25th IAHR International Symposium on Ice

PROCEEDINGS OF THE 25th INTERNATIONAL SYMPOSIUM ON ICE

Trondheim, Norway, 23rd – 25th November 2020

Editors
Knut Alfredsen, Knut Vilhelm Høyland, Wenjun Lu, Per Ludvig Bjerke, Leif Lia and Sveinung Løset.

International Association for Hydro-Environment Engineering and Research (IAHR)
ISSN 2414-6331
ISBN 978-82-7598-120-0

Table of contents

Front picture: Frazil ice in river Gaula,Norway (Photo: Knut Alfredsen)

Introduction

The IAHR symposium on ice is a biannual conference covering engineering and research on ice in fresh and salt water. The conference was first arranged in Reykjavik, Iceland in 1970. The 25th conference was planned for Trondheim, Norway in June of 2020, but due to the Covid19 pandemic it was arranged as a virtual conference in November of 2020. The conference gathered 105 participants and 87 papers were submitted and peer reviewed for the technical sessions of the conference. In addition, two plenary key note lectures were given covering the challenges of hydropower operation in the arctic and the history of ice research in Norway.

The technical sessions covered a range of topics within research on ice processes, utilisation of remote sensed data and engineering aspects related to ice jams, loads on structures and hydropower operation in fresh water and ships, floaters and fixed structures in coastal areas and on the ocean. All presentations and discussions were carried out live on a digital platform, and this fostered many interesting exchanges of information across countries and time zones.

The IAHR Ice Symposium were arranged by financial support from the Norwegian Research Council and the Norwegian University of Science and Technology. We gratefully acknowledge the support received to arrange the conference. The organising committee also wishes to thank the NTNU Centre for Continuing Education and Professional Development for support with the administration and technical arrangement. The transition from a traditional conference to a virtual meeting could not have been done without this support.

The organizing committee also want to thank the scientific committee for handling the peer review of the papers, the reviewers of the papers and not the least all authors and conference participants who made this event possible.

Knut Alfredsen
Chairman of the organizing committee.

Scientific and Organisation committee

Scientific committee

Arttu Polojärvi, Aalto University, Finland
Petteri Uotila, Helsinki University, Finland
Hayo Hendrikse, Delft University of Technology, Netherlands
Aleksander Milakovic, Hamburg University of Technology, Germany
Marina Karulina, Krylov State Research Centre, Russia
Tatiana Uvarova, Far Eastern Federal University, Russia
Tomasz Kolerski,Gdansk University of Technology, Polen
Zhi Jun Li, Dalan University of Technology, China
Steve Bruneau, Memorial University, Canada
Rocky Taylor, Memorial University, Canada
Paul Barette, National Research Council, Canada
Karl-Erich Lindenschmidt, Univ. Saskatchewan, Canada
Hayley Shen, Clarkson University, USA
Ian Knack, Clarkson University, USA
Adrian Law, Nanyang Technological University, Singapore
Akihisa Konno, Kogakuin University, Japan
Yuntong She, University of Alberta, Canada
Torbjørn Eltoft, University of Tromsø, Norway
Mats Granskog, Norwegian Polar Institute, Norway
Aleksey Marchenko, University Centre of Svalbard, Norway
Knut Høyland, NTNU, Norway
Raed Lubbad, NTNU, Norway
Wenjun Lu, NTNU, Norway
Morten Stickler, University of South-Eastern Norway, Norway
Sveinung Løset, NTNU, Norway
Bjørnar Sand, SINTEF Narvik, Norway

Organisation committee

Knut Alfredsen, NTNU
Knut Vilhelm Høyland, NTNU
Wenjun Lu, NTNU
Leif Lia, NTNU
Sveinung Løset, NTNU
Per Ludvig Bjerke, The Norwegian Water Resources and Energy Directorate.

List of papers

Keynote

Løset *Ice Research in Norway from an Engineering perspective*

1. Ice Mechanics

Barrette et al. *Beam testing of reinforced ice in the context of winter roads*
Barrette et al. *Plate testing of reinforced ice in the context of winter roads*
Frederking *Ice Behaviour under Indentation Loading - Medium-Scale Field Tests*
Gribanov et al. *Field investigation and numerical analysis of the deformation of L-shaped ice beams*
Høyland et al. *Ice properties in the updated ISO 19906*
Karulina et al. F*ield tests of ice compressive strength using thermally balanced samples*
Marchenko, A. et al. *Elastic moduli of sea ice and lake ice calculated from in-situ and laboratory experiments*
Marchenko, A. et al. *Influence of vibrations on indentation and compression strength of sea ice*
Murdza et al. *Results of preliminary cyclic loading laboratory experiments on natural lake and sea ice*
Polojärvi et al. *Scale effects in lattice-based modelling of ice sheets*
Pramanik et al. *The Adhesion of Fresh Water Ice to Concrete at Varying Pressure and Duration for Dry and Wet Conditions*
Visich et al. *Influence of water freezing in tidal cracks on the formation of ice stresses in coastal zone of the Arctic seas*

2. Sea Ice Remote sensing

Ansari et al. *Real-time classification of the sea ice interacting on a bridge pier using artificial intelligence techniques*
De Santi et al. *Grease-pancake sea ice thickness retrieval from SAR image wave spectra with the close-packing wave model*
De Silva et al*. Medium range sea ice prediction for Japanese research vessel IRAI's expedition cruise in 2019*
Gedikli et al. *On the ocean environment in the northern part of the Gulf of Bothnia leading ice induced vibrations*
Gerland et al. *Svalbard fjord sea ice environments as arenas for climate research, monitoring, remote sensing validation, and controlled process studies*
Khachatrian et al. *Unsupervised information selection in multimodal sea ice remote sensing*
Marchenko, N. *Marginal Ice Zone (MIZ) field investigation in the Western Barents Sea in April 2017-2019*
Pedersen et al. *Evaluating Human and Machine Performance on the Classification of Sea Ice Images*
Petrich et al. *A Note on Remote Temperature Measurements with DS18B20 Digital Sensors*
Turner et al. *Comparison of in-situ measurements from the Norströmsgrund lighthouse to Copernicus reanalysis products*
Wang et al. Physical Properties of Summer Arctic Sea ice during 2008–2018.
Yu et al. *Seasonal changes of sea ice condition along the Arctic Northeast Passage from 2010 to 2019*

3. Fixed offshore structures

Gagnon *Spallation-Based Numerical Simulations of Ice-Induced Vibration of Structures*
Hornnes et al. *Combined distribution of ice thickness and velocity based on local measurements at the Norströmsgrund lighthouse 2000-2003*
Shestov et al. *Scale-model ridges and interaction with fixed structures*
Stange et al. *Development of an experimental setup to investigate the impact of higher structural modes on dynamic ice-structure interaction*

4. Ships in ice

Huiling et al. *Research on Mechanism and Application of Ship Resonance Ice-Breaking*
Gagnon et al. *Numerical Simulations of Naval Vessel Collisions with Ice*
Karulina et al. *Evaluation of ship icebreaking capability based on a simple criterion*
Li et al. *Model-scale test of icebreaking pattern and comparison with state-of-the-art methods*

Sawamura et al. *Ramming distance of icebreaker "SHIRASE" during Antarctic voyage and numerical modeling of ship ramming in heavy ice conditions*
Zhaka et al. *Physical and mechanical properties of ice from a refrozen ship channel ice in Bay of Bothnia*

5. Floaters in ice

van den Berg et al. *Statistical analysis of the results from ice tank tests with broken ice*
Qu et al. *Mooring analysis of an ice resistant drilling semi in arctic region*
Zu et al. *Sheltering Effect in the Wake of a Ridge Keel in Uniform and Two-layer Flows*

6. Waves in ice

Boutin et al. *Impact of wave-induced sea ice fragmentation on sea ice dynamics in the MIZ*
Cheng et al. *Calibrating viscoelastic wave-in-ice models for different types of sea ice covers*
De Santi et al. *Modelling ocean gravity wave dispersion of young sea ice in the MIZ*
Kalisch et al. *Fully dispersive models for flexural-gravity waves*
Korobkin et al. *Vertical impact onto floating ice*
Li et al. *Signal processing techniques to estimate surface-wave parameters in laboratory studies of wave-ice interactions*
Løken et al. *A comparison of wave observations in the Arctic marginal ice zone with spectral models*
Marchenko, A. *Elasticity and viscosity of ice measured in the experiment on wave propagation below the ice in HSVA ice tank*
Ni Bao-Yu et al. *Numerical simulation of the interaction between the plane wave and the shore-connecting ice plate*
Rabault et al. *Development of open source instruments for in-situ measurements of waves in ice*
Shen et al. *Modeling new ice formation under the influence of ocean waves*
Sree et al. *An experimental study on surface wave propagation along segmented floating viscoelastic covers*
Sturova et al. *The response of semi-infinite ice sheet to a moving load*
Waseda et al. *Uncertainty in ocean wave estimate in the Arctic Ocean*
Zeng et al. *Theoretical model for predicting the breakup of ice covers due to wave ice interaction*
Zhang et al. *Theoretical model for predicting the breakup of ice covers due to wave ice interaction*

7. Oil and Pollution in ice

Goncharov et al. *Possibly approaches for under ice oil pollution detection*

8. Harbours and coastal challenges

Nesterov et al. *Thermal deformations of frozen clay caused by cyclic changes of temperature and thermal impacts*
O'Sadnick et al. *Ice Formation in Norwegian Fjords- Findings from the 2018 Field Season*
Ruud *Sufficient independence between barriers*

9. Icings

10. Icebergs

Marchenko, A. et al. *Monitoring of 3D motion of drifting iceberg with an ice tracker equipped with accelerometers*

11. Aufeis

12. River and Lake ice

Barrette *A review of laboratory studies on frazil ice*
Boyd et al. *Observations of Supercooling in Rivers*
Dai et al. *Analysis of factors affecting ice use in Harbin winter landscape*
Ghobrial et al. *Observations of anchor-ice in a Canadian river using photographic and acoustic devices*
Hashiba et al. *Study on the occurrence factors of anchor ice in observation of actual rivers*
Howley et al. *A Modeling Study of Complex River Ice Processes in an Urban River*

Inami et al. *Examination of the Applicability of a Model for Predicting Ice Sheet Thickness*
Kazemian et al. *Investigation of flow velocity in ice- covered channels*
Knack et al. *Two-Dimensional Modeling of Pier Type Ice Control Structures*
Koike et al. *Ice jam flood experiment using real ice around bridge piers*
Kolerski *Ice transport in rivers with training structures - the Odra River case study*
Turcotte *Will there be an ice bridge this winter? Predicting spatio-temporal freeze-up patterns along the Yukon River, Canada*
Vasiliev *Creation of Artificial Mountain Glaciers as a Way of Water Supply in Arid Regions of Central Asia*
Yabe et al. *Flow Discharge Estimation Method considering River and Crystal Ice Thickness, HQ Equation, and Measured Values during the Freezing Period*
Yokoyama et al. *Observation and simplified simulation of ice melting process in ice covered river*
Yoshikawa et al. *Simple ice jam simulation around bridge piers*

13. Ice actions on dams and bridges

Foss *Measurement of static ice loads on dams, with varied water level*
Hellgren et al. *Numerical studies of the thermal ice pressure along a concrete dam*
Petrich et al. *Static thermal ice loads on a dam in a small Norwegian reservoir*
Rødtang *Evaluating SAMS as a tool for predicting ice forces on river bridge piers in small steep rivers*
Seger et al. *Numerical analysis of ice loads on Taraldsvikfossen dam*
Sigtryggsdóttir *Riprap to resist wave and ice loads acting on the upstream slope of an embankment dam*

14. Environmental aspects of river ice

Alfredsen et al. *Modelling stranded river ice using LiDAR and drone-based models*
Lindenschmidt et al. *A novel fully-operational fully-automated real-time ice-jam flood forecasting system*
Lindenschmidt et al. *Parameter and process identification of a cold-region integrated catchment-river-lake water quality system*

15. Ice and hydropower

Hranfsdóttir *Design considerations for the ice skimming spillway on the new intake for Laxá Power Plant III – North Iceland*
Lia et al. *Reducing ice accumulation on Coanda Screen intakes*

16. Ice actions on morphology

Maznev et al. *Ice gouging conditions of the Northern Caspian depending on the severity of winters*

Keynote

25th IAHR International Symposium on Ice
Trondheim, November 23 to 25, 2020

Ice Research in Norway from an Engineering perspective

Sveinung Løset, Dr., Professor
Department of Civil and Environmental Engineering
Faculty of Engineering
Norwegian University of Science and Technology (NTNU), Trondheim
sveinung.loset @ntnu.no

Abstract

The current paper gives a historical review of research on ice in Norway from an engineering perspective, both covering ice in rivers and lakes, as well as ice in the ocean.

Pioneering work is mentioned for both categories. For river and lake ice formation Dr. Olaf Devik was a pioneer developing instrumentation that could measure supercooling of water in rivers and lakes. He was followed by Dr. Edvigs Kanavin and others. This part of the paper is followed by studies of atmospheric icing and sea spray icing. The rest of the paper has a focus on research related to ice in the ocean, both sea ice and glacial ice. Pioneering work on sea ice was done by meteorologist Torgny Vinje at the Norwegian Polar Institute. In the 1980ies the oil and gas industry active on the Norwegian Continental started to pay attention to the Barents Sea. The information for engineering purposes related to design and operation of offshore structures in these icy waters was quite limited. Thus several companies realized that a proper design database on ice in the ocean for these waters should be established. The first well documented sea ice and iceberg study in the Barents Sea became the multi-sensor ice data acquisition programme ICEBASE. This programme was led by Dr. Sveinung Løset and later followed by the programme IDAP. This first wave of studies was followed by more dedicated surveys after the millennium of which the centre for research-based innovation SAMCoT (*Sustainable Arctic Marine and Coastal Technology*) hosted by NTNU was the major one.

1. Ice in Rivers and Lakes – Pioneering Research

Hydropower has a long tradition in Norway. Hydropower regularly accounts for more than 95% of the total Norwegian power production, with a small remainder made up by thermal and, only recently, wind. At the end of 2020, Norway's inland waters powered 37 GW installed capacity, and a normal-year production of 151 TWh of clean power.

In the very beginning of hydropower production, more than 120 years ago, it was soon discovered that water regulation was needed and behind that there is a long technology development leading to this achievement ranging from hydrological studies of water catch and drainage to construction of water intakes and dams, and effects on river discharge. Most of the terrestrial areas in Norway are exposed to freezing during winter. Frequently that leads to formation of ice that may cause ice pressure on dams, flooding during winter and spring discharge, ice jamming, and loads from river ice on bridge pillars and other structures.

This caught the interest from the Norwegian physicist and meteorologist Olaf Devik, (1886–1987). He received his education from the University in Oslo, Dr. philos. He was a lecturer at the Norwegian Institute of Technology (NTH; Trondheim) from 1923 to 1932.

Figure 1. Physicist and meteorologist Olaf Devik, Dr. Philos (Photo, NVE).

Dr. Devik was a pioneer in studying river and lake ice physics applicable to engineering. The lake Aursunden at the head of the Glomma river was regulated in 1924 causing increased winter discharge that lead to more sever ice runs than before (Asvall, 1994). A better understanding of the physics and mechanics behind these phenomena was needed. A commission was appointed to investigate the cause of the increased ice problems. Here Devik was a central member and saw the need of doing fundamental studies of heat exchange at the water surface, i.e. cooling of river water including supercooling. Further, he studied formation of frazil ice, formation of bottom ice (anchor ice), description of ice runs and jamming.
He developed his own measurement technic to measured supercooling of water where he managed to capture a supercooling of -1.4°C at Festa, Oppdal around 1930.

Later on, the pioneering work of Devik was followed by Dr. Edvigs Kanavin. He was born in Latvia and became a leading hydrologist at the Norwegian Water and Resources Energy Directorate (NVE)'s history, founder and head of NVE's Ice Office from 1950 to 1973. His main topic was frazil ice formation and formation of ice in rivers in general. He did also study ice in rivers on Iceland.

Another person working with river ice was Dr. Einar Tesaker. He started out at NVE's Ice Office in Oslo, but moved to Trondheim after some years and started at the Watercourse and Harbour Laboratory (SINTEF/VHL). His research was focused on ice formation in steep rivers where anchoring ice could form causing water level rise leading to reduced water velocity and thereby ice formation.

More or less at the same time Dr. Torkild Carstens had returned from the USA where he had obtained a PhD degree from Berkeley, California. His supervisor there was professor Hans Albert Einstein, the son of Albert Einstein. Carstens started at (SINTEF/VHL) and worked in parallel with Tesaker mainly on problems related to ice and hydraulics in rivers and powerplants.

Another bauta in the sixties and later was Randi Pytte Asvall. She was a hydrologist and active at NVE's Ice Office from 1962 and on. Among different scientific and engineering activities she did a lot of snow balance studies on the glaciers Jostedalsbreen and Folgefonna.

Edvigs Kanavin Einar Tesaker Torkild Carstens Randi Pytte Asvall

Figure 2. Photos of major of pioneers in river and lake ice engineering, Norway.

2. Atmospheric Icing

Atmospheric icing on structures such as antennas, masts and power lines typically occurs when snow and sleet hit members of these structures. The ice accreted in this manner is porous and has normally a low mechanical strength. However, it may also form from super-cooled water droplets, with a temperature that can go down to –40°C (Makkonen, 1984), while the water is still liquid, freeze solid on contact with a cold surface. Super-cooled water droplets can exist in the form of frost smoke, super-cooled fog, freezing rain and drizzle.

In Norway electric power lines are built and run through any type of terrain, from the maritime coast to the continental inland. Such power lines in Norway are frequently exposed to atmospheric icing that may lead to galloping in wind and following breakdown. Figure 3 depicts such a situation. A leading person in Norway in this field has been Mr. Svein M. Fikke, meteorologist and consultant.

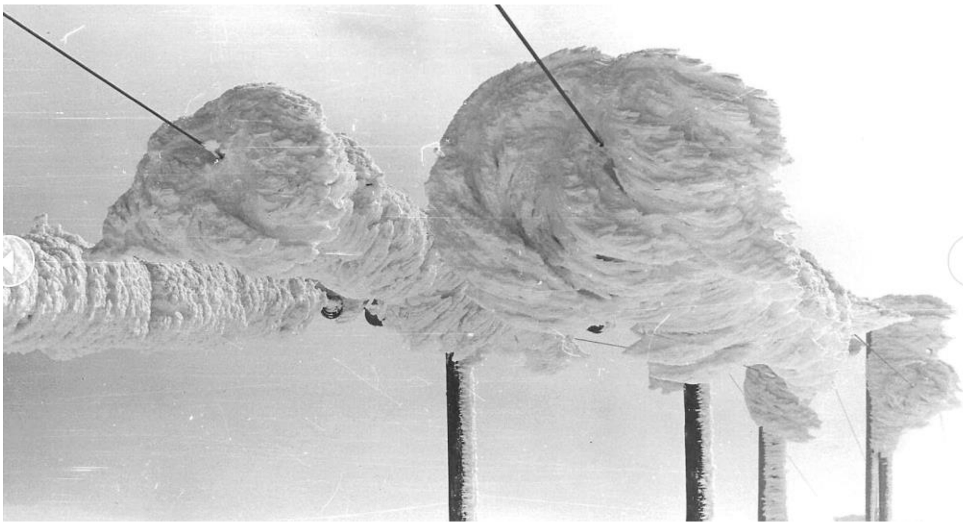

Figure 3. Rime icing on a 22 kV electric power line in Norway April 1961, 1 400 m above sea level. The ice load was measured to 305 kg/m (Photo: O. Wist).

3. Sea Spray Icing

Sea spray icing may occur at temperatures below freezing on ships and structures at sea. The ice accretion is 1) either caused by sea spray that is generated by a structure/ship that is piercing the sea surface and the interaction at the sea surface generates droplets that hit the structure and may freeze to it, or 2) when the wind blows droplets of water off the wave crest. The latter phenomena is called spume and depends on the form and steepness of the waves and wind speed.

There are two main scenarios of ice accretion in accordance with the factors limiting the growth rate. The first scenario is the "mass limited" (ML) scenario, in which the total water mass arriving on the cold surface can be frozen due to the cooling; the water mass is therefore the limiting factor for the accretion rate. The second scenario, the TL scenario, represents conditions when the water impingement on the surface is high and the heat fluxes are insufficient to freeze all of the water; as a result, some of the water runoff representing "wet" icing conditions.

The first really study of icing offshore in Norway was the research programme "Offshore Icing", 1982-85 (SINTEF/NHL). The programme was financed by Operator Committee North (OKN), a cluster of oil/gas companies active on the Norwegian Continental Shelf. Measurements of sea spray were performed on several structures offshore, a numerical model established and an outdoor wind tunnel with sea water spray injection constructed in Trondheim. Instrumental in these efforts were Dr. Torkild Carstens and Mr. Tore S. Jørgensen. The physical measurements both offshore and in the icing tunnel were used for calibration of a numerical icing prediction model.

There are several examples of icing on vessels in the Barents Sea. However, there is probably just one that is documented properly, the voyage I had with K/V Nordkapp from Tromsø to Bjørnøya 25-26 February 1987. About 110 tons of sea spray ice accreted on this vessel in a period of 17 hours during storm and air temperatures of -15°C. The estimation of the accreted ice mass was enabled by reading of the ballast water in addition to volumetric measurements of accreted ice.

Figure 4 depicts the effect of obstacles on the ice accretion. Ice accumulates more easily when it can adhere to non-plane objects. Stiffeners and horizontal surfaces act as anchors for the ice and huge accumulations may result. In this case ice accreted on the railing to a thickness of 1 m. The relatively high porosity of the accreted ice led to a density of about 600 kg/m^3.

Figure 4. Ice accretion on the foreship/lifeboat of K/V Nordkapp, 27th February 1987. (Løset et al., 2006).

In the latest decade, numerical simulations combined with field experiments, see Figure 5, performed at Spitsbergen have increased the understanding of the processes behind sea spray icing (Kulyakhtin, 2014).

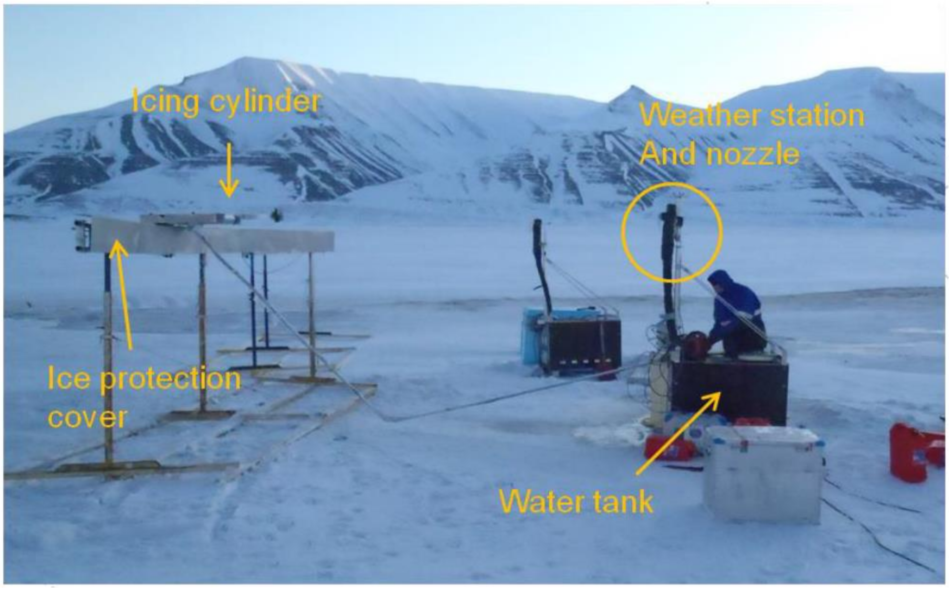

Figure 5. Physical simulation of sea spray icing in Adventsdalen, Spitsbergen (Kulyakhtin, 2014).

4. Ice in the Ocean

4.1 Sea ice

Learnings from sailings in the Arctic more than 100 years ago gave a practical understanding of the movement and behavior of sea ice under stress from wind and current. This is related to sailing voyages for sealing and hunting, but also commercial trading with Russians at the Siberian Coast. Then we had the voyages of Dr. Fridtjof Nansen, in particular the one with *Fram* towards the North Pole from 1893 to 1896. During this voyage he combined oceanographical and meteorological studies with observations of drift and deformation of sea ice. He experienced a lot of ridge building at *Fram* and how the hull shape prevented them from being screwed down by the ice.

Figure 6. Photo of Torgny Vinje (polarhistorie.no).

In more recent history I want to highlight Mr. Torgny Vinje (1929-2015, Figure 6). He obtained a cand. real degree in 1956 in meteorology from the University in Oslo. Soon after he travelled to Antarctica and overwintered there for three seasons at the Norway Station, Dronning Mauds Land. From 1964 he had almost annual surveys in the Arctic where he mainly studied sea ice drift, composition of ice fields and ice morphology. He was also a pioneer in using Upward Looking Sonars to detect ice ridges, both in the Western Barents Sea and the Fram Strait.

With respect to assessment of loads from ice on structures offshore and operations in ice, the type of ice (first-year or multiyear ice), its frequency of occurrence, thickness and drift velocity is of importance.

In the 1980ies the oil and gas industry active on the Norwegian Continental started to pay attention to the Barents Sea. The information for engineering purposes related to design and operation of offshore structures in these icy waters was quite limited. Thus the companies realized that a proper design database on ice in the ocean for these waters did not exist, and the first well documented sea ice and iceberg study in the Barents Sea became the multi-sensor ice data acquisition programme ICEBASE (Sea Ice Investigations in the Barents Sea) established in 1987. The research programme was funded by BP Norway, Esso Norway and Mobil Exploration Norway. ICEBASE was executed during the mid-winter and fall campaigns of 1987 (Løset and Carstens, 1996). The programme was led by Dr. Sveinung Løset (SINTEF/NHL, Figure 7).

The main purpose of the research programme was to obtain comprehensive information about sea ice and icebergs in the western Barents Sea. The specific elements of the mapping were satellite imaginary, precision stereo aerial photography, airborne synthetic aperture radar (SAR), helicopter-borne impulse radar and three ground truthing field campaigns. Field Survey 1 employed the Norwegian Coast Guard vessel K/V "Nordkapp" from 24th February to 10th March 1987, a second field survey (late March to early April 1987) used aircrafts and helicopters as platform from Longyearbyen Airport on Spitsbergen. Finally, Ship Survey 2, with the Norwegian Coast Guard vessel K/V "Senja", was conducted in the period 13th October to 25 October 1987.

Figure 7. Dr. Sveinung Løset in front of a huge pressure ridge in the Central Barents Sea. The top of the helideck of the expedition vessel is seen in the upper right part of the picture.

4.2 Glacial Ice

The programme of 1987 was the only viable source of much-needed data and was also seen as a model for future investigations in the Barents Sea. Thus, it was important to compare the various observation methods, both their field performance, data catch and the overlapping output.

The different campaigns of ICEBASE aimed at mapping the population and characteristics of icebergs, and sightings were made as indicated in Figure 8. In total the programme observed 180 icebergs, of which 105 were made from stereo photos made by a fixed wing aircraft. All pictures taken from the aircraft were stereographic with 60 % overlap. The advantage of the stereo photos is the high resolution (in the order of 0.1 m) and that it yields vertical dimensions. The stereo photos were acquired at two different scales, 1:2000 and 1:6000. The total areal coverage of these photos, excluding overlaps, was about 160 km^2.

The stereo technique was used to obtain above water volume, maximum sail height, maximum length, and other geometric parameters of 52 icebergs (43 in the 1:2000 scale photos and 9 in the 1:6000 scale photos). Of these icebergs, 37 were located in Storfjorden, 14 icebergs around the northern tip of Hopen Island. A significant sighting of ICEBASE was a tabular iceberg in position 78°34'N 26°32'E, just south of Svenskøya. The estimated mass was 6.35 million tonnes with a maximum length of 499 m and width of 253 m.

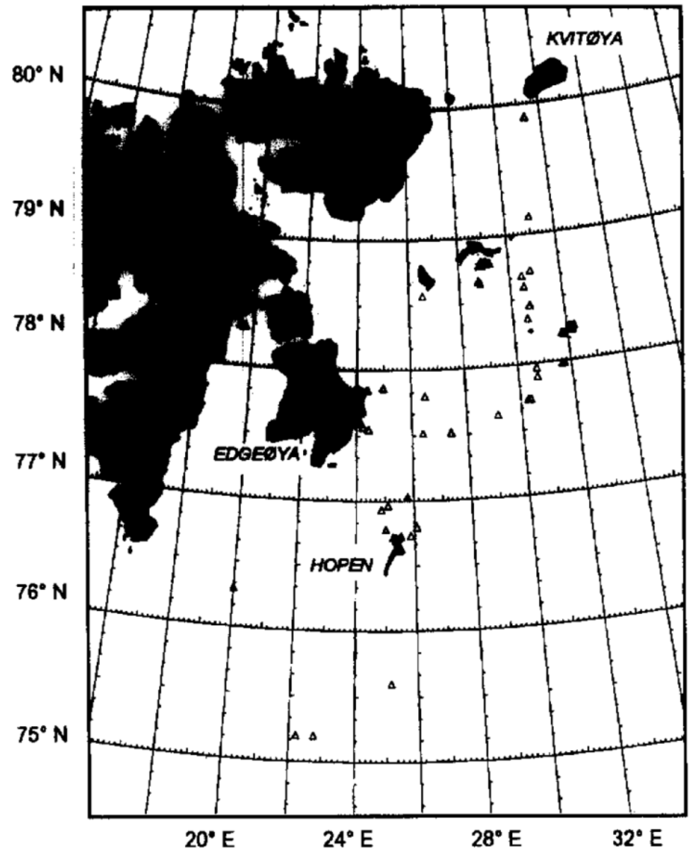

Figure 8. Location of iceberg sightings made of ICEBASE (Løset and Carstens, 1996).

The estimation of iceberg mass from the 52 digitized iceberg pictures gave an average total mass of 847 000 tonnes. The total number of icebergs observed was 180, overlaps excluded.

ICEBASE became a model for its successor IDAP ("Ice Data Acquisition Program") conducted by OKN ("Operator Committee North of 62°N") through the years 1988-1992 (Spring, 1994).

5. The Research Centre SAMCoT

The centre for research-based innovation (CRI) SAMCoT (*Sustainable Arctic Marine and Coastal Technology*) was established at NTNU in 2011 and run to the end of 2019. It was a long term funding with the Research Council of Norway (RCN) as the main sponsor. All together SAMCoT had 23 partners (8 research partners, 13 industry partners and 2 public). From the very beginning the vision of the research programme was to be a leading national and international centre for the development of robust technology needed by the industry operating in the Arctic region.

The aim of SAMCoT was to provide necessary research based knowledge as required by the industry to develop Arctic technology for the energy sector in particular and for society as a whole. In this way SAMCoT addressed the implications of the presence of ice and permafrost, and produce knowledge to ensure sustainable and safe exploration, exploitation and transport from and within the vulnerable Arctic region. SAMCoT became also the basis for the development of environmentally adapted coastal infrastructure (Kuiper and Løset, 2015).

The research strategy of SAMCoT is very much reflected in Figure 9. From a hypothesis or theory we search to understand the engineering problem by studying the phenomena at full- or lab scale.

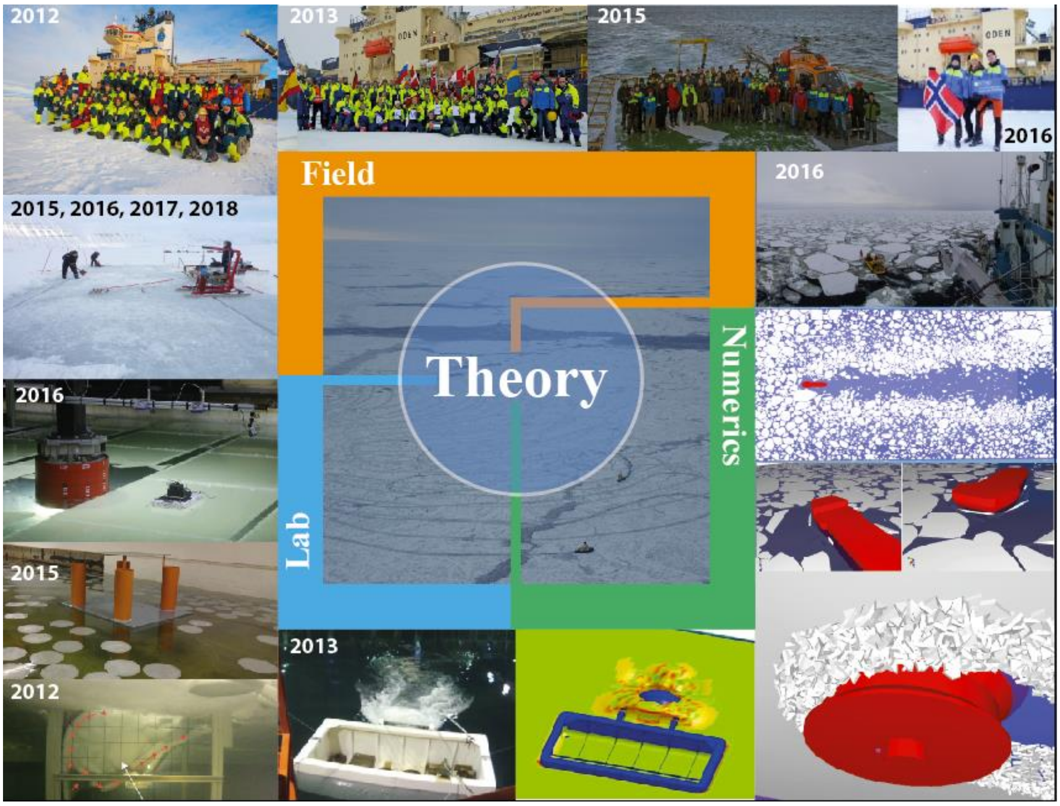

Figure 9. The research approach of SAMCoT.

From these learnings theoretical approaches and numerical models were developed, calibrated and applied to the best for the society.

In 2012, NTNU and the Swedish Polar Research Secretariat (SPRS) established a collaboration in polar research. A manifestation of the collaboration between NTNU and SPRS included a series of Arctic research cruises. In each of the autumns in 2012 and 2013 a research cruise with the Swedish icebreaker Oden was performed to the waters off the East Coast of Greenland (Oden Arctic Technology Research Cruise 2012 - OATRC2012 and OATRC2013). See the upper-left corner in Figure 9. The surveys were fully funded by Equinor.

In the autumn of 2015, NTNU and SPRS performed a third research cruise named the OATRC2015, which involved the two Swedish icebreakers, Oden and Frej, in the international waters north of Spitsbergen. The survey was fully funded by ExxonMobil. The major purpose of the latter research cruise was to establish procedures for efficient ice management (IM). The IM operations are characterised by breaking the incoming ice features by one or several icebreakers, such that the downstream offshore structures are protected from dangerous ice features.

A very important part of the efforts at SAMCoT has been contributions to relevant education of MSc and PhD students. By linking the education to field/lab attendance and working with real data, the students got first-hand knowledge of some of the challenges and solutions in e.g. an offshore field development. SAMCoT has delivered more than 30 PhDs and published more than 450 international papers.

Development of numerical models had a strong position at SAMCoT. Three prominent software packages have been developed and matured after the SAMCoT years:

- Simulator for Arctic Marine Structures (SAMS); a simulator for design and operation of floating structures and ships for ice-infested waters (NTNU spin-off company ArcISo - Arctic Integrated Solutions).

- Software for assessment of ice-induced vibrations caused by ice actions on fixed offshore wind turbines.

- Theory for frost heave and thawing settlement implement in the software package “Plaxis”.

6. Remarks

Cold climate research in Norway in the years after the 1920ies increased the understanding related to physical processes involving ice in rivers and lakes. Dr. Olaf Devik was leading the way and became a bauta in this area with theoretical work also applicable to engineering.

In the 1980ies a new era started with the aim of establishing data bases on the physical environment in the Barents Sea – in particular for sea ice and glacial ice in the ocean. In some way this culminated lately by the emphasis of SAMCoT providing research based knowledge as required by the industry to develop Arctic technology for the energy sector in particular and for society as a whole.

References

Asvall, R.P., 1994. River ice investigations in Norwegian Watercourses – A Review. Proc. 12th IAHR Symposium on Ice, Trondheim, Norway, pp. 1-10.

Devik, O., 1931. Thermische und Dynamische Bedingungen der Eisbildung in Wasserlaufen auf Norwegische Verhalniss Angewandt. *Geofysiske Publikasjoner*, Vol. IX. No. 1, Utgitt av det Norske Videnskaps-Akademi i Oslo, 1931, 100 p.

Kulyakhtin, A., 2014. Numerical Modelling and Experiments on Sea Spray Icing. Doctoral theses at NTNU, 2014: 338, 203 p.

Kuiper, G. and Løset, S., 2015. SAMCoT: Leveraging cross sector collaboration to drive sustainable energy developments in the Arctic. ATC Copenhagen, March 2015, OTC 25494.

Løset, S. and Carstens, T., 1996. Sea ice and iceberg observations in the western Barents Sea in 1987. *Cold Regions Science and Technology,* 24**,** pp. 323-340.

Løset, S., 1993. Thermal energy conservation in icebergs and tracking by temperature. *Journal of Geophysical Research: Oceans,* 98**,** 10001-10012.

Løset, S., Shkhinek, K., Gudmestad, O.T., Høyland, K., 2006. Actions from Ice on Arctic Offshore and Coastal Structures, Krasnodar, St Petersburg, Russia, 271 p.

Makkonen, L., 1984. Atmospheric Icing on Sea Structures, U.S. Army CRREL report, April 1984.

Spring, W., 1994. Ice Data Acquisition – Summary Report. Mobil Research Dev. Corp., Dallas E&P Eng., 90 p.

01
Ice mechanics

25th IAHR International Symposium on Ice
Trondheim, 23 – 25 November, 2020

Beam testing of reinforced ice in the context of winter roads

Paul D. Barrette
Ocean, Coastal and River Engineering (OCRE)
National Research Council (NRC), Ottawa, ON, Canada
paul.barrette@nrc-cnrc.gc.ca

Bradley Butt
Ocean, Coastal and River Engineering (OCRE)
National Research Council (NRC), St. John's, NL, Canada
bradley.butt@nrc-cnrc.gc.ca

A laboratory study was conducted to provide additional information on ice reinforcement and its field implementation to strengthen segments of floating ice (referred to as ice bridges, ice crossings or ice roads) that are commonly weak links in a winter road operation. In addition to preventing breakthroughs, this option would increase the predictability of the ice's bearing capacity. Four-point beam bending tests were conducted on freshwater ice with and without reinforcement, for comparison purposes. A steel mesh, a polypropylene geogrid and threaded steel rods were used as reinforcement material. In all tests, the load and the loading rate increased with time up to a peak load. For the non-reinforced ice, there was a sudden drop in load at which point the tests ended. For the reinforced ice, a drop in load also followed the peak load, but the load climbed again up to another peak in a repetitive fashion. The ice reinforced with the threaded rods had the highest resistance (exceeding the load cell capacity). Thin section observations showed that the crystal structure was forming around the material. However, cleavage surfaces along the ice/material interface after beam failure indicate that the interface could be a strength reduction factor.

1. Introduction

Most engineering materials used today (e.g. steel, metals and alloys, ceramics, concrete, asphalt) are 'human-made' and, consequently, their properties are relatively homogeneous. This makes their mechanical behavior predictable. In the context of a floating ice cover (ice bridges/roads/crossings), which are common components within a winter road infrastructure, ice is also considered an engineering material. But it is produced and controlled by nature, which does not promote uniformity or consistency. For instance, ice covers are typically made from layers of different densities and do not have a constant thickness across them. They also have an extensive, random network of internal cracks. Moreover, ice growth, natural or via artificial flooding and/or spray icing is only possible if the air temperature is low enough. At times, it is not.

Incorporating an engineered material – an adequate geogrid, geotextile, geogrid, or any other types of reinforcement - into ice is not a new concept. It has been investigated in the past century, including in the early 1940's, with the unlikely proposal to construct a floating anti-submarine base out of ice and wood pulp – the Habbakuk project (Gold, 2004, Charlebois et al., 2019). Since then, a variety of reinforcing materials have been incorporated in ice to improve its ability to support a vertical load (e.g. Michel et al., 1974, Ohstrom and DenHartog, 1976, Haynes et al., 1992) – a summary of that work is presented elsewhere (Charlebois and Barrette, 2019).

2. Purpose

This paper presents the outcome of a recent experimental program aimed at providing additional information on the response of reinforced ice beams subjected to a flexural load (Figure 1). More specifically, it was to investigate the effect of different reinforcement materials. It was also to see if and how they were incorporated into the ice, thereby addressing the question: to what extent can reinforcement weaken the ice, for instance, by introducing a plane of weakness. More information is provided elsewhere (Barrette, 2020).

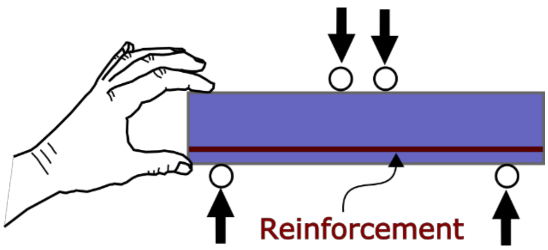

Figure 1: Four-point flexural test to assess the response of reinforced ice.

3. Rationale for beam testing

Ice cover response to a vertical load induces a flexural regime that induces a tensile stress along the bottom surface of the ice cover, leading to initial cracking. This may be followed by the formation of radial and circumferential crack networks and, eventually, breakthrough (e.g. Gold, 1971, CRREL, 2006). Given the scale difference and its two-dimensional nature, beam testing cannot hope to simulate the behavior of a real scenario. However, it can provide qualitative information on the initial ice response, and afford insights on the difference between reinforced and non-reinforced ice. In this paper, the term 'resilience' designates the ice's endurance in achieving full breakthrough, which contrasts with 'resistance' to initial cracking.

4. Reinforcement

An overview of investigations on previous ice reinforcement material, and of the factors playing a role in the selection of a candidate material, is presented (Charlebois and Barrette, 2019). On that basis, three materials were chosen for testing:

- Tensar's biaxial Type 2 geogrid, a polypropylene geogrid by Tensar International (Figure 2)
- Stratagrid SG 150, a steel mesh by Strata Systems (Figure 3)
- Standard off-the-shelf ¼ in. (6 mm) threaded rods (Figure 4)

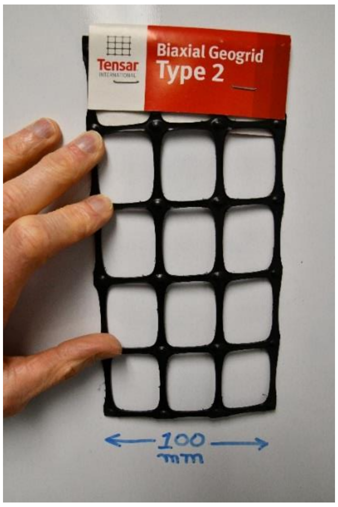

Figure 2: Sample of Tensar's polypropylene geogrid.

Figure 3: Sample of Stratagrid steel mesh.

Figure 4: A 6 mm diameter threaded rod.

5. Procedures

All test were done using the cold room facilities of the National Research Council, in St. John's, Canada. Tap water was used for the production of the test specimens. The ice was grown in a basin 1600 mm in length, 600 mm in width and 520 mm in depth (Figure 5 is a schematic diagram). The beams' target width and thickness was set at 75 mm and 60 mm, respectively (Figure 6 and Figure 7). The test set-up is shown in Figure 8. All tests were done at an ice temperature of -5°C. Displacement rate was from 0.1 to 9 mm per second. Output from the load cell and from a displacement transducer (string potentiometer) was recorded at an interval of 0.002 seconds (500 Hz). In the foregoing, tests without reinforcement and with reinforcement are referred to as the *N-series* and *R-series*, respectively.

6. Beam response

Load traces plotted against time

In Figure 9, all the load traces are plotted as a function of time. The following observations can be made:

- In all cases, the load increases with time up to a peak load.
- For the N-series tests, only one peak is observed in most cases, at which point there is a sudden drop in load as the test ends.
- For the R-series tests, a drop in load also follows the first peak load, but the load climbs again up to another peak in a repetitive fashion, so as to produce a saw tooth pattern, to a significant amount of time.

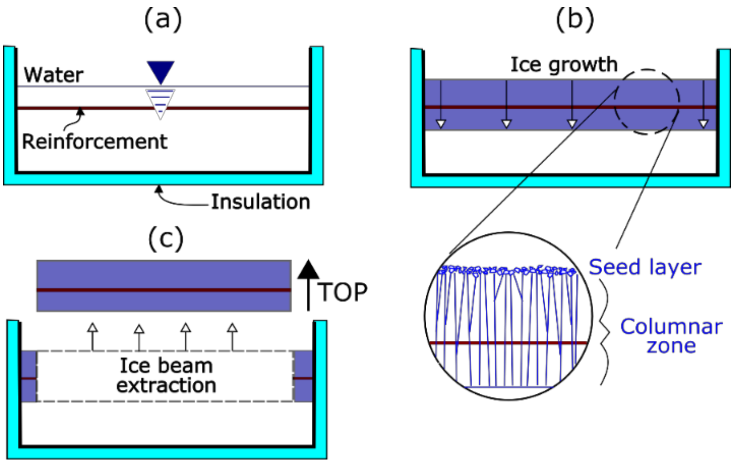

Figure 5: Ice growth (with reinforcement in this illustration): a) The reinforcement is set at the desired depth; b) Downward growth of columnar-grained ice; c) Beam extraction.

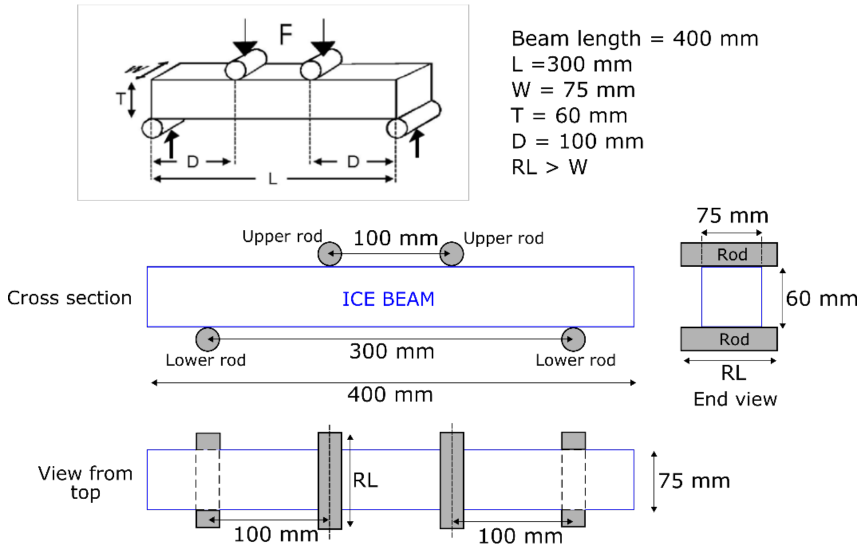

Figure 6: Beam testing configuration and target beam size. L: Beam length; W: Beam width; T: Beam thickness; D: Distance between upper and lower support; RL: Rod length.

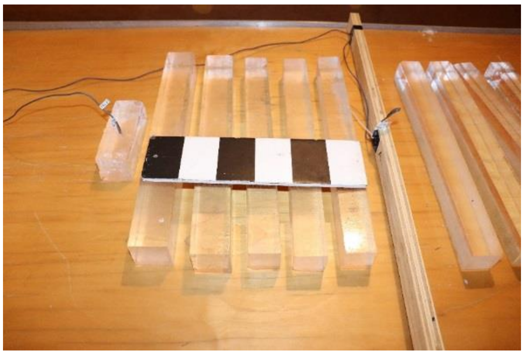

Figure 7: Beams machined to final dimensions, ready for testing. Scale partitions are 50 mm in width. Note on the left side, a dummy ice specimen with a temperature probe in it, to monitor ice temperature.

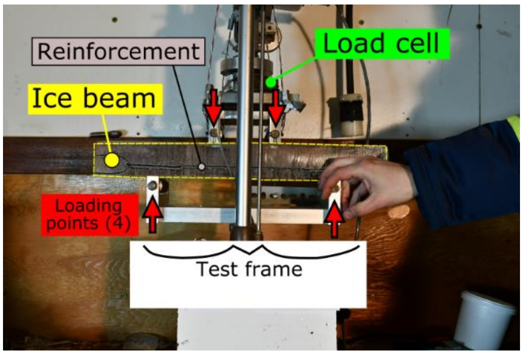

Figure 8: The test frame about to apply the load on the ice beams (at the four points – the red arrows).

- The N-series peak loads are relatively consistent, with one exception, where a test required 2 seconds to break, twice as much as the others, and incorporated two small load drops beforehand. A careful look at the video sequence suggests this could be due to local crushing at the load application points. The maximum load for that test is consistent with the others'.
- In the R-series, deformation up to the first peak load is similar to that of the N-series.
- The steel mesh material shows comparable initial loads but afterward, the beams did not carry as much load as those reinforced with the other materials. They show an initial peak load that is higher than the later peak loads.
- The two R-series tests with a threaded rod as reinforcement showed the highest resistance, but we are not able to appreciate the load response, since it exceeded load cell capacity.

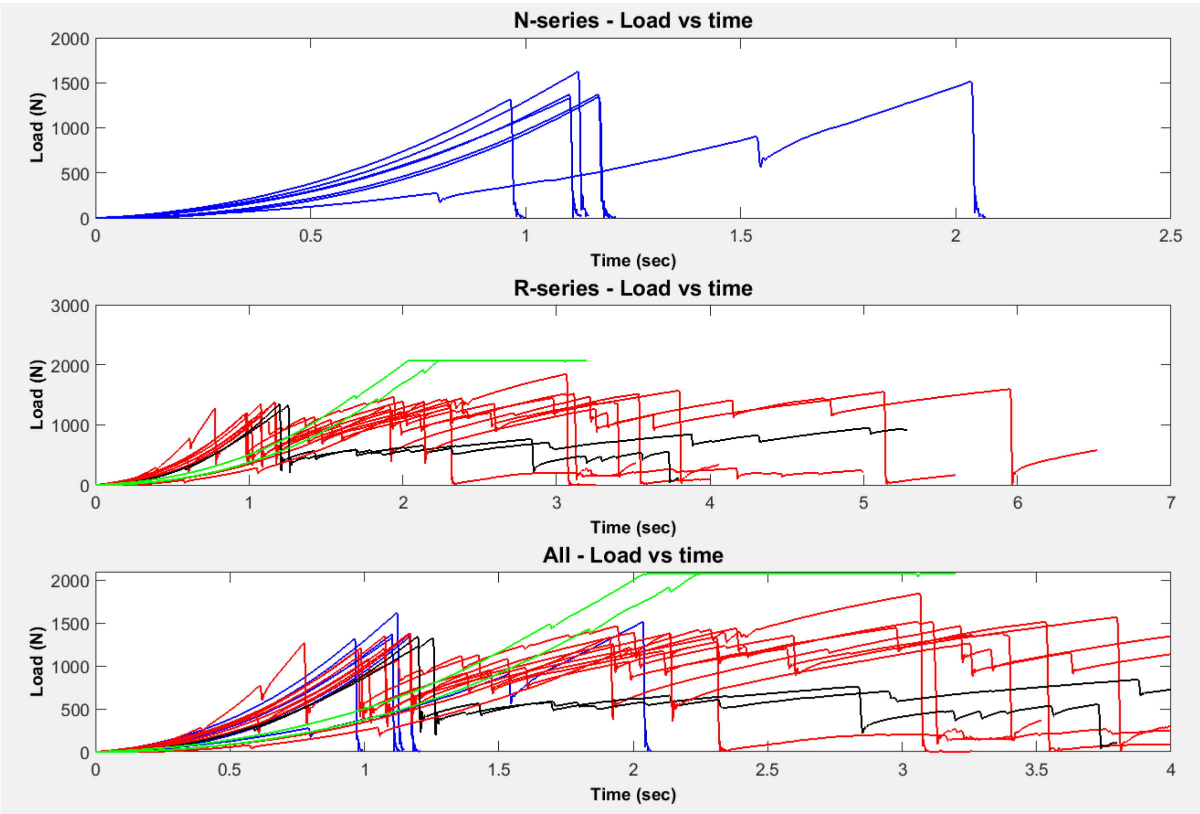

Figure 9: Load traces as a function of time for all tests – note the difference in time scale between the three plots. Blue traces are N-series. Red traces are R-series with the propylene reinforcement; black traces are with the steel mesh material; green traces are with the threaded rods.

Test parameters

Several test parameters were of interest: maximum load, total test time to maximum load, displacement to failure, strength and work. The maximum load was the maximum recorded load value. The strength was obtained with the standard formula for a flexural loading regime:

$$\sigma_f = \frac{3FD}{WT^2} \quad \textbf{[1]}$$

where

- σ_f is the flexural strength
- F is the applied load

- D, W and T are explained in Figure 6

For the N-series, this formula provides a strength estimate. For the R-series, the load used in the formula is the maximum, which is reached later in the deformation. It provides a nominal value, for comparison purposes between tests.

Work is a measure of the energy stored in the system, namely in the ice and in the way it accommodates that energy, mainly in the form of elastic distortion and the creation of free surfaces (cracks). Work is determined from

$$W = Fx \quad \textbf{[2]}$$

where x is the distance traveled by the indentor while it is in contact with the beam's surface. The unit for W is newton-meter, or joule. This equation is for a scenario where the load is constant. In our tests, however, the load is not constant but varies with displacement. Computationally, i.e. using the output of the data acquisition system, this can be dealt with by determining each work increment, and performing a summation of all:

$$W \sim \sum_{i=0}^{n} F(x_i^*)\,\Delta x \quad \textbf{[3]}$$

where Δx is the displacement increment between each reading, $F(x_i^*)$ is the load at each increment, from the point of contact ($i = 0$) to when the load vanishes ($i = n$). That equation allows addressing scenarios in which F is not necessarily constant, i.e. it can vary during the loading event, which is the case of the testing described in this report. It is the basis for the strain-energy criterion (Beltaos, 1978, 2001), stated as follows:

$$W = \int_S^B F(x)\,dx \quad \textbf{[4]}$$

Hence, W is the area under a load-time plot. In the above equation, it is determined between S, the time of load application, and B, the time when the load vanishes. The strain-energy criterion is very helpful in quantifying the effectiveness of the reinforcement in being able to resist ultimate failure, i.e. ice cover breakthrough.

Effects of displacement rate

A summary of test outcome is shown in Figure 10. Maximum load is the highest value in the force-time plot. Total test time is that required by the specimen to break (the load either vanishes or becomes negligible). Total displacement is that achieved at beam breakage. Strength and work are discussed above. The following two main observations may be drawn from that figure:

- For the non-reinforced ice, no particular trend is observed, i.e. the displacement rate does not appear to affect the other test parameters, at least within the range of displacement rates used in this test series.
- For the reinforced ice, the plots suggest a slight increase in displacement rate associated with an increase in all other parameters. Although the evidence is not strong, i.e. due to the data scatter, it is fairly consistent. This trend could have been more obvious had we used a wider range of displacement rates.

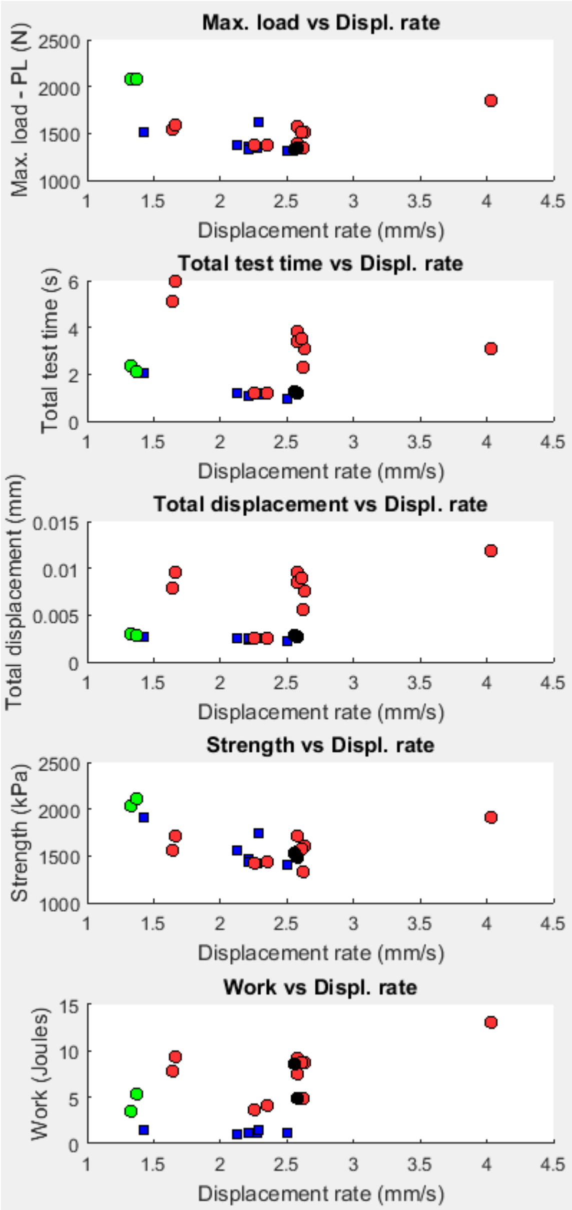

Figure 10: The various parameters plotted against displacement rate. Blue squares are N-series; red circles are propylene-reinforced; black circles are steel mesh-reinforced; green circles are the threaded rods.

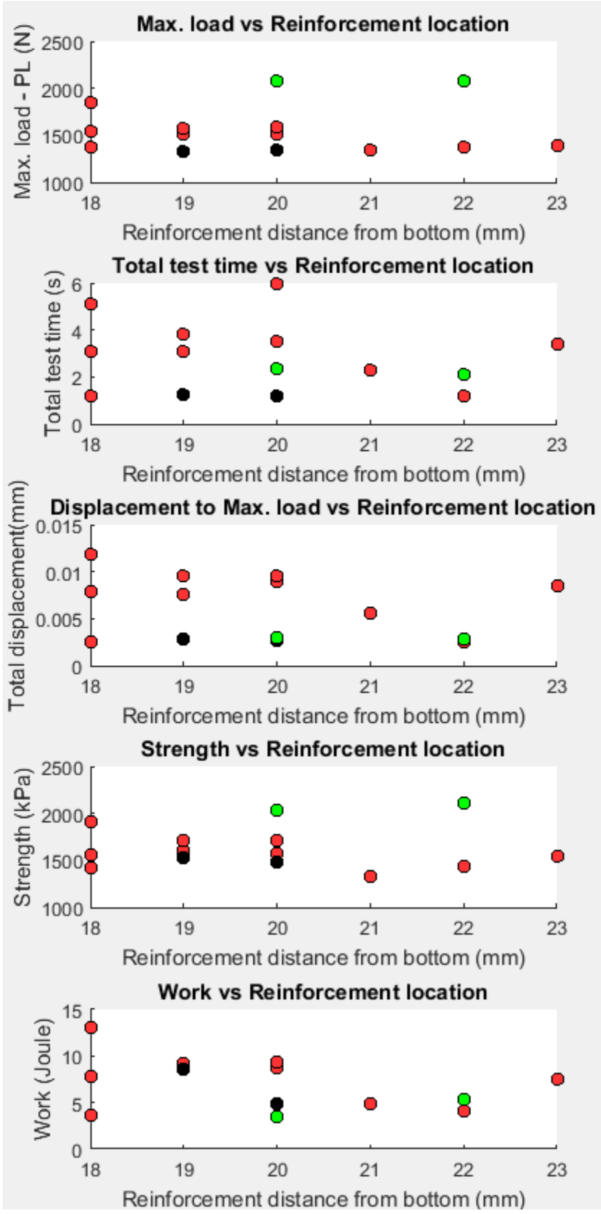

Figure 11: The various parameters (for R-series only) plotted the distance between the reinforcement and the bottom surface of the beam. Symbols are the same as in Figure 10.

Effects of reinforcement location in the beam

In Figure 11, a weak trend may be noticed: the further away the reinforcement is from the bottom surface, the lower the value is for the parameters on the y axis. This is to be expected – tension is maximal along the beam's lower surface. The closer the reinforcement is to that surface, the more effective it is at absorbing the energy associated with the loading event.

7. How does the ice incorporate the reinforcement material during growth?

Ice is notorious for not accepting anything inside its crystal structure. This is why the air contained in water does not get incorporated inside the crystal lattice, and instead occurs in the form of air bubbles. Although the incorporation of a geogrid into the ice is a different scenario altogether, it is an important question because in a flexural loading regime, shear action is expected to occur. Hence, if the presence of the ice-geogrid interface creates a weakness plane, this could conceivably defeat the purpose, at least to some extent, of ice reinforcement.

Figure 12 provides evidence that the crystal structure grew around the reinforcement material. Figure 13 documents the production of cleavage surfaces during testing, whose existence could be due to a preferred accumulation of air entrapment. In that case, any new interface (such as that between the reinforcement material and the ice) would likely promote sliding along it. This is what appears to have happened, as shown by the cleavage cracks in Figure 13.

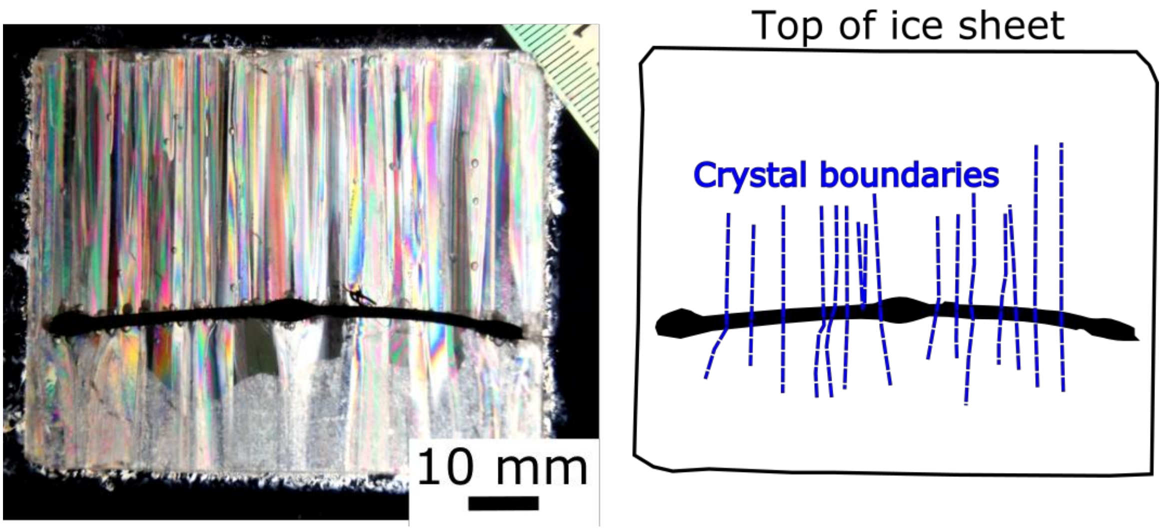

Figure 12: Left) Thin section in cross-polarized light across the thickness of the ice sheet grown in the laboratory, with the enclosed Tensar geogrid. Right) Outline of crystal boundaries and geogrid. Note how the crystal are able to grow through the geogrid, i.e. the geogrid does not promote a discontinuity.

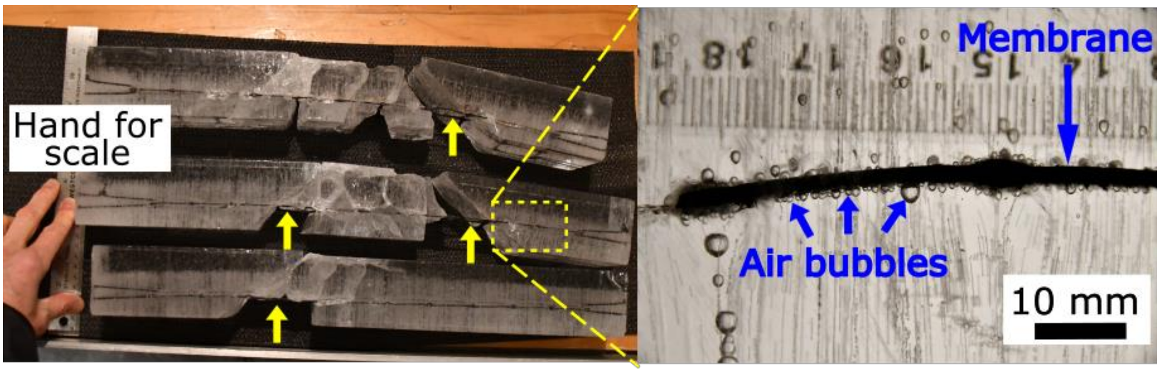

Figure 13: Left) Three polypropylene-reinforced beams after breakage pointing to a cleavage surfaces (arrows). Right) Close-up (in thin section under plain light) of the interface between the geogrid and the ice. Note the presence of air bubbles – these could be responsible for the cleavage.

Observations of the interface between the threaded rods and the ice were not obtained. From video observations, it could be seen that significant cracking initiated at the rod-ice interface. It is not known how much that could have played a role in making that material more effective (than the others) in strengthening the ice. If it did, however, it would have mobilized the elastic modulus of the metal, which is considerably higher than that of the ice. Without further evidence, that remains an assumption.

8. Significance for an ice crossing

In the context of a floating ice cover that is used for surface transportation, two concepts were retained for the purpose of these investigations: first crack and breakthrough. The above observations allow some preliminary appreciation of these concepts.

Resistance to first crack

When estimating the required ice thickness for a given ice crossing, first crack governs design. This concept is not new (Gold, 1967, Sinha, 1982, CRREL, 2006, Fransson, 2009). From an operational perspective, the consequence can be a 'wet crack', one that cuts across the ice full ice thickness, leading to local flooding of the ice cover (e.g. Government of the NWT, 2015). When and where this happens, traffic is no longer allowed, until the damage is repaired or an alternative routing is made available. If the reinforcement is stiffer than the ice, and well bonded to it, it can conceivably increase resistance to first crack. This would happen if its strength is mobilized as it absorbs the tensile stress at the bottom of the ice cover during vertical loading.

In the work reported herein, if the first peak load is assumed to represent first crack, the mesh and the geogrid have not achieved that purpose. This is indicated by the fact that they led to initial 'peak' loads that were not higher than those recorded by the un-reinforced ice. The threaded rods, however, appear to have been effective in raising that resistance. Although we are unable to further appreciate its performance in the beams, this speaks to the relevance of using a reinforcement material that is stiffer than the ice. Note that the cross-sectional area occupied by the rods is about 0.6% (i.e. the area of the rods divided by beam cross-section), which is relatively high from a field deployment scenario.

Resilience to breakthrough

Risks of vehicles breaking through an ice cover is a day-to-day concern for winter road operators. A breakthrough follows up on the rapid development of crack networks, until vertical support either vanishes or becomes too low to keep the load from sinking into the ice cover and the water below it. Beam testing is not meant to simulate these complex, three-dimensional scenarios. However, it can allow some insights on the difference between the response of un-reinforced and reinforced floating ice covers.

The mesh and the geogrid allowed the loading episode to extend to a significant amount of time. During that time interval, the energy was absorbed by the reinforced ice, which underwent considerable cracking activity before the load vanished. This is what is meant by 'resilience'. The beam tests reported herein provide an indication that this could be how a reinforced ice cover would respond. Moreover, assuming the strength of this reinforcement is sufficient to withstand the weight of the vehicle, it could conceivably prevent breakthrough.

9. Conclusion

The following statements can be derived from the foregoing:

- The polypropylene geogrid and the steel mesh did not increase the maximum peak load of the ice beams, but the threaded rods did.
- Reinforced beams absorbed considerably more energy from the loading event than did the non-reinforced ice.
- Reinforcement materials promote the development of air enclosures at their interface with the ice. This causes a cleavage to form at that interface – this may play a role in weakening the ice.

A tentative link is made between 1) the peak load in a beam test and the resistance to first cracks in an ice cover, and 2) the ability of an ice beam to absorb the energy delivered by the load and resilience to breakthrough of an ice cover. The relevance of these relationship to a three-dimensional scenario is dealt with in a companion paper.

Acknowledgments
The work reported herein is part of a project that was financed by Transport Canada's Northern Transportation Adaptation Initiative (NTAI) Program, the First Nation Adapt Program of Crown Indigenous Relations and Northern Affairs Canada (CIRNAC) and the Arctic Program of the National Research Council of Canada. Comments from R. Frederking were very helpful. Appreciation is extended to two anonymous reviewers.

References
Barrette, P., 2020. *Reinforcement of ice covers for transportation: Beam and preliminary plate testing*. NRC-OCRE-2019-TR-034. National Research Council. Ottawa.

Beltaos, S., 1978. *A strain energy criterion for failure of floating ice sheets*. Canadian Journal of Civil Engineering, 5, p. 352-361.

Beltaos, S., 2001. *Bearing capacity of floating ice covers: Theory versus fact*, 11th Workshop on the Hydraulics of Ice Covered Rivers. Committee on River Ice Processes and the Environment (CRIPE), Ottawa, Canada.

Charlebois, L. and Barrette, P., 2019. *Ice reinforcement: Selection criteria for winter road applications and outcomes of preliminary testing*, Proceedings of the 18th International Conference on Cold Regions Engineering and of the 8th Canadian Permafrost Conference, Quebec City, pp. 119-127.

Charlebois, L., Frederking, R. and Browne, T., 2019. *Making ice stronger: From the design of an aircraft carrier in WWII to applications in a changing climate* Proceedings of Geo St. John's, St. John's.

CRREL, 2006. *Ice Engineering Manual*. EM 1110-2-1612. Department of the Army, U.S. Army Corps of Engineers. New Jersey.

Fransson, L., 2009. *Ice Handbook for Engineers*. Luleå Tekniska Universitet.

Gold, L.W., 1967. *Time to formation of first cracks in ice*. In: H. Oura (Editor), Physics of Snow and Ice. The Institute of Low Temperature Science, Hokkaido, Japan, p. 359-370.

Gold, L.W., 1971. *Use of ice covers for transportation*. Canadian Geotechnical Journal, 8, p. 170-181.

Gold, L.W., 2004. *Building ships from ice: Habbakuk and after*. Interdisciplinary Science Reviews, 29(4), p. 373-384.

Government of the NWT, 2015. *Guidelines for safe ice construction*. Department of Transportation, Yellowknife, Canada, pp. 44.

Haynes, F.D., Collins, C.M. and Olson, W.W., 1992. *Bearing capacity tests on ice reinforced with geogrid*. Special Report 92-28.

Michel, B., Drouin, M., Lefebvre, L.M., Rosenberg, P. and Murray, R., 1974. *Ice bridges of the James Bay Project*. Canadian Geotechnical Journal, 11, p. 599-619.

Ohstrom, E.G. and DenHartog, S.L., 1976. *Cantilever beam tests on reinforced ice*. CRREL Report 76-7.

Sinha, N.K., 1982. *Delayed elastic strain criteria for first cracks in ice*. In: P.A. Vermeer and H.J. Luger (Editors), Proceedings of IUTAM Symposium on Deformation and Failure of Granular Materials. The Netherlands, Rotterdam, p. 323-330.

IAHR AIRH

25th IAHR International Symposium on Ice

Trondheim, 23 – 25 November, 2020

Plate testing of reinforced ice in the context of winter roads: Experimental set-up and preliminary results

Paul D. Barrette
Ocean, Coastal and River Engineering (OCRE)
National Research Council (NRC)
paul.barrette@nrc-cnrc.gc.ca

David Hnatiw
Ocean, Coastal and River Engineering (OCRE)
National Research Council (NRC)
david.hnatiw@nrc-cnrc.gc.ca

John Marquardt
Ocean, Coastal and River Engineering (OCRE)
National Research Council (NRC)
john.marquardt@nrc-cnrc.gc.ca

Yvan Brunet
Ocean, Coastal and River Engineering (OCRE)
National Research Council (NRC)
yvan.brunet@nrc-cnrc.gc.ca

Winter road networks generally comprise segments that run over land and over floating ice (rivers and lakes). The latter commonly are weak links in these operations, especially in a warming climate, because they rely on cold temperatures to achieve a thickness that is safe enough for the intended traffic. A testing program was designed to investigate the performance of steel cables and a polypropylene geogrid as reinforcement materials. This paper reports on the first stage of the test program, which was to design and implement a procedure to generate that information. One ice sheet was grown from freshwater in the NRC ice tank facility in Ottawa, and was partitioned into a series of eight plates 100 mm in average thickness. Forces and displacements were recorded while a downward vertical load was exerted on the plate at a constant displacement rate. Cracking activity was monitored via an acoustic sensor system. All plates underwent radial cracking. A good correlation existed between the response of the vertical load and cracking activity. Prospective follow-up on this preliminary testing is discussed.

1. Introduction

In Canada, Northern communities rely on winter roads – seasonal roads that only exist in the winter – for their supply of fuel, construction supplies and other bulk goods. These networks relieve Northerners of isolation, and allow them to commute between communities or to access the all-weather road network in the south. Winter roads generally comprise segments that run over land and/or over floating ice expanses (rivers and lakes). The latter are commonly weak links in these operations, because they rely on cold temperatures to achieve a thickness that is safe enough for the intended traffic. A safe ice cover is one where the buoyancy of the ice and its mechanical resistance provide the necessary support without failing, that is, without crack development, since these can lead ultimately to breakthrough. The over-ice segments are thus commonly a limiting factor in a winter road operation. In the years during which the air temperatures are higher than normal, this has important implications, namely:

1. The road will open later, delaying the delivery of critical supplies to northern communities.
2. Some users will expect the ice to be trafficable and will be tempted to use the ice without being fully aware it is unsafe, thereby increasing the risks of breakthroughs.

One solution to this challenge is to incorporate an engineered material into the ice cover (Figure 1). This will achieve a number of goals:

- It will increase the bearing capacity of the ice.
- It will do so in a predictable fashion.
- Even if the ice does fail, the reinforcement material inside the ice would support the load, thereby preventing breakthrough, and potential loss of life.
- This solution would become a tool available to operators to strengthen known weak links and prevent these locations from shortening the road's yearly operational lifespan.

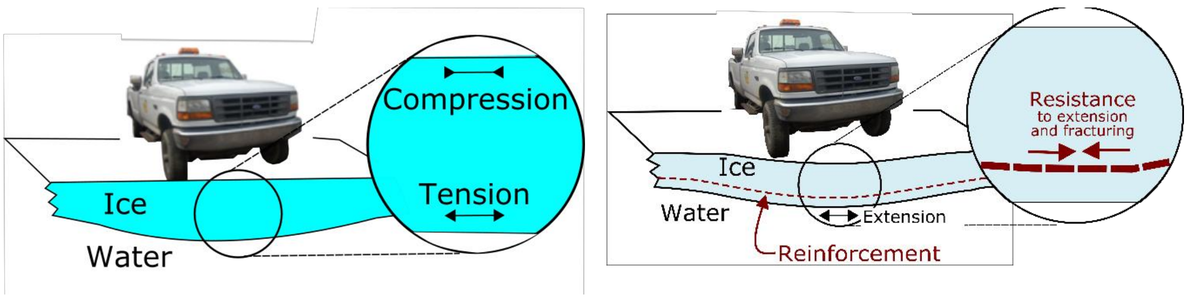

Figure 1: Left) Stress regime inside an ice cover loaded vertically. Right) Incorporation of a reinforcement inside an ice cover, to increase its resistance to the extensional component.

This solution has been used in the past in winter road operations (e.g. Gold, 1971, Michel et al., 1974). It has also been tested in the field and in the laboratory. Cederwall (1981), using steel bars, and Haynes et al. (1992), with a polymeric mesh, are examples of macro-reinforcement. Kuehn and Nixon (1988), with sawdust, Nixon and Weber (1991), with alluvium, and Gold (1993), with wood pulp, offer examples of micro-reinforcement.

2. Purpose of this paper

Drawing from work done in the past by various research groups, a project was initiated with the aim of identifying candidate reinforcement materials suitable for field deployment and retrieval, and to generate enough information on their performance to guide prospective follow-up work in the form of one or more pilot studies in a real ice cover. The purpose of this paper is to summarize the procedures that were used to generate that information, and to provide preliminary results, so as to guide follow-up testing (which will be reported elsewhere).

3. Rationale

Information on ice response due to loading can be investigated in various ways. Beam testing in a laboratory is a simple and very elementary approach to gaining insights into these scenarios (see companion paper). Plate testing is an extension of it, but it is not meant to reproduce the exact target scenario. For the present investigations, the ice plates were not floating, such that buoyancy was not factored in. Also, in floating ice, there is a temperature variation across the ice thickness (0ºC at the ice water interface). That factor was not captured either, i.e. the temperature was uniform across the full plate thickness. Further, the thickness to diameter ratio is too high to capture the characteristic length of the ice plate.

4. Reinforcement

The choice of materials used for reinforcement was based on the outcome of an earlier inquiry (Charlebois and Barrette, 2019)(Figure 2):

- Triaxial TX7 geogrid, by Tensar International, a punched polypropylene sheet, whose specifications are available on-line.
- Several parallel strands of standard steel cables 3.2 mm and 6.4 mm in diameter.

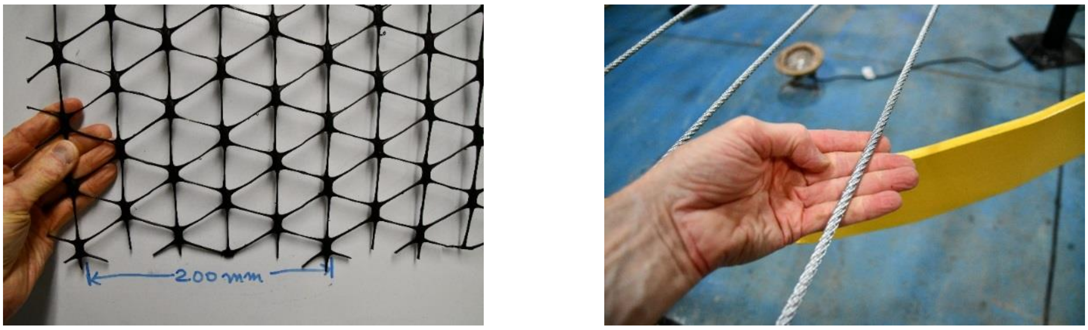

Figure 2: The two reinforcement material used for plate testing:
Left) Geogrid. Right) Steel cables.

5. Procedures

All test were done in OCRE's ice tank in Ottawa, a concrete basin 21 m in length, 7 m in width and 1.1 m in depth. It is equipped with a carriage, which is a structure spanning the full width of the tank, traveling on rails, and used for towing or for carrying instrumentation and actuators. A four-step procedure was adopted to conduct these tests (Figure 3):

1. Installation of eight 2.5 m diameter load frames, and of the reinforcement above them (Figure 4).
2. Tap water (freshwater) in tank cooled down and seeded ice (columnar-grained S2) was allowed to grow downward to enclose the reinforcement (Figure 5).
3. Cutting ice plates from the ice sheet above each frame, and lowering the water level to allow the plate to rest on them (Figure 6).
4. Removal of the remaining water and vertical loading (Figure 7).

The aim was to have the ice plate resting freely on the frame below it before testing, i.e. without being bounded (ad-frozen to it) or otherwise restricted along the frame's circumference. Available evidence shows that this was mostly achieved. However, for future testing, a plastic liner will be installed along the frames' upper circumference, so as to mitigate that effect.

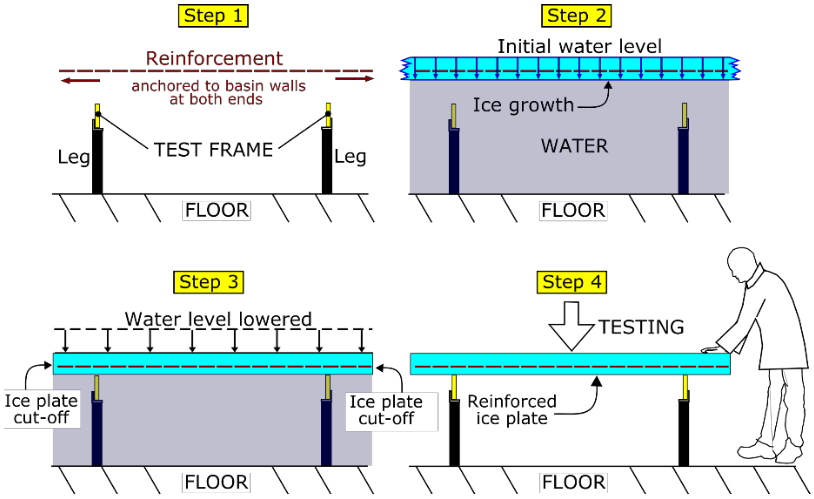

Figure 3: Four-step procedures designed and implemented for plate testing of reinforced ice. In step 4, an actuator has been used to deliver the vertical force (Figure 8).

Figure 4: Lay-out of circular frames in the OCRE ice tank, and of the reinforcement above them (person for scale at far end).

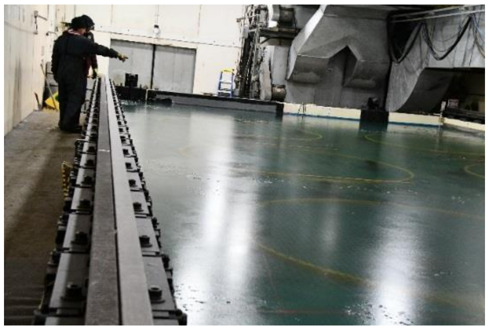

Figure 5: Tap water brought into the tank was cooled down and seeded. The yellow frames can be seen through the ice.

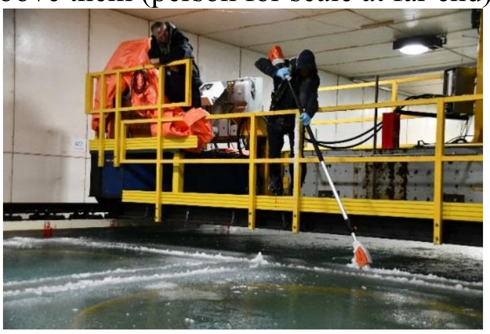

Figure 6: Once the ice above the test frames had achieved target thickness (thereby incorporating the reinforcement), it was cut around each test frame. This was done from the carriage.

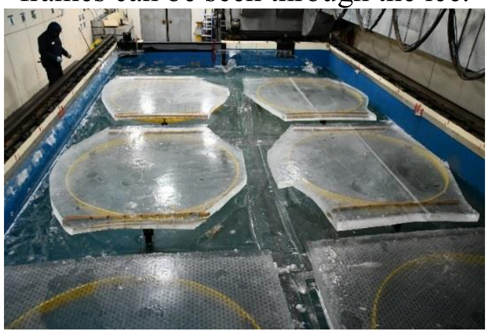

Figure 7: View of ice plates resting on the yellow frames, ready for testing (person at upper left for scale).

6. Instrumentation

The instrumentation included:

- An actuator, consisting of a 95 kN capacity hydraulic piston and a 45 kN capacity load cell. The actuator, which also incorporated a transducer to monitor displacement, was used to apply the load onto the ice at a desired displacement rate (1.4 mm per second), via a circular platen 100 mm in diameter that was connected to the load cell (Figure 8).

- Six spring-loaded linear variable inductance transducers (LVIT), with a 0-50 mm range and a 0-10 VDC output, and an accuracy of 0.01 mm. These were used to monitor ice deflection (Figure 8).
- An acoustic emission system, consisting of two channels, but only one sensor. It was a wideband frequency sensor, with an operating frequency range of 200-850 kHz. This system was used to monitor cracking activity (Figure 8, Figure 9).
- Data acquisition for load and displacement sensors was done at a rate of 500 Hz.
- A temperature profiler to monitor the temperature of the water, the ice and air, at a given location in the ice tank. That location was away from all tests. The target ice temperatures for all tests was -5 deg. C.

Figure 10 is a simplified depiction of the test set-up.

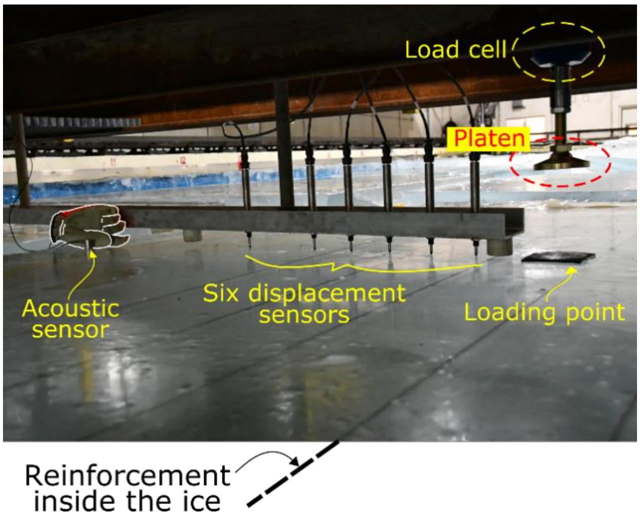

Figure 8: Instrumentation set-up below the carriage, here for test done on ice reinforced with steel cables. Glove for scale.

Figure 9: Close-up view of the acoustic sensor frozen onto the ice (no grease), here on ice reinforced with the geogrid.

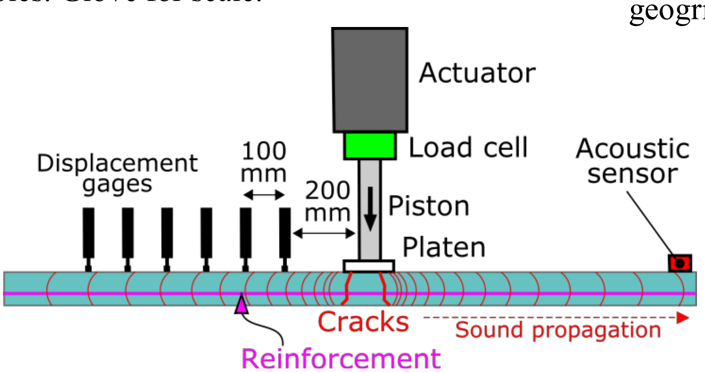

Figure 10: Schematics of instrumentation set-up (not to scale).

7. Acoustic sensing

Acoustic emission testing (AET) is key to understanding crack formation, an important aspect of structural health monitoring (SHM). This technique has been implemented on engineered material such as metals, asphalt and concrete (e.g. Sinha, 1996, Soulioti et al., 2009, Oh et al., 2020). It has also been used on ice in experimental set-ups (e.g. Gold, 1960, St. Lawrence and Cole, 1982, Li and Du, 2016), and in the field (Langhorne and Haskell, 1996, Lishman et al., 2020). Information was thereby generated on stress-induced cracking activity, the effects of temperature, and source location.

AET is a type of non-destructive monitoring technique applied to a large number of engineering scenarios. The basic principle is that a crack emits an elastic wave that travels through the ice – an AE sensor is able to detect that activity. It contains a piezoelectric crystal, which upon responding to the pressure associated with such a wave, generates an electric signal. Hence, when a crack forms, two things happen (Figure 11):

1) A permanent change inside the material, i.e. the existence of an additional crack,
2) A wave travels in all directions – it is a short-lived (e.g. microseconds) pulse-like event, characterized by a duration and an amplitude.

A simplified diagram of an AE event is shown in Figure 12, where the voltage generated by the sensor is plotted against time:

- *Threshold*: Minimum voltage required to be considered a significant event, e.g. above background noise (this parameter was set to 40 dB in our tests).
- *Rise time*: Time required to reach maximum amplitude.
- *Counts*: A single event may have several counts, which are voltage peaks exceeding the threshold limit.
- *Duration*: The time window that includes all counts – it may be in the order of microseconds.
- *MARSE*: The area that includes all counts, including below the threshold.

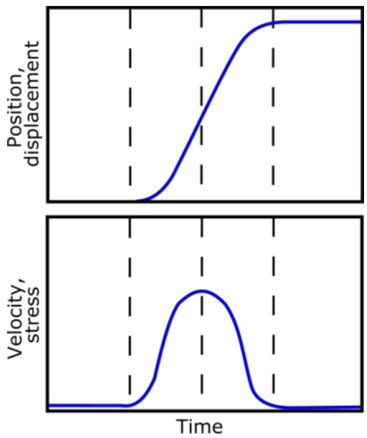

Figure 11: Top) A wave associated with the formation of a crack, the later expressed as a position/displacement as a function of time. Bottom) The wave is also associated with a transient, or recoverable, motion or stress in the material, which reaches a maximum before reversing to zero.

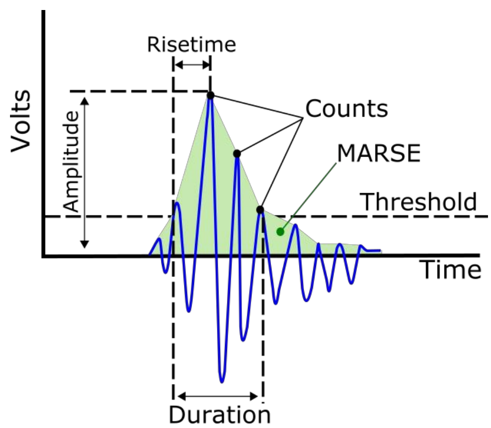

Figure 12: AE event and the various parameters typically used to describe it. See text for explanations.

These parameters were all recorded by the AE software. For the purpose of these preliminary investigations, only the counts were be monitored, as a preliminary step toward a more comprehensive assessment.

8. Preliminary testing

There was a drastic difference between un-reinforced and reinforced ice. The former underwent an instantaneous collapse, via a set of radial cracks (Figure 13). The reinforced ice showed considerable resilience to collapse. For a test done on the geogrid-reinforced ice, there was an instantaneous development of a set of radial cracks (within 2-3 seconds of load application), which was followed by additional radial cracking. Limited tangential cracks then occurred within 400 mm of the load application point, alongside progressive shearing along existing cracks. Near the end of the loading event, cracking was concentrated around the platen, to a point where it was driven through the ice surface (Figure 14). A similar scenario was observed with the cable-reinforced plates, with the difference that, as the loading event unfolded, shearing along the cables became a significant load-accommodating factor. Some of that shearing occurred preferentially at the intersection of a cable and a crack surface (Figure 15).

Figure 13: Outcome of a test done with non-reinforced ice.

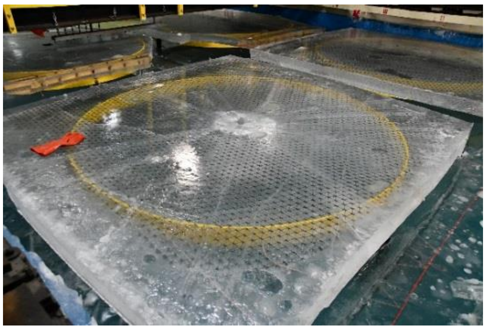

Figure 14: Outcome of a test done on an ice plate reinforced with the geogrid.

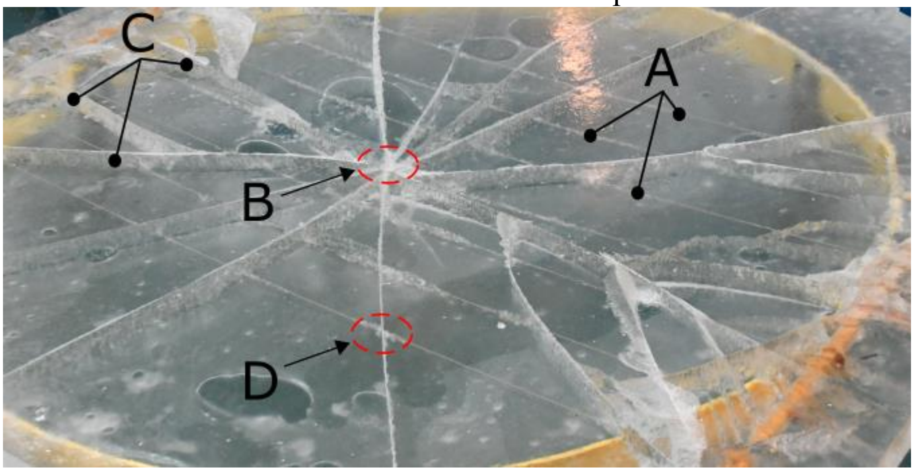

Figure 15: Outcome of a test done on an ice plate reinforced with the steel cables. A: Three cables (out of seven for this test), B: point of load application, C: examples of radial cracks, D: example of shearing along the cables, here initiating at the intersection with a crack.

The instrument response for one test is shown in Figure 16 as an example. A relatively good correlation between load and cracking activity can be observed, with the largest load drops often generating the more AE counts. Figure 17 shows the ice surface deflections recorded by the LVITs, at three time intervals very early in the loading event. The general downward deflection trends are seen, but it is uncertain as to why these trends are not smooth, as one might expect. A closer inspection of the load and AE responses (Figure 18) shows that no cracking activity occurred before the very first peak load, which occurred in this case about 4 seconds after load application.

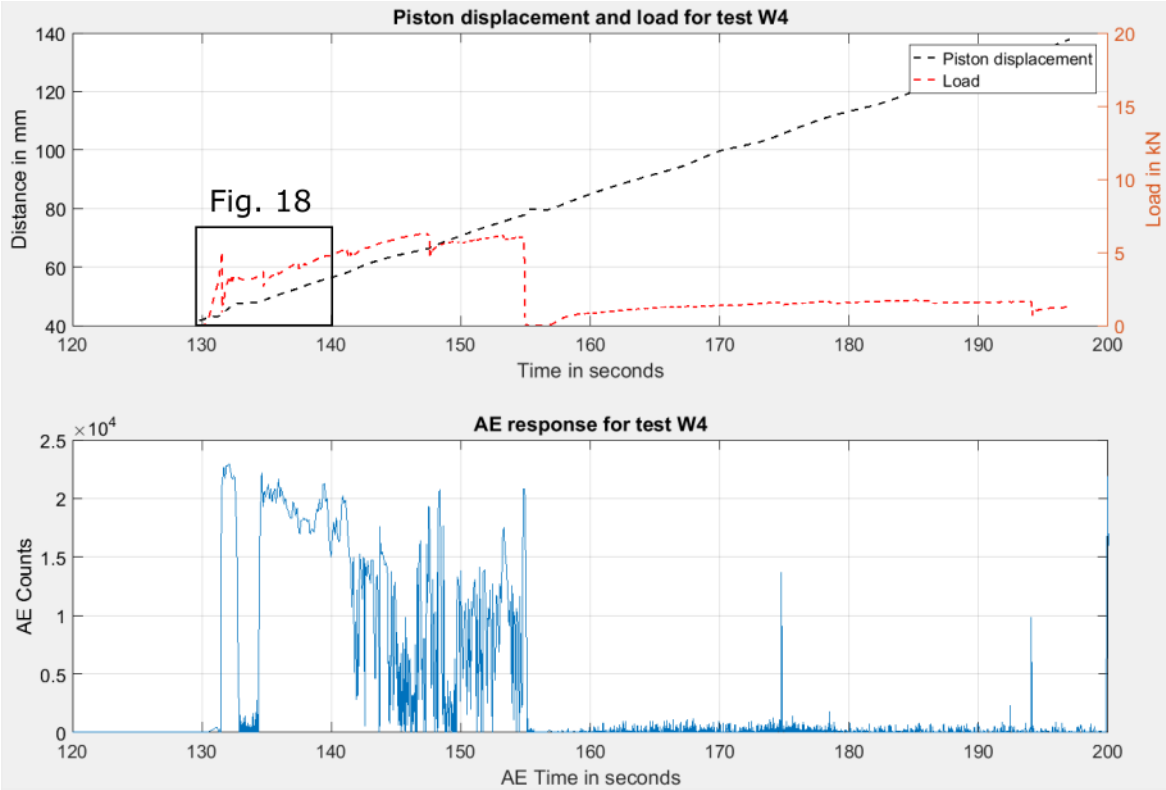

Figure 16: Example of instrument response (steel cables): Top) Piston displacement, load response and deflection vs time - the rectangular inset lower left corresponds to Figure 18; Bottom) Synchronized AE emission.

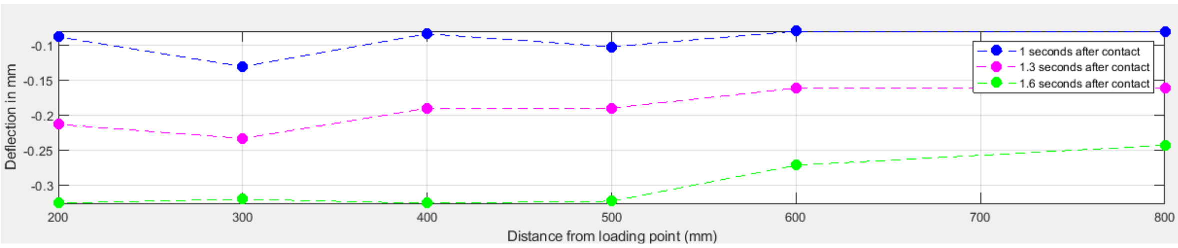

Figure 17: Ice deflection vs distance from the loading point at three different time interval for the same test. This example is also with steel cables.

9. Way forward

The exploratory nature of this preliminary testing points to a number of avenues that could be investigated in the follow-up testing.

- Is reinforced ice stronger than non-reinforced ice: This is, of course, a fundamental question. Unfortunately, because of two failures in the refrigeration system and an oversight in the data acquisition procedures, no information was generated on unreinforced ice that could be compared with that from the reinforced ice. Follow-up testing will provide these data, along with a comparison between responses from all tests.

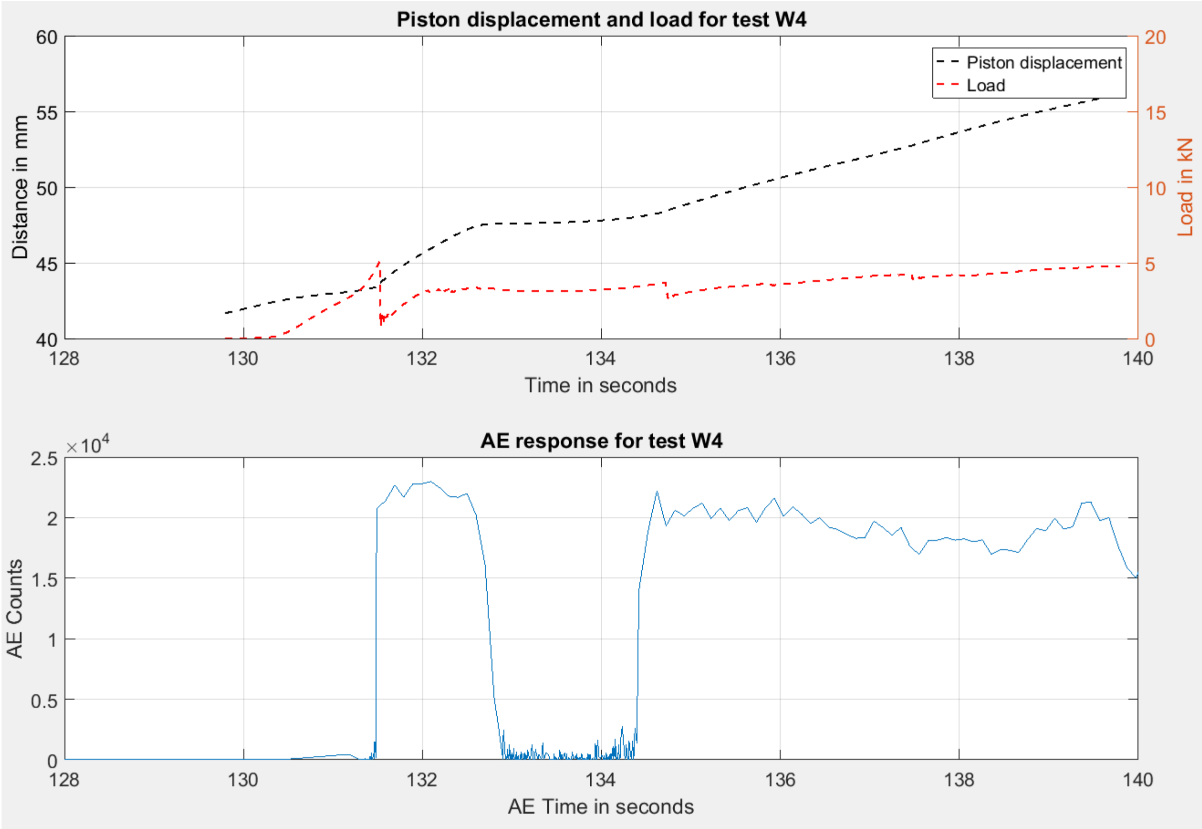

Figure 18: Inset in Figure 16.

- Correspondence between visual and instruments: A better understanding of the plate response could be gained via a close comparison between the visual information on the video sequence of each test and the instrumentation output for that test. Does all cracking activity lead to load drops? What are the extent and location of the cracks responsible for the most important load peaks and AE activity? Can reinforcement reduce cracking activity, or even induce it?
- Numerical modeling: Numerical modeling of the ice behavior in the elastic domain could be validated against the outcome of the plate test series. The ultimate purpose of this endeavor would be to assess the capability of this tool to foresee ice failure of non-reinforced and reinforced ice. Its ultimate aim is to develop a predictive tool for field scenarios.
- AE response – further analyses: Elastic wave energy in deforming ice can be examined in a number of ways – this can generate instructive insights on ice response with and without reinforcement. It could be followed up with additional analyses, for instance addressing AE energy, as guidance into prospective SHM implementation for floating ice covers and other ice engineering scenarios.
- Preliminary feasibility assessment: This task would include material certification and an investigation of further deployment options, which is an important consideration. The choice of reinforcement would also be discussed further. Material availability, density (whether if floats or not), ease of transportation (rolls, weight) are aspects that could be looked into further.
- Field deployment and retrieval: This study focused on the performance of reinforced ice, as opposed to the practicality of field deployment and retrieval. The latter is a very important consideration, and would be addressed after confirming the validity of ice reinforcement.

Acknowledgments

The work reported herein is part of a project that was financed by Transport Canada's Northern Transportation Adaptation Initiative (NTAI) Program, the First Nation Adapt Program of Crown Indigenous Relations and Northern Affairs Canada (CIRNAC), Infrastructure Canada (INFC) and the Arctic Program of the National Research Council of Canada. Comments by R. Frederking are gratefully acknowledged, as well as those from three anonymous reviewers.

References

Cederwall, K., 1981. *Behaviour of a reinforced ice-cover with regard to creep*, Proceedings of the 6th International Conference on Port and Ocean Engineering under Arctic Conditions (POAC), Quebec City, Canada, pp. 562-570.

Charlebois, L. and Barrette, P., 2019. *Ice reinforcement: Selection criteria for winter road applications and outcomes of preliminary testing*, Proceedings of the 18th International Conference on Cold Regions Engineering and of the 8th Canadian Permafrost Conference, Quebec City, pp. 119-127.

Gold, L.W., 1960. *The cracking activity in ice during creep*. Canadian Journal of Physics, 38(9), p. 1137-1148.

Gold, L.W., 1971. *Use of ice covers for transportation*. Canadian Geotechnical Journal, 8, p. 170-181.

Gold, L.W., 1993. *The Canadian Habbakuk Project - A project of the National Research Council of Canada*. Lochem Prepress and Periodiekenservice, The Netherlands, 323 p.

Haynes, F.D., Collins, C.M. and Olson, W.W., 1992. *Bearing capacity tests on ice reinforced with geogrid*. Special Report 92-28.

Kuehn, G.A. and Nixon, W.A., 1988. *Reinforced ice: Mechanical properties and cost analysis for its use in platforms and roads*, Proceedings of the 7th International Conference on Offshore Mechanics and Arctic Engineering (OMAE). The American Society of Mechanical Engineers (ASME), Houston, pp. 193-200.

Langhorne, P.J. and Haskell, T.G., 1996. *Acoustic emission during fatigue experiments on first year sea ice*. Cold Regions Science and Technology, 24, p. 237-250.

Li, D. and Du, F., 2016. *Monitoring and evaluating the failure behavior of ice structure using the acoustic emission technique*. Cold Regions Science and Technology, 129, p. 51-59.

Lishman, B., Marchenko, A., Sammonds, P. and Murdza, A., 2020. *Acoustic emissions from in situ compression and indentation experiments on sea ice*. Cold Regions Science and Technology, 172.

Michel, B., Drouin, M., Lefebvre, L.M., Rosenberg, P. and Murray, R., 1974. *Ice bridges of the James Bay Project*. Canadian Geotechnical Journal, 11, p. 599-619.

Nixon, W.A. and Weber, L.J., 1991. *Flexural strength of sand-reinforced ice*. Journal of Cold Regions Engineering, 5(1), p. 14-27.

Oh, T.-M., Kim, M.-K., Lee, J.-W., Kim, H. and Kim, M.-J., 2020. *Experimental investigation on effective distances of acoustic emission in concrete structures*. Applied Sciences, 10, p. 6051.

Sinha, N.K., 1996. *Acoustic emissions in asphalt subjected to thermal cycling at low temperature*, Proceedings of the 6th Conference on Acoustic Emission/Microseismic Activity in Geologic Structures and Materials, Zellerfield, pp. 109-120.

Soulioti, D., Barkoula, N.M., Paipetis, A., Matikas, T.E., Shiotani, T. and Aggelis, D.G., 2009. *Acoustic emission behavior of steel fibre reinforced concrete under bending*. Construction and Building Materials, 23, p. 3532-3536.

St. Lawrence, W.F. and Cole, D.M., 1982. *Acoustic emissions from polycrystalline ice*. Cold Regions Science and Technology, 5, p. 183-199.

IAHR AIRH

25th IAHR International Symposium on Ice

Trondheim, 23 - 25 November 2020

Ice Behaviour under Indentation Loading - Medium-Scale Field Tests

Robert Frederking
Ocean, Coastal and River Engineering Research Centre
National Research Council of Canada
Ottawa, Ontario K1A 0R6. Canada
Robert.Frederking@nrc-cnrc.gc.ca

Indentation testing at medium scale has been carried out on four occasions, between 1984 and 1990, in the Canadian Arctic. Iceberg ice and multi-year ice were tested. Forces up to 16 MN were exerted on contact areas up to 3 m2 at rates up to 0.4 m/s. All testing was done with the same servo-hydraulic controlled system. Results of the test programs have been previously reported individually. Here the results have been compared in terms of force versus penetration, global pressure versus nominal contact area and volumetric specific crushing energy versus crushed volume of ice. Various geometries of indenter and ice face were used but the volumetric specific crushing energy was relatively independent of geometry of ice or the indenter for the cases examined. Specific energy is lower for lower penetration rates. There was a strong numerical similarity between volumetric specific energy (MJ/m^3) and pressure (MPa) for the same test, whether plotted against crushed ice volume or nominal contact area. This paper explores whether volumetric specific crushing energy can provide helpful insights to defining global ice pressures on relatively small global areas, those less than 3 m^2. While this linkage may provide an additional data source for global pressure-area relations needed for structural design, further understandings are needed before their application.

1. Introduction

Information on ice loading is required to advance the safe design of structures placed in environments where they may be exposed to drifting ice. Observations and measurements on existing structures have been the basis for progress in definition of design ice loads. Instrumented structures have played an important role, for example measurements on the Molikpaq, Norstromsgrund Lighthouse, Bohai Bay jacket structures and the Confederation Bridge. This approach requires first of all the structure to be built, instrumented, and then waiting for nature to deliver a range of ice conditions. However when new structures or new conditions are encountered, a more active approach may have to be taken. This is where field testing comes into play. A loading scenario is envisioned and a test apparatus is design and built, and taken to the field to collect test data for this scenario. An early example of this approach was the drop tests carried out on lake ice in the late 1960s by the Arctic and Antarctic Research Institute (Likhomanov and Kheisin, 1971). Another example was the “Nutcracker” tests in the Beaufort Sea (Croasdale, 1970). These tests provides some insights which helped define hull strength requirements for ice breaking ship and guided approaches for design of offshore structures in the Beaufort Sea. These tests were either limited by the mass of object dropped on the ice or the capacity of the hydraulic system which loaded the ice. The Hibernia development off the east coast of Canada, which proposed deployment of a fixed structure, would have to contend with iceberg impact loading. This imposed a new set of requirements in terms of scale and loading rate. Masterson et al, 1992, described an entirely new test system, which was developed for the tests, and presented results from loading on iceberg ice at a scale heretofore not achieved. Forces up to 12 MN, loading rates up to 100 mm/s and contact areas up to 3 m^2 were attained. The results were analysed and presented in terms an empirical ice pressure versus area relation. This empirical approach has been used in design and is incorporated in offshore structures standards ((ISO, 2019).

There has also been parallel work looking for a more fundamental explanation of ice failure which could explain the more empirical findings. Kim and Høyland (2014) examined experimental data and conclude that for ”medium scale tests” the specific energy of the ice crushing process is scale and size independent. Subsequently larger scale tests were analysed (Kim and Gagnon, 2016) and again concluded there was scale and size independence and that such results could be used in modeling ice crushing, but that it would be desirable to examine a broader range of test results. Recently Kim and Tsuprik (2018) have questioned whether examining field data in terms of specific energy might lead to a more fundamental understanding of ice failure.

Design requires a pressure area relation, and while the units of volumetric specific crushing energy are the same as pressure, one is left with the question of how to relate the crushed volume of ice to a design area. This paper will explore how one might relate average global pressure and volumetric specific energy. Indentation tests have used a shaped indenter against a flat ice surface, in nature usually the structure/ship is relatively flat and the ice has a shape. Are both loading cases analogous? This paper will present an analysis and discuss results of several medium scale indentation test series to see what light can be shed on these questions.

2. Test Apparatus

A specialized test system was designed which could generate large forces and exert them at relative high velocities. Details of the system can be found in Masterson et al (1992). The system comprises a skid-mounted loading frame into which from one to four 4.5 MN capacity hydraulic actuators can be fit. In order to allow the system to exert loads at a relatively high rate a hydraulic accumulator with a power output of 1.8 MW for 3 s was the core of the system. A servo control system allowed a predetermined process variable to be controlled, for most of the tests this was the position of the actuator. Four field test campaigns were carried out with the same basic equipment; Pond Inlet 1984, Byam Martin Channel 1985 and Hobson's Choice Ice Island 1989 and 1990. Because the system was deployed in 4 different configurations and locations, each one will be described separately.

3. Test Results

A brief overview of the four test series is presented in the Table 1. Analysis of each series follows.

Table 1. Indentation test series analysed in this paper.

Test Series	Test ice	Indenters and speed
Pond Inlet, May 1984	Iceberg, -10 C	Spherical, decreasing from 100 mm/s
Byam Martin, May 1985	Multi-year, -10 C	Spherical, decreasing and constant at 10 mm/s and 100 mm/s
Ice Island, April 1989	Multi-year, -14 C	Flat, constant, 20 mm/s and 80 mm/s
Ice Island, May 1990	Multi-year, -10 C	Flat and wedge, constant 100 mm/s and 400 mm/s

Pond Inlet: The Pond Inlet test system (Masterson et al, 1992) employed 4 actuators in parallel for a capacity of 18 MN. Tests were carried out in three tunnels excavated into a grounded iceberg. Each tunnel was approximately 3 m wide, 3 m high and 15 m long. The ice of the test faces was shaved to be flat over an area 3 m by 3 m. Temperature of the ice faces was about -10°C. Several sizes of spherical indenters were used, but only the results from the two largest ones, which attained final contact areas of 1 m^2 and 3 m^2, will be reported here. The 1-m^2 spherical indenter had a radius of 1280 mm and the 3-m^2 spherical indenter a radius of 2300 mm. The system was programmed to start with an initial rate of 100 mm/s decreasing according to a cosine function to 0 mm/s after a displacement equivalent to 10% of the spherical radius. Normal movement of the indenter with respect to the test face was the controlled parameter. All together results of eight of the Pond Inlet tests are presented here, four (P3 t-n) for the 3-m^2 indenter and four (P1 t-n) for the for the 1-m^2 indenter. The 't-n' refer to test locations, t = tunnel number and n = test number.

Basic results of test P3 1-5 with the -m^2 indenter is presented in Figure 1. The test duration was slightly longer than 3 s. The decreasing rate of the indenter is apparent and the saw-tooth force-time record is typical of brittle ice failure and a decreasing frequency with decreasing rate. The larger drops in load are when a larger piece of ice spalled off. Note that the indenter has to move a few mm before it contacts the ice face and loading begins. This gap is taken into account in calculating the nominal contact areas and crushed volumes from the indenter movement signal.

The maximum force in this test was 10 MN, well under the system capacity of 18 MN, as was the case for all tests.

Given the geometry of the spherical indenter, the nominal contact area, A, and nominal crushed volume, V, are given by

$$A(x) = \pi\, x\, (2R - x) \tag{1}$$

$$V(x) = (\pi/3)\, x^2\, (3R - x) \tag{2}$$

where x is penetration into the ice face and R is the radius of the spherical indenter. Note that penetration x is a function of time, as discussed earlier and shown in Figure 1. With these geometric relations for area and volume, global pressure, p, an average pressure over the nominal area, and volumetric specific crushing energy, VSE, can be determined using the following expressions

$$p = F(x) \,/\, A(x) \tag{3}$$

$$VSE = \Sigma\, F(x)\, \Delta x \,/\, V(x) \tag{4}$$

where $F(x)$ is the indenter force at a penetration of x (a point in time), as is $A(x)$ and $V(x)$. Nominal crushing energy, $\Sigma\, F(x)\, \Delta x$, is the area under the force-penetration curve up to a particular amount of penetration, x, and is calculated here by a simple numerical integration with small penetration steps of Δx. The original analysis of the Pond Inlet iceberg indentation tests was in term of a cross plot of average pressure versus area from time-series records (Masterson et al, 1992).

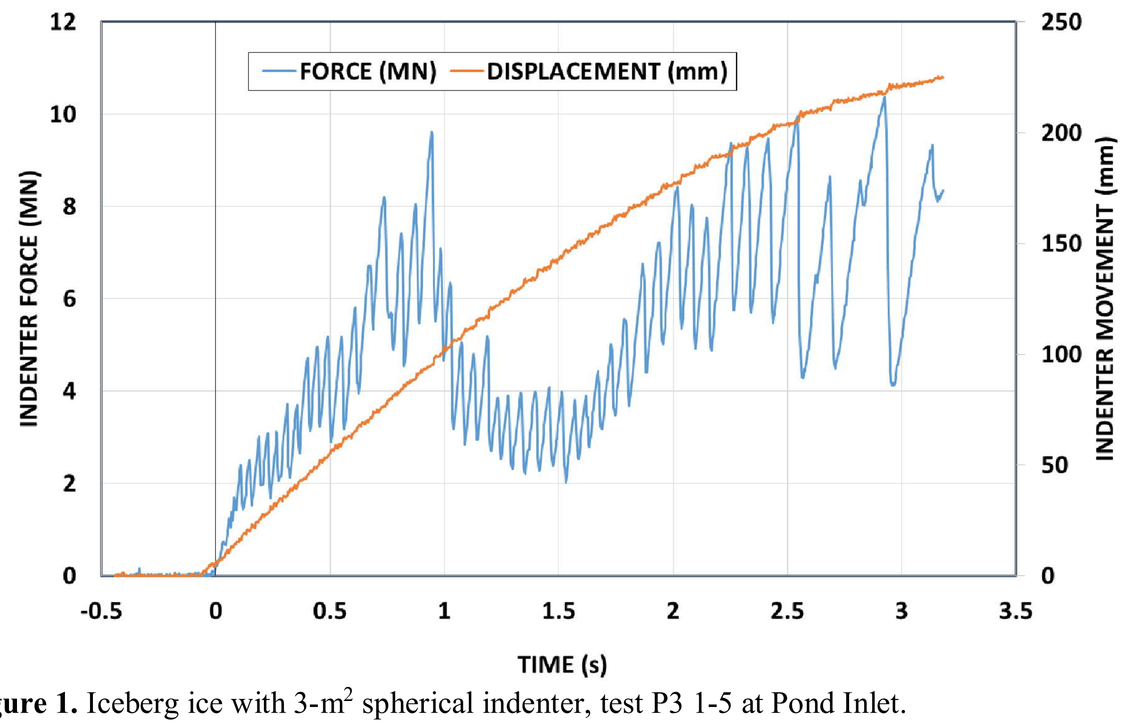

Figure 1. Iceberg ice with 3-m^2 spherical indenter, test P3 1-5 at Pond Inlet.

The result of such an analysis of the data from the test illustrated in Figure 1 is presented in terms of pressure and area in Figure 2 (a). A cross-plot of volumetric specific crushing energy versus nominal crushed volume is presented in Figure 2 (b). Both of these plots represent a process that progresses with time, as indicated by the arrows on the plots. The areas and volumes are termed nominal, since they are determined from simple geometric relations and are not actual values. The volumetric specific crushing energy (MJ/m^3) has the same effective units as pressure (MPa).

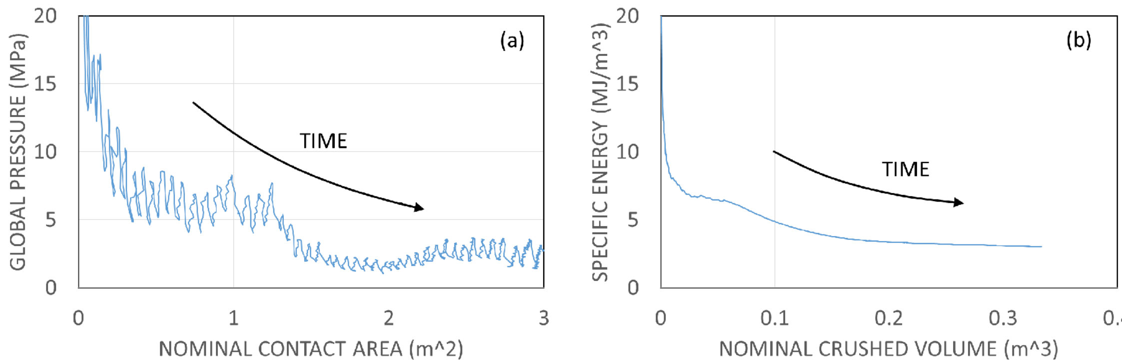

Figure 2. Analysis of results from Figure 1, (a) pressure-area, (b) volumetric specific energy-crushed volume.

Pressure-area plots for the four tests performed with the large, 3 m^2 spherical indenter are presented in Figure 3. The corresponding rate at which the indenter is advancing is also indicated. There are significant differences in the results for the first part of the indentation, probably reflecting randomness in spalling in the earlier part of the indentation, but surprising similarity in the later part of the indentation. The results combine the effects of an increasing nominal area and a significantly decreasing indentation rate in the latter part of the tests.

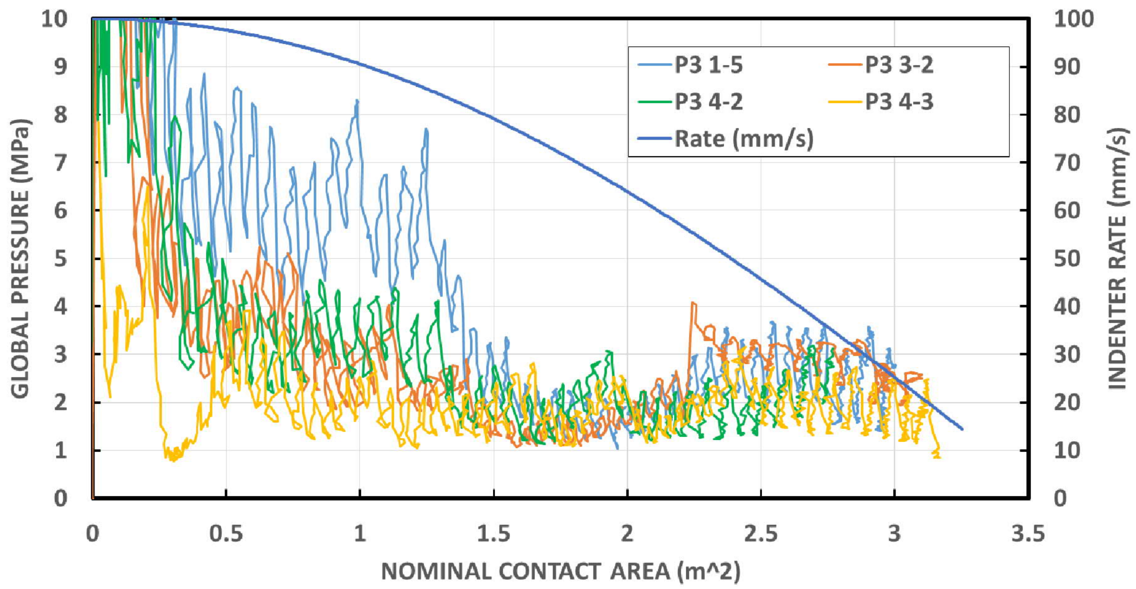

Figure 3. Global pressure as a function of nominal contact area for 3 m^3 indenter, Pond Inlet.

Results of the volumetric specific crushing energy for the tests that attained a nominal contact areas of 1 m^2 and 3 m^3, eight in total, are plotted in Figure 4. Kim and Gagnon (2016) in their analysis of the same data did not present any results for small indenters, to avoid possible scale effects. Also they did not analyse results for small crushed volumes. With the 3-m^2 indenter crushed volumes up to 0.35 m^3 were attained, and some size effect is noted for volumes less than 0.1 m^3. There was also some consistency in specific energies for volumes greater than 0.15 m^3. The 1-m^2 spherical indenter only attained crushed volumes of 0.05 m^3. There was considerable variability between the 1-m^2 tests.

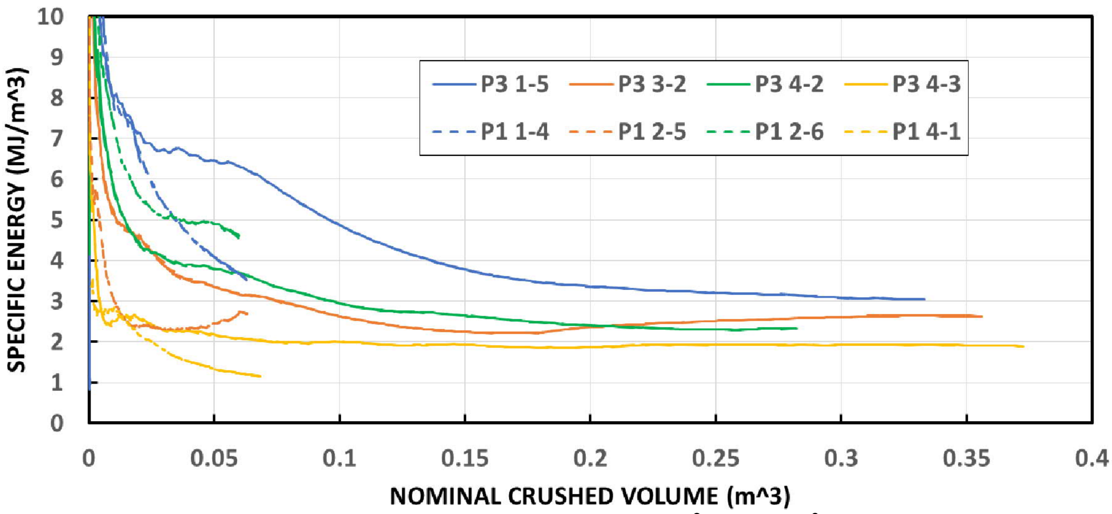

Figure 4. Volumetric specific crushing energy of the 1 m^2 and 3 m^3 indenters, Pond Inlet.

Byam Martin Channel: Indentation tests of multi-year ice were carried out in a floe in Byam Martin Channel (Masterson et al, 1999). In this case the testing was done in a multi-year floe about 5 m thick. Ice face temperatures were between -10°C and -9°C. Three trenches 2.5 m wide by 3.5 m deep and about 50 m long were excavated in the floe. All but one of the tests were conducted with the 1-m^2 spherical indenter on a flat ice face, similar to Pond Inlet. The same equations for relating contact area and crushed volume to penetration were employed. For these tests three actuators in parallel were used to generate the loading force. The primary test parameter was rate, with constant values from 0.1 mm/s to 100 mm/s, as well as decreasing rate tests as done at Pond Inlet. Only the tests at velocities of 10 mm/s and 100 mm/s are considered for analysis here. The maximum force was 9.2 MN, well under the system capacity of 13.5 MN.

Seven tests with higher rates were selected for analysis. The conditions for each test are described in Table 2.

Table 2. Test conditions for Byam Martin Channel test series

Indenter	Indenter speed	Test designation
1 m^2 spherical	Constant, 100 mm/s	BM 06, BM 09
1 m^2 spherical	Decreasing from 100 mm/s	BM 07, BM 08
1 m^2 spherical	Constant, 10 mm/s	BM 05, BM 10
Flat on spherical ice	Constant, 10 mm/s	BM 14

Volumetric specific crushing energy of the selected tests is presented in Figure 5. The four tests at velocities of 100 mm/s (solid lines in the plot) generally have higher specific energies than the two tests at 10 mm/s (dashed lines), suggesting a speed effect. For one test (BM 14) the geometry was reversed, a 1280 m radius spherical ice face, the same as the 1-m^2 indenter, was prepared and loaded with a flat indenter at a rate of 10 mm/s (heavier weight dashed line in Figure 5). Note that with the reversed geometry of test BM 14 the specific crushing energy is increasing in the latter part of the test.

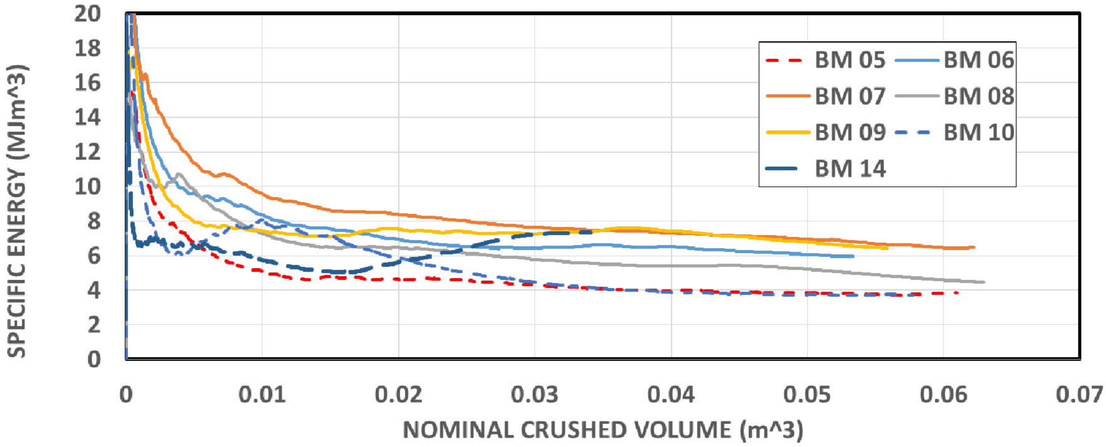

Figure 5. Volumetric specific crushing energy of the 1 m^2 indenter, Byam Martin

Ice Island 1989: Testing in multi-year ice was done at the Ice Island in 1989 (Frederking et al, 1990). A trench similar to Byam Martin was excavated. In this case loading was on specially shaped ice faces by flat indenters, as well as on flat faces with the 1280 mm radius spherical indenter. One of the flat indenters was deformable, representing ship structure, and the other one was rigid. Only a single actuator was employed so the maximum force was 4.5 MN and the scale of the testing was limited. Ice face temperatures were between -14°C and -13°C. All testing was at a constant indentation rate. An overview of the test conditions of the five tests selected is given in Table 3.

Table 3. Test conditions at the Ice Island in 1989

Indenter	Ice face; width – slope	Indenter speed	Test designation
Flat deformable	120 mm – 1:3	Constant, 20 mm/s	II89 06
Flat deformable	270 mm – 1:3	Constant, 70 mm/s	II89 07
Flat rigid	200 mm – 1:5	Constant, 80 mm/s	II89 08
Flat rigid	400 mm – 1:5	Constant, 10 mm/s	II89 09
Flat rigid	200 mm – 1:5	Constant, 20 mm/s	II89 10

Results of the five tests are plotted in Figure 6. The maximum nominal crushed volumes were much smaller that for the Byam Martin tests since the penetration amounts were smaller. Because of the variety of indenters, each test will be described, but details can also be found in Frederking et al, (1990). Tests with the 1280 mm spherical indenter gave similar results to those from Byam Martin, so were not presented here.

Tests 6 and 7 were with a flat deformable indenter, 1 m in diameter, on a shaped ice face. The shape of the ice face was a vertically-oriented truncated shallow wedge. The flat face was 120 mm wide and the sides were a shallow slope of 1:3, so each mm of penetration into the ice increased the width of loading by 6 mm. The geometry of the shaped ice face and the size of the indenter was used to calculate nominal contact area and nominal crushed ice volume during indenter penetration into the ice. Test 6 was at a nominal speed of 20 mm/s and Test 7 at a nominal speed of 70 mm/s, so the specific energy appears to be greater at higher rates. Tests 8, 9 and 10 were done with a rigid indenter 500 mm high and 750 mm wide. The ice face was again a vertically-oriented shallow wedge with face widths of 200 mm or 400 mm and side slopes of 1:5. Tests 8 and 10 were on a 200 mm wide face and a nominal rate of 80 mm/s for Test 8 and an effective rate of about 20 mm/s for Test 10. Test 9 was on a 400 mm wide face and while the actuator force reached 4.4 MN, for a stress on the ice face of 22 MPa, the ice did not fail and the loading system stalled out. Actually both Tests 9 and 7 reached the capacity of the actuator loading system.

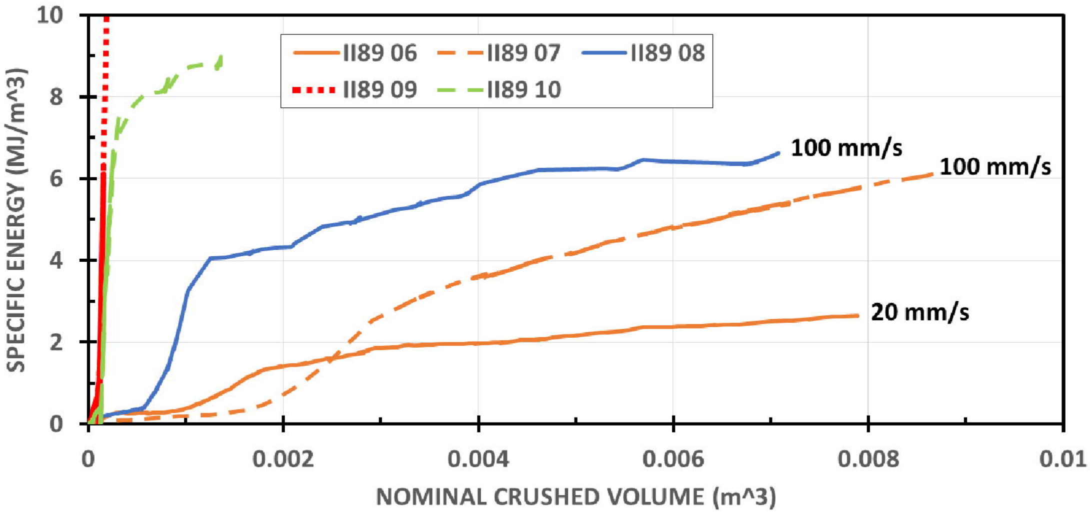

Figure 6. Volumetric specific crushing energy various indenters, Ice Island 1989.

Ice Island 1990: A more extensive test program was carried out at the Ice Island in 1990 (Masterson et al 1993). A trench similar to the one in 1989 was excavated in multi-year ice. All testing was on shaped ice faces with flat indenters or with wedge-shaped indenters on a flat ice face. The geometry of the shaped ice face and the size of the indenter was used to calculate nominal contact area and nominal crushed ice volume during flat indenter penetration into the ice. The inverse was done with the geometry of the wedged-shaped indenters for penetration of a flat ice face. Two deformable and one rigid flat indenter were used. A three-actuator loading skid with a capacity of 13.5 MN was used so larger contact areas and crushed volumes than in 1989 could be attained. Testing was at constant indentation rates of 100 mm/s and 400 mm/s. To achieve a speed of 400 mm/s the oil in the pressure accumulator was fed through 3 servo-valves in parallel to a single actuator. Ice face temperatures were between -9°C and -10°C for testing with the 100 mm/s tests and had increased to about -5°C for the 400 mm/s testing, which was conducted at the end of the test program..

Fourteen tests, with a variety of indenters and ice faces, are described in Table 4. Because of the complexity of the tests, the results will be grouped for presentation purposes.

Table 4. Test conditions at the Ice Island in 1990

Indenter	Ice face and shape	Indenter speed	Test designation
Flat Flexible	Vertical wedge, 1500x300 mm	100 mm/s	TFF 01
Flat Flexible	Vertical wedge, 1500x300 mm	100 rum/s	TFF 02
Flat Flexible	Horizontal wedge, 1200x300 mm	100 mm/s	TFF 03
Flat Flexible	Vertical wedge, 1000x100 mm	400 mm/s	SFF 01
Flat Flexible	Vertical wedge, 1000x100 mm	400 mm/s	SPF 02
Flat Flexible	Vertical wedge, 1000x100 mm	100 mm/s	SFF 03
Flat Rigid	Pyramid, 100x100 mm	100 mm/s	TFR 02
Flat Rigid	Pyramid, 500x500 mm	100 mm/s	TFR 03
Flat Rigid	Pyramid, 100x100 mm	100 mm/s	TFR 04
Flat Rigid	Pyramid, 500x500 mm	100 mm/s	TFR 05
Wedge 1:1	Flat	100 mm/s	TW1 01
Wedge 1:1	Flat	100 mm/s	TW1 02
Wedge 1:3	Flat	100 mm/s	TW3 04
Wedge 1:3	Flat	100 mm/s	TW3 05

The first group comprises the deformable indenters, the large one 1500 mm high by 1220 mm wide and the small one 1000 mm high and 700 mm wide, each representing hull structure. Results are presented in Figure 7. For the large indenter (TFF) the first two tests were on vertically-oriented truncated wedges with a 300 wide ice face and 1:3 side slopes. The third test was with the face of the wedge horizontally oriented. For the small indenter (SFF) the truncated wedge was vertically-oriented and the flat front edge was 100 mm wide. Tests 1 and 2 were at 400 mm/s and 3 was at 100 mm/s. Permanent deformations of the indenters after each test were noted and measured.

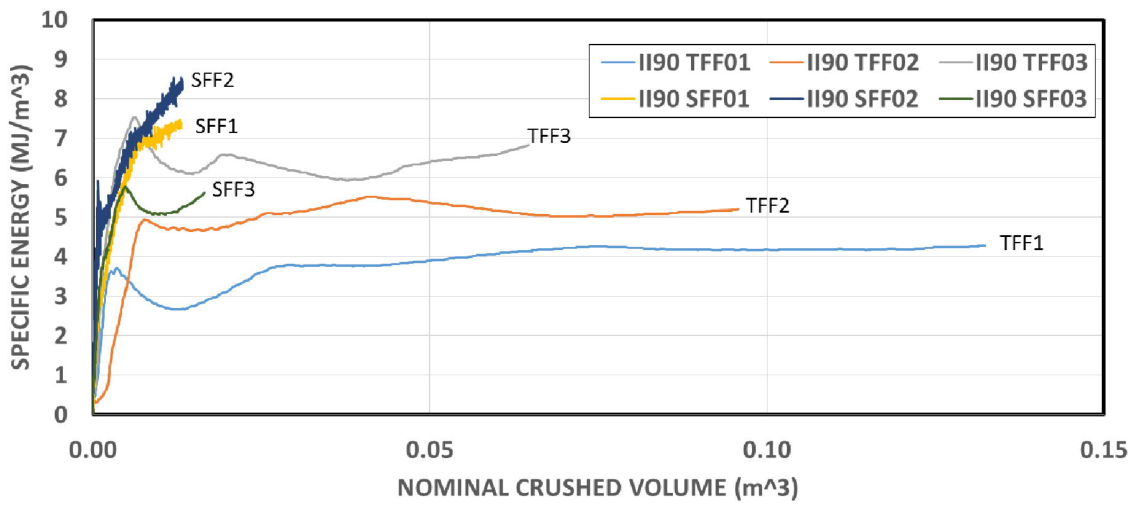

Figure 7. Volumetric specific crushing energy for flexible indenters, Ice Island 1990.

The second group of tests were with a rigid indenter (TFR). It was 1500 mm high and 1220 mm wide. The ice shapes prepared were a truncated pyramid with 1:3 side slopes. Results of these tests ae presented in Figure 8. For tests TFR02 and TFR04 the top of the pyramid was 100 mm by 100 mm and for tests TRF03 and TFR05 the top of the pyramid was 500 mm by 500 mm. The two test starting with a small initial contact (TFR02 and TFR04) had consistently higher specific energies.

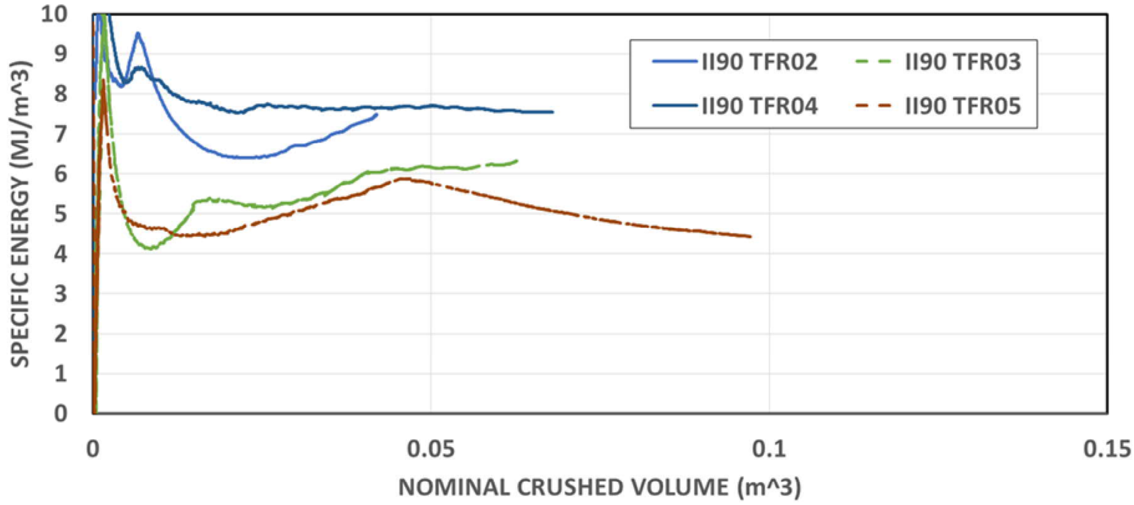

Figure 8. Volumetric specific crushing energy for the rigid indenter, Ice Island 1990.

The third group of tests were with wedge-shaped indenters (TW), 1800 mm long, 100 wide flat nose, and side slopes 1:1 or 1:3. They were oriented vertically and loaded a flat ice face. Results of these tests ae presented in Figure 9. For larger crushed volumes the 1:1 sloped wedges, TW101 and TW102 had consistently lower specific energies that the 1:3 sloped wedge, TW304 and TW305.

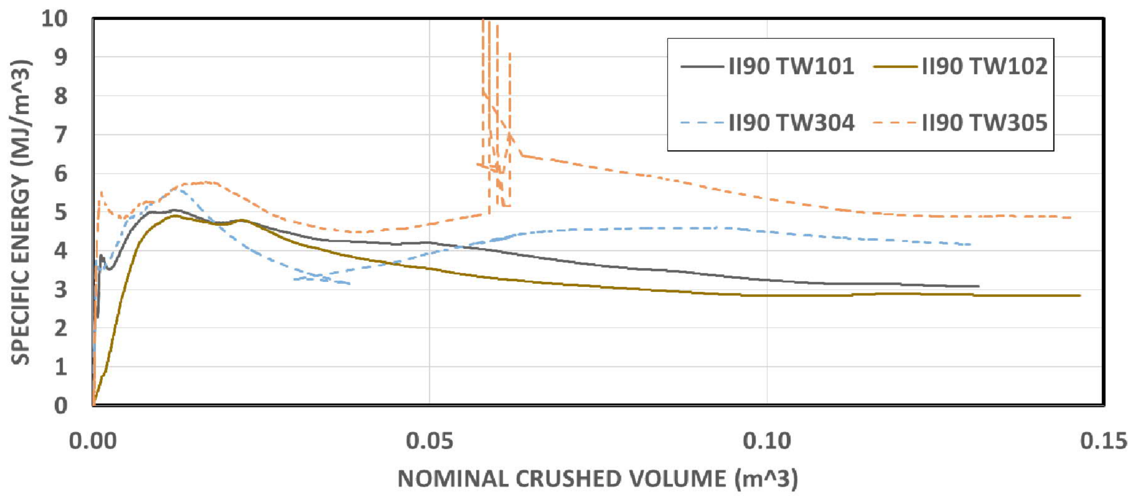

Figure 9. Volumetric specific crushing energy for wedge indenters, Ice Island 1990.

4. Discussion

The volumetric specific energy of iceberg ice in Pond Inlet and multi-year ice in Byam Martin Channel were quite similar, taking into account the size of the crushed volume of ice. All testing was done at ice temperatures within a couple degrees of -10°C. At this temperature there does not appear to be any difference between the two types of ice. Reversing the geometry of a spherical indenter into a flat ice face with a flat indenter impinging on a spherically-shaped ice face (BM14) gave increasing specific energy with increasing crushed volume, in contrast to the continuing shallow decrease in specific energy seen in all the other spherical indenter tests. Confinement conditions in the latter part of this test may have been greater due to the proximity of a 'semi-infinite' ice mass behind the spherical ice face.

At Byam Martin two tests at 10 mm/s had lower specific energies than the two 100 mm/s tests, showing a speed effect. Tests at the Ice Island in 1989 with a flat flexible on shaped ice had significantly lower specific energies at 20 mm/s compared to one at 70 mm/s. The 1990 Ice Island tests revealed a greater specific energy at 400 mm/s compared to the 100 mm/s tests. The specific energy from the Byam Martin spherical indenter and both Ice Island series indicated lower specific energies at lower indentation rates, independent of indenter or ice face geometries. At Byam Martin there was no significant difference between tests at a constant 100 mm/s and 100 mm/s decreasing with a cosine function.

At the Ice Island tests were performed with both rigid and deformable indenters. For deformable indenters the volumetric specific energy determined from force and penetrate records is reflects both the energy in crushing the ice and yielding the steel. The deformed shape of the indenter was measured and conducting a rough order of magnitude calculation, the energy of the plastic deformation of the steel indenter plate was two order of magnitude smaller than the total energy of the corresponding indentation test.

With the spherical indenters and the pyramid-shaped ice faces the shape of the loaded volume or area remains constant during the test, even as area and volume increase. Flat indenters on wedge-shaped ice faces and wedge-shaped indenters had initially elongated contact shapes which became less elongated as the indentation progressed. Kim and Gagnon (2016) observed that the shape of a spherical or wedge indenter might promote high lateral loading due to spalling, which would induce error in the specific energy determination. The truncated pyramid or wedge shaped ice faces minimize this issue of energy dissipation in lateral movements.

Referring to Figure 2 it can be seen that there is some similarity in the shape of the two plots, which is not surprising since they both are based on the same input data, only processed in different manners. Kim (Personal Communication, 2019) suggested that specific energy might be a more stable means of describing ice indentation test results. For a select number of test cases both nominal global ice pressure and volumetric specific crushing energy have been plotted against nominal contact area in Figure 10.

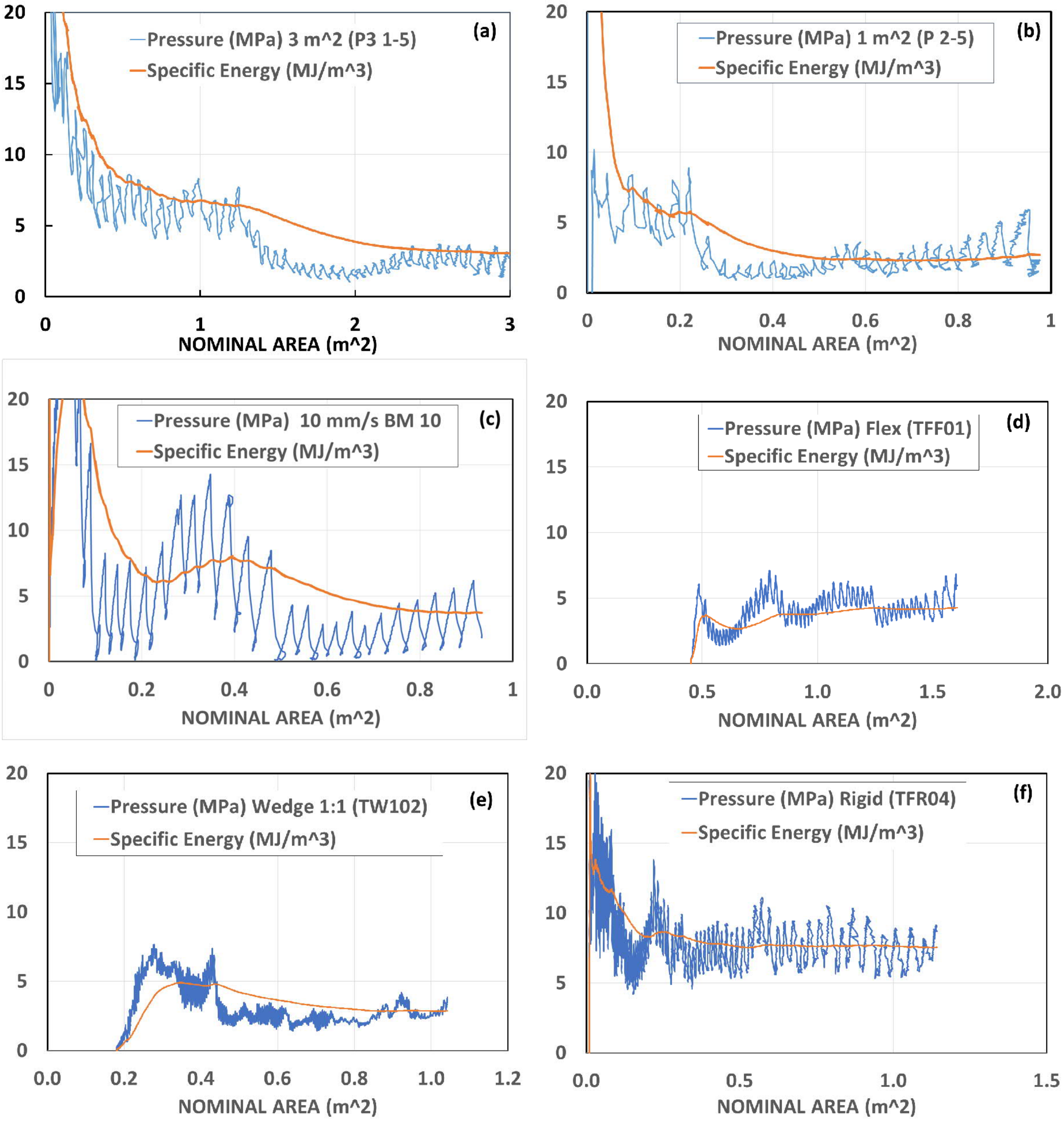

Figure 10. Volumetric specific crushing energy and global pressure versus nominal contact area for medium-scale indentation tests.

It can be seen that in all cases the two calculated values are numerically similar, the volumetric specific energy being much smoother due to the integrative process used in calculating it. There is a significant size effect, with specific energy and pressure decreasing for areas up to 1 m^2 in all cases presented here and in this case for all 4 large area (3-m^3 indenter) tests at Pond Inlet. For the 2 selected Pond Inlet tests with 3 m^2 and 1 m^2 indenters, Figures 10 (a) and (b) respectively, the specific energy curve is a reasonable upper limit on average pressure. In Figure 10 (c), a lower rate test at Byam Martin, the pressure oscillations are much larger, even dropping to zero and are lower frequency. Note the integrating effect of the specific energy, maintaining a higher value between 0.5 and 0.7 m^2. A similar effect was noted in Figure 10 (a) and (b). For the three

1990 Ice Island results in Figure 10 (d), (e) and (f) specific energy and pressure are quite similar, except in (e) the integrating effect has the specific energy numerically greater than the pressure. The results for the small initial area truncated pyramid, Figure 10 (f), are quite similar to those of the spherical indenter, Figure 10 (a), at corresponding areas.

5. Applications to Design

As already discussed, the requirement for structural design is an average ice pressure which can be applied to a specific area of the structure. In the indentation tests discussed here both the geometry of the indenter and the ice face are known, so the crushed volume and nominal contact area can be related to each other. Given a volumetric specific energy of ice, some knowledge of the shape of the crushed volume is needed in order to determine a corresponding nominal contact area. Until a workable volume-area relation is developed and understood, conventional pressure-area relations will continue to be the basis used in design.

6. Conclusions

- Volumetric specific crushing energy is relatively independent of geometry of ice or indenter for the cases examined here.
- For smaller crushed volumes there is a volume effect similar to the one seen in the pressure-area relation (decreasing specific energy with increasing crushed volume).
- Indentation should be examined as a process that extends over a period of time.
- There is a rate effect; for comparable conditions specific energy is lower for lower penetration rates.
- Volumetric specific crushing energy and nominal global ice pressure have the same units and numerical magnitude whether compared on a basis of crushed volume or nominal contact area, however there is a significant reduction in the information content of the specific energy due to the integrating function used to generate it.
- Other sources of field tests from which data that provide force and penetration or crushed volume of ice merit examination, e.g. ship impacts on ice, bergy bit or ice floe impacts on instrumented structures
- Further insights into the relation between crushed volume and contact area and specific energy are needed before they can applied in the aid of design.

Acknowledgments

I would like to acknowledge the suggestion by Ekaterina Kim that specific energy merits examination in relation to ice failure behavior and how it relates to pressure and area. I would also like to thank the Ocean, Coastal and River Engineering Research Centre of the National Research Council of Canada for the opportunity of preparing this paper.

References

Croasdale, K.R., 1970. The nutcracker ice strength tester and its operation in the Beaufort Sea, IAHR Ice Symposium, Paper 6.4, Reykjavik, September 7-10, 1970.

Frederking, R.M.W., Jordaan, I.J., and McCallum, J.S., 1990. Field Tests of Ice Indentation at Medium Scale, Hobson's Choice Ice Island, 1989. Proc. IAHR 10th International Symposium on Ice. August 20-23, 1990. Espoo, Finland, Vol. 2. pp. 931-944.

ISO 19906:2019, 2019. Petroleum and natural gas industries – Arctic offshore structures. International standard: 2nd edition, 2019 July.

Kim, E. and Høyland, K.V., 2014. Experimental investigations of the energy absorption capacity of ice during crushing: Is the specific energy scale independent? Proc. of the 22nd IAHR International Symposium on Ice.

Kim, E. and Gagnon, R., 2016. A preliminary analysis of the crushing specific energy of iceberg ice under rapid compressive loading. Proc. of the IAHR International Symposium on ice.

Kim, E. and Schulson, E.M., 2015. A phenomenological explanation of the pressure–area relationship for the indentation of ice: Two size effects in spherical indentation experiments. Cold Regions Science and Technology, 115, 48-55.

Likhomanov V.A. and Kheisin D.E., 1971. Experimental investigation of solid body impact in ice, Problemy Arktiki I Antarktiki, Vol. 38, pp. 105-111 (in Russian), English translation of Problemy Arktiki i Antarktiki, Vol. 38, pp. 128-136.

Masterson, D. M., Frederking, R.M.W., Jordaan, I.J. and Spencer, P.A., 1993. 1990 Field ice indentation Tests at Medium Scale-Hobscn's Choice ice island, OMAE '93 Conference, Glasgow, Scotland, June Paper OMAE93-127.

Masterson, D.M., Nevel, D.E., Johnson, R.C., Kenny, J.J. and Spencer, P.A., 1992, The medium scale iceberg impact test program. 11th International Symposium on Ice IAHR, Vol. 2, pp 930-966.

Masterson, D.M., Nevel, D.E. and Nordgren, R.P., 1999. Velocity Effects from Multi-Year Ice Tests. 18" lntemational Conference on Offshore Mechanics and Arctic Engineering. Paper OMAE99-1127.

25th IAHR International Symposium on Ice
Trondheim, 23 - 25 November 2020

Field investigation and numerical analysis of the deformation of L-shaped ice beams

Igor Gribanov[1], Aleksey Marchenko[2], Rocky S. Taylor[1]
[1]Memorial University of Newfoundland, St.John's, Canada
[2]The University Centre in Svalbard, Longyearbyen, Norway
ig1453@mun.ca

Complex bending deformation of L-shaped beams was previously investigated experimentally at several locations near the University Centre of Svalbard. The breaking force of the beam was related to the mechanical properties of ice by performing finite element analysis and by deriving analytical expressions for the state of stress on the surface of the sample. In the present work, we advance the analysis of the complex bending using the recently collected data. New field tests were performed in November 2019 on fresh water lake near Longyearbyen. Five extensometers were installed on the top surface of the beam to measure vertical displacements, which allow estimating the deformation of the sample. The collected data is compared with the results of numerical simulations with a particular interest in the deflection profile of the surface of the beam.

1. Overview

Field tests on uniform ice covers provide an affordable way of investigating the fracture properties on a medium scale. Because nature provides most of the essential components, such tests require minimal equipment and are easy to set up. Standard tests, such as cantilever beam bending, are performed regularly in many parts of the world for environmental observations, as a part of student research and other activities. Basic requirements for conducting such tests include the safe thickness of the cover, reasonable weather conditions, and accessibility of the test site by transport.

Utilizing natural ice formations for testing has a few downsides. If a test is performed on a floating sample, then there is no control over its thickness, the submerged surface is uneven, and there is limited access to the submerged portions. Properties of natural ice are highly variable, and the samples may have inclusions that cannot be visually identified. Seemingly intact ice covers may contain cracks that propagate across the whole water reservoir or parallel to the shore. The presence of surrounding water in the floating beam tests excludes bending of the sample under its weight but adds to the mass of the sample, complicating the data analysis.

Tests on L-shaped beams were conceived as a way of studying fracture behavior with complex states of stress. The beams are loaded vertically by applying force to the floating free end, and the bend creates the effect of torsion on the fixed portion of the beam. In addition to tensile and compressive stresses, the shear component is introduced, primarily at the fixed end. The fracture may occur either by shear or tension, depending on the dominating component.

The bending of a cantilever beam is described by straightforward analytical expressions, and its curvature can be related to the modulus of elasticity (Karulin et al. 2019). The curvature is constant along the length of the beam and is proportional to the applied bending moment. By placing several extensometers along the central axis, the curvature can be measured, and the modulus of elasticity can be inferred. In theory, the readings of the extensometers for the isotropic beam are shown to be linearly dependent. In practice, the displacements are quite small (around 1mm before fracture), and the readings are affected by surrounding oscillations and by the bending of surrounding ice on which the equipment is mounted.

The bending of an L-shaped beam is more complex than that of a cantilever beam, and the relationship between its deflection, modulus of elasticity, and the applied bending moment is not obvious. In this work, we investigate this relationship experimentally and numerically. In the experiment, extensometers are installed on the surface of the beam to measure its vertical deflection at several selected locations. Then, a numerical simulation is conducted using a finite element method with cohesive zones to generate the complete deflection profile of the surface.

2. Test description, location and ice conditions

Two tests that are described in this section were conducted as a part of a larger series of measurements that took place between October 26 and November 1, 2019. A large group of students and researchers participated in this project, so the test site was selected from the perspective of convenience and easy access. Coal mine #7 in Longyearbyen, Svalbard, is the last operating mine on the island and has a technical water reservoir that is well-suited for in-situ floating beam tests. In October and November, the thickness of its ice cover is sufficient for the presence of people and heavy equipment. The testing procedure was similar to the experiments that were performed previously, the details of which were described in earlier work (Karulina, Karulin, and Marchenko, 2013). Previous tests of L-shaped beams took place between 2014 and 2016 and focused on recording the loading force at the indenter and the location of the fracture (Murdza et al. 2016). Subsequent analysis of stress distribution showed how the dimensions of the beam influence the stress distribution, and the location of the fracture (Gribanov et al. 2019). The main interest in the L-shaped beam experiment is to observe the behavior of ice under a complex state of stress. For that purpose, the dimensions of the sample must be properly selected to cause a fracture at the fixed end, which corresponds to a torsional load.

The thickness of the ice cover at the test site was 50±1 cm. Measurements at nearby locations, within several meters from the selected location, showed that the thickness varied between 40 and 55 cm. Other dimensions of the beam are shown in Figure 1. The loading force was applied via a square indenter measuring 15×15 cm and recorded with a load cell.

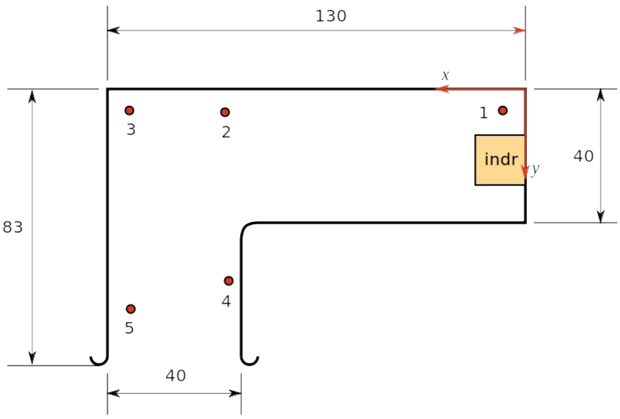

Figure 1. Dimensions of the L-shaped beam and locations of the extensometers. Sizes are shown in centimeters.

Table 1. Coordinates of extensometer placements. Offsets are measured relative to the top-right corner of the beam.

Extenso-meter	Horizontal offset, cm	Vertical offset, cm
DS1	7	7
DS2	85.5	7.5
DS3	116	7
DS4	93	61
DS5	123	70

Deflection of the beam was measured by five displacement sensors (DS1, DS2,...,DS5), installed on the top surface. The following types of HBM sensors were used: 1WA/2MM-T, 1-WA/10MM-T, and 1-WA/50MM-T, differing by their measurement range. Larger ranges were expected at DS1 and DS2, whereas smallest range was expected at DS5. Figures 1 and 2 show the locations of the extensometers, which were mounted on the wooden beams and attached to metal frames. Their exact positions are listed in Table 1. DS1 was mounted on the main loading frame near the indenter, while the other four sensors were placed on a separate frame, which was re-purposed from another experiment. The frame was attached to the surrounding ice with screws. Measurements were taken from the moment the hydraulic cylinder was activated until the fracture developed (Figure 2c). The average indentation rate, inferred from extensometer readings, was 0.57 mm/s.

(a)

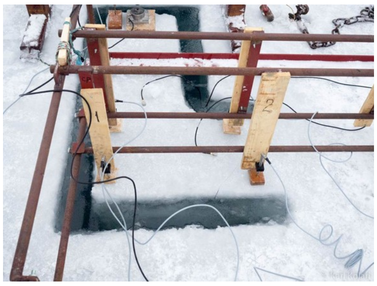

(b)

(c)

Figure 2. (a) Metal frame is holding the extensometers over the fixed portion of the L-shaped beam. (b) The extensometers are mounted on wooden beams; numbers on the plates do not correspond to sensor numbers. (c) Resulting fracture is visible to the left of the plate.

The force measured at the indenter is shown in Figure 3a. Extensometer readings are shown in Figure 3b. Normalized values (Figure 3c) were obtained by dividing all displacements by the readings of DS1 and indicate the displacements as proportions of the first extensometer. Such adjustment reveals the linear dependence of the readings.

In the measured forces and displacements, low-frequency oscillations were identified. The frequency of these oscillations was estimated to be 30Hz. The most likely source of these oscillations was the working hydraulic pump, which was a part of the experimental setup. The recorded data also included high-frequency noise, which was subsequently removed by feeding the data through a low-pass filter. Force measurements before and after filtering are shown in Figure 3a. Extensometer readings in Figures 3b and 3c are presented after the removal of high-frequency noise.

(a)

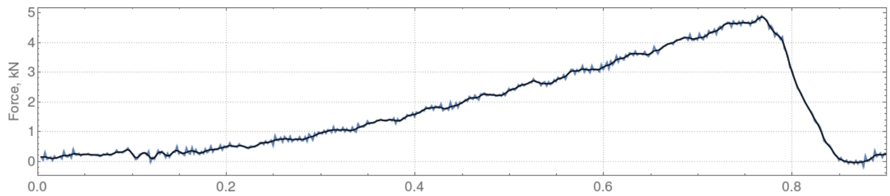

(b)

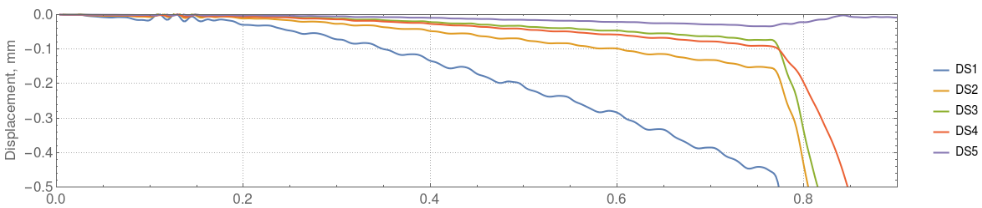

(c)

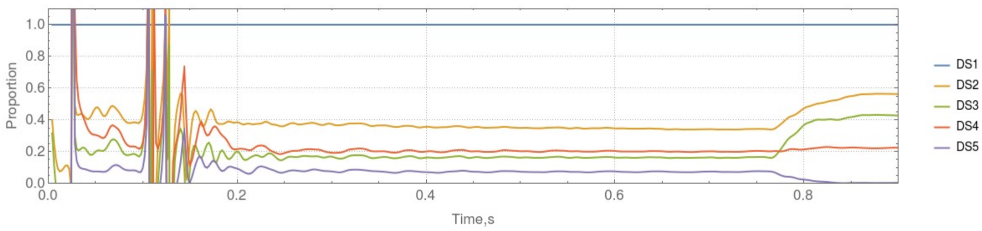

Figure 3. Measured (a) force on the indenter, (b) extensometer readings on the top surface, (c) normalized extensometer readings vs. time. A low-pass filter was applied to the recorded data to remove high-frequency noise.

The time range between 0.20 s and 0.75 s corresponds to a “steady regime,” during which the displacements are larger than extraneous noises, and the loading force increases linearly. Readings of DS1, DS3, DS4, and DS5 are linearly dependent. The exception is DS2, whose relative reading smoothly decreases from 0.39 to 0.35. Note that this deviation is caused by a steady process and not by noise. The linear dependence coefficients of DS1-DS5 are {1., 0.39-0.35, 0.16, 0.19, 0.070}.

Measurements of Young’s modulus via deflection of a cantilever beam

Young’s modulus of natural ice depends on the type of ice, its growing conditions, and may vary in a broad range. The modulus mainly determines the relationship between the beam’s deflection and the applied force. Exact measurements of Young’s modulus are necessary for conducting computer simulations.

The deflection of a regular cantilever beam can be related to its Young’s modulus (Karulin et al. 2019) using the expression $E=M/(kJ)$, where M is the bending moment, k is the curvature of the beam and J is the moment of inertia of the cross-section. The moment of inertia is computed as $J=bh^3/12$, where b is the width of the cross-section, and h is its height. The bending moment M is calculated as a product of the applied force F and the position of force application from the reference point. The curvature can be calculated by inspecting the deflection of the surface at three locations.

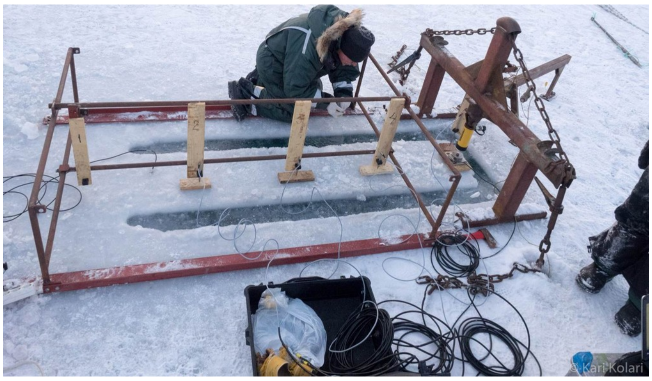

Figure 4. Cantilever beam setup with five extensometers.

Measurement of Young’s modulus was performed on a cantilever beam that was 301 cm long, 53 cm wide, and 51.5 cm thick (Figure 4). Five displacement sensors were placed with offsets {33cm, 103cm, 163cm, 223cm, 281cm} from the root of the beam. Only three points are needed for curvature computation, whereas readings from five sensors are available. The combinations of sensors for computing the curvatures are selected as {234, 125, 134, 135, 235, 245, 345}. The applied force, extensometer readings, and computed Young’s moduli are shown in Figure 5. The average value of all readings in the time span [6.6s, 7s] was calculated to be 3.7 GPa.

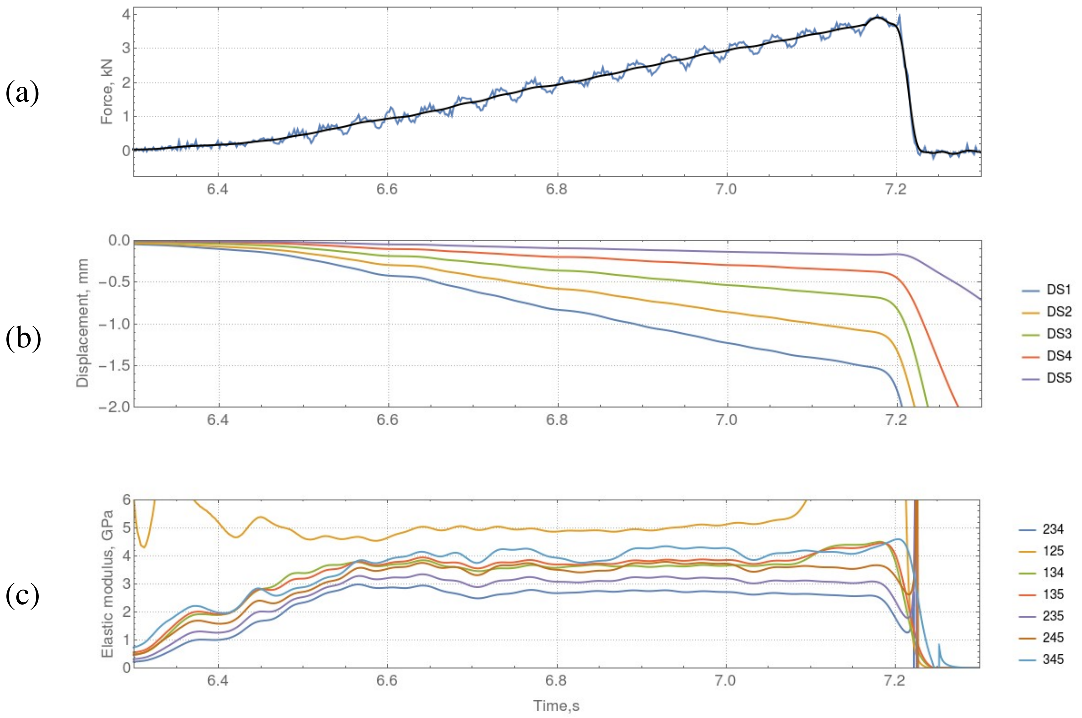

Figure 5. Measured (a) force on the indenter, (b) extensometer readings on the top surface, (c) calculated elastic moduli based on various combinations of sensors.

3. Numerical simulation

The simulation helps to understand the distribution of stress in the beam, deflection of its surface, and other properties that are difficult to observe directly. Unwanted factors, such as vibrations of hydraulic pump and possible bending of the sensor array frame, are excluded from the model, which results in an idealized view of the process. Comparing the simulation results with the experiment may confirm the analysis of the field measurements or hint at possible issues with the experimental setup. Of particular interest is the linear dependence between the extensometer readings. If the readings are linearly dependent, the model can predict their ratios.

In the past, we used a finite element method coupled with cohesive zones to investigate the formation and propagation of cracks in polycrystalline samples (Gribanov, Taylor, and Sarracino, 2018) and beams (Gribanov et al. 2019). The first version of the modeling code was a product of trial and error that used several programming languages for implementation. For simplicity, the code was re-written in C++ and is freely available at the GitHub repository (Gribanov, 2020). Ice is modeled as linearly elastic material, whereas fracture is represented by Park-Paulino-Roesler cohesive zones.

The dimensions of the beam were set identical to the field experiment, i.e., 50 cm thickness, 40 cm width, 83 cm length of the fixed portion, and 130 cm length of the free portion. The tetrahedral mesh, generated by the *Gmsh* library, consists of 30123 elements, 18242 nodes, and 6422 cohesive zones. The placement of cohesive zones is shown in Figure 6a. In comparison with the field test, several simplifications are made. The loading frame is replaced with a standalone indenter that is driven downward at constant velocity (17 mm/s). The interaction between the indenter and the deformable material is a penalty-based collision response, so the actual displacement velocity of the beam is 0.67 mm/s (Figure 7b). The anchors are not modeled in the simulation, which means that the surrounding mass does not participate in the motion. Neither water nor gravity is included in the model. The complete set of parameters is shown in Table 2; their effects on the modeled material are described in the previous work (Gribanov, Taylor, and Sarracino, 2018).

Table 2. Parameters of cohesive zones and elastic elements.

Notation	Description	Value
σ_{max}, τ_{max}	Cohesive strength in normal and tangential directions	230 kPa
φ_n, φ_t	Mode I and II fracture energies	3 J m^{-2}
α, β	Brittleness parameters for shapes of traction-separation curves	4
λ_n, λ_t	Non-dimensional slope indicators in PPR model	0.015
k	Penalty coefficient for collision model	5000
Y	Young's modulus	3.7 GPa
ν	Poisson's ratio	0.3
ϱ	Density of the material	917 kg/m^3

The typical density of freshwater ice, 917 kg/m^3, is used in the simulation, but this value incorrectly predicts the dynamic of the system after development of the fracture. In the experiment, the force decreases from its maximal value to zero in about 1/10th of a second after the fracture. Three factors affect this timing: the spring constant of the loading frame, the total mass involved in the motion, and the damping effect of the surrounding water. It is difficult to estimate the spring constant of the frame and the damping effect because of their combined complexity. Another factor that affects timing is the total mass. In the model, only the geometry of the L-shaped beam is considered. Setting the density higher than the normal density of ice accounts for the influence of the surrounding material. The effect of selecting a larger density is shown in dashed force-time curve in Figure 7a.

(a) (b) (c)

Figure 6. (a) Cohesive zones are shown as triangles on the surface. The fracture occurs at time 0.77 s of the simulation. (b) Modeled vertical displacement of the top surface of the beam before fracture at time 0.755 s. (c) Locations of modeled extensometers are shown as vertical white lines.

The simulation begins with the indenter touching the surface and completes after the beam fractures (Figure 6a). The location and the shape of the fracture are nearly identical to the field observations (Figure 2c). The crack propagates diagonally from the lower-right corner of the channel across the fixed portion of the beam. Figure 6b shows the displacement of the top surface in the form of discretized colored bands before the fracture occurs. When the displacements are small, the shapes of the bands remain unchanged, meaning that the beam behaves as a linear spring, and the surface displacement is proportional to the applied force.

This observation is consistent with the experimental measurements where extensometer readings were linearly dependent.

Modeled “extensometers” were introduced into the simulation at the same locations as the field test placements (Table 1, Figure 6c). They recorded vertical displacement at the surface, and the readings are presented in Figures 7b and 7c. The slopes of displacement curves are increasing until they reach the linear steady state after 0.3 seconds from the beginning. This period is consistent with the experimental observation and reflects the initial transition in load application, i.e., settling the indenter on the ice surface. Once the loading process achieves a steady regime, the readings become linearly dependent with the following coefficients {1., 0.38, 0.19, 0.17, 0.029}. The simulation gives an idealized representation of the process; hence there is no noise in the displacements up until the point of fracture. After the fracture, the modeled extensometer readings do not present any interest as they no longer indicate any deformation.

(a)
(b)
(c)

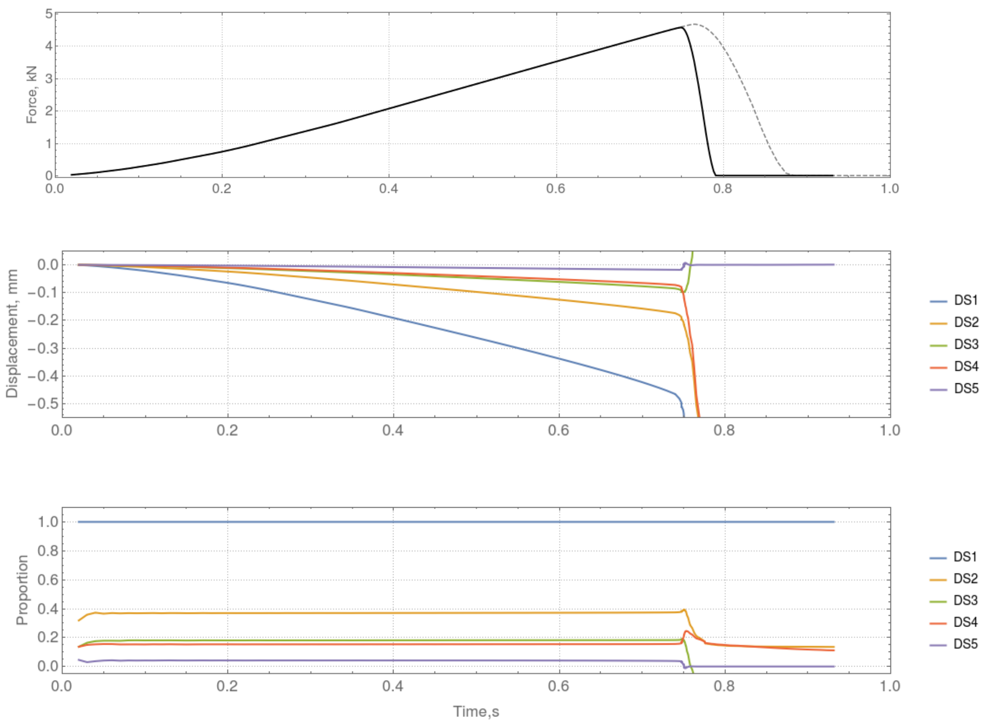

Figure 7. Modeled (a) force on the indenter; solid curve shows the simulation result with normal ice density; grey dashed curve shows the effect of added mass, (b) “extensometer” readings on the top surface, (c) normalized extensometer readings vs. time.

4. Discussion of the results and conclusion

Significant simplification in the numerical model is the absence of the loading frame with the hydraulic cylinder and the separate frame for sensor mounting. The model does not account for the deflection of the surrounding ice, which may be the source of the discrepancies between the recorded and predicted readings.

The model shows that the surface deflection profile is proportional to the applied bending moment, and the extensometer readings are linearly dependent. Experimental measurements from four sensors confirm this prediction, whereas the measurements from DS2 deviate from it. There are several possible explanations for the deviation. First, the behavior of ice may be nonlinear due to its anisotropy or due to the presence of imperfections. Another explanation is the displacement of the frame on which the sensors were installed.

Table 3 compares the extensometer ratios between the experiment and the modeled results. The values from DS2 are consistent by average magnitude. However, the readings of DS3 and DS4 seem to have switched places. This happens in the simulation if a different thickness of the beam is selected. The current thickness is set to 50 cm, but at thickness 70 cm, readings of DS3 and DS4 do switch places, as the overall surface deflection changes. Readings of these two sensors are very close, and slight adjustments of their positions affect the results substantially. Finally, readings of DS5 are not consistent with the model. That sensor is located in the area that is least affected by the overall displacement, and the discrepancy between the predicted value and the experimental measurement should be investigated.

Table 3. Comparison between the extensometer readings in the experiment and in the numerical model.

	DS1	DS2	DS3	DS4	DS5
Experiment	1.00	0.39-0.35	0.16	0.19	0.070
Model	1.00	0.38	0.19	0.17	0.029

In the experiment, the columnar grained S2 ice was used, which has orthotropic elasticity due to its structure. The orthotropy was not considered in the model, which may have added to the discrepancies with the experimental data. The analysis performed in this work leaves several unanswered questions, and more experimental data is needed to answer them definitively. If the anisotropic properties could be definitively related to the surface deflection of the L-shaped beam, this type of test could become an in-situ method of measuring the horizontal and vertical Young's moduli without physically extracting the samples. Further exploration of this concept is planned.

Acknowledgments
The authors gratefully acknowledge funding from the Natural Sciences and Engineering Research Council of Canada (NSERC) and Arctic offshore and coastal engineering in changing climate (AOCEC) program that allowed to perform this work. The authors also acknowledge the assistance of Evgeny Karulin, Aleksandr Sakharov, and Peter Chistyakov in the conduction of the experiments. The photographs in this work are included with the permission from Kari Kolari.

References

Gribanov, I. 2020. Github Repository. https://github.com/igorg520b/icyFlow2.

Gribanov, I., Marchenko, A., Murdza, A., Taylor, R., and Sarracino, R., 2019. Investigation of Mixed Mode Fracture of L-Shaped Sea Ice Beams. Proc. 25th International Conference on Port and Ocean Engineering under Arctic Conditions.

Gribanov, I., Taylor, R., and Sarracino, R., 2018. Cohesive Zone Micromechanical Model for Compressive and Tensile Failure of *Polycrystalline Ice. Engineering Fracture Mechanics* 196 (June), 142–56.

Karulin, E., Marchenko, A., Sakharov, A., Karulina, M., Chistyakov, P., and Onishchenko, D., 2019. Features of Determining the Ice Flexural Strength and the Elastic Modulus

Based on Floating Cantilever Beam Tests. Proc. 25th International Conference on Port and Ocean Engineering under Arctic Conditions.
Karulina, M., Karulin, E., and Marchenko, A., 2013. Field Investigations of First-Year Ice Mechanical Properties in North-West Barents Sea. Proc. International Conference on Port and Ocean Engineering under Arctic Conditions.
Murdza, A., Marchenko, A., Sakharov, A., Chistyakov, P., Karulin, E., and Karulina, M., 2016. Test with L-Shaped Cantilever Beam for Complex Shear and Bending Strength. Proc. 23rd IAHR International Symposium on Ice.

25th IAHR International Symposium on Ice
Trondheim, 23 – 25 November, 2020

Ice properties in ISO 19906's second edition

Knut V. Høyland
Dep. Civil and Env. Eng. NTNU
knut.hoyland@ntnu.no
Ekaterina Kim
Department of Marine Technology
Norwegian University of Science and Technology (NTNU)
Otto Nielsens vei 10, 7491 Trondheim, Norway
ekaterina.kim@ntnu.no
Aleksey Marchenko
Arctic Technology Dep. UNIS
alekseym@unis.no
Ben Lishman
London South Bank University
b.lishman@bristol.ac.uk
Paul D. Barrette
Offshore, Coastal and River Engineering (OCRE)
National Research Council of Canada (NRCC)
paul.barrette@nrc-cnrc.gc.ca

The second edition of ISO 19906 Arctic Offshore structures was issued in 2019. In this paper, we describe the changes that were made to sections dealing with ice properties and discuss the relationship between them and ice actions. The changes can be divided into five groups: 1) Physical properties (temperature, density and porosity), 2) modulus of elasticity, 3) ice friction, 4) mechanical properties in level ice (uniaxial and multi-axial compressive strength, flexural strength and borehole jack strength), and 5) the keel properties of first-year ridge (Mohr-Coulomb, macro-porosity). The standard is written in such a way so that simple approaches in design guidelines complement more elaborate models. Both currently face at least three challenges, namely, the lack of full-scale data, a complicated physical environment, and a lack of understanding of the deformation mechanisms taking place in the ice.

1. Introduction

The first international standard for ice actions on Arctic offshore structures was issued in 2010 and its second edition was published in 2019 (ISO 19906, 2019). Ice engineering and mechanics are important components of this standard. These are a relatively small niche in terms of expertise in science, technology, and engineering. Such that a stakeholder with an ocean engineering background, but without special ice competence, could find it challenging to use the standard if it is not adequately adapted for such users. Instead of developing simple engineering formulas to be used in design, there is a tendency in ice engineering to focus on complicated processes in the ice. The standard aims instead at a balance between presenting simple practical solutions and more elaborate theoretical and empirical solutions. The advantage of the simple formulas is that they can easily be used in probabilistic approach, and provide general guidance. Whereas the advantage of more advanced numerical and scaled models is that they include more physical phenomena and are often based upon well-established physical laws.

2. Purpose and scope of this paper

In this paper, we summarize the salient changes that were made to ice properties that occurred from ISO 19906's first edition (2011) to its second one (2019). We first describe general cases of ice action on structures, and briefly explain the importance of these properties. We then proceed with a summary of the changes in the properties themselves (temperature, density, porosity), followed those of level ice (strength properties) and rubble properties in the unconsolidated first-year ridge keels. We close off with a short discussion and a conclusion.

3. Ice actions in ISO 19906

ISO 19906 addresses ice actions on fixed and floating structures, global and local loads, and sloping and vertical waterlines. However, it has two basic cases: a) ice interaction with a vertical wall inducing crushing failure and b) ice interaction with a sloping wall or conical structure and corresponding flexural ice failure. The recommendations for these two cases illustrate diametrically opposite ways of dealing with ice actions and ice properties. In the first case, no ice properties are included, and in the second case, a number of physical processes and corresponding ice properties are identified.

The discussion in the following paragraphs pertains specifically to limit-stress ice-structure interactions, which occurs when there is sufficient energy or driving force to envelop the structure and generate ice actions across its total width. The limit energy interactions such as ice/icebergs impacts are not addressed herein.

For ice against vertical structures, the standard presents a simple empirical equation for the estimation of a deterministic design ice force (F_G) on fixed vertical structures exposed to drifting level ice where the driving forces are high enough to keep the ice drift velocity almost constant so that limit stress scenario occurs:

$$F_G = h_i \cdot w \cdot p_G = h_i \cdot w \cdot C_R \left[\left(\frac{h}{h^*} \right)^n \left(\frac{w}{h} \right)^m + f_{AR} \right] \qquad \textbf{[1]}$$

In that equation, p_G is the global average ice pressure [MPa], w is the projected width of the structure [m], h_i is the thickness of the ice sheet [m], h^* is a reference thickness of 1 m, m is an empirical coefficient equal to -0.16, n is an empirical coefficient equal to $-0.50 + h/5$ for $h < 1.0$ m, and equal to -0.30 for $h \geq 1.0$ m, C_R is the ice strength coefficient [MPa] (note that

C_R is not the same as the uniaxial compressive strength of ice!). Finally (new to the 2019 edition), f_{AR} is an empirical term taken from Määttänen and Kärnä (2011) and given by:

$$f_{AR} = e^{\frac{-w}{3h_i}} \sqrt{1 + 5\frac{h_i}{w}} \quad \textbf{[2]}$$

Equation 1 acknowledges a size effect as the global pressure decreases for increasing ice thickness and increasing structure width. However, it does not try to express any of the physical and mechanical processes that take place and govern this process, nor any ice properties.

For ice failing against a sloping wall or conical cross-section, the approach identifies a number of different physical mechanisms, such as bending and breaking of the ice cover, sliding against structure wall, ice-ice friction, etc. For this type of scenarios, unlike the previous one, specific ice properties such as the flexural strength, ice-ice friction coefficient and ice-structure friction coefficient are factored in. The equations are quite long and will not be reproduced here. For more information, the reader is referred to section A.8.2.4.4 in the standard. Interestingly, one of the most critical parameters is also one of the most difficult to quantify: pile-up height.

Scale-model testing in basins is an important part of ice engineering. It requires identification of relevant full-scale (in-situ) ice properties, theoretical scaling (dimensionless ratios, etc.) and scaled-down ice properties in the basin. This is not trivial, and here we will only underline the difference between scaling of flexural and compressive ice failure. The flexural strength is an integrated property over the full ice thickness, and it is relatively easy to compare full-scale and basin scale values. Compressive failure is far more difficult because the same tests cannot (or only with great difficulties) be done in the field and in the basins.

4. Changes in ice properties in the second edition

In this section, we will summarize the changes that occurred in the new edition which relate with ice properties, both physical and mechanical. These are mostly dealt with in 8.2.4, 8.2.8, and 6.5.1, i.e. in the normative part of the standard, and in their corresponding clauses in the informative part. Some changes did occur in the normative part. For instance, in 'Global ice actions' (8.2.4), it is stated that ice-on-ice friction shall be considered. Also, for evaluation of local ice action (8.2.5), ice encroachment shall be considered. Otherwise, most of the changes are in the informative part.

Physical properties – temperature, density, and porosity

The ice temperature is by far the most important physical characterization of sea ice, and together with ice salinity and air fraction it largely governs the ice's physico-mechanical properties. Sea ice is a multiphase material consisting of ice, brine, and air. The ice and brine are often assumed to be in thermal equilibrium so that any change in temperature causes some melting or freezing and a corresponding change in the brine (and corresponding ice) fraction. By measuring the salinity, temperature, and density of an ice sample the air and brine fractions can be estimated with the equations given by Cox and Weeks (1983) for ice colder than -2˚C, and by Leppäranta and Manninen (1988) in warmer ice. Both these equations are derived through first-order principles, but one may also find many empirically-derived relationships between brine fraction, ice salinity, and temperature that may fit over a limited range.

The density is an important parameter, especially in scenarios where the ice buoyancy is vital, such as those involving a ship, floater interaction with ice and ridges and ice rubble interaction. In these cases, it is the difference between ice and water density that is important, and this magnifies any uncertainty in ice density determination. Ice is driven under the hull, creating buoyant forces and corresponding frictional resistance. In the case of an ice ridge, ice density, water density, and rubble porosity can be used to determine the effective buoyancy of its keel. If applying estimates for the ice density in ice action calculations, the uncertainty regarding density can have a significant impact on the results. As the rubble volume can change during a ridge-structure interaction event, the ice rubble density can also change. A particular care is needed for modelling of density in ice model basins, due to deviations between water density and ice rubble density from full-scale magnitudes. Validated numerical methods can be used to assess these sensitivities.

There are several ways of measuring ice density – the most commonly used in the field is direct mass/volume determination. The ice mass is relatively easy to measure, but the volume is challenging. The second edition acknowledges there are alternative methods, but points out they are more difficult to perform in the field. It also raises the importance of this parameter in assessing rubble porosity, particularly in model-scale studies (numerical methods can be used to assess these sensitivities). An alternative approach, not mentioned in the standard, is the hydrostatic method, where the ice mass is measured in air and submerged in a fluid. This method avoids the uncertainty of a direct estimation of volume and achieves a much better accuracy and precision (Pustogvar and Kulyakhtin, 2016). The method takes more time, but should be considered in future editions of the standard.

Modulus of elasticity

The elastic modulus of ice can be either the *'true'* (Young's, E) or *'effective'* (quasi-static, E_f) elastic moduli. Young's modulus of ice is representative of deformation mechanisms of a purely elastic, time-independent nature, and is obtained from dynamic measurements (e.g. acoustic), involving very high deformation rates. However, ice naturally exists at a temperature that is very close to its melting point, which is why the concept of an effective modulus becomes relevant. It implies the deformation is not only elastic, but also comprises time-dependent recoverable strain, and non-elastic non-recoverable deformation (creep). The effective modulus is significantly lower at lower strain rates, in most scenarios of engineering relevance (Sinha, 1978, 1982). The 2019 edition of ISO 19906 explicitly acknowledges this challenge by recommending usage of an 'effective' modulus and 'effective' Poisson ratio. The 2019 edition offers this equation for guidance, where ν_b is the brine volume fraction and E is given as [GPa]:

$$E_f = 5.31 - 0.436{\nu_b}^{0.5} \qquad \textbf{[3]}$$

The standard also recommends a value of 0.42 for the effective Poisson ratio, and 0.33 for the true Poisson ratio.

Ice friction

The 2010 edition of the standard gave values for the friction of ice on concrete and of ice on steel, at three different sliding speeds. The new standard also includes a discussion of the friction of ice on ice, since this value is included in many models of ice-ice interactions, including discrete element models (see e.g. Ranta et al., 2018). The dependence on sliding speed was made explicit: "*Ice-ice friction decreases with increasing sliding speed, from a maximum of $\mu = 1$ at $v_s = 10^{-6}$ m/s to $\mu = 0,02$ at $v_s = 1$ m/s, with $\mu = 0.1$ at $v_s = 10^{-2}$ m/s*" (ISO 19906, 2019, p. 260). This description is the standard's attempt to concisely summarise the experiments discussed in Maeno et al. (2003). In many situations, either the sliding speed is not known or the sliding speed varies within the model, in which case a single friction coefficient is needed. For these situations, the standard recommends using $\mu = 0.1$. In models where it is possible to include more complexity, the standard notes that temperature and memory effects (i.e. previous sliding history) may be relevant, and directs users to Schulson and Fortt (2012) for further information. Understanding how these second-order friction effects (e.g. dependence on memory, temperature, sliding speed) affect models of ice dynamics is an ongoing research topic (see e.g. Lishman and Polojärvi, 2015).

Two further changes have been made to the discussion of friction in the standard. First, a statement that "*the static friction coefficient can be up to five times greater than the kinetic friction coefficient at 0.1 m/s*" has been amended to read "*the static friction coefficient has been measured to be up to five times greater than the kinetic friction coefficient at 0.1 m/s, and higher ratios are possible*" (ISO 19906, 2019, p. 269). This reflects recent research showing that static friction can continue to increase until it approaches the shear strength of level ice (see e.g. Scourfield et al., 2015). When updating this change, it was felt that the original statement suggested an upper limit on the static friction of ice, and that this statement is contradicted by experiments and by intuition. Taken as originally written, the statement could have led users to underestimate potential ice forces due to friction. Second, a suggestion was added for users of the data on ice-concrete and ice-steel friction, that if sliding speed is not known, a value of 0.01 m/s should be used for this parameter. This sliding speed leads to the highest listed values of ice friction, which in turn should lead to conservative design in situations where sliding speeds are not known.

The changes made, then, can be summarised as: 1) Inclusion of data on ice-ice friction; 2) removal of a potentially misleading reference to an upper limit on static friction; and 3) inclusion of a suggested single value for friction of ice on steel and ice on concrete. The rest of the discussion of friction, and the recommendations to users, have otherwise been left unchanged.

Level ice

The standard focusses mostly on properties that can be measured in-situ, i.e. in the field. The most commonly used approach is the small-scale uniaxial compressive strength (σ_c) test, the flexural strength (σ_f) test and the borehole jack (BHJ) strength test. These three different tests are a compromise between 1) testing something with a clear theoretical basis, which can be used effectively in mechanical modelling (σ_c), and 2) testing something that simulates the state of the ice in a real interaction scenario (BHJ or σ_f).

The uniaxial compressive strength of ice is the most commonly measured mechanical property in the field, because it is manageable and it is readily applicable to scenarios involving a narrow structure, taking into account a relation to ice actions for limits stress crushing (Korzhavin, 1962). When the structure gets wider, other effects related with the aspect ratio come into play and the relationship between ice action and σ_c is lost. A sufficient number of tests are performed, so as to be able to obtain trends of the uniaxial compressive strength versus ice porosity. The new edition of the standard includes the equations of Moslet (2007), which are based on porosities up to 0.38. In contrast, the equations of Timco and Frederking (1990) had data with porosities up to 0.19. The equations derived from Moslet (2007), for horizontally- and vertically-loaded sea ice uniaxial strength [MPa] respectively, are:

$$\sigma_c = 8\left(1 - \sqrt{\frac{\nu_t}{0.7}}\right)^2 \qquad \textbf{[4]}$$

$$\sigma_c = 24\left(1 - \sqrt{\frac{\nu_t}{0.7}}\right)^2 \qquad \textbf{[5]}$$

In these equations, ν_t is the total porosity. **Figure 1** is a corresponding plot. As this figure shows, the variability is large and the equation express some kind of upper limit. It would perhaps be more useful to define an average function and study the spread.

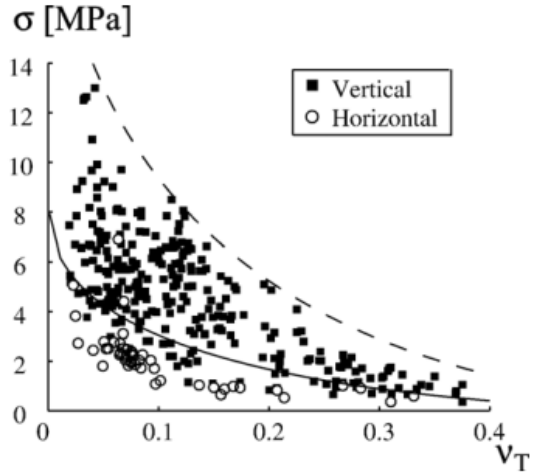

Figure 1. Uniaxial compressive strength plotted as a function of total porosity (from Moslet, 2007, Fig. 3).

The flexural strength is usually defined by linear elastic beam theory with homogeneous material properties. Because it is an integrated property (averaged over the whole ice thickness), it should not be compared directly with the tensile strength, even though the values are similar and linked. The beam size requirements are such that the water foundation effect is accounted for. A possible size-effect was also examined, but could not be documented from the published literature, e.g. Parsons et al. (1992) were not able to clearly demonstrate its existence.

The text about multi-axial behaviour was rewritten so as to explain that there is no such thing as multi-axial strength, and that a three-dimensional failure envelope is necessary to analyse and use data from multi-axial tests. **Figure 2** shows an example of a failure envelope, obtained from the yield stress for various confining conditions. These parameters typically have a large variability, such that a large number of tests in the field are required.

Both tensile and shear strength can be used to establish failure envelopes. Direct testing of tensile strength has mostly been done in the laboratory, although an increasing number of these tests done in the field are also reported. The text is unchanged from the 2010 edition. As for shear strength, few results have since been published. One challenge with these tests is to be able to carry them out with zero normal stress on the sample.

The borehole jack is used in-situ and the ice is multi-axial state of stress. This test is more representative of an ice crushing scenario than is a uniaxial test. However, it is difficult to use these data for mechanical modelling because the stresses spread and dissipate in the ice sheet. Several failure modes are typically observed, and the definition of the borehole strength, $\underline{p_u}$, depends on the failure mode (Sinha et al., 2012, Justad and Høyland, 2013, Johnston, 2014). When expressed over the full thickness of the ice, the depth-averaged borehole strength ranges from 3 MPa to 30 MPa for FY sea ice, and up to 34 MPa for MY sea ice over the range of ice temperatures tested. Strengths of 49 MPa have been measured in cold MY ice (Johnston, 2014, Johnston, 2016).

Ice fractures frequently when interacting with structures, but so far neither of the ice action models in the standard requires fracture properties. The discussion around fracture properties was limited to fracture toughness. The text was modified to express the scientific disagreement on whether or not a one-parameter model (fracture toughness) can be useful.

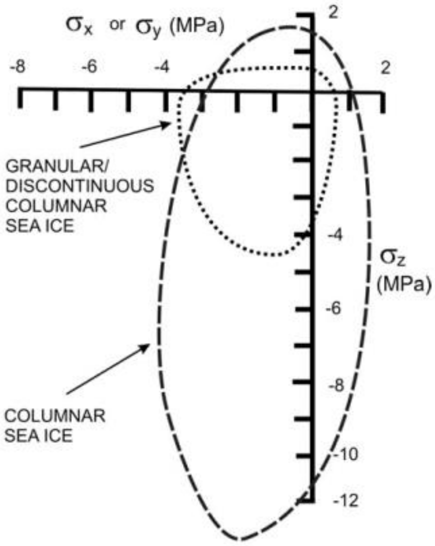

Figure 2: Example of a failure envelope for two ice types (from Timco and Weeks, 2010, Fig. 13). Stresses (σ) along x, y and z are taken into consideration. Positive and negative stresses are tensile and compressive, respectively.

First-year ice ridge keels (rubble properties)

In ISO 19906 (2019), the text on ice ridges, or ice rubble properties, has been extended and rewritten, focussing on friction angles, cohesion and macro-porosity through explaining some of large variability reported is due to systematic seasonal (temporal) and spatial variations. We have changed the title to reflect that it only deals with the properties of *the unconsolidated part of first-year ridges*. The section starts with describing the two approaches to describe the material; so-called *continuous* and *discrete*. Both have their advantages, but since the formulas describing the load (A.2.8.4.5.1, Eq. A.8.50) are based on the continuous approach and require the two material properties – cohesion and friction angle – as well as the macro-porosity, the text deals only with these three parameters.

The two-parameter Mohr-Coulomb model does not include volumetric compressibility, but in reality, the friction angle depends on the volumetric compression. In experiments, one will find different friction angles for the same material if the boundary conditions give different volumetric compression (Kulyakhtin and Høyland, 2015). The range of suggested values are modified to 24-45 degrees. The cohesion decreases with depth, and is probably at maximum just below the consolidated layer. This is partly due to stronger freeze-bonds because of higher confining stress, perhaps also due to lower macro-porosity higher up in the keel. Finally, the reported values of cohesion from both laboratory and field tests seem to increase with increasing block thickness. It is not clear why, but the standard suggests that it might be the box size / block size ratio that actually gives the variability in reported cohesions.

Macro-porosity values range from about 10% to 50% and the new text suggests that is mostly due to systematic variations. These are reported somewhat differently from the Baltic Sea (low salinity water) and other more saline waters. In saline ridges, it seems to increase from a minimum value just below the consolidated layer, while Baltic ridges are reported to have a mid-keel minimum. We do not know why. The melting also seems to be different as saline ridges are reported to have macro-porosities down to 10% in early summer, whereas no such values were measured in the Baltic. In summary, it looks like the differences between low-saline Baltic and saline ridges occur in the melt season. This corresponds to the fact that the growth rate for freshwater ice and saline ice is approximately equal, but the melting rate is quite differently.

5. Discussion

As mentioned in the introductory section, the standard is written in a way that simple approaches in design guidelines complement more elaborate models. Both currently face at least three challenges:

- A lack of full-scale data, particularly a combination of ice loads, structural response, ice properties, and failure modes.
- A complicated physical environment – the ice field is neither stationary, nor ergodic, and the ice properties are many and uncertain (compared, for instance, to waves where water density and viscosity are well known). This is related with the first challenge.
- A lack of understanding of how small-scale mechanical properties and failure mechanisms (cracking, pressure melting, solid-state recrystallization, etc.) scale-up and govern ice actions. Such an understanding of floating ice faces difficulties not encountered in other fields of structural and mechanical engineering, such as time-independent parameters (Young's modulus) which have de facto values (in these other fields). The reason is that ice is a high-temperature material, i.e. it naturally exists at very high homologous temperatures, such that, even at high engineering strain rates, time-dependent deformation processes occur alongside the pure elastic response (Sinha, 1978, 1984). To compensate, 'effective' values have to be resorted to, which at times may either be educated guesses or are used as a curve-fitting parameter.

Nonetheless, significant progress has been achieved in this second edition. The new guidance provided in section A.8.2.8.2 on ice strength under multi-axial stress state is an example of such an improvement. A failure envelope is much better suited to describe ice strength under multi-axial loading conditions and to analyse and use data from multi-axial testing. Moreover, the new standard suggests a systematic seasonal variability in properties, and this can be useful when modelling the load for different times of the year. In a probabilistic modelling, this will reduce the uncertainty and help to estimate better ridge load distributions.

There are gaps in information also. For instance, several properties that are discussed in the standard (e.g. the strength of granular ice) are not incorporated into ice load calculations using the analytical methods provided by the standard. This could mean that, if numerical approaches are used, the properties that are provided may be insufficient to model the constitutive response of ice. Moreover, the role of damage mechanics in ice failure and fracture is not discussed. Uniaxial testing requirements have been established, but what about those for biaxial and triaxial testing?

6. Conclusions

The second edition of ISO 19906 Arctic Offshore Structures was issued in 2019 and we have described the changes in the sections dealing with ice properties and discussed the relationship between these properties and ice actions – the ice properties combined with structural characteristics govern the ice actions. The ice environment is more complex to characterize than the corresponding ocean environment, i.e. wave, current and wind regimes. Fundamentally, ice is characterized by a much larger spatial and temporal variability, and ice properties are more challenging to measure, estimate or monitor, compared to human-made engineering materials. Any progress in the development of ISO 19906 for assessing ice actions will rely on a combination of:

- More full-scale data on ice-structure interactions.
- Better quantification and understanding of fundamental ice properties, both physico- and thermo-mechanical, as well as adequate statistical representations.

Acknowledgments
The authors of this paper were part of a task group responsible for coordinating the review of the 2010 edition with regards to the physical and mechanical properties of ice and related aspects. We would like to thank R. Frederking for his role as lead of TP2a, the technical panel that addressed ice actions, and everyone else having contributed with their comments and suggestions to the 2019 edition. The authors also wish to thank two anonymous reviewers for their comments on a draft.

References

Cox, G.F.N. and Weeks, W.F., 1983. *Equations for determining the gas and brine volumes in sea ice samples*. Journal of Glaciology, 29(102), p. 306-316.

CSA/ISO 19906, 2011. *Petroleum and Natural Gas Industries — Arctic Offshore Structures*. Canadian Standards Association, Toronto, Canada.

ISO 19906, 2019. *Petroleum and natural gas industries — Arctic offshore structures*. International Standard Organization, Geneva.

Johnston, M., 2016. *Compendium of NRC property measurements on first-year Ice, old Ice and ice island ice (2000 – 2015): Vol. I.* OCRE-TR-2016-009. National Research Council of Canada. Ottawa.

Johnston, M.E., 2014. *A decade of probing the depths of thick multi-year ice to measure its borehole strength*. Cold Regions Science and Technology, 99, p. 46-65.

Justad, J.A. and Høyland, K.V., 2013. *The UNIS-borehole jack: Description, experiments 2012 and a refined classification system*, Proceedings of the 22nd International Conference on Port and Ocean Engineering under Arctic Conditions (POAC), Espoo, Finland.

Korzhavin, K.N., 1962. *Vozdeystviye l'da na inzhenernryye sooruzheniya [Action of ice on engineering structures]. Novosibirsk, Izdatel'stvo Sibirskogo Otdel, Akademiye Nauk SSSR. [English translation: U.S. Cold Regions Research and Engineering Laboratory. Draft Translation 260, 1971.] Action of ice in engineering structures*.

Kulyakhtin, S. and Høyland, K.V., 2015. *Ice rubble frictional resistance by critical state theories*. Cold Regions Science and Technology, 119, p. 145-150.

Leppäranta, M. and Manninen, T., 1988. *The brine and gas content of sea ice with attention to low salinities and high temperatures*. Finnish Institute of Marine Research. Helsinki, Finland.

Lishman, B. and Polojärvi, A., 2015. *2D DEM of ice rubble: The effect of rate-dependent friction*, Proceedings of the 23rd International Conference on Port and Ocean Engineering under Arctic Conditions (POAC), Trondheim, Norway.

Määttänen, M. and Kärnä, T., 2011. *ISO 19906 Ice crushing load design extension for narrow structures*, Proceedings of the 21st International Conference on Port and Ocean Engineering under Arctic Conditions (POAC), Montreal, Canada.

Maeno, N., Arakawa, M., Yasutome, A., Mizukami, N. and Kanazawa, S., 2003. *Ice-ice friction measurements, and water lubrication and adhesion shear mechanisms*. Canadian Journal of Physics, 81, p. 241-243.

Moslet, P.O., 2007. *Field testing of uniaxial compression strength of columnar sea ice*. Cold Regions Science and Technology, 48, p. 1-14.

Parsons, B.L., Lal, M., Williams, F.M., Dempsey, J.P., Snellen, J.B., Everard, J., Slade, T. and Williams, J., 1992. *The influence of beam size on the flexural strength of sea ice, freshwater ice and iceberg ice*. Philosophical Magazine A, 66(6), p. 1017-1036.

Pustogvar, A. and Kulyakhtin, A., 2016. *Sea ice density measurements. Methods and uncertainties*. Cold Regions Science and Technology, 131, p. 46-52.

Ranta, J., Polojärvi, A. and Tuhkuri, J., 2018. *Limit Mechanisms for Ice Loads on Inclined Structures: Buckling*. Cold Regions Science and Technology, 147, p. 34-44.

Schulson, E.M. and Fortt, A.L., 2012. *Friction of ice on ice*. Journal of Geophysical Research, 117, p. B12204.

Scourfield, S., Sammonds, P., Lishman, B. and Marchenko, A., 2015. *The effect of ice rubble on ice-ice sliding*, Proceedings of the 23rd International Conference on Port and Ocean Engineering under Arctic Conditions (POAC), Trondheim, Norway.

Sinha, N.K., 1978. *Short-term rheology of polycrystalline ice*. Journal of Glaciology, 21(85), p. 457-473.

Sinha, N.K., 1982. *Constant strain- and stress-rate compressive strength of columnar-grained ice*. Journal of Materials Science, 17, p. 785-802.

Sinha, N.K., 1984. *Intercrystalline cracking, grain-boundary sliding, and delayed elasticity at high temperatures*. Journal of Materials Science, 19, p. 359-376.

Sinha, N.K., Shkhinek, K. and Smirnov, V., 2012. *On borehole indentor (BHI) measurements and analysis*. Cold Regions Science and Technology, 76-77, p. 109-120.

Timco, G.W. and Frederking, R.M.W., 1990. *Compressive strength of sea ice sheets*. Cold Regions Science and Technology, 17, p. 227-240.

Timco, G.W. and Weeks, W.F., 2010. *A review of the engineering properties of sea ice*. Cold Regions Science and Technology, 60, p. 107-129.

IAHR AIRH

25th IAHR International Symposium on Ice

Trondheim, 23 - 25 November 2020

Field Tests of Ice Compressive Strength Using Thermally Balanced Samples

M. Karulina[1], E. Karulin[1], A. Marchenko[2], A. Sakharov[3], P. Chistyakov[3], A. Sliusarenko[4]

[1]*Krylov State Research Centre, St.-Petersburg, Russia*

[2]*The University Centre in Svalbard, Longyeabryen, Norway*

[3]*Lomonosov Moscow State University, Moscow, Russia*

[9]*Soft Engineering, Kiev, Ukrain*

for.marina.m.k.@gmail.com

The compressive strength of sea ice is one of the primary mechanical ice properties. This parameter can be found by tests on small (10 to 20 cm) samples picked from different layers across the ice sheet thickness as well as full-scale tests where the compressive ice strength is referred to the full ice thickness. Full-scale tests with loading of floating ice across its full thickness are preferable for compressive ice strength evaluations but involve more technical challenges in the field compared to tests on small-scale samples. However the relationship between the ice compressive strength values obtained by small- and full-scale tests is not yet sufficiently understood and needs further investigations. Sea ice has inhomogeneous structure, temperature and brine content across its thickness. The problem with strength evaluation procedures based on small samples picked from different horizontal layers of ice is that these samples fail to keep the layer-specific temperature of ice. This paper describes a special-purpose experimental technology that has enabled researchers to maintain the temperature of small-scale ice samples as close as possible to the original temperature up to compressive ice strength tests. These tests provided compressive strength distribution curves across ice thickness, and thus obtained average integral values of ice compressive strength are compared with the data from full-scale tests.

1. Introduction

Ice compressive strength is to be obtained to assess ice loads on offshore structures when a failure due to compression is the primary type thereof failure. One of two below methods is generally used for direct estimation of ice compressive strength in-situ:

- uniaxial compressive strength test on ice specimen afloat over the whole ice thickness in horizontal direction (full-scale tests);
- evaluation of ice strength based on uniaxial compression tests of small samples drilled off various horizontal ice layers (small-scale tests).

Indirect evaluation methods for full-thickness ice compressive strength are based on the below tests:

- Indentation tests of vertical cylinder into ice sheet (Karulina et al., 2013);
- loading of beam with two fixed ends with horizontal force applied mid-length (Marchenko et al., 2015).

Compression tests of ice sample over the whole ice thickness are labor-intensive and need powerful equipment. Application of small samples taken from various horizontal ice layers for the experiments makes the task technically easier. Alongside with that other issues are here:

- how can we maintain temperature and salinity of samples obtained from different layers up to uniaxial compression tests?
- what is the coincidence accuracy between ice compressive strength obtained with small samples and values thereof derived during direct measurements of strength over the whole ice thickness?

As well as other ice characteristics ice compressive strength depends on a number of factors: ice temperature, salinity, porosity, strain rate, etc. The inhomogeneity of these parameters over the ice thickness causes a corresponding change in ice compressive strength through the thickness.

The above dictated main purposes of this study:

1) development and implementation of compression test procedure for small samples ensuring maintenance of temperature and salinity of ice layers they are taken from;
2) experimental study of the ice compressive strength distribution over the ice thickness;
3) comparison of full-thickness ice compressive strength obtained from the tests with small samples and one from the full-scale tests.

This paper describes the offered procedure for uniaxial compressive strength test on small ice samples in-situ ensuring maintenance of samples' temperature as close as possible to the temperature of relevant horizontal layer they were taken from. The experiments were carried out on fast sea ice of Van Mijen fjord, Svalbard, Norway, in March 2019 and 2020. Small samples' strength averaged over ice thickness was compared with direct measurement results for ice strength over the whole ice thickness. The results of the performed tests revealed the discrepancy in ice compressive strength obtained with two above-mentioned methods. It's safe to assume that one of the reasons thereof is the effect of the sample dimensions in the full-scale tests.

2. Background

The necessity to convert from strength values obtained in small-scale tests to ice strength over the whole thickness is primarily dictated by inclusion of this parameter into computational formulae to assess ice loads on vertical structures; secondly, this parameter is to be specified for simulation in case model tests in ice basin are carried out. For objective reasons, measurement methods for compressive strength of model ice offered in ISO 19906 (2019) do not include compression tests on small samples.

In passing to ice full-thickness compressive strength the results of small-scale tests may be used in a number of ways. As consistent with Russian regulatory document SP 38.13330 (2018) root-mean-square value of ice compressive strength taken from various ice layers shall be defined to assess ice compressive strength using formula:

$$\sigma_c = \left[\frac{1}{n}\sum_{i=1}^{n}\left(\sigma_{c\_i}\right)^2\right]^{1/2} \quad \textbf{[1]}$$

where σ_{c_i} – uniaxial compressive strength of ice sample from i-th layer, n – number of layers ($n \geq 3$).

Some other researchers use arithmetic mean values of the small-tests results to assess full-thickness ice compressive strength. Major studies aimed at comparison of small samples' strength and full-scale ice strength were carried out in 1980-1981 in Beaufort Sea by EXXON order (Timko and Frederking, 1990). The full-scale tests on uniaxial compressive strength were performed in field condition, while the small-scale tests were carried out in laboratory conditions. The small samples were cut from different horizontal layers, packed in dry ice and shipped to the cold laboratory. One day prior the testing, the small samples were placed in the test room of temperature of relevant ice layer. Fig. 1a presents the scheme of ice fragmentation by layers wherefrom ice samples were taken. Ice strength over the whole thickness σ_c was defined as arithmetic mean value of strength obtained for each layer σ_{c_i} :

$$\sigma_c = \frac{1}{n}\sum_{i=1}^{n}\sigma_{c\_i}. \quad \textbf{[2]}$$

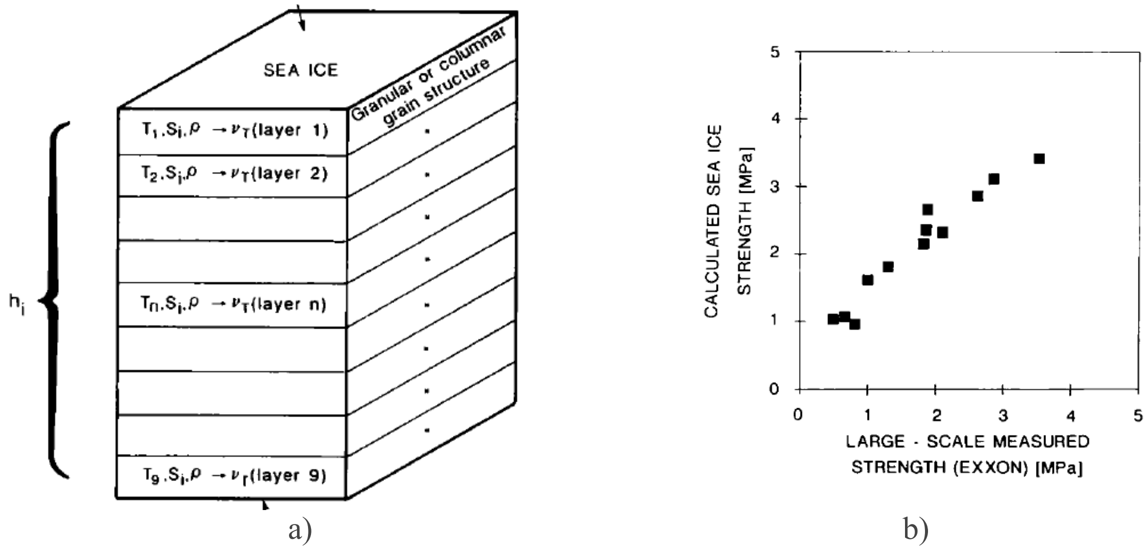

a) b)

Figure 1. a) Ice fragmentation by layers over thickness, and b) comparison of ice compressive strength obtained with small samples using formula (2) and measured during full-scale tests (from Timco and Frederking, 1990)

Strength values computed with formula (2) were correlated with results of compression tests on large-scale ice samples afloat (Chen and Lee, 1986). At that ice thickness achieved 1.2 – 1.8 m, samples were 3.05 m in width and 6.10 m in length. Strain rate $\dot{\varepsilon}$ in full-scale tests varied within 10^{-7}–$5 \cdot 10^{-5}$ s^{-1}. As seen in Fig. 1b close correlation of strength values obtained with two methods was obtained.

Small samples taken from different layers over ice thickness were repeatedly subjected to temperature variations during transportation to the laboratory, while the uniaxial compression tests were carried out at a significant time interval after the samples were taken from ice. This could affect the quality of the obtained results. This paper offers in-situ test procedure using small thermally balanced samples free from the above problems.

3. Tests description

Procedure of the uniaxial compression tests of small ice samples included several stages. First of all several holes were drilled in ice sheet. The depth of the holes was about 5 cm less than ice thickness. Round tubes with watertight bottom cap were inserted into the holes. The tubes with inner diameter of 110 mm and 90 mm were used in 2019 and 2020, respectively. The tubes were left for 24 hours to be frozen in ice. Cylindrical ice samples taken from various layers of ice sheet were used for tests. To obtain the samples block over the whole ice thickness was cut out in ice sheet and then it was extracted from water. Horizontal ice cores approximately 73 mm in diameter were drilled at four different levels over ice thickness (see Fig. 2). Ice thickness was in the range 0.75 – 0.82 м.

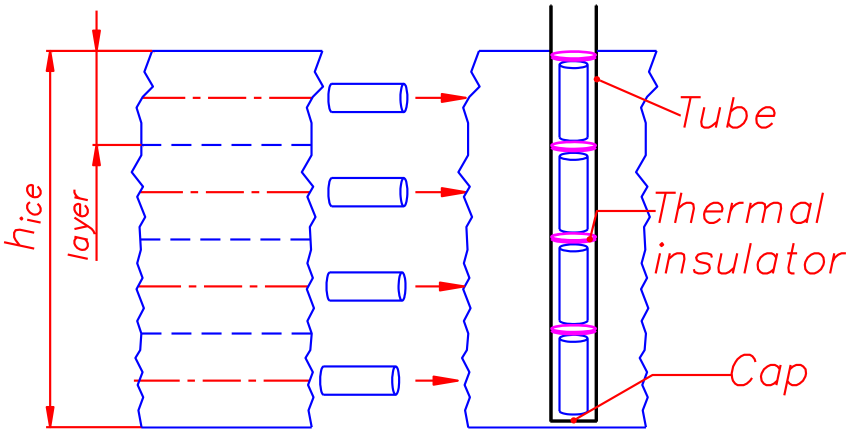

Figure 2. Preparation of thermally balanced ice samples

Two series of the tests were carried out: 3 tubes were used in 2019 and 4 tubes in 2020. Depths of axes of drilled horizontal cores are given in Table 1.

Table 1. Location of layers small samples are taken from

No. of horizontal layer	Distance from ice top to the horizontal axis [mm]	
	Year: 2019	Year: 2020
1	115	100
2	265	300
3	415	500
4	565	700

After the samples of required dimensions (73 mm in diameter and 180 mm in height) were prepared they were placed in plastic bags. The bags were placed into the earlier prepared tubes to depth corresponding to that of layer they were taken from. Vertical spaces between samples were filled with thermal insulation material (see Fig. 2). Then the tubes with samples were left for several days in natural environmental conditions to ensure thermal balance for the whole system (see Fig. 3). Thus the samples maintained the temperature close to that of layer they were taken from.

Figure 3. Workplace with tubes frozen into the ice cover. Next to the red stick is a thermistor string

7 days later the samples were sequentially extracted from pipes and subjected to uniaxial tests. The tests were performed with the Kompis rig designed for the use in the field conditions (Moslet, 2007). Strain rate during all the tests was the same $\dot{\varepsilon} = 10^{-3}\mathrm{s}^{-1}$. The load and displacement in the small scale tests were recorded with sampling frequency of 10 Hz in the field laptop connected to the Kompis rig.

The tests with each sample were carried out as quickly as possible so that the temperature of sample remained stable. Ice temperature in the small scale tests was registered with temperature probe immediately after each test. For the measurement of salinity the ice samples were taken and delivered in a warm place in plastic boxes for the melting. Then salinity of melt water was measured with salinometer Toledo.

Uniaxial compressive strength of a sample from i-th layer was calculated using formula $\sigma_{c\_i} = \frac{4F}{\pi d^2}$ where F is breaking force of the sample, d is the sample diameter.

The setup of full-scale uniaxial compression tests is shown in Fig. 4*a*. For these tests, a floating ice cantilever was cut over the whole ice thickness. The load F is applied to the vertical face of the cantilever by flat plate of 60 cm width and 80 cm height. The equipment has been designed and manufactured under the support of SAMCoT project. The rig shown in Fig. 4b consists of flat plates connected by two horizontal hydraulic cylinders (Enerpack) equipped with displacement sensor and load cell. Upper cylinder A is visible in the Figure and another one is under water. The cylinders are connected to the electrical pump powered by three phase generator 400 V. The stroke of the hydraulic cylinder is 37 cm and it has a load capacity of 300 kN. Recorded after the test data included loads, stroke and oil pressure in each cylinder. The data were recorded with sampling frequency of 100 Hz on the hard disk of the field computer. The test rig ensured average strain rate $\dot{\varepsilon}$ of the sample equal to $\sim 10^{-3} s^{-1}$.

Ice temperature (temperature profile) was registered with thermistor string GeoPrecision placed into the hole drilled in the beam (Fig. 4b). The salinity profile was obtained by measurement of ice samples salinity taken from different vertical layers of ice sheet.

Full-thickness ice compressive strength was calculated from these tests as $\sigma_c = \frac{F}{wh}$ where F is a breaking force of the ice cantilever (sample), w is the sample width, h is ice thickness.

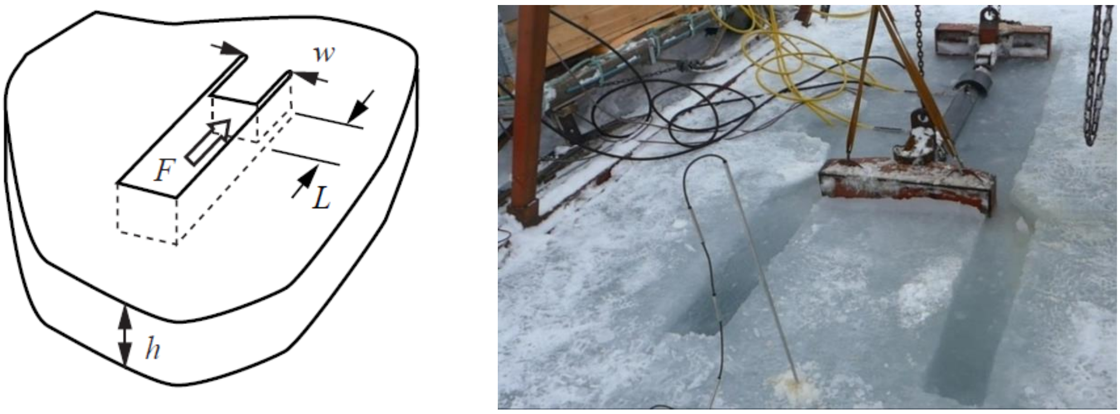

a) b)

Figure 4. Full-scale compression test: a) layout, and b) set-up

To study the ice structure through entire thickness, horizontal and vertical thin sections were made, which were then analyzed in polarized light.

4. Test results and analysis

Table 2 gives uniaxial compression test results for small thermally balanced samples.

Fig. 5 shows temperature distributions of samples in tubes, as well as temperature profile over ice thickness, as measured by a thermistor string near frozen-in tubes (see Fig. 3). In 2019 some samples in tubes were somewhat above their parental ice layers, so the temperature profiles in Fig. 5 (left) are above ice surface. It can be seen that temperature distribution over small samples has rather good correspondence with temperature profile over ice thickness measured by a thermistor string, which confirms the applicability of suggested technology for sample temperature preservation till the moment of compression tests.

The profiles of ice salinity over the ice thickness are given in Fig. 6. It must be noted that, unlike the relatively stable temperature profile, salinity distribution varied from one test site to another. Still, average salinities of ice within the testing area in spring period belong to rather a narrow range of 5–6 ppt. Fig. 6 shows a trend towards a certain decrease in salinity of small samples, which might suggest partial outflow of brine during sample preparation.

The thin section analysis, carried out in the same field studies and given in Marchenko et al. (2020), showed that the upper layer of ice about 20 cm thick had a granular structure, and below it was columnar one. Thus, the top ice samples in each tube had a granular structure, whereas the other three samples below were columnar.

Table 2. Uniaxial compression test results for small thermally balanced samples

Sample Year_No. of tube_ No. of layer (from top)	Salinity [ppt]	Temperature [degree C]	Sigma, [MPa]
2019_1_1	2.82	-12.2	6.88
2019_1_2	5.00	-7.9	4.23
2019_1_3	5.13	-6.0	3.23
2019_1_4	7.45	-3.8	1.94
2019_2_1	2.32	-15.8	7.63
2019_2_2	2.87	-8.8	4.45
2019_2_3	5.08	-6.4	3.68
2019_2_4	3.87	-4.0	2.99
2019_3_1	3.17	-16.9	8.06
2019_3_2	4.70	-12.1	5.24
2019_3_3	6.07	-7.5	3.68
2019_3_4	4.53	-5.1	3.20
2020_1_1	5.82	-17.8	6.08
2020_1_2	3.63	-14.0	5.13
2020_1_3	2.77	-10.4	5.04
2020_1_4	4.16	-6.8	3.95
2020_2_1	5.24	-17.6	5.09
2020_2_2	3.39	-14.9	5.64
2020_2_3	2.79	-10.4	3.78
2020_2_4	3.88	-6.6	2.81
2020_3_1	6.63	-15.5	2.58
2020_3_2	3.73	-11.9	4.63
2020_3_3	3.80	-9.3	5.06
2020_3_4	3.81	-5.9	4.48
2020_4_1	5.54	-15.0	5.48
2020_4_2	4.01	-12.0	4.17
2020_4_3	4.02	-9.3	5.90
2020_4_4	2.62	-6.0	3.33

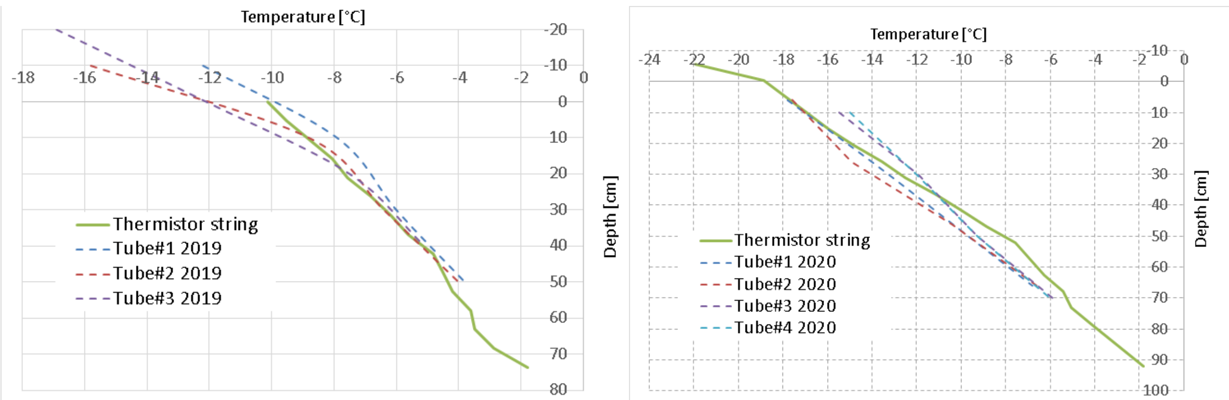

Year 2019 Year 2020

Figure 5. Temperature profiles over ice thickness, as measured on small ice samples and in ice cover using a thermistor string

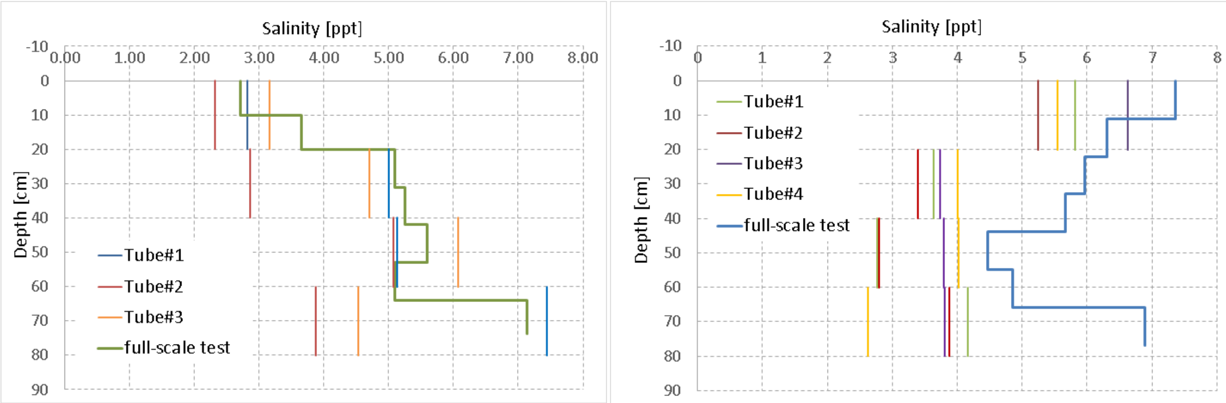

Year 2019 Year 2020

Figure 6. Salinity profiles over ice thickness, as measured on small ice samples and on ice cores drilled from ice cover next to full-scale tests

Fig. 7 shows test results for thermally balanced samples as distribution of uniaxial compression strengths over ice thickness. Some of the samples in tubes were above the surface of ice sheet, so these results only include the data for the samples within the ice sheet. Linear approximations of test data are given as follows:

Year 2019	$\sigma_c(depth) = 5.114 - 0.0565 \cdot depth,$	$R^2 = 0.8728$	**[3]**
Year 2020	$\sigma_c(depth) = 6.645 - 0.0518 \cdot depth$	$R^2 = 0.5815$	**[4]**

Here, $\sigma_c(depth)$ is in megapascals (MPa), and $depth$ is in centimeters (cm). Both test series have shown a trend towards weakening of deeper ice layers. The year 2020 as a whole and its winter and spring time in particular were considerably colder than 2019, which was reflected in ice strength.

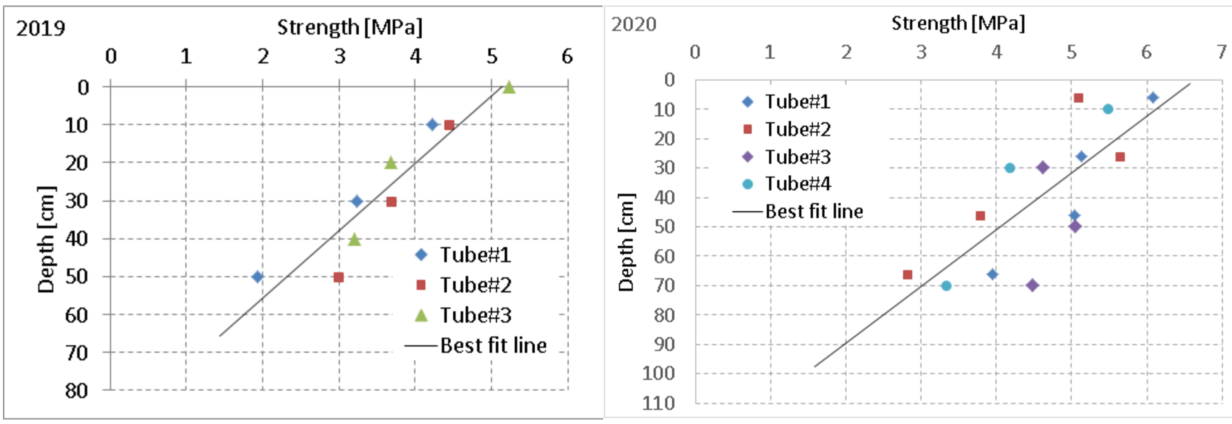

Year 2019 Year 2020

Figure 7. Distribution of uniaxial compressive strength of ice over its thickness as per the test data for thermally balanced samples

It might be interesting to compare the test results for uniaxial compression strength of small ice samples with the estimates obtained as per the expressions recommended by ISO 19906 (2019). For calculations the following expressions suggested by Timco and Frederking (1990) were applied:

for columnar ice $$\sigma_c = 37\dot{\varepsilon}^{0.22}\left(1-\sqrt{\frac{\nu_t}{0.27}}\right) \quad \textbf{[5]}$$

for granular ice $$\sigma_c = 49\dot{\varepsilon}^{0.22}\left(1-\sqrt{\frac{\nu_t}{0.28}}\right) \quad \textbf{[6]}$$

where ν_t is total porosity defined as the sum of the brine and gas fractions. Knowing the salinity, temperature and density of sea ice, the brine and gas fractions were calculated as given in Cox and Weeks (1983) for ice temperatures less than −2°C. Ice density was 900 kg/m^3.

Additional calculations have been performed for columnar ice using a formula suggested by Moslet (2007) and given in ISO 19906 (2019). The formula is based on results of field work on Svalbard in 2004 and 2005 when the same Kompis rig for small-scale compression tests was used. Strain rate during those tests was the same $\dot{\varepsilon} = 10^{-3}\mathrm{s}^{-1}$. The formula provides an upper limit of the compressive strength for horizontally loaded ice samples:

$$\sigma_c = 8\left(1-\sqrt{\frac{\nu_t}{0.7}}\right)^2. \quad \textbf{[7]}$$

The results of this comparison are shown in Fig. 8. Calculated estimates mostly demonstrate a good correlation with experimental results obtained in presented research. Considerable discrepancies were found on rather cold (below -10°C) samples.

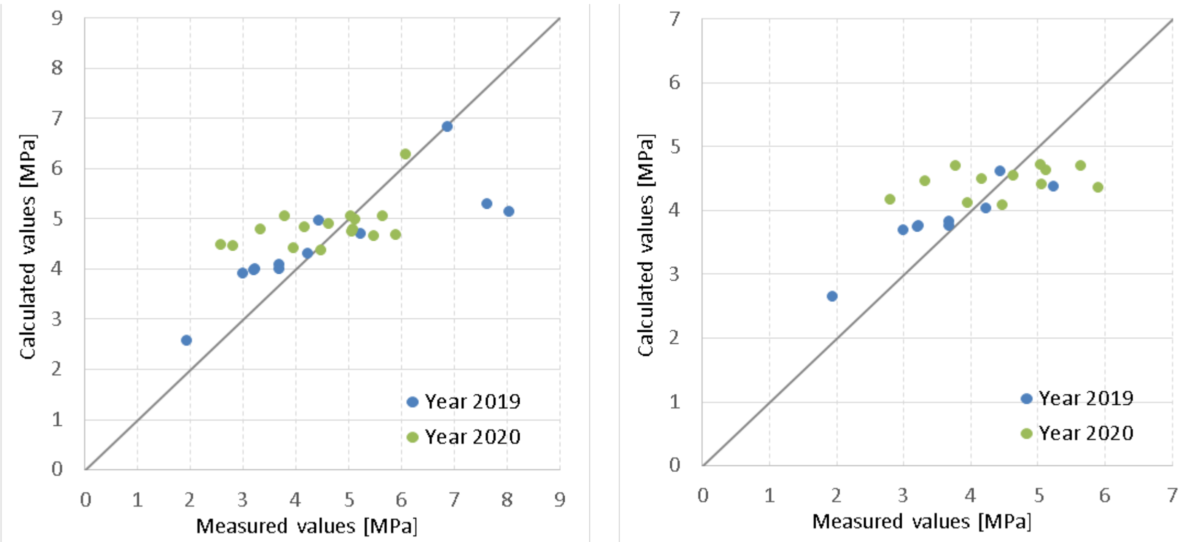

a) Calculation as per formulas [5] and [6] (Timco and Frederking, 1990)

b) Calculation as per formula [7] (Moslet, 2007)

Figure 8. Comparison of small-tests results and calculations based on ISO 19906

Expressions [5], [6] and [7] make it possible to estimate uniaxial compression strength of ice samples in the assumption that their properties, like structure, temperature, salinity, are uniform. As mentioned in Løset et al. (2006), these expressions do not yield ice compression strength over its entire thickness, so they are not suitable for ice load estimates. Two main factors must be taken into account when processing results of full-thickness uniaxial compression tests of ice samples: on one hand, growing pressure inside the sample due to

constrained compression and, on the other hand, non-uniform thickness-wise distribution of ice properties and the presence of lower layers with rather high temperatures.
In this study, full-thickness ice strength obtained through a certain averaging of the small-test results with samples from different layers was compared with compressive strength (pressure) measured directly in full-scale tests. The distribution of compression strength over ice thickness was calculated as per formulas [3] and [4]. The next step was the calculation of mean arithmetical, as per Timco & Frederking (1990), and root-mean-square (RMS), as per SP 38.13330.2018, full-thickness ice compressive strength. It must be taken into account that RMS calculation depends on the number of layers used to split the ice sheet. These calculations were performed for 4 ice layers of equal thickness. The results are given in Table 3 below.

Table 3. Full-thickness ice compressive strength [MPa] based both on small-scale and full-scale tests

Year	Calculations based on small-scale tests		Full-scale tests
	Arithmetical mean	RMS	
2019	3.00	3.25	1.29
2020	4.18	4.43	1.95

In contrast with similar field tests undertaken in 1981 under EXXON program (Petrie and Poplin, 1986), see Fig. 1b, these tests have not shown any close correspondence in full-thickness compressive strength based on small-scale tests and measurements in full-scale tests. The latter gave compressive strength more than 2 times less than averaged results for small samples.

Probable reasons for this discrepancy could be as follows. In the full-scale tests of 1981 performed under EXXON program (Lee et al., 1986), the proportions in size of large ice sample (thickness × width × length) were approximately 1×2.5×5, whereas in the presented studies these proportions were approximately 1×0.8×1. Such dimensions of full-scale sample in our tests were adopted so as to suit the capabilities of the test rig (plate size and maximum achievable load). Larger samples are likely to have stronger effect of constrained compression (see above) and, accordingly, exert greater pressure on the loading plate, and it is the key criterion in determination of ice strength during full-scale tests. So, the full-scale tests of 1981 demonstrated high values of compressive strength, which was close to the values in small-scale tests. This outcome means that dimensions of ice sample in the full-scale compression tests is an important factor.

Another reason is a non-uniformity of ice properties, which leads to the differences in strength over the thickness. In addition to temperature and salinity, the presence of defects in the ice that reduce its strength should be considered. In our study, we assumed a uniform distribution of defects in the ice structure over its thickness. In this case, the uniform arrangement of the small ice samples over the ice thickness made it possible to take into account the presence of defects to some extent. However, the total thickness of ice layer subjected to the small-scale tests is determined by the sum of the sample diameters, and it is approximately 35% of total ice thickness. If the distribution of defects over the ice thickness is uneven, then the presence of larger defects in other layers of ice can lead to a decrease in compression strength related to entire ice thickness. When the full-thickness sample is loaded, the contribution of specific layers to the total load is hard to estimate unambiguously.

5. Conclusion

This paper studies methods for determination of ice full-thickness compressive strength based on small ice samples and full-scale tests. One of the challenges in conducting small-scale tests in field condition is preserving the ice sample properties for a long time. The paper suggests a method which can be used for this: preparation of thermally balanced ice samples. The described field tests on sea ice have demonstrated the feasibility of this method and showed a good correlation in the temperature of ice samples immediately before the tests and the temperature profile over the ice thickness. However, the salinity of samples was slightly less than in their respective parental layers, which might mean that the samples lost some of their brine.

The tests with thermally balanced samples made it possible to obtain the distribution of uniaxial compression strength over ice thickness. Strength results for small samples were averaged by thickness and compared with the results of compression strength measurements performed on full-scale specimens over their entire length. In contrast to EXXON 1980-1981 experiments, these studies have shown the discrepancies in averaged compression strengths of small samples and the results of full-scale measurements. Apart from thickness-wise variations in strength and other properties of ice, these discrepancies could also be due to the size and proportions of the ice sample tested afloat in full-scale test.

Acknowledgments

The work was supported by the Research Council of Norway through the IntPart project Arctic Offshore and Coastal Engineering in Changing Climate.

References

Chen, A.C.T. and Lee, J., 1986. Large-scale ice strength tests at slow strain rates. Proc. OMAE'86, Tokio, Vol. 4, pp. 374–378

Cox, G.F.N. and Weeks, W.F., 1983. Equations for determining the gas and brine volumes in sea ice samples, *Journal of Glaciology*, Vol. 29, No. 102, pp. 306–316

Lee, J., Ralston, T.D. and Petrie, D.H., 1986. Full-thickness sea ice strength tests. Proc. IAHR Ice Symposium, Iowa City, Vol.1, pp. 293–306

Loset, S., Shkhinek, K.N., Gudmestad, O.T. and Hoyland, K.V., 2006. Actions from ice on Arctic Offshore and Coastal Structures, St. Petersburg, Publisher "LAN", 272 p.

Marchenko, A., Karulin, E., Frederking, R., Cole, D., Brown, J., Karulina, M., Sakharov, A., Chistyakov, P., Sodhi, D., Markov, V., Lishman, B., M. Shortt, and Sliusarenko, A., 2020. Influence of vibrations on indentation and compression strength of sea ice. Proc. of the 25th IAHR Symposium on Ice, Trondheim, Norway

Marchenko, A., Karulin, E., Karulina, M., Sakharov, A., Chistyakov, P., Sodhi, D. and Sliusarenko, A., 2018. Scale effects in compressive strength of sea ice. Proc. of the 24th IAHR Symposium on Ice, Vladivostok, paper 18-004.

Moslet, P.O., 2007. Field testing of uniaxial compression strength of columnar sea ice. *Cold Regions Science and Technology*, 48 (1), pp. 1–14.

Petrie, D.H. and Poplin, J.P., 1986. Comparison of small scale and large-scale sea ice strengths. Proc. IAHR Ice Symposium, Iowa City, Vol.1, pp. 265–277

Petroleum and natural gas industries – Arctic offshore structures. ISO/FDIS 19906, 2019

SP 38.13330.2018, 2018. Construction norms and rules: Loads and influences on hydrotechnical constructions (due to waves, vessels and ice), Moscow.

Timco, G.W. and Frederking, R.M.W., 1990. Compressive strength of sea ice, *Cold Regions Science & Technol.*, Vol. 17, pp. 227–240

25th IAHR International Symposium on Ice

Trondheim, 23 - 25 November 2020

Elastic moduli of sea ice and lake ice calculated from in-situ and laboratory experiments

A. Marchenko[1], J. Grue[2], E. Karulin[3], R. Frederking[4], B. Lishman[5], P. Chistyakov[6], M. Karulina[3], D. Sodhi[7], C. Renshaw[8], A. Sakharov[6], V. Markov[6], E. Morozov[9], M. Shortt[10], J. Brown[11], A. Sliusarenko[12], D. Frey[9]

[1]*The University Centre in Svalbard*
PO Box 156, N-9171 Longyearbyen, Norway
Aleksey.Marchenko@unis.no
[2]*University of Oslo, Oslo, Norway*
[3]*Krylov State Research Centre, St.-Petersburg, Russia*
[4]*National Research Council Canada, Ottawa, Canada*
[5]*London South Bank University, London, UK*
[6]*Lomonosov Moscow State University, Moscow, Russia*
[7]*Cold Regions Research and Engineering Laboratory, USA*
[8]*Dartmouth College, Hannover, USA*
[9]*Shirshov Institute of Oceanology, Moscow, Russia*
[10]*London South Bank University, London, UK*
[11]*National Research Council Canada, St. John's, Canada*
[12]*Soft Engineering, Kiev, Ukraine*

The effective elastic modulus of ice is an important physical parameter for the calculation of ice stresses in different situations when ice deformations are small. In the present paper the review of methods used for the calculation of the elastic modulus of ice is performed, new tests for the calculation of the elastic modulus are described, and their results are discussed. Field experiments with floating vibrating ice beams with fixed ends were performed in March and November 2019 on sea ice of the Van Mijen Fjord and fresh-water ice of a lake near Longyearbyen. Laboratory experiments with vibrating cantilever beams were performed in the cold laboratory of UNIS in November 2019. The results are compared with the values of the effective elastic modulus obtained in quasi-static tests with floating cantilever beams, and with in-situ dynamic tests where the effective elastic modulus was measured by the speed of sound waves.

1. Introduction

Elastic moduli of ice are important characteristics used for the formulation of rheological models of ice. Measurements of elastic constants of ice crystal were performed by Jona and Scherrer (1952) using ultrasonic waves with frequencies of 15-18 MHz, and by Zarembovitch and Kahane (1964) using the same method with wave frequencies of 6-14 MHz. Green and Mackinnon (1956), Bogorodskii (1964) and Dantl (1969) used the direct ultrasonic pulse propagation method. Gammon et al (1980) and Gagnon et al (1988) determined the elastic constants of ice by Brillouin spectroscopy. It was discovered that elastic constant characterizing propagation of longitudinal waves increases with the temperature decrease and changes in the range from 9.8 GPa to above 13 GPa. Dantl (1969) determined the frequency dependence of elastic constant of ice in the range of 4-190 MHz and the temperature dependence in the range from 0° C to -140° C.

Sinha (1989) derived the practical elastic moduli for polycrystalline ice using the data of Dantl (1969) and averaging procedure applied to a polycrystalline mass having randomly oriented grains (Voight, 1910). For the columnar-grained ice with horizontal and randomly oriented c-axes Sinha (1989) derived the formula describing temperature dependence of the longitudinal elastic modulus in the vertical and horizontal directions $E_v = E_{v,0} - c_v T$ and $E_h = E_{h,0} - c_h T$, where $E_{v,0} = 9.61$, $E_{h,0} = 9.39$ GPa, $c_v = 0.011$ GPa/C, $c_h = 0.013$ GPa/C, and T is the temperature (°C). According to formula (1) the vertical and horizontal elastic moduli increases respectively from 9.61 GPa to 9.72 GPa and from 9.39 GPa to 9.52 GPa when the ice temperature decreases from 0°C to -10°C. Dependencies of E_v and E_h from the temperature are shown in Fig. 1.

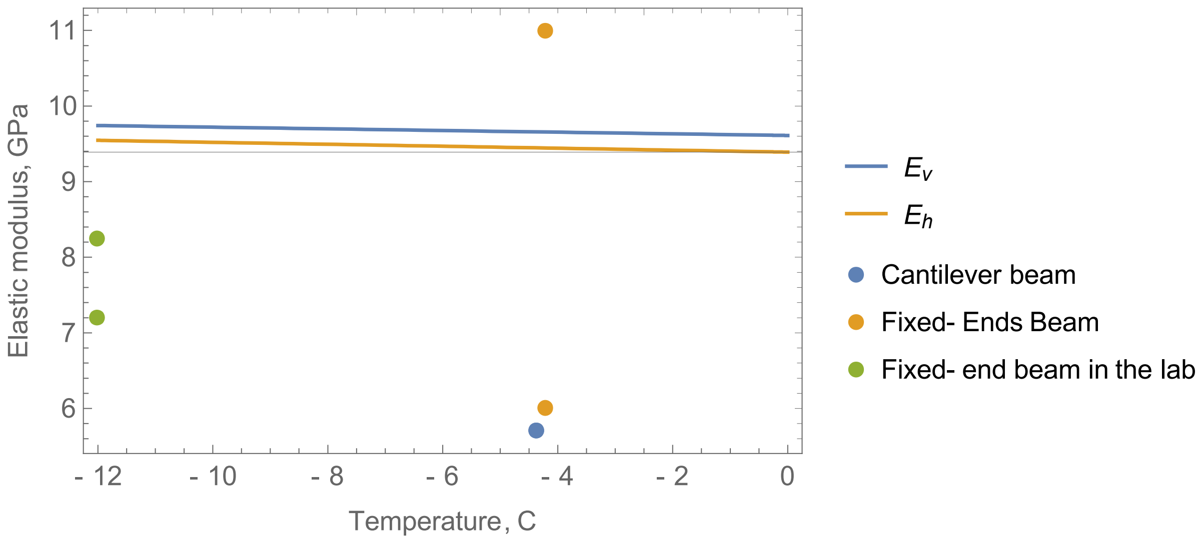

Figure 1. Elastic moduli of fresh ice versus the temperature.

Elastic modulus of sea ice was measured by Langleben and Pounder (1963) by seismic resonance experiments. Their data are approximated by the formula $E = 10 - 0.0351\,\nu_b$, where ν_b is the liquid brine content (ppt). Their measurements were performed for $0 < \nu_b < 90$ ppt. Slesarenko and Frolov (1972) measured elastic modulus of sea ice by the ultrasonic pulse method in the range $0 < \nu_b < 220$ ppt. Vaundrey (1977) calculated apparent elastic modulus from the results of laboratory and field tests on flexural strength. His empirical equation was included in ISO19906 as $E = 5.31 - 0.436\sqrt{\nu_b}$. Assur (1971) recommended for practical use the formula $E = E_f(1 - 0.001\nu_b)^4$, where E_f is the elastic modulus for fresh ice assumed equal to 9.5 GPa. All above mentioned results are shown in Fig. 2.

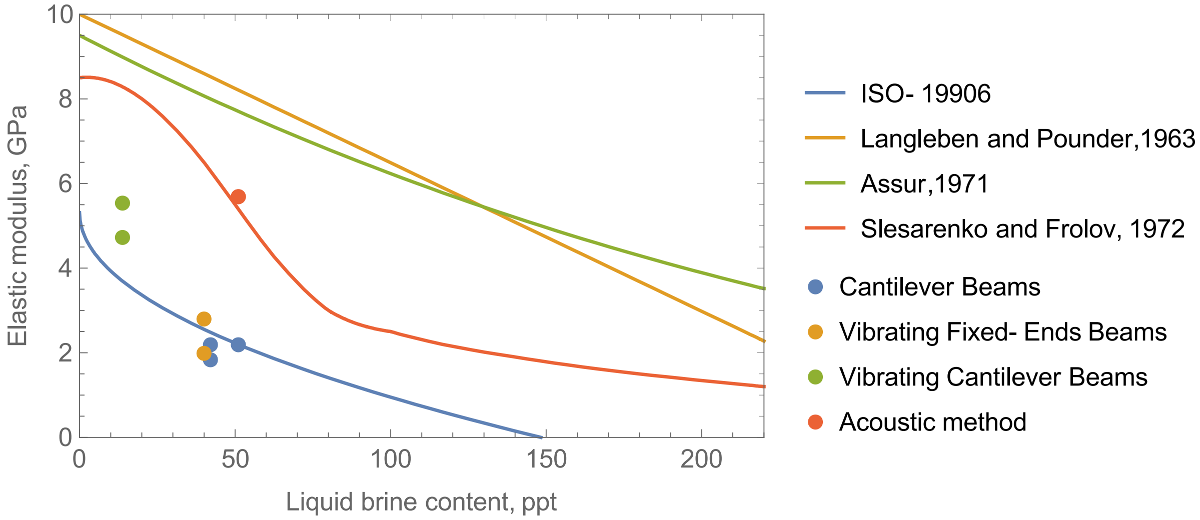

Figure 2. Elastic modulus of sea ice versus the liquid brine content.

In the present paper we perform the elastic modulus of fresh-water lake ice and sea ice calculated from the field tests with floating cantilever beams, floating fixed-ends beams, and laboratory tests with fixed end beams. All field tests were performed on sea ice in the Van Mijen fjord, and fresh ice in the lake near Longyearbyen in Spitsbergen. Laboratory tests were performed with ice beams sawn from sea ice in the places of the field works.

2. Tests with floating cantilever beams

Tests with floating cantilever beams (FCB tests) of sea ice were performed in the Vallunden lake (lagoon) near Svea in the Van Mijen fjord in March of 2019. Tests with floating cantilever beams of fresh ice were performed on the lake near Longyearbyen in November 2019. Figure 3 shows schematic of the test with downward bending of floating cantilever beam. Hydraulic equipment used in the tests is described in (Karulina et al., 2019). In 2019 measurements of vertical displacements was performed at several points located in the middle of the beam surface with LVDT displacement sensors (HBM). Data of the load cell and displacement sensors were collected by the amplifier SomatXR MX840B-R. Locations of the displacement measurements in the four tests are shown in Fig. 3c. The hydraulic cylinder and the displacement sensors were mounted on different metal frames R1 and R2 (Fig. 3b). The frames were fastened on the ice with ice screws. Figure 6 shows similar frame with the displacement sensors mounted near the beam with fixed ends. Further three tests (1,2,3) with sea ice beams and one test (4) with fresh ice beam are described.

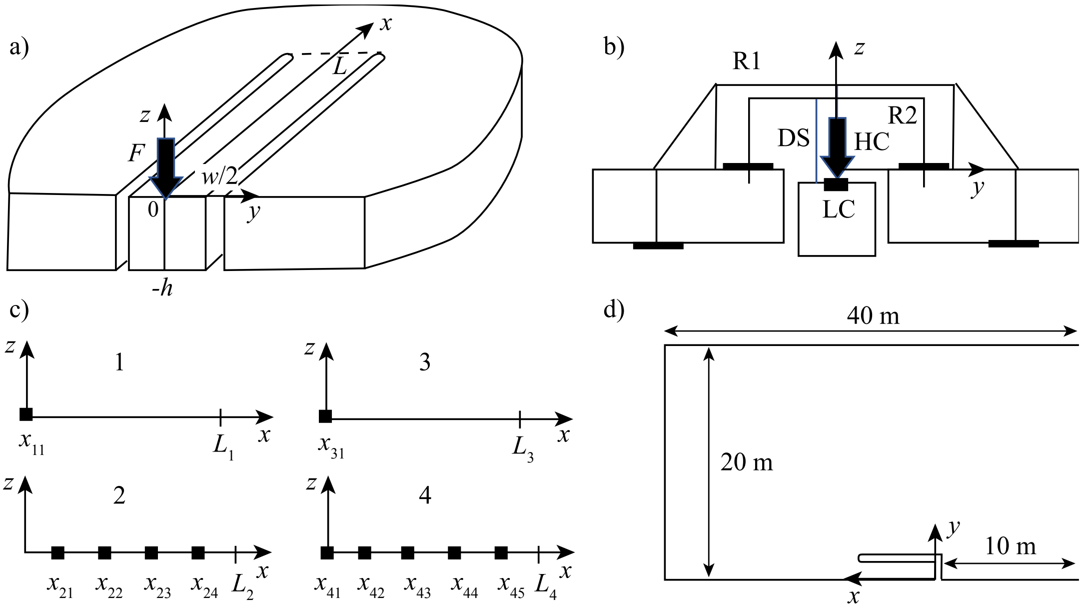

Figure 3. Schematic of the test with floating cantilever beam (FCB test) (a). Rig R1 is equipped with hydraulic cylinder (HC) and load cell (LC), rig R2 is equipped with displacement sensors (DS) (b). Locations of the measurements of vertical displacements at the beam axis in tests 1-4 (c). Dimensions of the computational domain (d).

Lengths and widths of the cantilever beams, ice thickness and locations of displacement sensors in the frame reference (x, y, z) shown in Fig. 3a are given below

1: $L_1 = 3.4$ m, $w_1 = 0.7$ m, $h_1 = 0.72$ m, $x_{11} = 0.0$ m; [1]
2: $L_2 = 3.36$ m, $w_2 = 0.68$ m, $h_2 = 0.73$ m, $x_{21} = 0.67$ m, $x_{21} = 0.67$ m, $x_{22} = 1.28$ m, $x_{23} = 1.88$ m, $x_{24} = 2.44$ m;
3: $L_3 = 3.94$ m, $w_3 = 0.74$ m, $h_3 = 0.75$ m, $x_{31} = 0.0$ m;
4: $L_4 = 3.0$ m, $w_4 = 0.53$ m, $h_4 = 0.515$ m, $x_{41} = 0.0$ m, $x_{42} = 0.70$ m, $x_{43} = 1.30$ m, $x_{44} = 1.90$ m, $x_{45} = 2.48$ m.

The mean values of the ice temperatures and salinities measured during the tests near the beams are $T_1 = -6.14$°C, $S_1 = 4.93$ ppt, $T_2 = -6.11$°C, $S_2 = 4.93$ ppt, $T_3 = -5.86$°C, $S_3 = 5.74$ ppt, $T_4 = -4.39$ °C, $S_4 = 0.0$ ppt. For the calculation of the elastic modulus numerical simulations were performed by the finite element method in the program COMSOL Multiphysics 5.4. The simulations are performed to model the beam deformations near the root (Karulin et al., 2019). Figure 3d shows the computational domain including a half of the cantilever beam. Symmetry boundary condition was used along the axis x and on the right boundary of the computational domain parallel to the axis y. Other boundaries on the plane (x, y) and the upper surface at $z = 0$ were free. At the ice bottom the elastic foundation imitating buoyancy force was used as a boundary condition. Sea density was equal to 920 kg/m3, and fresh ice density was set to 916 kg/m3. The Poisson's ratio was taken to be equal to 0.33. Linear elastic analysis was used for the modeling.

Measured forces were used directly in the simulations of each test. Elastic modulus was chosen by iteration to minimize the difference between calculated and measured displacements. Forces versus measured and computed displacements are shown in Fig. 4 for each of the tests. The values of adjusted elastic moduli are $E_1 = 2.2$GPa,$E_2 = 1.83$GPa,$E_3 = 2.2$GPa,$E_4 = 5.7$GPa.

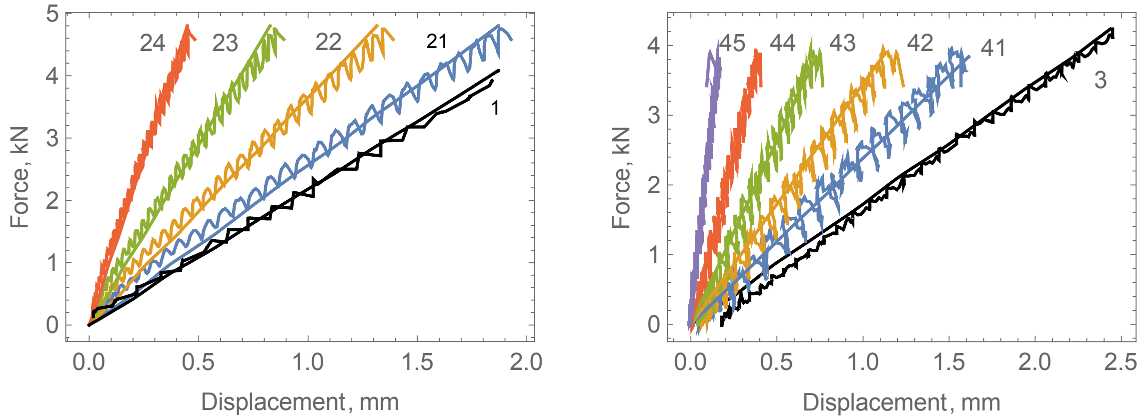

Figure 4. Forces versus displacements in tests 1-4. Solid straight lines correspond to the results of numerical simulations, curved lines correspond to the experimental data.

3. Tests with floating vibrating fixed-ends beams

Floating fixed-ends beam is shown in Fig. 5a. Natural frequencies of bending oscillations of the beam depend on the elastic modulus. In the test the beam oscillations are excited by a mechanic pulse and the beam motion is registered with accelerometers deployed on the beam surface. In the test on sea ice the beam was lifted in the middle by a chain connected to a winch, and then the chain was released by a release-hook (Fig. 6). This test is further named VFEB test. Two accelerometers are visible in the figure at the beam axis in the middle of the beam and to the left from the middle. In the test on fresh-water lake ice the pulse was applied by a jump of a person on the beam in the middle. Accelerometers Bruel & Kjær DeltaTron Type 8344 designed for the measurements of vibrations in the frequency range from 0.2 Hz to 3 kHz were used. The data of accelerometers were collected by the amplifier.

It is assumed that oscillations of an ice beam on hydraulic foundation are described by the equation

$$(\rho_i h + m_{ad})\frac{\partial^2\eta}{\partial t^2} + \frac{Eh^3}{12}\frac{\partial^4\eta}{\partial x^4} + \rho_w g\eta = 0, \quad [2]$$

where η is the beam elevation, ρ_i and ρ_w are the ice and water densities, h is the ice thickness, m_{ad} is the added mass per unit area of the beam surface, E is the elastic modulus of ice, g is the gravitational acceleration, t and x are the time and the coordinate directed along the beam axis.

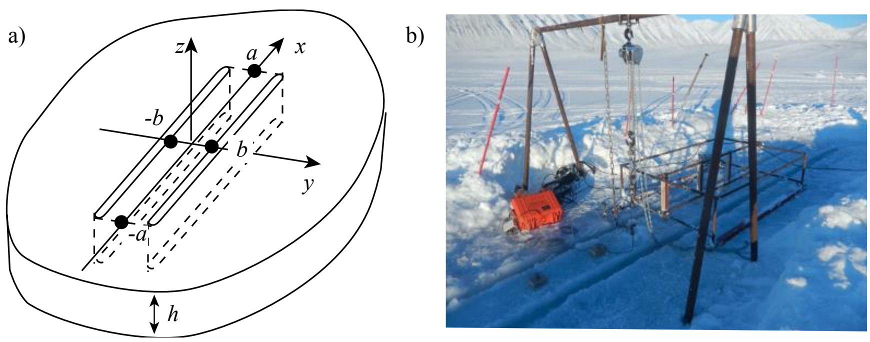

Figure 5. Schematic of the test with floating vibrating fixed-ends beam (VFEB test) (a). Photograph of in-situ VFEB test. Svea, March 2019 (b).

Boundary conditions for the fixed ends beam are

$$\eta = 0, \frac{\partial \eta}{\partial x} = 0, x = \pm a, \tag{3}$$

where $2a$ is the beam length. Periodical solution of [2] is expressed by formulas

$$\eta = e^{i\omega t} \sum_{j=1}^{4} C_j e^{ik_j x} + C.C., \tag{4}$$

where ω is the frequency, C_j are constants and k_j are the roots of the equation

$$\omega^2 - \omega_b^2 = \frac{Eh^3k^4}{12(\rho_i h + m_{ad})}, \omega_b^2 = \frac{\rho_w g}{\rho_i h + m_{ad}}. \tag{5}$$

Here ω_b is the frequency of the natural oscillations of the floating ice due to the balance between the gravity and buoyancy forces.

The roots of equation (5) are determined by the formulas

$$k_{1,2} = \pm\alpha, k_{3,4} = \pm i\alpha, \alpha = \sqrt[4]{\frac{12(\omega^2-\omega_b^2)(\rho_i h + m_{ad})}{Eh_i^3}}, \omega^2 > \omega_b^2, \tag{6}$$

$$k_{1,2} = \pm\alpha e^{i\pi/4}, k_{3,4} = \pm\alpha e^{-i\pi/4}, \alpha = \sqrt[4]{\frac{12|\omega^2-\omega_b^2|(\rho_i h + m_{ad})}{Eh^3}}, \omega^2 < \omega_b^2, \tag{7}$$

Substituting formulas [4] and [6] or [4] and [7] in boundary conditions [3] we find a system of linear homogeneous equations for the calculation of constants C_j. The determinant of the system should be zero for the existence of nonzero solution. It is known that there is no nonzero solution in static case by $\omega = 0$. Therefore, nonzero solution is also absent in case $\omega^2 < \omega_b^2$, since the solution is expressed through the same eigen function as in the static case. Thus, the natural modes have frequencies greater ω_b.

The characteristic equation for symmetric mode by $\omega^2 < \omega_b^2$ has the form

$$\tan(\alpha a) + \tanh(\alpha a) = 0. \tag{8}$$

Since the first root is equal to $\alpha = 2.365/a$ then the first natural frequency is expressed by the formula

$$\omega_1 = \sqrt{\omega_b^2 + \frac{Eh^3}{12(\rho_i h + m_{ad})}\left(\frac{2.365}{a}\right)^4}. \tag{9}$$

The shape of the first mode is described by the equation

$$\eta/\eta_0 \approx 0.883\cos(2.365x/a) + 0.117\cosh(2.365x/a); \eta = \eta_0, x = 0. \tag{10}$$

Formula (9) could be used for the calculation of the elastic modulus E as follows

$$E = \frac{12(\omega_1^2-\omega_b^2)(\rho_i h + m_{ad})}{h^3}\left(\frac{a}{2.365}\right)^4. \tag{11}$$

The added mass effect was estimated from the consideration of potential motion of the water in the region $z < -h$ (Fig. 4a). Normal water velocity at the boundary $z = -h$ is specified by the formulas

$$V_n = V, |x| < a, |y| < b; V_n = 0, |x| > a \text{ or } |y| > b, \quad [12]$$

where the vertical velocity of the ice beam $V = V(t)$ is a function of the time. The velocity potential was constructed in analytical form with using of Fourier transform (Grue, 2017). The mean added mass per unit area of the beam surface equals

$$\langle m_{ad} \rangle = \frac{4\rho_w b}{\pi^2} \int_0^\infty \int_0^\infty \frac{(\sin u)^2 (\sin v)^2}{uv\sqrt{(ub/a)^2+v^2}} du\, dv. \quad [13]$$

The characteristics of ice beams used in the experiments are $a_1 = 5$ m, $b_1 = 0.2$ m, $h_1 = 0.72$ m, $T_1 = -6.5\,°\text{C}$, $S_1 = 4.94$ ppt; $a_2 = 2.4$ m, $b_2 = 0.25$ m, $h_2 = 0.515$ m, $T_2 = -4.2\,°\text{C}$, $S_2 = 0.0$ ppt. The calculated added masses in the experiments are $\langle m_{ad} \rangle_1 = 0.561\rho_w(\text{kg/m}^2)$ $(\rho_w = 1020 \text{ kg/m}^3)$ and $\langle m_{ad} \rangle_2 = 0.554\rho_w(\text{kg/m}^2)$ $(\rho_w = 1000 \text{ kg/m}^3)$.

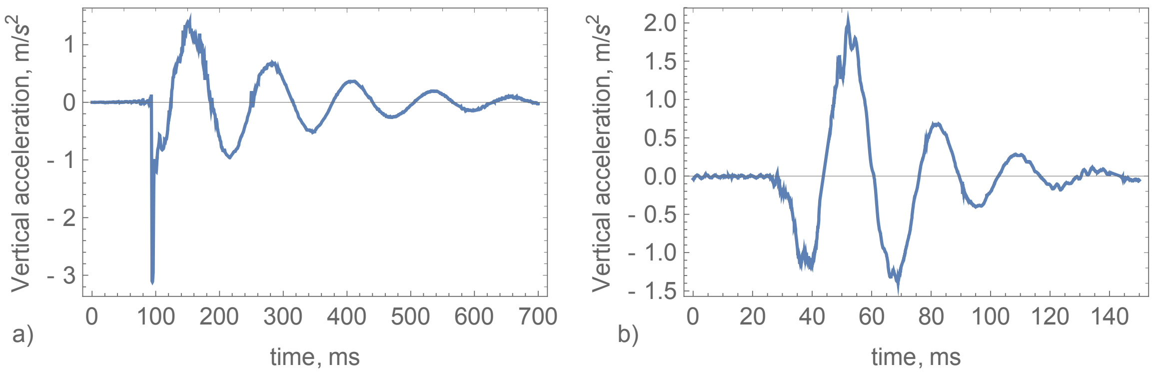

Figure 7. Examples of the vertical accelerations of the beams recorded in the test 1 in sea ice (a) and in the test 2 in lake ice (b).

Examples of the acceleration records are shown in Fig. 7. The frequencies of the beam oscillations in the test 1 and 2 are estimated as $\omega_1 \approx 16\pi$ rad/s (8 Hz) and $\omega_2 \approx 80\pi$ rad/s (40 Hz). The elastic moduli calculated with formula [11] are $E_1 = 2$ GPa annd $E_2 = 6$ GPa.

Numerical simulations in Comsol Multiphysics 5.4 were performed to calculate natural frequency of the plates on elastic foundation. The goal of numerical simulations was to account displacements of the fixed-ends beams near their roots. Boundary conditions [3] don't correspond to real situation because the ice near the beam roots may have vertical displacements excited by the beam oscillations. Numerical simulations were performed in the plate mode, where the thickness of the plate was equal to the beam thickness. The added mass was programmed as a property of the beams, while the added mass of the other parts of the plate in the computational domain were equal to zero. We adjusted the elastic modulus of the frequency of a natural mode with big amplitude of the beam and relatively small amplitudes in the rest of the computational domain to the measured frequencies by iterations. Obtained values of the elastic moduli in the test 1 and 2 are $E_{1,fe} = 2.8$ GPa and $E_{2,fe} = 11.0$ GPa.

4. Tests with vibrating cantilever beams

Two horizontal beams were made from sea ice collected in the Vallunden lake (lagoon) in the Van Mijen fjord in March 2019 and from fresh-water ice in the lake near Longyearbyen in November 2019. Their dimensions were $a_1 = 8.0$ cm, $b_1 = 7.25$ cm, $l_1 = 48$ cm and $a_2 = 7.0$ cm, $b_2 = 6.0$ cm, $l_2 = 50$ cm. In the experiments the beams temperature was -12ºC. The subscripts 1 and 2 are related to sea ice beams and fresh ice beams. The beam shape is shown in Fig. 8 (right panel). Two accelerometers Bruel & Kjær DeltaTron Type 8344 are also visible in the photograph. The beam oscillations were excited by a finger. The accelerometers measured vertical accelerations directed along the axis z (left panel in Fig. 8). The optical axes of ice were perpendicular the axis z. This test is further named VCB test.

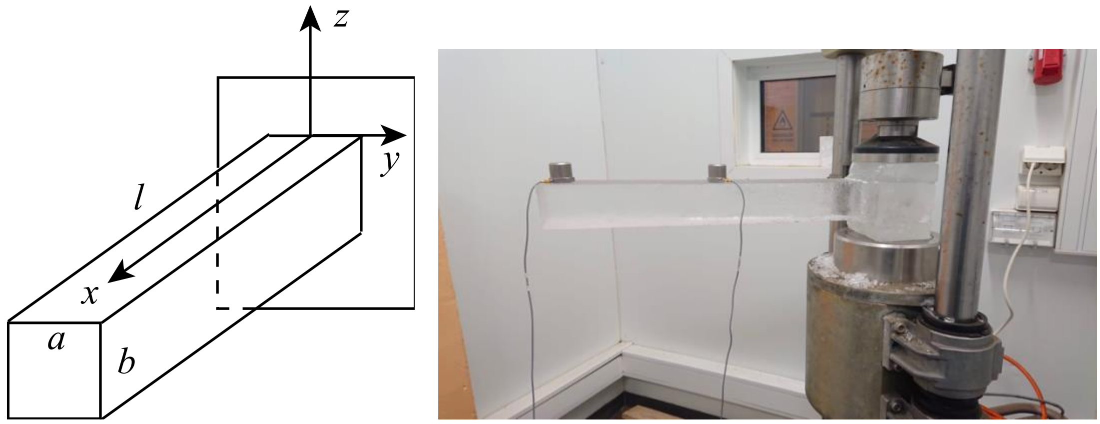

Figure 8. Schematic of the test with vibrating cantilever beam (left panel) (VCB test). Photograph of the test, the accelerometers are mounted on the top surface of the beam (right panel).

The first natural frequency of cantilever beam is calculated with formula (Landau and Lifshitz, 1965)

$$E = \frac{\omega^2 l^4}{3.52^2}\frac{\rho_i S}{I_y},\ S = ab,\ I_y = \frac{ab^3}{12}, \qquad [14]$$

where l is the beam length, and a and b are dimensions of the beam in the transversal direction to the axis (left panel in Fig. 8).

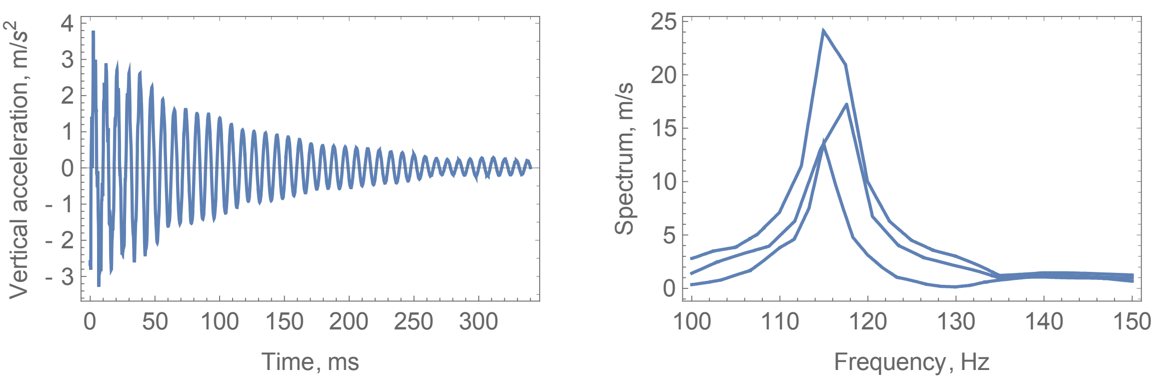

Figure 9. Example of the acceleration record (a) and spectra of the vertical accelerations (b) in the tests with sea ice beam.

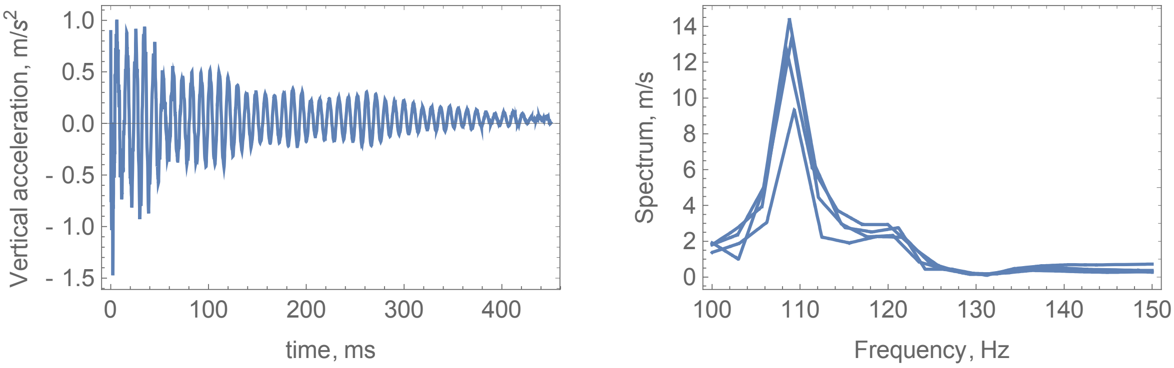

Figure 10. Example of the acceleration record (left panel) and spectra of the vertical accelerations (right panel) in the tests with fresh ice beam.

The example of the accelerometer record in the test with sea ice and fresh ice beams are shown in the left panel of Fig. 9, and Fig.10. The right panels on the same figures show the Fourier-spectrum of the acceleration signal. The values of the frequencies in the spectral maxima were $\omega_1 = 230\,\pi$ rad/s (115 Hz) for the sea ice beam, and $\omega_2 = 218\,\pi$ rad/s (109 Hz) for the lake ice beam. The elastic moduli calculated with formula (25) were $E_1 = 4.7$ GPa and $E_2 = 7.2$ GPa respectively.

Numerical simulations in Comsol Multiphysics 5.4 were performed to calculate natural frequencies of the oscillations of the beams with the shapes similar the shapes of the beams used in the experiment. The right panel in Fig. 8 shows that the fixed ends of the beams were wider than their main body. Simulations were performed in the 3D elastic mode of the program. The elastic moduli were adjusted by the iterations approaching the measured natural frequency to the calculated natural frequency. Obtained values of the elastic moduli were $E_{1,fe} = 5.55$ GPa for the sea ice beam and $E_{2,fe} = 8.25$ GPa for the lake ice beam.

5. Acoustic measurements

Acoustic measurements were performed on March 9, 2016, in the same location (Van Mijen fjord, Vallunden lake). The air temperature was of around -4°C, the surface ice temperature was -3°C, and the bottom ice temperature was at the freezing point of around -1.87°C. The ice thickness was 60 cm. Sea ice salinity varied from 6 ppt near the bottom to 2 ppt near the surface. The mean salinity averaged over the ice thickness was 4.38 ppt. We used a Vallen AMSY-5 to send and receive acoustic pulses with peak frequency of 150 kHz through PZT-5H compressional crystal transducers. The transducers were frozen onto the surface of an ice core taken from the naturally formed sea ice cover. Experiments were conducted within one hour of coring. Some brine drainage occurred. The core was 600mm long, covering the full vertical extent of the ice, with fragile and mushy ice removed from the bottom. The core was 140mm in diameter. The Vallen acoustic processing unit has a calibration setting which allows us to send out pulses at one transducer and then detect them at other transducers (AT test). Pulsing from transducer 1 to transducer 4, and vice versa, we found travel times of 197μs over a distance 600 mm, which corresponds to a speed of sound of 3040ms^{-1}. The elastic modulus calculated with the formula $E = \rho_i c_p^2 (1+\nu)(1-2\nu)/(1-\nu)$ is equal to 5.7 GPa when the ice density is $\rho_i = 917$ kg/m^3, the speed of p-wave is $c_p = 3040$ m/s, and the Poisson's ratio is $\nu = 0.33$.

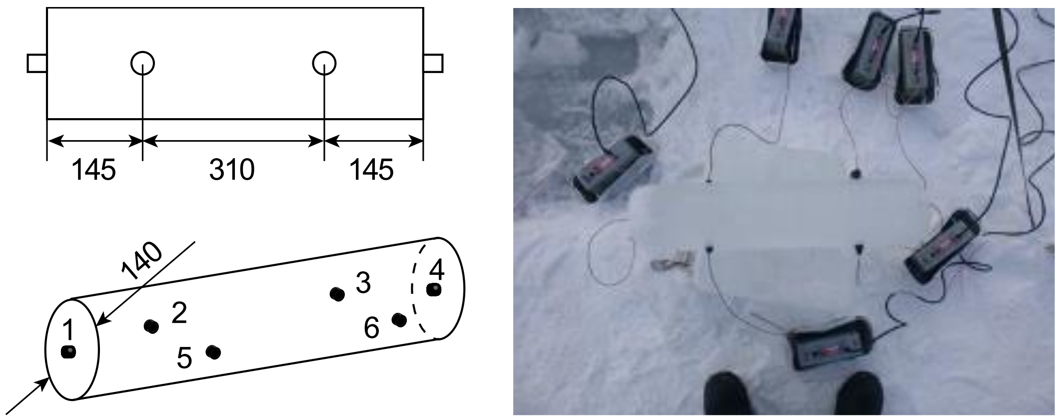

Figure 11. Dimensions of the ice core and locations of acoustic transducers in AT test (left). Photograph of the AT test on acoustic measurement of p-waves speed (right).

Any errors are most likely to occur in measurement of distance, since the measurements in time are software-controlled and highly repeatable. We tried to be careful measuring the distance between transducers 1 and 4, but the measurement could be out by as much as 20mm either way. This gives a range of 2940ms^{-1}-3140ms^{-1}. Transducers 5 and 6 give results which are difficult to interpret, and we suspect they may have had loose wiring. This means we're not able to compare vertical and horizontal sound speeds in the ice.

6. Conclusions and discussion

Results of the calculation of the elastic moduli from the experimental data are shown in Fig. 1 for the tests with fresh-water ice and in Fig. 2 for the tests with sea ice. The liquid brine content is calculated according to formula of Frankenstein and Garner (1967). Most of elastic moduli of fresh ice are lower than it is predicted by Sinha's formulas (1). The value of the elastic modulus of 11 GPa obtained by the numerical simulations of the natural frequency of fixed-ends beam is higher than it is predicted by formula (1). This result can't be considered as reliable because the model of water was simplified to the elastic foundation below the main part of the computational domain, and only below the beam the water effect was accounted by the added mass. VCB tests showed higher values of the elastic modulus than FCB and VFEB tests in the experiments with sea ice and fresh ice. Higher frequencies in VCB tests in comparison with VFEB tests may explain higher elastic modulus measured in VCB test.

Frequency response of effective elastic modulus was investigated by Sinha (1978) for polycrystalline fresh ice. He explained a reduction of the elastic modulus with frequency decrease by the influence of viscous-elastic rheology. The reduction exceeded 50% when the frequency changed from 10 Hz to 0.001 Hz, i.e. in the range of very low frequencies. The redaction was less than 10% when the frequency changed from 1 MHz to 1 Hz. For fresh columnar ice we obtained the reduction of elastic modulus from 7.2 GPa in VCB tests performed with the frequency of 109 Hz, to 6 GPa in VFEB tests performed with the frequency of 40 Hz, and to 5.7 Hz in FCB tests which frequency is around 1 Hz. It means 20%-reduction when frequency changes from 109 Hz to 1 Hz. The ice temperature in VFEB and FCB tests was -4°C, and VCB test was performed with ice temperature -12°C. According to formula (1) temperature effect on elastic modulus can't explain this difference.

The frequencies of oscillations of sea ice beams in VCB tests were 115 Hz, and in VFEB tests – 8 Hz. Elastic moduli obtained from FCB and VFEB tests on sea ice are well approximated by the ISO19906 line described by formula (3). Elastic moduli obtained from VCB tests showed higher values of the elastic modulus than it is predicted by formula (3), The ice temperature in the tests was -12°C. Therefore, the liquid brine content of ice and ice porosity in VCB tests are lower than in FCB and VFEB tests performed on sea ice with mean temperature of -6°C. The elastic moduli were found similar and of around 2 GPa in FCB and VFEB tests. Acoustic measurements performed on similar ice with the frequency of 150 kHz showed the elastic modulus of 5.7 GPa. This result fits well to the measurements of Slesarenko and Frolov (1972) performed by ultrasonic method. Seismic measurements performed in March 2019 in the same place (Vallunden lake, Van Mijen fjord) in the frequency range of 1-200 Hz show the elastic modulus of 4.5 GPa (Moreau et al, 2020). The frequency dependence of elastic modulus of sea ice seems very significant: it increases from 2 GPa to 5.7 GPa when the frequency increases from 1 Hz to 150 kHz.

Strong damping of beams oscillations was observed in VCB and VFEB tests both. In VFEB tests damping in the test with fresh ice was stronger than in the test with sea ice, and the frequency of beam oscillations in the tests with fresh ice (40 Hz) was higher in 5 times than in the test with sea ice (8 Hz). The source of the damping can be related to the viscous processes in ice, with vorticity production in the water, and with water-ice friction. The damping time was about 5 periods of the beam oscillations in the tests. Damping of the beam oscillations in VCB tests was smaller, and the damping time is estimated about 40 periods of the beam oscillations. Damping is these tests is related mainly to viscous properties of ice, but the interaction of the beam with the air also could be important over relatively long time. Further estimates should be performed to quantify physical nature of the damping observed in the tests.

Acknowledgments
The work was supported by the Research Council of Norway through the IntPart project Arctic Offshore and Coastal Engineering in Changing Climate and Petromaks-2 project Dynamics of Floating Ice.

References

Assur, A., 1971. Forces in moving ice fields. POAC-1971, 1, 112-118.

Bogorodskii, V.V., 1964. Elastic moduli of ice crystals. Soviet Physics Acoustics, 10, 124-126.

Dantl, G., 1969. Elastic moduli of ice. Physics of Ice, Editors Riehl, N., Builemer, B., and Engelhardt, H., Plenum Press, New York, 223-230.

Frankenstein, G.E., Garner, R., 1967. Equations for determining the brine volume of sea ice from 0.5 to 22.9oC. J. Glaciology, 6(48), 943-944.

Green, R.E., Mackinnon, L., 1956. Determination of the elastic constants of ice single crystals by an ultrasonic pulse method. The Journal of the Acoustic Society of America, 28(6), 1292.

Iona, F., Scherrer, F., 1952. Die elastischen Konstanten von Eis-Einkristallen. Helv. Phys. Acta, 25, 35-54.

Grue, J., 2017. Ship generated mini-tsunami. J. Fluid Mech., 816, 142-166.

Karulin, E., Marchenko, A., Sakharov, A., Karulina, M., Chistyakov, P., Onishchenko, D., 2019. Features of determining the ice flexural strength and the elastic modulus based on floating cantilever beam tests. POAC-12.

Karulina, M., Marchenko, A., Karulin, E., Sodhi, D., Sakharov, A., Chitsyakov, P., 2019. Full-scale flexural strength of sea ice and freshwater ice in Spitsbergen Fjords and North-West Barents Sea. Applied Ocean Research. 90, 101853.

Landau, L.D., Lifshitz, E.M., 1970. Theory of Elasticity (Volume 7 of A Course of Theoretical Physics). Pergamon Press.

Langleben, M.,P., Pounder, E.,R., 1963. Elastic parameters of sea ice. In: W.D.Kingery (Editor), Ice and Snow, M.I.T. Press, Cambridge, Mass, 69-78.

Sinha, N., 1978. Short-term rheology of polycrystalline ice. J. Glaciology, 21(85), 457-472.

Sinha, N., 1989. Elasticity of natural types of Polycrystalline ice. CRST, 17, 127-135.

Ludovic Moreau, Agathe Serripierri, Pierre Boué, Jérôme Weis, 2020. Monitoring sea ice thickness and mechanical properties with seismic noise, in Proc of the Forum Acusticum, Lyon, April 2020

Slesarenko, Yu, E., Frolov, A.D., 1972. Comparison of elasticity and strength characteristics of sal-water ice. Proc. of the IAHR Symp. on Ice, 2, 85-87.

Vaundrey, K., 1977. Ice engineering – study of related properties of floating sea ice sheets and summary of elastic and viscoelastic analysis. U.S. Naval Civil Engineering Lab., Rep. TR860, Port Huenem, CA.

Voight, W., 1910. Lehrbuch Der Krystallphysik. Feubner, Berlin.

Zarembovitch, A., Kahane, A., 1964. Determination des vitesses de propagation d'ondes ultrasoneres longitudinales dans la glace, Academic Science, Paris, 2629-2532.

25th IAHR International Symposium on Ice

Trondheim, 23 - 25 November 2020

Influence of vibrations on indentation and compression strength of sea ice

A. Marchenko[1], E. Karulin[2], R. Frederking[3], D. Cole[4], J. Brown[5], M. Karulina[2], A. Sakharov[6], P. Chistyakov[6], D. Sodhi[4], V. Markov[6], B. Lishman[7], M. Shortt[8], A. Sliusarenko[9]

[1]*The University Centre in Svalbard*
PO Box 156, N-9171 Longyearbyen, Norway
Aleksey.Marchenko@unis.no
[2]*Krylov State Research Centre, St.-Petersburg, Russia*
[3]*National Research Council Canada, Ottawa, Canada*
[4]*Dartmouth College, Hannover, USA*
[5]*National Research Council Canada, St. John's, Canada*
[6]*Lomonosov Moscow State University, Moscow, Russia*
[7]*London South Bank University, London, UK*
[8]*University College London, London, UK*
[9]*Soft Engineering, Kiev, Ukraine*

Indentation and compression strengths of floating sea ice subjected to vibrations is discussed. The experiments were performed on the land-fast ice of Van-Mijen Fjord in March of 2018 and 2019. The ice thickness was around 70 cm, and the ice salinity was 4-5 ppt. Vibratory loading was applied to the ice surface by a 400-kg commercial compactor used for compacting road fills. The vibration was applied for 10 to 15 minutes at a fixed location. The spectrum of vibrations was analyzed from accelerometer signals. Analysis of thin sections of ice was performed onsite. Indentation tests were performed on natural ice and ice subjected to the action of vibrating plate using the same hydraulic loading apparatus previously employed at the field site. It was found that indentation stroke rates were higher in the tests performed on the ice subjected to vibrations. Uniaxial compression tests were also performed on ice cores taken from the natural ice and from the ice subjected to the vibrations. Uniaxial compression strength of ice cores taken from the ice subjected to vibrations was higher than in the tests with natural ice.

1. Introduction

Vibrations can penetrate and influence ice properties due to the motions of aicrafts on ice runways, motions of cars or trains by ice roads, work of drilling rigs mounted on floating ice etc. A large group of inventions deal with vibration devices mounted on vessels or ice near vessels. It could be rotating unbalanced masses or power cylinders with a freely moving mass (Bogorodsky et al., 1987). An icebreaker attachment with a vibratory system has been developed and patented in few countries (Lezin, 1977).

Vibrations can influence ice properties in the vicinity of offshore structures due to the interaction of ice and structures. Frequency lock-in effect influence resonance interaction between structure and ice at natural frequencies of the structure (ISOPE 19906). Penetration of vibrations in the ice can change ice properties near the structure. For example, vibrations can influence micro-cracking of ice, make ice more "viscous" and influence synchronization of ice failure events along the contact surface with the structure.

In this paper we present results of field experiments performed on sea ice in 2018 and 2019. Vibrations were introduced in the ice by the vibrating plate (VP) designed for road works. Full scale indentation tests and uniaxial compression tests of ice cores were performed on natural sea ice and on sea ice subjected by VP action. The paper is organized as follows: first the action of VP on ice is described followed by results of full-scale indentation tests are formulated and then results on uniaxial compression tests are formulated. Finally, conclusions and discussions are given.

2. Action of vibrating plate on sea ice

The field works were performed on land fast ice in the Van Mijen Fjord near mining settlement Svea in March 2018 and 2019. In 2018, March 8-14, the ice thickness varied from 60 cm to 65 cm. The air temperature changed from -16 C to -22 C, and the mean ice temperature averaged over the ice thickness changed from -8.4 C to -11.35 C. The mean ice salinity was in the range of 5-7 ppt.


Figure 1. Vibrating plate on ice (left). Pulverization of ice surface by vibrating plate (right).

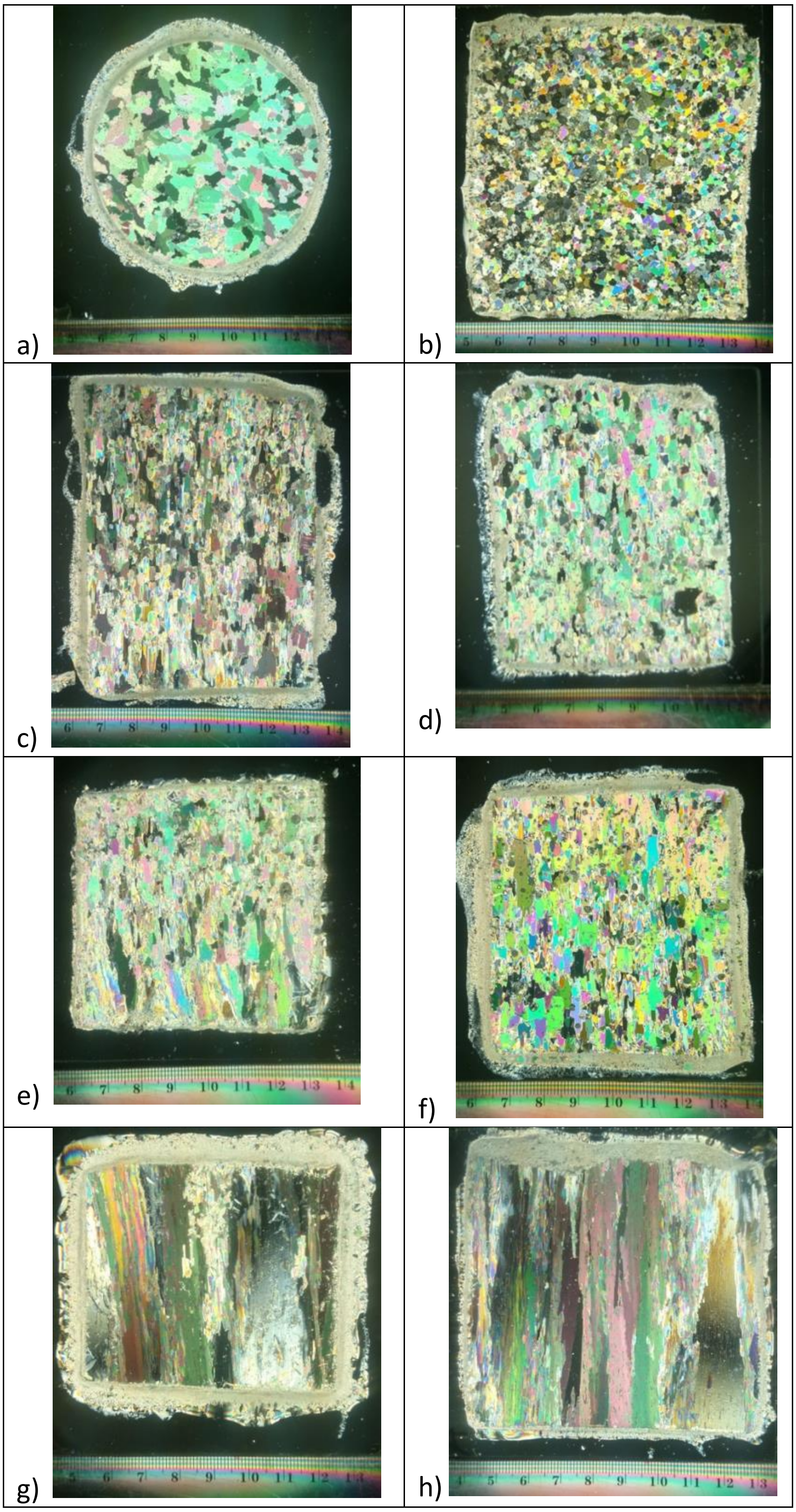

Figure 2. Horizontal sections of ice layer at 20 cm from the ice surface before VP action (a), and at 5 cm from the ice surface after VP action (b). Vertical sections of top layer of ice (10 cm from the surface) before (c) and after VP action (d). Vertical sections of ice layer at 20 cm from the ice surface before (e) and after VP action (f). Vertical sections of ice layer at 30 cm from the ice surface before (g) and after VP action (h). March 2018.

Vibrating plate with weight of 400 kg was used during the field works (Fig. 1, left panel). VP can move forward or back and the intensity of vertical vibration of VP is regulated. Standing on a spot VP pulverizes ice below and gradually submerges into the ice (Fig. 1, right panel). Spectrum of accelerations of VP was measured with vibration recorder VibraCorder™ 4400A with the sampling frequency of 3.2 kHz. Maximum energy of vibrations was released at the frequency of about 80 Hz. VP was working on the ice during 10-15 min with maximal intensity of vibrations in each test, and then tests on the ice subjected by VP action were performed.

The ice cores taken from natural ice and from the ice subjected to the VP action, and thin sections were made from these ice cores with Microtom machine. Photos of thin sections in polarized light were made in Rigsby stage. All equipment for thin section analysis was installed in the tent on the place of the field works. Figure 2 shows the horizontal thin sections taken from the top layer of ice with thickness of 20 cm before (a) and after (b) of VP action on the ice. Since top layer of ice with thickness 8-10 cm was pulverized, we prepared thin section from the ice at 5 cm distance from the new surface. Thus, both sections shown in Figs. 2a and 2b were prepared from the same ice. Fig. 2b shows very fine grain structure of ice immediately below VP. Figures 2c-h show vertical thin sections taken from the ice before (c, e, g) and after (d, f, h) VP action. The ice columns are damaged up to 20 cm depth, and don't have significant changes at the depth of 30 cm below the ice surface.

3. Indentation tests

Full-scale indentation tests were performed with the original rig equipped with hydraulic cylinders A (upper cylinder) and B (lower cylinder) (Fig. 3). The capacity of each cylinder is 30 t. Each cylinder is equipped with stroke sensor and load cell. The principles of the functioning of the hydraulic system are described in (Marchenko et al, 2019). The indenter is vertical semi-circular cylinder of 15 cm diameter made from reinforced steel. Results of indentation tests were described in (Karulin et al., 2014; Marchenko et al., 2018). Lishman et al (2020) investigated acoustic emission in the indentation tests. The data of indentation tests includes records of strokes and loads on the cylinders A and B with sampling frequency 50 Hz.

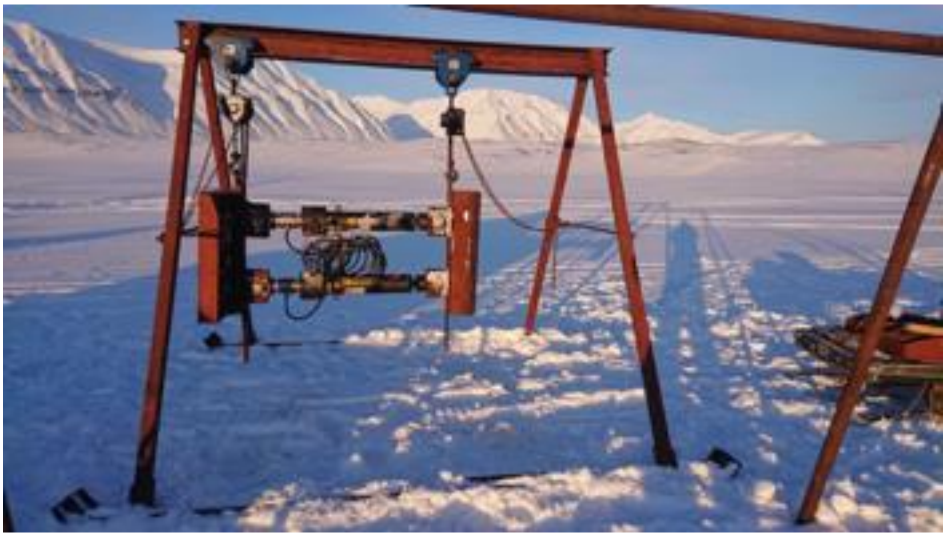

Figure 3. Hydraulic rig for indentation tests.

It was visible during the indentation tests performed in March 2018 that the speed of indentation was higher in the tests performed in ice subjected to VP action. Figure 4 shows interaction of the indenter with ice subjected to VP action (left panel) and with natural ice (right panel). The indenter practically didn't move in natural ice. Ice subjected to VP action failed by the formation of broken ice blocks or spoils on the surface. One can see in the left panel of Fig. 4 that top layer of ice with thickness of 7-8 cm is worn away due to VP action.

Figure 4. Indentation tests in the ice subjected to VP action (left) and in natural ice (right).

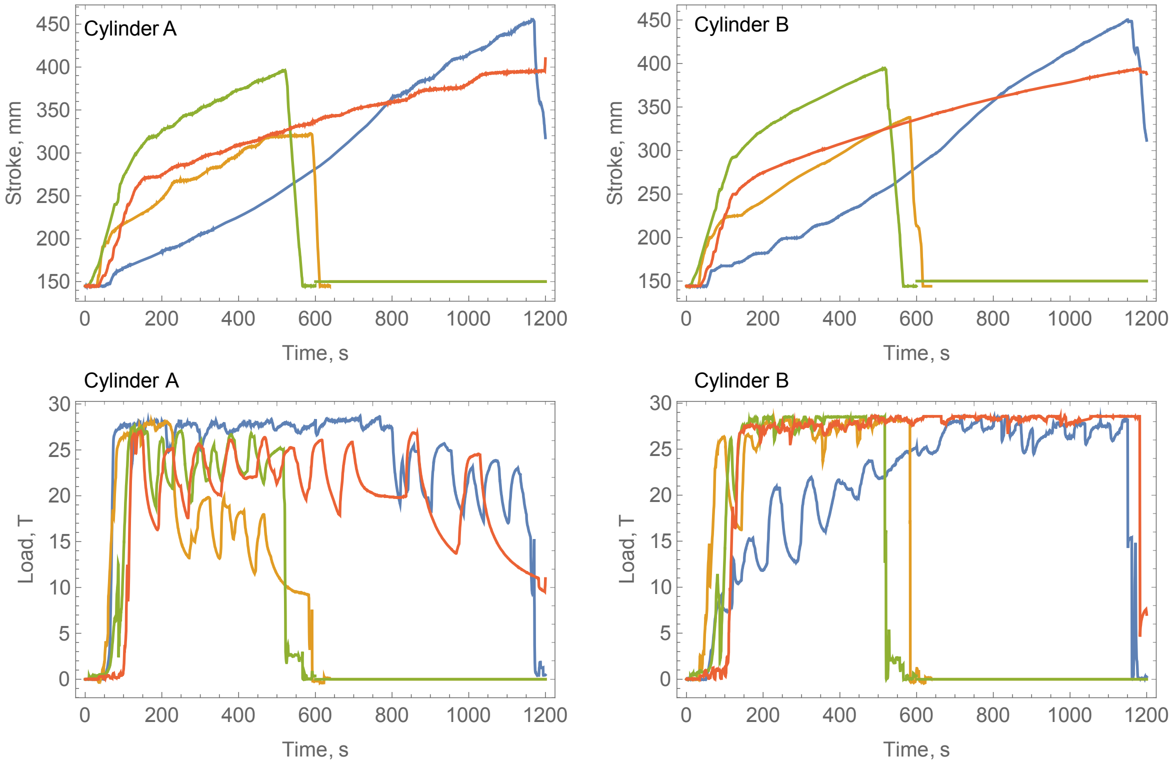

Figure 5. Records of strokes and loads in four indentation tests performed after VP action on natural ice. Blue, yellow, green and red colors correspond to the tests 1, 2, 3 and 4. March 2018.

Figure 5 shows records of strokes and loads on cylinders A and B recorded in four indentation tests performed after VP action on natural ice. The dependencies of strokes versus the time are similar for the cylinders A and B. Note that during the first 75 mm of penetration into the ice, the contact area of the circular-shaped indenter is increasing. This explains why the stroke speed is initially faster (tests 2, 3 and 4) and then slows down. The load on the cylinder A becomes smaller than the load on the cylinder B with the time because top layer of the ice was damaged by VP action and was, thus, 'softer'. The load oscillations on the cylinder A corresponds to events of ice break up in the surface layer similar shown in Fig. 4 (left panel).

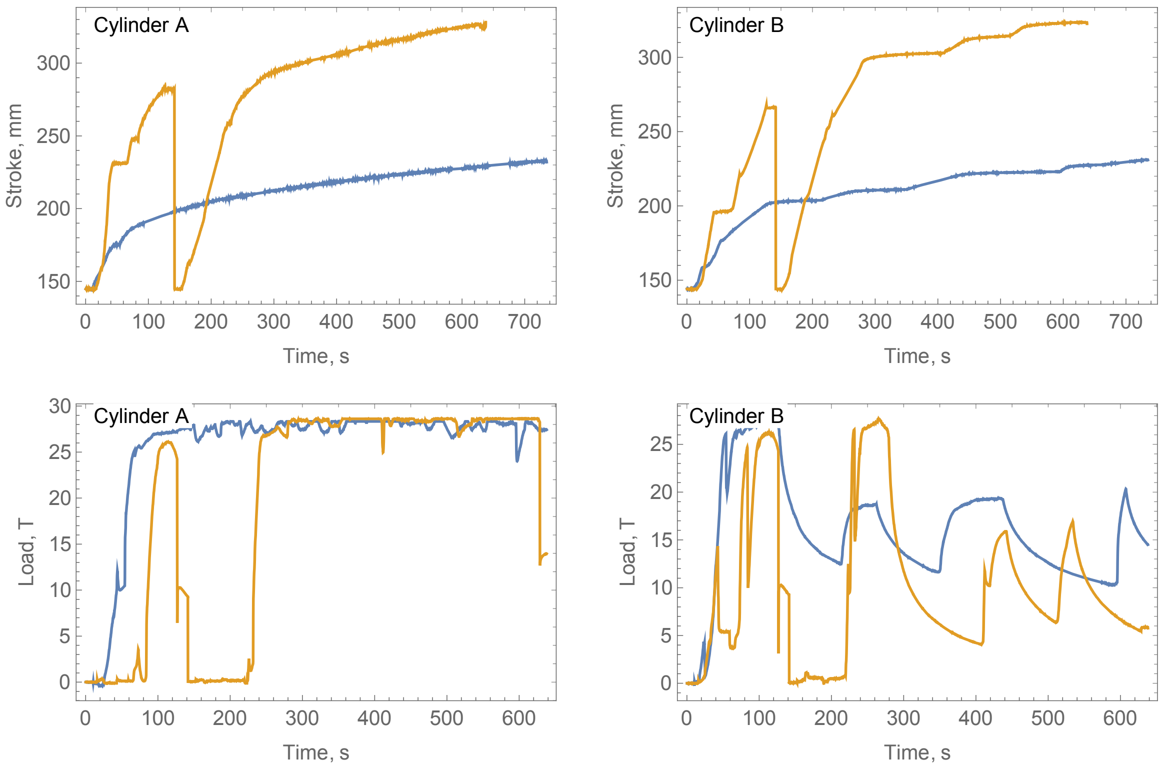

Figure 6. Records of strokes and loads in two indentation tests performed on natural ice. Blue and yellow lines correspond to the tests 5 and 6. March 2018.

Table 1. Mean stroke rates in the cylinders A (SRA) and B(SR) in Tests 1-6

Test number	1	2	3	4	5	6
SRA, mm/s	0.277	0.240	0.271	0.132	0.076	0.102
SRB, mm/s	0.276	0.255	0.276	0.125	0.065	0.085

Figure 6 shows the records of strokes and loads in the indentation tests performed on natural ice. One can see that in contrast to Fig. 5 the load on the cylinder A is stable, and the load on cylinder B oscillates. It is explained by the failure of bottom layer of the ice which strength is smaller than the strength of surface ice layers because of the temperature effect.

Figure 7 shows the dependencies of stroke rates of the cylinders A and B in the tests 1-4 where ice was subjected to VP action, and Fig. 8 shows the dependencies of stroke rates of the cylinders A and B in the tests 5,6 in natural ice. Table 1 shows the mean values of the stroke rates averaged over the time intervals in Fig. 7 and Fig. 8. It is obvious that the stroke rates are greater in the tests 1-4 then in the tests 5, 6.

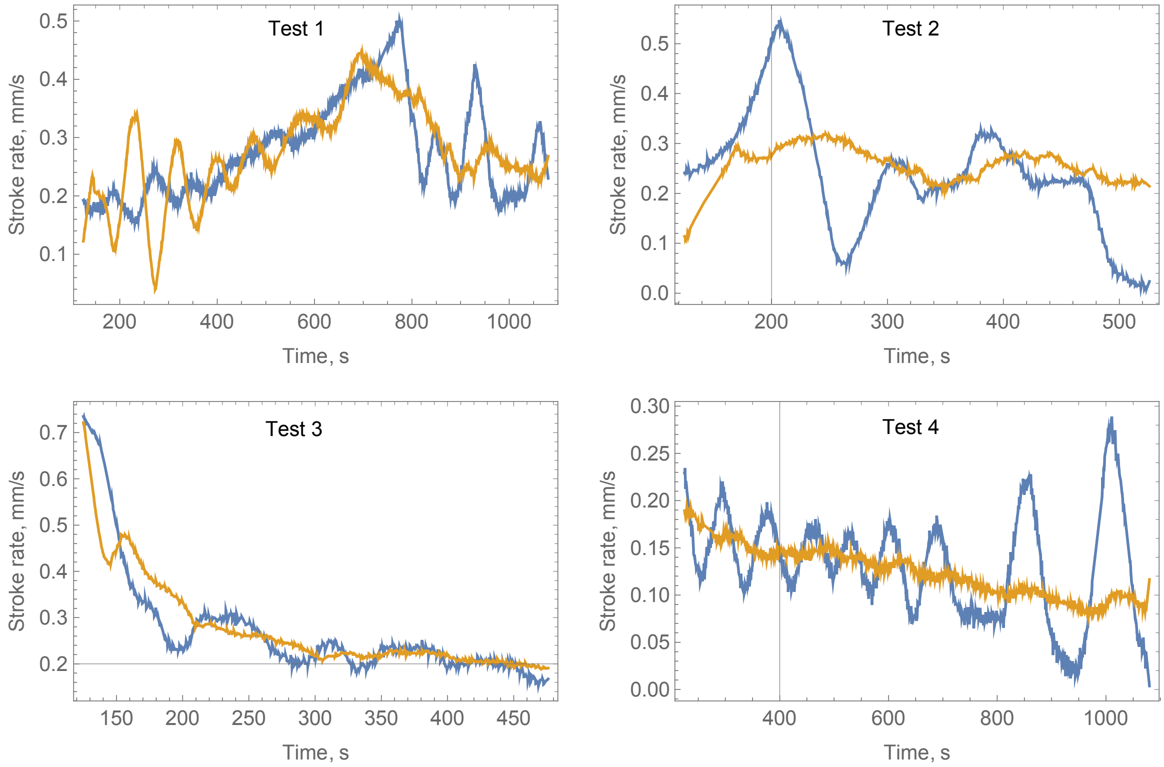

Figure 7. Stroke rates versus the time in four indentation tests performed after VP action on natural ice.

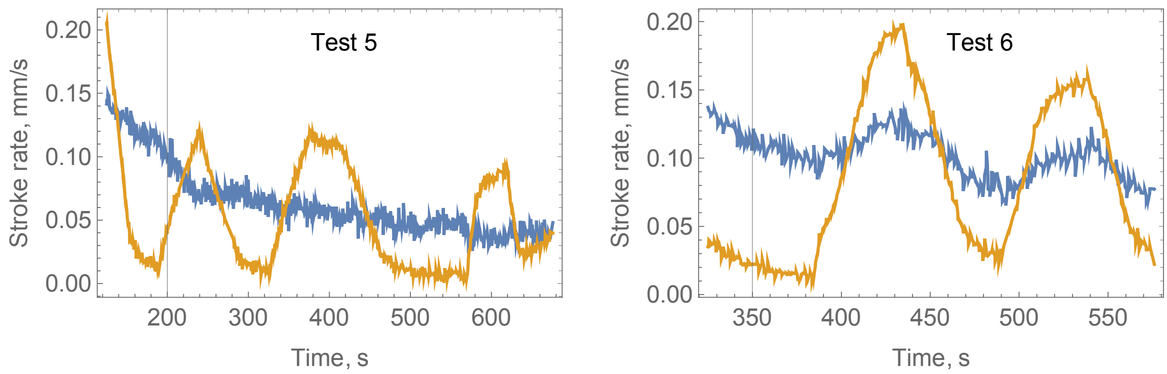

Figure 8. Stroke rates versus the time in two indentation tests performed on natural ice.

4. Uniaxial compression tests

Uniaxial compression tests were performed with vertical ice cores taken from the ice subjected to VP action on March 15 and from natural ice on March 10, 2019. All ice cores have the air temperature during the tests. The air temperature was -18C on March 10, and -14C on March 15. A representative temperature profile of ice cores is shown in Table 2. The salinity of ice cores varied within 5-7 ppt. The ice thickness was 70-75 cm. Tests were performed by the Kompis Rig (Moslet, 2007). Some of the tests were performed with cores (new cores) drilled soon after the ice was subjected by VP action. The other tests were performed with cores (old cores) drilled a few hours later after the ice was subjected by the action of the vibrating plate. Depth from which the new and old cores were taken was documented. We designate 'top layer' of ice extended from the ice surface to the depth of 20 cm, 'middle layer' of ice extended from the depth 20 cm to the depth 50 cm, and 'bottom layer' of ice located below 50 cm depth. Depth of the cores of natural ice was not written. All tests were performed at similar strain rate of $2 \cdot 10^{-4}$ s^{-1}. The length of all ice cores was 16 cm, and their diameter was 7.25 cm.

Table 2. Example of core temperature profile from March 10th

Depth (cm)	0	10	20	30	40	50	60
Temperature	-18.9	-18.3	-18.1	-17.7	-17.6	-17	-18

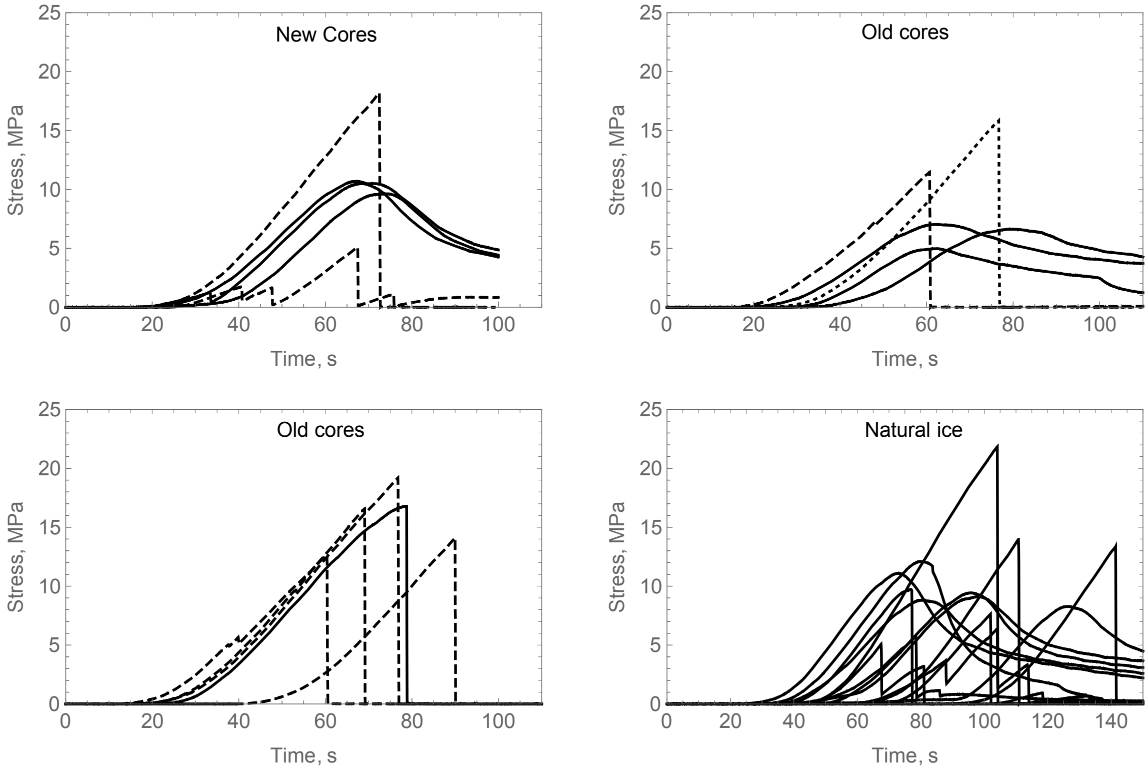

Figure 9. Stress versus the time in uniaxial compression tests with vertical ice cores. Solid, dashed and dotted lines correspond to the ice cores taken from 'top', 'middle' and 'bottom' layers of ice.

Figure 9 shows records of ice stress versus the time for all performed tests. One can see that most of the ice cores had brittle failure. Maximal stress in each test was interpreted as ice strength in uniaxial compression. Table 3 shows the ice strengths calculated from the tests performed with ice cores taken from the ice subjected to VP action. One can see that the strength of ice cores taken from the top layer of ice is smaller than the strength of ice cores taken from the middle and bottom layers. Figure 10 shows the ice strengths of ice cores taken from natural ice. The mean strengths of the new and old cores are 10.8 MPa and 12.5 MPa. The mean strength of the ice samples from natural ice is 10.2 MPa.

The mean values and standard deviations of compression strength are shown in Table 4. We excluded the value 16.8 MPa (marked by gray color in Tab. 3) of the strength of old ice core taken from the top layer because this core demonstrated very different behavior from the other cores. Table 4 shows that the mean strength of old ice cores taken from the top layer of ice is smaller the mean strength of new ice cores after vibrations. Standard deviation of the strength of ice cores after vibrations is lower than ice cores from natural ice.

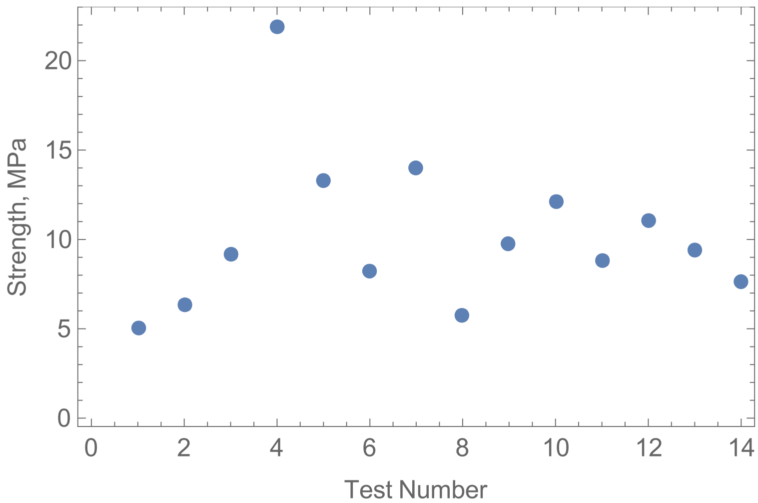

Figure 10. Ice strength after the uniaxial compression tests with vertical ice cores taken from natural ice.

Table 3. Uniaxial compression strength of new and old cores taken from 'top', 'middle' and 'bottom' layers of ice (MPa). D and B means ductile and brittle failure.

New	Top	9.63, D	10.69, D	10.5, D		
	Middle	18.19, B	5.1, B			
Old	Top	6.62, D	7.03, D	4.97, D	16.8, B	
	Middle	11.47, B	19.21, B	14.12, B	12.66, B	16.59, B
	Bottom	15.85, B				

Table 4. Uniaxial The mean values and standard deviation of compression strength.

	New, Top	Old, Top	Old, Middle	Natural ice
Mean	10.27	6.2	14.81	10.18
St. Dev.	0.56	1.09	3.11	4.29

We assume that VP influenced the top ice layer stronger than the middle and the bottom layers. Experiments showed higher strength in the middle (14.81 MPa) and bottom (15.85 MPa) layers than in the top layer (10.27 MPa) of ice subjected to VP action. The averaged strength of natural ice (10.18 MPa) was almost the same as in the top layer ice (10.27 MPa). If the strength of top layer natural ice would be 6.2 MPa, and the strengths of middle and bottom layers of natural ice would be respectively 14.81 MPa and 15.85 MPa then the mean strength of natural ice would be 12.29 MPa. It indicates strengthening of the top ice layer immediately after the VP action and decreasing of the ice strength in the top layer after several hours.

5. Discussion and Conclusions

The influence of cyclic deformation on ice properties was discussed in several papers. Usually cyclic deformations of materials lead to fatigue failure after certain number of cycles. Haynes et al (1993) investigated the influence of pulsating load on bearing capacity of floating fresh ice. The pulsation frequencies of 21.5 Hz and 15 Hz were applied in the experiments. After ice failure was not observed in the experiments, they were turned to investigate the influence of pulsating load on bearing capacity of ice. Test results showed lowering the bearing capacity due to the oscillations. Haskell et al (1996) performed in-situ tests on cyclic deformations of floating cantilever beams made of sea ice in the Antarctic. The periods of bending deformations were ~10 s. The dependence of bending stress at the beam failure from the number of cycles was investigated. It was discovered that ice doesn't fail if maximal stress is lower a half of the flexural strength.

In contrast to above mentioned effect of ice weakening under cyclic loading the ice strengthening was also discovered mainly for laboratory made ice. The ice strengthening due to uniaxial cyclic deformations tension-compression was described by Cole (1990). The experiments were performed in the frequency range of 0.001-10 Hz. Limited observations indicated an increase of brittle tensile strength of specimens after cycling loading. Increase of the flexural strength of laboratory made ice beams after their cyclic bending was discussed in the papers (Iliescu et al, 2017; Murdza et al, 2020a). Most of the bending cycles were performed with period of 10 s. It was discovered that flexural strength may increase even when the stress amplitude during cycling exceeds a half of flexural strength of not cycled samples. Similar experiments on cyclic 3-ponts bending of beams made from fresh-water lake ice also demonstrated small strengthening in comparison with tests with laboratory made ice beams (Murdza et al, 2020b).

In the present paper we investigated the influence of vibrations with higher frequency (80 Hz) on the strength of natural columnar sea ice. Vibrations were introduced in the ice in parallel direction to ice columns by vibrating plate working on the ice during 15 min. Vibrating plate pulverized surface layer of ice with thickness smaller 10 cm and caused strongest influence on the property of ice layer below the pulverized ice. Two types of in-situ tests were performed: full scale indentation tests on floating ice and uniaxial compression tests with ice cores. The indentation tests showed weakening of ice in the horizontal directions after the action of vibrating plate. The uniaxial compression tests indicated an increase of ice strength in the vertical direction in the top layer immediately after the action of vibrating plate on ice, and further reduction of this strength with the time.

Obtained results demonstrate the influence of the direction of applied vibrations on the strengthening of columnar sea ice. In combination with results from (Haynes et al, 1993) it is possible to conclude that vertical vibrations increase compression strength in the vertical direction and reduce ice strength in the horizontal directions. For the further studies we plan to perform more uniaxial compression tests with vertical and horizontal ice cores taken from natural ice and ice subjected to the action of vibrating plate. It is of interest to investigate the influence of vibrations applied in perpendicular directions to ice columns.

Acknowledgments
The work was supported by the Research Council of Norway through the IntPart project Arctic Offshore and Coastal Engineering in Changing Climate.

References

Bogorodsky, V.V., Gavrilo, V.P., Nedoshivin, O.A., 1987. Ice destruction. Methods and Technology. D.Reidel Publishing Company, Dordrecht, Holland.

Cole, D.M., 1990. Reversed direct-stress testing of ice: Initial experimental results and analysis. Cold Regions Science and Technology, 18, 303–321.

Haynes, F.D., Kerr, A.D., Martinson, C.R., 1993. Effect of fatigue on the bearing capacity of floating ice sheets. Cold Regions Science and Technology, 21, 257–263.

Haskell, T.G., Robinson, W.H., Langhorne, P.J., 1996. Preliminary results from fatigue tests on in situ sea ice beams. Cold Regions Science and Technology, 24, 167–176.

Iliescu, D., Murdza, A., Schulson, E.M., Renshaw, C.E., 2017. Strengthening ice through cyclic loading. J. Glaciology, 63 (240), 663-669.

Karulin, E., Marchenko, A., Karulina, M., Chistyakov, P., Sakharov, A., Ervik, A., Sodhi, D., 2014. Field Indentation Tests of Vertical Semi-Cylinder on First-Year Ice. Proc. of the 22th IAHR Symposium on Ice, Singapore, paper 1125.

Lezin, D.L., 1977. Icebreaker attachements. Proc. of Research Institute of Water Transport, 126, 3-15. (in Russian).

Lishman, B., Marchenko, A., Sammonds, P., Murdza, A., 2020. Acoustic emissions from in situ compression and indentation experiments on sea ice. Cold Regions Science and Technology, 172, 102987.

Marchenko, A., Karulin, E., Karulina, M., Sakharov, A., Chistyakov, P., Sodhi, D., Sliusarenko, A., 2018. Scale effects in compressive strength of sea ice. Proc. of the 24th IAHR Symposium on Ice, Vladivostok, paper 18-004.

Marchenko, A., Karulin, E., Sakharov, A., Chistyakov, P., 2019. On the influence of the hydraulic characteristics of the rig during full-scale compression and indentation tests on sea ice. POAC-32.

Moslet, P.O., 2007. Field testing of uniaxial compression strength of columnar sea ice. Cold Regions Science and Technology, 48 (1), 1–14.

Murdza, A., Schulson, E.M., Renshaw, C.E., 2020a. Strengthening ice through cyclic loading. J. Glaciology, 1-11.

Murdza, A., Marchenko, A., Schulson, E.M., Renshaw, C.E., 2020b. Cyclic strengthening of lake ice. J. Glaciology, 1-11. (accepted)

25th IAHR International Symposium on Ice

Trondheim, June 14 to 18, 2020

Results of preliminary cyclic loading experiments on natural lake ice and sea ice

Andrii Murdza[1], Aleksey Marchenko[2], Erland M. Schulson[1], Carl E. Renshaw[1,3], Alexander Sakharov[4], Evgeny Karulin[5], Peter Chistyakov[4]

[1]Thayer School of Engineering, Dartmouth College, Hanover, NH, USA
[2]The University Centre in Svalbard, Longyearbyen, Norway
[3]Department of Earth Sciences, Dartmouth College, Hanover, NH, USA
[4]Lomonosov Moscow State University, Moscow, Russia
[5]Krylov State Research Centre, Saint-Petersburg, Russia
14 Engineering Drive, Hanover, NH, USA, 03755
Andrii.Murdza@dartmouth.edu
alekseym@unis.no
erland.m.schulson@dartmouth.edu
carl.e.renshaw@dartmouth.edu

Abstract

This paper describes preliminary results of laboratory non-reversed 3-point flexural cyclic loading experiments under displacement control on natural S2 columnar lake and sea ice harvested on Svalbard. Freshwater ice was loaded normal to the columns; sea ice was loaded along the columns. The experiments were conducted at -12ºC, 0.1 Hz frequency and outer-fiber stress in the range from ~ 0.1 to ~ 0.7 MPa. The results show that the flexural strength of the lake ice increases linearly as average cycled stress amplitude increases, similar to the behavior of laboratory-grown ice (Murdza and others, 2020). Acoustic emissions detected in sea ice during cycling show a significant reduction of amplitude over 12 hrs, while acoustic emissions in lake ice look similar at the beginning and at the end of cycling.

1. Introduction

There is now an evidence that the propagation of ocean swells into a floating ice cover results in the instantaneous breakup of the parent ice cover into smaller ice floes (e.g., Asplin and others, 2012; Collins and others, 2015). These observations raise a question about how cyclic loading affects the flexural strength of ice, i.e., is the sudden breakup a result of fatigue failure under wave-driven cyclic loading, as discussed earlier (Haskell and others, 1996; Langhorne and Haskell, 1996; Bond and Langhorne, 1997; Langhorne and others, 1998, 1999)?

Cyclic loading of ice was recently studied in a systematic manner (Iliescu and others, 2017; Murdza and others, 2018, 2019, 2020). There, columnar-grained S2 freshwater ice was produced in the laboratory and, upon cyclic loading across the columns in a 4-point manner, was observed to strengthen significantly (by about a factor of 2 or more). This observation is reminiscent of an effect firstly reported by Cole (1990) who noted that upon alternating tension/compression uniaxial loading (Cole and Gould, 1990) freshwater, granular ice, also produced in the laboratory, could be cycled at stress amplitudes about twice as great as the tensile strength of non-cycled ice.

The question addressed in this paper is whether ice produced under natural conditions also exhibits cyclic strengthening.

2. Procedure

We conducted a series of non-reversed, cyclic flexural tests in the laboratory on both freshwater lake ice and natural sea ice. Lake ice was harvested from the ~50 cm thick cover on a lake in the Arctic, located near Mine 7 in Longyearbyen, Svalbard. Sea ice was harvested from landfast ice near Svea on Svalbard in March 2019. Figure 1 shows the microstructure of both lake and sea ice. The ice was columnar-grained with the S2 growth texture, as defined by Michel and Ramseier (1971). Thin-section analyses showed that c-axes were randomly oriented within the horizontal plane of the ice and confined more or less to that plane; no preferred orientation within the horizontal plane was evident. The average column diameter of lake ice was 17±3 mm and of sea ice 9±4 mm. The salinity of sea ice was 4 psu.

From large (~120 x 70 x 50 cm) blocks cut from the covers of both the sea ice and the lake ice and then transported to and stored at UNIS, plate-shaped specimens were first roughly cut to dimensions of ~600 mm x 120 mm x 100 mm using a chain and band saw. Later, using massive metal plates of room temperature (~20 ºC), the specimens were melted to the final dimensions of $h \sim 45$ mm in thickness (parallel to the long axis of the grains), $b \sim 100$ mm in width and $l \sim 600$ mm in length. The long axis of the grains was parallel to the specimen thickness in the case of lake ice and parallel to the specimen length in the case of sea ice. To prevent thermal cracking while processing, the specimens were slowly warmed up to about -3 °C before contact with the warmer metal plates. The procedure ensured the top and bottom surfaces of the samples to be reasonably parallel at ±0.5 mm accuracy. Following this procedure, we prepared seven lake ice samples and one sea ice sample.

The lake specimens were non-reversed loaded across the columns. A single specimen of sea ice was loaded along the columns at -12ºC and at 0.1 Hz frequency and at outer-fiber stress in the range from ~ 0.1 to ~ 0.7 MPa, using a custom-built 3-point rig, Figure 2, attached to a uniaxial loading system termed "Knekkis" (for details see Nanetti and others (2008); Sukhorukov and Marchenko (2014)). Although free from cracks, at least of a size detectable by the unaided eye, the lake ice specimens contained narrow (< 1 mm dia.) air channels oriented parallel to the long axis of the grain columns (one sample had about 3-8 air channels over 600 mm x 100 mm surface area).

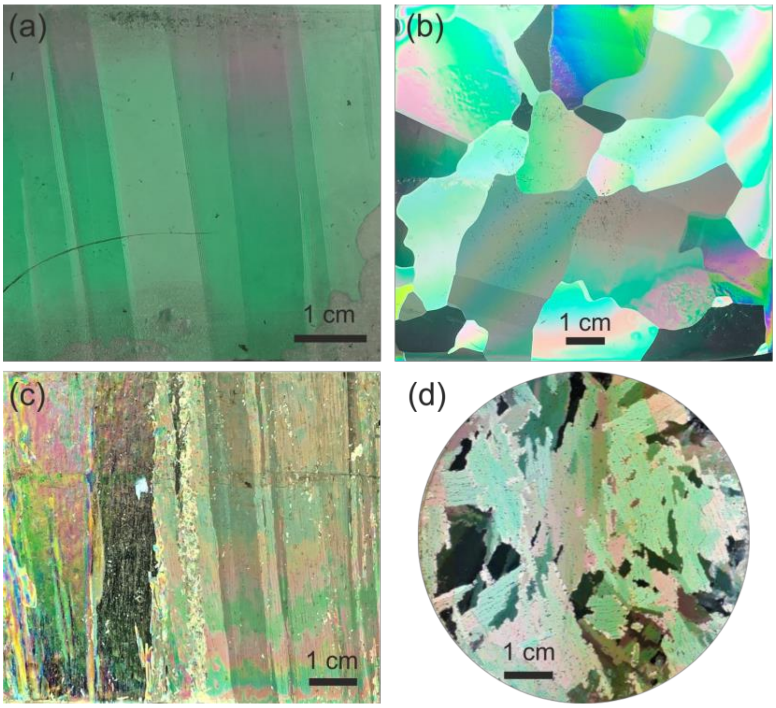

Figure 1. Photographs showing the vertical (a) and horizontal (b) microstructure of lake ice and vertical (c) and horizontal (d) microstructure of sea ice.

The distance L between the outer pair of loading cylinders was 460 mm; the diameter of the cylinders was 40 mm. The middle loading span had a square cross-section with rounded edges to reduce stress concentrations and had an edge length of ~18.5 mm. To minimize contact stresses the loading spans were warmed up before placing an ice plate so the ice was slightly melted at the contact.

During cyclic loading, the mechanical actuator of "Knekkis" was driven up and down under displacement control with the displacement limited in both directions. In addition to a built-in load cell, an external more accurate calibrated HBM load cell was placed between the middle loading span and press (Figure 2). As the results showed, there was no significant difference in measurements made using the two load cells. The displacement of the top surface of the ice plate (or outer-fiber strain) was measured using three calibrated HBM LVDT gauges placed at different positions along the length of the specimen (see Figure 2). The major outer-fiber stress σ_f was calculated from the relationship:

$$\sigma_f = \frac{3PL}{2bh^2}, \quad [1]$$

where P is the applied load.

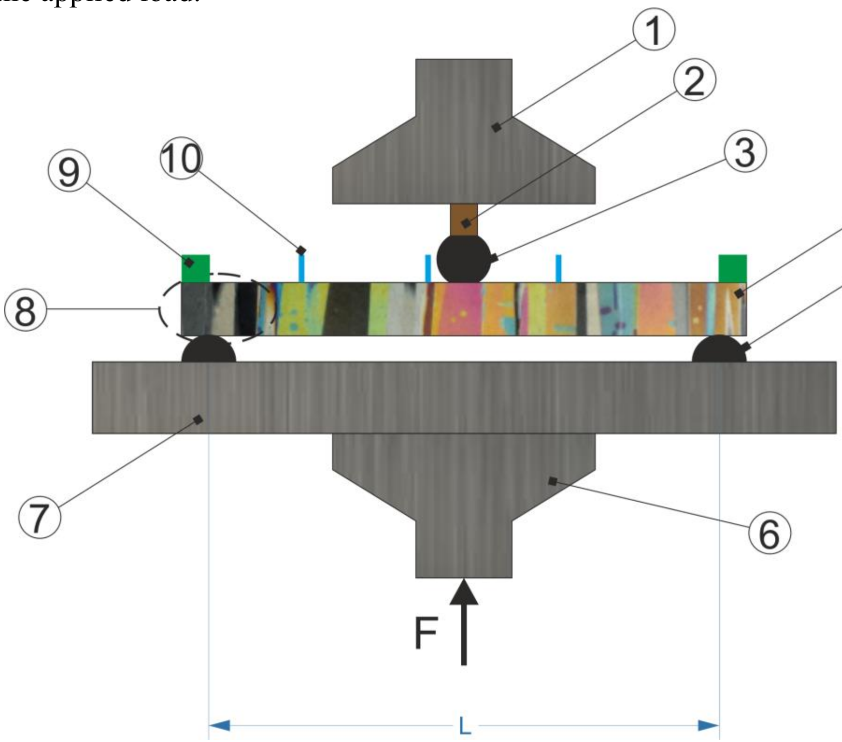

Figure 2. Sketch of the three-point bending apparatus connected to a "Knekkis" mechanical testing system: 1 – immobile steel plate; 2 – HBM load cell; 3 – mid-loading span; 4 – ice specimen; 5 – outer loading span; 6 – loading press; 7 – steel plate; 8 – schematics of columns within the ice specimen; 9 – AE sensor; 10 – LVDT. The upper immobile part 1 is attached to the frame of the machine while the mobile lower part 6 is attached through a fatigue-rated load cell to the piston.

3. **Result and Observations**

Firstly, we conducted three tests where the flexural strength of non-cycled lake ice was measured. Table 1 lists the results. The average and standard deviation of the measured flexural strength are 1.52±0.04 MPa which indicates good reproducibility. These values compare favorably with the values of 1.73±0.25 MPa reported by Timco and O'Brien (1994) for S2 freshwater ice at temperatures below -4.5°C and with the values of 1.67±0.22 MPa reported by Murdza and others (2020) for S2 freshwater ice at -10°C.

Subsequently, we cycled four lake ice specimens in a non-reversed manner for a certain number of cycles (up to 12000) and then brought the ice to a forced monotonic failure by bending in the same sense as cycled. Table 1 lists the stress amplitude during cycling, the number of cycles imposed and the flexural strength after cycling. Figure 3 plots the flexural strength of lake ice versus average amplitude of outer-fiber stress and compares the present results with those obtained earlier (Murdza and others, 2020) from laboratory-grown ice. Despite different loading conditions and a different origin of ice (Table 2), the lake ice behaves similarly to the laboratory-grown freshwater ice under cycling, i.e. flexural strength increases in an apparent linear manner as stress amplitude (and outer-fiber stress) increases. In other words, the answer to our question is yes: lake ice produced under natural conditions, like that produced in the laboratory, exhibits cyclic strengthening when cycled in the laboratory.

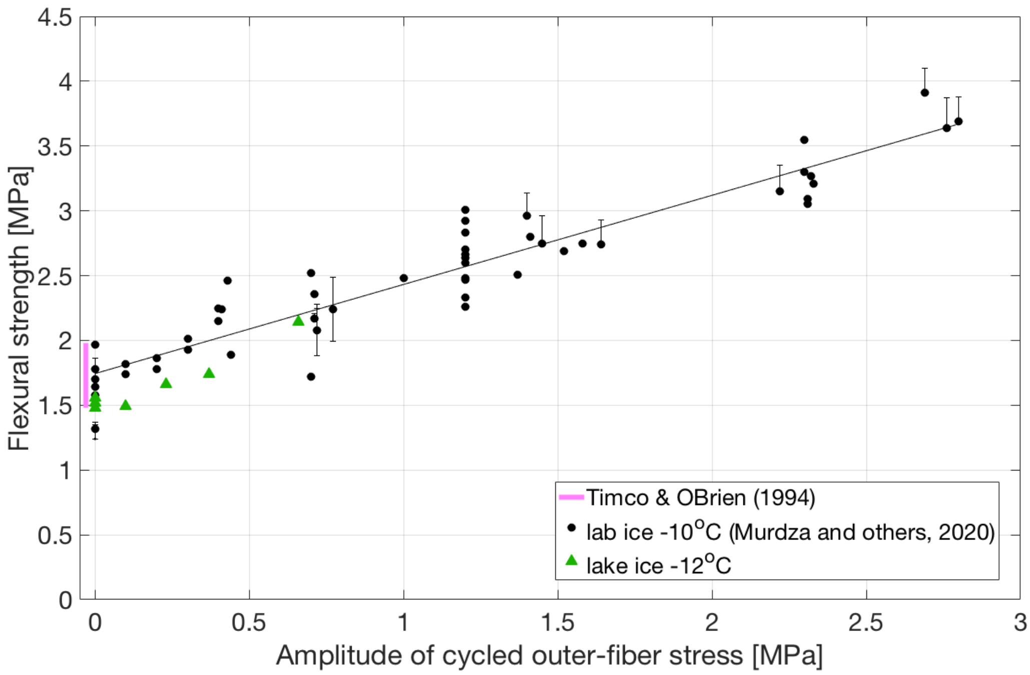

Figure 3. Flexural strength of freshwater ice as a function of stress amplitude/average amplitude of outer-fiber stress. The solid pink line indicates the average flexural strength of non-cycled freshwater ice plus and minus one standard deviation, i.e. 1.73±0.25 MPa (Timco and O'Brien, 1994). Black points represent laboratory tests presented in Murdza and others (2020) which were conducted on laboratory-grown freshwater ice at -10ºC and 0.1 mm s-1 outer-fiber center-point displacement rate in a reversed manner. Green points represent new tests on the lake ice. During all depicted tests the ice did not fail during cycling, but was broken by applying one unidirectional displacement until failure occurred.

In contrast to experiments reported by Iliescu and others (2017) and Murdza and others (2020), where samples were cycled between two specified load limits, in the present experiments specimens were cycled between two specified displacement limits. We observed inelastic deformation during cycling and, as a result, both mean load and maximum load per cycle gradually decreased during cycling. Therefore, stresses in Figure 3 and Table 1 are the average amplitudes of outer-fiber stresses.

One sea ice specimen was cycled and then brought to a forced monotonic failure in bending in the same sense as cycled. As mentioned earlier, the sea ice specimen was loaded parallel to the columns, i.e. columns were oriented along the length of the sample. The flexural strength after cycling resulted in 2.72 MPa. Interestingly, the sample was cycled for ~15 hrs and no significant inelastic deformation of the specimen was detected as well as a maximum load during a cycle was constant throughout the test, unlike the lake ice specimens. This observation is consistent with ice anisotropy where creep rate of S2 ice is greater when loaded perpendicular to the long axis of the ice grains.

Table 1. Flexural strength of both non-cycled and cycled lake ice samples.

TEST #	Flex. Strength non-cycled [MPa]	TEST #	Flex strength cycled [MPa]	Type of Ice	Average amplitude of outer-fiber stress [MPa]	Number of cycles
1	1.48	**4**	1.49	Lake ice	0.1	11961
2	1.52	**5**	1.66	Lake ice	0.23	3909
3	1.56	**6**	2.14	Lake ice	0.66	2860
		7	1.74	Lake ice	0.37	4182
		8	2.72	Sea ice	0.2	5263

Table 2. Comparison of the test setup and ice parameters between laboratory-grown ice (Murdza and others, 2020) and present lake ice.

	Lab-grown ice (Murdza and others, 2020)	Lake ice (present study)
Type of Ice	Freshwater	Freshwater
Type of loading	4-point	3-point
Texture of ice	S2	S2
Grain size [mm]	5.5±1.3	17±3
Density [kg/m^3]	914.1±1.6 [a]	915
Sample dimensions (*L x w x h*)	300 x 75 x 13 mm	600 x 100 x 45 mm
Loading direction	across-column	across-column
Temperature [°C]	-3, -10, -25	-12
Frequency [Hz]	0.03 – 2	0.1[b]
Outer-fiber strain rate [s^{-1}]	1.4 x 10^{-5}, 1.4 x 10^{-4}, 1.4 x 10^{-3}	2.5 x 10^{-5}
Outer-fiber stress rate [MPa s^{-1}]	0.1 – 5	0.05 – 0.2
Average amplitude of outer-fiber stress during test [MPa]	0.1 – 2.6	0.1 – 0.66
Maximum amplitude of outer-fiber stress during test [MPa]	0.1 – 2.6	0.25 – 1.4
Cycling type	Reversed; non-reversed	Non-reversed
Type of control	Load control	Displacement control

[a] Density of ice grown in the same manner is taken from (Golding and others, 2010).
[b] In the non-reversed experiments frequency is lower by a factor of two than in the reversed experiments at the same conditions.

We measured acoustic emissions (AE) during cycling for both lake and sea ice in a similar way as previously by other researchers (Langhorne and Haskell, 1996; Cole and Dempsey, 2004, 2006;

Lishman and others, 2020). Figure 4 shows the results. A few comments should be made based on these data:

1. The amplitude spectrum of lake ice at the beginning and at the end of cycling (~11 hrs) shifted to its higher values, though the width of the spectrum is about the same.
2. The hit rate of lake ice did not change significantly during testing.
3. Sea ice after ~14 hrs of cycling showed a significant reduction in hit amplitudes, i.e. the range of hit amplitudes decreased from ~35-70 dB to ~35-50 dB.
4. Upon cycling of sea ice the number of hits that are generated increased during the experiment by about a factor of 2.
5. The amplitude spectrum of lake ice at the end of the cycling looks very similar to the amplitude spectrum of sea ice at the end of cycling, although the number of hits generated in lake ice is twice the number in sea ice.

When comparing AE of lake ice (specimen #5) with sea ice (specimen #8) one should remember that the lake ice was cycled at ~0.2 MPa which is ~14% of its strength while the sea ice specimen was also cycled at ~ 0.2 MPa which appeared to be only 7% of its strength. Moreover, major stress in the sea ice sample during cycling was along its columns while in the lake ice specimen it was perpendicular to the columns.

Based on AE data presented in Figure 4, no acoustic emissions were detected upon cycling of the lake ice specimen above AE amplitude of ~45-50 dB until the ice broke into two pieces, similar to the earlier experiments on freshwater laboratory-grown ice (Murdza and others, 2020). In addition, the remnant pieces contained no cracks large enough to be detected by eye. This means that the flexural strength of both the lake ice and the freshwater laboratory-grown ice was governed by the tensile stress to nucleate the first crack. Once nucleated, the crack propagated.

It is worth pointing out that Murdza and other (2020) and Iliescu and others (2017) observed decohesions along grain boundaries upon cycling, which were taken to be evidence of grain boundary sliding. In our experiments on the natural ice we did not find any evidence of decohesions. Why is there a difference? Perhaps, type of loading, i.e. 4-point vs 3-point, has an effect. Indeed, the highest stress produced in the 3-point bending test is located at the specimen mid-point with reduced stress elsewhere. The 4-point bending test, however, results in a stress state where the highest stress is distributed uniformly over the entire mid-section of a specimen surface. Therefore, since the area at the highest stress under 3-point loading is relatively small, there could be no grain boundaries that are favorably oriented for grain boundary sliding. Indeed, Figure 10 in Murdza and others (2020) shows that not all the boundaries are favorably oriented for decohesion development.

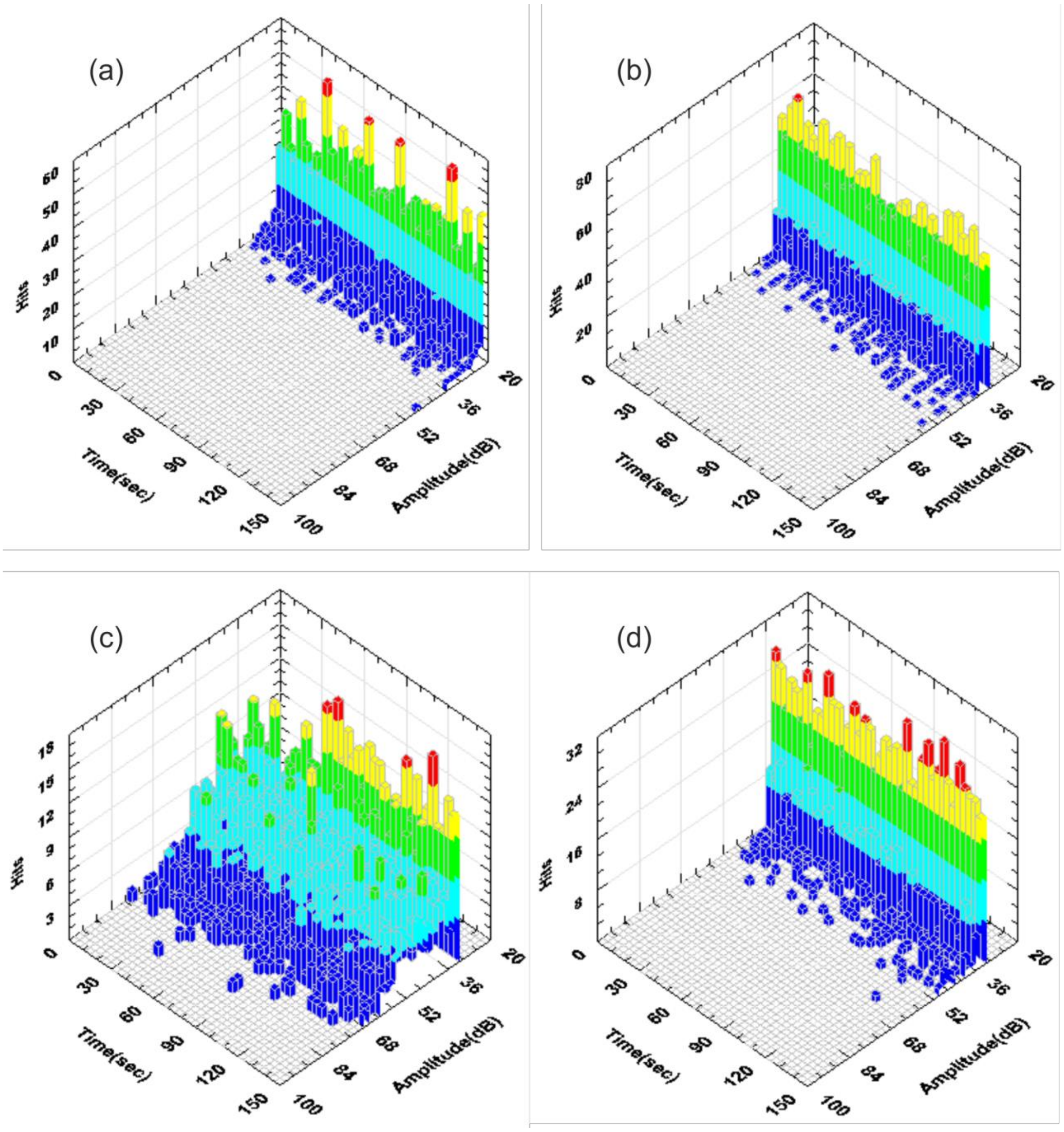

Figure 4. Acoustic emissions: hits as a function of amplitude and time for a) lake ice at the beginning of the test #5; b) lake ice at the end of the test #5 before the forced failure; c) sea ice at the beginning of the test #8; d)sea ice at the end of the test #8 before the forced failure.

4. Discussion

On the process responsible for strengthening the lake ice, our sense is that it is probably the same as the one discussed in Murdza and others (2020) for laboratory-grown ice; namely the development of an internal back stress that opposes the applied stress in nucleating cracks. It may be significant that of the two possible mechanisms proposed earlier (Murdza and others, 2020) for generating back stress, namely dislocation pileups and grain boundary sliding, the latter may be the less likely, given that the strengthening measured in the present experiments is very close to that measured earlier, but that decohesions were not detected within the fractured ice. Further work is required.

The reduction of "loud" AE during cycling of sea ice may indicate either the effect of loading supports, i.e. specimen is adapting to the stress concentrators from the rigid steel cylinders, or initial greater cracking of small weak defects within the sample.

5. Conclusions

Although few in number, the new results show that ice produced under natural conditions on an Arctic lake, when flexed cyclically in the laboratory in a non-reversed manner under 3-point loading at -12 ^{o}C and 0.1 Hz, is strengthened. In other words, although different in origin from ice produced in the laboratory and although loaded somewhat differently from lab ice, albeit cyclically, the natural material exhibits essentially the same behavior as its laboratory analogue.

Acknowledgments

This work was supported by Research Council of Norway (RCN) and Norwegian Centre for International Cooperation in Higher Education (SIU) through the Arctic Offshore and Coastal Engineering in Changing Climate (AOCEC) project, no. 274951, 2018–2020. The work was also partially supported by the US Department of the Interior-Bureau of Safety and Environmental Enforcement (BSEE), contract no. E16PC00005.

References

Asplin MG, Galley R, Barber DG and Prinsenberg S (2012) Fracture of summer perennial sea ice by ocean swell as a result of Arctic storms. *J. Geophys. Res. Ocean.* **117**(6), 1–12 (doi:10.1029/2011JC007221)

Bond PE and Langhorne PJ (1997) Fatigue behavior of cantilever beams of saline ice. *J. Cold Reg. Eng.* **11**(2), 99–112 (doi:10.1061/(ASCE)0887-381X(1997)11:2(99))

Cole DM (1990) Reversed direct-stress testing of ice: Initial experimental results and analysis. *Cold Reg. Sci. Technol.* **18**(3), 303–321 (doi:10.1016/0165-232X(90)90027-T)

Cole DM and Dempsey JP (2004) In situ Sea Ice Experiments in McMurdo Sound: Cyclic Loading, Fracture, and Acoustic Emissions. *J. Cold Reg. Eng.* **18**(4), 155–174 (doi:10.1061/(ASCE)0887-381X(2004)18:4(155))

Cole D and Dempsey J (2006) Laboratory observations of acoustic emissions from antarctic first-year sea ice cores under cyclic loading. *18th International POAC Conference*. Vol 3, 1083-1092

Cole DM and Gould LD (1990) Reversed direct-stress testing of ice: Equipment and example results. *Cold Reg. Sci. Technol.* **18**(3), 295–302 (doi:10.1016/0165-232X(90)90026-S)

Collins CO, Rogers WE, Marchenko A and Babanin A V. (2015) In situ measurements of an energetic wave event in the Arctic marginal ice zone. *Geophys. Res. Lett.* **42**(6), 1863–1870 (doi:10.1002/2015GL063063)

Golding N, Schulson EM and Renshaw CE (2010) Shear faulting and localized heating in ice: The influence of confinement. *Acta Mater.* **58**, 5043–5056 (doi:10.1016/j.actamat.2010.05.040)

Haskell TG, Robinson WH and Langhorne PJ (1996) Preliminary results from fatigue tests on in situ sea ice beams. *Cold Reg. Sci. Technol.* **24**(2), 167–176 (doi:10.1016/0165-232X(95)00015-4)

Iliescu D, Murdza A, Schulson EM and Renshaw CE (2017) Strengthening ice through cyclic loading. *J. Glaciol.* **63**(240), 663–669 (doi:10.1017/jog.2017.32)

Langhorne PJ and Haskell TG (1996) Acoustic emission during fatigue experiments on first year sea ice. *Cold Reg. Sci. Technol.* **24**(3), 237–250 (doi:10.1016/0165-232X(95)00021-3)

Langhorne PJ, Squire VA, Fox C and Haskell TG (1998) Break-up of sea ice by ocean waves. *Ann. Glaciol.* **27**, 438–442 (doi:10.3189/S0260305500017869)

Langhorne PJ, Squire VA and Haskell TG (1999) Role of fatigue in wave-induced break-up of sea ice- a review. *Ice in Surface Waters: Proceedings of the 14th International Symposium on Ice*. Rotterdam, The Netherlands, 1019–1023

Lishman B, Marchenko A, Sammonds P and Murdza A (2020) Acoustic emissions from in situ compression and indentation experiments on sea ice. *Cold Reg. Sci. Technol.* **172**, 102987 (doi:10.1016/j.coldregions.2019.102987)

Michel B and Ramseier RO (1971) Classification of river and lake ice. *Can. Geotech. J.* **8**(1), 36–45 (doi:10.1139/t71-004)

Murdza A, Schulson EM and Renshaw CE (2018) Hysteretic behavior of freshwater ice under cyclic loading : preliminary results. *24th IAHR International Symposium on Ice*. Vladivostok, 185–192

Murdza A, Schulson EM and Renshaw CE (2019) The Effect of Cyclic Loading on the Flexural Strength of Columnar Freshwater Ice. *Proceedings of the 25th International Conference on Port and Ocean Engineering under Arctic Conditions*. Delft, Netherlands

Murdza A, Schulson EM and Renshaw CE (2020) Strengthening of columnar-grained freshwater ice through cyclic flexural loading. *J. Glaciol.* **66**(258), 556–566 (doi:10.1017/jog.2020.31)

Nanetti M, Marchenko A and Høyland K V. (2008) Experimental Study on Friction between Saline Ice and Steel. *Proceedings of the 19th IAHR International Symposium on Ice*. Vancouver, British Columbia, Canada, 1131–1146

Sukhorukov S and Marchenko A (2014) Geometrical stick-slip between ice and steel. *Cold Reg. Sci. Technol.* **100**, 8–19 (doi:10.1016/j.coldregions.2013.12.007)

Timco GW and O'Brien S (1994) Flexural strength equation for sea ice. *Cold Reg. Sci. Technol.* **22**(3), 285–298 (doi:10.1016/0165-232X(94)90006-X)

25th IAHR International Symposium on Ice

Trondheim, 23 - 25 November 2020

Scale effects in lattice-based modeling of ice sheets

Arttu Polojärvi, Ville-Pekka Lilja, Jukka Tuhkuri and Jani Paavilainen

Aalto University School of Engineering,
Department of Mechanical Engineering
P.O. Box 14100, FI-00076 Aalto
arttu.polojarvi@aalto.fi

Three-dimensional numerical modelling of an intact ice sheet can be performed using different techniques. Models aiming for computational efficiency often rely on lattices of beams or different types of springs, that is, ice sheet is modelled using a network of beams or springs, which connect rigid bodies to each other. This technique is often used in the context of discrete element method, combined finite-discrete element method, and bonded particle models. Often the use of lattices introduces scale effects, which show in the response of a modeled ice sheet to external loading. Another source of scale effects can be the used material model. This paper discusses the scale effects of a model, which is based on a network of Timoshenko beams that fracture through a cohesive softening process. The results appear to scale as would be expected for quasi-brittle materials.

1. Introduction

In an ice-structure interaction process, ice sheet collides with a structure, deforms and breaks into a myriad of ice fragments. The fragments form a rubble pile and affect the subsequent failure process. Detailed understanding of the interaction process is important as it may lead to safer and more sustainable Arctic structures related to, for example, marine transportation and offshore wind energy. Numerical models have a central role in the studies on ice-structure interaction processes, even if the modeling still remains a computationally demanding task.

One technique for modeling an ice sheet in a three-dimensional simulation is to use lattices of beams or springs, that is, to model the ice sheet using a network of beams or springs connecting rigid bodies (Figure 1). This technique is often used in the context of combined finite-discrete element method (FEM-DEM) and bonded particle models (Cundall and Strack, 1979; Munjiza, 2004; Potyondo and Cundall, 2004). Lattice-based models introduce scale effects, which show in the mechanical response of the modeled ice sheet. Here this effect appears to be related to the quasi-brittle material model used.

This paper presents results from hundreds of numerical experiments performed by using a lattice-based model. The quantities studied are the tensile strength and the breakthrough strength of an ice sheet. The work is based on a 3D FEM-DEM model, where the ice sheet comprises of polyhedron-shaped rigid discrete elements connected by a network of Timoshenko beams (Figure 1). The examples presented demonstrate how the scale and the discretation of the sheet affect the model behavior. The paper is a short summary of our recent work (Lilja et al., 2019a,b, 2020).

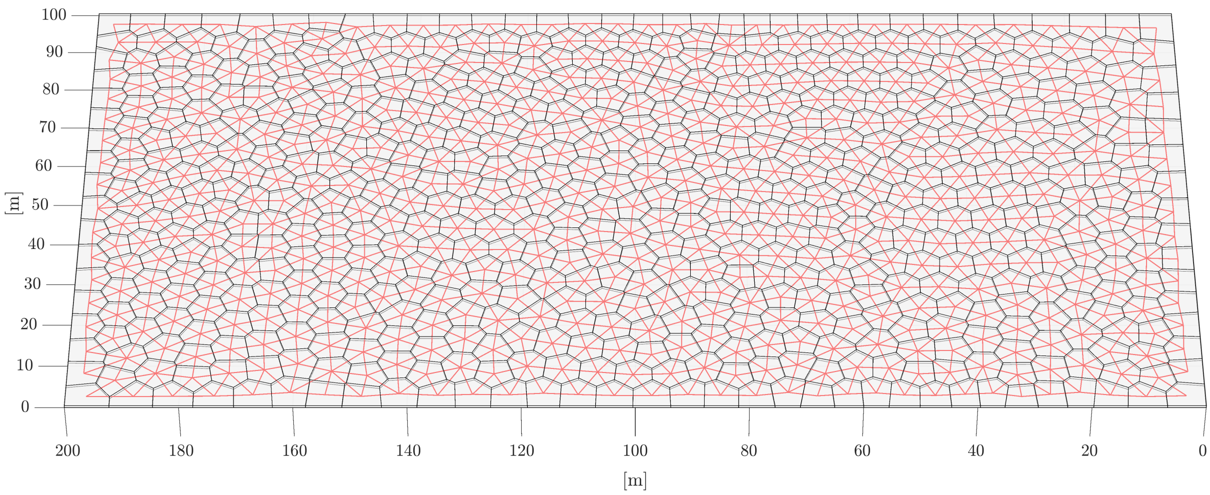

Figure 1. Ice sheet modeled using 3D FEM-DEM and a lattice of Timoshenko beams. In this example, an ice sheet having dimensions $200\ \mathrm{m} \times 100\ \mathrm{m} \times 0.5\ \mathrm{m}$ has been discretized into 600 rigid discrete elements. The centroids of the discrete elements are connected by the beams shown with red lines. Cross-sectional area of each beam was equal to that of the common face of the pair of the discrete elements it connected.

2. Simulations

The in-house 3D FEM-DEM simulation tool of Aalto University Group of Arctic Marine Technology and Ice Mechanics was used in this work. Discrete element shapes and, consequently, the beam networks result from a tessellation routine called centroidal Voronoi tesselation, used to discretize the sheets. The mechanics of the simulations are described in detail by Lilja et al. (2020), but in principle, the tool is a 3D extension of that introduced by Paavilainen et al. (2009).

The beam elements used are elastic-viscous and they were implemented following Crisfield (1990, 1997). The ice sheet failure occurs at locations, where the beams meet a predefined failure criterion. The failure criterion used is a mixed mode failure criterion presented by Schreyer et al. (2006). 2D implementation of the failure model is described in detail by Paavilainen et al. (2009). Upon failure, the beams go through a cohesive softening process (Hillerborg et al., 1976). The cohesive softening is implemented as described in Lilja et al. (2020) by using initially rigid cohesive elements (Sam et al., 2005). Normal contact forces between the discrete elements are solved using a viscous-elastic contact force model, which is here based on the overlap volume of the elements in contact (Feng et al., 2012). Tangential contact forces were solved using an incremental contact force model with Coulomb friction (Hopkins, 1992).

Figures 2a and b describe the numerical tests performed in this paper. Simple uniaxial tensile tests were used to investigate how the scale affects on the tensile strength of the modeled sheet (Figure 2a). Tests were performed by pulling two opposing sides of the sheet with a constant velocity. No other boundary conditions were applied on the sheet and there were no external loads acting on it. Post-fracture contacts were not considered in these tests. Tensile strength of the sheet was defined from the internal forces applied by the beams on the particles on one of the moving boundaries as follows. The loads were first summed into a force resultant, of which component into the direction opposite to the motion of the boundary was monitored. The maximum value of this component was divided by the cross sectional area of the sheet to arrive to the tensile strength. In the vertical breakthrough tests, a rigid cylindrical indentor moved upwards from under a freely floating ice sheet and penetrated it (Figure 2b). In addition to the contact forces due to the indentor, gravitational and buoyant forces were applied on the sheet. The ice sheet fragments forming during the breakthrough test could interact with each other through contacts.

Table 1 gives the main parameters, the sheet side lengths, and the sheet thicknesses used in the simulations. Both test types were performed on square ice sheets of five different sizes and three different thicknesses: The side lengths, L, of the sheet varied from 10 m to 160 m and thicknesses, h, from 0.5 m to 1.5 m. In addition, two different element sizes, beams with average lengths $l = 2h$ and $3h$, were used. Simulations with each set-up were repeated ten times with different tessellations of the sheet, excluding the uniaxial tensile tests with largest sheets, for which six different tessellations were used; about 650 simulations were performed in total. With the element and sheet sizes used, the number of discrete elements in the simulations varied from about 10 up to about 25000.

3. Results and discussion

Figures 3a and b show typical load, F, records from the uniaxial tensile tests and the vertical breakthrough tests, respectively. In the tensile strength tests, F was calculated by using the sum of the internal nodal force vectors of the beams having nodes on the boundary of the sheet; F is the

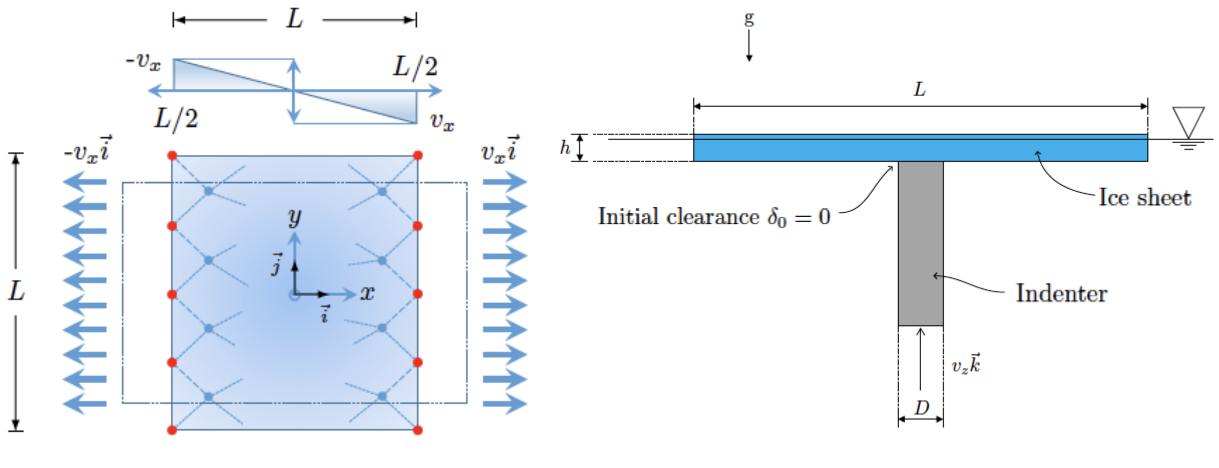

(a) (b)

Figure 2. Numerical experiments of this paper: (a) the uniaxial tensile tests had two opposing sides of an ice sheet moving with horizontal velocity and stretching the sheet and (b) vertical breakthrough tests a rigid cylindrical indentor penetrating a floating ice sheet. L and h, respectively, are the side length and the thickness of the sheet, D is the indentor diameter and g the gravitational acceleration. Figure reproduced from Lilja et al. (2020).

Table 1. Main simulation parameters.

	Parameter	Symbol	Unit	Value or range
General	Gravitational acceleration	g	m/s^2	9.81
	Drag coefficient			1.0
	Coefficient of friction			0.05
	Contact stiffness		GPa	4
	Contact damping ratio			0.95
	Indentor diameter		m	$3h$
	Time step		s	$1.0\ldots5.0\times10^{-5}$
Ice sheet	Side length	L	m	10, 20, 40, 80, 160
	Thickness	h	m	0.5, 1.0, 1.5
	Density		kg/m^3	920
Beams	Effective modulus		GPa	4
	Damping ratio			1.0
	Poisson's ratio			0.3
	Critical axial stress	σ^b_{cr}	kPa	125
	Critical shear stress		kPa	125
	Specific fracture energy		J/m^2	15
Water	Density		kg/m^3	1010

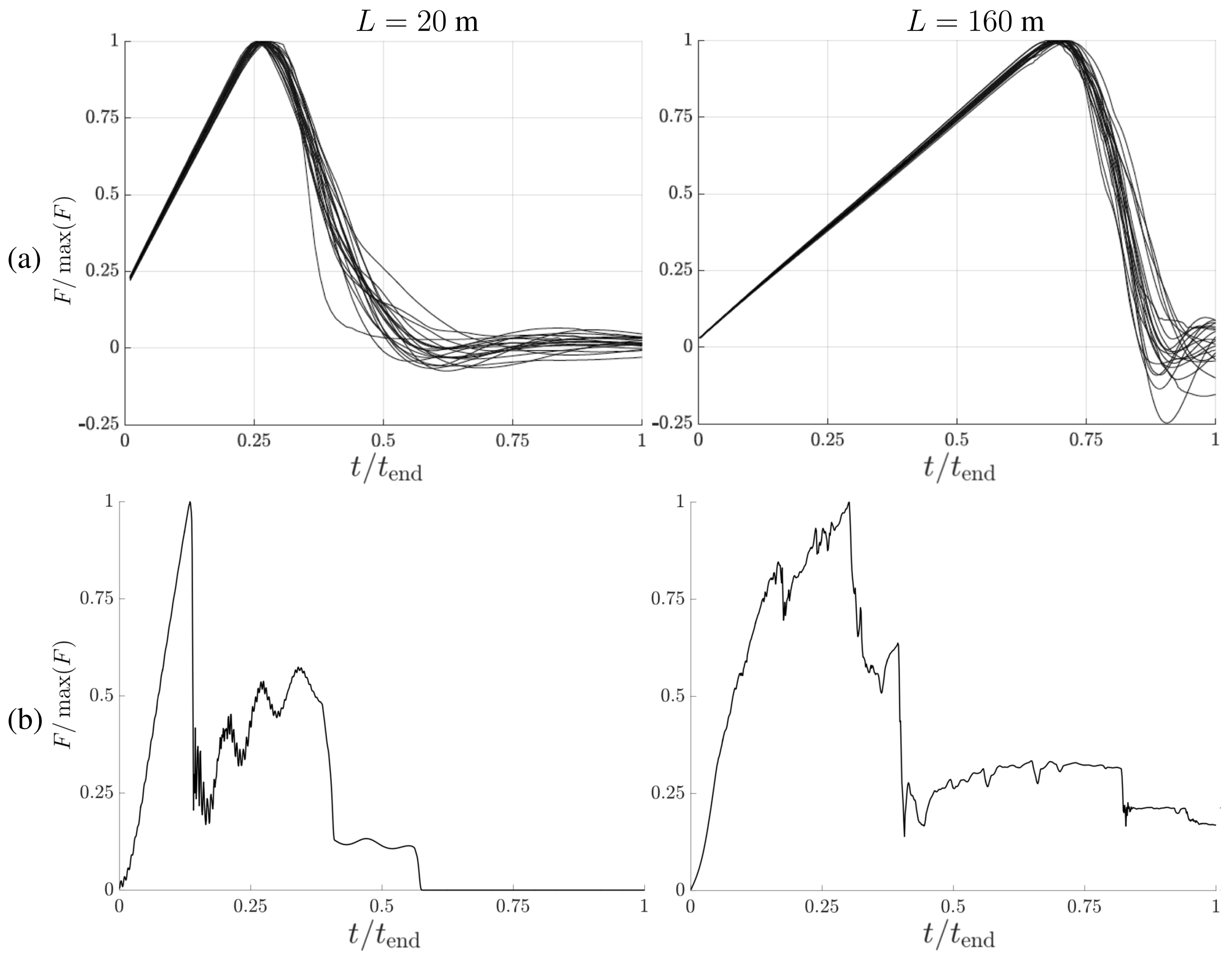

Figure 3. Typical load, F, histories from (a) uniaxial tensile tests and (b) vertical breakthrough tests from simulations having sheet side length $L = 10$ m and $L = 160$ m in left and right column, respectively. Sheets thickness $h = 0.5$ m and the element size $l = 2h$. F is normalized by it maximum value, $\max(F)$, and time, t, by the time at the end of the simulation, t_{end}. Figures reproduced from Lilja et al. (2020).

load component parallel to the direction of the motion on the boundary (Figure 2a). In the vertical breakthrough tests, F refers to sum of the vertical contact forces acting on the indentor penetrating the sheet (Figure 2b). Figure 3 shows the F-records for the smallest and largest ice sheets tested, and in each graph of the figure, F has been normalized by its maximum value, $\max(F)$.

As Figure 3a shows, in the uniaxial tensile tests F first increased approximately linearly up to the onset of the sheet failure. Then F abruptly dropped towards zero and momentarily reached negative values due to the inertia of discrete elements. In the vertical breakthrough tests, F initially started to increase, but with larger plates, the increase was not linear as illustrated by Figure 3b. After the sheet failure, F either dropped to zero or to a value equal to the weight of the ice fragments remaining on top the moving indentor and slowly sliding away from it.

Figure 4 shows the mean values and the standard deviations for the tensile strength, σ_{cr}, of the

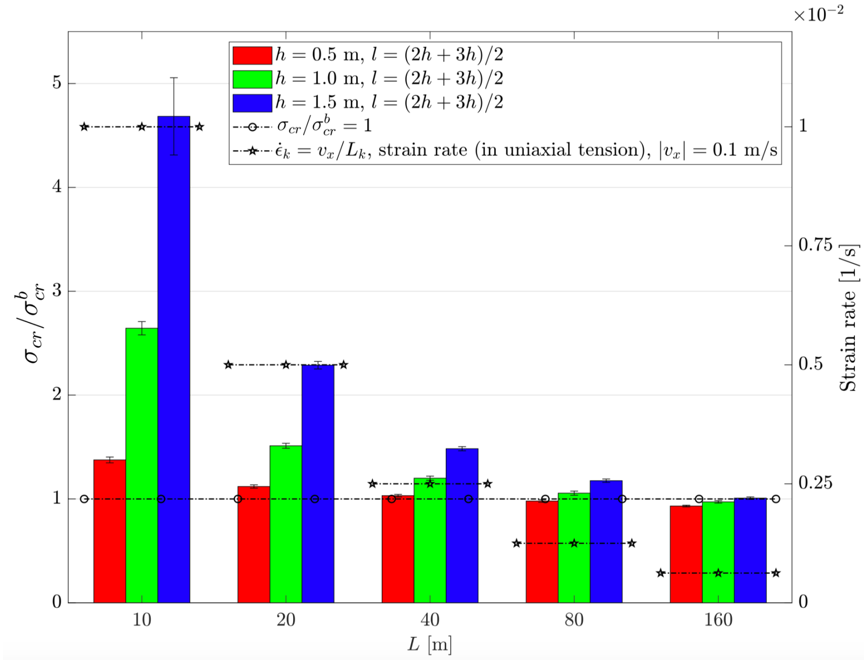

Figure 4. Mean values and standard deviations of the tensile strengths, σ_{cr}, for the ice sheets of all side lengths and thicknesses, L and h, respectively. The results are normalized by the critical tensile strength, σ_{cr}^b, of the beams connecting the discrete elements. Figure reproduced from Lilja et al. (2020).

sheets. Results are shown for the sheets with all side lengths, L, and thicknesses, h, tested. The values of σ_{cr} are normalized by the tensile strength used for the Timoshenko beam elements, σ_{cr}^b (Table 1). For each parameterization, the mean value of σ_{cr} was calculated using the data from the simulations with both element sizes, $l = 2h$ and $3h$, as it was observed that l had no significant effect the results. This means that each mean value for σ_{cr} is based on 20 simulations, excluding the results for sheets with $L = 160$ m, in which case 16 simulations were used to calculate each of them.

Figure 4 shows how the model scale affects the values of σ_{cr}: Thick and small sheets appear to have higher σ_{cr} than thin and large sheets. (Simulation with two discrete elements connected by a beam aligning with the direction of the pull would, however, yield the strength of the beam.) Further, the scale effect shows most clearly in the case of the thickest sheets, since for them σ_{cr} shows the strongest decrease with increasing L. The thinnest sheets have $\sigma_{cr} \approx \sigma_{cr}^b$ for all $L > 10$ m. For two largest sheet sizes, $\sigma_{cr} \approx \sigma_{cr}^b$ for all h. Since every sheet was pulled with an equal velocity from its two opposing boundaries (Figure 2a), the strain rate decreased with increasing L; increase in σ_{cr} with decreasing L is at least partly explained by the increase in strain rate. It should be noticed, that σ_{cr} changes with scale as would be expected for an ice sheet modeled as quasi-brittle material. It is important to notice that, in general, the scatter in the results for each parameterization is negligible; tessellation does not affect the tensile strength of the modeled sheet.

Figure 5 gives the mean values and the standard deviations for the breakthrough force F_{cr}, for all

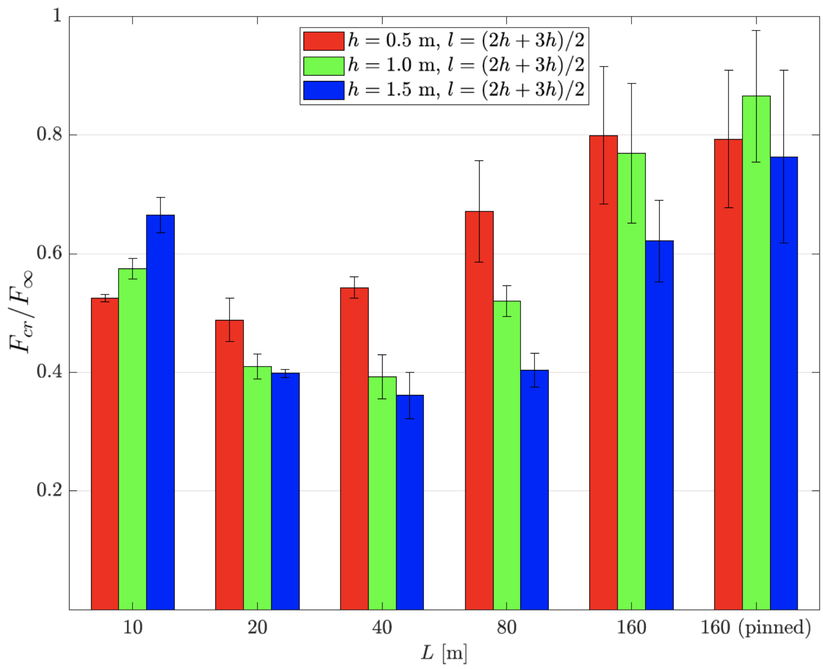

Figure 5. Mean values and standard deviations of the breakthrough loads, F_{cr}, for the ice sheets of all side lengths and thicknesses, L and h, respectively. The results are normalized by an analytic solution for the breakthrough load of an infinite ice sheet, F_∞ (Wyman, 1950). Figure reproduced from Lilja et al. (2020).

sheet sizes and thicknesses tested. The data in this case has been normalized by analytic solution for the breakthrough force of an infinite ice sheet, F_∞ (Wyman, 1950). Data from the simulations with $l = 2h$ and $3h$ was, again, combined to calculate each mean value of F_{cr}, since the effect of l on the results was small. Thus, each data point is based on the results from 20 simulations.

As Figure 5 shows, the breakthrough force, F_{cr}, increased and approached F_∞ with increasing L, when $L > 20$ m. With $L = 10$ m, there was significant upwards rigid body motion of the sheet before its failure, and thus, the static load due to the sheet weight shows in the results. For all L, the thinnest sheets appeared to result into F_{cr} values, which compare better with F_∞ than those yielded by the thick sheets. In this case the tessellation has a moderate effect on the results with the relative standard deviations having values up to about 20 % at maximum. With the largest ice sheet, F_{cr} appears to scale with h as would be expected for quasi-brittle materials. Scatter in the results appears to increase with the sheet size.

Figure 6 shows how the ice sheets typically failed in a breakthrough test. The snapshot at simulation time $t = 4$ s shows four radial cracks. Since the boundaries of the ice sheets were free, the radial cracks often reached the sheet boundaries. With more constrained boundary conditions, the advancement of the radial cracks would have been arrested close to the indentor (Lilja et al., 2020). Further, at $t = 8$ s, the radial cracks have been accompanied by the circumferential ones, and finally by $t = 12$ s, the sheet fragments are floating and interacting with each other. The smaller fragments in the middle of the sheet are still moved by the indentor.

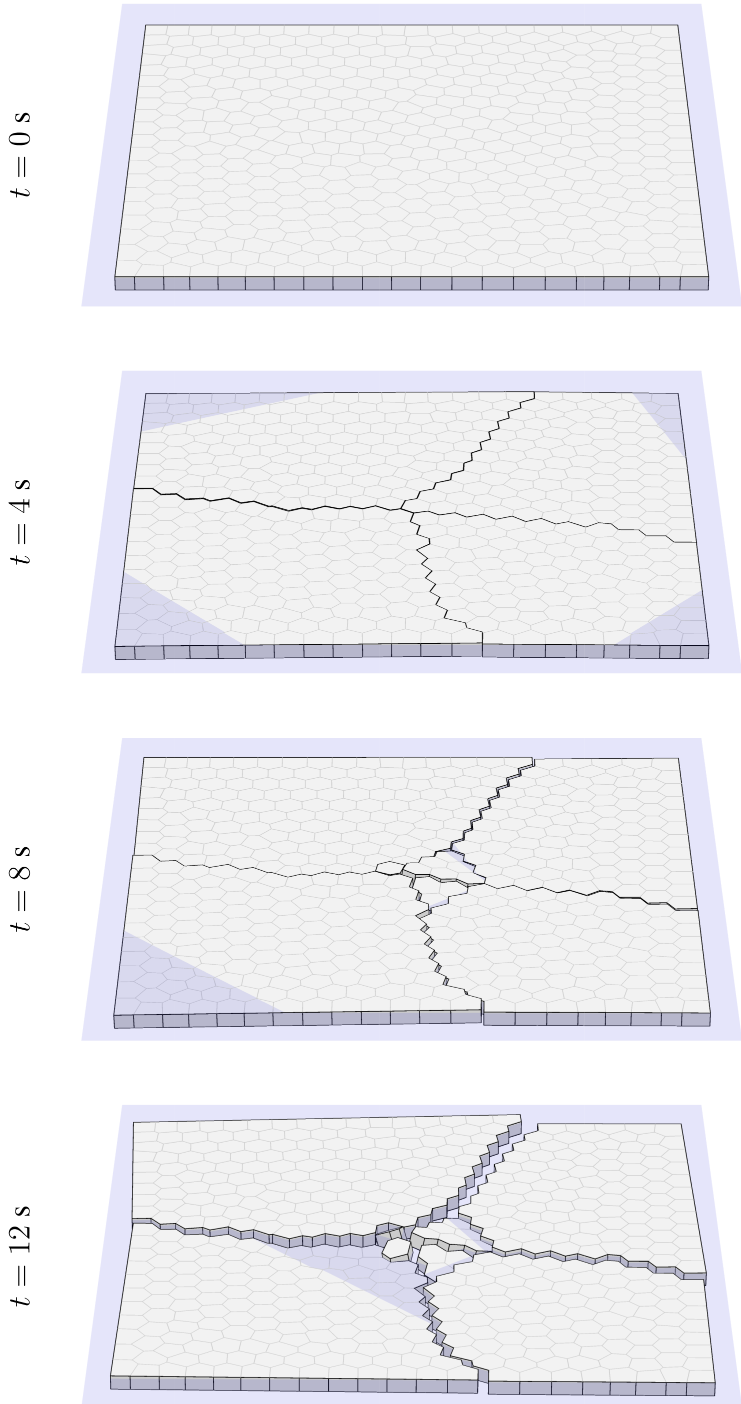

Figure 6. Freely floating square ice sheet of side length $L = 20$ m and thickness $h = 0.5$ m failing due to an upwards moving indentor breaking through it (indentor not visible). The snapshots show how the radial cracks form first and are followed by the circumferential ones as the simulation time, t, increases.

4. Conclusions

This paper presented a short summary on our work on the scale effects in lattice-based modeling of ice sheets Lilja et al. (2019a,b, 2020). The studied quantities were the tensile strength and the vertical breakthrough strength of an ice sheet. The side lengths of the sheets varied from 10 m to 160 m, and the thicknesses form 0.5 m to 1.5 m. The tensile strength of the modeled sheets decreased with the sheet size, while the breakthrough strength increased with it, and approached a value given by an analytical formula. Both quantities showed scaling that would be expected for quasi-brittle materials. Importantly, both test types indicated that the effect of tessellation on the measured quantities was either moderate or even negligible, and further, that the element size, within the variation used here, did not have a significant effect on the studied quantities. The failure patterns from the vertical breakthrough tests resembled those observed in nature, as the radial cracks appeared first and were followed by the circumferential ones.

Acknowledgements

The authors are grateful for the support from the Academy of Finland research projects (268829) Discrete Numerical Simulation and Statistical Analysis of the Failure Process of a Non-Homogenous Ice Sheet Against an Offshore Structure (DICE) and (309830) Ice Block Breakage: Experiments and Simulations (ICEBES). AP worked on the article while visiting Thayer School of Engineering at Dartmouth College (Hanover, NH, USA) during spring 2020, thanks are extended to Prof. Erland Schulson for hosting. Finnish Maritime Foundation is acknowledged for partial funding of the visit.

References

Crisfield, M. (1990). A consistent co-rotational formulation for non-linear, three-dimensional, beam-element. *Computer methods in applied mechanics and engineering*, 81:131–150.

Crisfield, M. (1997). *Non-linear Finite Element Analysis of Solids and Structures, Volume 2: Advanced Topics*. John Wiley & Sons, Inc.

Cundall, P. and Strack, O. (1979). A discrete numerical model for granular assemblies. *Géotechnique*, 29(1):47–65.

Feng, Y., Han, K., and Owen, D. (2012). Energy-conserving contact interaction models for arbitrarily shaped discrete elements. *Computer Methods in Applied Mechanics and Engineering*, 205-208(1):169–177.

Hillerborg, A., Modéer, M., and Petersson, P.-E. (1976). Analysis of crack formation and crack growth in concrete by means of fracture mechanics and finite elements. *Cement and Concrete Research*, 6:773–82.

Hopkins, M. (1992). Numerical simulation of systems of multitudinous polygonal blocks. Technical Report 92-22, Cold Regions Research and Engineering Laboratory, CRREL. 69 p.

Lilja, V.-P., Polojärvi, A., Tuhkuri, J., and Paavilainen, J. (2019a). Effective material properties of a finite element-discrete element model of an ice sheet. *Computers and Structures*, 224.

Lilja, V.-P., Polojärvi, A., Tuhkuri, J., and Paavilainen, J. (2019b). A free, square, point-loaded ice sheet: A finite element-discrete element approach. *Marine Structures*, 68.

Lilja, V.-P., Polojärvi, A., Tuhkuri, J., and Paavilainen, J. (2020). Finite-discrete element modelling of sea ice fracture. *Manuscript submitted to International Journal of Solids and Structures*.

Munjiza, A. (2004). *The combined finite-discrete element method*. John Wiley & Sons Ltd., Chichester, England.

Paavilainen, J., Tuhkuri, J., and Polojärvi, A. (2009). 2D combined finite–discrete element method to model multi-fracture of beam structures. *Engineering Computations*, 26(6):578–598.

Potyondo, D. and Cundall, P. (2004). Abonded-particle model for rock. *International Journal of Rock Mechanics & Mining Sciences*, 41:1329–1364.

Sam, C.-H., Papoulia, K. D., and Vavasisc, S. A. (2005). Obtaining initially rigid cohesive finite element models that are temporally convergent. *Engineering Fracture Mechanics*, 72(14):2247–2267.

Schreyer, H., Sulsky, D., Munday, L., Coon, M., and Kwok, R. (2006). Elastic-decohesive constitutive model for sea ice. *Journal of Geophysical Research: Oceans*, 111(11).

Wyman, M. (1950). Deflections of an infinite plate. *Canadian Journal of Research 28*, pages 293–302.

25th IAHR International Symposium on Ice
Trondheim, June 14 to 18, 2020

The Adhesion of Fresh Water Ice to Concrete at Varying Pressure and Duration For Dry and Wet Conditions

Titli Pramanik[1], Stephen Bruneau[1], Bruce Colbourne[1], Anne Barker[2]
[1]Memorial University of Newfoundland, St. John's, NL, Canada
[2] National Research Council of Canada, Ottawa
[1]240 Prince Philip Drive, 40 Arctic Avenue, St. John's , NL, A1B3X7
[2]1200 Montreal Road, Ottawa, ON
[1]titli.megh@gmail.com,[1]sbruneau@mun.ca,[1] s2dbc@mun.ca,
[2]cab816@mun.ca

Abstract: The purpose of this work is to improve the understanding of the adhesion of ice to concrete. This study is a part of the ICEWEAR* program to determine the effects of ice-concrete bonding on concrete abrasion. Experiments have been carried out in which fresh water ice samples have been placed in contact with mid strength concrete surfaces at varying pressures and for varying durations, after which they are pulled apart. A lever arm machine was designed so that the action of gravity provided steady long term compressive loads, and a controlled-rate scissor jack was used to gently reverse the loading direction to break the adhesive bonds. The result of the experiment confirmed the growth of the adhesive bond strength with time and pressure and provided sufficient data to fully characterize the non-linearity of the relationships.

**ICEWEAR "Ice Wear and Abrasion Effects on Concrete Surfaces" MUN, Kvaerner, NLIC, NSERC(CRD)2017-2022.*

1. Introduction

Ice interaction is a significant factor that structures in colder regions deal with. Concrete structures can be abraded due to continuous or intermittent ice interaction. The wear rate can be influenced by different parameters such as origin, feature, thickness or strength of the ice. Other environmental factors such as temperature, current, or wind may also influence the abrasion process. The adhesive property of ice is a possible significant factor for concrete abrasion as ice can generate pressure in the concrete pores even in a submerged condition(Shamsutdinova, Hendriks and Jacobsen, 2015), (Jacobsen et al., 2015). This surface material abrasion repeatedly causes serious damage for marine and hydraulic structures (Hiroshi Saeki, 2011). Often times, severe concrete wear occurs from ice movement of sea ice or fresh water ice for marine structures or river structures.

Previous studies have addressed the concrete abrasion mechanism causes due to sea ice in different temperatures by conducting sliding friction tests between sea ice and several materials with different surface roughness (H. Saeki et al., 1984). it was found that ice abrasion is dependent on the surface roughness, and temperature. This observation leads to another set of experiments where sliding friction tests were done under varying pressure and temperature by using various concrete samples with different aggregate as the surface roughness and compressive strength highly depend on the type of aggregate used in mix design (Itoh et al., 1988). A later, experiment was conducted under a fixed temperature of -10^{o}C, to determine the ice load effect on a concrete surface from a biaxial collision loads for dry conditions (Tijsen et al., 2015). This paper describes the conduct and results of an experiment to measure pure tensile adhesion of fresh water ice and mid strength concrete under a controlled temperature of -1^{o}C. A series of tests were conducted under varying pressure and duration for both dry and underwater conditions. The adhesion pressure was measured and the failure of the bond interface was observed for ice damage and concrete degradation.

2. Experimental Setup

Ice loads have complex impact on vertical structures which can be static or dynamic (Jacobsen et al., 2015)Besides several factors the abrasion rate depends on the normal stress or contact pressure and a previous report has already documented structure failure due to vertical forces (Hiroshi Saeki, 2011)Generally in cold regions, temperatures are defined by the 0^{o}C isotherm for engineering purpose (Saeki et al. 2010). This background information indicates the impact of temperature and contact pressure that directs the current study to an experiment under a fixed temperature of -1^{o}C with varying contact duration and pressure.

The instrument setup and mechanism of the experiment are illustrated in Figures 2.A and 2.B respectively. The contact pressure was varied by changing the weight hanging from the end of the lever arm. Contact and adhesion pressure were recorded using a 1000lb load cell attached to the lever arm and the concrete cylinder resting on the ice. Fresh water ice and a mid-strength concrete cylinder were used as samples, both produced in the laboratory using standardized methods to ensure uniform and constant physical properties. A supporting plate was used to keep the ice sample stable while a test was ongoing. The concrete sample was clamped in an aluminum holder and attached to the load cell without affecting the sample. Prior to the test (Fig 2.B) the concrete cylinder was not in contact with the ice surface. At the start of an experiment, the concrete was brought into contact and maintained for 0 – full duration by the weight-applied pressure. At the end of the contact duration time the two were pulled apart by reverse loading to obtain the adhesive bond strength resulting from the contact pressure. A controlled rate scissor jack was used with a rate of approximately 4mm/second to gently reverse the loading direction to break the adhesive bond. The entire setup was located inside a cold room for 24 hours prior to and during the experiment, while contact pressure and adhesive strength were recorded from outside the cold room, using a computer data acquisition system attached to the load cell.

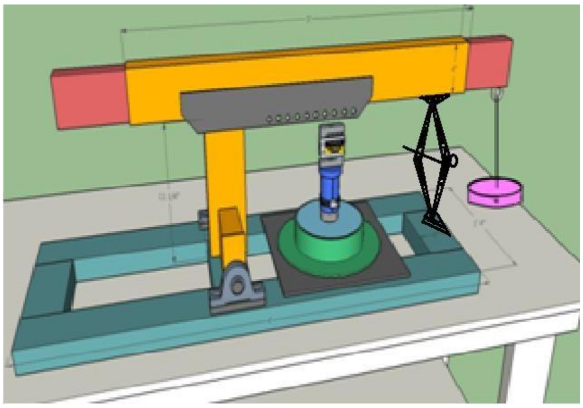

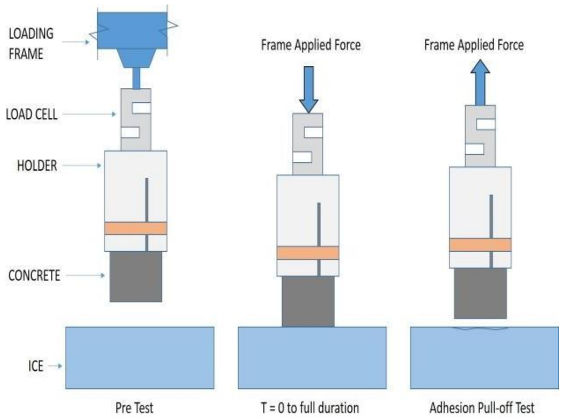

Figure 2.A: Instrumental Setup of Experiment **Figure 2.B:** Mechanism of Experiment

Figure 2.A illustrates the instrumental setup where a lever arm was designed so the action of gravity provided steady long term compressive pressures. The hanging weight bar was used to produce contact pressure on the concrete cylinder attached to the load cell for ascertain duration of time and pulled apart by reverse loading using the scissor jack. The entire setup was done inside a cold room at a controlled temperature of -1^{o}C

Figure 2.B illustrates the mechanism of the experiment conducted to measure ice-concrete adhesion with varying contact pressure and duration. Prior to the test, the concrete cylinder in a holder was attached to load cell and not in contact to the ice. The cylinder then came in contact with the ice surface by applying pressure for 0-full duration and was finally pulled apart by reverse loading after the stated time. The adhesion pressure was measured by the attached load cell without affecting the concrete sample

2.1 Ice Sample

Several ice features, such as origin, strength, thickness have significant impact on concrete abrasion (Jacobsen et al., 2015),and the water salinity and impurities are responsible for varying the strength of ice. To obtain the pure adhesive strength and corresponding abrasion, this experimental study was designed with non variable samples. The ice samples were produced in the laboratory by following a method, documented in earlier work (Bruneau et al., 2012; Dillenburg, 2012). This relatively simple preparation method has established a standardized procedure for producing ice samples with consistent mechanical properties and internal structures which can be reasonably considered as a replica of natural ice that is polycrystalline and anisotropic. The ice was prepared with seeded ice and water using a unidirectional freezing method. Commercial ice cubes were crushed mechanically to obtain the ice seeds which are then mixed well with deaerated, deionized, distilled water in cylindrical mould and support frame. Freezing occurs unidirectionaly from the bottom up due to thick insulation covering the other surfaces at -15 to -20^{o}C temperature. This method avoids the internal cracks and trapped air inside the freezing sample which occurs due to multi directional freezing method. The frozen samples were de-moulded, turned upside down and rubbed over an aluminum plate to get a smooth and flat contact surface of the ice sample.

The dimension of the ice sample was constant at 228.6 mm diameter and 101.6 mm height. A metal frame was used to clamp the sample during the experiment to reduce the chance of displacement, as illustrated in figure 2.1.1. The crystal structure of the ice was observed using a technique documented in Bruneau, Dillenburg and Ritter, 2013. A thin section of the laboratory made ice sample was cut and observed under a polarized microscope (Figure 2.1.1). The ice was found to be polycrystalline with no preferred orientation and the crystal sizes were 1-6 mm in width. Each sample was pre-prepared and wrapped in plastic cover before storing in the freezer to avoid frost. For each test, a new ice sample was used and no ice sample was reused for any dry and submerged experiment.

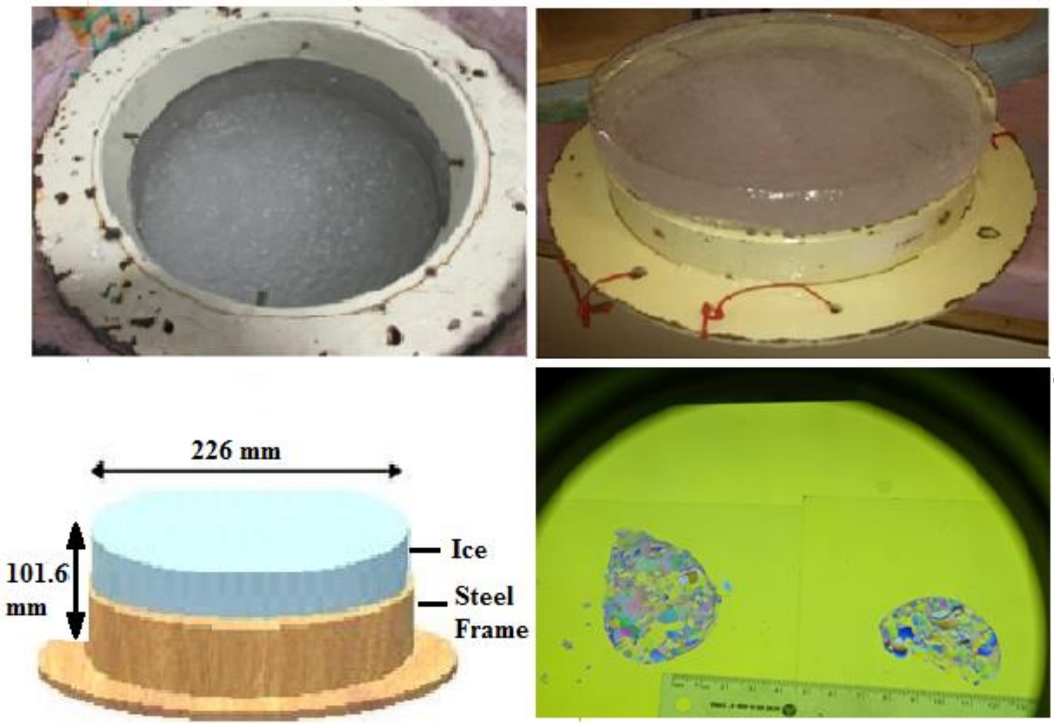

Figure 2.1.1: Fresh water Ice Sample

Top left: Seeded and de-aerated, de-ionized, distilled water were mixed in a mould with metal frame and ready to freeze in an unidirectional method ; Top right: the ice sample was demoulded and flattened with an aluminium plate; Bottom left: The schematic diagram of ice sample with dimension; Bottom right: Thin section of ice sample under polarized microscope.

Figure 2.1.1 Illustrates the fresh water ice sample with228.6 mm diameter and 101.6 mm height, prepared in laboratory with seeded ice and deaerated, deionized, distilled water by freezing the mixture in unidirectional method. The attached metal clamp used to clamp the sample during the experiment. The crystal structure of this sample was observed under polarized microscope. The ice was found polycrystalline and the crystal sizes were 1-6mm in width

2.2 Concrete Sample

The main purpose of designing the concrete mix was to standardize a consistent sample that can be easily compared with the other concrete mixes used for ice interaction experiments. Such mid strength concrete mixes are generally used in marina and harbor constructions. Samples were 50.8 mm in diameter and 101.6 mm in height cylinders. This mix was designed according to an ASTM standard and the compressive strength was found to be 45 and 47

MPa after 14 and 28 days respectively.

Table 1: Concrete Mix Design for m^3

Ingredients	Amount
Cement	400 kg
Coarse aggregate	112.8 kg
Fine Aggregate	94 kg
Water	19.2 kg
Plasticizer	50 ml
Ratios	
Water Content W/C	0.4
Cement Factor C/F	1.2

Table 1 describes the mid-strength concrete mix in details design for 1 m3.The compressive strength for this mix was found 45Mpa (approximately).

Figure 2.2.1 shows the 50.8 mm diameter, 101.6mm height concrete cylinder made from mid-strength concrete mix listed in table 2.2. The aluminum clamp is used to hold the concrete and attach it to load cell during the experiment

2.3. Test Plan

In past studies push-out, pullout and friction tests were done between sea ice and different materials under varying temperature to find the adhesion strength of ice where the adfreeze bond strength was found to be both material dependent and contact pressure dependent (Hiroshi Saeki, 2011).

Table 2: Test Matrix Plan of Ice-Concrete Adhesion Test with Varying Contact Pressure and Duration Under fixed Temperature and Other Non-Changing Variables

Contact Pressure (kPa)	Contact Duration (Minute)						
112	1	5	15	30	60	90	120
177	1	5	15	30	60	90	120
264	1	5	15	30	60	90	120
321	1	5	15	30	60	90	120
427	1	5	15	30	60	90	120
585	1	5	15	30	60	90	120
826	1	5	15	30	60	90	120

Non Changing Variables	
Temperature	-1◦ C
Surface area of concrete sample	2027 Area sq mm
Mechanical property of Ice sample	Replica of natural ice
Loading Rate	4 mm/s

Table 2 describes the 7x7 matrix test-plan with variable contact pressure to duration under constant temperature of -1◦ C. Other non changing parameters: surface area of concrete sample, mechanical property of ice and loading rates, are listed as well.

This experiment was designed with variable contact pressure and temperature using the replicated freshwater ice and concrete samples under constant temperature. A series of experiments were designed for varying contact pressure and duration using a 7x7 matrix in ranges from 1-120 minutes and 112.49-126.41 kPa under the controlled temperature of -1C (table 2). The corresponding adhesion pressure was measured and is listed in table 3..

Three replications were taken for each of the tests and the average result was considered as final output. Photographs were taken prior to and after testing for both samples, and the weight of the concrete sample was recorded prior to and after the test as well. This experiment was done for both dry and wet cases in order to compare the adhesion bond for the two different case scenarios. The dry test was conducted by resting the concrete over the ice in a controlled temperature whereas the submerged test was conducted in a water bath.

2.4 Submerged Test

In reality, marine structures are partially submerged in water and exposed to ice collision for both dry and submerged state. To observe the adhesion bond for both conditions, the test was conducted for both dry and underwater conditions. The experiment was initially designed under controlled temperature (at 1°C) inside the coldroom. However the temperature for the submerged tests was slightly higher than the dry test to prevent the water from freezing. The equipment was stored inside the coldroom 12 hours prior to the experiment, the ice sample was stored separately to avoid from melting and distilled water was used in this experiment.

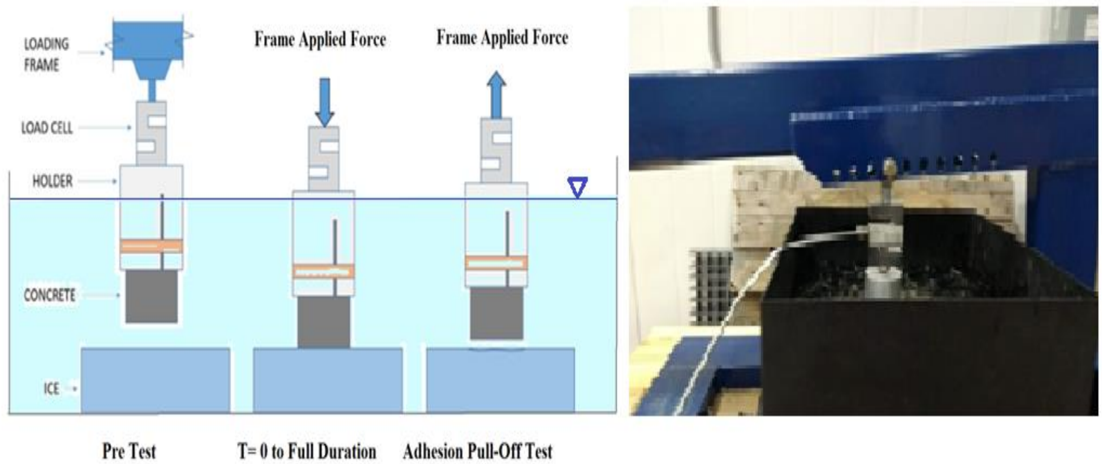

Figure 2.4.1: Methodology and Experimental Setup of Submerged Experiment

Figure 2.4.1illustrates the methodology and experimental setup of the submerged experiment. The ice sample was bolted inside a leakage resistant box that box was filled with distilled water near 0 °C temperature and distilled water made ice cubes were added to maintain the water temperature. The experiment was conducted under the controlled temperature of 1°C .

The water temperature was near 0°C and some distilled water made ice cubes were added to maintain the temperature during the experiment. The ice sample was bolted inside a leakage-resistant metal box (figure 2.4.1) and the concrete cylinder was attached to the load cell and lever arm but was not in contact with the water prior to the experiment. Once the box was filled with water, the concrete cylinder was placed using the same methodology and loading rate (4mm/s) as the dry test. After the contact duration, the concrete cylinder was pulled away from the ice using the scissor jack in the reverse loading direction. The ice cylinder was observed before and after the experiment and the water was drained after the experiment. The average of three replications was considered as final data for each test.

3. Results

The series of tests was conducted with multiple replications; the adhesion bond was recorded, and abrasion or surface damage was observed for each of the tests. Three replications was taken for each test and the average was considered as the final output, listed in table 3 and plotted in figure 3.1.

Table 3: Adhesion Strength between Ice and Concrete with Varying Pressure and Duration Under -1C temperature

SL No.	Contact Pressure (kPa)	Contact Duration(Min)						
		1	5	15	30	60	90	120
1	112	0	0	1.21	1.32	1.36	1.38	2.62
2	177	0.6	0.64	1.29	1.37	1.44	1.51	3.01
3	264	0.79	0.69	1.35	1.46	1.61	1.73	3.29
4	321	0.64	0.74	1.46	1.58	1.76	2.48	4.0
5	427	0.61	0.77	1.97	2.07	3	5.66	8.79
6	585	0.66	0.89	3.89	4.01	5.54	7.15	9.28
7	826	00.82	0.91	5.49	5.55	7.29	9.13	11.84

Table 3 shows the results obtained (average of three replications) from ice concrete adhesion under varying contact pressure and duration where adhesive strength increased with increasing contact pressure and duration. A parallel relationship was obtained for adhesion strength after the full series of experiments. The maximum adhesion pressure was observed for 826 kPa contact pressure and 120 minutes duration

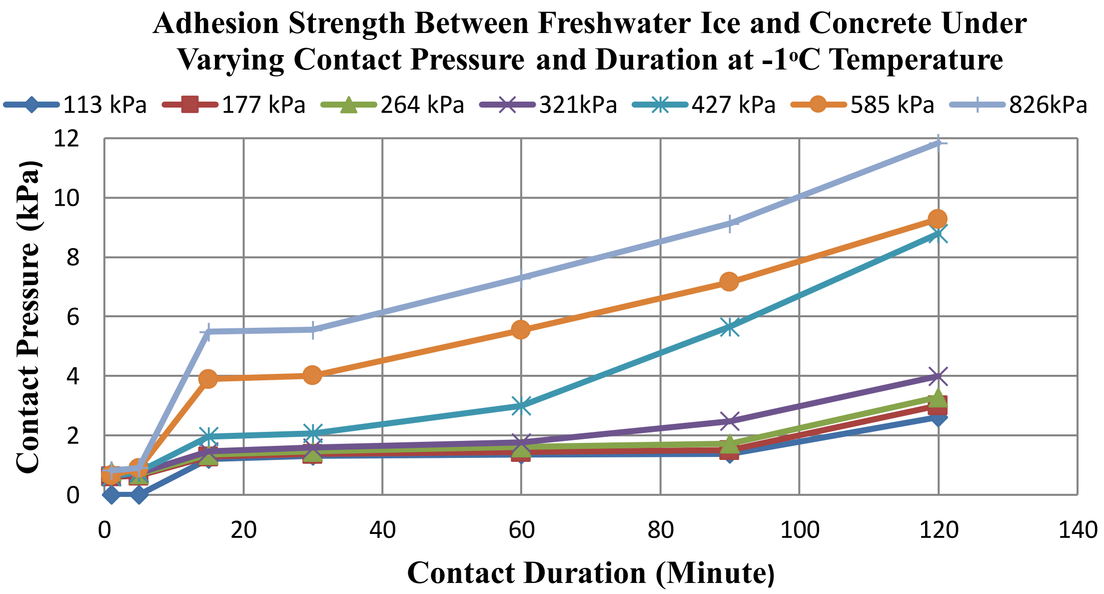

Figure 3.1: Ice-Concrete Adhesion Pressure versus Contact Duration at Various Normal Stresses

Figure 3.1 illustrates the ice- concrete adhesion strength for varying contact pressure and duration with contact duration in x axis and the adhesion pressure in y axis. Each of the series represents the nonlinear trend of adhesion pressure, where that adhesion pressure induced for stronger contact pressure and duration in a non linear way.

In each of the seven series, adhesive pressure was found to be directly proportional to the contact pressure and duration. The maximum adhesion pressure was observed to be 11.8 kPpa for the 826 kPa contact pressure at 120 minutes duration. A parallel relationship was obtained from the recorded data set and nonlinearity was observed from the data plotted in figure 3.1. The adhesion strength moderately increases for 15-30 minutes and in some cases up to 60 minutes and then more rapidly increases after that time point. On the other hand at weaker contact pressures 112.49, 176.63, 263.95, 320.69 kPa the adhesion was also comparatively weaker. It also increased after 5 minutes of contact duration but tended to remain linear up to 15-90 minutes of duration followed by a more significant increase at 120 minutes of duration.

The adhesion bond was observed to be significantly higher for the submerged experiment, compared to the dry test. For 265.9 kPa contact pressure with 60 minutes of contact duration under the water, the adhesion strength was observed to be 18.8 kPa, whereas for the comparable dry test, the bond strength was found 1.61 kpa

4. Observation

Photographs were taken after every experiment to observe the changes for both the ice and concrete samples.

Before Experiment **After Experiment**

Figure 4.1: Ice Surface Before and After Experiment

Figure 4.1 illustrates the ice surface before and after experiment. Though the abrasion rate is minimal, the abraded concrete particles are clearly observed over the ice surface after experiment.

An indentation was found in the ice almost after every test, it was deeper when the applied pressures and times were higher. For some lower applied loads with short time duration, the indentation was negligible but a thin layer of ice was found sticking on the concrete surface. In some of the experiments that showed strong bond breaking forces, a piece of ice was observed to come out with the concrete surface after the pull-up and concrete particles were found around the ice surface. Figure 4.1 illustrates the difference in the ice surface before and after an experiment where concrete particles can clearly be observed on the ice surface after the experiment. The abrasion of concrete was found to be very small after each single experiment, so the same concrete sample was used repeatedly for the series of experiments in order to determine the cumulative abrasion of the concrete by regular observation. The abrasion was observed after the series of tests.

The submerged experiment was conducted at a small scale and thus it was not possible to measure the material loss of concrete because the abraded particles were dissipated in the water. The experiment was conducted at 1°C temperature so the ice sample also started to melt after a certain time, so the changes in the ice surface due purely to the applied pressure were also not possible to obtain. The concrete cylinder was submerged in the water and there is a good chance of water absorption. Thus measuring the concrete sample before and after the experiment was also not an appropriate way to measure the material loss. However, the material loss was evident from the amount of ice piece sticking to the concrete (figure 4.2)

Figure 4.2: Ice Chunk Sticking on Concrete Surface after Submerged Experiment

Figure 4.2 illustrates the ice chunk sticking on the concrete surface after the submerged experiment. As the ice sample was started to melted due to the submerged condition, this was found as the most evident way to observe the material loss.

5. Conclusion

This paper describes an experiment that has been performed to determine a basic ice concrete bonding interaction and any corresponding abrasion. The dry pull up test was performed to measure the pure adhesion bond between ice and concrete under varying pressures and load durations . Based on the results and analysis, the adhesion of ice to concrete is quite dependent on the applied forces and time duration. The abrasion on the other hand could only be measured as a cumulative process due to the small amount of damage associated with each test. Thus a clear link between wear and load or duration could not be established although overall wear was evident.

In real life cases, ice concrete collisions occur both above and under the water. Some of the tests were also performed under-water and the bond strength was found to be significantly stronger than the dry tests. The concrete can causes a significant indentation on ice surface under medium ranges of applied force within a very short time duration compared to the dry tests.

The dry and underwater tests were conducted in a controlled temperature of -1 and 1 degree Celsius which can be considered as the most sensitive parameters this experiment. As the tests were conducted at a relatively small scale, and with a little bit of variation in temperature, the test results can have some variation or error. The laboratory was not able to provide a controlled temperature for more than 120 minutes. For further studies, the duration ranges should be extended up to 24 hours or even more to observe the maximum ice concrete adhesion bond under a constant applied force.

The water temperature was near 0 °C temperature during the submerged test so the ice sample started to melt after a certain contact duration and it was found difficult to hold the ice sample inside the metal ring during the experiment. Future submerged test are suggested to be conducted at a larger scale to observe the effect of longer contact duration.

Acknowledgement

The authors would like to acknowledge Memorial University of Newfoundland and Kvaerner Canada Limited for their technical and financial support in this research. Special thanks to Matthew Curtis, Craig Mitchell, David Snook, William Bidgood, Trevor Clark and other laboratory technicians for their continuous advice and help during the experiment. The authors would like to acknowledge Ali Eid Abdel Hafez and Mr. Mohamed Zurgani for helping in concrete mix design. We would also like to thank Bart Westerveld, Bob Tulp, Yiran Liu, Mwaria Emmanuel Richmond for their continuous advice and assistance.

References

Saeki, H., Ono, T., Nakazawa, N., Sakai, M., & Tanaka, S. (1984). The coefficient of friction between sea ice and various materials used in offshore structure. Proceedings of the Annual Offshore Technology Conference, 1984-May(March 1986), 375–382. https://doi.org/10.4043/4689-ms

Itoh, Y., Yoshida, A., Tsuchiya, M., Katoh, K., Sasaki, K., & Saeki, H. (1988). An experimental study on abrasion of concrete due to sea ice. In: Otc 88 Proc., Twentieth Annual Offshore Technol. Conf., (Houston, U.S.a.: May 2-5, 1988), 2, Richar, 61–68. https://doi.org/10.4043/5687-ms

Saeki, Hiroshi. (2011). Mechanical properties between ice and various materials used in hydraulic structures: The Jin S. Chung award lecture, 2010. International Journal of Offshore and Polar Engineering, 21(2), 81–90.

Bruneau, S. E., Dillenburg, A. K., & Ritter, S. (2013). Ice sample production techniques and indentation tests for laboratory experiments simulating ship collisions with ice. Proceedings of the International Offshore and Polar Engineering Conference, 1268–1271.

Jacobsen, S., Scherer, G. W., & Schulson, E. M. (2015). Concrete-ice abrasion mechanics. Cement and Concrete Research, 73, 79–95. https://doi.org/10.1016/j.cemconres.2015.01.001

Shamsutdinova, G. R., Hendriks, M. A. N., & Jacobsen, S. (n.d.)(2015). CONCRETE-ICE ABRASION : SURFACE ROUGHNESS.

Tijsen, J., Bruneau, S., & Colbourne, B. (2015). Laboratory examination of ice loads and effects on concrete surfaces from bi-axial collision and adhesion events. Proceedings of the International Conference on Port and Ocean Engineering under Arctic Conditions, POAC, 2015-Janua.

25th IAHR International Symposium on Ice
Trondheim, June 14 to 18, 2020

Influence of water freezing in tidal cracks on the formation of ice stresses in coastal zones of the Arctic seas

Aleksandra Visich[1,2], Aleksey Marchenko [2]
[1] Moscow Institute of Physics and Technology (MIPT), 9 Institutskiy per., Dolgoprudny, Moscow Region, 141701, Russian Federation
[2] The University Centre in Svalbard (UNIS), P.O. Box 156 N-9171 Longyearbyen, Norway
aleksandra.visich@phystech.edu

The project work included experiments in the cold laboratory of the University Centre in Svalbard and in-situ observations of land fast ice in the Van Mijen Fjord, Spitsbergen. The laboratory experiments were performed in 2018-2019 to investigate thermal response of ice samples due to cyclic changes of the room temperature and due to the freezing of water in the preliminary made ice cuts. The samples of natural lake ice and sea ice were used for the experiments. Duration of each laboratory experiment with lake ice and sea ice was of about one month. Granular structure of ice formed inside the cracks was investigated by thin section analysis in the laboratory and in the field conditions. Fiber optics sensors AOS GmbH were used to measure ice strains and temperatures in the laboratory. It was discovered that ice deformations are mostly related to the release of the latent heat during the water freezing in the cracks. Numerical simulations in COMSOL Multiphysics were performed to calculate the ice stresses near the crack caused by the heat transfer from the freezing water.

1. Introduction

Investigation of ice action on coastal zone of Arctic seas is important for designing engineering structures to protect shorelines from erosion, as well as for development of coastal infrastructure (ISO 19906). Tidal variations of water level cause cyclic deformations of coastal ice and regular formation of tidal cracks and floods on the ice surface in the hinge zone. We define here coastal ice as the part of the ice cover that is attached to the shore, which forbids large-scale horizontal movements and limits vertical movements with the sea surface. The hinge zone is located between coastal ice and land fast ice, where the latter moves up and down together with water according to tidal phase. The movements of coastal ice and floods, in turn, influence mechanical ice stresses and variations of ice temperature that result in thermally induced stresses.

Mechanical actions of sea ice on coastal zones of the Arctic were discussed in numerous papers (Prinsenberg et al. 1997; Caline 2010; Bogorodskiy et al. 2010; Ogorodov et al. 2013; Blæsterdalen et al. 2016; Wranborg et al. 2016). Thermal actions of sea ice are less known. ISO 19906 states that “in sheltered areas and areas near the shore, ice actions can occur due to rising temperatures when ice expansion is restricted by fixed structures or other obstructions”, and “in Russian and Canadian sea areas, sea ice does not expand appreciably for ice temperatures above -10 ^oC for salinities greater than 3 ppt or above -7 ^oC for salinities greater than 1 ppt”. Thermal stresses in sea ice of the Van Mijen fjord in Spitsbergen were investigated by Teigen et al. 2005. They measured largest stresses up to 0.2 MPa and discovered that tidal phase may influence thermal stresses in ice due to the confinement, and the boundaries and cracks are also vital. Marchenko 2018 measured cyclic ice pressures with semidiurnal period on the cofferdam of coal quay in Kapp Amsterdam in the Van Mijen fjord with maximal amplitude up to 0.5 MPa which were accompanied by cyclic changes of the ice temperature and sea water migration through the ice. Maximal pressures were registered in ice when its temperature was above -10 ^oC.

Thermal expansion of saline ice is different from that of fresh ice because of the phase changes that dominate over thermal expansion of brine and ice in the range of relatively high temperatures depending on the ice salinity. Malmgren 1927 derived the coefficient of thermal expansion assuming that permeability of the ice is low. This simplification was criticized by Cox 1983 and Johnson et al. 1990, who proposed that all the brine existed in permeable channels. Golden et al. 2007 investigated the permeability of sea ice and showed that it is not permeable when the ice temperature is below -5 ^oC, and the ice salinity is lower than 5 ppt. Marchenko and Lishman 2017 measured the coefficient of thermal expansion of saline ice between the values determined by Malmgren’s formula and the coefficient of thermal expansion of fresh-water ice. Renshaw et al. 2018 discovered that ice compression reduces sea ice permeability.

In the present paper we describe laboratory experiments on thermal deformations of natural sea ice and lake ice caused by cyclic changes of the air temperature and water freezing in the ice cracks. In addition, we present preliminary results of numerical simulations of ice stresses on shore line caused by water freezing in tidal cracks. Experimental setup and the results are described in the second and in the third sections of the paper, respectively. Results of numerical simulations are given in the fourth section. Main results of the investigations and conclusions are formulated in the last section of the paper.

2. Experiment description

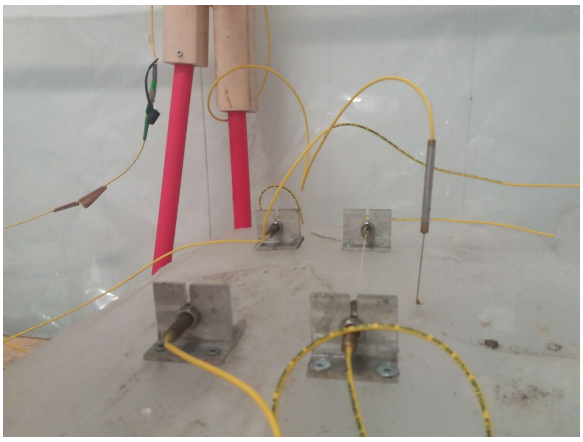

(a)

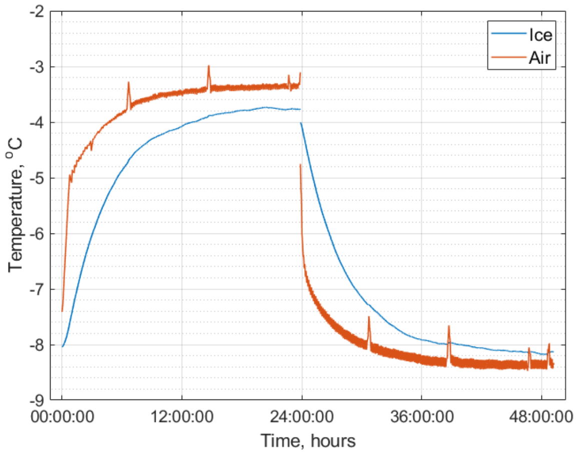

(b)

Figure 1: (a) FBG (Fiber Bragg Grating) strain sensors (on the left) and an FBG thermistor string (on the right, sticking out of the ice); the red sticks are holding the plastic covering of the sample (b) Typical temperature curve in thermal expansion experiments

Thermal expansion experiments (2018-2020)

Experiments on thermal expansion were conducted in 2018 (fresh ice), 2019 (sea ice) and 2020 (both). Although thermal expansion of ice itself has been studied multiple times since 1920s, it mostly focused on artificially grown ice, both fresh and saline. However, in these experiments we used samples cut of natural ice. Ice blocks had horizontal dimensions of about 50 cm and thickness of about 30 cm; they were placed on the side so that the deformations both parallel to the original surface and perpendicular to it could be investigated. Deformations were measured with FBG (Fiber Bragg Grating) strain sensors (see Marchenko, Thiel, et al. 2015) fixed on the ice block surface with brackets screwed to the ice. On a fresh ice block in 2018 two strain sensors were installed, matching the two directions mentioned above. On a sea ice block in 2019 we used three strain sensors in a form of a triangle (Figure 2), which was supposed to allow for calculation of the whole surface strain tensor. In both experiments temperature of the ice was logged using another type of FBG-based sensors, namely, thermistor strings of 12 temperature sensors each, which were installed into pre-drilled holes next to each strain sensor. Temperature in the laboratory was changed in cycles between approximately -15 and -5 ^{o}C, making the samples expand and contract accordingly. However, the cold lab equipment only allowed for setting the room temperature to a certain value, so that the cooling system brought the temperature down quite rapidly and then maintained it oscillating around this value with a period of 12 minutes. The typical temperature curve for one up-down cycle is showed in Figure 1b.

The experiments of 2018 and 2019 were aimed to estimate anisotropy of natural ice, i.e. how big the difference is between the CTEs (Coefficients of Thermal Expansion) if measured along the c-axis of the ice grains (horizontally) or perpendicular to them (vertically). After it was found that this anisotropy, if existent, could not be captured within experiments of this kind (see below), we moved to another factor that was assumed to be affecting the measurements. It was seen possible that, since the temperature was not changing uniformly across the cross section of the ice blocks, the length of the screws in relation to the thickness of ice may play a significant role. Therefore, the experiments in 2020 were not designed to measure anisotropy but involved sensors fixed with screws of different length instead.

Experiments on water freezing in artificial cracks (2019)

The main configuration and the equipment used for these experiments were exactly the same as for the ones in 2019, except that there was sawed a slot of approximately 10 cm of length, 6 mm of width and 13 cm of depth in the ice block (Figure 2). This slot was then filled with preliminary cooled water, and subsequent changes in ice temperature and deformations were recorded with the same sensors. The experiment was performed on both freshwater and sea ice samples, and the layout of the sensors was essentially the same.

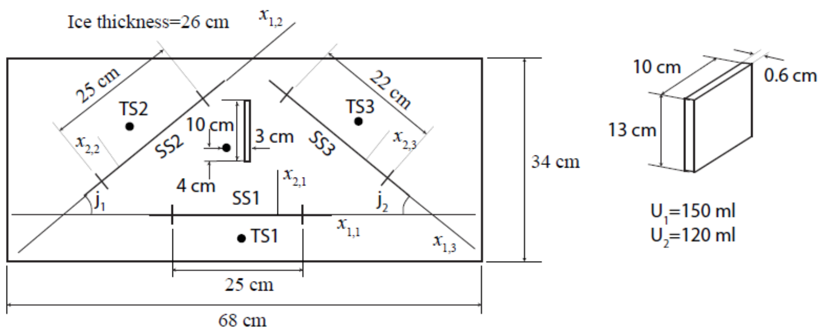

Figure 2: Sketch of the experimental setup for the experiments on water freezing in cracks

3. Results

Thermal expansion experiments: fresh ice 2018

Figure 3, top graph, shows an example of the results obtained in fresh ice experiments in 2018. A certain hysteresis loop appears for each up-down pair. Temperature was raised in three steps and after that decreased symmetrically, with the ”nodes” of the graphs corresponding to the change of the room temperature settings. Therefore, it must be assumed that the reasons for such patterns are strongly linked to uneven temperature changing rate. The possible linking factor can be the delay in heat transfer from the surface to the inner layers of the ice block.

Still, temperature-strain curves for horizontal and vertical deformations go parallel and quite close to each other compared to the difference due to hysteresis issues, which makes the phenomenon of anisotropy of freshwater ice negligible in these experiments compared to other effects.

Despite the loops, it is possible to perform a linear approximation of the temperature-strain curves for long multiple-steps cycles. This approximation gives a value between $6.3{\cdot}10^{-5}$ and $6.5{\cdot}10^{-5}$ 1/K, which is relatively close to the CTE values of about 5.0-$5.3{\cdot}10^{-5}$ found in literature [Butkovich 1959].

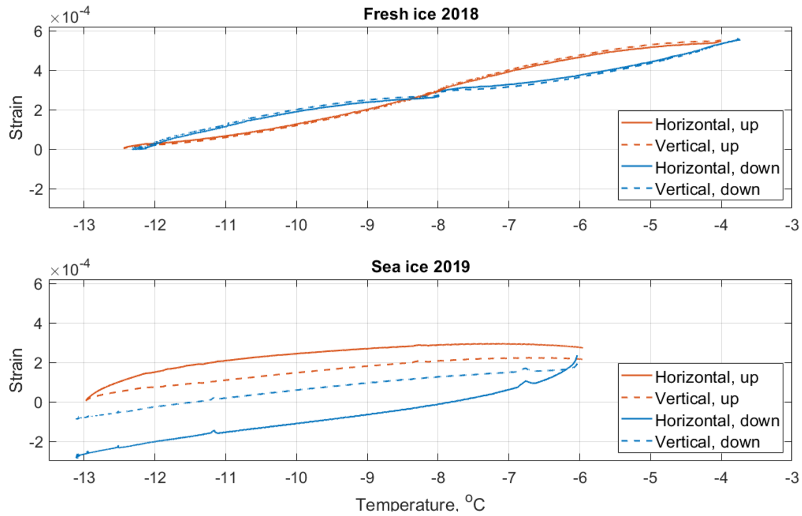

Figure 3: Strain-temperature curves for fresh ice (top graph) and sea ice (bottom graph), one up-down cycle (example); negative strain means contraction and positive strain means expansion

Thermal expansion experiments: sea ice 2019

Temperature-strain curves for sea ice showed hysteresis cycles similar to the ones observed for freshwater ice, but they are not closed anymore. When the temperature drops to its initial value, some residual strain is recorded by the sensors. It might be due to different reasons. On one hand, negative coefficients of thermal expansion of sea ice were observed several times by different scientists, and it is well known that cyclic heating and cooling of a saline ice sample causes the brine to drain down through the brine channel network, resulting in a certain decrease of the salinity of the sample. However, it seems more likely that the main cause of this effect is the screws creeping through the ice, being loaded by the strain sensors. This hypothesis is supported by the following idea: as shown before, the technical conditions in the cold lab are such that the ambient temperature change is rapid during the first several hours of the experiment and slows down as the time goes. In the first part of the experiment (warming-up) the temperature is raised and the strain sensor, which is essentially a thin cable, becomes more and more tensioned, loading the screws that fix the brackets. The screws we used in this experiment were rather short (about 3 cm), which means that they did not reach down to the colder inner layers of the ice blocks. This creep phenomenon may release the tension of the sensor, resulting in lower strain values, and since a decrease in tension that follows the cooling-down part would not “push” the brackets back, this residual negative strain will remain in place.

As for the obvious anisotropy in this case, we believe that it is mostly due to the fact that while the “horizontal” strain measurements were taken as they were from a single sensor, the “vertical” strains were calculated from all three sensors (see Figure 2) as if all of them showed ideal strains. The creep effects described above may have overlapped, increasing non-linearities of the curve.

However, the curves for sea ice within the same temperature range have a slightly less steep angle compared to the ones of fresh ice (Figure 3), although obtaining an accurate value is somewhat difficult due to the asymmetric effects discussed above.

Thermal expansion experiments: fresh ice & sea ice 2020

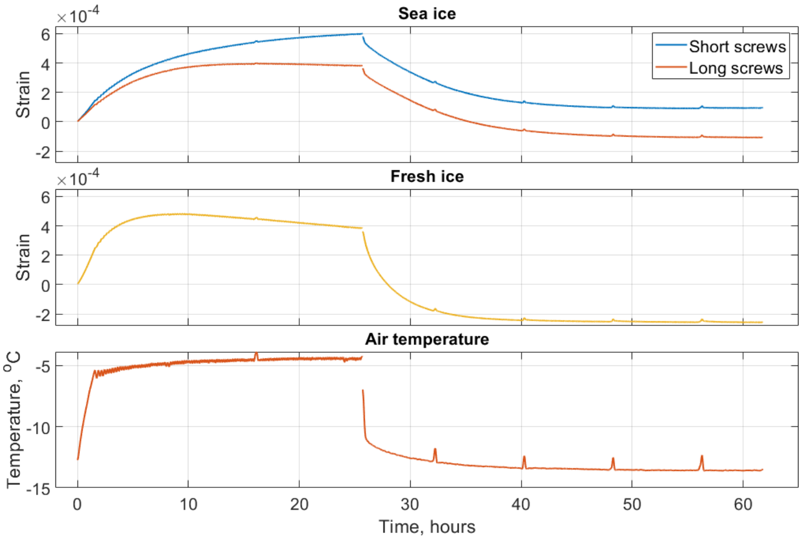

Figure 4: Time-strain curves and the air temperature for a coupled thermal expansion test in 2020

In 2020, it was decided to investigate closer the effect of screws on strain measurements in both freshwater and saline ice.

During these experiments, after each temperature switch both samples were left to stay at constant temperature for some time (about 20 hours). It had been assumed that using longer screws to fix the sensors on the ice surface could reduce the strain relaxation effect that was observed in the sea ice experiments of 2019. But in reality, on the sea ice block it was actually the long-screw sensor that showed a more significant curve decline in the first part of the experiment (Figure 4), while the opposite was expected. The reasons for this were not completely understood. However, the strain curve for the freshwater ice block has a clear downward tendency as well, which indicates that salinity issues are not the reason for this decline. In the second part of the experiment (cooling down) the strain curves remained flat together with the air temperature curve, which is in a good agreement with the "creeping screws" hypothesis.

The role of the fixating screws was confirmed in the experiments of 2020, but it cannot be concluded that using longer screws instead of short ones improves the quality of the experiment in any way. Therefore, it must be admitted that using FBG strain sensors in this configuration allows for obtaining data of acceptable quality only for relatively rapid temperature changes, and possible creep effects around the screws must be taken into account.

Water freezing experiments

This experiment, as mentioned above, was performed for natural freshwater and sea ice. The two experiments were not conducted simultaneously, but in Figure 5 they are aligned in time for comparison purposes. Although in both cases the temperature anomalies had a comparable time scale, the curve for freshwater ice shows steeper slopes for both warming up and for cooling down. Such

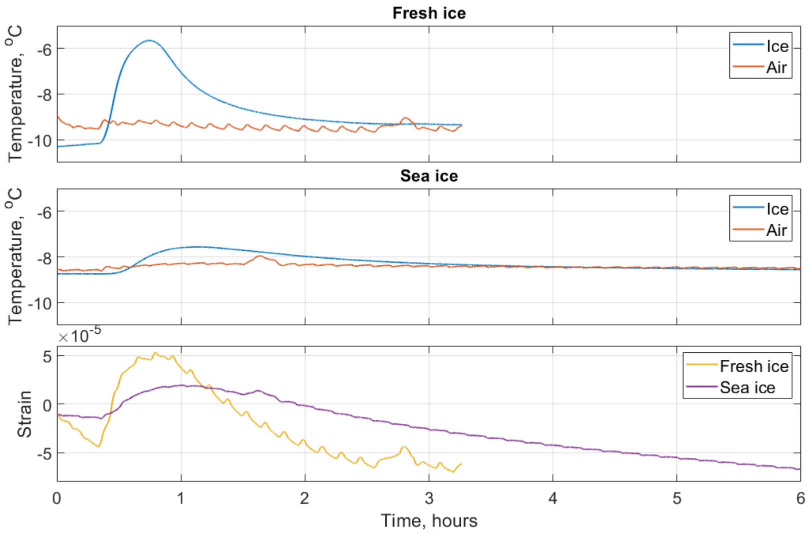

Figure 5: Temperature and strain curves in water freezing experiments

behavior is predictable, as specific heat of sea ice is known [Schwerdtfeger 1963] to grow significantly with temperature at high enough temperatures due to phase change in brine pockets. Similar patterns can be noticed when the strain curves for both types of ice are compared. It must be noted that although the water solidifies quite fast, the strains remain significant for several hours, which means that the main cause of the strains in the surrounding ice (and the stresses, should the ice be constrained) is the release of latent heat during water solidification.

4. Fieldworks: in-situ observations of tidal cracks

During the fieldworks of spring 2019, natural tidal cracks were observed on Vallunden lake (Sveabukta, Van Mijen Fjord, Svalbard). No quantitative investigations were performed, but ice cores were taken from one of the cracks, and the structure of ice inside the crack was examined through thin sections (Figure 6b).

Even on a simple slice of an ice core the boundary between the original ice of the crack side and the ice that formed from the penetrating water can be clearly seen. The newly formed ice tends to be less bubbly, which probably indicates its relatively slow and undisturbed process of formation as compared to the surrounding ice. In the thin section it is also visible that grains of the new ice are bigger in size and oriented from one side of the crack to the opposite one, exactly how it could be expected and similar to what was seen in laboratory experiments (Figure 6a).

5. Numerical simulations

Numerical simulations were performed in COMSOL Multiphysics to estimate stresses in a rectangular sample of confined fresh ice caused by the freezing of water in a crack. The computational domain was extended in the horizontal and vertical directions on 2 m and 1 m respectively. The crack of triangular shape (0.5 m deep and 10 cm wide at the surface) was placed at the left boundary of the domain. Boundary conditions were symmetric at the left and fixed at the right face of

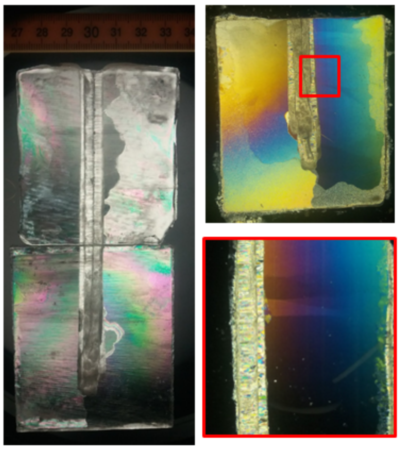

(a) Freshwater ice, laboratory

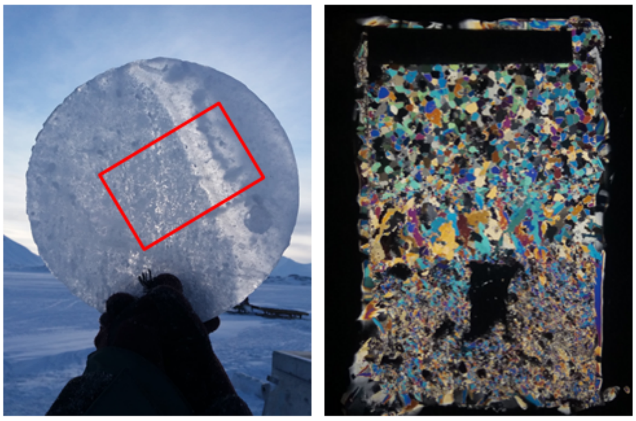

(b) Sea ice, natural crack

Figure 6: Thin section investigations

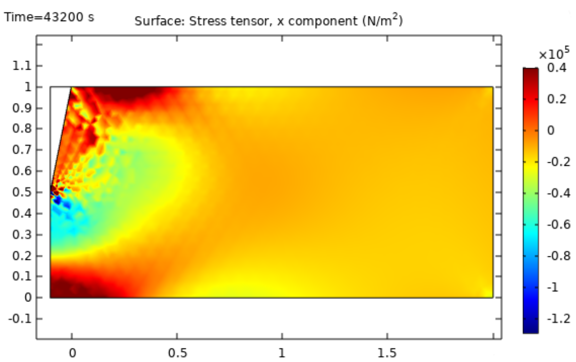

(a) Model

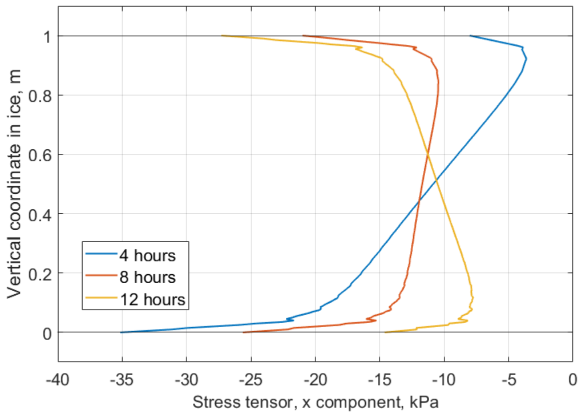

(b) X-component of the strain tensor along the right edge, kPa (10 cm wide crack)

Figure 7: Numerical modeling

the domain, and free surface boundary conditions were applied on the top and the bottom of the domain.

The right boundary of the computational domain was associated with a shoreline, and the left boundary was associated with the middle of a crack in land fast ice at a 2 m distance from the shoreline. The top and the bottom surface temperatures of ice were set to -20^{o}C and 0^{o}C (freezing point), respectively. Such boundary conditions assume a linear temperature profile through the ice until the crack is filled with water. A linear temperature profile was set as the boundary condition at the right boundary of the domain and as the initial condition for the whole domain, while the symmetric condition (in terms of heat transfer) was set at the left boundary.

We used the model of linear elastic solid with creep (Norton model) to describe temporal evolution of thermally induced deformations in ice. The COMSOL module Heat transfer with phase changes was used to describe the temperature evolution. Time dependent simulations were performed starting from the moment when the crack was filled with water at 0^{o}C. The creep rate coefficient, the reference stress and the stress exponent were set to 10^6 1/s, 1 MPa and 3 respectively. The thermodynamic characteristics of ice were taken from [Schwerdtfeger 1963].

The simulations aimed to describe time evolution of stresses, strains and temperature inside the ice caused by water freezing in the crack. Colours in Figure 7a show the distribution of the stress component σ_{xx} (x is the horizontal coordinate) at 12 h after the crack was filled with water. The lines show the vertical profiles of σ_{xx} at the shoreline in different times pointed out in Figure 7b. The local increase of the stresses near the ice surface and the ice bottom is deemed to be due to the influence of the corner points. Ice compression is caused by the increase of ice temperature due to the latent heat release in the crack. The stress averaged over the ice thickness is about 12 kPa. The vertical profile of the stress changed significantly over time. Maximal stresses are observed near the ice bottom at 4 h, and near the ice surface at 12 h after the crack was filled with water.

6. Conclusion

Laboratory experiments and numerical investigations have been performed on the role that thermal expansion of ice due to water freezing in tidal cracks plays in development of stresses in the coastal zone. The main conclusions are as follows:

- Mounting method of strain sensors on the ice is important for long term measurements. Even small tension of 2-3 N of FBG sensors causes creep of the screws that fix the sensor.
- Thermal expansion coefficients of sea ice were found to be slightly lower than those of fresh ice within the temperature range between -15^{o}C and -5^{o}C.
- It was discovered that when water freezes in ice cracks, the main stresses are due to the release of latent heat that causes heating and consequent thermal expansion of the surrounding ice.
- After water freezing in the crack temperature stabilization takes much longer time in sea ice than in fresh ice. In the experiments the difference reached 10-12 hours.
- Through numerical simulations for fresh ice it was found that onshore stresses averaged over the ice thickness related to the aforesaid water freezing can reach values of 12 kPa. This value can be significantly higher for sea ice, as its thermal properties (mostly specific heat capacity) are larger than that for fresh ice and strongly depend on temperature. Other factors that may increase the stresses are the size (in terms of volume of the freezing water) and the number of cracks.

Acknowledgements

The experiments and the fieldworks were funded by the Research Council of Norway through the AOCEC project. Special thanks to Nataly Marchenko and Dmitri Frey for their invaluable assistance during the fieldworks.

References

Blæsterdalen, B., Wranborg, D., Marchenko, A., & Høyland, K. V. (2016). Geometry and thermo-mechanical properties of coastal ice in a micro-tidal climate in Svalbard, part I, permeability and geometry. *Proceedings of the 23rd IAHR Symposium on Ice, Ann Arbor, Michigan, USA*.

Bogorodskiy, P., Marchenko, A., & Ogorodov, S. (2010). Formation of fast ice and its influence on the coastal zone of the Arctic seas. *Oceanology*, *50*(3), 317–326.

Butkovich, T. R. (1959). Thermal expansion of ice. *Journal of Applied Physics*, *30*(3), 350–353.

Caline, F. (2010). *Coastal-sea-ice action on a breakwater in a microtidal inlet in Svalbard* (Doctoral Thesis). NTNU.

Cox, G. F. N. (1983). Thermal expansion of saline ice. *Journal of Glaciology*, *29*(103), 425–432.

Golden, K., Eicken, H., Heaton, A., Miner, J., Pringle, D., & Zhu, J. (2007). Thermal evolution of permeability and microstructure in sea ice. *Geophysical Research Letters*, *34*.

ISO 19906: Petroleum and natural gas industries – Arctic offshore structures (International Standard). (2019(E)). ISO Copyright Office. Geneva, CH.

Johnson, J., & Metzner, R. (1990). Thermal expansion coefficients for sea ice. *Journal of Glaciology*, *36*, 343–349.

Malmgren, F. (1927). On the properties of sea ice. *The Norwegian North Polar expedition with the "Maud" 1918-1925, Scientific results*, *1*(5), 1–67.

Marchenko, A. (2018). Thermo-mechanical loads of confined sea ice on structures. *Philosophical Transactions of the Royal Society A: Mathematical, Physical and Engineering Sciences*, *376*, 20170341.

Marchenko, A., & Lishman, B. (2017). The influence of closed brine pockets and permeable brine channels on the thermo-elastic properties of saline ice. *Philosophical Transactions of The Royal Society A: Mathematical Physical and Engineering Sciences*, *375*.

Marchenko, A., Thiel, T., & Sukhorukov, S. (2015). Measurements of thermally induced deformations in saline ice with Fiber Bragg Grating sensors. *Proceedings of the 21st IAHR International Symposium on Ice "Ice Research for a Sustainable environment"*.

Ogorodov, S., Arkhipov, V., Kokin, O., Marchenko, A., Overduin, P., & Forbes, D. (2013). Ice effect on coast and seabed in Baydaratskaya Bay, Kara sea. *Geography, Environment, Sustainability*, *6*(3).

Prinsenberg, S., Fowler, G., van der Baaren, A., & Beanlands, B. (1997). Ice stress measurements from land-fast ice along Canada's Labrador Coast. *Cold Regions Science and Technology*, *25*, 1–15.

Renshaw, C. E., Marchenko, A., Schulson, E. M., & Karulin, E. (2018). Effect of compressive loading on first-year sea-ice permeability. *Journal of Glaciology*, *64*(245), 443–449.

Schwerdtfeger, P. (1963). The thermal properties of sea ice. *Journal of Glaciology*, *4*(36), 789–807.

Teigen, S. H., Høyland, K. V., & Moslet, P. O. (2005). Thermal stresses in first-year sea ice. *Proceedings of the 18th International Conference on Port and Ocean Engineering under Arctic Conditions (POAC)*, 893–906.

Wranborg, D., Vindegg, C. M., Marchenko, A., Blæsterdalen, B., & Høyland, K. V. (2016). Geometry and thermo-mechanical properties of coastal ice in a micro-tidal climate in svalbard, part II, in-situ stresses. *Proceedings of the 23rd IAHR Symposium on Ice, Ann Arbor, USA*.

02
Sea ice remote sensing and forecasting

25th IAHR International Symposium on Ice
Trondheim, June 14 to 18, 2020

Real-time classification of the sea ice interacting on a bridge pier using artificial intelligence techniques

Ansari, S., Rennie, C.D., Poirier L.
Department of Civil engineering, University of Ottawa, Ottawa, ON, K1N 6N5, Canada
Oceans, Coastal and River Engineering Research Centre, National Research Council Canada, Ottawa, ON, K1A 0R6, Canada

This research focuses on the development of a novel approach for monitoring and classifying different kinds of sea ice interacting with bridge piers in Northumberland Strait. Different ice types can have a varying impact on the navigability of a vessel or the loads on a structure. As such, the ability to monitor and classify different ice types automatically is an added strength to the existing ice load monitoring system present at the Confederation Bridge since 1997 and should allow for further automation. A deep learning algorithm based on Convolutional Neural Networks (CNN) has been utilized for training an algorithm to classify four different types of sea ice interacting with the bridge pier. Despite the fact that classification of different ice types from images is sometimes very challenging even when performed manually by experts, the developed algorithm is able to identify different classes accurately and on a real-time basis. The accuracy of the results demonstrates high practical utility of the method for similar applications.

1. Introduction

Ice loading on the Confederation Bridge has been monitored by the University of Calgary (Brown, 2001, Brown et al., 2010, Shrestha and Brown, 2018) and the NRC (Kubat et al., 2000, and Poirier et al., 2015) since its construction in 1997. This long term data record is the only one of its kind that provides ice loads on structures. The next longest comparable dataset is LOLEIF/STRICE which acquired 4 seasons of ice interactions against the Norströmsgrund lighthouse (Li et al., 2016).

Visual examination of video data from the Confederation Bridge has provided researchers valuable information on the volume and type of ice interacting with the instrumented bridge piers, as well as the ice failure mechanisms. Visual observation is currently the most reliable means of ice characterization. However, this task is challenging, expensive and requires specialized training. New technologies in image processing and computer vision can be applied for this purpose. These would improve automation and reduce the time and effort required to collect these data. Attempts have previously been made for river ice detection and characterization using computer vision algorithms (Ansari *et al.*, 2017); machine learning methods (Kalke and Loewen, 2018) and deep learning techniques (Singh *et al.*, 2019) and (Ansari et al., in prep.). In this study, an automated sea ice characterization algorithm was developed to detect and characterize the sea ice interacting with a bridge pier.

2. Study area and data

Confederation Bridge is the longest structure in the world constructed in ice-covered waters. The Confederation Bridge as part of the Trans-Canada Highway is the 13-kilometre linkage between the provinces of Prince Edward Island and New Brunswick across the Northumberland Strait. This bridge has 45 main spans, each 250 m long, that rest on a total of 44 piers (Poirier, Babaei and Frederking, 2015). Figure 1 illustrates the bridge and its location. As part of a comprehensive ice load monitoring program, two Sony SNC-EB632R cameras are installed to examine ice failures on two of the bridge piers. Cameras are connected to the network, and they are programmed to collect an image every 3 seconds. According to the Canadian Ice Service (CIS) Gulf of St. Lawrence, the ice season in this location is between December 31st to April 15 (Johnston M.E. and Timco, G.W. 2008).

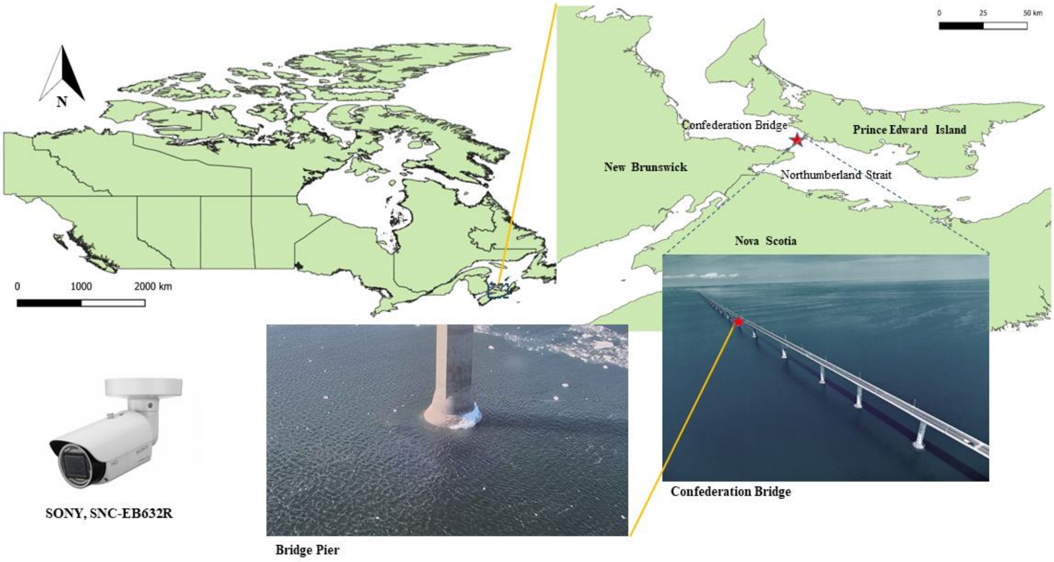

Figure 1. Project location, Confederation Bridge, and the SONY, SNC-EB632R

The vast number of images not only helps in the monitoring task but also provides the possibility of developing data-driven approaches for sea ice characterization. In this study, four different classes of sea ice have been defined for automatic recognition. These classes include *Icefloe, Broken, Ridge,* and *Flex.* The majority of the ice in any given image is ice floe (*Icefloe*). *Icefloe* is generally a piece of level ice that is at least half as large as the pier base, i.e., ≥ 5 m in diameter (Figure 2a). An *Icefloe* can also include deformed (ridged or rafted) ice. *Broken* sea ice is considered as the least imposing ice on a vessel or a structure. These are pieces of ice no larger than half of the pier base; in this dataset they are usually broken as a result of interacting with the bridge pier (Figure 2b). Deformed ice (ridged or rafted) is identified as *Ridge* (Figure 2c). Rafted ice occurs when two level ice sheets collide with each other and one is pushed over the other one leading to thickening of ice. Ridged ice, on the other hand, is when levelled ice interacts with an object, causing broken ice pieces to accumulate above or under the ice sheet. Finally, due to the conical shape of the bridge pier, ice interaction with the bridge leads to flexural failure; this is characterized as *Flex* in the presented algorithm (Figure 2d).

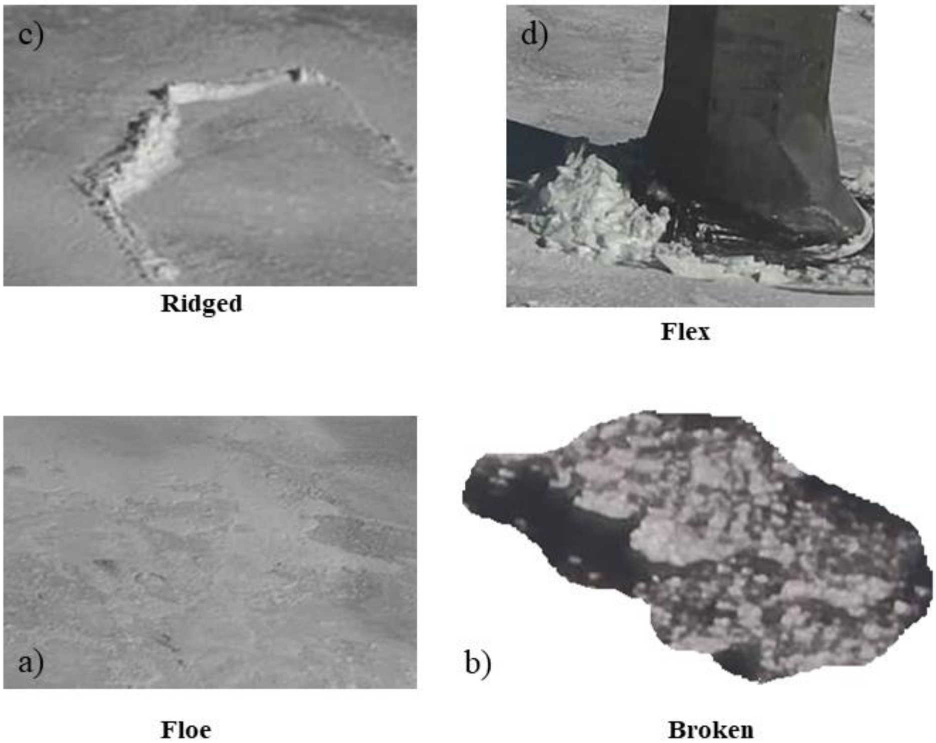

Figure 2. Different ice type classes; a) Floe; b) Broken ice; c) Ridged; d) Flex

3. Methodology

An instance image segmentation and object detection algorithm was employed to develop a real-time sea ice detection and classification algorithm. Mask RCNN model (He *et al.*, 2017) is the base model to establish the sea ice recognition algorithm. The Mask RCNN model used in this study was built on the Faster RCNN (Ren *et al.*, 2017) model. In the Mask RCNN a convolutional neural network first is used to generate object proposals within the image. An object proposal is essentially a rectangular area within the image that is identified to have a classifiable sea ice object within it. Then the Mask RCNN classifies the bounding boxes and adds an extra mask over the region of interest (RoI) (He *et al.*, 2017) to specify the polygon of the classified sea ice object. The architecture of the used model consists of a feature extraction model using a 101 layer Residual Neural Network (ResNet) (He *et al.*, 2006). After the feature extraction, the Region Proposal Network (RPN) is used to generate the correct RoI. The generated RoIs are then classified using the RoI classification algorithm. In the next step, a bounding box regressor is used for refining the bounding boxes of the classes and another methodology named as RoIAlign based on a bilinear interpolation is used for pixel-wise prediction of the masks (He *et al.*, 2017). Figure 3 illustrates the developed algorithm used for automated classification of the sea ice interacting with the bridge pier.

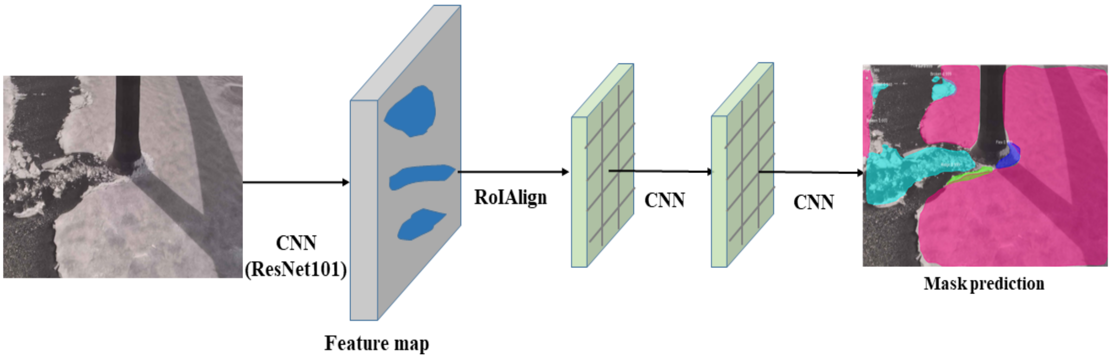

Figure 3. Architecture of the utilized improved version of the Mask RCNN

3.1. Implementation

The developed algorithm utilizes the Mask RCNN model on TensorFlow (Abadi et al. 2015). The training of the model was conducted on a Graphics Processing Unit (GPU) equipped machine. Parallel GPU computing was utilized to accelerate the training process of the model. The training was performed on the backbone structure of ResNet101 (101 layers), with a batch size of 2 images with a training rate of 0.0015 and learning momentum of 0.88 and weight decay of 0.0002. The trained Mask RCNN model was performed on the pre-trained weights of the COCO data (Common Objects in Context) set (Lin *et al.*, 2014). 120 images with the size of 1920 × 1080 were annotated to be used in the training procedure. The image data set was split into 80 percent for training and 20 percent for validation. Moreover, in order to increase the generalization of the algorithm, simple data augmentation techniques such as random flips, left zoom, right zoom were employed in the model. The inference process was also conducted with a detection confidence of 70%.
The utilized model was optimized during the training process to evaluate the accuracy of the model and the sufficient number of the annotated images for the training process. The training process was performed with 100 epochs.

4. Results and discussion

After the investigation of the loss and validation parameters, the results indicate that validation loss values quickly reach their lowest after a few ephochs and then continue to fluctuate. However, training loss values continue to decend. This suggests that the model memorizes before the 20th epoch. Thus running the model for the 100 epochs does not give any advantage. Based on the validation loss increase no more than 20 epochs should be utilized, because otherwise the model is overfit to the training data-set. The reason for this is that the training process has been conducted on a weighted data set as a result of pertaining COCO dataset. Moreover, this is an indication of the insufficiency of the labelled images for the training process.

Figure 4 shows some results of the sea ice characterization algorithm. Four different classes of floe, broken, flex, and ridge have been detected. The detected ice types have been segmented with masks and their associated colors. The results show that the developed algorithm was able to detect, identify and characterize the four different classes accurately and with acceptable pixel-wise accuracy. While the results are promising, two sets of errors were discovered. Although the classification and detection tasks were conducted correctly the mask prediction has some errors. The errors include the marginal error in the boundaries of the masks and some overlaps in the mask prediction pixels. As this was predictable from the loss graphs in the optimization process, there is still a need to perform the manual labelling task on a greater number of images to ensure the reliability of the system.

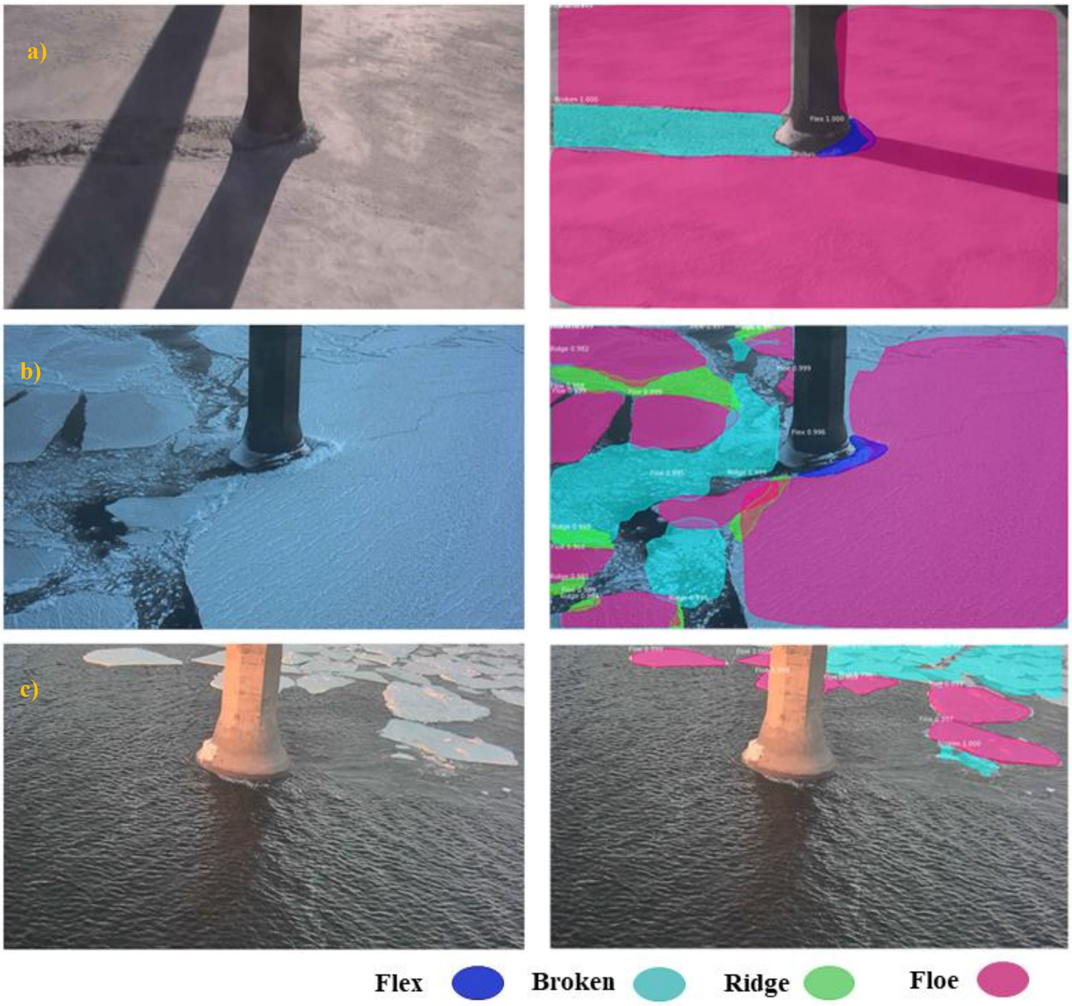

Figure 4. Sample results of the sea ice segmentation algorithm

5. Conclusion

As part of a comprehensive and automated monitoring network a sea ice characterization algorithm was developed to detect and recognize different classes of ice interacting with a bridge pier. With a changing climate, results of such a study are crucial, since monitoring, and specifically automated smart monitoring, is vital in providing the public with high-standard safe and reliable infrastructure. The developed algorithm employed an improved version of the Mask RCNN to improve sea ice characterization. The results indicated an acceptable outcome with some minor shortcomings, which should be investigated in future studies. Annotation of more images is a key factor in the generalization of the developed algorithm, which should be conducted in future work.

6. Acknowledgments

The authors would like to acknowledge the support of Strait Crossing Bridge Limited and Public Services and Procurement Canada for providing access and support to perform research on the Confederation Bridge. The National Research Council Canada (NRC) for giving access to the collected imagery data on the Confederation Bridge and David Hnatiw for technical support of the project.

7. References

Abadi, M., Agarwal, A., Barham, P., Brevdo, E., Chen, Z., Citro, C., . . . Zheng, X. (2015). Large-scale machine learning on heterogeneous systems, Software available from tensorflow.org.

Ansari, S. *et al.* (2020) 'River Ice Detection and Characterization Using Aerial Photography', in preparation for submission to *Cold Regions Science and Technology*.

Ansari, S. *et al.* (2017) 'Automated monitoring of river ice processes using shore-based imagery', *Cold Regions Science and Technology*. Elsevier, 142(June), pp. 1–16. doi: 10.1016/j.coldregions.2017.06.011.

Brown, T.G. (2001) "Four Years of Ice Force Observations on the Confederation Bridge", *Proceedings of the 16th International Conference on Port and Ocean Engineering under Arctic Conditions,* Ottawa, Canada, 12-17 August.

Brown, T.G., Tibbo, J.S, Tripathi, D., Obret, K. and Shrestha, N. (2010) "Extreme ice load events on the Confederation Bridge", *Cold Regions Science & Technolgy*, 60: 1-14.

He, K. *et al.* (2006) 'Deep Residual Learning for Image Recognition', in *IEEE conference on computer vision and pattern recognition*, pp. 1951–1954. doi: 10.1002/chin.200650130.

He, K. *et al.* (2017) 'Mask R-CNN', in *Proceedings of the IEEE International Conference on Computer Vision (ICCV)*. Venice, Italy, pp. 2980–2988. doi: 10.1109/ICCV.2017.322.

Kalke, H. and Loewen, M. (2018) 'Support vector machine learning applied to digital images of river ice conditions', *Cold Regions Science and Technology*. Elsevier, 155(September 2017), pp. 225–236. doi: 10.1016/j.coldregions.2018.08.014.

Kubat, K., Frederking, R. and Hayakawa, T. (2000) 'Response of the Confederation Bridge to Ice Action, in *Proceedings 2000 Annual Conference of the Canadian Society for Civil Engineering,* Vol. S, pp 434-441, London, Canada.

Lin, T. *et al.* (2014) 'Microsoft COCO : Common Objects in Context', pp. 740–755.

Poirier, L., Babaei, H. and Frederking, R. (2015) 'Statistical analysis of the ice loading events on the confederation bridge', in *Proceedings of the International Conference on Port and Ocean Engineering under Arctic Conditions, POAC*.

Ren, S. *et al.* (2017) 'Faster R-CNN: Towards Real-Time Object Detection with Region Proposal NEtworks', *IEEE Transactions on Pattern Analysis and Machine Intelligence*, 39(6), pp. 1137–1149. doi: 10.1109/TPAMI.2016.2577031.

Shrestha, N. and Brown, T.G. (2018) '20 years of monitoring of ice action on the Confederation Bridge piers', *Cold Regions Science and Technology*. Elsevier, 151 (July 2018), pp. 208–236. doi: 10.1016/j.coldregions.2018.03.025.

Singh, A. *et al.* (2019) 'River Ice Segmentation with Deep Learning', *arXiv preprint*, p. 1901.04412.

25th IAHR International Symposium on Ice
Trondheim, June 14 to 18, 2020

Grease-pancake sea ice thickness retrieval from SAR image wave spectra with the close-packing wave model

Giacomo De Carolis and Francesca De Santi
National Research Council of Italy (CNR)
Institute for Electromagnetic Sensing of Environment (IREA)
Via Corti, 12 – 20133 Milano (Italy)
(decarolis.g, desanti.f)@irea.cnr.it

A new SAR inversion scheme to estimate the thickness of sea ice in the marginal ice zone through observation of wave decay from SAR imaging is proposed. This scheme applies to sea ice composed by mixtures of sea ice prevalently composed by grease and pancake ice (GPI) and thin ice floes. A close packing (CP) model (De Santi & Olla 2017) is adopted where GPI is treated as a three-layer model, with an infinitely thin top layer accounting for the effect of the pancakes, an infinite depth inviscid layer representing the ice-free ocean on the bottom and a viscous layer in the between accounting for the effect of grease ice. Predicted waves attenuation depends on GPI thickness and the grease ice viscosity. Comparison between waves decay observed from SAR imaging and waves decay predicted by the CP model is the bedrock of the proposed scheme (De Carolis 2001). Unfortunately, as it happens for any viscous layer model, infinite combinations of thickness and viscosity predict a same value for attenuation. The resulting SAR inversion problem results therefore undetermined (De Santi et al. 2018). Removal of such inconsistency is performed by calibrating the SAR inversion scheme with modeled GPI thicknesses in the Odden Sea (Pedersen & Coon 2004). A physically consistent GPI viscosity-thickness relationship is obtained. Two examples of application for the proposed scheme will be presented: a Sentinel-1 C band, HH polarized SAR image taken in the Beaufort Sea on 1 November 2015 and a COSMOSkyMed X band, VV polarized SAR image taken in the Weddell Sea on 30 March 2019. The estimated GPI thicknesses are consistent with SMOS measurements with somewhat higher variability due to the higher spatial resolution of the estimates.

1. Introduction

The effects of global climate change on the Arctic seas have been detrimental due to the dramatic reduction in the extent and thickness of sea ice. This results in progressively higher waves that affect sea ice formation during the freezing season. The region of sea ice extensively affected by the wave action is called the marginal ice zone (MIZ). In the outer part of the MIZ, a chief role is played by the massive production of grease and pancake ice (GPI) whose role in the global cryosphere is not yet fully studied. To face up this problem, there is the need of effective monitoring of the GPI's properties, with particular concern of its thickness. This task cannot be entrusted to in situ activities because of the vast extent and the intrinsic dynamic nature of GPI fields. Remote sensing technology can help by exploiting the synthetic aperture radar (SAR) imaging capability to measure the full wave directional spectrum in open sea and sea ice.

In the literature there are a series of papers since 1997 where various SAR wave spectral inversion methodologies aimed at estimate the GPI thickness are described. In the earlier papers (Wadhams et al. 1997; 1999; 2002; De Carolis 2001) the GPI thickness was estimated by assuming a mass-loading ice rheology. Following the SAR observed ocean wave peak from open sea throughout the GPI cover, the estimated ice thickness resulted too high to be credible. In the latest papers (De Carolis 2003; Wadhams et al. 2004; 2018) the mass-loading approach was abandoned and the viscous wave propagation model (Keller 1998) was adopted. Furthermore, instead of the SAR dominant wave, the whole directional ocean wave spectrum in open sea was considered and SAR-tracked into the GPI field.

By analyzing a set of wave buoy data gathered in the advancing MIZ of the Weddell Sea, Antarctica, Doble et al. (2015) found that the GPI wave attenuation rates scaled with the "equivalent solid ice thickness", which is defined as:

$$h = c_{gr}h_{gr} + c_p h_p, \qquad \textbf{[1]}$$

where c and h are respectively the concentration and thickness of grease (gr) and pancake (p) ice. This outcome physically sounds as it states a relationship between wave decay and ice volume per unit area of the sea surface traveled by the waves. As a result, the SAR inferred GPI thickness should be related to the average thickness per unit area, i.e. the "effective ice thickness", rather than the thickness of pancakes. The effective ice thickness is the quantity most relevant to the overall changes in ice volume and is used in numerical dynamic-thermodynamic sea ice models (Holland et al. 2014).

In this paper we have considered a new viscous wave propagation model, called "close-packing" (CP) (De Santi & Olla 2017). Unlike the Keller model, the CP model parametrically accounts for the presence of disk-like impurities embedded in a viscous matrix to represent pancakes of given average radius. However, the CP model includes the Keller model as limiting case to describe pure grease ice layer or matrix of grease with dilute pancake ice. The CP model was successful in analyzing wave attenuation data collected by SWIFT buoys in GPI fields during the research cruise carried on the R/V Sikuliaq in the autumn 2015 (De Santi et al. 2018). The results obtained from in situ wave instruments led us to investigate the structure of the SAR-wave cost function over several orders of magnitude for the ice viscosity and up to 50 cm for the thickness, that is for a range of values much higher than those expected. It was found that the condition of minimum for the SAR cost function was not fulfilled for spotted values of the ice parameters to be inverted.

3. The SAR-wave inversion procedure in sea ice

The approach considers the ocean waves generated in open sea that cross the ice edge and finally propagate in the GP icefield. A SAR cost function is defined for measuring the distance between the observed SAR image spectrum and the one simulated as a function of the CP model parameterization, i.e., thickness and viscosity.

In sea ice, a series of adjacent SAR tiles of 256x256 pixels centered at the position $\vec{x}$ in the SAR reference frame and running from the ice edge along a straight line parallel to the direction of the incoming dominant wave are selected through the GPI field. For each of them, the SAR image spectrum is then computed. For the SAR images analyzed in this paper, the pixel sizes were 12.5 m for ERS2, 10 m for Sentinel-1A (S1A) and 15 m for COSMO-SkyMed (CSK) SAR images. Thus, the spatial resolution of the final GPI thickness and viscosity estimates is of the order of ~10 Km^2. It is assumed that the GPI cover alters the incoming ocean wave spectrum $S_w(\vec{k})$ according to the following expression (Wadhams et al. 2004; Sutherland & Gascard 2016):

$$S_i(\vec{x};\vec{k}) = S_w(\vec{k})\exp[-\alpha_k \Delta(\vec{x};\varphi)], \qquad \textbf{[2]}$$

where $\Delta(\vec{x};\varphi)$ is the distance traveled from the ice edge to the position $\vec{x}$ by the wave of wavenumber k heading the direction φ, and α_k is the wavenumber dependent energy attenuation rate. The latter is predicted by the CP model (De Santi & Olla 2017), which is parametric with respect to the effective ice thickness, h, and the ice layer viscosity ν. For each window located at position $\vec{x}$ into the SAR image, the SAR inversion scheme computes the waves-in-ice spectrum that minimizes the cost function defined as the global difference between the observed SAR spectrum, $\widetilde{P}_i(\vec{x};\vec{k})$, and the simulated one $P_{sim}(\vec{x};\vec{k};h,\nu,\gamma)$:

$$\Psi(h,\nu;\gamma) = \iint \left(\Re\left[\widetilde{P}_i(\vec{x};\vec{k}) - P_{sim}(\vec{x};\vec{k};h,\nu;\gamma)\right]\right)^2 d\vec{k}, \qquad \textbf{[3]}$$

where $\Re(\cdot)$ stands for the real part of the argument.

4. Which GPI thickness for the SAR inverted waves

Figure 1 shows the typical contoured cost functions obtained with the CP model under the assumption of compact GPI field where pancakes' horizontal motion is hampered (peristaltic motion). The absolute minimum of the cost functions was marked with a green star; red points mark those locations (h,ν) where the cost function values are within 1% of the corresponding absolute minimum. These points were fitted with a power-law curve of the type:

$$h = \beta\nu^{\alpha}. \qquad \textbf{[4]}$$

The parameters β and α were estimated through a straight line fit in the log-log 2D viscosity-thickness domain (blue straight line in figure 1) for all the analyzed SAR image tiles. It resulted that the values of the exponent were on average equal to $\alpha \simeq 1/3$ (cubic) with very small variability within a few percent. A similar structure of the cost functions was reported in De Santi et al. (2018) where wave attenuation rates in GPI fields measured by wave buoys were compared with the CP model. It is, therefore, to be expected that this is a property of the employed viscous model. In contrast, the values assumed by the parameters β were markedly variable, apparently featuring the physical characteristics of the SAR imaged portion of the actual GPI field. We assume that β depends on the GPI thickness, according to the following expression:

$$\nu_{cp} = \delta_{cp}(h)\sqrt{g}h^3 \quad \textbf{[5]}$$

where g is the acceleration due to gravity; δ_{cp} collect the dependency of β on the ice layer thickness h.

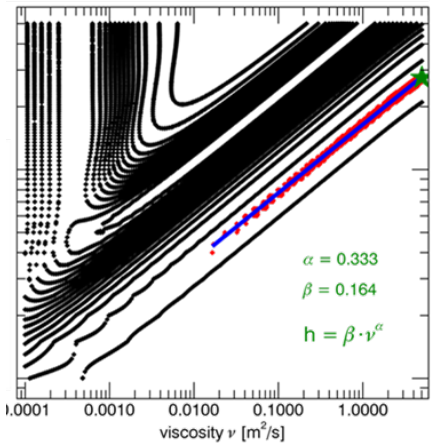

Figure 1. Example of contoured SAR cost function in GPI field with the CP model.

After performing a dimensional analysis, it is straightforward to show that $\delta_{cp} \sim h^{-1.5}$, so that the following relationship holds for the CP model:

$$\nu_{cp} = \eta\sqrt{g}h^{1.5}, \quad \textbf{[6]}$$

where η is an unknown dimensionless parameter to be estimated by using external ice thickness information. The value to be assigned to η can be determined by using a calibration procedure that fixes the relationship between the known GPI layer thickness h and the corresponding ice viscosity ν_{cp} estimated after applying the inversion method from a co-located SAR image.

5. SAR sea ice thickness calibration procedure

A reliable representation of the GPI thickness distribution in a given area was given by the salt-flux model developed specifically to describe the formation, transport and desalinization of GPI in the Odden region of the Greenland Sea (Pedersen & Coon 2004). The Odden is a large sea ice feature, largely consisting of GPI fields, that appeared almost regularly in winter seasons till the early years 2000, typically between 8°W and 5°E and between 73°and 77°N (Rogers & Hung 2008; Shuchman et al. 1998). The salt-flux model provided daily concentration, thickness and salinity of frazil and pancakes for the autumn/winter 1996/1997 (Pedersen & Coon 2004).

As the Odden sea ice was almost all composed by GPI, salt-flux model's predictions were used here to form the equivalent sea ice thickness, according to expression [1]. The field measurements carried by the oceanographic campaign into the Odden from March 3 to March 13 1997 permitted to test salt-flux results against measured values, thus leading to estimate the relative error of the equivalent GPI thickness $\Delta h/h \simeq 0.26$ (Wadhams & Wilkinson

1999; Pedersen & Coon 2004). The Odden locations visited during the cruise operations were imaged by a couple of ERS2 SAR images gathered on March 9 and 11, 1997 in coincidence with several sea ice data takes (Wadhams et al. 1997), thus allowing us to establish the quantitative relationship and dependence between GPI viscosity and thickness.
SAR inversions were carried out for a total of 24 instances to study the ice viscosity-GPI equivalent thickness relationship. Figure 2 shows the ERS-2 retrieved viscosities as a function of the GPI thicknesses for the two dates. The linear regression was performed using a Bayesian approach with errors in both thickness and viscosity (Kelly 2007). As expected, the retrieved GPI viscosity values were monotonically increasing with thickness and also compatible with the Newyear & Martin (1999) results. Therefore, a consistent ice viscosity-thickness relationship was found, which allowed to estimate the parameter η in [6] after imposing the least square fit with slope 1.5 as:

$$\eta = 0.963 \pm 0.093. \quad \textbf{[7]}$$

Finally, by combining [4], [6] and [7], the best SAR measurement of GPI thickness can be expressed as follows:

$$h = (0.975 \pm 0.064)\sqrt[3]{g}\beta^2, \quad \textbf{[8]}$$

where the value of the parameter β can be measured directly from the cost function of the actual SAR inverted tile. In [8] it was assumed negligible the uncertainty associated to β when compared to the one associated to the determination of η.

6. Examples of SAR inverted GPI thicknesses

The SAR-wave inversion procedure was applied to map the GPI distribution thickness from a couple of SAR images gathered by the S1A in Arctic, Beaufort Sea, and by the CSK in Antarctica, Weddell Sea, respectively.

6.1 Arctic – Beaufort Sea

On 1 November 2015, an IW-mode S1A SAR image was collected in the advancing MIZ of the Beaufort Sea (Figure 3). At the time of the SAR acquisition, the R/V Sikuliaq was in operation to carry out a field cruise as part of a large collaborative program to study the coupled air-ice-ocean-wave processes occurring in the Arctic during the autumn ice advance (Thomson et al. 2018).
A sharp ice edge can be detected on the SAR image separating the open sea (bottom part) to the ice field. GPI mainly compos the areas of icefield directly exposed to open sea. A number of directional wave buoys were deployed from the R/V Sikuliaq in proximity of the ice edge either in open sea and inside the GPI in proximity of the ice edge. At the time of SAR acquisition, a SWIFT wave buoy was floating in the area around the ice edge close to the ship, where an incoming wave spectrum was measured with $H_S \simeq 1.2m$. The application of the SAR inversion procedure returned a consistent wave directional spectrum, only slightly higher in wave height $H_S \simeq 1.5m$. Following the dominant wave direction, three transects were selected, each formed by 7 SAR image tiles of size 256x256 pixels. The retrieved ice thicknesses are shown in Figure 4 along with SMOS thicknesses (Huntemann et al. 2014) and ASSIST estimates (http://www.iarc.uaf.edu/icewatch). The overall trend shows increasing thicknesses going from the ice edge (0.43 cm) up to values close to 25 cm deep inside the GPI field. Close to the ship, the average thickness of 8.9±0.6 cm was estimated by SAR on the first three locations of T1 compares well with the 5.3±0.7 cm reported from visual

observations and 9.6±3.8 cm from pancake measurements collected in six recovery locations (Wadhams et al. 2018). SMOS thicknesses are bounded in the range 5.2-9.7 cm throughout the transects, thus failing in gather the overall trend of increasing thicknesses up to 25 cm for the points belonging to transect T2. In situ observations carried out 15-20 Km in the ice confirmed the increase in the retrieved thickness as a function of distance from the ice edge. These measurements reported thicknesses up to 30 cm, with pancake values in the range 10-18 cm and ASSIST observations ranging from 5 to 15 cm (Wadhams et al 2018).

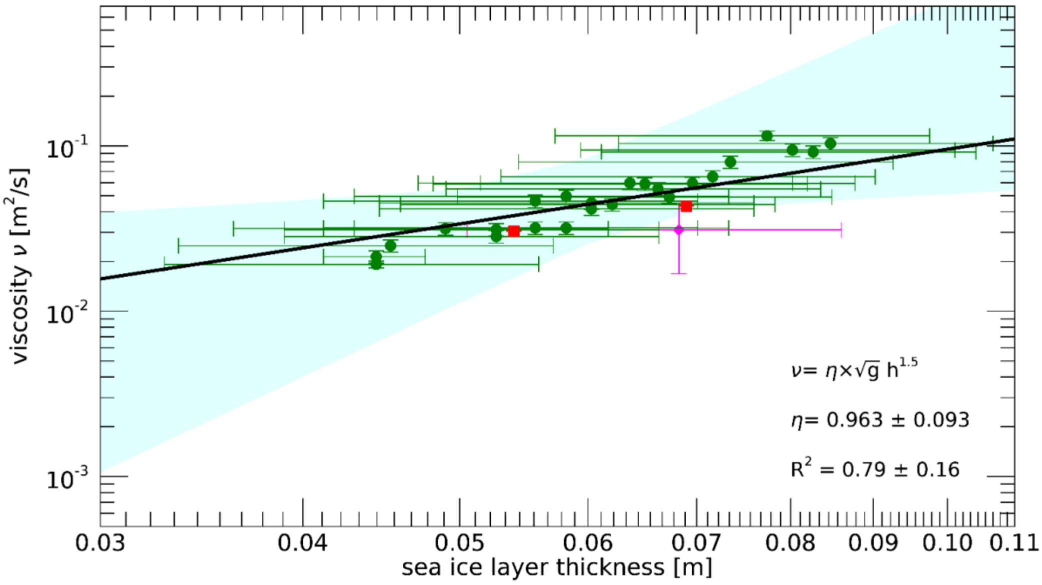

Figure 2. GPI viscosity vs equivalent thickness using the CP model for the instances selected on the ERS2 SAR images in the Odden region. The two red points represent the pure grease ice viscosity grown in laboratory (Newyear & Martin 1999).

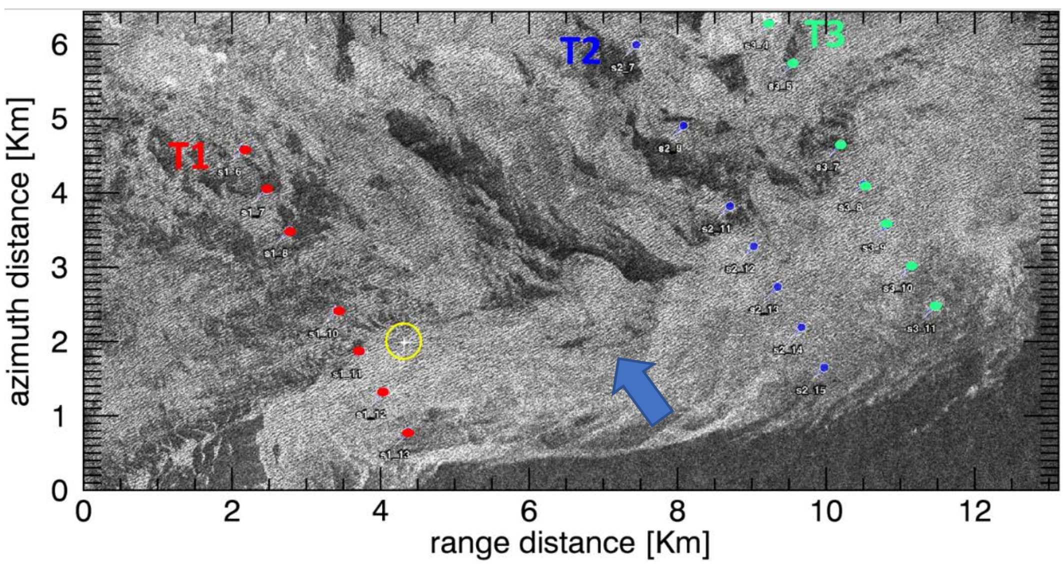

Figure 3. Portion of the S1A IW-mode SAR image acquired on 1 November 2015 in the Beaufort Sea. T1 (red), T2 (blue), and T3 (green) are the three transects selected for ice thickness estimation. The yellow ring encloses the imaged R/V Sikuliaq. The blue arrow represents the propagation direction of the dominant waves.

6.2 Antarctica – Weddell Sea

In the context of the Year of Polar Prediction (YOPP) initiative of the World Meteorological Program (Jung et al., 2016), a survey of the advancing ice edge of the Weddell Sea was performed during March-May 2019 by exploiting the fourth SAR satellite of the CSK constellation. The SAR inversion technique was applied on the SAR WIDEREGION image acquired by the CSK4 on 30 March 2019 at 10:00 UTC. Figure 5 represents a portion of the CSK4 image, where the interface separating the open sea with a developed GPI field was imaged. The dark areas adjacent to the ice edge and at direct contact with the open ocean are bands of pure frazil/grease ice from which pancakes originate. The selected SAR image was suitable to estimate the GPI thickness as an open ocean wave field of $H_S \simeq 1.9m$ and dominant wavelength $\lambda \simeq 168m$ traveled across the icefield with inclination 234 deg from the azimuth direction. A couple of transects was selected approximately following the propagation of the dominant wave. For each location of the transect the estimated thicknesses are plotted in Figure 6 according to the distance inside the icefield.

The SMOS thicknesses over the area covered by the transects are also reported as band of variability. Compared to the Beaufort Sea case study, thinner thicknesses much closer to the SMOS estimations resulted from the SAR inversion. In contrast, the region closer to the ice edge showed thicker ice up to about 3 cm higher the extremal SMOS value with a trend to decrease when running towards inside of the icefield. We cannot explain this, but it could be caused the action of the wave field that tends to compact the GPI in the region immediately surrounding the ice edge.

7. Discussion and Conclusions

A new technique aimed at the estimation of GPI thickness from the inversion of SAR wave image spectra has been described. The technique exploits the close-packing (CP) viscous model to approximate wave propagation in GPI. The CP model accounts for the presence of pancakes as circular floes of given radius whose compactness is parametric through a parameter $\gamma \geq 0$. For $\gamma \neq 0$ the overall ice viscosity is the one relevant to the grease ice matrix. In the limit of compact pancakes ($\gamma = 10$) a relationship between ice viscosity and thickness was found in the form $\nu = \delta(h)\sqrt{g}h^3$ by analyzing the SAR cost function that penalizes the differences between the observed and simulated SAR image spectra. The unknown parameter δ as a function of the GPI ice layer thickness was estimated through the application of an external SAR calibration procedure. To achieve the task, external thickness information provided by the salt-flux model, which ran for the 1997 Odden Ice Tongue collocated with ERS2 SAR imagery were used as reference data. The ice viscosity values were comparable with the one found for grease ice grown in wave tank at the corresponding thicknesses. This is a pretty new result that needs to be confirmed through extensive validation over selected cases study.

Acknowledgments

This work was developed within the FP7 EU project ICE-ARC (grant agreement 603887) and the PNRA project "WAMIZ – Waves in the Ice" (grant PNRA18_00109). This is also a contribution to the Year of Polar Prediction (YOPP), a flagship activity of the Polar Prediction Project (PPP), initiated by the WWRP of the WMO. We acknowledge the WMO WWRP for its role in coordinating this international research activity.

The Project was carried out using CSK® Products © ASI (Italian Space Agency), delivered under the ASI license to use ID 714 in the framework of COSMO-SkyMed Open Call for

Science. The Sentinel-1A used in this work was freely delivered by ESA through the Copernicus Open Access Hub (https://scihub.copernicus.eu/dhus/#/home).

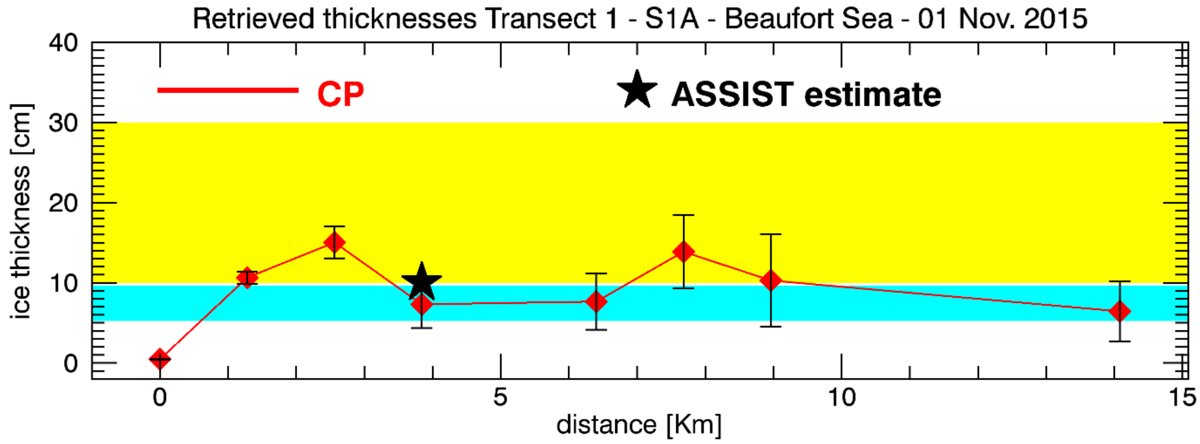

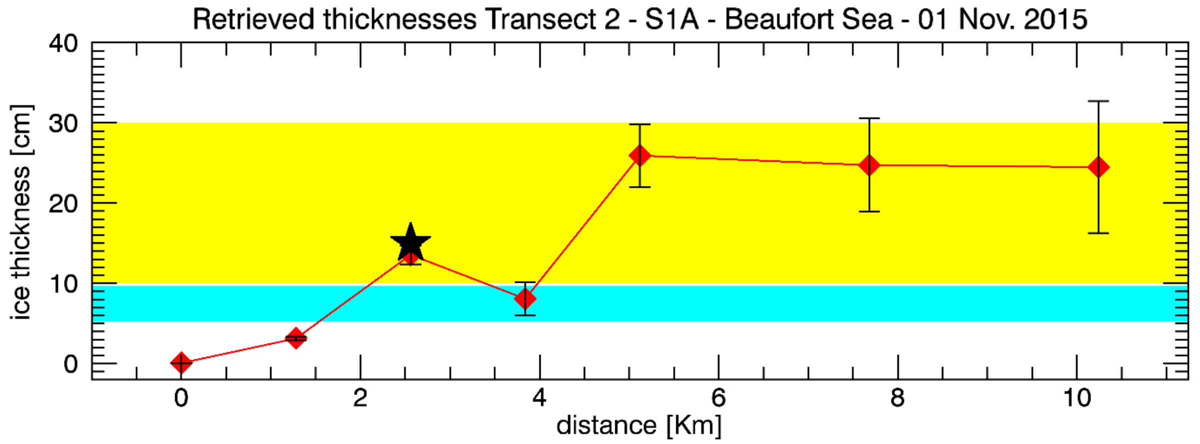

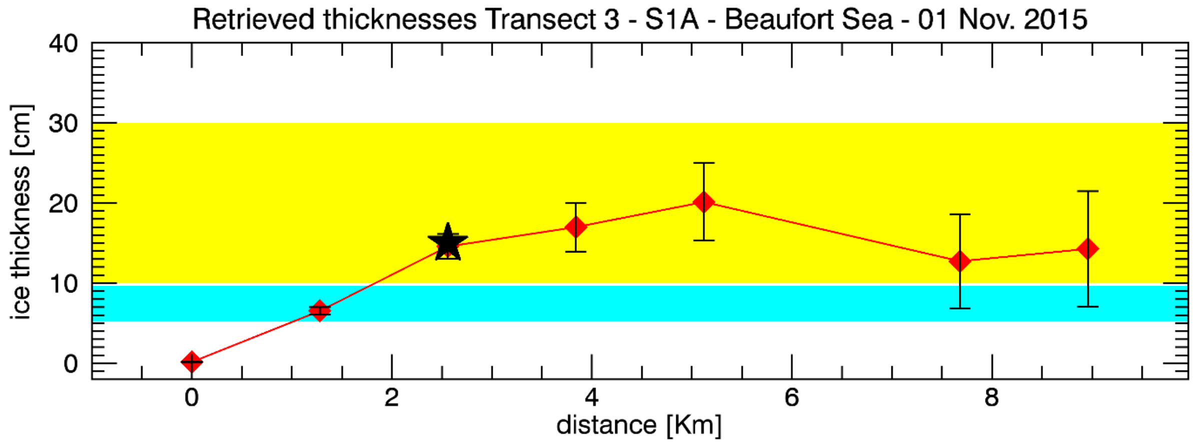

Figure 4. Estimated ice thicknesses over the three transects selected on the S1A SAR image. The cyan band represents the variability of the SMOS thicknesses in the area covered by the transects; the yellow band represents the variability of the in situ estimated ice thicknesses with the ASSIST protocol.

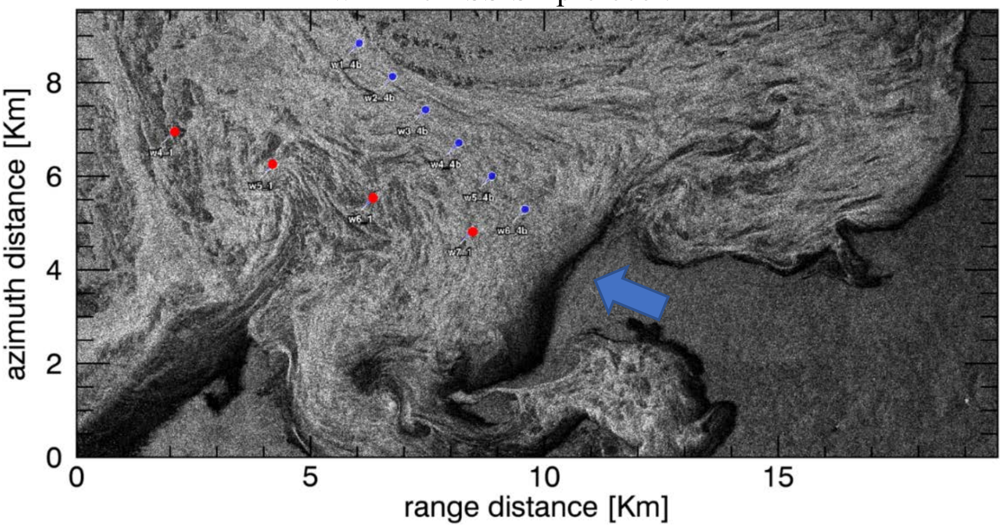

Figure 5. Portion of the CSK SAR image acquired on 30 March 2019 in the Weddell Sea. T1 (red) and T4b (blue) are the transects selected for ice thickness estimation. The blue arrow represents the propagation direction of the dominant waves.

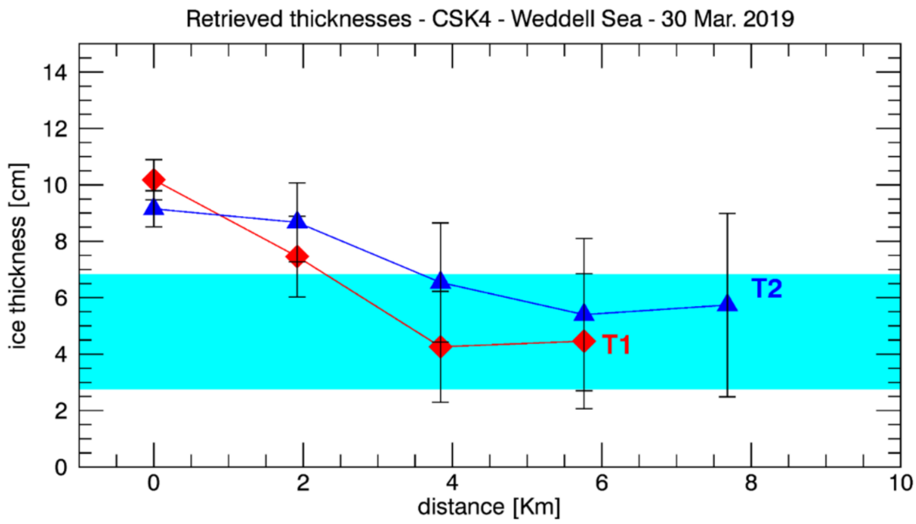

Figure 6. As for Figure 4, relevant to the two transects selected on the CSK SAR image of figure 5.

References

De Carolis, G. (2001). Retrieval of the ocean wave spectrum in open and thin ice covered ocean waters from ERS Synthetic Aperture Radar images. Nuovo Cimento C, 24 C (1), 53-66.

De Carolis, G. (2003). SAR measurements of directional wave spectra in viscous sea ice. Rivista Italiana di TELERILEVAMENTO, n. 26, 27, 28, pp. 31-36.

De Santi, F., & Olla, P. (2017). Effect of small floating disks on the propagation of gravity waves. Fluid Dynamics Research, 49(2), 025512.

De Santi, F., De Carolis, G., Olla, P., Doble, M., Cheng, S., Shen, H. H., & Thomson, J. (2018). On the ocean wave attenuation rate in grease-pancake ice, a comparison of viscous layer propagation models with field data. J. Geophys. Res., 123, 5933–5948. https://doi.org/10.1029/2018JC013865.

Doble, M., De Carolis, G., Meylan, M. H., Bidlot, J. R., & Wadhams, P. (2015). Relating wave attenuation to pancake ice thickness, using field measurements and model results. Geophys. Res. Letters, 42, 4473–4481. https://doi.org/10.1002/2015GL063628.

Holland, P. R. et al. (2014). Modelled trends in Antarctic Sea ice thickness. Journal of Climate, 27, 3784-3801. https://doi.org/10.1175/JCLI-D-13-00301.1.

Huntemann, M., Heygster, G., Kaleschke, L., Krumpen, T., Mäkynen, M., & Drusch, M. (2014). Empirical sea ice thickness retrieval during the freeze-up period from SMOS high incident angle observations. The Cryosphere, 8, 439-451, doi:10.5194/tc-8-439-2014, 2014.

Jung, T., et al. (2016). Advancing Polar Prediction Capabilities on Daily to Seasonal Time Scales. Bulletin of the American Meteorological Society. doi: 10.1175/BAMS-D-14-00246.1.

Keller, J. (1998). Gravity waves on ice-covered water. J. Geophys. Res., 103, 7663–7669.

Kelly, B. C. (2007). Some aspects of measurement error in linear regression of astronomical data. The Astrophysical Journal, 665:1489–1506, August 20.

Newyear, K., & Martin, S. (1999). Comparison of laboratory data with a viscous two-layer model of wave propagation in grease ice. J. Geophys. Res., 104, 7837–7840.

Pedersen, L. T., & Coon, M. D. (2004). A sea ice model for the marginal ice zone with an application to the Greenland Sea. J. Geophys. Res., 109, C03008, doi:10.1029/2003JC001827.

Rogers, J. C., & Hung M.- P. (2008). The Odden ice feature of the Greenland Sea and its association with atmospheric pressure, wind, and surface flux variability from reanalyses. Geophys. Res. Letters, 35, L08504, doi:10.1029/2007gl032938.

Shuchman, R. A., et al. (1998). Greenland Sea Odden sea ice feature: Intra-annual and interannual variability, Journal of Geophysical Research, 103, 12,709-12, 724.

Sutherland, P., & J.-C. Gascard (2016). Airborne remote sensing of ocean wave directional wavenumber spectra in the marginal ice zone, Geophys. Res. Letters, 43, 5151-5159, doi:10.1002/2016GL067713.

Thomson, J., et al. (2018). Overview of the Arctic Sea state and boundary layer physics program. J. Geophys. Res., 123, 8674–8687. https://doi.org/10.1002/2018JC013766

Wadhams, P., Wilkinson, J. P., Hall, R. J., & Down, S. J. (1997). Ice-ocean physics cruise to the Odden region of the Greenland Sea. R/V Jan Mayen cruise report. Internal report of the ESOP-2 project of the EU MAST-III programme. Contract MAS3-CT95-0015.

Wadhams, P., De Carolis, G., Parmiggiani, F., & Tadross, M. (1997). Wave dispersion by frazil-pancake ice from SAR imagery. IGARSS '97, 1997 IEEE International, Vol. 2, September 1997, DOI: 10.1109/IGARSS.1997.615280

Wadhams, P., & Wilkinson, J. (1999). The physical properties of sea ice in the Odden ice tongue. Deep-Sea Research II, 46, 1275-1300.

Wadhams, P., Parmiggiani, F., De Carolis, G., & Tadross, M. (1999). Mapping the thickness of pancake ice using ocean wave dispersion in SAR imagery. In G. Spezie & G. M. R. Manzella (Eds.), The oceanography of the Ross Sea, Antarctica (pp. 17–34). Milan, Italy: Springer.

Wadhams, P., Parmiggiani, F., & De Carolis, G. (2002). The use of SAR to measure ocean wave dispersion in frazil-pancake icefields. Journal of Physical Oceanography, 32, 1721–1746.

Wadhams, P., Parmiggiani, F., De Carolis, G., Desiderio, D., & Doble, M. J. (2004). SAR imaging of wave dispersion in Antarctic pancake ice and its use in measuring ice thickness. Geophys. Res. Letters, 31, L15305. https://doi.org/10.1029/ 2004GL020340.

Wadhams, P., Aulicino, G., Parmiggiani, F., Persson, P. O. G., & Holt, B. (2018). Pancake ice thickness mapping in the Beaufort Sea from wave dispersion observed in SAR imagery. J. Geophys. Res., 123, 2213–2237. https://doi.org/10.1002/2017JC013003.

IAHR AIRH

25th IAHR International Symposium on Ice
Trondheim, June 14 to 18, 2020

Medium range sea ice prediction for Japanese research vessel MIRAI's expedition cruise in 2019

L.W.A. De Silva[1] and H. Yamaguchi[1]
[1]The University of Tokyo, Japan
Kiban-tou 6H1, Graduate School of Frontier Sciences, The University of Tokyo, 5-1-5 Kashiwanoha, Kashiwa 277-8561, Japan
waruna@edu.k.u-tokyo.ac.jp , h-yama@edu.k.u-tokyo.ac.jp

To understand the state of the atmosphere, ocean and sea ice in the Chukchi Sea and Beaufort Sea of the Arctic Ocean, a Japanese research vessel (RV) MIRAI entered the Arctic water from 7 to 29 October 2019. The Arctic sea ice conditions, which is very critical for this ice-strengthen ship, can change over short timescales due to dynamics and thermodynamics during the cruise periods. Leads may open and close in a very short time, and heavy ice pressure may build up in the compression of compact ice. These short-time and small-scale processes have a strong influence on shipping on the ice infested water. Therefore, precise ice distribution and ice edge predictions in the medium range (10–day scale) are one of the key issues to keep safe and efficient navigation. In this study, a high-resolution (about 2.5 km) ice-ocean coupled model is developed for forecasting the medium range sea ice distribution in the Chukchi and Beaufort Seas. European Center for Medium-Range Weather Forecast atmospheric high-resolution 10-day forecasted forcing data is used for the sea ice prediction simulations. Initial sea ice distribution is given by observational AMSR2 sea ice concentration. Temperature and salinity boundary conditions at the Bering Strait is supplied using the RIOPS model data. Since MIRAI is an ice-strengthened ship that has to avoid the thick sea ice with high ice cover as much as possible. Forecast skill is measured by ice edge error, which is the average distance between forecast and observed ice edges. Using a threshold of 15% sea ice concentration to indicate the ice edge, the maximum ice edge error in the ice–ocean coupled model in the Chukchi Sea is 40 km.

1. Introduction

Since 1998 Japanese RV MIRAI has been conducted the research expedition cruise in the Arctic ocean for sea ice and ocean conditions observations. All the past expeditions in the Arctic were conducted in the summer and autumn. However, in 2018 they have conducted the Arctic research expedition in early winter for the first time and 2019 in the autumn. The MIRAI ship track and the sample collection locations of 2019 are shown in Fig.1.

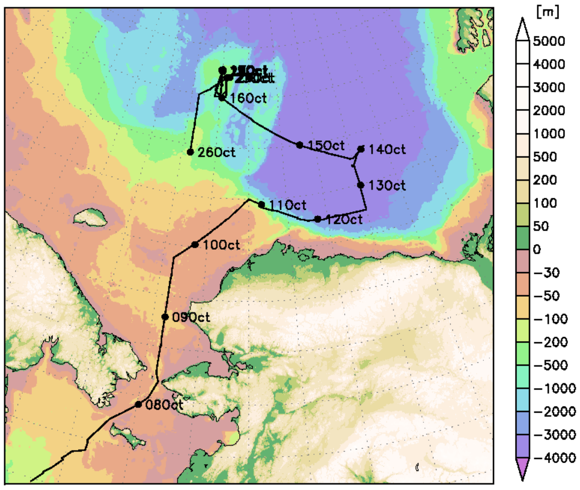

Figure 1. Ship track and sample collection locations of RV MIRAI in 2019

The Arctic sea ice conditions can change over short timescales due to dynamics and thermodynamics in autumn. Lead may open and close in a very short time, and heavy pressure may build up in the compression of compact ice. These short timescale processes have a strong influence on shipping on the ice infested water. The MIRAI ship is not an ice class vessel and thus, it navigates to avoid the sea ice as much as possible. Therefore, precise ice distribution prediction in the short-term (10–days scale) is one of the key issues to realize safe and efficient navigation.

Global climate models and regional models have been employed to assess the predictability of Arctic sea ice on seasonal and decadal time scale (Kubat et al. (2010); Turnbull and Taylor (2017)), and a few others focused on short time scales (Inoue et al. (2015); Ono et al. (2016); De Silva et al. (2015) Schweiger and Zhang (2015)).

Most of the available numerical models (Preller and Posey (1989); Schweiger and Zhang (2015)) have shown high uncertainties in the short-term (about 5-days) and narrow-area predictions. Nakanowatari et al. (2018) discussed the 10-day sea ice thickness distribution in the East Siberian Sea with the TOPAZ4 ice-ocean data assimilation system. They have found the TOPAZ4 system accurately predict the sea ice distribution in the summer up to the 3 days lead time. However, IcePOM model sea ice forecast shows a better agreement with the satellite observations (De Silva et al. (2015)) in Laptev Sea.

The purpose of this study is to predict the medium range (10-day) sea ice conditions in the Chukchi Sea using mesoscale eddy resolving ice-ocean coupled model within the ice edge error of ±20 km, which can meet MIRAI ship crew requirement. The correlation score of ice edge error and sea ice concentration distribution compared to the satellite observation of

Advanced Microwave Radiometer2 (AMSR2) quantifies the forecast skill. Skill scores are computed from 10-day forecasts which initialized from 01 October 2019 to 30 October 2019 during the MIRAI research expedition.

2. Model description and experimental design

Ice–ocean coupled model used in this study is based on the model developed by De Silva et al. (2015). The ocean model is based on generalized coordinates, the Message Passing Interface version of the Princeton Ocean Model (POM; Mellor et al. (2002)). The level-2.5 turbulence closure scheme of Mellor and Yamada (1982) is used for the vertical eddy viscosity and diffusivity. The horizontal eddy viscosity and diffusivity are calculated using a formula proportional to the horizontal grid size and velocity gradients (Smagorinsky 1963); the proportionality coefficient chosen is 0.2. The ice thermodynamics model is based on the zero-layer thermodynamic model proposed by Semtner (1976). Surface fluxes; shortwave radiation, longwave radiation, sensible heat flux, and latent heat flux are calculated according to the bulk formulation proposed by Parkinson and Washington (1979). The snow effect is parameterized according to Zhang and Zhang (2001). The ice rheological model is based on the elastic–viscous–plastic (EVP) rheology proposed by Hunke and Dukowicz (2002) and is modified to take ice floe collisions into account, following Sagawa and Yamaguchi (2006), Fujisaki et al. (2010), and De Silva et al. (2015). Model domains are constructed using Earth Topography 1 arc-minute Gridded Elevation Dataset (ETOPO1) as shown in Fig. 2. The zonal and meridional grid spacing are approximately 2.5 × 2.5 km for the high-resolution regional model (Fig. 2(b)) and 25× 25 km for the whole Arctic model(Fig 2(a)). To resolve the surface and bottom ocean dynamics, we use the logarithmic distribution of the vertical 33 z-sigma layers near the top and bottom surfaces. Satellite observation of sea ice concentration is assimilated into the IcePOM model with nudging method described by Mudunkotuwa et al. (2016). They claimed that assimilating sea ice concentration improved the ocean and ice conditions in the numerical model. Bering strait temperature and salinity boundary conditions are given by the Canadian Regional Ice Ocean Prediction System (RIOPS) model outputs.

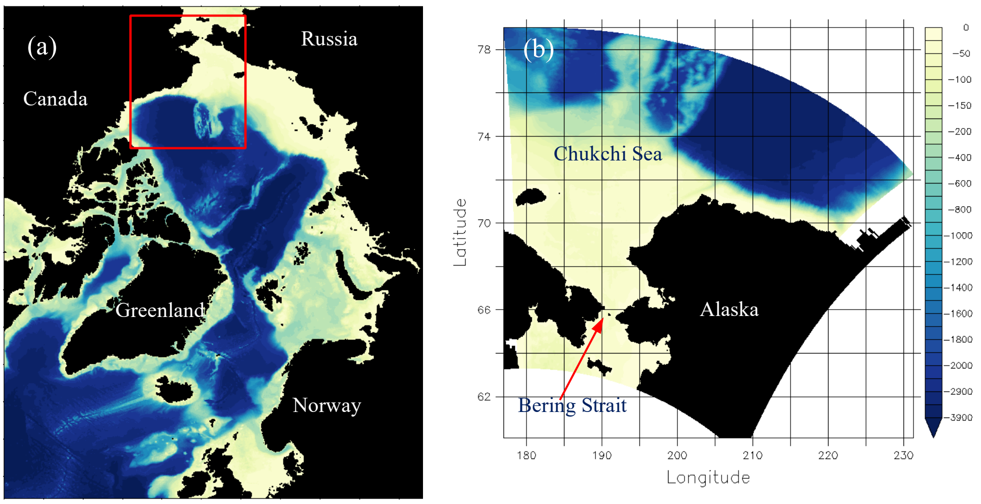

Figure 2. Model bathymetries (m). (a) Whole-Arctic model. (b) High-resolution regional 4model domain, consisting of the Chukchi Sea and Bering Strait. Red rectangle box in the whole-Arctic model shows the regional model domain.

Series of computations are performed in this study as described below. Firstly, we have run the whole Arctic model (Fig. 2(a)) with 6 hourly atmospheric reanalysis data from the European Centre for Medium-Range Weather Forecasts Re-Analysis Interim (ERA-Interim) and monthly mean river-runoff data from the Arctic Ocean Model Intercomparison Project [http://www.whoi.edu/page.do?pid=30587] from 01 January 2004 to 01 January 2019. Sea ice concentration data of Advanced Microwave Scanning Radiometer for Earth Observing System (AMSR-E) and AMSR2 data are assimilated into the whole Arctic model with nudging method.

Secondly, we have run the hindcast simulation of high-resolution regional model (Fig 2(b)) from 01 January 2018 to 01 October 2019. Hindcast computation is initialized using interpolated whole Arctic model results (sea ice concentration, thickness, ocean temperature and salinity). For the regional hindcast computation we also used the 6 hourly reanalysis data from ERA-Interim. Please note that ERA-Interim data has 2 months delay period and therefore, we used ECMWF forecasted data from 01 August 2019 to 01 October 2019. ECMWF atmospheric forecast data with 0.5 degree spatial resolution derived from THORPEX Interactive Grand Global Ensemble through its data portal [http://tigge.ecmwf.int]. AMSR2 sea ice concentration data is assimilated using nudging method. The main reason for preforming the hindcast high-resolution computation is, as described in De Silva and Yamaguchi (2017), high-resolution (2.5km) hindcast computation gives better initial conditions for future forecast computations than the medium-resolution (25km) whole Arctic computation.

Finally, high-resolution 10-day forecasting computations are initialized using high-resolution hindcast model ocean output data from 01 October 2019. Note that the hindcast model run sea-ice concentration and thickness are not used for high-resolution forecast computations; rather, AMSR2 derived concentration and thickness are used. When the initial AMSR2 sea ice concentration is not zero in the open water areas of the hindcast simulation, we interpolated the sea-ice thickness from neighboring grid cells. In this case, water surface temperature under those cells was set to the freezing temperature to avoid the rapid melting of sea ice. Moreover, when the initial AMSR2 observed concentration is zero and the hindcast regional simulation concentration is not zero, we set the sea-ice thickness to zero in those cells. For those cells, the temperature under the ocean surface was assigned by interpolating the open water neighboring grid cells. Note that, in both situations, ocean salinity is unchanged and the same as the hindcast model output value. For the forecast computation we have used the ECMWF atmospheric forecast data with 0.1 degree spatial resolution derived from Set I - Atmospheric Model high-resolution 10-day forecast (HRES) through Arctic Data Archive System (ADS) data portal [https://ads.nipr.ac.jp/].

3. Results and discussion

MIRAI ship cruise requesting following forecasted sea ice and ocean variables every day at 00:00UTC; sea ice concentration distribution, ice edge location at 5% and 15% threshold concentrations, sea ice thickness distribution, sea ice pressure distribution, and sea surface temperature distribution for safe navigation.

The icePOM model take about 55minutes to compute the 1 computational day. Every day icePOM download the AMSR2 data at 05:00UTC and ECMWF forecasted data at 05:45UTC from ADS server. After interpolating the AMSR2 and ECMWF data into the computational grid icePOM start the forecast computation at 06:30UTC. Results of forecasted computations, 1st-day is uploaded into the ADS server at 07:45UTC and 10th-day uploaded into the ADS server at 14:45UTC.

Preliminary analysis results are summarized as follows. We have investigated the 10-day sea ice prediction accuracy of icePOM model in the Chukchi Sea area. Since MIRAI ship navigates to avoid the sea ice as much as possible, a factor to score the forecast skill is considered to be ice edge error and bias which is an averaged distance between forecasted and observed ice edges.

Figure 3 shows the schematic diagram of predicted (blue) and observational (red) ice edges. Yellow areas indicate model overestimation (*O*), which is the spatial integral of all sea ice extents where predicted ice concentration is above 15% but observed sea ice concentration is below 15%. Green areas indicate model underestimation (*U*), which is the spatial integral of all sea ice extents where predicted ice concentration is below 15% but observed ice concentration is above 15%. Light blue and white areas indicate ocean extent that has been correctly predicted and sea ice extent that has been correctly predicted, respectively. Ice edge error and bias are defined in Eq. 1 and 2, respectively:

$$\text{Ice edge error} = \frac{O+U}{\frac{1}{2}\left(L_m + L_o\right)} \quad \textbf{[1]}$$

$$\text{Bias} = \frac{O-U}{\frac{1}{2}\left(L_m + L_o\right)} \quad \textbf{[2]}$$

where L_m and L_o are length of predicted ice edge and length of observational ice edge, respectively.

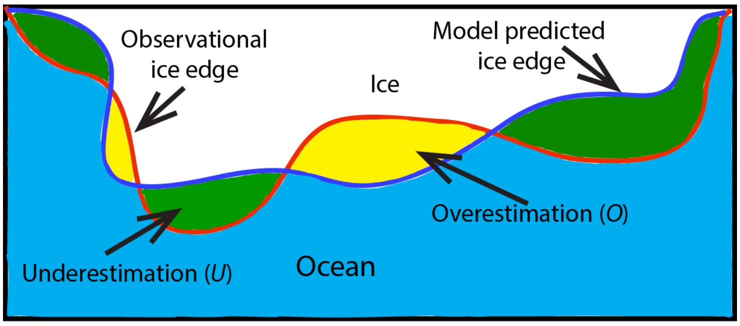

Figure 3. Schematic diagram of predicted (blue) and observational (red) ice edges. Yellow areas indicate model overestimation (*O*), which is the spatial integral of all sea ice extents where predicted ice concentration is above 15% but observed ice concentration is below 15%. Green areas indicate model underestimation (*U*), which is the spatial integral of all sea ice extents where predicted ice concentration is below 15% but observed ice concentration is above 15%. Light blue and white areas indicate ocean extent that has been correctly predicted and sea ice extent that has been correctly predicted, respectively.

Time series of 10-day forecasted ice edge errors and bias of IcePOM, ECMWF, TOPAZ4 and Persistence are shown in Fig 4. The computations stared from 01 to 30 October 2019 are used as the analyzed period. The maximum ice edge error of IcePOM model is about 40 km during the analyzed period. All computational results show similar ice edge error variations in the 10-day forecast. On the other hand ECMWF and TOPAZ4 shows the negative bias and IcePOM shows the positive bias.

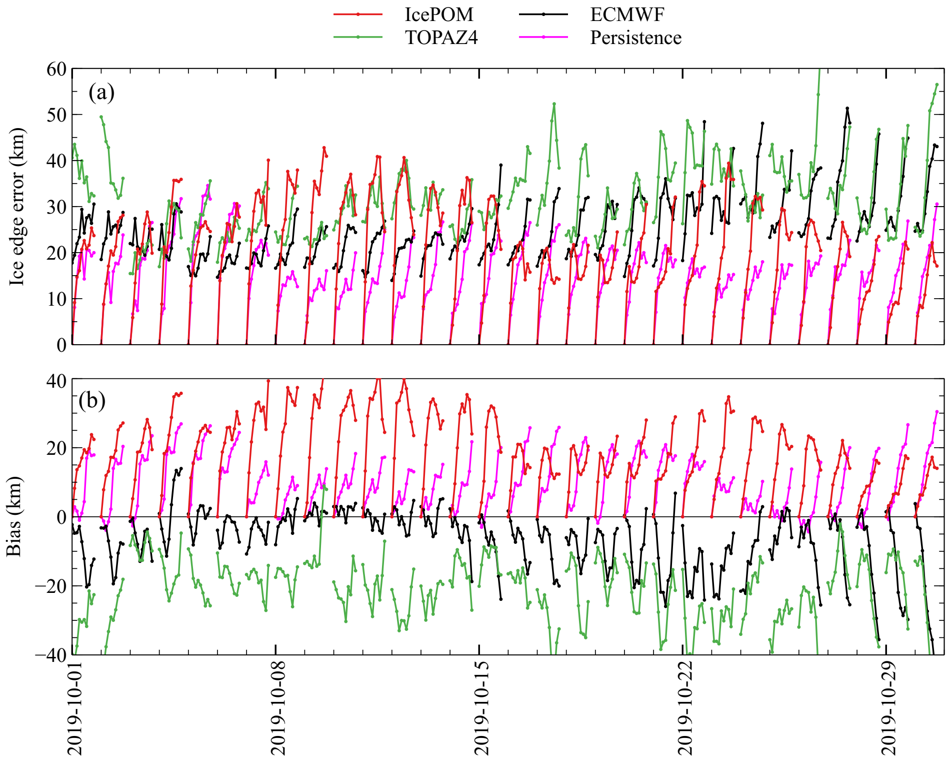

Figure 4. Evolution of ice edge errors and bias for 1 to 30 October 2019 from 10-day IcePOM forecast, TOPAZ4 forecast, ECMWF forecast and Persistence. Errors and biases were calculated with respect to Advanced Microwave Scanning Radiometer 2 (AMSR2) ((a) and (b)). Ice edge was defined by thresholds of 15% ice concentrations for comparison with AMSR2.

To further understand model bias, we plotted time–depth cross sections of ocean temperature (figure 5) and salinity (figure 6) at the marginal ice zone (MIZ) for 10 to 20 November 2018. Data sources include CTD observations from MIRAI (figures 5(a) and 6(a)), initial field from RIOPS forecast (figures 5(b) and 6(b)), and initial field from IcePOM forecast (figures 5(c) and 6(c)). Locations of CTD observations are shown in figures 5(d) and 6 (e). Temporal variation of salinity in all models is lower than that in MIRAIS observations at the MIZ. Variability of the upper mixed layer temperature in IcePOM and RIOPS are of the same magnitude as that from MIRAI observations.

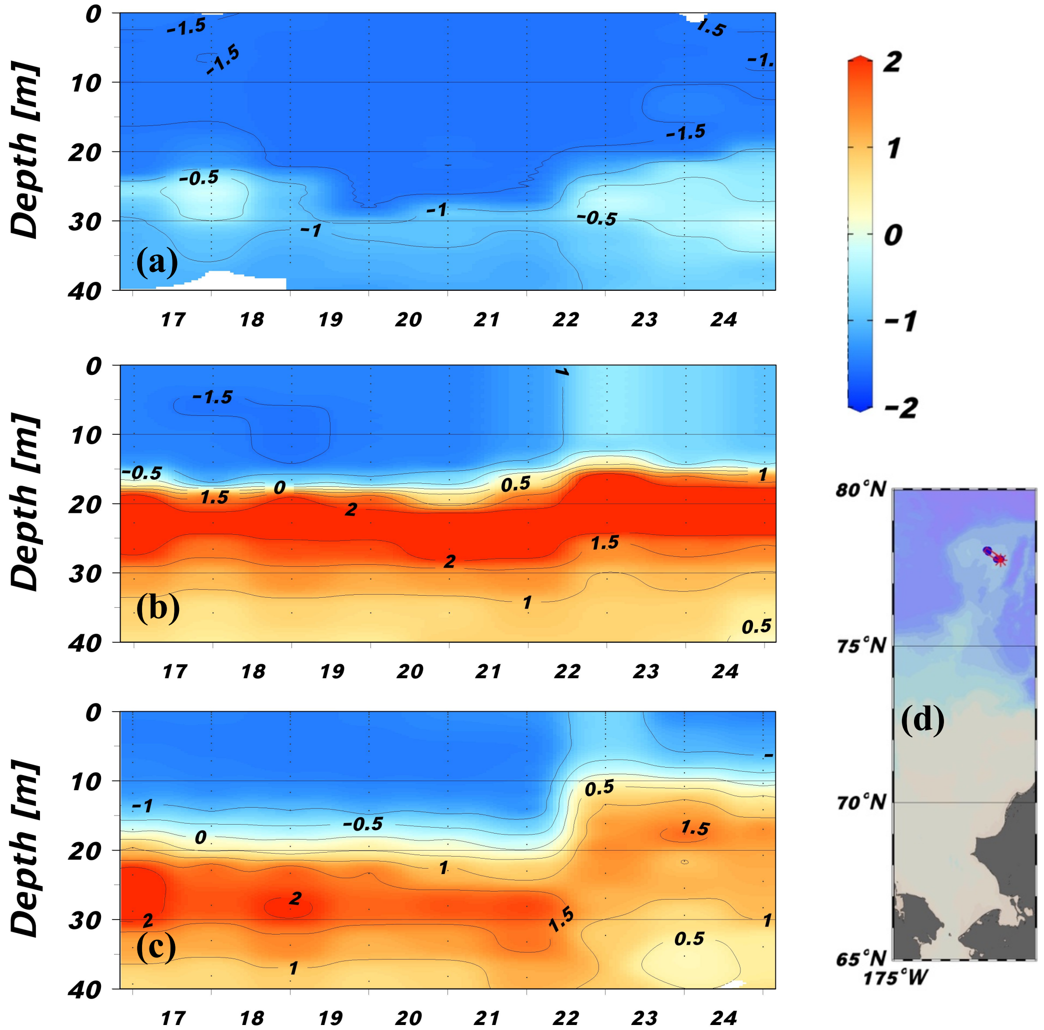

Figure 5. Time–depth cross section of ocean temperature for 17 to 25 October 2019 at the marginal ice zone. (a) results from conductivity, temperature and depth (CTD) observations from MIRAI, (b) RIOPS forecast, (c) IcePOM forecast, and (e) locations of CTD observations.

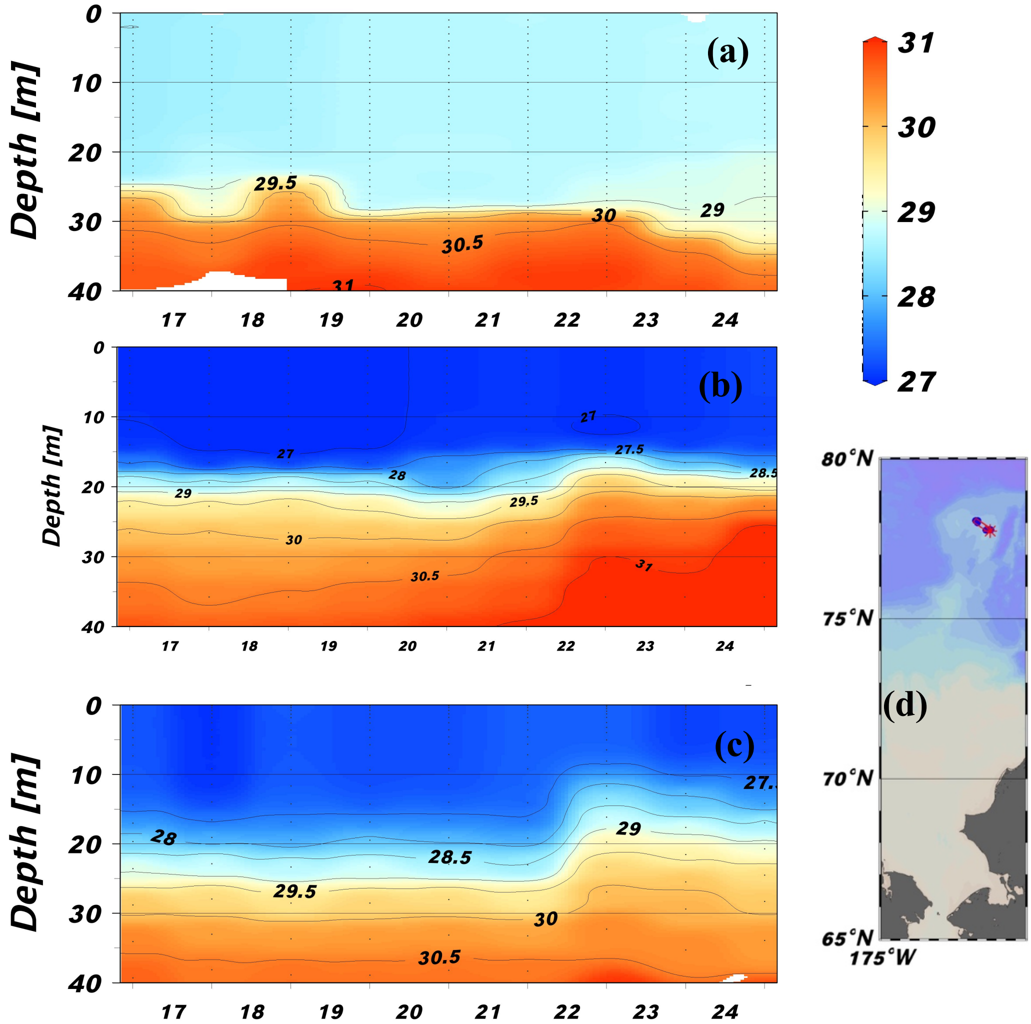

Figure 6. Time–depth cross section of ocean salinity for 17 to 25 October 2019 at the marginal ice zone. (a) results from conductivity, temperature and depth (CTD) observations from MIRAI, (b) RIOPS forecast, (c) IcePOM forecast, and (e) locations of CTD observations.

4. Conclusion

This paper has explained the detailed plan of real time sea ice prediction for the MIRAI research expedition. The location of sea ice edge, sea ice concentration, sea ice thickness and sea ice pressure distributions maps are important for operational planning of maritime activities. This study suggests that icePOM model can predict the maximum sea ice edge error within 40 km for 10-day computation in October 2019 that is in good agreement with the requirement of MIRAI ship crew.

References

De Silva, L.W.A. and Yamaguchi, H., (2017): The impact of data assimilation and atmospheric forcing data on predicting short-term sea ice distribution along the Northern sea route. *Okhotsk Sea Polar Ocean. Res.* **1**, 1–6.

De Silva, L.W.A., Yamaguchi, H., and Ono, J., (2015): Ice–ocean coupled computations for sea-ice prediction to support ice navigation in Arctic sea routes. *Polar Res.* **34**, 18pp. doi: 10.3402/polar.v34.25008.

Fujisaki, A., Yamaguchi, H., and Mitsudera, H., (2010): Numerical experiments of air–ice drag coefficient and its impact on ice–ocean coupled system in the Sea of Okhotsk. *Ocean Dyn.* **60**, 377–394. doi: 10.1007/s10236-010-0265-7.

Hunke, E.C. and Dukowicz, J.K., (2002): The elastic-viscous-plastic sea ice dynamics model in general orthogonal curvilinear coordinates on a sphere-incorporation of metric terms. *Mon. Weather Rev.* **130**, 1848–1865.

Inoue, J., Yamazaki, A., Ono, J., Dethloff, K., Maturilli, M., Neuber, R., Edwards, P., and Yamaguchi, H., (2015): Additional Arctic observations improve weather and sea-ice forecasts for the Northern Sea Route. *Sci. Rep.* **5**, 16868. doi: 10.1038/srep16868.

Kubat, I., Sayed, M., Savage, S.B., and Carrieres, T., (2010): Numerical simulations of ice thickness redistribution in the Gulf of St. Lawrence. *Cold Reg. Sci. Technol.* **60**, 15–28. doi: 10.1016/J.COLDREGIONS.2009.07.003.

Mellor, G.L., Hakkinen, S., Ezer, T., and Patchen, R., (2002): A generalization of a sigma coordinate ocean model and an intercomparison of model vertical grids., in: In Ocean Forecasting: Conceptual Basis and Applications. Springer, Berlin Heidelberg, pp. 55–72.

Mellor, G.L. and Yamada, T., (1982): Development of a turbulence closure model for geophysical fluid problems. *Rev. Geophys.* **20**, 851–875. doi: 10.1029/RG020i004p00851.

Mudunkotuwa, D.Y., De Silva, L.W.A., and Yamaguchi, H., (2016): Data assimilation system to improve sea ice predictions in the Arctic Ocean using an ice-ocean coupled model, in: 23rd IAHR International Symposium on Ice. Ann Arbor, Michigan USA, pp. 1–8.

Nakanowatari, T., Inoue, J., Sato, K., Bertino, L., Xie, J., Matsueda, M., Yamagami, A., Sugimura, T., Yabuki, H., and Otsuka, N., (2018): Medium-range predictability of early summer sea ice thickness distribution in the East Siberian Sea based on the TOPAZ4 ice–ocean data assimilation system. *Cryosph.* **12**, 2005–2020. doi: 10.5194/tc-12-2005-2018.

Ono, J., Inoue, J., Yamazaki, A., Dethloff, K., and Yamaguchi, H., (2016): The impact of radiosonde data on forecasting sea-ice distribution along the Northern Sea Route during an extremely developed cyclone. *J. Adv. Model. Earth Syst.* **8**, 292–303. doi: 10.1002/2015MS000552.

Parkinson, C.L. and Washington, W.M., (1979): A large-scale numerical model of sea ice. *J. Geophys. Res.* **84**, 311–337. doi: 10.1029/JC084iC01p00311.

Preller, R.H. and Posey, P.G., (1989): The Polar Ice Prediction System - A Sea Ice Forecasting System, Naval Ocean Research and Development Activity Rep. 212. Mississippi.

Sagawa, G. and Yamaguchi, H., (2006): A Semi-Lagrangian Sea Ice Model For High Resolution Simulation, in: The Sixteenth International Offshore and Polar Engineering Conference. International Society of Offshore and Polar Engineers, San Francisco, California, pp. 584–590.

Schweiger, A.J. and Zhang, J., (2015): Accuracy of short-term sea ice drift forecasts using a coupled ice-ocean model. *J. Geophys. Res. Ocean.* **120**, 7827–7841. doi: 10.1002/2015JC011273.

Semtner, A.J., (1976): A Model for the Thermodynamic Growth of Sea Ice in Numerical Investigations of Climate. *J. Phys. Oceanogr.* **6**, 379–389. doi: 10.1175/1520-0485(1976)006<0379:AMFTTG>2.0.CO;2.

Smagorinsky, J., (1963): General circulation experiments with the primitive equations. *Mon. Weather Rev.* **91**, 99–164. doi: 10.1175/1520-0493(1963)091<0099:GCEWTP>2.3.CO;2.

Turnbull, I.D. and Taylor, R.S., (2017): An Operational Thermodynamic-Dynamic Model for the Coastal Labrador Sea Ice Melt Season. *Geosci. Model Dev. Discuss.* **2017**, 1–57. doi: 10.5194/gmd-2017-39.

Zhang, X. and Zhang, J., (2001): Heat and freshwater budgets and pathways in the Arctic Mediterranean in a coupled ocean/sea-ice model. *J. Oceanogr.* **57**, 207–234.

25th IAHR International Symposium on Ice

Trondheim, 23 – 25 November 2020

On the ice and wind conditions in the northern part of the Gulf of Bothnia leading ice-induced vibrations

Ersegun Deniz Gedikli[1,2], Morten Bjerkås[3], Knut Vilhelm Høyland[1], Vegard Hornnes[1], Joshua Turner[1]

[1]*Department of Civil and Environmental Engineering, Norwegian University of Science and Technology, Trondheim, Norway*

[2]*Department of Ocean and Resources Engineering, University of Hawaii at Manoa, Honolulu, USA*

[3]*DIMB Consult AS, Trondheim, Norway*

In ice infested regions drift ice can cause serious damage to offshore structures and ships. The origin of the drifting ice is the winds and the currents. However, it is known that the Gulf of Bothnia does not have strong currents; therefore, it is the wind conditions and wind force that drive large ice sheets. In this study, we analyze the met-ocean data including measured wind speeds, wind directions, ice speeds, ice directions and ice concentrations on the Norströmsgrund lighthouse for the years of 2001-2003. We also examine the met-ocean conditions at the neighboring structures to understand how ocean environments differ in the region. For example, we find that the northern part of the Gulf of Bothnia has a typical crescent shaped wind profile and it is possible for ice floes to change their direction suddenly, depending on the stable wind directions both in early and late seasons where large ice sheets are not present. However, structural vibration can occur in any direction depending on the ice concentration near the structure, severity of the winter and the sea ice extent in the Bay. Because all met-ocean data are eventually coupled with the structural motions, it is important to understand how these parameters interact with each other and how they vary when large vibrations are observed so that one could use them for forecasting. In the end, we also present the results of the updated version of the met-ocean based FLI prediction method (Bjerkås and Gedikli, 2019) and discuss the results.

1. Introduction

Ice induced vibration (IIV) is an inherent problem seen in offshore structures in ice infested regions (i.e., Arctic and Subarctic regions) where coupled ice-structure interaction may lead to significant structural motions. These motions can influence structural fatigue and offshore operations. During such interactions, offshore structures may also experience resonance, oscillating at a frequency that is close to one of the natural frequencies of the structure. This extreme vibration case is referred to as frequency lock-in or FLI (Nord et al., 2018). In their study, Nord et al. (2018) identified 61 significant FLI events on the Norströmsgrund (referred as NSG from now on) lighthouse between the years of 2001 and 2003. Therefore, understanding the conditions leading to IIV is of utmost importance for the offshore industry to operate safely in ice infested regions.

ISO (2019) classifies IIV regimes as intermittent crushing, frequency lock-in (FLI) and continuous brittle crushing based on ice speeds; intermittent crushing occurs when the ice speeds are low, FLI occurs at intermediate ice speeds and continuous brittle crushing occurs when ice speeds are high (Yue and Bi, 2000). Although this classification gives a general idea of IIV, it does not give any information regarding the onset conditions of such vibrations. For example, the coupled effect of the met-ocean conditions on the offshore structures are far from being understood.

The main goal of this study is to get an in depth understanding of the met-ocean conditions at a given site and discuss how these conditions are and might be related with the observed ice loading on the structures. The data that we analyze comes from the projects "Measurements of Structures in Ice" (STRICE) and "Validation of Low Level Ice Forces" (LOLEIF). In this work, we first compare the wind and ice drift directions with the logbook readings from NSG. This type of exercise shows us how reliable the measured data are. In addition, because these test campaigns only include three years of data, we further extend the data by including the environmental readings from the Rødkallen Meteorological Station (See Figure 1). Comparing the wind conditions between NSG and Rødkallen, we 1) identify the directional relationship between those structures, and 2) extend our dataset beyond the three-year period. Since we are using historical data, any data fitting/ post-processing is subject to error which is easily quantifiable.

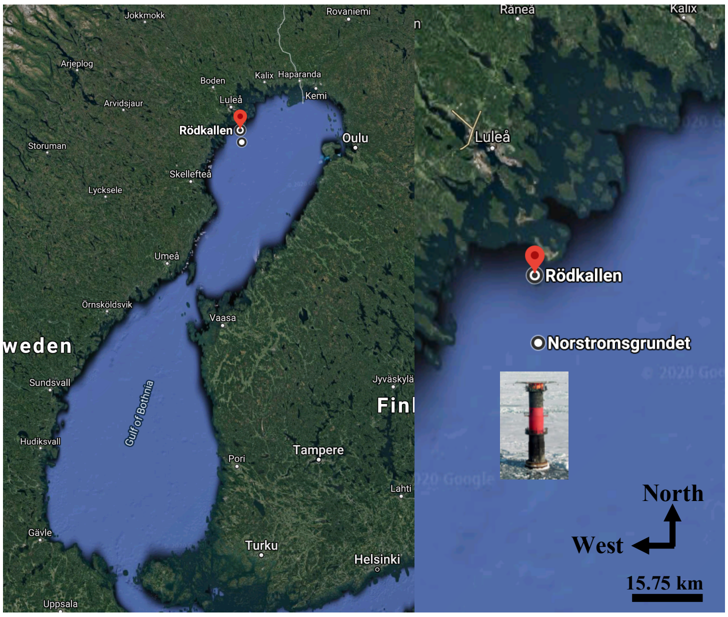

Figure 1. Locations of Rødkallen Meteorological Station and Norströmsgrund Lighthouse. Right image is the close-up version of the left image showing the region of interest. Distance between Rødkallen and Norströmsgrund is close to 15km.

As a result of this exercise, we make some unique observations where the results help to further improve the met-ocean data based IIV prediction method that has been introduced by Bjerkås and Gedikli (2019). For example, we identify that there is a crescent type of wind distribution in the region where the dominant wind direction tends to be more in the north-east direction (around 30 degrees) for NSG lighthouse when compared with Rødkallen. This is important because Bjerkås and Gedikli (2019) previously used the wind data from Rødkallen directly without any correction, with the assumption that the wind direction does not vary much for such close locations (apparently not true). In this study we also update the IIV prediction method and present the results. Therefore, we provide new insights on the conditions of IIVs using dominant wind directions and circular mean wind profiles.

2. Methods

2.1. Data Description

In this paper, three different datasets are studied: 1) LOLEIF and STRICE test campaigns 2001 – 2003 (both force measurements and logbook readings of local environmental conditions on the Norströmsgrund lighthouse); 2) EUMETSAT OSI SAF[1] (OSI SAF, 2017) for the ice concentration data, and; 3) Swedish Meteorological and Hydrological Institute (SMHI) for air temperatures, wind speeds and directions for the Rødkallen meteorological station and Luleå airport for the time interval of 1952-2015 (SMHI, 2020), where the third dataset is used for the update of the prediction method (Bjerkås and Gedikli, 2019). However, because sea ice concentration data obtained from EUTMETSAT OSI SAF was only available for the time period of 1972 and 2015, the final database was limited to this time period.

2.2 Norströmsgrund Lighthouse (NSG)

NSG is a bottom founded gravity-based structure with a diameter of 7.52m at mean water level (MWL) (Jochmann and Schwarz, 2000). It is located in the northern part of Gulf of Bothnia in the south of Luleå archipelago in Sweden (N65°6.6′ E22° 19.3′, see Fig. 1). The north-east and east-south portion of the lighthouse (covering 162° of the outer perimeter) is covered with nine load panels measuring the local ice loads at the MWL of 14.5m as illustrated in Fig. 2a.

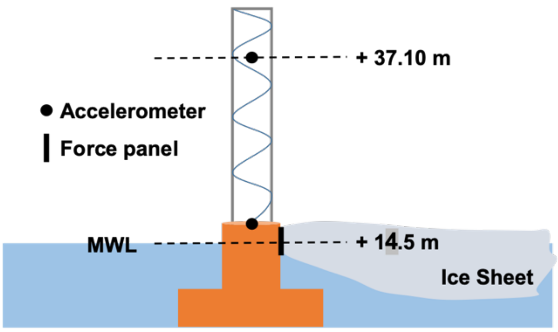

(a) Sideview of the lighthouse showing the locations of the accelerometers and force panels at MWL.

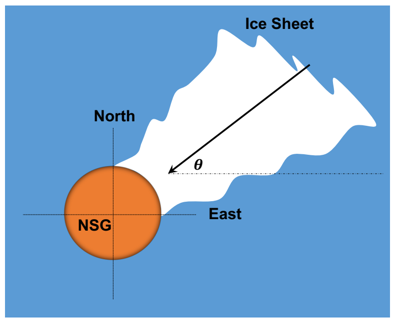

(b) Illustrative top view of the lighthouse showing an example ice sheet interacting with the structure.

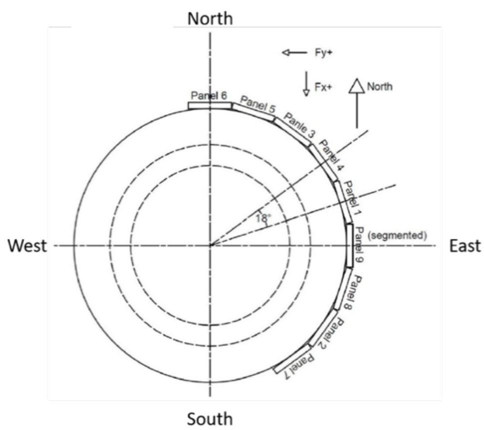

(c) Load panel orientation and sign convention (+F_y is the east – west Direction, +F_x is the north – south direction).

Figure 2. Sketch of the Norströmsgrund lighthouse. (a) sideview of NSG, (b) top view with moving ice sheet, and (c) cross-section of NSG with load panel orientation and sign convention.

[1] EUMETSAT stands for European Organization for the Exploitation of Meteorological Satellites and OSI SAF stands for Satellite Application Facility on Ocean and Sea Ice

The lighthouse was instrumented so that ice thickness, met-ocean data, ice loads and structural responses were measured. Parts of the lighthouse was also equipped with cameras to record the ice motion for some of the events. Other met-ocean data such as wind directions and ice drift directions at the lighthouse were also recorded in the logbooks for validation purposes. Fig. 2b shows an example ice sheet moving towards to NSG and Fig. 2c illustrates the cross-section of the lighthouse with force panels on it.

2.3 Wind and ice data

Wind data (speed and direction) was obtained from NSG logbooks and validated against the SMHI database. In the SMHI database two locations are considered: Luleå airport (because it gives us a complete met-ocean dataset covering the years between 1972 and 2015) and Rødkallen Metrological Station (because this location is close to the Norströmsgrund lighthouse, see Fig.1). In the SMHI (2020) dataset, the wind speed is measured at 10 m above the ground level and it is scaled down to 0.1 m (Bjerkås and Gedikli, 2019). After that, the ground level wind speed is multiplied with the Nansen number to find the theoretical ice drift speeds (Weiss, 2013). Here, it should be remembered that theoretical ice drift assumes the free drift of thin ice. These values are validated against the values presented in Nord et al. (2018). For completeness, we use the following numerical values based on Leppäranta and Omstedt (1990) and Leppäranta (2011)'s work on Gulf of Bothnia, some of which were chosen incorrectly in Bjerkås and Gedikli (2019) : $\rho_a = 1.23$ kg/m^3, $\rho_w = 1005$ kg/m^3, $C_a \approx 1.5 \times 10^{-3}$ and $C_w \approx 3.5 \times 10^{-3}$ (new values do not affect the results much).

It is important to note that Leppäranta (2011) uses hydrodynamic coefficients for 10 m level assuming they represent the wind speeds at the surface. However, using 10 m level wind speeds give significantly higher ice speed estimates compared to measured ice speeds. Therefore, we continue to use scaled down wind speeds in this work simply because the results match well with the observed wind speeds on NSG. That being said, regardless of the measured height of the wind speed, this only changes the ice drift speed condition in the prediction method, hence the ice speed interval in the model should be adjusted so that the specific criterion in Sec. 3.2 is met (in other words, we should include more physics in it).

As a result, the data matrix that we construct consists of daily mean values (wind direction, ice direction, wind speed), ice thickness, air temperature values (both Rødkallen and Luleå) and four-day average air temperature values as described in Bjerkås and Gedikli (2019). Mean wind and ice directions are estimated using the circular mean method due to the circular nature of the data (Berens, 2009). Consider a wind that is blowing towards 355° and another wind that is blowing towards 5°. Those two winds essentially represent a similar path (say north), yet their arithmetic mean is 180° (south) which is wrong and misleading.

The *circular mean* method is simple and straightforward. In the method, the directions are first transformed to unit vectors in the two-dimensional plane, and then vector averaged.

$$\Psi_i = \begin{pmatrix} \cos \alpha_i \\ \sin \alpha_i \end{pmatrix} \quad \rightarrow \quad \overline{\Psi_\iota} = \frac{1}{N} \sum_i \Psi_i \qquad \textbf{[1]}$$

where α represents mean of a sample, Ψ_i represents the transformed vectors and $\overline{\Psi_\iota}$ represents the mean resultant vector. Finally, $\overline{\Psi}$ is transformed using the four-quadrant inverse tangent function to find the mean angular direction $\bar{\alpha}$. For more information regarding the circular means, readers of this work are encouraged to read Berens (2009).

In addition, ice speed values were calculated using the Nansen number (Bjerkås and Gedikli, 2019) and compared with the previously reported ice speed values (Nord et al., 2018) and NSG logbook readings (not shown).

3. Results

Figures 3, 4 and 5 illustrate the distribution of wind and ice directions on NSG lighthouse where direction represents the coming direction of ice and wind, and it is counted clockwise from 0^o in the North. The black circles show the measured wind direction values on NSG, red squares show the reported ice directions (from logbook) on NSG, the black dashed line shows the circular mean values of measured wind directions on NSG, and purple plus-signs illustrates the circular mean (daily) of wind directions for Rødkallen Meteorological Station. The specific dates on the x-axis represent the observed IIV days that are available in the logbooks as in Nord et al. (2018). One common observation is that all three figures show a large variability in the resulting wind and ice directions. Figure 3 shows that ice and wind directions generally follow the same path where mean wind direction on NSG generally matches with the ice drift directions. Note that in some cases there are fewer red squares than black circles illustrating that there are fewer ice direction values. This is because the logbook is not complete i.e. where we have wind direction values but not the ice directions. Another important point is that these values represent different times of the days and they may sometimes be misleading when not read carefully. For example, the wind direction is either close to 350 degrees or around 5 degrees between March 23 and March 26, 2001, which results an arithmetic mean of 180 degrees which is incorrect and misleading. But, when the circular mean of the data is computed, the resulting values generally resemble the ice directions that are reported in the logbooks.

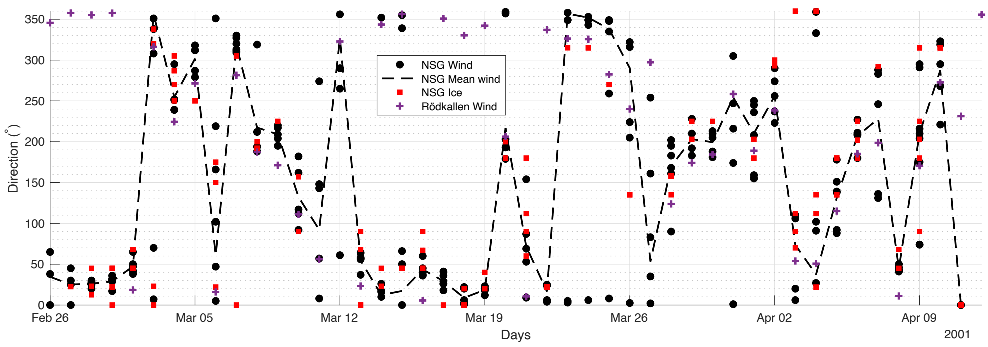

Figure 3. Measured wind and observed ice directions (logbook) for NSG and circular daily mean wind directions for Rødkallen Meteorological Station for the winter of 2001.

In addition to great variability in the wind, there is sometimes a large variability in the ice drift direction in a given day. For example, Figure 4 shows the ice direction for an April 9, 2001 event where ice is drifting in the east-west direction early in the day, then it changes its direction and moves in the south-north direction in the morning, and then drifts in the south-east direction in the night of the same day, at which point large IIVs are observed (Nord et al., 2018). In other words, although there is a large variability in the ice drift directions that align with the wind directions on NSG, large vibrations only occurred when ice moved in the South-East direction.

Figure 4. Ice drift directions at the NSG at different times on April 9, 2001.

Similar to Figure 3, Figure 5 also shows that there is a large variability both in wind and ice drift directions at NSG. One interesting observation here is that, even though there is a persistent wind direction between March 24 and March 30, 2002, the structure does not undergo resonance during these days, although they have comparable wind speeds when compared with other resonant events.

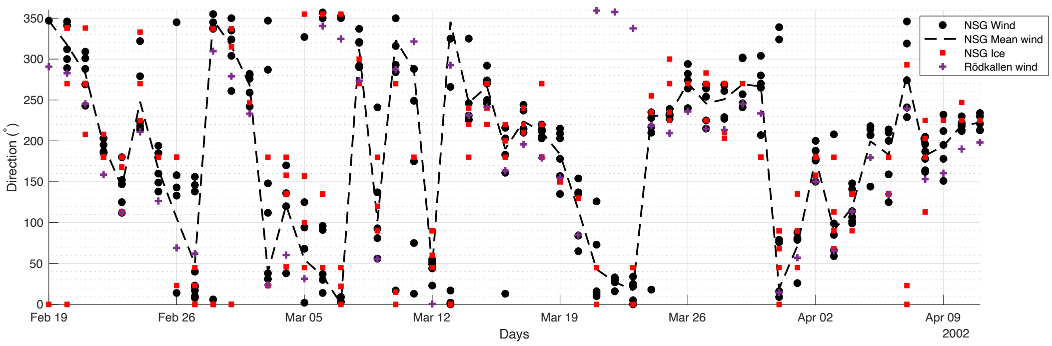

Figure 5. Measured wind and observed ice directions (logbook) for NSG and circular daily mean of wind directions for Rødkallen Meteorological Station for the winter of 2002.

Figure 6 shows the measured wind and ice directions on NSG. As one can clearly see there is less variability in the mean wind directions than the two previous years (especially in February and March), which resulted in more resonant events. One common observation in all three years is that large vibrations mostly occur when the structure is subjected to the winds in the north-south/south-north direction pairs (with some wind angle variations as described in Sec. 3.2 when determining the wind angle criterion), which forms a kind of wind channel system.

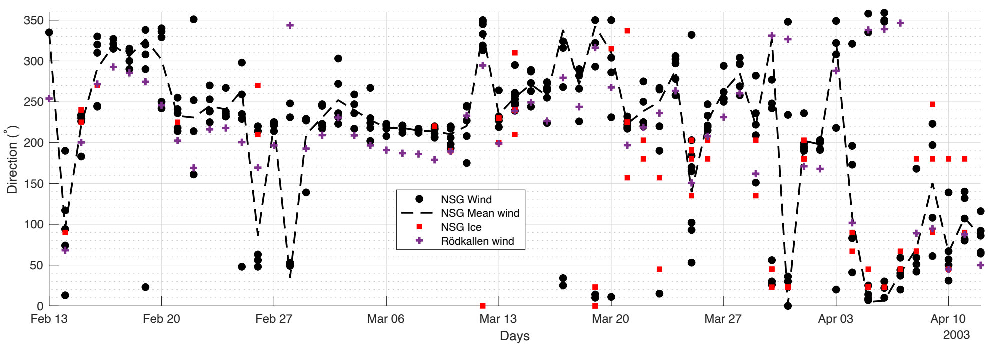

Figure 6. Measured wind and observed ice directions (logbook) for NSG and circular daily mean of wind directions for Rødkallen Meteorological Station for the winter of 2003.

In addition to the aforementioned data, the wind and ice readings also agree well with the Finnish Meteorological Institute's (FMI) reports which provide additional insights on the weather parameters. According to FMI, the ice season 2000/2001 was mild and shorter than average and "late in February the wind direction changed and the ensuing northerly winds pushed the deformed ice field out to sea, whereby a wide lead opened up along the fast ice boundary on the Finnish coast of the Bay of Bothnia" (FMI, 2020). This is also when NSG started to witness large IIVs which lasted until early April, when the weather was warmer than average and ice was thinner than usual, as mentioned in FMI report (in the Sea of Bothnia there was no ice left by the end of April). For the ice season of 2001/2002, FMI reported that the entire Bay of Bothnia was ice covered as early as January 24 in 2002, and the ice season was reported as mild. This year winter weather was variable which is also apparent in Figure 5. Finally, FMI reported that the ice conditions in winter of 2002/2003 were average when classified by the extent of the ice cover. Interestingly, this is also the year where 1) the directional wind and ice variations are lower than the previous two winter seasons as apparent in Figure 6, and 2) NSG experienced more events (Nord et al., 2018). One additional interesting observation that was reported by FMI is that weather became mild later in March and there were winds blowing from south-west which drove the ice against the Finnish coast of Gulf of Bothnia. This observation also matches with the ice and wind directions reported in NSG logbook (see Fig. 5) where a great variability in the wind directions started in late March, 2003 (in fact, NSG experienced several resonant vibration events in March 30, 2003). Later, in early April, the FMI reports that the ice in the Gulf of Bothnia drifted to the open sea changing its dominant direction from north towards south. Ervik et al. (2019) also show satellite images of the ice movement during this period which aligns with the FMI reports.

3.1 On the angles between wind and ice drift directions at NSG

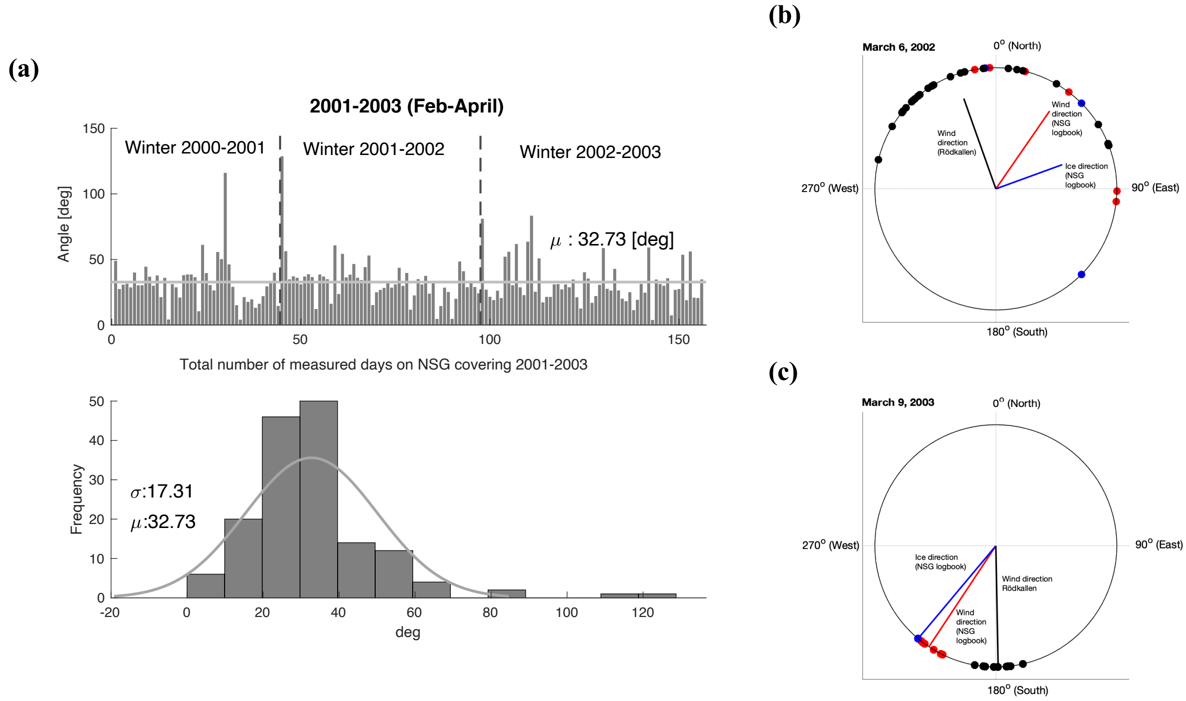

Figure 7. (a) Top image: Angle difference between NSG and Rødkallen Meteorological Station covering all winter days similar to Figures 3,5,6. Bottom image: Corresponding normal distribution of the angle difference with mean ($\boldsymbol{\mu = 32.73}$) and standard deviation ($\boldsymbol{\sigma = 17.31}$). (b-c) Wind and ice directional variations on NSG and Rødkallen on March 6, 2002 and March 9, 2003, respectively.

The circular mean method is applied to the dataset that includes wind data from Rødkallen Meteorological Station and ice and wind data from NSG logbooks. The left image in Figure 7 illustrates the wind angle variations between NSG logbooks and Rødkallen and the normal distribution of the comparison between 2001 and 2003. Figure 7b and 7c are example illustrations of daily wind - ice direction comparison at NSG for March 6, 2002 and March 9, 2003, respectively. Red and blue points illustrate the data readings from NSG logbooks, their color matching lines represent the circular mean of those values. Similarly, black points represent the wind directions measured on Rødkallen Meteorological Station and the matching black colored line represent the circular mean of the wind data. Also see that the resultant vector lengths in Figure 7b and 7c are different. This is because the circles showing the distributions represent unit circles, and within the circles the closer the quantity is to one, the more concentrated the data sample around the mean direction as described in Berens (2009).

Analysis of all data covering winter seasons between 2001-2003 show that wind directions at NSG are generally greater (in the clockwise direction) than wind directions at the Rødkallen Meteorological Station. In fact, although there are sometimes large variations between the two data sources on different days, this seems to be a trend as apparent in Figure 7a, where the mean angle difference between the two datasets is around 32 degrees. In addition, ice and wind directions at NSG are generally close to each other since both of them are taken from the NSG logbooks, however there are also some discrepancies which was illustrated earlier in Figure 4 showing that it is possible to have multiple ice drift directions in a given day.

These new insights regarding the wind and ice directions are important since some of which were completely ignored earlier in Bjerkås and Gedikli (2019). For example, 1) wind directions on Rødkallen and NSG were assumed to be very close, and 2) ice and wind directions were assumed to be highly correlated (but not all the time). Regarding the first point, we see that there is a persistent angle difference between the wind angles of NSG and Rødkallen data, and wind and ice are not highly correlated all the time. They seemed to be correlated more in mid-season where ice extent was large, but later and earlier in the season (i.e. when the Gulf of Bothnia is not fully covered), the correlation is subject to directional effects of winds.

3.2 Updated results to find intervals with probability of harsh IIV

Previously, Bjerkås and Gedikli (2019) introduced a met-ocean data based prediction method to estimate the number of days that a structure experiences harsh ice induced vibrations. In short, the method analyzes five environmental parameters for the NSG lighthouse (ice thickness, ice concentration, air temperature, ice drift speed and wind direction), and if all the parameters simultaneously exceed a threshold value or they fall into a specified range, we say that the structure is prone to IIV (or "harsh IIV" which is a term which contains both resonant events and large vibrations). In this study, we present the updated results given the aforementioned new insights on the environmental data for NSG.

Year	Feb		Mar		Apr		Total	
	OBS	EST	OBS	EST	OBS	EST	OBS	EST
2001	0	0	1	1	3	14	4	15
2002	1	0	2	12	3	18	6	30
2003	0	4	6	14	0	18	6	36

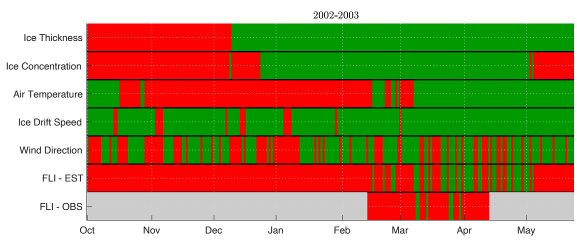

Figure 8. Left: Table showing the observed (OBS) and estimated (EST) number of days with harsh IIV at NSG, Right: Example model results for 2002-2003 where FLI stands for frequency lock-in (green color indicates that the specific criterion is met for the highlighted parameter; red color indicates that specific criterion fails for the same parameter and grey color indicates that there is no data available for that period).

We redefine the five criteria as follows: 1) Ice thickness should be greater than 0.2 m (Bjerkås and Skiple, 2005), 2) Ice drift speed should be within 0.02 – 0.08 m/s (2 day average), 3) Wind should be blowing between 350-50 degrees from the north or between 100-260 degrees from the south, 4) Air temperature should be large enough so that it makes the ice edge ductile, and 5) ice concentration should be greater than 65%.

The left table in Figure 8 illustrates the total number of days that the structure is experiencing harsh IIVs in a given month and year when the model prediction is used. This calibration test clearly shows that the model overestimates the total number of days the structure is prone to harsh IIV. This is an important result, because from an engineering perspective, it is always better to overestimate the vibrations than to underestimate them. In addition, the right image in Figure 8 illustrates the example model result for 2003. As clearly seen, it is generally the wind direction parameter that decides whether the structure is prone to harsh IIV or not. When compared with the STRICE measurements, the proposed method successfully finds the time intervals that may have high probability of IIV (years 2001, 2002 not shown because of the space limitations). This updated version of the method estimates the individual lock-in events with 70-100% accuracy over the three years of period (similar to Bjerkås and Gedikli (2019)). But the difference is that the total estimated number of the days in each year is significantly reduced increasing the overall accuracy in this updated version.

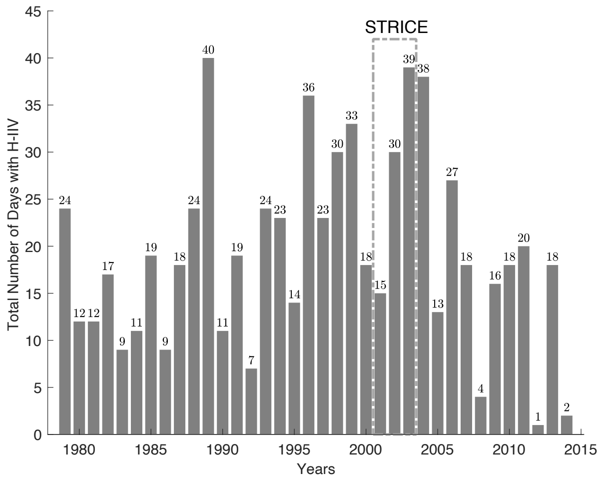

Figure 9. Total number of days with Harsh-IIV (H-IIV) between 1979 and 2015.

Figure 9 illustrates the total number of days with H-IIV predicted by the method (this can be thought of as hindcasting and forecasting since we estimate the total number of days before and after 2001-2003 period). It is important to note that the year 2003 is one of the winters where the structure experienced one of the largest number of days with H-IIV, and the results illustrated in Figure 9 also agree with this fact. Figure 9 also suggests that there is a great variability in the total number of days with a peak in 1989 with 40 days and with a single day in 2012. It seems that a typical year may include between 15 to 25 days with high probability of H-IIVs.

4. Concluding remarks

As a result of this exercise we make some unique observations and also further improve the met-ocean data based IIV prediction method using the insights obtained in this study. Some observations and results can be summarized as:

- Daily ice direction values may be highly variable in the late and early seasons, but they do not necessarily cause resonant events. This is mainly because the ice is not strong enough.
- There is a crescent type of wind profile in the northern part of Gulf of Bothnia where wind directions at NSG is around 32 degrees in the clockwise direction compared to the measurements obtained at the Rødkallen Meteorological Institution (although there are some instances where this is not true as shown in Figure 7).
- Stable strong wind speeds do not necessarily result in resonant vibrations (i.e. 24-30 March 2002).
- Ice directions are highly dependent on wind directions. This is important because field data shows discrepancies between wind and ice drift directions near the structure.
- The IIV prediction method introduced by Bjerkås and Gedikli (2019) is improved significantly with the new insights (see Fig. 8) and the following discussion.

It is important to note that these results are true for a given location, in particular the northern Gulf of Bothnia and NSG lighthouse. And it is not possible to extend this method to other locations with this version of the method, and there is still a gap between met-ocean conditions and structural responses. But, understanding the onset met-ocean conditions of IIVs is extremely important for the design of offshore structures in all ice infested regions. It is believed that the model can be improved further by including advanced geophysical models into the decision tools. Therefore, the next steps in the improvement process would be 1) development of a physical ice-drift model, 2) generalization of the criteria that are applied, 3) looking the effect of some other met-ocean parameters such as current, ice extent and strength etc. on IIV 4) calibrate the results with other datasets, 5) estimate the number of vibration cycles using a method to estimate fatigue life similar to Bjerkås et al. (2014), and 6) use reduced order modeling techniques to identify the dominant parameters that are hidden in these complex ice-structure interactions, and connect structural motions to met-ocean data which also helps improving second point (Gedikli et al., 2020, 2019; Li et al., 2020).

Acknowledgments
The authors wish to acknowledge to support to the FATICE project from the MarTERA partners, the Research Council of Norway (RCN), German Federal Ministry of Economic Affairs and Energy (BMWi), the European Union through European Union’s Horizon 2020 research and innovation programme under grant agreement No 728053-MarTERA and the support of the FATICE partners.

References

Berens, P., 2009. CircStat: A MATLAB Toolbox for Circular Statistics. J. Stat. Softw. 31, 1–21. https://doi.org/10.18637/jss.v031.i10

Bjerkås, M., Alsos, H.S., and Wåsjø, K., 2014. Estimates of the Number of Vibration Cycles From Frequency Locked-in Ice Loads. Presented at the ASME 2014 33rd International Conference on Ocean, Offshore and Arctic Engineering, American Society of Mechanical Engineers Digital Collection. https://doi.org/10.1115/OMAE2014-23134

Bjerkås, M., Gedikli, E.D., 2019. A method to find intervals with probability of ice induced vibrations, in: The International Conference on Port and Ocean Engineering under Arctic Conditions (POAC 2019). Presented at the POAC, Delft, The Netherlands.

Bjerkås, M., Skiple, A., 2005. Occurrence of Continuous and Intermittent Crushing During Ice-Structure Interaction, in: Proceedings of the International Conference on Port and Ocean Engineering Under Arctic Conditions. Presented at the 18th International Conference on Port and Ocean Engineering under Arctic Conditions (POAC’05).

Ervik, Å., Nord, T.S., Høyland, K.V., Samardzija, I., and Li, H., 2019. Ice-ridge interactions with the Norströmsgrund lighthouse: Global forces and interaction modes. Cold Reg. Sci. Technol. 158, 195–220. https://doi.org/10.1016/j.coldregions.2018.08.020

FMI, 2020. Ice season in the Baltic Sea - Finnish Meteorological Institute [WWW Document]. URL https://en.ilmatieteenlaitos.fi/ice-season-in-the-baltic-sea (accessed 9.13.20).

Gedikli, E.D., Chelidze, D., and Dahl, J., 2020. Empirical Mode Analysis Identifying Hysteresis in Vortex-Induced Vibrations of a Bending-Dominated Flexible Cylinder. Int. J. Offshore Polar Eng. 30, 186–193.

Gedikli, E.D., Nord, T.S., Hendrikse, H., and Ziemer, G., 2019. On pressure modes in ice-induced vibrations using multivariate analysis. Cold Reg. Sci. Technol. 160, 150–162. https://doi.org/10.1016/j.coldregions.2019.02.003

ISO 19906, 2019. Petroleum and natural gas industries — Arctic offshore structures. International Organization for Standardization. Geneva, Switzerland.

Jochmann, P., Schwarz, J., 2000. Ice Force Measurement at Lighthouse Norströmsgrund - Winter 1999. (LOLEIF Report). Hamburgische Schiffbau-Versuchanstalt GmbH.

Leppäranta, M., 2011. The Drift of Sea Ice, 2nd ed, Geophysical Sciences. Springer-Verlag, Berlin Heidelberg. https://doi.org/10.1007/978-3-642-04683-4

Leppäranta, M., Omstedt, A., 1990. Dynamic coupling of sea ice and water for an ice field with free boundaries. Tellus Dyn. Meteorol. Oceanogr. 42, 482–495. https://doi.org/10.3402/tellusa.v42i4.11892

Li, H., Gedikli, E.D., Lubbad, R., and Nord, T.S., 2020. Laboratory study of wave-induced ice-ice collisions using robust principal component analysis and sensor fusion. Cold Reg. Sci. Technol. 172, 103010. https://doi.org/10.1016/j.coldregions.2020.103010

Nord, T.S., Samardžija, I., Hendrikse, H., Bjerkås, M., Høyland, K.V., and Li, H., 2018. Ice-induced vibrations of the Norströmsgrund lighthouse. Cold Reg. Sci. Technol. 155, 237–251. https://doi.org/10.1016/j.coldregions.2018.08.005

OSI SAF, 2017. Global Se Ice Concentration Climate Data Record Product User Manual (Product OSI-450), Ocean and Sea Ice SAF. EUMETSAT.

SMHI, 2020. Data och analyser för väder samt Sveriges klimat och miljö | SMHI [WWW Document]. URL https://www.smhi.se/data (accessed 9.20.20).

Weiss, J., 2013. Drift, Deformation, and Fracture of Sea Ice: A Perspective Across Scales, SpringerBriefs in Earth Sciences. Springer Netherlands. https://doi.org/10.1007/978-94-007-6202-2

Yue, Q., Bi, X., 2000. Ice-Induced Jacket Structure Vibrations in Bohai Sea. J. Cold Reg. Eng. 14, 81–92. https://doi.org/10.1061/(ASCE)0887-381X(2000)14:2(81)

25th IAHR International Symposium on Ice
Trondheim, 23 - 25 November 2020

Svalbard fjord environments with land-fast sea ice as arenas for climate research, monitoring, remote sensing validation, and dedicated process studies

S. Gerland[1], D.V. Divine[1], A. Fransson[1], M.A. Granskog[1], O. Pavlova[1], M. Chierici[2], K. Høyland[3], A.M. Johansson[4], and A. Marchenko[5]

1: Norwegian Polar Institute, Fram Centre, Tromsø
2: Institute of Marine Research, Fram Centre, Tromsø, Norway
3: The Norwegian University of Science and Technology, Trondheim, Norway
4: UiT The Arctic University of Norway, Tromsø, Norway
5: The University Centre in Svalbard, Longyearbyen, Norway

gerland@npolar.no; dmitry.divine@npolar.no; agneta.fransson@npolar.no; granskog@npolar.no; olga.pavlova@npolar.no; melissa.chierici@imr.no; knut.hoyland@ntnu.no; malin.johansson@uit.no; aleksey.marchenko@unis.no

During winter and spring, parts of Svalbard fjords are covered with land-fast sea ice. The extent of fast ice areas has decreased during the last two decades, and seasons with fjord ice cover have on average become shorter. However, the different settings (e.g. size and shape of coastline, islands, connection to ocean water masses) of Svalbard fjords still give the opportunity to find fast ice with a variety of thicknesses, snow cover and physical properties. The variety of fast ice that is reasonably accessible, the fact that it is not moving and laterally relatively homogenous ("1-dimensional") gives unique opportunities for climate research, monitoring, remote sensing calibration and validation, and dedicated process studies. Here, we present examples of such studies within sea-ice physics and biogeochemistry, satellite remote sensing, and ice mechanics from three Svalbard fjords: Kongsfjorden, Storfjorden, and van Mijenfjorden. These three fjords have different settings, with different width, length and connections to the sea. Kongsfjorden and van Mijenfjorden in the west of Svalbard are more exposed to warmer water masses and have a thinner snow cover, while Storfjorden is exposed to colder water masses and has a larger amount of snow covering the fast ice. Different to Kongsfjorden and Storfjorden, van Mijenfjorden is protected by the island Akseløya at the fjord mouth restricting influence of swell, and to some extent also reducing warm Atlantic water inflow.

1. Introduction

Svalbard fjords give unique opportunities for climate research, monitoring, remote sensing calibration and validation, and controlled process studies on young and first-year sea-ice surfaces with a variety of physical properties. While many Svalbard fjords are located quite far from settlements and infrastructures, some fjords are closer or within reasonable distance to those and can be reached within a few hours by snow machine or boat. In the following we first introduce three such Svalbard fjords; Kongsfjorden, Storfjorden, and van Mijenfjorden (section 2), with focus on fjord ice. These three fjords (Fig. 1) have different settings, including different width, length, coastlines, atmospheric and oceanic conditions, and infrastructures that can be used for research. Then we briefly describe some examples of sea-ice studies and observations in those fjords (section 3). Several of the processes and changes observed have also relevance and implications for other polar regions.

Figure 1. Map of Svalbard, with the three fjord locations discussed in the text (KF for Kongsfjorden; VMF for Van Mijenfjorden; SF for Inglefieldbukta, Storfjorden).

Why a specific fjord is picked for a study can have several reasons: First one often evaluates whether the so far known conditions of a fjord fit well to a planned study. Then, especially for long-term monitoring, access conditions play an important role, as well as the local infrastructure. Some studies require presence of tidewater glaciers in a fjord, while other experiments might be interested in certain oceanic or atmosphere conditions, leading to specific timing of onset of freezing and melt, freezing and melt rates, and the desired amount of snow. Especially for interdisciplinary studies it can be important what other variables are overserved at a fjord. Since Svalbard fjords have different conditions, often one can find a fjord suitable for a planned study.

This contribution is only discussing three examples of more work happening; a full overview and review on Svalbard fjord sea-ice environments and related research infrastructures would be beyond the limitations of such an article, therefore this cannot be given here.

Other Svalbard fjords than those three detailed here, with both infrastructures and research and monitoring going on, include Isfjorden (see, e.g. Muckenhuber et al. 2016) and its side fjords with the settlements Longyearbyen (at Adventfjorden) and Barentsburg (at Grønfjorden, see, e.g. Zhuravskiy et al. 2012), as well as in the southwest of Svalbard Hornsund (see, e.g. Muckenhuber et al. 2016) with its Polish research station, and in the northeast Rijpfjorden (Wang et al. 2013; Johansson et al. 2020).

2. Three Svalbard fjords

Differences in local and regional climatic conditions across Svalbard lead to different sea-ice scenarios (see, e.g. Dahlke et al. 2020). Kongsfjorden and van Mijenfjorden in the west of

Svalbard are exposed to relatively warm Atlantic water masses. The thickness of both sea ice and snow cover here has been observed to be smaller than in Storfjorden, east of Spitsbergen (Gerland et al. 2008), which is exposed to colder Arctic water masses. These differences in the settings are also clearly visible in the ice conditions in each of the fjords. In the following, some more information on each of the three fjords is given.

Kongsfjorden

Kongsfjorden is located on the west coast of Spitsbergen, at 78° 55' N, 12° E. The fjord is hydrographically connected by the Kongsfjordenrenna to the North Atlantic, and receive warm Atlantic water masses from the West Spitsbergen Current, a main cause of the late onset of ice formation each winter. Atlantic water enters Kongsfjorden along the southern coast and mixes with meltwater and runoff water in the inner part, before it exits the fjord on the northern edge. The wide mouth of the fjord enables ocean swells from storms to reach the central part of the fjord, and this can break up the fast ice. Further details on the physical fjord system of Kongsfjorden can be found in Svendsen et al. (2002). Land-fast ice is forming during winter/spring in inner and the central part of the fjord, but in recent years this was often restricted to the innermost parts of the fjord (Pavlova et al. 2019; Gerland et al. 2020). Infrastructures can be found in Ny-Ålesund at the Ny-Ålesund Research Station (Fig. 2).

Figure 2: Ny-Ålesund Research Station and Kongsfjorden (Photo: S. Gerland).

The station has activities from institutions from many countries. Out from the Sverdrup unit of the Norwegian Polar Institute, sea ice in Kongsfjorden has been monitored since 2003 (Gerland and Renner 2007; Pavlova et al. 2019). Kongsfjorden fast ice has been the stage for numerous process studies within sea-ice physics and biogeochemistry, which are more detailed below. Ny-Ålesund can be reached by flights from Longyearbyen several times a week.

Van Mijenfjorden

Van Mijenfjorden is located on the west coast of Spitsbergen, at 77° 45' N, 16° E, and seasonal fast ice is forming during winter in its inner part, or over the entire fjord (see, e.g. Gerland and Hall 2006). As Kongsfjorden, it is exposed to Atlantic water from the West Spitsbergen Current, but for van Mijenfjorden the island Akseløya at the mouth of the fjord limits water mass exchange, it hinders swell from the ocean reaching the inner parts of the fjord, and it prevents ice from drifting out of the fjord. The (previous) coal-mining site Sveagruva was used frequently by scientists and student groups from UNIS and other institutes to perform studies in the inner fjord (Fig. 3).

Storfjorden

Storfjorden, a larger and wider fjord southeast of Spitsbergen, can be reached from Longyearbyen by snow machine. The surface water of Storfjorden is not exposed to Atlantic water as it is the case for the two other fjords. Only little infrastructure exists at Storfjorden; Norwegian Polar Institute has two light huts placed at the western shore of the fjord, giving space for personnel when monitoring fast ice in Inglefieldbukta (77° 53' N, 18° 15' E) in spring, as well as for instrumentation, consisting of an automatic weather station and an automatic camera (Fig. 4). While at Inglefieldbukta level, land-fast sea ice is common in winter and spring, other parts of Storfjorden can have ice types and features related to dynamical processes (ridging and rafting), which are more typical for pack ice environments than for (smaller) fjords. Storfjorden is also characterized in winter by a recurring polynya that forms offshore of the fast ice, with implications for ice formation and water masses (Haarpaintner et al. 2001; Skogseth et al. 2004).

Figure 3: Inner van Mijenfjorden and infrastructures from the (former) coal-mining site Sveagruva (Photo: S. Gerland).

Figure 4: Light hut with automatic weather station in Inglefieldbukta, Storfjorden (Photo: R. Krapp).

3. Examples of studies

Sea-ice-related climate research in Kongsfjorden and Storfjorden

Monitoring of the Kongsfjorden area has been carried out by the Norwegian Polar Institute systematically since 2003, and sporadic observations were made since 1997 (Gerland and Renner 2007; Pavlova et al. 2019; Gerland et al. 2020). Concept and methodology of the systematic fast-ice monitoring in Kongsfjorden are described in Gerland and Hall (2006), Gerland and Renner (2007), and Pavlova et al. (2019) and include visual sea-ice extent observations from the mountain Zeppelinfjellet (mapping) as well as *in situ* measurements of snow and ice thickness, and freeboard (Gerland and Renner 2007; Pavlova et al. 2019). The monitoring was designed to be relatively inexpensive, robust, and consistent over time. The permanent presence of staff at the Sverdrup unit and daily visits to the observatory on the mountain Zeppelinfjellet just south of Ny-Ålesund enable regular *in situ* thickness measurements and ice observations. During annual field campaigns, typically conducted in a week late April/early May when land-fast ice reaches its maximum extent, some 4-6 locations on fast ice in different parts of Kongsfjorden are visited to study the physical properties of sea ice and snow cover. In some years, the same sites were opportunistically revisited later in the melt season to measure ice thickness before the final break up of fast ice. The collected dataset demonstrated a consistent reduction of a maximum seasonal fast ice extent over the last two decades in Kongsfjorden, occurring in parallel with the ice thinning and decreasing snow thickness (Pavlova et al. 2019). The observed changes were attributed to the overall warming in the area, both oceanic and atmospheric, driving the associated shortening of the ice and on-ice snow accumulation seasons.

Kongsfjorden has also been a location for several process studies of the optical sea ice and snow properties, and snow-to-ice transformation processes (Gerland et al. 1999; Nicolaus et al. 2003; Hamre et al. 2004; Taskjelle et al. 2016; Wang et al. 2015). The proximity and infrastructures of Ny-Ålesund gives the possibility of repeated visits in order to follow snow and sea-ice changes during different stages of the seasonal development closely.

Storfjorden, without larger infrastructures, is usually visited once a year in spring for monitoring the fast ice conditions in Inglefieldbukta. A sea-ice thickness intercomparison done in winter 2006/07 (Gerland et al. 2008) showed that annual maximum fast ice thickness was in that specific winter with 90 cm larger than in Kongsfjorden (40 cm) and van Mijenfjorden (66 cm). Regional sea-ice surveys with transects across the fjord done in several years (Hendricks et al. 2011) illustrate the spatial and inter-annual variability of sea ice in Storfjorden. Substantial amounts of snow on sea ice observed in Inglefieldbukta make the site attractive for studies as a "look-alike" for sea ice north of Svalbard, where also thick snow was observed (Rösel et al. 2018).

Sea-ice related biogeochemical studies in Kongsfjorden

Various biogeochemistry studies have been conducted in Kongsfjorden over more than a decade. Sea-ice samples for biogeochemistry monitoring have been collected/analyzed since 2012 by the Norwegian Polar Institute, in collaboration with the Institute of Marine Research. Sea-ice parameters for biogeochemistry include total alkalinity (AT), total inorganic carbon (DIC), nutrients and dissolved oxygen isotopic ratio ($\delta^{18}O$). In addition, snow, frost flowers, brine and water samples have been collected and analyzed for biogeochemistry (Fransson et al. 2016). A specific study on the development of the biogeochemistry in Kongsfjorden land-fast sea ice was carried out for one month in March-April (Fransson et al. 2015). It was found that brine and frost flowers contributed to the change in sea-ice chemistry and CO_2 exchange in the air-ice-water interfaces. Within a process study back-to-back with Norwegian Polar Institute's long-term sea-ice monitoring, in spring 2008 ikaite (calcium carbonate crystals, CaCO3·6H2O) was discovered, showing that precipitation of calcium carbonate during freezing of sea ice can occur in the Arctic (Dieckmann et al. 2010). Ikaite crystals observed in sea ice, brine and frost flowers during the field studies in Svalbard fjords were largely responsible for the observed alkalinity and CO_2 changes (Fransson et al. 2015 2020). Another study on sea ice in Kongsfjorden aimed at finding out more about ion fractionation in young sea ice; Maus et al. (2011) found that the role of coupled diffusive–convective salt transport through complex pore networks is important in this context.

Validation of satellite sea-ice observations in Kongsfjorden

The long-term monitoring with *in situ* and visual observations of sea ice in Kongsfjorden (Pavlova et al. 2019) makes it a suitable study site for validating remote sensing sea-ice classification, sea-ice extent and sea ice versus open water algorithms (e.g. Negrel et al. 2018; Johansson et al. 2020). During the polar night, synthetic aperture radar (SAR) sensors are essential to monitor sea ice, and they are routinely used for sea-ice charts by e.g. the Norwegian Ice Service. ESA's Sentinel-1 satellites offers twice daily images over most areas around Svalbard, and are continuing a long record of C-band SAR satellites used for operational sea-ice monitoring e.g. ERS-1/2, Envisat ASAR and RADARSAT-2. Johansson et al. (2020) presented a record of fjord-ice area from 2002-2019 using a range of previous and current operational C-band SAR sensors starting with the ERS-1/2 and ending with the newest, Sentinel-1A/B. They used the method outlined in Cristea et al. (2020) as it is transferable between different SAR sensors and therefore can produce a consistent fjord-ice record essential for long-term climate studies (Eisenman et al. 2014). Furthermore, Johansson et al. (2020) compared SAR-based Kongsfjorden ice extent estimates with near-coincident visual observations from the mountain Zeppelinfjellet (see above; Pavlova et al. 2019) for a 5-year period, 2014-2018. The visual observations represent manually registered ice edges based on known reference landmarks. The two different records showed good agreement (R=0.7), where some differences between the two records were attributed to the time laps between the observations and the satellite passage and the associated ice drift in and out of the fjord. The largest discrepancies between the two area estimate data records were found when observing newly formed sea ice, as the SAR sensor typically observes a lower radar energy return from this ice type making separation from open water areas difficult, especially under conditions with little wind. In general, Johansson et al. (2020) results from 2002-2019 have confirmed the observation of a trend towards a reduced surface areal coverage, shorter ice seasons and later seasonal sea-ice formation than at the start of the century. A study by Muckenhuber et al. (2016) showed similar result for the fjord ice in the Svalbard fjords Isfjorden and Hornsund for 2000-2014.

Ice mechanical studies in van Mijenfjorden
The stable ice cover in van Mijenfjorden, the relative easy access from Longyearbyen and the Sveagruva settlement have made it a good place to study *in situ* thermo-mechanical properties of ridges and level ice. Numerous studies have been carried out by UNIS students and employees. Both the thermo-mechanical properties and the processes in ridges, level ice and coastal ice were studied. Ridge consolidation was first studied in natural ridges (Høyland 2002), and later in medium-scale man-made ridges (Liferov and Høyland 2004; Salganik et al. in press). Level ice thickness, growth and salinity were studied by Høyland (2009). The coastal ice is different from the free-floating ice as it hangs on the coast so that it bends and is partly flooded due to tidal processes. This induces stresses in the ice, makes it thicker and more saline that the free-floating level ice (Caline 2010; Blæsterdalen et al. 2016; Wrangborg et al. 2016). Similar processes influence ice loads on the coal quay in Kapp Amsterdam (Løset and Marchenko 2008; Marchenko 2018). *In situ* or field measurements of ice mechanical properties need to be combined with measurements of essential physical properties, at least temperature, salinity and density, so that gas and brine fractions can be estimated. This was started by Moslet (2007), who did uni-axial compressive tests and examined how it varies with gas and brine fractions. Beam tests, both with free and fixed ends, were carried out to study flexural, compressive, tensile and indentation strengths of the entire ice cover (Chistyakov et al. 2016; Marchenko et al. 2018; Karulina et al. 2019). A larger hydraulic setup has also allowed for compression of the full ice cover, but only up level ice thicknesses of about 80 cm. The large-scale test setup was used to investigate acoustic emission caused by ice failure (Lishman et al. 2020) and the influence of ice compression on its permeability by seawater (Renshaw et al. 2018). *In situ* fracture tests of the full ice thickness were carried out while carefully measuring the applied forces and the displacement field around the crack tip (Lu et al. 2015, 2019). Finally, also medium-scale ice structure interaction tests were carried out (Moslet 2008).

Acknowledgments
We are grateful for support by Norwegian Polar Institute staff at the Sverdrup unit of Ny-Ålesund Research Station and in Longyearbyen, and for the support from logistics staff at UNIS. We thank Anders Skoglund, Norwegian Polar Institute, for help with preparing the map, and Rupert Krapp, Norwegian Polar Institute, for providing the photo from Inglefieldbukta. This work was supported in parts by the Research Council of Norway (RCN) through "Centre for Integrated Remote Sensing and Forecasting for Arctic Operations" (CIRFA, RCN project 237906), and the project "Oil spill and newly formed sea-ice detection, characterization, and mapping in the Barents Sea using remote sensing by SAR" (OIBSAR) (RCN project 280616), by the projects "ALSIM" and "Mapping Sea Ice" (Fram Centre flagships "Arctic Ocean" and "Fjords and Coasts", respectively) and by Norwegian Polar Institute's long-term monitoring of Svalbard sea ice in the institute's Svalbard programme. The biogeochemical studies of sea ice in Svalbard fjords were funded by the Fram Centre flagship "Ocean acidification and ecosystem effects in Northern waters".

References

Cristea, A., Van Houtte, J., and Doulgeris, A.P., 2020. Integrating Incidence Angle Dependencies into the Clustering-Based Segmentation of SAR Images. IEEE Journal of Selected Topics in Applied Earth Observations and Remote Sensing. doi: 10.1109/JSTARS.2020.2993067.

Blæsterdalen, B., Wrangborg, D., Marchenko, A., and Høyland, K.V., 2016. Geometry and Thermo-Mechanical Properties of Coastal Ice in a Micro-Tidal Climate in Svalbard, Part I, Permeability and Geometry. Proc. 23rd IAHR Symposium on Ice, Ann Arbor, USA, paper #4878716.

Caline, F., 2010. Coastal-sea-ice action on a breakwater in a microtidal inlet in Svalbard. PhD thesis, NTNU, 978-82-471-2440-6(print)/978-82-471-2441-3 (elec), 263 p.

Chistyakov, P., Karulin, E., Marchenko, A., Sakharov, A., and Lishman, B., 2016. The tensile strength of saline and freshwater ice in field tests. Proc. 23rd IAHR Symposium on Ice, Ann Arbor, USA, paper #4872921.

Dahlke, S., Hughes, N.E., Wagner, P.M., Gerland, S., Wawrzyniak, T., Ivanov, B., and Maturilli, M., 2020. The observed recent surface air temperature development across Svalbard and concurring footprints in local sea ice cover. International Journal of Climatology, 40, 5246–5265. doi: 10.1002/joc.6517.

Dieckmann, G.S., Nehrke, G., Uhlig, C., Göttlicher, J., Gerland, S., Granskog, M.A., and Thomas, D.N., 2010. Ikaite (CaCO3*6H2O) discovered in Arctic sea ice. Brief communication, The Cryosphere, 4, 153-161.

Eisenman, I., Meier, W., and Norris, J., 2014. A spurious jump in the satellite record: has Antarctic sea ice expansion been overestimated? The Cryosphere, 8, 1289–1296. doi: 10.5194/tc-8-1289-2014.

Fransson, A., Chierici, M., Abrahamsson, K., Andersson, M., Granfors, A., Gårdfeldt, K., Torstensson, A., and Wulff, A., 2015. CO_2-system development in young sea ice and CO_2-gas exchange at the ice/air interface mediated by brine and frost flowers in Kongsfjorden, Spitsbergen. Annals of Glaciology, 56(69), 245-257. doi: 10.3189/2015AoG69A563.

Fransson, A., Chierici, M., Hop, H., Findlay, H., Kristiansen, S., and Wold, A., 2016. Late winter-to-summer change in ocean acidification state in Kongsfjorden, with implications for calcifying organisms. Polar Biology. doi: 10.1007/s00300-016-1955-5.

Fransson, A., Chierici, M., Nomura, D., Granskog, M.A., Kristiansen, S., Martma, T., and Nehrke, G., 2020. Influence of glacial water and carbonate minerals on wintertime sea-ice biogeochemistry and the CO_2 system in an Arctic fjord in Svalbard. Annals of Glaciology. doi: 10.1017/aog.2020.52.

Gerland, S., Gascard, J.-C., Ivanov, B., Nielsen, C.-P., Nilsen, F., Pavlova, O., Leu, E., Tverberg, V., and Barrault, S., 2008. Fast ice evolution in Kongsfjorden compared with other Svalbard fjords. Extended abstract. Proc. NySMAC Seminar: Ny-Ålesund and IPY, Cambridge, U.K. Polarnet, NRC, Italy, 44-46.

Gerland, S., and Hall, R., 2006. Variability of fast-ice thickness in Spitsbergen fjords. Annals of Glaciology, 44, 231-239.

Gerland, S., Pavlova, O., Divine, D., Negrel, J., Dahlke, S., Johansson, A.M., Maturilli, M., and Semmling, M., 2020. Long-term monitoring of landfast sea ice extent and thickness in Kongsfjorden, and related applications (FastIce). In: Van den Heuvel et al. (eds.): SESS report 2019, Svalbard Integrated Arctic Earth Observing System, Longyearbyen, Chapter 6, 160-167.

Gerland, S., and Renner, A.H.H., 2007. Sea ice mass balance in an Arctic fjord. Annals of Glaciology, 46, 435-442.

Gerland, S., Winther, J.-G., Ørbæk, J.B., and Ivanov, B., 1999. Physical properties, spectral reflectance and thickness development of first year fast-ice in Kongsfjorden, Svalbard. Polar Research, 18(2), 275-282.

Haarpaintner, J., Gascard, J.-C., and Haugan, P.M., 2001. Ice production and brine formation in Storfjorden, Svalbard. Annals of Glaciology, 33, 430-436.

Hamre, B., Winther, J.-G., Gerland, S., Stamnes, J.J., and Stamnes, K., 2004. Modeled and measured optical transmittance of snow-covered first-year sea ice in Kongsfjorden, Svalbard. Journal of Geophysical Research, 109, C10006. doi: 10.1029/2003JC001926.

Hendricks, S., Gerland, S., Smedsrud, L.H., Haas, C., Pfaffhuber, A.A., and Nilsen, F., 2011. Sea ice thickness variability in Storfjorden, Svalbard archipelago. Annals of Glaciology, 57(52), 61-68.

Høyland, K.V., 2002. Consolidation of first-year sea ice ridges. Journal of Geophysical Research, 107, C6, 15,1-15,15. doi: 10.1029/2000JC000526.

Høyland, K.V., 2009. Ice thickness, growth and salinity in van Mijenfjorden on Svalbard, Norway. Polar Research, 28, 339-352.

Johansson, A.M., Malnes, E., Gerland, S., Cristea, A., Doulgeris, A.P., Divine, D.V., Pavlova, O., and Lauknes, T.R., 2020. Consistent ice and open water classification combining historical synthetic aperture radar satellite images from ERS-1/2, Envisat ASAR, RADARSAT-2, and Sentinel-1A/B. Annals of Glaciology. doi: 10.1017/aog.2019.52.

Karulina, M., Marchenko, A., Karulin, E., Sodhi, D., Sakharov, A., and Chitsyakov, P., 2019. Full-scale flexural strength of sea ice and freshwater ice in Spitsbergen Fjords and North-West Barents Sea. Applied Ocean Research, 90, 101853.

Liferov, P., and Høyland, K.V., 2004. In-situ ice ridge scour tests: Experimental set up and basic results. Cold Regions Science and Technology, 40, 97-110.

Lishman, B., Marchenko, A., Sammonds, P., and Murdza, A., 2020. Acoustic emissions from in situ compression and indentation experiments on sea ice. Cold Regions Science and Technology, 172, 102987.

Lu, W., Løset, S., Shestov, A., and Lubbad, R., 2015. Design of a field test for measuring the fracture toughness of sea ice. Proc. International Conference on Port and Ocean Engineering under Arctic Conditions, Trondheim, Norway.

Lu, W., Shestov, A., Løset, S., Salganik, E., and Høyland, K.V., 2019. Medium-scale Consolidation of Artificial Ice Ridge–Part II: Fracture Properties Investigation by a Splitting Test. Proc. International Conference on Port and Ocean Engineering under Arctic Conditions, Delft, The Netherlands.

Løset, S., and Marchenko, A., 2009. Field Studies and Numerical Simulations of Ice Bustles on Vertical Piles. Cold Regions Science and Technology, 58, 15-28.

Marchenko, A., 2018. Thermo-mechanical loads of confined sea ice on structures. Philosophical Transactions of the Royal Society, A 376, 20170341.

Marchenko, A., Karulin, E., Karulina, M., Sakharov, A., Chistyakov, P., Sodhi, D., and Sliusarenko, A., 2018. Scale effects in compressive strength of sea ice. Proc. 24th IAHR Symposium on Ice, Vladivostok, paper #18-004.

Maus, S.,1 Müller, S., Büttner, J., Brütsch, S., Huthwelker, T., Schwikowski, M., Enzmann, F., and Vähätolo, A., 2011. Ion fractionation in young sea ice from Kongsfjorden, Svalbard. Annals of Glaciology, 52(57), 301-310.

Moslet, P.O., 2007. Field testing of uniaxial compression strength of columnar sea ice. Cold Regions Science and Technology, 48(1), 1-14.

Moslet, P.O., 2008. Medium scale ice-structure interaction. Cold Regions Science and Technology, 54(2), 143-152.

Muckenhuber, S., Nilsen, F., Korosov, A., and Sandven, S. 2016. Sea ice cover in Isfjorden and Hornsund, Svalbard (2000–2014) from remote sensing data. The Cryosphere, 10, 149–158. doi: 10.5194/tc-10-149-2016.

Negrel, J., Gerland, S., Doulgeris, A., Lauknes, T., and Rouyet L., 2018. On the potential of hand-held GPS tracking of fjord ice features for remote sensing validation. Annals of Glaciology, 59(76 part 2), 173–180. doi: 10.1017/aog.2017.35.

Nicolaus, M., Haas, C., and Bareiss, J., 2003. Observations of superimposed ice formation at melt-onset on fast ice on Kongsfjorden, Svalbard. Physics and Chemistry of the Earth, 28, 1241–1248.

Pavlova, O., Gerland, S., and Hop, H., 2019. Changes in sea-ice extent and thickness in Kongsfjorden, Svalbard (2003–2016). In Hop, H. and Wiencke, C. (eds.), The Ecosystem of Kongsfjorden, Svalbard. Advances in Polar Ecology. Springer Verlag, 105–136. doi: 10.1007/978-3-319-46425-1.

Renshaw, C.E., Marchenko, A., Schulson, E.M., and Karulin, E., 2018. Effect of compressive loading on first-year sea-ice permeability. Journal of Glaciology, 64(245), 443-449.

Rösel, A., Itkin, P., King, J., Divine, D., Wang, C., Granskog, M.A., Krumpen, T., and Gerland, S., 2018. Thin sea ice, thick snow, and widespread negative freeboard observed during N-ICE2015 north of Svalbard. Journal of Geophysical Research: Oceans, 123, 1156-1176. doi: 10.1002/2017JC012865.

Salganik, E., Shestov, A., and Høyland, K.V., in press. Medium-scale experiment in consolidation of an artificial sea ice ridge in Van Mijenfjorden, Spitsbergen. Cold Regions Science and Technology. doi: 10.1016/j.coldregions.2020.103194.

Skogseth, R., Haugan, P.M., and Haarpaintner, J., 2004. Ice and brine production in Storfjorden from four winters of satellite and in situ observations and modeling. Journal of Geophysical Research, 109, C10008, doi:10.1029/2004JC002384.

Svendsen, H., Beszczynska-Møller, A., Hagen, J.O., Lefauconnier, B.,Tverberg, V., Gerland, S., Ørbæk, J.B., Bischof, K., Papucci, C., Zajaczkowski, M., Azzolini, R., Bruland, O., Wiencke, C., Winther, J-G., and Dallmann, W., 2002. The physical environment of Kongsfjorden-Krossfjorden, an Arctic fjord system in Svalbard. Polar Research, 21(1), 133-166.

Taskjelle, T., Hudson, S.R., Granskog, M.A., Nicolaus, M., Lei, R., Gerland, S., Stamnes, J.J., and Hamre, B., 2016. Spectral albedo and transmittance of thin young Arctic sea ice. Journal of Geophysical Research: Oceans, 121, 540–553. doi: 10.1002/2015JC011254.

Wang, C., Cheng, B., Wang, K., Gerland, S., and Pavlova, O., 2015. Modelling snow ice and superimposed ice formation on landfast sea ice in Kongsfjorden, Svalbard. Polar Research, 34, 20828. doi: 10.3402/polar.v34.20828.

Wang, C., Shi, L., Gerland, S., Granskog, M.A., Renner, A.H.H., Li, Z., Hansen, E., and Martma, T., 2013. Spring sea ice evolution in Rijpfjorden (80°N), Svalbard, from in situ measurements and Ice Mass Balance Buoy (IMB) data. Annals of Glaciology, 54(62), 253-260.

Wrangborg, D., Vindegg, C.M., Marchenko, A., Blæsterdalen, B., and Høyland, K.V., 2016. Geometry and Thermo-Mechanical Properties of Coastal Ice in a Micro-Tidal Climate in Svalbard, Part II, In-situ stresses. Proc. 23rd IAHR Symposium on Ice, Ann Arbor, USA, paper #4878739.

Zhuravskiy, D., Ivanov, B. and Pavlov, A. 2012. Ice conditions at Gronfjorden Bay, Svalbard, from 1974 to 2008. Polar Geography, 35(2). doi: 10.1080/1088937X.2012.662535.

25th IAHR International Symposium on Ice
Trondheim, 23 - 25 November 2020

Unsupervised Information Selection In Multimodal Sea Ice Remote Sensing

Eduard Khachatrian, Saloua Chlaily, Torbjørn Eltoft, Andrea Marinoni
Dept. of Physics and Technology, UiT the Arctic University of Norway,
NO-9037, Tromsø, Norway
E-mail: {eduard.khachatrian, saloua.chlaily, torbjorn.eltoft, andrea.marinoni}@uit.no

In the new millennium, sea ice research has become a hot topic in the Earth observation disciplines, due to its importance for the climate and polar ecosystem. At the same time, it strongly affects a vast amount of anthropogenic activities, including shipping and navigation, oil and gas industry, fisheries, tourism and lifestyle of the indigenous population of Arctic. Therefore, sea ice monitoring becomes a key interest in protecting the Arctic and ensuring safe and efficient activities and polar navigation.

Currently, the most commonly used source of information about sea ice is remote sensing data, especially obtained from synthetic aperture radar (SAR), due to its independence of weather conditions. Nevertheless, sea ice can be monitored by various sensors, using different spectral, temporal, or spatial resolutions. Advanced characterization of sea ice can be achieved by combining relevant information from different sensors in order to obtain useful details about various aspects of sea ice properties. However, it is also true that the additional information may be redundant, corrupted, or unnecessary for the given task, hence increasing the computational complexity of the analysis framework. Thus, we propose a new method to select relevant information from multimodal remote sensing datasets.

Compared to existing dimensionality reduction methods, our algorithm has several fundamental advantages: 1 – It is unsupervised, which means that it is application-independent. 2 – It can be applied to several types of data, at different levels of data fusion. 3 – Since it is applied patch-wise, it emphasizes the particularity and diversity of homogeneous regions. 4 – It exploits a new reversible representation of data that enables a powerful separability without loss of physical meaning. 5 – It employs two similarity measures that account for local and global particularities of the dataset and in turn improves the accuracy of sea ice classification.

1. Introduction

Sea ice research has become one of the key areas in Earth observation disciplines, due to its fluctuations in the last few decades. It plays an essential role in the polar environment and climate, however, it also affects anthropogenic activities, such as shipping or oil and gas industry, therefore, information about sea ice conditions is extremely important for many countries and companies that operate in the Arctic (Funder et al., 2010).

Currently, the universal source of information about sea ice is remote sensing data, especially synthetic aperture radar (SAR), due to its independence of atmospheric conditions (clouds, daylight), which is particularly significant when operating in polar regions. It is challenging to interpret remote sensing data and usually requires expert's knowledge; however, it is necessary to have an automatic sea ice analysis method to conduct operational monitoring on a global scale (Sandven et al., 2006).

Multimodal remote sensing refers to the use of various sensors of similar or several types, using different spectral, temporal, or spatial resolutions. The information provided by multiple sensors reflects on different aspects of the area of interest, thus, combining information from multiple datasets is mandatory to achieve the best characterization for the region of interest (Dalla Mura et al., 2015). However, not all the complementary information is relevant, it can be redundant, corrupted or simply unnecessary for the particular task. Consequently, the use of these data can significantly deteriorate the performance of the algorithm in terms of accuracy and time complexity. Thus, the selection of relevant information is a crucial step in multimodal data fusion (Longbotham et al., 2012).

Information selection can be performed using dimensionality reduction methods, such as feature extraction (or transformation) and feature selection (Theodoridis et al., 2008). Feature extraction consists of projecting the data into a lower-dimensional space, while feature selection picks a relevant subset of features according to specific criteria. In contrast to feature selection, feature extraction increases the separability of the features but at the expense of data interpretability, which is essential in remote sensing analysis.

The aforementioned methods can be divided into two approaches, supervised (require training labels) and unsupervised. In the sea ice case, there are limited training sets, therefore, supervised methods can be hardly used to conduct an accurate performance.

In this paper, we introduced an unsupervised, flexible, accurate, and efficient method for attribute selection. It retains the main benefits of feature extraction and feature selection algorithms (increasing the separability and preserving the physical interpretability of original feature set). The fundamental advantages of the proposed method which fully distinguish it from the existing ones are:

1. *Unsupervision*: it does not require any primary information about the data, which makes it application-independent.

2. *Flexibility*: it is adequate for several types of data and valid at different levels of data fusion, data-level, and feature level.

3. *Accuracy*: it employs two similarity measures that account for global and local particularities of the original dataset.

4. *Efficiency*: the method is performed patch-wise, therefore it selects the relevant features for each patch.

The rest of this paper is organized as follows: Section 2 demonstrates details of the proposed method. Section 3 represents the experimental results of our method on sea ice dataset. Finally, the conclusion is presented in Section 4.

For notational convenience, random scalars are denoted by lower case letters, e.g., z. Random vectors are designated by bold lower case letters, e.g., $\mathbf{z}$. Bold upper case letters refer to matrices, e.g., $\mathbf{A}$. $|\mathbf{A}|$ denotes the determinant of the matrix $\mathbf{A}$. diag$\{d_1, \ldots, d_N\}$ refers to a diagonal matrix whose diagonal elements are $d_1, \ldots, d_N$ starting from upper left. The ddiag ($\mathbf{A}$) operator set to zero the off-diagonal entries of $\mathbf{A}$.

2. Method

We propose to implement the attribute selection on the superpixel level, i.e., homogeneous patches, to preserve the particularity of each patch. This superpixels of an image can be obtained using different segmentation methods. In our work, we use the Watershed superpixel segmentation algorithm (Neubert et al., 2014, Beucher, 1992).

Let M be the number of available images, including bands and polarizations, and L the number of superpixels in each image. We denote by $\mathbf{X} = (x_{lk})_{lk} \in \mathbb{R}^{L\times K}$ the matrix of attributes (bands, polarizations, extracted features, etc.). Where K is the total number of attributes. At data-level fusion $K = M$. We denote the k-th column of $\mathbf{X}$, that corresponds to the k-th attribute by x_{*k}, $\mathbf{X} = [\mathrm{x}_{*1}, \ldots, \mathrm{x}_{*K}]$. Analogously, we denote the l-th row of $\mathbf{X}$, that details the values of attributes at the l-th superpixel, by x_{l*}., $\mathbf{X} = [\mathrm{x}_{1*}^T, \ldots, \mathrm{x}_{L*}^T]^{\mathrm{T}}$.

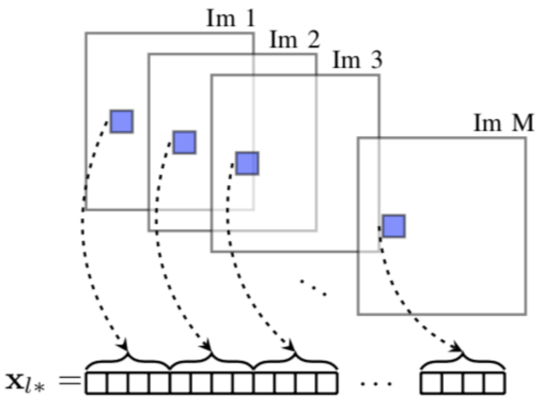

Figure 1. The attributes of the l-th pixel are stacked in one vector x_{l*}

The main goal of this paper is to find, for a given superpixel l, the smallest subset of attributes, $\{x_{l1}, \ldots, x_{lK}\}$, that preserves the structure and information content of the original set. We perform such selection at a local scale and global scale, in order to maintain the particularity of each superpixel, while accounting for the global content of the scene.

In the proposed method we use two similarity measures: Gaussian kernel (GK) and Mututal information (MI). GK used at the local level selection and preserves the structure of the attributes set. MI is performed image-wise and maintains the global information content of the attribute set. To increase the relevance of the selected attributes (improve accuracy), we propose to use both similarity measures.

The K attributes compose the vertices of the graph $G_l(V_l, E_l)$, and to the k-th vertex we assign the vector x_{*k}. However, instead of a single edge, we use two edges to connect vertices, as shown in **Figure 2**. Gaussian kernel determines the weight of one edge and it is introduced as follows:

$$\omega_{lig}^{GK} = \exp\left(-\frac{(x_{li}-x_{lj})^2}{2\sigma}\right), \quad \textbf{[1]}$$

where σ controls the width of the neighborhood in the graph, i.e., the number of connected vertices. The width of the neighborhood increases with σ. In this work, we set σ to 1. Due to the fact that the Gaussian kernel is applied at the local level, the weights are particular to each superpixel.

The weight of the second edge connecting two attributes, k_1 and k_2, is defined using mutual information,

$$\omega_{k_1k_2}^{MI} = I\left(\mathrm{x}_{*k_1}, \mathrm{x}_{*k_2}\right) = \sum_{i=1}^{L}\sum_{j=1}^{L} P\left(x_{ik_1}, x_{jk_2}\right)\log\left(\frac{P(x_{ik_1}, x_{jk_2})}{P((x_{ik_1})P(x_{jk_2}))}\right), \quad \textbf{[2]}$$

where P (x_i, x_j) is the joint density function of x_i and x_j, and P(x_i) and P(x_j) are the marginals. Mutual information quantifies the shared information between two random variables (Vergara et al., 2014). Mutual information is applied image-wise, therefore, the weights are the same for all superpixels.

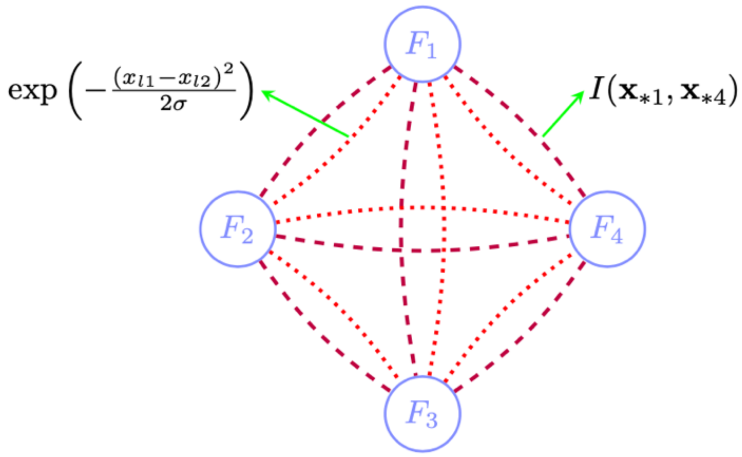

Figure 2. Graph of four attributes with two similarity functions at the l-th pixel.

The graph G_l can be represented and analyzed by a symmetric semi-definite matrix $\boldsymbol{L}$, known as the Graph Laplacian matrix. $\boldsymbol{L}$ can be defined in multiple ways. In this work, we use the symmetric normalized Laplacian (Ng et al., 2001).

To select the relevant subset of features based on both measures, we would like to partition the graph G_l into subgraphs, such that two vertices of the same subgraph have strong connections via both links. Two vertices from different subgraphs show at least one weak connection, either GK or MI.

To this aim, we associate two graph Laplacians with the graph G_l, one based on gaussian kernel metric, $\boldsymbol{L}_l^{GK}$ defined by equation **[1]**, while the other one is based on mutual information, $\boldsymbol{L}^{MI}$ defined by equation **[2]**. Each of the similarities carries different unique information, therefore, in order to apply them in the same space simultaneously and to increase the separability of the data, we map them to another common space by using joint eigen decomposition. We embed the original set of attributes into a lower-dimensional manifold using the *joint* null eigenvectors of $\boldsymbol{L}_l^{GK}$ and $\boldsymbol{L}^{MI}$. Then, we perform the clustering on the new Manifold using k-means. Finally, the centroids of the clusters will form the set of selected attributes.

The joint eigenvectors of the graph Laplacians, $\boldsymbol{L}_l^{GK}$ and $\boldsymbol{L}^{MI}$, are defined such as,

$$\boldsymbol{L}_l^{GK} = \mathbf{V}_l \boldsymbol{\Lambda}_l^{GK} \mathbf{V}_l^T , \qquad \textbf{[3]}$$

$$\boldsymbol{L}^{MI} = \mathbf{V}_l \boldsymbol{\Lambda}_l^{MI} \mathbf{V}_l^T , \qquad \textbf{[4]}$$

Where $\boldsymbol{\Lambda}_l^{GK} = \text{diag}\,(\lambda_{l1}^{GK}, \ldots, \lambda_{lK}^{GK})$, $\boldsymbol{\Lambda}_l^{MI} = \text{diag}\,(\lambda_{l1}^{MI}, \ldots, \lambda_{lK}^{MI})$, are diagonal matrices of the corresponding eignevalues, and $\mathbf{V}_l$ is the matrix of eigenvectors. $\mathbf{V}_l$ can be determined us- ing joint diagonalization (JD) algorithms, which minimize a criteria of diagonality of $\mathbf{V}_l^T \boldsymbol{L}_l^{GK} \mathbf{V}_l$ and $\mathbf{V}_l^T \boldsymbol{L}^{MI} \mathbf{V}_l$. Different diagonalization constraints and distances can be used leading to a multitude of algorithms. In this work, we perform the joint diagonalization using the Quasi-Newton algorithm (Ablin et al., 2018), which minimizes the log-likelihood measure (D.-T. Pham et al., 2001),

$$\mathcal{L}(\mathbf{V}) = \frac{1}{4}\left(\log\frac{|\text{ddiag}(\mathbf{V}_l^T \boldsymbol{L}_l^{GK} \mathbf{V}_l)|}{|\mathbf{V}_l^T \boldsymbol{L}_l^{GK} \mathbf{V}_l|} + \log\frac{|\text{ddiag}(\mathbf{V}_l^T \boldsymbol{L}^{MI} \mathbf{V}_l)|}{|\mathbf{V}_l^T \boldsymbol{L}^{MI} \mathbf{V}_l|}\right). \qquad \textbf{[5]}$$

In comparison to other methods that use two similarities, we apply them simultaneously. We strongly believe that mutual use of both similarities allows selecting the most relevant attributes, due to the fact that they preserve global and local information about the data. Throughout the next sections, we refer to our method as GKMI.

3. Experimental Results

To evaluate the performance of the proposed attribute selection method we used a multisensor dataset acquired from two satellite platforms: Radarsat-2 (SAR) and Landsat-8 (optical). The datasets were resampled to the same resolution, geolocated and labeled by Centre for Integrated Remote Sensing and Forecasting for Arctic Operations (CIRFA). **Figure 3** illustrates the overlapping area of SAR and optical data along with the example of superpixel segmentation, where yellow lines indicate the superpixel boundaries.

Along with original attributes (optical bands and SAR polarizations), we extracted Gray-Level Co-Occurrence Matrix (GLCM) textural features for each of the attribute (Haralick et al., 1973; Kandaswamy et al., 2005; Albregtsen, 1974). **Table 1** illustrates the extracted features as well as their mathematical definitions. Specifically, $g_{i,j}$ denotes the element of the GLCM matrix **G**. Q is the number of gray levels used, and $\mu = \sum_{i=0}^{Q-1}\sum_{j=0}^{Q-1} i g_{ig}$ and $\sigma^2 = \sum_{i=0}^{Q-1}\sum_{j=0}^{Q-1}(i -$

$\mu)g_{i,g}^2$ are, respectively, the GLCM mean and variance. ASM refers to angular second momentum. Finally, the dataset consists of 91 attributes (14 SAR and 77 optical).

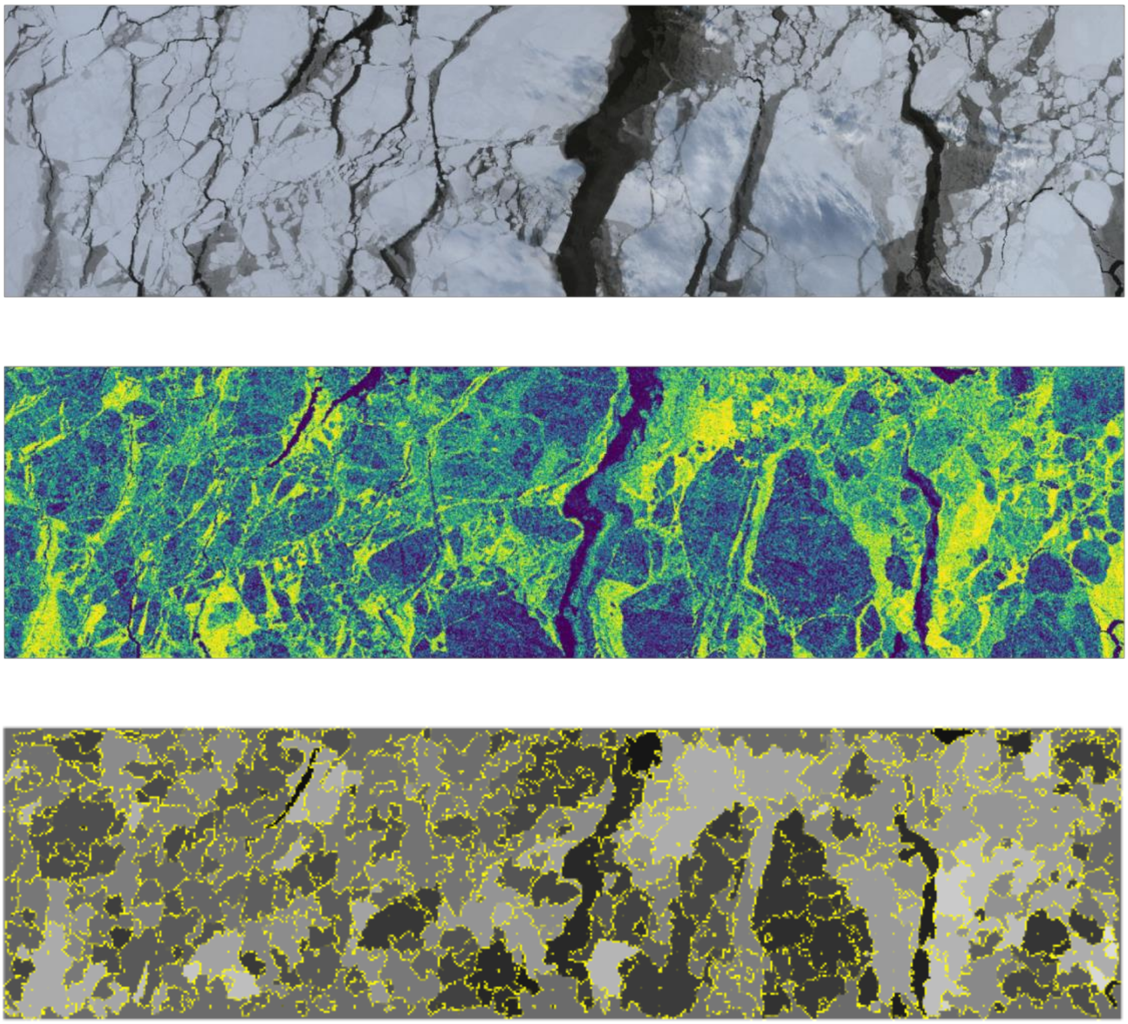

Figure 3. Overlapping area of multisensor dataset. **Top**: Natural color composite (RGB) of Landsat-8. **Middle**: HH polarisation of Radarsat-2. **Bottom**: HH polarization after superpixel segmentation.

Table 1. GLCM Texture Features.

Features	Definition	Features	Definition
Contrast	$\sum_{i,j=0}^{Q-1} g_{i,j}\,(i-j)$	ASM	$\sum_{i,j=0}^{Q-1} g_{i,j}^2$
Dissimilarity	$\sum_{i,j=0}^{Q-1} g_{i,j}\,\lvert i-j\rvert$	Energy	$\sqrt{ASM}$
Homogeneity	$\sum_{i,j=0}^{Q-1} \frac{g_{i,j}}{1+(i-j)^2}$	Correlation	$\sum_{i,j=0}^{Q-1} g_{i,j}\left[\frac{(i-\mu_i)(i-\mu_j)}{\sigma_i\sigma_j}\right]$

Dimensionality reduction methods can be implemented as a preprocessing step of several remote sensing applications, in our case we use it to improve classification accuracy. For the experiment, we randomly choose 20% of the samples from each label as the training set, while remaining 80% are used as test set. To estimate the accuracy of our algorithm, we use two commonly applied classifiers, support vector machine (SVM) and random forest (RF).
SVM is a classification method that determines a set of hyperplanes that separate the dataset into different classes (Gunn, 1998; Theodoridis et al., 2008). To perform a non-linear classification, we choose as a kernel the radial basis function (RBF).
Random Forest generates an ensemble of individual decision trees and combines their outputs to get an accurate prediction of the class (Liaw et al., 2001). In other words, RF is a classifier consisting of a collection of tree-structured classifiers.

Two main parameters of the proposed method that can potentially affect the classification performance are the number/size of superpixels and the number of selected attributes.
Figure 4 shows the overall accuracy (OA) as a function of the number of selected attributes for both classifiers. It is clear that using the whole attributes set does not lead to the best accuracy, moreover, maximum classification accuracy achieved with less than half of the original attribute set. However, the optimal number of attributes, after which there was no significant increase in accuracy, was reached even earlier with 20 attributes.

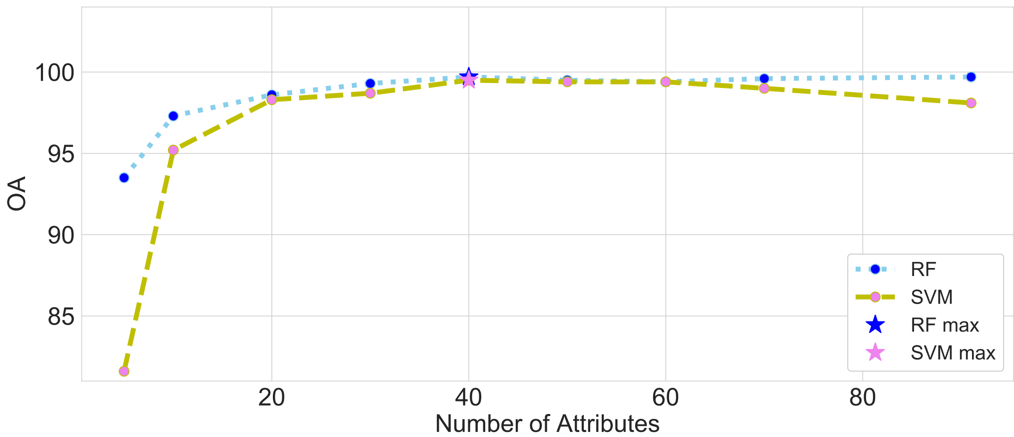

Figure 4. Overall accuracies of GKMI over a different number of selected attributes for two classifiers.

GKMI method is performed on a superpixel level, therefore it can be potentially affected by the size of superpixels, that can hold different information depending on the size. **Figure 5** illustrates overall accuracy with respect to the number of superpixels. It is evident from the curve that there are no significant fluctuations in overall accuracy. Consequently, the number of superpixels does not strongly affect classification accuracy.

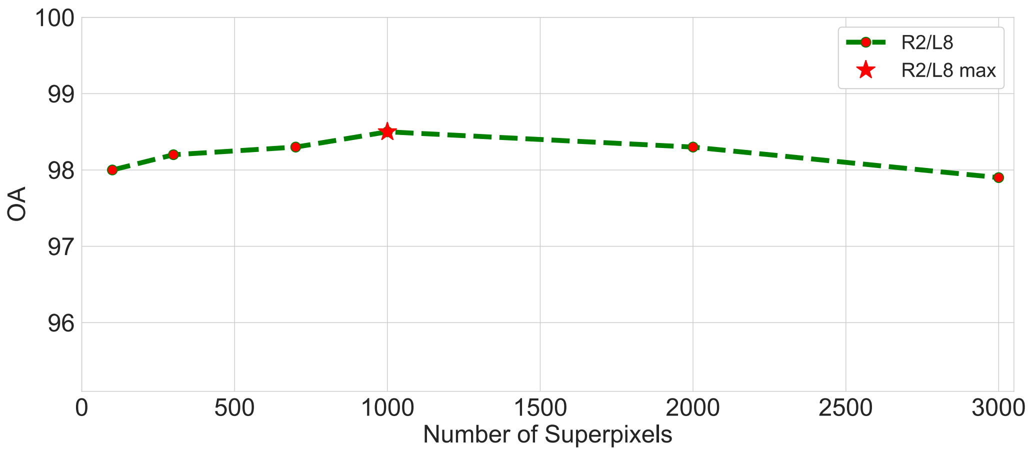

Figure 5. Overall accuracies of GKMI over a different number of superpixels using SVM classifier.

Figure 6 demonstrates the classification result obtained from optimal number of attributes by GKMI attribute selection method. It is complicated to precisely set the same labels that will simultaneously correspond both to WMO Sea Ice Nomenclature (Bushuyev, 1970) and radar classes since multisensor data can provide different information about the same region. Therefore, in our case Open Water corresponds to ice-free area, Thin Ice corresponds to any of young ice types, either grey or grey-white ice, Thick Ice 1 corresponds to thin first year ice/white ice, Thick Ice 2 corresponds to medium first-year ice, and Nilas remains the same according to nomenclature.

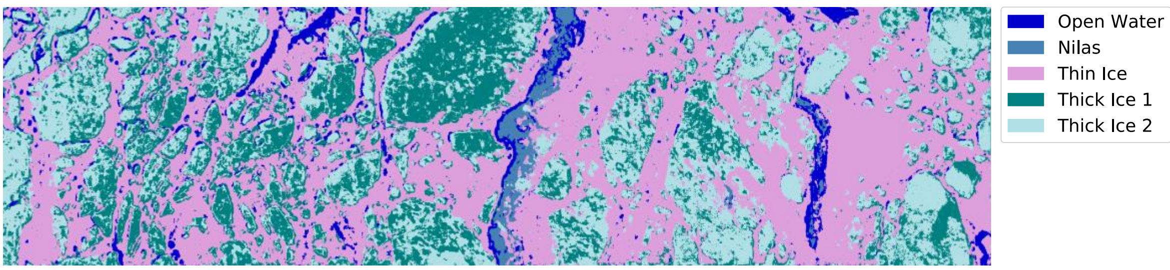

Figure 6. Classified map obtained from optimal number of attributes by means of the proposed method.

5. Conclusions

We designed an automatic framework for information selection that is:

- **Flexible**: can be applied for datasets obtained from various sensors.
- **Interpretable**: preserves the physical meaning of the original datasets.
- **Efficient**: produces high classification accuracy with less number of attributes.

The experimental results based on the multimodal sea ice dataset illustrated the accuracy and precision of the proposed information selection method. Our future work will be focused on studying the relevance of the attributes for different water and sea ice types, as well as testing the proposed method on various data combinations for diverse sea ice conditions.

Acknowledgments
This work is funded by Centre for Integrated Remote Sensing and Forecasting for Arctic Operations (CIRFA), the Research Council of Norway (RCN Grant no. 237906), and the Automatic Multisensor remote sensing for Sea Ice Characterization (AMUSIC) "Polhavet" flagship project 2020.

References

Ablin, P., Cardoso, J.-F., and Gramfort, A. (2018). Beyond Pham's algorithm for joint diagonalization, (December). Retrieved from http://arxiv.org/abs/1811.11433

Albregtsen F. (1974). Statistical Texture Measures Computed from Gray Level Coocurrence. *Boundary 2*, *3*(1), 45. https://doi.org/10.2307/302397

Beucher, S. (1992). The Watershed Transformation Applied to Image Segmentation. *Proceedings of the 10th Pfefferkorn Conference on Signal and Image Processing in Microscopy and Microanalysis*, 299–314. https://doi.org/10.1.1.24.5229

Bushuyev, A. V. (1970). WMO sea-ice nomenclature, terminology, codes and illustrated glossary, WMO/OMM/BMO 259, TP 145. https://doi.org/10.1109/SSST.1997.581627

Dalla Mura, M., Chanussot, J., Benediktsson, J. A., Prasad, S., Pacifici, F., and Gamba, P. (2015). Challenges and Opportunities of Multimodality and Data Fusion in Remote Sensing. *Proceedings of the IEEE*, *103*(9), 1585–1601. https://doi.org/10.1109/jproc.2015.2462751

Funder, S., et al. (2010). History of sea ice in the Arctic. *Quaternary Science Reviews*, *29*(15–16), 1757–1778. https://doi.org/10.1016/j.quascirev.2010.02.01

Gunn, S. R. (1998). Support Vector Machines for Classification and Regression.

Haralick, R., Shanmugam, K., and Dinstein, I. (1973). Textural Features for Image Classification. IEEE Trans Syst Man Cybern. SMC-3. 610-621.

Kandaswamy, U., Adjeroh, D. A., and Lee, M. C. (2005). Efficient texture analysis of SAR imagery. *IEEE Transactions on Geoscience and Remote Sensing*, *43*(9), 2075–2083. https://doi.org/10.1109/TGRS.2005.852768

Liaw, A., Wiener, M. (2001). Classification and Regression by RandomForest. Forest.23.

Longbotham, N., et al. (2012). Multi-modal change detection, application to the detection of flooded areas: Outcome of the 2009-2010 data fusion contest. *IEEE Journal of Selected Topics in Applied Earth Observations and Remote Sensing*, *5*(1), 331–342. https://doi.org/10.1109/JSTARS.2011.2179638

Neubert, P., and Protzel, P. (2014). Compact watershed and preemptive SLIC: On improving trade-offs of superpixel segmentation algorithms. *Proceedings - International Conference on Pattern Recognition*, 996–1001. https://doi.org/10.1109/ICPR.2014.181

Ng, A.Y., Jordan, M., and Weiss, Y. (2001). On Spectral Clustering: Analysis and an Algorithm. Advances in Neural Information Processing Systems.

Pham, D.-T., and Cardoso, J. F. (2001). Blind separation of instantaneous mixtures of nonstationary sources. *IEEE Transactions on Signal Processing*, *49*(9), 1837–1848. https://doi.org/10.1109/78.942614

Sandven, S., Johannessen, O. M., and Kloster, K. (2006). Sea Ice Monitoring by Remote Sensing. *Encyclopedia of Analytical Chemistry*, *1993*(March 1993), 1–43. https://doi.org/10.1002/9780470027318.a2320

Theodoridis, S., and Koutroumbas. K., Pattern Recognition, Fourth Edition, Academic Press, Inc., Orlando, FL, USA, 4th edition, 2008.

Vergara, J. R., and Estévez, P. A. (2014). A review of feature selection methods based on mutual information. *Neural Computing and Applications*, *24*(1), 175–186. https://doi.org/10.1007/s00521-013-1368-0

25th IAHR International Symposium on Ice
Trondheim, 23 – 25 November 2020

Marginal Ice Zone (MIZ) field investigation in the Western Barents Sea in April 2017-2019

Nataliya Marchenko
The University Centre in Svalbard
P.O. Box 156. Longyearbyen, N-9171, Norway
natalym@unis.no

Knowledge of sea ice state (distribution, characteristics and movement) is interesting both from a practical point of view and for fundamental science. The western part of the Barents Sea is a region of increasing activity – oil and gas exploration may grow in addition to traditional fishing and transport. So, the information is requested by industry and safety authorities.
Three last years (2017-19) the University Centre in Svalbard (UNIS) Arctic Technology Department performed expeditions on MS Polarsyssel in April in the sea ice marginal zone of the Western Barents Sea, as a part of teaching and research program. In (Marchenko 2018b), sea ice maps were compared with observed conditions. The distinguishing feature of ice in this region is the existence of relatively small ice floes (15-30 m wide) up to 5 m in thickness, containing consolidated ice ridges. In (Marchenko 2019) we described several such floes investigated by drilling, laser scanning and ice mechanical tests, on a testing station in the place with very shallow water (20 m) where ice concentrated. In this article, we summarize three years results with more attention for level ice floes and ice floe composition, continuing to feature ice condition in comparison with sea ice maps and satellite images.
These investigations provided a realistic characterization of sea ice in the region and are a valuable addition to the long-term studies of sea ice in the area performed by various institutions.

1. Introduction

The ice edge in the western part of the Barents Sea became the subject of much discussion in the Norwegian government in 2017 and 2020. Its position is associated with the possible expansion of hydrocarbon production in the region to the north of Bear Island, new licensed areas and therefore became the subject of heated political disputes (Rommetveit and Topdahl 2020).

Indeed, the position of the ice edge also changes throughout the year, with a maximum usually at the end of April and from year to year, reflecting climatic trends and the peculiarities of water circulation associated with currents. For the historical past, the ice boundary was reconstructed using seafarers' reports (Vinje 1985, 2001). In the era of the aerospace information, the ice boundary is determined by an ice concentration of 15%. 15% is the so-called threshold value, which is the detection limit for ice remote sensing. Based on this definition, the Norwegian Polar Institute has summarized the available information and various options for drawing the border on its website (Norwegian Polar Institute 2020). The so called "Plan 2015 boundary", announced in the report to the Norwegian Parliament (Ministry of Climate and Environment 2015), defines the ice boundary "Where there is ice for 30 per cent of the days in April, measured over the preceding 30 years (ice concentration greater than 15 per cent". This line goes far north of Bear Island and close to our study area, that was inspired by industry request for knowledge on sea ice as potential risk factor here. The expedition tracks, places of ice floe investigations and various versions of ice edge are shown in Fig. 1.

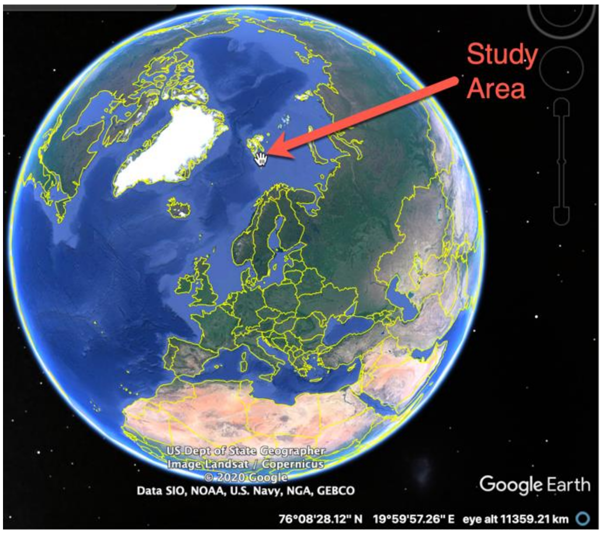

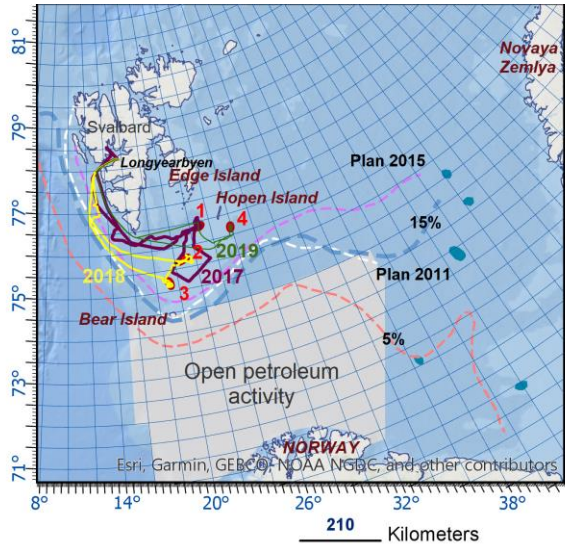

Figure 1. Study area. Place of fieldwork on the globe (left side) and detail map (right side). Three track lines show the trajectories of the vessel by years (the years are signed): 2017 – purple , 2018 – yellow, 2019 – green. Dashed lines show various options for drawing the ice boundary according to (Norwegian Polar Institute 2020 ; Bay-Larsen, Bjørndal, and Hermansen 2020). Dark blue spots show Russian deposits. Red spots with red number show investigated ice floes with ridges. These floes are presented in the table 2.

2. Natural conditions and previous research

The sea ice regime in the Barents Sea has been extensively studied by various institutions (Vinje and Kvambekk 1991; Zubakin 2006; Buzin 2009; Årthun, Eldevik, and Smedsrud 2019; Koenigk et al. 2009), both to ensure the development of regional industry and to understand global processes. As shown in (Lind, Ingvaldsen, and Furevik 2018), a significant increase in temperature has been observed in the Arctic in recent decades, especially in the northern part of the Barents Sea, which is associated with a decrease in sea ice imports. The Barents Sea, locating on the route of Atlantic water entering the Arctic, is the site of conjugate interaction processes that affect the variability of the entire Arctic air-ice-ocean system. When the waters of the Atlantic flow through the Barents Sea, they lose heat, giving it back to the atmosphere. Warm periods, including those observed now, are associated with high heat transfer to the north, a decrease in the Arctic sea ice cover, and high surface air temperatures (Smedsrud et al. 2013). Particular attention was paid to the western and central part of the Barents Sea in connection with the possible hydrocarbons exploration: the western region between the Bear and Hopen islands (Norwegian license areas) and the Shtokman fields in the east. Fishing and transport are actively developing here.

The study area is an extremely dynamic and interesting region both in an economical and in a natural sense, where the behaviour of sea ice affects both industry and understanding of global climate processes. In the west, where the Atlantic and Arctic waters meet and interact, an interesting natural phenomenon is observed - the tongue of ice, extending southward to 75°N and sometimes the surrounding Bear Island. This tongue appears in March-April and is visible on satellite images and ice maps even in the current warm season. T. Vinje estimated the possibility of observing multiyear ice near Bear Island as 1% of the total number of ice observations in 1970-1981 (Vinje 1985). According to Russian ice reconnaissance data from the archives of air and ice charts, the spread of old ice along Spitsbergen to more southern regions (Bear Island) is more frequent (Buzin 2009).

S. Gerland et al. (Gerland et al. 2008), based on more than 40 years of monitoring of land-fast ice in the area of Hopen Island, found a tendency to anomalies in ice thickness - 0.11 m per decade, coinciding with a decrease in the seasonal maximum of ice thickness and an increase at local surface air temperatures and water.

Measurement of ice thickness using an electromagnetic field antenna east of Svalbard (King et al. 2017) showed a range of possible ice thickness distributions. In colder years, like 2003, the dominant ice was over two years old; and its thickness varied within the region from 0.6 to 1.4 m, and the thinner ice was either one-year or multiyear ice that came into contact with warm Atlantic water. In 2014, the ice cover was predominantly local, less than a month old and 0.5–0.8 m thick.

Calculations based on the analysis of space information show that ice from the Arctic basin (from the area west of Franz Josef Land) can reach Bear Island, as it was the case in 2003 and may include multiyear ice and icebergs (Marchenko 2018a). At the end of May 2020, Bear Island was densely surrounded by ice as seen on ice maps and photographs (Norwegian Meteorological Institute 2020)

3. Organization of the expeditions

The Arctic Technology Department of the University Centre in Svalbard (AT UNIS) has been conducting field studies of sea ice in the western Barents Sea by the expeditions and drifting buoys installed on ice since 2003 (Marchenko and Marchenko 2015; Marchenko 2019). The cruises in the frame of AT-211 UNIS Bachelor's Course "Ice Mechanics, Structural Loads and Instrumentation" at the end of April provide valuable scientific data for this rarely visited part of the Barents Sea (Marchenko and Marchenko 2017). The participation of scientists from various institutes and countries (NTNU, C-Core, UCL, Cambridge University, Shirshov Institute of Oceanology) contributes to the setting of new experiments, enlivened scientific discussions. During the cruises, sea ice properties are investigated, and oceanographic measurements are taken.

Until 2017, the research vessel Lance was mainly used for the cruises, and it was possible to go to the solid ice (red) zone. For the last three years, cruises have been carried out on the MS Polarsyssel in the edge ice zone between Hopen and Bear islands (Fig. 1). Polarsyssel is a fire fighting vessel built-in 2014, IMO: 9690949, gross tonnage: 4324 t, deadweight: 3,700 t, length 88.5 m, width 18.3 m. The Governor of Spitsbergen uses the vessel for rescue operations and daily needs. Polarsyssel has ice class 1B, but due to the need to be constantly ready for an emergency situation, she usually does not work in ice.

Of the 8-10 days allocated for the expedition, several days are spent on the sailing from Longyearbyen to the research area and searching for a suitable site. In the marginal zone, it is necessary to find a suitable ice floe - sufficiently thick (at least 50 cm) and large (at least 20 m). In 2017-2018, the vessel was moored to the ice floe (Fig.2a). In 2019, groups landed on the ice from small motorboats (Fig. 2b). When working on ice floes, drilling is carried out to identify the thickness of the ice, laser scanning helps to determine the size and shape of the surface, mechanical tests reveal ice properties, and drifting buoys are installed to follow ice movement. Over the years, this "standard set" has been supplemented with studies of ice permeability, wave penetration and attenuation in an ice field, the effect of tides on the drift, etc. In 2017, a kind of new expedition motive was the crossing of the ice tongue and comparison with ice maps. In 2018 - the study of ice at the shallows and the southern limit was the speciality, in 2019 - the study of flat ice floes was the main feature.

Figure 2. Carrying out research on ice floes. 2a - mooring to the ice floe, 2b - "landing" from the boat. Drilling sites for measuring ice thickness are marked with red poles

4. Results

Three expeditions to the marginal zone have revealed the features of sea ice in the study area.

<u>*Comparison with ice charts*</u>

During the expedition at the end of April 2017, we crossed twice the ice tongue extending to Bear Island and monitored the sea ice to find out how the real situation was reflected on the ice map (Fig. 3). Such maps are published daily (except weekends and holidays) at 15:00 on the portal of the Norwegian Meteorological Institute. We have described the appearance of sea ice in different zones of the ice map, corresponding to the colour categories determined by ice concentration, in the marginal ice zone of the western Barents Sea (Marchenko 2018b).

Observations in April 2018 and 2019 confirmed the findings and made it possible to characterize the corresponding zones as follows (see Table 1).

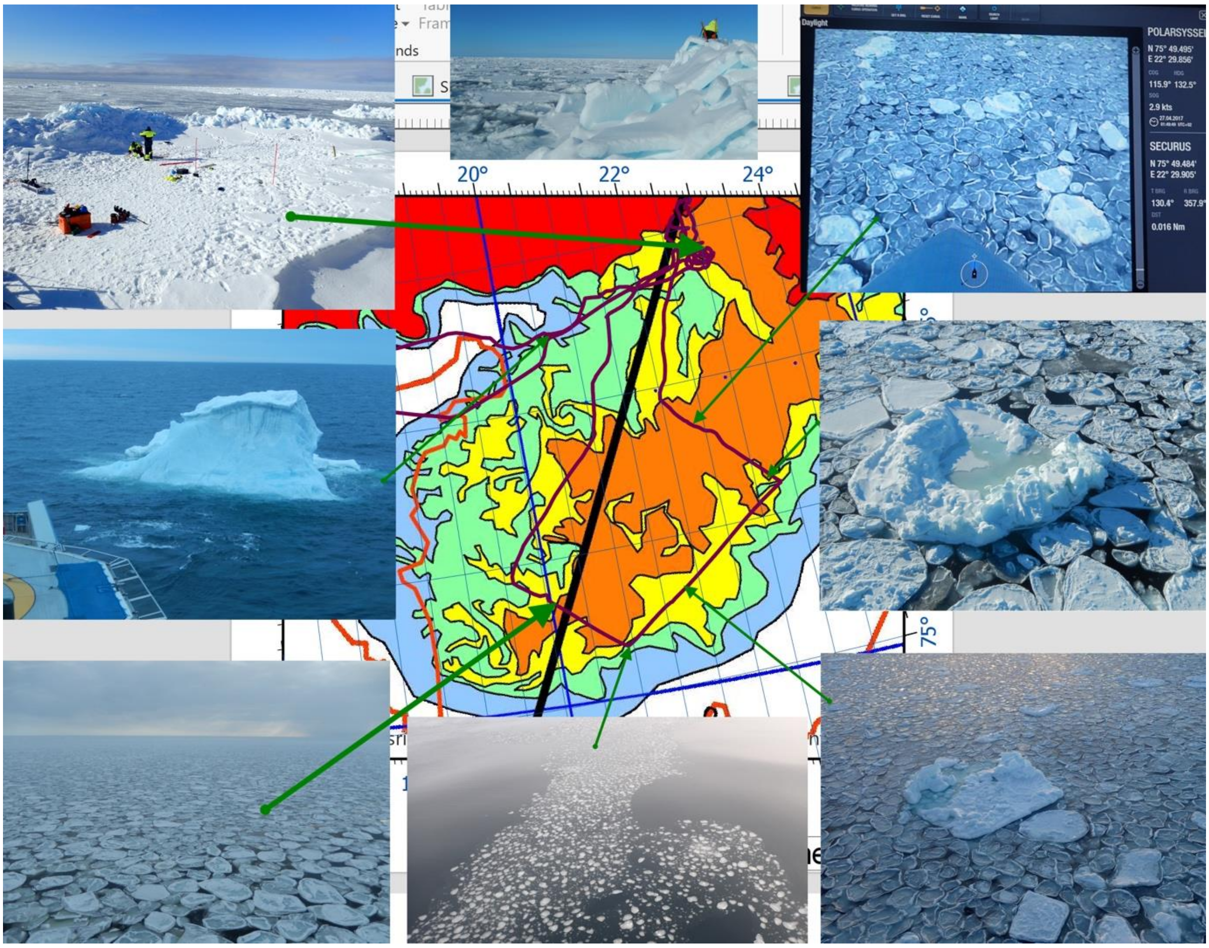

Figure 3. Ice map on 27 April 2017 and photographs of the actually observed situation when crossing the tongue of ice stretching towards Bear Island. The ship track is shown with a dark purple line. Explanations of colours on the map are given in Table 1.

Table 1. Correspondence between ice categories shown on the map and observed situation.

Colour / category on the map	Ice conditions
9-10/10ths Very Close Drift Ice Red zone. Ice concentration 9-10/10ths	a dense ice field, consisting of small (5-10 m) angular flat ice floes; repeating larger ice floes (20-30 m) with hummocks rising above the water surface up to 2 m and keel up to 4 m) and rounded fragments (less than 1 m) between them;
7-9/10ths Close Drift Ice Orange zone Ice concentration 7-9/10ths	in the northern part of the ice tongue (IT), there are round ice floes (2-4 m) with frequent intersperses of ice floes (10-15 m, up to 25 m), containing hummocks (with a sail up to 2 m and a keel up to 4 m); in the southern part of the ice tongue - dense and thick pancake ice, of a rather uniform oval shape (25-30 cm wide and 35-45 cm long) with occasional splashes of shaved ice;
4-7/10ths Open Drift Ice Yellow zone Ice concentration 4-7/10ths	in the northern part of IT - similar to the orange zone in terms of content, but with a lower concentration and fewer ice ridges; in the southern part of IT - thin pancake ice (20 cm in diameter) among the nilas;

1-4/10ths Very Open Drift Ice Green periphery Ice concentration 1-4/10ths	consist of ice strips from tens to hundreds of meters wide of the same composition as the yellow zone, located in ice-free water.

Icebergs

All categories mentioned above can include icebergs. In 2017, we observed an iceberg (up to 10 m high) in ice-free water (blue colour on the ice map – see Figure 3) at 76°N. In 2018, we saw and measured (using laser scanning of the topside) an iceberg in the orange zone between 75.11 and 75.26°N. During the observation, the ice field, together with our ship and the iceberg, made oval-shaped tidal loops 10x14 km in size (Fig. 4). The iceberg had a bizarre shape with five hills up to 4.2 m high, a pond in the middle and a significant visible underwater part.

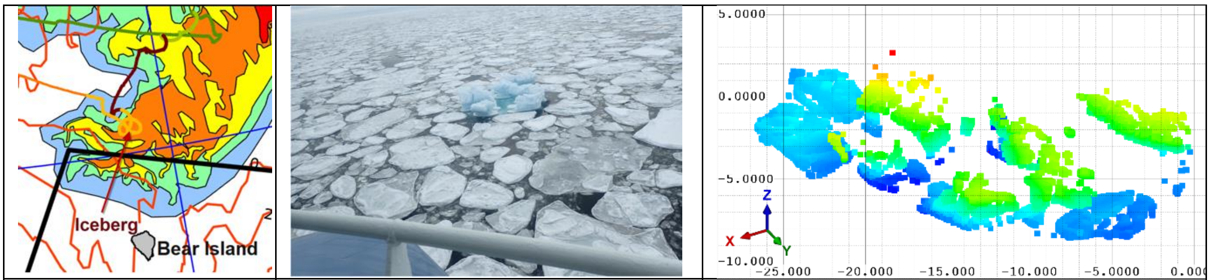

a. Ice map	b. Photo of the iceberg from the bridge	c. 3D point cloud, coloured in height above the water.

Figure 4. Observation and measurement of the iceberg 28 April 2018

Icebergs included in the solid ice field in the red zone were observed to the northeast of Edge Island in 2016, they are described in (Marchenko and Marchenko 2017).
In 2019, on the border of the yellow and orange zones at 75.11°N, an iceberg was observed. It had a complex shape, size of 23x23 m, rising up to 3.4 m. It was densely surrounded by ice floes of the most diverse shapes. Fig. 5 shows a photograph and a point cloud obtained by laser scanning, giving an idea of the geometry.

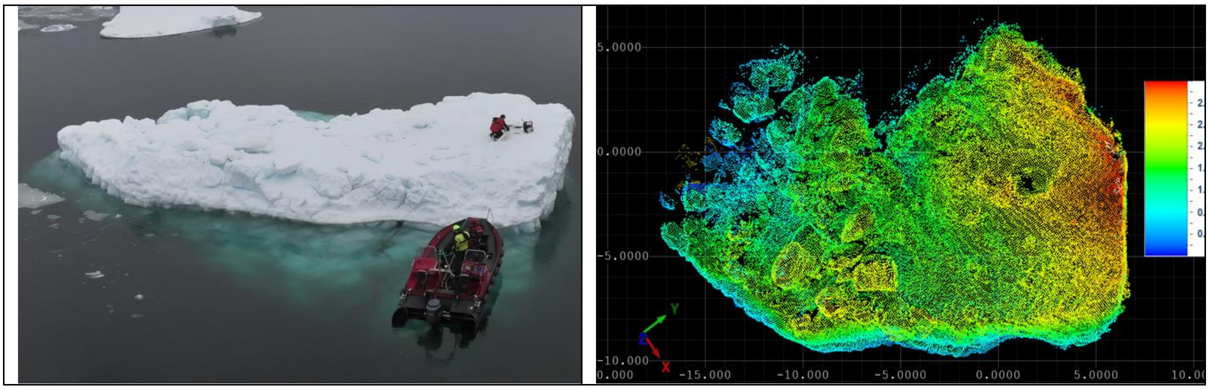

Figure 5. Observation and measurement of the iceberg 27 April 2019

Large ice floes with hummocks

Large ice floes with hummocks are a key feature of the marginal zone of the Barents Sea and are obviously a hazard to both navigation and industrial structures/platforms. Therefore, they represented the main object of research. Fig. 6 shows the progress of work and a three-dimensional model of the ice floe investigated in 2018 (ice floe number 3 in the table 1). Table 2 shows the main parameters of the studied typical ice floes.

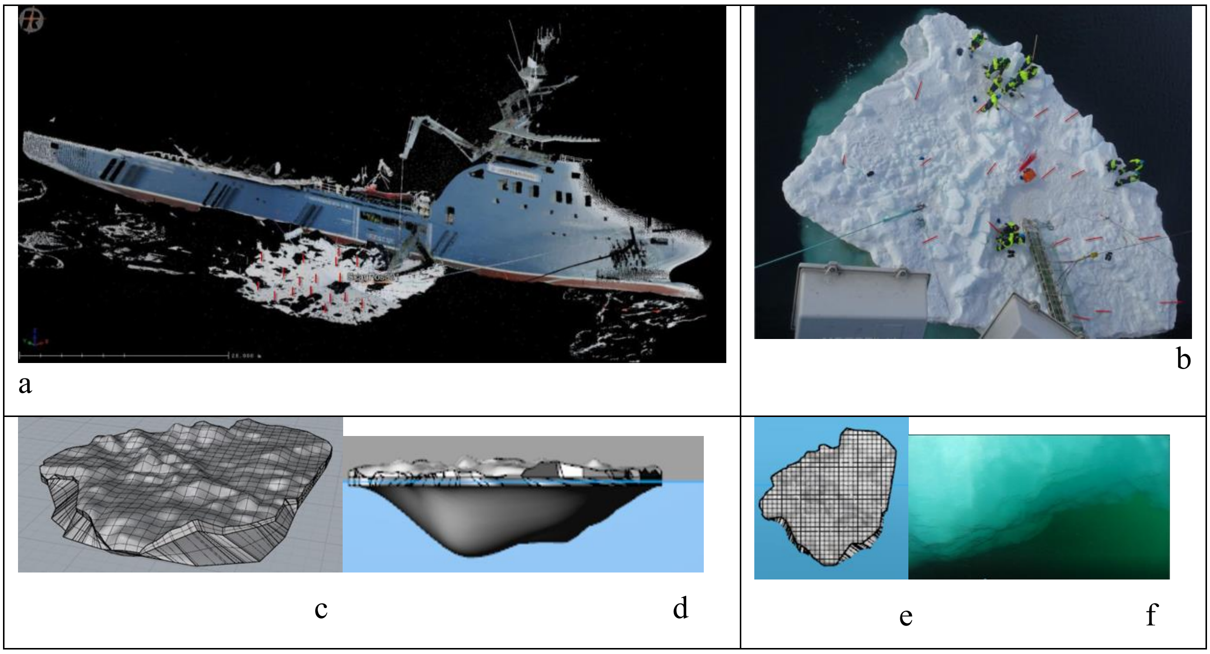

Figure 6. Study and modelling of ice floe (example of ice floe 2 - 2018).
6a - Three-dimensional cloud of points, coloured by photographs obtained during scanning. The ice floe is moored to the ship. 6b is a top view of the work process. Some of red poles, marking the regular drilling grid are visible on 6a and 6b.
6c - perspective view of the surface and sidewall (3D model), 6d - side view with the waterline, 6e - top view, 6f - underwater survey.

The RIEGL VZ1000 laser scanner was used to obtain a three-dimensional offset of points on the ice floe's surface (an example of the resulting cloud is shown in Fig.6a - the distance between points is a few millimetres), drilling on a regular grid gave information about the profile of the underwater part. In 2018 and 2019, underwater videos were taken to confirm the estimate. Inspired by the large keel measured by drilling in 2018, we attached the GoPro to a long pole and lowered it into the drilled hole to see the underwater part of the ice floe (Fig. 6f). In 2019, colleagues from the University of Oslo used an autonomous underwater vehicle.
We utilize three-dimensional modelling software (Rhinoceros 3D) to combine measurements from scans and drills and determine the numerical characteristics of floes presented in Table 2.

Table 2. Characteristics of ice floes
Explanations for the rows in the table: 1 - ice floe number and year of observation, 2 - coordinates, 3 - sea depth in situ, 4 - average air temperature / average ice salinity, 5 - horizontal size, m, 6 - maximum sail/draft, m., 7 - underwater volume / total ice volume, m^3, 8 - area, m^2, 9 - Ice volume above the water surface, m^3

1	Floe 1_2017	Floe 2_2018	Floe 3_2018	Floe 4_2019
2	76.39°N 22.86°E	75.58°N 21.57°E	75.18°N 19.20°E	76.20°N 25.94°E
3	90 m	45 m	22 m	120 m
4	- 7° C/ 7.7 ppt	- 8° C/ 4.5 ppt	- 5° C/ 4.5 ppt	- 2° C/ 3.1 ppt
5	43x30	26.9x26.5	22.6x22.8	35.5x31.3
6	2.16/3.82	2.2 /2.94	1.6/4.56	2.2/7.85
7	2655/3270	942/1469	752/1000	Not defined
8	934	613	343	730
9	615	527	247	1066

Flat ice floes

Ice in the marginal zone of the Barents Sea is a combination of relatively large flat ice floes, ice hummocks described in the previous section, and debris filling the space between these two types of ice floes (Fig. 2, 3, 7). Ice concentration is reasonably well reflected by ice maps, and the ratio of different types of ice changes when moving south. In 2017-2018, we focused on ice floes with hummocks, as the most remarkable and most dangerous ones. In 2019, at the request of the captain of the vessel, we examined the flat ice floes that were chosen by him, based on his considerations for the safety of navigation. It should be noted that in 2017 the captain was initially very sceptical about the idea of approaching the area shown on the map in orange colour and was quite surprised at how easily the tongue of ice was crossed. At the same time, the results of the drilling of ridged ice floes aroused obvious concern and the question of flat floes thickness. That's why we investigated the flat floes, which were of great interest. A group of three people was transported on the ice floes in a motorboat, disembarked and drilled at three points (Fig. 7a) measuring the ice thickness, freeboard and the thickness of the snow cover (Fig. 7b). To ensure the safety of the work, relatively large ice floes were selected. Simultaneously, laser scanning (Fig. 7c) and drone surveying with marking of places of grilling (Fig. 7d) were carried out.

a

Letter	Thickness [m]	Freeboard [m]	Snow [cm]
A	2.0	0.2	4-8
B	2.4	0.25	5-10
C	1.5	0.2	4-9

b

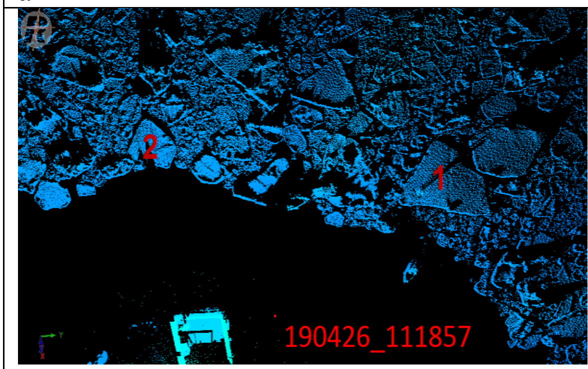

c

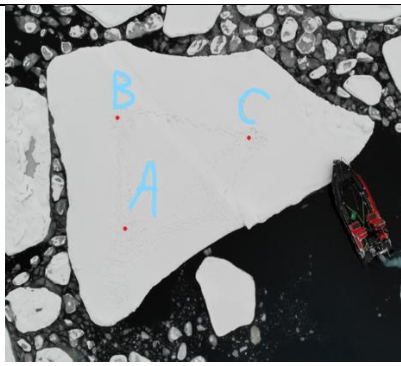

d

Figure 7. Study of flat ice floes on 26 April 2019

7a is a view from the helipad of the drilling process on ice floe 1 (ABC). 7b - measurement results, 7c - three-dimensional point cloud obtained during scanning. The composition of ice floes and ice floes 1 and 2 are visible, 7d - a photograph from a drone. Drilling sites are marked.

The results averaged over three points for seven ice floes are presented in Table 3. The average thickness of flat ice floes was 1.5 m, freeboard – 0.14 m, snow thickness – 0.05 m and size 18.3x12.7 m.

Table 3. Measurement of flat ice floes (readings in meters)

Floe	Ice thickness	Freeboard	Snow thickness	Length	Width
1	2.0	0.22	0.06	27	20
2	1.6	0.11	0.05	11	11
3	0.8	0.05	0.05	16	9
4	1.5	0.15	0.05	14	10
5	1.8	0.20	0.07	23	12
6	1.8	0.15	0.06	17	11
7	1.3	0.07	0.04	20	16
Average	1.5	0.14	0.05	18.3	12.7

CONCLUSION

Expeditions aboard the MS Polarsissel in April 2017–2019 made it possible to characterize the state of ice at the southernmost limit of its distribution in the Barents Sea in the area between the islands of Bear and Hopen. The sea ice is shown here on the map as a tongue extending from northeast to southwest and characterized by a dynamic combination of all ice categories from green to red with a concentration of 1 to 10 points. A distinctive ice feature in the area is the presence of small icebergs, ridged ice floe and hummocks up to 30 m in diameter and 5 m thickness in all these categories of ice. As you move southward, the frequency and size of such ice formation decrease. Such floes and icebergs can be potentially hazardous to navigation and offshore construction and must be taken into account and controlled.

Acknowledgements

The author would like to thank the crew of the MS Polarsyssel, the head of the expeditions Professor A.V. Marchenko, AT-211 course students and colleagues, and the AOCEC project (funded by the Research Council of Norway) for supporting this study.

References

Bay-Larsen, Ingrid, T. G. Bjørndal, and E. A. T. Hermansen. 2020. 'Mapping ice in the Norwegian Arctic – on the edge between science and policy', *Landscape Research*: 1-15.

Buzin, Igor V. 2009. 'On the Spreading of Old Ice In the Barents Sea', *Int. J of Offshore and Polar Engineering, ISOPE*, 19: 1-7.

Gerland, S., A. H. H. Renner, F. Godtliebsen, D. Divine, and T. B. Løyning. 2008. 'Decrease of sea ice thickness at Hopen, Barents Sea, during 1966–2007', *Geophysical Research Letters*, 35: n/a-n/a.

King, Jennifer , Gunnar Spreen, Sebastian Gerland, Christian Haas, Stefan Hendricks, Lars Kaleschke, and Caixin Wang. 2017. 'Sea‐ice thickness from field measurements in the northwestern Barents Sea', *Journal of Geophysical Research: Oceans*, 122: 1497-512.

Koenigk, Torben, Uwe Mikolajewicz, Johann H. Jungclaus, and Alexandra Kroll. 2009. 'Sea ice in the Barents Sea: seasonal to interannual variability and climate feedbacks in a global coupled model', *Climate Dynamics*, 32: 1119-38.

Lind, Sigrid, Randi B. Ingvaldsen, and Tore Furevik. 2018. 'Arctic warming hotspot in the northern Barents Sea linked to declining sea-ice import', *Nature Climate Change*, 8: 634-39.

Marchenko, N. A, and A.V. Marchenko. 2015. "Sea currents and ice drift in western part of Barents Sea. A comparison of data from floating and fixed on ice buoys " In *The 23rd Int. Conf. on Port and Ocean Eng. under Arctic Conditions (POAC 2015)*. Trondheim.
Marchenko, N., and A. Marchenko. 2017. "Investigation of large ice rubble field in the Barents Sea." In *Proceedings of the 24th International Conference on Port and Ocean Engineering under Arctic Conditions*. Busan, Korea.
Marchenko, Nataliya. 2018a. "Reconstruction of Ice Drifting lines in the Barents Sea, using IFREMER sea ice products." In *ISOPE - International Offshore and Polar Engineering Conference. Proceedings*, 8.
———. 2018b. 'Sea ice observation and comparison with ice maps during the cruise in the Western Barents Sea in April 2017', *Proceedings of the IAHR International Symposium on ice*: 8.
Marchenko, Nataliya A. 2019. "Ice at its southern limit in the Barents Sea: field investigation near Bear Island in April 2017-2018." In *25th International Conference on Port and Ocean Engineering under Arctic Conditions*, 9.
Ministry of Climate and Environment. 2015. "Update of the integrated management plan for the Barents Sea–Lofoten area including an update of the delimitation of the marginal ice zone." In, edited by Ministry of Climate and Environment, 56. Oslo: Norwegian Goverment.
Norwegian Meteorological Institute. 2020. "Archived Ice Charts." In. Oslo.
Norwegian Polar Institute. 2020. 'The marginal ice zone', Accessed 03.06.2020. https://www.npolar.no/en/themes/the-marginal-ice-zone/.
———. 2020 'The marginal ice zone'. https://www.npolar.no/en/themes/the-marginal-ice-zone/.
Rommetveit, Astrid, and Rolv Christian Topdahl. 2020. 'Derfor er iskanten politisk sprengstoff. Nok en gang diskuterer politikerne is så bustene fyker.', NRK, Accessed 30.05.2020. https://www.nrk.no/klima/xl/derfor-er-iskanten-politisk-sprengstoff-1.14985643.
Smedsrud, Lars H., Igor Esau, Randi B. Ingvaldsen, Tor Eldevik, Peter M. Haugan, Camille Li, Vidar S. Lien, Are Olsen, Abdirahman M. Omar, Odd H. Otterå, Bjørg Risebrobakken, Anne B. Sandø, Vladimir A. Semenov, and Svetlana A. Sorokina. 2013. 'THE ROLE OF THE BARENTS SEA IN THE ARCTIC CLIMATE SYSTEM', *Reviews of Geophysics*, 51: 415-49.
Vinje, T. 1985. *Drift, composition, morphology and distribution of the sea ice fields in the Barents Sea* (NPI: Oslo).
———. 2001. 'Anomalies and trends of sea-ice extent and atmospheric circulation in the Nordic Seas during the period 1864-1998', *Journal of Climate*, 14: 255-67.
Vinje, T., and A. S. Kvambekk. 1991. 'Barents Sea Drift Ice Characteristics', *Polar Research*, 10: 59-68.
Zubakin, G. K. 2006. *Ice formations of the seas of Western Arctic* (AARI: St.Petersburg).
Årthun, Marius, Tor Eldevik, and Lars H. Smedsrud. 2019. 'The Role of Atlantic Heat Transport in Future Arctic Winter Sea Ice Loss', *Journal of Climate*, 32: 3327-41.

25th IAHR International Symposium on Ice
Trondheim, 23 - 25 November 2020

Evaluating Human and Machine Performance on the Classification of Sea Ice Images

Ole-Magnus Pedersen, Ekaterina Kim
Department of Marine Technology, NTNU
NTNU Norwegian University of Science and Technology
ole-magnus.pedersen@ntnu.no, ekaterina.kim@ntnu.no

Safe navigation in Arctic seas requires qualified judgement of the ice conditions of ice around the vessel, a skill that takes years of training to master. At the same time, melting of the polar ice is allowing for more traffic, leading to less experienced operators navigating in the area. To ensure safe passage, the development of new systems for aiding ship operators in the Arctic is needed.

This work is a step towards computer-vision assisted navigation for the Arctic, by benchmarking the ability of human experts and novices on the task of classifying ice-objects in images and comparing them to an off-the-shelf computer vision model. This task can be seen as a lower bound on the difficulty of ice object recognition (compared to, say, instance segmentation), and gives an idea of how well computer vision fares in the Arctic in the best case.

Our method gives a good indication of the ability of both humans and computers trained on clean images to generalize to the difficult conditions often found in the Arctic. By applying realistic distortions, such as synthetic fog, to the images at test time, we can assess the ability of the human participants to generalize. These results are then compared to measurements from the computer vision system, to evaluate the models' ability to work in previously unseen, difficult conditions.

The main contribution of the work is to give a realistic benchmark of how well current computer vision models perform when classifying ice objects compared to humans. Furthermore, we discover which types of images and distortions pose challenges to both humans and computers. Together, these form a knowledge base that can help create new and improved computer vision models tailored for sea ice imaging, towards the goal of computer-aided navigation.

1. Introduction

The amount of optical data captured from vessels operating in icy environments is growing quickly. If these images could be analyzed automatically, they would give much information about the ice conditions in different parts of the world at different times, as well as providing decision-support for navigators in real-time. However, the visual conditions in these environments are often suboptimal, meaning an analysis system would need to generalize to a large variety of conditions. The purpose of this paper is to gauge the ability of a current state-of-the-art computer vision system to perform such generalization, and to compare them with humans performing the same task.

Convolutional neural networks (CNNs) are a class of artificial neural networks shown to perform exceptionally well on tasks like image analysis (He et al., 2016; Russakovsky et al., 2015) and generation (Goodfellow et al., 2014; Karras, Laine, Aittala, et al., 2019; Karras, Laine, and Aila, 2019), as well as non-image tasks such as audio analysis (Hershey et al., 2017). They work by stacking many convolution operations, together with non-linear functions and special functions that improve training (such as dropout (Srivastava et al., 2014) and batch normalization (Ioffe and Szegedy, 2015)). All or most of the functions are parameterized, whith parameters updated by gradient descent or a similar procedure (Kingma and Ba, 2015; Loshchilov and Hutter, 2019; Tieleman and Hinton, 2012) on a loss function measuring the distance from the output of the function to the desired output. A thorough description of neural networks can be found in most books on deep learning, such as Goodfellow et al., (2016).

Some previous work has compared human and computer performance on image classification. Dodge and Karam (2019) and Geirhos, Schütt et al. (2018) both compare the performance on classifying images with varying levels of distortion. Both found that neural networks do not generalize as well to most types of distortions as humans do. Geirhos, Schütt, et al. (2018) show that training networks on distorted images makes them robust to that exact type of distortion, but does not help the performance on other kinds of distortions. Dogde and Karam (2019) found that tuning a network trained on clean images with some distorted samples still left the network at a lower level than humans.

This work differentiates itself from the two above on two major points: First, the above works use images that are familiar to all participants, such as animals, while this work uses images of ice objects, a domain most people are very unfamiliar with. Second, both aforementioned works try to compare humans and computers on as fair a basis as possible, to find theoretical differences in how they operate. In the current work, the focus is to benchmark the best possible performance for humans and computers, without regard to the "fairness" of the experiment. A consequence of this is that images are shown for an unlimited amount of time for the human participants, without regard for firing off recurrent connections in the brain (Lamme et al., 1998). Furthermore, the image distortions used are chosen to imitate real visual conditions in the Arctic, to give a better representation of the real-world performance.

While much work has been done to analyze ice using other types of data, such as synthetic-aperture radar (SAR) images (e.g., Banfield and Raftery, 1992; Wang et al., 2016), the automatic classification of ice objects in optical images using deep learning has seen little focus. Kim et al. (2019) presented the first work in this area, where they compare several models on ice-object classification. This work extends upon their results by introducing image distortions and comparing the computer vision model to humans.

1.1. Limits of this study

While this study aims to compare humans and computers on the task of ice classification, it does not provide a completely accurate view of the best human performance in the real world. This is because human navigators use a variety of information sources when gauging the ice, including visual data, SAR-imaging, on-board radar images, infrared images, and the sound and feel of collision with the ice. Furthermore, the navigators may have a pre-learned classification bias that does not completely agree with the classification scheme used in this work, putting them at a disadvantage compared to computers and novices.

3. Methods

Two sets of experiments were conducted, one with human participants and one with a computer vision model. Following is a description of the dataset and image distortions used in this work, before the two experimental procedures are described.

3.1. Dataset

The dataset used for all our experiments consist of 738 unique images of ice cover. The images are taken either from cameras mounted on Arctic vessels or manually from onboard the ship. Most of the images are taken in high-visibility conditions, and each contains at least one (but possibly several) classes of ice objects. The images do not contain any major objects except for ice (such as other vessels or constructions), although some include minor distractions like

Table 1. Classes used in this work, and their definitions. Most of the classes are taken or adapted from the WMO Sea-Ice Nomenclature (2014)

Class	*Description*
Brash Ice	Accumulations of floating ice made up of fragments not more than 2 m across, the wreckage of other forms of ice.
Broken Ice	Predominantly flat ice cover broken by gravity waves or due to melting decay.
Deformed Ice	A general term for ice that has been squeezed together and, in places, forced upwards (and downwards). Subdivisions are rafted ice, ridged ice and hummocked ice.
Floeberg	A large piece of sea ice composed of a hummock, or a group of hummocks frozen together, and separated from any ice surroundings. It typically protrudes up to 5 m above sea level.
Floebit	A relatively small piece of sea ice, normally not more than 10 m across, composed of a hummock (or more than one hummock) or part of a ridge (or more than one ridge) frozen together and separated from any surroundings. It typically protrudes up to 2 m above sea level.
Iceberg	A piece of glacier origin, floating at sea.
Ice Floe	Any contiguous piece of sea ice.
Level Ice	Sea ice that has not been affected by deformation.
Pancake Ice	Predominantly circular pieces of ice from 30 cm - 3 m in diameter, and up to approximately 10 cm in thickness, with raised rims due to the pieces striking against one another.

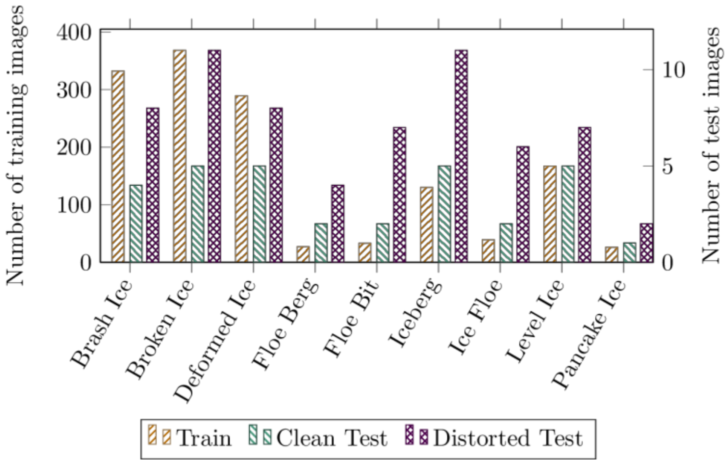

Figure 1. Distributions of the classes in the datasets. The data is very imbalanced, making training challenging.

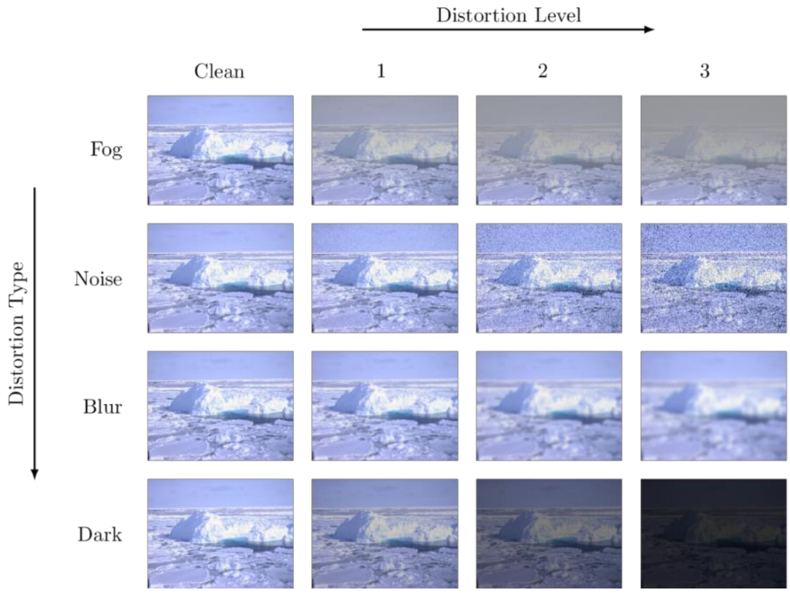

Figure 2. Different levels of the distortions used in this work.
Copyright of original image: Knut Vilhelm Høyland

animals. The goal of a classification system is to select all appropriate and no inappropriate classes for an image. The classes used in this work, along with their definitions, are shown in Table 1. The distributions of the classes in the datasets are shown in Figure 1.

To obtain data on the generalization ability of humans and computers, four kinds of semi-realistic image distortions have been used in this project:

- Synthetic fog
- Darkening of the image, simulating night
- Blur, simulating low visibility due to rain or snow
- Gaussian noise, simulating the effect of a high ISO on the cameras.

During the testing, we use three levels of each distortion, illustrations of which can be seen in Figure 2.

The data was split between training and test sets. 689 of the images were used for training (and validation for the computer system), and 49 were used for testing. Of the testing images, 16 were used as clean images as a baseline for the human trials, while the rest were distorted with one of the above distortions. To keep the setting equal in the different experiments, the data split was calculated only once.

3.2. Human Experiments

Two sets of experiments with humans were conducted: One with 8 novices with no previous experience with sea ice, and one with 6 experts experienced in recognizing ice features. All participants reported good or corrected to good vision, or slightly nearsightedness, which should not be a problem when working on a computer.

The experiments with human participants were performed after the following scheme: First, the participants went through a training phase, where they inspected images from all classes to become familiar with their definitions. They were free to go back and forth between classes for as long as they wished, and were also presented with the textual descriptions from Table 1. Following the training, they continued to a clean test phase, where they were asked to classify all 16 images in the non-distorted set. Finally, a distorted test was performed with the remaining 33 images. The two test phases were presented as a single phase to the participants.

During the distorted test, participants were first asked to classify an image at its highest level of distortion. If the participant failed to classify it correctly, the image was put back in the queue of images (at a random position), to be showed again at a later stage with a lower level of distortion. If correctly classified, it was assumed the participant would also be able to classify the image at a lower level of distortion, so no further tests were performed with that image. For an image to be correctly classified, the participant had to choose all correct and no incorrect classes for it. If the participants failed to classify the image at all levels of distortion (including the clean version of the image), the image was registered as a failed image, and not shown again. This general procedure is adapted from Dodge and Karam (2019).

During both test phases, each image was shown for an unlimited amount of time, and the participant was asked to choose any number of classes of ice objects in the image. Once they had submitted their answer, they were not allowed to change it.

3.3. Computer Vision Experiment

The neural network used for the computer vision experiment was implemented in PyTorch[1]. First, a pre-trained model was loaded, before the final fully connected layer was changed for a subnetwork that fit's the data. The subnetwork consists of a BatchNorm layer (Ioffe and Szegedy, 2015), followed by a Dropout layer (Srivastava et al., 2014), a fully connected layer with 512 output nodes, and a ReLU activation (Nair and Hinton, 2010), before another block of BatchNorm, Dropout and a fully connected layer with 9 outputs. The procedure is shown in Figure 3. The network chosen for this work after some preliminary experiments was the ResNet-50 (He et al., 2016), pretrained on the ImageNet dataset (Russakovsky et al., 2015).

Training of the network was done in two stages: First, the pretrained network was frozen and only the final subnet was trained. After the first stage, the rest of the network was unfrozen and fine-tuned. For both stages, the Adam optimizer (Kingma and Ba, 2015) with the improvements from Loshchilov & Hutter (2019) was used with the one-cycle policy from Smith (2018). Training parameters are shown in Table 2. Where the training parameters are not listed, the PyTorch default values were used. Five networks were trained using the same procedure, to

[1] https://pytorch.org

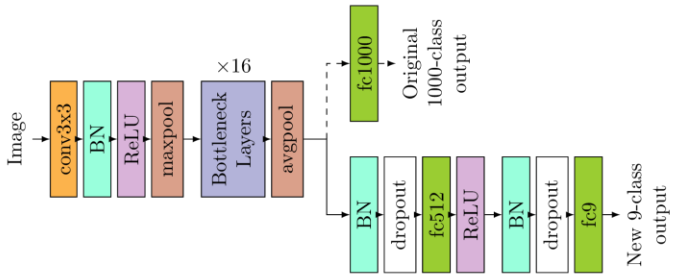

Figure 3. Reshaping of ResNet-50. The final 1000-class classifier was disconnected and replaced by a custom subnetwork.

get the mean, minimum, and maximum values reported in Section 4.

3.3.1. Data Preprocessing

Figure 1 makes it obvious that the dataset is very imbalanced. Training directly on such datasets will typically lead to a classifier very biased towards the majority classes. To avoid this, the datasets were oversampled before use in the computer vision experiments. The oversampling consisted of copying images with minority classes (the images were chosen randomly weighted by the mean frequency of their classes). This oversampling led to the class distributions of Figure 4. The test set was not oversampled, to keep comparisons between experiments fair.

Table 2. Hyperparameters used for training the ResNet-50. α is the learning rate, β_1, β_2 and weight decay are parameters of the Adam optimizer, and f_{init}, f_{end} are initial and final division factors for the one-cycle policy, so the learning rate starts at $\frac{\alpha_{max}}{f_{init}}$ and ends at $\frac{\alpha_{max}}{(f_{init}/f_{end})}$. The range in learning rate for stage 2 signifies the use of different rates in this range for the different layers (with the lowest for the first layer and highest for the last).

Parameter	*Stage 1*	*Stage 2*
α_{max}	$2 \times 10^{(-2)}$	$(10^{(-6)}, 10^{(-3)})$
f_{init}	25	25
f_{end}	1000	1000
$\beta_{(1,min)}$	0.80	0.80
$\beta_{(1,max)}$	0.95	0.95
β_2	0.99	0.99
Weight decay	$10^{(-3)}$	$10^{(-3)}$
Batch Size	32	32

85 % of the training images were used for training, while the remaining 15 % were used as a validation set. This split was randomized each run, and oversampling was performed after the split. Images were resized to 512×384 pixels, and random augmentation of horizontal flipping, rotation, zoom, brightness, contrast, saturation and hue was applied during training.

Images were normalized in the same manner as the ones used to pretrain the model[2].

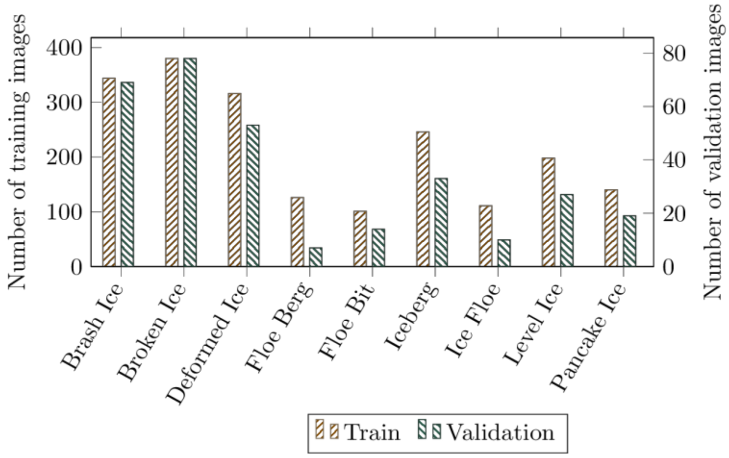

Figure 4. Distribution of classes in the datasets after oversampling was performed.

4. Results

The current section presents confusion matrices for the classification of clean images by humans and computer, and shows a selection of performance metrics. The chosen metrics are accuracy, balanced accuracy and F_1-score, defined as

$$acc = \frac{TP + TN}{TP + TN + FP + FN} \quad \textbf{[1]}$$

$$acc_b = \frac{1}{2}\left[\frac{TP}{TP + FN} + \frac{TN}{TN + FP}\right] \quad \textbf{[2]}$$

$$F_1 = \frac{2TP}{2TP + FN + FP} \quad \textbf{[3]}$$

		Predicted	
		False	True
Actual	False	TN	FP
	True	FN	TP

Figure 5. Definition of true and false positives and negatives, as used when calculating the metrics of a classifier.

where TP, TN, FP, FN are the number of true and false positives and negatives, as defined in Figure 5. Balanced accuracy and the F_1-score account for imbalanced datasets to a larger degree than plain accuracy, so comparing them will show the effect of class imbalance. We also report the *Correct Fraction*, i.e. the fraction of images where all correct and no incorrect classes were chosen.

Figure 6 shows the performance of humans and computer on varying levels of distortion. First, it is worth noting that some datasets seem more difficult than others, and that the difficulty depends on the person or model classifying. This is evident from the fact that the performance at distortion level 0 (i.e. no distortion) varies significantly from dataset to dataset in all experiments. For this reason, comparison of the absolute performance between different datasets makes little sense. Instead, this and the next section focuses on how the performance on the same data changes with higher levels of distortions.

Figure 6 shows how humans generally handle the distortions very well, with a relatively small decrease in the performance at higher levels of distortion. Even so, for the experts, we see that such a decline is present, especially for noise and blur. For novices, the performance seems

---

[2] https://pytorch.org/docs/stable/torchvision/models.html

more random, with performance at higher levels of distortion sometimes better than at lower levels. The effects of distortions are clearer in the computer vision trials, where there is a large decline in performance on higher levels of distortion. The effect of blurring is largest, followed by noise. Fog has a smaller, but still noticeable effect, while darkening of the images seem to have only a minor effect on the performance. When comparing humans and computers, it is obvious that there's a larger variety in the human performance than the computer performance. This is especially true when looking at the foggy images. In general, human novices have a larger variation than experts for all distortions except fog. The fraction of correctly classified

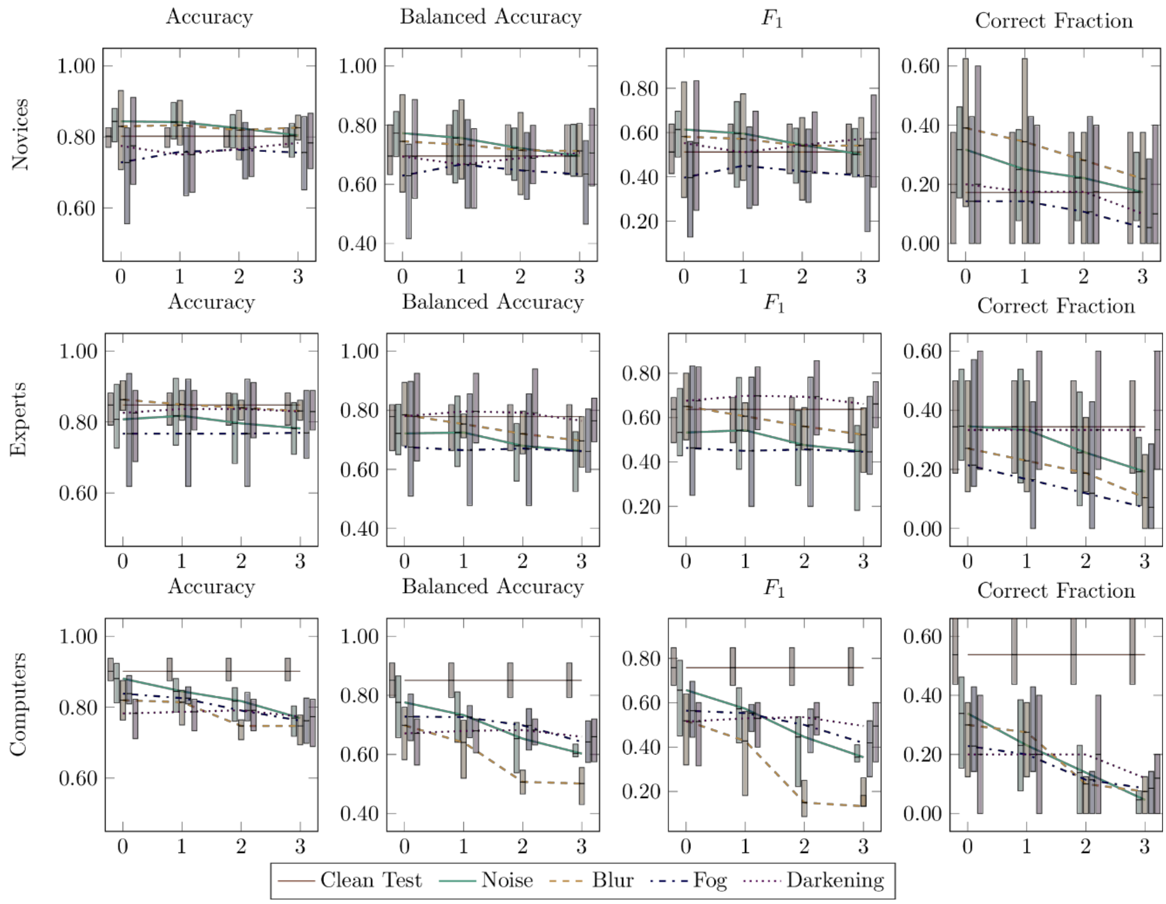

Figure 6. Mean metrics for the different experiments. The x-axis is the distortion level, and y-axis is the metric value. Minimum and maximum values in the data series are indicated by the colored bars.

	Brash Ice	Broken Ice	Deformed Ice	Floe Berg	Floe Bit	Ice Berg	Ice Floe	Level Ice	Pancake Ice
Novice	11 1 / 3 1	9 2 / 0 5	7 4 / 0 5	13 1 / 0 2	13 1 / 2 0	13 0 / 1 2	9 5 / 1 1	8 3 / 0 5	14 1 / 0 1
Expert	12 0 / 3 1	10 1 / 1 4	10 1 / 0 5	13 1 / 0 2	13 1 / 2 0	13 0 / 0 3	13 1 / 0 2	10 1 / 5 0	15 0 / 0 1
Computer	12 0 / 0 4	11 0 / 0 5	8 3 / 0 5	14 0 / 1 1	14 0 / 1 1	13 0 / 1 2	14 0 / 1 1	9 2 / 0 5	15 0 / 0 1

Figure 7. Confusion matrices for the best person/network in each experiment, based on their accuracy. All confusion matrices are from the experiments with clean images.

images declines with higher levels of distortion, which is expected due to the way correctly classified images are handled (see Section 3.2).

Figure 7 shows the confusion matrices for the best person or model in all experiments on the clean images. In the ideal case, only the main diagonal of each matrix should be larger than zero, as the secondary diagonal counts mistakes. However, we see that for all experiments and classes this is not the case.

5. Discussion

The fact that computers handle dark images so well is unsurprising, as images are normalized before being run through the networks, counteracting this effect. However, in the real world, the dark images are not uniformly darkened across the frame, but includes light spots and color shifts, possibly making them more difficult for the neural networks. For humans, we hypothesize that the darker images make people use more time to carefully inspect the image, thereby counteracting the effect of this distortion. We did not record the time used for each image, so this requires further testing to validate.

It is possible that the results with fog gains from the normalization as well, even though it is less effective as the distortion is not uniform over the entire frame. Regarding the foggy images, it should also be noted that the synthetic fog used here is less random than real fog tends to be. This could be a factor contributing to the good performance, and experiments with real fog must be performed to evaluate the effect of this.

Blur and noise have previously been noted to be challenging for neural networks (Karahan et al., 2016), while human vision is relatively robust to them. Furthermore, Geirhos et al. (2019) found that ImageNet-trained networks are biased towards recognizing texture over shape. As these distortions alter the textures of images, it is unsurprising that the network struggles with them. In other words, our results agree with previous work, indicating that these areas need improvement.

Comparing human experts and novices, the experts perform better at distortion level 0 except for the noise dataset, with an accuracy score of 0.85 compared to 0.80 on the clean test images. This difference increases when looking at the metrics accounting for class imbalance, with a balanced accuracy of 0.78 compared to 0.70. This indicates that novices tend to see that one class is common, and therefore choose it more often. Although experts also have a bias about which classes are more common, this bias is learned through years of experience and is therefore more correct, and less dependent on the exact training images used. The difference in performance between the two groups is smaller than expected, but this could be due to other parts of the demographics of the groups, such as age (novices have an average age of 20.5 years, and experts 48 years) or education.

In general, if we look at accuracy, computers perform at around the same or better level as human experts on clean images. However, looking at balanced accuracy and the F_1 score, the picture is more balanced, with the relative performance varying with the specific dataset inspected. We can still conclude that for clean images, the performance in general is at least around equal for the training and test sets used here. However, it deteriorates to much worse levels with some distortions. This shows that with the current technology, off-the-shelf solutions are not able to generalize to the difficult conditions often found in the Arctic, so as of now, this is not a dependable solution. It does, however, give a reason for further work in making networks more robust to distortions in the future, and indicates that if such work is successful, computer vision is indeed a relevant technology for such conditions.

It is also worth noting that computers are much better on the clean image test than humans, with balanced accuracy scores of 0.85 compared to 0.78 and 0.70 for experts and novices, respectively. The large gap here compared to the other trials can likely be explained by the way humans and computers work. For computers, the fact that images are undistorted seem most important for performance, while humans gain more from having several tries at the same image with different levels of distortions. In other words, it seems humans gain more from the way the experiment was designed, while computers are better at classifying correctly on the first try. In addition to this, it is likely the clean test set is easier for computers, perhaps due to the class balance of the images in that dataset.

Looking at the confusion matrices in Figure 7, a few interesting patterns can be noted. First, we can see that the best human expert and novice share some difficult classes not shared by the best computer. Specifically, brash ice, broken ice and floebits are classes where humans struggle slightly more than computers. We can hypothesize some reasons for this: For broken ice, it is often difficult to see if the ice is broken or not, due to snow cover and sometimes unclear images. Similarly for brash ice, it can sometimes be difficult to see if there actually is brash ice in an image, due to snow or waves. Floebits are difficult to distinguish from floebergs as the only difference is size, which is hard to measure in images. Furthermore, the novice and computer have problems spotting deformed ice, while the expert manage this very well. This is likely because deformed ice, and specifically ice ridges, is an important feature in icy waters, as they are often much harder to break than surrounding ice. Therefore, experts are trained to recognize such features. Finally, we see that all three have trouble recognizing level ice (where the novice and computer tend to label more images as level than true, and the expert opposite). A reason for this difficulty could be that the difference between level ice and broken ice is difficult to spot (as described above), and similarly the difference between an ice floe and level ice is not always obvious.

6. Conclusion

Based on the data, it is reasonable to conclude that neural networks perform at least on the level of, if not better than, human experts when classifying ice objects based only on clean image data. This is not the same as saying they could outperform human navigators, as there are a lot more factors to process in the real world. It does however encourage further research into this area.

The main challenge for neural networks observed in this work was with images distorted by noise and blur. With these images, computer vision proved far inferior to humans, and significant work must be done to improve this performance if computer vision is to become a viable help in Arctic navigation. Our result agree with those from Dodge and Karam (2019) and Geirhos et al. (2018).

Acknowledgments

We thank all the people who participated in our experiments. Furthermore, we thank Thomas Porathe and Erik Veitch for their comments on the experimental setup, and Knut Vilhelm Høyland, Roger Skjetne and Sveinung Løset for sharing their images with us. The network training and testing were performed on resources provided by UNINETT Sigma2 - the National Infrastructure for High Performance Computing and Data Storage in Norway.

References

Banfield, J. D., and Raftery, A. E., 1992. Ice floe identification in satellite images using mathematical morphology and clustering about principal curves. J. Am. Stat. Assoc., *87*(417), 7–16.

Dodge, S., and Karam, L., 2019. Human and DNN classification performance on images with quality distortions: A comparative study. ACM Trans. Appl. Percept., *16*(2), 1–17.

Geirhos, R., Michaelis, C., Wichmann, F. A., Rubisch, P., Bethge, M., and Brendel, W., 2019. Imagenet-trained CNNs are biased towards texture; increasing shape bias improves accuracy and robustness. 7th Int. Conf. Learn. Represent. ICLR 2019.

Geirhos, R., Schütt, H. H., Medina Temme, C. R., Bethge, M., Rauber, J., and Wichmann, F. A., 2018. Generalisation in humans and deep neural networks. Adv. Neural Inf. Process. Syst., *2018-Decem*, 7538–7550.

Goodfellow, I., Bengio, Y., and Courville, A., 2016. *Deep Learning* MIT Press.

Goodfellow, I., Pouget-Abadie, J., Mirza, M., Xu, B., Warde-Farley, D., Ozair, S., Courville, A., and Bengio, Y., 2014. Generative adversarial nets. Adv. Neural Inf. Process. Syst., *3*(January), 2672–2680.

He, K., Zhang, X., Ren, S., and Sun, J., 2016. Deep Residual Learning for Image Recognition. 2016 IEEE Conf. Comput. Vis. Pattern Recognit.

Hershey, S., Chaudhuri, S., Ellis, D. P. W., Gemmeke, J. F., Jansen, A., Moore, R. C., Plakal, M., Platt, D., Saurous, R. A., Seybold, B., Slaney, M., Weiss, R. J., and Wilson, K., 2017. CNN architectures for large-scale audio classification. ICASSP, IEEE Int. Conf. Acoust. Speech Signal Process. - Proc., 131–135.

Ioffe, S., and Szegedy, C., 2015. *Batch Normalization: Accelerating Deep Network Training by Reducing Internal Covariate Shift*.

Karahan, Ş., Yildirim, M. K., Kirtaç, K., Rende, F. Ş., Bütün, G., and Ekenel, H. K., 2016. How image degradations affect deep CNN-based Face recognition? Lect. Notes Informatics (LNI), Proc. - Ser. Gesellschaft Fur Inform., *P-260*.

Karras, T., Laine, S., and Aila, T., 2019. A style-based generator architecture for generative adversarial networks. Proc. IEEE Comput. Soc. Conf. Comput. Vis. Pattern Recognit., *2019-June*, 4396–4405.

Karras, T., Laine, S., Aittala, M., Hellsten, J., Lehtinen, J., and Aila, T., 2019. *Analyzing and Improving the Image Quality of StyleGAN*.

Kim, E., Dahiya, G. S., Løset, S., and Skjetne, R., 2019. Can a computer see what an ice expert sees? Multilabel ice objects classification with convolutional neural networks. Results Eng., *4*.

Kingma, D. P., and Ba, J., 2015. Adam: {A} Method for Stochastic Optimization. 3rd Int. Conf. Learn. Represent. (ICLR), Conf. Track Proceedings, Conf. Track Proc.

Lamme, V. A. F., Supèr, H., and Spekreijse, H., 1998. Feedforward, horizontal, and feedback processing in the visual cortex. Curr. Opin. Neurobiol., *8*(4), 529–535.

Loshchilov, I., and Hutter, F., 2019. Decoupled weight decay regularization. 7th Int. Conf. Learn. Represent. ICLR 2019.

Nair, V., and Hinton, G. E., 2010. Rectified linear units improve Restricted Boltzmann machines. ICML 2010 - Proceedings, 27th Int. Conf. Mach. Learn., 807–814.

Russakovsky, O., Deng, J., Su, H., Krause, J., Satheesh, S., Ma, S., Huang, Z., Karpathy, A., Khosla, A., Bernstein, M., Berg, A. C., and Fei-Fei, L., 2015. ImageNet Large Scale Visual Recognition Challenge. Int. J. Comput. Vis., *115*(3), 211–252.

Smith, L. N., 2018. *A disciplined approach to neural network hyper-parameters: Part 1 -- learning rate, batch size, momentum, and weight decay abs/1803.0*.

Srivastava, N., Hinton, G., Krizhevsky, A., Sutskever, I., and Salakhutdinov, R., 2014. Dropout: A simple way to prevent neural networks from overfitting. J. Mach. Learn. Res.,

15, 1929–1958.
Tieleman, T., and Hinton, G., 2012. Lecture 6.5-rmsprop: Divide the gradient by a running average of its recent magnitude. COURSERA Neural Networks Mach. Learn., *4*(2), 26–31.
Wang, L., Scott, K. A., Xu, L., and Clausi, D. A., 2016. Sea Ice Concentration Estimation during Melt from Dual-Pol SAR Scenes Using Deep Convolutional Neural Networks: A Case Study. IEEE Trans. Geosci. Remote Sens., *54*(8), 4524–4533.
WMO Sea-Ice Nomenclature 2014.

25th IAHR International Symposium on Ice
Trondheim, 23 - 25 November 2020

A Note on Remote Temperature Measurements with DS18B20 Digital Sensors

Chris Petrich[1,2], Irina Sæther[1], Nga P. Dang[1], Øystein Kleven[1], Megan O'Sadnick[1,3]
[1] *SINTEF Narvik, Narvik, Norway*
[2] *Ice Mate AS, Narvik, Norway*
[3] *UiT The Arctic University of Norway, Tromsø, Norway*
christian.petrich@sintef.no

Digital temperature sensors provide an attractive means to conveniently record ice and water temperatures in remote locations. Unlike conventional analogue techniques, a digital sensor performs a physical measurement, interprets its result in terms of temperature and transmits that result to a logger or display system in digital form. Processing of digital signals is comparatively robust and cheap. Custom calibration may be applied to increase measurement accuracy. A popular example of a digital temperature sensor is the Maxim Integrated DS18B20, which is readily available as a bare sensor in a standard transistor casing, or from third-part providers as a probe with the sensor encased in a waterproofed metal sleeve. We found that the quality of water protection of the probes varies widely, and that bare sensors and sensors in probes offered by most third-party providers (i.e. not by official distributors) are almost always clones, i.e. not produced by Maxim Integrated. We summarize in this paper the spectrum of counterfeit sensors currently available and how they differ from authentic parts and specifications in the Maxim Integrated data sheet. Currently sold sensors are grouped into 7 families, 6 of them representing counterfeits. Awareness of the prevalence and characteristics of counterfeit sensors will help avoid surprises during costly experimental field work.

1. Introduction

Digital sensors are attractive peripherals in environmental data acquisition systems as they remove the challenge of temperature compensation from the logger design. By allowing all-digital logging solutions, logger designs become comparatively cheap and simple. In many cases it is also possible to connect several sensors to the same data bus, thereby greatly reducing the number of wires required for strings of sensors (e.g., I2C, 1-Wire, SDI-12 protocols). One popular digital temperature sensor is Maxim Integrated DS18B20, which is the successor of the DS1820 (Maxim 2009), both of which had been developed and produced by Dallas Semiconductor prior to its acquisition by Maxim Integrated. The DS18B20 has been produced for approximately 20 years and is used in commercially available sea ice buoys and individual research projects (e.g., Cui et al., 2015; Hills et al., 2018; Planck et al., 2019). Our group has used DS18B20 temperature sensors in an ice-borne temperature string since 2013 (Petrich et al., 2014), and at a much larger scale in ocean applications and construction projects since 2018 (e.g., Petrich et al., 2019). The prevalence of counterfeit DS18B20 sensors became apparent to us in the context of the most recent measurement series when we started to reject probes for their poor signal-to-noise performance. Following our initial suspicion, a systematic attempt was made with the support of Ice Mate AS to survey the state of counterfeit DS18B20 as of 2019. The main result of this study is a list of characteristics that is backed up by observations on large numbers of sensors.

Maxim Integrated temperature sensors DS18B20 integrate a bandgap-based thermal circuit with an analogue-to-digital converter, temperature calibration unit, and digital communication circuitry (Maxim, 2019). The manufacturer states an absolute temperature accuracy of ±0.5 °C over the temperature range from -10 to +85 °C while the operating range extends from -55 to +125 °C with ±2 °C accuracy. The temperature resolution is 0.0625 °C. The remaining temperature error vs. temperature relationship is parabolic (Maxim, 2013). This characteristic of all bandgap-based sensors allows for higher order correction in post-processing to increase the temperature accuracy. The sensors expose three pins: ground, supply voltage, and bi-directional data transfer. The low power requirements and integrated capacitor allows them to operate in “parasitic power mode” where the supply voltage pin is tied to the ground pin and the chip derives its power from the data line. Each sensor contains a unique 64-bit address (called ROM by the manufacturer) which allows communication with multiple sensors on the same data bus. The sensors are available in a TO-92 case among other options. The TO-92 case is a flattened cylinder of approximately 5 mm height and diameter. There are many third-party suppliers that will produce waterproof probes by soldering wires to the sensor, placing the sensor in a 6 mm outer diameter metal sleeve and waterproofing the connection with epoxy, glue, heat shrink, or a combination of those. Those waterproof probes can be bought on eBay often for less than the costs of a sensor from a Maxim-authorized retailer (based on prices for individual sensors).

DS18B20 sensors communicate through the 1-Wire protocol that allows multiple sensors to share the same data bus. Communication is always initiated by a bus controller (e.g., Dallas, 2019). The bus controller begins by sending a 0.5 ms reset pulse followed by the “Match ROM” command byte and the ROM code of the sensor it wants to communicate with. Subsequent communication will be between the bus controller and the sensor addressed until another ROM command is sent. Each interaction with the sensor begins with a reset pulse, followed by a function code, followed either by additional data from the bus controller or by clock signals from the bus controller and data from the sensor in response. A peculiarity of the protocol is that sending clock signals is indistinguishable from sending hexadecimal data

0xFF, and receiving no response is indistinguishable from receiving a 0xFF response. While this is not a limitation when communications follow documented protocol, it does affect attempts to reverse engineer sensor behavior. The 1-Wire protocol also includes a mechanism for the bus controller to discover the ROM codes of all sensors attached to the bus.

To receive a temperature measurement, the bus controller sends a function code that makes the sensor initiate measurement and data conversion. Following this, the bus controller can either query the sensor for completion of the data conversion or wait the maximum time for data conversion specified in the datasheet (i.e., 750 ms; Maxim, 2019). Temperature data are retrieved by sending a "Read Scratchpad" function code and receiving 9 bytes of data: the temperature measurement (bytes 0 and 1), two alarm registers (bytes 2 and 3), a configuration register (byte 4), three reserved bytes (bytes 5, 6, and 7), and a checksum (byte 8). The configuration register specifies whether the sensor operates with 9-bit (fastest), 10, 11, or 12-bit (slowest) resolution. The reserved bytes are useful to identify counterfeit sensors. Bytes 2, 3, and 4 can be overwritten by the user and stored in an EEPROM on the DS18B20. The temperature stored in bytes 0 and 1 between power-up and the first successful temperature conversation is 85 °C (Maxim, 2019).

There is no uniform definition of counterfeit parts across engineering and legal domains (cf. AIR6273). According to the definition of AIR6273 (2019), a counterfeit electrical part is "an unauthorized (a) copy, (b) imitation, (c) substitute, or (d) modified materiel or [electronic] part, which is knowingly, recklessly, or negligently misrepresented as a specified genuine item from an authorized manufacturer; or a previously used materiel or [electronic] part which has been modified and is knowingly, recklessly, or negligently misrepresented as new without disclosure to the customer that it has been previously used.". According to our survey in this study, the main problem affecting DS18B20 sensors are imitations (clones) that are misrepresented as genuine parts.

Throughout this paper we will distinguish between DS18B20 sensors (Figure 1a) and waterproof probes that contain DS18B20 sensors (Figure 1b). With the exception of one subsection in the Discussion, this manuscript is about DS18B20 sensors, whether sold separately or encased in a probe.

2. Methods

Over 1000 waterproof probes and sensors were purchased from over 70 different vendors on eBay, AliExpress, Amazon, or Alibaba, in addition to Maxim-authorized international retailers including Digikey, Mouser, Farnell, and RS-Electronics, regionally-focused retailers including Reichelt and Conrad Electronics, Elfa Distrelec, or Elektroimportøren, an authorized retailer for DS18B20 clones, LCSC, independent stores such as Kjell & Co, TELMAL, DROK, YourDuino, SparkFun, Adafruit and Banggood, and speciality vendor Quest Components.

To characterize sensor performance and calibration, an Arduino Uno was used to communicate with the sensor using the 1-Wire library "OneWire", Version 2.3, maintained by Jim Studt and Paul Stoffregen. Sensors were powered at 5 V, and a 1.2 kOhm pull-up resistor was used on the data line. Sensors were powered through the sensor supply voltage pin except while testing the performance in parasitic power mode.

We performed temperature calibration measurements in an ice–water bath in a thermos flask at nominally 0 °C on hundreds of sensors. The data were automatically evaluated for average, and standard deviation (i.e., discretization noise), and drift was checked for quality control. We followed Mangum (1995) for the preparation of the ice–water bath. Temperatures were polled every 10 seconds during sensor calibration, which avoided signs of self-heating (based on our tests, polling every second resulted in measurable self-heating of one discretization step of up to 0.06 °C). Measurements were repeatable to within the measurement resolution of the sensors.

The following had been recorded systematically for the classification of sensors: the ROM code, scratchpad register start-up values and content of reserved bytes, time required for temperature measurement, response to undocumented function codes, response to power cycling, and performance in parasite power mode. In addition, a small subsample was used to assess electrical performance (skipped here due to space), and to photograph the die (i.e., the electronic circuit). In order to prepare a die, we broke the TO-92 case open with pliers and detached the die from the plastic case by boiling in colophony, removed the colophony with acetone, and cleaned the die in acetone ultrasonically. Photos were taken with a USB camera.

3. Results

The sensors tested fall naturally into seven groups, henceforth referred to as families. In our naming convention, the family letter indicates the pattern of undocumented function codes.

3.1 Sensor Families

3.1.1 Family A1: Authentic Maxim

- ROM pattern: 28-xx-xx-xx-xx-00-00-xx
- Package label lasered.
- Indent mark: “P” or “THAI <letter>”. All current sensors are marked “P”.
- At 0 °C, the average temperature error is smaller and of different sign and the spread between devices is less than suggested by the datasheet.
- Startup value of reserved byte 6 of the scratchpad register is 0x0C.
- Following a successful temperature conversion, reserved byte 6 of the scratchpad register is: <byte 6> = 0x10 – (<byte 0> & 0x0F)
- Two calibration parameters (Trim1, Trim2) can be read with undocumented function codes 0x93 and 0x68, respectively (Maxim, undated). Parameter spreads over approximately 20 units within a batch.
- Default alarm register setting: 0x4B, 0x46
- Time for temperature conversion (Figure 3c): 584 to 615 ms at 12 bits.

There are also authentic chips being sold by unauthorized sources that have their calibration parameters (and alarm and configuration registers) set to 0x00. Until set to reasonable values, those sensors report temperatures around -39 °C at room temperature, and too low conversation times even at 12-bit resolution (cf. Figure 3c, section A1).

3.1.2 Family A2

- ROM pattern: 28-00-xx-00-xx-xx-xx-xx, 28-xx-00-xx-xx-xx-xx-xx, 28-xx-00-00-xx-xx-00-xx
- Package label is printed, indent is unmarked.
- <byte 6> behavior as Family A1
- Two calibration parameters (Trim1, Trim2) can be read with undocumented function codes 0x93 and 0x68, respectively. Parameter spreads over approximately 200 units.

- Random content of alarm registers.
- Some samples retain scratchpad content over a 100 ms power cycle.
- Default alarm register setting: 0x4B, 0x46
- Time for temperature conversion (Figure 3c): 325 to 502 ms at 12 bits.

3.1.3 Family B1

- ROM pattern: 28-AA-xx-xx-xx-xx-xx-xx (GXCAS), 28-xx-xx-xx-xx-xx-xx-xx (UMW)
- Package label is printed, indent is unmarked. Some chips are marked GXCAS or UMW rather than DALLAS (cf. Figure 1a).
- <byte 6> and <byte 7> can be overwritten with the "Write Scratchpad" function (UMW, undated)
- Does not return data on function code 0x68. Does return data following function codes 0x90, 0x91, 0x92, 0x93, 0x95, and 0x97. Response to 0x97 is 0x22.
- Last 7 bytes of ROM code can be overwritten with command sequence "96-Cx-Dx-94"
- Default alarm register setting: 0x4B, 0x46
- Time for temperature conversion (Figure 3c): 589 to 728 ms at 12 bits.

3.1.4 Family B2

- ROM pattern: 28-FF-xx-xx-xx-xx-xx-xx
- Package label is printed, indent is unmarked. Some chips are marked 7Q-Tek rather than DALLAS (cf. Figure 1a).
- <byte 6> and <byte 7> can be overwritten with the "Write Scratchpad" function (7Q-Tek, undated)
- Does not return data on function code 0x68. Does return data following function codes 0x90, 0x91, 0x92, 0x93, 0x95, and 0x97. Response to 0x97 is 0x31.
- ROM code cannot be overwritten with command sequence "96-Cx-Dx-94"
- Default alarm register setting: 0x4B, 0x46
- Time for temperature conversion (Figure 3c): 587 to 697 ms at 12 bits.

3.1.5 Family C

- ROM pattern: 28-FF-64-xx-xx-xx-xx-xx
- Package label is printed, indent is unmarked.
- <byte 6> is fixed at 0x0C.
- Configuration byte <byte 4> is fixed at 0x7F, i.e., 12-bit resolution.
- EEPROM endures only approximately 8 write cycles.
- Does not return data on any undocumented function code.
- Default alarm register setting: 0x55, 0x00
- Time for temperature conversion (Figure 3c): 28 to 30 ms.

3.1.6 Family D1

- ROM pattern: 28-xx-xx-77-91-xx-xx-xx, 28-xx-xx-46-92-xx-xx-xx
- Package label is printed, indent is unmarked.
- <byte 7> defaults to 0x66 (vs. 0x10 according to Maxim (2019))

- Does not return data on function code 0x68. Does return data or shows reaction following function codes
    - 0x4D, 0x8B (8 bytes), 0xBA, 0xBB, 0xDD (5 bytes), 0xEE (5 bytes), or
    - 0x4D, 0x8B (8 bytes), 0xBA, 0xBB.
- First byte following undocumented function code 0x8B is
    - 0x06: Sensors do not work with Parasitic Power. Sensors leave data line floating when powered parasitically.
    - 0x02: Sensors do work in parasitic power mode (and report correctly whether they are parasitically powered).
- ROM code can be overwritten following undocumented function code 0xA3. The family code (0x28) can also be changed.
- Reserved <byte 5>, <byte 6>, and <byte 7> can be overwritten following undocumented function code 0x66.
- Chips contain a supercapacitor rather than an EEPROM to hold alarm and configuration settings. I.e., the last temperature measurement and updates to the alarm registers are retained between power cycles for seconds to minutes.
- Default alarm register setting: 0x55, 0x05
- Default temperature reading: 25 °C (rather than 85 °C)
- Time for temperature conversion (Figure 3c): 11 ms regardless of specified resolution.
- Poor calibration accuracy at 0 °C (Figure 3a).
- Temperature readings fluctuate significantly (Figure 3b).

3.1.6 Family D2

- ROM pattern: 28-xx-xx-79-97-xx-xx-xx, 28-xx-xx-94-97-xx-xx-xx, 28-xx-xx-97-A2-xx-xx-xx, 28-xx-xx-16-A8-xx-xx-xx
- Package label is printed, indent is unmarked.
- <byte 7> defaults to 0x66 (vs. 0x10 according to Maxim (2019))
- Does not return data on function code 0x68. Does return data or shows reaction following function codes
    - 0x4D, 0x8B (9 bytes), 0xBA, 0xBB, 0xDD (3 bytes), 0xEE (3 bytes), or
    - 0x4D, 0x8B (8 bytes), 0xBA, 0xBB.
- First byte following undocumented function code 0x8B is 0x00.
- Sensors do not work with Parasitic Power. Sensors pull the data line low when powered parasitically.
- Default alarm register setting: 0x55, 0x05
- Default temperature reading: 25 °C (rather than 85 °C)
- Time for temperature conversion (Figure 3c) is independent of specified resolution:
    - "-79-97-" and "-94-97-" ROM codes: 494-523 ms, and
    - "-97-A2-" and "-16-A8-" ROM codes: 462-486 ms
- Poor calibration accuracy at 0 °C (Figure 3a).

3.2 Dies and Manufacturers

According to the markings on the die (Figure 4), Family B1 and B2 are produced by GXCAS (Beijing Zhongke Galaxy Core Technology Co., Ltd.) and 7Q-Tek (Beijing 7Q Technology Inc.), respectively. Some sensors obtained were marked on the case GXCAS or UMW (Family B1), or 7Q-Tek (Family B2) instead of DALLAS. While the origin of the die of Family A2 is unknown, we note the visual resemblance with the style of families A1 and B2, and that the measured conversion time is compatible with the specifications on the 7Q-Tek QS18B20 datasheet (7Q-Tek, undated). The dies of Families D1 and D2 resemble each other, indicating the same origin (Figure 4). The die of Family C is not related to any of the other design efforts shown in Figure 4.

4. Discussion

4.1 Temperature Performance

Figure 3a shows that most sensors available in 2019 gave reasonable readings at 0 °C, although not necessarily within the specified error limit of 0.5 °C. The most notable exceptions are in Families A2 and D1. Noise level in Figure 3b is at the discretization limit except for Families D1 and D2, i.e. the usable resolution of those sensors is below 12 bits. The time for temperature conversion in Figure 3c differs between Families but was below the datasheet-specified 750 ms for all sensors.

Families A2 and D1 are practically obsolete while Family D2 is very common and thus of potential concern. Notable are high temperature offsets of +0.8 °C seen in some sensors of Family A1. Those measurements are reproducible and come from sensors that were bought from third-party vendors with uncertain handling history. The comparatively low conversion times of some Family A1 sensors were third-party supplied sensors with invalid calibration constants (Trim1 and Trim2), which are unlikely to be encountered.

4.2 Power-up Reading vs. Valid Measurement

After power-up and before the first valid temperature conversion, Maxim-produced DS18B20 and many counterfeits will return a temperature of 85 °C (Maxim, 2019), which is well within the operating range of the sensor. In chips of Family A, the power-up temperature reading can be distinguished from a valid temperature reading in a simple and undocumented manner. Upon power-up, <byte 6> of the scratchpad register is initialized to 0x0C. After a successful temperature measurement of 85 °C it is 0x10.

4.3 Quality of Waterproofing of Probes

Waterproofing is tangential to this study and not related to the question of whether or not a sensor is counterfeit. However, it is highly relevant for operation in saltwater environments. Figure 2 shows examples of the content of the metal cylinders used to provide waterproofing. We found that the spectrum includes a wide range from no waterproofing apart from heat shrink on the outside of the cylinder, to the use of a glue gun, and solid epoxy fill of the cylinder. Also, the quality of the outer heat shrink varied considerably. We submerged a small sample of 8 probes purchased from different vendors in 10 cm of saltwater for 2 months. 3 probes failed after 10 hours, 2 more probes failed after 10 days, the remaining probes operated through the end of the test. Also, we have successfully operated waterproofed probes in a fjord environment for 10 months (cf. Petrich et al., 2019). These observations highlight the importance of testing the quality of the waterproofing of those probes that are to operate in saltwater environment.

4.4 Obsolete Counterfeits

Based on web searches we are aware of counterfeit DS18B20 with the following ROM patterns:

- 28-61-64-xx-xx-xx-xx-xx, and
- 28-xx-xx-xx-00-00-80-xx.

However, in spite of a large number of purchases, we were not able to obtain sensors with these ROM patterns in 2019, leading us to believe that they are obsolete.

5. Conclusion

The results of a market survey of counterfeit DS18B20 sensors and waterproof probes containing DS18B20 sensors are presented. We found that counterfeit sensors are easy to identify and to classify by performance. A significant fraction of counterfeit sensors (i.e., Families D1 and D2) had temperature calibration problems and a signal-to-noise ratio that exceeded that of authentic Maxim Integrated-produced DS18B20 sensors. Those should be avoided in a research setting.

As of 2019, the simplest (and apparently sufficient) test questions for authenticity of a recently produced DS18B20 sensor are: does the indent on the case show the letter “P”? And does the ROM code follow the pattern 28-xx-xx-xx-xx-00-00-xx? However, other metrices should be tested (e.g., the value of <byte 6> of the scratchpad register (Section 3.1.1)) since some sensors allow the ROM code to be changed. Test software is available from the repository at https://github.com/cpetrich/counterfeit_DS18B20.

As a side-effect of our investigations we identified an undocumented mechanism to distinguish the power-up temperature reading from successful temperature measurements.

We suggest that, until tested, one should assume that every sensor bought from a third-part retailer is counterfeit, and that every waterproof probe contains a counterfeit sensor. There are few exceptions to this rule. The quality of waterproofing of probes also varies widely. Acquisition of waterproof probes that are epoxy-filled and use authentic, Maxim-produced DS18B20 sensors requires time and money to identify sources and test the products.

Producing integrated circuits involves high up-front costs. The existence of several manufacturers that currently produce DS18B20 clones (i.e., counterfeits) is evidence of the relevance of digital temperature sensors for industrial applications, research, and hobby. Since the performance of the counterfeits varies widely, awareness of their prevalence is needed to avoid unpleasant surprises.

Acknowledgments

The presentation of this work was supported by the Research Council of Norway through the SFI Center for Integrated Remote Sensing and Forecasting in the Arctic (CIRFA), grant number 237906. Ice Mate AS provided most of the sensors for testing as well as probes containing authentic sensors.

References

7Q-Tek, undated. QT18B20 Programmable Resolution 1-Wire Digital Thermometer. Datasheet Rev 061713, 7Q Technology, 22pp.

AIR6273, 2019. Terms, Definitions, and Acronyms Counterfeit Materiel or Electrical, Electronic, and Electromechanical Parts. SAE Aerospace Information Report, July 2019, 8pp.

Cui, L., J. Qin, and X. Deng, 2015. Freshwater ice thickness apparatus based on differences in electrical resistance and temperature. Cold Regions Science and Technology, 119, 37-46, https://doi.org/10.1016/j.coldregions.2015.07.009.

Hills, B.H., J.T. Harper, T.W. Meierbachtol, J.V. Johnson, N.F. Humphrey, and P.J. Wright, 2018. Processes influencing heat transfer in the near-surface ice of Greenland's ablation zone. The Cryosphere, 12, 3215–3227. https://doi.org/10.5194/tc-12-3215-2018.

Mangum, B.W., 1995. Reproducibility of the Temperature of the Ice Point in Routine Measurements. NIST Technical Note 1411. US Department of Commerce Technology Administration. 32 pp.

Maxim, 2009. Comparison of the DS18B20 and SD18S20 1-Wire Digital Thermometers. Application Note 4377, Maxim Integrated, 18 March 2009, 3 pp.

Maxim, 2013. Curve Fitting the Error of a Bandgap-Based Digital Temperature Sensor. Application Note 208, Maxim Integrated, 20 June 2002, 4 pp.

Maxim, undated. DS18x20 EEPROM Corruption Issue - Failure Description and Patch Recommendations. Application Note 247, Tag 040204, Maxim Integrated, 2 pp.

Maxim, 2019. DS18B20 Programmable Resolution 1-Wire Digital Thermometer. Datasheet. Maxim Integrated, Rev. 6, July 2019, 20 pp.

Petrich, C., I. Sæther, L. Fransson, B. Sand, and B. Arntsen, 2014. Preliminary Results from Two Years of Ice Stress Measurements in a Small Reservoir. In Proceedings of the 22nd IAHR International Symposium on Ice, Singapore, 11-15 August 2014, 8 pp.

Petrich, C., M. O'Sadnick, Ø. Kleven, I. Sæther, 2019. A low-cost coastal buoy for ice and metocean measurements. In Proceedings of the 25th International Conference on Port and Ocean Engineering under Arctic Conditions (POAC), 9-13 June 2019, Delft, The Netherlands, 6 pp.

Planck, C.J., J. Whitlock, C. Polashenski, and D. Perovich, 2019. The evolution of the seasonal ice mass balance buoy. Cold Regions Science and Technology, 165, 102792, https://doi.org/10.1016/j.coldregions.2019.102792.

UMW, undated. UMW DS18B20. Datasheet, 22pp, in Mandarin.

Figures

(a) 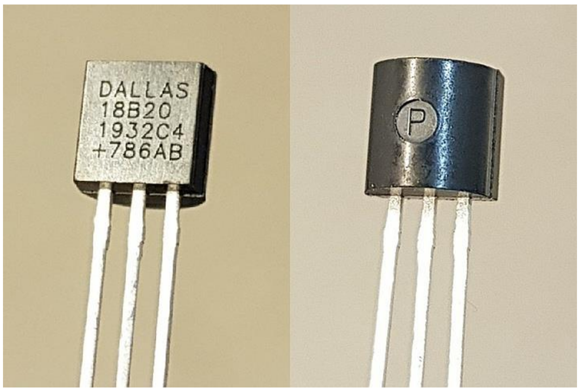

(b) 

Figure 1. (a) Maxim-produced DS18B20 sensor in TO-92 case (approx. 5 mm high), and (b) waterproof probe with 6 mm o.d. metal cylinder containing a DS18B20 sensor and cable attached.

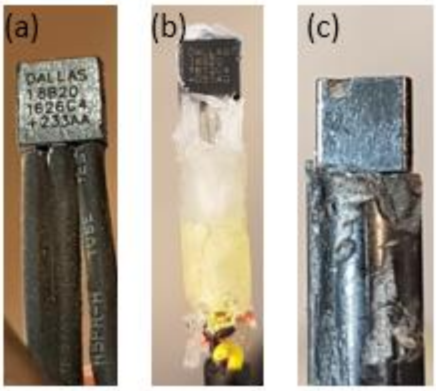

Figure 2. Example fill used inside the metal cylinders of waterproof DS18B20 probes: (a) air-fill, (b) glue gun-fill, and (c) epoxy-fill. All sensors are counterfeit, and (c) had been nicked during the opening of the cylinder.

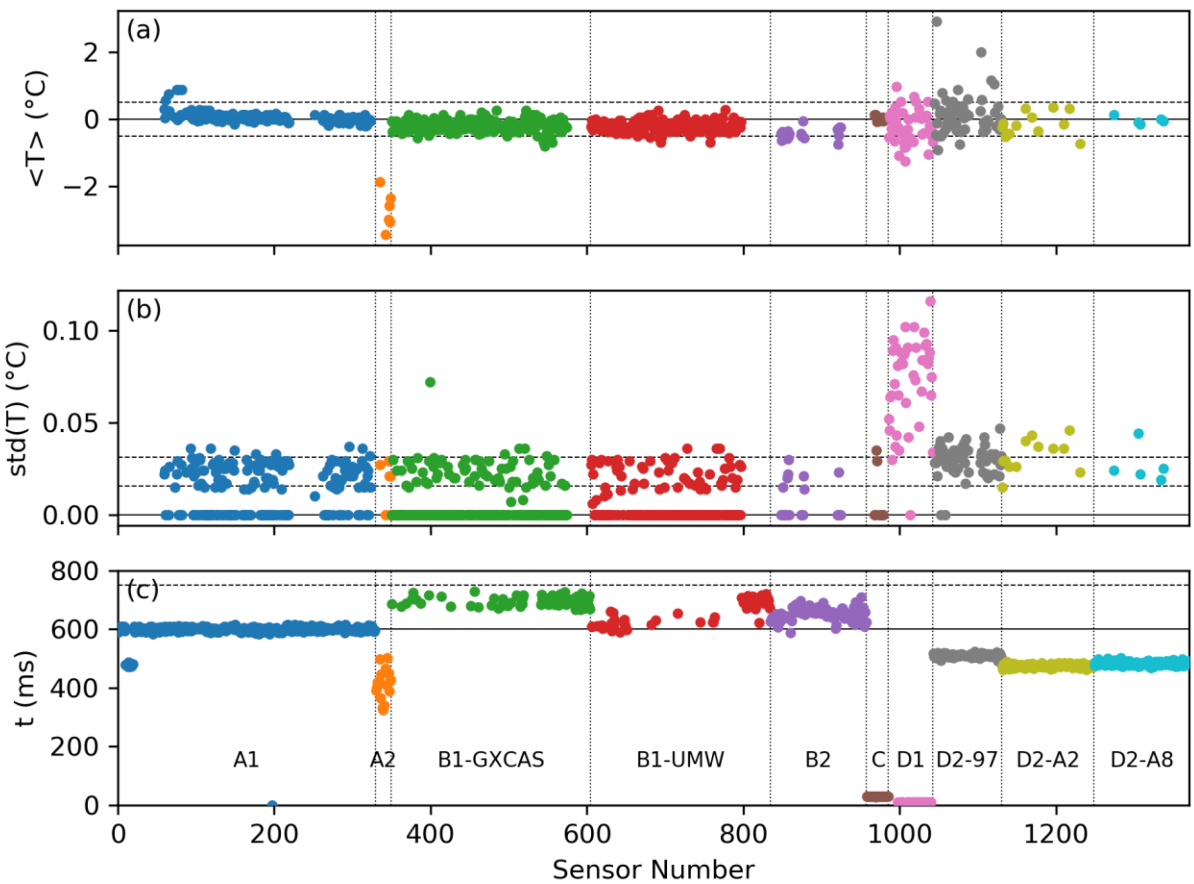

Figure 3. (a) Average temperature reading at 0 °C, (b) standard deviation of temperature readings at 0 °C (typically N=15 samples), and (c) reported time required for temperature conversion. Dashed lines indicate (a) allowable range according to data sheet, (b) expected standard deviation for fluctuations 1:14 and 1:2, (c) maximum time according to datasheet.

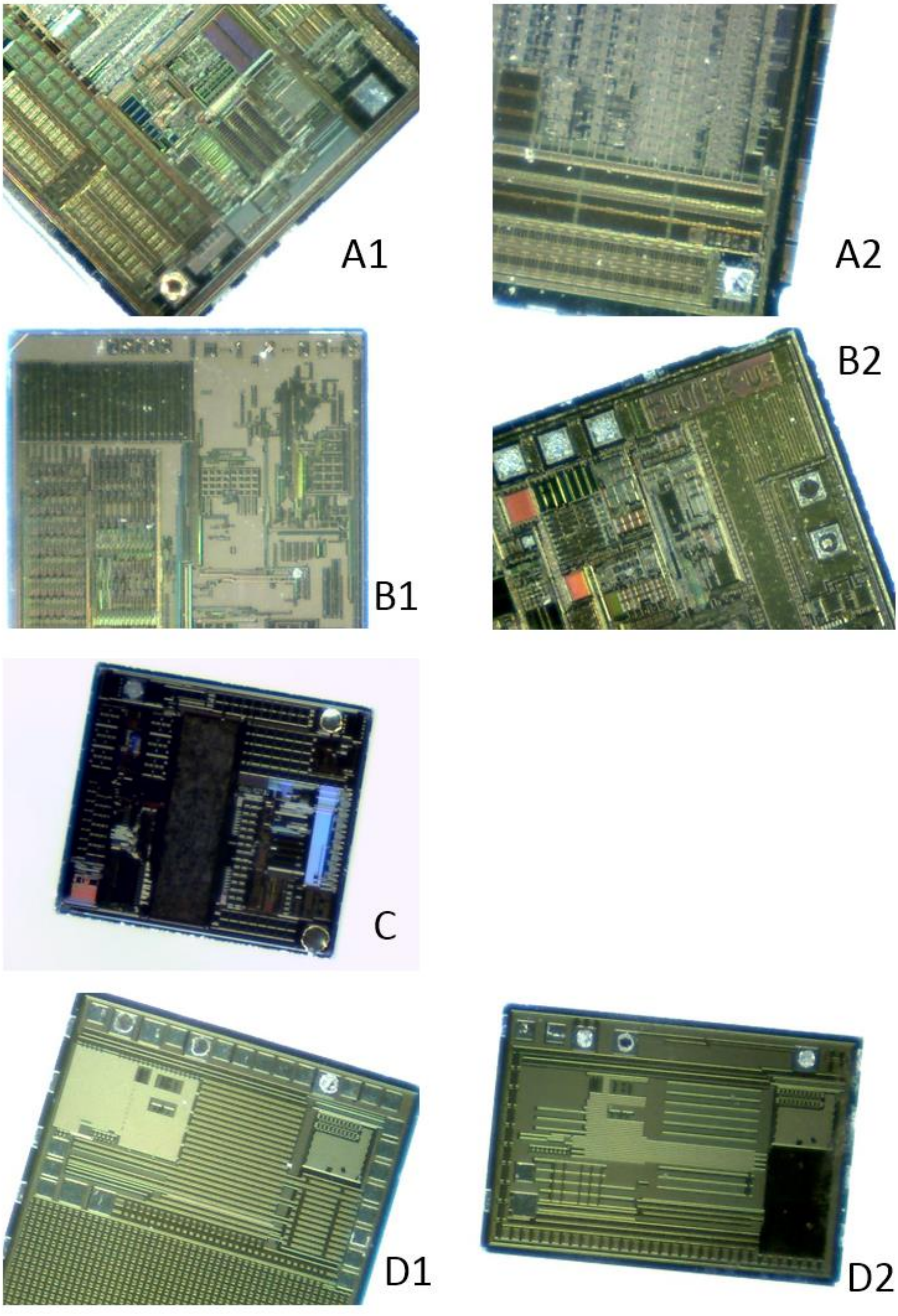

Figure 4. Photos of dies of Families A1, A2, B1, B2, C, D1, and D2. The width of each photo is approximately 1.4 mm.

25th IAHR International Symposium on Ice
Trondheim, 23 - 25 November, 2020

Comparison of in-situ measurements from the Norströmsgrund lighthouse to Copernicus reanalysis products

Joshua Dennis Turner[1], Knut Vilhelm Høyland[1], Vegard Hornnes[1], Ersegun Deniz Gedikli[1,2]
[1]*Department of Civil and Environmental Engineering, Norwegian University of Science and Technology, Trondheim, Norway*
[2]*Department of Ocean and Resources Engineering, University of Hawaii at Manoa, Honolulu, USA*
joshua.d.turner@ntnu.no

Here, we aim to extend the full-scale data measurements of ice conditions and the resulting structure behaviour at the Norströmsgrund lighthouse to other locations in the Baltic Sea via comparison to the met-ocean conditions from Copernicus reanalysis products. The sea ice velocity produced by the global reanalysis product of the Copernicus Marine Environment Monitoring Service compares favourably to the measurements taken at Norströmsgrund, producing a skewed lognormal similar to the distribution observed during the measurement campaigns. The sea ice thickness from the reanalysis is less applicable; the inspected model produces estimates of level ice thickness near Norströmsgrund over an area of approximately 9.3 km x 3.9 km, averaging out the effect of ridges and leads. A transformation from level ice statistics to first year ice statistics is thus required for application to other locations in the Baltic Sea. Atmospheric reanalysis of air temperature, barometric pressure, wind speed, and wind direction match perfectly over a much larger area (approximately 83 km x 35 km near the Norströmsgrund lighthouse). Comparison to met-ocean conditions both on-site and via Copernicus reanalysis products show some evidence that frequency lock-in events are connected to changes in local conditions; further analysis is required for confirmation.

1. Introduction

The effective design of offshore structures in ice-infested waters requires detailed knowledge of both the met-ocean conditions in the region and the expected loading response produced by such conditions. Design estimates are generally based on full-scale data previously gathered during ice-structure interactions (ISIs). This is both costly and of limited use; data gathered in such a way is only technically accurate for the specific structure and met-ocean conditions observed. Extending these limited data sets to other locations and structure designs is not without difficulty; the first step alone requires understanding how the met-ocean conditions at a given site produce the observed loading conditions, an as-yet unsolved problem.

Particular attention must be paid to the occurrence of ice-induced vibrations (IIVs). These vibrations make standard operations more dangerous for on-site personal and, in extreme cases such as the KEMI-1 lighthouse in the Gulf of Bothnia, can lead to the complete failure of the structure (Määttänen, 1975). ISO 19906 (2019) separates IIVs into three regimes of interest: intermittent crushing (IC) at low ice speeds; frequency lock-in (FLI) at intermediate ones; and continuous brittle crushing (CBC) during high speed interactions (Yue et al., 2009). FLI events are the most extreme form of ice-structure interaction. During FLI the structure vibrates at or near one of its natural frequencies and undergoes high-amplitude, periodic oscillations far in excess of what the loading conditions would normally indicate. This induces significantly more fatigue stress in structural members than would otherwise be expected. Predicting FLI events is therefore of great concern to the design of offshore structures.

Full scale measurements of ice-structure interactions are limited in space and time. Met-ocean model data covers oceans world-wide, dating back to the 1900s in some cases. Correlations between model data and in-situ ice measurements that could be applied to other locations of interest would be highly useful to the design of offshore structures. The "Measurements on Structures in Ice" (STRICE) measurement campaign at the Norströmsgrund (NSG) lighthouse was chosen as the basis for this investigation due to its extensive data collection and the noted occurrence of IIV events. The time period of the campaign (2000-2003) coincides with the period modelled by the marine and atmospheric reanalysis products of Copernicus (1993-2018 and 1979-2019, respectively), allowing for a direct comparison of model results and in-situ measurements.

a) b)

Fig. 1. (a) Map of the Baltic Sea with location of NSG lighthouse noted, and (b) NSG lighthouse after ice-structure interaction.

2. Data Description

2.1. In-situ Measurements

Extensive full-scale field measurements were gathered at the NSG lighthouse from 1999-2003 during the "Validation of Low Level Ice Forces" (LOLEIF) and STRICE projects (Schwarz, 2001). The site itself is described in Jochmann and Schwarz (2000a). In short: the lighthouse is located within the Bay of Bothnia at 65°6.6' N and 22°19.3' E at the edge of the landfast ice zone off the coast of Luleå, Sweden, approximately 20 km from the nearest shoreline, as shown in Figure 1a). The lighthouse stands at 42.3 m, with the waterline at approximately 13 m. The diameter at the waterline, including load panels, is 7.52 m (Note that later sources consistently state that the diameter at the water line is 7.58 m. See Bjerkås et al., 2003 for an example).

The exact location and specifications of the instrumentation, and the measurements taken with said instrumentation, changed from year-to-year. Li (2015) provides the complete history of the measurement campaign, as well as a discussion of the difficulties these changes present to the analysis of the NSG measurements. Of particular note is the method with which ice drift was measured; cameras were used to manually measure ice velocity by tracking conspicuous ice features across a 10 m x 10 m grid displayed on a screen (Jochmann and Schwarz, 2000b). Measurements were sporadic and heavily biased; see Hornnes et al. (2020) for further discussion and a detailed description of the steps necessary to prepare the sea ice velocity and thickness data for analysis. Ice loads were measured directly by nine panels covering 162 deg of the perimeter. An electromagnetic (EM) ice thickness sounding device was installed during the LOLEIF project. The device was suspended by a horizontal scaffold boom and extended 10 m from the lighthouse minimize disturbances from the existence of said lighthouse. The EM device was suspended approximately 2 m above the sea ice, out of consideration for the measurement resolution as well as to avoid collisions with ridges. The EM device was replaced by a sonic distance meter for the winter of 2003 (Haas and Jochmann, 2003). Wind speed and air temperature were measured approximately 28 m and 20 m above sea level, respectively, during the winters of 2002 and 2003.

The data gathered during the LOLEIF and STRICE projects has been thoroughly investigated in the nearly two decades since. Focus was on analyzing FLI events. Bjerkås et al. (2013) analyzed the FLI event of March 30, 2003, one of the longest and harshest events observed during the measurement campaign. Spatial synchronization of high-pressure zones (hpzs) was found to trigger the lock-in event, consistent with the laboratory results of O'Rourke et al. (2016). Bjerkås et al. (2014) showcased a method to estimate the number of vibration cycles during a FLI event, a necessary component of fatigue evaluations.

Nord et al. (2018) documented the occurrence of 61 resonant vibrations that match the criteria for FLI events postulated by ISO 19906 except they seldom reach a steady state, indicating that a sinusoidal response may not be a necessary condition for FLI. Therefore, to highlight the strict formulation of the ISO, Nord et al. (2018) called these resonant events, without any constraint put on the underlying mechanical system. Here these resonant events will also be referred to as FLI events, for ease of discussion. Events were selected based on the existence of a dominant response frequency, generally between 2.2 and 2.4 Hz. FLI was found to occur under a wide range of conditions, for all types of ice (level, rafted, ridged) observed at NSG. Bjerkås and Gedikli (2019) used the met-ocean conditions during these events to predict days where FLI events were more probable. The method was found to over-predict, perhaps indicating that the met-ocean conditions alone are a necessary but insufficient indicator of FLI events.

2.2. Model Data

The European Union's (E.U.) Copernicus program consists of six services. Here only two are relevant: 1) the Copernicus Marine Environment Monitoring Service (CMEMS), which provides regular and systematic reference info on the world's oceans and regional seas, and; 2) the Copernicus Atmosphere Monitoring Service (CAMS), which provides continuous data on atmospheric composition worldwide.

Together, these two services provide hundreds of different products which fill a wide range of needs. Linking these model outputs to full-scale observations would be useful for design worldwide. Products examined here are the Global Reanalysis data of CMEMS (E.U., 2020b) and the ERA-Interim data of CAMS (ECMWF, 2019). The global reanalysis product outputs data at noon daily every 1/12° of latitude and longitude. Higher resolution is available through the Baltic Reanalysis product (E.U., 2020a), but difficulties with the ice thickness output and lack of ice drift data led to the adoption of the global model. The ERA-Interim model outputs every 3/4° with a period of six hours. For a more detailed description of the respective models please refer to Garric et al., 2017 and Dee et al., 2011.

The two models provide numerous output parameters. We are interested in parameters that can be directly compared to those measured at NSG, namely sea ice (thickness and velocity) and some atmospheric (temperature, velocity, and pressure) parameters. Sea ice thickness and velocity were output at the grid cells sea surface height. Model wind speed and air temperature were output at heights of 10 m and 2 m, respectively.

3. Results

3.1. The Baltic Sea

To provide a baseline for comparison, statistics for the relevant parameters were examined across the entire Baltic Sea and its various sub-regions. Several restrictions were placed on the examined data. First, grid cells with a sea ice thickness less than 0.1 m were ignored, as at this thickness sea ice can be safely differentiated from open ocean and becomes strong enough to be relevant to ISIs (Leppäranta, 2005). Secondly, a lower limit of 5 mm/s (Oikkonen et al., 2016) was applied to total sea ice velocity to remove grid cells containing landfast ice, which is expected to play little role in the fatigue life of a structure. Sea ice conditions that meet these criteria will be referred to as drift ice throughout the text. Figures 1a) and b) illustrate the probability distribution functions for ice concentration (C) and thickness (h) within various regions of the Baltic Sea. Some regions show multipeak behavior characteristic of seasonal and regional variations. The secondary peak in sea ice concentration at 0.2 seems to be related to the restriction placed on ice thickness; 0.1 m thick ice appears to be normally distributed around a sea ice concentration of 0.2. Some grid cells erroneously report ice concentrations greater than 1. They are corrected to 1 during further analysis.

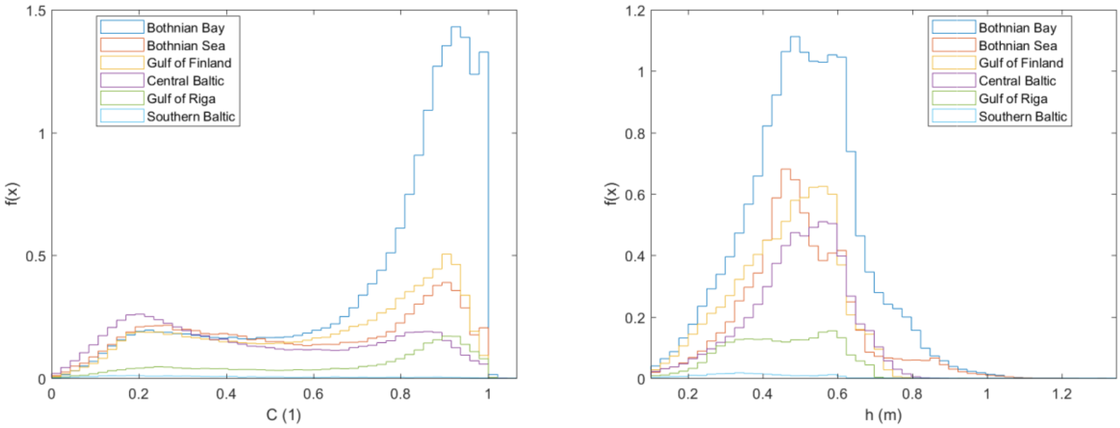

a) b)

Fig. 1. Model sea ice concentration (a) and thickness (b) within regions of the Baltic Sea. Bin counts are normalized such that the sum of the area under all histograms equals one.

Figure 2a) illustrates the regional composition of ice drift direction. Ice in the Gulf of Finland travels predominantly towards the east, as expected due to the geography of its coastline. Ice in the rest of the Baltic travels mostly in the north-northeast and south-southwest directions. Little to no ice drift is observed heading west due to the prevailing wind conditions in the Baltic Sea, which proceed predominantly towards the northeast and south-southwest. Ice velocity distributions are best presented via polar probability distribution functions (pdfs) of the type shown in Figure 2b). Quintile-based speed bands are used to capture the lognormal nature of the ice speed distribution. Notable changes in trends occur with increasing speed; high-speed ice is found to drift predominantly to the south-southwest and north-northeast. The Bothnian Bay, in which the NSG lighthouse is located, contains the highest concentrations of ice in the Baltic Sea, the thickest ice sheets, and ice speeds second only to the Bothnian Sea. Together, these factors combine to produce the harshest ice conditions, significantly increasing the probability of IIVs in the region.

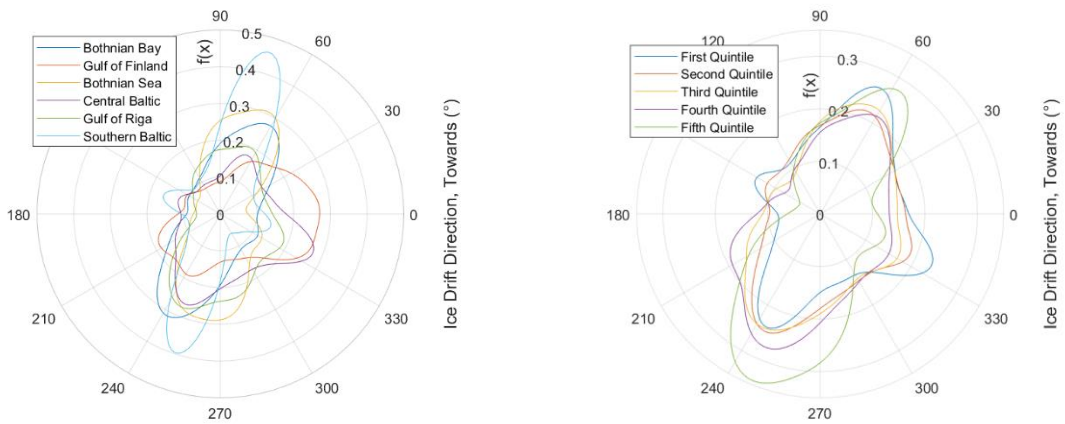

a) b)

Fig. 2. Model sea ice (a) drift direction pdfs for each region and (b) velocity pdfs for each speed quintile within the entire Baltic Sea.

3.2. Norströmsgrund

Once general trends in the Baltic were understood, data from the grid cell containing the NSG lighthouse was compared to measurements obtained during the STRICE project via time-series plots. Before comparing atmospheric data, corrections must be applied to account for differences in elevation. Air temperature decreases at a rate of 6.5 C per kilometer increase in elevation on average, for a difference of 0.117 C between measured and modelled data at NSG. The logarithmic wind profile is valid at the elevations of interest here, providing a method to compare the measured and modelled data. The simplified equation is given by:

$$u_2 = u_1 \frac{\ln(h_2/z_0)}{\ln(h_1/z_0)}$$

where u_2 and u_1 are the wind speeds at elevations h_2 and h_1, respectively, and z_0 is the roughness length, which accounts for differences in terrain. Note that zero-plane displacement has been ignored and neutral stability has been assumed. After corrections, the atmospheric parameters were generally found to correspond well to those measured on-site, as seen in Fig. 3. The measured air temperature (not shown) was found to be consistently higher than the model output, likely due to the lighthouse heating the surrounding air. Dates where FLI events occurred are denoted by a vertical line; notably, all events appear to occur at or near local extrema. Similar results are obtained from the 2003 data (not shown). Further research is necessary to determine if local extrema are a necessary component of FLI events.

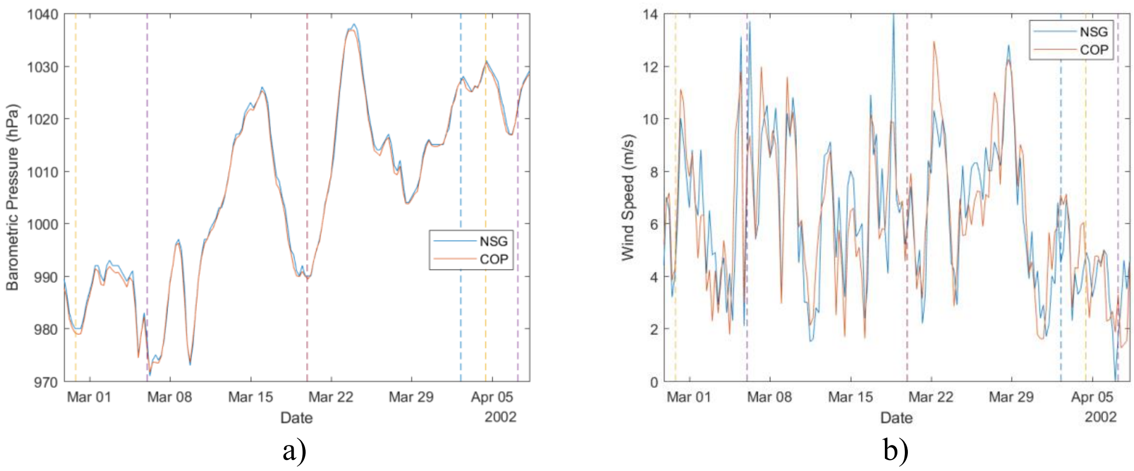

Fig. 3. Time series of Copernicus and NSG a) barometric pressure and b) wind speed data. Vertical lines note dates where FLI was observed. NSG data has been resampled to match Copernicus output frequency.

Comparisons of sea ice data were less successful, for two main reasons: 1) sea ice simply has a much larger spatial and temporal variability than either ocean or atmospheric parameters, and; 2) the STRICE project only measured sea ice parameters during loading events. The recorded sea ice parameters are thus only a subset of the total sea ice parameters in the region near NSG. Sea ice concentration is an important factor in ISIs that was unfortunately not recorded during the STRICE project. Sea ice velocity measurements were highly biased to round numbers, as seen in Figure 4a). Both model and field data follow underlying lognormal distributions from which useful information can be obtained, though the fit to measured data is skewed by human rounding bias. The thickness pdfs differ greatly. This can be attributed to a combination of three factors: 1) the nearby shipping channel increases the prevalence of thin ice near NSG, which is either averaged out of or ignored in the model results; 2) the calibration of the EM device used to measure ice thickness at NSG drifted by up to 0.05 m, producing cases where open water was mistaken for ice up to 0.15 m thick, and; 3) they simply measure different quantities; Copernicus provides an areal average which smoothes out the effect of ridged ice, producing a pdf that better represents level ice. The thickness distribution will thus include components for level, rafted, and ridged ice. A transform from level ice thickness to first-year ice statistics is required if Copernicus thickness output is to be used at other locations of interest.

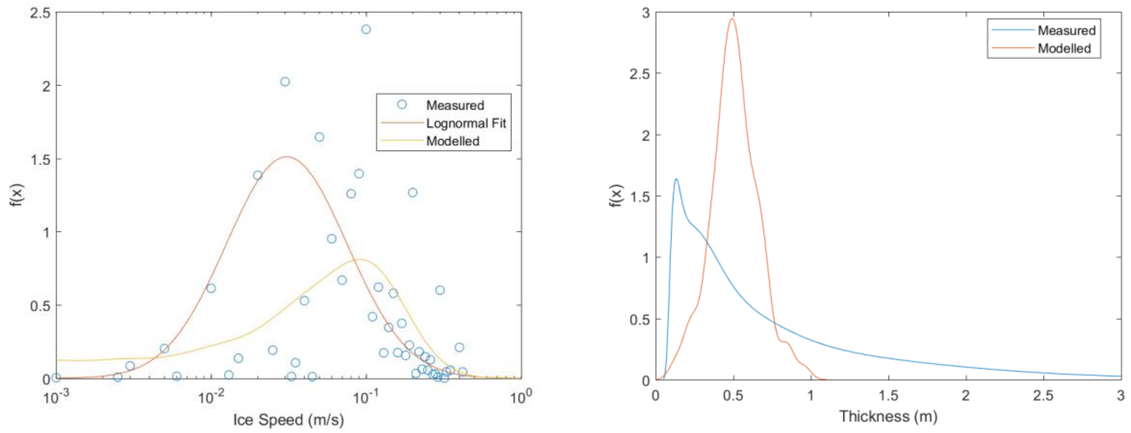

a) b)

Fig. 4. Modeled and observed empirical probability density functions for sea ice a) speed and b) thickness at NSG. Lognormal fit shown corresponds to data measured at NSG. Skewed nature of Copernicus speed data (which drops to zero at 0.00001 m/s) likely due to an artifact of the model.

3.3. Farstugrunden

A brief inspection of the model output at Farstugrunden (FSG) during the years of the LOLEIF and STRICE projects was also undertaken. The FSG lighthouse is a slightly stiffer structure (Nord et al., 2018), located in water that is 0.5 m deeper than the NSG location. It is approximately 6 km closer to the nearest shoreline and approximately 24 km further north. Little to no IIVs have been observed at FSG, and no structural fatigue has been noted. This is generally attributed to the higher proportion of landfast ice in this location, which does not induce vibrations. Sea ice statistics near FSG were checked for any other peculiarities, given that the predominance of landfast ice may not continue into the coming years due to the effects of climate change. The ice at FSG was found to be slightly thicker with a slightly lower concentration, as seen in the CDFs presented in Fig. 5. Drift velocity statistics (not shown) at both locations do not differ significantly, though drift direction shifts slightly to the east at FSG, due simply to the geography of the nearby coastline. Note that the two lighthouses share a grid cell in the model data, so no comparison can be made.

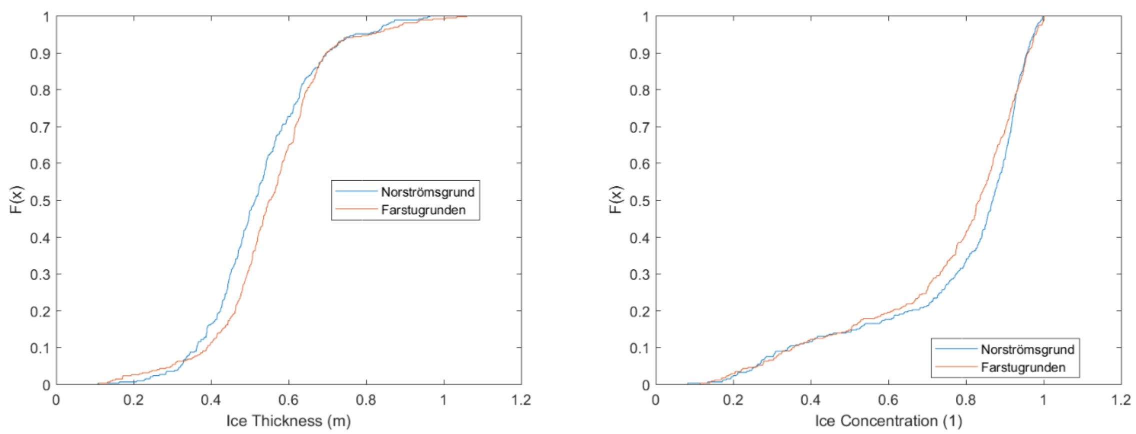

a) b)

Fig. 5. Empirical cumulative distribution functions for sea ice a) thickness and b) concentration within grid cells containing NSG and FSG lighthouses.

4. Discussion

The long-term goal of this study is to provide a systematic method to apply full-scale measurement results to locations where met-ocean conditions are available. As an initial test case the Baltic Sea region was examined using the met-ocean and atmospheric models of Copernicus. Significant differences in sea ice parameters (thickness, concentration, velocity) and wind velocity are observed between regions, indicating that forcing conditions on a structure will differ considerably from region-to-region.

The model output was then compared to observations at the NSG lighthouse. They were found to be sufficiently similar to be used as an initial estimate of forcing input for an ISI at other locations via methods such as those discussed in Nord et al. (2016) or Hendrikse and Nord (2019). Some difficulties are encountered; atmospheric model output more closely resembles the measured data than the sea ice output, due simply to the increased difficultly encountered when modelling sea ice. Drift ice thickness statistics of model output show a similar mode to the helicopter-towed EM measurements analyzed by Ronkainen et al., (2018). Rafted and ridged ice is underrepresented in the Copernicus data, producing a significantly lower mean ice thickness. A transform is necessary to produce true ice thickness statistics from model output; a preliminary analysis of the relationship between ridge ice and level ice statistics can be found in Samardžija and Høyland (2019). The model sea ice velocity data shares the same underlying lognormal distribution with the NSG data, but little else can currently be said due to human rounding bias during the measurement of ice drift at NSG. Methods with which to account for this human rounding bias are currently being investigated.

Copernicus model output near dates of FLI events discussed in Nord et al. (2018) was also examined during this study. No clear trend was observed, though events all appear to occur around local extrema in parameters. Combined with the FLI prediction method of Bjerkås and Gedikli (2019) this may provide sufficient conditions with which to predict FLI events. Further investigation is underway.

Model output at the two sister lighthouses was examined due to the noted lack of IIVs at FSG. Though generally assumed to be due to higher probability of landfast ice at its location, a more thorough analysis is warranted due to the changing climate in the Baltic Sea; regions of landfast ice may not remain so in the future. The lack of IIVs cannot be explained by the Copernicus models examined during the time period of interest; the overall statistics are practically identical at the two locations during the LOLEIF and STRICE projects. Misunderstanding of the necessary conditions for IIV may play a part; as previously presented in this study, there is some evidence that rates play an important role in triggering FLI. This may also be due to the model resolution; statistical downscaling in the region may provide better insight into met-ocean conditions at the FSG location. An analysis of statistically downscaled model output in the region is planned for the near future.

5. Conclusions

This study examines the sea ice and atmospheric model output in the Baltic Sea of two Copernicus products. These models are then compared against the full-scale data obtained during the STRICE project, particularly near FLI events. The study concludes that:

- There are significant differences in met-ocean conditions throughout the Baltic Sea which will affect fatigue and limit testing conditions for structures from region-to-region.

- Model output compares favourably to full-scale observations, with atmospheric parameters being a better fit than sea ice ones.
- FLI events appear to occur during local extrema in both model and full-scale measurements.

Acknowledgments
The authors wish to acknowledge the support to the FATICE project from the MarTERA partners, the Research Council of Norway (RCN), German Federal Ministry of Economic Affairs and Energy (BMWi), the European Union through European Union's Horizon 2020 research and innovation programme under grant agreement No 728053-MarTERA and the support of the FATICE partners.

References

Bjerkås, M., Moslet, P., Jochmann, P., and Løset, S., 2003. Global ice loads on the lighthouse Norströmsgrund in the winter 2001. Proc. of the International Conference on Port and Ocean Engineering Under Arctic Conditions, Trondheim, Norway.

Bjerkås, M., Meese, A., Alsos, H.S., 2013. Ice Induced Vibrations – Observations of a Full Scale Lock-in Event. Proc. 23rd International Offshore and Polar Engineering (ISOPE), Anchorage, Alaska, USA.

Bjerkås, M., Alsos, H.S., Wåsjø, K., 2014. Estimates of the Number of Vibration Cycles from Frequency Locked-in Ice Loads. International conference on Ocean, Offshore and Arctic Engineering (OMAE). San Fransisco, USA.

Bjerkås, M., Gedikli, E.D., 2019. A method to find intervals with probability of harsh ice induced vibrations. Proc. 25th International Conference on Port and Ocean Engineering under Arctic Conditions (POAC), Delft, The Netherlands.

Dee, D.P., Uppala, S.M., Simmons, A.J., Berrisford, P., Poli, P., Kobayashi, S., Andrae, U., et al., 2011. The ERA‐Interim reanalysis: configuration and performance of the data assimilation system. Q.J.R. Meteorol. Soc., 137: 553-597.

European Centre for Medium-range Weather Forecast (ECMWF), 2011. The ERA-Interim reanalysis dataset, Copernicus Climate Change Service (C3S) (accessed 25.11.2019), available from https://www.ecmwf.int/en/forecasts/datasets/archive-datasets/reanalysis-datasets/era-interim

E.U. Copernicus Marine Service Information, 2020a. BALTICSEA_REANALYSIS_PHYS_003_011. In: C.M.E.M. Service.

E.U. Copernicus Marine Service Information, 2020b. GLOBAL_REANALYSIS_PHYS_001_030. In: C.M.E.M. Service.

Garric, G., Parent, L., Greiner, E., Drévillon, M., Hamon, M., Lellouche, J.M., et al., 2017. Performance and quality assessment of the global ocean eddy-permitting physical reanalysis glorys2v4. In: Buch E, Fernandez V, Nolan G, Eparkhina D (eds) Operational oceanography serving sustainable marine development. Proceedings of the eight EuroGOOS international conference, 2018, 3–5 October 2017, Bergen, Norway.

Haas, C and Jochmann, P., 2003. Continuous EM and ULS thickness profiling in support of ice force measurements, Loeset, S., Bonnemaire, B., Bjerkas, M. (Eds.), Proceedings of the 17th International Conference on Port and Ocean Engineering under Arctic Conditions, POAC ´03, Trondheim, Norway.

Hendrikse, H. and Nord, T.S., 2019. Dynamic response of an offshore structure interacting with an ice floe failing in crushing. Marine Structures, 65, 271-290.

Hornnes, V., Høyland, K.V., Turner, J.D., Gedikli, E.D., Bjerkås, M., 2020. Combined distribution of ice thickness and speed based on local measurements at the Norströmsgrund lighthouse 2000-2003. Proc. 25th International IAHR Symposium on Ice, Trondheim, Norway.

International Organization for Standardization (ISO), 2019. Petroleum and natural gas industries – Arctic offshore structures. ISO/FDIS 19906.

Jochmann, P., Schwarz, J., 2000a. Ice Force Measurement at Lighthouse Norströmsgrund - Winter 1999. LOLEIF report. Hamburgische Schiffbau-Versuchsanstalt GmbH.

Jochmann, P., Schwarz, J., 2000b. Ice Force Measurement at Lighthouse Norströmsgrund - Winter 2000. LOLEIF report. Hamburgische Schiffbau-Versuchsanstalt GmbH.

Leppäranta, M., 2005. The Drift of Sea Ice.

Li, H., 2015. Measurement Setup at Lighthouse Norströmsgrund and Data Processing 1999 – 2003, Department of Civil and Transport Engineering, NTNU, Trondheim.

Li, H., Bjerkås, M., Høyland, K.V., Nord, T.S., 2016. Panel loads and weather conditions at Norströmsgrund lighthouse 2000-2003. Proc. 23rd IAHR International Symposium on Ice, Ann Arbor, Michigan USA.

Määttänen, M., 1975. Experiences of Ice Forces against a Steel Lighthouse Mounted on the Seabed, and Proposed Constructional Refinements. Proc. 3rd International Conference on Port and Ocean Engineering under Arctic Conditions (POAC), Fairbanks, Alaska, 857–867.

Nord, T.S., Øiseth, O., Lourens, E.M., 2016. Ice force identification on the Norströmsgrund lighthouse. Computers & Structures, Volume 169, 24-39.

Nord, T.S., Samardžija, I., Hendrikse, H., Bjerkås, M., Høyland, K.V., Li, H., 2018. Ice-induced vibrations of the Norströmsgrund lighthouse. Cold Regions Science and Technology, 155, 237-251.

Oikkonen, A., Haapala, J., Lensu, M., and Karvonen, J., 2016. Sea ice drift and deformation in the coastal boundary zone. Geophysical Research Letters, 43 (19), 303-310.

O'Rourke, B.J., Jordaan, I.J., Taylor, R.S., Gürtner, A., 2016. Experimental investigation of oscillation of loads in ice high-pressure zones, part 2: Double indentor system — Coupling and synchronization of high-pressure zones. Cold Regions Science and Technology, 124, 11-24.

Posey, P. G., Metzger, E. J., Wallcraft, A. J., Hebert, D. A., Allard, R. A., Smedstad, O. M., et al., 2015. Improving Arctic sea ice edge forecasts by assimilating high horizontal resolution sea ice concentration data into the US Navy's ice forecast systems. Cryosphere 9, 1735–1745.

Ronkainen, I., Lehtiranta, J., Lensu, M., Rinne, E., Haapala, J., and Haas, C., 2018. Interannual sea ice thickness variability in the Bay of Bothnia. The Cryosphere, 12 (11), 3459-3476.

Samardžija, I., & Høyland, K., 2019. Initial results of a study into the relationship between level ice draft and ridge keel draft. Proc. 25th International Conference on Port and Ocean Engineering under Arctic Conditions (POAC), Delft, The Netherlands.

Schwarz, J., 2001. Validation of Low Level Ice Forces On Coastal Structures. Proc. International Society of Offshore and Polar Engineers (ISOPE), Stavanger, Norway, 749-753.

Yue, Q., Guo, F., Kärnä, T., 2009. Dynamic ice forces of slender vertical structures due to ice crushing. Cold Regions Science and Technology, 56 (2–3), 77-83.

25th IAHR International Symposium on Ice
Trondheim, June 14 to 18, 2020

Physical Properties of Summer Arctic Sea ice during 2008–2018

Qingkai Wang[1], Peng Lu[1], Zhijun Li[1], Bing Tan[2]
1 State Key Laboratory of Coastal and Offshore Engineering, Dalian University of Technology, Dalian 116024, China
2 School of Mathematics and Statistics, Nanyang Normal University, Nanyang 473061, China
wangqingkai@dlut.edu.cn (Q. W.), lupeng@dlut.edu.cn (P. L.), lizhijun@dlut.edu.cn (Z. L.), tanbing111@126.com (B. T.)

As a part of Chinese National Arctic Research Expedition program, the physical properties of sea ice were investigated in the Pacific sector of the Arctic during the summers of 2008−2018. Sea ice salinity, density, and temperature were measured in field at 21 first-year ice (FYI) sites and 20 multi-year ice (MYI) sites. Results show that the bulk salinity ranged from 0.4 to 3.2 PSU for FYI and 0.4–2.4 PSU for MYI. The bulk density of FYI was 600−900 kg/m^3, and of MYI was 686−903 kg/m^3. Both the measured salinity and density were less than the previously reported values, and their earlier parameterization formulae were not appropriate for the current summer Arctic sea ice. Therefore, several modifications were proposed based on our measurements. Furthermore, the contents of brine and gas within sea ice were evaluated according to the volume fractions calculated using sea ice temperature, salinity, and density. The bulk brine volume fraction ranged from 3.0 to 25.9% for FYI and from 2.2 to 21.4% for MYI. The bulk gas volume fraction ranges were 2.7−35.4% and 3.6−26.1% for FYI and MYI, respectively. The typical variations of brine and gas volume fractions along ice depth were parameterized using quadratic polynomials. Large changes have been observed in the physical states of current Arctic sea ice compared with earlier observations, and the results can be helpful to improve the accuracy of existing sea ice models.

1. Introduction

A large number of variations have been seen in Arctic sea ice because of Arctic amplification occurred in the Arctic region in recent decades. Increased interior melt has been observed in the summer ice (Huang *et al*., 2016). The physical characteristics of sea ice are likely to be changing as well with the development of Arctic warming. Some of the parameterization formulae for sea ice physical parameters based on earlier observations may not be appropriate for current Arctic sea-ice state. Therefore, our knowledge on the physical properties of summer Arctic sea ice needs to be updated. While the measurements on the sea ice physics of high quality have been much sparser after the year 2000.

Sea ice temperature, salinity, and density are fundamental physical parameters influencing the thermal, optical, and mechanical properties of sea ice, and thus, attracted much focus in the previous work. The annual cycle of Arctic sea ice temperature has been investigated using thermistor strings (Perovich and Elder, 2001), and the temperature profile of Arctic sea ice with depth has also been observed using ice-core measurements (Carnat *et al*., 2013). The characteristics of salinity profile of first-year ice (FYI) and multi-year ice (MYI) were different due to desalination process (Tucker III *et al*., 1987; Vancoppenolle *et al*., 2006), and a parameterization formula was established for MYI salinity profile (Schwarzacher, 1959) which has been used in several existing sea ice models (*e.g*., Hunke and Lipscomb, 2008). Sea ice shows lower density in the part above the waterline than below in summer. Several sea ice density ranges have been reported using various methods (*e.g*., Timco and Frederking, 1996), and a mathematic equation has been established to describe the MYI density profile along ice depth (Eicken *et al*., 1995).

The Arctic sea ice is transiting from a predominantly MYI system to a FYI system, but there are limited studies on parameterizing the vertical profiles of FYI physical properties, especially salinity and density. Sea ice is a multicomponent medium consisting of ice crystals, brine pockets, gas, and other inclusions. The phases of sea ice change largely as it warms in melt season, and brine and gas can account for large proportions. While there have been only limited studies on the sea ice brine distribution and even fewer on the gas. Eicken *et al.* (1995) reported the distribution characteristics of brine and gas content within summer sea ice in the Eurasian sector of the Arctic, and Cannat *et al*. (2013) investigated the evolution of brine volume fraction of sea ice during a growth cycle in the Canadian Arctic.

Sea ice physical data has been collected from the Pacific sector of the Arctic Ocean during the past 10 years through the Chinese National Arctic Research Expedition (CHINARE) programs. In this paper, we presented the salinity and density of current summer Arctic sea ice and compared them with the previous parameterization formulae. Based on the field observations, the brine and gas contents within sea ice were evaluated and then parameterized. Finally, several potential improvements were suggested to promote existing sea ice models.

2. Study Area and Measurements

A total of 41 ice sites were set up on the floes with diameters of several kilometers in the CHINARE programs conducted mostly in the Pacific sector of the Arctic during the summers of 2008−2018 (Figure 1). Most of the ice sites were located within 76.3−88.4ºN and 147.1−179.6ºW, except the sites in 2012 that were located further west from 83.4−87.4ºN and 120.2−161.4ºE. Based on the division of the Arctic Ocean by the National Snow and Ice Data Center, most of the ice sites were located in the Central Arctic, and some were located in the Chukchi and Beaufort seas. The ice thickness ranged between 49.3 and 205.3 cm, and the snow thickness was 3−20 cm. The ice sampling was carried out mainly in August, and the air temperature at the time of sampling ranged between −4.2 and 3.6ºC. Ice sampling was conducted on wide and level areas at each site, and at least four vertical ice cores were extracted using a drilling auger.

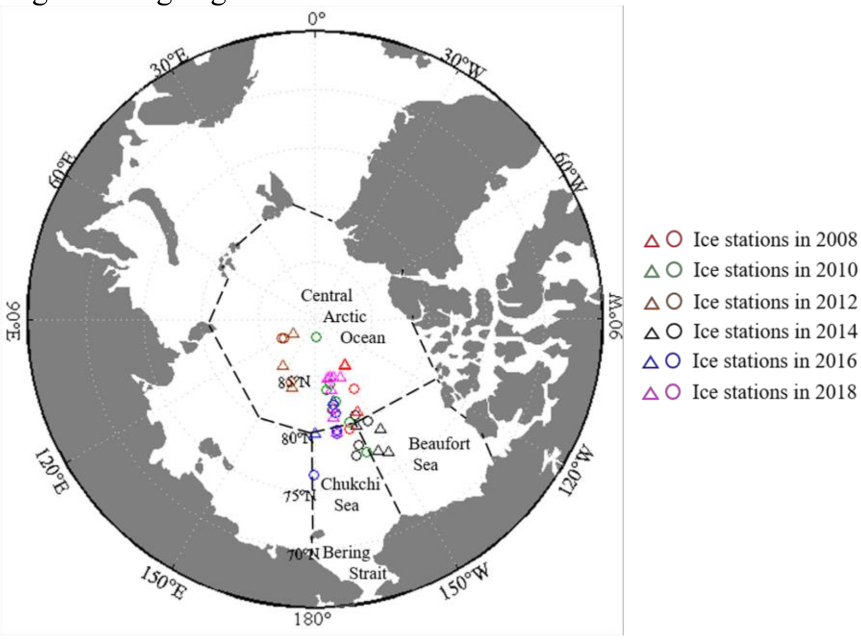

Figure 1. Maps of ice sites in the CHINARE programs during 2008–2018. The green part represents land and islands, and the white part represents seas.

Sea ice temperature

Once an ice core was extracted, ice temperature was measured immediately. Holes were drilled at 10-cm intervals along the length of the ice core, and a temperature probe sensor with an accuracy of ±0.1ºC inserted in the holes to measure the ice temperature.

Sea ice salinity

Ice salinity was measured using another ice core, which was cut into 10-cm-long segments from top to bottom with a handsaw immediately after extraction. These ice sections were then preserved in plastic bottles and taken back to the ship. A salinometer with an accuracy of ±0.1 PSU was used to measure salinity after the ice sections melted.

Sea ice density

Ice density was determined using the mass-volume method in the on-board cold laboratory. An ice core was cut into 10-cm-long sections. Each section was then machined into cubes with side length of 4 cm carefully using the band saw and weighed using a balance (±0.1 g), and the volume was calculated based on the dimensions measured with a caliper (±0.02 mm). An ice cube typically had a mass of 40–70 g, and thus, the uncertainty due to the measurement error was approximately 5% according to error propagation analysis.

Sea ice crystal structure

The observations of crystal texture were conducted by preparing vertical sections with size of 5−10 cm in length and 1 cm in thickness using the band saw in the cold laboratory. These sections were then attached to glass sheets and shaved to a thickness of less than 1 mm using a planer. These slices were then placed on a universal stage to observe the crystal texture under crossed polarizing light.

3. Results

The ice sites were classified into FYI and MYI according to the measured salinity profile and crystal texture. MYI generally shows a fresh layer in the uppermost of salinity profile and discontinuities in crystal structure along the depth due to the changes in the crystal size and shape. Based on the criteria, a total of 21 FYI and 20 MYI sites were finally identified.

3.1. Sea ice salinity

The salinity of both FYI and MYI samples mainly ranged between 0 and 5 PSU (grey points in Figure 2). A nearly fresh (< 0.5 PSU) layer existed in the upper of most MYI ice sheets, and this layer accounted on average for 30±9% of the ice thickness. A top layer with low salinity (< 1.0 PSU) was also found in the majority of FYI sheets due to the flushing of surface meltwater, accounting for 25±12% of the total thickness averagely. To better depict the salinity profiles of both ice types, the ice depth was normalized to the interval of [0, 1] and then divided into 10 even layers. The salinity of each layer at an ice site was averaged taking the measured section length as weight:

$$S_{i,j} = \frac{1}{L}\sum_{j=1}^{n} S_{i,j} \times l_j \qquad \textbf{[1]}$$

where S_i is the salinity of a layer, L is the layer length, n is the number of measured sections located within the layer, $S_{i,j}$ is the salinity of a measured section, and l_j is the measured section length. The profiles of all MYI and FYI sites were averaged finally as shown in the black lines in Figure 2. It could be clearly seen that the ice salinity of both ice types increased from top to bottom, and the salinity in the upper layer of FYI was a bit higher than that of MYI.

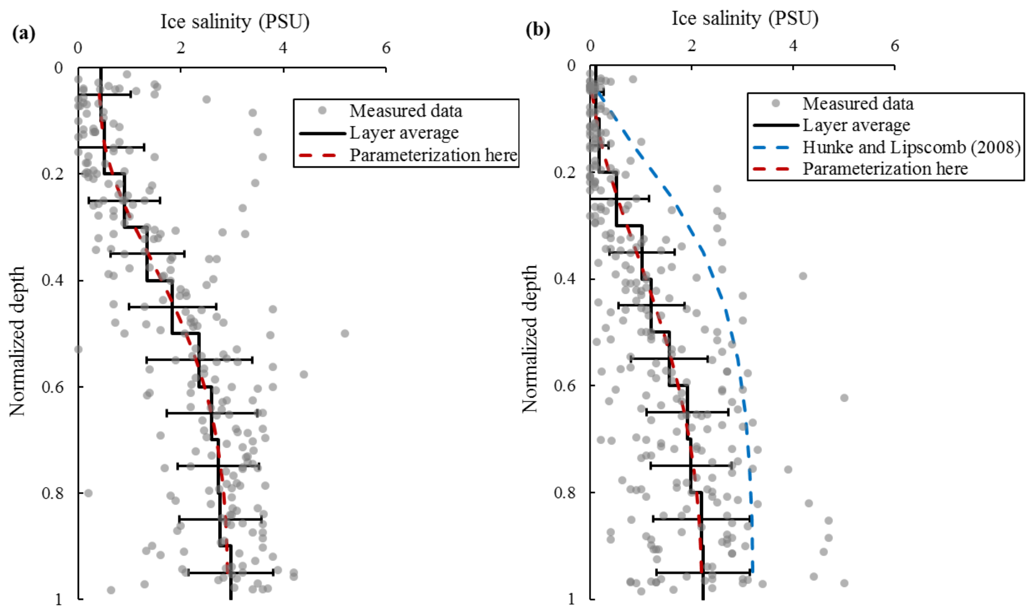

Figure 2. The measured sea ice salinity against normalized depth for FYI (a) and MYI (b). The error bar represents the standard deviations.

The most commonly used parameterization of the summer MYI salinity profile in sea ice models, such as in Hunke and Lipscomb (2008), is:

$$S(z) = \frac{1}{2} S_{\max}[1 - \cos(\pi z^{\left(\frac{a}{z+b}\right)})] \quad \textbf{[2]}$$

where S is sea ice salinity, z is the normalized ice depth, and a and b are fitted coefficients. In Hunke and Lipscomb (2008), S_{max} = 3.2 PSU, a = 0.407, and b = 0.573. The profile fitted by Eq. (2) was shown as the blue dashed line in Figure 2b. It could be seen that the previous parameterization showed much higher salinity than our data. Therefore, modifications were applied to this parameterization, and the fitted parameters were S_{max} = 2.2 PSU, a = 2.32, and b = 2.67. The coefficient of determination (R^2) was 0.99 and the significance level (p) was 0.01. The modified profile was shown as the red dashed line in Figure 2b.

Furthermore, we adopted a similar form as Eq. (2) to depict the FYI salinity profile, but a slight modification was added to give a positive value $S(0)$ at the ice surface.

$$S(z) = \frac{1}{2} S_{\max}[1 - \cos(\pi z^{\left(\frac{a}{z+b}\right)})] + S(0) \quad \textbf{[3]}$$

where $S(0)$ = 0.41 PSU, S_{max} = 2.5 PSU, a = 0.76, and b = 0.58. The goodness of fit was R^2 = 1.00 at p = 0.01. The profile was shown in the Figure 2a.

The bulk salinity of an ice sheet was determined by averaging the salinity of all measured sections taking the length as weight. Results showed that the bulk salinity ranged from 0.4–3.2 PSU for FYI with an average of 1.9±0.6 PSU, and for MYI, the salinity range and average were 0.4–2.4 PSU and 1.3±0.5 PSU, respectively.

3.2. Sea ice density

Sea ice density of our samples were 491–907 kg/m^3 for FYI and 521–906 kg/m^3 for MYI (gray points in Figure 3). The density in the freeboard (the ice section above the sea level) of the ice cores was less than in the draft (the ice section below the sea level) due to the heavy deterioration and large gas pores in the upper of ice sheet. The mean density in the freeboard was 718±87 kg/m^3 for FYI and 701±86 kg/m^3 for MYI; and the mean density in the draft was 804±80 kg/m^3 and 825±52 kg/m^3 for FYI and MYI, respectively. To describe the density profile in a quantitative way, the ice core was divided into 10 even layers, and a similar method as Eq. (1) was used to calculated the density of each layer. Finally, general depth profiles of sea ice density were obtained by averaging all FYI and MYI profiles (black lines in Figure 3). The density of both ice types decreased from top to bottom.

Eicken et al. (1995) has adopted a logarithm equation to describe the variation of MYI density along depth:

$$\rho(z_i) = 35.7 \times \ln(z_i) + 881.8 \quad \textbf{[4]}$$

where ρ is sea ice density in kg/m^3, and z_i is the real ice depth (in meters). As the blue dashed line in Figure 3b, this parameterization cannot follow the density variation of current Arctic sea ice. Furthermore, this equation cannot guarantee reasonable mathematical behavior when z_i = 0. Therefore, a quadratic polynomial is used in this paper to parameterize the sea ice density profile:

FYI: $\rho(z) = -103.4z^2 + 231.5z + 710.1$, $R^2 = 0.99$, $p < 0.01$ **[5]**
MYI: $\rho(z) = -218.1z^2 + 423.1z + 672.5$, $R^2 = 0.98$, $p < 0.01$ **[6]**

The bulk density ranged from 600–900 kg/m^3 for FYI with an average of 793±74 kg/m^3, and for MYI, the density range and average were 686–903 kg/m^3 and 810±49 kg/m^3, respectively. Compared with the earlier reported value in Timco and Frederking (1996), our measured density ranges were less and wider for both ice types.

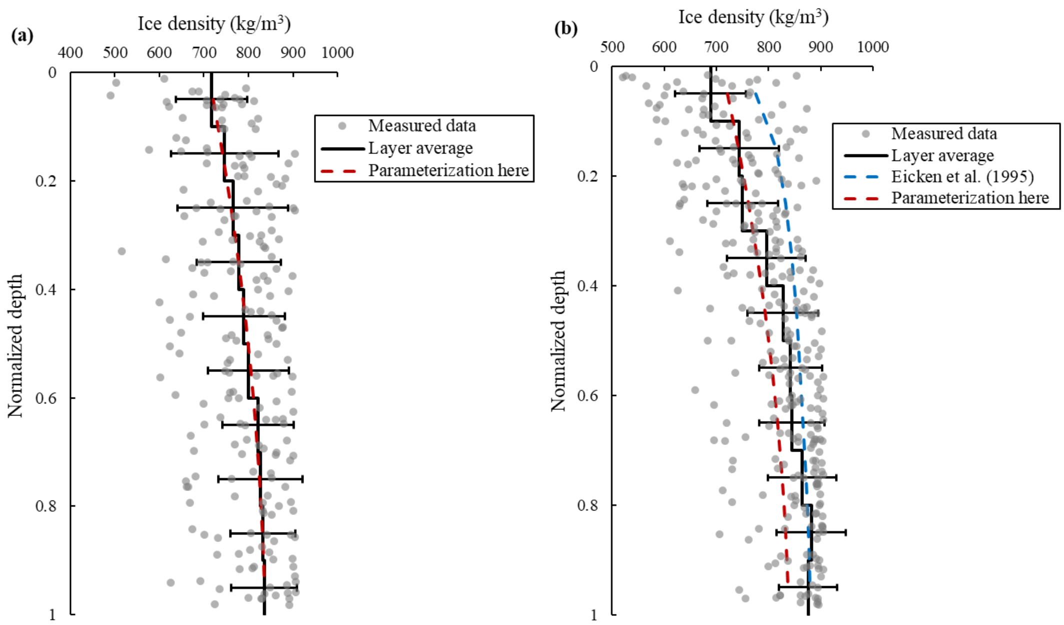

Figure 3. The measured sea ice density against normalized depth for FYI (a) and MYI (b). The error bar represents the standard deviations.

3.3. Sea ice brine and gas volume fractions

The contents of liquid brine and gas change as sea ice warms. The brine and gas are two important factors affecting sea ice thermal and optical properties. They are difficult to measure in field, but there are mathematical formulae to calculate their volume fractions using Cox and Weeks (1983) as well as Leppäranta and Manninen (1988).

Since each ice core has been divided into 10 layers within the normalized ice depth, and the salinity and density of each layer were obtained. We then calculated the ice temperature of corresponding layer assuming the ice temperature varies linearly between two adjacent measurement points and taking the length between adjacent measurement points as weight. Finally, the brine and gas volume fractions in each layer could be determined.

The brine volume fraction range of FYI samples was 0–61.8%, and of MYI samples was 0–37.3%. The bulk brine volume fraction of an individual ice core was taken as the mean value of the brine volume fractions of 10 layers, and the bulk value for FYI was between 3.0 and 25.9% with an average of 11.3±6.2%, and for MYI was between 2.2 and 21.4% with an average of 9.5±11.0%. To parameterize the general variation of brine volume fraction along depth, the profiles of FYI and MYI were averaged, respectively. As shown in Figure 4, the general profiles of both ice types showed a reversed "C-shape" with a maximum in the middle. Therefore, we used the quadratic polynomials to fit the profiles:

$$\text{FYI: } v_b = -32.9z^2 + 43.9z,\ R^2 = 0.91,\ p < 0.01 \quad \textbf{[7]}$$

$$\text{MYI: } v_b = -34.2z^2 + 42.1z,\ R^2 = 0.90,\ p < 0.01 \quad \textbf{[8]}$$

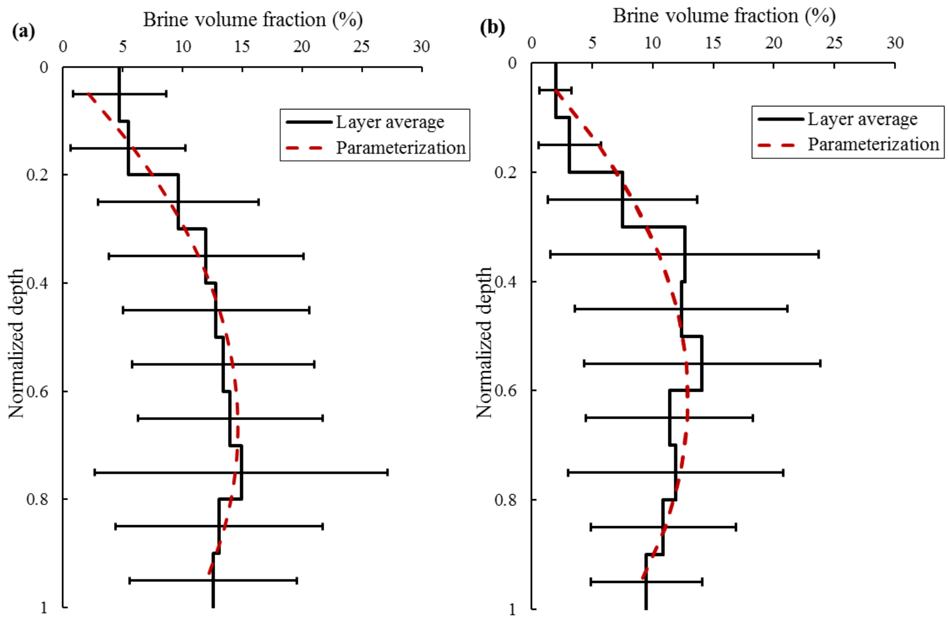

Figure 4. The mean brine volume fraction profiles for FYI (a) and MYI (b). The error bar represents the standard deviations.

The calculated gas volume fraction ranged between 0 and 65.4% for FYI, and between 0 and 34.4% for MYI. The bulk gas volume fraction was 2.7–35.4% with an average of 14.9±7.9% for FYI, and the bulk value was 3.6–26.1% with a mean value of 13.5±12.7% for MYI. Similarly, the general profiles of gas volume fractions were plotted for both ice types. As shown in Figure 5, both profiles showed that the gas volume fraction decreased from top to bottom against normalized ice depth. The profiles were also parameterized using the quadratic polynomials:

FYI: $v_a = 8.6z^2 - 21.3z + 22.7$, $R^2 = 0.99$, $p < 0.01$ **[9]**

MYI: $v_a = 14.1z^2 - 31.0z + 24.3$, $R^2 = 0.98$, $p < 0.01$ **[10]**

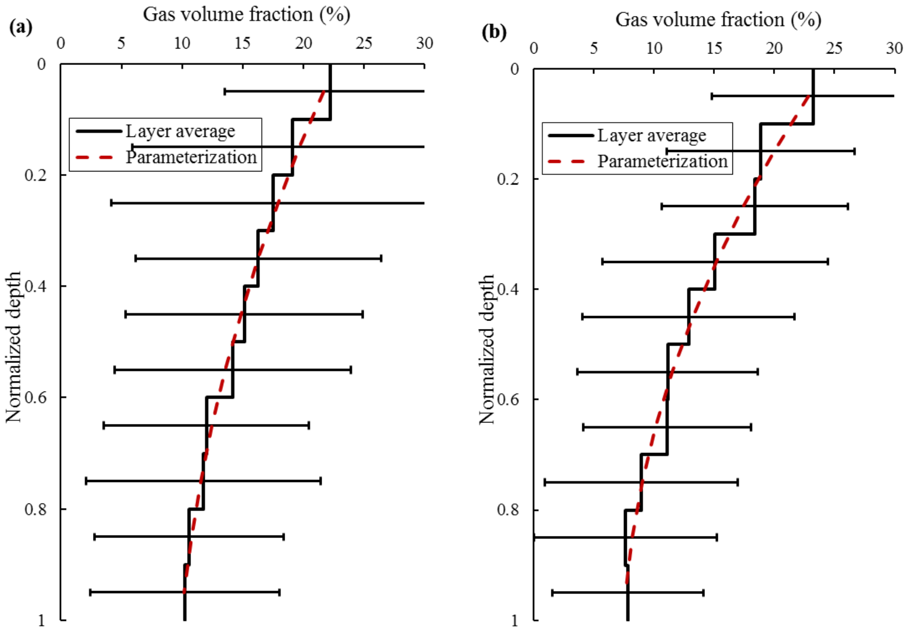

Figure 5. The mean gas volume fraction profiles for FYI (a) and MYI (b). The error bar represents the standard deviations.

The mean values of bulk gas volume fraction were greater than those of bulk brine volume fraction for both FYI and MYI, indicating that gas occupied more than brine of the summer Arctic sea ice. Especially, comparisons of the general profiles of brine and gas showed that the gas content was more than brine in the upper of ice sheet for both ice types. Permeability is the key factor affecting the hydrological evolution of summer sea ice. The percolation threshold $v_b^* \approx 5\%$ depends on the crystal structure; at $v_b > v_b^*$, brine or sea water can move through the ice (Golden et al., 1998, 2007). As shown in Figure 4 and 5, the lower sections were permeable with $v_b > 5\%$, and v_a in the top low-brine layers was higher than 5% because of drained-out brine. These sections had been permeable through the brine channels and were probably still permeable via the gas pores. In other words, both FYI and MYI were completely permeable through the whole thickness.

4. Conclusion

The physical properties of sea ice were collected during summers of 2008–2018 in the Pacific sector of the Arctic. We analyzed the sea ice salinity and density and calculated gas and brine volume fractions. The results could be used to improve the existing sea ice numerical models.

- Sea ice is less saline in the current Arctic, and thus the parameterization based on the earlier observations should be updated.
- Sea ice density is less than decades ago, and should not be regarded as a constant but a variable.
- Gas and brine occupy a large fraction of summer Arctic sea ice, and thus the variations of gas and brine should be fully considered in the future sea ice models.
- Gas occupies more than brine of summer sea ice, which could further affect the liquid transport within sea ice as well as the thermal and optical properties of sea ice.

Acknowledgments

This research was supported by the National Natural Science Foundation of China (41906198 and 41876219) and the National Postdoctoral Program for Innovative Talent (BX20190051).

References

Carnat, G., Papakyriakou, T., Geilfus, N.X., Brabant, F., Delille, B., Vancoppenolle, M., Gilson, G., Zhou, J., and Tison, J., 2013. Investigations on physical and textural properties of Arctic first-year sea ice in the Amundsen Gulf, Canada, November 2007–June 2008 (IPY-CFL system study). *J. Glaciol.*, 59(217), 819−837.

Cox, G.F.N., and Weeks, W.F., 1983. Equations for determining the gas and brine volumes in sea ice samples. *J. Glaciol.*, 29(102), 306–316.

Eicken, H., Lensu, M., Leppäranta, M., Tucker III, W.B., Gow, A.J., and Salmela, O., 1995. Thickness, structure, and properties of level summer multiyear ice in the Eurasian sector of the Arctic Ocean. *J. Geophys. Res.*, 100(C11), 22697−22710.

Golden, K. M., Ackley, S. F., and Lytle, V. I., 1998. The percolation phase transition in sea ice. *Science*, 282(5397), 2238−2241.

Golden, K. M., Eicken, H., Heaton, A. L., Miner, J., Pringle, D. J., and Zhu, J., 2007. Thermal evolution of permeability and microstructure in sea ice. *Geophys. Res. Lett.*, 34, L16501.

Huang, W., Lei, R., Han, H., and Li, Z., 2016. Physical structures and interior melt of the central Arctic sea ice/snow in summer 2012. *Cold Reg. Sci. Technol.*, 124, 127-137.

Hunke, E.C., and Lipscomb, W.H., 2008. The Los Alamos sea ice model documentation and software user's manual, Version 4.0. LA-CC-06-012, Los Alamos Nat. Lab., New Mexico.

Leppäranta, M., and Manninen, T., 1988. Brine and gas content of sea ice with attention to low salinities and high temperatures. Finnish Institute of Marine Research Internal Report, Helsinki.

Perovich, D.K., and Elder, B.C., 2001. Temporal evolution of Arctic sea-ice temperature. *Ann. Glaciol.*, 33, 207−211.

Schwarzacher, W., 1959. Pack-ice studies in the Arctic Ocean. *J. Geophys. Res.*, 64(12), 2357−2367.

Timco, G.W., and Frederking, R.M.W., 1996. A review of sea ice density. *Cold Reg. Sci. Technol.*, 24, 1−6.

Tucker III, W.B., Gow, A.J., and Weeks, W.F., 1987. Physical properties of summer sea ice in the Fram Strait. *J. Geophys. Res.*, 92(C7), 6787−6803.

Vancoppenolle, M., Fichefet, T., and Bitz, C.M., 2006. Modeling the salinity profile of undeformed Arctic sea ice. *Geophys. Res. Lett.*, 33, L21501.

25th IAHR International Symposium on Ice
Trondheim, 23 - 25 November, 2020

Seasonal changes of sea ice conditions along the Arctic Northeast Passage from 2010 to 2019

Miao Yu [1], Peng Lu* [1], Zhijun Li [1], Zhiyuan Li [2], Xiaodong Chen [3]

1 State Key Laboratory of Coastal and Offshore Engineering, Dalian University of Technology, Dalian 116024, China

2 School of Naval Architecture & Ocean Engineering, Dalian university of Technology, Dalian 116024, China

3 State Key Laboratory of Structural Analysis for Industrial Equipment, Dalian university of Technology, Dalian 116024, China

yumiao2411@mail.dlut.edu.cn; lupeng@dlut.edu.cn; lizhijun@dlut.edu.cn

lizhiyuan@dlut.edu.cn; chenxiaodong@mail.dlut.edu.cn

Abstract: With the change of global climate, sea ice conditions in the Arctic have changed significantly in the past decades, which brings opportunities for Arctic navigation and resource exploitation. In the present study, four different parts of the Arctic Northeast Passage (NEP) were selected as the research targets, two of them were routes from Sabetta port of Yamal Peninsula to the direction of Europe, and the others were to the direction of Asia. Seasonal and spatial changes of sea ice conditions and navigable period (NP) in the past decade were analyzed using multisource remote sensing data. Results of sea ice concentration (SIC) reveal that ice conditions of two Asian routes were more severe than the European routes, and the annual mean SIC was ~0.62 for the former and 0.2~0.3 for the latter, respectively. NP analyses indicate that the mean open days of two European routes were almost same, from mid-July to mid-October, lasting about 125 days for a threshold of SIC<0.7 and 110 days for a threshold of SIC<0.3. Concurrently, Asian routes only lasted for 78 days (SIC<0.7) and 64 days (SIC<0.3), from mid-August to mid-October. Results of ice thickness show that the mean value of two European routes was almost the same too, about open water in October and 1.16m in April. Thicker ice appears in the two Asian routes, achieving 0.3m and 0.54m in October, 1.2m and 1.55m in April, respectively.

Keywords: Arctic navigation, sea ice concentration, ice thickness

1 Introduction

Global air temperature has continued to rise in recent decades, which leads to the dramatically retreat of Arctic sea ice. Sea ice extent, thickness, and proportion of multiyear ice have changed a lot as a result. In 2007 and 2012, the ice extent had reached valleys of 4.1×10^6 km^2 and 3×10^6 km^2 respectively (Comiso and Parkinson et al., 2008; Parkinson and Comiso, 2013). The ice extent declined at a trend of -12.2% $decade^{-1}$ between 1979 to 2012 (Comiso, 2012).The maximum ice thickness of winter decreased from 3.64m to 1.89m from 1980 to 2008 (Kwok and Rothrock, 2009). The decline trend of annual mean ice thickness was -0.58±0.07m $decade^{-1}$ from 2000 to 2012 (Lindsay and Schweiger, 2015). Multiyear ice, represents the component of sea ice surviving from melt in summer, has suffered an inevitable change. The multiyear ice has been replaced by thinner first-year ice gradually, and the extent of multiyear ice remained negative at more than -15.1% $decade^{-1}$ from 1979 to 2011 (Comiso, 2012).

As climate models predict, the Arctic sea ice will continue to lose in future decades, which makes it possible to navigate in Arctic (Stroeve and Kattsov et al., 2012). Model results show that navigable periods for open water vessels will be double, and the shipping time between Europe and Asia will be 10 days faster than the traditional routes nowadays by midcentury (Melia and Haines et al., 2016). The Northeast Passage (NEP) connects Asia and Europe through the Chukchi Sea, East Siberian Sea, Laptev Sea, Kara Sea, and the Barents Sea, which shows noteworthy opportunity for Arctic shipping (Laliberté and Howell et al., 2016). NEP has immense economic potential, not only because it can save about 40% sailing distance than the conventional routes from Europe to Asia (Liu and Kronbak, 2010), but also the resource-rich Yamal peninsula is located in the Kara Sea. It is undoubtedly that the NEP will play a more and more crucial role in resource exploitation and intercontinental transport. But because of the complicated ice condition, only 9.3% of vessels travel in the Arctic are world's shipping traffic in 2014, the other shipping activities are almost confined in Norwegian and Barents Seas (Eguíluz and Fernández-Gracia et al., 2016).

Sea ice conditions, including sea ice concentration (SIC) and sea ice thickness (SIT), are the most significant factors that affect navigations in the Arctic Ocean. Therefore, it's necessary to understand the seasonal and spatial changes of sea ice clearly. The potential interest can benefit many industries such as fishing, cargo transport, tourism and research activity. For different industries, choosing different vessels according to the state of sea ice will be more safe and economical. So far, remote sensing is the only method to detect the up-to-date changes of sea ice on a large scale. Both SIC from passive microwave and SIT from altimeter sensors onboard satellites have mature databases published, and most of the previous studies on ice conditions were based on them (Comiso and Parkinson et al., 2008; Comiso, 2012; Parkinson and Comiso, 2013). However, these studies pay more attention to the influences of sea ice retreat on the global climate than navigation in the Arctic. In the present work, sea ice data from satellite remote sensing are employed to explain the seasonal variability of sea ice conditions and the navigable period along the NEP.

2 Study region and Data

2.1 Study region

The NEP connects several sea areas along the Siberian coast. There are many detail differences among these seas, although sea ice conditions in all regions show a negative trend (Comiso and Meier et al., 2017). Because of the warm flow from the Atlantic, the Barents Sea becomes nearly open in recent years even in winter (Smedsrud and Esau et al., 2013; Onarheim and Eldevik et al., 2015). Consequently, the retreat speed of sea ice in the Kara and Barents Sea is the greatest (Comiso and Meier et al., 2017), and the decline rate of SIC near New Siberian Islands is lowest among all (Comiso and Meier et al., 2017).

In the following study, the whole NEP is divided into four parts, as shown in Figure 1, which are common routes of Arctic shipping according to the information published on the website of *Northern Sea Route Information Office* (https://arctic-lio.com/). Sabetta port of Yamal peninsula is defined as the starting point, and routes 1 and 2 (R1, R2) are the European lines and routes 3 and 4 (R3, R4) are the Asian lines. R1 has shorter distance through Kara strait and R2 takes a detour to Novaya Zemlya for less ice area. R3 locates in the east Kara Sea, from the Yamal peninsula to Vilkitskoyo Strait (include strait), and the rest belongs to R4. The route R4 did not pass through the Sannikov strait (74.5°N, 142°E) or Dmitry Laptev strait (73°N, 142°E) because Dmitry Laptev strait cannot afford regular merchant ship pass due to its shallow depth, and Sannikov strait have shorter navigable period due to complicated ice condition and fickle wind there (Qin, 2014). The detailed information of these four routes are summarized in Table 1.

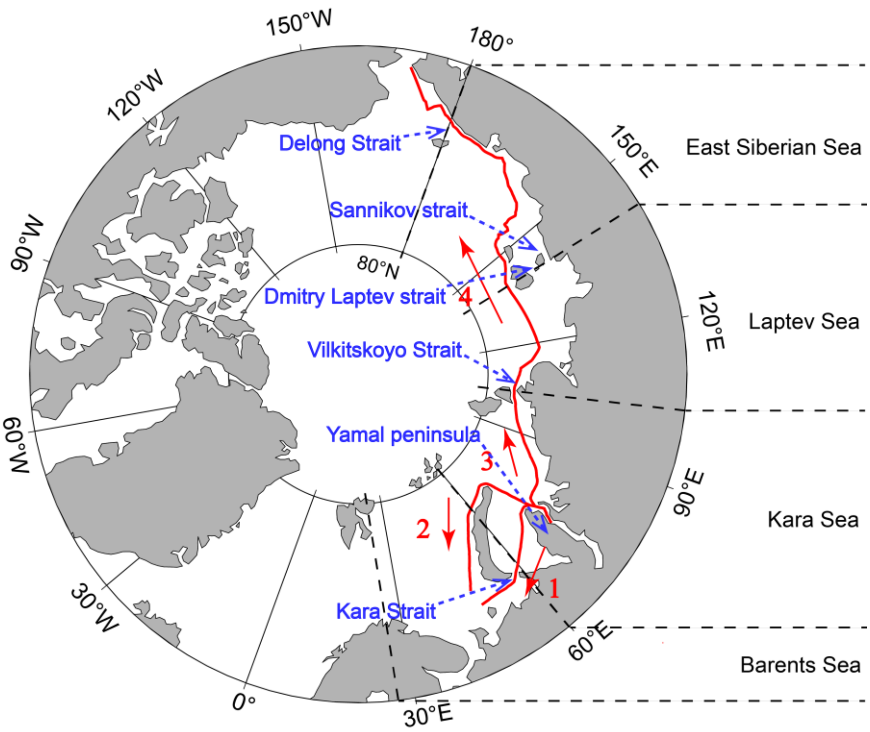

Figure 1 Four study routes with the red arrows indicate the navigation direction

Table 1 Information of study routes

Route	Start	End	Distance
1	Yamal peninsula	Barents Sea	1300km
2	Yamal peninsula	Barents Sea	1600km
3	Yamal peninsula	Vilkitskoyo Strait	1450km
4	Vilkitskoyo Strait	Bering Strait	3100km

2.2 Sea ice data

Sea ice in the Arctic Ocean has been continuously observed by satellite sensors since 1979. As summarized in Table 2, sea ice data from satellite remote sensing in the past 10 years were employed in the present study. SIC data were provided by the University of Bremen (Spreen and Kaleschke et al., 2008) and National Snow and Ice Data Center (NSIDC) (Cavalieri and Parkinson et al., 1996), covering every day from 2010 to 2019. SIC data from the University of Bremen were determined by the ARTIST Sea Ice (ASI) algorithm using the brightness temperature date from Advanced Microwave Scanning Radiometer for EOS (AMSR-E) between 2003 and September 2011, and from Advanced Microwave Scanning Radiometer 2 (AMSR-2) after July 2012. The spatial resolution of this SIC data was 3.125km. The gap period between AMSR-E and AMSR-2 was fed by SIC data from NSIDC. This data were determine by the National Aeronautics and Space Administration (NASA) Team 2 algorithm using the passive microwave data of Special Sensor Microwave Imager Sounders (SSMIS) with a spatial resolution of 25km. In the following study, time series SIC date will be employed to depict the ice conditions along the navigation routes.

Ice thickness data were derived from CryoSat-2 Synthetic Aperture Interferometric Radar Altimeter. There are two major steps to convert the radar signals into ice thickness: estimation of freeboard from radar waveforms, and calculation of thickness depending on the Archimedes principle (Laxon and Giles et al., 2013). Ice thickness data used in this study were published monthly and cover January to April and October to December by NSIDC with a spatial resolution of 25km. No date are available in summer because it is difficult to ascertain the freeboard of sea ice by discriminating seawater and melting ice (Peacock, 2004).

Table 2 Summary of satellite remote sensing data employed in this study

Product	Time period	Data source	Spatial resolution
Sea ice concentration	2010.01-2011.09	AMSR-E	3.125km
	2011.10-2012.06	SSMIS	25km
	2012.07-2019	AMSR-2	3.125km
Sea ice thickness	2010-2019	Radar Altimeter	25km

3 Results

3.1 Sea ice concentration

Daily variations in SIC along routes R1-R4 are shown in Figure 1, on which the horizontal axes represent the date and vertical axes represent the distance from the start point of the routes. In general, days with lower SIC (blue part in Figure 1) appear more in recent years, which demonstrates the feasibility of navigation. As mentioned above, the sea ice retreat speed in Kara Sea and Barents Sea was the greatest among all. So SIC along R1 and R2 were much lower than others. Just like Figure 1a and b shows, R1 and R2 have a steady low SIC period (blue part in figure) every year since 2010. The annual mean SIC of R1 was in the range from 0.49 to 0.27 and the decadal mean was 0.36. The largest annual mean SIC occurred in 2014, and the smallest one took place in 2012, corresponding to the recorded lowest Arctic sea ice cover in that year. Annual mean SIC of R2 changed less than R1, range from about 0.31 to 0.16 with a decadal mean of 0.24. The maximal annual mean SIC took place in 2010 and reached a minimum in 2012.

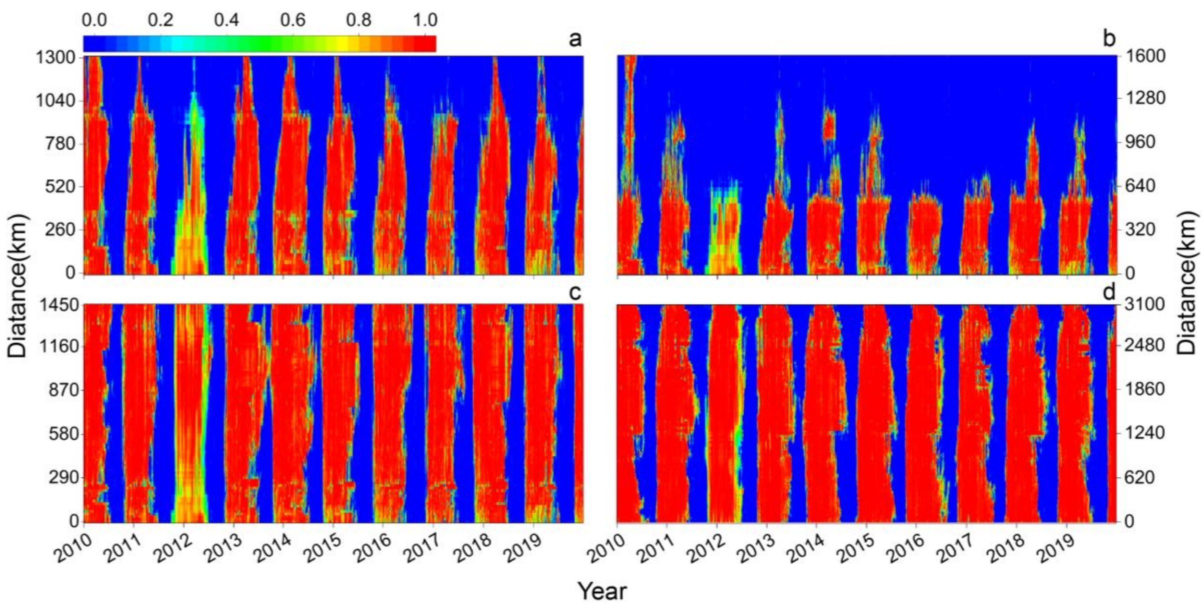

Figure 2 Sea ice concentration of four routes from 2010 to 2019. Section a-d represent R1-R4 respectively.

Obvious change in SIC along R1 occurred at about 1000km from the start point, where was the Kara Strait. Because of the warm flow from the Barents Sea, the low SIC period of the first 3/4 route was much less than that of the latter 1/4. That means, R1 was almost navigable once vessels passed the Kara Strait. A similar phenomenon was more obvious on R2. Sea ice decreased sharply after the first 1/3 distance from the start, where was the northwest corner of the Yamal peninsula. The Kara Strait is not only a separation of the Kara Sea and the Barents Sea, but also plays an important role in increasing the opportunity of navigation along the NEP.

Ice conditions of R3 and R4 were more severe than those of R1 and R2. It is obvious that the regions with SIC close to 1 is predominant in Figure 1c and d. The annual mean SIC was in the range of 0.73 and 0.54, and the decadal mean was 0.62. The largest and smallest annual mean SIC occurred in 2013 and 2011 respectively. Annual mean SIC of R4 changed within a relative narrow range from about 0.69 to 0.6, with the decadal mean of 0.64. The maximal value of the annual mean SIC took place in 2014, and the minimum was achieved in 2018.

There was a special area on R3 between 2013 and 2019, owing to the Vilkitskoyo Strait. In fact, the Vilkitskoyo Strait located in the distance of 1100-1300km from the start, but high SIC parts took place in the region from 600km to 1300km. It was because of the accumulated sea ice around the strait, and the degrees of sea ice accumulation were different year to year. There were two high SIC sections on R4, one was the Delong strait (at the distance of about 2600-2700km) and the other was floating ice of the East Siberian Sea (about 1200-2200km). These influences of two areas on SIC were similar in recent years.

3.2 Navigable period

There are different classification societies, such as Finnish-Swedish Ice Class Rules (FSICR) designed by Finnish Marine Agency and Swedish Marine Agency (FMA&SMA) and Polar Class (PC) designed by International Association of Classification Societies (IACS), that have designed the rules for icebreakers according to the ice conditions. Among which, the Polar Class (PC) takes several factors into account, including ice type, thickness and cruise speed (IACS, 2019) . This rule becomes more and more widely accepted by shipping companies. World Meteorological Organization (WMO) has also linked the ice concentration with the difficulty of navigation in ice. In the following study, we defined two SIC thresholds, namely 0.7 and 0.3, to calculate the navigable period of a route, which are based on Lei et al. (2015) and Shibata et al. (2013) . The SIC threshold of 0.7 means that PC4 icebreakers can navigate, and 0.3 means open-water vessels can pass with difficulty and icebreakers can navigate easily.

The navigable period (NP) and navigable days (ND) on the basis of the SIC thresholds are denoted by green dots and red lines on Figure 3. The light green dots and red dotted lines represent the NP and ND depending on the threshold of 0.7, and dark green dots and solid red lines stand for corresponding values under the threshold of 0.3. In consideration of the vessels can avoid sea ice by human intervention. SIC of more than 95% test points are lesser than the threshold are regarded as navigable.

As shown in Figure 3a, the mean ND of R1 with SIC<0.7 was 125 days, with the shortest ND of 100 days occurred in 2014, and the longest ND was 147 days occurred in 2016. Corresponding NP of R1 was from early July to early November. The mean ND defined by SIC<0.3 of R1 was 110, with the shortest ND of 92 days in 2014, and the longest ND was 138 days in 2016. An interesting phenomenon is that NP and ND defined by different thresholds were only about 10 days apart, which reveals that the melting speed was fast. A similar situation took place in R2. ND and NP were similar with R1 under different SIC thresholds. The mean ND defined by different SIC thresholds were 125 days and 111 days respectively. The corresponding NP is similar to R1(Figure 3b).

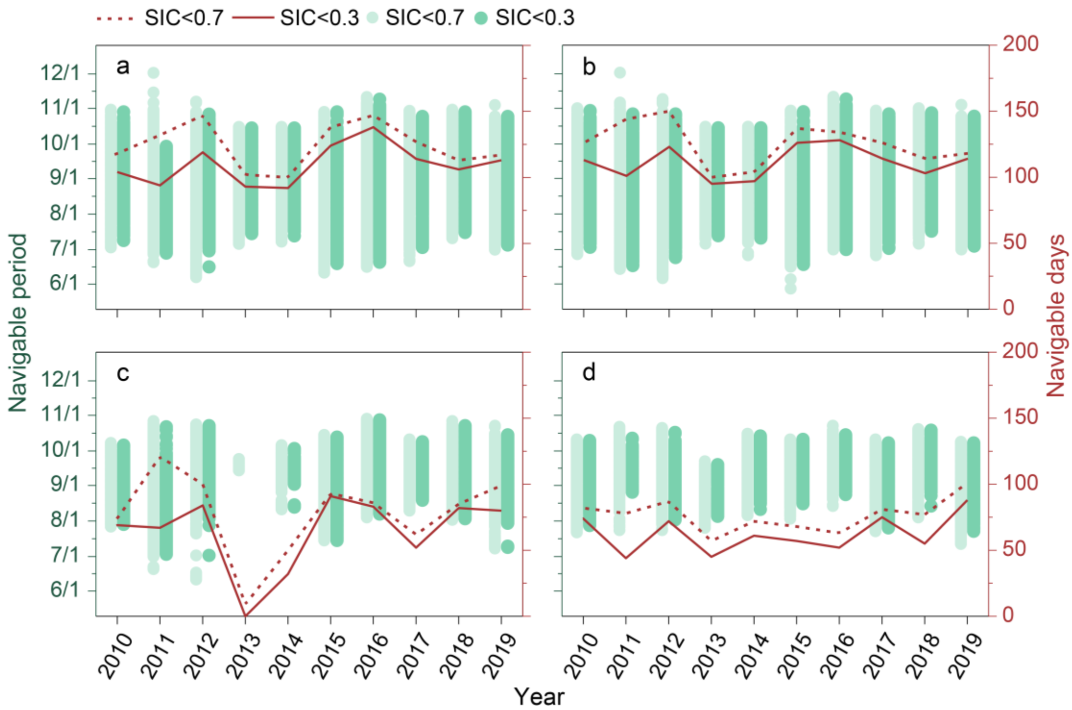

Figure 3 Navigable period (green dots) and navigable days (red lines) of four routes using ice concentration thresholds of 0.7 and 0.3. Section a-d represent R1-R4 respectively.

Comparing with R1 and R2, the navigability of R3 and R4 were different and more irregular. The mean ND of R3 defined by different SIC thresholds were 78 and 64 days respectively, corresponding maximum ND was 121 days (SIC<0.7) in 2011 and 91 days (SIC<0.3) in 2015 (Figure 3c). The SIC in 2013 is an exception because sea area around the west of Vilkitskoyo Strait was covered by floating ice, which had a strong impact on the ND and NP of R3. Similar to R1 and R2, ND and NP of R3 and R4 using different thresholds were only about 10 days apart. ND of R4 was less and NP was more regular than R3. The mean ND defined by SIC<0.7 of R4 was 77 days, with the shortest ND of 57 days in 2019, and the longest ND was 101 days in 2013. Defined by SIC<0.3, the mean ND of R4 was 62 days and reaches its maximum of 88 days in 2019 and the minimum of 45 days in 2013. The range of NP was about early August to mid-October (Figure 3d).

3.3 Ice thickness

The monthly ice thickness data of CryoSat-2 cover the period from January to April and October to December in 2010-2019. The mean ice thickness along the four routes in the recent decade are illustrated in Figure 4. Obviously, sea ice thickness (SIT) in different routes shows different status but obvious tendency is not clear. The SIT on R3 and R4 were higher than that on R1 and R2. In every month, mean SIT of R4 was the highest among all, up to 1.55m in April and reached about 0.54m in October. The second thickest ice existed on R3. The mean thickness of R3 was 1.2m in March and April, and that in October was 0.3m. Sea ice on R1 and R2 had a similar mean thickness. In October, R1 and R2 were nearly open water, so mean SIT were almost 0 m. And the ice grew to 1.16m in April. Ice got thicker gradually from October to April of next year on all routes, with an increase of 1.11m, 1.11m, 0.9m and 1.01m, respectively.

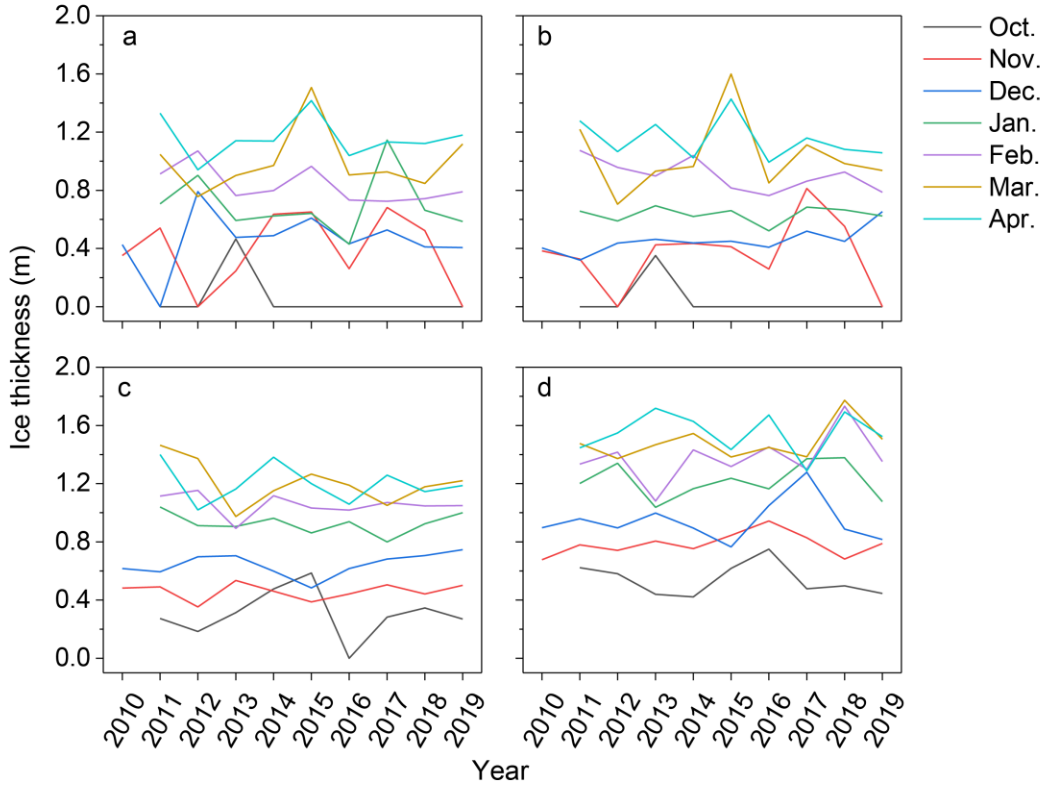

Figure 4 Ice thickness of four routes in Oct.-Apr..

4 Conclusion

Sea ice data of satellite remote sensing were analyzed to characterize seasonal and spatial changes in ice conditions along the NEP from 2010 to 2019. In this study, the NEP was divided into four parts, which are common routes of Arctic navigation. According to the SIC and thickness from multisource remote sensing data, the following results are obtained. In general, the ice conditions of the two Asian routes are more severe than that of the European routes. The SIT of two Asian routes is thicker from October to April and SIC are higher in the other months than those of European routes. So navigation from Yamal peninsula to Europe along the NEP is much easier than that to Asia. It is possibly navigable for two European routes from July to October. For the Asian routes, navigable periods are shorter, about August to September. In July or October, a powerful icebreaker is necessary along the Asian route when pass the East Siberian Sea.

Acknowledgements

This research was supported by the National Key R&D Program of China (Grant no. 2017YFE0111400), National Natural Science Foundation of China (Grant nos. 41922045 and 41876213), and the Fundamental Research Funds for the Central Universities.

References:

Cavalieri, D. J. and C. L. Parkinson, et al., 1996. updated yearly. Sea Ice Concentrations from

Nimbus-7 SMMR and DMSP SSM/I-SSMIS Passive Microwave Data, Version 1. Boulder, Colorado USA. NASA National Snow and Ice Data Center Distributed Active Archive Center..

Comiso, J. C., 2012. Large Decadal Decline of the Arctic Multiyear Ice Cover. Journal of Climate, 25 (4): 1176-1193.

Comiso, J. C. and C. L. Parkinson, et al., 2008. Accelerated decline in the Arctic sea ice cover. Geophysical Research Letters, 35 (1): L01703.

Comiso, J. C. and W. N. Meier, et al., 2017. Variability and trends in the Arctic Sea ice cover: Results from different techniques. Journal of Geophysical Research: Oceans, 122 (8): 6883-6900.

Eguíluz, V. M. and J. Fernández-Gracia, et al., 2016. A quantitative assessment of Arctic shipping in 2010 – 2014. Scientific Reports, 6 (1): 30682.

IACS, 2019. Requirements concerning POLAR CLASS. (Available at http://www.iacs.org.uk/publications/unified-requirements/ur-i/).

Kwok, R. and D. A. Rothrock, 2009. Decline in Arctic sea ice thickness from submarine and ICESat records: 1958-2008. Geophysical Research Letters, 36 (15): L15501.

Laliberté, F. and S. E. L. Howell, et al., 2016. Regional variability of a projected sea ice ‐ free Arctic during the summer months. Geophysical Research Letters, 43 (1): 256-263.

Laxon, S. W. and K. A. Giles, et al., 2013. CryoSat-2 estimates of Arctic sea ice thickness and volume. Geophysical Research Letters, 40 (4): 732-737.

Lei, R. and H. Xie, et al., 2015. Changes in sea ice conditions along the Arctic Northeast Passage from 1979 to 2012. Cold Regions Science and Technology, 119: 132-144.

Lindsay, R. and A. Schweiger, 2015. Arctic sea ice thickness loss determined using subsurface, aircraft, and satellite observations. The Cryosphere, 9 (1): 269-283.

Liu, M. and J. Kronbak, 2010. The potential economic viability of using the Northern Sea Route (NSR) as an alternative route between Asia and Europe. Journal of Transport Geography, 18 (3): 434-444.

Melia, N. and K. Haines, et al., 2016. Sea ice decline and 21st century trans-Arctic shipping routes. Geophysical Research Letters, 43 (18): 9720-9728.

Onarheim, I. H. and T. Eldevik, et al., 2015. Skillful prediction of Barents Sea ice cover. Geophysical Research Letters, 42 (13): 5364-5371.

Parkinson, C. L. and J. C. Comiso, 2013. On the 2012 record low Arctic sea ice cover: Combined impact of preconditioning and an August storm. Geophysical Research Letters, 40 (7): 1356-1361.

Peacock, N. R., 2004. Sea surface height determination in the Arctic Ocean from ERS altimetry. Journal of Geophysical Research, 109 (C7): C07001.

Qin, D., 2014. The Evaluation Research on the Navigation Environment of Arctic Northeast Route Based on Cloud Model (in Chinese), Dalian Maritime University.

Shibata, H. and K. Izumiyama, et al., 2013. Sea-ice coverage variability on the Northern Sea Routes, 1980 – 2011. Annals of Glaciology, 54 (62): 139-148.

Smedsrud, L. H. and I. Esau, et al., 2013. The role of the Barents Sea in the Arctic climate system. Reviews of Geophysics, 51 (3): 415-449.

Spreen, G. and L. Kaleschke, et al., 2008. Sea ice remote sensing using AMSR-E 89-GHz channels. Journal of Geophysical Research, 113: C02S03.

Stroeve, J. C. and V. Kattsov, et al., 2012. Trends in Arctic sea ice extent from CMIP5, CMIP3 and observations. Geophysical Research Letters, 39 (16): L16502.

03
Fixed offshore structures in ice

25th IAHR International Symposium on Ice
Trondheim, 23 - 25 November 2020

Spallation-Based Numerical Simulation of Ice-Induced Vibration of a Structure

R. Gagnon
OCRE/NRC
St. John's, NL, Canada
Robert.Gagnon@nrc-cnrc.gc.ca

A full-scale numerical simulation model of ice-induced vibration of structures has been developed (using LS-Dyna™) and applied to the Molikpaq facility for an ice-encroachment event similar to that which occurred on May 12, 1986 in the Beaufort Sea. The bulk ice sheet used for the simulations had elastic properties, and its dimensions were 6 km x 6 km x 2.5 m. Where ice crushing occurred at the structure-ice interface the ice model used was a crushable foam that incorporated regular spallation events. Typical characteristics of ice-crushing in the brittle regime were manifested by the model. That is, a narrow horizontal hard zone (relatively-intact high-interface-pressure ice) was present in the mid-height region of the ice-edge contact area. Soft-zone material (shattered spall debris from the hard zone) was also represented. Evolution of the hard-zone contact area involved rapid reductions in size during spallation events, immediately followed by fast growth during consequent elastic surging of the near-field ice sheet and structure towards each other, and then some slower growth (due to the bulk ice-sheet velocity) until the next spalling event. The specified 'thickness' of the spalls was 5.4 cm, as previously determined from Molikpaq records of the frequency of the spalling events as a function of ice-sheet speed. Spallation (and associated rapid drops in load) occurred at regular intervals whenever a critical amount of hard-zone stress was reached at the ice-structure interface. The amplitude of the Molikpaq repetitive movements in response to the sawtooth loading from the spalling events depended on whether the resonant frequency of the structure/ice system was higher (for a strong response) or lower (for a weak response) than the spalling frequency, where the spalling frequency is directly proportional to the ice-sheet speed. The continuously variable resonant frequency of the structure/ice system had a maximal limiting value (~ 2.1 Hz), designated as the At-Spallation-Resonant-Frequency (ASRF), that was essentially determined by the time duration of load drops at spallation events. The simulations inherently accounted for the variable effective mass and effective spring constant of the ice sheet.

1. Introduction

Ice crushing induced vibration has been the subject of interest in many investigations since problems were first encountered for some structures when ice sheets moved against them. Examples are structures in Cook Inlet, Alaska (Blenkarn, 1970), the Baltic Sea (Määttänen, 1978) and in Bohai Bay, China (Yue and Bi, 2000). The most widely known and studied events are those associated with the Gulf Canada Resources Ltd. Molikpaq caisson facility that occurred in 1986 during operations at the Amauligak I-65 site in the Canadian Beaufort Sea. Various analytical and numerical approaches (e.g. Määttänen, 1978; Kärnä et al., 1999; Hendrikse and Nord, 2019; Gagnon, 2012) have been applied to explain ice crushing induced vibration. Gagnon (2012) analytically showed that new understandings of ice crushing, with emphasis on spalling behavior, can be applied to the problem when large-scale aspects of the ice are sufficiently taken into account and that this can explain ice-induced vibrations, including so called 'lock-in' behavior. Here we present a full-scale numerical model of ice-induced vibration (IIV) that is fundamentally based on ice spallation at the structure-ice interface. The model is applied to a well-documented test case of ice-induced vibration of the Molikpaq structure that occurred on the May 12, 1986 in the Canadian Beaufort Sea (Jefferies et al., 2011). The Molikpaq structure, and the ice sheet that encroached on it on May 12, have been described before (e.g. Gagnon, 2012).

2.0. Spallation and Ice Induced Vibration – A Brief Review

In order to understand the makeup of the numerical simulation model, particularly the spallation components and the physical processes represented therein, it will be helpful to review some earlier work on ice-induced vibration of structures. As a convenience to the reader, a few aspects are included here that are taken directly from Gagnon (2012). Various studies have shown that ice crushing, at least at rates in the brittle regime, is highly geometrical (e.g. Daley, 1991; Evans et al., 1984; Gagnon, 1999; Spencer and Masterson, 1993). That is, spalling events are determined for the most part by the geometry of the ice formation and the depth of penetration, where both can influence the level of confinement. If the rate of penetration varies then the spalling frequency varies accordingly since spalls depend on depth of penetration. This has been discussed by Gagnon (2011) in the context of the development of an ice crushing numerical model that incorporates spalling. The process surface is the actual surface of the ice during the crushing interaction. The geometry of the process surface is determined by the spalling geometry, the hard-zone geometry and the presence of shattered spall debris, i.e. crushed ice. There have been many direct visual observations using normal and high-speed video cameras of regular spalling behavior, both in laboratory and field experiments, that coordinates with regular intervals of penetration as determined from displacement sensors and load sensors used in conjunction with known equipment compliances (Gagnon, 1999). Hence, it is not unreasonable to think that regular spalling events were happening in the case of the 12 May, 1986 Molikpaq event. We may represent the ice sheet and its ice process surface during crushing as in Figure 1 where the sequence of spalls and their occurrence according to depth of penetration is illustrated. The type of spalling event that ties in closely with the ice sheet speed involves a pair of spalls breaking away at approximately the same time, one from the lower and one from the upper edge portion of the ice sheet. As the sheet moves towards the structure there is elastic stress buildup in the ice and structure in between spalling events. For example, this is evident in Figure 2 where the portion of the load record shown occurred at the end of the 12 May 1986 event when the ice was moving slowly. The mechanisms that enable the rapid penetration of ice during a spalling event are complex (Gagnon, 1999). Referring again to the Molikpaq event we can see the rapid ice penetrations that occur, that are enabled by these processes, at the spalling-induced sharp load drops where sudden associated strain releases (surges) occur (Figure 3, from Gagnon (2012)).

3.0. Numerical Model Components and Properties

All simulations were run using LS-Dyna^{TM} commercial software. These were conducted on a HP Z840 Workstation using 38 CPU's. Depending on the initial ice-sheet speed (i.e. slower speeds took longer to run) and the number of spallation events included in a given simulation, the runtimes varied substantially and all but one were in the range (18 – 237 hours). One simulation, at the slowest ice-sheet speed, was deliberately left to run considerably past the point where spallations had stopped. Its runtime was ~ 336 hours. Characteristics of all model components are summarized in Tables 1 and 2. Here we are presenting results from one simulation primarily.

3.1. 'Molikpaq' Structure and Ice Sheet

The most efficient way to describe the model in a manner that gives the reader an appreciation for the large range of scales and element size is through a series of zoom-views from that of the full ice sheet down to the size of individual spalls at the ice/structure interface. Figure 4 shows the full model, i.e. using the 6 km x 6 km x 2.5 m ice sheet. Barely visible at this scale is the structure at the left edge mid position of the ice sheet that essentially represents a facility such as the Molikpaq. Figure 5 is a closer view at the scale of the structure. The model structure had a large Body-Block (22 m x 22 x 22 m) that represented the bulk effective mass of the Molikpaq. This was attached to a smaller Spring-Block (22 m x 22 m x 4 m) that had elastic properties and that served as the 'spring' component of the structure. The Spring-Block was in turn attached to a fixed rigid Base-Block (22 m x 22 m x 4 m). The three component structure system had a resonant frequency of 1.72 Hz, that is close enough to that of 1.80 Hz for the Molikpaq for our purposes. Figure 6 is a closer view of a stack of ridge-shaped entities called Hard-Zone-Spalls (HZS's) prior to their sequential crushing against the Crushing-Plate. Figure 7 shows details of a single HZS and its associated Support-Plate.

Another component, known as the Edge-Plate (Figure 5), is attached to the edge of the Ice-Sheet. The Edge-Plate has a length dimension along the edge of the Ice-Sheet of 60 m, that is, it spans the full width of the actual Molikpaq structure and transmits load to the Ice-Sheet associated with the crushing activity. In Figure 6 the Crushing-Plate is actually attached to the structure Body-Block. LS-Dyna enables one to attach one rigid body to another even if they are not in physical contact. In Figure 6, each HZS is supported underneath it by a thin rigid 'Support-Plate' (not visible) consisting of shell elements with rigid properties. This is illustrated in Figure 7 for one of the HZS's and a Support-Plate. In Figure 7 the two objects are separated for illustrative purposes, however, generally each HZS is in contact with the corresponding Support-Plate that supports it. All seven of the HZS Support-Plates are attached to the ice sheet Edge-Plate. Hence, when the ice sheet moves towards the structure the Support-Plates move with it and thereby push each HZS sequentially against the Crushing-Plate. This seemingly complicated arrangement is necessary to enable the Ice-Sheet and structure Body-Block (that both consist of large elements) to 'crush' against each other via the HZS's (that are part of the Ice-Sheet) and the Crushing-Plate (that is part of the structure Body-Block), where both have necessarily small elements. Note that the mesh nodes that comprise the HZS's, Support-Plate's and the Crushing-Plate are constrained to movement only in the Y-direction, i.e. the direction of the ice-sheet movement.

Here we note that in actual crushing of an ice sheet against a structure, such as the Molikpaq, the ice contact zone (that includes hard-zone spallation events) spans the full width of the structure, i.e. ~ 60 m in the Molikpaq case. In principle, we could have created HZS's that were 60 m in length, but the requirement of having small elements for the HZS's would necessitate an unwieldy large number of elements, roughly 60 times the number of elements we presently have for the HZS's. This would lead to memory issues and impractically long runtimes for the simulations. But one can achieve the intended behaviors in the simulation by enabling HZS's of reasonable length dimension (~ 0.9 m, in our case) to exert forces that are the same as what 60 meter long HZS's would generate. This is done simply by applying crushable-foam interface pressures that are sixty-six times the pressure values that would be assigned to a 60 m HZS. Hence, we can apply realistic loads to the structure face using HZS's of short length (and far fewer elements) that still provide all the characteristics of 60 m HZS's. This strategy provides high computational efficiency while maintaining the overall integrity of the spallation mechanisms and hard-zone evolution. The specific shape of the ends of the HZS's (Figures 6-7) is required so that when a HZS is crushing against the Crushing-Plate, no 'naked edges' (nodes without neighbors at the edge) interact with the Crushing-Plate. Such neighbor-less nodes would penetrate the crushing plate in an unrealistic manner that leads to error in interfacial forces.

4.0. Numerical Simulation Strategy

The load and displacement data from a simulation are shown below in Figures 8-10. At the beginning of any simulation (such as in Figure 8) the first thing that happens is that a uniform load of 100 MN is quickly applied to the surfaces of both the Crushing-Plate (associated with the structure) and the Edge-Plate (associated with the ice sheet). As discussed below, this load represents the 'ambient' load that is present throughout the simulation due to crushed ice that resides at the sides of the hard-zone contact area. Then the ice sheet is given an initial velocity (0.06 m/s in this case) towards the structure so that contact of the first HZS with the Crushing-Plate occurs and hard-zone load begins to accumulate. The load and HZS contact area continue to increase until the critical stress/strain is attained at the middle of the elongated ice-contact patch, at which point the HZS contact definition with the Crushing-Plate is automatically turned off by a switch that senses that the critical stress/strain has been attained. This results in an abrupt drop in load and onset of contact with the next HZS. Consequently load starts to increase again and the pattern repeats itself as the ice sheet continues its forward movement. Up to seven spallation events may be simulated in this fashion since the model presently contains seven stacked HZS's. Note that we did not include water in these simulations because the water-related shear force on the moving ice sheet is negligible compared to the inertial force of the sheet.

5.0. Description of a Spallation Event

The ice sheet is 2.5 m thick, however the process surface of the ice contact consists of hard-zone relatively intact ice and soft-zone crushed ice. The thickness of the horizontal band of hard-zone contact area is much less than the ice sheet thickness, roughly 1/10 (from ice crushing experiments) at load peaks, and it expands from an initial value (zero in this case) to its maximum value during the time between the load peaks as load increases. The force generated by actual crushed ice in this type of scenario is fairly constant because the change in contact area of the crushed ice is small whenever a new spallation occurs and shatters to become crushed ice. So it is convenient, justifiable and computationally efficient to forgo creating an object to apply the crushed-ice load. Instead, we need only use LS-Dyna to apply the appropriate force on the structure and the ice sheet (i.e. 100 MN in this case, in rough correspondence with the May 12, 1986 Molikpaq event) to adequately represent the 'constant' background force field that the crushed ice would have created. To be more specific, that force was numerically applied to the elements of the Edge-Plate and the Crushing-Plate. The images of the model components therefore do not show an object representing the crushed ice because it was not necessary. In the simulation hard-zone contact areas originate from the interaction of the ridge-shaped model entities (HZS's) consisting of intact ice that flatten against the Crushing-Plate as load is applied. The flattening is enabled by the crushable-foam property of these 'Hard-Zone-Spalls'. Each Hard-Zone-Spall plays two important roles in the simulation: 1. When the peaked ridge of the HZS is pressed against the Crushing-Plate it flattens by an amount proportional to the applied load, thereby creating a hard-zone area in direct contact with the plate where the interface pressure is high. 2. When the stress at the hard zone / Crushing-Plate interface reaches a critical prescribed value the simulation will switch off the contact definition of the Hard-Zone-Spall so that it no longer supports load, i.e. essentially taking it out of play. This corresponds to a spallation event where a portion of the hard-zone contact (in our case, all of it) separates and shatters to become crushed ice. There is consequently an abrupt drop in load at the ice / Crushing-Plate interface that is proportional to the size of the hard-zone contact area that was taken out of play. In the present case we have set up the simulation so that the spallation event happens when the next Hard-Zone-Spall entity in the sequential stack is about to make contact with the Crushing-Plate. This is achieved in LS-Dyna by using ON/OFF contact-definition switches that are triggered by a prescribed stress or strain in the Hard-Zone-Spall at the center of the flattened area

For elements of the HZS's that are undergoing volumetric compression in the flattening region at the HZS/Crushing-Plate interface the curve describing the pressure vs fractional volume change had a shape qualitatively similar to that used by Gagnon (2011). The actual quantitative x and y coordinate pairs for the four points defining the curve in the present case are: 0.0, 0.0; 0.015, 450; 0.5, 900; and 1.0, 900, where each pair corresponds to Fractional Volumetric Strain and Yield Stress (MPa) respectively. If the contact patch actually spanned the whole width of the structure face (~ 60 m), then the x and y coordinate pairs for the four points defining the curve would be: 0.0, 0.0; 0.015, 6.75; 0.5, 13.5; and 1.0, 13.5, where each pair corresponds to Fractional Volumetric Strain and Yield Stress (MPa) respectively. The former values were suitably chosen to generate the desired change in load (about 127 MN) that maximal compression of the HZS's, described above, would generate. With this strategy a reasonable facsimile of the magnitudes of the sawtooth load pattern generated near the end of the May 12, 1986 Molikpaq ice encroachment event could be obtained.

Figure 11 shows a sequence of 16 images from Simulation-2 depicting the behavior of two adjacent stacked HZS's during a time interval that spans portions of two sequential sawteeth in the sawtooth load pattern (Figure 8). Figure 8 has markers that correspond to the images in Figure 11. The far-field speed of the ice sheet (0.06 m/s) is near constant for this relatively short period of time. The sequence starts at the midpoint in time between two spallation events (sharp load drops). At this point a certain amount of load has accumulated, above and beyond the 'background load' associated with the crushed ice that is 'present' at the sides of the hard-zone contact areas, but not shown. The corresponding interfacial pressure distributions within the contact zones are also shown in Figure 11. We remind the reader that pressure indicated in the contact zone (that in the simulation is about 0.9 m in length) appear high because they need to be adjusted to represent the actual pressure that would be applied to the structure surface across its full 60 meter face length. That is, the actual pressure across the whole face of the structure is the pressure indicated in Figure 11 multiplied by 0.9/60. On the other hand, the maximal vertical extent of the pressure patch is the same in the images (~ 0.20 m) as it would be across the whole face of the structure. The hard-zone horizontal contact band, where the crushable foam has flattened against the Crushing-Plate, continues to gradually grow in thickness with the continuing ice-sheet movement up to the point where the load peaks and a spallation abruptly occurs between images 6 and 7. Image 7 shows only the second HZS since the first one has been 'switched off'. Note that Images 7 and 8 indicate a very rapid forward movement and flattening of the HZS compared to the earlier images. This is due to the rapid surge (Figure 10) of the Crushing-Plate (associated with the structure) and the HZS (associated with the Ice-Sheet) towards each other resulting from the release of elastic energy at the load drop. Following the rapid surge, the contact area of the HZS with the Crushing-Plate (as shown in images 9-16) continues to increase gradually as in images 1-6.

6. The Role of Resonance of the Structure / Ice System

We note that the simulation presented here is part of a larger set that we conducted for various ice-sheet speeds. The full set of results showed that the displacement amplitude response of the structure (e.g. Figure 9) to the sawtooth loading patterns (e.g. Figure 8) depended on whether the resonant frequency of the structure/ice system was higher (for a strong response) or lower (for a weak response) than the spalling frequency, where the spalling frequency is directly proportional to the ice-sheet speed. Furthermore, a maximal limiting resonant frequency (~ 2.1 Hz) of the structure/ice system was identified, designated as the At-Spallation-Resonant-Frequency (ASRF), as in Figure 9, and its value agreed reasonably well with the corresponding value (~ 2.0 Hz) identified in the Molikpaq May 12, 1986 event (Figure 3). The continuously variable resonant frequency of the structure/ice system partly depends on the effective mass and effective spring constant of the ice sheet, where both in turn depend on the cyclic loading frequency (i.e. spalling rate). Finally, amongst the simple simulations we conducted to obtain the effective mass and effective spring of the ice sheet using the method of Gagnon (2012), one involved directly applying a very fast cyclic load of 100 MN, with a half-cycle comparable to the duration of a load drop during spallation. The system resonant frequency determined for that case was ~ 2.1 Hz. This corroborates with the previously-identified ASRF.

7. Conclusions

We have presented a full 3D numerical model for ice induced vibration of structures that is based on documented aspects of ice crushing in the brittle regime. The model incorporates regular spallation events, and high-pressure and low-pressure zones. The simulation results agree quite well with the load and displacement data from a May 12, 1986 Molikpaq ice-induced vibration event. Furthermore, the results emphasized the important role that the resonant frequency of the structure/ice system plays.

Acknowledgements

The author is grateful to OCRE/NRC for its support of this work, and to Jungyong Wang for helpful technical discussions.

References

Blenkarn, K.A., 1970. Measurement and analysis of ice forces on Cook Inlet Structures. Proc. 2nd OTC Conf., Houston, TX, OTC 1261, vol. II, pp. 365‑378.

Daley, C.G., 1991. Ice edge contact and failure. Cold Regions Science and Technology 21, 1‑23.

Evans, A.G., Palmer, A.C., Goodman, D.J., Ashby, M.F., Hutchison, J.W., Ponter, A.R.S., Williams, G.J., 1984. Indentation spalling of edge-loaded ice sheets. Proceedings of IAHR 1984, Hamburg, pp. 113‑121.

Frederking, R., 2004. Ice Pressure Variations during Indentation. Proc IAHR Symposium on Ice, St. Petersburg, Russia, pp. 307‑314.

Gagnon, R.E., 1999. Consistent observations of ice crushing in laboratory tests and field experiments covering three orders of magnitude in scale. Proc. POAC-99, Helsinki, Finland, 2, pp. 858‑869.

Gagnon, R., 2011. A numerical model of ice crushing using a foam analogue. Cold Regions Science and Technology. 65 (3), 335‑350.

Gagnon, R., 2012. An explanation for the Molikpaq May 12, 1986 event. Cold Regions Science and Technology 82 (2012) 75–93.

Hendrikse, H., Nord, T.S., 2019. Dynamic response of an offshore structure interacting with an ice floe failing in crushing. Marine Structures 65 (2019), 271-290.

Kärnä, T., Kamesaki, K., Tsukuda, H., 1999. A numerical model for dynamic ice‐ structure interaction. Computers and Structures 72, 645‐658.

Määttänen, M., 1978. On conditions for the rise of self-excited ice-induced autonomous oscillations in slender marine pile structures. Winter Nav. Board, Finland, Res. Rep., 25.

Määttänen, M., Marjavaara, P., Saarinen, S., 2011. Ice crushing pressure distribution against a compliant stiffened panel. Proc. 21st Int. Conf. On Port and Ocean Engineering under Arctic Conditions, Montreal, Canada, POAC 2011, paper #038.

Spencer, P.A., Masterson, D.M., 1993. A geometrical model for pressure aspect-ratio effects in ice‐structure interaction. Proceedings of the 12th International Conference on Offshore mechanics and Arctic Engineering, OMAE 1993, vol. 4, pp. 113‐117.

Vaudrey, K.D., 1977. Determination of mechanical sea ice properties by large scale field beam experiments. In: Muggeridge, D.B. (Ed.), POAC'77—Fourth International Conference on Port and Ocean Engineering Under Arctic Conditions, vol. 1, pp. 529‐543.

Yue, Q.J., Bi, X., 2000. Ice-induced jacket structure vibrations in Bohai Bay Sea. Journal of Cold Regions Engineering 14 (2), 81‐92 (June 2000, Paper No 21698).

Figures and Tables

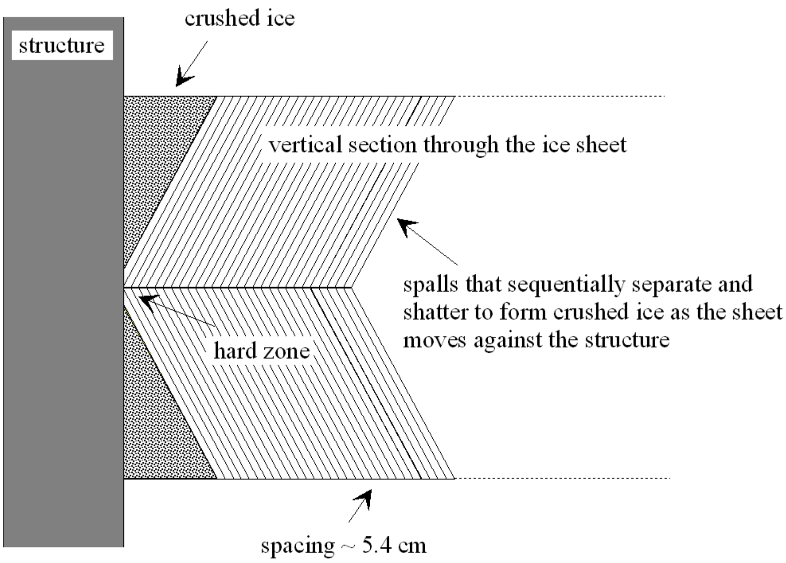

Figure 1. Schematic illustrating the sequence of spalls that will occur as the ice sheet moves to the left and crushes against the Molikpaq structure. Regions of relatively soft crushed ice, located above and below a central region of relatively intact hard ice, are also indicated. Note that experimental studies have observed higher pressures in the middle of ice sheets during crushing (e.g. Määttänen et al., 2011; Frederking, 2004). Taken from Gagnon (2012).

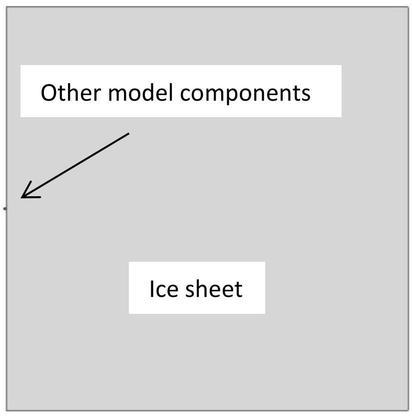

Figure 4. Full model components. The 6 km x 6 km x 2.5 m ice sheet is the main object visible at this scale. The other components are barely visible at the left edge of the ice sheet. Zoom-level 1.

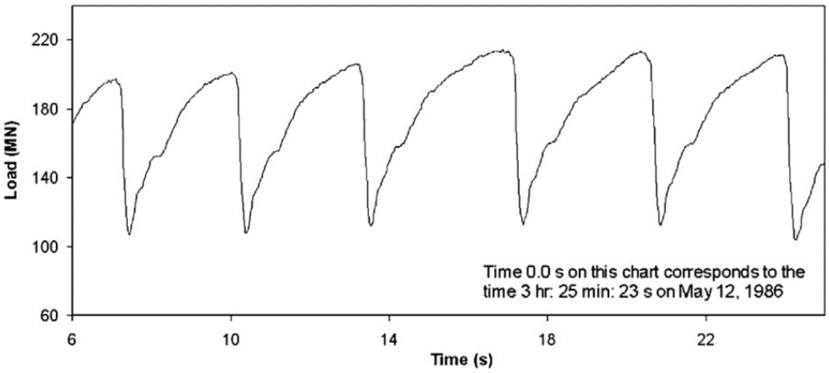

Figure 2. A portion of the load record acquired during the third 'burst file' data trace where the ice sheet was moving slowly against the Molikpaq structure. A spalling event is associated with each abrupt drop in load in the sawtooth pattern and these relieve the stress that builds up between the spalling episodes. Taken from Gagnon (2012).

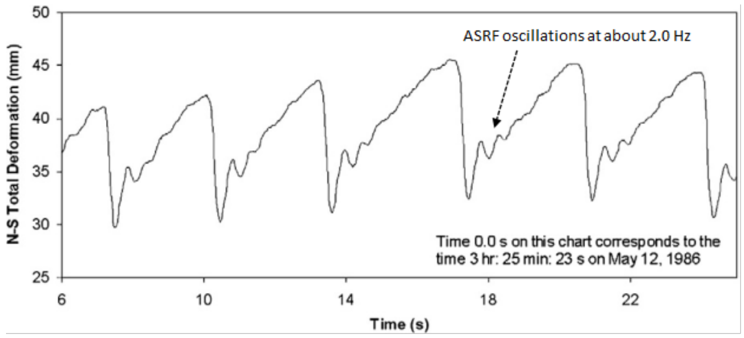

Figure 3. Movement of the north face of the Molikpaq in the north–south direction as the ice sheet crushes against it. The record corresponds to the same time period as shown in the load record in Figure 2. A rapid movement of the structure (about 10 mm) is evident at each spalling event. Taken from Gagnon (2012). Note: The 'ASRF oscillations' are explained below.

Table 1. Characteristics of Model Components.
Note: The ice modulus values are within the range given by Vaudrey (1977).

Object	Dimensions (m)	Element Type/Size (m)	Modulus (GPa)	Density (kg/m^3)	Strain Property	Mass (kg)
Ice-Sheet 1	6000 x 6000 x 2.5	Solid 15 x 15 x 0.625	3.0	900	Elastic	81 x10^9
Ice-Sheet 2	6000 x 6000 x 2.5	Solid 15 x 15 x 0.625	1.5	900	Elastic	81 x10^9
Ice-Sheet 3	7000 x 15000 x 2.5	Solid 15 x 15 x 0.625	3.0	900	Elastic	236.3 x10^9
Ice-Sheet 'Edge-Plate'	60 x 2.5 x 1.0	Solid 15 x .625 x .5	9.0	900	Rigid	150
Structure 'Body-Block'	22 x 22 x 22	Solid .5 x .5 x .5	5.0	8000	Rigid	85.2 x10^6
Structure 'Spring-Block'	22 x 22 x 4	Solid .5 x .5 x (.051-.759)	0.0826	2000	Elastic	3.87 x10^6
Structure 'Base-Block'	22 x 22 x 4	Solid .5 m x .5 m x .5 m	5.0	8000	Rigid	15.5 x10^6
Structure 'Crushing-Plate'	2.024 x 0.998 x 0.2	Shell .038 x .025	1000.0	8000	Rigid	Negligible ~ 3.2 x10^3
Hard-Zone-Spall (a.k.a 'HZS')	See Table 2	Solid Top view, .038 x .025 x .027	160.0	900	Crushable Foam	Negligible ~ 14.1
Hard-Zone-Spall 'Support-Plate'	Same as lower surface of spall	Shell Top view, .038 x .025	1000.0	8000	Rigid	Negligible ~ 554

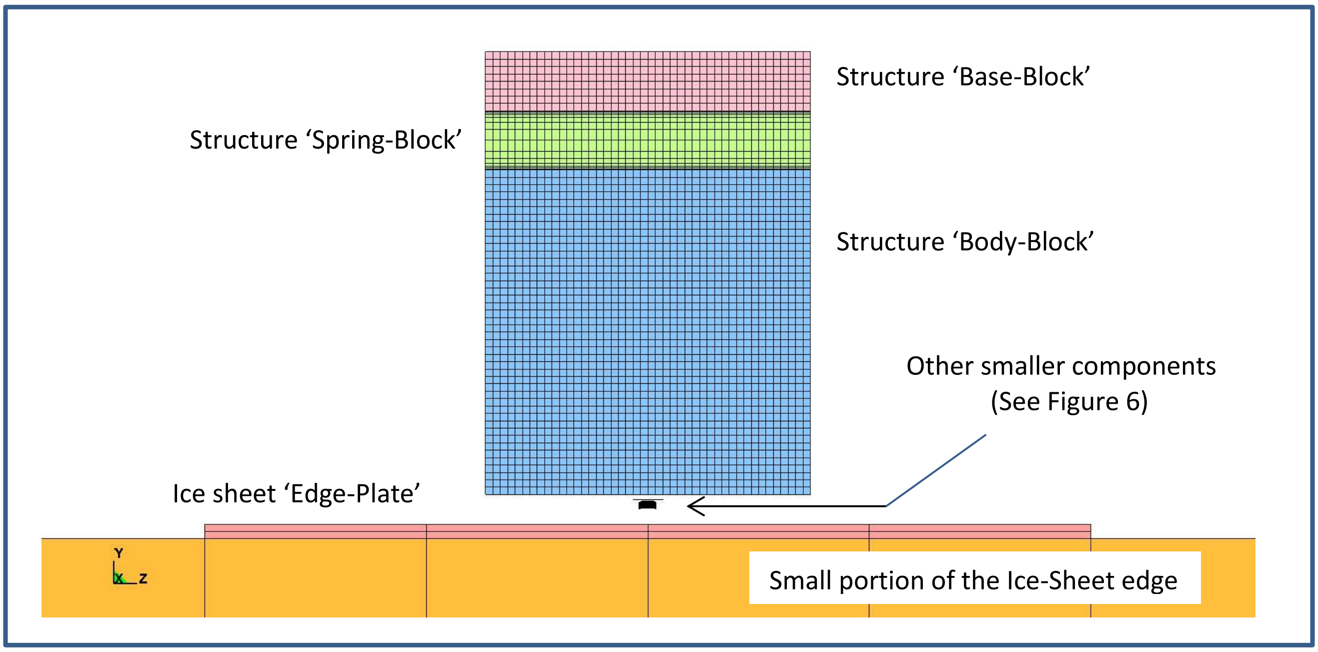

Figure 5. Various components of the model shown at a much smaller scale than that of Figure 4. Zoom-level 2.

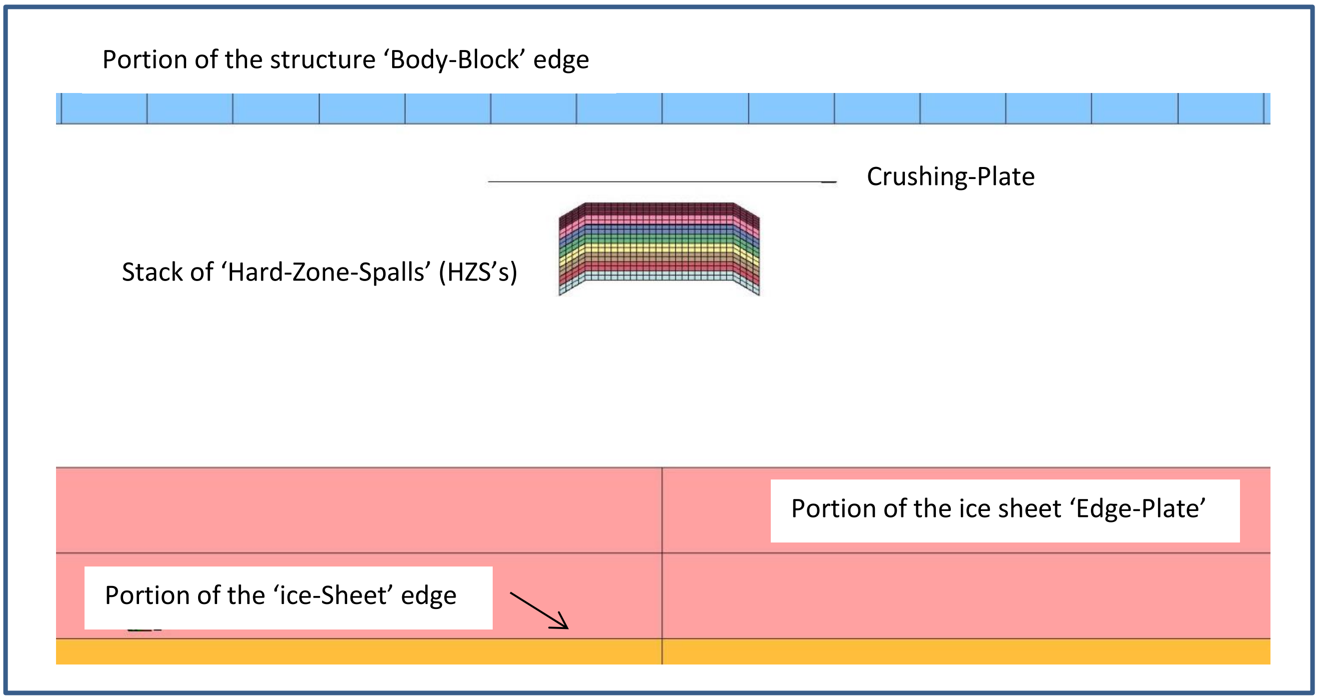

Figure 6. Various components of the model. Note that some objects are attached to other objects even though they may not be in physical contact. For example, the Crushing-Plate is attached to the structure Body-Block. Zoom-level 3.

Table 2. Characteristics of Model Components: Hard-Zone-Spall Dimensions - Particulars.

Full Length (m)	Ridge Length (m)	Width (m)	Base-to-Top Height (m)	Ridge Base-to-Top Height (m)	Thickness (m)
1.163	0.863	0.250	0.214	0.126	0.054

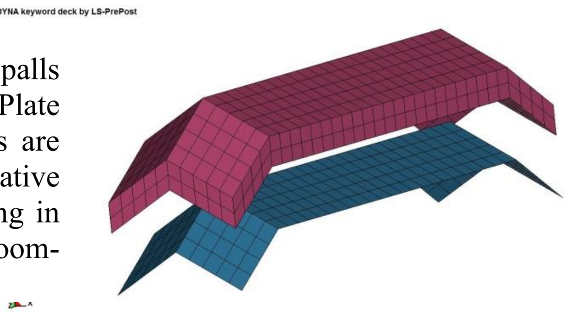

Figure 7. One of the Hard-Zone-Spalls (HZS's) with its associated Support-Plate underneath it. Note that the two objects are separated in this graphic for illustrative purposes, where normally during crushing in the simulation they are in contact. Zoom-level 4.

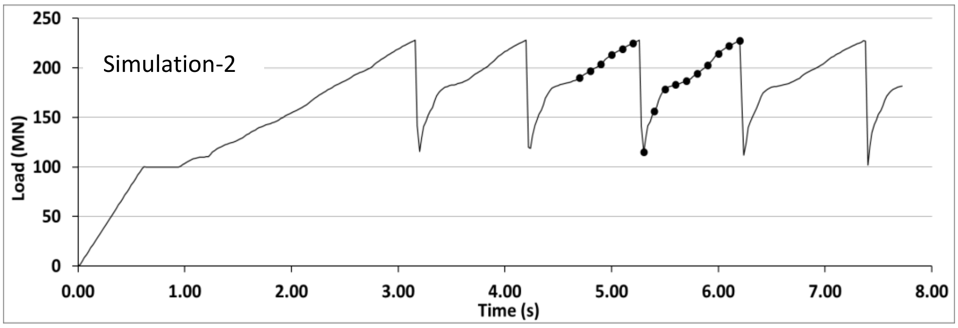

Figure 8. Load time series plot for Simulation-2. On the plot there are dark-circle markers that span portions of two of the load sawteeth. The markers correspond with simulation images shown in Figure 11 below.

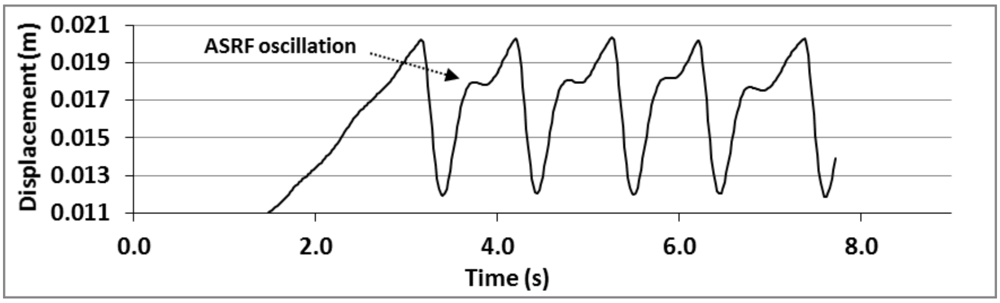

Figure 9. Structure displacement time series plot for Simulation-2.

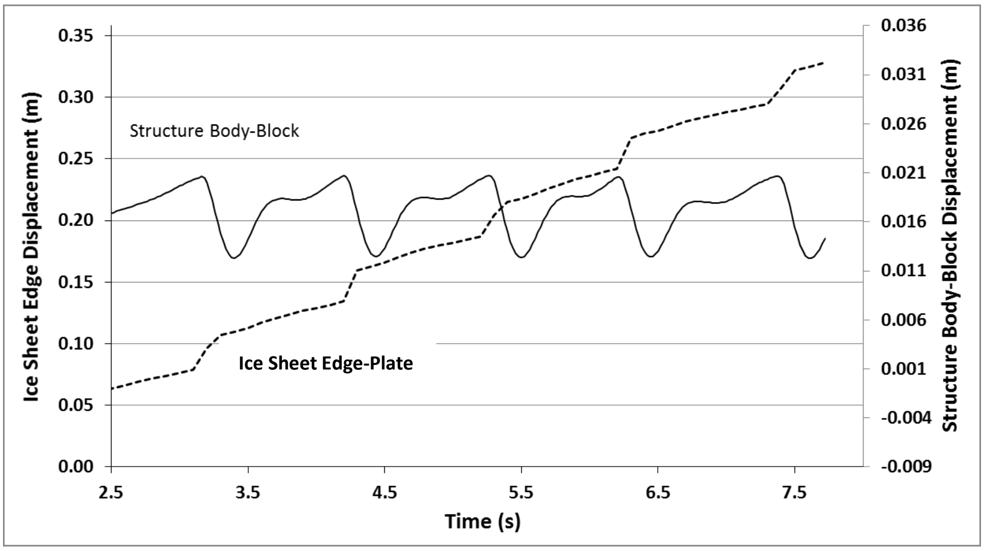

Figure 10. Displacement time series of the ice sheet Edge-Plate and the structure Body-Block for Simulation-2. Note that the structure and ice sheet edge surge towards each other at the spallation-induced load drops.

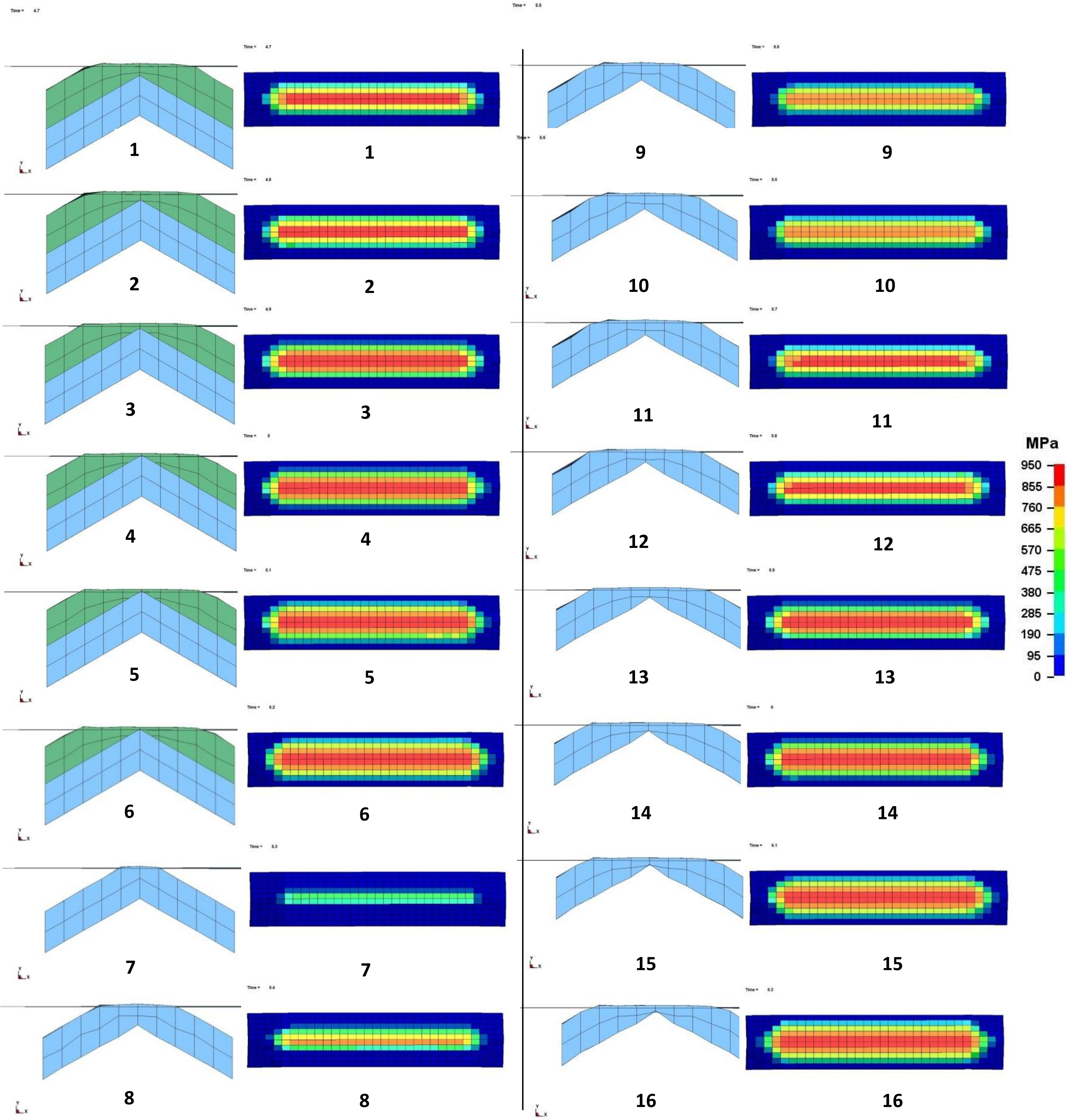

Figure 11. Sequence of 16 numbered pairs of images, from top left to bottom right. A pair consists of a sectional-view image of HZS's flattening against the Crushing-Plate and a corresponding image of the interfacial contact pressure pattern. The pairs correspond to the 16 dark-circle markers indicated on the load time series for Simulation-2 (Figure 8). The color-coded pressure scale for the pressure pattern images is at the right. Note that continuous horizontal contact area/pressure patterns have been observed in experimental studies involving structures interacting with ice sheets (e.g. Määttänen et al., 2011). The maximal vertical width of the contact patches is ~ 0.2 m.

25th IAHR International Symposium on Ice
Trondheim, 23 - 25 November 2020

Combined distribution of ice thickness and speed based on local measurements at the Norströmsgrund lighthouse 2000-2003

Vegard Hornnes[1], Knut Vilhelm Høyland[1], Joshua Dennis Turner[1], Ersegun Deniz Gedikli[1,2], Morten Bjerkås[3]

[1] *Department of Civil and Environmental Engineering, Norwegian University of Science and Technology,*
Høgskoleringen 7A, 7491 Trondheim, Norway
vegard.hornnes@ntnu.no
[2] *Department of Ocean and Resources Engineering, University of Hawaii at Manoa, Honolulu, USA*
[3] *DIMB Consult AS,*
Ellefsens vei 3, 7020 Trondheim, Norway

Fatigue caused by ice-induced vibrations (IIV) is an important design consideration for offshore structures exposed to drifting sea ice. The occurrence of IIV is promoted by, but not limited to, certain combinations of ice thickness and ice drift speed, which makes them fundamental input parameters for structure fatigue life estimation. To that end, this work identifies and analyses the frequency of combined ice thicknesses and ice drift speeds during all recorded ice-structure interaction events at the Norströmsgrund lighthouse during 2000 – 2003. The ice drift speed measurements were performed manually at the lighthouse, leading to bias towards multiples of 0.05 m/s. The ice thickness measurements by EM antenna underestimates ridge keel depth. The current approach gave a total of above 25 days of ice condition measurements. The cumulative distributions for ice thickness and speed were estimated. Given drifting ice conditions, the probability of encountering ice thicker than 0.8 m was 0.34, i.e. the probability of encountering thicker ice than most of the level ice in the area. A relatively frequent combination of ice conditions was ice thickness between 0.1 and 0.6 m and ice drift speed between 0.05 and 0.15 m/s, occurring with a probability of 0.29.

1. Introduction

Drifting sea ice can cause severe IIVs of offshore structures. One example is the Kemi-I lighthouse situated in the Bay of Bothnia, which eventually collapsed after a period of heavy vibrations caused by ice actions during the winter of 1973/74 (Määttänen, 1975). To ensure safe and reliable structures, the potential IIVs caused by ice conditions in an area must therefore be considered during design (ISO, 2019). IIVs can be divided into three regimes: intermittent crushing, frequency lock-in and continuous brittle crushing (ISO, 2019). The occurrence of each type of IIV will depend on the local ice conditions as well as parameters such as the structural flexibility (Hendrikse and Nord, 2019). Notably, frequency lock-in can lead to significant vibrations close to the natural frequencies of the structure and is therefore a concern when it comes to structural fatigue (Hendrikse and Koot, 2019).

For offshore wind turbines, fatigue load caused by wind and waves is a major design concern (Igwemezie et al., 2019), making it important to consider the addition of possible fatigue loads from ice. Different models have been developed to understand the impact of IIVs on structural fatigue, such as by Hendrikse and Nord (2019). The application of the model for an offshore wind project is described by Hendrikse and Koot (2019). In short, the model attempts to find the combinations of ice drift speed and ice thickness that lead to frequency lock-in for a structure. Then, the probability of occurrence of the relevant ice conditions can be used to determine the vibration cycles and the contribution to fatigue. A parallel can be drawn to structural reliability analyses based on wave conditions, which rely on simultaneous distributions of significant wave height and wave period (Vanem, 2016). Consequently, accurate statistics of local ice conditions in an area are necessary in order to determine the fatigue contribution from ice interactions.

A relevant source of statistics on local ice conditions were recorded through the 'Low Level Ice Forces' (LOLEIF) and the 'Measurements on Structures in Ice' (STRICE) projects. During the years 2000 – 2003, extensive full-scale measurements of ice thickness and ice drift speed were carried out at the Norströmsgrund lighthouse (Haas and Jochmann, 2003). Norströmsgrund is located in the Bay of Bothnia in the Northern Baltic sea (N65°6.6′ E22°19.3′), in a transition zone between land-fast and drift ice (Bjerkås, 2006, Ervik et al., 2019). The ice condition measurements at Norströmsgrund are advantageous in that they provide a temporal distribution of the conditions experienced by the structure, and that possible influences from the structure on the ice speed are included. The probability of occurrence of ice conditions at Norströmsgrund can thus be used as input for fatigue modelling. In addition, the statistics can provide a starting point for connecting local ice conditions and met-ocean data, in order to predict local ice conditions in other areas (Bjerkås and Gedikli, 2019, Turner et al., 2020).

2. Data and data analysis

The following outlines how the local measurements of ice thickness and speed were carried out during the LOLEIF/STRICE projects.

2.1. Ice drift speed

The ice drift velocity was estimated manually by the personnel stationed on the lighthouse during ice-structure interactions (Fransson, 2008). A video screen showing the ice was marked corresponding to a 10x10 m^2 grid, and the ice speed and direction was estimated by tracking distinct ice features through the grid. The manual measurement method resulted in a discrete distribution of speed values with at most two significant digits per value. The measurements were performed infrequently and irregularly, with gaps in time between measurements ranging from minutes to hours. No clear pattern in the timing of the measurements was observed. A measurement was often made when the load recording started and after significant shifts in speed, but this was not always the case, see Samardžija (2018) and Ervik et al. (2019).

2.2. Ice thickness

The ice thickness measurements at the Norströmsgrund lighthouse were carried out with several different combination of instruments during the four-year period (Haas and Jochmann, 2003). An upward-looking sonar (ULS) as well as a Geonics EM31 electromagnetic ice thickness sensor (EM) was employed in 2000 to measure the subsurface profile of the ice, while a laser distance meter measured the elevation above the surface. The laser distance meter was replaced by a sonic distance meter in 2003. The ULS was placed 6 – 7 m below mean water level, about 5 m southeast of the lighthouse. The EM sensor and laser distance meter were mounted on a rig extending 10 m away from the lighthouse, approximately 2 m above the mean water level. The ice thickness measurement frequency varied between 0.1 – 1 Hz. Note that the ice thickness was not always recorded due to instrument issues.

The EM measurements averaged the ice thickness over a certain footprint of some metres in diameter (Haas and Jochmann, 2003). For ridges, the EM most probably measured the thickness of the consolidated layer and some part of the rubble depending on their conductivities, which is affected by their salinities and the macroporosity (Ervik et al., 2019). As a result, the EM measurements underestimated the ridge keel depth. In contrast, the ULS always measured the deepest point on the ice keel, making it more accurate for ridge thickness. Haas and Jochmann (2003) found that EM measurements underestimated the keel depth by as much as 50%, but that EM and ULS measurements agreed well for level ice. Bjerkås (2006) multiplied the EM keel depths with 3.16 in order to reach similar values as measured by ULS. In what follows, no correction will be made for possible underestimation of keel depth by EM. In order to maintain a consistent measurement method between 2000 – 2003, this work focuses on the ice thickness measured through EM only.

2.3. Data structure

Measurements of loads, ice thickness, speed and other parameters were recorded and saved in a total of 519 time series known as events, with durations ranging from 10 minutes to 24 hours. Importantly, the measurements of ice speed were only recorded simultaneously with load measurements, primarily during ice-structure interactions. The loads were recorded when observers noticed interesting ice interactions with the lighthouse (Bjerkås et al., 2003). That is, the ice-structure interactions governed the collection of ice condition data. As such, the selection of recorded ice conditions during events will be inherently skewed towards conditions which produce ice-structure interactions.

2.4. Data analysis

A MATLAB routine was used to search through and extract recorded measurements from the 519 events. Errors in the dataset were removed. Subsequently, the collected data were processed as outlined in the following.

2.4.1. Stepwise interpolation

Because of variations in the measurement frequency of ice thickness and speed and the poor temporal resolution of the speed measurements, the parameters were interpolated as illustrated in Figure 1 within each event. The interpolation was not carried out outside the duration of the events. Stepwise interpolation schemes were preferred over alternatives like linear interpolation in order to avoid generating thickness and speed values that did not necessarily occur. The values were interpolated every second, effectively standardizing the measurement frequency to 1 Hz. Additionally, a comparison between the previous neighbour interpolation and nearest neighbour interpolation was carried out in order to investigate the resulting speed frequency distributions.

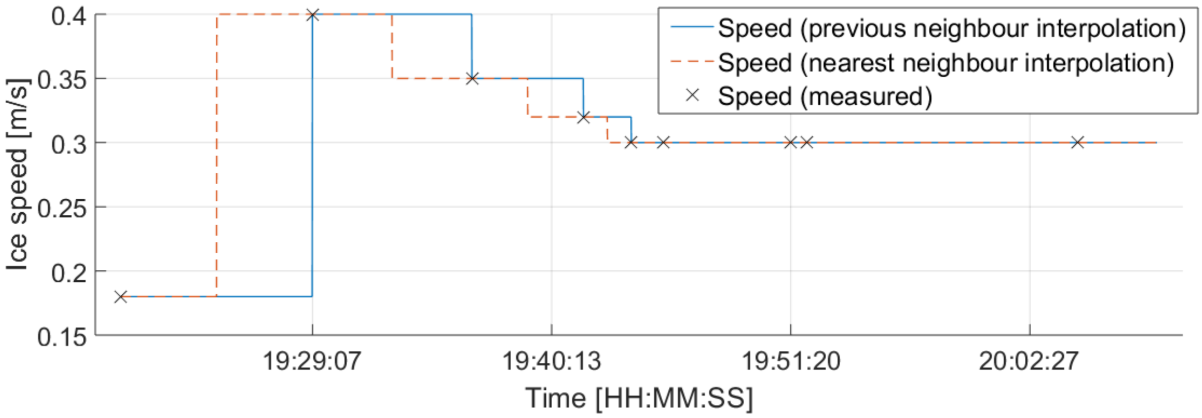

Figure 1. Example of a speed time series, showing measured speeds (crosses) along with stepwise interpolation methods (lines) between measurements.

2.4.2. Parameter constraints

To focus the analysis on conditions which may contribute to structural fatigue, only drifting ice with a certain ice thickness is considered. Static ice with a drift speed of 0 m/s is removed, as well as ice thinner than 0.1 m. The purpose of setting an ice thickness criterion is to eliminate false positives from open water, which restricts the analysis to conditions where sea ice has been confirmed to occur. Only common measurements that fulfil both parameter constraints simultaneously are considered for the analysis.

3. Results

Figure 2 shows the frequency of all local ice thickness and ice speed values that were recorded during the interaction events of the LOLEIF/STRICE campaigns, without interpolation and parameter constraints. A mean thickness of 0.86 m was measured during events, with a standard deviation of 0.77 m and where the most frequently measured thicknesses were in the interval 0.05 – 0.10 m. The frequency distribution shows a decreasing trend for thicknesses above 0.4 m, with the exception of local peaks at 0.7 m, 1.4 m and 1.9 m. The measurements contained fluctuations on the order of ± 0.05 m for level ice, giving a baseline uncertainty.

The measured speed shown in Figure 2 has a mean of 0.12 ± 0.09 m/s, with a mode of 0.1 m/s. The values contain at most two significant digits, and only 48 unique speed values were recorded in total. The frequency distribution contains prominent peaks for multiples of 0.1 m/s, with less prominent peaks at values such as 0.15 and 0.25 m/s. These peaks point to a significant underlying bias in the speed measurements towards multiples of 0.05 m/s. Although they follow the underlying trend of decreasing frequency with increasing speed, the prominence of the peaks are large outliers from the apparent underlying distribution.

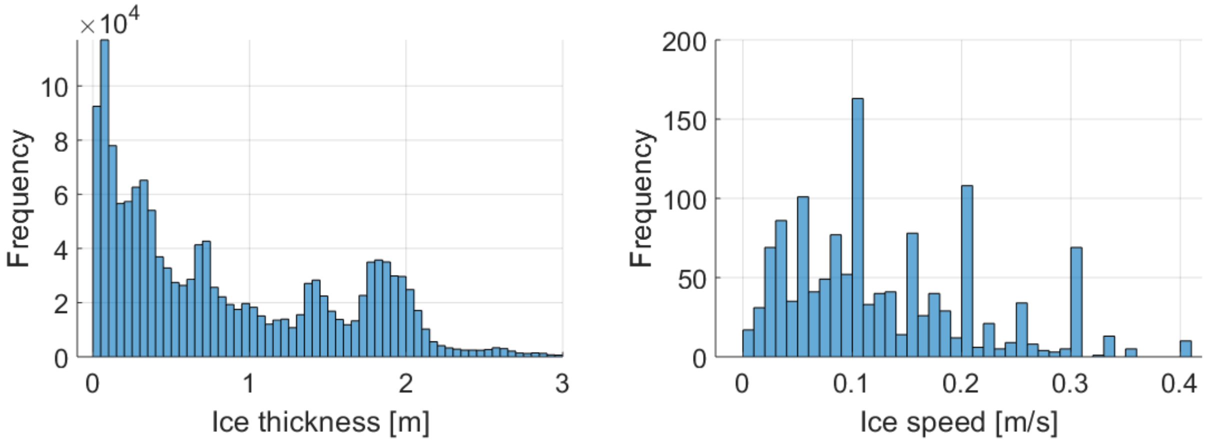

Figure 2. The frequency of measured ice thickness values (left, bin width 0.05 m) and non-zero ice speed values (right, bin width 0.01 m/s) recorded during the events of the LOLEIF/STRICE campaigns.

The previous neighbour and nearest neighbour interpolation methods result in similar speed frequency distributions. The relative difference between the two interpolation methods is below ± 0.1 for the most frequently occurring intervals. Because of the overall small difference in the resulting distribution for speed, the previous neighbour interpolation was utilized for the combined distribution for consistency.

Implementing previous neighbour interpolation and the parameter constraints results in the frequency distributions of ice thickness and speed shown in Figure 3. The mean thickness is 0.76 ± 0.70 m with a mode in the interval 0.10 – 0.15 m. Compared to the frequency distribution of the measured results (cf. Figure 2), the ice thickness has notably less prominent peaks at higher thicknesses, and the distribution is more evenly decreasing.

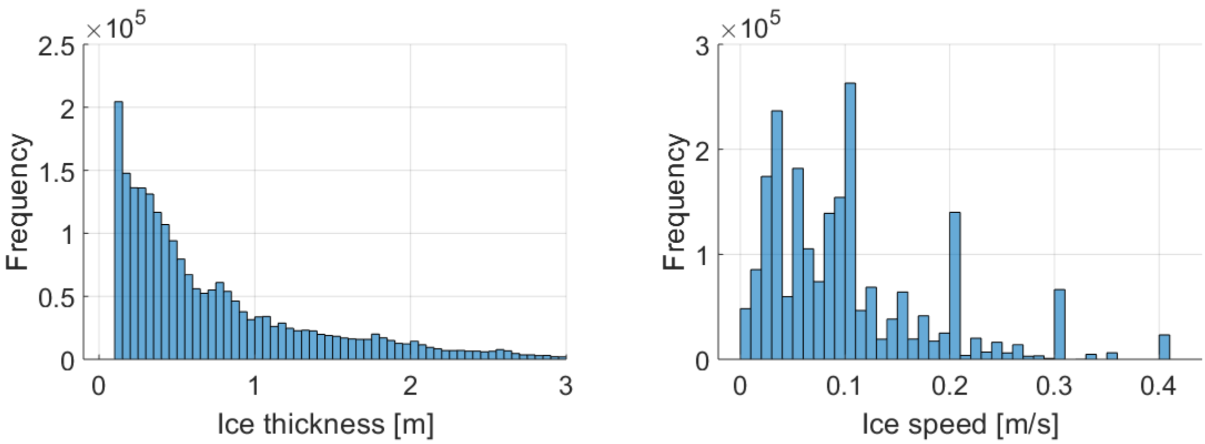

Figure 3. The frequency of interpolated ice thickness values (left, bin width 0.05 m) and ice speed values (right, bin width 0.01 m/s) that simultaneously fulfil the parameter constraints.

The mean speed after interpolation is 0.10 ± 0.08 m/s, and the mode is in the interval 0.10 – 0.11 m/s. The bias in the speed data is still present, although occurrences of 0.15 m/s and 0.25 m/s are relatively less frequent.

After interpolation, the frequency distribution of thickness and speed can be considered an estimate of the occurrence of each parameter in seconds, as the measurement frequency is standardized to 1 Hz. The result is thickness and speed data within the parameter constraints for a total of about 25 days and 5 hours between 2000 – 2003. In comparison, the total event duration is about 94 days and 16 hours across the four years. Most of the removed data was static ice, making up a total duration of above 52 days. Interpolation results in about 79 days of ice thickness measurements during events, where the ice was thicker than 0.1 m for roughly 67 days and 18 hours.

Figure 4 shows the interpolated thickness distribution per year, while Table 1 summarizes the mean, standard deviation and mode per year. 2003 is an outlier, with a large mean thickness and a frequency distribution skewed towards thicker ice compared to other years. This is, however, not reflected in the modes, as 2003 also contains a significant number of measurements between 0.10 – 0.15 m. These measurements were primarily recorded during the final weeks of the measurement campaign in April. If the final full week of measurements is not included, the mean thickness for 2003 is 1.23 ± 0.85 m with a mode between 0.45 – 0.50 m.

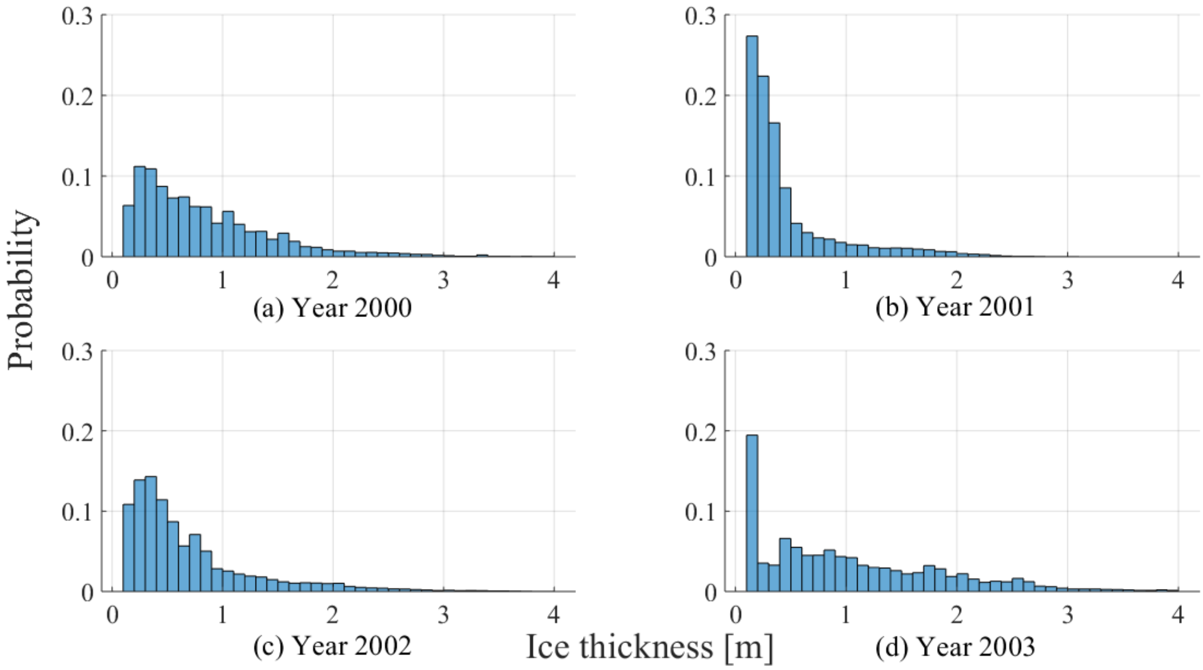

Figure 4. Interpolated ice thickness distributions per year for drifting ice, with bin widths 0.1 m. The bin heights are normalized by probability, summing to 1.

Table 1. Ice thickness means, standard deviations, and modes in total and per year for measured and interpolated ice thickness distributions with parameter constraints. The modes are the most frequent interval with interval widths of 0.05 m.

Year	**Measured ice thickness**		**Interpolated ice thickness**	
	Mean ± st. dev. [m]	**Mode [m]**	**Mean ± st. dev. [m]**	**Mode [m]**
Total	0.86 ± 0.77	0.05-0.10	0.76 ± 0.70	0.10-0.15
2000	0.69 ± 0.57	0.25-0.30	0.84 ± 0.62	0.25-0.30
2001	0.57 ± 0.51	0.20-0.25	0.46 ± 0.45	0.15-0.20
2002	0.67 ± 0.62	0.30-0.35	0.70 ± 0.59	0.30-0.35
2003	1.03 ± 0.85	0.05-0.10	1.06 ± 0.87	0.10-0.15

3.1. Combined distribution

The combined distribution of drifting ice thickness and speed is illustrated in Figure 5. The biased speed distribution affects the combined distribution, resulting in separate thickness distributions for certain speed values. The most frequently occurring combination is between 0.15 – 0.20 m and 0.03 – 0.04 m/s. The joint cumulative histogram of the ice thickness and speed is shown in Figure 5c, and can be used to estimate the probability of certain ice conditions. The most frequent combinations occurred for ice thicknesses in the interval 0.1 – 0.6 m and speeds in the interval 0.05 – 0.15 m/s with a total probability of 0.29. The thickness distribution had a long tail, resulting in a 0.34 probability of encountering ice thicker than 0.8 m. Multiplying the probabilities from the cumulative histogram with the total duration of 25 days and 5 hours gives approximate time durations that the conditions in question were encountered at the lighthouse. For example, drifting ice thicker than 0.8 m was encountered an estimated total duration of 8 days and 20 hours between 2000 – 2003.

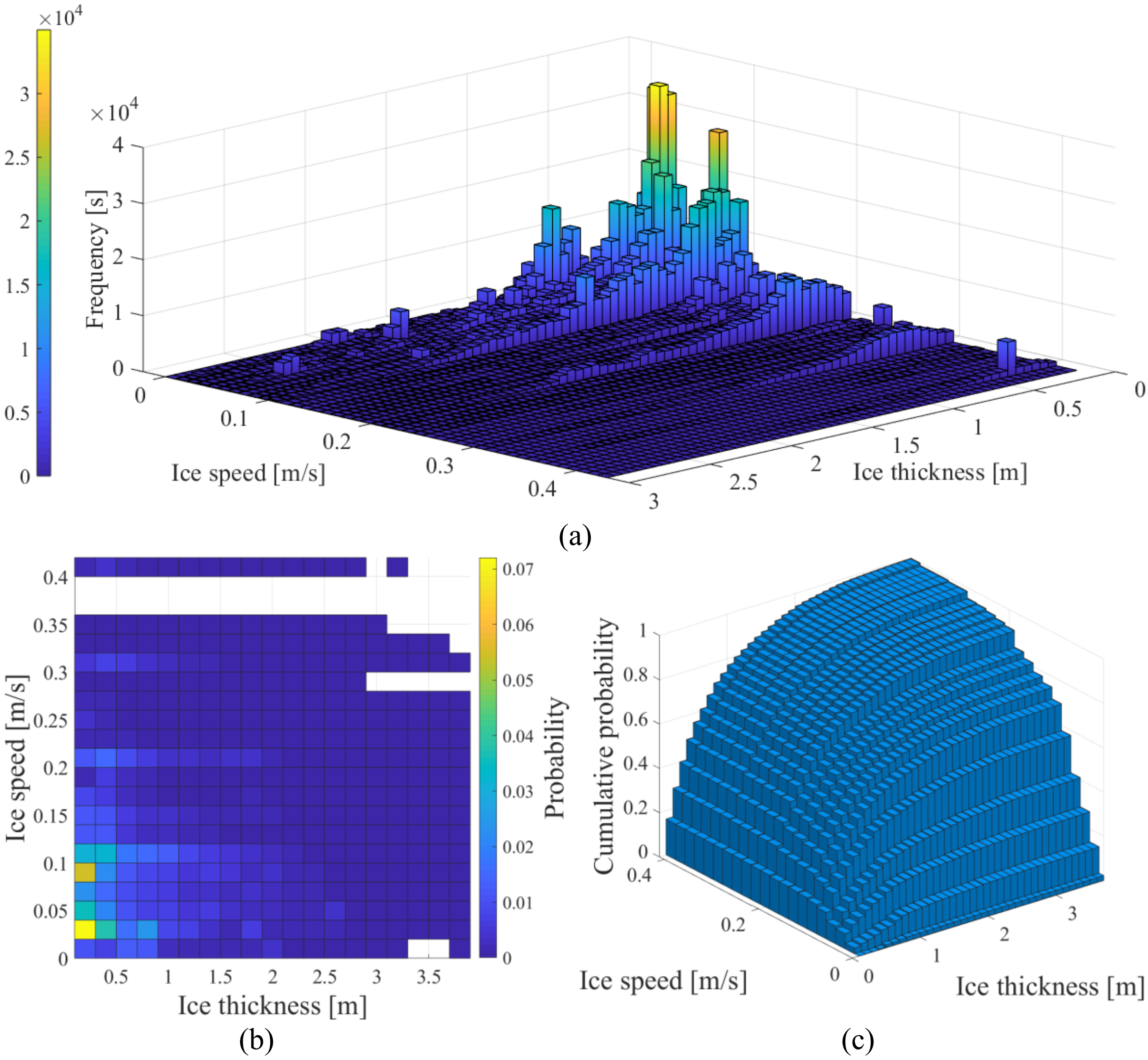

Figure 5. Figures showing the combined distribution of ice thickness and ice drift speed. (a) shows a bivariate frequency distribution of the two parameters with bin widths of 0.05 m x 0.01 m/s. (b) shows a heatmap of the frequency distribution in (a), where the colour of each field shows the probability of each combination of parameters, normalized over the visible bins. The heatmap has bin widths of 0.2 m x 0.02 m/s. (c) shows the same distribution as a joint cumulative histogram, with bin widths of 0.1 m x 0.02 m/s.

4. Discussion

After interpolation, the frequency distributions of ice thickness and speed can be interpreted as temporal distributions of ice conditions at the lighthouse, because the parameters are interpolated to every second. The frequency of a given combination of ice thickness and speed will equal an estimate of its total duration. The duration can then be divided by the total measurement time over four years to find the probability of occurrence of the conditions in question. Note that the durations will be a lower bound estimate, as the measurements and interpolation are limited only to the recorded events, with a total duration of 94 days and 16 hours over the four years. Despite this, much of the drifting ice encountered during the campaign periods are likely recorded in events. Drifting ice often caused ice-structure interactions, and recording these interactions was the focus of the campaign.

The significant bias in the speed data towards multiples of 0.05 m/s is likely caused by rounding to one or two significant figures, as the speed was manually estimated. Some information is lost when the values are rounded, which makes it difficult to recover the underlying distribution. The bias makes the combined distribution less accurate for small speed intervals, effectively reducing the resolution from which useful data can be extracted.

Some relevant ice thickness measurements by EM of drifting ice in the Bay of Bothnia are summarized by Ronkainen et al. (2018) and can be used for comparison to the measurements at Norströmsgrund. In 2003, several ice thickness measurement campaigns were carried out by using a helicopter-borne EM instrument (HEM), described by Haas (2004). The analysis of the dataset done by Ronkainen et al. (2018) focused on drifting ice, where they found a mean ice thickness of 1.39 m and a mode of 0.5 – 0.6 m on the 21st of February, east in the Bay of Bothnia. They also found that 63.1% of the drift ice was deformed. Haas et al. (2009) found a generally good agreement between HEM measurements and ground-based measurements using a Geonics EM31 instrument, which was also used at Norströmsgrund.

Except for the large mode at 0.1 – 0.2 m, the ice thickness distribution at Norströmsgrund follows a similar trend as the HEM measurements in 2003, with a local peak at 0.5 – 0.6 m and a gradual decline with a very long tail in the distribution. Importantly, the seasonal development of ice thickness will impact the Norströmsgrund statistics, as these were recorded over more than two months, while the HEM data is from a single day. Excluding the thin ice during the last week of measurements in April, the mean thickness at Norströmsgrund (1.23 m) is close to the mean thickness through HEM (1.39 m). Additionally, Ronkainen et al. (2018) writes that there was less ice in the west side of the Bay and a greater presence of coastal leads, which will reduce the mean ice thickness at Norströmsgrund compared to the helicopter measurements. Note that the frequency distribution of ice thickness at Norströmsgrund will depend on the ice speed, while the ice can be assumed static relative to the helicopter during HEM measurements.

Drift ice thicker than 0.8 m was encountered 35% of the time during events at Norströmsgrund, much of which was deformed ice. According to Määttänen and Kärnä (2011), the level ice thickness was less than 0.6 m in the area during the measurement years. Li et al. (2016) found a mean annual maximum ice thickness of 0.61 m between 2000 – 2003 based on Freezing Degree Days calculations, with 2003 being the most severe year with 0.71 m. The severity of the winter in 2003 is reflected in the long tail of the thickness distribution that year (see Figure 4d). Ronkainen et al. (2018) points out that 2003 was very windy, which likely contributed to the large amount of ridging.

Note that the temporal distribution of ice thickness at Norströmsgrund may be affected by the structure itself, but the magnitude of this effect is unknown. For example, when the driving forces on an ice floe are insufficient for limit stress failure to occur, the floe may get stuck on the lighthouse. The thickness of the stuck floe will continue to be measured for some time, increasing its relative frequency in the data.

5. Conclusions

The recorded ice thicknesses and ice drift speeds at Norströmsgrund during the LOLEIF/STRICE campaigns in the years 2000 – 2003 were extracted and analysed. By interpolating per second, the varying measurement frequencies were corrected, and a joint temporal frequency distribution of drift ice at the lighthouse was estimated. The joint distribution can provide input to fatigue modelling and as a basis for transferring local ice conditions to other areas. However, ridge keel depth was underestimated by EM measurements. In addition, the accuracy of the combined distribution was affected by significant underlying bias in the ice speed data. Establishing a more accurate local speed distribution is a target for further research.

The drift ice thickness distribution in 2003 followed a similar trend to helicopter EM measurements that year, with the addition of a large mode for thin ice measured late in the season. A significant fraction of the drift ice encountered was thicker than level ice, which is important to consider for distributions of local ice thickness. The influence of the structure on the local ice drift and resulting thickness distribution was not quantified but is highly relevant for fatigue simulations based on local ice conditions and should be investigated further.

Acknowledgments

The authors wish to extend their gratitude to Ilija Samardžija, Torodd S. Nord, Hayo Hendrikse, and other partners on the FATICE project who provided helpful feedback on the methods and findings in this work.

The authors also wish to acknowledge the support to the FATICE project from the MarTERA partners, the Research Council of Norway (RCN), German Federal Ministry of Economic Affairs and Energy (BMWi), the European Union through European Union's Horizon 2020 research and innovation programme under grant agreement No 728053-MarTERA and the support of the FATICE partners.

References

Bjerkås, M., and Gedikli, E. D., 2019. A method to find intervals with probability of harsh ice induced vibrations. Proc. 25th International Conference on Port and Ocean engineering under Arctic Conditions, Delft, The Netherlands.

Bjerkås, M., Ivanova, A., Bonnemaire, B., and Jochmann, P., 2003. Magnitudes of global and local ice loads on the lighthouse Norströmsgrund winter 2002. Report, Norwegian University of Science and Technology.

Bjerkås, M., 2006. Ice Actions on Offshore Structures–With Applications of Continuous Wavelet Transforms on Ice Load Signals. PhD thesis, NTNU.

Ervik, Å., Nord, T. S., Høyland, K. V., Samardžija, I., and Li, H., 2019. Ice-ridge interactions with the Norströmsgrund lighthouse: Global forces and interaction modes. Cold Regions Science and Technology 158, 195–220.

Fransson, L., 2008. Ice mechanics and shipping in ice-infested waters. Research report no 65, Finnish Transport Safety Agency.

Haas, C., and Jochmann, P., 2003. Continuous EM and ULS thickness profiling in support of ice force measurements. Proc. 17th International Conference on Port and Ocean Engineering Under Arctic Conditions, Trondheim, Norway.

Haas, C., 2004. Airborne EM sea-ice thickness profiling over brackish Baltic Sea water. Proc. 17th IAHR International Symposium on Ice, St. Petersburg, Russia, 12-17.

Haas, C., Lobach, J., Hendricks, S., Rabenstein, L., and Pfaffling, A., 2009. Helicopter-borne measurements of sea ice thickness, using a small and lightweight, digital EM system. Journal of Applied Geophysics 67(3), 234-241.

Hendrikse, H., and Nord, T. S., 2019. Dynamic response of an offshore structure interacting with an ice floe failing in crushing. Marine Structures 65, 271-290.

Hendrikse, H., and Koot, J., 2019. Consideration of ice drift in determining the contribution of ice-induced vibrations to structural fatigue. Proc. 25th International Conference on Port and Ocean engineering under Arctic Conditions, Delft, The Netherlands.

Igwemezie, V., Mehmanparast, A., and Kolios, A., 2019. Current trend in offshore wind energy sector and material requirements for fatigue resistance improvement in large wind turbine support structures – A review. Renewable and Sustainable Energy Reviews 101, 181-196.

ISO19906, 2019. Petroleum and natural gas industries – Arctic offshore structures. International Organization for Standardization, Geneva, Switzerland.

Li, H., Bjerkås, M., Høyland, K. V. and Nord, T. S., 2016. Panel loads and weather conditions at Norströmsgrund lighthouse 2000-2003. Proc. 23rd IAHR International Symposium on Ice, Ann Arbor, Michigan USA.

Määttänen, M., 1975. Experiences of ice forces against a steel lighthouse mounted on the seabed, and proposed constructional refinements. Proc. 3rd International Conference on Port and Ocean Engineering Under Arctic Conditions, Fairbanks, Alaska, 857–871.

Määttänen, M., and Kärnä, T., 2011. ISO 19906 ice crushing load design extension for narrow structures. Proc. 21st International Conference on Port and Ocean Engineering Under Arctic Conditions, Montréal, Canada.

Milaković, A.-S., Braun, M., Willems, T., Hendrikse, H., Fischer, C., and Ehlers, S., 2019. Methodology for estimating offshore wind turbine fatigue life under combined loads of wind, waves and ice at sub-zero temperatures. Proc. International Conference on Ships and Offshore Structures ICSOS 2019, Florida, USA.

Nord, T. S., Samardžija, I., Hendrikse, H., Bjerkås, M., Høyland, K. V., and Li, H., 2018. Ice-induced vibrations of the Norströmsgrund lighthouse. Cold Regions Science and Technology 155, 237–251.

Ronkainen, I., Lehtiranta, J., Lensu, M., Rinne, E., Haapala, J., and Haas, C., 2018. Interannual sea ice thickness variability in the Bay of Bothnia. The Cryosphere 12, 3459-3476.

Samardžija, I., 2018. Two applications of a cross-correlation based ice drift tracking algorithm; ship-based marine radar images and camera images from a fixed structure. Proc. 24th IAHR International Symposium on Ice, Vladivostok, Russia, 141- 151.

Turner, J., Høyland, K. V., Hornnes, V., and Gedikli, E. D., 2020. Comparison of in-situ measurements from the Norströmsgrund lighthouse to Copernicus reanalysis products. Proc. 25th IAHR International Symposium on Ice, Trondheim, Norway.

Vanem, E., 2016. Joint statistical models for significant wave height and wave period in a changing climate. Marine Structures 49, 180-205.

25th IAHR International Symposium on Ice
Trondheim, June 14 to 18, 2020

Scale-model ridges and interaction with narrow structures, Part 1 Overview and scaling

Aleksey Shestov[1], Aase Ervik[2], Jaakko Heinonen[3], Ilka Perälä[3], Knut V. Høyland[1,4], Evgenii Salganik[4], Hongtao Li[4], Marnix van den Berg[4], Zongyu Jiang[4] and Otto Puolakka[5]
1 The University Centre in Svalbard (UNIS), Norway
2 Multiconsult AS, Norway
3 Technical Research Centre of Finland (VTT), Finland
4 The Norwegian University of Science and Technology (NTNU), Norway
5 Aalto University, Finland
Aleksey.shestov@unis.no, knut.hoyland@ntnu.no, Evgenii.salganik@ntnu.no

Abstract
An experimental campaign to investigate sea ice ridge interaction with bottom-fixed structures was carried out in the Aalto ice basin. Ice ridges were produced, their consolidation was monitored, the properties of level ice and ridges were tested. Finally, a structure was pulled through the level ice and ridges while measuring the loads and monitoring the deformation pattern. Two different structures were tested, one with cylindrical and one with a conical waterline shape. We investigated a) the scaled ridge properties, b) how structures broke level ice and ice ridge, and c) the scaling of ridge forces with respect to a cylindrical and a conical structure at the waterline. Full-scale ridge structure interaction data are available for the Norströmsgrund lighthouse, so we used its size in scaling the tests. We assumed that gravity/buoyancy forces contribute and combined Froude and Strength scaling with a geometric scale-factor of 15. The initial ice temperature and accumulated air temperatures (FDD) during consolidation were varied to investigate how reasonably scaled ridge properties can be achieved. The campaign covered three different ice sheets and ridges. Punch tests, flexural strength, compressive strength tests were carried out. The main preliminary observations are that loads from level ice on vertical structure (F^{V}_{li}) gave the highest load. Next, in decreasing order of magnitude, followed the load from a ridge on vertical structure (F^{V}_{ri}), load from a ridge on sloping structure (F^{S}_{ri}), and finally, the load from level ice on sloping structure (F^{S}_{li}).

1. Introduction

Ice ridges are often key features when designing structures in ice-covered waters. In the case of only first-year ice and that icebergs do not exist or can be managed, first-year ice ridges give the quasi-static design load. In the Baltic, there are plans to expand electricity production from Offshore wind, and one of the essential questions concerning structure design is if a cylindrical or conical structure shape at the waterline should be used. A conical structure reduces the ice load as long as it provokes bending failure instead of crushing. However, there are several disadvantages. It is more expensive to produce. It gives higher hydrodynamic loads than the cylindrical structure. It makes ship access (for maintenance) more difficult, and the cone may become very large in waters with a high tidal difference. To estimate ridge loads, ISO19906 (2019) gives models for the ice rubble and recommends using level ice formulas for the consolidated layer. There are several problems with this. The formula for ice rubble action does not include surcharge even though it is included in the original paper (Dolgopolov et al., 1975), and Serré and Liferov (2010) argue that this is important. Further, the level ice action on sloping structures includes the effects of ice rubble accumulation. However, in a ridge, there are already large amounts of rubble. We think that the level ice interaction with accumulating rubble is not directly transferable to how the consolidated layer produces accumulating rubble and interacts with it. Finally, the effect of steep cones is not apparent even for level ice. It has not been shown which cone angles ensure bending failure.

Experiments in the Aalto ice basin were planned and conducted with ridge action on fixed vertical and steep-cone structures. There were two somewhat different, but connected topics:

a) The production and scaling of ice ridges in model-scale
b) The effect of the steep cone on the total load from ridges and surrounding level ice

The Norströmsgrund lighthouse offshore Luleå was instrumented in the LOLEIF and STRICE project and is still the best dataset for full-scale ice interaction with vertical structures. We will use a scaled version of this lighthouse as the vertical model-scale structure. An angle of 75˚ was chosen because it is steeper than normally being built, but no so steep that crushing is expected.

The is no accepted method for the production of ice ridges in model-scale; it applies both to the theoretical foundation and the practical procedures (Repetto-Llamazares, 2010). Complete thermo-mechanical testing is practically almost impossible (Høyland, 2010), and compromises must be made. In the project, we will investigate how the initial conditions and the consolidation after ridge production govern the thickness of the consolidated layer and the mechanical properties of the rubble and the consolidated layer.

2. Scaling

We assume that gravity and water and ice densities are similar in full-scale (prototype) and basin-scale (model). Further, inertia, gravity/buoyancy, ice strength, and ice elasticity may govern the process. One may attempt to scale the forces and/or the deformation patterns. In the latter case, the ice's elastic behavior is vital, but the elastic contribution to the total ice load on a rigid structure is probably not vital. When considering the full dynamic ice-structure interaction, the elasticity may be important. Let us concentrate on the scaling of the ice load, identify force contributions from inertia, gravity/buoyancy, and ice breaking (strength) so that the total force F can be expressed:

$$F = f\left(F_{in}, F_g, F_{is}\right) \quad [1]$$

where F_{in} is the inertia, F_g is the gravity/buoyancy, and F_{is} is the ice strength contribution. And they scale as follows:

$$F_{in} \sim \frac{v^2}{L} \qquad F_g \sim L^3 \qquad F_{is} \sim \sigma L^2 \quad [2]$$

where v is a vital velocity, L a vital length, and σ an ice strength. From these, we may identify two dimensionless ratios, the Froude number Fr and an *Ice strength* or *Strength of Materials number SOM*:

$$Fr = \frac{v^2}{gL} \qquad SOM = \frac{v^2}{\sigma} \quad [3]$$

Note that the Cauchy number does not directly come into play unless $\left(\frac{\sigma}{E}\right)_p = \left(\frac{\sigma}{E}\right)_m$ which is challenging to obtain.

In our case, we tested both a conical and a vertical structure shape so that we should consider both ice ride-up and bending failure as well as crushing. If ride-up (or down) and bending failure is vital, we assume F_{in}, F_g, and F_{is} are all vital, and further that ice strength is dominated by flexural strength (σ_f). It is then well known that the geometric, kinetic, strength, and dynamic scaling factors become:

$$\lambda = \frac{h_{i,p}}{h_{i,m}} = \frac{w_p}{h_m} \qquad \lambda_k = \sqrt{\lambda} \qquad \lambda_\sigma = \lambda \qquad \lambda_d = \lambda^3 \quad [4]$$

where h_i is the ice thickness, w the structure width, and the indices p and m refer to respectively prototype (full-scale) and model (basin-scale).

In the case of crushing, one may imagine that gravity/ buoyancy does not play a vital role so that the total force can be expressed:

$$F = f\left(F_{in}, F_{is}\right) \quad [5]$$

where the ice breaking is dominated by crushing and expressed through a compressive strength (σ_{cr}). Now the Froude number is irrelevant, and only the strength number governs the process so that there are no conditions on how to determine the ice strength (except that it should be proportional to velocity squared). The ice force is a function of length squared and the ice strength, and one may use any ice strength! In our case, we tested the two structure shapes with the same ice, and we had the ridge keels, so it is evident that we need to consider gravity/buoyancy contributions and use Fr so that the ice should be weakened ($\lambda_\sigma = \lambda$).

The next question that may come up is, what is the ice strength? How can one carry out a test in full-scale and basin-scale and compare them? When ice fails in bending, the flexural strength is used, and it is tested (more or less) the same way in full-scale and basin-scale. The full ice thickness is tested, and flexural strength is derived, often based on linear elastic beam theory, so that it is a force with units of stress. The ice compressive strength is more complicated, it is not a well-defined property, and in the field, there are three tests: a) Uni-axial compressive strength, with often cylindrical samples of diameter/length of

70mm/175mm; b) Borehole-Jack indentation tests, where the piston head is roughly 50mm; and c) a few compressive tests of full ice thickness have been done, but only for relatively thin ice or low loading-rate. Testing full ice thickness (e.g.1m) compressive strength in the field requires very large and heavy equipment and is practically difficult to carry out. In a basin, the compressive strength is tested either by a) Making short beams (width and length approximately equal) and compressing full thickness or b) Making indentation with a small cylinder into a strait ice edge. In other words, the compressive strength is not a well-defined property, and different tests are done in the field and in model-scale. A comparison between full-scale and model-scale is difficult. We also need thermal scaling as the consolidated layer is the result of thermal processes; the state-of-the-art, including challenges, are given in Høyland (2007), Høyland (2010), and Repetto-Llamazares (2010) and will not be repeated here.

3. Experimental set-up and procedures

3.1 Level ice and ridge production

The water in the Aalto basin is doped with ethanol, resulting in a concentration of ethanol 0.3%. The level ice was created in the standard, for this basin, procedure by spraying and letting the ice grow upwards. The air temperature during spraying was -10C, while the ice was isothermal at the freezing point. When the target ice thickness of 40 mm was reached, the spraying stopped, but the cooling continued to cool the ice and create a proper internal ice matrix and strength. Finally, the ice was tempered to achieve target strength. The ridges were produced in two steps. Firstly, by breaking the ice with the pushing plates on the main carriage, and secondly, by pushing it together with the carriage. When the ridge was formed, it had to be kept in place by a confining level ice floe (Figure 1). The campaign resulted in ten tests, varying shape of the structure, ridge consolidation degree, and level ice properties (Table 1). If the testing matrix required the run through the unconsolidated keel (Tests 2, 7, and 8), the experiment was conducted at once after ridge production. Otherwise (Tests 1, 5, 6, 9, and 10), cooling was applied overnight to run the ridge consolidation process; it followed by warming to maintain target level ice strength properties. During the test campaign, three cycles of ice level sheet production followed by ice ridge creation and consolidation were carried out; air temperature courses during these cycles were registered with regular basin sensor and thermistor string placed in the ice (Figure 2). Moments of structure-ice interaction tests and level ice strength tests are indicated on the temperature course plots.

Table 1. Testing matrix with varied structure shape, keel consolidation, and ice properties. Note that Tests 3 and 4 failed and their results are not used further in the discussion.

Ice sheet	Test #	Structure waterline	Structure Interactions with			Level ice flexural strength (MPa)
			Level ice before	Ridge	Level ice after	
1	1	Vertical	No	consolidated	No	73
2	2	Vertical	Yes	unconsolidated	Yes	60
	5	Sloping	No	consolidated	Yes	235
	6	Sloping	Yes	consolidated	Yes	-
3	7	Sloping	Yes	unconsolidated	Yes	51
	8	Sloping	Yes	unconsolidated	Yes	-
	9	Sloping	Yes	consolidated	Yes	78
	10	Vertical	No	consolidated	No	-

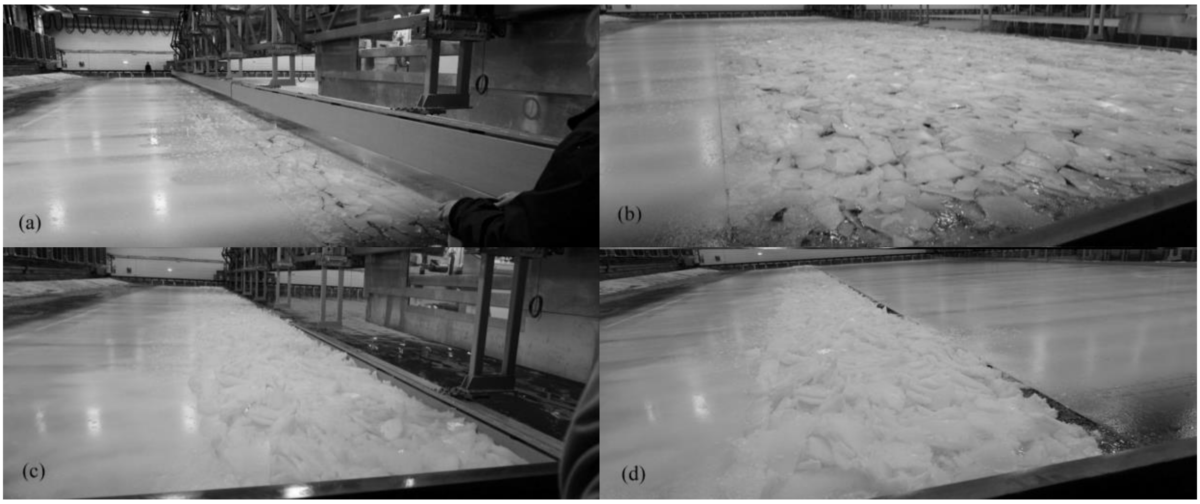

Figure 1. Ridge production. Cutting level ice (a), cutting completed (b), forming the ridge by pushing broken level ice (c), ridge production completed (d).

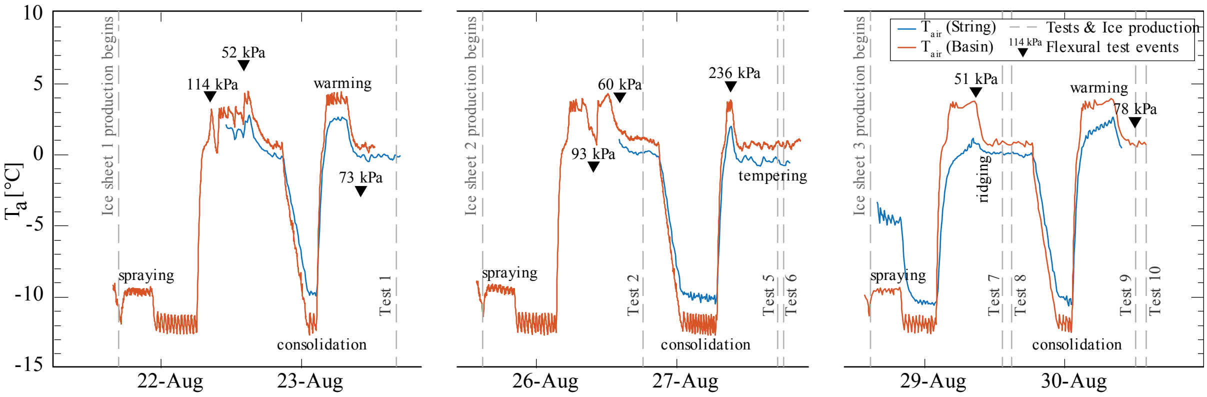

Figure 2. The air temperature history measured by the Aalto sensor and one of the thermistor strings.

3.2 Mechanical characterization level ice and ridges

Mechanical parameters were tested for both level ice and the ice ridges. For level ice, flexural and compressive strengths were measured, and for the ridges, punch tests were carried out using regular Aalto ice basin tests' procedures. The flexural strength was tested on cantilever beams 25 cm long and 8 cm wide (Figure 3). The compressive strength was tested by compressing short cantilever beams.

Figure 3. Testing level ice flexural strength

3.3 Structure, loads, and cameras

The structure with vertical and sloping walls was tested (Figure 4). The structure's position was adjusted for different scenarios: cylindrical shape at the waterline and conical shape at the waterline. The structure was assumed to be rigid, even though, in reality, neither the fixing of the structure to the wagon nor the wagon itself were completely rigid. We did not measure any structural response. The cylindrical structure diameter was 54.2 cm, and this was also the cone bottom's diameter on the conical structure. The cone angle was 74.8°and the cone height was 35.8 cm. The global load was measured with a three-dimensional load cell between the carriage and the structure. Also, local pressure distribution was registered with tactile sensors installed both at the cylindrical and conical structures. However, due to damage to the tactile sensors in the tests, data were only gathered from tests 1, 2, and 3. A system of cameras below and above water surface was installed. Cameras below water were intended to provide the view and depth measurement of rubble pile accumulation in front of the structure and the side view of the rubble pile passing the structure. The camera in the air was set to provide the top view covering structure-ice interaction and the zone ahead of that, such that if there is visible crack propagation, it was registered. GoPro cameras powered by power banks were packed in waterproof cases, which were mounted on a steel frame with long arms. The frame itself was mounted on the carrier behind the structure to avoid causing any interaction with ice or disturbances into load measurements. In turn, long arms below the structure were reaching out to provide the requested view of the process. Power banks kept cameras recording throughout the working day. This allowed us to mount and dismount the camera's frame only once per day, which helped for the tests program's efficiency.

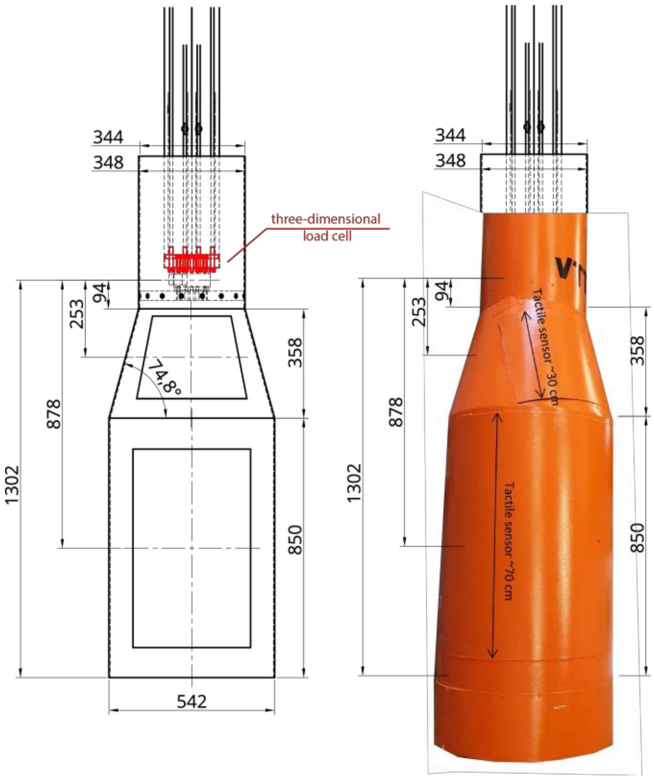

Figure 4. Front view cross-section sketch and photo of the structure used in the experiment. Dimensions and location of three-dimensional load cell and tactile sensors on the structure's vertical and sloping wall.

4. Some observations and preliminary results

4.1 Level ice and ridge - geometry and morphology

Three ice sheets were produced, and three ice ridges were built, resulting in ten structure test runs (Table 1). Some transverse profiles (cross-sections) of the ridge made in ice sheet three are shown in Figure 5. The maximum depth of keel was approximate 0.4 m. The width of the ridge was generally 4 m and started from the side close to the structure. One can see that the keel profile was roughly in the shape of a trapezoid, which is similar to the geometry of a natural ridge keel.

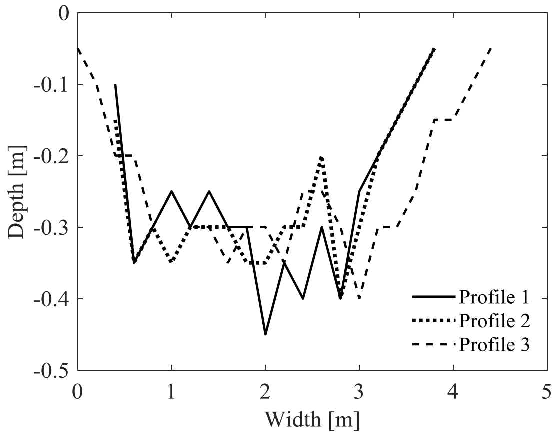

Figure 5. Cross-section profiles of the ridge made from ice sheet number three.

4.2 Ice forces

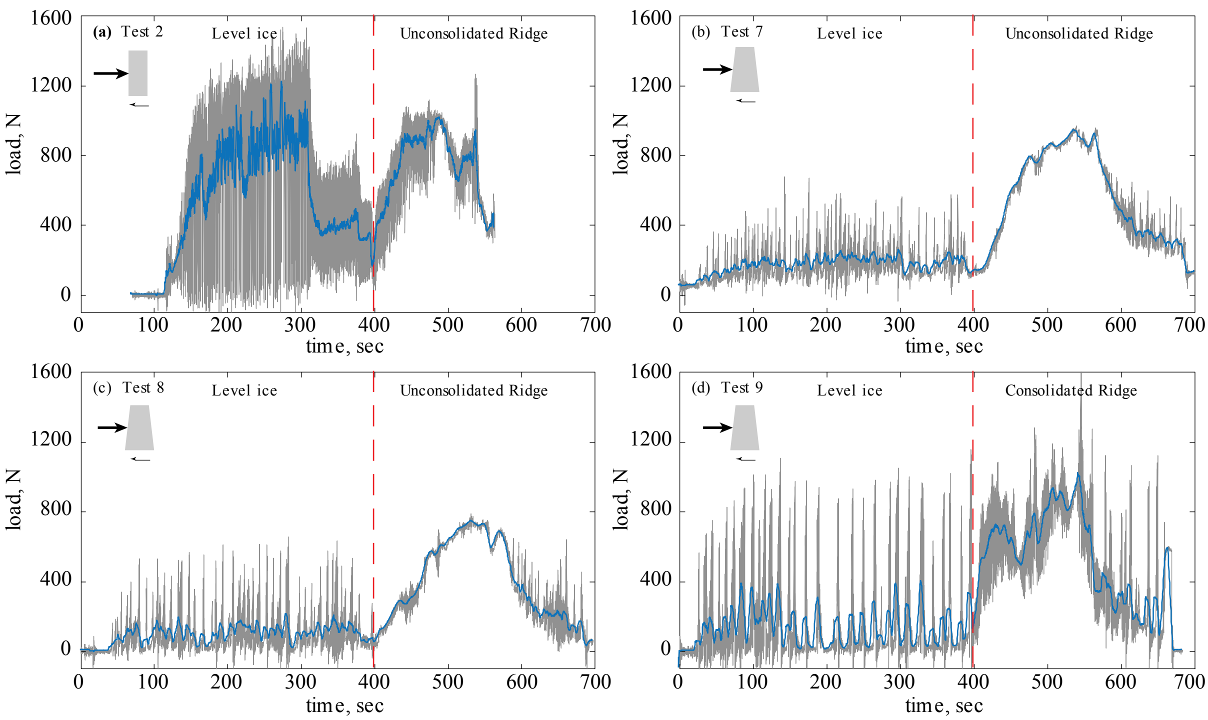

Figure 6. Horizontal ice load in the towing direction. In grey – raw signal, in blue – smoothed signal. a) Test 2, vertical structure, unconsolidated; b) Test 7, sloping structure, unconsolidated; c) Test 8, sloping structure, unconsolidated; d) Test 9, sloping structure, consolidated.

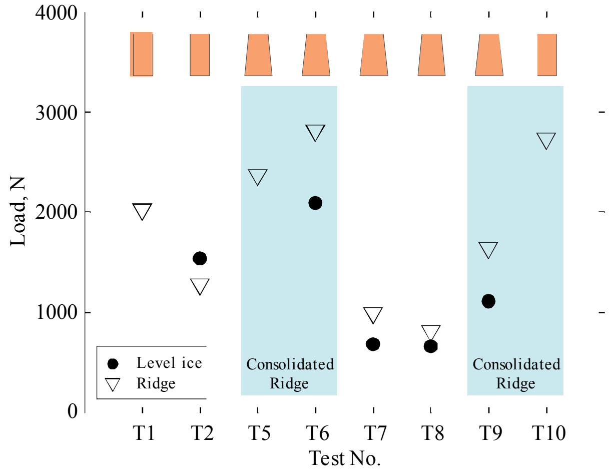

Figure 7. Peak loads from level ice and ridges in all tests.

The loads from level ice and ridges are given as time-series (Figure 6) and as peak loads (Figure 7). Let us compare loads of a) vertical and sloping structures, b) consolidated and un-consolidated ridges, and c) level ice and ridges.

The load on the vertical structure was generally higher than on the sloping structure (Tests 1, 2 versus Tests 7, 8; and Test 10 versus Test 9), and the load from consolidated ridges was higher than from unconsolidated ridges. Both these observations are as expected. The findings from the comparison of level ice and ridge loads are more interesting. For the vertical structure, the load from level ice was higher than from the ridge (Test 2), whereas it was the opposite of the sloping structure.

The difference between the raw signal and the smoothed signal (Figure 6) indicates significant dynamic amplification, but a proper dynamic analysis is outside the paper's scope and motivation. We neither measured the structural accelerations nor its dynamic properties. Figures 8 and 9 show the frequency domain of the load-time series for the level ice and ridge and allows for some observations. All the loads on the sloping structure contained a low-frequency component that could not be seen in the vertical structure's signals. This corresponds to the visual observations of ice ridging-up on and releasing from the cone. Further, it seems to be a difference between consolidated (Test 9) and unconsolidated (Tests 7 and 8) ridge action on the cone (Figure 9). In the consolidated ridge, the low-frequency component was smaller, indicating that the cone was less effective in avoiding crushing.

The differences between ice actions on vertical and conical structures for level ice and ridges indicate that the cone is less effective in reducing loads from ridges, and especially consolidated ridges, than from level ice. In level ice, the pile-up height mostly did not exceed the cone, while in ridge interaction, it often did. This argues that the ISO approach to treating the consolidated layer as thick level ice is questionable. Earlier observations from HSVA (Jensen et al., 2001) confirm that the ridge load on a ship-shaped vessel (sloping) was higher than from level ice.

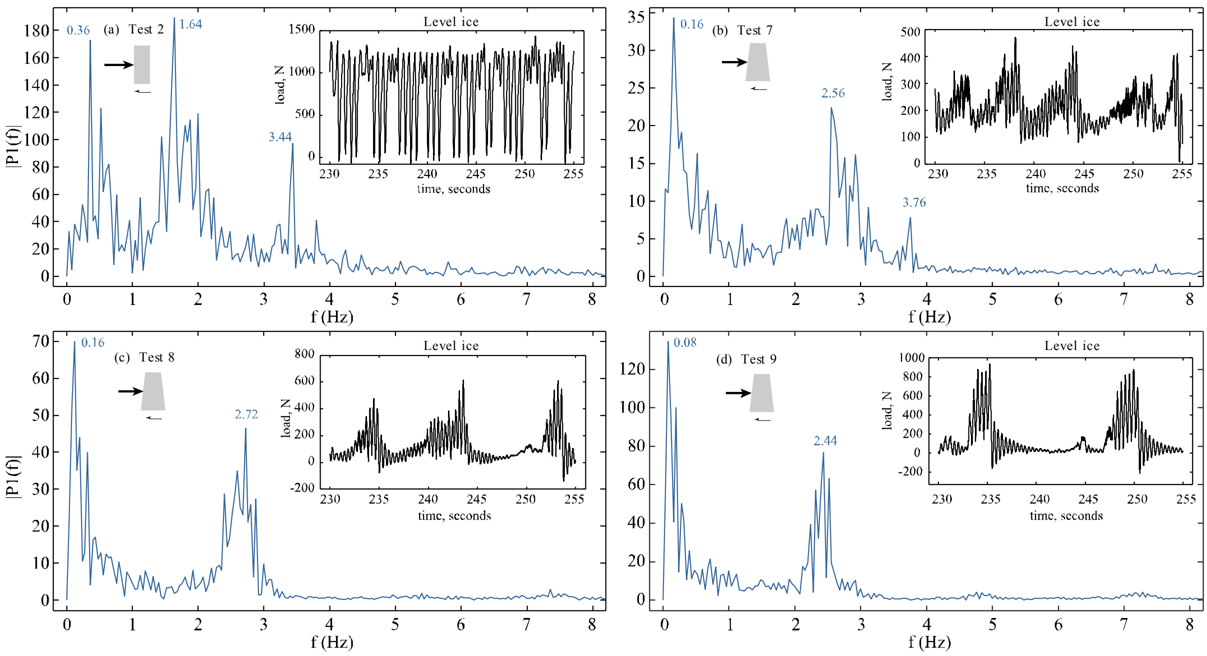

Figure 8. Frequency domain analysis of horizontal load signal during structure advancing through level ice. Note, the vertical scale is different both for load signal and FFT analysis.

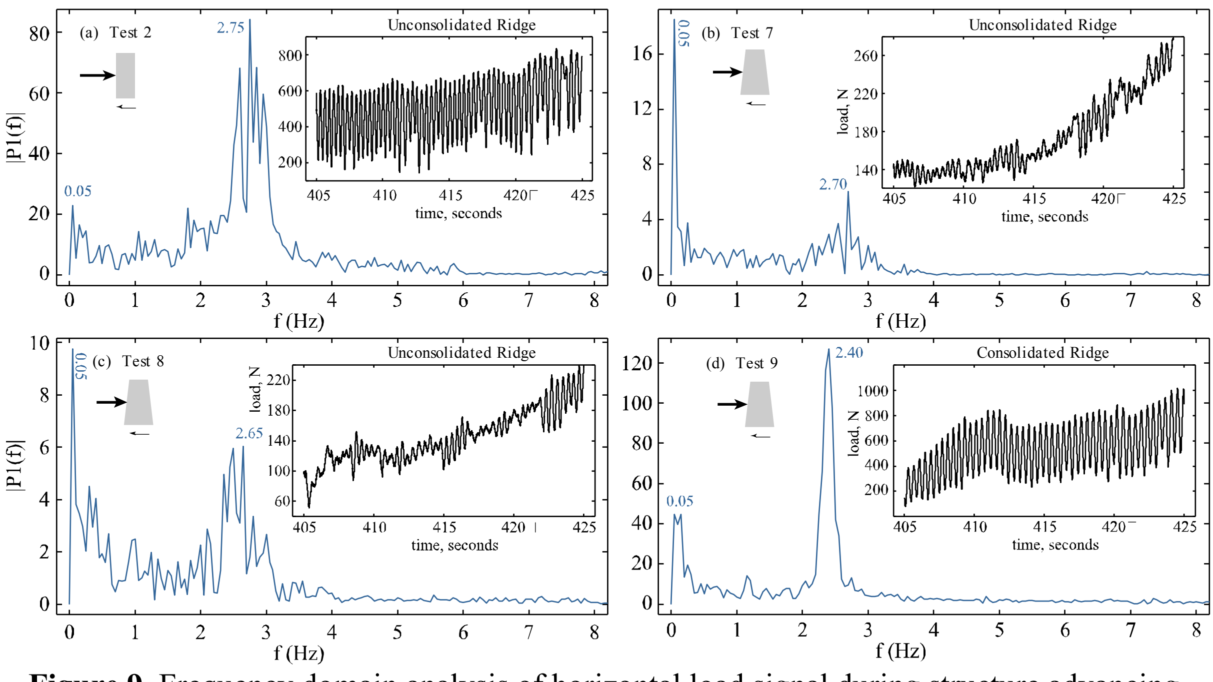

Figure 9. Frequency domain analysis of horizontal load signal during structure advancing through the ridge. Note, the vertical scale is different both for load signal and FFT analysis.

The main preliminary observations are that horizontal load from level ice on vertical structure ($F^{V}{}_{li}$) gave the highest level; the load from a ridge on vertical structure ($F^{V}{}_{ri}$) was higher than load from the ridge on sloping structure ($F^{S}{}_{ri}$); and, finally, the load from level ice on sloping structure gave the lowest level (Equation 6).

$$F_{li}^{V} > F_{ri}^{V} > F_{ri}^{S} > F_{li}^{S} \qquad \textbf{[6]}$$

5. Conclusions

A set of experiments were carried out in the Aalto ice basin to investigate the scaling of first-year ridges and the effect of cone angle on the ridge load on fixed structures. The ridges were produced by breaking the level ice and pushing the broken pieces together. The ridges were 40 m long, about 4 m wide, and approximately 0.4 m deep. After formation, half of the ridge was tested mechanically, and ridge-structure interaction testing was done. Then the ridge consolidated overnight, and the procedure of testing mechanical properties and interaction with structures repeated the next day. The load analysis's main preliminary results are that horizontal load from level ice on vertical structure (F^{V}_{li}) gave the highest level. Next, in decreasing order of magnitude, followed the loads from a ridge on vertical structure (F^{V}_{ri}), from a ridge on sloping structure (F^{S}_{ri}), and finally, from level ice on sloping structure (F^{S}_{li}).

Acknowledgments

The work described in this publication was supported by the European Community's Horizon 2020 Programme through the grant to the budget of the Integrated Infrastructure Initiative HYDRALAB+, Contract no. 654110. The authors would also like to thank the crew in the Aalto ice basin for the hospitality and fixing all practical matters during the long hours of testing.

References

Dolgopolov, Y., Afanasiev, V.P., Koren'Kov, V.A. and Panfilov, D.F., 1975. Effect of hummocked ice on the piers of marine hydraulic structures. International Symposium on Ice Problems, 3rd, Proceedings, Dartmouth College, Hanover, NH. Aug., 18-21. 1975.: 469-477.

Høyland, K.V., 2007. Thermal scaling of ice ridges, some dimensionless numbers. Proceedings of the 19th International Conference on Port and Ocean Engineering under Arctic Conditions (POAC), Dalian, China. pp. 517-523, ISBN 978-7-5611-3631-7.

Høyland, K.V., 2010. Thermal aspects of model basin ridges. Proceedings of the 20th IAHR International Symposium on Ice, June 14 to 18, Lahti, Finland, paper 66.

ISO19906, 2019. Petroleum and natural gas industries - Arctic offshore structures, Geneva, Switzerland, pp. 434.

Jensen, A., Løset, S., Høyland, K.V., Liferov, P., Heinonen, J., Evers, K.-U. and Maattanen, M., 2001. Physical modelling of first-year ice ridges - part II: mechanical properties. Proceedings of the 16th International Conference on Port and Ocean Engineering under Arctic Conditions, POAC'01, 3: 1493-1502.

Repetto-Llamazares, A.H.V., 2010. Review in model basin ridges. Proceedings of the 20th IAHR International Symposium on Ice, June 14 to 18, Lahti, Finland, paper 154.

Serré, N. and Liferov, P., 2010. Loads from ice ridge keels – experimental vs. numerical vs analytical. Proceedings of the 20th IAHR International Symposium on Ice, June 14 to 18, Lahti, Finland, paper 92.

25th IAHR International Symposium on Ice
Trondheim, 23 - 25 November 2020

Development of an experimental setup to investigate the impact of higher structural modes on dynamic ice-structure interaction

Timo Stange[1], Gesa Ziemer[1], Rüdiger U. Franz von Bock und Polach[2]
[1]Hamburg Ship Model Basin (HSVA), Hamburg, Germany
Bramfelder Straße 164, 22305 Hamburg, Germany
[2]Institute for Ship Structural Design and Analysis (M-10)
Hamburg University of Technology, Hamburg, Germany
Am Schwarzenberg Campus 4c, 21073 Hamburg, Germany
stange@hsva.de
ziemer@hsva.de
franz.vonbock@tuhh.de

Abstract
Dynamic ice-structure interaction is a major issue for bottom founded offshore structures subjected to drifting sea ice. The interaction can magnify the ice loads the structure has to withstand, and severe vibrations may occur which can lead to fatigue damage. However, today's understanding of dynamic ice-structure interaction is still insufficient, and available prediction tools and methods suffer from several uncertainties. One reason is the lack of data of sufficient quality which could be used for model validation. Full-scale data typically suffer from missing ice parameters and insufficiently defined ice conditions. Model scale data are usually obtained from tests with a single degree of freedom (SDOF) structure, thus neglecting the influence of higher structural modes on the interaction, although it was already pointed out in the 1970s that the second mode may have a considerable impact. In order to fill this gap, a new experimental setup was developed at HSVA as part of the FATICE project. This setup enables testing with a structure whose configuration could be changed from SDOF to multi-degree of freedom (MDOF, 2 natural frequencies) to compare the developing dynamic ice-structure interaction modes.

The paper describes the development of the experimental setup, its practical implementation, and its applicability and limitations for ice model tests. Basic results from the comparison of SDOF and MDOF conditions are discussed.

1. Introduction

Ice-covered waters such as the Baltic Sea stand out for excellent wind conditions or until now unused resource fields. The increasing energy demand worldwide shifted the focus on such unexploited areas. However, the occurrence of ice limits the accessibility and could harm the offshore structures, like wind turbines or exploration platforms.

Regarding bottom founded and pile shaped offshore structures, dynamic ice-structure interactions may lead to a magnification of the ice loads. By actuating one of the structure's natural frequencies severe vibrations and large loads and displacements may occur, leading to fatigue damages in the long run (Battisti et al., 2006; Høyland, 2017). Consequently, a safe offshore structure design requires a full understanding of occurring ice loads and the resulting dynamic ice-structure interaction. However, nowadays there is still a considerable variation in predicted ice loads even in static load scenarios (Timco and Croasdale, 2006). Considerable effort has been spent on investigating dynamic ice-structure interaction over the past decades and understanding has grown (Hendrikse, 2017), but the physics behind remains not yet fully deciphered (Nord et al., 2015). Consequently, dynamic model tests and dynamic ice-structure simulations are still subject to major uncertainties.

Both approaches were dominated by single degree of freedom (SDOF) configurations; see e.g. Barker et al. (2005), Ziemer (Ziemer and Evers, 2016; Ziemer and Hinse, 2017), Huang and Liu (2009) and Wu and Qiu (2019). The few attempts made with multi-degree of freedom (MDOF, two or more natural frequencies) configurations were not fully successful in reproducing the dynamic ice-structure interaction modes, in particular frequency lock-in, see e.g. Määttänen et al. (2015).

Accordingly, the influence of higher structural modes is largely unknown, despite the fact that Määttänen already measured in 1975 a great impact of the second mode in full-scale observations (Määttänen, 1975). In 2008 Kärnä also reported a critical impact of higher structural modes on the dynamic ice-structure interaction (Kärnä, 2008). In order to determine this impact in model-scale, a new experimental setup was developed at the HSVA, which provides a tunable second natural frequency. The contrast between a SDOF configuration containing only one low natural frequency and a MDOF configuration containing two low natural frequencies visualizes this impact.

The development of such an experimental setup, or more general the improvement of model-scale testing technologies, is one of HSVA's objectives in the on-going research project "Fatigue damage from dynamic ice action (FATICE)".

This paper describes the setup of the physical model including calculations and modeling that led to the experimental setup. This setup is then used in ice model tests and the measured excited frequencies are presented together with the ice failure modes.

2. Theoretical model

Basic principle

The main feature of the new experimental setup is the option to switch between a single degree of freedom (SDOF) and a multi-degree of freedom (MDOF) configuration. The switch between both configurations shall be executed with a low operating expense. This feature shall enable the comparability between a SDOF and MDOF configuration. The influence of the second low natural frequency with respect to dynamic ice-structure interaction has not yet been adequately deciphered. This setup shall give new insights into the influence of higher modes on dynamic ice-structure interaction. Herein, SDOF refers to a configuration with one dominant natural frequency, contrary to the MDOF configuration where two modes are examined. Nonetheless, both SDOF and MDOF setups naturally contain further eigenmodes,

which are supposed to be insignificant for the dynamic interaction due to low modal amplitudes.
The first two natural frequencies shall be adjustable in a range that is comparable to full-scale with adjustable stiffness and mass. Frequency lock-in (FLI) is considered as the most critical dynamic ice-structure interaction regime and it occurs mainly in a range up to 10 Hz (ISO, 2010). Ziemer and Hinse (2017) successfully created FLI in laboratory conditions with a first natural frequency varying between 5.4 up to 7.6 Hz. Therewith, the experimental setup is aiming for a first and second natural frequency below 10 Hz, to examine FLI. Furthermore, the second natural frequency should not be a whole multiple of the first natural frequency, to clearly differentiate between them during the excitation. Higher natural frequencies should be clearly above 10 Hz and have significantly lower amplitudes.

The theoretical setup providing the possibility to switch between SDOF and MDOF configuration with either one or two adjustable natural frequencies is shown in Figure 1. The two masses m_1 and m_2 are connected by a beam element, which serves as a spring element. The beam is divided into three lengths L_A, L_B, and L_C and supported by two dynamic leaf springs k_1 and k_2. This dynamic support enables a close to free vibration behavior of the setup. By changing the upper dynamic leaf spring support towards fixed support and remove the upper mass, the MDOF setup transforms into a SDOF setup. Thus a simple and fast switch between SDOF and MDOF configuration is possible.

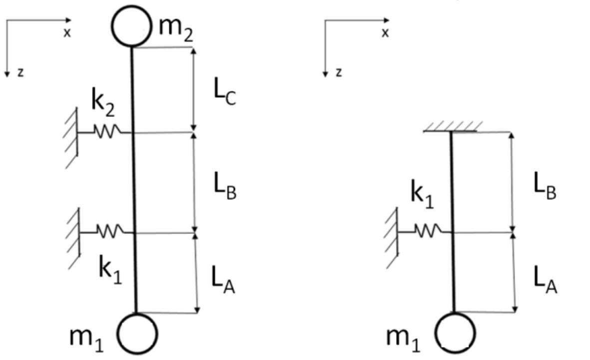

Figure 1. Schematic illustration of the MDOF setup (left) and SDOF setup (right)

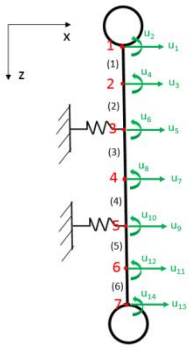

Figure 2. MDOF setup discretized by Euler-Bernoulli beam elements

The dynamic behavior of these two setups can be described by the equation of motion:

$$\bar{M}\ddot{x} + \bar{C}\dot{x} + \bar{K}x = F(t) \qquad \textbf{[1]}$$

With $\bar{M}$ being the oscillating mass matrix, $\bar{C}$ the damping matrix and $\bar{K}$ the stiffness matrix. x being the deflection vector with its first and second time derivatives $\dot{x}$ and $\ddot{x}$. $F(t)$ is an external force acting on the structure. The natural frequencies of such a system are determined with a free vibration analysis whereby damping and external forces are set to zero (Wu, 2013). This leads to the eigenvalue problem, see Equation [2], where ω is the natural circular frequency and Φ the column mode shape matrix.

$$(\bar{K} - \omega^2\bar{M})\Phi = 0 \qquad \textbf{[2]}$$

The eigenvalues $\lambda = \omega^2$ are the solution of the characteristic polynomial, see Equation [2]. The natural frequency can be determined by:

$$f = \frac{\omega}{2\pi} = \frac{\sqrt{\lambda}}{2\pi} \quad [3]$$

with f being the natural frequency. Equation [2] demonstrates the adjustability of natural frequencies for such a system by changing the stiffness properties, the mass properties or both.

Finite Element validation

In order to identify and validate feasible combinations of structural properties for the experimental setup, a finite element analysis (FEA) is executed. Both setups are discretized by Euler-Bernoulli beam elements. Those elements are capable to display the deflection and thereby the vibration in load direction. The discretization of the MDOF setup is shown in Figure 2. The dynamic leaf springs were treated as simply supported beams subjected to a center point load. Thus, the equivalent spring constant is set to:

$$k_{1/2} = \frac{192EI_s}{L_{Leaf}^3} \quad [4]$$

With E being the Young's Modulus, I_s being the leaf springs moment of inertia and L_{Leaf} the free leaf spring length. The resultant stiffness (k_1 and k_2) and the point masses (m_1 and m_2) are added to the global stiffness and mass matrices, according to their global position.
To find the best possible combination of structural dimensions the FE model is implemented into a brute-force analysis. The following structural criteria and boundary conditions were used for the brute-force search:

- Strength capacity to withstand a design ice load of at least 5 kN
- The global stiffness shall be greater than 450 N/mm
- The height and width of the leaf springs can be varied freely
- The free leaf spring length ($L_{Leaf1/2}$) can be varied between 0 to 0.5m
- The initial weight of m_1 is 340 kg and limited to 1500 kg
- The initial weight of m_2 is 50 kg and limited to 500 kg
- The length L_A shall be fixed to 0.5m
- The length L_B shall be fixed to 0.4m
- The length L_C can be varied between 0 and 0.8m

Consequently, the masses m_1 and m_2, the length L_C as well as the dimensions of the leaf springs were varied sequentially to find the best possible configuration for the MDOF and SDOF setup while accounting for basin limitation.

Results

Five feasible configurations for the MDOF setup were selected, which are shown in Table 1 along with the resulting properties, the natural frequencies f_1 and f_2, the maximum static deflection δ_{max} and the total global stiffness K_{Global}. Note that the best possible height with 50mm and width with 10mm of the leaf springs is found for all configurations and thereby fixed to those values. Configuration No. 1 is chosen for a detailed analysis. Figure 3 shows the corresponding theoretical mode shapes including mode one and mode two. Figure 1 shows the corresponding response amplitude. Emphasis was put on the magnitude of the second response amplitude, which should be as large as possible to facilitate noticeable impact on the structure-ice interaction. It should be noted that damping was not considered.

Damping should be as low as possible in the practical implementation to facilitate lock-in vibrations.

Table 1. Properties and results of selected configurations for the MDOF setup

No.	m_1 [kg]	m_2 [kg]	L_C [m]	L_{Leaf1} [m]	L_{Leaf2} [m]	f_1 [Hz]	f_2 [Hz]	δ_{max} [mm]	K_{Global} [N/mm]
1	1500	500	0.70	0.40	0.50	2.81	3.77	9.37	533
2	1460	450	0.70	0.45	0.45	2.81	4.00	10.77	464
3	1500	500	0.60	0.40	0.50	2.89	4.33	9.37	533
4	1165	500	0.60	0.50	0.50	2.84	4.42	11.78	424
5	1435	500	0.55	0.45	0.50	2.80	4.70	10.44	479

To transform the configuration into the SDOF configuration the free length of the upper leaf spring L_{Leaf2} is reduced to 0m, forming a fixed support, as it is shown in Figure 1. The free length of the lower leaf spring L_{Leaf1} is increased to 0.5m. The additional upper weight m_2 is reduced to 0kg. Only the fixed mass of the upper basis with 50kg remains. At last, the length L_C is reduced to 0m. In order to reach the first natural frequency of $f_1 = 2.81$Hz for the SDOF configuration, the lower mass m_1 is increased by 50kg. All properties of the SDOF configuration are listed in Table 2. The results for this SDOF configuration are listed in Table 3. As one can see a first natural frequency of $f_1 = 2.82$Hz is reached and thereby in range of the first natural frequency of the MDOF setup. The second natural frequency is high enough to define this configuration as a SDOF setup.

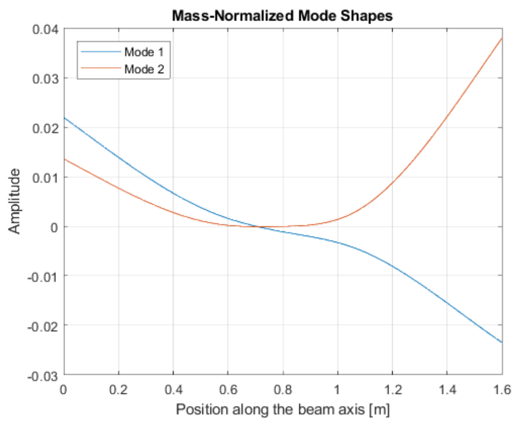

Figure 3. Mass normalized mode shapes from MDOF setup

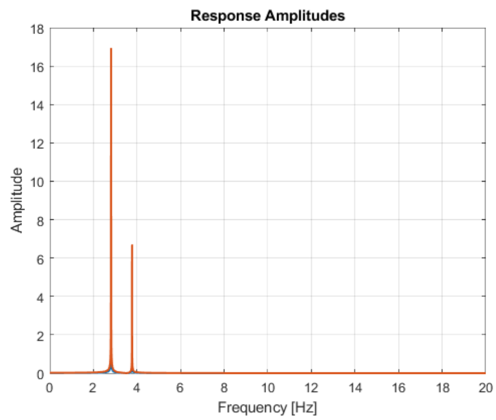

Figure 4. Response amplitude from MDOF setup

Table 2. Properties of selected configurations for the SDOF setup

No.	m_1	m_2	L_C	L_{Leaf1}	L_{Leaf2}
1	1550 kg	50 kg	0 m	0.5 m	0 m

Table 3. Results of the selected configurations for the SDOF setup

No.	f_1	f_2	δ_{max}	K_{Global}
1	2.82 Hz	213.4 Hz	10.3 mm	485 N/mm

3. Physical modeling and testing

The physical model is a further development of the one introduced by Ziemer and Hinse (2017). Figure 5 shows the resulting new experimental setup. Compared to the theoretical approach, instead of one beam element connecting the upper and lower mass, four beam elements are now used. Each beam element is supported by two dynamic leaf springs (green in Figure 5). On top of the beams a moveable platform, containing the mass m_2, is installed. The lower mass m_1 is located on the lower platform (yellow in Figure 5) at which the 6-component-scale (grey in Figure 5) and the actual model to be tested (red in Figure 5) are mounted. Assuming a symmetric setup the theoretical validation beforehand is still valid. It has to be noted that the 6-component-scale and the model to be tested are located off-centered in ice drift direction. But, in relation to the whole setup, the weight of those two components is rather small. Therefore, the resulting error of the first theoretical estimate can be neglected. Furthermore, the 6-component-scale, as well as the leaf spring clamping, show a different stiffness compared to the theoretical estimate due to additional softness. Besides this variation to the theoretical approach, all components are designed according to the presented requirements. As beam elements, a square hollow structural section with a 40x40 mm² profile and 2.5mm wall thickness is used. In the back part of Figure 5, the connection to the towing carriage by aluminum frames is hinted.

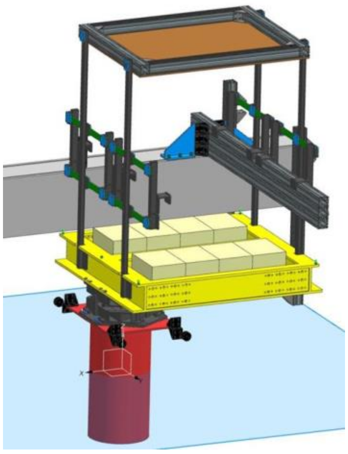

Figure 5. ISO view of the new experimental setup (MDOF configuration)

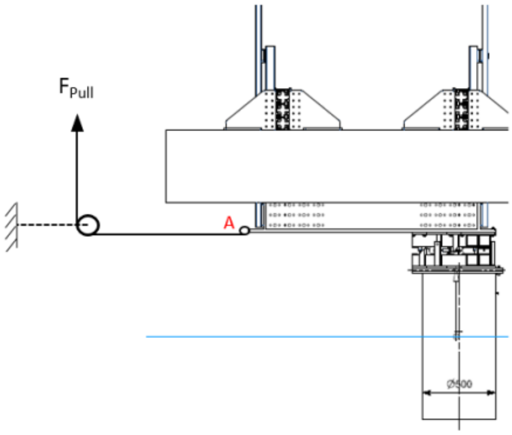

Figure 6. F_{Pull} point of attack

Pre-tests

Based on the theoretical design two dominant frequencies ($f_1 = 2.81$Hz and $f_2 = 3.77$Hz) regarding the MDOF configuration and one dominant frequency ($f_1 = 2.82$Hz) regarding the SDOF configuration should be found in the actual setup. The translational stiffness of the model should be linear. To examine the dynamic characteristics pullout and plucking tests are conducted. Therefore, the structure is deflected by a steadily increasing external force F_{Pull}. This external force is applied at a specified point on the setup, see point A in Figure 6.

To identify the setup's global stiffness pullout tests are conducted. After reaching a maximum pull force ($F_{Pull} \approx 2000$N) the force is steadily released. During the release, the hysteresis of deflection can be examined. The averaged results of all pullout tests for both configurations resulted in a stiffness of 830 N/mm for the SDOF configurations compared to 885 N/mm for the MDOF configuration. The noticeable higher global stiffness compared to the theoretical estimation can be explained primarily by the simplified structural FE model. Because of the different supports, the SDOF configuration shows a slightly lower global stiffness compared to the MDOF configuration.

To identify the setup's natural frequencies plucking tests were conducted. After reaching a maximum pull force of $F_{Pull} \approx 1000N$ the force was kept on a constant level for around 10 seconds. Following, the setup was released instantly via a release-shackle and could oscillate freely. The oscillations were recorded and by applying a Fast Fourier Transformation (FFT) the natural frequencies of the setup can be determined.

Table 4 shows the measured and theoretical estimated natural frequencies. FFTs are presented in Figure 7. Based on the higher global stiffness the estimated natural frequencies are lower compared to the measured ones. Although natural frequencies were higher than estimated they remain constant during all test runs and fulfill the initial criteria. Note that both, pullout and plucking tests were conducted with the model surrounded by water.

Table 4. Difference between estimated and measured natural frequencies (MDOF)

	f_1	f_2	Ratio f_1/f_2
Theoretical estimate	2.86 Hz	3.77 Hz	0.76
Measured properties	3.4 Hz	4.7 Hz	0.72
Difference	18.9 %	24.7 %	5.3 %

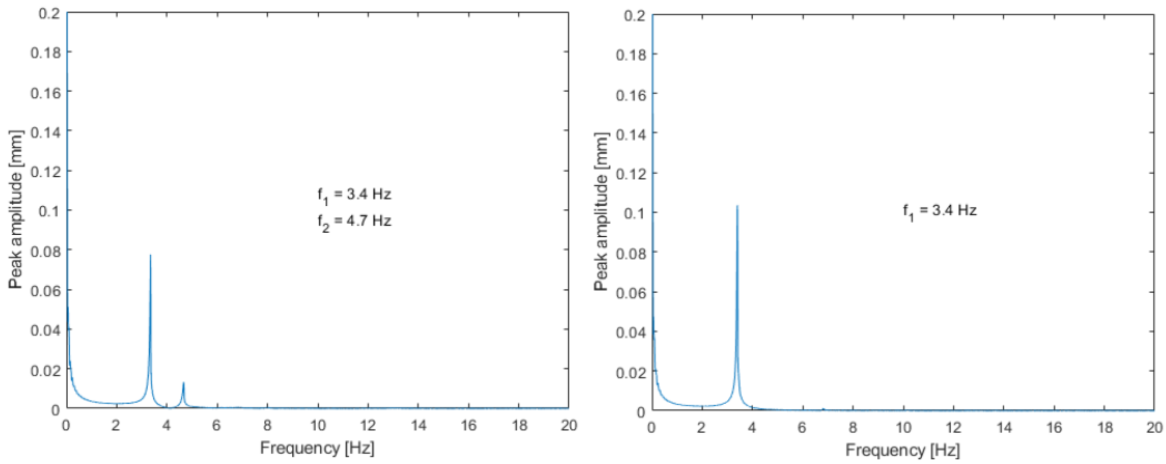

Figure 7. FFT of plucking tests in MDOF (left) and SDOF (right) configuration.

Model tests

The model tests were conducted in the large ice tank at HSVA. Four different series containing two runs each were conducted. Thereby, during each series the MDOF and the SDOF configuration were tested. Throughout all tests, two different types of ice, two different ice thicknesses and a speed range of 4-150 mm/s were applied. The detailed test matrix is given in Table 5. See Evers and Jochmann (1993) for further specifications on "Ice 1", which is HSVA's standard model ice, and Ziemer (2019) on "Ice 2", which is a current development of a model ice without fresh water top layer to improve the model ice' behavior in crushing. Though comparison of the standard and newly developed model ice was part of the FATICE project as well, it is beyond the scope of this paper.

Table 5. Test matrix

Run	11010	15010	21010	25010	31010	32010	42010	44010	46010
Configuration	MDOF	SDOF	SDOF	MDOF	SDOF	MDOF	SDOF	SDOF	MDOF
Ice type	1	1	2	2	1	1	2	2	2
Ice thickness	19 mm	19mm	23mm	23 mm	41mm	41mm	43mm	43mm	43mm

Results

All dynamic ice-structure interaction modes of interest, namely intermittent crushing (IC), frequency lock-in (FLI), and continuous brittle crushign (CBR) could be reproduced throughout the test series with the new experimental setup. Note that during Series 30000 the interaction modes of interest could not be reproduced due to unforeseen flexural failure of the ice. Therefore, Series 30000 is not taken into account for the overall comparison. For the MDOF configuration, an earlier transition towards FLI can be observed, which is shown exemplarily for Series 20000 in Table 6. This shift might be explained by the larger stiffness of the MDOF configuration. Huang et al. (2007) found that for increasing structure stiffness the FLI range shifts to lower ice sheet velocities. However, the difference in stiffness is small, and so is the difference in transition velocities. It cannot be concluded whether the change from SDOF to MDOF system might have an impact on the transitional velocities as well.

Table 6. Occurrence of IC, FLI and the transition in dependence of ice drift velocity during Series 20000.

Velocity [mm/s]	4	6	8	10	12	14	16	18	20	22
Run 21010	IC	IC	IC	IC-FLI	IC-FLI	IC-FLI	IC-FLI	FLI	FLI	FLI
Run 25010	IC	IC	IC-FLI	IC-FLI	IC-FLI	IC-FLI	FLI	FLI	FLI	FLI

The change from SDOF to MDOF setup has a noticeable impact on the global ice load acting on the structure just as on the deflection of the structure. In terms of global ice load, this impact is shown exemplarily for Series 20000 in Figure 8. In terms of structural deflection, it is shown exemplarily for Series 20000 in Figure 9. As it is clearly visible the change between configurations reduces the global ice load and consequently the structural deflection. The same observations can be made for Series 10000 and 40000.

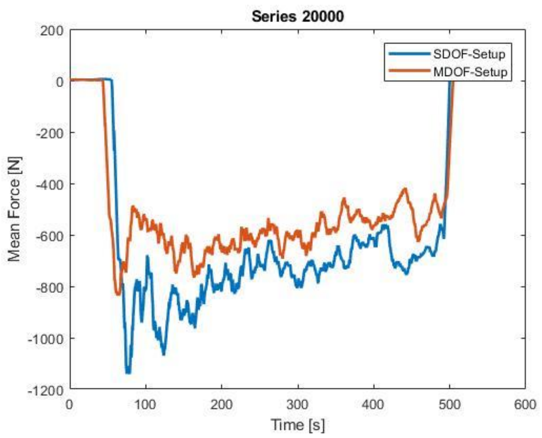

Figure 8. The moving load average of SDOF and MDOF configuration during Series 20000

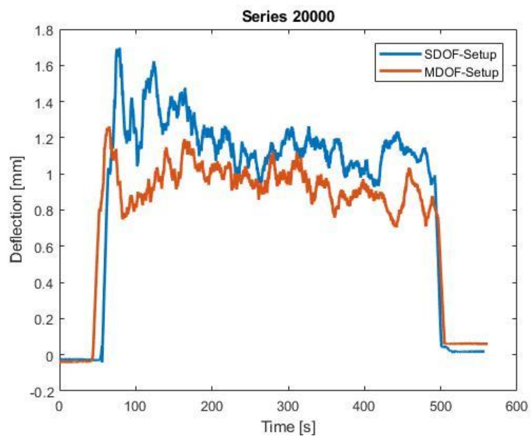

Figure 9. The moving deflection average of SDOF and MDOF configuration during Series 20000

The presented time series show full test runs 21010 and 25010 which were conducted wit the same automated speed control sequence for the main carriage pushing the setup through the level ice sheet. Thus, the ice drift speed changes throughout the time series, and failure type changes accordingly. The velocity was stepwise increased, meaning that the failure changes from IC over FLI to CBR. Differences are largest in IC, but time series of moving mean are also least steady, which is somewhat expected due to the nature of IC with global load buildup followed by load drop to zero after failure. The moving load and displacement average is most steady during the FLI range from about 200s to 310s.

The combined percentage differences between SDOF and MDOF configuration of the averaged global ice load and deflection are shown in Table 7, illustrating a significant load reduction for the MDOF setup compared to the SDOF configuration. The results in Table 7 also show that the differences between SDOF and MDOF in terms of deflection and load for IC and CBR are similar, while for FLI there is a clear difference between load and deflection reduction. This difference in the dynamic response amplification agrees to the close to resonant behavior of FLI (Huang and Liu, 2009).

Table 7. Averaged difference for Series 10000, 20000 and 40000 between SDOF and MDOF configuration in terms of load and deflection for IC, FLI, and CBR.

	IC	**FLI**	**CBR**
Load	14.9 %	15.3 %	22.0 %
Deflection	13.4 %	9.0 %	22.2 %

4. Conclusion

To provide new insights into the impact of higher modes on dynamic ice-structure interaction, in particular the second mode, a new physical test setup is developed. This new setup provides a tunable second low dominant natural frequency. Thereby the setup can serve as a SDOF or MDOF oscillator. The model's natural frequencies are adjustable in a wide range by varying the additional masses or the stiffness by varying the length of beams and the free length of leaf springs. The switch between the SDOF and MDOF configuration is easy to achieve. The desired properties of the model could be kept on a constant level during all series, as the pre-tests have shown.

All dynamic ice-structure interaction modes of interest, namely IC, FLI, and CBR could be reproduced during the tests with a SDOF and a MDOF system, thus the prototype development and model test campaign were successful and provide the first full set of experimental data with a MDOF setup oscillating in all relevant types of ice-induced vibrations. Furthermore, the second natural frequency may have reduced the magnitude of the global ice load and structure deflection. A difference between SDOF and MDOF in terms of load and deflection of 22% is remarkable regarding the design process and costs for offshore structures in ice-covered waters. These results show the importance of deciphering the influence of higher structural modes on dynamic ice-structure interaction. However, further analysis of the measured data is required to understand what causes the load reduction.

Acknowledgments

The authors wish to acknowledge the support to the FATICE project from the MarTERA partners, the Research Council of Norway (RCN), German Federal Ministry of Economic Affairs and Energy (BMWi), the European Union through European Union's Horizon 2020 research and innovation program under grant agreement No 728053-MarTERA and the support of the FATICE partners. The authors would also like to thank the HSVA ice tank crew for the professional execution of the model tests.

References

Barker, A., Timco, G., Gravesen, H., and Vølund P. (2005). Ice loading on Danish wind turbines: Part 1: Dynamic model tests. Cold Regions Science and Technology, 41(1):1-23

Battisti, L., Fredrizzi, R., Brighenti, A., and Laakso, T. (2006). Sea ice and icing risk for offshore wind turbines. Proc. of the OWEMES.

Evers, K.-U. and Jochmann, P. (1993). An Advanced Technique to Improve the Mechanical Properties of Model Ice Development at HSVA Ice Tank. Proceedings of the 12th International Conference on Port and Ocean Engineering under Arctic Conditions, Hamburg Germany, Vol. 2, pp. 877-888

Hendrikse, H. (2017). Ice-induced vibrations of vertically sided offshore structures. Ph.D. thesis

Høyland, K. V. (2017). Final Proposal Fatigue damage from dynamic ice action (FATICE). Full Proposal, Norwegian University of Science and Technology Department of Civil and Environmental Engineering, Trondheim, Norway.

Huang, G. and Liu, P. (2009). A dynamic model for ice-induced vibration of structures. Journal of Offshore Mechanics and Arctic Engineering, 131:6 pages.

Huang, Y., Shi, Q., and Song A. (2007). Model test study of the interaction between ice and a compliant vertical narrow structure. Cold Regions Science and Technology, 49:151-160.

ISO (2010). Petroleum and natural gas industries –Arctic offshore structures. International Standard ISO/FDIS 19906:2010(E), International Organization for Standardization (ISO).

Kärnä, T. (2008). Ice Induced Vibrations of Slender Structures. Modeling Ice-induced Vibrations of Vertical Structures. Winter Navigation Research Board Report No 65, 165-218

Määttänen, M. (1975). Experiences of ice forces against a steel lighthouse mounted on the seabed, and proposed constructional refinements. Port and Ocean Engineering under Arctic Conditions, POAC, pages 857-867.

Määttänen, M., Løset, S., Metrikine, A., Evers, K.-U., Hendriske, H., Lønøy, C., Metrikin, I., Nord, T., and Sukhorukov, S. (2012). Novel ice induced vibration testing in large-scale facility: Deciphering ice induced vibrations part 1. Proceedings of the 21st IAHR International Symposium on Ice, Pages 946-958.

Nord, T., Lourens, E.-M., Määttänen, M., Øiseth, O., and V. Høyland, K. (2015). Laboratory experiments to study ice-induced vibrations of scaled model structures during their interaction with level ice at different velocities. Cold Regions Science and Technology, 119.

Timco, G. and Croasdale, K. (2006). How well can we predict ice loads? Proc 18th IAHR International Symposium on Ice, 2006, Japan, 1:167-174.

Wu, J.-S. (2013). Analytical and Numerical Methods for Vibration Analyses. Wiley, Hoboken.

Wu, T. and Qiu, W. (2019). A dynamic ice-structure interaction model for prediction of ice-induced vibration. Periodica Polytechnica Civil Engineering.

Ziemer, G. (2019). Utilization of tactile sensors to investigate local ice pressure in scale model tests. Proceedings of the 6th International Conference on Advanced Model Measurements Technology for the Maritime Industry, AMT'19.

Ziemer, G. and Evers, K.-U. (2016). Model tests with a compliant cylindrical structure to investigate ice-induced vibrations. Journal of Offshore Mechanics and Arctic Engineering.

Ziemer, G. and Hinse, P. (2017). Relation of maximum structural velocity and ice drift speed during frequency lock-in. Proceedings of the 24th International Conference on Port and Ocean Engineering und Arctic Conditions, POAC'17.

04
Ships in ice

25th IAHR International Symposium on Ice
Trondheim, 23-25 November, 2020

Research on Mechanism and Application of Ship Resonance Ice-Breaking

Dai Huiling*, Pang Fuzhen, Lang Jicai, Li Haichao
College of Shipbuilding Engineering
Harbin Engineering University, Harbin, 150001, PR China
dhl@hrbeu.edu.cn

Aiming at the problem of low cost-effectiveness ratio in ice-breaking of traditional polar ships, this paper proposes a method of resonance ice-breaking based on resonance theory, and studies the mechanism of resonance ice-breaking. Firstly, a simplified model of infinite sea ice in the typical sea area is established. The analysis of vibration modals of the sea ice is carried out, and the relationship between the failure mode and the vibration modal is discussed. On this basis, the resonance effect of the sea ice is stimulated by the designed periodic excitation load, and its stress response and fracture process are analyzed. The effects of parameters such as the amplitude of exciting force and the excitation frequency on resonance ice-breaking effect are investigated. Finally, the method is applied to the structural design of ships, and its ability in ice-breaking is analyzed by a test, which provides a reference for the application and the related research in resonance ice-breaking of polar ships.

1. Introduction

With the development of polar resources, the significance of polar military strategic is highlighted, The polar region ships such as heavy icebreaker and high-icebreaker class ships are increasingly becoming the focus of the competition among the maritime powers, while the ice-breaking ability is crucial to the survival and operation ability of polar ships, which has attracted the close attention of scholars in related fields.

In this respect, Su *et al*. (2011) established a three-degree-of-freedom coupling equation between ice load and hull motion, and studied the ice-breaking load and ice-breaking capacity of the icebreaker. Choi *et al*. (2015) proposed a method for estimating the ice-breaking capacity required for polar ships with dynamic and uncertain conditions. Jordaan (2011) established a mathematical model of the interaction between sea ice and ocean structures, studied the damage mechanism of sea ice under different ballast actions, and proved that the force between ice and structures plays an important role in the damage form of sea ice. Shi *et al*. (2016) conducted numerical simulation studies on the collision of different bow shapes and ice floes, the results showed that the ice-breaking ability of forward bow and flying shear bow was stronger than that of upright bow and bulbous bow. Liu (2014) carried out numerical simulation of ice load of icebreaker and proposed a new type of double-pile structure of icebreaker to enhance ice-breaking ability. These research shows that the existing icebreaker mainly realizes ice-breaking function based on its own gravity, and ice-breaking ability is limited by ship displacement, main engine power and other parameters, so greatly improving ice-breaking ability will seriously affect the ship's performance.

While in the field of road ice-breaking, Chen *et al*. (2012) concluded that vibration ice-breaking is more efficient than static ice-breaking and the optimal vibration frequency should be selected according to the thickness of ice through experiments and finite element analysis of ice-breaking with a tool. Inspired, the method of vibration ice-breaking is used in the field of ship ice-breaking, puts forward a new technology of resonance ice-breaking. This paper carries out research on the mechanism of resonance ice-breaking, analyzes the stress response and the rupture process of ice during resonance ice-breaking, explores influence parameters of ice-breaking ability and applies it into the design of ship structures, aiming to significantly improve the ice-breaking ability of polar ships.

2. Ship - ice resonance principle

2.1. Model of ship-ice vibration system

During the operation of ice-breaking, sea ice bears the periodic force from the ship in the ice zone. Due to the elastic effect of ship and sea ice, a complex master-slave vibration system will be constituted. In order to explain the general principle and facilitate derivation, it is abstracted as a single-degree-of-freedom vibration system, as shown in **Figure 1**.

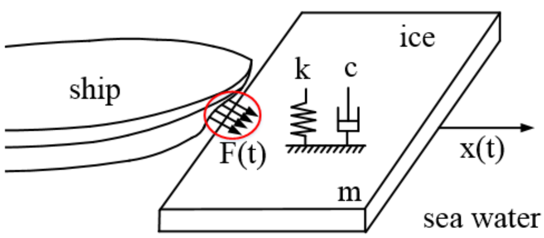

Figure 1. Simplified model of ship - ice vibration system.

Assuming that the center of gravity coincides with the geometrical center of the sea ice, and the sea ice moved only in the x direction. The static equilibrium position is taken as the origin of coordinates. Where, m is the mass of the sea ice, k is the sea ice stiffness coefficient, c is the sea ice damping coefficient, $F(t)$ is the simple harmonic excitation force, let $F(t) = F_0 \sin wt$, and w is the circular frequency of the excitation load.

2.2. Resonance principle of ship-ice vibration system

According to the knowledge related to structural dynamics, the dynamic amplification factor β of the vibration system under sinusoidal excitation force is (Ji, 1985):

$$\beta = \left| \frac{1}{\sqrt{(1-\gamma^2)^2 + (2\zeta\gamma)^2}} \right| \quad [1]$$

Where, γ and ζ are the frequency ratio and the damping ratio of the vibration system respectively.

Figure 2 shows the amplitude-frequency characteristic curve of the vibration system by MATLAB. In **Figure 2**, when γ approaches 1, β increases significantly, and the forced vibration response of the sea ice will reach the maximum value. At this point, the only limiting factor is the damping of the vibration system. The smaller ζ is, the lager the forced vibration response is. In the actual ice-breaking operation, the ship's excitation force is mostly non-harmonic periodic loads, which can be expanded into Fourier series and treated as infinite harmonic loads. Therefore, the above resonance theory is still applicable (Yao, 2004).

Wang *et al*. (2015) obtained the force when moves slowly and moves the tool under the specified vibration frequency and amplitude to chop the ice, and drew the relation curve between the static ice-breaking force, the vibration ice-breaking force and the ice thickness, as shown in **Figure 3**. It can be seen that, when the same thickness of ice is broken, the vibration ice-breaking force is much less than the static ice-breaking force, which is basically 0.1 times that of the static ice-breaking force. In other words, the effect of vibration ice-breaking is 10 times higher than that of the static ice-breaking force. This illustrates the excellent effect of vibration ice-breaking,

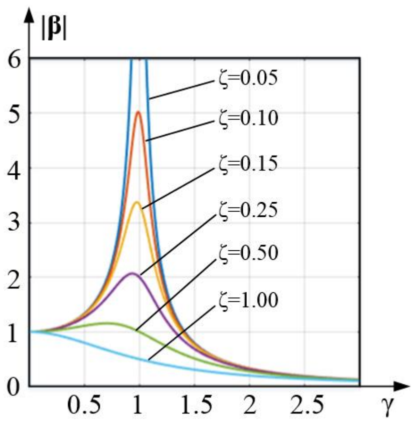

Figure 2. Amplitude-frequency characteristic curve of vibration system.

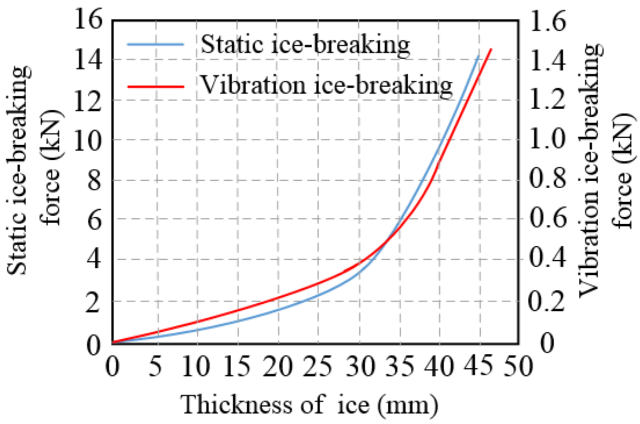

Figure 3. Curves of static and vibration ice-breaking force.

Based on the resonance principle and combined with the above analysis, it can be seen that if the low coordinated vibration of the hull can be effectively utilized to stimulate the resonance effect of sea ice, the stress inside sea ice can be significantly enhanced, leading to crushing, and then the ice-breaking ability of the ship can be greatly improved.

3. Analysis of vibration characteristics of ice at contact area

3.1. Computational model of ice at contact area

In this paper, the sea ice was regarded as an ideal elastic material, and its failure criterion used the von Mises criterion. Combining elastic mechanics and the elastic sheet bending theory in structural mechanics, the sea ice at contact area was simplified into an elastic rectangular sheet with uniform thickness in **Figure 4**, its length and width were set as a and b. It is assumed that the contact side between sea ice and the icebreaker is free, the other three sides are subject to fixed constraints, and the acting position of ice-breaking excitation load is the midpoint of the free side (Wang *et al.*, 2015).

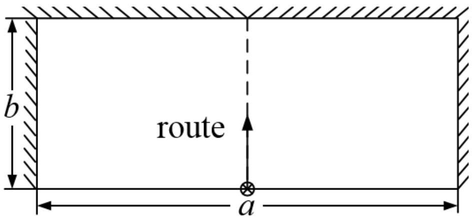

Figure 4. Calculation model diagram of the ice at contact area.

3.2. Vibration modals analysis of ice at contact area

The vibration of the structure has infinite inherent frequencies, only when the excitation frequency is the inherent frequency, the amplitude is larger. But amplitudes generated by different natural frequency are different, and vibration modes are also different. Therefore, the proper frequency and vibration modes can be selected by analyzing inherent modals of the structure to obtain the excitation conditions satisfying the amplitude requirements.

In this paper, the influence of fluid load was taken into account to establish the ice sound-solid coupling model, and vibration modals analysis of ice was carried out by ABAQUS. The parameters of ice were set as: ice size $a \times b \times h = 36 \times 20 \times 1.5$ m^3, elastic modulus $E = 5.4$ GPa, poisson ratio $\mu = 0.33$, sea ice density $\rho_1 = 915$ kg/m3, seawater density $\rho_2 = 1024$ kg/m3, failure stress $\sigma_0 = 2$ MPa. **Figure 5** exhibits results of typical modes and inherent frequencies (m and n are the longitudinal and the transverse wave number respectively).

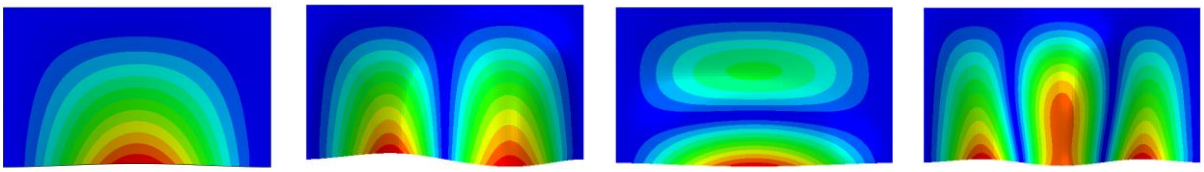

a) The first vibration mode 1.4 Hz	b) The second vibration mode (m=2, n=1) 4.2 Hz	c) The third vibration mode (m=1, n=2) 5.6 Hz	d) The fourth vibration mode (m=3, n=1) 8.4 Hz

Figure 5. Typical vibration modes of ice.

Since the higher the frequency, the more complex the sea ice mode is. The energy attenuation is very serious at this time, the ice-breaking effect is not obvious, so this paper mainly analyzes the first four order vibration modes. For the overall structure mode, when the excitation position is located at the crest/ trough of the mode, a better excitation effect will be generated (Miao *et al*., 2016). It is clear from **Figure 5** that only the first, third and fourth modals meet requirements, so the next step is to observe the stress of sea ice under these modals to analyze the relationship between vibration modal and failure mode of sea ice.

3.3. Preliminary study on the relationship between failure mode and vibration mode of ice

When the excitation frequency is close to the inherent frequency, the structure produces resonance effect, and the frequency is called resonance frequency. In this paper, the first, second and fourth resonance modals of sea ice were excited by unit force respectively to observe the sea ice stress. **Figure 6** and **Table 1** exhibit the stress cloud diagram of sea ice and the stress value at the typical position.

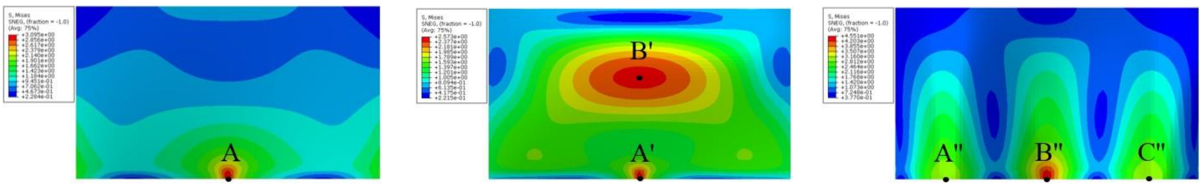

a) The first stress response b) The third stress response c) The fourth stress response

Figure 6. Stress response cloud diagram of sea ice.

Table 1. Stress values at typical locations of sea ice.

Location	Stress (Pa)	Location	Stress (Pa)
A	15.3	A''	4.0
A'	4.6	B''	5.3
B'	13.5	C''	4.0

It can be seen from **Figure 6** and **Table 1** that under the unit excitation force of single frequency, the sea ice stress at the crest/ trough of the mode is larger. When the frequency is 1.4 Hz, only the sea ice stress at A (trough) is large, which is 15.3 Pa. When the amplitude of excitation force is large enough, the sea ice here reaches the failure stress and begins to break firstly. When the frequency is 5.6 Hz, the sea ice stress at A' (trough) and B' (crest) are 13.5 Pa and 4.6 Pa, the stress at B' is larger than A'. When the amplitude of excitation stress is large enough, B' reaches the failure stress and cracks firstly, it can be used to rescue icebreaker trapped in B'. When the frequency is 8.4 Hz, the sea ice stress at A'' (crest), B'' (trough) and C'' (crest) has little difference, which is 4.0 Pa, 5.3 Pa and 4.0 Pa respectively. When the amplitude of excitation force is large enough, failure stresses of the sea ice at these three places are almost simultaneously reached and crack, causing the sea ice to break up in a large area. To sum up, the resonance ice-breaking directionally can be realized by stimulating the corresponding resonance modals of sea ice.

In addition, according to the excitation position, when the excitation frequency is 1.4 Hz, the sea ice stress is significantly larger than that at 5.6 Hz and 8.4 Hz, which corresponds to the first vibration modal of sea ice, that is, the ice-breaking effect is best when the excitation force stimulates the first vibration modal of sea ice.

4. Analysis of ice-breaking effect

4.1. Vibration ice-breaking load setting

In order to compare the failure effect of sea ice under static load and dynamic load, the vibration ice-breaking load was set as a sinusoidal periodic load with time variation, which is the superposition of gravity of the ice-breaking contact area of bow and simple harmonic excitation force. The load function is $\boldsymbol{F}(t) = G + F_0 \sin wt$, where G is the gravity of the ice-breaking contact area of bow, F_0 is amplitude of the vibration load, w is the vibration load frequency, let F_0 = 80 KN, w= 1.4 Hz (first resonance frequency of sea ice) (Yang *et al*., 2014).

4.2. Comparative analysis of gravity and resonance ice-breaking effects

In this paper, the unit failure method was adopted to simulate the damage of ice, the element will fail when the stress reaches the failure stress. Through finite element simulation analysis, It could not make the ice broken when the amplitude of static ice-breaking load is 500 KN (gravity of the ice-breaking contact area of bow is 500 KN), the stress at excitation position of the sea ice is 0.96 MPa, While when the amplitude of static ice-breaking load is 900 KN (gravity of the ice-breaking contact area of bow is 900 KN) can make the stress at excitation position reaches 2 MPa and break up, the damage effects are shown in **Figure 7**. In **Figure 7**, the blue area indicates that the ice has not been damaged, and as the color deepens, the extent of damage increases, while the gray area indicates that the sea ice has failed (Cheng *et al*., 2019).

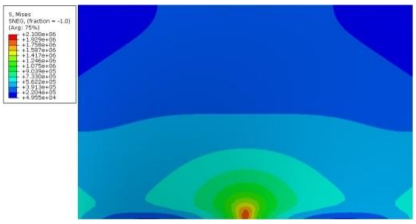
500 KN

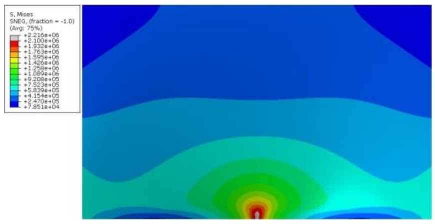
900 KN

Figure 7. Cloud diagram of gravity ice-breaking.

According to the test, G = 500 KN is enough to break the ice during the progress of resonance ice-breaking. Compared with gravity ice-breaking method, the mass of the ice-breaking contact area of bow required by resonance ice-breaking method is significantly reduced. The calculation time was set as 12s and the calculation step was 0.02s to simulate the process of ice rupture under the resonance ice-breaking load. **Figure 8** shows the degree of rupture of sea ice through stress diagrams at typical moments. **Figure 9** shows the stress response curve of the region near the excitation position.

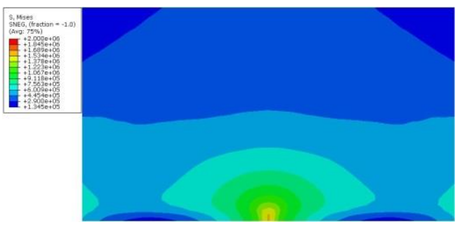
a）0.26s

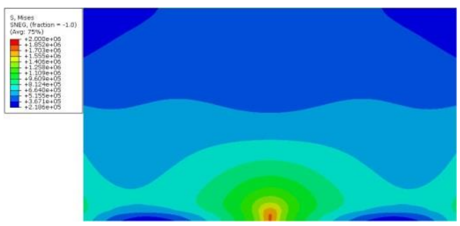
b）1s

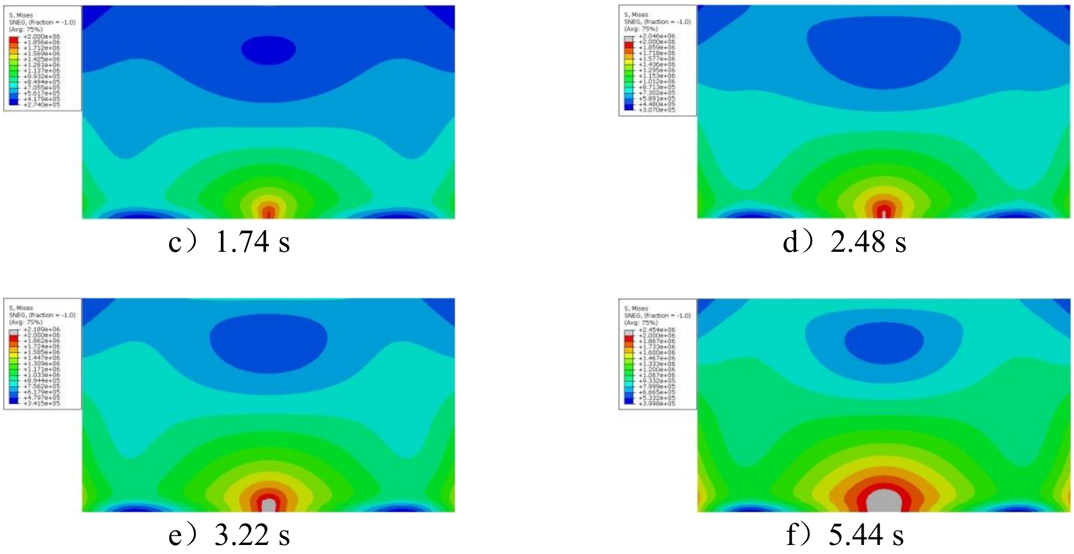

Figure 8. Cloud diagram of response ice-breaking.

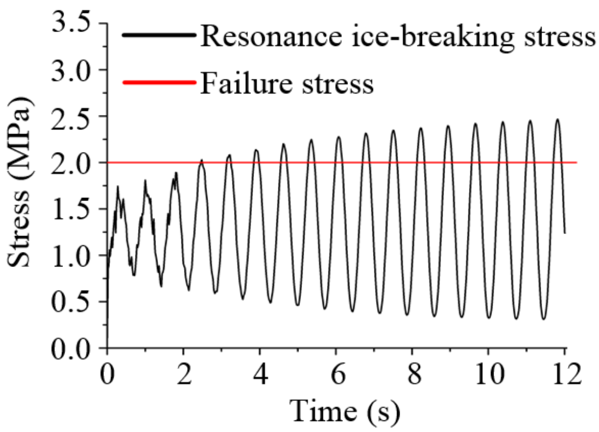

Figure 9. Stress response curve of the region near the excitation location.

Form **Figure 8** and **Figure 9**, the closer to the excitation position, the greater the stress response of the ice. Over time, the affected area increases, and the damage degree deepen. But resonance is not a periodic vibration of equal amplitude, its amplitude increases with time, so it takes time to break. After 2.48 s (about 3.5 cycles), the ice at the excitation position reached the failure stress, and it broke up in an annular direction around the excitation, it can reach 6.8 m^2 at 5.44 s.

4.3. Analysis of influencing factors and law of resonance ice-breaking ability

In order to explore the influence law of various parameters of vibration ice-breaking load on ice-breaking effect, the comparison conditions of the amplitude of excitation force and vibration frequency were respectively set as follows: F_0 = 60 KN, 80 KN, 100 KN; w = 0.4 Hz, 1.4 Hz, 2.4 Hz, where w = 1.4 Hz is the first resonance frequency of sea ice, and w = 0.4 Hz and 2.4 Hz both avoid the resonance frequency.

Figure 10 shows the curve of ice stress under the condition that the vibration frequency remains unchanged, while the amplitude of excitation force is changed. In **Figure 10**, when the vibration frequency is unchanged, with the increase of the amplitude of excitation load, the ice stress near the excitation position gradually increases, and the increasing trend is basically consistent. When F_0 = 60 KN, 80 KN and 100 KN, the time required for ice breakage are 1.72 s, 2.48 s and 4.62 s respectively, indicating that the failure time decreases with the increase of the amplitude of excitation load. **Figure 11** shows the curve of ice stress under the condition that the amplitude of excitation load remains unchanged, while the excitation frequency is changed. In **Figure 11**, when w = 1.4 Hz, the first resonance modal of sea ice was excited, and the stress response of ice increased with the increase of time, and the ice was broken at 2.48 s. However, when w = 0.4 Hz and 2.4 Hz, the stress response of the ice still presents approximate periodic changes, but the failure stress cannot be achieved, so the ice will not break up. So when the ice-breaking load causes the resonance of ice, the damage effect is most significant.

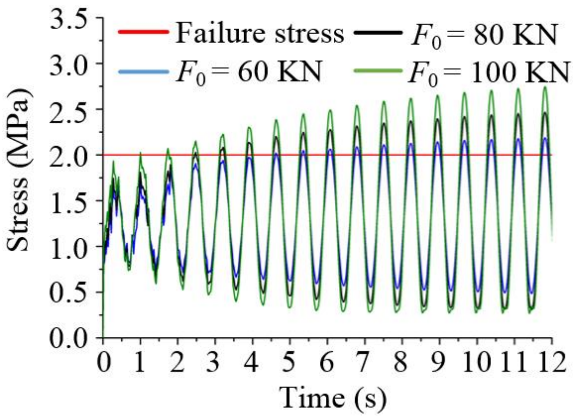

Figure 10. Relationship between ice stress and amplitude of excitation force.

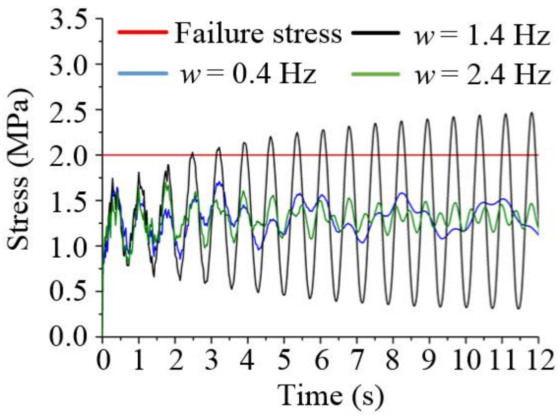

Figure 11. Relationship between ice stress and excitation frequency.

5. Structure design of the resonance ice-breaking bow

In this chapter, based on the resonance principle, the resonance ice-breaking bow was designed. The ice-breaking contact structure of bow was improved and the additional stiffener was added on the basis of the original bow, as shown in **Figure 12**. The ice-breaking contact area of bow was designed as a concave and convex wave-like structure, which was used to provide the excitation force for ice-breaking. The stiffener was installed inside the contact area, so that the stiffness of the area could meet the ice-breaking requirements. The specific structure is shown in **Figure 13**.

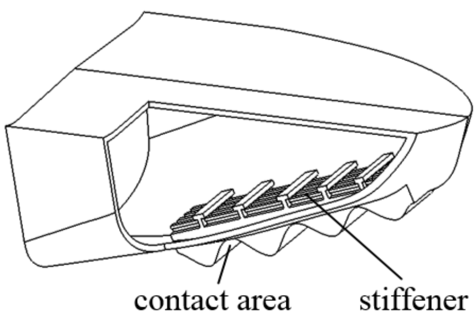

Figure 12. Diagram of resonance ice-breaking bow

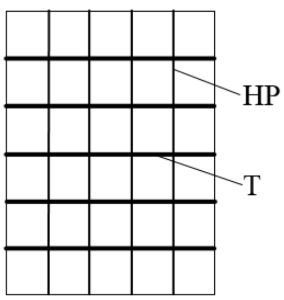

Figure 13. Diagram of stiffness

According to the speed v of the icebreaker and the resonance frequency w of the sea ice at contact area, the unit wavelength l of the wave-shaped structure was determined by $w = v / l$.

The modal mass m was obtained by modal analysis of the ice-breaking contact area of bow, and the stiffness k of the ice-breaking contact area of bow was determined by $w^2 = k / m$, which was guaranteed by the internal stiffener.

In order to verify the ice-breaking ability of resonance ice-breaking bow, **Figure 14** exhibits tests were conducted in the inflatable tank. In **Figure 14**, the thin paraffin was used to replace ice, and ships sailed to the paraffin at a steady speed and finally acted on the edge of one end of the paraffin. As shown in **Figure 15**, the bow is designed into two types: ordinary type and wave type, their weights were basically kept the same. It was found that the ordinary bow did not break the paraffin, while the wavy bow breaks a crack in the paraffin from the edge.

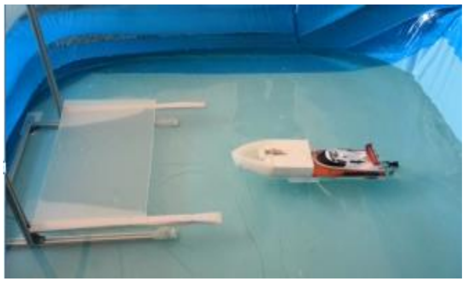

Figure 14. Diagram of ice-breaking test in inflatable tank

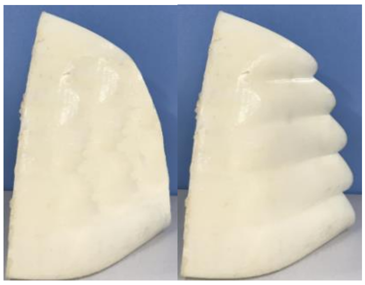

Figure 15. Contrast figure between a normal bow and a wavy bow

6. Conclusion

A resonance ice-breaking method based on resonance principle was proposed in this paper. The relationship between the failure mode and the vibration modal of sea ice was investigated, and the resonance ice-breaking process was simulated by ABAQUS. Finally, the resonance ice-breaking bow was designed and ice-breaking tests were carried out. The results show:

(1) Corresponding vibration modals of sea ice can be excited to achieve resonance directional ice-breaking. The ice-breaking effect is the best when the excitation force excitations the first vibration modal of sea ice.

(2) Compared with the gravity ice-breaking method, the mass of the bow required for resonance ice-breaking is significantly reduced, and the ice-breaking effect is significant. With the increase of the applied time of vibration ice-breaking load, the ice will be broken in an annular manner around the exciting position, and the failure area of will increase gradually.

(3) When the excitation frequency is fixed, the damage time of ice decreases with the increase of the force amplitude; Under the condition of certain force amplitude, the ice-breaking effect is remarkable when the vibration frequency is the resonance frequency of ice.

(4) The wavy bow has better ice-breaking effect than the ordinary bow. However, the quantitative analysis of the ice-breaking effect has not been achieved in the current test, so further tests can be carried out with the help of force sensors.

Acknowledgments

The paper is supported by Key research and development project of Shandong province (2019JZZY010125), National key research and development project (2016YFC0303406), National natural science foundation of China (51209052, 51679053), China postdoctoral fund (2014M522661), General assembly pre-research fund (6140210020105).

References

Su B., Riska K., Moan T., 2011. A numerical method for the prediction of ship performance in level ice. Cold Regions Science and Technology, 60(03): 177-188.

Su B., Riska K., Moan T., 2011. Numerical study of ice-induced loads on ship hulls. Marine Structures, 65(04): 1-21.

Choi M., Erikstad S.O., Ehlers S., 2015. Mission based ship design under uncertain arctic sea ice conditions. Proc. 34th ASME International Conference on Ocean, St John's, CANADA, 1-8.

Jordaan I.J., 2011. Mechanics of ice–structure interaction. Engineering Fracture Mechanics, 68 (11) 1923-1960.

Shi, J.H., Gui, H.B., and Li, D., 2016. Research on influence of bow shape to the collision between ship and ice. Ship Science and Technology, 38(01):8-13.

Liu, X., 2014. Research on the new icebreakers ice structure. Jiangsu University of Science and Technology.

Chen, L.G., Wang, S.L., Wang, J.F., Song, J.J., and Ma, W.X., 2012. Mechanism analysis of snow-ice removing using vibration and optimization of vibration roller. Construction Machinery, 2(03):102-105.

Ji, W., Fang, T., and Chen, S.Q., 1985. Mechanical Vibration. Beijing: Science Publication.

Yao, X.L, 2004. Ship Vibration. Harbin: Harbin Engineering University Publication.

Wang, J.W., Zou, Z.J, 2015. Ship's structural response during its collision with level ice based on nonlinear finite element method. Journal of Vibration and Shock, 34(23):125-130.

Miao, B., Zhu, C.L., and Zhu, C.X., 2016. Research on placement of piezoelectric actuators in plate piezoelectric de-icing system. Acta Aerodynamica Sinica, 34(06):732-737.

Yang, Q., Xiao, Y.J., Chen, F.Q., Liu, J.P., 2014. Method and application of numerical simulation for full process of pile driving by using high frequency hammers. Journal of Water Resources and Architectural Engineering, 12(02):44-50.

Cheng, W.X., 2019. Research on numerical simulation of ice breaking by under ice explosion based on PD. Harbin Engineering University.

25th IAHR International Symposium on Ice

Trondheim, 23 - 25 November 2020

Numerical Simulations of Naval Vessel Collisions with Ice

R. Gagnon[1], J. Wang[2], D. Seo[3] and J. Mackay[4]

[1, 2, 3] OCRE/NRC; [4] DRDC

[1, 2, 3] St. John's, NL, Canada; [4] Halifax, NS, Canada

[1] Robert.Gagnon@nrc-cnrc.gc.ca, [2] Jungyong.Wang@nrc-cnrc.gc.ca,

[3] DongCheol.Seo@nrc-cnrc.gc.ca, [4] John.Mackay2@forces.gc.ca

Numerical simulations (using LS-Dyna™) were initially conducted to show two scenarios for a naval vessel, one where little-to-no-damage occurs during an ice collision and the other where substantial damage occurs. NRC's crushable-foam ice model was used for all simulations. One instance of the first scenario corresponded to the vessel moving at a given vessel speed of 1.5 m/s and experiencing a bow-side collision with a block-shaped ice mass of approximately 181 tonnes that caused a relatively small amount of plastic damage to the vessel's hull (i.e. a wide-area shallow-depth plating dent with depth of ~ 11 mm). In contrast, the second scenario corresponded to the vessel colliding at the same speed with a 524 tonne similar-shaped ice mass at the same hull location that caused extensive, non-holing, plastic damage to the vessel grillage. That is, the hull plating experienced substantial plastic indentation (~ 60 mm) and the stiffener and frame in the region of impact underwent bending and buckling. Following those simulations, others were performed using progressively smaller ice masses in order to determine what the size of an ice mass would be that would cause no damage at all to the vessel. The results indicated that some level of damage, albeit diminishingly small, occurred (in a linear trend) as the ice masses and associated peak loads get smaller until eventually an ice mass of 8 tonnes produced no damage at all, where the peak load was 25 kN. The next ice-mass size up from that was 17 tonnes, that produced a tiny amount of damage during a simulation. An important observation from all the simulations concerns where the ice impact occurs with respect to supporting stiffeners and frames behind the plating. This can influence the peak loads and pressures that occur, and the extent of local damage. The 524 tonne ice mass collision simulation yielded average and peak contact pressures that were in reasonable agreement with average and hard-zone pressure values obtained in large double pendulum ice impact lab tests. This, and favorable comparisons with other lab and field data, bolster confidence in the ice model used.

1. Introduction and Background

Marine transportation in Arctic regions is seriously affected by the presence of glacial and sea ice masses. Of concern for ships (including naval vessels) are bergy bits and growlers (house-sized and car-sized glacial ice masses) and sea ice masses (e.g. a chunk of multi-year sea ice, a chunk from a dense sea ice rubble field or from a consolidated ridge, individual floes or smaller portions broken from floes). Detection of ice masses is sometimes difficult using marine radar in rough sea states. Should ice make contact with a ship's hull, the impact forces will depend on the masses of the vessel and ice, the hydrodynamics of the interaction, the ship structure, the shape of the ice mass and its local crushing properties.

Numerical simulations of a naval vessel colliding with ice were conducted. The simulations involved collisions with ice masses of varying size at the side of the vessel's bow. Some scenarios entailed relatively mild collisions (≤ 514 kN peak impact load) with a single ice mass (in the range of 8-181 tonnes) where moderate to little damage (or no damage in one case) to the vessel occurred. The other scenarios involved damaging, but non-holing, collisions with ice masses (in the range 98-524 tonnes) where greater permanent indentation of the vessel's grillage occurred and where peak loads were in the range 200-769 kN. Hit location, with respect to stiffeners and frames, was a factor. The simulations were run at NRC/OCRE STJ using NRC hardware (HP Z840 Workstation) and licensed LS-Dyna™ software. NRC's validated ice model was used for the simulations. The results are presented below.

2.0. Numerical Simulations of a Naval Vessel Colliding with Ice Masses

As mentioned above, the purpose of the simulations was to show various cases of a naval vessel colliding with ice, some cases where mild damage (or no damage) occurred and the others where significant permanent non-holing damage was done to the grillage. The strategy used to accomplish this was to utilize similar-shaped ice masses, of various sizes, to perform the collision simulations. The initial masses of the ice objects needed to fit these requirements had to be determined from a few trial-and-error simulations so that for the chosen vessel speed of 1.5 m/s the largest ice mass (~ 524 tonnes) caused obvious damage to the grillage and a smaller ice mass (~ 181 tonnes) caused substantially less damage. The trial-and-error tactic was necessary because the shape of the slender naval vessel, where the bow expanded at about 10^{o} from the vessel's length axis, was radically different from other vessels and structures for which ice-impact simulations had been conducted before by the NRC/OCRE simulation team. The initial trial runs were 'dry' runs that did not involve hydrodynamic effects.

2.1. Naval Vessel and Impacted Hull Segment Description

Figure 1 shows the full meshed volume used in the simulations. The front half portion of the vessel that was generated by NRC from the IGES file that was supplied by DRDC is visible. DRDC also supplied a report which contained all relevant information necessary to describe the properties of the hull portion which NRC had decided that ice impacts would most appropriately occur in the simulations. Table 1 gives information on the vessel and Table 2 gives properties of the target hull segment. Figure 2 shows the vessel body plan.

2.2. Bulk-Ice Mass and Target Ice-Knob

An ice mass is shown in Figure 3. In this instance the bulk-ice mass represents a block-shaped ice feature such as a glacial ice growler, a chunk of multi-year sea ice or a chunk from a dense sea ice rubble field or from a consolidated ridge. The hemispherical ice mass (a.k.a. the 'ice-knob') is attached at one of the corners of the ice mass feature. A validated 'crushable foam' material model (Gagnon and Derradji-Aouat, 2006) was used to characterize the ice-knob. To do this, LS-Dyna's material model MAT_63 was used with the following inputs: Density = 870 kg/m^3, Young's Modulus = 9 GPa, Poisson's Ratio = 0.003, Tensile Stress Cutoff = 800 MPa, and the Yield Strength versus Volumetric Strain curve the same as that used by Gagnon and Derradji-Aouat (2006). Table 3 gives information on the characteristics of the initial ice masses used for the simulations.

2.3. Meshing Considerations and Simulation Strategy

Following the methods of Gagnon and Wang (2012), the main large objects that do not interact with anything other than water and air, i.e. the vessel and the bulk-ice mass, are given a large, but adequately refined, mesh size that matches the mesh size of the water and air domains. On the other hand, the ice-knob and deformable grillage must be finely meshed, since their interaction volume is much smaller, in order to capture the appropriate behaviors during the impacts. These relatively small and finely meshed objects do not have to interact with the water and air because the main hydrodynamic effects are captured by the interactions of the vessel and the bulk-ice mass with the water and air. Furthermore, the deformable properties of the ice-knob and grillage do not have to be active until they come into contact with one another, that is, they can be treated as rigid objects until the impacts occur. This is computationally very efficient, and LS-Dyna provides the user with the convenient option to run a simulation and control the properties of objects by setting precise times when their deformable properties become active during a simulation. Consequently, a few trial simulations are conducted where the grillage and ice-knob are treated as rigid bodies in order to determine the precise time when contact occurs at the initiation of impact. This time is then used to control when the grillage and ice-knob properties are switched from rigid to deformable during the full simulations.

In order to run the full simulations in an efficient manner a simple strategy was used to reduce the run time by reducing the effective number of elements in the meshed volumes of the air and water. By cutting the vessel in half, and only using the bow half, a substantial number of superfluous water and air elements could be removed without affecting the simulated impact results. Note that the back half of the vessel would not have contributed to the bow wave that is created by the front half of the vessel. The full air and water domains encompassing the half-ship and ice mass for a typical impact simulation are shown in Figure 1.

During the simulated impacts with ice the ship moved at a constant speed and was assumed to be constrained from roll, yaw and sway movement. This is a valid assumption because the loads exerted on the vessel (25-769 kN, as seen in the results below) were not capable of influencing the ship movement in any substantive manner during the course of the brief (~ 1.0 s) ice/grillage primary interaction. Recall that the vessel has a displacement of 7600 tonnes, with an additional hydrodynamic added mass, so that the applied impact force could only influence the ship movement by a negligible amount during the impact. Indeed, even during a 'dry-case' HITS simulation (Gagnon and Quinton, 2017), the surge movement of the striking object, with a relatively tiny mass of 74 tonnes compared to the vessel in the present case, was shown to have a small influence (~ 15 %) on the forward speed of the striking object during impacts where the impact load was roughly 300 kN.

With these aspects in mind the 'wet-case' simulations involving the grillage were conducted by letting the vessel accelerate to the target speed of 1.5 m/s and then move through an adequate length of the water/air domain to create a realistic bow wave before actually making contact with the ice-knob on the bulk-ice mass. During this time the ice-knob and the grillage were assigned rigid properties. Then, just before contact, the deformable properties of the ice-knob and the grillage were switched on. This strategy ensured that the hydrodynamics of the interaction were adequately accounted for and that run times were only as long as necessary (up to 58 hours using 30 CPU's on a HP Z840 Workstation).

2.4. Simulation Results

Figure 4 shows the force time series for the case of the 524 tonne ice mass initially impacting the grillage segment at a stiffener location and near a frame. The secondary 'peak' corresponds to the sliding ice-knob contacting the hull plating that was supported by a frame. The oscillations in load at the top of the secondary peak correspond to elastic oscillations of the meshed hull segment due to the ice-knob impacting the frame. Further evidence (not shown here) of the elastic oscillations was observed in the normal-to-the-surface displacement of the hull at a particular location outside of the region of plastic damage. The resonant frequency is ~ 48 Hz. Figure 5 shows an image sequence from the simulation illustrating the progressive damage to the grillage structure during the sliding impact. The damage involves indentation of the plating, and bending/buckling of the stiffener and frame. Figure 6 shows the maximum deformable plate deflection associated with the impact. We note that the maximum load generated by the collision (~ 769 kN) was greater than the damaging load generated during the HITS simulation study conducted in 2017 where ice impacts occurred on a similar ship grillage. The load differences are associated with the generally larger impacted ice masses in the present study. As expected, some bow-wave induced surge and sway of the ice mass occurred prior to the impact (data not shown here).

Figure 7 shows the force time series for the case of the grillage segment impacting the 181 tonne ice mass. The maximum first-peak load value (~ 171 kN) induced significantly less plastic damage to the grillage than the larger ice-mass case. In contrast to Figure 5, that showed considerable plastic damage, relatively little damage was evident on the hull segment for the 181 tonne ice mass impact at the time of first-peak load. The sliding impact caused a wide-area shallow dent of ~ 11 mm depth, whereas the former heavier impact created a dent with a depth of ~ 59 mm.

Towards the end of this study we wished to determine what the size of an ice mass would be that caused no damage at all to the vessel. Consequently, a wet-case simulation was run using a smaller ice mass of 98 tonnes. This also showed some grillage damage. So additional simulations were conducted using progressively smaller ice masses until no damage was produced. The results for the additional cases, where the impacts for most occurred roughly at the midpoint between two vertical frames, are shown in Table 4 and Figures 8 and 9, along with the results from the former heavier ice mass cases. Note that due to time constraints most of these simulations were run in 'dry' conditions, that is, hydrodynamics associated with water were not included since these simulations took far less time to run than 'wet' ALE simulations (1 hour versus more than 25 hours). However, we did conduct two simulations (one 'wet' and one 'dry') using the 98 tonne ice mass, where the impact initiated at a frame, to confirm that the impact loads were in reasonable agreement (see Table 4).

The results in Table 4 and Figures 8 and 9 are illuminating. They indicate that some level of damage, albeit diminishingly small, occurred as the ice masses and associated peak loads get smaller until eventually an ice mass of 8 tonnes produced no damage at all, where the peak load was 25 kN. Not surprisingly, this ice mass is less than the hybrid structure/ice mass used in the study by Gagnon and Quinton (2017) where grillage damage was evident. Also noteworthy is that the data indicate a fairly linear trend in the degree of damage associated with peak loads and ice masses. Note that in these results we are using 'residual displacement', the maximum non-recoverable indentation of the hull plating, as an index of 'damage'. Using the fit equation in Figure 8, and the peak load value (260 kN) from Gagnon and Quinton (2017) for an ice impact on a similar grillage, we obtain a residual displacement of 18.4 mm, where those authors reported a value of 24 mm. These values corroborate when one considers that the similar grillages did have some structural differences, and in the present case the impacts were nearer to a stiffener than in the former case (leading to less displacement).

There have been many numerical simulation studies of ship interactions with ice. An extensive review has been provided by Xue et al. (2020). Much of the work has related to ship performance in broken ice and through ice sheets. Due to the particular focus of most of the studies, damage to the vessel was not considered and hydrodynamic aspects were treated in a simplified manner, or not included. The first ship-ice collision simulation to include damage to the vessel and full hydrodynamics was by Gagnon and Wang (2012), using a validated ice model.

A somewhat similar study to the present one, involving simulations of a ship collision with a bergy bit, has been conducted by Liu et al., 2011. It is difficult to compare our results with those results because the scenarios in both studies are very different. The grillage in the other study had a different configuration and was much stronger than the present case. Furthermore, that work did not incorporate water (i.e. hydrodynamics), while some of ours did, so the ice mass was not a free floating object and its velocity against the vessel was fixed. Also the collision was not a sliding load scenario. Perhaps the most important difference was the ice model used that had mesh elements that eroded in response to a critical stress. That led to the formation of gaps in places in the ice contact zone where elements disappeared. That may explain why the simulation did not appear to reflect the structure of the grillage in the pressure distribution patterns it produced. On the other hand, the damage to the grillage had some similarities with the present results, and those of Gagnon and Wang (2012), such as the apparent bending and buckling of structural members behind the plating.

For the case of the 524 tonne ice mass we performed further analysis to determine the average pressure and ice contact area as the impact progressed. Table 5 shows the contact area, average pressure and peak pressure at seven equally-spaced instances in time for a time span similar to that spanning the second to the seventh images in Figure 5. The average pressure was obtained by first determining what the contact area was, following the method of Gagnon and Wang (2012). This was done by viewing the grillage at specific instants in time where at each instant the interface pressure was shown for the grillage elements. By choosing an appropriate scale for the colored pressure display, in our case using the range 0.001–2 MPa, the contact area could be obtained by summing the individual areas of all elements showing any indication of interface pressure. The average pressure was determined for the set of elements that were in contact with ice at that particular instant in time by dividing the total force on the grillage by the contact area. Excluding the first and last data points, that correspond to the onset of plate contact and the collision with a supporting frame, the pressure is fairly constant (6.6 MPa), as was that of Gagnon and Wang (2012) at a value of ~ 3.8 MPa. The difference in the two pressure values is due to the fact that the load and contact area were much greater in the earlier work, even though the grillage segments were similar. This meant that in the former study the contact area fairly evenly spanned the plating in both unsupported areas and areas where there were stiffeners/frames, resulting in a representative average pressure. However, in the present case the loads and contact areas are much lower and consequently the contact zone does not span multiple stiffened and unstiffened regions of the plate. Hence, if the contact happens to occur in the proximity of a frame/stiffener, as was the case depicted in Figure 5, where the contact is at the location of a horizontal stiffener and is also in close proximity to a frame that it eventually collides with, the average pressure will consequently be higher. This point is further illustrated by the observation that both the average and peak pressures decrease between rows 3 and 6 in Table 5. This is due to the downward movement (on the impacted hull segment) of the contact area away from the horizontal stiffener as the ice rotates slightly downwards on the damaged sloping plating during the course of the sliding impact. This is discernible in Figure 5, but more clearly visible in other graphics that could not be included here due to paper-length limitations.

Another aspect of the pressure results from the simulation is the impressive degree of agreement with results of large double pendulum ice impact tests (Gagnon et al., 2020). These lab experiments involved fairly large (1 m base diameter) conically-shaped ice samples impacting a hard surface that was covered with high spatial and temporal resolution pressure-sensing technology. The highest loads from the impact tests (416-622 kN) were in approximately the same range of the load for the 524 tonne ice mass impact after the onset of contact (303-656 kN). The average pressure from the tests was about 7.4 MPa that compares reasonably well with 6.6 MPa from the simulation. The average hard-zone pressures from the tests were very consistent (~ 21.5 MPa), and compare with the peak pressures of the simulation (~ 20.4 MPa) quite well. One may ask how a 'peak' pressure value can match an 'average' hard-zone pressure. We conclude that this is due to the size of a unit pressure sensor ($\leq 3\ cm^2$) on the impact apparatus compared to the larger typical element size of the impacted hull segment in the simulation (~ 12 cm^2). The unit pressure sensor is small enough to resolve pressure distribution within a given hard-zone region, that may range from 15 MPa to 52 MPa (Gagnon et al., 2020), whereas the much larger size of an element in the simulation gives a pressure value more representative of the average pressure of hard zones. Recall that actual peak local interface pressures during ice crushing in the brittle regime almost invariably are associated with regions of hard-zone contact, where the ice is relatively intact and the pressure is high, as opposed to soft-zone regions consisting of crushed ice (shattered spall debris) where local pressure is low (Gagnon, 1999).

3. Conclusions

The simulation results indicated that some level of damage, albeit diminishingly small, occurred (in a linear trend) as the ice masses and associated peak loads get smaller until eventually an ice mass of 8 tonnes produced no damage at all, where the peak load was 25 kN. The next ice-mass size up from that was 17 tonnes, that did produce a tiny amount of damage during a simulation.

The simulations show the effect of where the ice impact occurs with respect to supporting stiffeners and frames behind the plating and how this can influence the peak loads and pressures that occur, and the extent of local damage.

Impressive agreement of average and hard-zone pressures from the 524 tonne ice mass collision simulation with those from large-scale ice impact lab tests on a rigid surface was noted. While this may bolster confidence in the ice model that was used in the simulation, the fact that the grillage plating was deforming during the collision in the simulation, whereas the lab impact tests were on a flat rigid surface, suggests the need for further study of impacts on rigid and deformable surfaces (e.g. ship grillages).

Acknowledgements

The authors are grateful to NRC and DRDC for their support of this work.

References

Gagnon, R.E., 1999. Consistent Observations of Ice Crushing in Laboratory Tests and Field Experiments Covering Three Orders of Magnitude in Scale. Proceedings of the 15th International Conference on Port and Ocean Engineering under Arctic Conditions, 1999, POAC-99, Helsinki, Finland, Vol. 2, 858-869.

Gagnon, R.E. and Derradji-Aouat, A., 2006. First Results of Numerical Simulations of Bergy Bit Collisions with the CCGS Terry Fox Icebreaker. Proceedings of IAHR, Sapporo, Japan, Vol. 2, 9-16.

Gagnon, R.E. and Wang, J., 2012. Numerical Simulations of a Tanker Collision with a Bergy Bit Incorporating Hydrodynamics, a Validated Ice Model and Damage to the Vessel. Cold Regions Science and Technology 81, 26-35.

Gagnon, R. and Quinton, B., 2017. Heavy Impact Test Site (HITS) Simulations. OCRE Report OCRE-TR-2017-012, Protected A.

Gagnon, R., Andrade, S.L., Quinton, B., Daley, C., and Colbourne, B., 2020. Pressure distribution data from large double-pendulum ice impact tests. Cold Regions Science and Technology 175 (2020) 103033.

Liu, Z., Amdahl, J., and Løset, S., 2011. Integrated numerical analysis of an iceberg collision with a foreship structure. Marine Structures 24 (4), 377–395.

Pearson, D. and Abbott, M., 2016. Notional Vessel Design Improvement. Contract Report DRDC-RDDC-2017-C100.

Xue, Y., Liu, R., Li, Z., and Han, D., 2020. A review for numerical simulation methods of ship–ice interaction. Ocean Engineering 215 (2020) 107853.

Figures and Tables

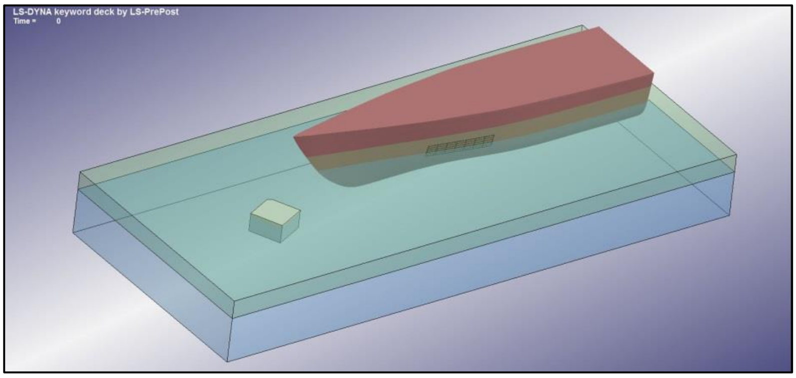

Figure 1. The full meshed volume used in the simulations: half-ship (red); air (green); water (blue); bulk-ice mass (yellow). The portion of the vessel hull that was given a high mesh density and deformable properties during ice impacts is visible. Note that the ice-knob (discussed below) is at the far corner of the bulk-ice mass and is not visible in this image.

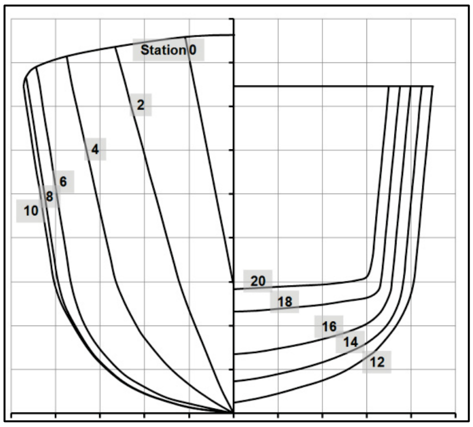

Figure 2. Notional Destroyer body plan. (From Pearson and Abbott (2016))

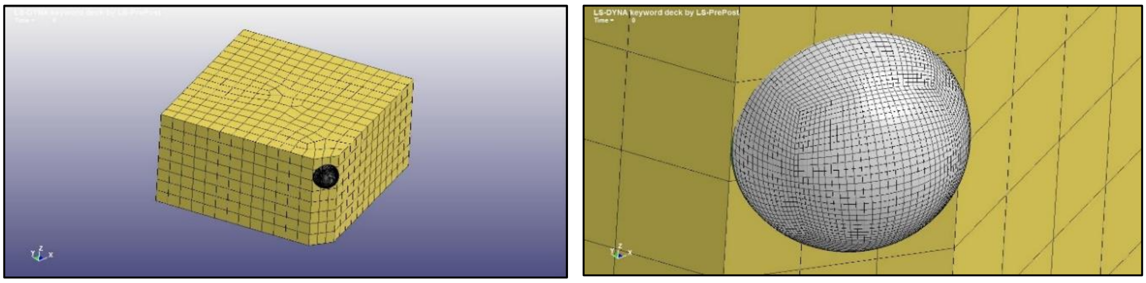

Figure 3. (Left) Bulk-ice mass with ice-knob attached at a corner. (Right) An expanded view of the ice-knob showing its refined mesh that suites the mesh size of the target hull segment (Figure 1).

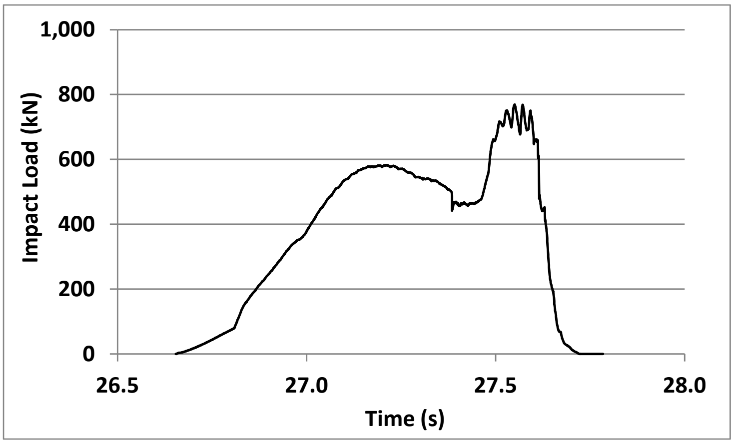

Figure 4. Load time series for the simulated impact with the 524 tonne ice mass. The secondary 'peak' corresponds to the ice-knob contacting the hull plating that was supported by a frame. The oscillations in load at the top of the secondary peak correspond to elastic oscillations of the meshed hull segment due to the sliding ice-knob impacting the frame.

Table 1. Notional Destroyer principal particulars. (From Pearson and Abbott (2016))

Loa	150.5 m
Lwl	142.6 m
B	18.9 m
Bwl	16.9 m
T	6.7 m
H (to 1 Deck)	14.0 m
Displacement	7600.0 tonne
Cruising Speed	18.0 kt
Sprint Speed	28.0 kt
Max Speed	29.0 kt

Table 2. NSR Primary shell scantling dimensions Frame 18 – 11. (From Pearson and Abbott (2016))

Primary Structure	Thickness (mm)	Material
Shell Plate	8.5	DH36 Steel*
Frame	10.0	DH36 Steel
Frame Flange	8.0	DH36 Steel
Longitudinal Stiffener	5.0	DH36 Steel
Longitudinal Flange	6.0	DH36 Steel

*350 MPa yield strength; based on Gagnon and Quinton (2017) the Young's Modulus is 200 GPa and the Tangent Modulus is 1.04 GPa

Table 3. Characteristics of the ice-knob and the initial bulk-ice masses.

Ice Mass Name	Shape/Dimensions	Mass (tonne)	Element Property During Impacts
Ice-knob (attached to all bulk-ice masses)	Hemisphere (1 m diameter)	0.24	Deformable
Medium Bulk-Ice Block	Brick (7.1 m x 7.1 m x 4 m)	181	Rigid
Large Bulk-Ice Block	Brick (12 m x 12 m x 4 m)	524	Rigid

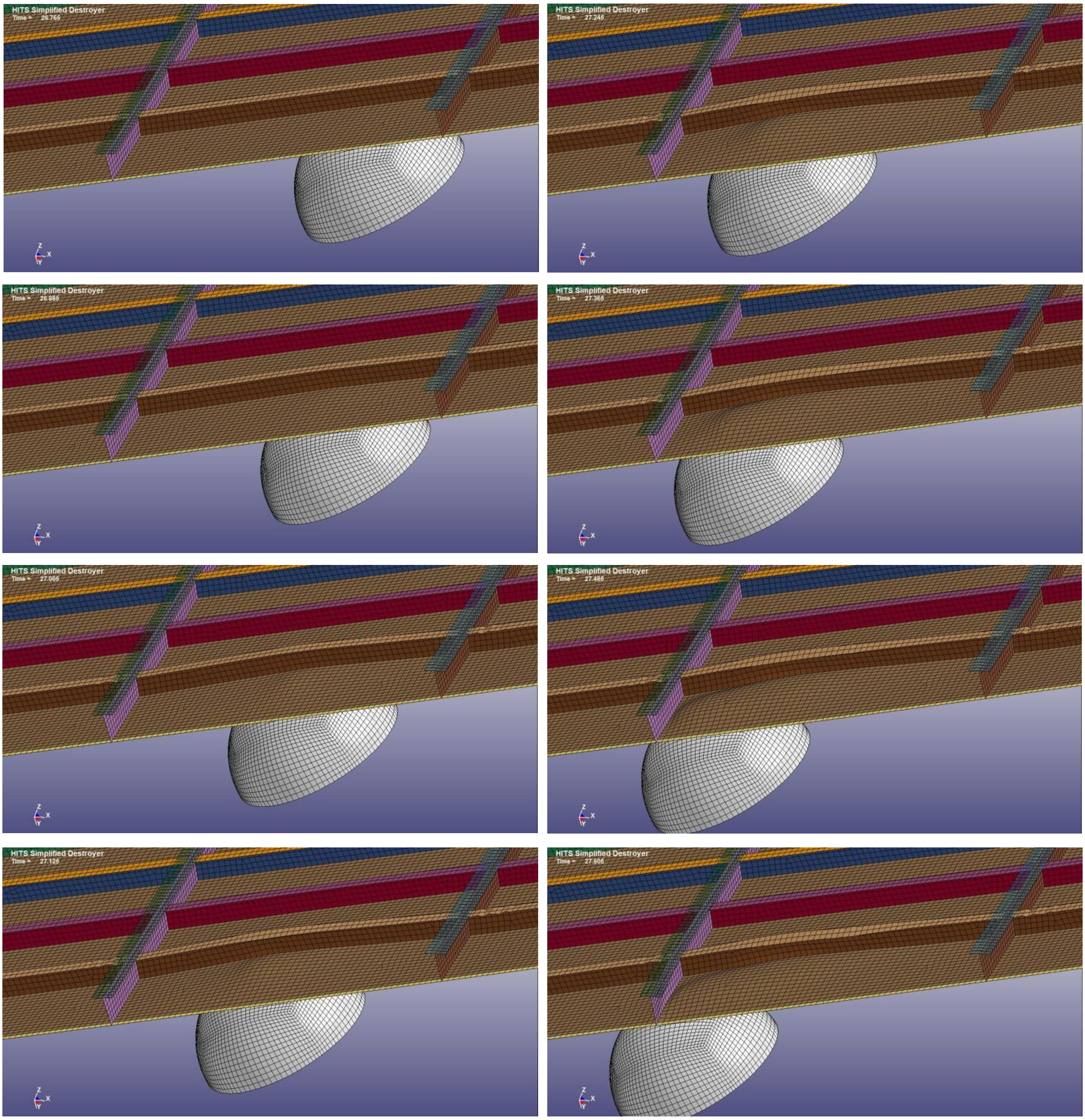

Figure 5. Sequence of images (top left to bottom right) from the simulation illustrating the progressive plastic damage to the grillage that developed during the sliding impact. The impact occurred on the lower portion of the meshed deformable segment of the vessel hull. The bottom edge of the hull segment is attached to a deck on the actual vessel and is therefore treated as a rigid boundary. As the ice-knob (white object) progresses to the left, and somewhat downwards, bending and buckling of the lowest horizontal stiffener and flange is evident. Crumpling of the flange on the stiffener is evident on the outsides of the two vertical frames where there is substantial compression of the flange due to the two vertical frames 'leaning away' from the prominent upward bending of the stiffener. Similarly, when the ice-knob reaches the vertical frame at the left, bending and buckling of the frame occurs. The flanges on the two vertical frames were given transparent characteristics to facilitate viewing of the local deformations. Time stamps are included on the images, where the real-time interval between successive images is 0.12 s.

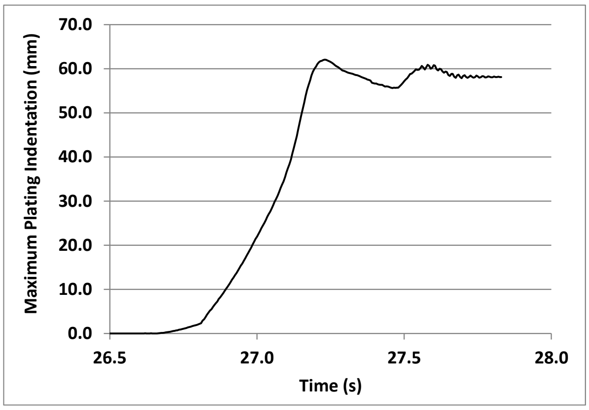

Figure 6. Maximum plating indentation time series for the simulated impact with the 524 tonne ice mass. The secondary 'peak' corresponds to the ice-knob sliding onto hull plating that was partially supported by a frame. The small oscillations in displacement at the top of the secondary peak correspond to resonant elastic oscillations of the meshed hull segment due to the ice-knob impacting the frame.

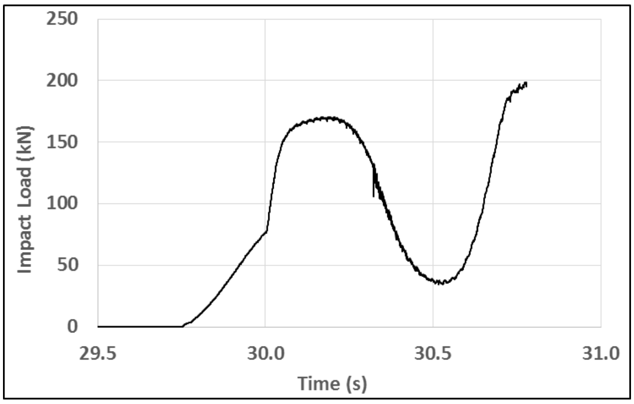

Figure 7. Load time series for the simulated ship impact with the 181 tonne ice mass. The initial impact peak at ~ 30.2 s is followed by a trough at ~ 30.5 s that corresponds to the ice mass bouncing off of, and almost losing contact with, the hull segment during the sliding collision. Hydrodynamic forces prevent the ice from fully rebounding away from the hull at the load trough and consequently load rises again towards a secondary peak as the ship and hull segment continue to move forward against the ice mass, as the ice-knob approaches a frame.

Table 4. Simulations summary: ice dimensions/mass; peak load; hull residual indentation depth.

Simulation Designation	Bulk-Ice Dimensions	Bulk-Ice Mass	Peak Load	Residual Displacement
	(m x m x m)	(tonne)	(kN)	(mm)
524 Tonne - ALE	12 x 12 x 4	524	769	58.8
181 Tonne - ALE	7.08 x 7.08 x 4	181	171 (first peak)	10.9
98 Tonne - Frame - ALE	6 x 6 x 3	98	550	16
98 Tonne - Frame - DRY	6 x 6 x 3	98	514	12.3
98 Tonne - Center - DRY	6 x 6 x 3	98	200	15.1
37 Tonne - Center - DRY	4.5 x 4.5 x 2	37	65	2.2
37 Tonne - Frame - DRY	4.5 x 4.5 x 2	37	149	2.2
17 Tonne - Center - DRY	3.5 x 3.5 x 1.5	17	40.7	0.42
8 Tonne - Center - DRY	3 x 3 x 1	8	25	0

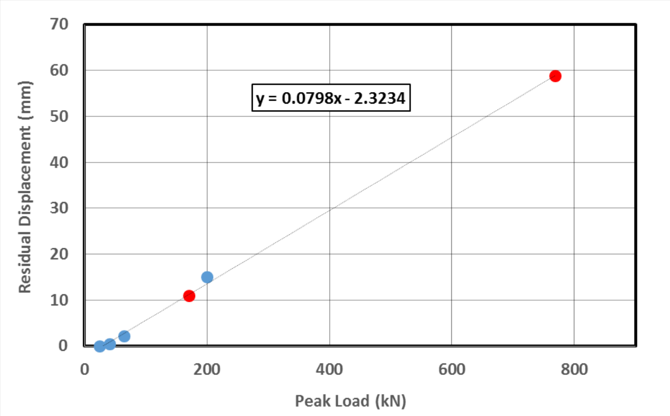

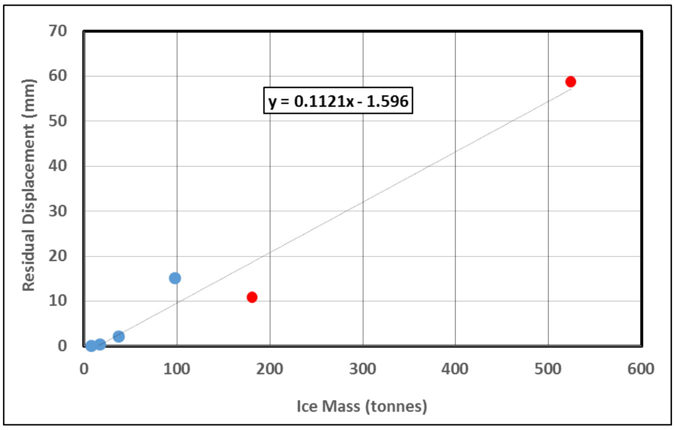

Figure 8. Residual displacement versus peak load for simulations covering a wide range of peak loads. Red-circle data points correspond to 'wet-case' ALE simulations, whereas the blue-circle data points relate to 'dry-case' simulations that did not include hydrodynamics. For all of the 'dry' simulations the ice impacts occurred between two vertical frames. Note that 'residual displacement' refers to the maximum non-recoverable indentation of the hull plating.

Figure 9. Residual displacement versus ice mass for simulations covering a wide range of ice masses. Red-circle data points correspond to 'wet-case' ALE simulations, whereas the blue-circle data points relate to 'dry-case' simulations that did not include hydrodynamics. For all of the 'dry' simulations the ice impacts occurred between two vertical frames. Note that 'residual displacement' refers to the maximum non-recoverable indentation of the hull plating.

Table 5. Contact Area, Load and Pressure Data for the 524 Tonne Ice Mass Simulation.

Time (s)	Number of Elements	Contact Area (sq. cm)	Load (kN)	Average Pressure (MPa)	Peak Pressure (MPa)
26.81	20	244.5	79.1	3.23	9.89
26.94	41	493.6	303.2	6.14	21.53
27.07	52	636.3	502.9	7.90	27.25
27.20	72	881.5	579.8	6.58	22.67
27.34	70	845.2	533.2	6.31	17.81
27.47	71	861.9	502.0	5.82	12.84
27.60	28	337.4	656.3	19.45	42.68
Averages (red data)	*61.2*	*743.7*	*484.2*	*6.55*	*20.42*

25th IAHR International Symposium on Ice
Trondheim, 23 - 25 November 2020

Evaluation of Ship Icebreaking Capability Based on a Simple Criterion

E. Karulin, M. Karulina
Krylov State Research Centre
St.-Petersburg, Russia
Evgeny@ek17106.spb.edu

In planning and performance of marine operations it may well be required to assess the icebreaking capabilities of icebreaking ships involved in these operations. The icebreaking capability of a ship is defined by the maximum thickness of solid level ice that the ship in question can negotiate at the minimum steady speed (2-3 knots) under full power. This characteristic depends on the ship hull form and propulsion system details as well as power output. This paper presents an approach intended to derive a simple criterion to assess such capability for icebreakers. The formula for icebreaking capability criterion is structured based on simple physical considerations: icebreaking capability is proportional to the total shaft power of propellers and inversely proportional to the ship beam on waterline. The formula coefficients are found using the least-square treatment of actual data collected from known icebreakers. Icebreaking capability assessments are done for vessels not included in the reference data samples. Specific aspects related to extension of the formula from icebreakers to commercial ice-class carriers and supply vessels are considered. It is shown that the said criterion is useful in prompt icebreaking capability evaluations for practical decision-making tasks like choice of suitable vessels for certain icebreaker operations related to convoy assistance, towage or ice-management operations.

1. Introduction

Icebreaking capability that is ultimate ice thickness to be negotiated by ship by keeping moving at full engine power is one of characteristics of practical importance for ice-going ship. This parameter is obviously dependent on a number of factors: ship hull and displacement, propulsion system and propulsive output, as well as hull plating condition – ice/ship hull friction coefficient. Several formulae considering the effect of the above factors to a greater or lesser degree are offered to evaluate ship icebreaking capability. The formulae are generally focused on a specific type of vessels featuring common hullforms. In particular, Choi (2003) formula enables evaluating icebreaking capability of icebreakers in case detailed data on lines drawing are available. Another evaluation method for icebreaking capability offered by Kashtelyan et al. (1981) is based on quite a simple formula, at that it covers not only icebreakers but ice-class commercial vessels, as well. As per the current investigation results the Kashtelyan formula significantly underestimates icebreaking capability of up-to-date ice-class ships.

The necessity to formulate the fairly simple criterion for prompt icebreaking capability evaluations for practical decision-making tasks like choice of suitable vessels for certain icebreaker operations related to convoy assistance, towage or ice-management operations, on the one hand, and availability of collected data on ice-going capability of existing and active ice-class ships to be analyzed and used for criterion development, on the other hand, served the background for this investigation.

Icebreaking criterion was developed based on analysis of sample list including more than 20 icebreakers. The obtained formula was thereafter used for icebreaking capability evaluations of modern ice-class ships not covered by the initial sample list. The available individual data on icebreaking capability of these ships validate feasibility and expedience of the developed criterion to be used for addressing practical icebreaking tasks.

2. Structure of Criterion Formula

For the sake of analysis the ship is assumed to move in solid level ice at a steady average speed, thus, ship motion is affected by a constant average ice resistance force and a constant average thrust from propulsor supplied with a constant average power. Also, the analysis assumes ship movement in conditions close to ultimate ice-going capability. It means the ship speed is 2-3 knots (1.0-1.5 m/sec) under almost full power. At that water resistance may be neglected due to low motion speed.

In accordance with Ionov and Gramuzov (2013) ice resistance/speed relationship may be presented by two components: purely ice resistance defined by resistance value at zero speed, and speed component supplementing purely ice component up to overall ice resistance growing together with the increasing speed. Considering the above assumption on ship speed smallness in ice it may be assumed that overall ice resistance does not depend on speed within the examined range.

Ultimate ice-going capability is traditionally defined at certain standardized values of physical and mechanical ice properties (for instance, ice bending strength is assumed to be 500 kPa). Consequently relationship between ultimate icebreaking capability and ice strength is not addressed here.

For further analysis, the Table 1 with key characteristics of several icebreakers offered in Ionov et al. (2014) is used. It's worth noting that this table contains data on icebreakers with both "conventional" and "innovative" hull shapes like bows of "*Fennica*", "*Oden*" and stern rimmers of "*Oden*". As per the analysis these ships may not be classified as conventional icebreakers in terms of their icebreaking capabilities. The data on the above ships will be neglected in the analysis on a regular basis.

Table 1. Main parameters of icebreakers

Ship	Year built	Design waterline length, m	Design waterline breadth, m	Shaft power, kW	Icebreaking capability, m	Power/ breadth
Lenin, Project 92	1959	124.0	26.8	28800	1.65	1.0746
Moskva	1960-1969	112.4	23.5	16200	1.45	0.6894
Ermak	1974-1976	130.0	25.6	26500	1.80	1.0352
Arktika, Project 1052	1974-2007	136.0	28.0	49000	2.25	1.7500
Kapitan Dranitsyn	1977-1981	121.0	25.6	16200	1.30	0.6328
Taimyr, Project 10580	1989-1990	140.6	28.0	32500	1.95	1.1607
Moskva, Project 21900	2008	97.2	26.5	16000	1.20	0.6038
Kapitan Belousov	1954-1956	77.5	18.7	7700	1.00	0.4118
Project 97	1962, 1971	62.0	17.5	3450	0.70	0.1971
Kapitan Izmaylov	1976	52.2	15.6	2500	0.60	0.1603
Dikson	1982-1983	78.5	20.0	7000	0.95	0.3500
Louis S. St. Laurent	1969	101.9	23.8	10900	1.20	0.4580
Atle	1974-1977	96.0	22.5	16240	1.40	0.7218
Polar Star	1976, 1977	107.3	23.8	13400	1.20	0.5630
*Polar Star**	1976, 1977	107.3	23.8	44100	1.80	1.8529
Almirante Irizar	1978	113.4	24.8	11900	1.00	0.4798
Pierre Radisson	1978, 1982	88.0	19.2	10140	1.10	0.5281
Shirase	1982	124.0	27.8	22080	1.50	0.7942
Otso	1986, 1987	90.0	23.4	15000	1.40	0.6410
Henry Larsen	1987	94.0	19.5	12000	1.20	0.6154
Botnica	1998	77.9	23.1	10000	1.20	0.4329
Healy	1999	120.9	24.4	22400	1.40	0.9180
*Oden***	1988	93.2	25.0	17600	1.80	0.7040
*Fennica***	1993, 1994	96.7	25.2	15000	1.80	0.5952

Notes:
* "*Polar Star*" being operated under gas turbine unit (GTU) mode will be addressed individually.
** "*Fennica*" and "*Oden*" featuring "unconventional" hull lines with rimmers and will be addressed individually.

Propeller is the main type of icebreaker propulsors. The below notions are used in ship propulsor theory (Rusetzkiy et al., 1971):

$$K_T = \frac{T}{\rho n^2 D^4} \quad \textbf{[1]}$$

$$K_Q = \frac{Q}{\rho n^2 D^5} \quad \textbf{[2]}$$

where K_T is thrust coefficient, K_Q is torque coefficient, T is propeller thrust, Q is propeller torque, n is number of propeller revolutions, D is propeller diameter, ρ is water density.

Efficient propeller thrust T_E and power consumed therewith may be expressed as:

$$T_E = \overline{K}_T \rho n^2 D^4 (1-t) \quad [3]$$

$$P_S = 2\pi \overline{K}_Q \rho n^3 D^5 / \eta_S \quad [4]$$

where $\overline{K}_T$ – propeller thrust coefficient behind ship hull, $\overline{K}_Q$ – propeller torque coefficient behind ship hull, t – thrust deduction coefficient (under modes close to bollard pull ones in this case), η_S – mechanical efficiency. After certain transformations by assuming water density as $\rho = 1025$ kg/m^3 the below relation may be obtained (Basin and Miniovich, 1963):

$$\frac{T_E}{{P_S}^{2/3}} = 2.96 \cdot \left(\frac{\overline{K}_T}{{\overline{K}_Q}^{2/3}}\right) \cdot D^{2/3} \cdot (1-t) \cdot {\eta_S}^{2/3} \quad [5]$$

or

$$T_E = 2.96 \cdot \left(\frac{\overline{K}_T}{{\overline{K}_Q}^{2/3}}\right) \cdot D^{2/3} \cdot P_S^{2/3} \cdot (1-t) \cdot {\eta_S}^{2/3} \quad [6]$$

Formula [6] gives the below expression for the specific ship under close to bollard pull mode which is important for our problem:

$$T_E \sim P_S^{2/3} \quad [7]$$

By assuming that the mean value of propeller thrust T_E at continuous ship motion in solid level ice is equal to the mean value of ice resistance force R_{ICE} we obtain:

$$R_{ICE} = T_E \sim P_S^{2/3} \quad [8]$$

Analysis of available computational methods for ice resistance demonstrates (Ionov and Gramuzov, 2014; Kashtelyan et al., 1968] that ice resistance force is assumed to be proportional to ship breadth B, i.e.:

$$R_{ICE} \sim B \quad [9]$$

To complete the logical chain ice resistance force is assumed to be proportional to ice thickness raised to a certain power. Taking into account formula [9] we have:

$$R_{ICE} \sim B \cdot h^x \quad [10]$$

And, by shifting to evaluation of ultimate icebreaking capability – maximum ice thickness h_{lim} that may be negotiated by ship moving continuously, it may be written as:

$$R_{ICE} \sim B \cdot h_{lim}^x \quad [11]$$

By assuming $x = 1$, the formula [11] can be written as $h_{lim} \sim \frac{R_{ice}}{B}$, and finally the below expression is obtained:

$$h_{lim} \sim \frac{{P_S}^{2/3}}{B} \quad [12]$$

Another relation for more general criterion is to be considered as well:

$$h_{lim} \sim \frac{P_S{}^p}{B^q} \qquad \textbf{[13]}$$

For descriptive reasons equation (12) is hereinafter referred to as the "physical", while (13) – as "formal" one.

3. Evaluation of Correlation Relationship between Criterion Components and Icebreaking capability

Formula [7] offers relationship between propeller thrust and power supplied thereto. Certain assumptions were used to obtain it. Statistical analysis of two types is carried out to precise the type of relationship between these values:

- correlation analysis to assess the extent these values are close to linear dependency;
- regression analysis to define numerical values of relationship parameters under consideration.

Let us consider procedure to establish correlation relationship (Ventzel, 2005). Let there be two random variables X and Y. Correlation coefficient concept is used here: r_{XY}. Correlation coefficient characterizes the extent random values' relationship is close to linear one. If random values X and Y are correlated with linear functional relationship, then $r_{XY} = \pm 1$. Correlation coefficient sign depends on whether this linear dependency is increasing or decreasing. In general case when random values X and Y are correlated with arbitrary probability relationship, correlation coefficient lies within -1 to +1 range.

Data on icebreakers given in Table 1 were used for correlation analysis (Fig. 1). Here we use the concept of "total specific power on the shaft", which represents the total power on the shaft, referred to the width of the ship waterline.

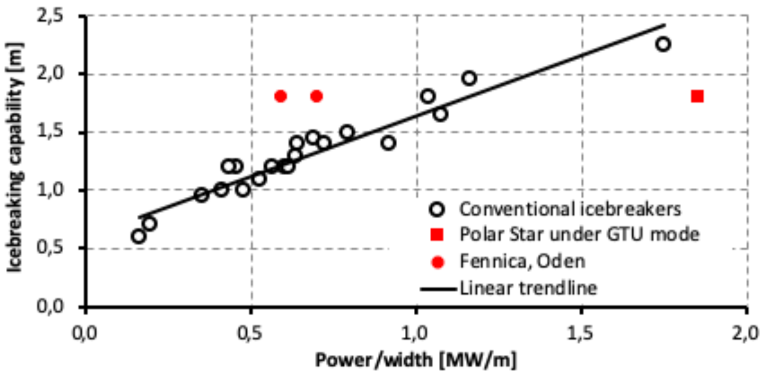

Figure 1. Relationship between ultimate icebreaking capability and overall specific shaft power.

As seen in the Fig. 1:

- the relationship is close to linear one if we consider conventional icebreakers;
- points indicating "*Oden*" and "*Fennica*" icebreakers do not follow the general trend and are little bit higher than imaginary straight line (unconventional hull lines not typical for classic icebreakers prevent from using their data when analyzing homogeneous data);
- as may be supposed, "*Polar Star*" point is significantly below the general trend line due to peculiarities in combining propulsive output involving gas-turbine plant and propulsor system;

−point corresponding to *Arktika* icebreaker, Project 1052 (the right point in the diagram), slightly deviates the general trend and rests just below the imaginary straight line.

Computation of correlation coefficients results in the correlation matrix shown in Table 2 and Table 3. Analysis of the Table 2 reveals that ship icebreaking capability/power relationship is the closest to linear one, while icebreaking capability/specific power (power per breadth unit) relationship is the second one. Relevant correlation coefficients are higher for correlation analysis of truncated sampling (Table 3 – ignoring "*Fennica*", "*Oden*" and "*Polar Star*" under special mode), at that correlation between icebreaking capability and specific power prevails.

Table 2. Correlation coefficients' matrix based on full analysis.

	Shaft power, MW	Design waterline breadth, m	Power/Breadth, MW/m	Icebreaking capability, m
Shaft power, kW	1.0			0.867
Design waterline breadth, m		1.0		0.785
Power/Breadth, MW/m			1.0	0.838
Icebreaking capability, m	0.867	0.785	0.838	1.0

Table 3. Correlation coefficients' matrix ignoring "*Fennica*", "*Oden*" and "*Polar Star*".

	Shaft power, MW	Design waterline breadth, m	Power/Breadth, MW/m	Icebreaking capability, m
Shaft power, kW	1.0			0.955
Design waterline breadth, m		1.0		0.809
Power/Breadth, MW/m			1.0	0.961
Icebreaking capability, m	0.955	0.809	0.961	1.0

4. Establishing Regressional Relationship between Propeller Power, Design Waterline Breadth and Icebreaking Capability

The above evaluation method for random values' relationship enables assessing relationship type proximity to linear dependency. Correlation analysis method is not applicable for determination of relationship of some specific type. Regressional analysis method is used to solve the stipulated problem. Basic principles thereof are given in Ermakov and Zhiglyavskiy (1987), for example. Brief description of the method used is offered below.

Regressional relationship between two random values X and Y may be expressed as:

$$y_j = \sum_{i=1}^{m} \theta_i \cdot f_i(x_j) + \varepsilon_j = \theta^T \cdot f_i(x_j) + \varepsilon_j \qquad \textbf{[14]}$$

where y_j- ultimate ice-going capability for j-th ship; $\theta = (\theta_1, \dots \theta_m)^T$- vector of unknown coefficients of regressional relationship; $f(x_j) = \left(f_1(x_j), \dots f_m(x_j)\right)^T$ - vector of basis functions; x_j - j-th point of factor space (i.e. parameters' value for j-th ship); ε_j – random error for j-th ship (for the sake of simplicity errors are considered to be uncorrelated and of equal dispersion σ). The model is linear with respect to unknown coefficients θ_i.

The best linear unbiased estimate of these coefficients may be obtained as:

$$\hat{\theta} = (F^T \cdot F)^{-1} \cdot F^T \cdot Y \qquad \textbf{[15]}$$

By defining evaluation vector $\hat{\theta}$ regressional model may be used to obtain value prediction vector $\hat{Y}$ for the experimental design points. Difference between vectors Y and $\hat{Y}$ is residual vector e. Vectors $\hat{Y}$ and e are used for evaluation of regressional model quality.

Relationship between ultimate icebreaking capability and ship breadth and power of interest is to be examined in greater details (formulae 12 and 13). The offered structures of the above relationships may be written as follows:

$$h_{lim} = a \cdot \frac{P_S{}^{2/3}}{B} \quad \textbf{[16]}$$

$$h_{lim} = b \cdot \frac{P_S{}^{p}}{B^q} \quad \textbf{[17]}$$

where $a, b, p\ and\ q$ of certain real numbers are unknown coefficients and regression indices.

The diagram in Fig. 3 is plotted to evaluate a value using truncated sampling of icebreakers. Straight line approximation results in the below expression for "physical" model [12]:

$$h_{lim} = 4.984 \cdot \frac{P_S{}^{2/3}}{B} \quad \textbf{[18]}$$

At that 8 points of 21 are below the obtained line, 13 – above it (Fig. 2). Consequently, greater deviations are attributable to points below the straight line (featuring lower actual icebreaking capability as against prediction).

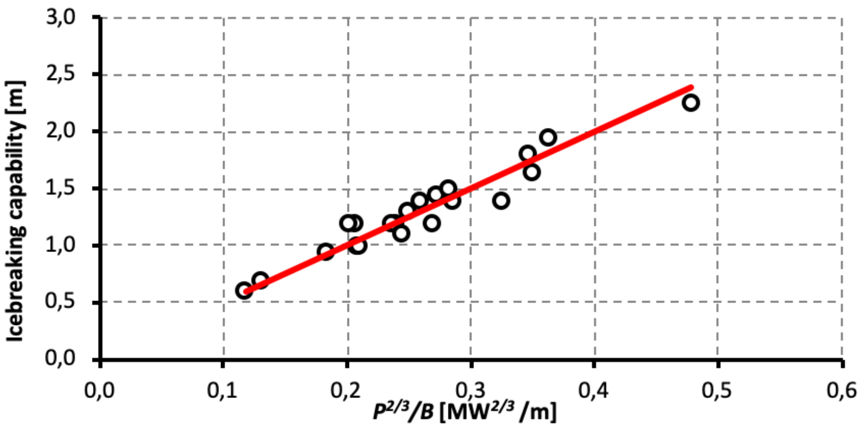

Figure 2. Relationship between icebreaking capability and $\frac{P_S{}^{2/3}}{B}$

Let us now consider "formal" format of the criterion (formula 17). "Formal" interpretation is not applicable for mathematical tool of the above-mentioned least-square method due to its nonlinearity with respect to unknown regression coefficients p and q. Both parts of formula [17] are to be presented in logarithmic form to make it linear:

$$\ln h_{lim} = \ln b + p \cdot \ln P_S - q \cdot \ln B \quad \textbf{[19]}$$

where $\ln b$, p and q are unknown values. This formula is identical to:

$$y = a_0 + a_1 \cdot x_1 + a_2 \cdot x_2 \quad \textbf{[20]}$$

Evaluation of regression coefficients with least-square method using formula [15] finally results in:

$$h_{lim} = 0.87720 \cdot \frac{P_S^{0.496}}{B^{0.299}} \qquad \textbf{[21]}$$

It should be noted that the effect of the ship's breadth in this expression is significantly less than in the formula [18].

In case power is raised to 2/3 degree, the below expression is obtained:

$$h_{lim}^{1.345} = 0.8384 \cdot \frac{P_S^{2/3}}{B^{0.402}} \qquad \textbf{[22]}$$

Taking expression [7] into account, it can be seen from formula [22] that ice resistance is proportional to ice thickness to the power of about 1.35.

The difference between actual icebreaking capability value and criterion value is called residual. The analysis into the above results (Fig. 3, Table 4) reveals that missing trend in residuals' distribution evidences arbitrary nature of this relationship that validates unbiasedness and, consequently, the accuracy in selecting the structure of relationship between ultimate ice-going capability and breadth and power.

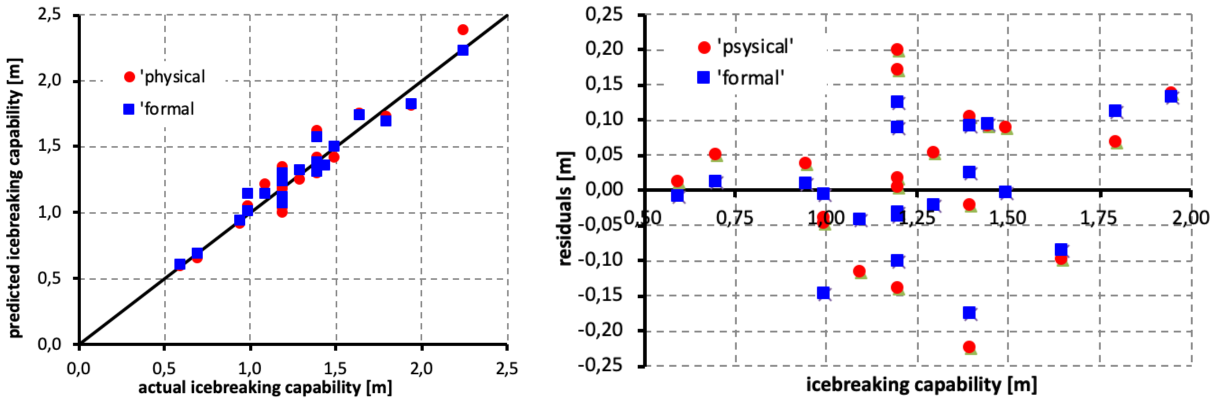

a) b)

Figure 3. Comparison of actual icebreaking capability and elaborated criteria: a) relationship between actual icebreaking capability and criteria-predicted one; b) relationship between residuals and icebreaking capability for "physical" and "formal" criteria

At that regression coefficient between actual value of icebreaking capability and its value obtained with "physical" method [18] is 0.844, while the same value for "formal" one is 0.976 that is significantly closer to 1. Thus, icebreaking criterion defined with the truncated sampling (ignoring "*Fennica*" and "*Oden*") is as follows:

for "physical" model $$h_{lim} = 4.984 \cdot \frac{P_S^{2/3}}{B} \qquad \textbf{[23]}$$

for "formal" model $$h_{lim} = 0.87720 \cdot \frac{P_S^{0.496}}{B^{0.299}} \qquad \textbf{[24]}$$

where P_S – power of engines' propeller shafts [MW], B– ship waterline breadth [m].

Analysis into deviation of ice-going capability from the obtained regressional relationships seems to be interesting. Computation results for deviations (residuals) are given below (Table 4). Deviations of ultimate icebreaking capability downside as to criterion value are marked with blue colour; the same upside as to criterion value are marked with red colour.

Table 4. Residual values for truncated sampling of icebreakers

Icebreaker	Deviation of "physical" model from actual values	Deviation of formal model from actual values	Concurrent deviations
Lenin, Project 92	-0.10	-0.08	+
Moskva	0.09	0.09	+
Ermak	0.07	0.11	+
Kapitan Dranitsyn	0.05	-0.02	-
Taimyr, Project 10580	0.14	0.13	+
Moskva, Project 21900	0.01	-0.10	-
Kapitan Belousov	-0.04	0.00	+
Project 97	0.05	0.01	+
Kapitan Izmaylov	0.01	-0.01	-
Dikson	0.04	0.01	+
Louis S. St. Laurent	0.17	0.09	+
Atle	-0.02	0.02	-
*Polar Star**	0.02	-0.03	-
Almirante Irizar	-0.05	-0.15	+
Pierre Radisson	-0.12	-0.04	+
Shirase	0.09	0.00	-
Otso	0.10	0.09	+
Henry Larsen	-0.14	-0.04	+
Botnica	0.20	0.13	+
Healy	-0.22	-0.18	+
Arktika, Project 1052	-0.13	0.02	-

Fig. 4 presents correlation of the developed icebreaking "physical" criterion and "formal" criterion. The same figure gives the ships icebreaking capabilities obtained using formula of Kashtelyan et al. (1981). It can be seen that these points are significantly lower: the explanation here is probable consideration of transport vessels by the authors, as well.

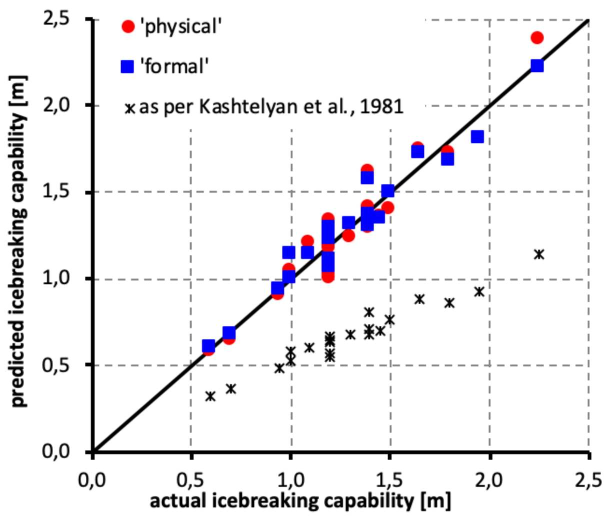

Figure 4. Correlation with criterion as per [8]

It can be seen from the Table 4:

–Icebreaking capability lower than “average” one (lower than criterion value) is observed for 8 icebreakers as per the “physical” format and 11 icebreakers as per the “formal” format.

–Above-“average” icebreaking capability is typical for 13 icebreakers as per “physical” format and 10 icebreakers as per the formal one. "Healy" features the most serious lack of icebreaking capability under both criterion formats. "Botnica" has the biggest excess for criterion of “physical” format. “Formal” criterion smooths these deviations significantly.

–The below points are within ∓0.05m deviation: 9 points of “physical” format criterion; 11 points of “formal” criterion.

The computed values of icebreaking criterion for ships not initially included in criterion development are offered in Table 5. Some of these ships are still under construction. Unfortunately, there are very few published reliable data on the actual icebreaking capability of these ships. The results of full-scale ice trials of icebreaker *Tor Viking II* (Riska et al., 2001) and of icebreaker *Araon* (Kim et al., 2011) indicated that the icebreaking capabilities of them were 1.20 m and 1.10 m, respectively. These values are in good agreement with the values of the “formal” icebreaking criteria given in the table for these ships: 1.34 m and 1.14 m, respectively.

Table 5. Evaluation of ships not included in the sampling using icebreaking criterion

Ship	Shaft power, MW	Waterline breadth, m	Icebreaking criterion, m	
			“physical”	“formal”
Vladislav Strizhov (Moss 828)	15.0	19.00	1.60	1.39
Vladivostok (21900M)	18.0	26.50	1.29	1.38
Christophe de Margerie	45.0	50.00	1.26	1.80
LK-60	60.0	33.00	2.31	2.34
Aker ARC 123	40.0	31.40	1.86	1.95
Shturman Skuratov	22.0	34.00	1.15	1.41
Kirill Lavrov	13.6	34.00	0.84	1.11
Kapitan Gotskiy	20.0	34.00	1.08	1.35
Aleut	14.0	19.50	1.48	1.33
Alexander Sannikov	21.5	25.00	1.54	1.53
Polaris	19.0	24.00	1.48	1.46
Kigoriak	12.3	17.25	1.54	1.30
Varandey	16.8	21.70	1.51	1.41
LK-25	25.0	29.00	1.47	1.58
Mackinaw	6.8	17.70	1.01	0.96
Xue Long 2	15.0	23.30	1.30	1.31
Araon	10.0	19.00	1.22	1.14
Tor Viking II	13.4	18.00	1.57	1.34

Conclusions

The offered simple criterion ensures quite a reliable evaluation of icebreaking capability for icebreakers. Attention shall be paid to the below important issues:

- the criterion parameters were obtained based on the data of icebreakers with conventional hullforms, fitted with stern propeller and moving ahead;

- based on the above assumption the criterion shall be prudently used in evaluating icebreaking capability of ships which hullforms are different from those of conventional icebreakers. Thus, icebreaking capability of transport vessels with extended dead flat assessed with the criterion will be within the computed limits, not higher, while that of ships moving astern will be most probably underestimated;

- “formal” criterion is notably higher affected by ship waterline breadth – decrease in icebreaking capability with breadth increase is not so obvious here as against to “physical” criterion;

- the criterion is useful in prompt icebreaking capability evaluations for practical decision-making tasks like choice of suitable vessels for certain icebreaker operations related to convoy assistance, towage or ice-management operations.

References

Ionov, B.P., Gramuzov, E.M., 2013. Ice performance of ships. / 2-nd edition, revised. - SPb: Sudostroenie, 504 p.

Ermakov, S.M., Zhiglyavskiy, A.A., 1987. Mathematical theory of optimal experiment: Study guide. -M.: Nauka. Ch. Ed. Phys. math. Lit., 320 p.

Ionov, B.P., Gramuzov, E.M., Zuev, V.A., 2014. Icebreaker design. SPb: Sudostroenie, 512 p.

Rusetzkiy, A.A., Zhuchenko, M.M., Dubrovin, O.V., 1971. Ship propulsors: guide. Leningrad: Sudostroenie, 288 p.

Basin, A.M., Miniovich I.Ya., 1963. Theory and computation of propellers. Leningrad: Sudpromgiz, 760 p.

Kashtelyan, V.I., Poznyak, I.I., Ryvlin, A.Ya., 1968. Ice resistance to ship motion. Leningrad: Sudostroenie, 238 p.

Ventzel, E.S., 2005. The theory of probability: guide. 10-th edition, reprint. Moscow: Akademia. 576 p.

Kashtelyan, V.I., Ionov, B.P., Ilchuk, A.N., 1981. Evaluation of ice-going capability of icebreakers and ice-class commercial vessels under initial design stage. Proc. AARI, vol. 376, p. 22-25

Choi, L.G., 2003. Icebreakers. Design peculiarities. Study guide. SMTU, SPb, 110 p.

Riska, K., Leiviskä, T., Nyman, T., Fransson, L., Lehtonen, J., Eronen, H., Backman, A., 2001. Ice performance of the Swedish multi-purpose icebreaker Tor Viking II. Proc. of the 16th Int. Conference on Port and Ocean Engineering under Arctic Conditions POAC’01, Ottawa, Ontario, Canada

Kim, H.S., Lee, C.-J., Choi, K., 2011. The study on the ice sea trial in Chukchi sea using Korean icebreaker “Araon”. Proc. of the 30th International Conference on Ocean, Offshore and Arctic Engineering, OMAE’2011, Rotterdam, Netherlands, OMAE201149482

25th IAHR International Symposium on Ice

Trondheim, June 14 to 18, 2020

Model-scale testing of icebreaking pattern and comparison with state-of-the-art methods

Fang Li [1], Tam Aaron [1], Pentti Kujala [1]

1. Aalto University, School of Engineering, Department of Mechanical Engineering
P.O. Box 14100, Aalto, FI-00076, Finland
fang.li@aalto.fi

Icebreaking pattern has been recognized as an important factor in ship ice resistance prediction for decades. It involves the shape and size of ice pieces broken from an intact ice sheet when a ship is going through. For the estimation of icebreaking pattern, various methods were proposed, which could be divided into semi-empirical and mechanics-based theoretical methods. Due to limited availability of data, the validity of these methods has not been systematically evaluated. In order to understand the accuracy of these methods in predicting model-scale icebreaking pattern and find the most applicable ones, a set of model tests was conducted in Aalto Ice Tank. Two Gopro cameras were instrumented at two positions at bow and took videos of the icebreaking process. Image analysis tools are implemented to measure the ice pieces size and shape from the photos extracted from the videos. The measurement results are then compared with selected methods. The accuracy is analysed and discussions on the advantages and shortcomings of each method are presented.

1. Introduction

For the estimation of ship performance in level ice, icebreaking pattern has been recognized as one of the main factors influencing the prediction of ice breaking resistance (Li et al. 2018). Icebreaking pattern in this paper refers to the size and shape of ice pieces after bending failure. There are several methods available in the literature to estimate the icebreaking pattern, which can be divided into semi-empirical (e.g. Wang 2001) and mechanics-based theoretical methods (e.g. Li et al. 2019). Although some of these methods have been widely adopted by other models, the validations of these icebreaking pattern models are still insufficient. This paper is based on Tam (2019), which investigates the applicability of these models in model-scale ice test. For this aim, photos extracted from video record of a model ship MT Uikku going through level ice at Aalto Ice Tank are analysed and compared with the predictions by several methods. The results indicate that semi-empirical formulae and mechanics-based theoretical methods can give reasonable estimations of icebreaking pattern in single-contact scenario for model-scale ice. Finally, suggestions on further development of icebreaking pattern methods are given.

2. Review of icebreaking pattern estimation methods

Measures used to characterize an ice piece differ among different methods. According to the measurement of full-scale ice pieces by Li et al. (2019), and to enable the comparison with data and comparison between methods, we firstly characterize the geometry of an ice piece with parameters as illustrated in Figure 1. Here W and L are termed as the width and length of the arc; L_{edge} the breaking lengths at the edges and L_{center} the breaking length at the center; θ the wedge opening angle.

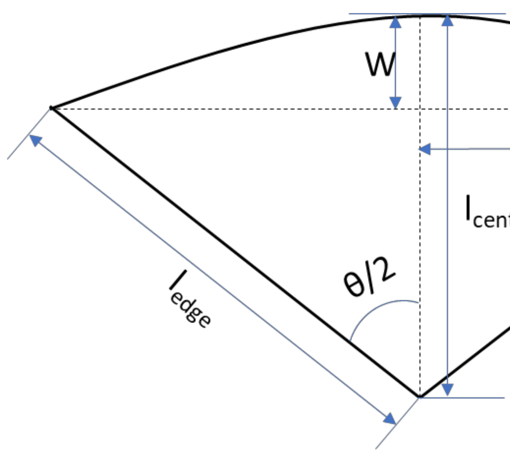

Figure 1. Ice pieces geometry

2.1. Semi-empirical methods

Semi-empirical methods combine measurement information with theoretical inference. This usually involves non-dimensionalized parameters such as describing the breaking length as a fraction of characteristic length. Measurements are obtained either from full-scale or model-scale tests.

One of the earliest studies on icebreaking pattern is McKindra and Lutton (1981), where the authors performed tests with the USCG 140' Bay-class tugboats and use lognormal distribution to fit the measured length of broken ice pieces. The results were for full-scale test in the Great Lake river fresh waters in the St. Mary's River. The tests cover varying speed ranging from 0.98 knots to 11.6 knots. However, the tests are conduct only with ice thickness 0.33m, therefore no thickness dependency can be obtained from the measurement. Based on this work, Tatinclaux (1985) conducted a series of model-scale tests with simple wedges, which confirmed lognormal fit to describe the distribution of ice piece size. Using dimensionless linear fitting, Tatinclaux (1985) established the following formulae to estimate the area and length of ice pieces for urea ice:

$$A/h^2=0.105(\sigma_f/\gamma h)^{0.5} \quad \textbf{[1]}$$
$$L/h=0.540(\sigma_f/\gamma h)^{0.5} \quad \textbf{[2]}$$

with σ_f being the flexural strength; h the thickness of ice and γ the specific weight of water.

Izumiyama et al. (1992) conducted model scale test on conical structures interaction with level ice sheet, and use normal distribution to fit into the measured breaking length, i.e. L_{center} in Figure 1. The distribution is combined with non-dimensional parameters to generalize the results for different ice thicknesses. The results can be expressed as

$$Z \sim \text{Normal}(0.937, 0.268), \text{ where } Z = L_{center}/l_{br};\ l_{br}=(\sigma_f h/\gamma)^{0.5} \quad \textbf{[3]}$$

Kotras et al. (1983) proposed a semi-empirical formula to describe L and W as functions of ice characteristic length and the Froude number, by which ice thickness and ship speed are both taken into account. The formula takes ship hull angles into account as well, which accounts for the hull angle influence on bending failure. The empirical factors are obtained based on five icebreaking ships, resulting in the following formulae

$$L= \eta_3 l_c[1.7153+4.2653(\sin(\alpha)/\tan(\beta)(v/(gl_c)^{0.5})]^{-1}; \quad \textbf{[4]}$$
$$W=L(10\ meters/h)^{0.5} \quad \textbf{[5]}$$

where η_3 is the directional cosine of the forward 20 percent of the ship; α and β the waterline angle and normal flare angle of the ship; v the ship speed; g the gravity constant and l_c the characteristic length of ice.

Wang (2001) proposed a semi-empirical formula to estimate the icebreaking length L_{center} assuming the crack as an arc, expressed as

$$R = C_l(1+C_v v_n)l_c, \text{ where } C_v=B_e\tan\beta\cos\alpha \quad \textbf{[6]}$$

Here C_l and B_e are constants of value 0.320 and -0.144 respectively. It is worth noting that C_l is an empirical coefficient obtained from regression of data, while B_e is a parameter obtained through regression of numerical simulation results from Varsta (1983). It should be noted that B_e is dimensional, therefore should be scaled while used for model-scale calculation.

2.2. Mechanics-based theoretical methods

Mechanics-based theoretical methods are based on the calculation of stress in the ice field and searching for the location of the maximum stress. Ice failure is commonly defined as the instant when the maximum stress exceeds a threshold value. Ice is often assumed as pure elastic to enable analytical derivation or fast numerical computation.

Nevel (1961) derived a closed-form solution for a narrow wedge resting on elastic foundation. The solution is adopted by Lubbad and Løset (2011) for the calculation of ice bending failure. The deflection of a wedge at a position with distance x from the wedge tip can be written as

$$y=A*\mathrm{du}_2(x)+B*\mathrm{du}_3(x) \quad \textbf{[7]}$$

where $\mathrm{du}_2(x)$ and $\mathrm{du}_3(x)$ are derived functions of x; A and B the coefficients solved from boundary conditions with regards to loading. The stress $\sigma(x)$ can be calculated by the section modulus dividing the moment, which is obtained through second derivative of Eq. [7]. The breaking length of an ice piece is then

$$x=x_m, \text{ where } \sigma(x_m)=max(\sigma(x)) \text{ and } \sigma(x_m)=\sigma_f \quad \textbf{[8]}$$

Li et al. (2019) presented an expanded version of Nevel (1961) into three-dimensional wedge, thereby improving the fidelity of numerical simulation models. The solution is derived with discretized narrow wedges, each governed by Nevel's solution and interacting with neighboring wedges. This results in a one-dimensional differential equation which could be solved easily with Finite Difference Method. The size of an ice piece can be found with Eq. [8] as well. The main difference is that according to this method, L_{edge} differs from L_{center}. The ice pieces are therefore sections of elliptical, instead of being sections of circular as assumed by most other methods.

A revision is made to Li et al. (2019) model by Li et al. (2020) through combining the speed dependency part of Wang (2001) (see Eq. [6]) with Li et al. (2019) model. This overcomes the deficiency of Li et al. (2019) model that hydrodynamic effect is not considered. Denote the estimated breaking length by Li et al. (2019) as l_{19}, the revised breaking length, denoted by l_{20}, is expressed as

$$l_{20}= (1+C_v v_n)l_{19} \quad \textbf{[9]}$$

3. Measurement of ice pieces geometry

3.1. Test arrangement

Model-scale tests of ship going through a level ice field were conducted at Aalto Ice Tank in 2019 after its renovation. The model used in the test is MT *Uikku*, which is the model of a 16000 DWT tanker which has been extensively instrumented for scientific research. In order to measure the size of ice pieces, two Gopro Black 7 cameras were mounted at station 9 and 10 at ship bow region (see Figure 2(a)), which looked down to the level ice sheet with the scope of vision illustrated in Figure 2(b). The hull flare angle, which is the angle between the normal vector and the vertical direction, is 50 degrees. The outer ship profile in Figure 2(b) shows the upper deck of the model and the inner ship profile illustrates waterline at the test draft (also the design draft). In this way the interaction between ship and ice at waterline is captured. The scopes of visions are set to overlap so that the scopes of the two cameras can be combined. The Gopros were controlled remotely to capture videos of the ice pieces at 60 FPS.

The tests were performed on May 15th, 2019. Ice properties including compressive strength σ_c, flexural strength σ_f, and Young's modulus E are measured prior to the tests. The model ship was towed by the carriage through the level ice sheet with two set speeds, 0.162m/s and

0.270m/s, corresponding to full-scale speeds of 0.9m/s and 1.5m/s. Table 1 summarizes the ice parameters and test conditions.

Table 1. Test parameters and ice properties

Test No.	v (m/s)	h_i (m)	σ_f (kPa)	σ_c (kPa)	E (MPa)
1	0.162	0.028	45	108	14.8
2	0.270				

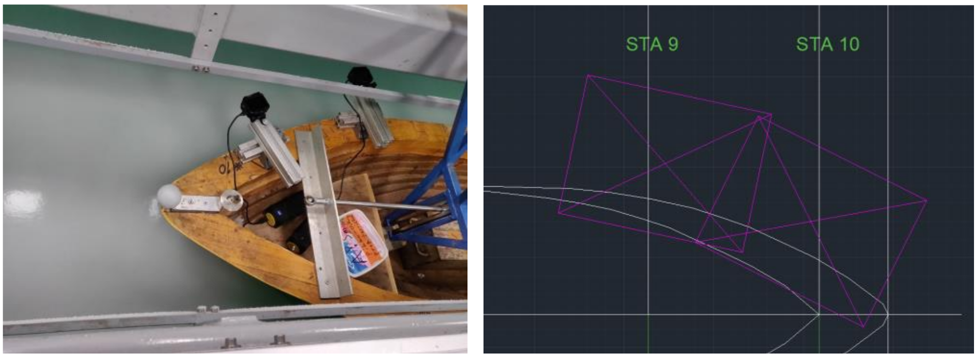

(a) (b)

Figure 2. Installed Gopro cameras; (a) photo of ship bow region; (b) Gopro scopes of vision

3.2. Digital processing

The videos from the two cameras during the two tests were extracted for processing. The videos were then rotated and positioned into the appropriate positions and orientations so that the videos overlapped as the scope of cameras did in Figure 2. Then the brightness is adjusted for clear observation and the camera positions, station 9 and station 10, are marked in the video, see Figure 3.

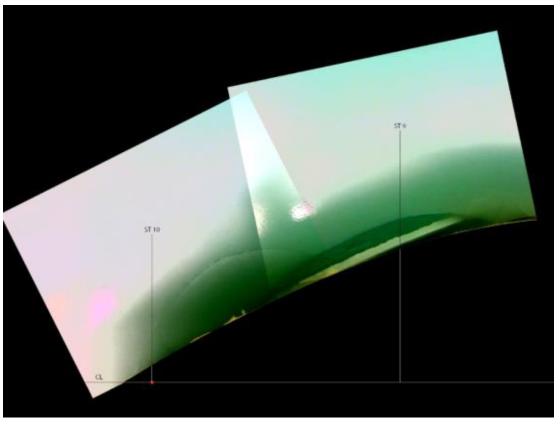

Figure 3. Overlapping videos with adjusted brightness and added markers

Each frame of the overlapped video was then extracted, resulting around 10000 frames from each test. The frames are manually examined to find the ones where cracks are clearly seen and have propagated through the top surface of ice sheet. This results in about 500-600 frames from each test, which are valid for measurements. After that, a Matlab script is written to manually locate points on the photos and automatically analyze the size and shape of the ice pieces. Each ice piece is measured with six points among which one is on ship waterline and others around the crack. Two examples are shown in Figure 4. The left one shows an example of a *single contact* case, where there is one contact point between ship and ice. The right one shows an example of a *multiple contact* case, where there are more than one contact points simultaneously. A clearer example of multiple contact case is given later in Figure 7.

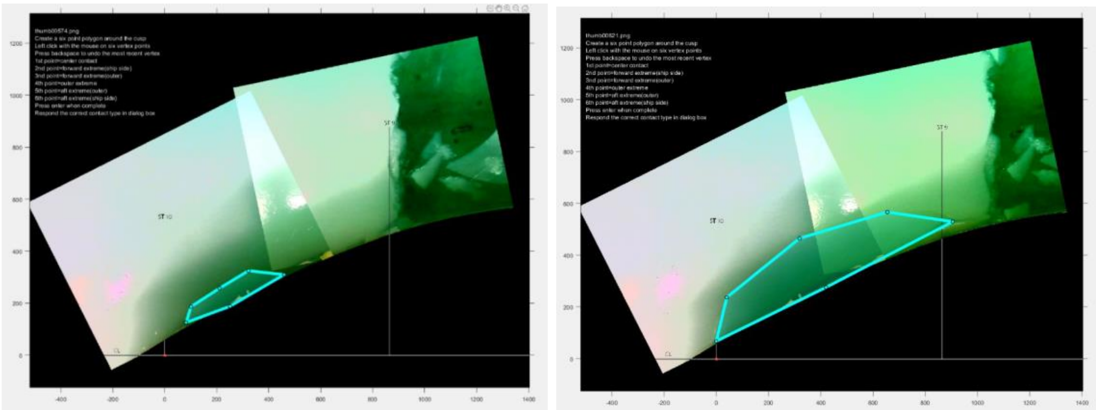

(a) (b)

Figure 4. Examples of ice piece measurement, (a) single contact case; (b) multiple contact case

4. Measurement results and comparisons with estimations

4.1. Statistics of measurement results

Figure 5 shows the icebreaking pattern at the end of the tests after reversing a small distance. It can be roughly seen that ice pieces size with 0.27m/s is smaller than with 0.162m/s. However, the ice pieces in the figure have gone through extensive re-breaking after being broken by ship hull, therefore do not reflect the real statistics of ice breaking by ship hull.

Figure 5. Icebreaking pattern at the end of the tests after reversing; left: v=0.162m/s, right: v=0.270m/s

The photos obtained from the videos can be easily divided into single contact and multiple contact groups (see Figure 4), which is clearly reflected from the histograms in Figure 6. In the former case the crack is formed as the result of one ship-ice contact while in the latter case the crack covers multiple contacts. Another example of multiple contact is shown in Figure 7, where it is clearly seen that there are two separate contact areas simultaneously, together contributing to the crack formation, resulting in a large ice piece. The distinction between single contact and multiple contact cases gives a reasonable explanation to the observation of Daley (1992), who measured the ice pieces areas from full-scale test of MS Kemira, and identified clearly two groups of ice pieces from the cumulative probability plot.

Table 2 summarizes the mean values of the measured quantities. The mean ice piece area of multiple contact cases is about one order higher than that of single contact. The numbers also clearly indicate the speed effect in the size of ice pieces. When ship speed increases from 0.162m/s to 0.270m/s, area of ice pieces decrease by 25.7% and 29.3% in single contact and multiple contact cases. As the result, the number of icebreaking cases increases from 507 to 557 for the same distance. The number of multiple contact cases is approximately half of the number of single contact cases.

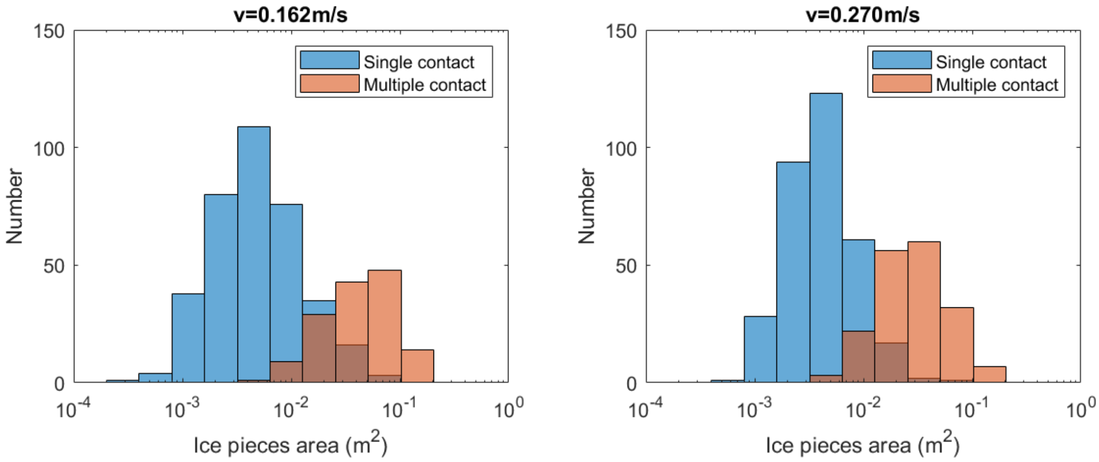

Figure 6. Histograms of ice pieces area

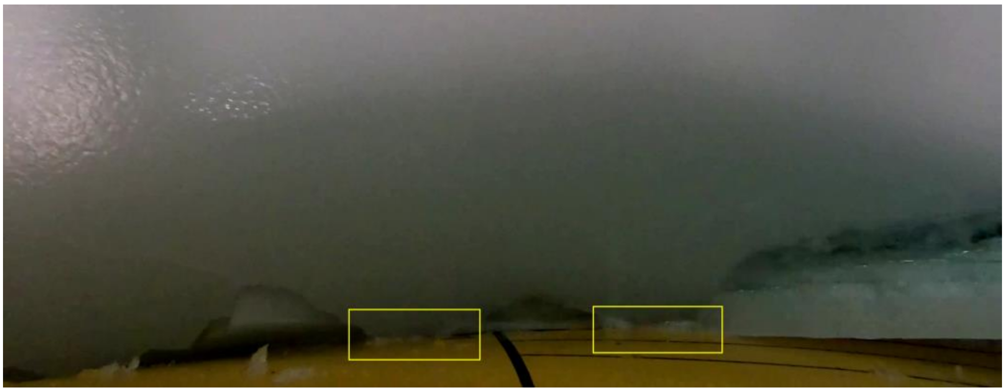

(a)

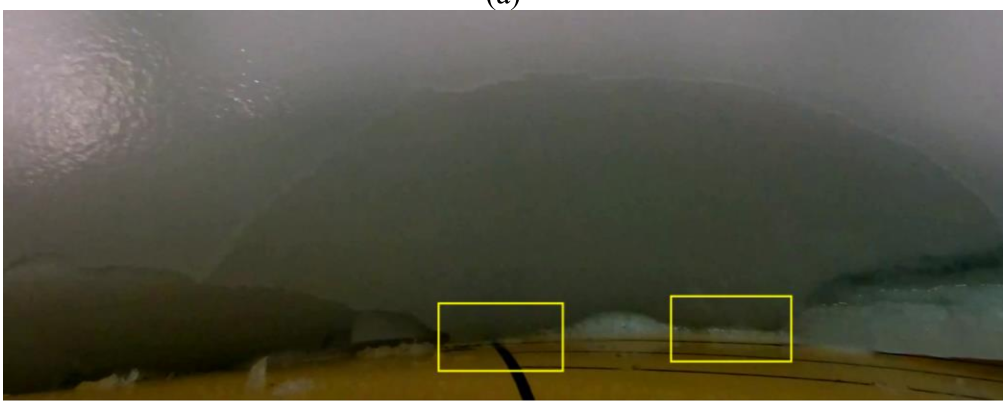

(b)

Figure 7. Example of an ice piece formed by multiple contact, (a) before crack formation and (b) after crack formation

Table 2. Mean values of the measured quantifies

	All cases			Single contact			Multiple contact		
v (m/s)	A (m^2)	L_{center} (m)	L_{edge} (m)	A (m^2)	L_{center} (m)	L_{edge} (m)	A (m^2)	L_{center} (m)	L_{edge} (m)
0.0162	0.0208	0.0858	0.141	0.0074	0.0623	0.0893	0.0543	0.145	0.269
0.0270	0.0171	0.0779	0.132	0.0055	0.0593	0.0769	0.0384	0.112	0.234
	W (m)	L (m)	Number	W (m)	L (m)	Number	W (m)	L (m)	Number
0.0162	0.0858	0.276	507	0.0623	0.171	362	0.145	0.536	145
0.0270	0.0779	0.258	557	0.0593	0.145	360	0.112	0.465	197

4.2. Comparison with estimations

The mean prediction errors by the reviewed methods are summarized in Table 3. The indices L and W are used for Tatinclaux (1985) and Kotras et al. (1983) methods, while L_{edge} and L_{center} are applied for the rest, so that we compare the quantities which the methods predict. In terms of ice pieces from single contact cases, methods of Tatinclaux (1985) and Izumiyama et al. (1992) significantly overestimate the size of ice pieces, while other methods manage to predict to the same order mostly within 50% deviation. The pure mechanics-based theoretical models by Nevel (1961) and Li et al. (2019) show similar performance and especially the same drawback, which is the lack of speed dependency. This enlarges the deviation when ship speed increase from 0.162m/s to 0.270m/s. It seems that the by introducing the speed dependence correction term with Li et al. (2020) model, the estimations becomes much better. None of the methods demonstrate distinctive performance over others, but overall, the semi-empirical formula of Wang (2001) and the Li et al. (2020) model gives the least prediction error.

In terms of ice pieces as results of multiple contact, none of the methods give very satisfactory predictions, but the predictions of Tatinclaux (1985) and Izumiyama et al. (1992) methods become rather reasonable and give better results than others. It is possible that the empirical data used by Tatinclaux (1985) and Izumiyama et al. (1992) contains mainly multiple contact cases where ice pieces are rather large, while those used by Kotras et al. (1983) and Wang (2001) contains mainly single contact cases. The mechanics-based theoretical methods are derived for single contact cases thus not applicable for multiple contact cases.

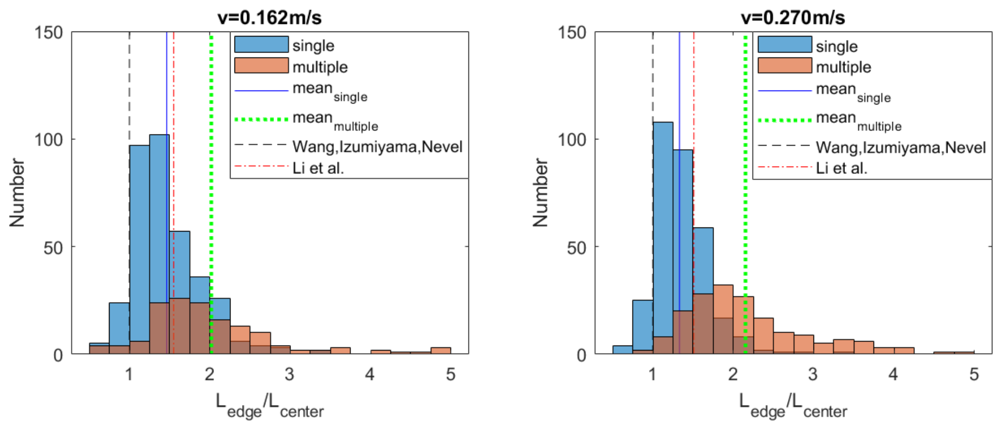

Figure 8. Comparison of predicted and measured ice piece shape

Table 3. Summary of mean prediction errors by different methods

	Single contact			Multiple contact		
v=0.162m/s	*L or* L_{edge} (m)	*W or* L_{center} (m)	*A* (m^2)	*L or* L_{edge} (m)	*W or* L_{center} (m)	*A* (m^2)
Tatinclaux (1985)	NA*	+211%	+82%	NA	+34%	-75%
Izumiyama et al. (1992)	+141%	+246%	NA	-20%	+49%	NA
Kotras et al. (1983)	+41%	+16%	NA	-57%	-52%	NA
Wang (2001)	-31%	-0.64%	NA	-77%	-57%	NA
Nevel (1961)	+1.1%	+45%	NA	NA	NA	NA
Li et al. (2019)	+33%	+24%	NA	NA	NA	NA
Li et al. (2020)	+15%	+7%	NA	NA	NA	NA
v=0.270m/s						
Tatinclaux (1985)	NA	+226%	+145%	NA	+73%	-65%
Izumiyama et al. (1992)	+180%	+263%	NA	-8%	+92%	NA
Kotras et al. (1983)	+58%	+15%	NA	-54%	-43%	NA
Wang (2001)	-20%	+4%	NA	-74%	-45%	NA
Nevel (1961)	+17%	+52%	NA	NA	NA	NA
Li et al. (2019)	+51%	+30%	NA	NA	NA	NA
Li et al. (2020)	-1%	-15%	NA	NA	NA	NA

*NA: not applicable

Another important characteristic of ice pieces is the shape, which can be described by the ratio L/W or L_{edge}/L_{center}. The mean measured value of L/W with 0.162m/s and 0.270m/s are 2.80 and 2.56 for single contact cases. With Kotras et al. (1983) method, the ratios are 3.36. The comparisons of L_{edge}/L_{center} are summarized in Figure 8. Here only predictions of single contact cases are averaged and plotted. Methods which assume the ice piece as a part of a circular give a constant L_{edge}/L_{center} as 1, while Li et al. (2019, 2020) method predicts elliptical ice pieces with L_{edge}/L_{center} over 1. The measurement confirms the elliptical shape with L_{edge}/L_{center} close to the prediction of Li et al. (2019, 2020) method. Another observation from the figure is that ice pieces of multiple contact cases are more elliptical than single contact cases.

5. Discussions and conclusions

The data used to develop the comparison are obtained with model-scale ice, therefore the findings should be limited to the scope of ship-ice interaction in model scale, especially fine-grained granular ice with ethanol solution. In full-scale the conclusions obtained here may not be valid. Based on the analysis, the following should be addressed.

The first important finding is the distinction between single contact and multiple contact cases. The size and shape differ a lot between the cases. Existing research regarding icebreaking pattern has been mostly devoted to single contact scenario. However, multiple contact clearly plays an important role and may affect the resistance and channel width estimation. The apparent existence of multiple contact cases indicates that the assumption of independence between ship-ice contacts may not always be valid. This assumption, however, is commonly adopted in numerical simulation models of ship going through level ice. The occurrence of multiple contact may be due to ship hull with small curvature or locally strong ice with high flexural strength.

The comparisons indicate that Li et al. (2020) method, which is a combination of Li et al. (2019) and Wang (2001) methods, gives the best overall estimations performance both on the size and the shape of ice pieces. This method overcome the deficiency of Li et al. (2019) that hydrodynamic effect is missing. The semi-empirical formula by Wang (2001) shows reasonable estimation in terms of size but not the shape. This implies the value of empirical approaches, where the value of empirical information can be utilized to reflect reality. The overestimation of ice pieces size by pure mechanics-based theoretical methods address the importance of hydrodynamic effect to be taken into account.

The data utilized in this paper were obtained from one ice sheet with the same ice thickness. Another test series has been conducted after this one with another ice thickness, but the results are still under processing. This will give a more comprehensive comparison as a supplement to this paper.

Acknowledgments
This work has received funding from the South-eastern Finland–Russia CBC 2014–2020 program via the project Future Potential of Inland Waterways (INFUTURE).

References

Daley, C., 1992. *Aspects of Ship-Ice Interaction in a Natural Ice Cover, M-120,* Otaniemi, Espoo, Finland: Helsinki University of Technology.

Izumiyama, K., Kitagawa, H., Koyama, K. & Uto, S., 1992. *A numerical simulation of ice-cone interaction.* Banff, Alberta, IAHR.

Kotras, T., Baird, A. & Naegle, J., 1983. Predicting Ship Performance in Level Ice. *SNAME Transactions Vol 91,* pp. 329-349.

Li, F., Goerlandt, F., Kujala, P., Lehtiranta, J., Lensu, M., 2018. Evaluation of selected state-of-the-art methods for ship transit simulation in various ice conditions based on full-scale measurement. Cold Regions Science and Technology, 151, 94-108.

Li, F., Kotilainen, M., Goerlandt, F., & Kujala, P. 2019. An extended ice failure model to improve the fidelity of icebreaking pattern in numerical simulation of ship performance in level ice. Ocean Engineering, 176, 169-183.

Li, F., Goerlandt, F., & Kujala, P. 2020. Numerical simulation of ship performance in level ice: A framework and a model. Applied Ocean Research, 102, 102288.

Lubbad, R. & Sveinung, L., 2011. A numerical model for real-time simulation of ship-ice interaction. *Cold Regions Science and Technology,* Issue 65, pp. 111-127.

Mckindra, C. & Lutton, T., 1981. *Statistical analysis of broken ice dimensions generated during 140' WTGB icebreaking trials,* Washington, D.C., USA: United States Coast Guard.

Nevel, D. E., 1961. *The Narrow Free Infinite Wedge on an Elastic Foundation,* Hanover, New Hampshire, USA: U.S. Army Cold Regions Research and Engineering Laboratory - Corps of Engineers.

Tam, A. (2019). A systematic analysis of test-based model-scale icebreaking patterns. Master thesis, Aalto University.

Tatinclaux, J.-C., 1985. *Level ice breaking by a simple wedge,* Hanover, New Hampshire, USA: US Army Corps of Engineers: Cold Regions Research and Engineering Laboratory.

Varsta, P., 1983. On the Mechanics of Ice Load on Ships in Level Ice in the Baltic Sea. D.Sc. Thesis. Helsinki University of Technology.

Wang, S., 2001. A dynamic model for breaking pattern of level ice by conical structures. D.Sc. Thesis, Helsinki University of Technology.

IAHR AIRH

25th IAHR International Symposium on Ice

Trondheim, 23 - 25 November 2020

Penetration distance of icebreaker "SHIRASE" during her Antarctic voyage and the calculation of ship ramming in heavy ice condition

Junji SAWAMURA[1], Hajime YAMAGUCHI[2], Shuki USHIO[3], Shigeya MIZUNO[4]

[1] *Naval Architecture and Ocean Engineering, Osaka University*
2-1 Yamada-oka, Suita, Osaka, 565-0871, Japan
sawamura@naoe.eng.osaka-u.ac.jp

[2] *Graduate School of Frontier Sciences, The University of Tokyo*
5-1-5, Kashiwanoha, Kashiwa, Chiba, 277-8561 Japan
h-yama@edu.k.u-tokyo.ac.jp

[3] *Meteorology and Glaciology Group, National Institute of Polar Research*
10-3 Midori-cho, Tachikawa-shi, Tokyo 190-8518, Japan
ushio@nipr.ac.jp

[4] *Technical Research Center, Japan Marine United Corporation*
l-3,Kumozu- kokan- cho,Tsu,Mie 514- 0398,Japan
mizuno-shigeya@jmuc.co.jp

The understanding of ramming performance of an icebreaker is important for a safe and efficient navigation when the icebreaker encounters heavy ice conditions such as ridge ice and multi–year ice. Antarctic research icebreaker *Shirase* II is often compelled to a ramming icebreaking during her Antarctic voyage. The ramming performance strongly influences on the schedule of her voyage. The icebreaking in heavy ice condition, however, has not been understood yet. This paper analyzes the ship ramming (penetration distance and ship motions) when the Japanese icebreaker *Shirase* II rams into multi-year ice. The relation between the ice thickness, penetration distance and ship motions are shown. The calculation method based on energy conservation is proposed to predict the penetration distance. The results compared with the penetration distance of icebreaker *Shirase* II.

1. Introduction

The Japanese Antarctic research icebreaker *Shirase II* has transferred cargoes and scientists to the Japanese Antarctic research station (Syowa station) since 2009. Syowa station is located in Lützow–Holm Bay, where is often covered with the multi–year ice. *Shirase II* is frequently compelled to a ramming icebreaking during her Antarctic voyage. The ramming performance affects her Antarctic voyage schedules and safe operations. Ramming icebreaking needs different ship handling from continuous icebreaking. During ship ramming, the icebreaker collides with the ice edge and slides up onto the ice plate. The ice is broken by the ship–ice collision and gravitational force of the ship's sliding. The large impact loads occurs when the ship rams the ice edge. The ship penetrates into the ice using the repetition of the ship ramming operation, which includes the ship backward move, ship acceleration, ship–ice collision and ship slide–up. For the safe and efficient ramming operation, it is necessary to understand the ship response during ship ramming and to predict the ship ramming performance.

A difficulty of the studies for ship ramming is the difficulty of obtaining the reliable data from ice basin and real sea ice. The icebreaker *Shirase* II has recorded the ship motion data during her voyage since her first voyage in 2009 (Yamauch et al., 2011). Takahashi et al (2019) analyzed the measured impact velocity, penetration distance, and turning angle of the icebreaker *Shirase* II. They predicted the time of ship turning in ramming icebreaking. Earlier studies related to calculation of ship ramming was conducted by Popov et al., (Dalay et al., 1990). They assumed the ship–ice interactions during ship ramming to be the ship–ice impact problem and applied the energy conservation to derive a simple formula of ramming force. Vaughan (1986) included the flexural response of ship longitudinal motion during ship ramming. They analyzed the effect of the ship flexure using the maximum bending moment. Ringsberg et al. (2014) analyzed the relation between measured ship motions and ice loads. They proposed the computational model to identify ramming force during ship–ice events in the heavy ice conditions. A number of papers related to ship ramming have been published. The present researches of ship ramming is limited in the available ship and ice conditions. The more reliable ramming data and analysis is necessary to predict the ramming performance.

This paper analyzed the ship motion data when the Japanese icebreaker Shirase II rams in multi–year ice. The relation between the ship response and ice condition during ship ramming are realized. The calculation of ship ramming in multi–year ice based on energy conservation is proposed. The method includes the ship–ice collision, ship slide–up onto ice and ice failure. The calculated penetration distance are compared with measured ones. The icebreaking of ship ramming are discussed using measured and calculated results.

2. Ship ramming in multi–year ice

Ship monitoring system

Japanese icebreaker *Shirase* II is equipped with a ship–monitoring system that records ship motion data during her voyage. The ship–monitoring system records the ship speed, motion (head, pitch and roll angle), shaft power, thrust, steering, frame stress etc. with the time interval of 0.01 s (Yamauch and others, 2011). The ice thickness was measured by electro–magnetic induction sensor (EM sensor) installed at the starboard shoulder. EM sensor measures the total sea ice thickness (snow + ice). The time interval of the EM sensor is 1.0 s. The ship locations are recorded by GPS whose time interval is 1.0 s. For the measurement of the structural response, the strain gauges were installing on the side frames in the starboard shoulder and on the main deck plating. The strain measured by two (upper and lower) gauges equipped on the vertical frame of the outer hull at the starboard shoulder. The strain data transferred to the shear stress acting on the frame. The strain on the deck recorded at 3 locations. The shear stress on the frames recorded at 10 flames. This paper used ship speed, ship power, ice thickness, deck strain, flame shear stress and GPS locations recorded when *Shirase* II penetrates in multi–year ice with ramming breaking. Table 1 shows the principal dimension of Japanese icebreaker *Shirase* II. Fig. 1 shows the outline of the ship–monitoring system installed *Shirase* II.

Table 1. The principal dimension of Japanese icebreaker *Shirase II*.

Length of water line	126.0 m
Maximum breadth	28.0 m
Design draft	9.2 m
Bow angle	19 deg.
Maximum displacement	abt. 20,000 t
Continuous icebreaking (at 3kt.)	1.5 m level ice
Maximum speed	19.5 kt.
Propulsion power	abt. 22,000 kW
Number of propeller	2
Number of rudder	2

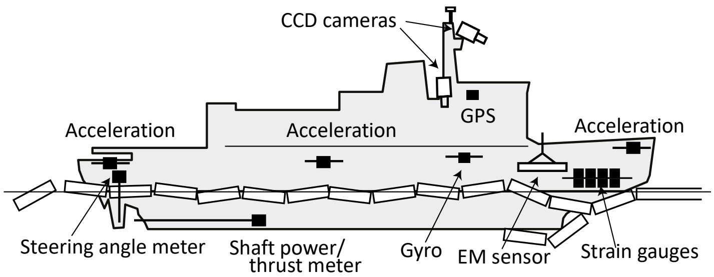

Fig. 1 The ship-monitoring system.

Ice thickness

Shirase II conducted her operations in the Antarctic sea ice for the 55th Japanese Antarctic Research Expedition (JARE 55) during December 2013 through March 2014. During the outbound voyage to Showa station, *Shirase* II started her ramming operations from December 18, 2013, when she entered the multi–year ice (69°00'N, 39°05'E), and continued until January 4, 2014 when she berthed at Showa station (69°00'N, 39°38'E). This paper selected two areas for analyzing the ship responses in the multi–year ice. One is during 2013/12/18-23 (Area 01) that is the beginning of the ramming operation in the outbound voyage of Antarctic sea ice. Another is 2014/01/01-04 (Area 02) that is ending of the ramming operation. Fig. 2 shows the ship route of the *Shirase* II in the multi–year ice and the analyzed sea ice area. Table 2 shows the average, standard deviation and coefficient of variation of ice thickness in Area 01 and Area 02. The average and standard deviation of the thickness in Area 01 and Area02 were 5.08 ± 0.58 m and 3.78 ± 0.79 m, respectively. The thickness of multi-year ice in the Lützow–Holm Bay gradually decreases with approaching to Showa station. The sea ice conditions in the early period of ramming operations were extremely heavy (thick sea ice). Those in the end period close to Showa station were moderate.

Table 2 Measured sea ice thickness (ice + snow).

	Area 01 (2013/12/18 - 23) 69°00'N,39°08'E - 69°02'N,39°13'E	Area 02 (2014/01/01 - 04) 69°06'N,39°30'E - 69°00'N,39°62'E
Avg. [m]	5.08	3.78
SD [m]	0.58	0.79
RSD [%]	16.69	20.82

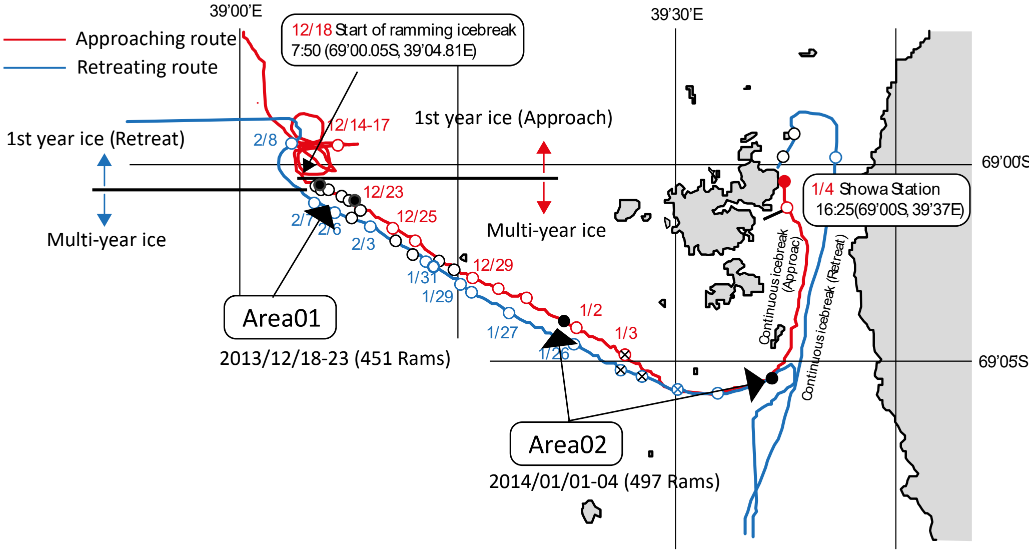

Fig. 2 The ship route in multi–year ice and the analyzed sea ice area.

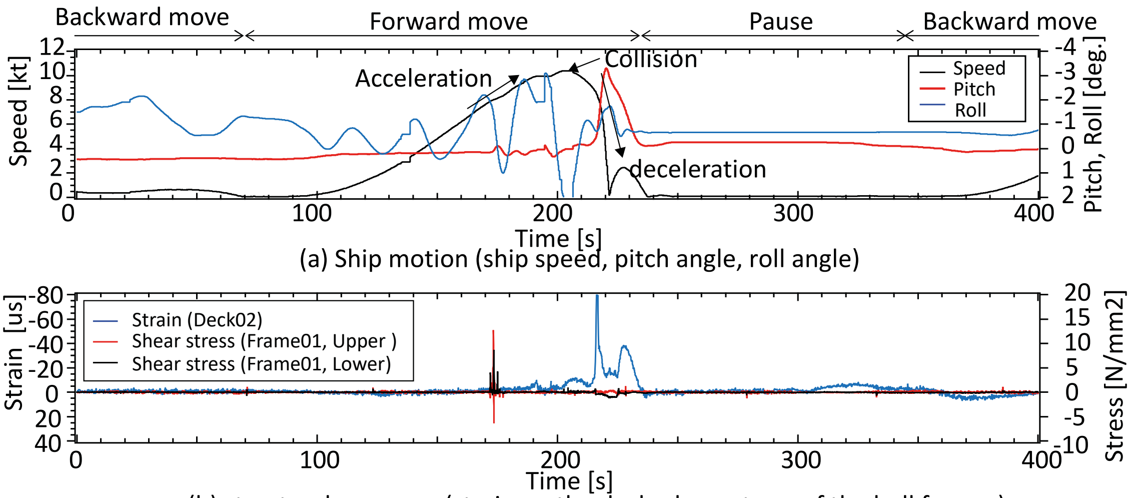

Fig. 3 The history of the ship response during ramming (Area 01: 69°017'N, 39°117'E).

Ship response

The ramming in multi–year ice during the outbound voyage to Showa station was done 1952 times. The ramming in Area 01 was 451 times, and in Area 02 was 497 times. Fig 3 shows time history of the ship response during ones cycle of the ship ramming. The ship speed shows on an absolute value. The pitch motion in the bow up direction expresses negative value. The ship moves backward to make the accelerating distance (around 300 m). The ship accelerates at around 10 kt of ship speed and collies with the plate ice edge at 210 s of the time in Fig. 3. The ship speed is decreased quickly by the collision with ice edge. At the same time, the pitch angle increases quickly by the sliding–up onto the ice after the ship–ice collision. The roll angle fluctuates with not only during the ship–ice collision but also the ship acceleration. The strain on the deck increases quickly at the ship–ice collision of the ship ramming and decreases with decreasing the pitch angle. The shear stresses of the hull frame dese not increase at the ship–ice collision, but the spiked–shape stress is shown during the ship acceleration. The deck strain is concerned with the longitudinal response of the ship hull structure. The longitudinal bending of the ship occurs by the decreasing of the bow draft during the ship slide–up onto the ice. The strong correlation between the deck strain and pitch angle are shown. The shear stresses of the hull frames are concerned with the structural response of the ship local structure of starboard shoulder. The deformation of the hull frames occurs when the ship starboard shoulder hull collide with not only the plate ice during the ship ramming but also with the broken ice floes during the ship acceleration.

Relation between ship response and ice thickness

Table 3 shows the average, standard deviation and coefficient of variation of the maximum speed, thrust and pitch angle during one cycle of ship ramming. The maximum speed and thrust in Area 01 are 10.87 ± 0.58 [kt] and 1309.97 ± 117.76 [kN]. The maximum speed and thrust in Area 02 are 10.67 ± 0.80 [kt] and 1268.08 ± 107.68 [kN]. The maximum speed and thrust of one cycle of the ship ramming are almost unchanged between Area 01 and Area 02, which reveals that ship operates with same condition during her ramming operation. The maximum pitch angle in Area 01 is -2.81 ± 0.48 [deg.] (the coefficient of variation, 17.01 %), and in Area 02 is -1.97 ± 0.73 [deg.] (the coefficient of variation, 36.91 %), respectively. The pitch angle between Area 01 and 02 shown relative large difference, which depends on the sea ice thickness (See Table 2). The large coefficient of variation of the pitching motion in Area 02 concerned with the large variation of the sea ice thickness in Area 02.

Table 3 Average, standard deviation and coefficient of variation of the maximum speed, thrust and pitch angle during one cycle of ship ramming.

		Speed [kt]	Thrust [kN]	Pitch angle [deg.]
Area 01	Avg.	10.87	1309.97	-2.81
	SD	0.58	117.76	0.48
	RSD [%]	5.35	8.99	17.01
Area 02	Avg.	10.67	1268.08	-1.97
	SD	0.80	107.68	0.73
	RSD [%]	7.51	8.49	36.91

Fig. 4 shows the relation between the ice thickness and the maximum pitch angle during one cycle of the ship ramming. The strong correlation between the ice thickness and the pitch motion are shown (correlation coefficient = 0.63). The pitch angles proportionally increase with the sea ice thickness. The linear relation between the maximum pitch angle and the ice thickness can be obtained as;

$$h = 2.09270 + 0.97563, \qquad \textbf{[1]}$$

where h represented ice thickness and θ is the maximum pitch angle of the one cycle of ship ramming. This proportional relation between ice thickness and the pitch angle implies that the maximum pitch angle can estimate the ice thickness during ship icebreaking operation. Fig. 5 shows the relation between the penetration distance and the maximum pitch angle. The penetration distance of ramming is defined as the distance between arrival points of the present and preceding ram. The penetration distance rapidly increases below the maximum pitch angle 1.5°. The penetration distance becomes below about 25 m when the maximum pitch angle becomes larger than about 1.5°. The ice thickness 4.11 m is obtained using the liner relation described by Eq. (1), when the pitch angle equals to 1.5°. Consequently, *Shirase* II ramming performance is approximately assumed that the penetration distance becomes below about 25 m when the ice thickness is larger than 4 m. These relations between ice thickness and the ship responses show possibility that the ship response to the icebreaking can estimate the ice conditions along the ship route. However, further investigations are necessary to identify above estimations.

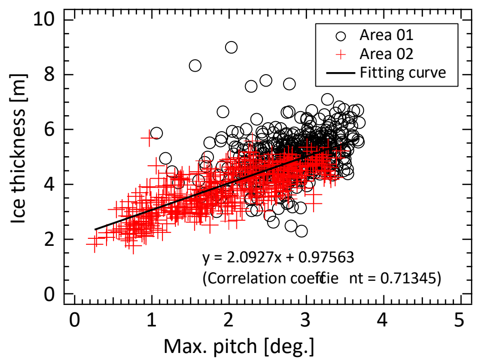

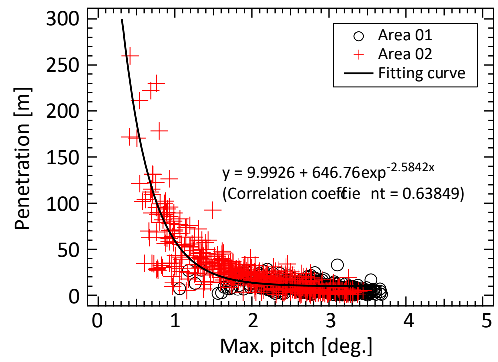

Fig. 4 Relation between pitch angle and ice thickness (left).
Fig. 5 Relation between pitch angle and penetration distance (right).

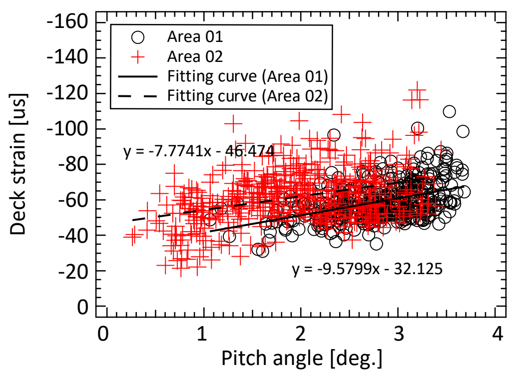

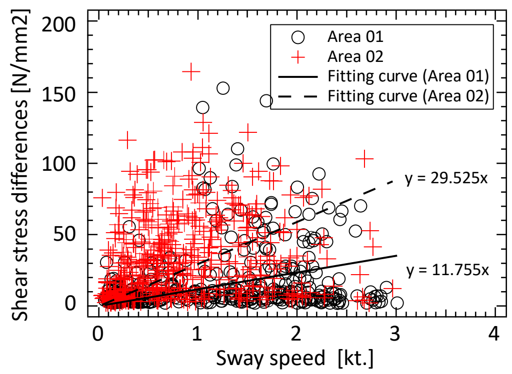

Fig. 6 Relation between pitch angle and deck strain (left).
Fig. 7 Relation between sway speed and shear stress differences of the hull frame (right).

Table 4 Average, standard deviation and correlation coefficient of the deck strain and share stress differences of the hull frame during one cycle of ship ramming.

		Strain [μs]	Stress [N/mm^2]
Area 01	Avg.	59.07	16.92
	SD	11.21	23.31
	Correlation coefficient	0.4156 (with pitch) 0.0609 (with sway)	0.0611 (with pitch) 0.2322 (with sway)
Area 02	Avg.	61.93	35.72
	SD	15.12	30.12
	Correlation coefficient	0.3748 (with pitch) 0.0586 (with sway)	0.3337 (with pitch) 0.1553 (with sway)

Relation between ship structural response and ship motion

Fig. 6 shows the relation between the maximum deck strain and the maximum pitch angle during one cycle of the ship ramming. Fig. 7 shows the relation between the maximum shear stress differences of the hull frame and the maximum speed in sway during one cycle of the ship ramming. The shear stress differences is obtained by subtracting the lower shear stress from the upper shear stress of the frame. Table 4 shows the average, standard deviation and correlation coefficient of the deck strain and shear stress differences during the ship ramming. The proportional relation between the deck strain and the pitch motion are shown (correlation coefficient = 0.42 in Area 01 and 0.38 in Area 02). The maximum deck strain in Area 01 is 59.07 ± 11.21 [μs], and Area 02 is 61.93 ± 15.12 [μs]. The maximum deck strain in Area 01 is smaller than those Area 02. The snow thickness which observed by the eye observation and the image data from the CCD camera in Area 01 was thicker than in Area 02. The snow gives negative effect to the ship longitudinal response which is called cushioning effect. Furthermore, the water flushing system has been operated during Area 01. The water flushing reduces the friction between hull and sea ice, and elongates the penetration distance to the sea ice. The water flushing may affect to the ship longitudinal response. However, further investigations are needed to identify the effect of the water flushing to the ship longitudinal response. No correlation can been seen between the sway motion and the share stress differences of the hull frame (correlation coefficient = 0.23 in Area 01 and 0.16 in Area 02). The average value of the maximum shear stress 16.93 ± 23.31 [N/mm^2] was measured in Area 01, and 35.72 ± 30.12 [N/mm^2] in Area 02. The average speeds in sway was 1.135 ± 0.826 [kt] in Area 01 and 0.876 ± 0.628 [kt] in Area 02. The average value of the maximum shear stress during ramming does not depend on the sway speed. It is shown that the shear stress of the hull frame is affected by not only the sway motion but also other ship motions. The correlation between the structural response of the hull frames and the ship motions was not been found in this investigation.

3. Calculation of ship ramming

Energy conservation model

This paper applied the energy conservation model proposed by Vinogradov (Nozawa, 2006) to the calculation of penetration distance during the ship ramming. His formula is to predict the maximum ice force during ship ramming. Vinogradov's approach is as follows;

– The ship strikes the ice, and slides up on the ice using the kinetic energy and thrust energy.
– The ice downward force increases with increase of gravitational force during the ship slide–up on ice.
– The kinetic energy and propeller thrust energy is expended in the ship–ice collision, potential energy and friction during the ship slide–up on ice.
– The ship breaks the ice when the ice downward force exceeds the ice breaking force before all available kinetic energy is expended.

The energy balance during ship ramming is expressed as;

$$(E_0 - E_1) + E_2 = E_3 + E_4 + E_5, \qquad \textbf{[2]}$$

in which the following variables are defined.

E_0 = kinetic energy before ship ram
E_1 = kinetic energy after ramming icebreaking
E_2 = propulsive thrust energy
E_3 = energy dissipation of ship–ice collision
E_4 = potential energy of ship slide–up on ice
E_5 = energy dissipation of ship-ice friction.

E_0 ~E_5 are expressed as shown below.

$$E_0 - E_1 = \frac{W}{2g}({v_0}^2 - {v_1}^2), \qquad \textbf{[3]}$$

$$E_2 = T \cdot S,$$

$$E_3 = \frac{W}{2g}({v_0}^2 \sin^2\phi)(1 - e^2),$$

$$E_4 = \int_0^{Z_1} P_1 dz + \int_0^{\theta_1} P_1 q d\theta,$$

$$E_5 = \frac{1}{\sin\phi}\int_0^{Z_1} F dz + \frac{1}{\sin\phi}\int_0^{\theta_1} F q d\theta \ .$$

In those equations, v_0 represents the ship velocity before the ship ramming, v_1 denotes the ship velocity after ramming icebreaking, W stands for ship displacement, g is the gravitational constant, T denotes the mean propulsive thrust during ship ramming, S expresses the penetration distance into the ice, ϕ signifies the stem angle, and e is the coefficient of restitution of the ship–ice collision. Z_1 represents the reduction of the average draft. Also, θ_1 is the change of trim angle during the ship ramming. P_1 stands for the vertical force at the ship–ice collision surface. F expresses the friction force on the collision surface. Eq. (3) are substituted into Eq. (2), with the vertical ice force, P_1, expressed by Eq. (4).

$$P_1 = XT - \left[X^2T^2 + \frac{Y}{A}W^2\frac{v_0{}^2\{1-(1-e^2)\sin^2\phi\}-v_1{}^2}{gd}\right]^{\frac{1}{2}}. \qquad \textbf{[4]}$$

In that equation, the following variables are used.

$$A = \frac{W}{\rho A_{\mathrm{W}} gd} + \frac{q^2}{KM_{\mathrm{L}}d}, \qquad \textbf{[5]}$$

$$X = \frac{1-\frac{f_i}{\cos\beta}\tan\phi}{1+\frac{f_i}{\cos\beta}\cot\phi}\cot\phi,$$

$$Y = \frac{1}{1+\frac{f_i}{\cos\beta}\cot\phi}.$$

In those equations, q denotes the distance between the ship–ice collision point and the center of floatation, β is the cosine of the frame angle, f_i is the coefficient of ship–ice friction, A_w represents the area of waterline, KM_L represents the height of longitudinal metacenter, ρ denotes the seawater density. The ice is broken by ship ramming when P_1 is greater than the ice bearing force P_{ice}.

Modeling of ship ramming

Failure mechanisms by ship ramming include the local and global failure of bending, crushing, splitting, and flaking. Because few data have been collected on the behavior of icebreaking during ship ramming, the mechanism of the failure in ship ram has not been understood precisely. The analysis of this paper relied upon the simple assumption that icebreaking by ship ram occurs by local crushing on the ice edge and the bending failure of the plate ice. A ship ramming scenario is idealized using the Vinogradov's approach. The ship ramming scenario is portrayed in Fig. 8. The penetration distance is calculated as described below.

– The ship strikes the ice edge with initial velocity v_0, and slides up on the sea ice.
– The ice edge is broken by ice crushing during ship slide–up, and ice downward force increases by the increase of the ice crushing area and ship slide–up.
– Ice bending failure occurs when the ice downward force P_1 exceeds the ice bearing force P_{ice}. The ship velocity decreases v_i ($i = 1 \sim n$) by the ship slide–up and ice failure.
– The penetration distance S_i is calculated by the distance between arrival (ice breaking) points of the present and preceding ram. The total penetration distance S_{total} is calculated as the sum of each penetration distance S_i ($i = 1 \sim n$).

Bending failure of the plate ice occurs when the bending stress in the plate ice, σ_b, increases as the ship advances and exceeds the flexural strength of the ice, σ_f. σ_b is calculated using fluid–structure interaction (FSI) in which the dynamic effect of fluid underneath the plate ice is included along with plate ice bending (Sawamura et al., 2008). Ice bending in various ship–ice conditions (e.g. ice edge angle, thickness, and ship speed) have been calculated using FSI. A database of the icebreaking force P_{ice} and icebreaking length was prepared. In the ship ramming calculations for different ship–ice conditions, the icebreaking force and icebreaking length is obtainable from this database (Sawamura et al., 2009). The detailed description of the ship ram modeling are shown in Sawamura et al., 2020.

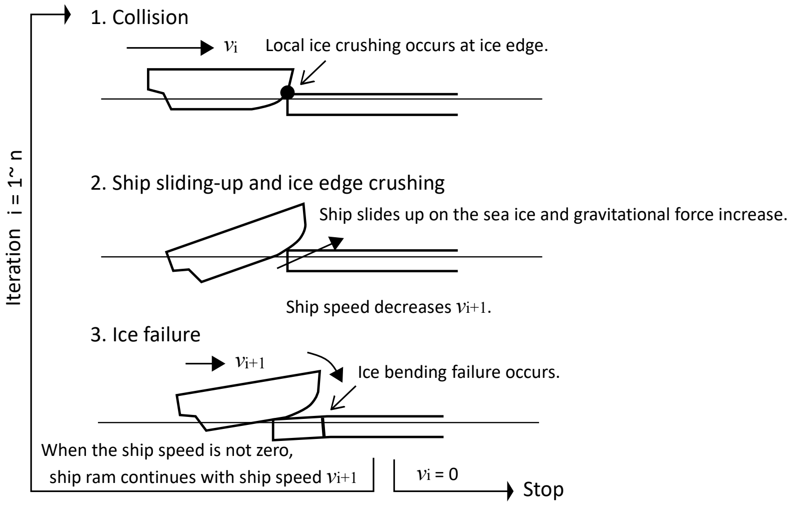

Fig. 8 Ship ramming scenario.

Calculation conditions

The measured ship speed, thrust, and the ice thickness were used for ramming distance calculations. The maximum speed when the ship collides with the ice edge and the mean thrust during the ship ram was used as the input data for calculations. The ice thickness measured by the EM sensor at zero speed when the ship ramming has ended is used. The mechanical properties of sea ice were not measured in JARE 55. The flexural strength estimated using the empirical formula based on the brine volume of sea ice which were measured in JARE 51 (Dec. 2009 – Mar. 2010) was used. The coefficient of restitution obtained from the collision tests with pure ice block and ice sphere are available (Araoka and other, 1978). Young's modulus, compression strength, and coefficient of friction of ice used in the model test of ship in level ice (Sawamura et al., 2017) are selected, because the flexural strength used in the motel test are similar values of those in JARE 51. The principal dimensions of the icebreaker *Shirase* II and the mechanical properties of the sea ice are presented respectively in Tables 1 and 5.

Table 5 Mechanical properties of sea ice.

Young's modulus	E	300 MPa
Flexural strength	σ_ϕ	0.5 MPa
Compression strength	σ_c	0.7 MPa
Coefficient of friction		0.1
Coefficient of restitution		0.7

Comparison of penetration distance

The calculated penetration distance of ship ramming were compared with measured ones. Fig. 9 portrays the measured penetration distance and measured sea ice thickness for Area 02. Fig. 10 shows the calculated penetration distance and measured sea ice thickness for Area 02. The measured penetration distance gradually increases with the decreasing the sea ice thickness. The calculated ones show stable penetration distance within 20 m during the ice thickness above 3 m. The calculated distance rapidly increases below 3 m. The calculation is significantly sensitive to the ice thickness. Table 6 shows the total, average and standard deviation of the penetration distance in Area 01 and Area 02. In the calculation, the more than 10 times consecutive ice failure during one ship ram calculation assumes to be a continuous icebreaking. The iterative calculation of ship ramming is ended when 10 consecutive ice failures are continued, that is *n* equals 10 in Fig. 8. For that reason, the penetration distance obtained from 10 consecutive ice failures (continuous icebreaking) was excluded from the results of Table 6. 444 times ramming in Area 01 and 375 rams in Area 02 were used for the calculations of the penetration distance of Table 6. The calculated total and average penetration distance in Area 01 (in heavy ice conditions) moderately agrees with the measured values. The standard deviation of the calculation in Area 01 is larger than that of measured one. The calculated penetration distance in Area 01 fluctuates more than that of the measured one. The calculated total and average penetration distance in Area 02 (in light ice conditions) are less than the measured values. The standard deviation of the calculation in Area 02 are smaller than those of measured one. The calculated penetration distance in Area 02 was more stable than the measured one.

Table 6 Measured and calculated penetration distance.

		Measured [m]	Calculated [m]
Area 01 (444 rams)	Total	3663	3516
	Avg.	8.268	7.936
	SD	5.385	9.104
Area 02 (375 rams)	Total	6484	5250
	Avg.	17.38	14.04
	SD	7.51	6.67

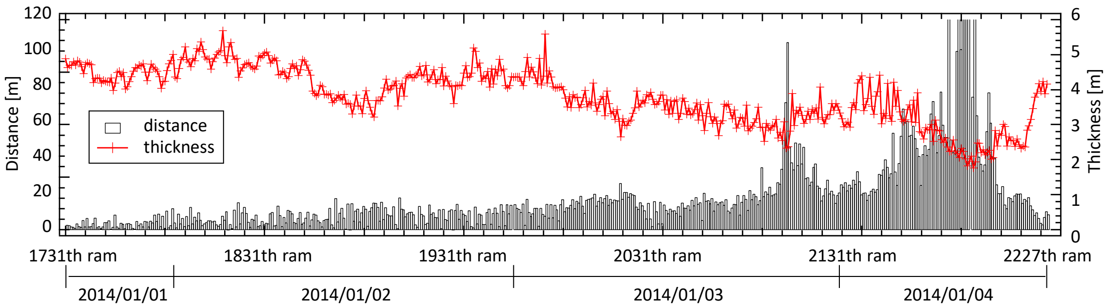

Fig. 9 Measured penetration distance and ice thickness on Jan.1 and 4, 2014 (Area 02).

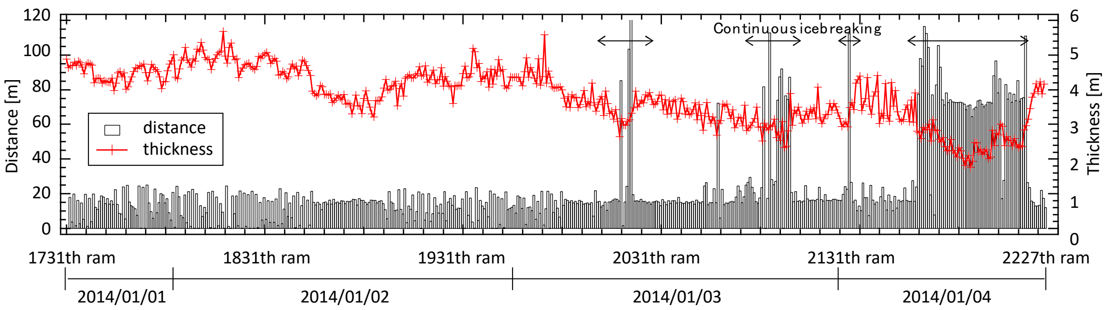

Fig. 10 Calculated penetration distance and ice thickness on Jan.1 and 4, 2014 (Area 02).

The penetration distance is strongly affected by the snow and water flushing. The snow thickness negatively affects the penetration distance. Water flushing elongates the ramming distance. The measured penetration distance in Area 01 includes both effect of snow thickness and water flashing. Ice melted ponds were frequently distributed in Area 02. The ice melted water reduces the friction between hull and ice, and elongates the penetration distance. The calculations did not include effects of snow, water flushing and ice melted water. Additionally, in the calculations, the ice thickness and the mechanical properties of sea ice were assumed to be constant. Only local ice crushing and bending failure are included as the icebreaking phenomena of the ship ramming. The propeller–ice interactions occurs normally in actual ship ramming, which reduces the propeller thrust. The flexural response of the ship longitudinal hull during the ship–ice conditions and slide–up on the ice consumes the kinematic energy of the ship, which reduces the penetration distance. Those problems are anticipated as reasons for the discrepancy between the calculated and measured values. They must be investigated and include in the calculation.

4. Conclusion

This paper described the distributions of ice thickness and ship motion when the Japanese icebreaker *Shirase* II rams in multi–year ice. The relation between ship response and ice thickness were analyzed. The maximum pitch angles during ship ram proportionally increase with the sea ice thickness. The penetration distance rapidly increases less than the ice thickness 4 m. The strong correlation between the ice thickness and the penetration distance were shown. These relations between ice thickness and the ship responses have possibility that the ship response to the icebreaking can estimate the ice conditions along the ship route. The calculation method to predict the penetration distance of ship ramming in multi–year ice is proposed. The calculated penetration distance is compared with measured ones. The calculated distance in the heavy ice conditions moderately agreed with the measured ones, but in the light ice condition showed less penetration distance. The penetration distance during ship ramming is affected from the sea ice conditions (snow thickness, ice melted water and ice strength) and the ship operational conditions (water flushing, steering and cargo conditions) The ice breaking criterion, propeller–ice interactions and ship flexural response also affect the penetration distance. Those effects must be included in calculations.

Acknowledgments

Authors would like to thank members of the 55th Japanese Antarctic Research Expedition and crews of Japanese icebreaker *Shirase* II for great support in field tests and measurements in Antarctic sea ice. We also acknowledge the Antarctic Research Support Section, Ministry of Defense, for their permission to publish this work. This work was partially supported by the National Institute of Polar Research (NIPR) through General Collaboration Project no. 31-18 and this work was partially supported by the Arctic Challenge for Sustainability II (ArCS II), Program Grant Number JPMXD1420318865.

References

Araoka. K., and Maeno. N., 1978. Measurements of Restitution Coefficients of Ice, Low Temperature Science, A, 36, 55-65 (in Japanese).

Daley, C. G. and K. Riska, 1990. Review of Ship–ice Interaction Mechanics, Report from Finnish–Canadian Joint Research Project No. 5 “Ship Interaction with Actual Ice Conditions” Interim Report on Task 1A. Helsinki, Finland: Helsinki University of Technology.

Nozawa, K., 2006. Sea ice Engineering, Seizando-Shoten Publishing Co. Ltd. Japan, 259-264 (in Japanese).

Ringsberg, J. W., M. Broman and P. Nordqvist, 2014. Development of a Model for Global Response of Ship Hull during Ramming of Heavy Ice Features, Proc. of the ASME 2014 33rd International Conference on OMAE, OMAE2014-23186.

Sawamura, J., K. Riska and T. Moan, 2008. Finite Element Analysis of Fluid–Ice Interaction during Ice Bending. Proc. of 19th IAHR International Symposium on Ice, 191-132.

Sawamura, J., K. Riska and T. Moan, 2009. Numerical Simulation of Breaking Pattern in Level Ice at Ship's Bow, Proc. of the 19th International Offshore and Polar Engineering Conference, 600-607.

Sawamura, J et al., 2017. Simulation of Ice Force and Breaking Pattern for Icebreaking Ship in Level Ice, CD-ROM, OMAE2017-61583

Sawamura, J et al., 2020. Calculation of penetration distance during ship ramming in multi-year ice, Okhotsk Sea and Polar Oceans Research, 4, 10-17.

Takahashi, Y., H. et al., 2019. Turning features of an icebreaker during ramming operations: a case study. Okhotsk Sea and Polar Oceans Research, 3, 13-19.

Vaughan, H., 1986. Flexural Response of Ice-Breaking Ships to Impact Loads", RINA Transactions, 7, 259-267.

Yamauchi, Y., S. Mizuno and H. Tsukuda, 2011. The icebreaking performance of SHIRASE in the maiden Antarctic voyage. Proc. of the 21st International Offshore and Polar Engineering Conference. 1093-1099.

25th IAHR International Symposium on Ice

Trondheim, 23 - 25 November 2020

Physical and mechanical properties of ice from a refrozen ship channel ice in Bay of Bothnia

Vasiola Zhaka [1,*], Victoria Bonath [1], Bjørnar Sand [2], Andrzej Cwirzen [1]

[1] *Luleå University of Technology, Sweden,* [2] *Northern Research Institute Narvik, Norway*

vasiola.zhaka@ltu.se, victoria.bonath@ltu.se, bjoernar.sand@norut.no, andrzej.cwirzen@ltu.se

Winter navigation in the North Sea is expanding with respect to vessel size and traffic volume. Icebreakers create routes for ice-going vessels by breaking the level ice cover. Repeated vessel passages in the fairways and harbors initiate the formation of brash ice. The brash ice has the ability to refreeze quickly. In the current work, a field study was conducted on a refrozen brash ice ship channel located in Marjaniemi harbor in Bay of Bothnia. Aim of this study is to evaluate the structure and the strength of ice in the fully refrozen ship channel. Ship channel geometry, ice temperature and salinity were assessed in the field. The ice thickness was in average 45 cm covered by a snow layer with an average of 20 cm. The temperature profiles showed approximately -15^{O}C at the ice surface and close to 0^{O}C in the depths above 10 cm. Salinity varied from 0 to 1.5 ppt. Ice texture, density and compressive strength of refrozen brash ice were measured in the laboratory on 200 mm diameter cores. The behavior of refrozen brash ice with random ice texture was more ductile and stronger in uniaxial compression compared to the adjacent level ice.

1. Introduction

Bay of Bothnia located in the northern basin of Gulf of Bothnia is subjected to sea ice formation during winter season. The ice layer reaches its maximum thickness from February till early March (Kujala and Arughadhoss, 2012). Navigation in fairways and harbors break and erode the initial ice layer into ice pieces known as brash ice. Accumulation and growth of brash ice in frequently navigated channels occur faster than the growth of undisturbed ice layer. Heavy brash ice accumulation makes the navigation harder and unsafe (Mellor, 1980).

After each vessel passage the cold brash ice pieces submerges in the warmer water that causes heat loss and subsequently ice growth (Sandkvist, 1980). The brash ice regain strength between two vessel passages due to refreezing process. Thus, when a ship channel is subjected to very low temperatures for a long time, the full consolidation of the brash ice can occur and its breaking becomes harder (Greisman, 1981). The sailing resistance in a brash ice channel was found to be proportional with the brash ice thickness (Kitazawa and Ettema, 1985). Field measurements from a brash ice channel located in Bay of Bothnia, Luleå coast conducted by (Sandkvist, 1986) showed that the thickness of brash ice after 33 ship passages was 2.5 m.

The physical and mechanical properties of the refrozen brash ice are not well known and their study can give insight in the history of brash ice development. The detailed evaluation of properties and behavior of brash ice are necessary to develop accurate models (Riska et al., 2019). On the other hand, accurate models can assist the establishment of ice management strategies in ports and fairways (Bridges et al., 2020). The current work present results obtained from specimens sampled in a refrozen ship channel in Bay of Bothnia. The term refrozen ship channel refers to a brash ice filled channel that was consolidated prior to sampling due to navigation ban. The aim of this study was to characterize the physical and the mechanical properties of refrozen brash ice from the material perspective and compare these properties with the adjacent level ice. The investigation of refrozen brash ice properties can give a better understanding for brash ice formation and accumulation in the ship channels.

2. Measurements

2.1 Field measurements

Fully consolidated brash ice and sea level ice located at Marjaniemi Harbor in Bay of Bothnia were investigated during February 2019. Nine ice cores with 200 mm diameter were drilled along the consolidated ship track and seven cores were drilled along adjacent level ice. The distance between measuring points was 2 m. The top part of ice cores and the position in the profile were marked and the ice cores were placed in plastic bags and were transported quickly from the field to a freeze box. The samples were stored in -20^{o}C until laboratory tests were conducted in December 2019. The thickness and structure of the channel was measured by mechanical drilling with a 50 mm auger. A measuring stick with a horizontal protrusion at one end was used to measure the ice thickness in each hole and the gaps between the ice blocks. Vertical ice salinity and ice temperature profiles were measured at 2 points along the measured channel cross-section. Measurements of ice salinity and temperature profiles were done on 70 mm ice cores. For salinity measurements, the ice core was cut into 5 cm thick slices, stored in plastic bags and melted in room temperature. Mettler Toledo pH meter apparatus was used to measure the salinity of the melted sea ice based on conductive properties of the dissociated salts in water.

2.2 Laboratory tests

Ice cores were stored for 10 months in the laboratory at -20ᴼC, until the sample preparation was conducted. Unconfined compressive strength was measured for 26 samples of refrozen brash ice and for 20 sample of level ice. The ice cores were removed from the freezing box 2 hours before the sample preparation started and were stored during this time in a refrigerator room that maintained a constant temperature of -10ᴼC. Cylinders with an approximate diameter of 70 mm and height of 170 mm were drilled horizontally along the 200 mm ice cores. The depth of sampling was determined for each cylinder. Specimens were sawed to level the surface and were smoothed with fine sandpaper to reduce the radial restraint that can be caused from the steel plates applied at the top and bottom of the ice samples during compressive tests. Diameter, height and weight of samples were measured to determine the ice density. Thin slices were cut using a band saw from the cores to study the ice texture. Ice slices were stored in the refrigerator for one day in order to achieve clearer texture results. Pictures of ice texture were recorded under crossed polarized light. The test set up for the unconfined uniaxial compression and calibration of system deformation for different load levels are shown in Figure 1 and were described in details by (Bonath et al., 2019). During the compression tests, the temperature of the ice samples varied from -6ᴼC to a minimum of -13ᴼC. The ice samples where compressed at strain rates from 10^{-1} to 10^{-4} s^{-1}. After the horizontal uniaxial compression tests, specimens were stored in plastic bags and melted in the room temperature. Salinity measurement were done for each sample. The total porosity was calculated as the sum of air and brine relative volume (Cox and Weeks, 1983). The brine, pure ice and solid content were expressed as a function of temperature valid for temperatures within the range of -2ᴼC to -22.9ᴼC. The relative brine volume was computed as the ratio between the measured sea ice density and salinity with the empirical temperature function and the relative air volume were computed as the difference of the total sea ice bulk fraction with brine, ice and solid salt relative volumes.

3. Results and discussion

3.1 Properties and texture of sea ice

The sea ice salinity measured in field was relatively low, between 0 and 1.5 ppt (Figure 2). One reason is that the Bay of Bothnia generally consists of brackish water with low salinity that varies within the range of 2.5 to 4.5 ppt (Marmefelt and Omstedt, 1992). Despite that, a high amount of snow ice was observed on top of the ice cover contributing to sea ice with low salinity. Salinity measured in the laboratory after samples were stored for 10 months were even lower between 0 to 0.7 ppt. The observed difference indicated a brine loss due to brine drainage. Possibly occurred in the field due to physical transportation of the cores from the sampling area to the freezing box where samples were stored. The distance was approximately 500 m. Brine drainage does not change the total porosity of the sea ice but affects it by increasing the air volume and decreasing the brine volume. No significant correlation was observed between the salinity and the depth. The ice temperature was generally close to zero, due to a warm period with air temperatures constantly above zero during the week before the measurements. The air temperature during sampling was approximately -15°C, thus the uppermost ice layer had the ice temperatures colder than 0°C, Figure 2.

Refrozen brash ice (RBI) and level ice (LI) texture was investigated by recording images of thin ice sections under cross-polarized light. In both studied sea ice types RBI and LI, it was observed a mixed ice structure of granular and columnar ice. Figure 3 shows representative images of horizontal and vertical profiles for both refrozen brash ice and level ice. The microstructure of 8 RBI cores were investigated from the 9 cores sampled in total. Two different types of mixed ice were noticed in the RBI samples. The first type contained mainly randomly orientated fragments of columnar ice crystals with sizes varying from 1 up to 10 cm, mixed with granular crystals of sizes smaller than 1 cm. The second type of the observed ice mainly contained granular ice crystals of sizes smaller than 1 cm mixed with some crystals bigger than 1 cm. The second type containing mainly granular crystals was recorded in five from the 8 cores investigated while in the three other cores both microstructure types were observed. The high amount of granular ice maybe subjected to snow ice imply the possibility of the RBI thicknesses increase due to snowfall. The hypothesis that a significant increase in RBI thickness occurs due to snowfall agitation with brash ice during vessel passages should be further investigated. In addition, the snow-ice effect in the brine change due to agitation and refreezing process in channels should be further studied. Six cores of LI were observed under cross-polarized light. Level ice contained vertically orientated crystals of columnar ice that were interrupted from possible frazil ice entrapped beneath the ice cover. In all six cores investigated, the frazil ice layers were present. Columnar ice regrowth occurred after these interruptions. Based on the level ice and ridges texture classification presented elsewhere (Bonath et al., 2019) the refrozen brash ice can be classified as $IIIB_1$ and $IIIB_2$ ice types that are described respectively as refrozen ice fragments containing small and big random crystals. Grain size of ice crystal for refrozen brash ice and level ice in the horizontal direction of viewing varied from few mm up to 10 cm. (Bridges et al., 2019) recently recorded the microstructure of the laboratory produced refrozen brash ice. The crystals had random orientation and size variation.

3.2 Uniaxial compression and stress strain curves

Deformation history of compression test and crack propagation within ice samples were observed to have a high impact on the maximum strength (Sinha, 1982). The loading history during uniaxial compression test was studied and representative stress-strain curves are presented in Figure 4. Refrozen brash ice and level ice showed a brittle behavior at high strain rates equal to $10^{-2}s^{-1}$. Brittle behavior could be related to the immediate loss of the loading capacity after reaching the maximum compressive strength (Moslet, 2007). The level ice showed both brittle and ductile behaviors for strain rates equal to 10^{-3} and 10^{-4} s^{-1}. Ductile behavior can be described as the ability of ice to bear the load after the maximum strength is achieved and was observed in the stress-strain curves as the softening branch occurring after the maximum compressive strength. The refrozen brash ice showed a ductile behavior for strain rates of 10^{-4} s^{-1} and $10^{-3}s^{-1}$. In addition, a clear transition zone between brittle and ductile behavior was present. The studied RBI samples showed a ductile behavior in a bigger number of samples compare to level ice. The intrinsic properties of ice like the grain size, temperature and porosity could affect the behavior variation of LI and RBI samples. Earlier study indicated that the ice fracture under the uniaxial compression was affected by the stress state at the ice-platen interface (Schulson et al., 1989). In the current work to reduce this effect, the ice surface was smoothened. The splitting failure was common for all the samples with brittle behavior leading to a uniform internal damage. In the case of the ductile failure, the cracking nucleated and scattered to random sites in the sample leading to a failure without splitting. The uniaxial compression strength results for different loading rates and the standard deviation are presented in Table 1. The average compressive strength for 16 LI samples was 4.05 MPa. The refrozen brash ice had an average compressive strength of 5.04 MPa for 23 samples. Three samples of refrozen brash ice and for samples of level ice were not evaluated due to possible measurement errors. The uniaxial compression in the horizontal loading direction showed higher average strength values for the refrozen brash ice with granular and randomly oriented columnar grains compare to the level ice. Earlier studies by (Schulson, 1990) showed that decreasing the strain rate up to $10^{-3}s^{-1}$, the grain size and the temperature tended to increase the maximum compressive strength for fresh water granular ice with a brittle behavior. The compressive strength of the sea ice decreased with decreasing the strain rate below $10^{-3}s^{-1}$ (Timco and Frederking, 1990). In the present work, the same trend was observed for RBI samples that had higher ultimate compressive strength for strain rate equal to $10^{-3}s^{-1}$ and a lower ultimate compressive strength for higher and lower strain rates, Table 1 and Figure 4. On the other hand, the LI samples had a higher compressive strength for strain rates equal to $10^{-4}s^{-1}$. A possible explanation could be that the number of samples tested is small for a representative stress-stain rate trend.

Another engineering property of ice that is very commonly determined from the stress-strain curves is the elastic modulus that was determined by dividing the maximum compressive strength by the corresponding measured strain. Both level ice and refrozen brash ice showed an increase in modulus of elasticity at higher strain rate, $10^{-2}s^{-1}$. Others observed similar trends (Sinha, 1982).

3.3 Compressive strength vs physical properties

Ice physical properties have a major influence on the compressive strength. (Shafrova and Høyland, 2008) studied the compressive strength of ridges and level ice and their results for the level ice showed that the compressive strength increase with depth. The strongest ice layer was in the bottom of the ice cover. Independently of the applied strain rate the compressive strength of level ice sheet tended to increase with depth due to lower salinity in the bottom part (Timco and Frederking, 1990). Recently the compressive strength for laboratory grown refrozen brash ice was reported to be higher in the top layer compare to the bottom layer (Bridges et al., 2019). The variation of uniaxial compressive strength of refrozen brash ice and level ice with depth and different strain rates is shown in Figure 5. The compressive strength appeared to be higher for samples taken from depths between 15 and 40 cm. In the present case, the compressive strength was probably lower in the top due to snow ice presence.

No clear dependency between the ice porosity and the depth was observed in any of the ice types in this study, Figure 5. All the samples of the refrozen brash ice taken from the depth between 15 and 40 cm had very low porosity. Similar trends were observed in the case of the level ice. The calculated average density of the studied level ice samples was 0.893 g/cm^3 and for the refrozen brash ice was 0.897 g/cm^3. The refrozen brash ice samples had a higher slightly calculated average density. Average porosity, average density and density standard deviations for a certain number of samples are shown in Table 1. The relation of maximum compressive strength with total porosity, air and brine relative volume is shown in Figure 6. The total porosity was computed as the sum of brine and air relative volume (Cox and Weeks, 1983). The results showed that the effect of those parameters on the measured compressive strength were in the same trend as the results presented by others (eg, Moslet, 2007; Shafrova and Høyland, 2008; Timco and Frederking, 1990), where the sea ice compressive strength increased with decreasing porosity. In the current work, the brine volume did not had the main influence in the total porosity. The air volume was the main contributor to the total porosity of refrozen brash and level ice, Table 1. The correlation between the maximum strength and the total porosity was evaluated by using the equation 1 for the horizontal loading direction (Moslet, 2007). Equation 2 was used previously to evaluate the compression strength of granular ice for strain rate equal to$10^{-3}s^{-1}$ (Timco and Frederking, 1990):

$$\sigma = A \cdot \left(1 - \sqrt{\frac{v_T}{B}}\right)^2 \quad \textbf{[1]}$$

$$\sigma = 49(\dot{\varepsilon})^{0.22}\left[1 - \sqrt{\frac{v_T}{0.28}}\right] \quad \textbf{[2]}$$

A and B are empirical coefficients. (Timco and Frederking, 1990) described B as the total ice porosity that causes the ice maximum strength to approach zero. For the granular ice, B was 0.28 and for columnar ice, B was held constant at 0.7 (Moslet, 2007). Coefficient A was introduced as a constant that depends on loading direction and ice temperature (Bonath et al., 2019). Fitting curves for the maximum compressive strength for the refrozen brash ice and level ice are shown in Figure 7. The maximum compressive strength of ice samples decreased with increasing the total porosity. On the present fitting curves for level ice the best fit had an A equal to 8 and for the refrozen brash ice the best fit had an A equal to 12.5.

4. Conclusions

Refrozen brash ice and level ice properties were studied for cores sampled during winter 2019 in Marjaniemi harbor in Bay of Bothnia. Horizontal uniaxial compression were evaluated for 23 samples of RBI and 16 samples of LI. Sea ice density was computed from the mass - volume method. Total porosity was computed as the sum of brine and air relative e volume. Sea ice texture was assessed from pictures of ice yielded under cross-polarized light.

1. Two types of microstructure were recorded in refrozen brash ice samples. The first type with higher amount of big randomly orientated crystals was in a smaller proportion compare to the second type with a higher amount of small random crystals. Level ice microstructure contained mainly elongated ice crystals with a vertical crystal growth. RBI structures were similar to the IIIB1 and $IIIB_2$ ice structures observed by (Bonath et al., 2019).

2. Refrozen brash ice samples were stronger in horizontal direction compare to the adjacent level ice and showed a higher ductility than level ice. LI maximum compressive strength increased with decreasing strain rate. RBI maximum compressive strength was higher for strain rates of $10^{-3}s^{-1}$, where the transition from brittle to ductile occurred. Both ice types exhibit a brittle behavior in strain rates equal to $10^{-2}s^{-1}$. Refrozen brash ice samples showed only ductile behavior for strain rates equal to $10^{-3}s^{-1}$. Level ice for strain rates from 10^{-3} to $10^{-4}s^{-1}$ showed both brittle and ductile behavior.

3. For both level ice and refrozen brash ice sampled in Bay of Bothnia the maximum compression strength decreased with increasing porosity. Brine volume was very low and its influence in total porosity and maximum strength was probably lower than air volume.

Acknowledgment

This work was supported by the Kolartic Project ICEOP in collaboration with the 5th Snow science winter school 2019, Hailouto, Finland.

References

Bonath, V., Edeskär, T., Lintzén, N., Fransson, L., and Cwirzen, A., 2019. Properties of Ice from First-Year Ridges in the Barents Sea and Fram Strait. Cold Regions Science and Technology 168, 102890.

Bridges, R., Riska K., and Haase A., 2019. Experimental Tests on the Consolidation of Broken and Brash Ice. Proceedings of the 25th International Conference on Port and Ocean Engineering under Arctic Conditions.

Bridges, R., Riska, K., Suominen, M., and Haase, A., 2020. Experimental Tests on Brash Ice Channel Development. International Society of Offshore and Polar Engineers.

Cox, G.F.N., and Weeks W.F., 1983. Equations for Determining the Gas and Brine Volumes in Sea Ice Samples. CRREL Report: US Army Cold Regions Research and Engineering Laboratory. 29(102),306–16.

Greisman, P., 1981. Brash Ice Behavior. U.S. Coast Guard Research and Development Center: Report No. USCG-D-30-81.

Kitazawa, T., and Ettema R., 1985. Resistance to Ship-Hull Motion through Brash Ice. Cold Regions Science and Technology 10(3), 219–34.

Kujala, P., and Sankar A., 2012. Statistical Analysis of Ice Crushing Pressures on a Ship's Hull during Hull-Ice Interaction. Cold Regions Science and Technology 70, 1–11.

Marmefelt, E., and Omstedt, A., 1992. Deep water properties in the Gulf of Bothnia. Continental Shelf Research 13(2-3), 169-187.

Mellor, M., 1980. Ship Resistance in Thick Brash Ice. Topics in Catalysis 3(4), 305–21.

Moslet, P. O. 2007. Field Testing of Uniaxial Compression Strength of Columnar Sea Ice. Cold Regions Science and Technology 48(1), 1–14.

Riska, K., Bridges, R., Shumovskiy, S., Thomas, C., Coche, E., Bonath, V., Tobie, A., Chomatas, K., and Oliveira, R.C.D., 2019. Brash Ice Growth Model – Development and Validation. Cold Regions Science and Technology 157, 30–41.

Sandkvist, J., 1980. Observed growth of brash Ice in ship's tracks. Research Report Series. Water Resources Engineering University of Lulea, Lulea, Sweden.

Sandkvist, J., 1986. Brash ice behaviour in frequented ship channels. Water Resources Engineering. Research Report Series A, No.139 Luleå University of Technology, Luleå, Sweden.

Schulson, E. M. 1990. The Brittle Compressive Fracture of Ice. Acta Metallurgica Et Materialia 38(10), 1963–76.

Schulson, E. M., M. C. Gies, G. J. Lasonde, and W. A. Nixon. 1989. The Effect of the Specimen-Platen Interface on Internal Cracking and Brittle Fracture of Ice under Compression: High-Speed Photography. Journal of Glaciology 35(121), 378–82.

Shafrova, S., and Høyland K.V., 2008. Morphology and 2D Spatial Strength Distribution in Two Arctic First-Year Sea Ice Ridges. Cold Regions Science and Technology 51(1),38–55.

Sinha, N. K. 1982. Constant Strain- and Stress-Rate Compressive Strength of Columnar-Grained Ice. Journal of Materials Science 17(3),785–802.

Timco, G.W, and Frederking R.M.W., 1990. Compressive Strength Of Sea Ice Sheets. Cold Regions Science and Technology 17(3), 227–240.

Table 1. Summary of test results for refrozen brash ice and level ice under different strain rates, number of samples tested, avarage maximum compressive strength, standard deviation for the maximum compressive strength, avarage measured salinity, avarage relative air and brine volume, total porosity, avarage ice density and the standard deviation for the ice density.

Nr.Samples		Strain Rate (s^{-1})	σ_{max} (Mpa)	σ_{std} (Mpa)	S (ppt)	ν_a (-)	ν_b (-)	ν_t (-)	ρ_{avg} (g/cm³)	ρ_{std} (g/cm³)
RBI	4	$1.1 \cdot 10^{-2}$	4.89	1.26	0.35	0.008	0.002	0.010	0.912	0.004
	4	$1.1 \cdot 10^{-3}$	6.29	0.67	0.37	0.037	0.002	0.039	0.884	0.019
	5	$1.1 \cdot 10^{-4}$	4.16	1.61	0.36	0.010	0.019	0.012	0.910	0.006
LI	3	$5.3 \cdot 10^{-2}$	2.90	0.71	0.39	0.048	0.002	0.050	0.874	0.084
	3	$1.1 \cdot 10^{-3}$	4.47	1.19	0.26	0.034	0.001	0.035	0.888	0.020
	3	$5.3 \cdot 10^{-4}$	5.09	0.74	0.32	0.023	0.002	0.025	0.897	0.013

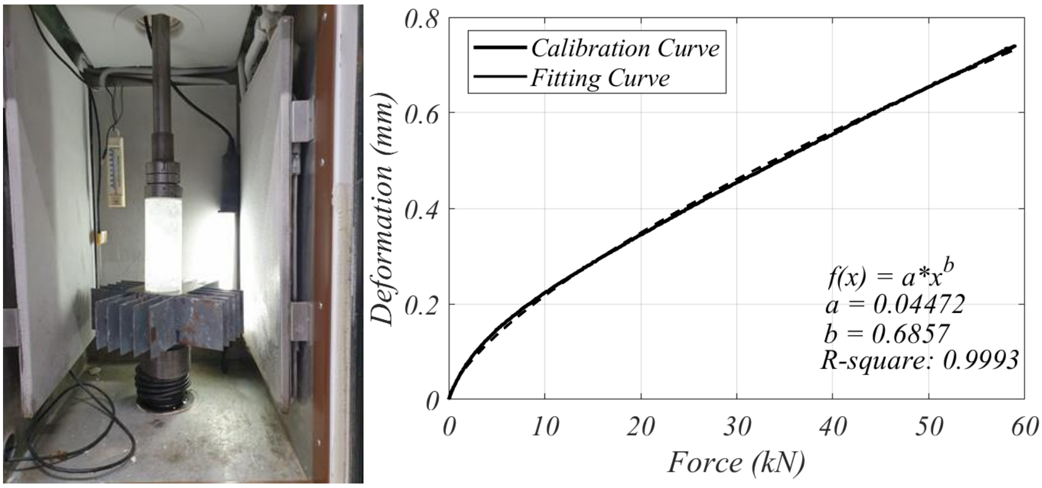

Figure 1. Unconfined uniaxial test set up and deformation calibration curve.

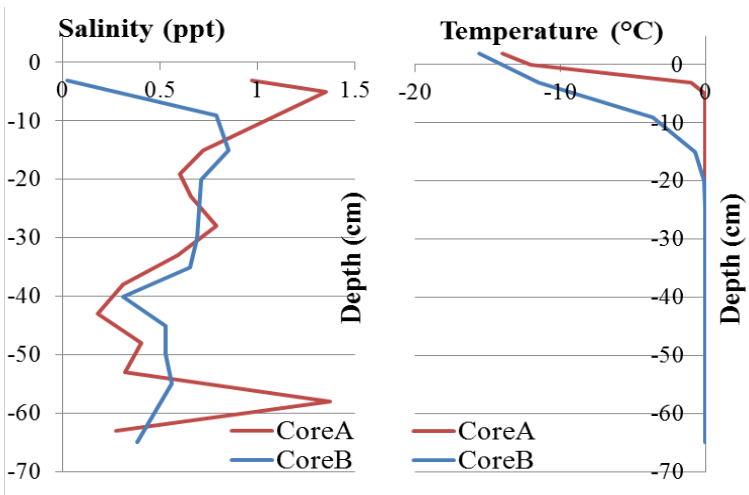

Figure 2. Salinity and temperature profile for refrozen brash ice sampled at two different positions.

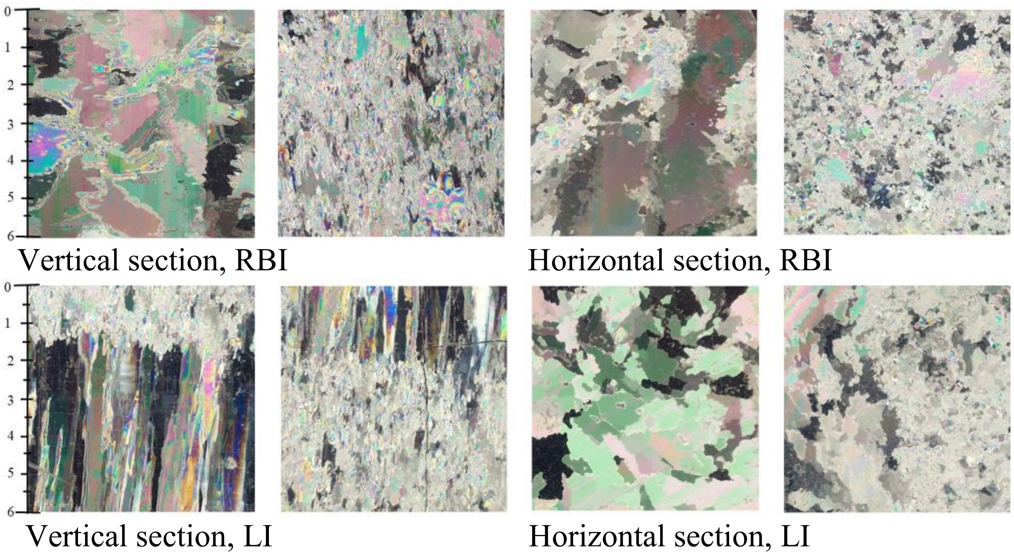

Figure 3. Texture of refrozen brash ice (RBI) and level ice (LI) observed under cross-polarized light in vertical and horizontal direction. Appeared scale represents a microstructure equal to 6x6 cm.

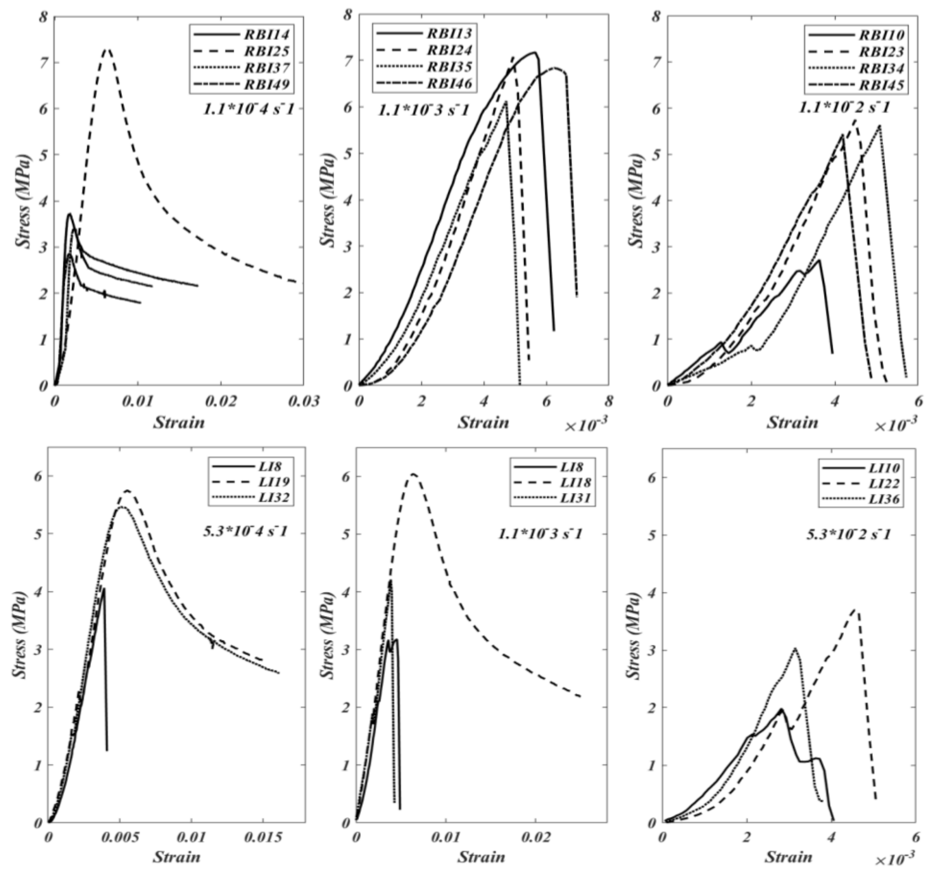

Figure 4. Stress-strain curves for the refrozen brash ice (RBI) and level ice (LI) in different strain rates and sampled in different depths in cm, indicated from numbers in the legends, i.e RBI10 was refrozen brash ice specimen sampled in the depth of 10 cm.

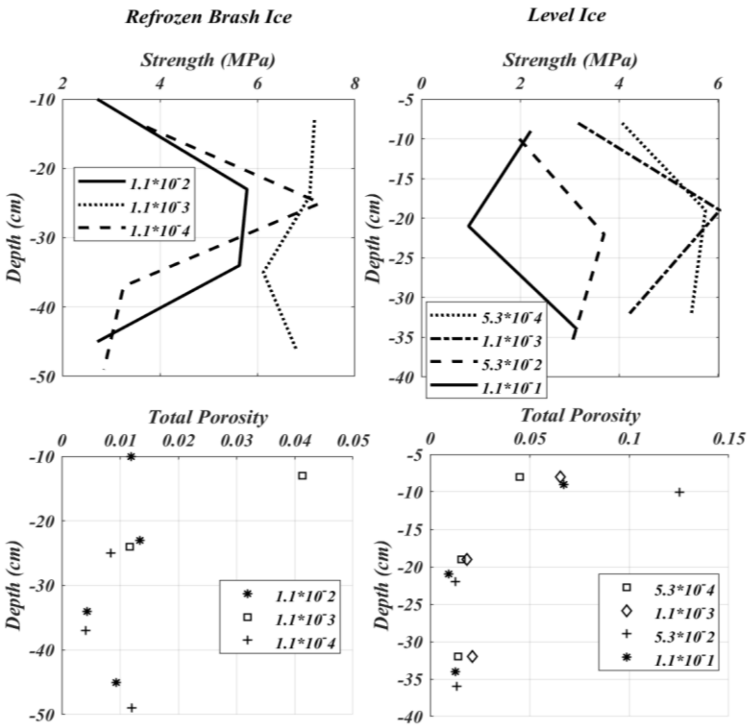

Figure 5. Maximum compressive strength and total porosity variation of refrozen brash ice and level ice with the depth**.**

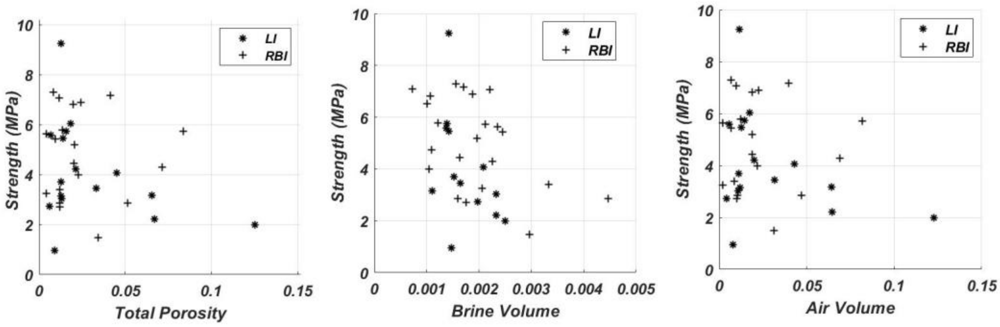

Figure 6. Compressive strength vs total porosity, relative brine volume and relative air volume for refrozen brash ice and level ice.

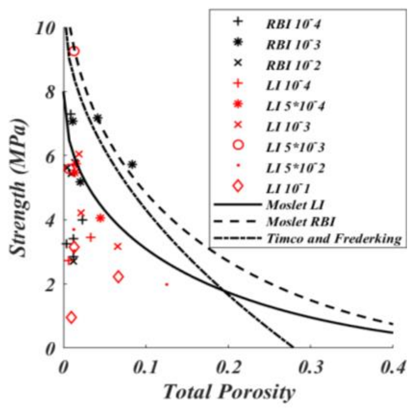

Figure 7. Maximum compressive strength presented as function of total porosity.

05
Floaters in ice

25th IAHR International Symposium on Ice
Trondheim, Norway Nov 23 to 25, 2020

MOORING ANALYSIS OF AN ICE RESISTANT DRILLING SEMI IN ARCTIC REGION

Yan Qu, Dongchang Chen，Haoyang Yin， Ziwei Huang
Southern University of Science and Technology (SUSTech)
Shenzhen,Guangdong,China 518055
quy3@sustech.edu.cn
Former DMAR Engineering Inc, Houston, USA

Shunying Ji， Dayong Zhang
State Key Laboratory of Structural Analysis for Industrial Equipment of Dalian University of Technology

Dahui Liu
CIMC Offshore Engineering Institute Co., Ltd

Abstract
This paper presents a mooring analysis result of a new drilling Semi-sub concept which intended to operate in the arctic region. The SEMI was designed to be able to operate in open water season and in level ice less than 1 meter thick in the Arctic. In order to reduce the ice load on the SEMI, 6 inclined columns were designed to break the ice sheet in a bending failure mode. A total of 12 mooring lines were considered to be installed on the SEMI to provide a station-keeping capacity against wave load and ice load. The SEMI was also designed to have the station-keeping capacity in 1.5 meter thick level ice as survival condition. The analysis shows that the SEMI with inclined columns is able to operate in the arctic wave condition and ice condition.

1. Introduction

According to the US National Petroleum Council (NPC) investigation, the Arctic has about 30% of undiscovered reserves of world oil and gas (2015). The NPC study shows that the global Arctic has 525 BBOE of resource potential with 70% (372 BBOE) expected to be gas. And globally, 75% (389 BBOE) of the Arctic resource potential is expected to be offshore. With the increasing of the global demands and limited undiscovered conventional reservoir, development of the Arctic will be an inevitable option for the human being to meet the needs although the process has been postponed by the boom of shale oil and gas.

Technically speaking exploration of the arctic offshore oil and gas is not an impossible mission. In the Beaufort Sea over 140 wells were drilled from the 1970s to early 1990s. [G.W. Timco and R. Frederking, 2009]. Several different approaches, including the floating drillships, conical floating drill platform, caisson structures, had been used for oil exploration. After 2000, several arctic drilling activities were carried out in the Russian offshore filed and US Chukchi sea. Several semi-submersible drilling rigs have been selected by the operators to drill the wells. ExxonMobil contracted the West Alpha semi-submersible rig to drill in the Kara sea for the East Prinovozemelsky-1well [Exxon, 2014]. Shell used Polar Pioneer to drill in the Chukchi sea.[Shell Terminates Contract for Polar Pioneer Drilling Rig, 2015] Gazprom Neft used Nanhai-VIII and Nanhai-IX to drill in Leningradskoye field, Nyarmeyskoye field and Skuratovskoye field of Kara sea. And discovered two major discoveries, Dinkov and Nyarmeyskoy.[Kevin Hewitt, TEKNA Conference, 2007]


West Alpha semi-submersible rig


Polar Pioneer semi-submersible rig


Nanhai-VIII semi-submersible rig

Nanhai-IX semi-submersible rig

Figure 1 Semi-submersible drilling platforms used for Arctic offshore drilling operations after 2000

It should be mentioned that all those semi-submersibles contracted to drill in the Arctic were ordinary rigs just with winterized upgradation and structural strengthen modification. These drill rigs were only able to operate in the open water season at the filed. The total well costs were highly affected by the length of the drilling season .If a drilling campaign can not be accomplished in one season, the mobilization, start-up and abandonment cost will all add to the cost of the well(s).[Li Zhou, Biao Su, Kaj Riska, Torgeir Moan, 2012] Therefore, extending the drilling window by enhancing the drill rig capacity is a key factor to make more arctic offshore exploration economically applicable.

Alain Wassink and Remco van der List (2013) indicated that in order to reduce the drilling cost, the rig is needed to be able to work in sea ice conditions. This could enable an earlier start of the operation as the rig can be towed in when the sea ice is deteriorating. The rig can continue to work in autumn when the sea ice is forming. That will further extend the operation period into autumn or even early winter.

In order to work in sea ice conditions, the SEMI submersible drill rig should be designed with ice resistant capacity. The ice resistant capacity is composed of at least the following features:

- The SEMI needs to meet the station keeping request in moving ice.
- The hull has enough strength under the moving ice action.
- The risers should be kept away from direct level ice action, and should be able to work in the broken ice floes.
- The station-keeping system should be able to work in the moving ice.

In this paper, a new ice resistant drilling SEMI concept was presented and the station-keeping capacity of the SEMI was verified against the ice load in the extended season and design wave load in the summer.

2. Global performance requirement of the new arctic drilling SEMI concept

The offset of the SEMI submersible is one of the most concerned factors for the drilling rigs design. An offset exceeding limit value will create a large tilt angel on the drilling riser, which can cause failure of the riser. Typically 5% and 10% of the water depth had been used as the limit offset in the operational and extreme wave condition [Alain Wassink and Remco van der List, 2013]. Thus in the shallow water, the offset limit proposed a challenge for the floating drilling system. For the rig intended to be used in the extended ice season, the same offset limit can be set for the operational and extreme ice condition. In this paper, a drilling site of 70 m water depth is considered to verify the feasibility of an arctic drilling SEMI. The level ice 1 m and 1.5 m thick were defined as the operational and extreme ice condition. Environmental parameters for the operational and extreme condition in wave and ice were defined in **Table 1**.

Table 1 Environmental parameters for the arctic operation and extreme condition

Parameters	*Operating*	*Extreme*
Water depth [m]	70	70
Wave Height Hs [m]	5	7
Wave period Tp [s]	11.8	12
Gama	1.5	1.5
Wind [m/s]	21.5	24
Surface current [m/s]	1.37	2.0
Depth average current [m/s]	0.97	1.2
Ice thickness [m]	1	1.5

3. The new ice resistant drilling SEMI concept

The new SEMI submersible was a hull structure with 6 columns and 2 pontoons. A sketch of the new ice resistant SEMI submersible concept was shown in **Figure 2** Sketch of the ice resistant SEMI submersible drilling rig..

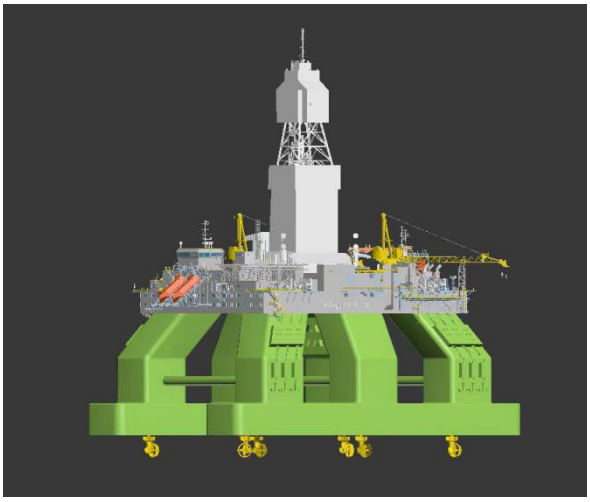

Figure 2 Sketch of the ice resistant SEMI submersible drilling rig.

To mitigate the ice load on the drill rig, the columns were designed with an inclined section over the vertical section as shown in **Figure 2**. When drilling in the ice, the draft will be lowered to the inclined column elevation. The moving ice will act on a sloped surface, which will force the ice to fail in bending and reduce the global ice load on the rig. When drilling in the open water, the rig will be de-ballasted and change the draft to the vertical column elevation, which will improve the global performance of the SEMI. It should be mentioned that the columns are inclined towards center of the deck. The 4 columns at the bow and stern have a tilt angle both at the X (bow) and Y (starboard) direction. The other 2 columns only have the tile angle at X direction. That allows the ice from every direction to act on a sloped surface of the hull.

Mooring system of the platform is composed by 4 groups of anchor chains. For floating structures in ice covered sea, the sea ice may cause abrasion of the mooring chain if ice directly acts on it. The ice floe may also affect operation of the anchor chain. Therefore, it was suggested that the mooring chain should be protected from direct ice action. A steel plate cover was proposed to be used as a mooring line protector against the ice action as shown in **Figure 3**. Besides the mooring lines, drilling riser is also fragile to the ice action. It was suggested that the drilling riser should be protected from level ice and large ice floe action as well. **Figure 3** also shows a riser protection fence for the arctic drilling platform for this propose. The riser protection fence was composed by horizontal beams below the moon pool area between the pontoon pairs in the middle of the rig. The horizontal beams was strengthened by the V or X shape braces. The ice fence will block the level ice and large ice floe act on the risers directly.

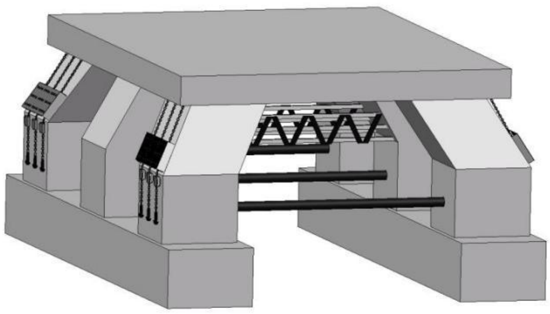

Figure 3 Ice resistant features of the new SEMI submersible drilling rig.

The main dimensions of the new SEMI are given in **Table 2** Main dimensions of the ice resistant SEMI. Typical dimensions for a conventional semi-submersible with 6 columns and 2 pontoons was used for the new SEMI. In this case, the SEMI has a global performance similar to the existing rigs.

Table 2 Main dimensions of the ice resistant SEMI

	Length (m)	*Width (m)*	*Height (m)*	*Disp. (m^3)*	*Spacing (m)*	*Inclined Angle (deg)*
Deck	90	70	6	-	-	-
Hull	110	80	40	-	-	-
Pontoon	110	18	12	47520	80	-
Column(vertical)	16	16	14	16896	42	-
Column(inclined)	16	16	14		36→42	60
				Draft(m)		
Open water				23		
Ice				25		

4. Mooring system of the drilling SEMI.

Alain Wassink and Remco van der List (2013) indicated that for the arctic drilling, a practical water depth of 50 to 80 meters is the upper limit for jack-up rigs, 300 to 400 meter for mooring system. Dynamic Position system is used for water depth higher than 300 to 400 meters. At present, the exploration frontier of the arctic oil and gas is still at shallow water areas. Therefore, the arctic SEMI is expected to be able to operate in the shallow water. To provide the positioning capacity against the ice load, mooring lines listed in **Table 3** are used for the new SEMI.

Table 3 Mooring system parameters

Line Properties	*Line Segment*		
	Platform chain	*Riser Wire*	*Ground Chain*
Grade	R4	Spiral strand	R4
Length (m)	30	240	430
Diameter (mm)	122	132	122
Weight (MT/m)			
Air	0.319	0.085	0.319
Water	0.277	0.071	0.277
EA Elasticity (MT)	1.271E6	1.610E6	1.271E6
Breaking Strength (MT)	1398	1383	1398

5. Environmental loads

Operation of the arctic SEMI requests the rig has a limited offset under the action of environmental loads. For the SEMI operated in the arctic, the environmental load combination are different between open water and ice. When operating in the open water, the environmental load is a combination of wind, wave and current, while in ice, the load is a combination of wind, ice and current. The environmental loads can be estimated using the methods recommended in regulation and code. The following methods are used in this paper by using the environmental parameters in **Table 3** as input.

- The ice loads are calculated using the method presented in ISO19906[ISO, 2010]. The sloped column is considered as a conical structure with waterline diameter equal to width of the column. The ice load from bow and starboard direction will be verified. It should be considered that in the bow direction, two columns will be exposed to the ice action, and in the starboard direction, the ice will act on 3 columns. The ice failure on each column is considered as independent. For the offset verification, the ice load generated by the level ice action is calculated. The ice action from a level ice of 1 m thickness is considered as operational condition and 1.5 m thick ice is considered as extreme condition. That implies that the rig will keep drilling operation under ice action less than 0.5 m thickness. And the mooring system is able to keep positioning capacity when ice thickness is less than 1 m.
- The wind load is estimated using the method presented in API 2SK [American Petroleum Institute, 2005]. A typical wind speed listed in **Table 4** is used for the calculation. In the analysis, different projected areas were evaluated considering the wind from bow and starboard direction. To combine with ice load and wave load, the projected areas also vary due to change of the draft.
- The current load is estimated using the method presented in DNV-RP-C205. The current speed listed in **Table 4** is used for the calculation. Similar to the wind load, the current loads from bow and starboard direction were both considered. When combined with ice and wave, the draft verification will also affect the current loads.
- The wave load is calculated in Orcaflex 10.0 using the RAO of the SEMI obtained in SESAM. Motion and mooring analysis are also carried out in Orcaflex 10.0.

Results of the environmental loads analysis are listed in **Table 4**.

Table 4 Environmental loads on the arctic SEMI

Load case	***Env. Condition***	***Env. Parameters***	***Surge (MT)***	***Sway (MT)***
Operation	**Wind**	25.4 (m/s)	172.6	211.4
	current	1.37 (m/s)	248.4	740.4
	Ice	1 (m)	177.4	266.1
Extreme	**Wind**	28.3 (m/s)	214.2	262.5
	current	2.25 (m/s)	669.1	1996.9
	Ice	1.5 (m)	600.6	901.4

6. Mooring analysis of the arctic SEMI in ice condition

To verify the mooring capacity of the arctic SEMI, an integrated hull-mooring system model was built in the mooring analysis software package Orcaflex 10.0. The model is shown in **Figure 4**.

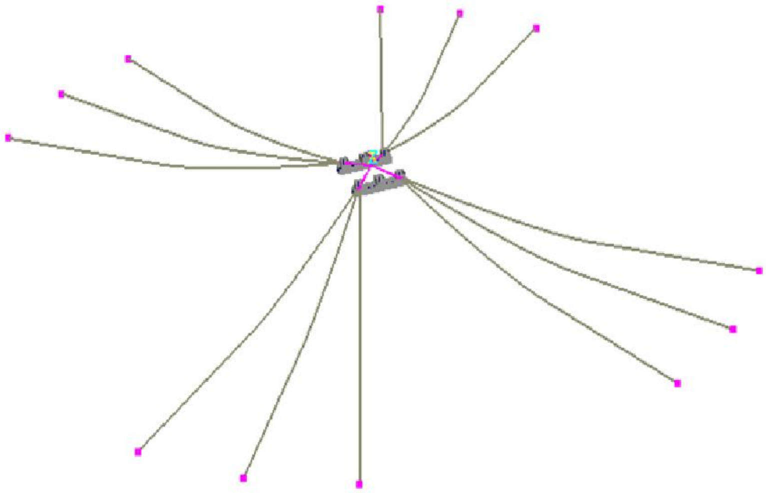

Figure 4 Hull / mooring system model of the arctic SEMI.

When operating in level ice, the offset of the drilling SEMI is driven by action of ice, current and wind. The maximum offset can be estimated by considering the environmental loads combinations as a static force in the same direction. **Figure 5** shows restoring force results by imposing different offsets to the SEMI. The results show that when imposing an offset of 3.5 m, which is 5% of the water depth, the restoring force is at the level of 12,000 kN at bow direction and 21,055 KN at starboard direction. That is higher than the total environmental loads of 5984 KN and 12179 KN at the corresponding directions. That implies that the mooring system has adequate stiffness to withstand the environmental loads and keep the rig offset in a safe magnitude.

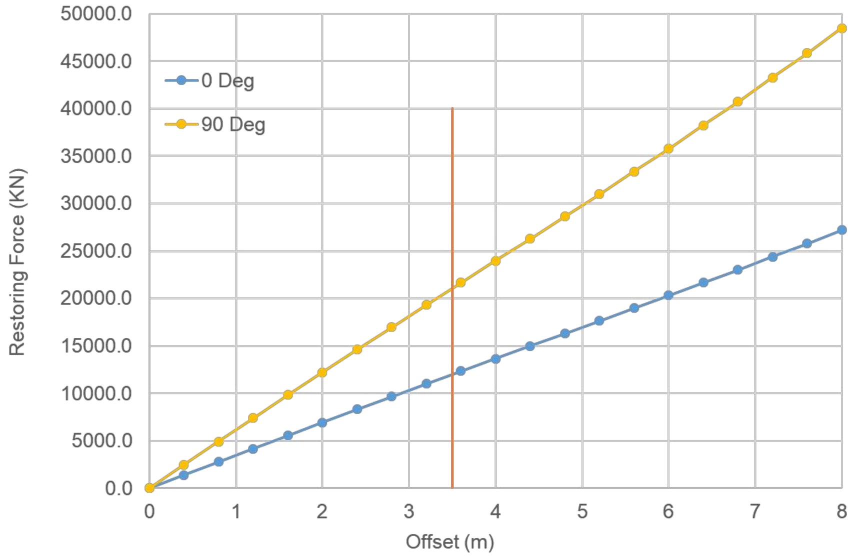

Figure 5 Restoring force as a function of drilling SEMI offset.

The max mooring tension results against the rig offsets is shown in **Figure 6** The result shows that when the rig offset is 3.5 m for the operating condition, which is 5% of the water depth, the max tension in the mooring line is 5,707.3 KN. That is about 40% of the breaking strength, and the safety factor is 2.45 which is more than the value 2.0 requested in the code.

While for the extreme condition that the offset is 7 m, the max tension is 8,685.1 KN, safety factor 1.58, which is less than 1.67 [DNVGL, 2010] that requested in the code.

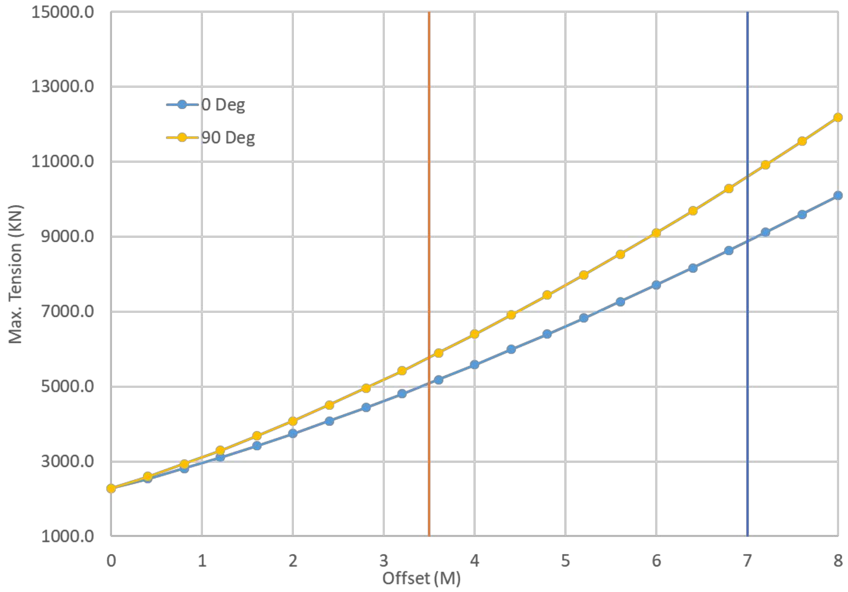

Figure 6 Max mooring tension as a function of offset of the drilling SEMI.

7. Mooring analysis of the arctic SEMI in open water condition

Though the arctic SEMI is capable of drilling in the sea covered by ice, the open water season is still its major operating window. The SEMI needs to have a reasonable hydrodynamic global performance to ensure its drilling capacity. When operating in the open water, the arctic SEMI adjusts its draft to the vertical column elevation. In this case the submerged part of the rig is identical to a traditional drilling SEMI. The existing drilling SEMI global sizing experience can be used to determine dimensions of the pontoon and column. By using the sizing result in **Table 2**, mooring system parameters in **Table 3** and environmental parameters in **Table 4**, the mooring capacity of the arctic SEMI was investigated by a standard mooring analysis for the wave condition. The analysis results are listed in **Table 5** .

The analysis results show that for the operational condition defined in **Table 4**, the arctic SEMI has an offset less than 5% of the water depth, and the safety factor of mooring tension is larger than 2, which means that the drill rig has an adequate safety margin in the operational condition. But for the extreme condition the offset exceeded a little bit of the design limit, 10% of the water depth. The mooring tension for the 90-degree wave direction has a safety factor 1.47, which is a little bit less than requested in the code. It should be noted that although the results exceeded the design limit, it does not mean that the arctic SEMI is not applicable. Firstly, the main dimension of the arctic SEMI in this paper used typical sizing of the drilling SEMI without any optimization, the global performance could be improved by modifying the sizing parameters. Secondly the results presented here are based on the environmental parameters listed in **Table 4**. Those parameters vary at different sites. For those sites with harsh environmental condition, the SEMI can also be used by narrowing the operation window.

Table 5 Mooring analysis results of the arctic SEMI in open water

	offset (m)				*Mooring Tension (KN)*			
	0 deg	% WD	90 deg	% WD	0 deg	safety factor	90 deg	safety factor
Operation	3.26	4.66%	3.44	4.91%	5236	2.64	6076	2.28
Extreme	7.35	10.50%	7.59	10.84%	6897	2.01	9429	1.47

8. Conclusion

Exploration and development of the arctic offshore oil & gas is an inevitable choice for the northern countries. At present Russia is leading the role by developing several oil field in the arctic and sub-arctic shallow water region. There are also other countries attempting to drill in the arctic but failing to conclude a commercial development in the past decades. In the drilling campaign launched, the operating companies all met challenges that the operation window was narrow due to the limited open water season. The industry needs facilities that can be used in the shoulder ice season to reduce the drilling cost.

In this paper a drilling semi concept with the capacity to operate in level ice condition was presented. The semi is a 6 column 2 pontoon structure. The column has a lower vertical section and an inclined top section. The inclined column section was the main feature of the semi that helps to reduce the ice load by breaking the level ice in bending failure. Two other accessory structures, the riser ice fence below the moon pool and the mooring line protector are also designed to increase the safety of the rig in the ice.

Positioning capacity of the drilling semi is verified by using the Orcaflex 10.0 software. The results show that the mooring system is strong enough to hold the rig in a safe position under level ice action. But for the open water operation, the rig offset exceeded the design requirement. That implies the ice load is lower or at least in the same level of wave loads. It is technically feasible to design a semi that is able to operate in open water and shoulder ice season.

Acknowledgement

The authors would like to acknowledge support from State Key Laboratory of Structural Analysis for Industrial Equipment of Dalian University of Technology (GZ19120), National Natural Science Foundation of China (41976195). National Key Research and Development Program (2016YFC0303400).

References

National Petroleum Council, 2015, Arctic Potential: Realizing the Promise of U.S. Arctic Oil and Gas Resources

G.W. Timco and R. Frederking, 2009, Overview of Historical Canadian Beaufort Sea Information, NRC Canadian Hydraulics Centre Technical Report CHC-TR-057

Exxon, (2014) https://cdn.exxonmobil.com/~/media/global/files/other/2014/kara-sea-fact-sheet.pdf

Alain Wassink, Remco van der List, 2013, Development of Solutions for Arctic Offshore Drilling, SPE Arctic and Extreme Environments Technical Conference and Exhibition, 15-17 October, Moscow, Russia

Shell Terminates Contract for Polar Pioneer Drilling Rig, 2015, https://gcaptain.com/shell-terminates-contract-for%20-polar-pioneer-drilling-rig/

Kevin Hewitt, TEKNA Conference, 2007, Offshore Arctic Exploration Development challenges, Oslo

Li Zhou, Biao Su, Kaj Riska, Torgeir Moan, 2012, Station Keeping Capacity of a Moored Structure with Heading Control in Level Ice, 21st IAHR International Symposium on Ice

International Organization for Standardization, 2010, ISO 19906 Petroleum and natural gas industries-Arctic offshore structures[S]. Europe: International Standardization for Organization

American Petroleum Institute, 2005, API RP 2SK Design and analysis of stationkeeping systems for floating structures[S]. Washington, D.C.: API Publishing Services

DNVGL, 2010, DNVGL RP C205 Environmental conditions and environmental loads[S]. Norway: Det Norske Veritas

25th IAHR International Symposium on Ice
Trondheim, 23 - 25 November 2020

Statistical Analysis of Results from Ice-Tank Tests with Broken Ice

Marnix van den Berg
Raed Lubbad
Sveinung Løset
Norwegian University of Science and Technology (NTNU)
[2]Department of Civil and Environmental Engineering, NO-7491, Trondheim, Norway email
marnix.berg@ntnu.no, raed.lubbad@ntnu.no, sveinung.løset@ntnu.no

Loads from broken ice may be regarded as the governing design load for structures supported by ice management. Ice-tank tests are often used in the assessment of loads from broken ice. This study uses measurements from an ice tank in combination with results from numerical simulations in order to assess the uncertainty in results from ice-tank tests with broken ice. The numerical simulations are performed with the Simulator for Arctic Marine Structures (SAMS). The ice-tank measurements belong to a test that was performed at Hamburg Ship Model Basin (HSVA) in 2012. The test involved a multi-leg structure in 60% (initial) ice concentration. The test was part of a test campaign supported by the HYDRALAB-IV European research grant. In this study, the ice-tank test is reproduced numerically for 300 times. Each time, a different initial floe position is used. The results show a strong dependency of the simulated ice loads and the governing interaction mechanisms on the initial conditions (i.e., the initial floe positions herein). A strong dependency of ice tank test results on uncontrolled initial conditions, such as the initial floe positions, leads to a high random uncertainty in the test results. This random uncertainty should be considered in the statistical interpretation of test results from ice tank tests with broken ice.

1. Introduction

Ice tank tests are often used in the analysis of broken-ice loads on structures. Test campaigns involving broken-ice conditions generally perform a single test for each specific condition to be tested. It is often unclear to what extent the test results could vary if the test would be repeated. The repeatability of a test is important in the interpretation of the test results. A test with pour repeatability (i.e., a test where the results are strongly influenced by uncontrolled conditions) has a high random uncertainty and thus a practically limited value.

A method to investigate the random uncertainty in ice tank test results is proposed in the *Procedure for assessing the experimental uncertainty in ship resistance testing in ice* (ITTC, 2005). The procedure describes the assessment of random uncertainty for a test case of a ship in level ice, but it is also applicable to other conditions as it is based on general principles of uncertainty assessment. The procedure is based on the division of the time series of a measured parameter of interest, such as the ice load, into statistically independent segments with (close to) identical properties.

This study uses numerical simulations to analyse the repeatability of ice tank tests in broken ice. It builds on the study described in van den Berg et al. (2020), in which the repeatability of ice tank tests in broken ice was studied for a multi-leg structure and a ship in a range of broken-ice conditions. In van den Berg et al. (2020), 20 numerical simulations were performed for each ice-tank test run (in total 15 different ice tank test runs, each with a different structure type and/or ice conditions). The main conclusion drawn by van den Berg et al. (2020) was that a high random uncertainty exists in the results of ice tank tests with broken ice; and that the results of a test with the same ice properties (ice concentration, thickness, mechanical properties) can be significantly different if the test is initiated with different initial floe positions. Although 20 numerical simulations for each ice-tank test run were sufficient to support the conclusions in the study described in van den Berg et al. (2020), they may be insufficient for a reliable statistical analysis of the simulation results.

This study selects a single ice-tank test run from van den Berg et al. (2020), and simulates this test run 300 times. Only the initial position of ice floes is changed in each simulation. The larger simulation batch enables a more thorough statistical analysis of the variability in results that may occur due to uncontrolled initial conditions such as the initial positions of ice floes. The simulation results are used to define certainty bounds of the mean ice loads. In addition, differences in the ice accumulation and clearing processes are studied.

2. Numerical model characteristics

The numerical simulations were performed with the Simulator for Arctic Marine Structures (SAMS). SAMS is a numerical simulator designed for the modelling of ice-structure and ice-ship interaction. SAMS uses the non-smooth discrete element method. In each time step, contact forces are calculated implicitly by solving a mixed linear complementarity problem. The method allows for relatively large time step sizes, but the resolution of forces within each time step is more demanding than in explicit methods. The method is described in detail in van den Berg et al. (2018). Bending and splitting failure of ice floes is considered using analytical solutions described in (Lu et al., 2018, 2015a, 2015b). Hydrostatic and hydrodynamic forces on ice floes are considered by using drag coefficients and the local velocity of the triangulated ice floe geometries, as described in Tsarau (2015). An overview of the combined model components is given in Lubbad et al. (2018).

For the specific conditions modelled in this study, ice-ice rafting was observed to be an important load releasing mechanism. Therefore, a description of the ice-ice rafting mechanisms in SAMS was provided in van den Berg et al. (2020).

3. The ice-tank test run and the numerical simulation setup

The test-run analysed in this study was part of an Hydralab IV test campaign described in Hoving et al. (2013). The test was performed using a multi-leg structure with four cylindrical legs that are vertical at the waterline. The waterline geometry and orientation of the structure is shown in Figure 1. The tests were performed at a scaling factor of 32, leading to full-scale leg diameters of 7 m and a leg center-to-center spacing of 50 m. Table 1 shows the approximate floe size distribution.

Table 1. Floe size distribution; dimensions in model scale.

Percentage of ice Area [%]	45	40	15
Size [m]	0.5	1.0	1.5

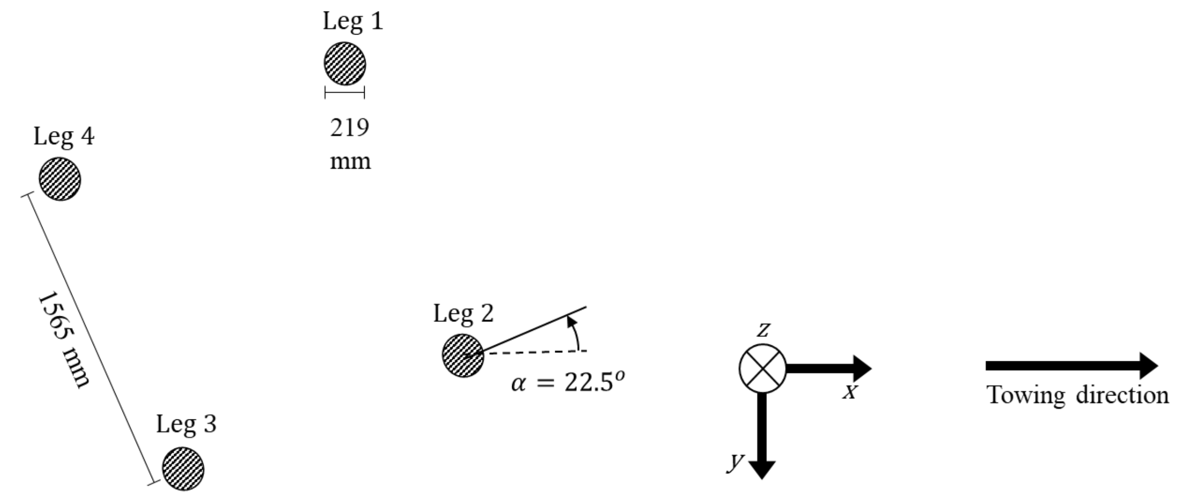

Figure 1. Waterline geometry and orientation of the structure, dimensions in model scale.

The analysed test run has a (reported) initial ice concentration of 60%. The numerical broken ice field is created by digitizing stitched top-view photos of the broken ice field used in the ice tank test. Figure 2 shows the stitched top-view photos of the broken ice field and the numerical reproduction of the ice field constructed from the stitched top-view photos.

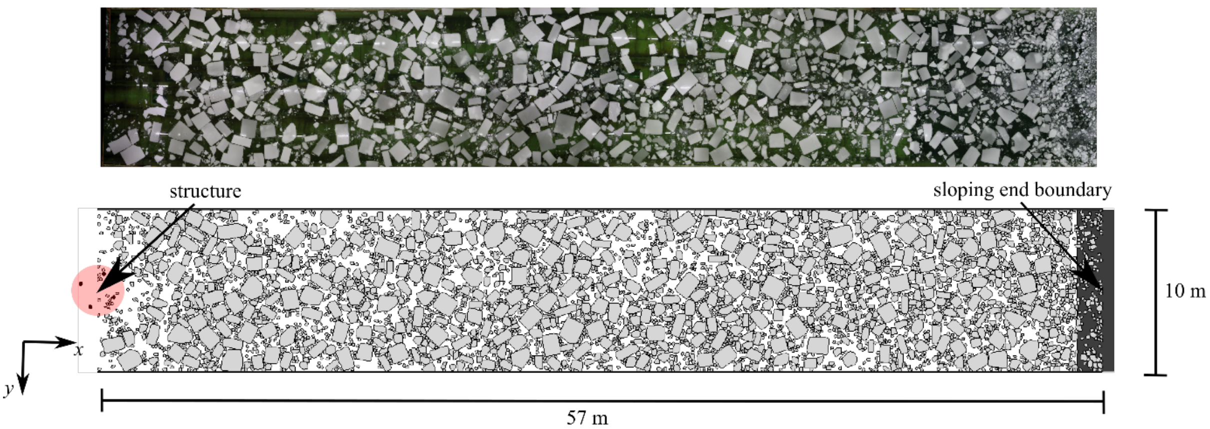

Figure 2. Stitched top view photos of the broken ice field (top) and a numerical reproduction of the ice field (bottom), showing the tank dimensions, axis system, and initial structure location.

The structure moved with a constant speed of 0.09 m/s for the first one third of the total test distance, and with a speed of 0.18 m/s for the remaining two thirds, resulting in an equal amount of test time at 0.09 m/s and 0.18 m/s.

The other simulation parameters are listed in Table 1. The ice flexural strength is based on values measured during the tests. The fracture toughness is based on measured values reported by (Dempsey et al., 1986) (not specifically for the model ice used in this test). The ice-ice friction coefficient is determined by calibrating the numerical model to another test case of the same test campaign. The procedure is described in detail in van den Berg et al. (2020). The crushing specific energy is the energy consumed in crushing a unit volume of ice. It is equivalent to the crushing pressure averaged over space and time. Its values is determined from tests with the same structure in level ice, as described in van den Berg et al. (2020).

Table 2. Simulation parameters.

Friction coefficient ice-ice	0.25
Friction coefficient ice-structure [-]	0.1
Ice form drag coefficient [-]	0.1, 0.5 (horizontal, vertical)
Ice skin friction drag coefficient [-]	0.005
Fracture toughness [$\mathrm{kPa}\sqrt{\mathrm{m}}$]	6.0
Crushing specific energy [$\mathrm{kJ/m^3}$]	30.0
Ice flexural strength [kPa]	60.0
Water density [$\mathrm{kg/m^3}$]	1020.0
Ice density [$\mathrm{kg/m^3}$]	900.0

In the numerical simulations, randomness was introduced in the initial position of the ice floes by initializing each floe with a uniformly distributed random horizontal velocity between 0 and 0.2 m/s. Floes moved with their random horizontal velocity for a period of 7 s, after which the velocity of all floes was set to zero and the structure propagation started. Floes could not fail, rotate or displace vertically during the randomization period.

4. Results

A selection of the 300 simulation results has been inspected visually and compared to the ice tank test recordings. Both in the simulations and in the ice tank test, the most important ice-structure interaction mechanisms are splitting failure of the ice, rafting of the ice, clearance of the ice around the structure, accumulation of the ice in front of the structure and the jamming of the ice between the structure legs. A snapshot showing jamming of ice between the structure legs in the simulation and the experiment is shown in Figure 3.

Figure 3. Jamming of ice between the structure legs in the numerical simulation (left) and in the ice tank test (right).

Figure 4 shows a time-domain comparison of the total absolute ice loads in x-direction ($|F_x|$) as a function of time. The numerical simulations with the lowest and highest mean loads among the 300 simulations are displayed together with the ice load measured during the ice tank test. Note that an exact match between the numerical results and ice tank test results should not be expected because of the chaotic nature of the interaction process; a small change in the beginning of the interaction may result in different conditions later in the test.

All numerical simulations capture the strong increase in ice load in the second half of the test. A consistent discrepancy between the numerically simulated ice loads and measured ice loads is a higher variability of the simulated loads, which can be quantified by calculating the ice load's autocorrelation. A visual comparison of the simulation results and the ice tank test recordings indicates that the lower autocorrelation might be caused by the discrete nature of ice rubble in the numerical simulations. Ice rubble is considered as discrete small ice bodies in the numerical simulations, while it appears more like a continuous slush in the experiment recordings. This is visible in Figure 3. The slush might have a smoothing effect on the measured ice loads.

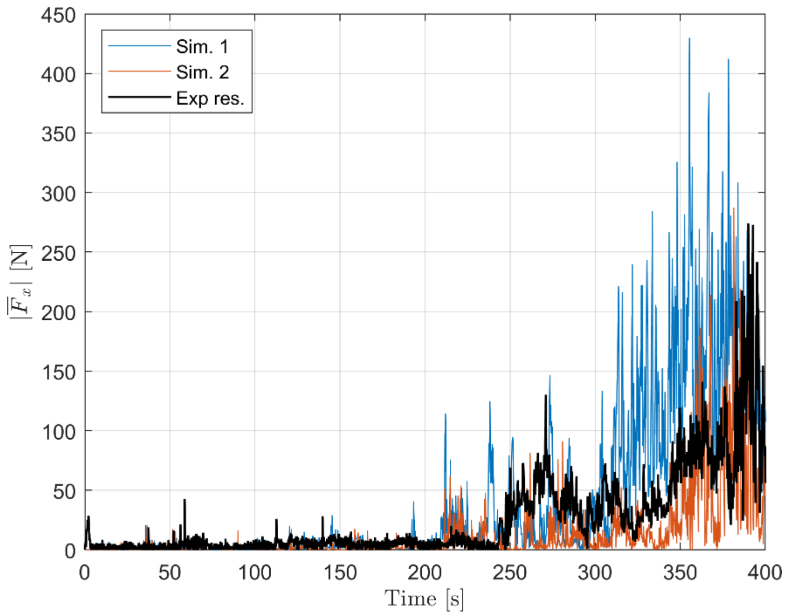

Figure 4. Time-domain comparison of the experimental result and two simulation results; simulation with the lowest mean load (sim. 1) and the simulation with the highest mean load (sim. 2).

The random uncertainty in the simulation results is assessed for the mean total ice loads in the low-velocity and high velocity segments of the test, respectively. The mean load is often one of the primary results of tests in broken ice. In the calculation of the mean loads, all load data measured while propagating at the low or the high velocity are considered. It is a common procedure in the processing of ice tank test data to discard the data at the start of the test and the data right after the velocity change, as the transient conditions may invalidate the measured data. However, the results of the numerical simulations presented in this study show that the assertion based on which the data are discarded may be an incorrect one for the analysed tests; the conditions remain transient throughout the test, and the transient nature is not limited to the test start and the velocity change. This is further discussed in the remainder of this section.

Figure 5 and Figure 6 show the histograms of the mean loads resulting from the 300 simulations performed for this study. The mean value of the measured load is displayed in reference to the simulated mean loads. The figures show the 95% confidence bounds of the mean loads derived from the numerical simulation results. The confidence bounds are derived by sorting the simulation results from low to high based on the mean simulated load, and taking the 8th result as the lower bound and the 392nd result as the upper bound. The confidence bounds and the mean values of the measured loads are listed in Table 2. The measured and simulated loads both include the hydrodynamic resistance of the structure. In the numerical simulations, the hydrodynamic resistance of the structure is assumed equal to the hydrodynamic resistance measured in open-water tests.

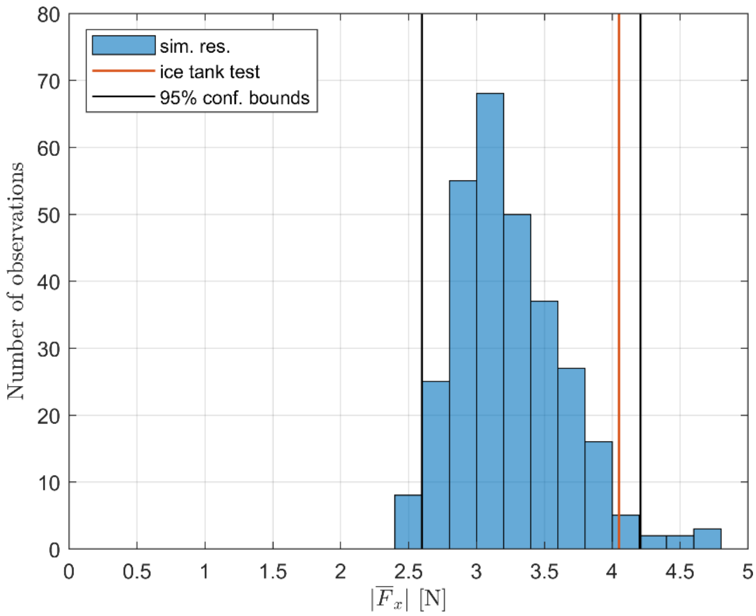

Figure 5. Histogram of mean loads resulting from the simulations of the low-velocity segment of the tests, showing the mean experimental load and the 95% confidence bounds.

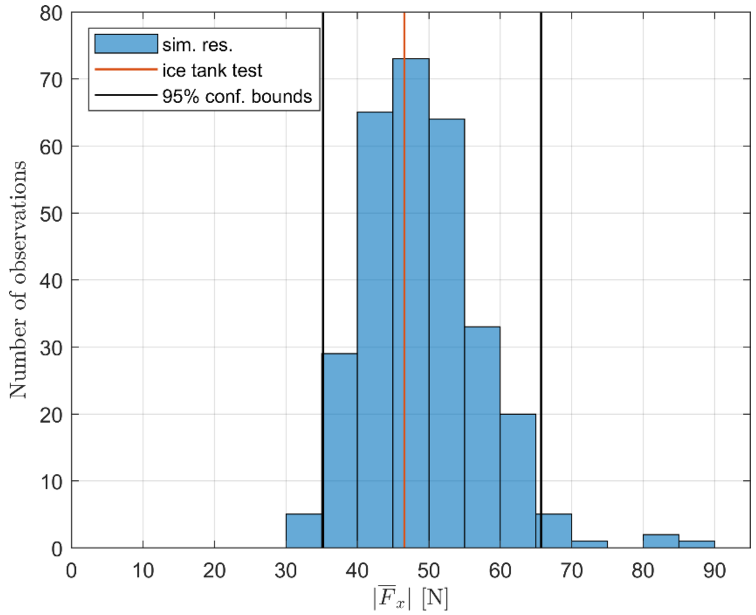

Figure 6. Histogram of mean loads resulting from the simulations of the high-velocity segment of the tests, showing the mean experimental load and the 95% confidence bounds.

The random uncertainty in the results is mainly related to differences in the floe accumulation process. In all numerical simulations, ice accumulated ahead of the structure, leading to an increase in ice concentration as the simulation progressed. The rate of accumulation is different for each simulation and depends on the specific floe positions.

Table 3. 95% confidence bounds of the mean loads in the low-velocity segment of the simulations and the high velocity segment of the simulations, respectively.

Velocity [m/s]	Simulation - 95% conf. Lower bound [N]	Simulation - 95% conf. Upper bound [N]	Ice tank test result [N]
0.09	2.6	4.2	4.0
0.18	35.2	65.7	46.7

Figure 7 demonstrates the effects of floe accumulation. It visualizes the stresses in the broken ice field using a body load value, which is calculated similar to Paavilainen and Tuhkuri (2013) as the maximum eigenvalue of load tensor $\hat{\alpha}_{\mathrm{ij}}$:

$$\hat{\alpha}_{ij} = \sum_{c=1}^{Nc} f_i^c r_j^c \quad \textbf{[1]}$$

in which N_c is the number of contacts of each floe, f_i^c are the contact force vectors, and r_j^c are normalized vectors from the body's centre of gravity to the contact point. The figure shows four top-view snapshots of ice-structure simulations. a and b show snapshots of the simulation with the highest mean load (sim. 1 in Figure 4) and c and d show snapshots of the simulation with the lowest mean load (sim. 2 in Figure 4). In the simulation with the highest mean load, more floes have accumulated ahead of the structure, leading to the occurrence of extensive force networks (also described as force chains, see Paavilainen and Tuhkuri (2013)) within the broken ice field from 310 s onwards. In the simulation with the lowest mean loads, it takes up to 352 second before extensive force networks start to occur.

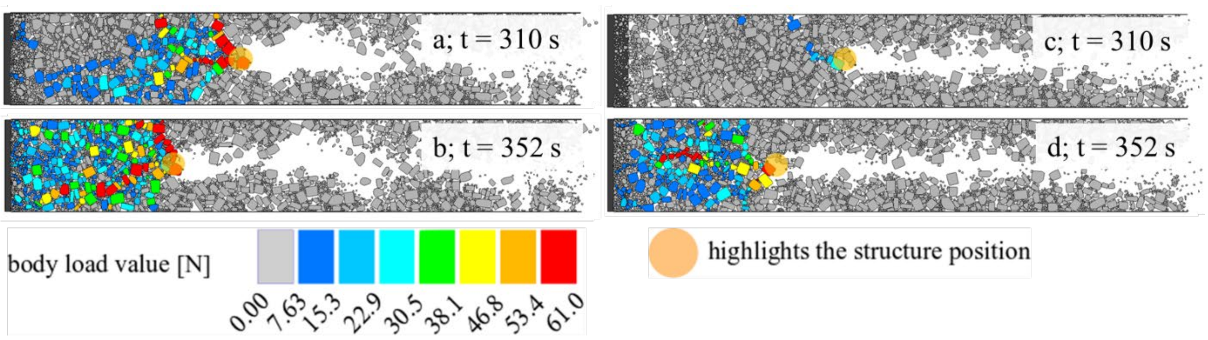

Figure 7. Stress state in the broken ice field; simulation with the highest mean load (left) and simulation with the lowest mean load (right).

The ice concentration development during the tests is analysed for the numerical simulation results. The aerial ice concentration is extracted from the simulation results for the region between the structure's centre of gravity and the end of the ice tank. The region over which the concentration is analysed, for a specific structure position, is visualized in Figure 8.

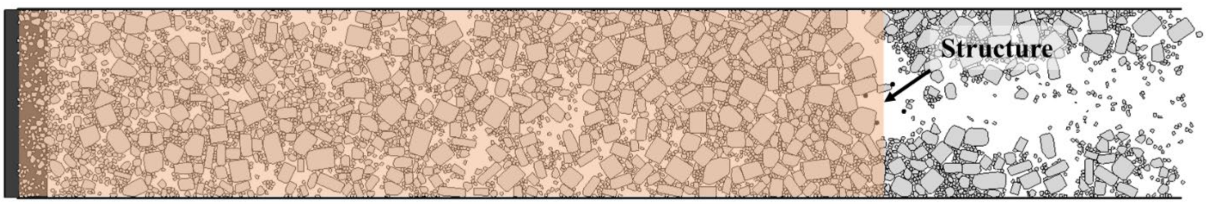

Figure 8. The orange area shows the region over which the ice concentration is calculated.

A similar analysis on the ice-tank test results is unfortunately not possible because there are no recordings available capturing the full domain. Figure 9 shows the development of ice concentration ahead of the structure as a function of structure displacement. In addition, it displays three theoretical displacement-concentration curves constructed using simplified assumptions on the ice accumulation and clearing process.

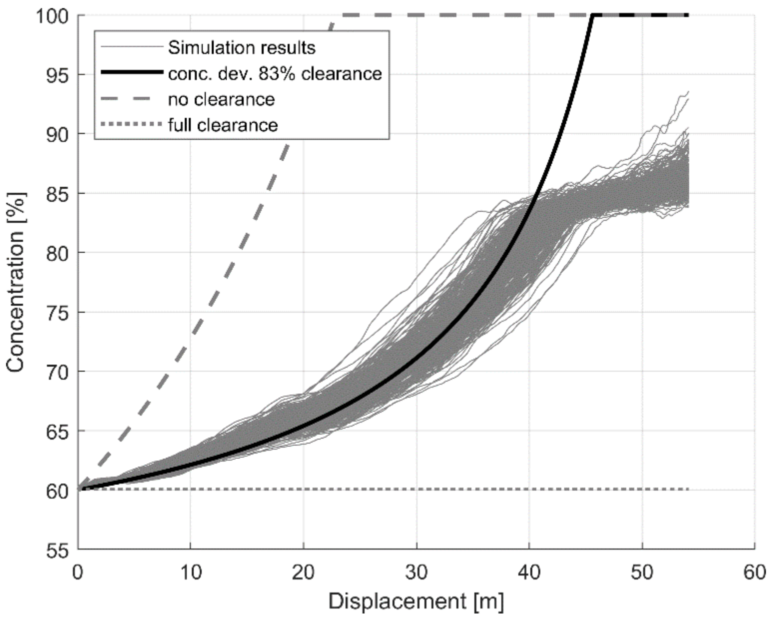

Figure 9. Ice concentration as a function of structure displacement in the numerical simulations, and theoretical concentration developments following from different clearing assumptions.

The simulation results show a consistent development of ice concentration as a function of structure displacement. In all simulations, the concentration increases relatively smoothly up to a concentration of ~83%. Above this concentration, the increase in concentration slows down considerably. The visual simulation results show that at a concentration of around 83%, the broken ice forms a continuous contact network between the structure and the end of the ice tank, leading to a strong increase in load. Similar results were observed by Comfort et al. (1999) and by Hopkins and Tuhkuri (1999) who both found a strong increase in ice loads around 80% concentration. The exact concentration at which a continuous contact network occurs depends on the ice floe shapes and size distribution.

The increase in ice concentration as a function of displacement is a result of the ice accumulation and clearing process. If, on average, the amount of ice 'clearing' around the structure is lower than the ice accumulating ahead of the structure, the ice concentration will increase (rafting will also influence the ice concentration, as the concentration is measured in terms of areal coverage in this study). Theoretical displacement-concentration curves are constructed using the following simplifying assumptions:

- The broken ice is evenly distributed over the domain.
- No rafting occurs.
- The ice clears with a constant concentration.

Using these assumptions, the ice concentration in the domain ahead of the structure c_s can be describes as:

$$c_s = \frac{L \cdot c_i - D \cdot c_c}{L - D} \quad \textbf{[2]}$$

In which L is the total domain length, c_i is the initial ice concentration, D is the structure displacement and c_c is the concentration of the ice clearing around the structure. Assuming that all ice clears ($c_i = c_c$), the ice concentration remains constant, resulting in the dotted line in Figure 9. If no ice clears around the structure, the ice concentration develops as indicated by the dashed line in Figure 9. The simulation results roughly coincide with a clearing concentration c_c of 50%, thus 83% $(50/60 * 100)$ of the accumulating ice clears around the structure.

Clearly, this idealization is a simplification of reality. Comparing the simulation results to the theoretical curve, it appears that at the beginning of the simulations the ice clears less than the theoretical curve, leading to a stronger increase in concentration, while later in the simulations the ice clears at a higher rate than the theoretical curve, leading to a weaker increase in concentration. Nevertheless, it is interesting to observe that a consideration of concentration development based on an assumption of a constant ice clearing concentration matches the simulated concentration development relatively well.

5. Discussion

The numerical simulation results give 95% confidence bounds of the mean loads of 2.6 – 4.2 N for the low-velocity segment of the simulation (the first half) and 35.2 – 65.7 N for the high-velocity segment of the simulation (the second half). A crucial question is if the random uncertainty observed in the numerical simulations is representative of the random uncertainty that may occur in physical ice-tank tests. Clearly, this can only be proven by performing multiple repetitions of the same physical test. However, the validity of random uncertainty predicted by the numerical simulations can be further substantiated by examining the mechanisms leading to the random uncertainty and performing a comparison against the observations made in the ice tank tests. From such a comparison, and the result analysis as discussed in van den Berg et al. (2020), the following observations are made:

- The random uncertainty in the numerical simulation results is caused by differences in the ice accumulation process, leading to different developments of the ice concentration ahead of the structure.
- In the ice-tank tests, the ice concentration in the test domain ahead of the structure (as shown Figure 8) was not captured. However, it can be concluded from the measured load time series, from local observations of the ice concentration and from the ice-structure interaction process that a significant concentration increase also occurred during the experiments.
- The mechanisms influencing the ice accumulation process in the numerical simulations, such as the jamming of ice between the structure legs and the subsequent clearing of the jammed ice, occur also in the ice tank tests. This can be observed in the ice tank test recordings.

Considering these observations, it is expected that a random uncertainty similar to the random uncertainty observed in the numerical results would also occur in the physical test results if an ice-tank test similar to the one analysed in this study would be repeated several times.

Independent from the random uncertainty, the strong concentration change as observed in the simulations is identified as a factor that compromises the usefulness and validity of the analysed ice tank test with broken ice.

6. Conclusions

The random uncertainty in the results of ice tank tests with broken ice was investigated by performing 300 numerical simulation of the same test, with different initial floe positions but otherwise identical simulation properties. The simulations results show that the 95% confidence bounds of the mean ice loads as predicted by the numerical simulations are 2.6 – 4.2 N for the low-velocity segment of the simulation (the first half) and 35.2 – 65.7 N for the high-velocity segment of the simulation (the second half). The mean loads measured in the ice tank test fall within these confidence bounds. An analysis of the processes leading to the random uncertainty indicates that a similar random uncertainty could occur in the ice-tank if the ice- tank test analysed in this study would be repeated several times. Whether the random uncertainty as predicted by the numerical simulations would be acceptable depends on the aims of the tests. However, it should always be considered in the interpretation and subsequent usage of ice-tank test results that there may be a high random uncertainty in the measured ice load values. Separate from the random uncertainty, the continuous increase in ice concentration ahead of the structure is identified as a factor potentially compromising the validity and usefulness of the test results.

Acknowledgments

The authors would like to acknowledge the support of the SAMCoT CRI through the Research Council of Norway and all of the SAMCoT Partners. The analysed ice-tank tests were supported by the European Community's 7th Framework Program through the grant to the budget of the Integrated Infrastructure Initiative HYDRALAB-IV, Contract no. 261520.

References

Comfort, G., Singh, S., Spencer, D., 1999. Evaluation of Ice Model Test Data for Moored Structures - PERD/CHC Report 26-195, pp. 1-77, 1999-04.

Dempsey, J.P., Bentley, D.L., Sodhi, D.S., 1986. Fracture toughness of model ice, in: Proceedings 8th IAHR Symposium on Ice. Iowa City, Iowa, pp. 365–376.

Hopkins, M. a., Tuhkuri, J., 1999. Compression of floating ice fields. J. Geophys. Res. 104, 15815–15825. https://doi.org/10.1029/1999JC900127

Hoving, J.S., Vermeulen, R., Mesu, A.W., Cammaert, G., 2013. Experiment-Based Relations between Level Ice Loads and Managed Ice Loads on an Arctic Jack-Up Structure. Proc. 22nd Int. Conf. Port Ocean Eng. under Arct. Cond.

ITTC, 2005. ITTC – Recommended Procedures and Guidelines Experimental – Uncertainty Analysis for Ship Resistance in Ice Tank Testing. Qual. Syst. Gr. 28th ITTC.

Lu, W., Lubbad, R., Løset, S., 2015a. In-plane fracture of an ice floe: A theoretical study on the splitting failure mode. Cold Reg. Sci. Technol. 110, 77–101.

Lu, W., Lubbad, R., Løset, S., 2015b. Out-of-plane failure of an ice floe: Radial-crack-initiation-controlled fracture. Cold Reg. Sci. Technol. 119, 183–203.

Lu, W., Lubbad, R., Shestov, A., Løset, S., 2018. Parallel channels' fracturing mechanism during ice management operations. Part I: Theory. Cold Reg. Sci. Technol. https://doi.org/https://doi.org/10.1016/j.coldregions.2018.07.010

Lubbad, R., Løset, S., Lu, W., Tsarau, A., van den Berg, M., 2018. An overview of the Oden Arctic Technology Research Cruise 2015 (OATRC2015) and numerical simulations performed with SAMS driven by data collected during the cruise. Cold Reg. Sci. Technol. 156, 1–22.

Paavilainen, J., Tuhkuri, J., 2013. Pressure distributions and force chains during simulated ice rubbling against sloped structures. Cold Reg. Sci. Technol. 85, 157–174. https://doi.org/10.1016/j.coldregions.2012.09.005

Tsarau, A., 2015. Numerical Modelling of the Hydrodynamic Effects of Marine Operations in Broken Ice. Norwegian University of Science and Technology.
van den Berg, M., Lubbad, R., Løset, S., 2020. Repeatability of ice-tank tests with broken ice. Mar. Struct. 74, 102827. https://doi.org/https://doi.org/10.1016/j.marstruc.2020.102827
van den Berg, M., Lubbad, R., Løset, S., 2018. An implicit time-stepping scheme and an improved contact model for ice-structure interaction simulations. Cold Reg. Sci. Technol. 155, 193–213. https://doi.org/https://doi.org/10.1016/j.coldregions.2018.07.001

IAHR AIRH

25th IAHR International Symposium on Ice

Trondheim, June 14 to 18, 2020

Sheltering Effect in the Wake of a Ridge Keel in Homogeneous and Stratified Flows

Yongheng Zu, Peng Lu*, Zhijun Li

Dalian University of Technology

No.2 Linggong Road, Ganjingzi District, Dalian City, Liaoning Province, P.R.C., 116024

lupeng@dlut.edu.cn

Abstract: The two-dimensional flow structure in the wake of a ridge keel was investigated in this paper. The laboratory experimental results of two-component Particle Image Velocimetry (PIV) data are compared with numerical simulations. Vortex shedding area is linearly increased with keel depth and slope angle in both uniform and two-layer flow. And there is a flow velocity decay zone in the wake which is related with the location of vortex center. For the laminar region, we use the results to obtain a skin friction relationship; For the turbulent region, we obtain the velocity decay function of a 45º wedged shape model. The results of the present study provide a priori recommendations for the sheltering function in the parameterization scheme of ice-ocean drag coefficient.

Key words: drag coefficient; ridge keel; vortex; sheltering effect

Introduction

The momentum flux from atmosphere to ocean plays an important part in the Arctic climatology model. The cover of sea ice alters boundary conditions of Atmosphere Boundary Layer (ABL) and Ocean Boundary Layer (OBL) due to the characteristics of sea ice morphology. Sea ice drag coefficient reflects momentum fluxes exerted by atmosphere and ocean. In the parameterization scheme of drag coefficient, skin drag and form drag are considered respectively. Arya (1973) finds that the form drag on pressure ridges is much larger than the shear stress on the ice surface. Garbrecht et al. (1999) present a case study of the flow around of a single pressure ridge and propose a formulation for the determination of the form drag of a single pressure ridge based on the ridge height. Birnbaum and Lupkes (2002) use the approach to calculate the form drag by the friction velocity in the ABL and roughness parameters of ice floes. Thus the morphology parameters of ice surface, including ice concentration, ice draft and ridge density, have taken into account in the parameterization scheme of form drag.

Pressure ridges is a type of deformed ice due to the pressure mechanical action. Different from other small roughness of ice surface, the influence of pressure ridge on momentum flux is mainly reflected in form drag, and other small roughness affects skin drag. The classification of these roughness is identified by the cutoff height which is lower than pressure ridges height. (Tan et al., 2012) Using the Rayleigh criterion, the distribution of sail heights and keel depths are obtained respectively from aeronautic laser profiles and submarine sonar profiles. (Lowry and Wadhams, 1979; Lepparanta, 1981; Wadhams and Davy, 1986) Thus we can obtain the pressure ridge drag coefficient combined with the individual pressure ridge effect and the distributions of ridge heights and spacings (Lu et al, 2011; Lupkes et al, 2012; Tan et al, 2017).

The sheltering effect of an individual ridge keel on the flow induce a vortex wake in the ridge leeward area. Numerous investigations have been conducted to improve the understanding of airfoil vortex structure which is influenced by wings attack angle and shape models. (Wu, 1986; Birch et al, 2004; DelPino et al., 2011) Similar to the wings conditions, the sheltering effect of a ridge keel considers the strength of vortex along the flow direction and the velocity profiles in the downstream vicinity of ridge keels. Hoerner (1965) investigate a pair of circular cylinders in the turbulent flow and the drag of rear one is evidently reduced due to the vortex shedding on the downstream side of the former. HanssenBauer (1988) assumes that wind profile decays with negative exponential relationship as distance from the obstacle increases and obtain the aerodynamic form drag coefficient resulting from the reduction of wind pressure on the ice edge. Steele et al. (1989) suggest that the strength of a wake reduces with $x^{-1/2}$, where x is distance away from the object.

These methods are adopted in recent parameterization schemes of sea ice drag coefficient. (Lu et al., 2011; Tsamados et al., 2014) However, the above assumptions are originally applied to floe edges, not pressure ridges. And wake flow structure mainly depends on the size and shape of the body. The objective of this work is to investigate the turbulent wake flow structure after an independent ridge keel. We use the wedged shape obstacle to simulate the ridge keel in the laboratory environment. The paper is organized as follows, section 2 introduces the laboratory experimental setup and numerical model and discusses the validity between laboratory experiments and numerical simulations. In section 3, we present vortex shedding velocity field results of a ridge keel. Then we use the numerical model to obtain the decayed velocity profiles of the turbulent wake flow in section 4. Conclusions are made in section 5.

Model Setup

The physical experiments were conducted at the Particle Image Velocimetry (PIV) flume, which is 0.45m long, 0.23m wide and 0.45m deep. In the homogeneous fluid experiment, the flume is full of fresh water with 0.35m depth. And in the stratified fluid experiment, fresh water is added to the flume and then saline water is added to form the upper and lower layers. The upper layer is 0.15m deep and the lower layer is 0.2m deep. The ridge keel model was made of perspex, with a cross-section of wedged shape. A movable tractor used to fix the ridge keel model were installed along the track on the flow flume, and the platform was linked to an electric motor by a wire rope, so that the velocity of the platform can be changed by turning the rotation rate of the motor. The force tensor is combined with motor and tractor. The draft of ridge keel model into water can be altered by changing the installation height of the model on the tractor. The flume and keel model are shown on Figure 1 and experiment parameters are listed in Table 1. Details of the physical modeling can refer to Li et al. (2015).

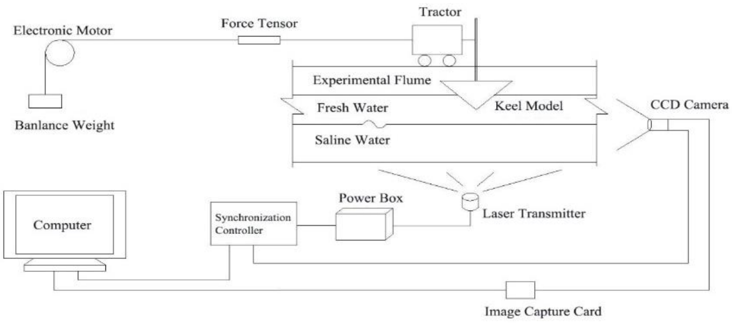

Figure 1 Sketch of experimental flume and PIV system

Table 1. Parameters used in experiments

Parameters		Symbols	Values	Units
Flume	dimensions	$L \times W \times H$	4.4×0.23×0.45	m
Ridge keel	slope angle	θ	20,45,60	°
	keel depth	h	0.04-0.1	m
	towing speed	U	0.01-0.3	m/s
Fluid 1	depth	h_1	0.15	m
	density	ρ_1	998.2	kg/m3
	viscosity coefficient	μ_1	1.003×10^{-3}	kg/(m·s)
Fluid 2	depth	h_2	0.2	m
	density	ρ_2	1025	kg/m3
	viscosity coefficient	μ_2	1.12×10^{-3}	kg/(m·s)

As a comparative experiment, numerical experiments also simulate the motion of the ridge keel in the homogeneous fluid and the stratified fluid. Considering the symmetry of the flow field and the slight variations along the width of floe model, the simulation is simplified to a two-dimensional flow problem. That is, the vertical cross section along the length of the flume is chosen as the computational domain of the numerical simulation, which is shown on Figure 2. To ensure a fully developed wake flow in the lee side of the ice floe, the ridge model is placed at the 1/3 length of the flume, agreeing with the general conditions for a fully developed wake flow. In the computational domain, AG is the water inlet, and it has a uniform velocity distribution, so a velocity inlet boundary condition is applied at AG. Boundary BC, CD, FG are solid walls and no-slip wall boundary conditions are used. The outlet EF is described by the free out-flow condition, on which the flow rate can be fully developed because the wake flow region behind the ice is long enough. A rigid lid assumption is employed for the free surface AB and DE, taking them as symmetry surfaces, namely free-slip walls. We choose the typical cases with angle of 45° computed for grid independency study. When the space size is between 0.5cm and 0.9cm, the calculation results are stable. We choose 0.5cm as the final space size.

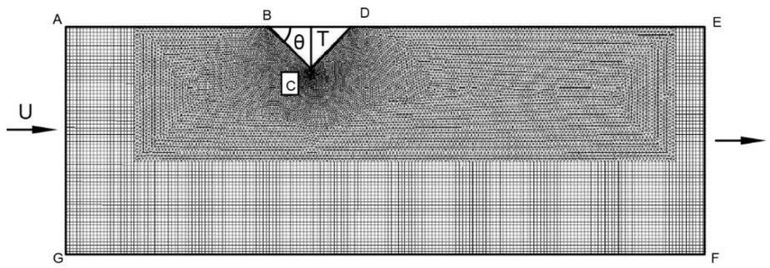

Figure 2 Numerical computational domain and U is fluid velocity, θ is keel slope angle, and T is keel depth into water. In the vicinity of keel, there are unstructured grids.

The control equation calculated by the flow field is the k-ε turbulence model based on the Reynolds stress average equation. For the RNG k-ε two equation model, C_μ=0.0845, $C_{1\varepsilon}$=1.42, $C_{2\varepsilon}$=1.68, α_ε=α_k=1.39. The control equation of numerical simulation adopts first-order implicit integration in the temporal discretization, and the second-order upwind scheme is adopted in the spatial discretization. The pressure-based solver for homogeneous fluid chooses SIMPLEC algorithm. In the stratified fluid simulation, the model belongs to multi-phase flow and the solver need to calculate transient flow field information. And the PISO coupling algorithm is chosen. The motion of ice ridge adopts dynamic mesh module, which is solved by using the layering scheme. The Volume of fluid (VOF) model is applied for the tracking of the interface of stratified fluid, and the interpolation near the interface selects geometric reconstruction approach. This is also a more accurate interface tracking method at present, which is recommended by most transient VOF calculations.

Results

We obtain drag force results and velocity field information around the keel. For force results, the Reynolds number Re and the drag coefficient C_d are defined as follow:

$$Re = \frac{UL}{\upsilon},\ C_\text{d} = \frac{D}{2\rho U^2 Lb} \quad [1]$$

Where U is the keel velocity, L is the keel base length and varied with the keel depth T into water, υ is the fluid kinematic viscosity coefficient and here υ=1.003×10^{-6}m^2/s, ρ

is the fluid density and here ρ=10^{3}kg/m^3, and b is the keel transverse length.

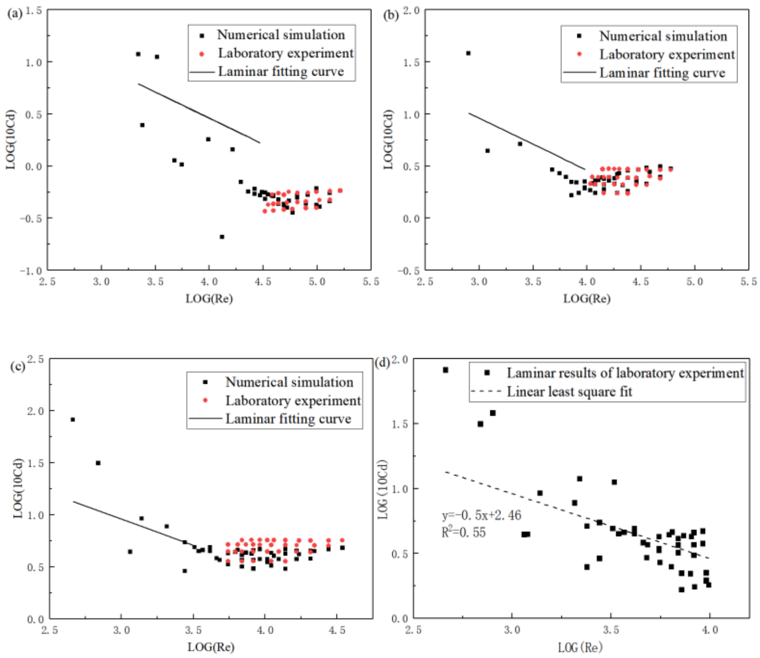

Figure 3 plots of C_d with Re, red dots represent numerical results and black squares represent laboratory results. The black line at (d) is fitting curve by linear least squares regression with formula LOG(C_d)=-0.5LOG(Re)+2.46 and the square of correlation coefficient R^2=0.44. The keel slope angle θ is (a) 20º, (b) 45º and (c) 60º.

The above results are obtained in the homogeneous fluid experiments. It's shown in Fig. 3 that experiments cover full range from laminar flow to turbulent flow. For laminar flow, viscous stress dominates the drag force of a keel. In the surface boundary layer, the friction coefficient of a flat plate is related to the Reynolds number $Re^{-0.5}$. Hoerner (1965) has sorted out the results of previous experiments and get the formula with C_d=1.328$Re^{-0.5}$. In Pite's (1995) keel model experiments, the data without flow separation are well fitted by a laminar skin friction relationship of the form C_d=2.8$Re^{-0.5}$ and the coefficient is about twice that a flat plate. We obtain similar results with Pite's results in laminar flow, C_d=24.5$Re^{-0.5}$, using the linear least square regression of physical data. This result is lager than Pite's formula due to the fact that our keel model is wedged shape not the streamline model.

The comparison between numerical and the physical experiments shows that the results of laminar flow are somewhat different because the numerical simulation solver uses a turbulence model. In the turbulent region, as the keel slope angle θ increases, the mean value of the drag coefficient also increases. The numerical simulation results agree with the physical model experiments, and they all fluctuate with the keel depth in a small range. In next section, we will analyze the sheltering effect using numerical model results.

In addition to the results of the homogeneous flow experiment, the stratified flow has similar laws in the laminar region. However, as the generation of internal waves, additional resistance will be generated. The drag coefficient of the stratified flow will increase under the same conditions. When the internal wave is far away from the ridge keel, the drag coefficients of the stratified flow will tend to be the same as homogeneous flow. Details about the drag coefficient of stratified flow can refer to Zu et al. (2019).

C_d is no longer associated with *Re* in turbulent flow. Then the streamlines around the keel model are no longer smooth, and a vortex wake is formed in the lee side. The pressure in the vortex zone is lower than the pressure at the same horizontal level in front, and the form drag force created by the pressure difference is much greater than the skin friction drag force. The variation of C_d with D/h when $U = 0.15$ m/s and $\alpha = 45^\circ$ is shown in Fig. 5a as an example. In other cases of constant U and α, the variation of C_d with D/h are all similar in turbulent flow.

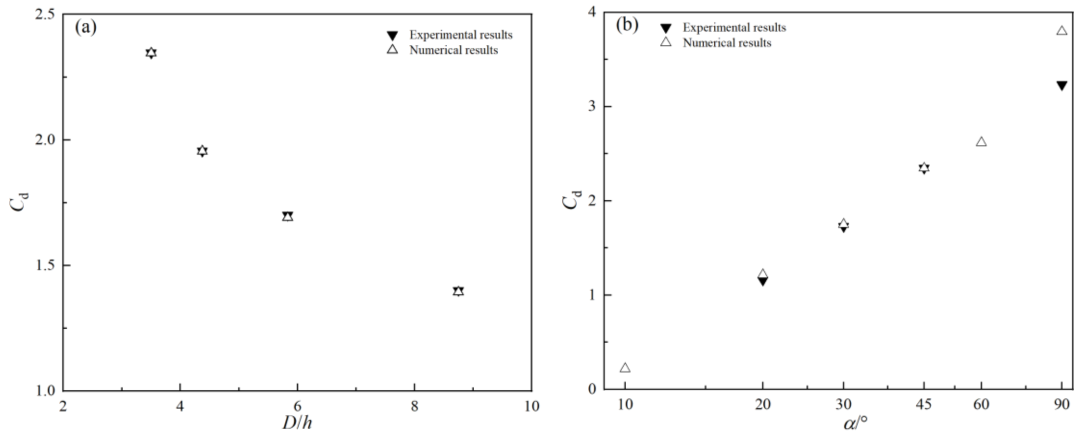

Figure 4 The variation of C_d with (a) D/h (h=4cm, 6cm, 8cm and 10cm) when U=0.15m/s and α=45˚ and (b) α (10˚≤α≤90˚) when U=0.15m/s and h =10cm in experimental and numerical results

It is clear from Fig. 4a that C_d decreases with D/h. The total drag force is determined by the size and shape of the keel model, which decides the distribution of pressure around the keel. Physical experiments were conducted in the tank with finite depth. For the flow past the keel, there was a sheltered area behind the keel (Garbrecht et al., 1999). With the increase of h, the flow passage channel will become narrower. The upstream–downstream pressure difference $\triangle p$ is proportional to $0.5\rho\triangle U^2$ according to the Bernoulli equation in fluid dynamics. According to the law of mass conservation, we have that $0.5\triangle U^2 = 0.5(h/(D\text{-}h))^2U^2$. Consequently, $C_d \sim \triangle p/\rho U^2 = 0.5/(D/h\text{-}1)^2$. Based on the inviscid flow theory, the increase of C_d with D/h is nonlinear especially when $2 < D/h < 10$ (Fig. 4a). As D increases, the influence of h on C_d weakens with $C_d \to 1.2$ for $D >> h$. In real conditions, the depth of the mixed layer is an order of magnitude greater than the keel depth. Thus, the keel movement in a deeper tank would be more appropriate but by scaling analysis our results are well applicable to nature scale conditions.

For U=0.15m/s and h=10cm, then $Re > 10^5$ and the flow is fully turbulent for all keel shapes. Fig. 4b shows that C_d increases linearly with $\ln(\alpha)$. The slope angle α is a key parameter of the keel shape for the influence on C_d. It is ob vious that the numerical results agree well with the physical experiments in the turbulent regime.

Analysis

In the physical model experiment, the velocity field information near the ridge keel is obtained by the PIV system, and then compared with the turbulent velocity field information obtained by numerical simulation.

Figure 4,5 and 6 show streamlines in the vicinity of keels of different slope angle. It's obvious that a shedding vortex is formed in the lee side of the keel. With the increase of the slope angle of the ice ridge, the affected area of the flow field and wake field gradually increased. The existence of ice ridges makes the cross-section under ice narrow, so the velocity under ice increases. Compared with homogeneous fluid in similar condition, the vortex area in the stratified fluid tends to be narrow due to that the peak of internal wave also is a vortex.

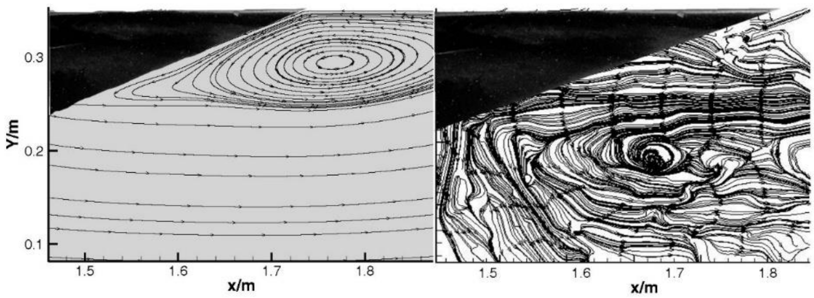

Figure 5 Comparison of streamlines between numerical simulation (left) and laboratory experiment (right) in homogeneous fluid with θ=20º, T=0.1m and U=0.08m/s.

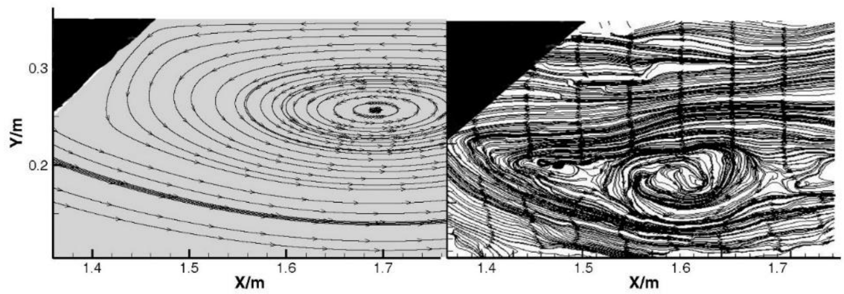

Figure 6 Comparison of streamlines between numerical simulation (left) and laboratory experiment (right) in homogeneous fluid with θ=45º, T=0.1m and U=0.08m/s.

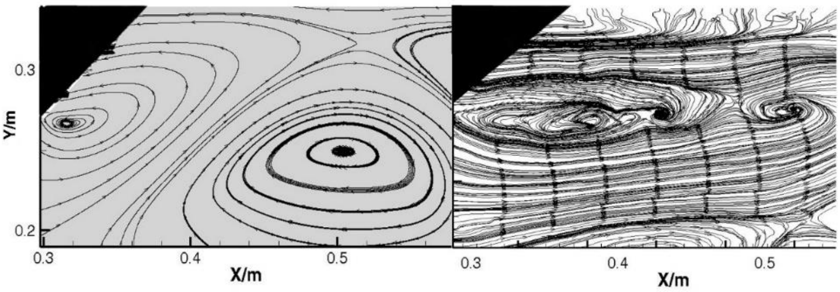

Figure 7 Comparison of streamlines between numerical simulation (left) and laboratory experiment (right) in stratified fluids with θ=45º, T=0.08m and U=0.07m/s.

In order to study the effect of sheltering vortex on velocity profiles, we use the average dynamic pressure over the vertical distance to describe the attenuation of velocity profiles. The dynamic pressure p_{dyna} is defined as follow form:

$$p_{dyna} = \frac{1}{2}\rho(u^2 + v^2) \qquad [2]$$

Where u and v are fluid velocity components at x and y direction. p_{dyna} represents the momentum flux in the fluid. (Garbrecht et al., 1999) As shown in Fig. 6, there is a velocity decay region in the lee side of the keel. Figure 8 and 9 are results in homogenous fluid, and with the increase of keel depth, the difference of dynamic pressure around the keel is growing but field structures are similar. In stratified fluids, the fluid's momentum flux is not only transmitted to the ice ridge, but also maintains the generation of internal waves. However, as keel depth increases, the momentum distribution of fluid near the ice ridge tends to that of homogeneous fluid.

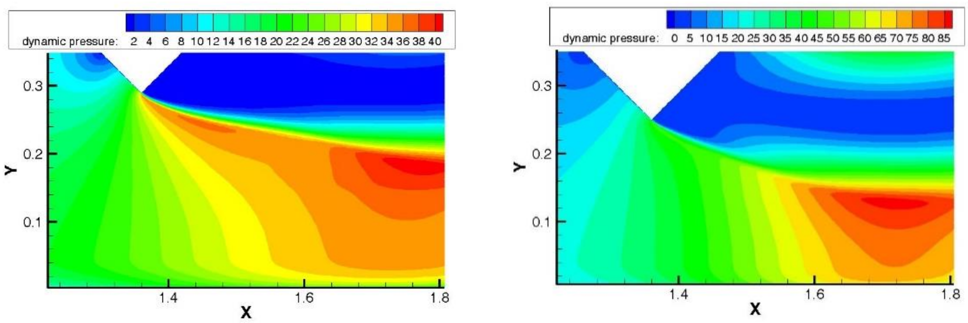

Figure 8 Comparison of dynamic pressure (unit: Pa) contours between T=0.06m (left) and T=0.1m (right) with θ=45º, U=0.18m/s in homogeneous fluid

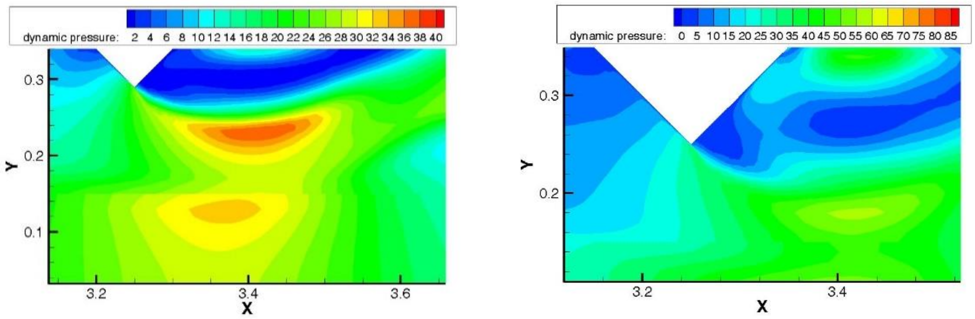

Figure 9 Comparison of dynamic pressure (unit: Pa) contours between T=0.06m (left) and T=0.1m (right) with θ=45º, U=0.18m/s in stratified fluids

For the convenience of quantitative analysis of velocity decay, we use the average dynamic pressure p_{ave} of the vertical section and p_{ave} is defined as follow:

$$p_{ave} = \frac{1}{T}\int_{-T}^{0} p_{dyna} dy \tag{3}$$

We can obtain the variation of p_{ave} with the distance away from the keel x. By dimensionless processing, the velocity decay function is shown in Fig. 7. HanssenBauer (1988) uses that velocity profile decays with negative exponential relationship with s=0.18:

$$\frac{u}{U} = 1 - \exp(-sX/T) \tag{4}$$

Where u is the velocity in decay region and U is the undisturbed velocity upstream, X/T is dimensionless distance and here we adopt keel depth as T. s is an empirical parameter that is related to the sheltering area. In our 45º wedged shape numerical simulations, s is 1.9 which results in smaller sheltering effect than before. (Lupkes et al., 2012)

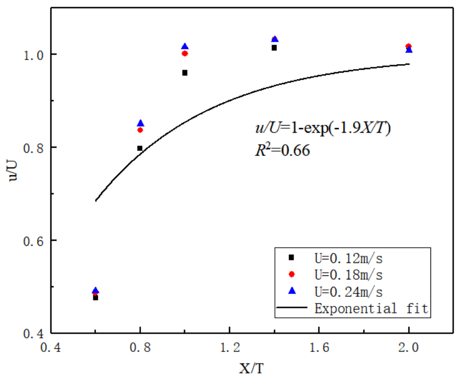

Figure 9 Velocity decay function of u/U vs. X/T with θ=45º

Conclusions

Laboratory experiments and numerical simulations are conducted to study the keel motion in homogeneous and stratified fluids. The momentum flux from fluid to keel model is concentrated by the drag coefficient C_{d}. The results of numerical simulation agree well with laboratory data in turbulent region. For the laminar region, we use the physical results to obtain a skin friction relationship, C_d=24.5$Re^{-0.5}$.

For the turbulent region, the velocity fields between two type experiments have similar structure. A shedding vortex is formed in the lee side of the keel, and velocity decays in this area. We obtain the velocity decay function of a 45° wedged shape model, u/U=1-exp(-1.9X/T).

The results obtained here are obtained from laboratory experiments and numerical simulations. Based on the parameterization concept, we study parameters about the keel drag. In future work, these parameters varied with real ocean conditions should be studied to establish accurate parameterization scheme of sea ice drag coefficient.

Acknowledgements

This research was supported by the National Key R&D Program of China No 2017YFE0111400, National Natural Science Foundation of China (Grant No. 41922045 and 41876213), and the Fundamental Research Funds for the Central Universities.

References

Arya, S. P. S. "Contribution of form drag on pressure ridges to the air stress on Arctic ice." Journal of Geophysical Research 78.30 (1973): 7092-7099.

Birch, D., et al. "Structure and induced drag of a tip vortex." Journal of Aircraft 41.5 (2004): 1138-1145.

Birnbaum, Gerit, and Christof Lüpkes. "A new parameterization of surface drag in the marginal sea ice zone." Tellus A: Dynamic Meteorology and Oceanography 54.1 (2002): 107-123.

Del Pino, C., et al. "Structure of trailing vortices: Comparison between particle image velocimetry measurements and theoretical models." Physics of Fluids 23.1 (2011): 013602.

Garbrecht, Thomas, et al. "Influence of a sea ice ridge on low - level airflow." Journal of Geophysical Research: Atmospheres 104.D20 (1999): 24499-24507.

HANSSEN - BAUER, I. N. G. E. R., and Yngvar T. Gjessing. "Observations and model calculations of aerodynamic drag on sea ice in the Fram Strait." Tellus A 40.2 (1988): 151-161.

Hoerner, Sighard F. "Fluid Dynamic Drag, published by the author." Midland Park, NJ (1965): 16-35.

Lepparantam, M. Statistical features of sea ice ridging in the Gulf of Bothnia, Winter Navig. Res. Board Helsinki, Tech. Rep. 32(1981), 46 pp.

Li, B, Wu, Y, and Lu, P (2015). “Study on the ice ridge drag coefficient in stratified flow,” Proc 17th China Ocean Offshore Eng Symp, Nanning, China, 317-321. (in Chinese)

Lowry, R. T., and P. Wadhams. "On the statistical distribution of pressure ridges in sea ice." Journal of Geophysical Research: Oceans 84.C5 (1979): 2487-2494.

Lu, Peng, et al. "A parameterization of the ice‐ocean drag coefficient." Journal of Geophysical Research: Oceans 116.C7 (2011).

Lüpkes, Christof, et al. "A parametrization, based on sea ice morphology, of the neutral atmospheric drag coefficients for weather prediction and climate models." Journal of Geophysical Research: Atmospheres 117.D13 (2012).

Pite, H. D., D. R. Topham, and B. J. Van Hardenberg. "Laboratory measurements of the drag force on a family of two-dimensional ice keel models in a two-layer flow." Journal of Physical Oceanography 25.12 (1995): 3008-3031.

Steele, Michael, James H. Morison, and Norbert Untersteiner. "The partition of air‐ice‐ocean momentum exchange as a function of ice concentration, floe size, and draft." Journal of Geophysical Research: Oceans 94.C9 (1989): 12739-12750.

Tan, Bing, et al. "A novel strategy to analyse the form drag on pressure ridges and the air–ice drag coefficient in the north-western Weddell Sea." Applied Mathematical Modelling 58 (2018): 158-165.

Tan, Bing, et al. "Morphology of sea ice pressure ridges in the northwestern Weddell Sea in winter." Journal of Geophysical Research: Oceans 117.C6 (2012).

Tsamados, Michel, et al. "Impact of variable atmospheric and oceanic form drag on simulations of Arctic sea ice." Journal of Physical Oceanography 44.5 (2014): 1329-1353.

Wadhams, Peter, and Tom Davy. "On the spacing and draft distributions for pressure ridge keels." Journal of Geophysical Research: Oceans 91.C9 (1986): 10697-10708.

Wu, J., J. Hackett, and D. Lilley. "A generalized wake-integral approach for drag determination in three-dimensional flows." 17th Aerospace Sciences Meeting. 1979.

06
Waves in ice

25th IAHR International Symposium on Ice
Trondheim, 23 - 25 November 2020

Numerical simulation of the interaction between the plane wave and a shore-connecting ice plate

Ni Bao-Yu*, He Kang-Jian, Hu Wen-Jin, Zeng Ling-Dong
College of Shipbuilding Engineering, Harbin Engineering University, Harbin 150001, P. R. China
nibaoyu@hrbeu.edu.cn

Based on Fluid-Structure Interaction (FSI) model, the interaction between a plane wave and a shore-connecting ice plate was studied by using CFD method. Firstly, the numerical wave tank model was constructed to simulate the wave-making and wave-eliminating. The numerical results were compared with theoretical results to verify the accuracy of numerical water tank. On this basis, the shore-connecting ice plate was simplified as rigid and elastic plate, respectively, and interacted with the incident wave. The hydrodynamic forces were both obtained and the structural response of the elastic ice plate was obtained directly. On the other hand, the rigid ice was further assumed as a cantilever beam and its stress was obtained by adding the hydrodynamic forces on its surfaces. In this way, the responses between rigid and elastic ice plates were compared. The response characteristics of different ice models in waves were obtained, which was expected to provide references for ship navigation in ice zone from the perspective of external loads.

1. Introduction

Due to the global warming, the arctic sea ice melts more, which leads to the rise number of ice plates around Marginal Ice Zone. On the one hand, the interaction between wave and ice is of great scientific meaning, which is helpful of the development of fluid mechanics (Squire et al., 1995). On the other hand, the interaction between wave and ice is of great significance for ship navigation in the Marginal Ice Zone, from the perspective of external loads (Ni et al., 2020).

The interaction between wave and ice has a long history. Related theoretical methods can refer to the reviews from Squire et al. (1995), Squire (2007, 2020), etc. With development of computer capacity, numerical simulation between wave and ice has been developing fast. According to ice size to wavelength, there are usually two kinds of problems. One is the interaction between wave and ice floe. For this kind of problem, ice floe can be seen as a rigid body, as it is small relevant to wave length. In this way, the motion response such as surge, heave and drift has been paid more attentions. Shen and Ackley (1991), Shen and Zhong (2001), Meylan et al. (2015) adopted Slope Sliding theory to simulate the surge and drift motion of a small ice floe under wave loading. Bai et al. (2017) used the potential flow model HydroSTAR and the viscous flow computational fluid dynamics (CFD) model OpenFOAM to investigate the kinematic response of rigid sea ice floes in waves. Numerical results were compared with experimental data of Mcgovern and Bai (2014). On this basis, the velocities in surge, heave and drift motion were analyzed for various ice floe shapes.

The other is the interaction between wave and ice sheet. For this kind, ice deformation should be considered, because the ice sheet is large enough compared with wavelength (Korobkin et al., 2014). In this kind, the interaction between wave and shore-connecting ice sheet or ice shelf can be seen as a sub-category, where the one end of the ice sheet is fixed and the other end is free. Yang et al. (2017) and Hu et al. (2018) used CFD method to simulate the hydrodynamic forces of a rigid shore-connecting ice sheet under Airy wave and Stokes wave, respectively. Ilyas et al. (2018) and Kalyanaraman et al. (2019) adopted finite element method to study the structural response, such as vibration, of ice shelf under wave forcing.

One may concern the elastic effects of an ice sheet, compared with the rigid ice sheet assumption, on the interaction between ice sheet and wave. This forms the motivation of this paper. In this paper, the ANSYS Workbench software was adopted to simulate the fully FSI between wave and a shore-connecting ice sheet. Rigid and elastic ice models were both studied and compared to investigate the influence of ice elasticity.

2. Numerical model and validation

2.1 Governing equations and boundary conditions

The basic governing equations for a two-dimensional flow are continuity equation and Navier-Reynolds equation as below:

$$\rho\left(\frac{\partial u}{\partial x}+\frac{\partial v}{\partial y}\right)=0 \qquad \textbf{[1]}$$

$$\frac{\partial u}{\partial t}+u\frac{\partial u}{\partial x}+v\frac{\partial u}{\partial y}=-\frac{1}{\rho}\frac{\partial p}{\partial x}+\upsilon\left(\frac{\partial^2 u}{\partial x^2}+\frac{\partial^2 u}{\partial y^2}\right)+S_x \qquad \textbf{[2]}$$

$$\frac{\partial v}{\partial t}+u\frac{\partial v}{\partial x}+v\frac{\partial v}{\partial y}=g-\frac{1}{\rho}\frac{\partial p}{\partial y}+\upsilon\left(\frac{\partial^2 u}{\partial x^2}+\frac{\partial^2 u}{\partial y^2}\right)+S_y \quad \textbf{[3]}$$

where ρ is fluid density, u and v are the velocity components in the direction of X and Y, respectively, t is time, p is pressure, υ is kinetic viscosity coefficient, S_x and S_y are the source of momentum in the direction of X and Y, respectively.

The sea bed satisfies non-penetrable and non-slip conditions:

$$u=v=0 \quad \textbf{[4]}$$

VOF method was taken to simulate the deformation of free surface and wave, and the boundary condition on free surface can be written as:

$$\frac{\partial \alpha_i}{\partial t}+\frac{\partial (u\alpha_i)}{\partial x}+\frac{\partial (v\alpha_i)}{\partial y}=0, \quad \sum \alpha_i=1, \quad i=1,2 \quad \textbf{[5]}$$

where α_i is the volume fraction of the ith phase fluid (i=1 means water and i=2 means air), and $0\le\alpha_i\le1$.

2.2 Numerical wave tank with ice plates

Firstly, a 2D numerical wave tank without ice plate is established. The wave is generated by using 'Boundary wave-making' method. Wave elimination method can refer to Hu et al. (2018). The dimensions of the wave tank are 10m long, 1.1m deep with water depth 0.8m. Relative boundary conditions are set as: upside is pressure outlet, downside is wall surface, left side is velocity inlet, and right side is pressure outlet with 'Numerical Beach' selected to absorb wave. In particular, for the wave maker, an Airy wave is selected with given wavelength and wave height:

$$\eta=A\cos(kx-\omega t) \quad \textbf{[6]}$$

and horizontal and vertical velocities are

$$V_x=A\omega\frac{chk(z+h)}{shkh}\cos(kx-\omega t) \quad \textbf{[7]}$$

$$V_z=A\omega\frac{shk(z+h)}{shkh}\sin(kx-\omega t) \quad \textbf{[8]}$$

where A is wave amplitude, ω is wave frequency, k is wave number and h is water depth. For the wave absorber, an artificial damping is added on the vertical velocity (Choi & Yoon, 2009),

$$S_z^d=\rho\left(f_1+f_2|V_z|\right)\frac{e^{\kappa}-1}{e-1}V_z \quad \textbf{[9]}$$

where $\kappa=\left(\frac{x-x_{sd}}{x_{ed}-x_{sd}}\right)^{n_d}$, in which x_{sd} and x_{ed} are the starting and ending points on the wave surface, f_1, f_2 and n_d are parameters of the damping. Here we take f_1, f_2 and n_d as 10, 10 and 2, respectively. In multi-phase module, VOF model and K-epsilon turbulence model are selected.

Secondly, a rigid shore-connecting ice plate is added in the wave tank. The dimensions of the ice sheet is 3.0m long and 0.06m thick. Its draft is 0.054m. The boundary conditions of the ice sheet is rigid walls. Unstructured triangular meshes are adopted to discrete the flow and the meshes are refined in the regions near wave surfaces and ice plates, as shown in Fig.1. 100 meshes are plotted in a wave length and 20 meshes are plotted in a wave height.

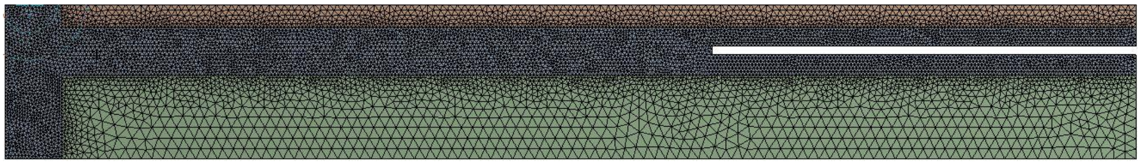

Figure 1. Meshes in numerical wave tank with a rigid shore-connecting ice plate

Thirdly, an elastic shore-connecting ice plate is added in the wave tank. As the deformation of the ice needs to be calculate, the 'Fluid-Structure Interaction model' should be adopted. In ANSYS Workbench software, three modules including 'Fluid Flow (FLUENT)', 'Transient Structural' and 'System Coupling' are used. Fluid Flow (FLUENT) module is used to calculate flow domain and all the parameters are set same to the above. Transient Structural module is used to calculate the response of ice. Besides the above-mentioned geometrical parameters, material parameters of the ice plate are also needed, including Young's modulus (2GPa), Poisson's ratio (0.35), density (900kg/m^3). The numbers in the bracket are the parameters used in this paper. In addition, in Transient Structural module, the ice plate must be in 3D, thus the width of the ice plate is taken as 0.025m and the flow domain in Fluid Flow (FLUENT) is also extended to 0.025m wide with symmetry plane as the boundary conditions of front and back surfaces of the wave tank. For the elastic ice plate, its boundary conditions are: rigid fixed at right end, free at left end, symmetry at front and back surfaces, fluid-solid interfaces are set at upside, downside and left sides, which satisfy both impermeable condition and non-slip condition, namely,

$$\boldsymbol{u}_f \cdot \boldsymbol{n} = \boldsymbol{u}_s \cdot \boldsymbol{n} \tag{10}$$

$$\boldsymbol{u}_f \cdot \boldsymbol{\tau} = \boldsymbol{u}_s \cdot \boldsymbol{\tau} \tag{11}$$

where $\boldsymbol{u}_f$ and $\boldsymbol{u}_s$ are the fluid velocity and ice velocity, respectively, and $\boldsymbol{n}$ and $\boldsymbol{\tau}$ are unit normal and tangential vector of the ice surface. System Coupling is used to transfer the data at these fluid-solid interfaces in real time. Time step is set as 0.002s.

2.3 Validation of numerical wave tank

Numerical wave tank is first validated by comparing with theoretical waveform. Wave length λ is taken as 2.6m, wave height H is 0.1m. Wave elimination zone is also taken as 2.6m, namely a wavelength. A monitoring point 0.1m away from left side of tank is set on the wave surface, whose waveform is compared with theoretical one, as shown in Fig. 2. It can be seen from the figure that numerical results coincide with theoretical ones well after the wave is stable, which validates the numerical wave tank in this paper.

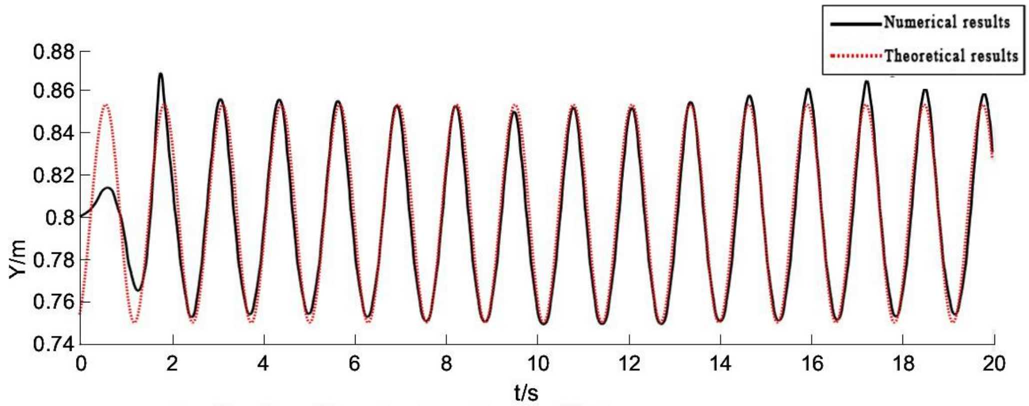

Figure 2. Comparison of numerical and theoretical waveforms

3. Results and discussions

3.1 Interaction of wave and rigid ice plate

Firstly, the results of the interaction of wave and rigid ice plate is investigated. λ is 2.5m, H is 0.1m, and other parameters are same to those in section 2.2. The development of wave propagation is shown in Fig.3. It can be seen that as the wave continues to propagate, a part of wave is reflected by the ice sheet, and a small part of wave overwashes the upper surface of the ice and propagates along the ice surface (Skene et al., 2015, Nelli et al., 2020), until to the right end of the ice sheet, where there exists a small outlet and the wave flows out there.

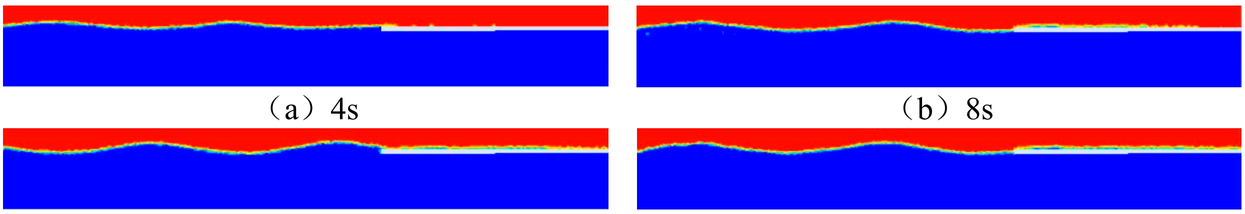

Figure 3. Interaction of wave and rigid shore-connecting ice plate

The forces on the three surfaces of the ice plate is measured in Fig.4. For the vertical force, the positive direction is upward, while for the horizontal force, the positive direction is rightward. From Fig.4 (a), one can see the force F_1 increases along with the accumulation of water on the upper side of ice plate. Minus presents that the direction of F_1 is downward. As wave overwashes the ice periodically, F_1 presents a rise in cycle also. From Fig.4 (b), one can see the F_2 on the lower surface of ice plate is dominant, with same cycle with that of incident wave. Compared with Fig.4 (a) and (b), it can be seen that the F_3 on the free end of ice plate in Fig.4 (c) is much small and can be negligible in most time. It also indicates that the compression induced by the wave on the ice is quite small.

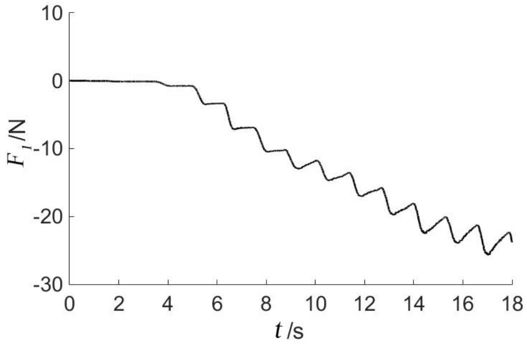

(a) upper surface

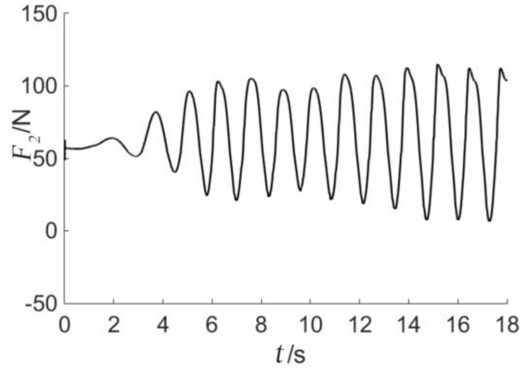

(b) lower surface

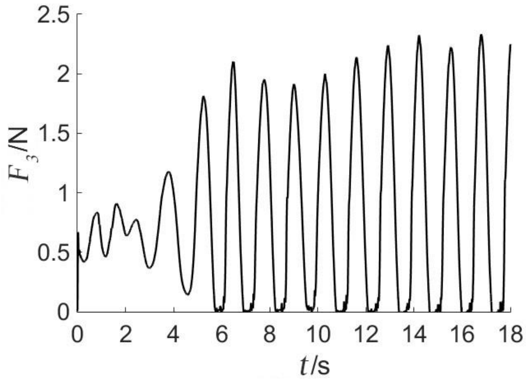

(c) free-end surface

Figure 4. Time histories of forces on the surfaces of the rigid ice plate

In order to compare the structural response of the rigid ice with that of elastic ice, we introduce an approximate method to study the bending stress of the rigid ice (Hu et al., 2018). As shown in Fig.5, the ice plate is seen as a cantilever beam and the external fluid force is equivalent to a uniformly distributed loads. Considering the effect of gravity force G of the ice plate $G=mg$, where m is mass of the plate and g is gravitational acceleration, the uniformly distributed loads q can be obtained by:

$$q = \frac{F_1 - F_2 + G}{LB} \qquad \textbf{[12]}$$

where L and B are the length and beam of the ice plate, respectively, in which B is taken as 1 for 2D simulation.

By using the knowledge of materials mechanics, one can easily obtain the maximum bending stress $\sigma_{\max}$ of the ice plate as:

$$\sigma_{\max} = \frac{M_{\max}}{W} = -\frac{1}{2}qL^2B^2 / (\frac{1}{6}Bh^2) = -3\frac{(F_1 - F_2 + G)L}{h^2} \qquad \textbf{[13]}$$

where $M_{\max}$ is the maximum bending moment of the ice plate, which is realized at the fixed end of the beam from structural analysis; W is section modulus and h is the thickness of the ice plate. It is easy to know that $\sigma_{\max}$ exists at the fixed end of the ice plate due to the maximum bending moment. From Eq. (13), one can also predict that $\sigma_{\max}$ increases linearly with ice length L.

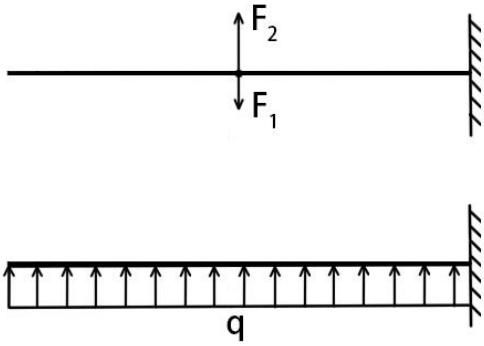

Figure 5. Sketch of the external fluid force on the rigid shore-connecting ice plate

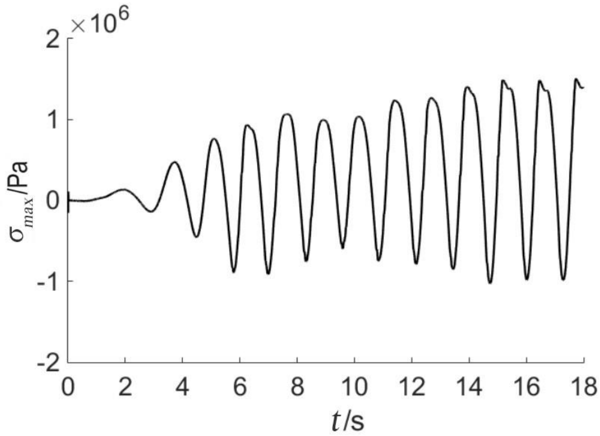

Figure 6. The maximum bending stress of the rigid shore-connecting ice plate

Fig. 6 provides the time history of the maximum bending stress $\sigma_{\max}$ of the ice plate. Compared with Fig. 4 (b), one can see that the tendency of $\sigma_{\max}$ is similar to that of F_2. Considering Eq. (13), it can be easily understood because the fluid force on the lower surface F_2 dominates the total force.

3.2 Interaction of wave and elastic ice plate

Secondly, the results of the interaction of wave and elastic ice plate is investigated, with same parameters as those in section 2.2 and 3.1. Fluid forces and structural response can be obtained directly in Fluid Flow (FLUENT) module and Transient Structural module, respectively.

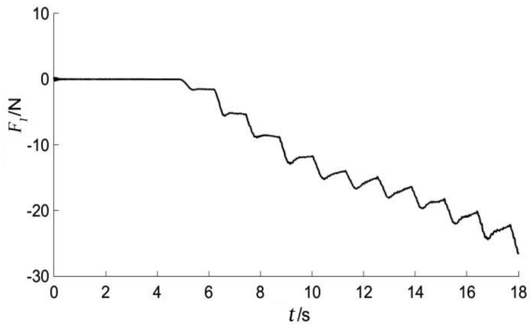

（a）upper surface

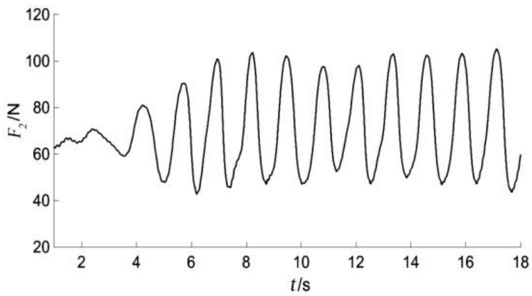

（b）lower surface

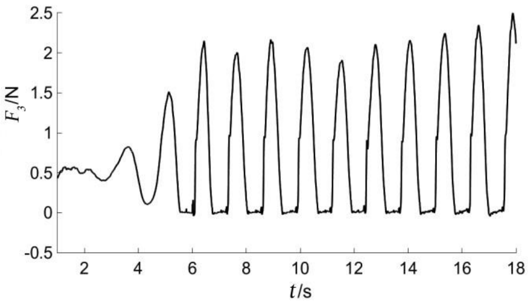

（c）free-end surface

Figure 7. Time histories of forces on the surfaces of the elastic ice plate

Fig.7 presents the time histories of forces on the surfaces of elastic ice plate. It can be seen their tendencies coincide with those of rigid ice plate in Fig.4. The detailed differences will be checked and discussed in section 3.3.

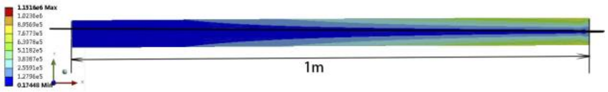

（a）6.92s

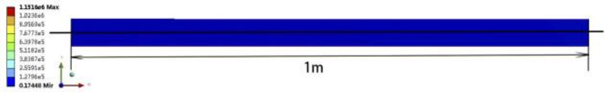

（b）11.77s

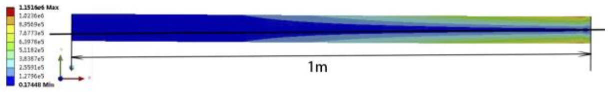

（c）15.23s

Figure 8. Bending stress contour of the elastic ice plate

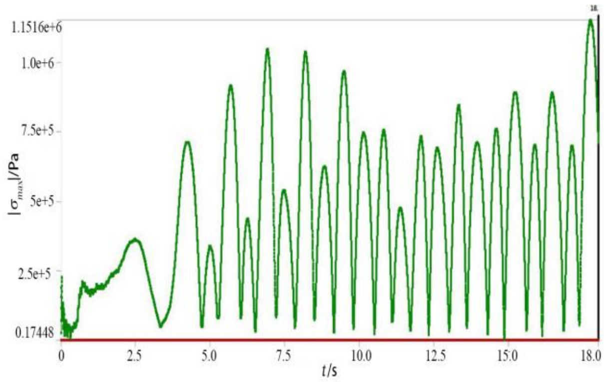

Figure 9. The absolute maximum bending stress of the elastic shore-connecting ice plate

Fig.8 and Fig.9 provide the bending stress contour and the absolute maximum bending stress of the elastic shore-connecting ice plate. In Fig. 8, we just provide 1m near the fixed end of the ice. These three moments correspond to the ice plate bends downwards most, to the central position and upwards most, respectively. From Fig.8, one can see the maximum bending stress happens on the upper surface at the fixed end of the ice plate, which denotes the ice will be broken and cracked at the upper surface first. From Fig.9, one can notice the largest bending stress in this case is 1.149×10^6Pa around t=17.75s. Once this bending stress is over the allowable bending stress, the crack will generate along the upper surface at the fixed end of the ice plate.

3.3 Comparison between rigid ice and elastic ice

Based on section 3.1 and 3.2, this section provides the comparison between these two cases.

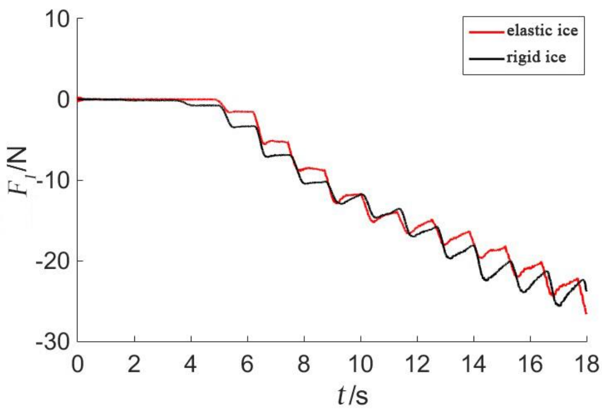

（a）upper surface

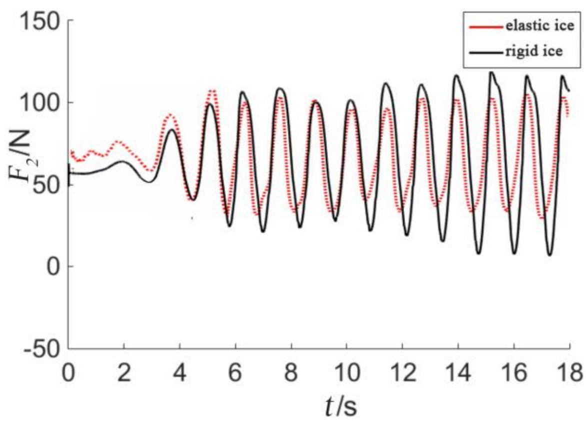

（b）lower surface

Figure 10. Comparison of fluid force between rigid ice and elastic ice

Fig. 10 provides the comparison of fluid forces on the upper and lower surfaces of rigid ice and elastic ice. Overall, there are not large differences between these two cases, which denotes the elasticity of the ice plate has not too much influences on the fluid forces under this case. One can see the amplitudes of the fluid force of the rigid ice are larger than those of elastic ice. This can be understood, given that the elastic ice can absorb part of wave energy as elastic energy of the plate and reduces the external fluid force as a result.

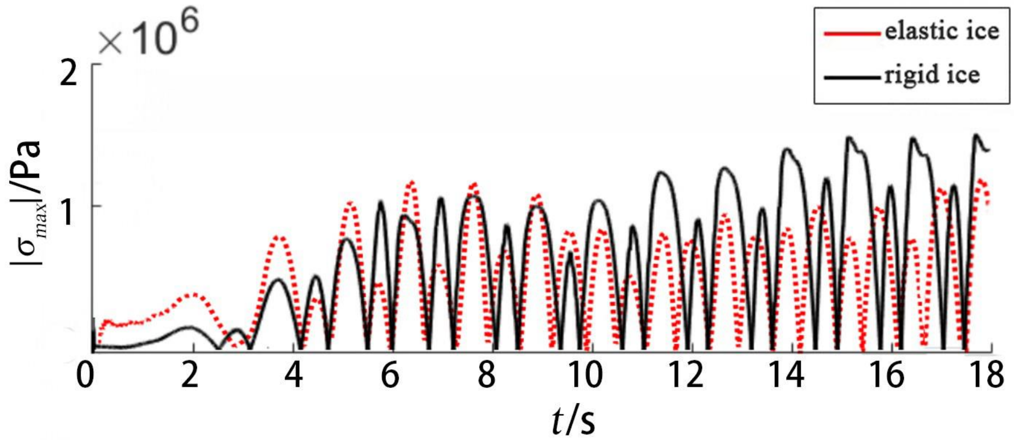

Figure 11. Comparison of absolute maximum bending stress between rigid ice and elastic ice

Fig.11 presents the comparison of absolute maximum bending stress $|\sigma_{\max}|$ between rigid ice and elastic ice. One can see that the oscillation frequency of the elastic ice sheet is greater than that of the rigid ice after around 10s. This is because the flexural oscillation of the elastic ice sheet causes extra wave. This wave propagates and superimposes with incident wave, and the superposition of wave frequency is greater than that of the rigid ice, so the response of the elastic ice sheet gets faster. On the other hand, as mentioned above, due to the induced elastic energy, the amplitudes of bending stress of elastic ice sheet are normally smaller than those of rigid ice sheet.

4. Conclusions

Based FSI model, the interaction between the wave and a rigid ice plate or an elastic ice plate was studied. The results of rigid ice and elastic ice were compared and some conclusions has been drawn:

1) A simplified method was presented to approximate the structural response of the rigid ice sheet. It was found that maximum bending stress $\sigma_{\max}$ of the rigid ice sheet increases linearly with ice length L.
2) For elastic ice sheet, $\sigma_{\max}$ happens on the upper surface at the fixed end, which denotes the ice will be broken and cracked at the upper surface first, once the $\sigma_{\max}$ is over the allowable stress.
3) Compared with rigid ice sheet, elastic ice sheet is subjected to an external fluid force with smaller amplitudes and higher frequency, thus generates bending stresses with smaller amplitudes and higher frequency.

Acknowledgments

This work is supported by the National Key R&D Program of China (2017YFE0111400), the National Natural Science Foundation of China (Nos. 51979051, 51979056 and 51639004) and National Natural Science Foundation of Heilongjiang Province (A2018003), to which the authors are most grateful.

References

Bai W, Zhang T, Mcgovern D J. Response of small sea ice floes in regular waves: A comparison of numerical and experimental results [J]. Ocean Engineering, 2017, 129:495-506.

Choi J, Yoon S B. Numerical simulations using momentum source wave-maker applied to RANS equation model [J]. Coastal Engineering, 2009, 56(10):1043-1060.

Hu W J, Ni B Y, Han D F, et al., 2018, Numerical simulation of interaction between two-dimensional wave and sea ice, 13th International Marine Design Conference, Espoo, Finland, Jun., 10-14.

Ilyas M , Meylan M H , Lamichhane B , et al. 2018, Time-domain and modal response of ice shelves to wave forcing using the finite element method. Journal of Fluids and Structures, 80:113-131.

Kalyanaraman B, Meylan M. H., Lamichhane B., Bennetts L. G., 2019 A linear elasticity model for ice shelf vibrations, Proc 34th IWWWFB workshop, Newcastle, Australia. Apr. 7-10.

Korobkin A A , Khabakhpasheva T I , Papin A A . 2014, Waves propagating along a channel with ice cover[J]. European Journal of Mechanics, 47:166-175.

Mcgovern D J, Bai W. Experimental study on kinematics of sea ice floes in regular waves. Cold Regions Science & Technology, 2014,103(103):15-30.

Meylan M H, Yiew L J, Bennetts L G, et al., 2015, Surge motion of an ice floe in waves: comparison of a theoretical and an experimental model. Annals of Glaciology, 2015, 56(69):46-52.

Nelli, F. Bennetts, L. Skene D., Toffoli A., 2020, Water wave transmission and energy dissipation by a floating plate in the presence of overwash, Journal of Fluid Mechanics, 889, DOI: https://doi.org/10.1017/jfm.2020.75.

Ni B Y, Han D. F., Di S. C., Xue Y Z, 2020, On the development of ice-water-structure interaction, Journal of Hydrodynamics, 32(4):629-652.

Shen H H, Zhong Y. 2001, Theoretical Study of Drift of Small Rigid Floating Objects in Wave Fields. Journal of Waterway Port Coastal and Ocean Engineering, 2001, 127(6): 343-351.

Shen H H, Ackley S F. 1991, A one-dimensional model for wave-induced ice-floe collisions. Annals of Glaciology, 15:87-95.

Skene D. M., Bennetts L. G., Meylan M. H., 2015, Toffoli A. Modelling water wave overwash of a thin floating plate, Journal of Fluid Mechanics, 777, R3, http://dx.doi.org/10.1017/jfm.2015.378.

Squire V A, Dugan J P, Wadhams P, et al., 1995, Of ocean waves and sea ice. Annual Review of Fluid Mechanics, 27(1): 115-168.

Squire V A. Of ocean waves and sea-ice revisited. Cold Regions Science and Technology, 2007, 49(2): 110-133.

Squire V A, 2020, Ocean wave interactions with Sea Ice: A Reappraisal, Annual Review of Fluid Mechanics, 52: 37-60.

Yang C Z, Liu C G, Fang H Y, et al. 2017, Numerical simulation of wave impact on sea ice in the Bohai sea, Chinese Journal of Hydrodynamics, 32(2):141-147. (in Chinese)

25th IAHR International Symposium on Ice
Trondheim, 23 - 25 November 2020

Impact of wave-induced sea ice fragmentation on sea ice dynamics in the MIZ

Guillaume Boutin[1], Timothy Williams[1], Pierre Rampal[1], Einar Olason[1], Camille Lique[2]
[1]*Nansen Environmental and Remote Sensing Center, Bergen, Norway*
[2]*Univ. Brest, CNRS, IRD, Ifremer, Laboratoire d'Océanographie Physique et Spatiale (LOPS), IUEM, Brest 29280, France*
guillaume.boutin@nersc.no
timothy.williams@nersc.no
pierre.rampal@nersc.no
einar.olason@nersc.no
camille.lique@ifremer.fr

The recent decrease in Arctic sea ice extent leaves more open water available for the generation of surface ocean waves. When they propagate in sea ice, these waves are attenuated, limiting the wave-ice interactions to the area at the interface between the pack ice and the open ocean, commonly referred to as the marginal ice zone (MIZ). In this region, waves can bend and break the ice floes, thus fragmenting sea ice. The consequences of this fragmentation on sea ice dynamics are poorly known, although it has often been suggested that fragmented sea ice is likely to have its resistance to deformation reduced. Here, we investigate the potential impact of wave-induced sea ice fragmentation on sea ice dynamics using a new coupled framework between a spectral wave model and the sea ice model neXtSIM, which includes a Maxwell-Elasto Brittle rheology. Using a case study in the Barents Sea, we find that fragmented sea ice, for which the internal stress is reduced, is significantly more mobile than when it is unbroken. This increase in mobility is particularly visible for high sea ice concentrations. We describe two effects of fragmentation on sea ice dynamics: it maintains high velocities when the wind speed of a storm starts decreasing, and it allows for sea ice to be mobile even in very calm conditions. This modulation of sea ice mobility by waves has important implications for both sea ice forecast applications and longer-term simulations.

1. Introduction

The decrease in sea ice extent occurring in the Arctic leaves more space for ocean waves to develop and propagate. It results in more frequent and more energetic wave events (Thomson et Rogers, 2014) that can break the sea ice over tens to hundreds of kilometres before the waves get completely attenuated by their interactions with sea ice (eg. Collins et al., 2015, Ardhuin et al., 2018). The partially ice-covered area in which these wave—sea ice interactions take place is generally referred to as the marginal ice zone (MIZ). Fragmentation of sea ice by waves has received great attention recently (eg., Roach et al., 2018; Boutin et al., 2020a, Voermans et al., 2020) as it could enhance lateral melting in summer (Asplin et al., 2012; Horvat et al., 2017). At the same time, wave-induced fragmentation could also affect sea ice mobility, as a fragmented sea ice cover is likely to be easier to deform than a consolidated one (McPhee 1980).

Very little is known about the relationship between the fragmentation of sea ice and its ability to be deformed in the MIZ. Shen et al. (1986) applied a granular flow theory to represent the behaviour of fragmented sea ice. They used a collisional stress term dependent on the floe size, but their results largely underestimated the magnitude of fluctuations of the velocity field observed during the MIZEX campaigns. A collisional stress term was also introduced by Feltham (2005) to explain the generation of ice jets in the MIZ, but the spatial scale of the resulting jet was smaller than the one observed by Johanessen et al. (1983). There is therefore no consensus on the proper way to model the behaviour of a fragmented MIZ, and until now most state-of-the-art sea ice models do not take into account sea ice fragmentation in their rheology. Instead, sea ice resistance to deformation depends mostly on sea ice concentration.

There are, however, some elements that confirm the importance of fragmentation on sea ice rheology. During the N-ICE-2015 expedition for instance, Oikkonen et al. (2017) reported deformation rates that are an order of magnitude higher in fragmented sea ice than in the pack. Satellite images of the MIZ, whether they are optical or from SAR, also show a large number of mesoscale features deforming the ice cover, even in places where sea ice looks compact. These observations, combined with the potential importance of ocean mesoscale activity in the export and melt of sea ice (Manucharyan and Thomson, 2018) strongly motivate our investigations of the effects of fragmentation on sea ice dynamics in the MIZ.

Recent progress in both wave and sea ice numerical models have greatly extended the possibility of studying wave-ice interactions without the need of costly and risky polar expeditions. Wave models like WAVEWATCH III® (WW3) now include a variety of wave—sea ice interactions parameterizations (The WAVEWATCH III Development Group, 2019), some of them including a representation of the wave-induced sea ice breakup (Boutin et al., 2018). The addition of a floe size distribution (FSD) in sea ice models (eg. Horvat et Tziperman, 2015) has also been an important step forward as it has enabled the exchange of floe size information between sea ice and wave models, making possible the development of coupled wave—sea ice models (Roach et al., 2019; Boutin et al.; 2020a).

The very recent wave-sea ice coupled model developed by Boutin et al. (2020b) involves the sea ice model neXtSIM (Rampal et al., 2016), which uses the Maxwell-elasto-brittle rheology (Rampal et al., 2019). This rheology includes a variable called *damage* representing the density of cracks that form during high-deformation events. A high level of *damage* lowers the resistance of sea ice to deformation. If deformation events stop happening, the *damage* decreases slowly, over a timescale of a few weeks. The *damage* variable therefore keeps track of previous deformation events. The Maxwell-elasto-brittle rheology was found to reproduce the scaling of sea ice deformations in pack ice very well (Rampal et al., 2019). Hypothesising that fragmentation could be considered as a very strong deformation event, Boutin et al. (2020b) related the wave-induced fragmentation to the sea ice *damage* and found an increase in sea ice mobility in the MIZ.

In this study, we push further the investigations of Boutin et al. (2020b) and comment on the impact of wave-induced fragmentation on sea ice velocities and thickness in the MIZ. We first provide a quick summary of the coupled framework used by Boutin et al. (2020b) and introduce the domain and the simulations that we use here. We then analyse our results and conclude with a discussion on the hypothesis made in this study.

2. Methods

Here, we re-use the same wave—sea ice coupled framework as introduced by Boutin et al. (2020b). In this section, we will give a short summary of this coupling, but for more details please refer to the study by Boutin et al. (2020b).

The coupling involves the spectral wave model WAVEWATCH III ® (The WAVEWATCH III Development Group, 2019) in which we use the wave—sea ice interactions developments introduced by Boutin et al. (2018). They include 3 wave attenuation processes (scattering, friction, and inelastic dissipation) that depend on sea ice concentration, thickness, and floe size. They also include a representation of wave-induced sea ice breakup built on the model introduced by Williams et al. (2013), allowing for feedback between the floe size and the wave field. The wave model computes two variables that are sent to the sea ice model. The first one is the breakup wavelength, which corresponds to the wave wavelength for which the stress exerted by the waves on the sea ice is maximum. The second one is the wave radiation stress (WRS), that corresponds to a transfer of momentum from the attenuated waves to the sea ice in the direction of the wave propagation. The value of the WRS is added as an external stress to the momentum balance equation of neXtSIM as described in Williams et al. (2017). In turn, WW3 receives from neXtSIM sea ice information necessary to compute the wave attenuation (sea ice concentration, thickness, maximum and average floe size).

The information on whether fragmentation has occurred or not is included in the breakup wavelength sent to the sea ice model. If the stress applied to sea ice, computed in WW3, is lower than the flexural failure limit, the value of the breakup wavelength is equal to 1000m, and waves have no impact on the FSD in neXtSIM. If the stress induced by the waves is greater than the flexural failure limit, the breakup wavelength is computed with values in [D_{minF} 1000m[, D_{minF} being the smallest ice floe size for which flexural failure can occur (see Mellor, 1986). The FSD in neXtSIM is then redistributed to represent the fragmentation of large sea ice floes into smaller ones as explained in Boutin et al. (2020b).

The main originality of the FSD implementation in neXtSIM is the parallel evolution of two FSDs, each being associated with a different timescale of the floe size growth. These two FSDs are used to distinguish between a continuous ice cover made of small floes joined together by a thin sea ice cover, and a sea ice cover made of large consolidated ice plates, for which the mechanical properties are certainly very different. The first FSD, called the thermodynamical FSD, is used in processes associated with thermodynamics. The timescale associated with this growth is between a few hours to a few days, corresponding to the time needed for a thin sea ice layer to create joints between consolidated ice floes. It allows for a quick growth of the floe size under the action of refreezing and floe welding, for which we use a parameterization derived from Roach et al. (2018). This FSD also represents the impact of floe size on lateral melting. The second FSD is called the mechanical FSD and is associated with a slow floe size growth taking from days to weeks. It represents the time needed for the ice layer between the consolidated floes to become solid and thick enough for the ensemble of floes to be considered as a coherent ice plate. This FSD is used for mechanical processes, like the impact of fragmentation on sea ice dynamics and wave attenuation, for which the floe size associated with the rigidity of the ice cover is the important factor.

To investigate the impact of wave-induced fragmentation on sea ice, Boutin et al. (2020b) suggest increasing the level of damage d of a sea ice cell assuming that broken sea ice is associated with a very high value of damage d_{broken}=0.99 (the theoretical maximum value for d is 1).

$$d=\min(1,\ d\,(1-c_{broken})+d_{broken}\,c_{broken}) \qquad \textbf{[1]}$$

To distinguish the impact of fragmentation from the rest of the changes induced by the coupling, we proceed similarly to Boutin et al. (2020b) and run 2 simulations. The first one, we call CPL_WRS, involves all the features of the coupling introduced by Boutin et al. (2020b) and summarized here but the link between fragmentation and damage. The only direct impact of wave on sea ice dynamics compared to a stand-alone simulation of neXtSIM is therefore the momentum injected by the WRS. The second simulation is called CPL_DMG, and is similar to CPL_WRS in everything but the fact that it includes the relationship between fragmentation and damage presented above.

Like in Boutin et al. (2020b), these simulations are run on a regional 0.25° grid (CREG025), which covers the Arctic Ocean at an approximate resolution of 12 km, as well as some of the North Atlantic. neXtSIM is a sea ice model that is solved using a finite element method on a moving Lagrangian mesh - i.e., it is not run on a grid. Its initial mesh is, however, based on a triangulation of the CREG025 grid, giving a mean resolution of 12 km. neXtSIM is run with a timestep of 20s, and WW3 with a timestep of 800s. Fields between the two models are exchanged every 2400s. Atmospheric forcings are provided by 6-hourly fields from the CFSv2 atmospheric reanalysis (Saha et al., 2014). neXtSIM is also forced by ocean fields from the TOPAZ4 reanalysis (Sakov et al., 2012). The wave-in-ice parameterization used in WW3 is the one called REF2 in the evaluation performed by Ardhuin et al. (2018) as it gives the best match with observations. For more details on these simulations, refer to Boutin et al. (2020b).

Because the effects of wave-induced sea ice fragmentation strongly depend on waves and sea ice conditions, we limit our study to the Barents Sea. Just like in Boutin et al. (2020b), the domain we define to perform our analysis is limited south and north by the 69°N and 84°N parallels respectively, and west and east by the 16°E and 60°E meridians (see for instance Fig.3a).

The simulations are run over all October 2015, as it includes storm events in the Barents Sea, enabling us to analyze the impact of waves on the MIZ under different wind conditions. Both simulations start on September 15th to allow for 15 days of spin-up.

3. Impact of wave-induced fragmentation on the sea ice velocity distribution in the MIZ

Here we focus on the impact of wave-induced fragmentation on sea ice velocities in the MIZ. Boutin et al. (2020b) have shown how the damage added by wave-induced fragmentation was making compact sea ice more mobile in both on-ice and off-ice conditions but have not commented much on the way the sea ice drift velocity was increased. In particular, it is still unclear how the distributions of sea ice velocity in the MIZ is affected by wave-induced fragmentation.

In Fig.1a., we plot the mean distributions of sea ice drift velocity from the two simulations over all October 2015. In our analysis, we only consider compact sea ice that has recently been broken. Following Boutin et al. (2020b), compact sea ice is defined as sea ice for which the sea ice concentration is greater than 0.8. Sea ice that has recently been broken is defined as sea ice with a maximum floe size D_{max} lower than 200m. Justifications of these thresholds can be found in Boutin et al. (2020b), who found that the impact of fragmentation was mostly visible for sea ice obeying these two criteria, with for instance a ~6.5% increase of the mean ice drift velocity between CPL_DMG and CPL_WRS in October 2015. In the velocity distribution, this increase corresponds to two changes (Fig.1a,b):

i. A reduction in the proportion of sea ice drifting at velocities between 0 and 0.1m/s associated with an increase for velocities between 0.1 and 0.15m/s.
ii. A reduction in the proportion of sea ice drifting at velocities between 0.15m/s and 0.2m/s and a clear increase for greater speeds (with the exception of the interval 0.375-0.4m/s)

To better understand the mechanisms at play in the changes (i) and (ii), we look more closely at the same two events as reported in Boutin et al. (2020b), each corresponding to a maximum in the increase of ice drift velocity in CPL_DMG compared to CPL_WRS. These two events, like all the maxima in the ice drift velocities differences between the two simulations occurring in October 2015, were found by Boutin et al. (2020b) to happen in the wake of storms, once the drift slows down (Fig.2a,b).

The first event corresponds to the wake of a storm occurring on October 15th, just after the wind speed has started to decrease (Fig. 2). This event is associated with on-ice winds and characterized by high ice drift velocities over all the studied domain (Fig.3a). This fast drift of the ice is visible in the velocity distribution with a peak centered at ~0.2m/s (Fig.3b). The sea ice velocity distribution in CPL_DMG is shifted towards higher velocities than the distribution in CPL_WRS (Fig.3c). This is associated with an increase of the proportion of sea ice with velocities higher than 0.2m/s (Fig.3b,c). This is coherent with the change (ii) reported in the monthly distribution.

The second event occurs after strong off-ice winds. This time, the wind speed and ice drift velocities reach a minimum when the maximum difference in ice drift velocity between the two simulation occurs (Fig. 2). The event is characterized by an overall slow drift of the ice in the studied domain: in CPL_WRS, most of the sea ice has a velocity lower than 0.05m/s (Fig. 4a,b). Adding the effect of fragmentation modifies the shape of the velocity distribution that in CPL_DMG shows a peak centered around 0.1m/s. This change is explained by a strong reduction in the amount of ice with very low velocities (lower than 0.05m/s) and an increase of the amount of sea ice with velocities between 0.1 and 0.2m/s (see Fig.4c). This is coherent with the change (i) reported in the monthly distribution.

4. Discussion and conclusion

In our model, we have identified two changes in the sea ice drift velocity distribution when the link between fragmentation and damage is activated in our simulations. The first one corresponds to a shift in the ice drift towards higher velocities once wind speed decreases after reaching its maximum. In this case, the added damage associated with fragmentation is likely to support the high drift velocities by maintaining a low ice resistance to deformation. The second one occurs in calm conditions, when the wind speed and ice drift velocity reach a minimum. Without the effect of fragmentation on damage, sea ice drifts very slowly, as its resistance to deformation overcomes the low stresses applied to it. Fragmentation lowers this resistance and maintains the mean drift velocity around 0.1m/s.

The acceleration of the modeled sea ice drift reported by Boutin et al. (2020b) is therefore not uniform, but instead corresponds to an increase in the amount of sea ice in the high-velocity tail of the ice drift velocity distribution. This behaviour is observed for all the maxima in the ice drift velocity between the CPL_DMG and CPL_WRS simulations occurring in October 2015 in the Barents Sea and visible on Fig. 2b. Our conclusions are therefore likely to apply every time compact sea ice is fragmented by waves.

To obtain these results, we have assumed that broken sea ice is associated with a very high value of damage, therefore behaving almost as in free drift. We therefore neglected the potential impact of floe-floe interactions that may dominate the sea ice internal stress in the MIZ (Shen et al., 1986). This stress is likely to affect the increase in sea ice mobility found in Boutin et al. (2020b) and in this study, and our results should therefore be considered as an upper-bound of the effects of fragmentation on sea ice mobility. This is particularly true in convergent events, when floe-floe collisions are expected to be numerous.

The changes in sea ice dynamics due to waves have significant implications on the sea ice drift of compact ice and are worthy of further investigation. Sea ice is the main hazard for ships navigating in the MIZ, and the safety of human activities in this area requires the production of accurate sea ice forecasts (Azzara et al., 2015). Our results and the ones of Boutin et al. (2020b) suggest that waves have a strong impact on the drift of compact sea ice, and therefore illustrate how the addition of waves to operational sea ice models could strongly impact sea ice forecasts. Our results also suggest that waves can modulate sea ice mobility in the MIZ, hence the volume of ice that could be exported to the open ocean by the mesoscale activity taking place in this region (Manucharyan and Thompson, 2018).

Acknowledgments
This work has been carried out as part of the Copernicus Marine Environment Monitoring Service (CMEMS) WizARd project. CMEMS is implemented by Mercator Ocean in the framework of a delegation agreement with the European Union. It has also been funded by institutional support from the Nansen Center.

References

Ardhuin, F., Boutin, G., Stopa, J., Girard-Ardhuin, F., Melsheimer, C., Thomson, J., Kohout, A., Doble, M., and Wadhams, P.: Wave attenuation through an Arctic marginal ice zone on 12 October 2015: 2. Numerical modeling of waves and associated ice breakup, Journal of Geophysical Research: Oceans, 123, 5652–5668, 2018.

Asplin, M. G., Galley, R., Barber, D. G., and Prinsenberg, S. J.: Fracture of summer perennial sea ice by ocean swell as a result of Arctic storms, J. Geophys. Res., 117, https://doi.org/10.1029/2011JC007221, 2012.

Azzara, A. J., Wang, H., Rutherford, D., Hurley, B. J., and Stephenson, S. R.: A 10-year projection of maritime activity in the US Arctic region, Tech. rep., 2015

Boutin, G., Ardhuin, F., Dumont, D., Sévigny, C., Girard-Ardhuin, F., and Accensi, M.: Floe Size Effect on Wave-Ice Interactions: Possible Effects, Implementation in Wave Model, and Evaluation, Journal of Geophysical Research: Oceans, 123, 4779–4805, https://doi.org/10.1029/2017JC013622, 2018.

Boutin, G., Lique, C., Ardhuin, F., Rousset, C., Talandier, C., Accensi, M., and Girard-Ardhuin, F.: Towards a coupled model to investigate wave–sea ice interactions in the Arctic marginal ice zone, The Cryosphere, 14, 709–735, https://doi.org/10.5194/tc-14-709-2020, 2020.

Boutin, G., Williams, T., Rampal, P., Olason, E., and Lique, C.: Wave–sea-ice interactions in a brittle rheological framework, The Cryosphere Discuss., https://doi.org/10.5194/tc-2020-19, in review, 2020b.

Collins, III, C. O., Rogers, W. E., Marchenko, A. V., and Babanin, A. V.: In Situ Measurements of an energetic wave event in the Arctic marginal ice zone, Geophys. Res. Lett., https://doi.org/10.1002/2015GL063063, 2015.

Feltham, D. L.: Granular flow in the marginal ice zone, Phil. Trans. R. Soc. Lond. A., 363, 1677–1700, 2005.

Horvat, C., & Tziperman, E. (2015). A prognostic model of the sea-ice floe size and thickness distribution. The Cryosphere, 9(6), 2119–2134. https://doi.org/10.5194/tc-9-2119-2015

Horvat, Christopher, Tziperman, E., & Campin, J.-M. (2016). Interaction of sea ice floe size, ocean eddies, and sea ice melting. Geophysical Research Letters, 43(15), 2016GL069742. https://doi.org/10.1002/2016GL069742

Johannessen, O. M., Johanessen, J. A., Morison, J., Farrely, B. A., and Svendsen, E. A. S.: Oceanographic Conditions in theMarginal Ice Zone North of Svalbard in Early Fall 1979 With an Emphasis on Mesoscale Processes, J. Geophys. Res., 88, 2755–2769,1983.

Manucharyan, G. E. and Thompson, A. F.: Submesoscale sea ice-ocean interactions in marginal ice zones, Journal of Geophysical Research:Oceans, 122, 9455–9475, 2017.

McPhee, M. G.: An analysis of pack ice drift in summer, Sea ice processes and models, pp. 62–75, 1980.

Mellor, M.: The Mechanics of Sea Ice, in: The Geophysics of Sea Ice, edited by Untersteiner, N., pp. 165–182, 1986.

Oikkonen, A., Haapala, J., Lensu, M., Karvonen, J., and Itkin, P.: Small-scale sea ice deformation during N-ICE2015: From compact pack ice to marginal ice zone, Journal of Geophysical Research: Oceans, 122, 5105–5120, 2017.

Rampal, P., Bouillon, S., Ólason, E., and Morlighem, M.: neXtSIM: a new Lagrangian sea ice model, The Cryosphere, 10, 1055–1073, https://doi.org/10.5194/tc-10-1055-2016, 2016.
Rampal, P., Dansereau, V., Óláson, E., Williams, T. D., and Samaké, A.: On the multi-fractal scaling properties of sea ice deformation, The Cryosphere, 13, 2457–2474, https://doi.org/10.5194/tc-13-2457-2019, https://www.the-cryosphere.net/13/2457/2019/, 2019

Roach, L. A., Horvat, C., Dean, S. M., and Bitz, C. M.: An emergent sea ice floe size distribution in a global coupled ocean–sea ice model, Journal of Geophysical Research: Oceans, 2018

Roach, L. A., Bitz, C. M., Horvat, C., & Dean, S. M. (2019). Advances in modeling interactions between sea ice and ocean surface waves. Journal of Advances in Modeling Earth Systems, 11, 4167–4181. https://doi.org/10.1029/2019MS001836

Shen, H. H., Hibler, W. D., and Leppäranta, M.: On Applying Granular Flow Theory to a Deforming Broken Ice Field, Acta Mechanica, 63,143–160, 1986.

Saha, S., Moorthi, S., Wu, X., Wang, J., Nadiga, S., Tripp, P., Behringer, D., Hou, Y.-T., Chuang, H.-y., Iredell, M., Ek, M., Meng, J., Yang,R., Mendez, M. P., van den Dool, H., Zhang, Q., Wang, W., Chen, M., and Becker, E.: The NCEP Climate Forecast System Version 2,Journal of Climate, 27, 2185–2208, https://doi.org/10.1175/JCLI-D-12-00823.1, https://doi.org/10.1175/JCLI-D-12-00823.1, 2014.

Sakov, P., Counillon, F., Bertino, L., Lisæter, K. A., Oke, P. R., and Korablev, A.: TOPAZ4: an ocean-sea ice data assimilation system for theNorth Atlantic and Arctic, Ocean Science, 8, 633–656, 2012

Thomson, J. and Rogers, W. E.: Swell and sea in the emerging Arctic Ocean, Geophys. Res. Lett., 41, 3136–3140,https://doi.org/10.1002/2014GL059983, 2014

The WAVEWATCH III Development Group (TWDG): User manual and system documentation of WAVEWATCH III version 6.07, Tech. Rep. 333,Environmental Modeling Center Marine Modeling and Analysis Branch, 2019.

Voermans, J., Rabault, J., Filchuk, K., Ryzhov, I., Heil, P., Marchenko, A., Collins, C., Dabboor, M., Sutherland, G., and Babanin, A.: Experimental evidence for a universal threshold characterizing wave-induced sea ice break-up, The Cryosphere Discuss., https://doi.org/10.5194/tc-2020-201, in review, 2020.

Williams, T. D., Bennetts, L. G., Squire, V. A., Dumont, D., and Bertino, L.: Wave-ice interactions in the marginal ice zone. Part 2: Numerical implementation and sensitivity studies along 1D transects of the ocean surface, Ocean Modelling, 71, 92–101,https://doi.org/10.1016/j.ocemod.2013.05.011, 2013.

Williams, T. D., Rampal, P., and Bouillon, S.: Wave-ice interactions in the neXtSIM sea-ice model, The Cryosphere, 11, 2117–2135,https://doi.org/10.5194/tc-11-2117-2017, 2017

Figures and Tables

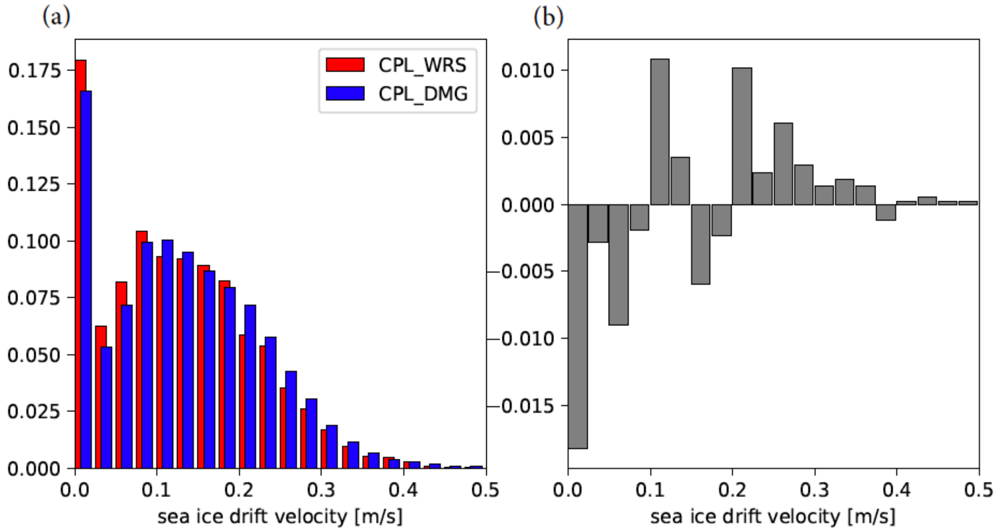

Figure 1. (a) Mean distribution of sea ice velocities in CPL_WRS (red) and CPL_DMG (blue) for compact sea ice that has recently been broken (defined as D_{max}<200m and sea ice concentration lower than 0.8), in the Barents Sea, over all October 2015. (b) Mean difference of the distributions of sea ice velocities between CPL_DMG and CPL_WRS for the same domain and period.

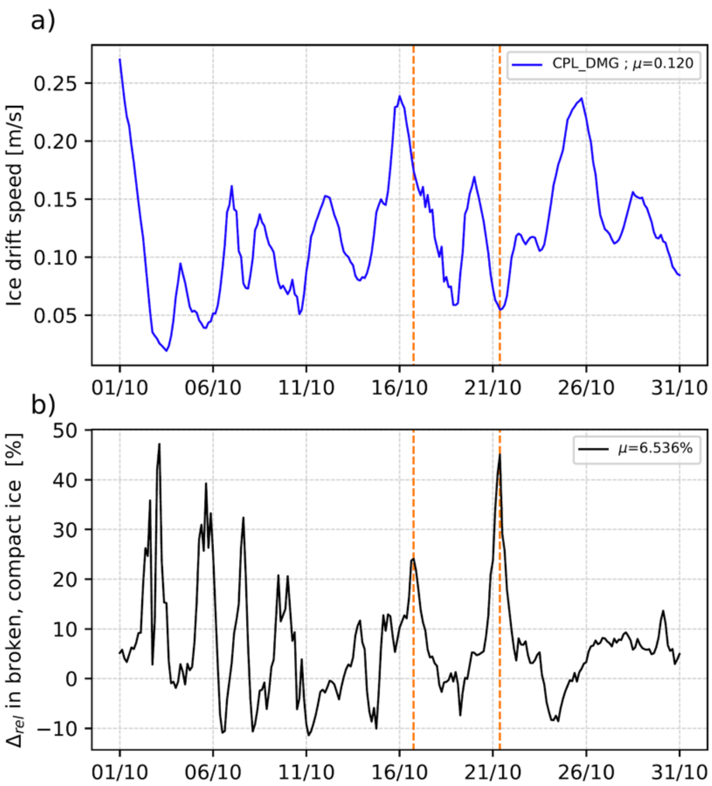

Figure 2. Figure extracted from Boutin et al. (2020b). Temporal evolution of (a) the ice drift velocity averaged over all the ice-covered part of the domain for the CPL_DMG simulation, over October 2015, and (b) of the difference of ice drift velocity in the region covered by

compact sea ice that has been recently broken (defined as D_{max}<200m and sea ice concentration lower than 0.8) between the CPL_WRS and CPL_DMG simulations. The sea ice-covered part of the domain corresponds to the area for which the sea ice concentration is greater than 0. The two orange vertical lines indicate the dates of the snapshots shown in Figures 3 and 4. In each panel legend, μ indicates the temporal mean of the plotted quantity.

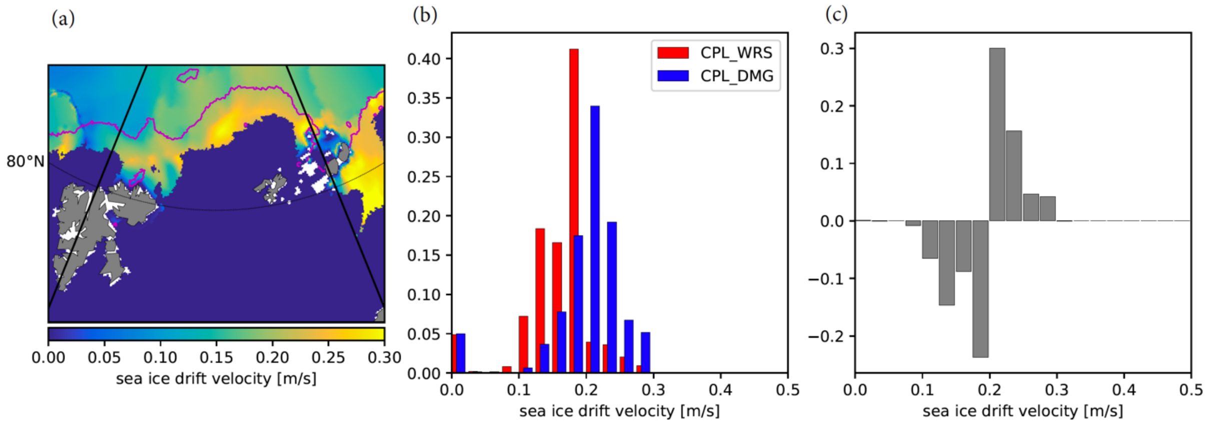

Figure 3. (a) Sea ice drift velocity distributions of sea ice drift velocity in the CPL_DMG simulation taken on October 16th at 18:00 GMT. The two black thick lines delimit the studied domain, and the magenta line corresponds to the contour D_{max}=200m. For this same date, (b) shows the distribution of sea ice velocities in CPL_WRS (red) and CPL_DMG (blue) for compact sea ice that has recently been broken (defined as D_{max}<200m and sea ice concentration lower than 0.8). and (c) is the difference of the distributions of sea ice velocities between CPL_DMG and CPL_WRS.

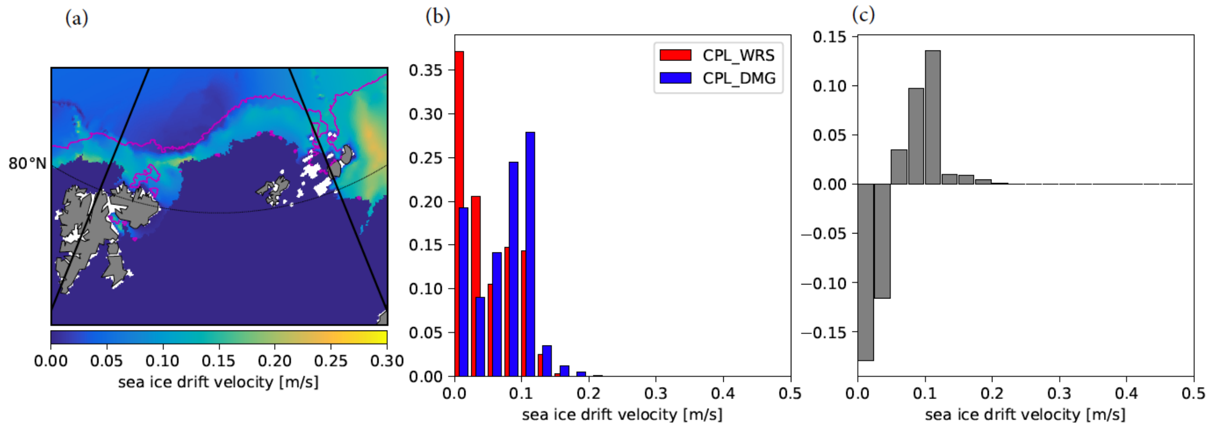

Figure 4. (a) Sea ice drift velocity distributions of sea ice drift velocity in the CPL_DMG simulation taken on October 21st at 09:00 GMT. The two black thick lines delimit the studied domain, and the magenta line corresponds to the contour D_{max}=200m. For this same date, (b) shows the distribution of sea ice velocities in CPL_WRS (red) and CPL_DMG (blue) for compact sea ice that has recently been broken (defined as D_{max}<200m and sea ice concentration lower than 0.8). and (c) is the difference of the distributions of sea ice velocities between CPL_DMG and CPL_WRS.

25th IAHR International Symposium on Ice

Trondheim, 23 - 25 November 2020

Calibrating viscoelastic wave-in-ice models for different types of sea ice covers

Sukun Cheng[1], Justin Stopa[2], Fabrice Ardhuin[3] and Hayley H. Shen[4]

[1]*Nansen Environmental and Remote Sensing Center, Bergen, Norway*

[2]*Department of Ocean and Resources Engineering, University of Hawaii, Mānoa, HI, USA*

[3]*Univ. Brest, CNRS, IRD, Ifremer, Laboratoire d'Océanographie Physique et Spatiale (LOPS), IUEM, Brest, France*

[4]*Department of Civil and Environmental Engineering, Clarkson University, Potsdam, NY, USA*

ABSTRACT

Sea ice reduction has increased the fetch and wave intensity in the Arctic Ocean. Reliable wave forecasts will be useful for the potential increase of engineering activities in the region, and help to evaluate present and future oceanographic and meteorological processes that may be affected. The global wave model WAVEWATCH III® has implemented several "switches" to determine the propagation of ocean waves through an ice cover. Except for one switch which is entirely data-driven, each of the other switches is based on a different theory and requires field data to calibrate the parameters. These switches, when trained with large amounts of data, can become robust for applications. In this paper, we present the methodology and results of using field data to calibrate one of these switches based on a viscoelastic theory. In this theory, the ice covers are assumed to be solely responsible for the observed change in wave dispersion and attenuation. The two parameters of an ice cover, equivalent elasticity and viscosity, depend on the type of the ice cover. We study two types of ice covers. One predominantly consists of grease and pancake ice near the ice edge. The other is pack ice further into the ice cover. We also divide the pack ice zone into two subzones delineated by the first appearance of leads. The calibrated equivalent shear modulus (viscosity) of the pack ice are roughly two orders (one order) of magnitude greater than that in grease/pancake ice. Small but notable changes of viscoelastic parameters are also found before and after the first appearance of leads. The same methodology used in the analysis is also applicable to calibrate other switches. These completed switches may then be used in WAVEWATCH III® to evaluate their forecast capabilities.

1. Introduction

The decline of sea ice impacts the Arctic sea state in many ways. One of the observed changes is the increase of wave intensity even without changes from the atmospheric forcing (Thomson et al., 2018). Less ice cover means more fetch to help wind generate and grow waves. The increase of wave intensity heightens the need for better wave forecasts, which is particularly important in the Marginal Ice Zone (MIZ), where the ice conditions are most dynamic. To meet this need, the global wave model WAVEWATCH III® (WW3, WAVEWATCH III® Development Group, 2019) recently has included several "switches" to account for the ice effects on wave propagation. These effects include the wave attenuation and the change of dispersion (the relation between wavelength or wave speed and frequency). One of these switches are fully data-driven while others are based on theoretical considerations. The advantage of a theory-based model for wave-in-ice is its broader applicability, provided that the theory captures the major underlying mechanisms. In WW3, each of these theory-based switches contains unknown parameters. Deriving these parameters following a "first principle" approach is extremely challenging. The alternative is to use field data to calibrate these parameters. That is, varying the model parameters to produce an outcome that is measured under field conditions. The parameters which yield the best match with the measured data are the calibrated model parameters. In the present study, we show the results of this calibration for two types of ice covers. One is in predominantly populated with grease/pancake ice. The other is the pack ice zone further into the ice cover. The pack ice zone is further separated into two regions. One consists of large floe aggregates and the other consists of semi-continuous ice populated with leads. We use two types of field data. For the grease/pancake ice zone, time series of the directional wave spectra obtained by buoys is used. For the pack ice zone, spatial distributions of the directional wave spectra obtained from SAR imagery are used. We use these two datasets to calibrate a viscoelastic wave-in-ice model. The same method can be used to calibrate other switches. In this paper, we present a summary of the calibration process and results. Details are referred to Cheng et al. (2017) for the grease/pancake part and in Cheng et al. (2020, under review) for the pack ice part.

2. Description of field data

Both datasets used for calibration were obtained in October 2015 during a storm event in the western Arctic Ocean (Thomson et al. 2018). The buoy dataset included in this study covered 10-13 October and the SAR dataset was taken around 16:50:00 UTC on 12 October. The buoy data were from an array of two different types of buoys, the spar shaped SWIFT buoys (Thomson, 2012) and the disk shaped WB buoys (Doble and Wadhams, 2006). The directional-frequency wave spectra at each of the buoy location were determined from the time series of each buoy's records. The SAR dataset was from the Sentinel-1A. Advanced image processing was developed as described in Stopa et al. (2018) to remove contamination by ice features with length scale on the order or the wavelength. The extracted directional wave spectra versus wavenumber in the pack ice zone was obtained in a roughly 300 × 400 km domain with 5.1 × 7.2 km resolution. From the SAR dataset obtained in the pack ice zone, we separated the region into the lower (south) and upper (north) parts delineated by the first appearance of leads (FAL). The FAL was defined in Stopa et al. (2018). North of FAL, the appearance of the ice cover is semi-continuous populated with leads. South of FAL, the appearance of leads is no longer visible and the ice cover presumably consists of fragmented floes.

Figure 1 shows the general ice condition around the study domain. From north to south, the red box indicates the region containing the SAR data selected for this study. The FAL locations is marked by a cyan curve. Ice concentration from AMSR2 is superimposed as yellow contours with label values indicating ice concentration. The locations of wave buoys (orange dots) and the Sikuliaq ship duirng the experiment (green dimand) are near ice edge. The Alaska coastline at the bottom is marked by a thick gray cruve.

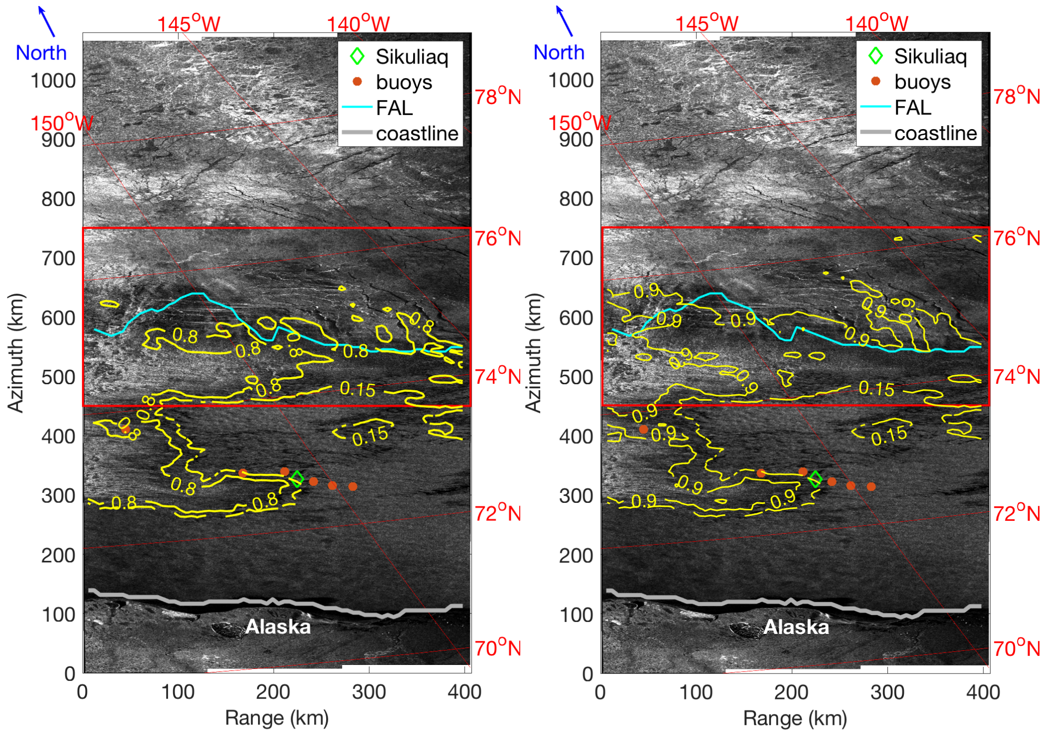

Figure 1. Sentinel-1A imagery acquired around 16:50:00 UTC on 12 October 2015. Yellow contours show ice concentration from AMSR2. The FAL is marked by a cyan curve. The domain of SAR dataset is within the red box. The buoy dataset is collected from the region around the wave buoys (orange dots).

Assume an exponential attenuation pattern of wave energy in ice field. By pairing two buoy records with known separation distance and wave direction, we obtained an attenuation rate α at each frequency f as

$$\alpha(f) = \frac{1}{2D\cos(|\theta(f)-\theta_{AB}|)} \ln\left(\frac{E_{\mathrm{A}}(f,\theta_A(f))}{E_{\mathrm{B}}(f,\theta_B(f))}\right) \qquad \textbf{[1]}$$

where D is the distance from location A to location B, and θ_{AB} is the vector direction. $E_{\mathrm{A}}(f,\theta_A(f))$ and $E_{\mathrm{B}}(f,\theta_B(f))$ are the directional spectral energy density, where $\theta_A(f)$ and $\theta_B(f)$ represent the mean directions depending on frequency f. The average of the main wave directions at A and B, $\theta(f) = \frac{\theta_A(f)+\theta_B(f)}{2}$, is used to estimate propagation distance for the wave component. The attenuation directly measured by pairing two buoy data is the result of many source/sink terms other than the contribution from the ice cover. These additional source/sink terms include the wind input, the dissipation due to white-capping and and the nonlinear transfer of energy between different frequency components. After removing these additional source/sink effects, we may obtain the net attenuation k_i shown below for each frequency due to ice alone (see details in Cheng et al., 2017),

$$k_i = \frac{2c_g\alpha E+(1-C)(S_{in}+S_{ds})+S_{nl}}{2Cc_gE} \qquad \textbf{[2]}$$

where c_g is the group velocity, E is the wave energy density, C is the ice concentration, S_{in} is the wind input, S_{ds} is the dissipation through wave breaking, S_{nl} is the energy transfer due to nonlinear interactions among spectral components, and S_{ice} is the damping due to ice cover. Note the variables in Eq. (2) depend on frequency except C.

The processed spectral attenuation data from the SAR imagery were first determined by pairing the directional wave spectrum at two locations. We note that the SAR data are near instantaneous spatial information. Hence the retrieved wave energy corresponds to wavenumber. The distance between the two locations and the energy components in each of the wavenumber is used to calculate the apparent attenuation through Eq. [1] except that freqeuncy is replaced by wavenumber k_r. Then using the same procedure as for the buoy pairs, the extra energy source/sink contribution is removed to obtain the spectral attenuation due to ice alone as Eq. [2] but depends on the wavenumber. The pairs of locations used in these calculations were either both south of the FAL or north of the FAL, so that to detect any differences between these two regions. Results of the attenuation from the buoys measured in the grease/pancake ice and from the SAR imagery measured in the pack ice are given in Figure 2. These plots show the two-dimensional histograms of k_i from (a) grease/pancake ice by wave buoys and (b)(c) pack ice separated by the FAL. In each panel, $\log_{10} k_i$ data are presented by a two-dimensional histogram against frequency in panel (a) and wavenumber in panels (b)(c). The attenuation domain is equally divided into 60 bins in the log scale from 10^{-6} to 10^{-2} m^{-1}. Grayscale indicates the occurrence frequency of k_i in each k_i-f or k_i-k_r bin from the selected pairs. The highest occurrence frequency is marked by a red curve.

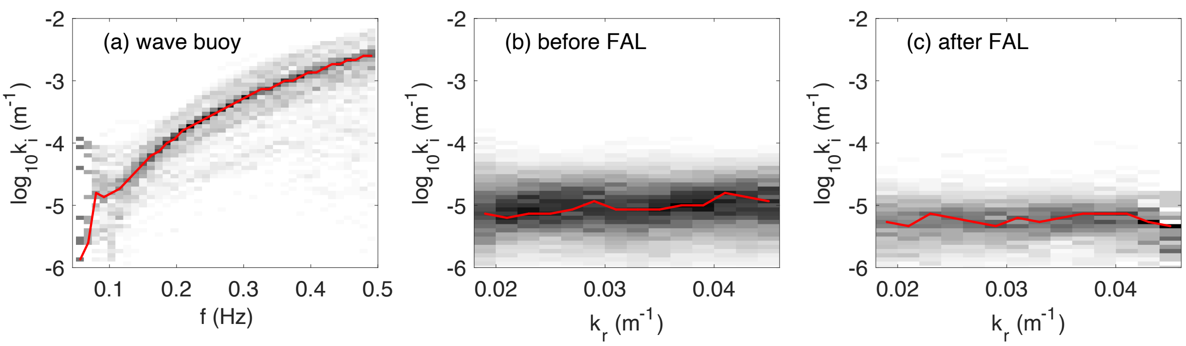

Figure 2. Ice-induced attenuation rates collected from (a) wave buoys in grease/pancake ice and (b)(c) pack ice separated by the FAL.

3. Methodology

The calibration is conducted through an optimization procedure by minimizing the differences between the measured data and the model results using a range of model parameters. First, we describe the model which we are calibrating now. In this model, the ice cover is viewed as a viscoelastic layer. Its constitutive behavior, when modeled as a continuum, is described as a Voigt material with a linear spring and a dashpot connected in parallel, so that the total internal stress is the sum of the elastic stress $G\epsilon$ and viscous stress $\nu\dot{\epsilon}$. In which, G is the equivalent shear modulus of the ice layer and ν is its equivalent viscosity, ϵ and $\dot{\epsilon}$ are the strain and strain rate respectively. This model was described in Wang and Shen (2010). The dispersion relation between the complex wavenumber $k = k_r + ik_i$ and the angular frequency $\sigma = 2\pi f$ is shown to be

$$\sigma^2 - Qgk \tanh kH = 0 \qquad \textbf{[3a]}$$

$$Q = 1 + \frac{\rho_{ice}}{\rho_{water}} \frac{(g^2k^2 - N^4 - 16k^6a^2\nu_e^4)S_kS_a - 8k^3a\nu_e^2N^2(C_kC_a - 1)}{gk(4k^3a\nu_e^2S_kC_a + N^2S_aC_k - gkS_kS_a)} \quad \textbf{[3b]}$$

where H is water depth, ρ_{ice} and ρ_{water} are densities of ice and water, respectively, h is ice thickness, $a^2 = k^2 - \frac{i\sigma}{\nu_e}$, $S_k = \sinh kh$, $S_a = \sinh ah$, $C_k = \cosh kh$, $C_a = \cosh ah$, $N = \sigma + 2ik^2\nu_e$, $G_\nu = G - i\sigma\nu\rho_{ice}$ and $\nu_e = \nu + \frac{iG}{\rho_{ice}\sigma}$, V is Poisson's ratio. In this study, we use H = 1000 m for deep water, ρ_{water} = 1025 kg/m^3, ρ_{ice}= 922.5 kg/m^3 and V = 0.3 for ice. The complex wavenumber contains the real part k_r associated with wavelength $\lambda = 2\pi/k_r$ and the imaginary part k_i associated with attenuation, so that the wave profile decays exponentially as $E = e^{2i(kx-\sigma t)} = e^{-2k_ix}\, e^{2i(k_rx-\sigma t)}$. For each pair of (G, ν), Eq. [3] can be used to calculate the $k_r - f$ relation and the $k_i - f$ relation.

From the buoy dataset obtained in the grease/pancake ice, we have 148 cases of $k_i - f$ spectral attenuation curves. The $k_r - f$ relation could not be found from the buoy pairs that were far apart. Instead, such information was obtained from the marine radar data (Lund et al., 2016). The results showed that within the conditions encountered in the field, open water dispersion relation $\sigma^2 = gk_{ow}$ applied. We then used the following objective function

$$\mathcal{F}_1 = \min_{G,\nu} \| k_{ow} - k_r \|_2 \quad \textbf{[4]}$$

$$\mathcal{F}_2 = \min_{G,\nu} \| w(k_i^t - k_i^m) \|_2 \quad \textbf{[5]}$$

where superscript t indicates theoretical values from Eq. [3] and m indicates measured data, $w = \int E(\theta, f)d\theta\, f^4$ is a weighting function that emphasized the high-frequency part of the wave spectra. The choice of this weighting factor is to focus on the type of ice encountered consisting mostly grease/pancake ice. Because this type of ice attenuates the high-frequency waves very effectively.

For the SAR data obtained in pack ice, we have 2194 pairs before the FAL, and 440 pairs after the FAL. An independent study using overlapping bursts of Sentinel-1 A SAR imagery separated by a time lapse of ~2 s showed that open water dispersion relation still applies at least to wavenumbers in the range of 0.01-0.025 m^{-1} (about 12-20 s waves, Monteban et al., 2019). Their study was conducted in the Barents Sea with similar ice conditions. Using these measured attenuation data, we perform the calibration by searching for the global optimal G and ν. Since the measured data from the spatial imagery are in terms of k_i-k_r relationship while the theoretical results are in terms of k_i-f and k_r-f relationship. Before applying the optimization, we map the theoretical values for each chosen G, ν to the k_i^t-k_r^t domain. For each k_r^m, we first determine f from the theoretical k_r-f curve from Eq. [3], then use this f to determine the corresponding k_i^t. The objective function is Eq. [5], since Eq. [4] is redundant in this case. Furthermore, we define $w = \sqrt{\int E(\theta, k_r)d\theta}$, considering the quite flat attenuation rate in the range of wavenumbers available in Fig. 2. Hence a broad band weighting is selected.

4. Results

The results are an array of pairs of the calibrated equivalent shear modulus and viscosity. The array size corresponds to the pairs selected from the grease/pancake ice and the pack ice zone before and after the FAL. Figure 3 provides a simultaneous visualization of the ice cover property and the ice morphology. The calibrated shear modulus and viscosity in $\log_{10}$ scale are superimposed on the SAR imagery. To aid visualization, each data point represents the mean value of the parameters obtained in a 5 km by 5 km cell.

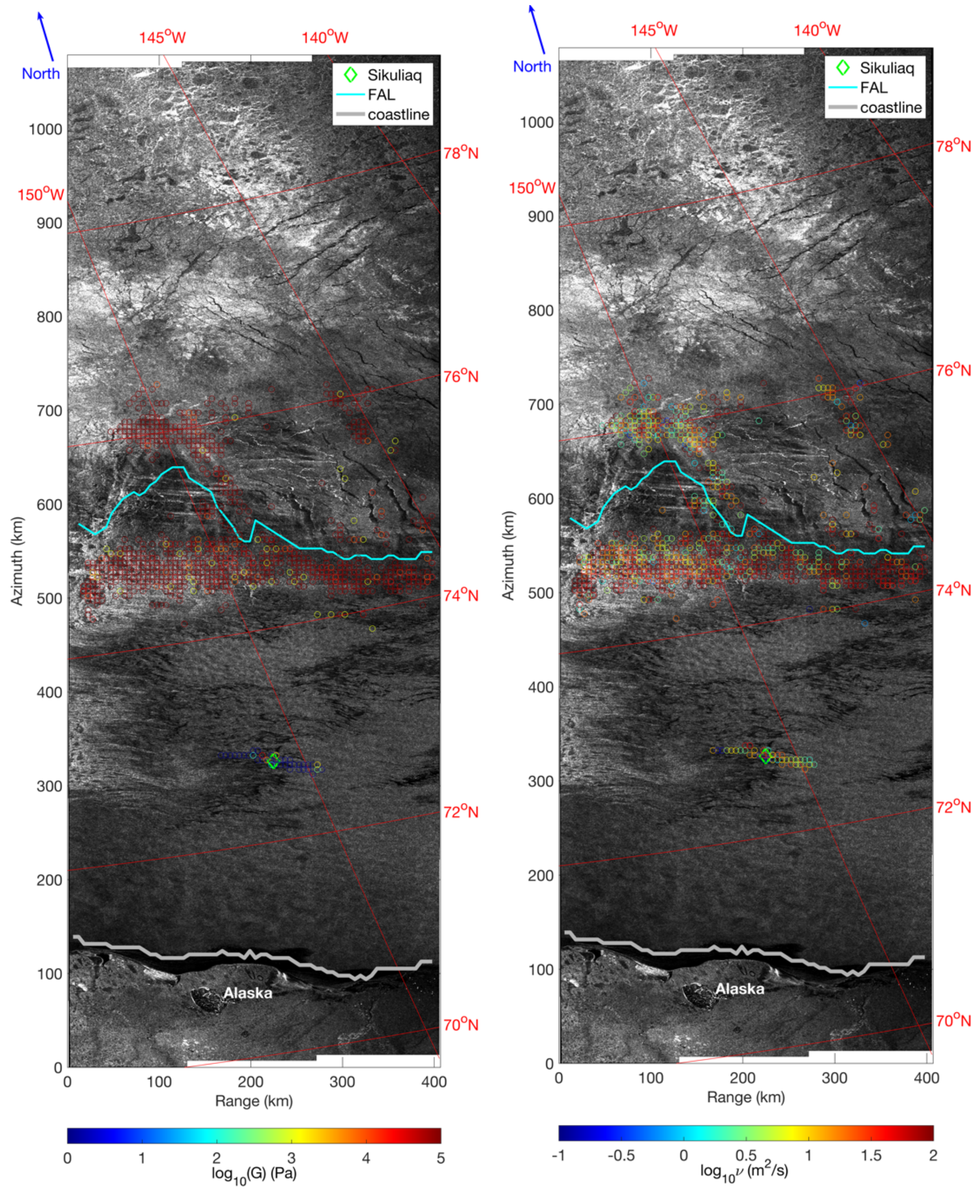

Figure 3. Superposition of the calibrated (a) elastic modulus G and (b) viscosity ν in log scale on the Sentinel-1 A SAR imagery. The color bar indicated the value of these parameters.

Furthermore, these calibrated data in the shear modulus and viscosity domain are clustered using bivariate Gaussian distribution functions. Statistics of the obtained functions including the means and covariances of $\log_{10} G$ and $\log_{10} \nu$ are given in Table 1. From the mean values, in the grease/pancake ice, data are clustered in two clusters with low or zero elasticity, indicating ice layer behaves as a viscous layer. The pack ice layer preserve more viscoelastic property. The difference between the south and north of the FAL is slight, with higher elastic and less viscous properties north of the FAL.

Table 1. Statistics of the log scaled shear modulus (Pa) and viscosity (m^2/s).

	μ_X	μ_Y	$cov(X,X)$	$cov(X,Y)$	$cov(Y,Y)$
Grease/Pancake					
	-5.65	0.93	0.17	0.11	0.15
	2.82	0.41	0.17	-0.03	0.03
Pack ice					
Before FAL	5.07	1.51	0.07	0.07	0.81
After FAL	5.25	1.32	0.11	0.27	1.26

*$X = \log_{10} G$, $Y = \log_{10} \nu$, μ: mean, cov: covariance.

5. Discussion and conclusions

From Fig. 3, we observe that the calibrated values of elastic modulus and viscosity of pack ice are higher than those of grease/pancake ice. The difference of elasticity from the ice types are more significant than the viscosity. The equivalent elasticity of pack ice is roughly two orders of magnitude higher than the grease/pancake ice (but still much less than the intrinsic ice elastic modulus, ~10^9Pa).

This study shows how to use field data to calibrate wave-in-ice models. With more field experiments that are ongoing in both Arctic and Antarctic regions, we envision that parameterization of models for various ice types may be performed. At the same time, different wave-in-ice models may also use the procedure described here to complete the parametrization. These models may then be applied to test their capability of wave forecasts in the ice-covered seas.

Detailed results of this study have been reported in Cheng et al. (2017) and Cheng et al. (2020, under review). Wave-ice interaction may include many physical mechanisms. In this study, the total attenuation rate from all processes, Eq. [1], and attenuation from ice, Eq. [2], are obtained. The dataset can potentially be used in many future studies.

Acknowledgments

The authors would like to thank the Isaac Newton Institute for Mathematical Sciences, Cambridge, for support and hospitality during the programme Ice-fluid interaction (SIPW02) where work on this paper was initiated. This programme was supported by EPSRC grant numbers EP/K032208/1 and EP/R014604/1. The concept presented here was based on many discussions during the ONR sponsored Seastate and Boundary Layer Physics Program under Drs. Scott Harper and Martin Jeffries.

References

Cheng, S., Rogers, W. E., Thomson, J., Smith, M., Doble, M. J., Wadhams, P., ... and Ackley, S. F., 2017. Calibrating a viscoelastic sea ice model for wave propagation in the Arctic fall marginal ice zone. J. Geophys. Res.-Oceans, 122(11), 8770-8793.

Cheng, S., Stopa, J., Ardhuin, F., and Shen, H. H., 2020. Spectral attenuation of ocean waves in pack ice and its application in calibrating viscoelastic wave-in-ice models. The cryosphere, under review.

Doble, M.J. and Wadhams, P., 2006. Dynamical contrasts between pancake and pack ice, investigated with a drifting buoy array. J. Geophys. Res.-Oceans, 111(C11S24), https://doi.org/0.1029/2005JC003320.

Lund, B., C. O. Collins III, H. Tamura, and H. C. Graber, 2016. Multidirectional wave spectra from marine X-band radar. Ocean Dyn., 66, 973–988, doi:10.1007/s10236-016-0961-z.

Monteban, D., Johnsen, H., and Lubbad, R., 2019. Spatiotemporal observations of wave dispersion within sea ice using Sentinel-1 SAR TOPS mode. J. Geophys. Res.-Oceans. https://doi.org/10.1029/2019JC015311.

Rogers, W. E., Thomson, J., Shen, H.H., Doble, M.J., Wadhams, P., and Cheng, S., 2016. Dissipation of wind waves by pancake and frazil ice in the autumn Beaufort Sea. J. Geophys. Res.-Oceans, 121, https://doi.org/10.1002/2016JC012251.

Stopa, J., Ardhuin, F., Thomson, J., Smith, M. M., Kohout, A., Doble, M., and Wadhams, P., 2018. Wave attenuation through an Arctic marginal ice zone on 12 October 2015: 1. Measurement of wave spectra and ice features from Sentinel 1A. J. Geophys. Res.-Oceans, 123, 3619-3634. https://doi.org/10.1029/2018JC013791

Thomson, J., 2012. Wave Breaking Dissipation Observed with “SWIFT” Drifters. J. Atmos. Oceanic Technol., 29:1866–1882, https://doi.org/10.1175/JTECH-D-12-00018.1

Thomson, J., Ackley, S., Girard-Ardhuin, F., Ardhuin, F., Babanin, A., Boutin, G., 2018. Overview of the Arctic Sea state and boundary layer physics program. J. Geophys. Res.-Oceans, 123, 8674– 8687. https://doi.org/10.1002/2018JC013766

The WAVEWATCH III® Development Group (WW3DG), 2019. User manual and system documentation of WAVEWATCH III® version 6.07. Tech. Note 333, NOAA/NWS/NCEP/MMAB, College Park, MD, USA, 465 pp. +Appendices.

Wang, R., and Shen, H. H., 2010. Gravity waves propagating into an ice-covered ocean: A viscoelastic model, J. Geophys. Res.-Oceans, 115.

25th IAHR International Symposium on Ice
Trondheim, June 14 to 18, 2020

Modelling ocean gravity wave dispersion of young sea ice in the MIZ

De Santi F. [1] , Passoni G. [2] , Olla P. [1] , Abbà A. [2] ,
Valdettaro L. [2] , De Angelis E. [4] , De Carolis G. [1]
(1) National Research Council Of Italy, Milan, Italy
desanti.f@irea.cnr.it, decarolis.g@irea.cnr.it,olla.dsf@unica.it
(2) Politecnico di Milano, Milan, Italy
Giuseppe.passoni@polimi.it, antonella.abbà@polimi.it, lorenzo.valdettaro@polimi.it
(3) Università di Bologna, Bologna, Italy
e.deangelis@unibo.it

The young sea ice that develops in the marginal ice zones (MIZ) of the Polar Seas during the freezing period mainly consists of mixtures of grease-pancake ice and thin ice floes (GPTI). GPTI properties are exceedingly difficult to measure in situ, due to the small floe size, the transient nature of the processes involved and the hostile environment where they take place. As the surface gravity waves coming from the open ocean are affected by GPTI, a tool to infer GPTI properties could rely on waves' measurements.

This procedure requires the application of a suitable model of wave propagation in the ice-covered ocean. Viscous wave propagation models have demonstrated their ability to predict the observed spectral wave attenuation in GPTI, although concerns remain about their calibration. The recently developed waves-in-ice model, called close packing model, has had reasonable success, at least in the case of very thin ice, in predicting both the attenuation and the dispersion of the waves as a function of the frequency. However, to apply the CP model to thicker sea ice, such as the one found in the Antarctica oceans, further theoretical efforts are required.

With this research, we want to estimate the relative importance and the parametrization of those mechanisms that are not considered in close packing. This is the case of pancakes inertia and wave diffraction.

1. Introduction

Grease-pancake ice and thin ice floes (GPTI) are the major types of young sea ice that grow in the turbulent waters of the marginal ice zones (MIZ) of the Earth planet. Almost ubiquitous in the Antarctica MIZ, the GPTI is also becoming the "new normal" in western Arctic MIZ where, in the past, there was scarce evidence of it (Thomson et al. 2018). A fact highly related to the dramatic shrinking of sea ice occurring in the Arctic during the summer, followed by thinner sea ice growth in the autumn. The situation leads to longer fetches of open waters where bigger waves are allowed to grow, which is contributes to hindering ice formation (Stopa et al. 2016).

Waves propagating from the open ocean change their speed and amplitude as they enter in an ice-covered area. These waves changes depending on the ice layer properties and due to two main mechanisms: the scattering by individual flows and the dissipation from friction and other processes in the ice cover.

Wave scattering conserves energy and waves' attenuation results from an accumulation of scattering events by individual floes. Conventionally scattering models treats the floes as thin floating elastic plates (e.g., Bennetts & Williams, 2010), and they agree reasonably well with experimental measurements (e.g., Kohout & Meylan, 2008), but only when wavelengths are comparable to floe lengths.

For waves much longer than floes waves' attenuation is assumed to result from dissipation of wave energy, e.g., due to viscosity. In this case, if the ice cover is sufficiently homogeneous, waves' modification can be described by a complex dispersion relation, which accounts for the material properties of ice cover. These properties can be expressed as explicit terms for additional inertia at the surface (Squire 1993), effective ice layer viscosity (Keller 1998), effective eddy viscosity (De Carolis & Desiderio 2002), effective ice cover elasticity (Wang & Shen 2010), and horizontal compression at the surface (De Santi & Olla 2017).

Validation of the prediction by different models is challenging because it requires simultaneous measurements of the ice cover properties, i.e., sea ice concentration and thickness, and the associated wave spectral properties. Some studies using remote sensing data from SAR imagery (De Carolis & Laurenza, 2016) and, when available, field measurements (Doble et al. 2003; Thomson et al. 2018) have found that:
- the elasticity contribution to waves dynamics is negligible when the ice cover consists mostly of pancake ice, frazil ice, or small floes of thin young ice (Cheng et al. 2017);
- pure viscous or visco-elastic models require a large variability of the rheological parameters to reproduce the attenuation of the waves showed by satellite and buoy data which makes difficult to properly calibrate such models (Cheng et 2017; De Santi et al. 2018; Doble et al. 2015);
- pure viscous and visco-elastic models fail to predict the waves shortening observed in recent measurements (Collins et al. JGR:Oceans 2018);
- the model that only accounts for additional inertia at the surface, called mass loading model, can predict the wave-shortening but overestimates the ice thickness and does not predict any wave attenuation (Collins et al. JGR:Oceans 2018).

The problems experienced with the above models are partially overcome by the recently proposed Close Packing (CP) model, where the effect of the ice viscosity is combined with a horizontal compression at the surface due to the presence of pancakes or thin floes (De Santi & Olla 2017). For very thin ice, CP model can reproduce the measured waves attenuation and wave shortening with reasonable values for the ice thickness and ice viscosity. However, the CP model overestimates the ice thickness for ice layers thicker than 20 cm, thus suggesting that some essential ingredients of the wave dynamics in the MIZ is still missing.

This work aims to assess whether this "missing ingredient" can be related to ideal effects such as, e.g. wave scattering. Scattering phenomena are known to play an important role when the size of the floating objects is comparable to the wavelength. The present study intends to provide an estimate of the scattering contribution to wave attenuation in the case of smaller bodies of the size of a pancake. In this preliminary study we do not take into account the interaction of the pancakes, even though, given the high surface density and compactification rate of the GPTI, it is worthwhile to quantify the mutual interaction among floes. Indeed, when an incident wave propagates into a matrix of bodies, each body diffracts waves towards the others, which in turn respond to this excitation and send back radiation that contributes to the total excitation of the original body, and so on (Kagemoto & Yue 1986). We have proved, and we are going to report all the details in a work-in-progress manuscript, that pancakes result in a coherent scattering so that we can neglect their mutual interaction.

The computation of water wave interaction effects amongst floating bodies is also relevant for the analysis of a variety of offshore and coastal problems. As an example, in the emerging field of offshore renewable energy, wind turbines and wave energy converters (WECs), must be deployed in arrays where wave interactions have significant effects on wave loads, dynamics, and performance (e.g., McNatt, J. C., et al., 2015; Simon 1982).
.to generate cost-effective electricity, devices, such as offshore

However, to the authors' knowledge, none of these applications considers a length scale separation typical of the autumn marginal ice zone (i.e. mostly composed by pancakes and small floes). With this preliminary study, we want to analytically estimate the effective role of scattering processes in such conditions.

2. Problem formulation

We want to assess the contribution by ideal effects to wave damping in the grease-pancake ice-covered ocean focusing our analysis on the scattering due by the pancakes.

Under the hypothesis that wave dynamics obeys to linearized Euler equation and assuming an elastic scattering, each pancake responds to the field of the incoming wave by generating a radial wave with identical frequency. The velocity potential of the perturbation measured at x is:

$$\phi(\boldsymbol{x}, t) \backsim \sum_j \exp\left[i\left(\boldsymbol{k}\cdot\boldsymbol{x} + \delta + \boldsymbol{q}_j\cdot\left(\boldsymbol{x}-\boldsymbol{x}_j\right) - \omega t\right)\right], \qquad \textbf{[1]}$$

where $\boldsymbol{k}$ is the wavevector of the incoming wave, $\omega = \sqrt{kg}$ is the wave frequency, with g the gravitational acceleration, $\boldsymbol{x}_j$ is the position of the j-th pancake, and $\boldsymbol{q}_j$ is the wavevector of the radial wave at $\boldsymbol{x}$, and δ is the constant phase shift in the radiation process.
If $\boldsymbol{x}$ is very far from the region containing the pancakes, $\boldsymbol{q}_j$ will be almost constant, $\boldsymbol{q}_j \simeq q$, and

$$\phi(\boldsymbol{x}, t) \backsim exp[i(\boldsymbol{k} \cdot \boldsymbol{x} + \delta - \omega t)] \sum_j \exp[i(\boldsymbol{q} \cdot (\boldsymbol{x} - \boldsymbol{x}_j) - \omega t)] . \quad \textbf{[2]}$$

Consistently with the assumption of inviscid system, we assume potential flow both for the wave field, $\overline{\boldsymbol{U}} = \nabla \overline{\Phi}$ and for the perturbation by the pancakes, $\boldsymbol{u} = \nabla \varphi$. We disregard the presence of grease ice and consider the pancakes neutrally buoyant and fully submerged in the water column.

To obtain an order of magnitude estimate of the radiated energy, we consider a simplified picture in which pancakes are so widely separated that their mutual interactions are negligible and the interference of the radiated waves has random character. This allows us to neglect cross terms in the double sum in the expression of the energy flux at the region containing the pancakes is much larger than one wavelength, the terms at x, which is quadratic in ϕ.
Therefore the energy flux results in the sum of the energy fluxes by the individual pancakes.

Let us indicate with I_ϕ the energy radiated by pancakes. It is evaluated from the total energy current $\boldsymbol{J}_\phi$ as

$$I_\phi = \int_0^{2\pi} d\varphi x_\perp \cdot \boldsymbol{J}_\phi(x), \quad \textbf{[3]}$$

where $\boldsymbol{x} = (\boldsymbol{x}_\perp, x_3)$ and x_3 is taken to point upward. The scattering cross section is thus defined as $\sigma = I_\phi / J^{inc}$, with J^{inc} the energy flux density of the incident wave. The total energy lost by the incoming wave to diffusion by the pancakes in an area S will be $S n_p \sigma J$, where n_p is the surface density of the pancakes. This leads to the extinction length,

$$\lambda = (n_p \sigma)^{-1}, \quad \textbf{[4]}$$

and the whole business is to evaluate the parameter σ from the hydrodynamics interaction of the waves and the pancakes.

2. Scattering cross section for pancakes scale length

The wave dynamics obeys the linearized Euler equation

$$\rho \partial_t \boldsymbol{U} + \nabla P + \boldsymbol{e}_3 \rho g = 0, \quad \textbf{[5]}$$

where $\boldsymbol{U} = \overline{\boldsymbol{U}} + \boldsymbol{u}$ is the total fluid velocity, P is the total pressure, and ρ is the water density.
Energy conservation is accounted for by the presence of a conserved current

$$\boldsymbol{J} = \langle P\boldsymbol{U} \rangle = -\rho[(\nabla\Phi)\partial_t\Phi^* + (\nabla\Phi^*)\partial_t\Phi] = i\omega\rho[\Phi\nabla\Phi^* - \Phi^*\nabla\Phi] \quad \textbf{[6]}$$

which obeys the local conservation law

$$\frac{\rho}{2}\frac{\partial|\nabla\Phi|^2}{\partial t} + \nabla \cdot J = 0 \quad \textbf{[7]}$$

The structure of this conservation law is very similar to that for probability in quantum mechanics. This gives some indication on how to evaluate the energy transfer to the diffused wave. The treatment is adapted from the one of quantum mechanical elastic scattering described e.g. in (Landau & Lifshitz, 2013). We postpone technical details to a later publication and illustrate here the result of the analysis in the case of submerged bodies of simple shape (spheres and cylinders). In the case of the pancakes, the mechanics of the process can be outlined as follows.

For an analytical treatment of the problem, we expand incident and diffusion wave in partial waves through Bessel functions of the first and the second kind. For now, we can limit our analysis to the scattering produced by a single small floating body of characteristic size R.

Taking inspiration from analogous strategies in the treatment of electromagnetic radiation, we exploit the scale separation and subdivide the domain into far ($kx_\perp$ >>1) and near ($kx_\perp$ <<1) field regions. In the near field region, U evolves on a time scale ω^{-1} much slower than that of a wave with wavelength $x_\perp$, so that near field disturbance is enslaved to the incident wave field. The far field is then determined by imposing continuity of the energy flux in the two regions. Following such procedure allows us to estimate the scattering cross section for a floating object with generic shape:

$$\sigma \simeq 4k^{-1} \textstyle\sum_{n=0}^{\infty} \delta_n^2, \qquad \textbf{[8]}$$

where δ_n are the scattering phases associated with the$n$-th Bessel function.
Radially symmetric outgoing waves dominate scattering in the case of bodies much smaller than a wavelength, so that phases with $n = 0$ dominate the scattering cross section.

Determination of the scattering phases requires to solve the fluid dynamic problem in the vicinity of the ice body, for which the analytical solution is available only for particular geometries. We consider the case of a spherical object of radius R at depth z such that $R \ll z \ll k^{-1}$. We obtain in this case

$$\delta_0 \simeq (\pi k^4 R^5)/(3z). \qquad \textbf{[9]}$$

3. Discussion

The characteristic scales of a typical pancake ice field are $R = 0.5$ m, $10^{-2}\text{m}^{-1} \leq k \leq 10^{-1}\text{m}^{-1}$ and $z = 0.5$ m. As defined in Eq. [9], the resulting scattering phase is very small, $10^{-9} \lesssim \delta_0 \lesssim 10^{-5}$. Three different operations could, in principle, make δ larger.

1) Operate in the limit $z \to R$, i.e. to consider a floating object. This would remove a factor R/z in Eq. [9] ($\delta \sim 1.6 \cdot 10^{-5}$)

2) Lastly, we may try to refine the argument leading to the extinction length in Eq. [3] by taking into account that, in a close-packing regime, a large number of pancake pairs are less than a wavelength away, and that localized fluctuations produce a coherent contribution to the radiation field. Let us take for simplicity fluctuations of amplitude $\sim n_p$ and indicate with $l \lesssim k^{-1}$ their correlation length. We have from Eq. [2]

$$\langle|\phi(\boldsymbol{x},t)|^2\rangle \backsim \sum_{s,j}\left\langle exp\left[i\left((\boldsymbol{k}-\boldsymbol{q})\cdot(\boldsymbol{x}_s-\boldsymbol{x}_j)\right)\right]\right\rangle. \quad \textbf{[10]}$$

If A is the area of the pancake containing region, the number of pairs separated by less than l will be $\sim n_p^2 A l^2 \sim A\, l^2/R^4$, much larger than the number of pancakes in the region, A/R^2. Extinction length formula Eq. [3] is then replaced by

$$\lambda \sim \left(n_p^2 l^2 \sigma\right)^{-1} \sim \left(n_p^2 l^2 k^5 R^6\right)^{-1} \gtrsim (k^3 R^2)^{-1} \sim 1.6 \cdot 10^4 \mathrm{m} \quad \textbf{[11]}$$

Unfortunately, it is difficult to justify a finite l without invoking a nonlinear mechanism. The extinction length results, therefore one hundred times the wavelength. We can conclude that the effect is very small.

Acknowledgments

This research has been funded by PNRA PNRA18_00109 project WAMIZ.

References

Thomson, J., et al., 2018. Overview of the arctic sea state and boundary layer physics program. Journal of Geophysical Research: Oceans, 123(12), 8674-8687.

Stopa, J. E., Ardhuin, F., & Girard-Ardhuin, F., 2016. Wave climate in the Arctic 1992-2014: seasonality and trends. Cryosphere, 10(4).

Bennetts, L. G., & Williams, T. D., 2010. Wave scattering by ice floes and polynyas of arbitrary shape. Journal of fluid mechanics, 662, 5-35.

Kohout, A. L., & Meylan, M. H., 2008. An elastic plate model for wave attenuation and ice floe breaking in the marginal ice zone. Journal of Geophysical Research: Oceans, 113(C9).

Squire, V. A., 1993. The breakup of shore fast sea ice. Cold Regions Science and Technology, 21(3), 211-218.

Keller, J. B. (1998). Gravity waves on ice-covered water. Journal of Geophysical Research: Oceans, 103(C4), 7663-7669.

De Carolis, G., & Desiderio, D., 2002. Dispersion and attenuation of gravity waves in ice: a two-layer viscous fluid model with experimental data validation. Physics Letters A, 305(6), 399-412.

Wang, R., & Shen, H. H., 2010. Gravity waves propagating into an ice-covered ocean: A viscoelastic model. Journal of Geophysical Research: Oceans, 115(C6).

De Santi, F., & Olla, P., 2017. Effect of small floating disks on the propagation of gravity waves. Fluid Dynamics Research, 49(2), 025512.

De Carolis, G., & Laurenza, L. M., 2016. SAR Monitoring of Waves in Pancake Ice in the Marginal Ice Zone. In Living Planet Symposium (Vol. 740, p. 338).

Doble, M. J., Coon, M. D., & Wadhams, P., 2003. Pancake ice formation in the Weddell Sea. Journal of Geophysical Research: Oceans, 108(C7).

Cheng, S., et al., 2017. Calibrating a viscoelastic sea ice model for wave propagation in the Arctic fall marginal ice zone. Journal of Geophysical Research: Oceans, 122(11), 8770-8793.

De Santi, F., et al., 2018. On the Ocean Wave Attenuation Rate in Grease-Pancake Ice, a Comparison of Viscous Layer Propagation Models With Field Data. Journal of Geophysical Research: Oceans, 123(8), 5933-5948.

Doble, M. J., et al., 2015. Relating wave attenuation to pancake ice thickness, using field measurements and model results. Geophysical Research Letters, 42(11), 4473-4481.
Collins, C., et al., 2018. Observations of surface wave dispersion in the marginal ice zone. Journal of Geophysical Research: Oceans, 123(5), 3336-3354.
Kagemoto, H., & Yue, D. K., 1986. Interactions among multiple three-dimensional bodies in water waves: an exact algebraic method. Journal of fluid mechanics, 166, 189-209.
McNatt, J. C., et al., 2015. A novel method for deriving the diffraction transfer matrix and its application to multi-body interactions in water waves. Ocean Engineering, 94, 173-185.
Simon, M. J., 1982. Multiple scattering in arrays of axisymmetric wave-energy devices. Part 1. A matrix method using a plane-wave approximation. Journal of Fluid Mechanics, 120, 1-25.
Landau, L. D., & Lifshitz, E. M., 2013. Quantum mechanics: non-relativistic theory (Vol. 3). Elsevier.
Abramowitz, M., Stegun, I. A., & Romer, R. H., 1988. Handbook of mathematical functions with formulas, graphs, and mathematical tables

25th IAHR International Symposium on Ice

Trondheim, 23 - 25 November 2020

Fully Dispersive Models for Flexural-Gravity Waves

Evgueni Dinvay[1,2], Henrik Kalisch[2], Emilian I. Parau[3]

[1]*UFR mathématiques, Université de Rennes 1, 35042 Rennes CEDEX, France*
evgueni.dinvay@uib.no
[2]*University of Bergen, Department of Mathematics, PO Box 7800, 5020 Bergen, Norway*
henrik.kalisch@uib.no
[3]*University of East Anglia, School of Mathematics, Norwich, NR4 7TJ, UK*
E.Parau@uea.ac.uk

We propose a mathematical model which describes the time-dependent response to of a floating ice sheet to a load moving at an arbitrary, possibly time-dependent velocity. The model is validated using a number of test cases from existing field studies, such as the field campaign of Takizawa at Lake Saroma and the campaign of Wilson at Mille Lacs. Good agreement between the deflectometer records from the field studies and the numerical simulations is observed in most cases.

The model allows for an accurate description of waves across the whole spectrum of wavelengths and also incorporates nonlinearity, forcing and damping. The load can be a point load or have a described weight distribution, moving at a time-dependent velocity. In this respect, the present model is more versatile than existing models for steady waves excited by moving loads.

1. Introduction

Hydro-elastic waves can be found in ice sheets in the arctic regions and on frozen lakes and sounds in the winter season. The study of such waves has a long history going back to the 1950's and was prompted by attempts to use solid ice covers as a means of supporting mechanized transportation (Squire et al., 1988). For example, in cold regions, some winter truck routes are partially on ice-covered lakes, and in some cases air strips have been built on thick ice covers. Indeed as mentioned in (Squire et al., 1988), in some cases, train tracks have been laid on ice.

As many of these enterprises experienced problems resulting in loss equipment, and sometimes even endangering the life of the crews, it became clear that there was a need to improve our understanding of the properties of ice covers such as bearing capacity, resonant behavior, and the susceptibility to crack formation. A number of experimental campaigns were mounted with the goal of understanding the wave response to moving loads on ice covers (Takizawa, 1987), (Takizawa, 1988), (Wilson, 1955). In addition, mathematical models were developed in order to predict the wave response to a moving load (Davys, Hosking and Sneyd, 1985). This purely linear conservative model was later improved by including nonlinearity (Parau and Dias, 2002), (Guyenne and Parau, 2014a, 2014b) and various forms of damping or visco-elasticity (Hosking, Sneyd and Waugh, 1988), (Wang, Hosking and Milinazzo, 2004).

In the current contribution, we use a fully dispersive model equation developed in (Dinvay, Kalisch and Parau, 2019a, 2019b) which is able to give more detailed information on the waves excited by a moving load than many previous works. The derivation is based on an idea due to G.B. Whitham (Whitham, 1967) to couple fully dispersive models with weakly linear terms, which has recently been extended to systems of equations (Aceves-Sanchez, Minzoni, and Panayotaros, 2013), (Carter, 2018), (Dinvay, Dutykh and Kalisch, 2019), (Moldabayev, Kalisch, Dutykh, 2015). Using this new model in connection with a split-step method for numerical discretization, we are able to study the time-dependent development of flexural-gravity waves. The versatility of the model system allows the study of a wide range of situations including the motion of a combination of point loads, or indeed loads of arbitrary shape and time-dependent velocity.

A point of departure for the linear study of flexural-gravity waves is the dispersion relation for small-amplitude waves. This relation is given by

$$c^2(\xi) = \frac{g/\xi + D\xi^3/\rho}{\coth \xi H + h\xi\rho_I/\rho} \qquad (1.1)$$

where H is the depth of the undisturbed fluid, h is the thickness of the elastic cover, ρ is the fluid density, ρ_I is the density of the elastic cover, and D is the flexural rigidity of the elastic material. In stating the relation (2.1), the assumption is made that the wavelength is greater than the thickness of the ice sheet. This assumption is generally reasonable. On the other hand, for very long waves the above relation may be approximated by

$$c^2 = \frac{g}{\xi}[1 + \xi^4 D/g\rho\,] \tanh \xi H \qquad (1.2)$$

which is used in Takizawa (1987) and many other works. Figure 1 shows the two dispersion relations (1.1) and (1.2) for the parameter sets corresponding to the field experiments reported in (Takizawa, 1987,1988) and (Wilson, 1955). In the following we shall look at the derivation of the hydro-elastic equations, then state the weakly nonlinear approximation, and finally present numerical simulations of the field experiments of Takizawa and Wilson.

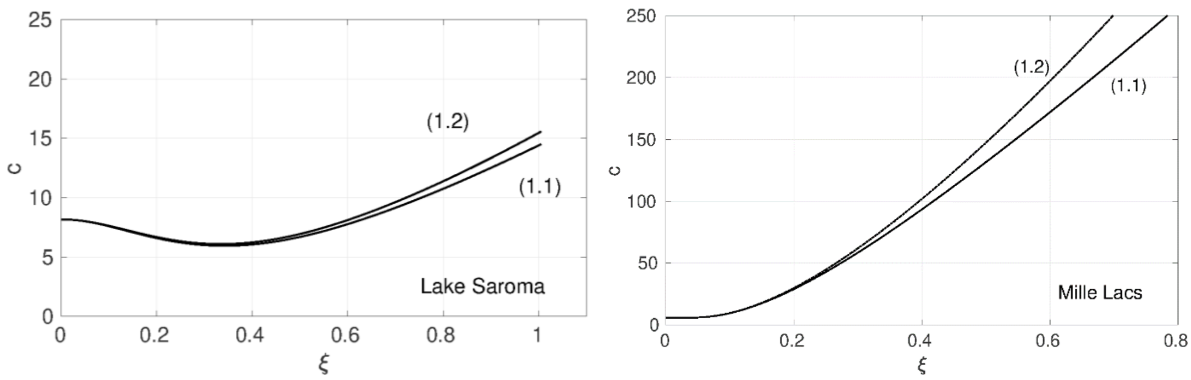

Figure 1. Dispersion of flexural gravity waves on Lake Saroma (Takizawa, 1987) and on Mille Lacs (Wilson, 1955).

2. The hydro-elastic system

We consider irrotational motion of an inviscid and incompressible fluid of undisturbed mean depth H, and with gravity g acting in the negative z-direction. The fluid is covered by an elastic solid described by the Kirchhoff–Love plate theory (cf. Squire, Hosking, Kerr & Langhorne (1988)). The flow of the underlying liquid is described by the velocity potential Φ(x, z, t) and by the fluid surface elevation η(x,t) that coincides with the vertical deformation of the underside of the elastic cover. The surface z = 0 corresponds to the fluid-solid interface at rest. The fluid flow is describe by the Euler equations, i.e. the Laplace equation

$$\Phi_{xx} + \Phi_{zz} = 0 \qquad \text{for } x \in \boldsymbol{R}, \qquad -H < z < \eta(\mathrm{x,t}) \tag{2.1}$$

the Neumann boundary condition at the bottom

$$\Phi_z = 0 \qquad \text{at } z = -H, \tag{2.2}$$

the kinematic condition at the interface between the cover and the liquid

$$\eta_t + \Phi_x \eta_x - \Phi_z = 0 \qquad \text{for } x \in \boldsymbol{R}, \qquad z = \eta(\mathrm{x,t}) \tag{2.3}$$

and the dynamic boundary condition

$$\Phi_t + \frac{1}{2}|\nabla\Phi|^2 + g\eta + \frac{p}{\rho} = C_B \qquad \text{for } x \in \boldsymbol{R}, \qquad z = \eta(\mathrm{x,t}). \tag{2.4}$$

Here C_B is the Bernoulli constant which will be specified later. The presence of the elastic solid is described via the pressure at the boundary. To model the elastic medium we regard a new coordinate system shifted up along the z-axis, so that the line z = 0 coincides with z = h/2, where h is the ice thickness. Thus at rest, the line z = 0 coincides with the the center line of the elastic plate. For ease of reading, the developments in this section are only given for the two-dimensional case. The three dimensional case can be treated analogously. Assuming small deformations in the horizontal and vertical directions respectively, one may consider the following material motion equations

$$\partial_x \sigma_{11} + \partial_z \sigma_{12} = \rho_I \partial_t^2 u_1 \tag{2.5}$$

$$\partial_x \sigma_{21} + \partial_z \sigma_{22} - \rho_I g = \rho_I \partial_t^2 u_2 \tag{2.6}$$

This system represents Newton's second law connecting the divergence of the stress tensor on the left hand side and the acceleration of particles on the right simplified due to smallness of the deformation. The plate density is constant. The stress tensor is symmetric, which means there are no volume or surface moments. As is common in hydro-elastic problems, we combine nonlinear equations for the fluid motion with linear elastic equations for the solid. This choice can be justified by noticing that liquid motions are of a different order of magnitude than deformations of the elastic solid cover. The equations are completed by adding the relation

$$u_1 = -z\partial_x u_2 \tag{2.7}$$

with u_2 not depending on z and

$$\sigma_{11} = \frac{E}{1-\nu^2}\partial_x u_1 \tag{2.8}$$

Here E is Young's modulus and ν is Poisson's ratio of the solid. Equation (2.7) is a consequence of the first Kirchhoff hypothesis stating that straight lines normal to the mid-surface remain normal and straight after deformation. It also assumes that the thickness does not change during deformation. Equation (2.8) is a Hooke relation modified by the second Kirchhoff hypothesis stating that normal stresses to surfaces parallel to the center surface are smaller than other stresses. The validity of the last assumptions (2.7)-(2.8) are well justified provided the plate thickness h is small with respect to horizontal scales. That is true since we consider a domain of infinite extent in the horizontal directions. Note that we do not assume anything concerning the relation between the thickness h and the depth H.

With regards to boundary conditions imposed on the elastic plate, we have an inviscid fluid below the plate, which means that the shear stress at the lower boundary is zero and the normal stress is due to the fluid pressure p. The top of the elastic plate is free, except for an imposed pressure P which can be used to model a moving load. Summing up, we have

$$\sigma_{22} = -P(x,t) \text{ on } z = h/2,$$
$$\sigma_{22} = -p(x,t) \text{ on } z = -h/2,$$
$$\sigma_{12} = \sigma_{21} = 0 \text{ on } z = h/2 \text{ and } z = -h/2.$$

An agreement is made here that the liquid pushes the plate up and the load pushes it down. In a real situation this will mean that the pressure P is positive, in case of a heavy truck for example. However, mathematically, negative values of the imposed load P are also allowed.

Following Squire, Hosking, Kerr & Langhorne (1988), a standard procedure of averaging the expressions (2.5)-(2.6) is now applied. Introduce a transverse force

$$Q_1 = \int_{-h/2}^{h/2} \sigma_{12}\, dz.$$

Integrating both parts of (2.6) over z one obtains

$$\partial_x Q_1 + \sigma_{22}\big|_{z=-h/2}^{z=h/2} - \rho_I g h = \rho_I h \partial_t^2 u_2.$$

Substituting (2.7)-(2.8) in the first equation (2.5), then multiplying by −z and integrating over z one arrives at

$$\frac{Eh^3}{12(1-\nu^2)} \partial_x^3 u_2 + Q_1 - z\sigma_{12}\big|_{z=-\frac{h}{2}}^{z=\frac{h}{2}} = \frac{\rho_I h^3}{12} \partial_t^2 \partial_x u_2.$$

These two equations together with the boundary conditions yield the relation

$$D\partial_x^4 u_2 - \frac{\rho_I h^3}{12} \partial_t^2 \partial_x^2 u_2 + \rho_I h \partial_t^2 u_2 + \rho_I g h + P - p = 0$$

where $D = Eh^3/12(1-\nu^2)$ is the flexural rigidity. This is a well known equation describing the deflection $u_2(x,t)$ of a beam. The second term in the equation which is due to horizontal acceleration of media particles is usually neglected, but in the present analysis, this term will actually be important.

The last step in the modelling of the elastic cover is to take into account energy dissipation. We assume a damping force proportional to the vertical velocity, which results in the addition of a damping term to the left part of equation (2.6). Repeating the above averaging procedure in the presence of damping leads to

$$D\partial_x^4 u_2 - \frac{\rho_I h^3}{12} \partial_t^2 \partial_x^2 u_2 + \rho_I h \partial_t^2 u_2 + b\partial_t u_2 + \rho_I g h + P - p = 0 \tag{2.9}$$

which is our main ice deflection model that we need to combine with Equations (2.1)-(2.4). As stated above, the vertical deformation does not depend on variable z. Moreover, we do not allow for cavitation, so that the underlying fluid is always in contact with the elastic plate. Therefore the curves $z = u_2(x, t) - h/2$ and $z = \eta(x, t)$ coincide. If we now choose the Bernoulli constant $C_B = g\,\rho_I h/\rho$, then the last equation (2.9) together with (2.4) can be written in terms of the hydro-elastic parameter $\kappa = D/(\rho g)$ as

$$\kappa g \partial_x^4 \eta - \frac{\rho_I h^3}{12\rho} \partial_t^2 \partial_x^2 \eta + \frac{\rho_I h}{\rho} \partial_t^2 \eta + \frac{b}{\rho} \partial_t \eta + g\eta + \Phi_t + \frac{1}{2}|\nabla\Phi|^2 + \frac{P}{\rho} = 0. \tag{2.10}$$

This equation holds on the interface $z = \eta(x, t)$. Note that both the horizontal acceleration of the solid media particles and the nonlinear hydrodynamical effects are taken into account here. The load P is taken as a distributed pressure

$$P(x,t) = \rho f(x - x_0 - X(t)) \tag{2.11}$$

propagating down the x-axis. The hydro-elastic system is given thus by the Laplace equation (2.1), with the boundary conditions (2.2), (2.3) and (2.10).

3. Weakly nonlinear models and simulations

Using an analysis such as presented in (Dinvay, Kalisch and Parau, 2019a, 2019b), a fully dispersive weakly nonlinear system can be found. The system has the form

$$\eta_t = -\frac{\tanh HD}{D} u_x - \partial_x(\eta u) \tag{3.1}$$

$$u_t = -g\frac{1+\kappa\partial_x^4}{K}\eta_x - \frac{b}{\rho}\frac{G_0}{K}u - \frac{\rho_I g h}{2\rho}\partial_x^3\eta^2 + \frac{b}{\rho}\partial_x^2(\eta u) - uu_x - \Gamma_x, \tag{3.2}$$

where $D = -i\partial_x$, $G_0 = D\tanh(HD)$ and $K = 1 + \rho_I h/\rho \; D\tanh(HD)$ are Fourier multiplier operators and Γ_x represents the forcing by the moving load. In the following, we present results of simulations of this system. In order to approximate solutions, a spectral method coupled with a second-order split-step scheme is utilized. Details of this process can be found in (Dinvay, Kalisch and Parau, 2019a).

First, we consider the field experiments of Takizawa. In this case, the ice thickness was 0.16m, the depth was 6.8m, and the load was a skidoo weighing 235kg. The skidoo was driven on a test track at various sub and supercritical speeds. Figure 2 shows the results of measurements taken at a fixed measurement point along the test track. The time series obtained by Takizawa are digitized and compared with numerical simulations of the model (3.1), (3.2). The comparison is favorable except for the near-critical speed 5.5 m/s.

In Figure 3, similar comparisons are made with the data obtained during the field campaign of Wilson on Mille Lacs (Wilson, 1955). In this case, the ice layer was 61cm thick, and the water depth was 3.26m. Two trucks were driven over the lake simultaneously. Several runs with varying separation are shown in Figure 3, and the agreement between the measurements and the simulations is very good.

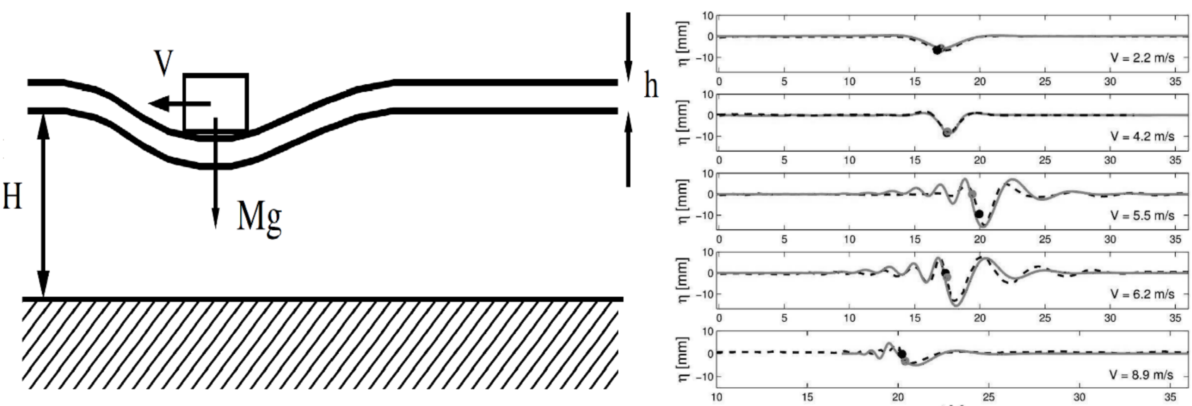

Figure 2. Single point load used by Takizawa during experiments on Lake Saroma. The right panel shows comparison between time series measured at a fixed measurement location, and

a time series taken from a simulation of the experiment using the parameters documented in (Takizawa, 1987).

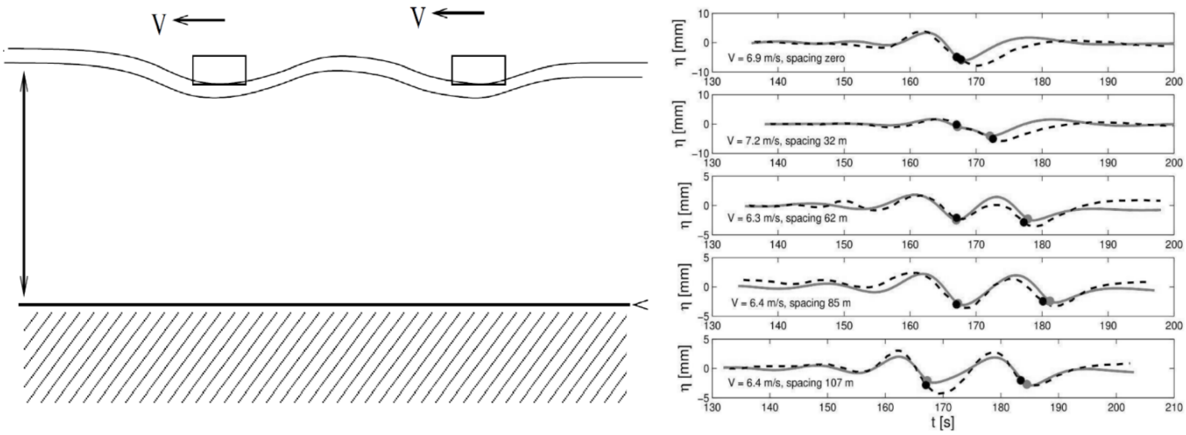

Figure 3. Double load used by Wilson during experiments on Mille Lacs. The right panel shows comparison between time series measured at a fixed measurement location, and a time series taken from a simulation of the experiment using the parameters documented in (Wilson, 1955).

Acknowledgments

This research was supported by the Research Council of Norway through grant no. 239033/F20 and by the EPSRC under grant EP/J019305/1. The authors would like to thank two anonymous reviewers for valuable comments.

References

Aceves-Sanchez, P., Minzoni, A.A. and Panayotaros, P., 2013. Numerical study of a nonlocal model for water-waves with variable depth. Wave Motion 50, 80–93.

Carter, J.D.. 2018. Bidirectional Whitham equations as models of waves on shallow water. Wave Motion 82, 51–61.

Davys, J.W., Hosking, R.J. and Sneyd, A.D., 1985. Waves due to a steadily moving source on a floating ice plate. J. Fluid Mech. 158, 269–287.

Dinvay, E., Dutykh, D. and Kalisch, H., 2019. A comparative study of bi-directional Whitham systems. Appl. Numer. Maths 141, 248–262.

Dinvay, E., Kalisch, H and Parau, E.I., 2019a. Fully dispersive models for moving loads on ice sheets. J. Fluid Mech. 867, 122-149.

Dinvay, E., Kalisch, H and Parau, E.I., 2019b. The Whitham equation for hydroelastic waves. Appl. Ocean Research 89, 202-210.

Guyenne, P. and Parau, E.I., 2014a., Finite-depth effects on solitary waves in a floating ice-sheet. J. Fluids Struct. 49, 242–262.

Guyenne, P. and Parau, E.I., 2014b., Forced and unforced flexural-gravity solitary waves. In Proc. IUTAM, vol. 11, pp. 44–57. Elsevier.

Hosking, R.J., Sneyd, A.D. and Waugh, D.W. 1988., Viscoelastic response of a floating ice ice plate to a steadily moving load. J. Fluid Mech. 196, 409–430.

Marko, J.R. 2003. Observations and analyses of an intense waves-in-ice event in the Sea of Okhotsk. J. Geophys. Res. 108 (C9), 3296.

Milinazzo, F., Shinbrot, M. and Evans, N.W., 1995. A mathematical analysis of the steady response of floating ice to the uniform motion of a rectangular load. J. Fluid Mech. 287,173-197.

Moldabayev, D., Kalisch, H. and Dutykh, D., 2015. The Whitham equation as a model for surface water waves. Physica D 309, 99–107.

Parau, E.I. and Dias, F., 2002. Nonlinear effects in the response of a floating ice plate to a moving load. J. Fluid Mech. 460, 281–305.

Squire, V.A., Hosking, R.J., Kerr, A.D. and Langhorne, P.J., 1988. Moving Loads on Ice Plates. Kluwer.

Takizawa, T. 1987 Field studies on response of a floating sea ice sheet to a steadily moving load. Contrib. Inst. Low Temp. Sci. A 36, 31–76.

Takizawa, T., 1988. Response of a floating sea ice sheet to a steadily moving load. J. Geophys. Res. 93, 5100–5112.

Wang, K., Hosking, R.J. and Milinazzo, F., 2004, Time-dependent response of a floating viscoelastic plate to an impulsively started moving load. J. Fluid Mech. 521, 295–317.

Whitham, G.B., 1967. Variational methods and applications to water waves. Proc. R. Soc. Lond. A 299, 6–25.

Wilson, J.T., 1955. Coupling between moving loads and flexural waves in floating ice sheets. US Army SIPRE Report 34.

25th IAHR International Symposium on Ice
Trondheim, 23 - 25 November 2020

Vertical impact onto floating ice

Alexander Korobkin, Tatyana Khabakhpasheva
School of Mathematics, University of East Anglia
Norwich, NR4 7TJ, UK
a.korobkin@uea.ac.uk

Haixuan Ye, Kevin Maki
Department of Naval Architecture and Marine Engineering, University of Michigan
Ann Arbor, MI, USA
kjmaki@umich.edu

The vertical impact of a rigid body on a floating ice plate is investigated. The problem is unsteady, two-dimensional and coupled. The hydrodynamic loads and elastic ice response are determined simultaneously. The ice deflection is described by the Euler beam equation. The beam is isotropic and of constant thickness. The plate and the water are initially at rest. The impact loads are calculated as part of the solution together with the region of contact between the impacting rigid body and the thin elastic ice plate. The intervals of contact are determined by the condition that the rigid body cannot penetrate the ice surface during the impact. The contact of the smooth body with the elastic plate may occur at separate points. This is demonstrated for a static problem of a floating ice plate of infinite extent and a circular rigid cylinder of variable mass sitting on the ice plate. The impact problem is regularized by introducing an elastic layer between the impacting body and the elastic ice plate. The local reaction force in the layer is a given function of the local compression of the layer. The stresses in the ice plate and the plate deflection are studied for the plate floating between two vertical walls with sliding edge conditions. It is shown that the elastic response of the floating plate is weakly dependent on the thickness and rigidity of the elastic layer on the top of the floating plate. The impact loads and the regions of contact between the impacting body and the ice plate are computed together with the deflections and strains of the ice plate. The problem of the impact of the body and a freely floating ice plate is also studied within the potential flow theory and a numerical Navier-Stokes solver.

1. Introduction

The vertical impact of a rigid smooth body on a floating ice plate is investigated within the linear theory of unsteady two-dimensional potential flows during an initial stage when the ice deflection is relatively small. Initially the plate is floating on the water surface. The plate is isotropic and of constant thickness. The water of infinite depth is initially at rest. The body touches the upper surface of the plate at a single point which is taken as the origin of the Cartesian coordinate system *Oxy,* see Fig. 1. At $t=0$ the body starts to move downwards at a constant speed V. The problem is coupled: the hydrodynamic loads and elastic ice response are determined simultaneously. The ice deflection is described by the Euler beam equation. The impact loads are not assumed but calculated as part of the solution together with the region of contact between the impacting rigid body and the plate. The contact region may consist of several intervals of contact, the positions of which are determined by the condition that the surface of the rigid body is always above the deflected ice surface at any time during the impact. The contact of the impacting body with the elastic plate may occur at separate points. The problems of elasticity with concentrated unknown loads and inequalities for elastic deflections are challenging both theoretically and computationally. A practical approach to such problems is to introduce an elastic layer between the impacting body and the elastic ice plate (Winkler, 1867; Fryba, 1995). The local reaction force in the layer is a given function of the local compression of the layer. Such a layer can model either some physical properties of the ice surface or can be considered as a regularization of problems with concentrated loads, or as a penalty method to satisfy the inequality concerning the positions of the body surface and the floating ice plate. In the present study, the lower surface of the ice plate is assumed to be in contact with water during the initial stage of the impact.

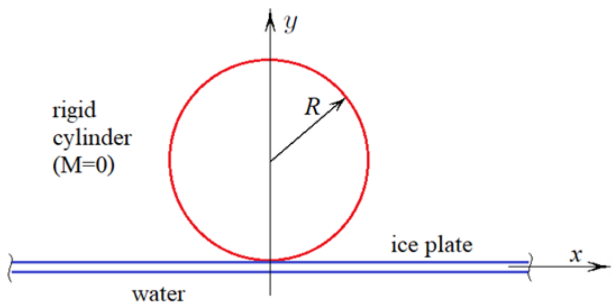

Figure 1. Initial position of the body touching the floating elastic plate. This configuration is also used in the static analysis with the zero mass of the cylinder.

The effect of floating ice floes on the impact loads experienced by a rigid body impacting onto the water surface near the ice field was studied by Khabakhpasheva et al. (2018a) using the Wagner model of water impact (Wagner, 1932). It was shown that the presence of floating ice is important only if the impact occurs in a close proximity of the ice. The motions of the ice floe during the water impact was taken into account. The ice floe may move towards the entering body and collide with the body surface by its edge, which may result in a knife-type damage of the body surface. Korobkin and Khabakhpasheva (2018) studied impact onto a floating ice with a pre-existing crack at the centre of the floe. Impact was modelled by a concentrated load described by a given function of time. The crack of time-dependent length was modelled by a torsional spring. It was shown that the presence of the crack reduces the stresses caused by the impact. The problem of impact onto a finite elastic plate floating on water of infinite depth was formulated and solved in (Korobkin, 2000) assuming that the impact loads are smoothly distributed along the plate and are given. The hydrodynamic problem was reduced to the added mass matrix for dry modes of a beam with free-free edges. The elements of the matrix were calculated in analytical form using the Bessel functions. Impact onto a floating ice plate was studied by Khabakhpasheva et al. (2018b) by CFD and by asymptotic model of water impact (Korobkin et al., 2014). The ice plate was assumed rigid with an elastic layer on the top of it. Only symmetric problem was considered. The present study can be considered as a generalization of that by Khabakhpasheva et al. (2018b) to elastic ice plate with calculations of stresses in ice caused by a body impact.

We shall determine the impact loads, the elastic deflections and the strains in the ice plate for given impact conditions. The model and numerical algorithm are demonstrated for the problem of a plate with sliding edge conditions, see Fig. 4. In this configuration, the problem is solved by the normal mode method. The modes are coupled only through the impact loads but not through the hydrodynamic loads. The problem is generalized to the case of a floating plate with free-free edge. In this problem, the modes of a dry beam are coupled through both the impact and hydrodynamic loads.

To justify the approach with an elastic thin layer on the upper surface of the floating plate, we study the static problem of a circular cylinder sitting on the top of a floating elastic plate without the additional layer between the plate and the cylinder, see Fig. 1 and 2. It is shown that the static contact always occurs at single points.

Finally, a CFD method is used to study the floating plate with free-free edges. The purpose of using the CFD is to consider the possible effects of nonlinearity in the fluid flow when the motion of the edges of the floating ice becomes large.

2. Static problem

To illustrate that the contact between a rigid body and a floating elastic plate may occur at single points in models of thin plates without non-zero intervals of contact, a circular cylinder of radius *R* on the top of a floating Euler beam of infinite extent is considered for variable mass *M* of the body. At *M=0*, see Fig. 1, the beam is horizontal and the cylinder touches the beam at the origin of the coordinate system. We assume that for small mass *M* the contact still occurs at *x=0*. We need to determine the limiting mass of the body such that the configuration with a single contact point is applicable for masses below this limiting value.

It is convenient to take the characteristic length of the ice plate, $L_c = \left(\frac{D}{\rho g}\right)^{\frac{1}{4}}$, where D is the rigidity coefficient of the plate, ρ is the water density and g is the gravitational acceleration, as the horizontal length scale, and *R/Y* as the deflection and vertical length scale, where $Y = (2\rho R^2)/(MX)$ and $X = R/L_c$. The dimensionless variables are denoted by tilde. The vertical coordinate is shifted to the lowest point of the deflected beam. In these new variables, the shape of the beam is independent of any parameters and the cylinder is transformed to the ellipse with semi-axis *X* and *Y*:

$$\tilde{y} = \frac{1}{\sqrt{2}} - e^{-\frac{\tilde{x}}{\sqrt{2}}} \cos\left(\frac{\pi}{4} - \frac{\tilde{x}}{\sqrt{2}}\right), \qquad \frac{\tilde{x}^2}{X^2} + \frac{(\tilde{y}-Y)^2}{Y^2} = 1. \qquad \textbf{[1]}$$

The ellipse touches the plate only at $\tilde{x} = 0$ if $Y > X^2/\sqrt{2}$, which corresponds to $M < 2\sqrt{2}\rho L_c^3/R$. Note that in the present analysis, the shape of the plate does not depend on the load but the body shape does, see [1]. This is illustrated in Fig. 2a for particular values of *X* and *Y*. The body is a circle in the stretched variables, *X*=*Y*, and we are at the limit of the configuration with a single contact point, $Y = X^2/\sqrt{2}$, for $X = Y = \sqrt{2}$. This case with second-order contact at the origin is shown in Fig. 2b. Note that the model of a thin elastic plate can be used only for deflections which are much smaller than the horizontal scale, $R/Y \ll L_c$, which gives $Y \gg X$. Therefore, the limiting case with $Y = X^2/\sqrt{2}$ can be achieved only for large X, which is for very thin plates.

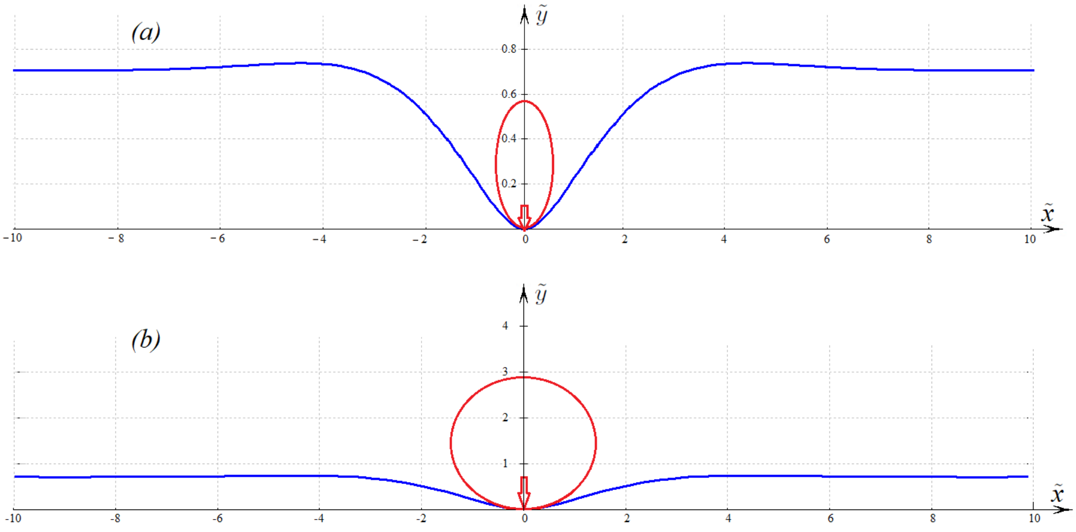

Figure 2. Relative positions of the body and the plate in the stretched coordinates where (a) $Y > X^2/\sqrt{2}$, and (b) $Y = X^2/\sqrt{2} = X$.

For a heavier cylinder with $M > 2\sqrt{2}\rho L_c^3/R$, there are two contact points at $x = \mp a$, where a depends on the mass of the cylinder through the following equation

$$e^{-\beta}\frac{\sin\beta}{\beta} = \frac{\tilde{Y}}{\sqrt{1-\frac{\tilde{a}^2}{X^2}}}, \quad \beta = \sqrt{2}\tilde{a}, \quad \tilde{a} = \frac{a}{L_c}, \quad \tilde{Y} = \frac{\sqrt{2}Y}{X^2} \;. \qquad \textbf{[2]}$$

For $\tilde{a} = 0.5$ and *X=0.7* equation [2] gives *Y=0.11*. The circular cylinder and the plate contact each other at two points for this condition, see Fig. 3a in the stretched coordinates. For larger mass of the cylinder its contact with the deformed plate is more complicated with several points of concentrated loads. The type of the contact depends also on the shape of the rigid body. Static deflection of a floating elastic plate with a rigid heavy plate on it is shown in Fig. 3b for the rigid plate length 1.314 L_c. In this case, the contact occurs at the edge of the rigid plate but the elastic plate under the rigid surface is deflected upwards touching the lower surface of the rigid plate. There are two contact points for shorter plates and three for longer plates.

We conclude that the contact between a rigid body and a floating elastic plate can be complicated even in static problems. To avoid the difficulties with the concentrated loads and point contacts, we add a thin elastic layer at the top of the floating plate and solve the problem numerically.

3. Impact on a floating plate with sliding edge

To simplify the hydrodynamic part of the impact problem, we consider water of infinite depth bounded by two vertical walls at $x = \mp L$. The elastic plate of thickness h_i covers the upper surface of water without gaps between the plate and the walls, see Fig. 4a. The edges of the plate can slide freely along the walls. There is an elastic layer of thickness h_e and rigidity K on the top of the ice plate. The rigid body is parabolic. The position of the body is described by the equation $y = x^2/(2R) + h_e - Vt$, where R is the radius of the body curvature, V is the impact velocity, and $t \geq 0$.

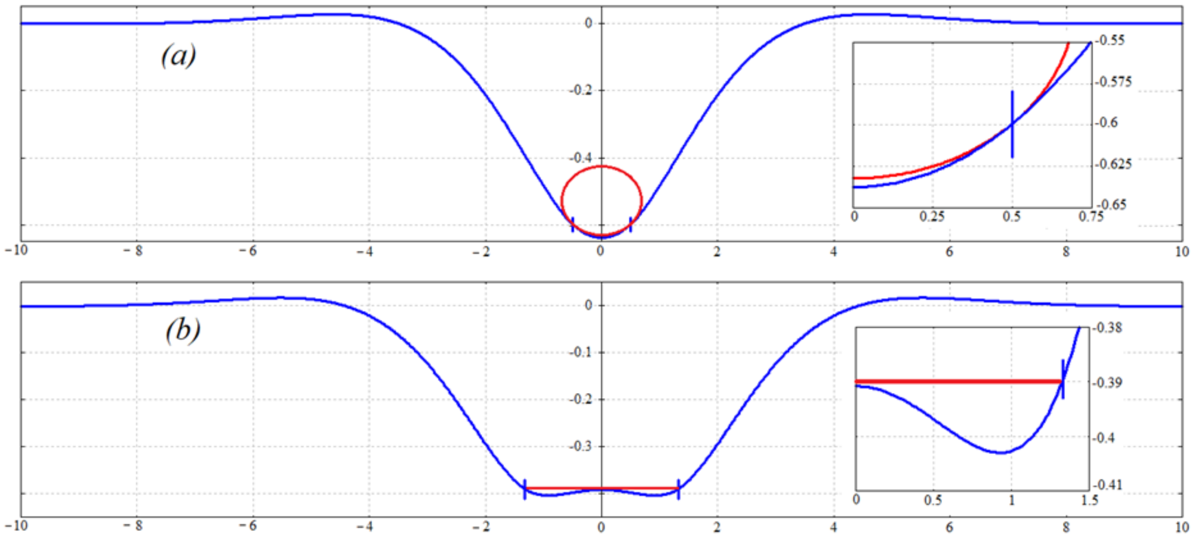

Figure 3. Relative positions of the body and the plate in the stretched coordinates for (a) circular cylinder with *X=0.7* and *Y=0.11,* (b) rigid plate of length 1.314 L_c.

The plate deflection, $w(x,t)$, satisfies the Euler beam equation (Timoshenko and Young, 1955),

$$m\frac{\partial^2 w}{\partial t^2} + D\frac{\partial^4 w}{\partial x^4} = p(x,0,t) - P_e(x,t) \qquad (-L < x < L, \qquad t > 0), \qquad \textbf{[3]}$$

the initial conditions,

$$w(x,0) = 0, \qquad \frac{\partial w}{\partial t}(x,0) = 0, \qquad \textbf{[4]}$$

and the edge conditions

$$\frac{\partial w}{\partial x} = 0, \quad \frac{\partial^3 w}{\partial x^3} = 0 \qquad (x = \mp L, \ \ t > 0), \qquad \textbf{[5]}$$

where $p(x,0,t) = -\rho\varphi_t(x,0,t) - \rho g w(x,t)$ is the hydrodynamic pressure acting on the ice-water interface, $\varphi(x,y,t)$ is the velocity potential of the flow under the ice, $m = \rho_i h_i$ is the mass of the ice plate per unit area, $D = Eh_i^3/[12(1-\nu^2)]$ is the rigidity coefficient, $P_e(x,t)$ is the reaction force of the elastic layer. The reaction force is modelled by $P_e(x,t) = K\,f(\mu)$, where K is the rigidity of the elastic layer and μ is the relative compression of the layer, $\mu = (h_e - h(x,t))/h_e$, and $h(x,t)$ is the current thickness of the layer, $h(x,t) = \frac{x^2}{2R} + h_e - Vt - w(x,t)$. In the present calculations, we assumed $f(\mu)$= $\mu/(1-\mu)$.

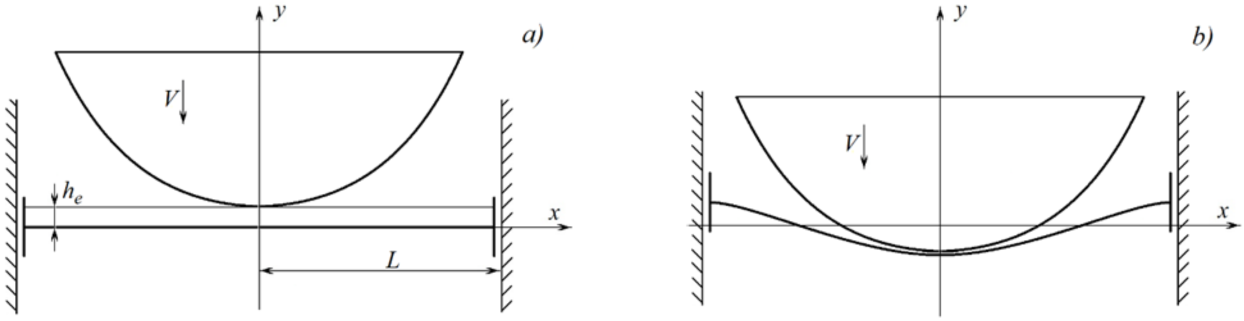

Figure 4. Vertical impact of a rigid body onto a floating elastic plate between two vertical walls: (a) Initial position of the body and notation, (b) Sketch of the elastic plate deflection.

The symmetric deflection of the ice plate is sought in the form,

$$w(x,t) = \sum_{n=1}^{\infty} a_n(t)\psi_n(x), \qquad \psi_n(x) = \cos(\lambda_n x), \qquad \lambda_n = \frac{\pi n}{L}. \qquad \textbf{[6]}$$

Then the velocity potential of the flow under the ice reads

$$\varphi(x,y,t) = \varphi_0(t) + \sum_{n=1}^{\infty} \frac{1}{\lambda_n} \dot{a}_n(t) e^{\lambda_n y} \psi_n(x) \ . \qquad \textbf{[7]}$$

This potential satisfies Laplace's equation, boundary conditions on the vertical walls, the kinematic condition on the ice/water interface, and decays as $y \to -\infty$. Note that the series in [6] starts from $n = 1$ excluding $n = 0$. This is because the rigid-body displacement of the ice plate should be zero in this problem without free surfaces. Substituting [6] and [7] in [3] and using orthogonality of the modes $\psi_n(x)$, we arrive at non-linear system of ordinary differential equations,

$$\ddot{a}_n + \omega_n^2 a_n = P_n(t), \qquad \dot{a}_n(0) = a_n(0) = 0,$$

which are truncated and integrated numerically by the fourth-order Runge-Kutta scheme. Here

$$P_n(t) = -\frac{1}{L\left(m + \frac{\rho}{\lambda_n}\right)} \int_{-L}^{L} P_e(x,t)\psi_n(x)\,dx, \qquad \omega_n^2 = \frac{D\lambda_n^4 + \varrho g}{m + \frac{\rho}{\lambda_n}} \ .$$

4. Numerical results

The results of the numerical simulations are presented for the rigidities of the elastic layer $K = 0.01$ MPa and $K = 1$ MPa, thickness of the layer $h_e = 1\ cm$, radius of curvature of the rigid body $R = 5$ m, speed of impact $V = 1$ m/s, thickness of the ice plate $h_i = 5\ cm$, length of the plate $L = 20$ m, the Young modulus of the ice $E = 4.2$ GPa, density of ice $\rho_i = 917\ kg\ m^{-3}$, density of water $\rho = 1000\ kg\ m^{-3}$, gravity acceleration g = 9.81 m/s^2.

The positions of the impacting body and the deflected plate are shown in Fig. 5 at four time instants for two values of the rigidity of the elastic layer. It is seen that the shape of the plate closely follows the shape of the body in the impact region and weakly depends on the rigidity of the elastic layer. The loads in the elastic layer caused by its compression are shown in Fig. 6 at the same time instants as in Fig. 5. The loads are in MPa. Even Fig. 5 shows contact regions which look as long continuous intervals, the computations provide that the actual contact intervals at some time instants are very short. At $t=0.224$ sec (dimensionless time is 0.4) the contact between the body and the elastic layer occurs in the interval 0.3 m $<x<0.6$ m and in the interval *0.9* m <*x*<*1.1* m at *t=0.9* sec (dimensionless time is 1.6). The gaps between the surface of the rigid body and the upper surface of the ice plate at *x=0* are shown for two rigidities of the elastic layer in Fig. 7. Here *y=0* corresponds to the surface of the moving body and *y=-0.01* m corresponds to the thickness of the elastic layer. The soft layer with *K=0.01* MPa is compressed at the plate centre for a main part of the process. As to the stiffer layer with *K=1* MPa, it is just slightly compressed, and around *t=1* sec the beam together with the elastic layer are losing their contact with the rigid surface for a substantial time interval.

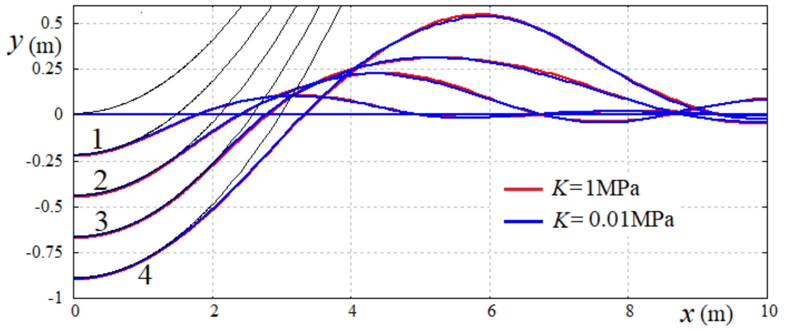

Figure 5. Relative positions of the body surface (black lines) and the elastic ice plate for rigidity of the elastic layer *K=1* MPa (red lines) and *K=0.01* MPa (blue lines) at the dimensionless time instants 0.4 (1), 0.8 (2), 1.2 (3), and 1.6 (4). The time scale is 0.56 sec.

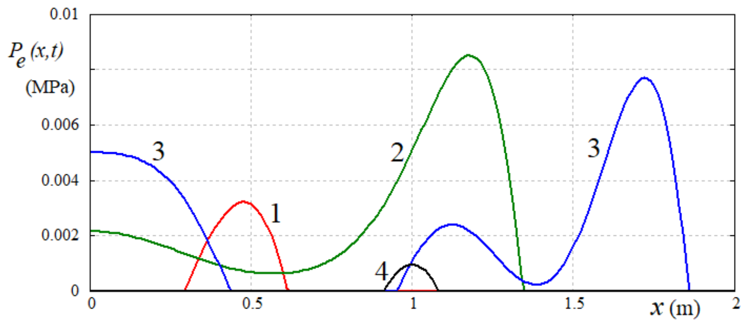

Figure 6. Reaction forces in the elastic layer, $P_e(x,t)$, as functions of *x* at the time instants from Fig. 5. Rigidity of the elastic layer is *K=1* MPa.

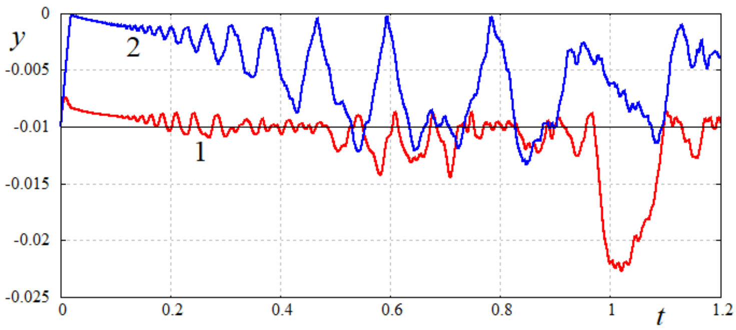

Figure 7. The gaps between the surface of the parabolic body and the upper surface of the ice plate at the plate centre, *x=0*, as functions of time for the rigidity of the elastic layer *K=1* MPa (red line) and *K=0.01* MPa (blue line). The thickness of the elastic layer, *1* cm, is shown by the black line.

The strains at four points, *x=0*, *1*, *2* and *3* m of the upper surface of the floating plate, are shown in Fig. 8a and 8b for the rigidity of the elastic layer *K=1* MPa and *K=0.01* MPa correspondingly. The dashed straight line, $\varepsilon = -0.005$, shows the strain for the shape of the plate approximated by the shape of the body in the contact region. Note that the strains are much higher than the yield strain for the ice (Brocklehurst et al., 2011) which is estimated as 0.00008. The strains are computed up to $t=1.2$ sec, which corresponds to the body displacement 1.2 m. This displacement is still small compared with the length of the floating plate 20 m. To justify the high-frequency oscillations of the strains, the calculations were performed with 20, 30 and 40 modes in [6]. The convergence of the results is demonstrated in Fig. 9.

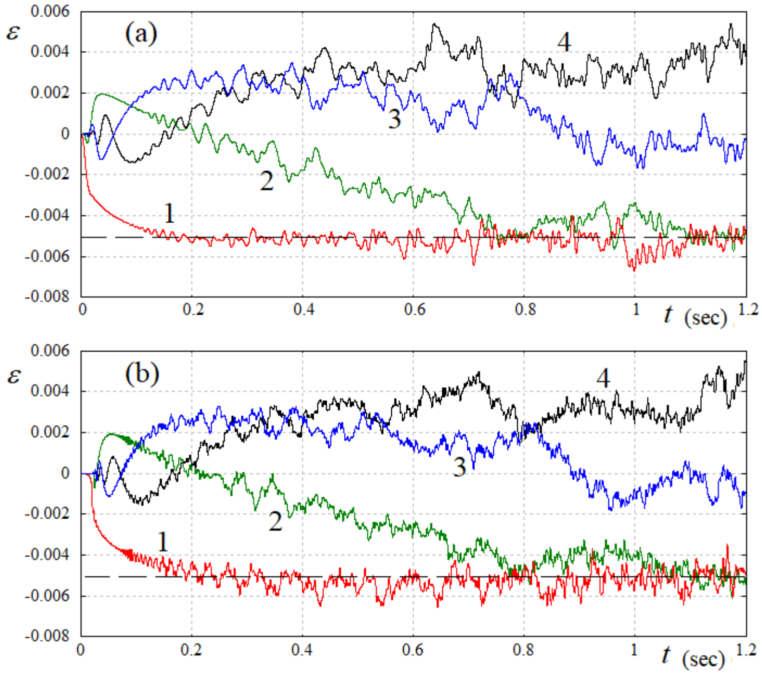

Figure 8. The strains on the upper surface of the ice plate at four distances from the impact point: $x=0$ (1), $x=1$ m (2), $x=2$ m (3), $x=3$ m (4), for the rigidity of the elastic layer $K=1$ MPa (a) and $K=0.01$ MPa *(b)*.

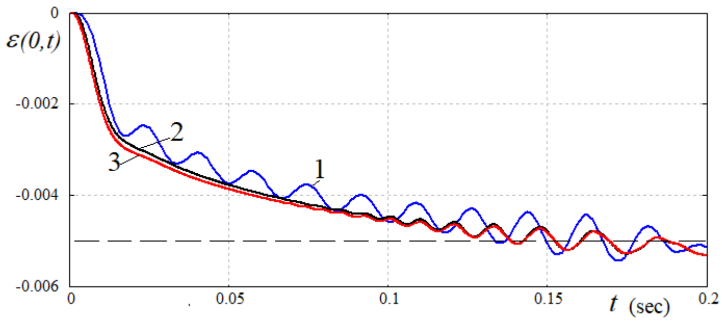

Figure 9. The strains on the upper surface of the ice plate at $x=0$ as functions of the dimensional time calculated with 20 (1), 30 (2), and 40 (3) elastic modes. The rigidity of the elastic layer is $K=1$ MPa.

The floating ice plate problem is also solved with a CFD method. The Navier-Stokes equations are solved numerically with a finite-volume method from the OpenFOAM opensource CFD software. The ice plate is described by [3], and solved with the modal method [6]. The hydrodynamic pressure in [3] is calculated with the CFD solver that uses a deforming mesh method to account for the deflection of the ice plate.

Results are computed using a CFD grid with 60 points along the length of the ice sheet. The CFD solution is discrete in space and time, whereas the structural modal model is discrete in time, but uses a basis of continuous mode shapes. Due to the finite representation of the spatial discretization, the CFD solution effectively limits the number of structural modes that can be used. For example, it is required that at least two CFD points on the plate are required per wavelength, although this is still far too coarse. For 60 points on the plate, a total number of modes of 10 is used. This corresponds to 6 points per wavelength for the last mode.

The relative position of the impacting body and the ice sheet as computed with the CFD method is shown in Fig. 10 (left). The instant of time is 0.4, and comparison can be made with the results from the linear potential flow formulation used in Fig. 5. Agreement for the long plate is quite good even the edge conditions in Fig. 10 and Fig. 5 are different. Also at this time instant the pressure field under the deforming ice plate is shown in Figure 10 (right). It can be seen that the flexure of the ice sheet is dominated by the first modes, but the pressure field shows response for a higher (shorter wavelength) mode.

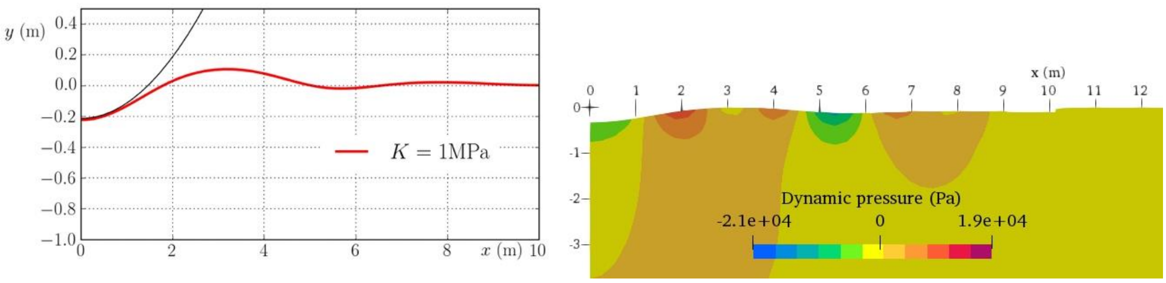

Figure 10. (left) Relative position of the body surface (black line) and the elastic ice plate for rigidity of the elastic layer $K=1$ MPa (red line) at the dimensionless time instant 0.4. (right) Dynamic pressure in water under ice sheet computed with CFD method.

5. Conclusion

An approach to estimate the response of a floating ice plate to the vertical impact by a rigid smooth body has been proposed. It was assumed that the ice could not be crushed by the impact and the bending of the ice plate is the major phenomenon leading to a possible breaking of the ice. To avoid difficulties with concentrated impact loads, the problem was regularized by including an elastic thin layer at the top of the ice plate. The problem was studied within the linearized potential theory and by Computational Fluid Dynamics. We conclude that a thin elastic layer makes it possible to compute the deflections and stresses of the ice plate but does not affect significantly their values.

The present model can be developed further to model ice crushing in the impact region by a thin viscoelastic layer of variable thickness. A possible approach to account for ice crushing is to introduce a critical value P_* of the impact load $P_e(x,t)$, see [3], such that the interface between the viscoelastic layer and the ice plate moves into the ice plate if $P_e(x,t) > P_*$. The displacement of the interface is determined using the condition $P_e(x,t) \leq P_*$. The present model does not account for acoustic waves caused by the impact and propagating in water from the floating plate. It is challenging to include water compressibility in a model of floating elastic plate, see Korobkin (1996) for some discussions.

Acknowledgments

This work was supported by the NICOP research grant "Vertical penetration of an object through broken ice and floating ice plate", N62909-17-1-2128.

References

Brocklehurst, P., Korobkin, A.A., and Parau, E.I., 2011. Hydroelastic wave diffraction by a vertical cylinder. Philosophical Transactions of the Royal Society of London A: Mathematical, Physical and Engineering Sciences, 369(1947), 2832-2851.

Fryba, L., 1995. History of Winkler foundation. Proc.3rd Herbertov Workshop Interaction of Railway Vehicles with the Track and its Substructure, Herbertov, Czech Republic, 24, 7-12.

Khabakhpasheva, T.I., Chen Y., Korobkin A.A., and Maki K.J., 2018. Water impact near the edge of a floating ice sheet. Proc. 33rd International Workshop Water Waves Floating Bodies, Guidel-Plages, France, 4pp.

Khabakhpasheva, T.I., Chen, Y., Korobkin, A.A., and Maki, K.J., 2018. Impact onto an ice floe. Journal of Advanced Research in Ocean Engineering, 4(4), 146-162.

Korobkin, A.A., 1996. Water impact problems in ship hydrodynamics. In: Ohkusu M (ed) Advances in Marine Hydrodynamics, Chap 7. Computational Mechanics Publications, Southampton, Boston, 323-371.

Korobkin, A.A., 2000. Unsteady hydroelasticity of floating plates. Journal of Fluids and Structures, 14(7), 971-991.

Korobkin, A.A., Khabakhpasheva, T.I., Malenica, S., and Kim, Y., 2014. A comparison study of water impact and water exit models. International Journal of Naval Architecture and Ocean Engineering, 6(4), 1182-1196.

Korobkin, A.A., and Khabakhpasheva, T.I., 2018. Impact on an Ice Floe with a Surface Crack. In *ASME 2018 37th International Conference on Ocean, Offshore and Arctic Engineering*. American Society of Mechanical Engineers Digital Collection.

Timoshenko, S., and Young, D.H., 1955. Vibration Problems in Engineering, D. van Nostrand Company.

Wagner, H., 1932. Uber Stoss- und Gleitvorgange an der Oberflache von Flussigkeiten. ZAMM, Journal of Applied Mathematics and Mechanics/Zeitschrift fur Angewandte Mathematik und Mechanik, 12(4), 193-215.

Winkler, E., 1867. Die Lehre von der Elasticitaet und Festigkeit: mit besonderer Rücksicht auf ihre Anwendung in der Technik für polytechnische Schulen, Bauakademien, Ingenieue, Maschinenbauer, Architecten, etc. Dominicus.

IAHR AIRH

25th IAHR International Symposium on Ice

Trondheim, 23 - 25 November 2020

Systematic investigation of data analysis methods in wave-ice interaction problem

Hongtao Li[1,2], Ersegun Deniz Gedikli[1,3], Raed Lubbad[1]

[1] *Department of Civil and Environmental Engineering, Norwegian University of Science and Technology, Trondheim, Norway*
Høgskoleringen 7A, 7491 Trondheim, Norway
hongtao.li@ntnu.no, honglia@space.dtu.dk
[2] *DTU Space, Technical University of Denmark, Lyngby, Denmark*
[3] *Department of Ocean and Resources Engineering, University of Hawaii at Manoa, Honolulu, USA*

Wave climate and extent of ice cover in the Arctic ocean have changed significantly in recent decades. Concomitantly, interest in studying wave-ice interaction has rapidly increased in the last two decades. Laboratory-scale experiments present a fundamental approach to understand the detailed processes involved in wave-ice interaction and to validate theoretical models. One key parameter that describes how waves evolve under ice cover is the spatial attenuation coefficient. To estimate this parameter from laboratory measurements, wave amplitudes at different positions along the wave propagation direction should be estimated. In addition to wave amplitudes, it is also critical to confirm that the period of incoming waves agree with a preset wave period since this parameter is involved in evaluating wave dispersion relation. In this study, we systematically explore various measurement (signal) processing techniques to extract wave parameters such as wave amplitudes and periods. The contamination of wave measurements with noise and wave reflection in addition to the sometimes use of low-sampling frequency and the possible lack of stationarity in the measurement require dedicated care when selecting the suitable analysis method. In this study, we investigate several methods including: Bandpass filtering in frequency domain (bp), Tikhonov regularization (Tikhonov), two MATLAB built-in functions, fir1 and smooth (Smooth), Fast Fourier Transform (FFT), Peak Analysis (Peak), Dynamic Mode Decomposition (DMD), Genetic Algorithm (Genetic) and Prony's method (Prony). By using experimental measurements (from Qualisys systems, ultrasound and pressure sensors) and synthetic signals, we show that bp gives equivalent filtering results as fir1 (difference expressed by normalized root mean squared error less than 3.5%). Moreover, Tikhonov and Smooth produces similar smoothing of signal. Additionally, we find that Prony, DMD and FFT in combination with interpolation quantify incoming wave period accurately (normalized error less than 2.5%). As for wave amplitudes, FFT combined with interpolation, Genetic, a variant of DMD, Hilbert transform and its combination with interpolation and Peak combined with interpolation results in similar estimates with respect to FFT (normalized error less than 3%).

KEY WORDS: Surface gravity waves, ice, Prony, Dynamic mode decomposition, Hilbert transform, Genetic algorithm, Tikhonov regularization.

1. Introduction

The interest in wave-ice interaction studies has resurged in recent decades. The driving factors are multiple. One of them is the increasing concern of potential implications brought by accelerating melting of ice in waves in both Arctic and Antarctic. To fully comprehend how waves are changed by ice cover, more high-quality field datasets are in urgent need (Rabault et al., 2017, Kohout et al., 2015). This is attributed to: (1) diverse proposed theoretical models for waves propagating in ice need to be calibrated and validated by using field measurements (Rabault et al., 2017, Mosig et al., 2015, Cheng et al., 2017); (2) various damping patterns of waves in ice should be investigated (Rabault et al., 2017); (3) dominant mechanisms in attenuating waves travelling in ice remain to be clarified (Voermans et al., 2019, Ardhuin et al., 2020). Especially, these information should be systematically and meticulously measured, i.e., wave elevation, wave travelling direction, ice concentration, ice types, ice extent, ice thickness, wave speed and wind (Cheng et al., 2017, Kohout et al., 2015). However, well-controlled laboratory studies are also indispensable, because of its advantages over the field measurements. Firstly, laboratory studies can be designed to fulfill the assumptions introduced in those theoretical models. Secondly, ambient conditions could be comprehensively measured and controlled. Despite these superiorities, proper data analysis methods are essential in interpreting the laboratory measurements to reveal the detailed physical processes involved in wave-ice interaction. Hitherto, there have not been any dedicated systematic investigation of data analysis methods used in wave-ice interaction community for laboratory study.

Noise is inevitable in real measurements. Smoothing and filtering the recorded data are necessary pre-processing steps for reliable analysis of data. Physical meaningful signal of wave and ice motion is typically narrowband. This implies that a narrowband pass filter should be designed to filter raw measurements. However, narrowband filter design using the preferred finite impulse response (FIR) approach requires long kernel and hence reduces temporal precision (Cohen, 2014). In some cases, measurements from small wave flumes have short time series. Consequently, high-quality narrowband filter designed via FIR is virtually impossible to be used for short signal. To avoid this kind of caveat of FIR filter, we propose to use fast Fourier transform (FFT, Cooley and Tukey (1965)) in conjunction with inverse fast Fourier transform (IFFT) to perform filtering in frequency domain. Despite the sharp edge of this filtering method in frequency domain gives rise to ripple/ringing effect in temporal domain (Cohen, 2014), we show that the ripple/ringing effect seems to be minimal in real application.

Move-mean filter and MATLAB function *smooth* with option *lowess* were employed in previous studies (Zhao and Shen, 2015, Meylan et al., 2015, Yiew et al., 2016). However, these two methods are severely prone to subjective bias, because span of data (or number of data points) used by move-mean filter and *smooth* must be chosen by trial-and-error procedure. In this study, we introduce the Tikhonov regularization method (Mueller and Siltanen, 2012) and propose for the first time to use it to smooth data on wave-ice interactions. Regularization parameter involved in this method can be determined by generalized cross-validation and L-curve criteria (Aster et al., 2018).

Though Wang and Shen (2010) compared four different estimation methods for wave frequency, in their study, only pressure sensor measurements from one experimental facility were analyzed. In contrast, we apply the methods presented in this study on measurements collected from various devices (i.e., Qualisys systems, ultrasound and pressure sensors) from four different experimental facilities. Moreover, we introduce for the first time Prony's method and dynamic mode decomposition (DMD) to estimate frequency in wave-ice related studies.

Peak analysis (Wang and Shen, 2010, Sree et al., 2018, Yiew et al., 2019, Li and Lubbad, 2018, Meylan et al., 2015) and the methods based on Fourier transform (Bennetts and Williams, 2015, Zhao and Shen, 2015, Rabault et al., 2019, Sutherland et al., 2017) have been used to estimate wave amplitude. To the best knowledge of the authors', a comparative study of these two methods have not been performed. In the present study, we evaluate the difference of amplitude estimates derived from various methods including peak analysis and those methods based on Fourier transform. Herein, we introduce for the first time a variant of DMD, and Hilbert transform to wave-ice research community to estimate wave amplitude. Furthermore, we propose to apply truncated singular value decomposition (TSVD) to judiciously determine the number of modes to be retained in DMD.

In the following sections, we will start with the description of data used in this study. This is followed by methods to pre-process data. Methods to estimate incoming wave period/frequency and wave amplitude are then presented. Thereafter, results of applying various methods to analyze data are given. The final section summarizes our findings.

2. Description of Data

Table 1 lists the data analyzed in this study. f_w is target wave frequency, $k_w a$ is wave steepness and F_s is sampling frequency. Cases #1 - # 19 are experimental measurements collected during four different experimental campaigns that were conducted in four wave/ice tanks.

Case #20 is a synthetic signal that imitates recorded laboratory measurements. Equation [1] shows the synthetic signal:

$$\mathbf{z} = \sum_{j}^{10} a_j \exp(-\alpha_j \mathbf{t}) \sin\left(2\pi / T_j + \varphi_j\right) + \boldsymbol{\varepsilon} \quad \textbf{[1]}$$

where a_1 = 18, and $a_2, a_3, \cdots, a_{10}$ are sampled from uniform distribution [0, 0.5]. $\mathbf{t}$ represents a time vector. α_j is the grow/decay rate and sampled from uniform distribution $[0,\ 0.001]$. The sign of α_j is determined by sample from uniform distribution $[0,\ 1]$. When sample exceeds 0.5, a positive sign is assigned for α_j, otherwise a negative sign is imposed on α_j. $T_j = [4,\ 1,\ 1.1, 1.2,\ 1.5, 1.6,\ 1.8,\ 2,\ 2.2,\ 8]$ in seconds, where $T_1 = 4$ [s] represents the preset period of the generated waves. φ_j is sampled from uniform distribution $[0,\ 0.02\pi]$. $\boldsymbol{\varepsilon}$ denotes 1% white noise.

Table 1. Data description

Case #	f_w [Hz]	$k_w a$ $[10^{-3}]$	F_s [Hz]	Device	Label	Remark	Source
1-3	0.6	32.58	64	Qualisys	Marker 5	disk	Montiel et al.

4-6	0.8	32.99	64	Qualisys	Marker 5	thickness D = 3 mm (cases #1, 4, 7, 10), 5 mm (cases #2, 5, 8, 11) and 10 mm (cases #3, 6, 9, 12).	(2013)
7-9	1.1	32.87	64	Qualisys	Marker 5		
10-12	1.3	31.42	64	Qualisys	Marker 5		
13-15	1.5	62.83	50	Ultrasound sensors	$US_{4.25}$, $US_{4.75}$, $US_{5.25}$		Yiew et al. (2019)
16	1.25	91.06	200	Qualisys	Disk 2		Yiew et al. (2016)
17-18	0.5	12.51	50	Pressure sensors	P7 and P8	test series 3310, see also Figure 1 in Li et al. (2019)	Haase and Tsarau (2019)
19	0.5	12.51	100	Qualisys	Marker 8		
20	0.25	-	200	-	-	-	

3. Data Filtering and Smoothing Methods

Bandpass filtering (bp) implemented by using FFT and IFFT

Bandpass filter can be realized by using FIR filter and infinite impulse response (IIR) filter (Proakis, 2001). For motion measurements of ice and waves collected in laboratory study, we recommend another way to implement bandpass filtering, which is easier to use. This filtering approach is based on Shmuel (2020) and is denoted as bp onwards.

FFT outputs Fourier coefficients that correspond to following frequency consecutively (Trefethen, 2000, Kutz, 2013).

$$ff = \frac{F_s}{l}[0, 1, 2, \cdots, j, \ -k, \ -(k-1), \ \cdots, \ -1] \qquad \textbf{[2]}$$

where $j = \left\lfloor \frac{l}{2} \right\rfloor + \left(l - 2\left\lfloor \frac{l}{2} \right\rfloor \right) - 1$, $k = \left\lfloor \frac{l}{2} \right\rfloor$ and l is the length of selected data (see below).

The steps to achieve bandpass filtering (bp) of measured time series $\mathbf{z} \in \mathbb{R}^{n \times 1}$ using FFT and IFFT are as follows:

(1) Select the cyclic part of $\mathbf{z}$ (denoted as $\mathbf{z}^l$ with a size of $l \times 1$), that is far before the beginning and well after the ending of steady part of $\mathbf{z}$ (denoted as $\mathbf{z}^s$ with a size of $s \times 1$), with periodic boundary having zero values.
(2) Conduct FFT on data $\mathbf{z}^l$.
(3) Select out Fourier coefficients, which are output from FFT, in correspondence with desired frequency to be retained.

(4) Populate a zero-matrix that has a size of $l \times 1$ with chosen Fourier coefficients having the same index as output from FFT.
(5) Perform IFFT on the populated matrix and take out the real values.

The requirements for the chosen section of data when using FFT and IFFT results from that FFT and IFFT assume periodic boundary condition (Kutz, 2013) and use cyclic Fourier series to do transformation between time and frequency domain. Imposing the condition $l > s$ subsides the edge artifact on filtering results of $\mathbf{z}^s$ (Kohout et al., 2015). The edge artifact is induced by the possibility that zero periodic boundary condition is not satisfied (Cohen, 2014) due to noise contamination and low resolution of data. To alleviate the edge artifact further, tapered cosine (i.e., Tukey) window could be applied at the first step just mentioned above (MathWorks, 2020e, Kohout et al., 2015, Tucker and Pitt, 2001).

Tikhonov regularization
Tikhonov regularization is one of the possible methods to denoise signal. For reducing noise, the model used for Tikhonov regularization is:

$$\mathbf{z} = \mathbf{f} + \boldsymbol{\varepsilon} \qquad \textbf{[3]}$$

where $\mathbf{z} \in \mathbb{R}^{n\times 1}$ is the measured time series, $\mathbf{f} \in \mathbb{R}^{n\times 1}$ is the signal that is free from noise and is to be inversely determined, $\boldsymbol{\varepsilon} \in \mathbb{R}^{n\times 1}$ is noise. According to Mueller and Siltanen (2012), this can be formulated as an optimization problem:

$$\mathbf{f}_\alpha = \underset{\mathbf{b}\in\mathbb{R}^{n\times 1}}{\arg\min}\left[\left(\| \mathbf{Ab} - \mathbf{m} \|_2\right)^2 + \alpha\left(\| \mathbf{L}_2\mathbf{b} \|_2\right)^2\right] \qquad \textbf{[4]}$$

where $\mathbf{A} = \mathbf{I}_{(n-2)\times n}$ is an identify matrix; α is a regularization parameter that makes a trade-off between the loss term $\left(\| \mathbf{Ab} - \mathbf{m} \|_2\right)^2$ and the penalty term $\left(\| \mathbf{L}_2\mathbf{b} \|_2\right)^2$; $\mathbf{m}$ is a vector, populated with the first $(n-2)$ elements of $\mathbf{z}$; $\mathbf{L}_2$ is a regularization matrix, herein a second derivative operator based on finite difference methods, and expressed as:

$$\mathbf{L}_2 = F_s^2 \begin{bmatrix} 1 & -2 & 1 & & & \\ & 1 & -2 & 1 & & \\ & & \ddots & \ddots & \ddots & \\ & & & 1 & -2 & 1 \end{bmatrix}_{(n-2)\times n} \qquad \textbf{[5]}$$

where F_s is sampling frequency in Hz. Here, this form of $\mathbf{L}_2$ implies that no any assumption about the boundary of signal is introduced. To handle various kinds of boundaries of signal, e.g., reflexive boundary, other forms of second derivative operator $\mathbf{L}_2$ are proposed in previous studies, see more details in chapter 5 in Mueller and Siltanen (2012) and chapter 8 in Hansen (2010). Mathematically, this optimization problem can be solved by using normal equation (Mueller and Siltanen, 2012):

$$\left(\mathbf{A}^T\mathbf{A} + \alpha\mathbf{L}_2^T\mathbf{L}_2\right)\mathbf{f}_\alpha = \mathbf{A}^T\mathbf{m} \qquad \textbf{[6]}$$

For computational convenience, the stacked form formulation is used (Mueller and Siltanen, 2012):

$$\begin{bmatrix} \mathbf{A} \\ \sqrt{\alpha}\mathbf{L}_2 \end{bmatrix} \mathbf{f}_\alpha = \begin{bmatrix} \mathbf{m} \\ \mathbf{0} \end{bmatrix} \quad \textbf{[7]}$$

For large scale problem, Equation [7] is solved by matrix-free method (Mueller and Siltanen, 2012). We propose to use LSQR algorithm (Paige and Saunders, 1982), which is efficiently implemented to avoid memory size limitations of computer for storing large-dimension matrices.

In this paper, the regularization parameter α is estimated by the robust L-curve method (Hansen, 2010, Mueller and Siltanen, 2012). As discussed in James et al. (2013), larger α results in smoother $\mathbf{f}_\alpha$ and if $\alpha \to \infty$, $\mathbf{f}_\alpha$ is a straight line. Conversely, $\alpha = 0$ results in that $\mathbf{f}_\alpha$ converges to $\mathbf{z}$.

Note that here we assume $\mathbf{f}$ is smooth, which is typical the case for the motion signals of ice and waves recorded in laboratory, therefore second derivative operator is used as the regularization matrix. Other commonly used regularization matrices include identity matrix and first derivative operator (Chen and Chan, 2017, Gedikli et al., 2018, Gedikli et al., 2020). The choice of the regularization matrix is data dependent. It should also be noted that the implementation of using Tikhonov regularization to denoise signal presented here is novel and has not been seen in other literatures.

Another approach to denoise the signal is the use of newly developed time-delay-based differentiation (TDD, Li et al. (2020a)) method which reduces the noise embedded in the signal in the derivation process.

Apply MATLAB built-in functions to directly filter and smooth data

It is a well-established knowledge that if data are sufficiently long and off-line analysis is performed, FIR filter is preferable to IIR filter. This is attributed to (1) performance of IIR filter at best matches with that of FIR filter (Cohen, 2020); (2) FIR filter is stable while IIR filter maybe not (Cohen, 2014, MathWorks, 2020c); (3) FIR filter results in constant phase delay for all frequency components whereas IIR filter yields nonlinear phase delay (MathWorks, 2020b, MathWorks, 2020a); (4) The approaches to construct FIR filter are primarily linear (MathWorks, 2020c).

MATLAB provides plentiful functions to design filter and smooth data. We only select commonly used *fir1* and *smooth* functions to compare with the other methods presented in this study. *fir1* is comparable to bp method since transition zones of both methods are tight (Cohen, 2014). Note that smoothing window is applied to smooth filter kernel in *fir1* function to mitigate ripple generation in time domain (Cohen, 2014).

The MATLAB *smooth* function with option *lowess* performs weighted least-squares local regression of data using first degree polynomial. This approach has been used by earlier studies to reduce noise (Meylan et al., 2015, Yiew et al., 2016). Here, we recommend using option *rloess* which smooths data via local regression of data using second degree polynomial. This option incorporates an outlier-rejecting mechanism and is used by Li et al. (2020b) to smooth wave-induced ice-ice interaction signals.

4. Methods to Estimate Wave Period and Wave Amplitude

Prony's method

Prony's method is a method to decompose data, which is analogous to Fourier series. The difference lies in the fact that Prony's method decomposes data into a complex exponential series that includes grow/decay rate (see Hu et al., 2013 and references therein). Regarding formula for discrete data, Prony's method can be expressed as:

$$z_k = \sum_{j=1}^{\beta} a_j \exp(i\theta_j)\left(\exp\left(\frac{k\lambda_j}{F_s}\right)\right) \qquad \textbf{[8]}$$

where k represents k^{th} element of the chosen steady signal $\mathbf{z}^s$, the a_j and θ_j are amplitude and phase for the j^{th} component, respectively; $\lambda_j = -\alpha_j + i2\pi f_j$, where α_j (1/sec) and f_j (Hz) are the grow/decay rate and oscillation frequency for j^{th} component, respectively.

In this study, we employ the implementation of Prony' method as in Hu et al. (2013), which is shown by Hu et al. (2013) to be insensitive to sampling frequency and robust against noise. For more extensive discussions about various implementations, readers are referred to Rodríguez et al. (2018).

Number of modes β is determined by TSVD (Mueller and Siltanen, 2012) method. Specifically, β is chosen as the maximum subspace dimension just before flat noise floor in singular value spectrum expressed in logarithmic scale (see e.g. Figure 4b).

Dynamic mode decomposition (DMD)

DMD (Schmid, 2010) is another method of decomposing data into complex modes. Here, we utilize the algorithm presented in Tu et al. (2014) and Kutz et al. (2016). The approach of estimating average amplitude by means of DMD is developed by Kutz et al. (2016) and this variant of DMD is referred to as DMDa henceforth. To the best knowledge of the authors', this is the first time that DMDa is employed in wave-ice interaction studies.

It should be noted that, both Prony and DMD methods can be related to system identification techniques, i.e., eigen realization algorithm (Juang and Pappa, 1985), in terms of the way to identify grow/decay rate and oscillation frequency (Hu et al., 2013, Kutz et al., 2016).

For DMD, we employ TSVD and the optimal hard thresholding method proposed by Gavish and Donoho (2014) to determine β, respectively. To distinguish these two methods in combination with DMD, the former is denoted as DMD and latter is represented as DMDr hereafter.

Genetic algorithm to fit a sinusoidal wave

The fitting to a sinusoidal wave can be formulated as a search for a set of parameters to minimize the objective function (Li et al., 2019):

$$\varepsilon_j = \sqrt{\sum_{k=1}^{s}\left[z_k - a_k^{(j)}\cos(2\pi f^{(j)} t_k + \varphi^{(j)})\right]^2} \quad \textbf{[9]}$$

where j represent the j^{th} group of parameters to fit to data $\mathbf{z}^s$ and k denotes the k^{th} element in $\mathbf{z}^s$. Genetic algorithm, implemented in MATLAB as function *ga*, is applied to solve this optimization problem.

Interpolation in combination with peak analysis and FFT

Inspired by the work of Sree et al. (2017) and Sree et al. (2018), we propose to interpolate low-frequency sampled data by using *makima* method in MATLAB. In comparison with *pchip* method (applied by Sree et al. (2017) and Sree et al. (2018)) and *spline* method, *makima* produces results that follow measured data trend much better (MathWorks, 2020d). After high resolution data are obtained by using the *makima* method, peak analysis and FFT are employed to estimate amplitude and preset wave period. These two methods are referred to as IntPeak and IntFFT onwards. Likewise, *Int* precedes all methods that involve interpolation henceforth.

Hilbert transform

Hilbert transform can be applied to compute the analytic signal of measurements, whereby instantaneous amplitude can be further determined as the magnitude of the analytic signal. The pertinent formulae take the form (Bruns, 2004):

$$S(f) = \mathcal{F}\{z\} \quad \textbf{[10]}$$

$$h(f) = iS(f) \quad \textbf{[11]}$$

$$S_H(f) = S(f) - i\,\mathrm{sgn}(f)h(f) \quad \textbf{[12]}$$

$$z_H = \mathcal{F}^{-1}\{S_H(f)\} \quad \textbf{[13]}$$

Where $\mathcal{F}$ and $\mathcal{F}^{-1}$ represent Fourier transform and inverse Fourier transform, respectively; f is frequency, z is vertical oscillation signal and z_H is the analytical signal of z. In implementation, FFT and IFFT are employed to perform Fourier transform and inverse Fourier transform. In addition, $\mathbf{z}^s$ substitutes for z. We propose to compute amplitude of $\mathbf{z}^s$ by taking the mean of the instantaneous magnitude of z_H (see e.g. Figure 5), which has the same length as $\mathbf{z}^s$. As mentioned earlier, because FFT and IFFT are involved in taking the Hilbert transform of $\mathbf{z}^s$, periodic boundary of $\mathbf{z}^s$ should be ensured to ameliorate edge artifact.

5. Results

Filtering and smoothing results

To demonstrate the efficiency of each method to remove noise, we show the data/signal and filtered and smoothed signals in frequency domain (Figure 1). It can be seen that bp is most effective followed by fir1. More importantly, fir1 amplifies low-frequency noise for some cases (see Figure 1d and Figure 1f). Tikhonov regularization and Smooth are more applicable to remove high frequency noise. Both Tikhonov regularization and Smooth yield similar smoothing results.

Note that here we preserve only the frequency components close to the incoming wave frequency (the most dominant peaks), similar to Sutherland et al. (2017), Rabault et al. (2019) and Nelli et al. (2017). The other frequency components are regarded as noise and should be eliminated. Actually, the amplitudes of frequency components in the regions where the smoothing and filtering methods modify the tails (Figure 1), are at least 5 times smaller than the predominant peaks (incoming wave frequency). This suggests that those frequency components with amplitudes changed by smoothing and filtering can be treated as noise. Figure 1 also demonstrates that both the smoothing and filtering methods effectively attenuate the high frequency components (noise) when comparing with original signals (represented by blue lines).

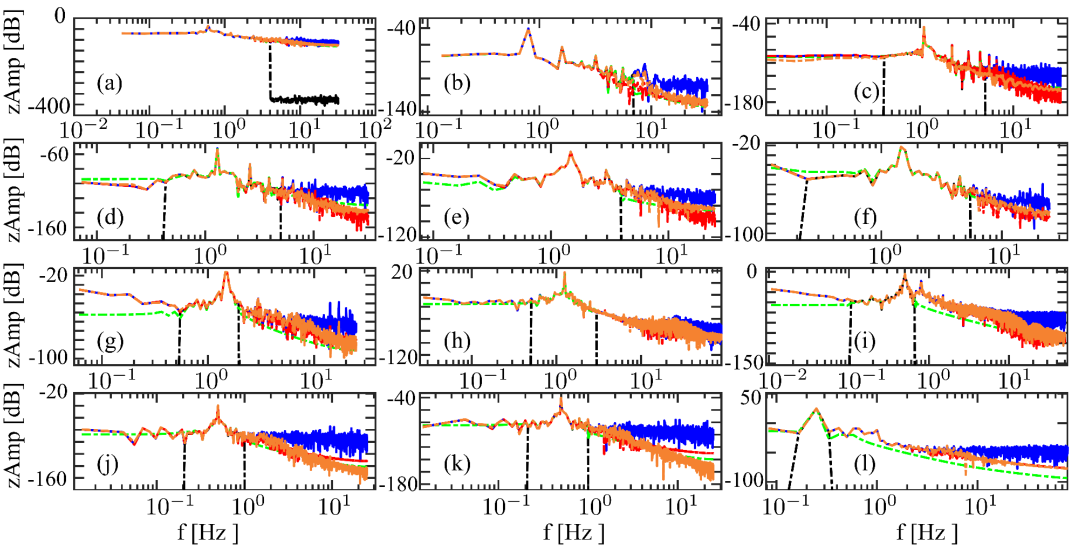

Figure 1. Data and corresponding filtered and smoothed results for different cases. (a) – (d) for cases #1, 4, 7 and 10. (e) – (l) for cases #13 – 20. Blue line represents original data. Black and green dash-dot lines denote filtered results by means of bp and fir1 respectively. Red and orange dashed line represent smoothed results by using Tikhonov regularization and Smooth, respectively. NOTE: black dash-dot floor around -400 dB in (a) represents numerical representation of zeros, and those floors in (b)-(l) are not shown.

A point-wise comparison is made for filtering results from bp and fir1 (Figure 2). Normalized-root-mean-squared errors (NRMSEs) for most cases are below 1.5% except for case #14, in which fir1 enlarges low-frequency noise (see Figure 1f). In addition, Figure 1 suggests that much of discrepancy between filtered results by bp and fir1 originates from the remainder after filtering low-frequency noise. To be more specific, the remainder after filtering high-frequency noise is much lower than that for low-frequency noise.

Considering the facts that bp and fir1 yield similar results and fir1 is devised to alleviate undesired ripple/ringing caused by sharp edge in narrowband filter design, ripple/ringing effect is minimal when using bp as well.

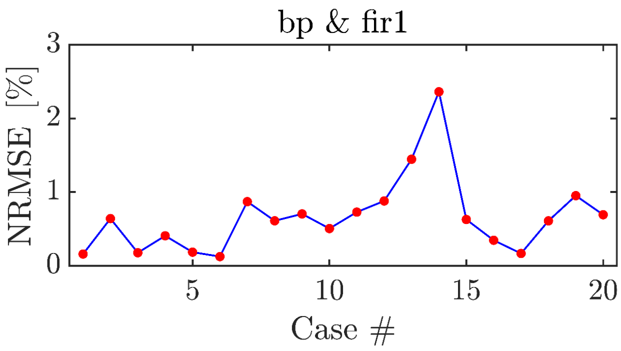

Figure 2. Comparison between filtered results by applying bp and fir1. Blue line with red dots is used to show clearly the NRMSE values.

Figure 3 compares the original signal, filtered and smoothed signals for case #18 using different filtering (bp, fir1) and smoothing methods (Tikhonov regularization, Smooth). It is evident that these different filtering and smoothing methods eliminate high frequency components. This is also apparent in frequency domain (Figure 1j), when comparing the original signals (blue lines) with the smoothed and filtered signals (other colorful lines).

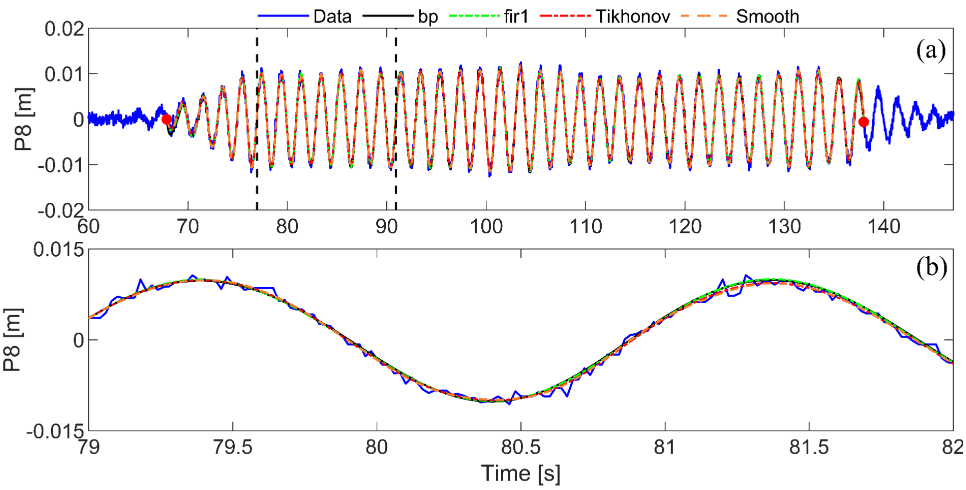

Figure 3. Case #18 and corresponding filtered and smoothed signals. Red filled dots in (a) highlight the zero periodic boundary selected for $\mathbf{z}^l$. Segment between two vertical dashed lines in (a) represent steady signal with zero periodic boundary chosen, i.e. $\mathbf{z}^s$.

Take case #18 as an example again, Figure 4a - Figure 4b illustrate using L-curve method to choose regularization parameter α for Tikhonov regularization and applying TSVD to choose number of components β to be retained for DMD, DMDa and Prony's method. The determined regularization parameter $\alpha = 6.40\times10^{-5}$. Number of components $\beta = 2$ since there is a significant gap between the second and third subspace dimension as exhibited in Figure 4b.

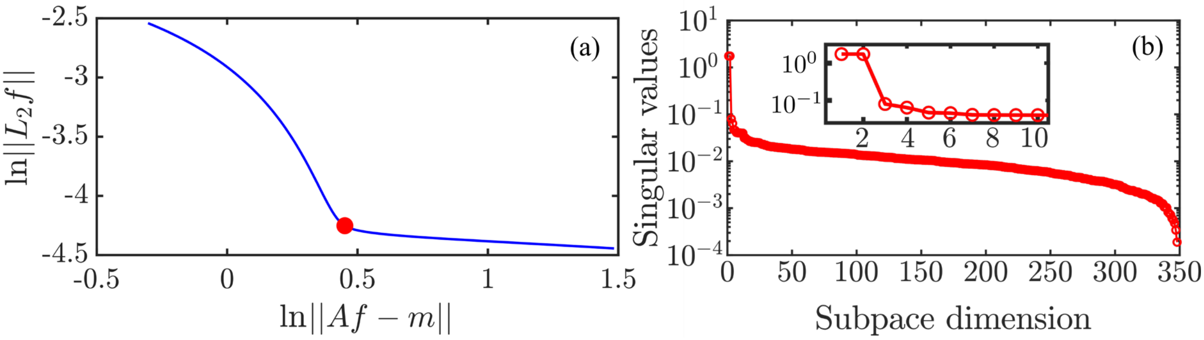

Figure 4. Methods to determine parameters for Tikhonov regularization, DMD, DMDa and Prony's method used for case #18. (a) regularization parameter determined by L-curve method for Tikhonov regularization. (b) number of modes β to be used (i.e. TSVD) for DMD, DMDa and Prony's method. Red dot in (a) denotes results corresponding to selected regularization parameter. Inset in (b) highlights that noise floor starts from 3rd subspace dimension.

Identifying the wave period and oscillation amplitude

Considering that bp and fir1 produce similar results, we perform analysis only on the filtered $\mathbf{z}^s$, which is obtained by applying bp on $\mathbf{z}^l$. Figure 5 serves as an example to illustrate the analytic signal obtained by Hilbert transform. As can be seen in Figure 5a, real part of analytic signal matches with the filtered signal. Figure 5b demonstrates the variation of the magnitude which is not noticeable in Figure 5a.

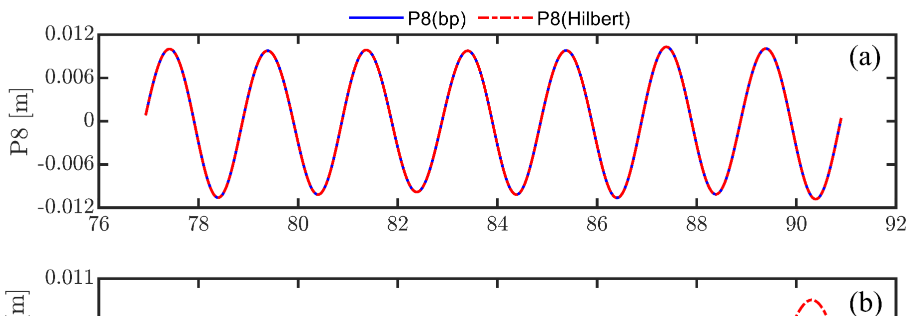

Figure 5. Hilbert transform of case #18. (a) compares the filtered signal obtained by bp and real part of the analytic signal. (b) shows the magnitude of the analytic signal.

Normalized error (NE) of estimated incident wave period by various methods compared with target wave period is displayed in Figure 6. As shown, all methods except for IntPeak give accurate estimates of incoming wave period (NE less than 2.5%). Prony's method, IntFFT and DMD are preferred methods because results produced by these methods are less scattered.

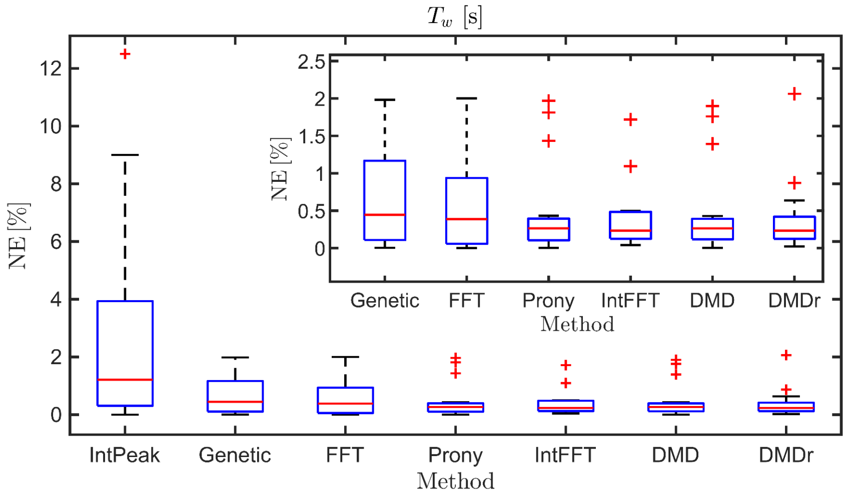

Figure 6. Normalized error (NE) of identified incoming wave period in comparison with target wave period by using various methods. Red plus sign denotes outliers. Inset shows more clearly the spread of NEs for all methods except for IntPeak.

Regarding amplitudes estimated by various methods, all methods except of Prony, DMD and DMDr yield similar results as FFT (NEs less than 3%). The significant deviation between results from Prony, DMDr, DMD and the other results can be explained as follows: (1) the amplitudes estimated by Prony, DMD and DMDr depend on initial data point due to grow/decay rate involved in these three methods; (2) other methods yield average amplitudes.

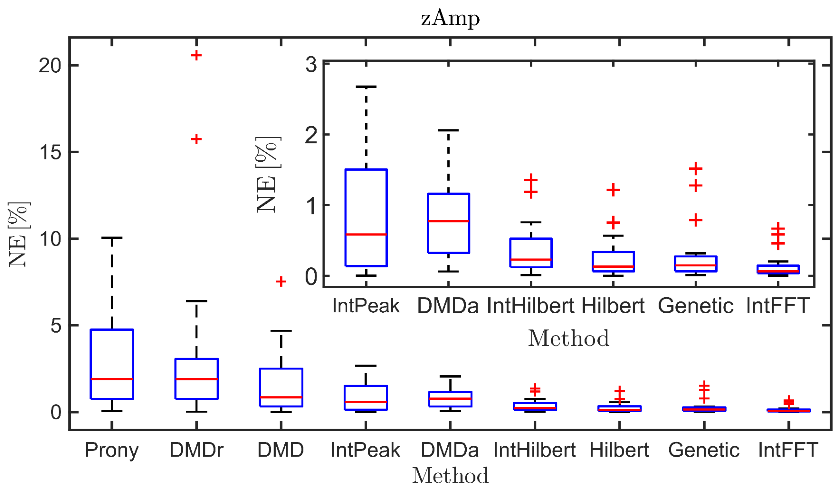

Figure 7. Normalized error (NE) of amplitudes identified in comparison with those obtained by FFT. Amplitudes here are for components having incoming wave frequency as oscillation frequency. Red plus sign denotes outliers. Inset displays more clearly the scatter of NEs for all methods except for Prony's method, DMDr and DMD.

The same analysis is also conducted on the smoothed $\mathbf{z}^s$ obtained by using Tikhonov regularization on $\mathbf{z}^l$. Similar spread of NEs for wave period and amplitude is observed. NEs for wave period are less than 4.5% for the various methods except for IntPeak, which has the largest NE around 11%. With regards to amplitude, the NEs are within 3% compared with results from FFT for those methods except for Prony's method, DMD and DMDr.

To validate the estimation procedures for wave period and oscillation amplitude, we reconstruct the signals based on the extracted largest oscillation amplitude and corresponding wave period. Figure 8 (case #18) illustrates that FFT, Genetic, Prony and DMD reliably reconstruct the filtered signal obtained by bp. The discrepancy quantified as NRMSE is within 1.7% with respect to the filtered signal.

The same validation steps are repeated for smoothed signal of case #18 obtained by Tikhonov regularization. The deviation of reconstructed signal by using the same aforementioned methods relative to the smoothed signal is negligible (NRMSEs less than 2.2%).

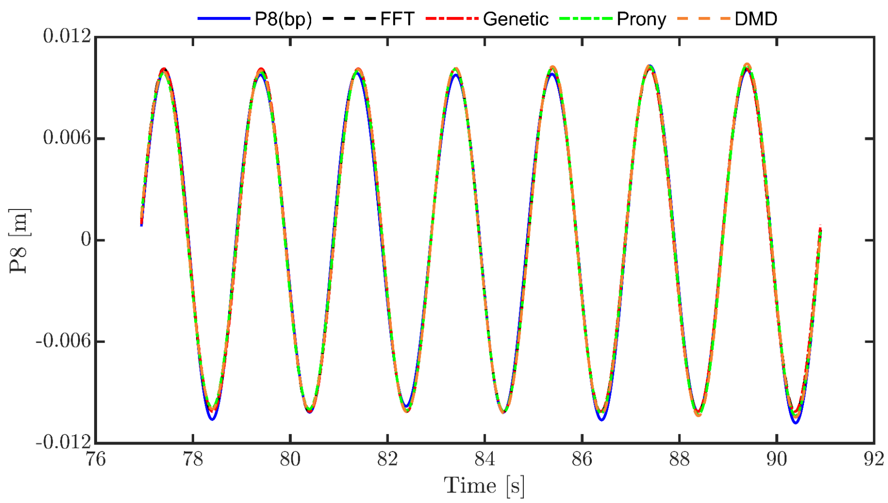

Figure 8. Filtered signals obtained by bp and reconstructed signals. The reconstructed signals are constructed by only utilizing component corresponding with target wave frequency.

6. Conclusion

In this paper, we present a systematic comparative study of methods involved in pre-processing data and analysis of data in wave-ice interaction studies.

In terms of pre-processing, we find that filtering by using FFT along with IFFT give equivalent filtering results as MATLAB function *fir1*. Tikhonov regularization produces similar results as MATLAB *smooth* function with option *rloess*. Tikhonov regularization denoising is superior to *smooth* owing to the existence of systematic approach to determine the regularization parameter involved in the former method.

Comparison of various wave period estimators shows that FFT combined with interpolation, Prony's method, DMD and DMDr reliably estimate incoming wave period with small variance. Lastly, we demonstrate that six methods (IntPeak, DMDa, Genetic, IntHilbert, Hilbert, IntFFT) give quantitively similar results with those obtained by using FFT (normalized error less than 3%).

Acknowledgments

The authors wish to acknowledge the support from the Research Council of Norway through the Centre for Research-Based Innovation SAMCoT and the support from all SAMCoT partners. The constructive discussions with Per Christian Hansen, and Yiqiu Dong at DTU Compute, and Zhengshun Cheng from Shanghai Jiao Tong University are greatly appreciated. The authors would like to extend great thanks to Lucas Yiew and Fabien Montiel for sharing the data used in this study. Lastly, the leading author feels very grateful towards the various supports provided by Jens Olaf Pepke Pederson during the author's research staying at DTU Space, where part of this work was conducted.

The MATLAB scripts employed in this study are planned to be provided online in near future.

References:

Ardhuin, F., Otero, M., Merrifield, S., Grouazel, A. & Terrill, E. (2020). Ice Breakup Controls Dissipation of Wind Waves Across Southern Ocean Sea Ice. *Geophysical Research Letters,* 47**,** e2020GL087699.

Aster, R. C., Borchers, B. & Thurber, C. H. (2018). *Parameter estimation and inverse problems*, Elsevier.

Bennetts, L. G. & Williams, T. D. (2015). Water wave transmission by an array of floating discs. *Proceedings of the Royal Society A: Mathematical, Physical and Engineering Science,* 471.

Bruns, A. (2004). Fourier-, Hilbert-and wavelet-based signal analysis: are they really different approaches? *Journal of neuroscience methods,* 137**,** 321-332.

Chen, Z. & Chan, T. H. (2017). A truncated generalized singular value decomposition algorithm for moving force identification with ill-posed problems. *Journal of Sound and Vibration,* 401**,** 297-310.

Cheng, S., Rogers, W. E., Thomson, J., Smith, M., Doble, M., Wadhams, P., Kohout, A. L., Lund, B., Persson, O., Collins, C. O., Ackley, S. F., Montiel, F. & Shen, H. H. (2017). Calibrating a Viscoelastic Sea Ice Model for Wave Propagation in the Arctic Fall Marginal Ice Zone. *Journal of Geophysical Research: Oceans* [Online]. Available: http://dx.doi.org/10.1002/2017JC013275 [Accessed October 21, 2017].

Cohen, M. X. (2014). *Analyzing neural time series data: theory and practice*, MIT press.

Cohen, M. X. (2020). *Signal processing problems, solved in MATLAB and in Python* [Online]. https./www.udemy.com. Available: https://www.udemy.com/course/signal-processing/learn/lecture/11864684#questions [Accessed January 14 2020].

Cooley, J. W. & Tukey, J. W. (1965). An algorithm for the machine calculation of complex Fourier series. *Mathematics of computation,* 19**,** 297-301.

Gavish, M. & Donoho, D. L. (2014). The optimal hard threshold for singular values is 4/ √ 3. *IEEE Transactions on Information Theory,* 60**,** 5040-5053.

Gedikli, E. D., Chelidze, D. & Dahl, J. (2020). Empirical Mode Analysis Identifying Hysteresis in Vortex-Induced Vibrations of a Bending-Dominated Flexible Cylinder. *International Journal of Offshore and Polar Engineering,* 30**,** 186-193.

Gedikli, E. D., Chelidze, D. & Dahl, J. M. (2018). Bending dominated flexible cylinder experiments reveal insights into modal interactions for flexible body vortex-induced vibrations. *The 28th International Ocean and Polar Engineering Conference*, 2018. International Society of Offshore and Polar Engineers.

Haase, A. & Tsarau, A. (2019). Hydralab+ HSVA-01 TA Kvaerner sensor_data. Zenodo.

Hansen, P. C. (2010). *Discrete inverse problems: insight and algorithms*, SIAM.

Hu, S.-L. J., Yang, W.-L. & Li, H.-J. (2013). Signal decomposition and reconstruction using complex exponential models. *Mechanical Systems and Signal Processing,* 40**,** 421-438.

James, G., Witten, D., Hastie, T. & Tibshirani, R. (2013). *An introduction to statistical learning*, Springer.

Juang, J.-N. & Pappa, R. S. (1985). An eigensystem realization algorithm for modal parameter identification and model reduction. *Journal of guidance, control, and dynamics,* 8**,** 620-627.

Kohout, A. L., Penrose, B., Penrose, S. & Williams, M. J. (2015). A device for measuring wave-induced motion of ice floes in the Antarctic marginal ice zone. *Annals of Glaciology,* 56**,** 415-424.

Kutz, J. N. (2013). *Data-driven modeling & scientific computation: methods for complex systems & big data*, Oxford University Press.

Kutz, J. N., Brunton, S. L., Brunton, B. W. & Proctor, J. L. (2016). *Dynamic Mode Decomposition: Data-driven Modeling of Complex Systems*, SIAM.

Li, H., Gedikli, E. D. & Lubbad, R. (2019). Identifying flexural-mode shapes of ice floes under wave actions using multivariate analysis. *The 25th International Conference on Port and Ocean Engineering under Arctic Conditions*, 2019 Delft, The Netherlands. Delft, The Netherlands.

Li, H., Gedikli, E. D. & Lubbad, R. (2020a). Exploring time-delay-based numerical differentiation using principal component analysis. *Physica A: Statistical Mechanics and its Applications,* 556**,** 124839.

Li, H., Gedikli, E. D., Lubbad, R. & Nord, T. S. (2020b). Laboratory study of wave-induced ice-ice collisions using robust principal component analysis and sensor fusion. *Cold Regions Science and Technology,* 172**,** 103010.

Li, H. & Lubbad, R. Laboratory study of ice floes collisions under wave action. *The 28th International Ocean and Polar Engineering Conference*, 2018. International Society of Offshore and Polar Engineers.

Mathworks. (2020a). *Compensate for the Delay Introduced by an FIR Filter* [Online]. Available: https://se.mathworks.com/help/signal/ug/compensate-for-the-delay-introduced-by-an-fir-filter.html [Accessed January 14 2020].

Mathworks. (2020b). *Compensate for the Delay Introduced by an IIR Filter* [Online]. Available: https://se.mathworks.com/help/signal/ug/compensate-for-the-delay-introduced-by-an-iir-filter.html [Accessed January 14 2020].

Mathworks. (2020c). *FIR Filter Design* [Online]. Available: https://se.mathworks.com/help/signal/ug/fir-filter-design.html [Accessed November 01 2020].

Mathworks. (2020d). *Modified Akima piecewise cubic Hermite interpolation* [Online]. Available: https://se.mathworks.com/help/matlab/ref/makima.html [Accessed January 08 2020].

Mathworks. (2020e). *tukeywin* [Online]. Available: https://se.mathworks.com/help/signal/ref/tukeywin.html [Accessed November 01 2020].

Meylan, M. H., Yiew, L. J., Bennetts, L. G., French, B. J. & Thomas, G. A. (2015). Surge motion of an ice floe in waves: comparison of a theoretical and an experimental model. *Annals of Glaciology,* 56**,** 155-159.

Montiel, F., Bonnefoy, F., Ferrant, P., Bennetts, L., Squire, V. & Marsault, P. (2013). Hydroelastic response of floating elastic discs to regular waves. Part 1. Wave basin experiments. *Journal of Fluid Mechanics,* 723**,** 604-628.

Mosig, J. E., Montiel, F. & Squire, V. A. (2015). Comparison of viscoelastic ‐ type models for ocean wave attenuation in ice ‐ covered seas. *Journal of Geophysical Research: Oceans,* 120**,** 6072-6090.

Mueller, J. L. & Siltanen, S. (2012). *Linear and nonlinear inverse problems with practical applications*, SIAM.

Nelli, F., Bennetts, L., Skene, D., Monty, J., Lee, J., Meylan, M. & Toffoli, A. (2017). Reflection and transmission of regular water waves by a thin, floating plate. *Wave Motion,* 70**,** 209-221.

Paige, C. C. & Saunders, M. A. (1982). LSQR: An algorithm for sparse linear equations and sparse least squares. *ACM Transactions on Mathematical Software (TOMS),* 8**,** 43-71.

Proakis, J. G. (2001). *Digital signal processing: principles algorithms and applications*, Pearson Education India.

Rabault, J., Sutherland, G., Gundersen, O. & Jensen, A. (2017). Measurements of wave damping by a grease ice slick in Svalbard using off-the-shelf sensors and open-source electronics. *Journal of Glaciology,* 63**,** 372-381.

Rabault, J., Sutherland, G., Jensen, A., Christensen, K. H. & Marchenko, A. (2019). Experiments on wave propagation in grease ice: combined wave gauges and particle image velocimetry measurements. *Journal of Fluid Mechanics,* 864**,** 876-898.

Rodríguez, A. F., De Santiago Rodrigo, L., Guillén, E. L., Ascariz, J. R., Jiménez, J. M. & Boquete, L. (2018). Coding Prony's method in MATLAB and applying it to biomedical signal filtering. *BMC bioinformatics,* 19**,** 451.

Schmid, P. J. (2010). Dynamic mode decomposition of numerical and experimental data. *Journal of Fluid Mechanics,* 656**,** 5-28.

Shmuel, B.-E. (2020). FFT filter - clean your signals and display results! (https://www.mathworks.com/matlabcentral/fileexchange/25017-fft-filter-clean-your-signals-and-display-results). MATLAB Central File Exchange.

Sree, D. K., Law, A. W.-K. & Shen, H. H. (2018). An experimental study on gravity waves through a floating viscoelastic cover. *Cold Regions Science and Technology,* 155**,** 289-299.

Sree, D. K. K., Law, A. W.-K. & Shen, H. H. (2017). An experimental study on the interactions between surface waves and floating viscoelastic covers. *Wave Motion,* 70**,** 195-208.

Sutherland, G., Halsne, T., Rabault, J. & Jensen, A. (2017). The attenuation of monochromatic surface waves due to the presence of an inextensible cover. *Wave motion,* 68**,** 88-96.

Trefethen, L. N. (2000). *Spectral methods in MATLAB*, SIAM.

Tu, J. H., Rowley, C. W., Luchtenburg, D. M., Brunton, S. L. & Kutz, J. N. (2014). On dynamic mode decomposition: theory and applications. *Journal of Computational Dynamics,* 1**,** 391-421.

Tucker, M. J. & Pitt, E. G. (2001). *Waves in ocean engineering*, Elsevier Science.

Voermans, J., Babanin, A., Thomson, J., Smith, M. & Shen, H. (2019). Wave attenuation by sea ice turbulence. *Geophysical Research Letters,* 46**,** 6796-6803.

Wang, R. & Shen, H. H. (2010). Experimental study on surface wave propagating through a grease–pancake ice mixture. *Cold Regions Science and Technology,* 61**,** 90-96.

Yiew, L., Parra, S., Wang, D., Sree, D., Babanin, A. & Law, A.-K. (2019). Wave attenuation and dispersion due to floating ice covers. *Applied Ocean Research,* 87**,** 256-263.

Yiew, L. J., Bennetts, L., Meylan, M. H., French, B. & Thomas, G. (2016). Hydrodynamic responses of a thin floating disk to regular waves. *Ocean Modelling,* 97**,** 52-64.

Zhao, X. & Shen, H. H. (2015). Wave propagation in frazil/pancake, pancake, and fragmented ice covers. *Cold Regions Science and Technology,* 113**,** 71-80.

IAHR AIRH

25th IAHR International Symposium on Ice

Trondheim, 23 - 25 November 2020

A comparison of wave observations in the Arctic marginal ice zone with spectral models

Trygve K. Løken (a), Jean Rabault (b,a), Erin E. Thomas (b), Malte Müller (b), Kai H. Christensen (b), Graig Sutherland (c) and Atle Jensen (a)

a. Department of Mathematics, University of Oslo, Moltke Moes vei 35, 0851 Oslo, Norway
b. Norwegian Meteorological Institute, 0371 Oslo, Norway
c. Numerical Environmental Prediction Research, Environment and Climate Change Canada, Dorval, Québec, Canada
trygvekl@math.uio.no, jeanra@math.uio.no, erinet@met.no, maltem@met.no, kaihc@met.no, graigory.sutherland@canada.ca, atlej@math.uio.no

Increased economic activity and research interest in the Arctic raise the need for better wave forecasts in the Marginal Ice Zone (MIZ). Mathematical and numerical models of wave propagation in sea ice would benefit from more in situ data for validation. This study presents shipborne wave measurements from the MIZ where altimeter readings are corrected for ship motion to obtain estimated single point ocean surface elevation. From the combined measurements, we obtain significant wave height and zero up-crossing period, as well as one-dimensional wave spectra. In addition, we provide spectra and integrated parameters obtained from Inertial Motion Units (IMUs) placed on ice floes inside the MIZ. The results are compared with integrated parameters from the WAM-4 spectral wave model over a period of three days in the open ocean. We also compare our measurements outside and inside the MIZ with hindcast data from the new pan-Arctic WAM-3 model and the Wave Watch III (WW3) model for the European Arctic, which both model wave attenuation in sea ice. A good agreement is found with WAM-4 and WW3 in zero up-crossing period and significant wave height outside the MIZ, where deviations are less than 23%. WAM-3 is on the other hand up to 60% higher than observations. WW3 and WAM-3 are able to estimate the trends for significant wave height and zero up-crossing period inside the MIZ, although the discrepancies with respect to the observations are larger than in the open ocean. Wave damping by sea ice is investigated by looking at the spatial attenuation coefficients. Predicted attenuation coefficients are found to be 72-83% smaller for WW3 and 3-64% larger for WAM-3 compared to observations. Hence, further model tuning is necessary to better estimate wave parameters in the ice.

1. Introduction

The recent decline in Arctic ice cover has allowed for increased human activities in the region, which raises the importance of better forecast models and improved physical understanding of the environment to ensure safe operations (Fritzner et al., 2019). This also applies in the interface between solid ice, such as land fast ice or pack ice, and the open ocean, called the Marginal Ice Zone (MIZ). In situ wave measurements can increase our understanding of global climate systems and provide data for calibration and validation of numerical and mathematical models to describe wave attenuation in ice. However, experimental data are relatively sparse due to the harsh and dangerous environment for both researchers and instruments, combined with the inaccessibility of the regions where sea ice is present (Squire, 2007).

In this study, we present results from shipborne wave measurements in the MIZ. The methodology, first described in Christensen et al. (2013), combines a bow mounted altimeter and a motion correction instrument. We provide estimated power spectra from ocean surface elevation and integrated parameters from spectra, which are important quantities when considering wave-ice interactions. The results are compared with the spectral wave models WAM-4, Wave Watch III (WW3) and WAM-3 in the open ocean and in the MIZ, as a validation for the capability of modelling wave attenuation by sea ice. We also compare measurements in the MIZ with data from wave measuring instruments consisting of Inertial Motion Units (IMUs) placed on ice floes. From the significant wave height, the spatial damping coefficient from the observations and models are found and compared with each other.

In this paper, the data acquisition and processing methods are described in Section 2. The results are presented in Section 3 followed by a discussion in Section 4. Finally, the concluding remarks are given in Section 5.

2. Data and Methods

The data were obtained during a research campaign in the Barents Sea with R/V Kronprins Haakon in September 2018. Shipborne wave measurements were made continuously during cruising in the open ocean and in the MIZ, into which the ship ventured on September 19.

Table 1. Time, WTD and location where measurements were carried out inside the MIZ.

Stop	Time	Position (N/E)	WTD [km]		
			Bow	WW3	WAM-3
1.1	04:22	82.126/20.736	0	5	0
1.2	06:28	82.246/20.245	28	34	15
1.3	08:59	82.355/19.803	61	58	31
1.4	12:20	82.436/19.674	82	65	53
2.1	13:11	82.421/19.579	77	65	51
2.2	14:32	82.359/19.544	65	61	32
2.3	15:40	82.294/19.389	46	43	27
2.4	16:54	82.228/19.275	18	27	20
2.5	18:00	82.163/19.183	7	12	7
2.6	19:08	82.099/19.046	0	0	1
2.7	20:09	81.994/18.982	0	0	0

Four stops were made on the way into the MIZ to deploy in situ Waves-In-Ice (WII) instruments on ice floes (Rabault et al., 2020). The sea ice concentration was visually estimated to be 10, 30, 90 and 100% for stops 1.1-1.4 respectively, and the ice thickness of the floes was approximately 1 m. Upon the return to the open ocean, a total of seven stops were made to carry out measurements unaffected by cruising speed. The location, starting time and wave travel distance (WTD) through the ice for each measurement in the MIZ are summarized in Table 1. WTD indicated "Bow" is found from the approximated ice edge from Fig. 1 and the estimated wave direction from WAM-4, while "WW3" and "WAM-3" are found by combining the ice edge and the wave direction estimated by the respective model. Prefix 1 denotes the four stops into the MIZ while prefix 2 denotes the seven stops out of the MIZ.

Figure 1(left) shows the ice edge at approximately 82.2 °N below the thin cloud cover and ship trajectory into (red) and out of (green) the MIZ. The cyan line indicates the longitudes over which the wave directions are averaged to find the mean. The ice edge is roughly recreated from the satellite image and shown in Fig. 1(right). This figure also indicates the ice edge and the mean wave direction at the ice edge at noon on September 19 estimated by the spectral models, which is further described in Section 2.2. We use the "going-to" convention for wave direction and define directions as clockwise rotation from the geographic north.

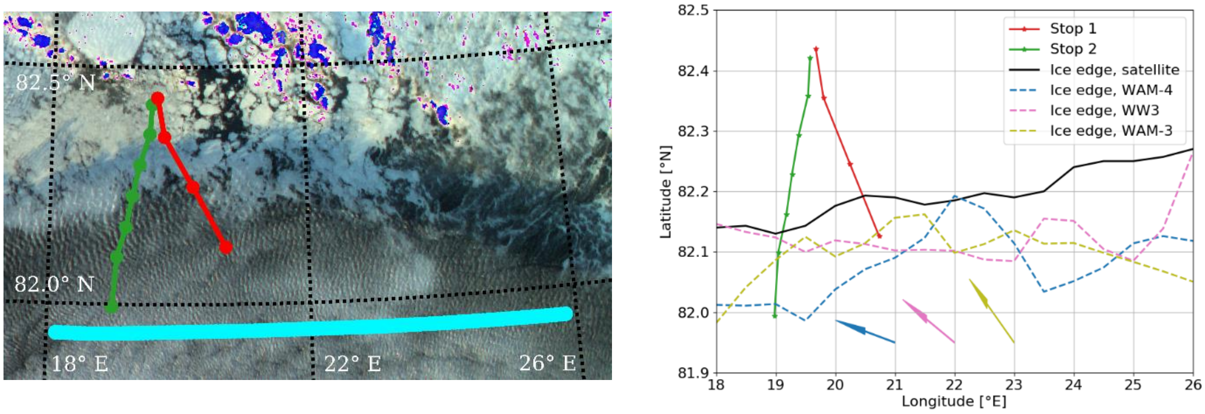

Figure 1. Ice edge and location of measurements. Left: Satellite image with ship trajectory into (red) and out of (green) the MIZ. The cyan line marks the averaging range for wave parameters from the models. Right: Ice edge and wave direction from models and satellite image.

The instrument setup consisted of an ultrasonic gauge (UG) mounted on a rigid pole that measured ocean surface elevation relative to the ship bow. We used a UG (Banner QT50ULB) with approximately 0.2-8 m range. The instrument emits 75 kHz ultrasonic pulses at a 10.4 Hz sampling rate. Estimated absolute surface elevation was obtained after correcting for ship motion by means of an IMU placed on deck, also in the bow section of the ship. As motion correction device, we used an IMU (VectorNav VN100). It features 3-axis accelerometers and 3-axis gyroscopes measuring at a rate of 800 Hz. After an internal Kalman filtering, the instrument gives an output frequency of 80 Hz. The gyros yield rotation angles about all three axis directly. Vertical acceleration is integrated twice to obtain ship vertical displacement about the mean. Details on the integral scheme, data filtering and other technical information on the instrument can be found in Rabault et al. (2020).

In order to obtain time series of the surface elevation, UG and IMU data at the same time instance were needed. We solved this by defining a common sampling rate of 10 Hz, which should be sufficient for resolving all relevant ocean surface features. All data were then interpolated on the common time base for the analysis. See Løken et al. (2019, Eq. 3) for details on the motion correction and estimates for the ocean surface elevation. The UG range was exceeded (saturated) at times with large wave amplitudes.We accept up to 10% saturation in a time series and will therefore discard the sample recorded at stop 2.7 in further analysis, which had a total saturation of approximately 20%.

2.1. Spectrum, statistical parameters and wave attenuation

Power spectra *S(f)* of the surface elevation is obtained with the Welch method, following Earle (1996). Samples are subdivided in q consecutive segments and ensemble averaged. Segment size is set to 200 s with 50% overlap. 20 min sampling time at 10 Hz yields a segment size of 2000 and a total number of 12000 sampling points for each measurement. A Hanning window is applied to each segment to reduce spectral leakage. Peak frequency f_P is defined as the frequency at the spectral peak. The mean zero up-crossing period and the significant wave height are obtained from the spectral moments:

$$m_j = \int_{f_{min}}^{f_{max}} f^j S(f) df, \quad \textbf{[1]}$$

where the cutoff frequencies f_{min} and f_{max} are set to 0.04 Hz and 1.0 Hz, respectively, which should include the most energetic ocean waves. Approximately the same cutoff frequencies are also applied in the spectral models. Zero up-crossing periods T_{m02} are estimated from:

$$T_{m02} = \sqrt{\frac{m_0}{m_2}}. \quad \textbf{[2]}$$

We investigate significant wave heights H_S estimated from spectra, defined as:

$$H_S = 4\sqrt{m_0}\,. \quad \textbf{[3]}$$

Confidence intervals for both spectra and significant wave heights are calculated from the Chi-squared distribution, following Young (1995). For spectra, the total degree of freedom (TDF) is calculated as $TDF = 2q$, and for significant wave height, TDF is found as described in ITTC (2017, p. 5). We use the Mean Absolute Percentage Error (MAPE) to compare model data with bow measurements. Systematic bias relative to observations is described with the Mean Percentage Error (MPE).

Previous field measurements indicate that waves decay exponentially in ice (Squire and Moore, 1980; Wadhams et al., 1988; Marchenko, 2018). We have investigated the attenuation of the significant wave height by fitting decreasing exponentials on the shape $H_S = Ce^{-\alpha x}$, where C and α are estimated parameters and x is wave traveling distance through the MIZ, by means of non-linear least squares. From the fitted curves, the spatial damping coefficients α, which describe wave attenuation per meter, are determined from:

$$\frac{\partial H_S}{\partial x} = -\alpha H_S. \quad \textbf{[4]}$$

2.2. Wave models

We have investigated the performance of the three wave prediction models; WAM-4, WW3 and WAM-3 in comparison to our observations. WAM-4 does not give wave parameter where there is assumed to be an ice cover present, whereas the two latter models contain wave attenuation through the ice cover. WW3 estimates power spectra, while the WAM models only provide integrated parameters.

The WAM-4 spectral wave forecast model is run operationally by the Norwegian Meteorological Institute (Carrasco and Gusdal, 2014). Spatial and temporal resolution of the model is 4 km and 1 hour, respectively, and it runs twice a day. A hard ice boundary based on satellite images (ice concentration larger than 30%) is defined in the model.

The WAM-3 model is a pan-Arctic wave forecasting system with an effective resolution of 3 km, operated in the framework of the Copernicus Marine Environmental Monitoring System's Arctic Marine Forecasting Center. The WAM-3 wave hindcast used in the present study is forced by hourly 10 meter winds from ERA-Interim reanalysis (Dee et al., 2011) with a horizontal resolution of around 80 km. The wave spectra from the ERA-Interim are used at the lateral boundaries. The daily sea-ice concentration, ice thickness, and surface current information is taken from the TOPAZ ocean model system (Sakov et al., 2014). In areas with a sea-ice concentration larger than 20%, for the wave propagation, the frictional dissipation by the overlying ice sheet is considered as a function of the sea-ice thickness and wavenumber (Sutherland et al., 2019). Epsilon, which describes the thickness ratio of the two layers, is 0.13.

The WW3 model is a two-way coupled atmosphere-wave numerical weather prediction system in the Arctic. The atmosphere model AROME-Arctic (Müller et al. 2017) is coupled to the 3rd generation spectral wave model WW3 v5.16 using the OASIS3 model coupling toolkit. To obtain the sea-ice variables required by the wave model, we utilize the simple sea ice scheme (SICE) within SURFEX (Batrak et al., 2018). The WW3 setup used in this study uses the ST3 physics setting (equivalent to WAM4 physics) and estimates wave damping by sea ice through dissipation caused by bottom friction below a continuous thin elastic plate of ice (IC2 setting). We assume no scattering by sea ice in this framework. The coupled model is configured over the AROME-Arctic domain with a horizontal grid resolution of 2.5 km. AROME-Arctic uses 1 min. time steps while WW3 uses 5 min. time steps. The coupling frequency is every 30 min.

3. Results

Bow measurements are compared with model data interpolated to the location of the ship in Fig. 2(left). Valid measurements inside the MIZ, which we define as time periods where total UG saturation is below 10% and Ship Speed over Ground (SOG) is below 0.5 m/s, are highlighted with gray background color. The whole comparison spans over three days. Error statistics are summarized in Table 2, where MAPE describes the mean absolute error and MPE describes the mean error. In general, there is a good agreement between observations and model. The WAM-4 model performs best outside the MIZ compared to the bow measurements with deviations less than 23% and 8% for H_S and T_{m02} respectively. Deviations are approximately equally high when comparing to WW3, while WAM-3 overestimates both wave height (approx. 60%) and period (approx. 17%), especially the day before the ship ventured into the MIZ. Inside the MIZ, both models capture the larger trends when comparing them to the observations. H_S is actually better predicted when the measurements are considered not valid for both models. T_{m02} is more sensitive to the motion of the ship and the models are closer to the observations within the valid times.

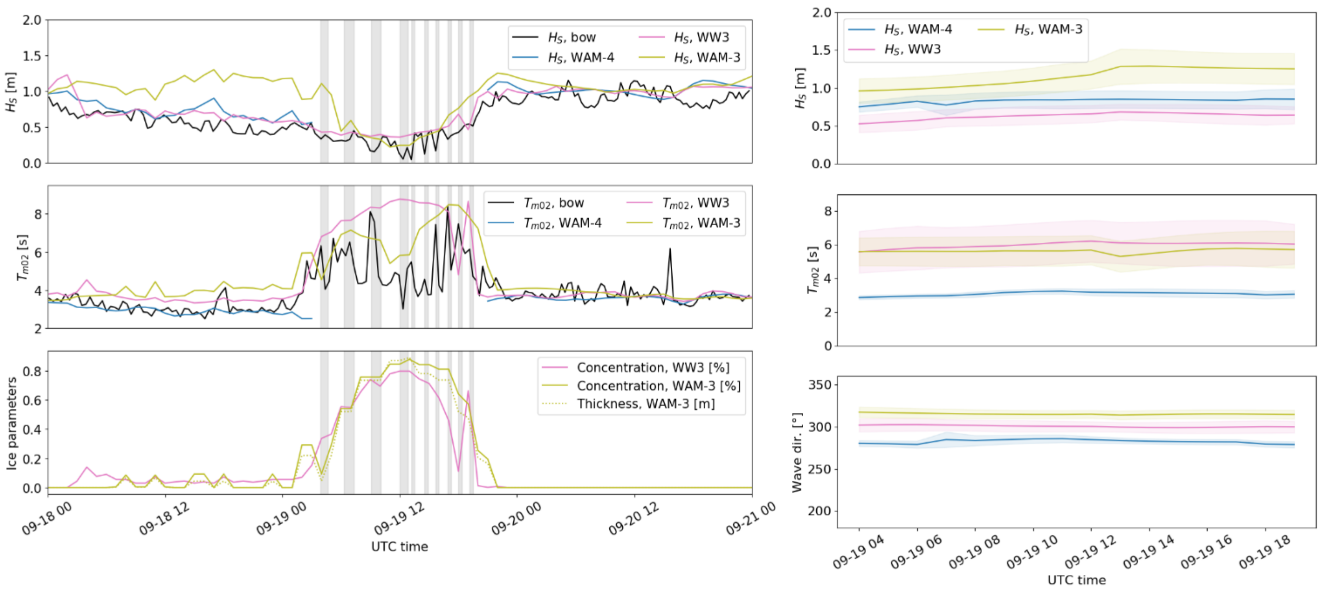

Figure 2. Left: long time comparison between bow measurements and the models for H_S (upper), T_{m02} (middle) and ice properties (lower). Measurements that are considered valid are highlighted with gray background color. Right: time series of H_S (upper), T_{m02} (middle) and wave direction (lower) from the wave models with spatial standard deviations shown as shaded regions. Values are extracted from locations indicated in Fig. 1.

A stationary sea state over the measurement period inside the MIZ is an advantage in our analysis. The sea state is investigated in Fig. 2(right) where time series of H_S, T_{m02} and wave direction from the models are presented. The model data are extracted from the ice edge defined in the respective models over the range of longitudes indicated in Fig. 1(left), and the standard deviation over this range is shown as shaded areas. None of the parameters change dramatically over the time period, and the data is overall quite consistent in space.

Table 2. Error statistics for H_S and periods T_{m02} when comparing model data with bow measurements.

	Error	WAM-4		WW3		WAM-3	
		H_S	$Tm02$	H_S	$Tm02$	H_S	$Tm02$
MAPE [%]	Outside MIZ	22.9	7.8	19.5	11.4	59.7	17.1
	MIZ, valid			107.5	58.2	85.7	32.7
	MIZ, not valid			32.8	53.7	67.2	39.0
MPE [%]	Outside MIZ	-20.6	5.4	-17.1	-7.4	-58.9	-14.4
	MIZ, valid			-107.4	-56.0	-83.1	29.9
	MIZ, not valid			-32.2	-49.6	-61.5	-37.3

Power spectra from bow measurements (black) and WII instruments (blue) with their respective 95% confidence intervals are compared to spectra from WW3 (magenta) and peak frequencies from WAM-3 (green) in Fig. 3. Stops into the MIZ are presented to the left, going successively from stop number 1.1 (upper panel) to 1.4 (lower panel) and stops out of the MIZ are presented to the right, going successively from stop number 2.1 (upper panel) to 2.6 (lower panel).

The observed power spectra from bow measurements and WII instruments in Fig. 3(left) are consistent for most frequencies for all stops in the left figure, except for stop 1.3, where the spectra deviates substantially for frequencies higher than 0.1 Hz. See Løken et al. (2019) for a discussion on this discrepancy. The spectrum from WW3 underestimates the wave energy content at stop 1.1, is consistent up to approximately 0.125 Hz at stop 1.2 and overestimates the energy at stops 1.3-1.4. The peak frequencies from WAM-3 decrease further into the ice in accordance with the observations, except for stop 1.4 where it is overestimated.

In Fig. 3(right), WW3 overestimates the wave energy content at stops 2.1-2.3 furthest into the MIZ. The model predicts a dual peak spectrum with the low frequency peak in the same frequency range as the observed spectra, but no high frequent peak was detected in the bow measurements. For stops 2.4-2.6, the spectra are comparable in strength and frequency. WAM-3 predicts an increasing peak frequency, but the growth in f_P is smaller than what was observed with the bow measurements.

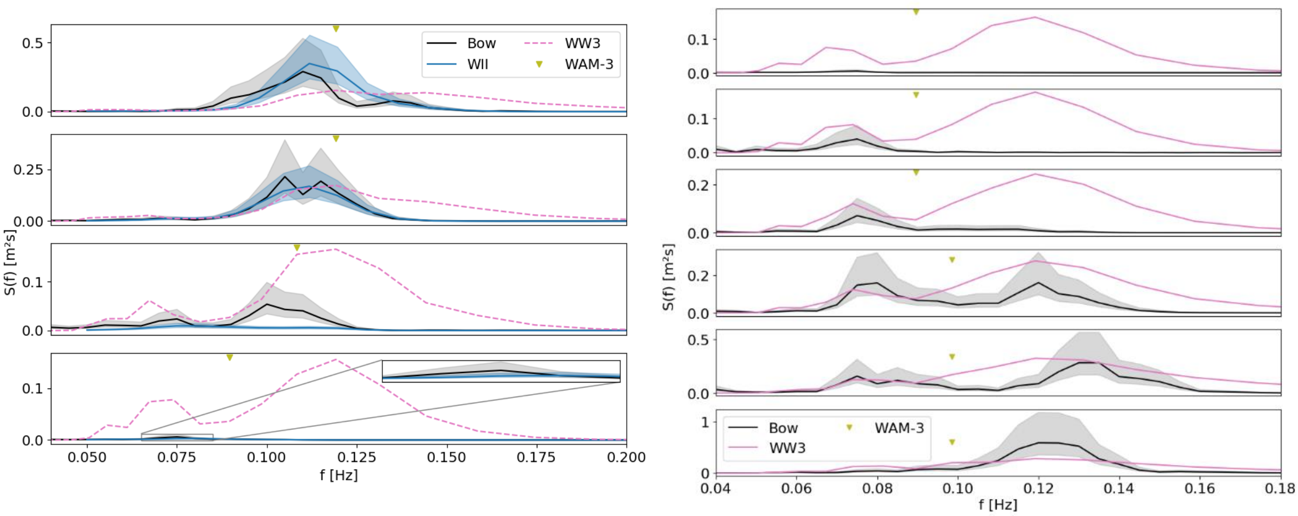

Figure 3. Power spectra from bow measurements (black) and WII instruments (blue) with their respective 95% confidence intervals shaded. Spectra from WW3 (magenta) and peak frequencies from WAM-3 (green). Left: going into the ice zone from upper (stop 1.1) to lower panel (stop 1.4). Right: going out of the MIZ from upper (stop 2.1) to lower panel (stop 2.6).

It is evident that waves are attenuated as they travel through the MIZ. Figure 4 shows the decrease in H_S from observations (with 95% confidence intervals) and the models as function of WTD through the MIZ on the way into (left) and out of (right) the ice. Decreasing exponentials are fitted to the data and the spatial damping coefficients are found from the fitted curves with Eq. 4. The damping coefficients from the different models and observations are summarized in Table 3. The bow measurements and the WII instruments are quite consistent. WAM-3 predicts a larger damping than observations into the MIZ (attenuation coefficient 64% higher than bow measurements), but is very close to observations out of the MIZ (attenuation coefficient 3% higher than bow measurements). WW3 substantially underestimates the damping compared to observations both into and out of the MIZ (attenuation coefficient 72-83% lower than bow measurements).

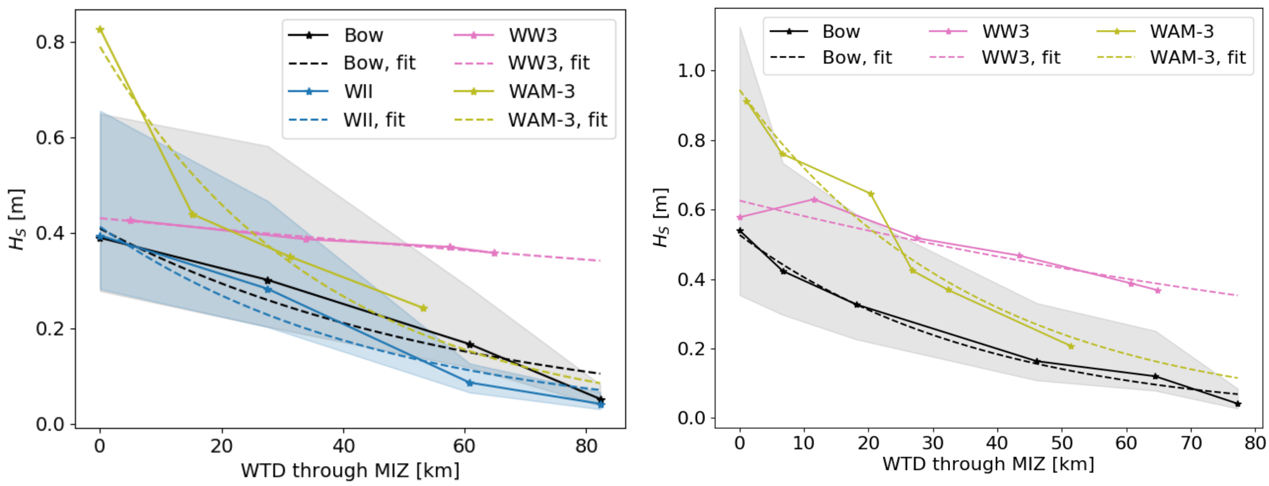

Figure 4. H_S as function of WTD with fitted exponential decays from bow measurements (black), WII instruments (blue) with their respective 95% confidence intervals shaded, WW3 (magenta) and WAM-3 (green). Left: into the MIZ. Right: out of the MIZ.

Table 3. Spatial damping coefficients from observations and models into (stop 1) and out of (stop 2) the MIZ.

α $[10^{-5}\ m^{-1}]$	Bow	WII	WW3	WAM-3
Stop 1	1.65	2.15	0.28	2.71
Stop 2	2.64		0.74	2.72

4. Discussion

The consistency in spectra between the bow and the WII instruments substantiates the validity of the wave measurements in the ice. The WTD through the MIZ is found from the mean wave direction and the location of the ice edge predicted by each model and therefore differs, as seen in Table 1.WAM-3 performs reasonably well compared to the observations in the MIZ when considering integrated parameters. Wave attenuation through the ice is satisfactory modeled in WAM-3 with the two-layer model of Sutherland et al. (2019), although a bit overestimated in terms of the spatial damping coefficient compared to observations. This deviation can be partly explained by the fact that the WTD found from WAM-3 is considerably smaller than the WTD found from WW3, which in again is smaller than the WTD found from WAM-4. WW3 also gives fair estimates of the integrated parameters, especially outside the MIZ, but the spectra and the damping coefficient reveals that the thin elastic plate modelling of the sea ice so far fails to estimate the attenuation of the waves.

Data recorded while a ship is in motion will contain a Doppler shifted frequency according to the wave heading angle (Collins III et al., 2017), which could be problematic in the calculation of periods. In the present study, we observe that measured T_{m02} is closer to the predicted value from WAM-3, which performs best of the models inside the MIZ, when the ship is stationary. Observations of H_S on the other hand, seem to be less affected by the moving ship when compared to the models, the deviations are in fact larger between models and observations at the times considered not valid. This is in agreement with the results of Cristensen et al. (2013), which reported that peak and mean periods were strongly biased by the Doppler shift in the time series, while the estimates of significant wave heights were reasonable since they only depend on the sea surface variance

5. Conclusions

We have presented shipborne wave measurements from the MIZ with a system combining an altimeter (UG) and a motion correction device (IMU). Our setup provides single point time series of ocean surface elevation outside of and inside the MIZ, which enables us to produce 1D power spectra and integrated parameters.

Observations have been compared with estimates from the spectral models WAM-4 (integrated parameters) in the open ocean, WW3 (integrated parameters and spectra) and WAM-3 (integrated parameters) in the open ocean and in the MIZ. We have found good agreement in zero up-crossing periods and significant wave height outside the MIZ. Predictions from WAM-4 and WW3 deviate with less than 23% over this timespan while H_S predicted by WAM-3 is up to 60% off. From the time series, it is clear that the two models which predict wave attenuation through ice are able to estimate the trends for H_S and T_{m02} inside the MIZ, although the errors with respect to the observations are larger here. Observed H_S actually matches the model prediction better when the measurement conditions are considered not valid, i.e. either when the altimeter measurement range was exceeded or when the ship was cruising. Measured T_{m02} matches model predictions better during the times considered valid, most likely due to the Doppler shift induced in the time series during cruising.

Both observations and models show an exponential decay in H_S through the MIZ. From the spectra and the spatial attenuation coefficients, we can conclude that WW3 underestimates the wave damping through the ice. The attenuation modeling of WW3 predicts coefficients 72-83% smaller than observations, and further tuning is therefore necessary to better estimate wave parameters in the ice. Spectra were not available from WAM-3, but the attenuation coefficients from this model match observations better and are 3-64% larger than bow measurements.

Acknowledgments

The authors are grateful to Øyvind Breivik for inviting us to the cruise and to the crew of RV Kronprins Haakon for their assistance. The Nansen Legacy project helped funding the campaign. Funding for the experiment was provided by the Research Council of Norway under the PETROMAKS2 scheme (project DOFI, Grant number 28062). The data are available from the corresponding author upon request.

References

Batrak, Y., Kourzeneva, E. and Homleid, M., 2018. Implementation of a simple thermodynamic sea ice scheme, SICE version 1.0-38h1, within the ALADIN–HIRLAM numerical weather prediction system version 38h1. *Geoscientific Model Development* **137**, 3347-3368.

Carrasco, A. and Gusdal, Y., 2014. Validation of the operational wave model wam for the years 2012 and 2013. *Section of Ocean and Ice, Norwegian Meteorological Institute*.

Christensen, K.H., Röhrs, J., Ward, B., Fer, I., Broström, G. Sætra, Ø. and Breivik, Ø., 2013. Surface wave measurements using a ship-mounted ultrasonic altimeter. *Methods in Oceanography* **6,** 1-15.

Collins III, C.O., Blomquist, B., Persson, O., Lund, B.R., Rogers, W.E., Thomson, J. Wang, J., Smith, M., Doble, M., Wadhams, P. and others, 2017. Doppler correction of wave frequency spectra measured by underway vessels. *Journal of Atmospheric and Oceanic Tech.* **34** (2)**,** 429-436.

Dee, D.P., Uppala, S.M., Simmons, A.J., Berrisford, P., Poli, P., Kobayashi, S., Andrae, U., Balmaseda, M.A., Balsamo, G., Bauer, D.P. et al., 2011. The ERA-Interim reanalysis: Configuration and performance of the data assimilation system. *Quarterly Journal of the royal meteorological society* **137** (656), 553-597.

Earle, M.D.,1996. Nondirectional and directional wave data analysis procedures. *NDBC Tech. Doc* **96**.

Fritzner, S., Graversen, R., Christensen, K.H., Rostosky, P. and Wang, K., 2019. Impact of assimilating sea ice concentration, sea ice thickness and snow depth in a coupled ocean-sea ice modelling system. *The Cryosphere* **12** (2), 491-509.

ITTC Specialist committee, 2017. Confidence intervals for significant wave height and modal period. *Tech. rep. International Towing Tank Conference*. Accessed: 2019-08-29

Løken, T.K., Rabault, J., Jensen, A., Sutherland, G., Christensen, K.H. and Müller, M., 2019. Wave measurements from ship mounted sensors in the Arctic marginal ice zone. *arXiv preprint arXiv:1911.07612*.

Marchenko, A., 2018. Wave attenuation in marginal ice zone of Arctic pack ice to the north of Spitsbergen. *Proceedings of the Twenty-eight (2018) International Ocean and Polar Engineering Conference Sapporo, Japan*, 1642-1647.

Müller, M., Y. Batrak, J. Kristiansen, M. Køltzow, G. Noer, A. Korosov, 2017 Characteristics of a Convective-Scale Weather Forecasting System for the European Arctic Monthly Weather Review **145** (12), 4771-4787

Rabault, J., Sutherland, G., Gundersen, O., Jensen, A., Marchenko, A. and Breivik, Ø., 2020. An open source, versatile, affordable waves in ice instrument for remote sensing in the polar regions. *Cold Regions Science and Technology* **170**.

Sakov, P., Counillon, F., Bertino, L., Lisæter, K.A., Oke, P.R. and Korablev, A., 2012. TOPAZ4: an ocean-sea ice data assimilation system for the North Atlantic and Arctic. *Ocean Science Discussions* **9** (2).

Squire, V.A. and Moore, S.C., 1980. Direct measurement of the attenuation of ocean waves by pack ice. *Nature* **283** (5745).

Squire, V.A, 2007. Of ocean and sea-ice revisited. *Cold Regions Science and Tech.* **49** (2), 110-113.

Sutherland, G., Rabault, J., Christensen, K.H. and Jensen, A., 2019. A two layer model for wave dissipation in sea ice. *Applied Ocean Research* **88**, 111-118.

Wadhams, P., Squire, V.A., Goodman, D.J. Cowan, A.M. and Moore, S.C., 1988. The attenuation rates of ocean waves in the marginal ice zone. *J. of Geophys. Research: Oceans* **93** (C6); 6799-6818.

Young, I.R., 1995. The determination of confidence limits associated with estimates of the spectral peak frequency. *Ocean engineering* **22** (7), 669-686.

25th IAHR International Symposium on Ice
Trondheim, 23 - 25 November 2020

Elasticity and viscosity of ice measured in the experiment on wave propagation below the ice in HSVA ice tank

Aleksey Marchenko[1], Andrea Haase[2], Atle Jensen[3], Benjamin Lishman[4], Jean Rabault[3], Karl-Ulrich Evers[5], Mark Shortt[6], Torsten Thiel[7]

[1]*The University Centre in Svalbard*
PO Box 156, N-9171 Longyearbyen, Norway
Aleksey.Marchenko@unis.no
[2]*Arctic Technology, Hamburgische Schiffbau-Versuchsanstalt GmbH,*
Hamburg Ship Model Basin, Hamburg, Germany
[3]*University of Oslo, Oslo, Norway*
[4]*London South Bank University, UK*
[5]*Solutions4arctic, Germany*
[6]*University College London, UK*
[7]*Advanced Optics Solutions GmbH, Germany*

An experiment on the propagation of flexural-gravity waves was performed in the HSVA ice tank in 2018. Physical characteristics of the water-ice system were measured in different locations in the tank during the tests, with several sensors deployed in the water, on the ice and in the air. Periodical waves with frequencies of 0.5-1.5 Hz were generated by HSVA wave maker during 10 min in each test. The phase speeds and wave damping associated with anelastic deformations of ice were analyzed in the paper. Elastic modulus of ice was calculated for each wave period from the dispersion equation of flexural gravity waves where measured values of wave frequencies and wave speeds were substituted. Viscous coefficient of ice was calculated after the analysis of wave damping. Obtained values have relatively big dispersion which can be explained by natural variability of ice properties.

1. Introduction

Sea ice coverage in the Arctic Ocean is decreasing. This leads to an increase in the probability of storms in ice-free areas (Sepp and Jaagus, 2011). Surface waves and swell penetrate from stormy regions of the ocean into ice-covered regions, and induce ice failure. The low frequency component of swell propagates across long distances under the ice without ice failure and with very little damping, causing bending oscillations of Arctic pack ice. Measurements of swell in Arctic pack ice have been made in the Beaufort Sea (Crary et al., 1952) and in the Central Arctic (Hunkins, 1962; LeSchack and Haubrich, 1964; Sytinskii and Tripol'nikov, 1964), using gravity-meters and seismometers. Recently, Mahoney et al., (2016) measured low frequency swell using short-temporal-baseline interferometric synthetic aperture radar. Hunkins (1962), Sytinskii and Tripol'nikov (1964), Gudkovich and Sytinskii (1965) and Smirnov (1996) measured waves with periods of 8-15s. These are associated with local processes in drift ice, caused by wind action on ice ridges, floe-floe interactions, etc. Physical mechanisms of wave damping in solid ice include viscous and anelastic bending deformations of ice, energy dissipation in the ice-adjacent boundary layer, and brine pumping (Marchenko and Cole, 2017; Rabault et al., 2020).

Wave actions on pack ice and land-fast ice are similar because both involve solid ice. The action of the land-fast ice on incoming waves is combined with the effects of bathymetry, shoreline and islands. These combined effects can lead to diffraction, refraction and reflection of waves, leading to waves with more complicated configurations. The amplitude of ocean swell in shallow water regions becomes higher, and the wavelength becomes shorter. This swell can also cause the breakup of land-fast ice near the shoreline. Zubov (1944) describes the breakup of landfast ice near Cape Chelyuskin and Tiksi Bay on 26th-28th January 1943 by large waves, despite the fact that the ice thickness throughout the Laptev Sea was greater than 1m. Bates and Shapiro (1980) recorded vertical displacements of ice with amplitude of several centimeters and with a period around 600s, prior to a significant ice push episode in land-fast sea ice (1.5-2m thick) near Point Barrow, Alaska. Further, over five years of near-continuous radar observations of near-shore ice motion in that area, similar oscillations were always observed to occur for several hours before the start of movement of land-fast ice or adjacent pack ice. Wave events were associated with momentum transfer from sea ice into the water during ice ridge buildup between land-fast ice and drift ice in the Beaufort Sea (Marchenko et al., 2002). The breakup of land-fast ice of 0.5m thickness, in shallow water near the shore in the Ice fjord of Spitsbergen, due to swell with period 7s and amplitude 10-15cm, is described by Marchenko et al. (2011). This work also shows that the maximum bending stresses in the ice during the breakup event were comparable to the flexural strength measured in the same place several days earlier. The action of a tsunami-wave on land fast ice (1m thick, near Tunabreen glacier in Temple Fjord, Spitsbergen) is described by Marchenko et al. (2013). The duration of the leading wave pulse was 40s, and the wave tail included waves with periods around 10s and 16s. Sutherland and Rabault (2015) investigated how swell penetrates from open water into land-fast ice (0.5m thick, in Temple Fjord, Spitsbergen), and were able to measure the attenuation of waves, with periods 4-10s, in the land-fast ice.

In 2015 and 2016, several tests on wave-ice interaction were performed at the Large Ice Model Basin (LIMB) of the Hamburg Ship Model Basin (Hamburgische Schiffbau-Versuchsanstalt, or HSVA) (Cheng et al, 2017; Tsarau et al., 2017; Hermans et al., 2018). The main goals of these tests were (1) to investigate the distribution of floe sizes when an initially continuous uniform ice sheet was broken by regular waves with prescribed characteristics, (2) to measure wave attenuation and dispersion in broken ice, and (3) to improve understanding of ice-structure interaction under wave conditions. Wave characteristics were reconstructed from the records of water pressure sensors mounted on the tank wall. Tests were performed with wave lengths around 2.5m and 6.17m. Both ice breakup (starting from the ice edge) and wave attenuation were observed in the tests with wavelength around 2.5m.

In this paper we present some results of tests performed in January 2018 in the Large Ice Model Basin (LIMB) of HSVA. The work was supported by the Hydralab+ project "Investigation of bending rheology of floating saline ice and physical mechanisms of wave damping". The aims are to observe and describe physical processes in solid ice during wave propagation; to investigate the bending rheology; and to investigate the damping of waves propagating below solid ice. These aims are realized by performing a suite of measurements during wave propagation below solid ice. The present paper is structured as follows. Section 2 provides a description of the rheological viscous-elastic model of ice and gives formulas for the calculation of elastic and viscous characteristics of ice from the experimental data. Organizing of the experiment is described in Section 3. Collected experimental data are described and estimates of elastic and viscous ice constants are given in Section 4. Results of investigations are summarized and discussed in Conclusions (Section 5).

2. Dispersion and damping of surface waves propagating below thin viscous-elastic plate
Propagation of waves with small amplitudes in water layer covered by thin sold ice plate is investigated with using of the following model including the second order equation for the velocity potential φ (Greenhill, 1887):

$$\left(\frac{\partial^2}{\partial x^2}+\frac{\partial^2}{\partial z^2}\right)\varphi=0,\ z\in(-H,0), \qquad [1]$$

and boundary conditions and the bottom and below the ice plate

$$\frac{\partial\varphi}{\partial z}=0,\ z=-H;\ \frac{\partial\eta}{\partial t}=\frac{\partial\varphi}{\partial z},\ z=0;\ \frac{\partial\varphi}{\partial t}+g\eta=\frac{1}{\rho_w}\frac{\partial^2 M_{xx}}{\partial x^2},\ z=0. \qquad [2]$$

Here η is the elevation of ice plate, M_{xx} is the bending moment in the ice plate, ρ_w and H are the water density and water depth, g is the gravity acceleration, t is the time, and x and z are the horizontal and vertical coordinates.

The bending moment and longitudinal strain are determined according classical theory of thin plates (Timoshenko and Woinowsky-Krieger, 1959)

$$M_{xx}=\int_{-h/2}^{h/2}\zeta\sigma_{xx}d\zeta,\ \varepsilon_{xx}=-\zeta\partial^2\eta/\partial x^2, \qquad [3]$$

where σ_{xx} is the longitudinal stress caused by bending deformations of the ice, ζ is the transversal coordinate perpendicular to the middle surface of the plate, and h is the plate thickness.

Rheology of small viscous-elastic deformations of ice is descried by a linear combination of the Maxwell and Voight units described by the equation (Ashton, 1986)

$$\ddot{\varepsilon}_{xx}+\frac{E_2}{\eta_2}\dot{\varepsilon}_{xx}=\frac{1}{E_1}\ddot{\sigma}_{xx}+\left(\frac{1}{\eta_1}+\frac{1}{\eta_2}+\frac{E_2}{E_1\eta_2}\right)\dot{\sigma}_{xx}+\frac{E_2}{\eta_1\eta_2}\sigma_{xx}, \qquad [4]$$

where E_1 and E_2 are the elastic moduli, and η_1 and η_2 are the coefficients of viscosity. Dots and double dots above the symbols mean the first and the second derivatives with respect to the time.

Solution of equations [1] and [2] is expressed by the formula

$$\varphi = \varphi_0 e^{i\theta} \frac{\cosh[k(z+H)]}{\cosh[kH]}, \eta = ae^{i\theta}, \varphi_0 = i\omega a/(k\tanh[kH]), \theta = kx + \omega t, \qquad [5]$$

where ω and k are the wave frequency and the wave number, and a is the wave amplitude. The wave frequency and the wave number satisfy to the dispersion equation

$$\frac{\omega^2}{k\tanh[kH]} = g + \frac{E_1 h^3 k^4}{12\rho_w} \frac{1 - iE_2/(\eta_2\omega)}{1 - \frac{iE_1}{\omega}\left(\frac{1}{\eta_1} + \frac{1}{\eta_2} + \frac{E_2}{E_1\eta_2}\right) - \frac{E_1E_2}{\omega^2\eta_1\eta_2}}. \qquad [6]$$

Wave damping is associated with the imaginary terms of equation [8]. These terms are small if wave damping occurs over a distance much greater than the wavelength. The imaginary terms are small when $E_1/\omega\eta_1 \ll 1$ and $E_2/\omega\eta_2 \ll 1$.

Now the dispersion equation can be approximated by the formulas

$$\omega = \omega_{fg}(1 + i\beta), \omega_{fg}^2 = k\tanh[kH]\left(g + \frac{E_1h^3k^4}{12\rho_w}\right), \ \beta = \frac{E_1h^3k^4}{24\rho_w\,(g + E_1h^3k^4/12\rho_w)}\frac{E_1}{\omega\mu}, \qquad [7]$$
$\mu = \eta_1\eta_2/(\eta_1 + \eta_2)$.

Spatial decay of the amplitude of a periodic wave is described by the equation (Caster, 1962)

$$\eta = \eta_0 e^{i\theta - \omega\beta c_g^{-1}x}, \qquad [8]$$

where $c_g = \partial\omega_{fg}/\partial k$ is the group velocity. Further we consider the wave damping coefficient $\alpha = \omega\beta c_g^{-1}$.

Assuming that in the leading order the phase speed is determined by the formula $c = \omega_{fg}/k$, the elastic constant E_1 is calculated with the formula

$$E_1 = 12\rho_w(c^2\coth[kH] - g)(k^4h^3)^{-1}. \qquad [9]$$

The viscous constant is calculated from formula [7] as follows

$$\mu = \frac{E_1^2k^4h^3}{24\alpha c_g\rho_w(g + E_1h^3k^4/12\rho_w)}. \qquad [10]$$

3. Organizing of experiment

During the experiment in HSVA ice tank wave maker produced periodic waves propagating below solid ice with thickness of 5 cm. The tank width is 10 m, and the tank length is 70 m. Locations of sensors used in the experiments are pointed out in the frame of reference (x, y, z), where the origin is located at the right corner at the bottom of the tank near the wave maker. The ice sheet affects actual wave heights in the tank due to damping in the ice covered region (12 m < x < 62 m) and due to reflections from the ice edge in the region with open water (0 <

x < 12 m). Wave reflection from the end of the tank can be ignored in the tests because of the small wave amplitudes at the end of the tank and the relatively small wave lengths.

Waves characteristics were registered with fiber optics strain sensors (FBGS sensors), optical system Qualisys, Ultra Sonic sensors and water pressure (WP) sensors. FBGS sensor measured longitudinal strain of the fiber with working length of 20 cm mounted on the ice surface with two brackets each of which was screwed to the ice by four screws (Fig. 1a). Bending deformations of ice influenced the change of fiber tension with the wave period. FBGS sensors were installed in the longitudinal and transversal directions of the tank around $x = 20$ m (FBGS 1-4, Fig. 1b) and $x = 50$ m (FBGS 5-8), where x is the longitudinal coordinate extended along the ice tank axis. The tank width is 10 m, and the tank length is 70 m. The ice edge was located at $x = 12$ m. Distance between sensors FBGS1 and FBGS2 was about 63 cm. Similar distance was between sensors FBGS5 and FBGS6. Air, ice and water temperature was recorded by temperature strings FBGT1 and FBGT2 with spatial resolution of 1 cm. Sampling interval of FBGS and FBGT sensors was 40 Hz.

A Qualisys™ motion capture system is used to detect the rigid body motions of the ice in all six degrees of freedom (6-DOF). The system uses four cameras, installed on the main carriage, to detect markers which are located at different positions on the model. Figure 2 shows locations of 5 markers of the system placed on the ice around $x = 28$ m by a cross: one marker was in the middle, two markers oriented in the longitudinal direction of the tank, and two markers oriented in the transversal direction of the tank. Distances between the middle marker 2 and two markers 1 and 3 oriented along the tank axis were 1.547 m and 1.344 m. Qualisys provided records of the displacements of each marker in the directions x, y, and z with sampling frequency of 200 Hz. Waves influenced mainly vertical displacements of the markers, while their horizontal positions were similar during the tests.

Eight water pressure sensors (WP) were mounted on the tank wall at 30 cm depth below the ice (Fig. 3). They were located at $x = 8$ m (1 WP sensor in open water area), $x = 24$ m (3 WP sensors with 30 cm distance between them), and $x = 56$ m (3 WP sensors with 30 cm distance between them). Measurements were performed with sampling frequency of 200 Hz. Further the results of measurements with FBGS, Qualisys and WP sensors are discussed.

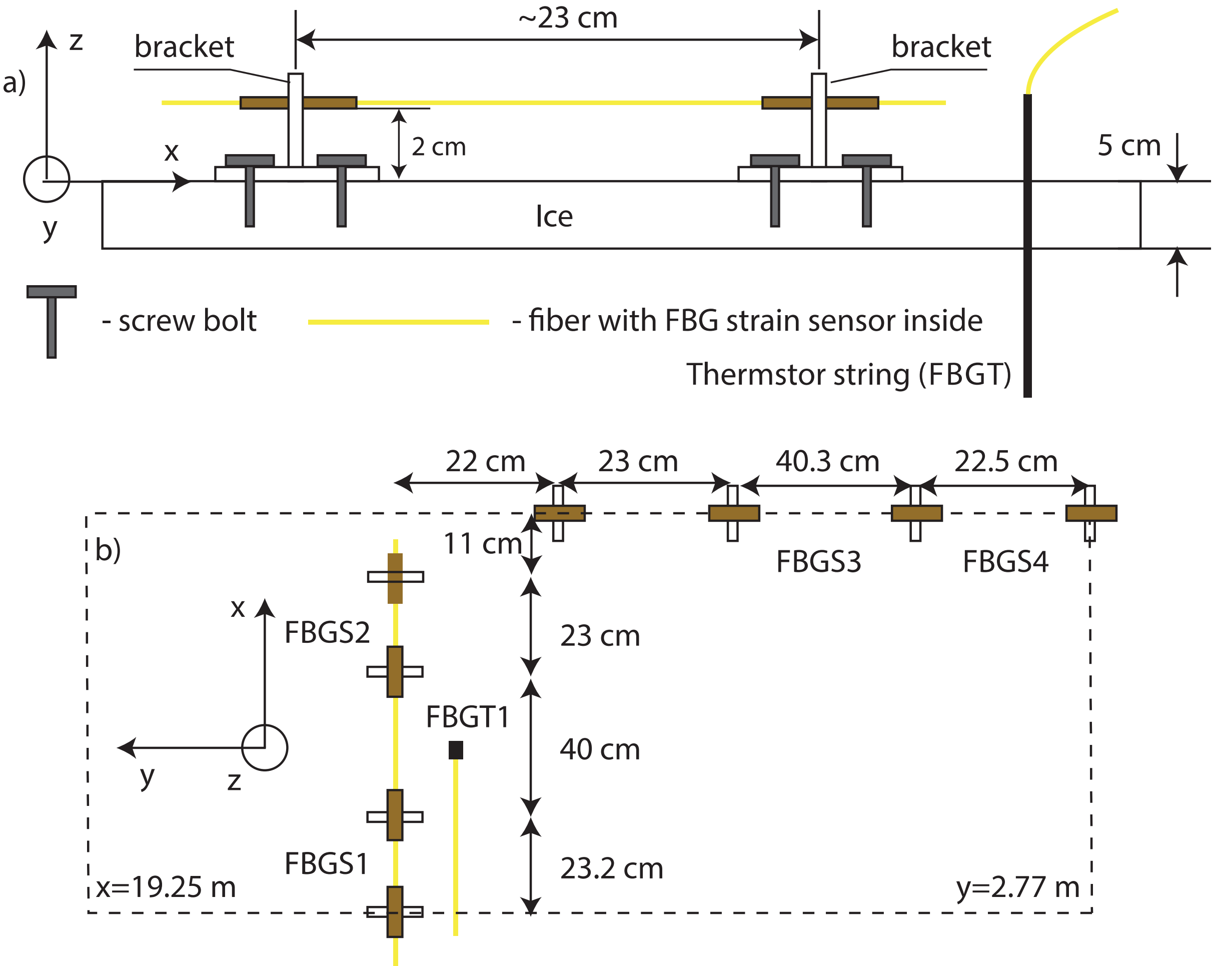

Figure 1. Mounting of the fibre optic strain sensor (FBGS) and temperature string (FBGT) on the ice (a). Spatial locations of FBGS 1-4 and FBGT sensors (b).

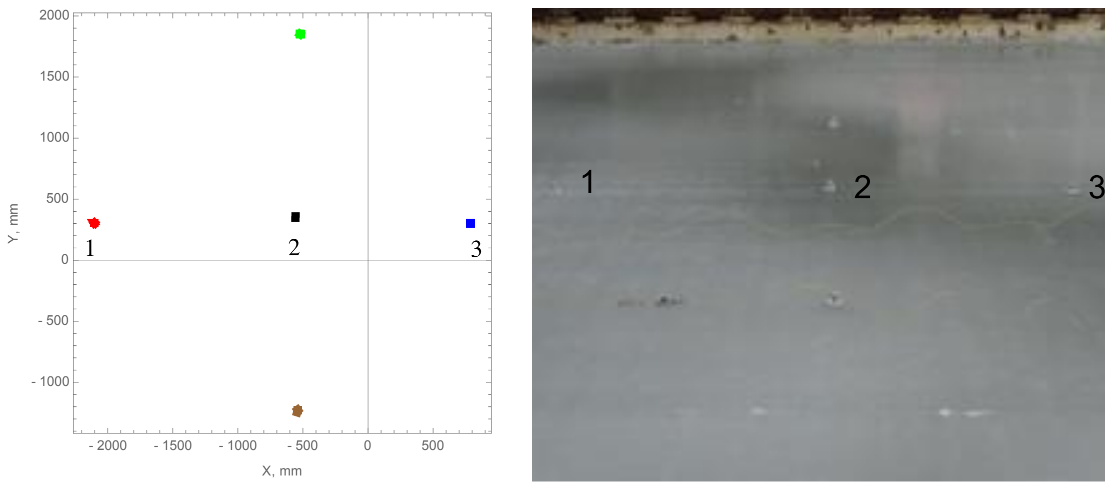

Figure 2. Locations of Qualisys markers in the local reference frame (left panel). Photographs of the markers on the ice. Markers 1, 2 and 3 are oriented along the tank axis. Marker 2 is located at $x = 28$ m.

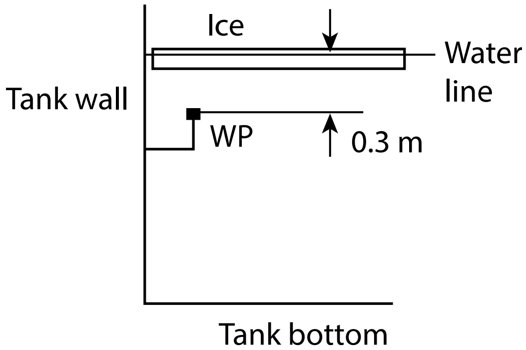

Figure 3. Mounting of the water pressure sensors at the tank wall.

4. Calculation of rheological constants

On the first stage the data were analysed to select time intervals were recorded amplitudes have relatively small dispersion. The duration of each test when the wave maker was programmed to generate periodic waves with prescribed height and frequency was 10 min. Usually the amplitudes of ice strains and vertical displacements changed in the beginning of each test during of approximately 50-100 sec, and then they became more stable. The dispersion of wave amplitudes was observed over each test, but in the beginning of the tests the amplitude dispersion was higher. All twelve tests disussed in the present paper were performed in one day of January 16. The ice temperature varied between -0.4°C and -0.45°C. The ice thickness was 5 cm. Wave height according to the wave maker setup was set to 5 mm in the first six tests and to 10 mm in the second six tests.

The analysis of phase speeds was performed for a fragment of each record with relatively small amplitude dispersion to minimize the influence of the modulations on the calculated phase speed. Time moments when strains recorded by FBGS 1-2, FBGS 5-6 reached local maxima were calculated for all performed tests. Time intervals Δt between local maxima recorded by FBGS1 and FBGS2 were used for the calculation of the phase speed of waves by the formula $c = L/\Delta t$, $L = 63$ cm. Similar calculations were performed with records of FBGS5 and FBGS6, and records of markers 1 and 2 and markers 2 and 3 of Qualisys system. Figure 4 shows phase velocities versus the wave frequency calculated with using of FBGS1-2 data (left panel) and Qualisys markers 1-2 (right panel). FBGS sensors showed a drop of the phase velocity to 2.8 m/s in two tests with wave frequency of 0.7 Hz, and an increase of the phase velocity to 3.6-3.8 m/s in two tests with wave frequency of 0.8 Hz. Qualisys data showed phase velocity in the range of 3.25-3.45 m/s in the tests with wave frequencies of 0.7 Hz and 0.8 Hz. In the most of the tests phase velocity is greater when the wave height is greater. Colored lines show analytical dependencies of the phase velocity from the wave frequency calculated with the formula $c = \omega_{fg}/k$ with three values of the elastic modulus $E_1 = 100, 150$ and 200 MPa.

Figure 5 shows elastic modulus versus the wave frequency calculated by formula (13) using the data of FBGS (left panel) and Qualisys system (right panel). Static point bending tests performed before and after the wave tests showed the values of elastic modulus of 88 MPa and 126 MPa respectively. Most of the whe wave tests showed higher values of elastic modules in the tests with bigger wave heights. The wave tests showed that the elastic modulus is around of 150 MPa or higher when the wave frequency was 0.9 Hz and 1 Hz. FBGS records showed that the elastic modulus is higher then 200 MPa in the tests with the wave frequency of 0.8 Hz, and it is of around 50 MPa in the tests with the wave frequency of 0.7 Hz. Qualisys data showed that elastic modulus varied between 110 MPa and 150 MPa in the tests with the wave frequency of 0.8 Hz, and between 130 MPa and 190 MPa in the tests with the wave frequency of 0.7 Hz.

The mean value of elastic modulus was around 120 MPa in the tests with the wave frequency of 0.5 Hz and 0.6 Hz according to FBGS data. Qualisys data showed similar values for these frequencies.

Figure 6 shows wave damping over 30 m distance according to the records of FBGS1 and FBGS5 sensors. One can see that damping of strains in stronger for higher wave frequencies. The wave damping coefficient can be calculated with the formula $\alpha = \log(a_1/a_2)/\Delta x$, where a_1 and a_2 are the strain amplitudes registered at different spatial locations, and $\Delta x = 30$ m is the distance between the locations. Then, the viscous constant is calculated from formula [10].

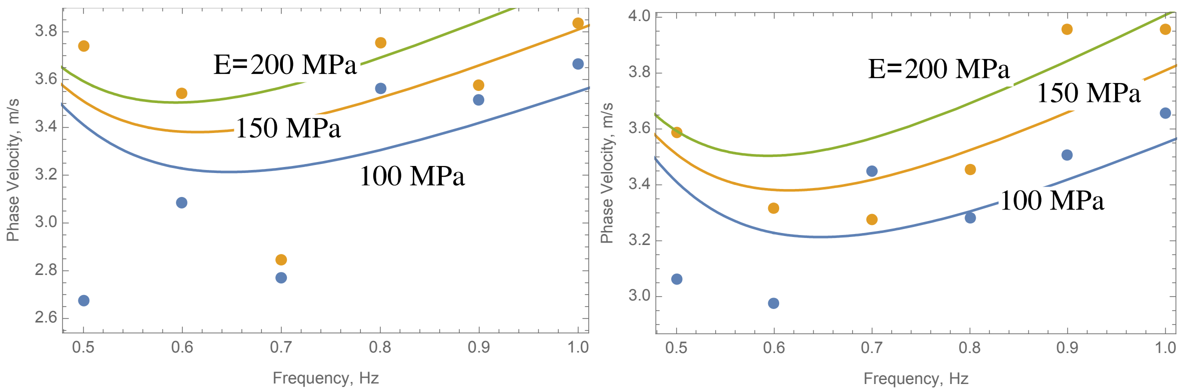

Figure 4. Phase velocities versus the wave frequency measured by FBGS sensors (left panel) and Qualisys system (right panel). Wave height according to the wave maker setup is 5 mm (blue points) and 10 mm (yellow points).

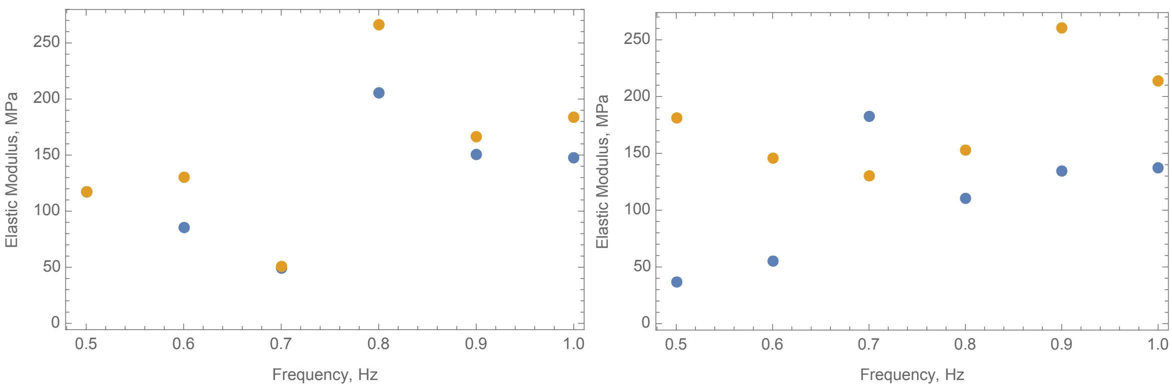

Figure 5. Elastic modulus versus the wave frequency measured by FBG strain sensors (left panel) and Qualisys system (right panel). Wave height according to the wave maker setup is 5 mm (blue points) and 10 mm (yellow points).

Figure 7 (left panel) shows the wave damping coefficient versus the wave frequency, and Fig. 7 (right panel) shows the viscous constant versus the wave frequency. The representative value of the viscous constant of ice is around $3 \cdot 10^8$ kg/(m s). Figure 8 (left panel) shows the dimensionless coefficient β specified in formula [7] versus the wave frequency. One can see that the approximation $\beta \ll 1$ is satisfied. The wave damping coefficient was calculated also from the data of WP sensors. The coefficient α was calculated using the absolute values of the discrete Fourier transforms of the WP data at the wave frequency. The values of a_1 and a_2 were equal to the discrete Fourier transforms applied to the records of WP sensors located at $x = 24$ m and $x = 56$ m. The results are shown in Fig. 8 (right panel). Left panel in Fig. 7 and left panel in Fig. 8 show that the wave damping coefficients calculated from FBGS data and WP sensors data are in the same range.

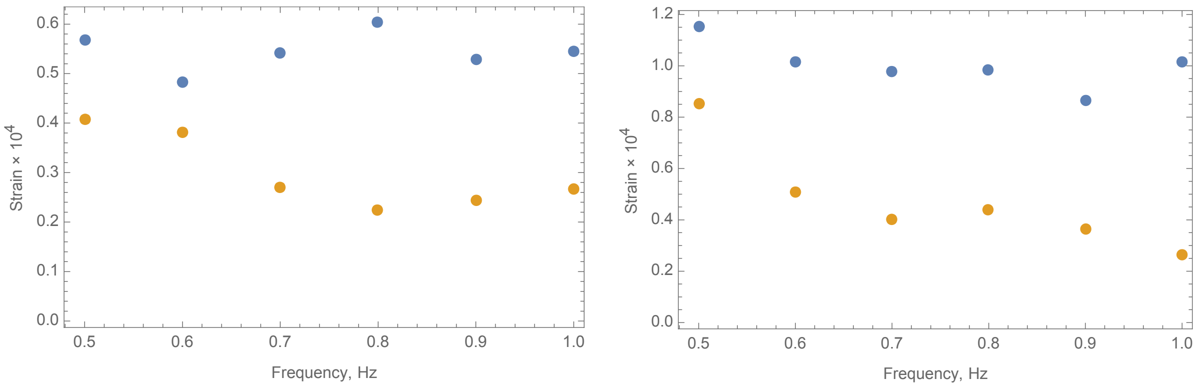

Figure 6. Longutudinal strains recorded by FBG strain sensors versus the wave frequency at the distances of 20 m (blue points) and 50 m (yellow points) from the beginning of the tank. Wave height according to the wave maker setup is 5 mm (left panel) and 10 mm (right panel).

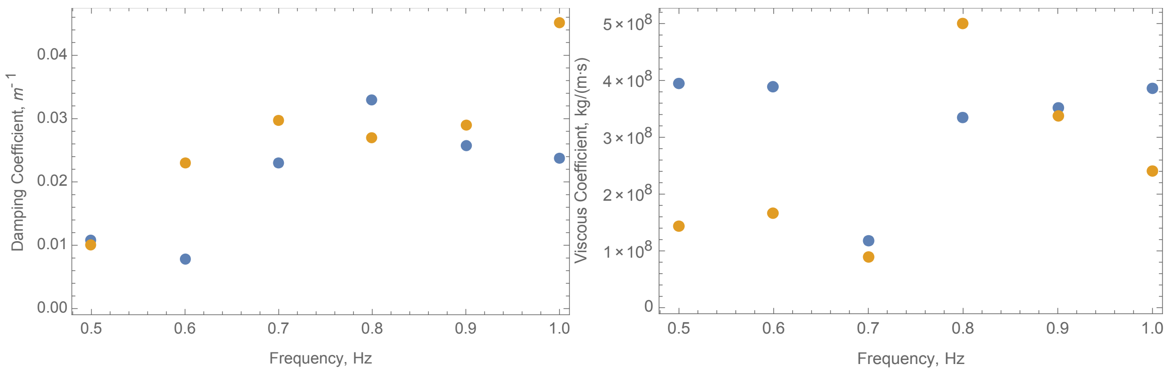

Figure 7. Damping coefficients (left panel) and viscous constant μ (right panel) versus the wave frequency reconstructed from the records of FBGS sensors. Wave height according to the wave maker setup is 5 mm (blue points) and 10 mm (yellow points).

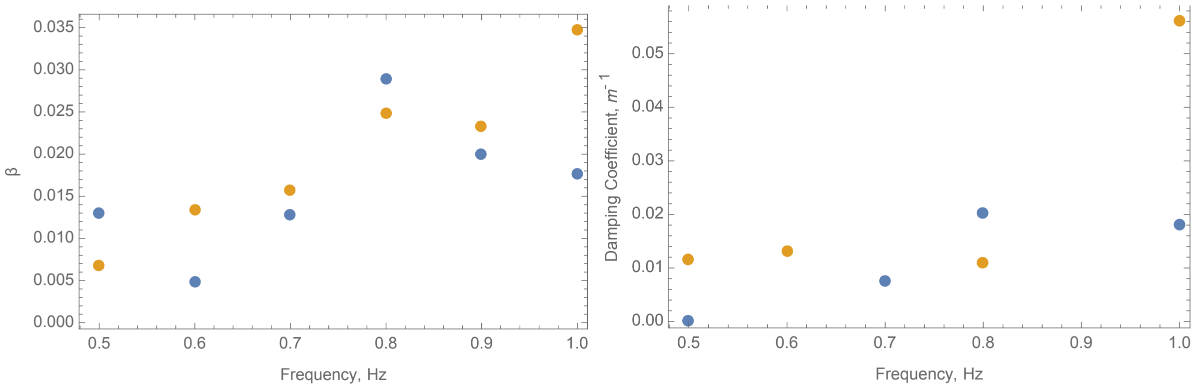

Figure 8. The dimensional coefficient β calculated with FBGS data (left panel) and the damping coefficient calculated with the records of the water pressure sensors versus the wave frequency. Wave height according to the wave maker setup is 5 mm (blue points) and 10 mm (yellow points).

5. Conclusions

Data of twelve tests on the propagation of flexural-gravity waves below solid ice with 5 cm thickness were processed and analyzed. The ice temperature during these tests was almost constant. Wave frequency changed in the tests from 0.5 Hz to 1.0 Hz with the step of 0.1 Hz. Wave maker was programmed to produce waves with amplitudes 5 mm in the first six tests, and 10 mm in the other 6 tests. Duration of each test was 10 min. Because of small wave amplitudes we assumed that creep behavior of ice is described by liear model (Schulson and Duval, 2009). Linear comination of the Mawell and Voight units was used to describe ice rheology under bending deformations.

Analysis of wave characteristics showed an increase of the elastic modulus of model ice with the wave frequency. Data of FBGS sensors showed maximal values of the elastic modulus up to 250 MPa for the waves of 0.8 Hz frequency. Qualisys records showed maximal values of the elastic modulus up to 250 MPa for the waves with the frequency of 0.9 Hz. The elastic moduli were higher in the tests with higher wave amplitudes. Minimal value of the elastic modulus of 50 MPa was obtained from FBGS data from the tests with the wave frequency of 0.7 Hz. Qualisys data showed minimal values of the elastic modulus of around 50 MPa in the tests with the wave frequincies of 0.5 Hz and 0.6 Hz. The elastic moduli measured from the tests with the wave frequencies of 0.8 Hz, 0.9 Hz and 1.0 Hz were higher than elastic moduli determined from quasi-static tests on point bending: 88 MPa (before the tests) and 126 MPa (after the tests). Nine values of the phase speed calculated from the Qualisys records in the twelve tests are located within theoretical dependencies of the phase speed of flexural-gravity waves constructed with the elastic moduli of 100 MPa and 200 MPa. FBGS data showed stronger dispersion of the phase speeds.

FBGS data showed wave damping over 30 m distance. The viscous ice constant derived from these data varied between 10^8 kg/(m s) and $5 \cdot 10^8$ kg/(m s). Tabata (1958) and Lindgren (1968) estimated the viscous coefficient in the Voight unit of 10^{13} kg/(m s) (sea ice at -10 C) and $(6 \div 43) \cdot 10^{10}$ kg/(m s) (fresh ice at -5°C ÷ -2.3°C). The damping coefficient increased from 0.01 m^{-1} to 0.05 m^{-1} when the wave frequency increased from 0.5 Hz to 1.0 Hz. Water pressure records showed similar values of the wave damping coefficient. The dimensionless coefficient β calculated with FBGS data was smaller than 0.036, i.e. the approximation $\beta \ll 1$ used to simplify the dispersion equation was satisfied in the all tests.

Acknowledgments
The work described in this publication was supported by the European Community's Horizon2020 Research and Innovation Programme through the grant to HYDRALAB+, Contract no. 654110. The work was also partially supported by the Research Council of Norway through the Petromks-2 project Dynamics of Floating Ice and IntPart project Arctic Offshore and Coastal Engineering in Changing Climate.

References

Ashton, G.D. (Editor), 1986. River and Lake Ice Engineering. Water Resources Publications. Michigan.

Bates, H., F., Shapiro, L.H., 1980. Long-period gravity waves in ice-covered sea. J. Geoph. Res., 85(2), 1095-1100.

Caster, M., 1962. A note on the relation between temporally-increasing and spatially-increasing disturbances in hydrodynamic instability. J. Fluid Mech., 14, 222-224.

Cheng, S., Tsarau, A., Li, H., Herman, A., Evers, K.-U., Shen, H., 2017. Loads on Structure and Waves in Ice (LS-WICE) Project, Part 1: Wave Attenuation and Dispersion in Broken Ice Fields. POAC17-046.

Greenhill, A.G., 1887. Wave motion in hydrodynamics. Am. J. Math., 9: 62-112.

Crary, A. P., Cotell, R. D. and Oliver, J. (1952). Geophysical studies in the Beaufort Sea, 1951. Transactions of the American Geophysical Union, Vol. 33, No. 2, p. 211–16.

Hermans, A., Evers, K.-U., Reimer, N., 2018. Floe-size distribution in laboratory ice broken by waves. The Cryosphere, 12, 685-699.

Hunkins, K., 1962. Waves in the Arctic Ocean. J. Geoph. Res., 67(6), 2477-2489.

Gudkovich, Z.M., Sytinskii, A.D., 1965. Some observation results of tidal phenomena in Arctic basin using tilt-meters. Okeanologia, 5(5), 75-85. (in Russian)

LeSchack, L.A., Haubrich, R.A., 1964. Observations of waves on an ice-covered ocean. J. Geoph. Res., 69(18), 3815-3821.

Lindgren, S., 1968. Effect of temperature increase o ice pressure. Institute of Hydraulic Engineering, Royal Institute of Technology, Stockholm.

Marchenko, A., Makshtas, A., Shapiro, L., 2002. On the excitation of shelf-edge waves due to self-induced oscillations of ice floes. In: Squire, V. A. and P. J. Langhorne (Eds), Ice in the Environment: Proc. 16th Intern. Symp. on Ice, vol. 2. Intern. Assoc. Hydraulic Eng. & Res., Dunedin, New Zealand, 301-309.

Marchenko, A., Shestov, A., Karulin, A., Morozov, E., Karulina, M., Bogorodsky, P., Muzylev, S., Onishchenko, D., Makshtas, A., 2011. Field studies of sea water and ice properties in Svalbard fjords. POAC11-148.

Marchenko, A.V., Morozov, E.G., Muzylev, S.V., 2013. Measurements of sea-ice flexural stiffness by pressure characteristics of flexural-gravity waves. Annals of Glaciology, 54(64), 51-60.

Marchenko, A., Cole, D., 2017. Three physical mechanisms of wave energy dissipation in solid ice. POAC17-086.

Rabault, J., Sutherland, G., Jensen, A., Christensen, K.H., Marchenko, A., 2019. Experiments on wave propagation in grease ice: combined wave gauges and particle image velocimetry measurements. J. Fluid Mech., 864, 876-898.

Schulson, E.M., Duval, P., 2009. Creep and fracture of ice. Cambridge University Press. 417 pp.

Sepp, M., Jaagus, J., 2011. Changes in the activity and tracks of Arctic cyclones, Clim. Change, 105(3–4), 577–595.

Smirnov, V.N., 1996. Dynamics processes in sea ice. St.-Petersburg, Gidrometeoizdat, 162 pp. (in Russian)

Sytinskii, A.D., Tripol'nikov, V.P., 1964. Some investigation results of natural oscillations of ice fields in Central Arctic. Izvestia AN SSSR. Geofizika. N4, 210-212. (in Russian)
Sutherland, G., Rabault, J., 2015. Observations of wave dispersion and attenuation in land fast ice. J. Geoph. Res. Oceans, 121, 1984-1987.

Tabata, T., 1958. Studies on visco-elastic properties of sea ice in Arctic Sea Ice, Arctic Sea Ice Conference, Easton, Maryland, 1958.

Timoshenko, S., Woinowsky-Krieger, S., 1959. Theory of plates and shells. 2nd ed., McGraw/Hill, New York, USA.

Tsarau, A., Sukhorukov, S., Herman, A., Evers, K.-U., Løset, S., 2017b. Loads on Structure and Waves in Ice (LS-WICE) project, Part 3: Ice-structure interaction under wave conditions, POAC17–068.

Zubov, N. N., 1943: Arctic Ice. Izdatel'stvo Glavsevmorputi, 360 pp. (English translation, AD 426 972, U.S. Nav. Oceanogr. Office, NTIS, 5285 Port Royal Rd., Springfield, VA 22161)

25th IAHR International Symposium on Ice
Trondheim, 23 - 25 November 2020

Development of Open Source instruments for in-situ measurements of waves in ice

J. Rabault (a, b, *), J. Voermans (c), G. Sutherland (d),
A. Jensen (b), A. Babanin (c), K. Filchuk (e)
(a): Norwegian Meteorological Institute, Oslo, Norway
(b): University of Oslo, Oslo, Norway
(*): jean.rblt@gmail.com
(c) : University of Melbourne, Melbourne, Australia
(d) : Environment and Climate Change Canada, Dorval, Canada
(e) : Arctic and Antarctic Research Institute, St. Petersburg, Russia

The interaction between surface waves and sea ice involves many complex physical phenomena such as viscous damping, wave diffraction, and nonlinear effects. The combination of these phenomena, together with considerable variability in ice configuration, ranging from viscous grease ice slicks to large icebergs through closed drift ice and landfast ice, makes it challenging to develop robust and accurate waves in ice models. In this context, a reason for the challenges modelers are facing may lie in the mismatch between the relative scarcity of waves in ice data available for testing theories, and the wide diversity of phenomena happening at sea. This lack of experimental data may be explained, at least in part, by the high cost of waves in ice instruments. Therefore, development of open source, low-cost, high-performance instrumentation may be a critical factor in helping advance this field of research. Here, we present recent developments of a new generation of open source waves in ice instruments featuring a high accuracy Inertial Motion Unit as well as GPS, on-board processing power, solar panel, and Iridium communications. Those instruments are now being used by several groups, and their simple and modular design allows them to be customized for specific needs quickly and at reduced cost. Therefore, they may be an important factor in allowing more data to be gathered in a cost-effective way, providing much-needed data to the waves in ice community. This approach is here validated by presenting recent sea ice drift and wave activity data, and comparing these results with those obtained with commercially available buoys. In addition, our design may be used as a general platform for cost-effective development of other in-situ instruments with similar requirements of low-power data logging, on-board computational power, and satellite communications.

1 Introduction

A number of complex phenomena are involved in the mechanics of wave-ice interaction. These include, to name but a few, viscous damping (Weber, 1987; Rabault et al., 2017), wave diffraction (Squire et al., 1995), and nonlinear effects in the ice (Liu & Mollo-Christensen, 1988). The complexity of these phenomena, their intrication and combination in all experimental datasets, and the (relative) similarity of their effect on waves propagating in ice (i.e., wave damping and wave-induced drift) are key factors that explain the challenges faced by the waves in ice community (Rabault, 2018; Squire, 2018; Babanin et al., 2019). This inherent complexity is unfortunate, as getting detailed understanding of wave-ice interaction is necessary for allowing safe human activities in the polar regions, as well as improving both weather and climate models. As a consequence of both the challenges presented by wave-ice interaction, and the practical interests at stake, several groups are actively working on the topic, and the field of wave-ice interaction presents a recent surge in activity (Sutherland & Rabault, 2016; Wang & Shen, 2010a,b; Zhao & Shen, 2015; Sutherland et al., 2019; Rabault et al., 2019; Marchenko et al., 2019; Voermans et al., 2019a; Squire, 2020, Voermans et. al., 2020).

A natural direction for improving both understanding of wave-ice interaction, and our modeling abilities, is to generate more data from field measurements under a variety of waves, ice, and currents conditions. There, several challenges have been encountered historically. First, the polar regions are famous for their harsh climate and strong storm events, therefore, putting demanding requirements on instruments to be deployed there. Second, instruments able to perform waves in ice measurements have traditionally been expensive black boxes, which both limits modularity and ease of use, and puts severe constraints on the number of instruments that can be deployed given constrained budgets. However, recent developments in free and open source electronics and software are opening new opportunities for bypassing the expensive, inefficient process of acquiring scientific instruments for waves in ice measurements from private companies. Such approach has notably been pioneered in a number of recent works (Rabault et al., 2017, 2020), which introduced hardware and software that through iterative evolution have reached the point where a fully operational wave in ice instrument is now available as Free Open Source Software and Hardware (FOSSH).

In this paper, we offer a short overview of the FOSSH waves in ice instruments, and we present a new dataset of both waves in ice and ice drift obtained recently in the Antarctic. During this deployment, commercial buoys were deployed at similar locations to the FOSSH instruments. Comparing the data from the FOSSH versus commercial instruments, we fully validate the wave measurements and in-situ data processing. Finally, we discuss in details the next steps to be taken for further improving the FOSSH instruments, therefore, laying the foundations for the next iteration of the design.

2 Full Open Source Software and Hardware instruments

The FOSSH instruments used in the present paper were developed over time by J. Rabault, G. Sutherland and O. Gundersen at the University of Oslo over the period 2016-2018, and used first for a real-world, full-scale deployment in September 2018 (Rabault et al., 2016, 2017, 2020). Since then, one more series has been built and deployed in the context of a collaboration between the University of Melbourne, AARI and the University of Oslo, following the design presented in Rabault et al. (2020). Two more series are awaiting deployment. The full design is released as FOSSH material, see: https://github.com/jerabaul29/LoggerWavesInIce_InSituWithIridium.

The central reason allowing the development of low-cost, easy-to-build, accurate instruments lies in the recent development and democratization of micro electronics that has been allowed by several Open Source projects. This means that one can now, with minimal previous electronics or programming knowledge, design, program, and assemble devices containing micro controllers, micro computers, GPS modules, Iridium satellite communications, and powerful sensors such as the high-accuracy VN100 Inertial Motion Unit (IMU) (Vectornav Corporation, 2016). In particular, laboratory testing (Rabault et al., 2016) and previous field deployments (Sutherland & Rabault, 2016) have confirmed the ability of the VN100 to measure waves of amplitude down to the millimeters range (see Fig. 1).

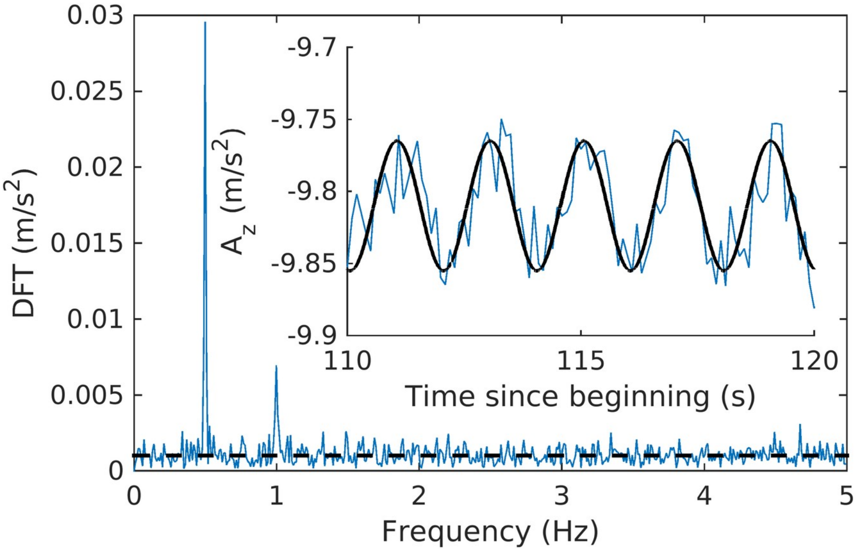

Figure 1: Test in the laboratory of the accuracy of the acceleration measurements provided by the VN100 Inertial Motion Unit. The VN100 IMU is positioned on a styrofoam floe in a wave flume, and waves of amplitude 3 mm (2 s period) are successfully recorded. Reproduced from Rabault et al. (2016). Since this work, more optimal configuration of the VN100 IMU has allowed to reduce even further the level of noise.

While more details are available in a recent paper (Rabault et al., 2020), we summarize here the main lines of the FOSSH design for the sake of completeness. The instrument features 4 main hardware components: a power control module, a micro-controller based logger, an on-board microcomputer, and a satellite communication unit (see Fig. 2). Each of these modules is built using inexpensive, off-the-shelf components. The combination of these modules constitutes a general purpose, flexible, cost-efficient platform from which instrument designs can be easily and quickly iterated.

More practically, the instruments are built based on a single Printed Circuit Board (PCB), available together with the software, on which common components are soldered (see Fig. 3). The PCBs can be inexpensively ordered from any producer, and the design choices were made so as to maximize the ease-of-assembly, so that any person with minimal soldering skill can mount all the components needed in typically no more than about 3 hours per instrument built.

To summarize, the FOSSH instruments have considerable advantages compared to commercially produced instrumentation:

Price: the cost of the FOSSH used in this study is around 2K USD. This is around 3-50 times less than commercial alternatives, which are commonly sold for 5K-100K USD. Though it should be noted that the FOSSH requires a few hours time for assembly and testing, and additional time to familiarize with the hardware and software specifications, the FOSSH is designed from commonly used software and off-the-shelf hardware thereby limiting the specific expertise required (particularly for academics) to build and work with the instrument. In addition, FOSSH are more flexible, and can be easily adapted to specific fieldwork needs.

Flexibility: as the complete instrument design is open-source, all aspects of the instrument can be altered to facilitate owner and project needs. Commercially-built instruments will always have a certain degree of hidden software and perhaps hardware that limits the full understanding of the instrument functioning. Both the software and hardware of the FOSSH are fully customizable, allowing changes in data recording, transmission and processing algorithms. This also allows accommodation of additional measurements, including temperature, wind speed, atmospheric pressure, by performing minor updates to the hardware and software.

Technology type: the FOSSH is currently based around a leading high-performance Inertial Motion Unit (IMU). Though this is the most expensive component of the FOSSH by far, it allows for wave motion accuracies down to a few millimeters.

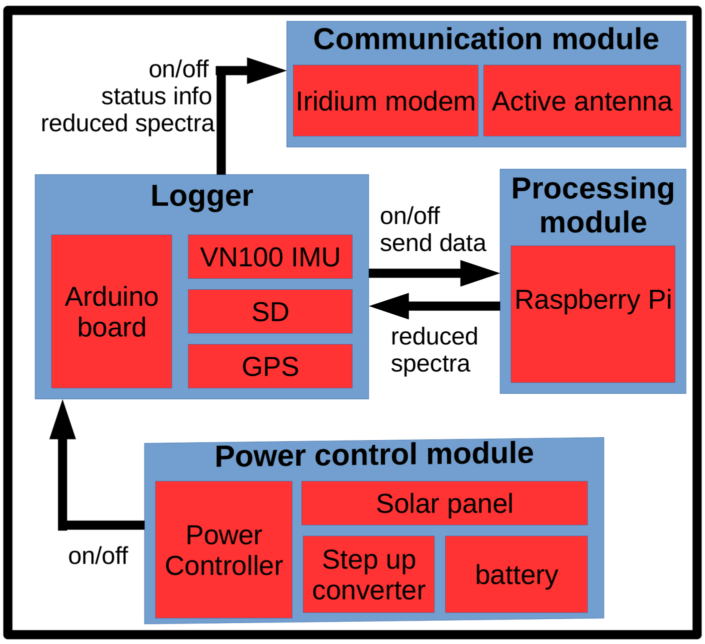

Figure 2: The instruments are built following a modular design. The different modules can be combined in a flexible way to implement a wide variety of in-situ data acquisition, data processing, and satellite communications. Reproduced from Rabault et al. (2020).

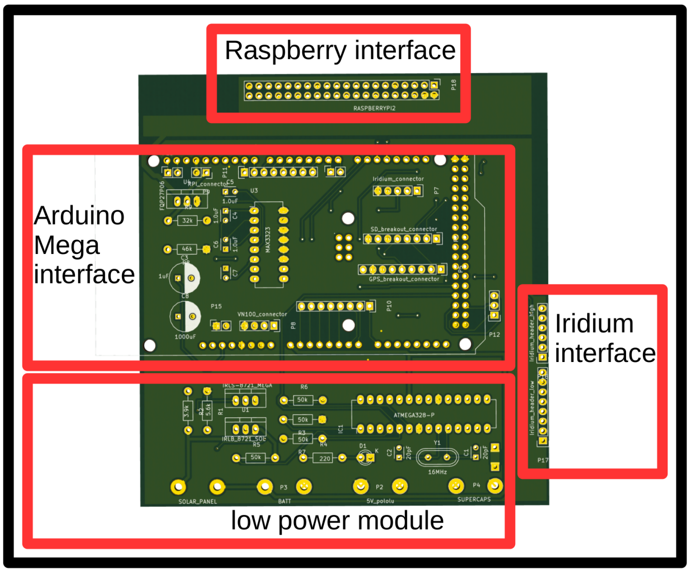

Figure 3: The instruments are organized around a single main PCB design, which is part of the fully released FOSSH material. Reproduced from Rabault et al. (2020).

The first real-world deployment of the instruments took place in 2018 (described by Rabault et al., 2020), and allowed to both fully test the instruments at sea, validate the results against a measurement of waves using a pressure sensor (see Fig. 4), and collect a first dataset that is currently under further analysis.

Following this first deployment, new series of instruments were built as previously named, and we will here present recent data from a measurement campaign during which two Sofar Spotter wave buoys were deployed close to FOSSH instruments in the Antarctic. The Spotter buoys are commercial wave buoys (https://www.sofarocean.com/ products/spotter), and have been extensively tested against the industry-standard Waverider buoys (Raghukumar et al., 2019) and NDBC weather stations (Voermans et al., 2019b). Though the Spotter wave buoys were initially deployed with the idea to measure ocean waves after the sea ice on which they were deployed would have disappeared, they provide a valuable opportunity here to further validate the performance of the FOSSH instruments.

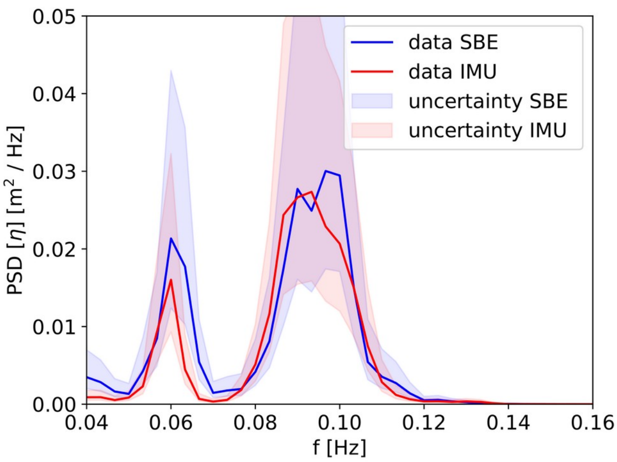

Figure 4: Validation of the open source instruments (relying on a VN100 IMU) against pressure sensor measurements of waves (SBE spectra). Reproduced from Rabault et al. (2020).

3 Recent deployment in the Antarctic, and validation against the Spotter buoy

Data from the Antarctic sea ice cover were obtained during the second measurement campaign using FOSSH buoys (the first campaign took place in September 2018 in the Arctic and was reported in Rabault et al. (2020)). The deployment took place in December 2019 on landfast ice in Antarctica (approximate deployment location: 69.25S, 76E). This deployment included two FOSSH instruments, as well as two Spotter wave buoys. While initially the ice remained still and attached to land, around one month after deployment the ice started breaking (see Fig. 5). The ice breakup happened close to the location of the instruments (both FOSSH and Spotter buoys). As a result, the instruments got separated and the trajectories of the different instruments diverged over time. After a few weeks, one FOSSH instrument (22-01) and then the two Spotter buoys (03-02) stopped transmitting, probably due to the combination of ice breakup and incoming waves crushing the instruments housings.

To confirm the hypothesis that the termination of transmission of at least one of the FOSSH instruments was due to crushing by the ice, battery levels of the FOSSH devices can provide guidance. Similar analysis over a deployment that lasted for about 2.5 weeks until loosing contact indicated that no significant battery level drop could be observed (Rabault et al., 2020). Here, we observe the same phenomenon, i.e. the batteries remained fully charged due to favorable weather conditions providing near-continuous solar panel input. It should be noted that an unknown minor technical issue created some spread in the battery voltage reported. We believe that this is a benign artifact probably due to some low level issue on the firmware side, and we are working towards resolving it. Nevertheless, the long deployment duration confirms that the solar panel is sufficiently powerful to allow for unlimited operation when solar input is provided.

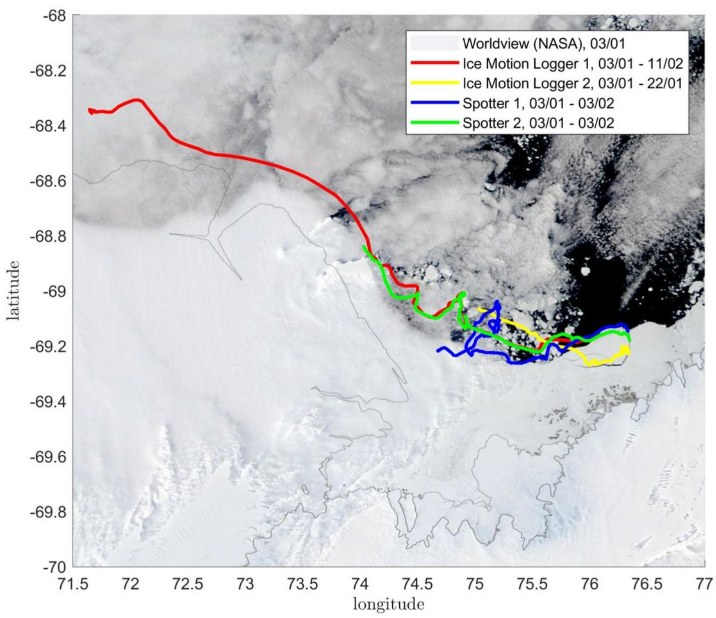

Figure 5: Illustration of the trajectories of the different instruments (satellite imagery on 03-01, Worldview NASA). Deployment took place on what was initially landfast ice. Following incoming waves, the ice broke up after around 1 month of deployment, and the instruments started to drift. As of the middle of February 2020, i.e. after around 2 months of deployment, only a single FOSSH instrument was still active. It is believed that the other instruments were crushed due to the combination of ice breakup and incoming waves.

As visible in Fig. 5, the trajectories of one of the FOSSH instruments and one of the spotter buoys remained close for an extended amount of time. Over this period of time, several significant wave events took place, which were recorded by both instruments. A summary of these measurements is provided in Fig. 6. As visible there, the time series for the significant wave height indicate excellent agreement between both instruments. Similar quantitative agreement is observed on the frequency spectra, as is also visible on Fig. 6. While minor differences are observed at the high-frequency end of the spectra, the energy in this range is considerably below the wave energy levels that can be reasonably resolved at these frequencies by these instruments. In addition, this difference may be explained by both artifacts in the processing used (for instance, the FOSSH instruments rely on a well-tested taper function for windowing when taking Fourier transform, and uses the Welch method), and the different sensors used to measure the motion.

4 Conclusion

In recent years, Fully Open Source Software and Hardware (FOSSH) instruments are becoming a promising avenue for gathering critical data in challenging remote environments. This, in turn, holds many promises for the waves in ice community. In this proceedings, we presented a summary of the technical results obtained so far with one such family of FOSSH instruments. They are shown to perform reliably in demanding polar conditions, and to compare satisfactorily with commercially available devices. Therefore, the barrier to entry for new actors who would want to participate in monitoring of ice drift, breakup, as well as wave propagation in the ice, is drastically reduced, and established groups can get access to new low-cost alternatives to traditional instrumentation solutions.

While several successes were obtained, this is by no means an end to the gradual improvements of our FOSSH instruments design. As new electronics are regularly released, we expect to be able to further improve the design so as to continue simplifying the assembly of the instruments, reduce their cost, and improve even further both power efficiency and accuracy of the measurements. We hope that these efforts may inspire new groups to join this collaborative project and contribute with their technical abilities. In the near future, we will be working towards incorporating additional measurements such as temperature, pressure, and hygrometry, in a standardised way, and we will as well investigate the possibility to monitor ice breakup by including acoustic sensors.

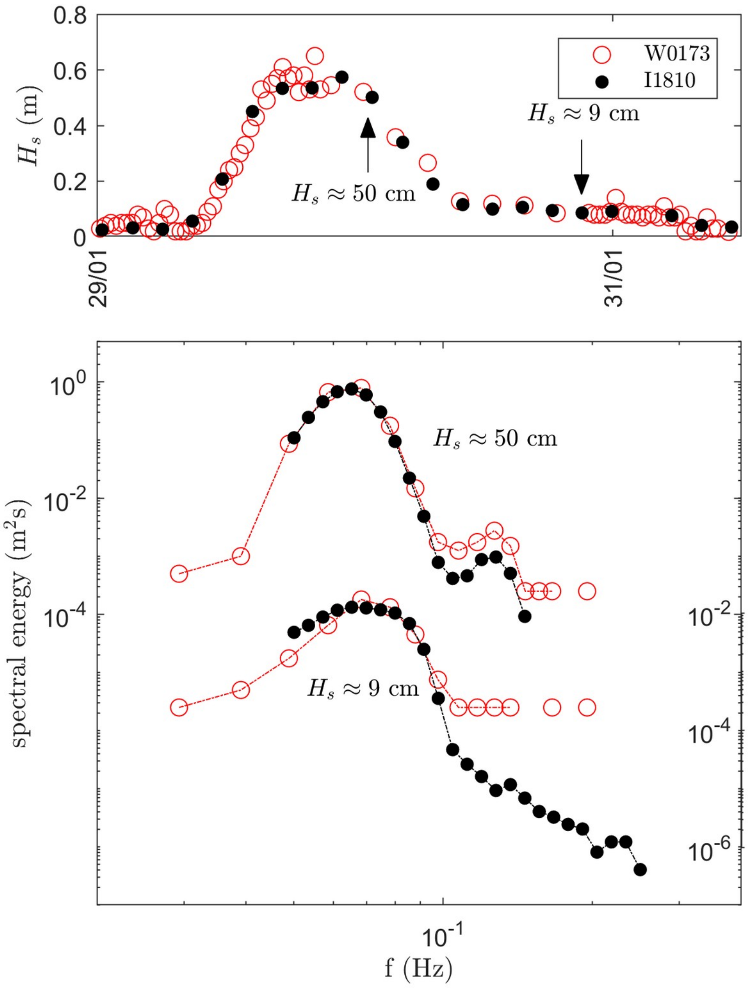

Figure 6: Comparison between the wave measurements obtained from the Spotter wave buoy (W0173) and the FOSSH waves in ice instrument (I810) that were closest to each other (see trajectories in Fig. 5). Top: comparison of the Significant Wave Height (Hs) reported by the two instruments over the period of time 29-31 January 2020. Both instruments report very similar results. Bottom: wave spectra reported at two different times (corresponding to Hs = 50 cm and Hs=9 cm, respectively, as highlighted on the top panel). The location and height of the peaks are very similar for both instruments. The second pair of spectra (Hs=9cm) has been slightly shifted vertically for ease of representation, and should be interpreted with the Y-label on the right edge of the figure.

References

Babanin, A., V, Rogers, W., De Camargo, R. , Doble , M., Durrant, T., Filchuk, K., Ewans, K., Hemer , M., Janssen, T., Kelly Gerreyn, B. & others 2019. Waves and swells in high wind and extreme fetches, measurements in the southern ocean. Frontiers in Marine Science 6, 361.

Liu , A K. & Mollo-Christensen, E. 1988. Wave propagation in a solid ice pack. Journal of Physical Oceanography 18 (11), 1702 – 1712.

Marchenko , A., Wadhams , P., Collins , C., Rabault , J. & Chumakov , M. 2019 Wave-ice interaction in the north-west barents sea. Applied Ocean Research 90, 101861.

Rabault , J., 2018 An investigation into the interaction between waves and ice. PhD Thesis, University of Oslo.

Rabault, J., Sutherland, G., Gundersen, O. & Jeansen, A., 2017. Measurements of wave damping by a grease ice slick in svalbard using off-the-shelf sensors and open-source electronics. Journal of Glaciology p. 1–10.

Rabault, J., Sutherland, G., Gundersen, O., Jensen, A., Marchenko , A. & Breivik, Ø., 2020. An open source, versatile, affordable waves in ice instrument for scientific measurements in the polar regions. Cold Regions Science and Technology 170, 102955.

Rabault, J. , Sutherland, G., Jensen, A. , Christensen , K. H. & Marchenko , A., 2019. Experiments on wave propagation in grease ice: combined wave gauges and particle image velocimetry measurements. Journal of Fluid Mechanics 864, 876–898.

Rabault, J., Sutherland, G., Ward, B., Christensen, K. H., Halsne , T. & Jensen, A. 2016. Measurements of waves in landfast ice using inertial motion units. IEEE Transactions on Geoscience and Remote Sensing 54 (11), 6399–6408.

Raghukumar, K. , Chang, G., Spada, F., Jones, C., Janssen, T. & Gans, A. 2019, Performance characteristics of “spotter,” a newly developed real-time wave measurement buoy. Journal of Atmospheric and Oceanic Technology 36 (6), 1127–1141, arXiv: https://doi.org/10.1175/JTECH-D-18-0151.1.

Squire, V.A., Dugan, J. P., Wadhams, P., Rottier, P. J. & Liu, K., A. 1995. Of ocean waves and sea-ice. Annual Review of Fluid Mechanics 27, 115 – 168.

Squire, V. A. 2018. A fresh look at how ocean waves and sea ice interact. Phil. Trans. R. Soc. A 376 (2129), 20170342.

Squire, V. A. 2020. Ocean wave interactions with sea ice: A reappraisal. Annual Review of Fluid Mechanics 52 (1), 37–60, arXiv: https://doi.org/10.1146/annurev-fluid-010719-060301.

Sutherland, G. & Rabault, J. 2016. Observations of wave dispersion and attenuation in landfast ice. Journal of Geophysical Research: Oceans 121 (3), 1984–1997.

Sutherland, G. , Rabault, J., Christensen , K. H. & Jensen , A., 2019. A two layer model for wave dissipation in sea ice. Applied Ocean Research 88, 111 – 118.

Vectornav Corporation 2016 VN100 specification datasheet. http://www.vectornav.com/products/n100-rugged/specifications, accessed 20/04/16.

Voermans, JJ, Babanin, AV, Thomson, J, Smith, MM & Shen, HH, 2019a. Wave attenuation by sea ice turbulence. Geophysical Research Letters 46 (12), 6796–6803.

Voermans, JJ, Smith, PB, Janssen, TT & Babanin, AV, 2019b. Estimating wind speed and direction using wave spectra. Journal of Geophysical Research: Oceans p. e2019JC015717.

Voermans, JJ, Rabault, J, Filchuk, K, Ryzhov, I, Heil, P, Marchenko, A, Collins, C, Dabboor, M, Sutherland, G, Babanin, A, 2020. Experimental evidence for a universal threshold characterizing wave-induced sea ice break-up, The Cryosphere.

Wang, R. & Shen, H. H. 2010A, Experimental study on surface wave propagating through a grease–pancake ice mixture. Cold Regions Science and Technology 61 (2–3), 90 – 96.

Wang, R. & Shen, H. H. 2010b. Gravity waves propagating into an ice-covered ocean: A viscoelastic model. Journal of Geophysical Research: Oceans 115 (C6).

Weber, JE, 1987. Wave attenuation and wave drift in the marginal ice zone. Journal of Physical Oceanography 17 (12), 2351–2361.

Zhao, X. & Shen, H. H. 2015 Wave propagation in frazil / pancake, pancake, and fragmented ice covers. Cold Regions Science and Technology 113, 71 – 80.

25th IAHR International Symposium on Ice
Trondheim, June 14 to 18, 2020

Modeling new ice formation under the influence of ocean waves

Hayley H. Shen[1], Stephen F. Ackley[2], Hung Tao Shen[1], Che Yue[1]
[1]Civil & Environmental Engineering Department, Clarkson University, Potsdam NY 13699 USA
[2]NASA Center for Advanced Meas. in Extreme Environments (CAMEE), Univ. Texas at San Antonio, San Antonio TX 78249 USA

ABSTRACT

In sea ice modeling the focus has been on the basin to climate scale processes. New ice formation has received less attention. Field observations in the Southern Ocean consistently reported the ubiquity of pancake ice in the marginal ice zone. The presence of this type of ice has become prevalent in the Arctic Ocean during the fall-winter season. Field observations have also shown that new ice is very effective in damping high frequency ocean waves. Such findings have motivated more refined sea ice models. In this paper, we briefly review the mathematical framework for the new ice formation in the sea. We then propose an algorithm to expand existing sea ice models to include new ice types in the presence of waves.

1. Introduction

Both river ice and sea ice initiate from frazil crystals in the turbulent water body. The early stages of frazil particles are small and disk shaped. As their concentration increases, neighboring discoids may clump together to form flocs. Once surfaced, the colder air and progressively increasing concentration from frazil accumulation allow the neighboring flocs to adhere and form ice pans or pancake ice. The size of the floc and ice pans depends on the level of agitation. In calm waters, ice crystals are not entrained into the water body. Instead, they form a thin smooth layer on the water surface called nilas. The rate of growth of frazil crystals, flocs, and surface pans is not known.

The initial formation of a sea ice cover is affected by several hydrodynamic processes: the Langmuir circulation (Leibovich, 1983) and the existence of ocean waves. At the early formation stage, long patches of grease ice (concentrated slurry of frazil) form in the convergence zone of the Langmuir circulation. With enhanced concentration and thickness at the leading edge of these patches, tiny pancakes may form. This highly heterogeneous formation of initial ice cover gradually evolves into larger and larger spans of relatively uniform grease ice cover as the ice production grows. With the presence of waves, the grease ice cover often evolves into pancakes. On the other hand, in calm waters at open seas or within leads of pack ice, thin films of nilas form. Nilas are easily deformed due to slight wind and wave stress to form finger rafting patterns. Further destruction creates more fragmented pieces.

While the ocean circulation is an important hydrodynamic process, its effect on the relatively much more dynamic changes on the surface is small. On the other hand, waves produce oscillatory flow with periods on the order of seconds, thus have much more impact on the morphology of the surface layer. With the presence of waves, frazil ice may progress from grease ice to pancake ice to the final solid cover. Under calm conditions, a thin smooth ice cover forms. In rough seas, such as in polynyas, a thick layer of grease ice may persist (for a recent study, see de Pace et al. 2019). Nilas, grease, and pancake ice are routinely observed in field experiments.

Grease and pancake ice are ubiquitous in the Southern Ocean, and are becoming more prevalent in the Arctic marginal ice zone (MIZ). Systematic studies of their evolution from the frazil stage are rare, let alone incorporating their formation into predictive ice models. At present, the most commonly used sea ice model is the Los Alamos sea ice model CICE (https://github.com/CICE-Consortium/CICE/wiki). In this model, an ice cover is characterized by its concentration and thickness. The thickness is further grouped into a number of categories. Formation of new ice from open water, i.e. frazil ice, is considered to instantly transition to the thinnest ice category (CICE documentation, 2019). To what extent such simplification may affect the largescale ice concentration and thickness, as well as ocean and atmosphere circulations are still under investigation (Notz, 2012, Shi and Lohmann, 2017).

The decline of Arctic ice has increased the wave intensity. How may the formation of new ice affect wave propagation? Rogers et al. (2016) used field data in the Arctic MIZ and the global wave model WAVEWATCHIII® (WW3) (Tolman et al., 2014) to analyze the spectral attenuation of waves through grease/pancake ice covers. Their analysis included ice damping effects where the spectral attenuation rate was inversely determined from the field data. They found that the attenuation rate, especially for the high frequency wave components (>0.2 Hz), was sensitive to the type of the newly formed ice cover, with pancake ice more effective in damping high frequency waves than grease ice.

In the present study, we first describe several key studies that have guided our conceptual model. These studies address the following processes: the initial frazil ice distribution, the evolution into small pancakes, and with the addition of waves, the criteria for the new ice to evolve through the initial grease, pancake, or nilas to finally become part of the solid ice cover. We then conclude with an algorithm which incorporates these processes for new ice formation in the ocean under wave actions. Actual implementation and testing of this algorithm are left for future work.

2. Formation and evolution of new ice

Frazil crystals first form in the supercooled water at the open water surface. In the quiescent zone these tiny particles quickly cover the water surface to form nilas. Thickening of this type of ice continues through congelation growth. In turbulent waters, frazil particles are immediately entrained into the water body to form the suspended ice. Supercooling can deepen into the water body, to allow in-situ frazil formation and growth as well. As the frazil particles become more numerous, they adhere to each other to form increasingly larger flocs so that eventually buoyancy overcomes turbulence entrainment to keep the flocs on the surface. Over time, supercooling in the water body is consumed by latent heat from frazil production. Meanwhile, surface ice layer continues to freeze to form a solid ice layer over the slushy frazil layer.

Because of the complexity of the frazil formation processes, and the inter-dependency among the processes, to implement the formation of new ice into a river model was achieved through simplifications (Shen et al. 1995, Shen 2010). To include processes of new ice formation in sea ice models, two lessons can be learned from the river ice model. First, simplifying the new ice into average properties of a few key categories appears to be an acceptable way to build a practical model. Second, even after simplifications there is a large number of parameters. Nevertheless, experience from the river ice modeling has shown that such models, as long as major mechanisms are properly considered with carefully chosen parameterization, may produce useful tools for engineering applications.

In the ocean, the initial formation of ice from frazil accumulation has been discussed by several theoretical papers (Daly 1994, and Omstedt 1985). Following the same basic processes, but adding the hydrodynamic forcing due to wind generated surface circulation, Matshumura and Ohshima (2015) expanded these early studies. In their study, they considered the basic physics of growth and melt, buoyancy and turbulence entrainment to quantify the development of frazil and grease ice in wind driven turbulent flows, while ignored details of nucleation and flocculation. Instead of using flocculation, they defined the transition from frazil to grease ice by the depth-weighted total frazil accumulation over depth. When this accumulation was greater than 0.1 m the frazil layer was considered to become grease ice. They applied a Lagrangian parcel method to track the three-dimensional distribution of frazil concentration in a fixed domain with periodic boundary conditions. Smedsrud and Martin (2015) built a sea ice model considering the formation of new ice with simplifications analogous to river ice, but without following the suspended frazil. They ignored the distinction between frazil and grease ice and separated the surface layer to grease (unsolidified) and pancake ice (solidified) layers. From open water, net heat loss due to all sources including wind and solar radiation created frazil ice. The frazil ice formed inside the water body was assumed to instantly float to the surface to form a layer of grease ice. The volume per surface area of grease ice produced, V_g, was determined from the rate of frazil production in open water due to net loss of heat. Following the theory developed in Smedsrud (2011), the thickness of the grease ice layer was determined by the wind and the current stresses, $h_g = \left(\frac{4}{9}\frac{V_g L}{K_r}|\vec{\tau}_a + \vec{\tau}_w|\right)^{1/3}$, where L was the grid length and K_r was the packing resistance of a grease ice pile. They acknowledged that such formulation was grid-resolution-dependent and thus further improvement was needed. The area concentration of this grease ice layer was then $a_g = V_g/h_g$. This layer of grease ice could melt quickly if in the following time steps the net heat flux into the ice layer from atmosphere and ocean was positive. Based on a laboratory observation (de la Rosa et al. 2011), the surface temperature and heat flux over grease ice were assumed to be the same as over open water. The grease ice solidified into pancake ice in time as described by $V_i = V_i(t_0) + V_g(t_0)\left(1 - e^{-\frac{t}{T_s}}\right)$. From a laboratory observation (de la Rosa et al. 2011), $T_s = 1.44$ days was proposed. This solid ice at first took the form of pancake ice. This newly formed pancake ice might either be tracked as a new ice thickness category, or be merged into the thinnest ice category of the existing ice cover at the end of each time step. Smedsrud and Martin (2015) found that, among other things, that the total ice volume in the Arctic Ocean was not affected by this refined model from the standard CICE type of ice categories, but the regional variability produced by the new model in the MIZ was much more pronounced than the standard model.

In the algorithm we will propose, we plan to build on the findings and concepts of the two key papers: Matsumura and Ohshima (2015) and Smedsrud and Martin (2015) with some modification. We will also introduce the wave field as another variable in the model, in the attempt to determine not just the concentration and thickness of the new ice, but also its type.

3. Ice morphology under the influence of waves

We now describe our approach to incorporate the wave effects, and how to couple the updated ice models with the existing wave models. Our proposition is that waves mainly alter the morphology of the ice cover. Their potential effects on heat fluxes through enhanced turbulence is neglected. Furthermore, in the field waves are never monochromatic. Instead, a spectrum of many components exists. As a simplification, our model will be built on the dominant wave component, hence can use the theoretical results from monochromatic wave fields. We may extend the models to consider wave spectra in future modifications by including effects from each component.

We first recap a conceptual theory behind the ice morphology under the influence of wave actions here (Shen et al. 2001). Because of the exponential downward decay of wave action in the water body, the most important wave effects are on the surface ice layer. Grease ice on the surface consisting of a dense layer of frazil crystals congeal to form progressively larger pancakes until either the wave bending or the differential velocity between neighboring pancakes prevent further growth. The pancakes then reach their maximum size dictated by the wave field and the freezing condition.

From this conceptual model, the limiting pancake diameter was determined from considering two opposing mechanisms: adhesion and breaking (Shen et al. 2004). One connects two objects together and the other disconnects them. The balance of the two determines the size of the pancakes. The adhesion comes from the freezing bonds between two ice elements (frazil crystals, flocs of many crystals, or pancakes). The breaking can be due to bending or tensile failure, each gives a different prediction of the relation between the pancake size and the wave field:

$$D_b \approx \frac{C_b \lambda^2}{2\pi^2 EA}\,;\, D_t \approx \sqrt{\frac{2C_t\lambda^2}{\pi^3 \rho_{ice} g A}} \qquad \textbf{[1]}$$

where "*b*" denotes the bending failure case and "*t*" the tensile failure case. The physical parameters involved in the above are: wavelength λ, wave amplitude A, Young's modulus E, gravitational acceleration g, ice density ρ_{ice}. Parameters C_b and C_t are both in the units of N/m^2, representing the cumulative strength of the freezing bonding between two ice elements against bending and tension, respectively. These two parameters should be related to temperature and salinity, with a decreasing trend as temperature or salinity increase.

We note that in Eq. [1] both cases are limited by $(1/wave\ curvature)^n$, where the power n is either 1 or 1/2. Statistical analysis of the data collected from laboratory studies showed that D versus λ^2/A relation was much closer to the power of 1/2 than 1 when growing pancakes from open water (Shen et al. 2004). Hence, it was suggested that tensile failure might be the controlling mechanism if the pancakes were formed strictly from an open water condition through lateral growth. In a recent study, Roach et al. (2018) analyzed field data collected from a camera mounted on top of a wave buoy. The pancake size and the local wave field were obtained from observations made in a 5-hr period. They showed that D had similar correlation with respect to $\sqrt{\lambda^2/A}$ and λ^2/A, where the wavelength and amplitude were associated with the peak wave. No further analysis on the confidence interval of the power law fit to their data. From physical considerations, bending failure presumes a pre-existing ice sheet or large floes on the order of wavelength or more, while tensile failure envisions a field of dispersed small elements that could freeze together. The latter appears to be more convincing for the new ice formed in open water under continued agitation. However, we also acknowledge the formation of pancake ice from nilas or pre-existing ice floes broken up by increasing wave intensity. In this case, bending failure would control the pancake ice that would form once the wave intensity increases. Hence, in field conditions, pancake ice size is history dependent. It is probably controlled by a combination of both tensile and bending failure. These considerations will be included in the algorithm to be proposed. One more new ice type not mentioned above is shuga ice, which describes flocs of ice crystals that are nearly spherical in shape. This type of ice is formed on the water surface under very rough seas. Shuga ice will be considered as an extreme case of grease ice.

4. Criteria for the Three Types of New Ice

The above summarizes the conceptual model for the limiting size of the pancakes that would form under the wave action. Laboratory experiments were conducted to test this theory (Shen et al., 2004). These experiments were designed to measure the pancake diameter formed under a given monochromatic wave field. The results supported the tensile controlled concept for the pancake size. An unintended result of these experiments was that under large waves the ice cover remained as grease ice. The critical condition that determined whether pancake ice could form was not investigated at the time. We now discuss how such conditions may be established.

To determine the criteria for whether pancakes could form, or instead one of the other two types of new ice, nilas or grease, would be produced, we first need to define what qualifies as a pancake. Consider a given wave with fixed amplitude and wavelength. If the freezing bonding between two pancakes with diameters equal to the wavelength is sufficient to survive the wave loading, then these pancakes can grow indefinitely because the loading experience with any larger size would be repetitive. Thus, if the maximum D calculated from either criteria of Eq. [1] equals to λ, the wave field would produce a continuous sheet, i.e. nilas. In the other extreme, the growth of pancakes is a continuous process starting from frazil discoids. The minimum pancake size is thus a subjective concept. From laboratory observations, when the ice elements become larger than a couple of centimeters, visually the surface texture begins to show the characteristic circular shape of pancakes with a thicker center and slightly raised edges. (Incidentally, the maximum length of capillary waves is 2 cm.) Thus from pure observational evidence, we choose the lower limit D_{min}= 2 cm. From these considerations, we can determine the criteria between nilas, grease, and pancake ice.

In dimensionless forms, the relationships between pancake size D and the controlling parameters C_b, C_t and A, λ are:

$$\frac{D_b}{\lambda} \approx \frac{C_b \lambda}{2\pi^2 EA}, \frac{D_t}{\lambda} \approx \sqrt{\frac{2C_t}{\pi^3 \rho_{ice} g A}} \qquad [2]$$

For a given wave field with the dominant wave described by A, λ, and the surface temperature and salinity condition, we define a dimensionless number δ to determine which ice type should form. For bending controlled cases, $\delta = \delta_b = \frac{C_b \lambda}{2\pi^2 EA}$, and for tensile controlled cases, $\delta = \delta_t = \sqrt{\frac{2C_t}{\pi^3 \rho_{ice} g A}}$. For either case:

$$\begin{cases} \delta \le \dfrac{D_{min}}{\lambda} & \text{grease} \\ \dfrac{D_{min}}{\lambda} \le \delta \le 1 & \text{pancakes} \\ \delta \ge 1 & \text{nilas} \end{cases} \qquad [3]$$

The most difficult parameters are C_b and C_t. The Young's modulus of pancake ice, E is also unknown. Provided these parameters remain constant, we may tentatively leave them out from the dimensionless formula and thus focus on the effect of $\frac{\lambda}{2\pi^2 A}$ for the bending control and $\sqrt{\frac{2}{\pi^3 \rho_{ice} g A}}$ for the tensile control. Table 1 summarizes the final pancake size in a laboratory wave tank (Shen et al. 2004). In this experiment, a twin tank exposed to the same room temperature and filled with the same saline water was used to study the relation between the pancake size and the wave characteristics. The tests were conducted with each wave paddle running at a similar wave period but different amplitude. The column labeled D is the size of the final pancake diameter from each test, or grease ice when no pancakes were able to form. In Figure 1, we plot the resulting $\delta_1 = \frac{\lambda}{2\pi^2 A}$ and $\delta_2 = \sqrt{\frac{2}{\pi^3 \rho_{ice} g A}}$. Both plots show that the data are distributed with pancakes forming when δ_1 or δ_2 are large. As δ_1 or δ_2 decrease, they reach their respective critical values that favor grease ice formation. At the critical values, both pancakes or no pancakes coexist. Below the critical values only grease ice form. We do not have data for the other critical value that separates the nilas and pancake ice regime. This value could only be found with very small wave amplitude corresponding to large δ_1 or δ_2.

Table 1. The final pancake size or only grease ice from the experiment in Shen et al. (2004).

	A (m)	λ (m)	D (m)	$\lambda/2\pi^2 A$	$\sqrt{2/\pi^3 \rho_{ice} g A}$
11/21 port	0.0086	5.30	0.13	31.1	0.029
11/21	0.038	3.930	grease	5.27	0.014
11/22 port	0.02	3.390	grease	8.79	0.019
11/22	0.025	2.850	0.10	5.71	0.017
11/23 port	0.014	3.61	0.26	13.2	0.023
11/23	0.015	2.86	0.23	9.50	0.022
11/26 port	0.011	1.76	0.11	8.15	0.026
11/26	0.035	1.86	grease	2.70	0.014
11/27 port	0.0095	2.39	0.15	12.8	0.028
11/27	0.031	2.43	grease	3.99	0.015
11/28 port	0.0069	5	0.13	36.7	0.032
11/28	0.03	4.45	0.15	7.50	0.016

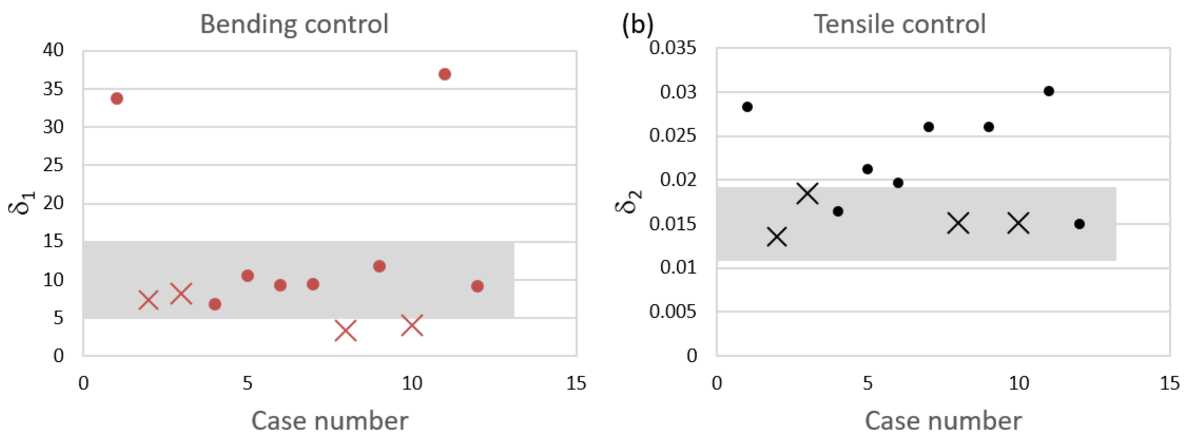

Figure 1. The dimensionless parameter (a) δ_1 (b) δ_2 measured in the cases from Table 1. $\times$: no pancake formation. $\bullet$: pancakes formed. Grey line marks the transition between the two regimes, above which pancakes would form, below which only grease form.

We now use the above criteria to examine the field data from Roach et al. (2018). In their case, only those wave conditions that produced pancakes were discussed. They summarized their pancake diameter D and associated wavelength and amplitude and then fitted the values to the relation $\propto \sqrt{\frac{\lambda^2}{A}}$. They reported that the least-square linear fit of the relation gave an estimate of $C_t = 0.167$ N/m^2. The peak wavelength in their cases was ~120 m with amplitude ~1 m, hence $\frac{0.02}{120} \leq \delta_t \approx \sqrt{\frac{2\times0.167}{\pi^3 \rho_{ice} g A}} = 0.001 \leq 1$, corresponding to the pancake regime consistent with the observation. We cannot perform a similar analysis using the bending control due to the lack of knowledge of C_b and E.

5. Incorporating wave effects in ice models

We now propose an algorithm which incorporates the regime of new ice formation under a given wave condition. We assume that the wave field is prescribed. For a fully coupled wave-ice model, we envision that the two models: ice and wave, are run in parallel, with information exchange at every time step. In this way, the current information of the wave through various ice covers can be simulated, and in turn, the formation of new ice can use the updated wave condition in the new time step. The algorithm is built on observations from Matsumura and Ohshima (2015) and the conceptual model of Smedsrud and Martin (2015). To include the wave effects into ice covers, we add one more variable into the model of Smedsrud and Martin (2015). This additional variable is the pancake diameter D. The thickness of the grease ice layer is h_g. However, instead of using the grid size dependent assumption for the frazil thickness (Smedsrud, 2011 and Smedsrud and Martin, 2015), we propose a formulation that is independent of the grid size as will be described later. At each time step, we will calculate the concentration, area, and thickness of both the solid ice as in CICE, and the new ice. The new ice will eventually become part of the solid ice. In each grid cell, the numerical model will determine the new ice type under the current wave condition. Depending on the wave condition, initially the new ice may be nilas, pancake, or grease. As they evolve towards the final solid ice state, the changing wave condition may turn them into any of the three types: sheet ice, pancake, shuga or brash ice (small ice fragments formed broken floes). Sheet ice forms when ocean waves diminish to an extent that surface ice elements, regardless of their evolution history, freeze together. Pancakes can change their size from time to time due to lateral growth or breaking. Grease ice may evolve into shuga under an intense wave condition. Brash ice forms in rough seas from disintegrated ice covers. For example, for existing pancakes, if the new wave condition admits pancakes larger than the existing one, existing pancakes grow to become a larger size, controlled by tensile failure. The lateral growth might be a continuous sheet if the wave field is gentle. However, if the wave condition admits only grease ice, the pancakes are pulverized to become brash ice. In which case, the bending control is activated to break the existing pancakes. We will use the same criteria shown in Eq. [3] to determine which of the three ice types is compatible with the wave condition at each time step. We also follow the thickness evolution of the new ice cover. When the thickness of new ice becomes the same as the thinnest category in the solid ice, we combine this new ice into the solid ice.

The following is the algorithm to include newly formed ice. For growth/melt and deformation of existing solid ice covers, there is no change from the CICE formulation.

1. The volume production of ice crystals in the open water portion, V_g, is determined from the net heat loss through the surface. This volume is assumed to instantly float to the surface as in Smedsrud and Martin (2015).
2. The thickness of this initial ice layer is $h_g = V_g/A_g$, where A_g is area concentration of the ice crystal layer. Instead of directly formulating h_g as in Smedsrud and Martin (2015), we propose a parameterization based on the area evolution. As shown in the numerical experiment of Matsumura and Ohshima (2015), the surface frazil was at first concentrated in the zone of convergence of the surface current, then gradually spread over the rest of the open water area. Hence, we formulate the time-dependent area concentration as $A_g(t) = 1 - e^{-t/T_g}$ where T_g is the time scale for the area increase of the grease ice layer.
3. As the ice crystal layer thickens the top layer freezes. The freezing process is time dependent, but we will assume that this time scale is short hence will let the top layer be frozen instantly. The exposed layer has a thickness of $\left(1 - \frac{\rho_{ice}}{\rho_w}\right) h_g \sim 0.1 h_g$. We will assume a minimum thickness (on the order of mm) for which further considerations of ice types will take place. For very thin crystal layers we calculate their growth but ignore its effect on thermodynamics and wave mechanics. When the thickness is above this threshold, to determine if this layer will form pancake ice, or accumulate as loose frazil

slurry, or freeze smoothly into a layer of nilas, we use the current wave characteristics, and the criteria described in Eq. [3].

4. In the next time step, the wave characteristics are calculated using the current ice condition, where the spectral attenuation of different ice types are considered. The ice condition is updated using CICE algorithm in the partially covered "old ice" zone. The partially covered new ice zone continues to grow more ice crystals through heat loss. The net heat flux over new ice is assumed to be the same as over open water. For grease ice this assumption is supported by the experimental result of De La Rosa and Kern (2011). For pancake ice the assumption is subject to future scrutiny.
5. At each time step, we check the new ice thickness including both the frozen top layer and the porous loose layer at the bottom. If the equivalent thickness of this layer is the same as the thinnest category of the solid ice, we combine it into the solid ice.

The above processes are summarized below.

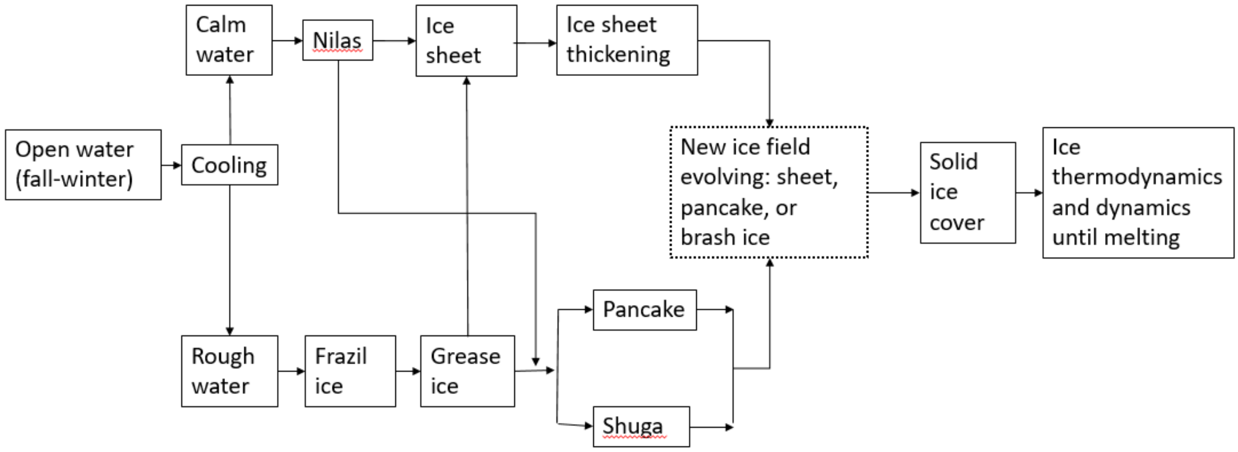

Figure 2. Diagram of the new ice formation and its evolution into solid ice. Calm and rough conditions correspond to the wave characteristics defined in Eq. [3]. In this diagram, the downward direction indicates increasing wave intensity.

6. Discussion and conclusions

In this paper, we present a conceptual model to determine the type of newly formed sea ice under the influence of a wave field. The study is prompted by the fact that wave attenuation, especially the high frequency band, depends on the ice type. Because of the increase of fetch in the Arctic as open water area has increased, regional wave forecasts will need more refined ice models. The present study combines the thermodynamic growth with wave effects to determine which of the three types of new ice would form: nilas, pancake, or grease ice. This new ice evolves under the action of wave forcing and thermal growth until they eventually become part of the solid ice cover. Under rough seas, i.e. intense wave condition, grease ice forms and continues to thicken. Under moderate seas, pancake ice forms. Under calm seas, nilas forms. Further growth can be subject to a different wave condition. Hence, nilas can turn into pancakes or brash ice, pancakes can grow in size or break into smaller pancakes or turn into brash ice, and grease ice can become pancakes, or freeze into an ice sheet. The layer of new ice evolves until its thickness becomes the same as the thinnest solid ice defined in CICE. We then combine it into the solid ice cover.

Despite many assumptions used in this conceptual model, it is the beginning of a much needed step towards combining an ice model with a wave model to predict the new ice type and assess its effect on wave propagation. We will implement this model in the very near future to test its capability in a seasonal ice zone.

Acknowledgments
The authors would like to thank the Isaac Newton Institute for Mathematical Sciences, Cambridge, for support and hospitality during the programme Ice-fluid interaction (SIPW02) where work on this paper was initiated. This programme was supported by EPSRC grant numbers EP/K032208/1 and EP/R014604/1. The concept presented here was based on many discussions during the ONR sponsored Seastate and Boundary Layer Physics Program under Drs. Scott Harper and Martin Jeffries.

References

CICE Consortium. 2019. CICE Documentation. 104 pp. https://buildmedia.readthedocs.org/media/pdf/cice-consortium-cice/master/cice-consortium-cice.pdf

Daly SF ed. 1994. *IAHR Working Group on Thermal Regimes: report on frazil ice*. CRREL Spec. Rep. 94-23, 52pp.

De la Rosa, S., Maus, S. and Kern, S. 2011. Thermodynamic investigation of an evolving grease to pancake ice field. *Ann. Glaciol*., doi: 10.3189/172756411795931787

De Pace, L., Smith, M., Thomson, J., Stammerjohn, S., Ackley, S. and Loose, B. 2019. Frazil ice growth and production during katabatic wind events in the Ross Sea, Antractica, *The Cryosphere*, https://doi.org/10.5194/tc-2019-213

Leibovich, S. 1983. The form and dynamics of Langmuir circulations. *Ann. Rev. Fluid Mech*. https://doi.org/10.1146/annurev.fl.15.010183.002135

Matsumura, Y., and Ohshima, K. 2015. Lagrangian modelling of frazil ice in the ocean. *Ann. Glacio.*, doi:10.3189/2015AoG69A657

Omstedt, A. 1985. Modelling frazil ice and grease ice in the upper layers of the ocean. *Cold Reg. Sci. Tech.* https://doi.org/10.1016/0165-232X(85)90009-6

Roach, L.A., Smith, M.M., and Dean, S.M. 2018. Quantifying growth of pancake sea ice floes using images from drifting buoys. *JGR-Oceans,* https://doi.org/10.1002/2017JC013693

Rogers, W. E., Thomson, J., Shen, H.H., Doble, M.J., Wadhams, P., and Cheng, S. 2016. Dissipation of wind waves by pancake and frazil ice in the autumn Beaufort Sea, *JGR-Oceans,* 121, doi:10.1002/2016JC012251.

Shen, H.H., Ackley, S.F., and Yuan, Y. 2004. Limiting diameter of pancake ice, *JGR-Oceans*, 109(C12035), doi:10.1029/2003JC002123.

Shen, H.T., 2010. Mathematical Modeling of River Ice Processes, *Cold Reg. Sci. Tech.* 62(1), 3-13, 2010. https://doi.org/10.1016/j.coldregions.2010.02.007

Shen, H.T., Wang, D.S., Lal, W.A.M. 1995. Numerical simulation of river ice processes. *J. Cold Reg. Eng.* https://doi.org/10.1061/(ASCE)0887-381X(1995)9:3(107)

Smedsrud LH (2011). Grease-ice thickness parameterization. *Ann. Glaciol*., doi:10.3189/172756411795931840

Smedsrud, L., & Martin, T. (2015). Grease ice in basin-scale sea-ice ocean models. *Ann. Glacio.*, doi:10.3189/2015AoG69A765

Thomson, J., Ackley, S., Girard-Ardhuin, F., Ardhuin, F., Babanin, A., Boutin, G., et al. 2018. Overview of the Arctic Sea state and boundary layer physics program. *JGR-Oceans*, https://doi.org/10.1002/2018JC013766

Tolman, H. L. and the WAVEWATCH III® Development Group. 2014. *User Manual and System Documentation of WAVEWATCH III®* version 4.18, Tech. Note 316, NOAA/NWS/NCEP/MMAB, 282 pp.1Appendices, National Centers for Environmental Prediction, College Park, Md.

25th IAHR International Symposium on Ice
Trondheim, June 14 to 18, 2020

An Experimental Study on Surface Wave Propagation along Segmented Floating Viscoelastic Covers

Dharma Sree[1,2], Adrian Wing-Keung Law[1,2*] and Hayley H. Shen[1,3]
[1]*Environmental Process Modelling Centre (EPMC), Nanyang Environment and Water Research Institute (NEWRI), Nanyang Technological University, 1 CleanTech Loop, CleanTech One, #06-08, Singapore 637141*
[2]*School of Civil and Environmental Engineering, Nanyang Technological University, N1-01a-29, 50 Nanyang Avenue, Singapore 639798*
[3]*Department of Civil and Environmental Engineering, Clarkson University, Potsdam, NY, USA 13699-5710*
**cwklaw@ntu.edu.sg*

Continuum-based viscoelastic model considers wave dispersion and attenuation under large stretch of ice by assigning effective mechanical properties for the ice cover, whereas discrete floe model considers the scattering mechanisms. This research work inspects the combined effects of material properties, scattering mechanism, and hydrodynamics on surface wave modifications. The study is a continuation of the experimental approach developed by Sree et al. (2017; 2018), with the incorporation of discontinuities on floating viscoelastic covers. The covers with required rheological properties were first prepared using oil-doped polydimethylsiloxane and tested in an oscillatory rheometer. Ultrasound sensors installed along a wave flume then recorded the surface elevation at various locations of the cover under wave action. These data were used to analyze wave dispersion and associated wave attenuation. With segmentation, notable change in wavenumber was obtained in terms of switching from wave lengthening to shortening for stiff and thick covers. The experimental results were compared with an existing theoretical model on segmented floating elastic cover; an empirical relation was also derived based on attenuation data (Sree et al. 2020). In this talk, we will present a summary of and the outlook from these results.

1. Introduction

Marginal Ice Zone (MIZ) is composed of diverse types of ice covers from newly formed frazil ice in open water to larger pancake ice, as well as huge closely packed broken multi- year-old ice chunks. The wave energy loss in MIZ is complex due to the combined action of different temporal and spatial processes. They consist of wave scattering by bending of ice floes (Kohout and Meylan, 2008), dissipation due to the boundary layer hydrodynamics above (i.e. overwash) and underneath the ice cover and its surface roughness (Kohout et al, 2011), and dissipation due to the rheological property of the type of ice cover considered, and many others. Together they result in the deterioration of waves, thus protecting the vast ice pack in the interior.

Many theoretical models have been developed in the past for wave-ice interactions with various assumptions for the ice covers, for example, mass-loading model (Weitz and Keller, 1950; Keller and Weitz, 1953; Shapiro and Simpson, 1953; Wadhams, 1986) for pancake ice which assumed no interaction between two floes, and the two-layer viscous model (Weber,1987; Keller,1998; De Carolis and Desiderio, 2002) for grease ice, and the thin elastic plate model for unbroke continuous sheet (Greenhill,1887; Wadhams, 1973; Fox and Squire 1990) as well as broken ice covers (Meylan and Squire, 1994; Kohout and Meylan, 2008). All these theories were experimentally examined in the laboratory using floating covers of known material property (Sakai and Hanai, 2002) as well as real ice (Newyear and Martin, 1999; Wang and Shen 2010a).

The viscoelastic model (Squire and Allan 1980; Robinson and Palmer 1990; Wang and Shen 2010b) was developed to bridge the pure viscous and pure elastic assumption and intended to describe general ice conditions. The validation of viscoelastic model for unbroken / continuous covers have been done so far (Sree et al, 2017; 2018), which considered how the rheological property of the viscoelastic covers modified the waves when it entered the covered region. This paper is a continuation of the previous work that experimentally investigates how the discontinuities along the viscoelastic covers would alter the wave properties.

2. Experimental Setup and Material Testing

The Environmental Processing and Modelling Centre, NEWRI, at NTU is equipped with a wave flume, 8.0m long, 1.0m deep and 0.3m wide, made of tempered glass supported using stainless steel framework. The detailed description about the flume was mentioned in Sree et al. (2018). In the present paper, the wave parameters used are: wave period, T = 0.5 s, wave height, $H = 1.70 \times 10^{-2}$ m, and water depth, d = 0.30 m (Figure 1).

The floating viscoelastic covers were made of polydimethylsiloxane (PDMS) doped with white oil extending 3.0 m long along the wave propagation inside the wave flume. Two viscoelastic covers were tested with mass percentages of curing agent, $m_{CA} = 4$, and 10 %, respectively. Their shear modulus (G) and kinematic viscosity (ν) were: (a) for $m_{CA} = 4\%$, G = 23.18 kPa and ν = 0.23 m^2/s, and (b) for $m_{CA} = 10\%$, G = 145.11 kPa and ν = 0.42 m^2/s (Sree et al., 2020). Both viscoelastic covers were tested with four different segment lengths, l_s = 3.0, 1.0, 0.5 and 0.25 m, in the present experiments. The cover thickness considered here was h_s = 0.01 m

Ultrasound sensors were used to record the vertical displacement of the segmented covers under wave action. The positions of the ultrasound sensors were fixed on top of the covers for all the experiments. The detailed description of their locations is provided in Sree et al. (2020). Since the displacement data is collected along the length of viscoelastic cover, the leading-edge reflection to the open water is not considered in the present study.

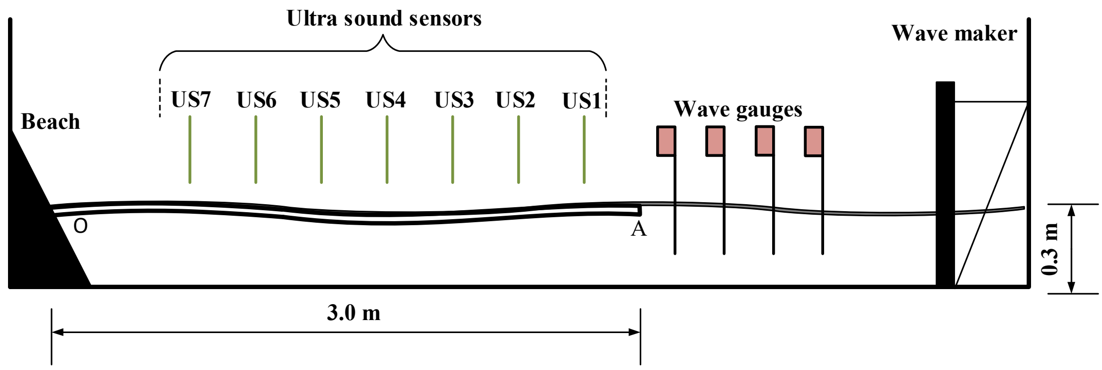

Figure 1. Schematic diagram of the wave flume (profile view, not in scale).

3. Data Analysis and Results

The surface displacement of the viscoelastic covers obtained during wave experiments from the DAQ system had a sampling frequency of 50 Hz. The sampling rate was increased to 200 Hz by the piecewise interpolation using the $PCHIP$ function in MATLAB. The data was smoothened using the $lowess$ function in MATLAB to determine the exact location of crest and trough. The location of the crest and trough were determined from the smoothed data using $findpeaks$ function in MATLAB.

The wave celerity, c_s , along the region covered with viscoelastic cover was determined by calculating the time taken for a fully developed wave to travel between consecutive sensors. Only the first three fully developed waves were considered for the analysis to avoid the effects from reflection. The celerity was calculated as

$$c_s = \frac{\Delta x}{\Delta t} \qquad \textbf{[1]}$$

where, Δx is the distance between two consecutive sensors and Δt is the time take for a fully developed wave crest to travel between the two sensors.

The variation of c_s along the cover region is given in Figure 2. For the flexible cover of m_{CA} = 4%, c_s was always less than open water celerity, c_o. while this was not the case with the stiffer cover of m_{CA} = 10% which showed a gradual decrease in the value of c_s with decreasing segment length. This shows that celerity of wave depends on the segment length of a discontinuous cover, in addition to other previously reported factors like the material property, thickness, and wave period (Sree et al., 2017; 2018).

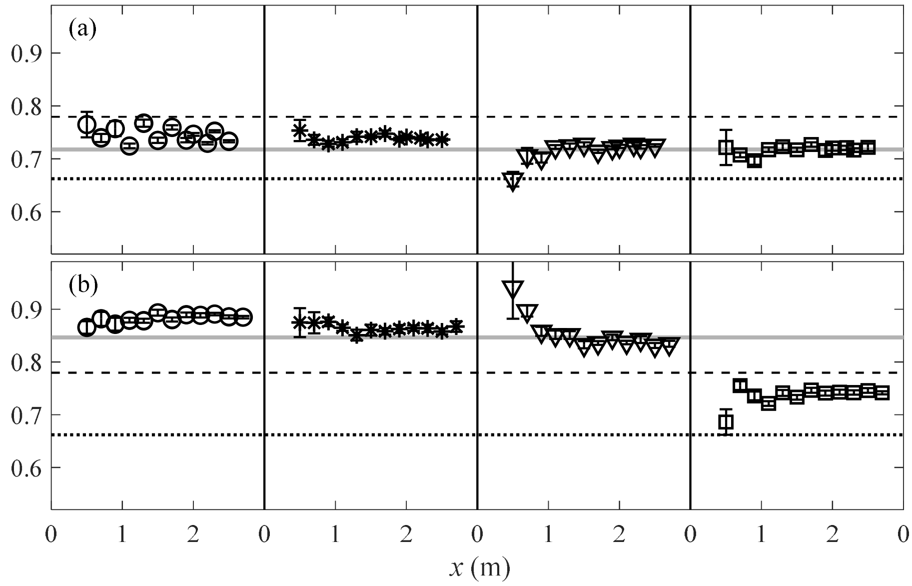

Figure 2. Wave celerity along the length of PDMS cover for T = 0.5 s, h_s = 0.01 m, m_{CA} = (a) 4%, (b) 10%. Segment length (l_s): ○ 3.0 m, ∗ 1.0 m, ∇ 0.5 m, and □ 0.25 m. Dotted line = Mass loading model, Dashed line = Open water case, and Grey solid line = Wang and Shen (2010b).

The attenuation coefficient was obtained by fitting the amplitude of surface displacement data at different locations of sensors, along the direction of propagation, with an exponential curve (Figure 3). The attenuation coefficient, α is given by

$$A_x = A_o\, e^{-\alpha x} \qquad \textbf{[2]}$$

where, A_x is the wave amplitude at the distance x from the leading edge (where x = 0).

The variation of attenuation coefficient obtained using Equation (2) with segment length for the two covers is shown in Table 1. The values clearly indicate that the attenuation coefficient depends on the number of discontinuities and the rheological property of the cover. For the flexible cover with m_{CA} = 4%, the coefficient initially decreased when the segment length reduced from l_s = 3.0 to 0.5 m, and then the trend reversed with further reduction to l_s = 0.25 m. For the stiffer cover with m_{CA} = 10%, the attenuation coefficient increases monotonically with the increase in the number of discontinuities for the cover.

4. Conclusions

The effect on waves travelling through segmented floating viscoelastic covers were experimentally investigated in this study. Viscoelastic covers of two different rheological properties and four segment lengths were tested. Notable differences were observed in the wave celery for different segment lengths, keeping wave period, cover thickness and material properties as constants. For the stiffer covers at T = 0.5 s, the change of wave celery with segment length can be clearly observed. The flexible covers on the other hand showed a complex zig-zag trend for the variation of celerity along the length of cover. In terms of attenuation, the attenuation coefficient was found to be directly proportional to the number of discontinuities for the stiffer cover. For the continuous cover, the attenuation coefficient decreased with increase in m_{CA}, but when the discontinuities were introduced the attenuation coefficient increased with m_{CA} instead. The energy dissipation due to discontinuities was also more significant for stiffer covers.

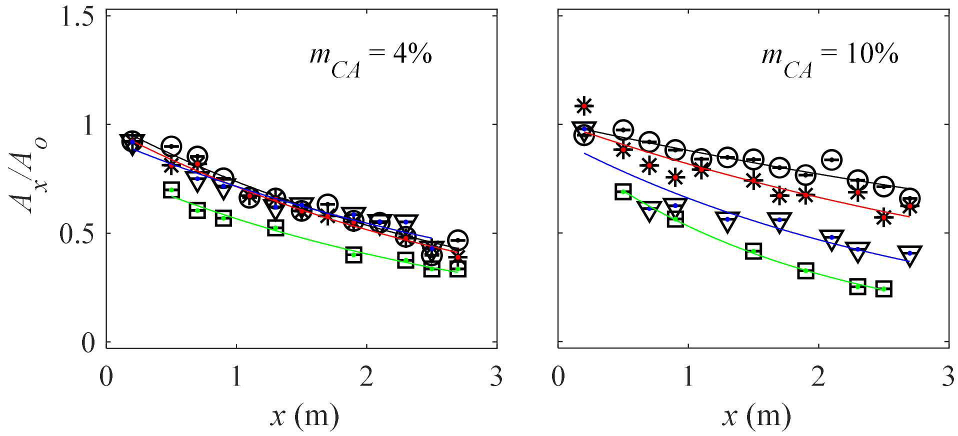

Figure 3. Variation of normalized wave amplitude with segment length. Segment length (l_s): ○ 3.0 m, ∗ 1.0 m, ∇ 0.5 m, and □ 0.25 m and their corresponding exponentially fitted curves are black, red, blue, and green. All error bars collapse to a point due to the repeatability of the tests.

Table 1. Wave attenuation coefficient for different covers

l_s (m)	m_{CA}	
	4%	10%
	α (rad/m)	
3.0	0.33	0.11
1.0	0.33	0.19
0.5	0.27	0.30
0.25	0.29	0.73

This paper is a condensed summary of the key points found in this experimental study. A more complete report may be found in Sree et al. (2020). The relative contribution of different dissipation mechanisms on wave attenuation are analyzed over a narrow range of wave parameters and cover properties considered in the laboratory. The results from the experimental study may be used to check theoretical models for wave propagation through segmented floating viscoelastic covers. However, due to scaling issues, these results may not be quantitatively extrapolated to field cases.

Acknowledgement

This work is supported by US Office of Naval Research Grant #N00014-17-1- 2862 and US Office of Naval Research Global Grant No: N62909-15-1-2069.

References

De Carolis, G. and Desiderio, D., 2002. Dispersion and attenuation of gravity waves in ice: a two-layer viscous fluid model with experimental data validation. Physics Letters A, 305(6), 399-412.

Fox, C. and Squire, V.A., 1990. Reflection and transmission characteristics at the edge of shore fast sea ice. Journal of Geophysical Research: Oceans, 95(C7), 11629-11639.

Greenhill, A.G., 1887. Wave motion in hydrodynamics (continued). American Journal of Mathematics, 97-112.

Keller, J.B. and Weitz, M., 1953. Reflection and transmission coefficients for waves entering or leaving an icefield. Communications on Pure and Applied Mathematics, 6(3), 415-417.

Keller, J.B., 1998. Gravity waves on ice‐covered water. Journal of Geophysical Research: Oceans, 103(C4), 7663-7669.

Kohout, A.L. and Meylan, M.H., 2008. An elastic plate model for wave attenuation and ice floe breaking in the marginal ice zone. Journal of Geophysical Research: Oceans, 113(C9).

Meylan, M. and Squire, V.A., 1994. The response of ice floes to ocean waves. Journal of Geophysical Research: Oceans, 99(C1), 891-900.

Newyear, K. and Martin, S., 1999. Comparison of laboratory data with a viscous two‐layer model of wave propagation in grease ice. Journal of Geophysical Research: Oceans, 104(C4), 7837-7840.

Robinson, N.J. and Palmer, S.C., 1990. A modal analysis of a rectangular plate floating on an incompressible liquid. Journal of sound and vibration, 142(3), 453-460.

Sakai, S. and Hanai, K., 2002, December. Empirical formula of dispersion relation of waves in sea ice. In Ice in the environment: Proceedings of the 16th IAHR International Symposium on Ice. 327-335.

Shapiro, A. and Simpson, L.S., 1953. The effect of a broken icefield on water waves. Eos, Transactions American Geophysical Union, 34(1), 36-42.

Squire, V.A. and Allan, A., 1977. Propagation of flexural gravity waves in sea ice. Centre for Cold Ocean Resources Engineering, Memorial University of Newfoundland.

Sree, D.K., Law, A.W.K. and Shen, H.H., 2017. An experimental study on the interactions between surface waves and floating viscoelastic covers. Wave Motion, 70, 195-208.

Sree, D.K., Law, A.W.K. and Shen, H.H., 2018. An experimental study on gravity waves through a floating viscoelastic cover. Cold Regions Science and Technology, 155, 289-299.

Sree, D.K., Law, A.W.K. and Shen, H.H., 2020. An experimental study of gravity waves through segmented floating viscoelastic covers. Applied Ocean Research, 101, 102233.

Wadhams, P., 1973. The effect of a sea ice cover an ocean surface waves (Doctoral dissertation, University of Cambridge).

Wadhams, P., 1986. The seasonal ice zone. In The geophysics of sea ice. 825-991. Springer, Boston, MA.

Wang, R. and Shen, H.H., 2010a. Experimental study on surface wave propagating through a grease–pancake ice mixture. Cold Regions Science and Technology, 61(2-3), 90-96.

Wang, R. and Shen, H.H., 2010b. Gravity waves propagating into an ice‐covered ocean: A viscoelastic model. Journal of Geophysical Research: Oceans, 115(C6).

Weber, J.E., 1987. Wave attenuation and wave drift in the marginal ice zone. Journal of physical oceanography, 17(12), 2351-2361.

Weitz, M. and Keller, J.B., 1950. Reflection of water waves from floating ice in water of finite depth.

25th IAHR International Symposium on Ice

Trondheim, 23 - 25 November 2020

The response of semi-infinite ice sheet to a moving load

Sturova I.V. and Tkacheva L.A.

Lavrentyev Institute of Hydrodynamics of Siberian Branch of Russian Academy of Sciences

Lavrentyev Prospect, 15, Novosibirsk, 630090

sturova@hydro.nsc.ru, tkacheva@hydro.nsc.ru

Dynamic perturbations occurring in fluid and ice cover as a result of the action of mechanical external force have been thoroughly studied in the linear treatment for an infinitely extended homogeneous ice cover. In reality, the ice cover is not homogeneous since it can cover not the entire upper boundary of a fluid, but only its part and also the cracks and the patches of ice-free water may take place in it. The research of a steady three-dimensional (3-D) problem for flexural-gravity waves (FGWs) generated by a local pressure distribution moving with uniform speed along the rectilinear edge of semi-infinite ice sheet is presented. This load simulates the motion of an air-cushion vehicle (ACV). Five cases are considered: 1) the movement of the load on the ice sheet while the remaining half of the fluid surface is free; 2) two semi-infinite ice sheets (may be of different thickness) divided by a crack with free edges; 3) the fluid is bounded by a rigid vertical wall and the edge of the ice sheet may be either free or clamped; 4) load movement on the free surface near the ice sheet; 5) moving load on open water lead between two semi-infinite floating ice sheets (ice channel). The fluid flow is described by the linearized velocity potential theory, while the ice sheet is modeled through a thin elastic plate floating on the water surface. The solutions are obtained by two methods: the Wiener-Hopf technique (WHT) and the matched eigenfunction expansions (MEE). The vertical displacements of ice sheet and free surface as well as strains in ice and the forces acting on vehicle in horizontal directions are determined at different speeds of ACV.

1. Introduction

A considerable interest is now related to the study of various types of water wave problems in the presence of a thin ice-sheet. The wave/ice sheet/body interaction problem received a great development in fluid mechanics due to its practical relevance. At the present time, the behavior of ice cover under dynamic action has been thoroughly studied for an infinitely extended homogeneous ice cover (Squire et al., 1996). An investigation of the effect of various types of inhomogeneous conditions at the upper boundary of the fluid has been started only in recent decades. In the 2-D case, wave motions caused by an oscillating horizontal submerged cylinder were considered and the linearized velocity potential theory was adopted in the frequency domain. The actuality of this problem is due to the fact that with the current intensive developing of polar regions of the World's oceans and seas, in particular in connection with oil and gas extraction on the shelf, the need to operate long submerged pipelines and floating tanks arises in these regions. It should be noted that the solution of the 2-D problem enables us to describe the hydrodynamic loads acting not only on long pipelines but also on elongated 3-D bodies using the method of plane sections. A detailed review of existing solutions for 2-D problems is presented by Li et al. (2019). In the 3-D case, some problems were investigated for time-periodic external pressure and for load uniformly moving along the rectilinear edge of semi-infinite ice sheet. For time-periodic external pressure, three configurations were considered: (i) a floating semi-infinite elastic plate contacting with a free water surface; (ii) two semi-infinite elastic plates connected by the vertical and flexural rotational springs as a model of partially frozen crack in an ice sheet; (iii) semi-infinite ice sheet near a rigid vertical wall while its edge can be either clamped or free (Sturova, 2017; Tkacheva, 2017a-d).

The solutions of the cases (i)-(iii) for a pressure distribution moving with constant speed along the edge of ice sheet at some distance from it are considered by Sturova (2018) and Tkacheva (2018, 2019a) for fluid of finite depth. In the moving coordinate system associated with the load, the considered problem is assumed to be steady. The behavior of ice sheet under the action of moving load is studied, on the one hand, to develop methods for ice breaking by ACV and, on the other hand, to investigate the possibility of using ice sheet as crossings, floating platforms for various purposes. It is well known that FGWs develop in fluid under an ice cover and surface gravity waves (SGWs) are in fluid with a free surface. These waves have different dispersion relations and, in particular, differ by the fact that SGWs can arise at any load travelling speed while FGWs arise only when the load speed is higher than their minimum phase velocity. Sturova (2018) considered only the subcritical regime of moving load for the cases (i) and (iii) that is the load speed was assumed to be not higher than the minimum phase velocity of FGW. This implies the absence of wave perturbations of ice sheet in the far field and their localization in the neighborhood of external pressure region. However, a wave wake exists in the ice-free water region for the case (i). The solution of linear problem is obtained by means of the integral Fourier transform and MEE. For the problem with the vertical wall, the bending moments are determined together with the deflections of ice sheet. It is shown that in the case of clamped edge the maximum moment can be reached not at the center of pressure region but in the neighborhood of the wall. The analytic solutions of the problem for the cases (i)-(iii) are obtained using WHT by Tkacheva (2018, 2019a). The results obtained using various methods (MEE and WHT) for the case (i) are in good agreement. For two identical plates with a crack, the solution is found in an explicit form. The wave forces (wave resistance and side force), the deflection of plate, and the elevation of the free surface of fluid at different load speeds (subcritical and supercritical) are investigated. Tkacheva considered the action of an external load moving with uniform speed both over a free surface along the edge of ice sheet in (2019b) and between two semi-infinite floating ice sheets (ice channel) in (2019c). References to the papers of other authors devoted to the study of the effect of moving loads on inhomogeneous ice cover can be found in the bibliography of these papers.

The outline of this paper is as follows. In Sect. 2, we give a mathematical formulation of the problem for the case when the load moves on the ice sheet while the remaining half of the fluid surface is free. In Sect. 3, numerical results are reported and discussed for all five cases of load movement indicated in the abstract. The brief conclusion is given in Sect. 4.

2. Mathematical formulation

The water is taken to be of constant density ρ and uniform depth H. The local external pressure distribution moves at constant speed V along the rectilinear edge of ice sheet at some distance from it. We consider the moving together with the load Cartesian coordinate system (x,y,z) with x - axis directed perpendicular to the edge of the plate, the y - axis directed along the edge, and the z - axis directed vertically upwards. The load moves in the positive direction of the y - axis. The upper boundary of fluid is covered by the ice sheet in the region $x>0$ and the surface of fluid is free outside of ice sheet in the region $x<0$. The fluid motion can be described by a velocity potential $\varphi(x,y,z)$. The ice sheet is assumed to be isotropic and homogeneous and is treated as an elastic thin plate using the Kirchhoff - Love model. The plate is assumed to be in contact with water at all points and the plate draft is ignored. The edge of ice plate is free. The boundary-value problem for the velocity potential and the free surface elevation or the plate deflection $w(x,y)$ can be written as

$$\Delta_3\varphi = 0 \quad (|x|,|y|<\infty, -H\le z\le 0), \quad \Delta_3 \equiv \Delta_2 + \partial^2/\partial z^2, \Delta_2 \equiv \partial^2/\partial x^2 + \partial^2/\partial y^2, \qquad \textbf{[1]}$$

$$gw - V\left.\frac{\partial\varphi}{\partial y}\right|_{z=0} = 0 \quad (x<0), \quad D\Delta_2^2 w + \rho_0 h V^2 \frac{\partial^2 w}{\partial y^2} + g\rho w - \rho V \left.\frac{\partial\varphi}{\partial y}\right|_{z=0} = -q(x,y) \quad (x>0), \qquad \textbf{[2]}$$

$$\partial\varphi/\partial z|_{z=0} + V\,\partial w/\partial y = 0, \quad \partial\varphi/\partial z|_{z=-H} = 0, \qquad \textbf{[3]}$$

$$\left(\partial^2/\partial x^2 + \nu\partial^2/\partial y^2\right)w = 0, \quad \left[\partial^3/\partial x^3 + (2-\nu)\partial^3/\partial x\partial y^2\right]w = 0 \quad (x=0+, |y|<\infty). \qquad \textbf{[4]}$$

Here $D = Eh^3/[12(1-\nu^2)]$; E, ν, h, ρ_0 are Young's modulus, Poisson's ratio, thickness and density of ice sheet, respectively; $q(x,y)$ is ACV pressure on ice surface; g is the acceleration due to gravity. For wave motion, the decaying conditions should be satisfied far from the pressure region. We shall assume that the function $q(x, y)$ is nonzero only in the rectangular domain of width $2a$ and length $2b$ whose center is located at the point ($x = x_0 > a$, $y = 0$). Inside this rectangular domain the pressure is constant:

$$q(x,y) = q_0 \quad (|x-x_0|\le a, |y|\le b). \qquad \textbf{[5]}$$

The tilts of ACV influence on the distribution of pressure below the ACV during the motion, but we neglect this effect.

We are interested in bending stresses in ice cover. In particular, it is of practical interest to know whether the moving load can lead to strains large enough to break the ice in the area of load or near the edge. The strain tensor $\varepsilon(x,y)$ is given by the matrix

$$\varepsilon(x,y) = -\frac{h}{2}\begin{Vmatrix} \partial^2 w/\partial x^2 & \partial^2 w/\partial x\partial y \\ \partial^2 w/\partial x\partial y & \partial^2 w/\partial y^2 \end{Vmatrix}. \quad \textbf{[6]}$$

This tensor describes the strain field in the ice sheet. To find the maximum strain ε_m in the ice sheet, we need to find the largest eigenvalue of the strain tensor **[6]** at each location. The fracture strain was determined for the Bering Sea ice as $4.4-8.5\times10^{-5}$ by Squire and Martin (1980). In this study, we use the estimate of the yield strain ε_* for destruction of ice cover as $\varepsilon_* = 8\times10^{-5}$ (see Brocklehurst et al. (2010) and discussion of this value there).

Similar to the case of movement of ACV over the free surface, we can determine the forces acting on ACV during its movement over the ice sheet due to arising FGWs. In general, the wave forces acting on ACV consist of wave resistance, side force and yawing moment. We shall restrict our consideration only to the side force R_x and wave resistance R_y and its non-dimensional values A_x, A_y which are determined by formulas

$$(R_x,R_y) = -q_0\int_{x_0-a}^{x_0+a}\int_{-b}^{b}\left(\partial w/\partial x, \partial w/\partial y\right)dydx, \quad (A_x,A_y) = -g\rho(R_x,R_y)/(2aq_0^2). \quad \textbf{[7]}$$

The relations **[7]** are obtained by the projection of pressure force on corresponding directions and by integration over the load domain. For infinitely extended ice cover, the effect of speed and aspect ratio of the vehicle, the depth of water, and ice characteristic on wave resistance of uniformly moving ACV was investigated by Kozin and Pogorelova (2003).

The solution of boundary value problem **[1]-[5]** is obtained by Sturova (2018) and Tkacheva (2018) in integral form using MEE and WHT, respectively, but due to a limited scope of this paper, we ignore it here.

3. Numerical results

Physical and mechanical properties of sea ice and ACV are highly variable and we can consider some typical values of ice sheet $E = 5G\mathrm{Pa}, \rho_0 = 900\,\mathrm{kg/m^3}, \nu = 1/3$ for $\rho = 10^3\,\mathrm{kg/m^3}$, $q_0 = 10^3\,\mathrm{Pa}$, $a = 10$ m, $b = 20$ m and $H = 350$ m, unless otherwise stated. The speed of load V, the thickness of ice sheet h and the distance between load center and plate edge x_0 are varied in calculations. According to Squire et al. (1996), the minimum phase velocity V_m of FGW for infinitely extended ice cover corresponds to the value of wave number k_m at which the values of phase and group velocity coincide. In non-dimensional variables, the values $F_m = V_m/\sqrt{gH}$ and $\bar{k}_m = k_m H$ are determined by solving a system of two equations:

$$F_m^2 = \frac{(1+\beta\bar{k}_m^4)\tanh\bar{k}_m}{\bar{k}_m(1+\sigma\bar{k}_m\tanh\bar{k}_m)}, \quad \beta = \frac{D}{\rho g H^4}, \ \sigma = \frac{\rho_0 h}{\rho H},$$

$$\beta^2\bar{k}_m^8 - 2\beta\sigma F_m^2\bar{k}_m^6 + \bar{k}_m^4[F_m^4\sigma^2 + \beta(2+3F_m^2)] - F_m^2\bar{k}_m^2[2\sigma + F_m^2(1+\sigma)] + 1 - F_m^2 = 0.$$

The value V_m is approximately equal to 18.112 and 21.862 *m/s* for the ice sheet thickness h=1.5 m and h=2.5 m, respectively.

Figure 1 shows 3-D plots for the vertical displacements $w(x,y)$ of ice sheet at $x>0$ and free surface at $x<0$ for the load speed V=20 m/s (subcritical regime) and V=23 m/s (supercritical regime), the ice thickness h=2.5 m and the distance of the line of motion from an ice sheet edge $x_0 = 50$ m. The load moves on the ice sheet from left to right. The subcritical regime implies the absence of wave perturbations of the ice sheet in the far field and their localization in the neighborhood of the external pressure region. However, a wave wake exists in the ice-free water region at $y<0$ typical of Kelvin ship wake. In the supercritical regime, wave motions also arise in the ice sheet and extend to sufficiently large distances from the edge of ice. The motion of load gives rise to both short flexural waves in front of the load region and long gravity waves behind it.

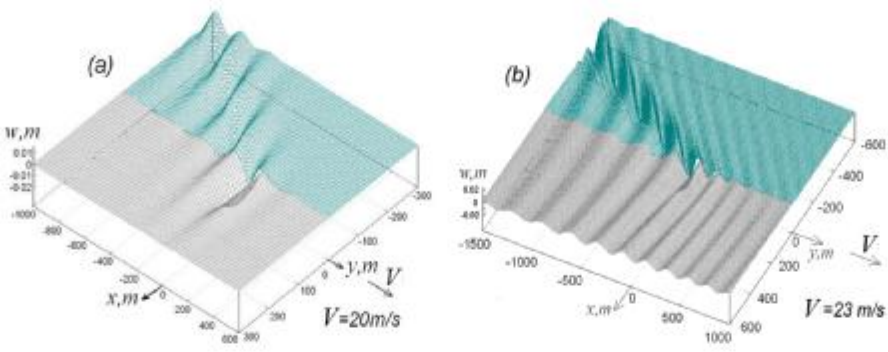

Figure 1. Vertical displacements of the ice sheet at $x>0$ and the free surface at $x<0$ for the load moving at the speed V=20 m/s (a) and V=23 m/s (b); $x_0 = 50$ m.

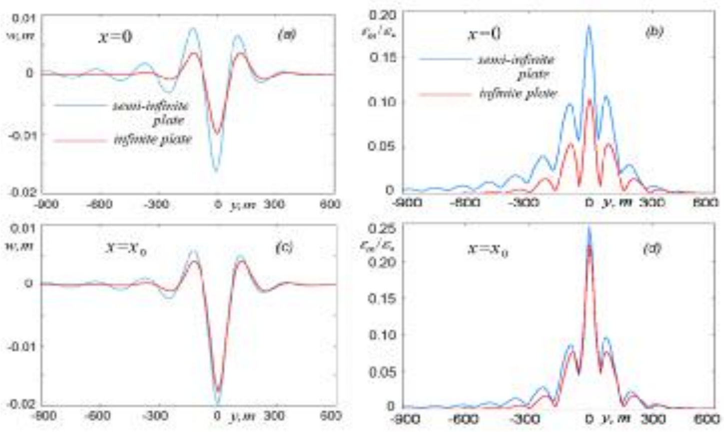

Figure 2. Deflections of ice sheet (a) and strains (b) on its edge, and the deflections of ice sheet (c) and strains (d) on the line of load motion at the load speed V=20 m/s, x_0= 50 m.

The deflections of ice sheet on its edge $w(0,y)$ and on the line of load motion $w(x_0, y)$ as well as their corresponding non-dimensional maximum strains $\varepsilon_m / \varepsilon_*$ are shown in figure 2 at h=2.5 m, x_0 =50 m and V=20 m/s. We have a subcritical case at this load speed and there are no FGWs in the infinitely extended ice cover. In the case of semi-infinite ice sheet, the moving deflection of sheet edge gives rise to waves in the fluid that generate waves in the ice sheet near its edge behind the moving load, which decay away from the edge. For an infinitely extended ice sheet, the deflection and strains are given in figure 2(c,d) on a line passing through the load center, and in figure 2(a,b) on a line parallel to the central one and at a distance x_0 from it. Both deflections and strains for the semi-infinite plate are higher than those for the infinite plate. The deflection and strain are maximal in the center of load.

Non-dimensional values of wave forces acting on moving vehicle A_x and A_y in **[7]** are presented in figure 3(*a,b*) as functions of the load speed at *h*=1.5 m and *h*=2.5 m, respectively. The values of wave forces for different distances $x_0 = 30$ m and $x_0 = 50$ m are compared in each figure. These figures also show the dependence of wave resistance A_y on load speed for an infinitely extended ice cover; the value of side force A_x is identically zero in this case. When the line of load motion becomes closer to the edge, then wave forces become larger as one would expect.

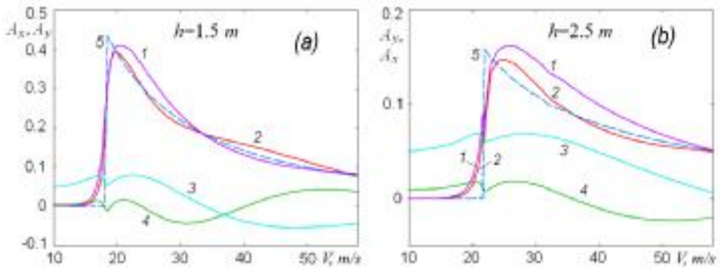

Figure 3. Non-dimensional values of side force A_x and wave resistance A_y for ice thickness *h*=1.5 m (*a*) and *h*=2.5 m (*b*). Curves *1, 2* correspond to the wave resistance and curves *3, 4* correspond to the side force at $x_0 = 30$ m and $x_0 = 50$ m, respectively. Curve *5* shows the wave resistance for infinitely extended ice cover.

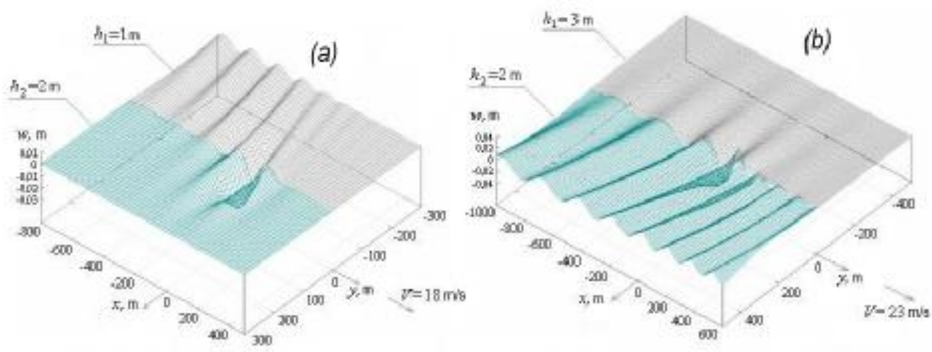

Figure 4. Vertical displacements of the ice plates at $h_2 = 2$ m: (*a*) - $h_1 = 1$ m at $V = 18$ m/*s*; (*b*) - $h_1 = 3$ m at $V = 23$ m/s.

The analytical solution to the problem of the behavior of ice sheet with rectilinear crack under the action of uniformly moving ACV is obtained using WHT by Tkacheva (2019a). Two configurations are considered. Firstly, two semi-infinite plates (whose thickness can differ) are separated by a crack with free edges. Secondly, the fluid is bounded by the vertical wall and the ice cover edge can be either free or frozen to the wall. In the case of the contact of plates of the same thickness, as well as in the presence of the wall, the solution is obtained in the explicit form. Two edge waves exist in the cases of identical plates and the plate near the wall with free edge at supercritical load speeds, one of them is spread in front of the load and other one behind it. In the figures 4 and 5, the thickness of loaded plate $h_2 = 2$ m and the thickness of left plate was taken equal to h_1 = 1, 2, or 3 m. The minimum phase velocities of FGW are equal to 15.594, 20.138, and 23.379 m/s for the plates of thickness 1, 2, and 3 m, respectively. Figure 4(a) shows 3-D plot for vertical displacements $w(x,y)$ of the plates of thickness h_1 = 1 m and h_2 = 2 m at speed V = 18 m/s. This velocity is subcritical for the right plate and supercritical for the left one. We can see that a wave motion appears in a thin plate. This motion excites waves in a thick plate in the neighborhood of the edge, these waves damp far from the edge. In figure 4(b), we reproduced a similar plot for the plates of thickness h_1 = 3 m and h_2 = 2 m at speed V = 23 m/s. This velocity is supercritical for the plate of thickness 2 m and subcritical for the plate of thickness 3 m. In the loaded plate, short bending waves propagate ahead of the load and long gravity waves propagate behind the load. They excite waves in the second plate in the neighborhood of the edge, the waves damp far from the edge.

Non-dimensional values of wave resistance A_y as functions of load speed for an ice sheet in the presence of vertical wall or in contact with free fluid surface as well as for the plates of various thickness values are shown in figure 5. We can see that for the ice sheet with free edge in the presence of vertical wall, the maximum wave resistance forces are reached at load speed close to a critical velocity of FGWs in the plate. For the plate of thickness h_1 = 3 m, as well as for the plate with free edge near the wall, the maximum wave forces are significantly greater than in other cases. Obviously, the action of thick plate is similar to reflection from the rigid wall. For the plate with clamped edge near the wall, the graphs of forces as functions of speed differ strongly from all other cases.

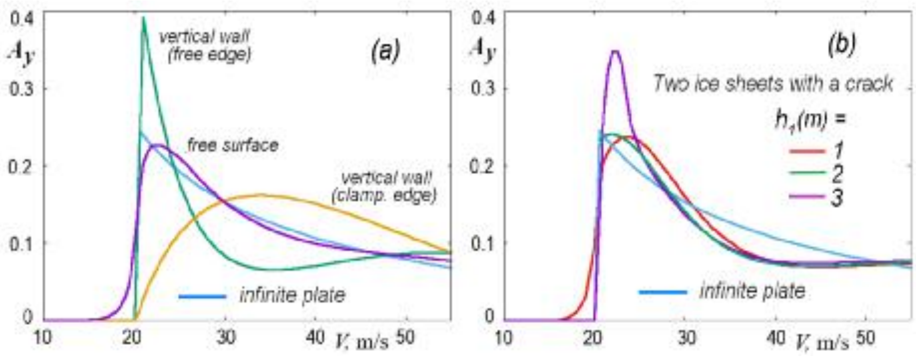

Figure 5. Non-dimensional values of wave resistance A_y as functions of load speed at $h_2 = 2\,\mathrm{m}$: (a) is for ice sheet in the presence of vertical wall or free surface; (b) is for ice sheets of different thickness $h_1 = 1, 2, 3\,\mathrm{m}$.

The problem of waves generated in fluid and ice sheet by a pressure region moving on the free surface of the fluid along the edge of semi-infinite ice sheet is solved by Tkacheva (2019b) using WHT. In contrast to the case of movement of the external load **[5]** on the ice sheet, in this case we restrict our consideration to the pressure distribution in the form

$$q(x,y) = q_0\{\tanh[\kappa(y+b)] - \tanh[\kappa(y-b)]\}/2 \ \ (|x-x_0|<a), \quad q(x,y)=0 \ \ (|x-x_0|>a), \quad \textbf{[8]}$$

where the rate of pressure decrease at the edges is controlled by the parameter κ . As shown by Doctors and Sharma (1972), when the load moves over a free surface, the constant pressure distribution in the rectangular planform leads to unrealistic oscillations in the wave resistance curve at the low Froude numbers. The results presented below were obtained with

$\kappa = 5/b$ and H=100 m. Figure 6 shows 3-D plots for the vertical displacements of free surface at $x > 0$ and ice sheet at $x < 0$ for the load speed V=15 m/s and different thickness of ice sheet: 0.5 and 1 m. The minimum phase velocity of FGWs is equal to 12.068 and 15.594 m/s for the ice plate of thickness 0.5 and 1 m, respectively. The load speed V=15 m/s is subcritical for the ice sheet 1 m thick and only weak wave motions appear in the ice sheet decaying rapidly away from the edge. The load speed V=15 m/s is supercritical for the ice sheet 0.5 m thick and wave motions are excited in the ice sheet, extending to a sufficiently large distance from the edge of ice cover.

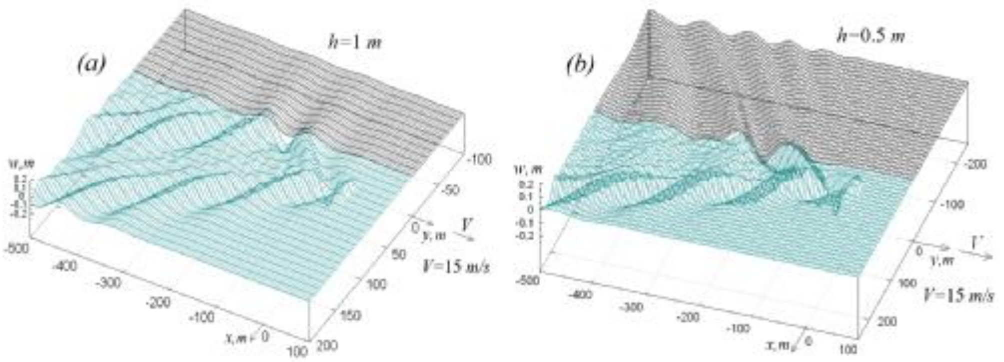

Figure 6. Vertical displacements of ice sheet at x<0 and free surface at x>0 for the load moving on free surface at the speed V=15 m/s for h=1 m (a) and h=0.5 m (b) for $x_0 = 50$ m, H=100 m.

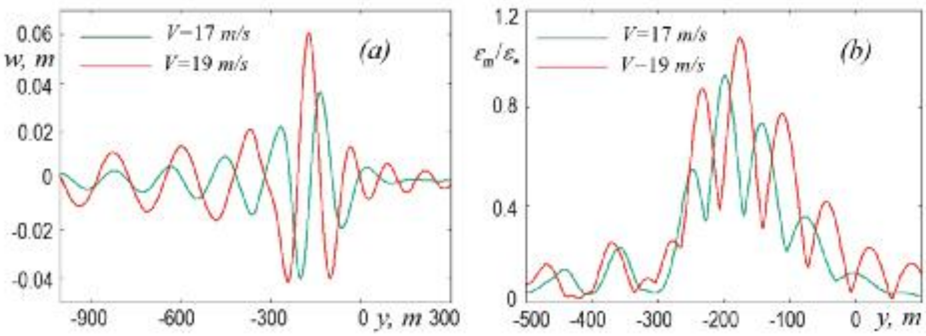

Figure 7. Dependences of vertical deflections (a) and non-dimensional strains (b) of an ice plate of thickness h = 1.5 m at the edge versus the coordinate y for V = 17 m/s and V = 19 m/s at $x_0 = 50\,\text{m}$, H=100 m.

The vertical deflections of ice plate at the edge and the non-dimensional maximum strains $\varepsilon_m/\varepsilon_*$ versus the coordinate y are presented in figure 7 at load speed 17 and 19 m/s and for ice sheet 1.5 m thick. The minimum phase velocity of FGW is equal to 18.104 m/s for the ice plate of thickness 1.5 m at H=100 m. The deflections of ice sheet and its strains are maximal at the edge when load moves on a free surface. It is seen that as the load speed increases, both the deflections of ice sheet and strains increase. For the plate of thickness h = 1.5 m, speed V = 17 m/s is subcritical and speed V = 19 m/s is supercritical and in the latter case, the destruction of ice cover on its edge is possible.

The analytical solution of the problem of waves produced in fluid and ice sheet by the uniform motion of pressure region **[8]** on the free surface of the fluid in an ice channel is obtained by Tkacheva (2019c) using WHT. The ice cover is modeled by two thin semi-infinite plates of constant thickness, floating on the surface of fluid and separated by a free surface of the fluid. Many edge waves exist in this case both at subcritical speeds and supercritical load speeds. The wave forces, the elevation of free surface of the fluid, and the deflection and deformation of the plates are investigated at different load speeds and ice sheet thickness. It is shown that for some values of the load speed, ice sheet thickness, and current pressure, the destruction of ice sheet near the edge is possible.

A comparison of wave resistance for the vehicle moving along the edge of ice cover at $x_0 = 25$ m and along the centerline of the channel of width 50 m is presented in figure 8. The minimum phase velocity of FGW is equal to 20.099 m/s for the ice plate of thickness 2 m at H=100 m. Dashed straight lines of the corresponding color show the values of critical velocity values for FGW at various ice thickness values. Difference of wave resistance in the channel from its value on the infinite free surface is cause by the influence of FGWs in plates and edge waves.

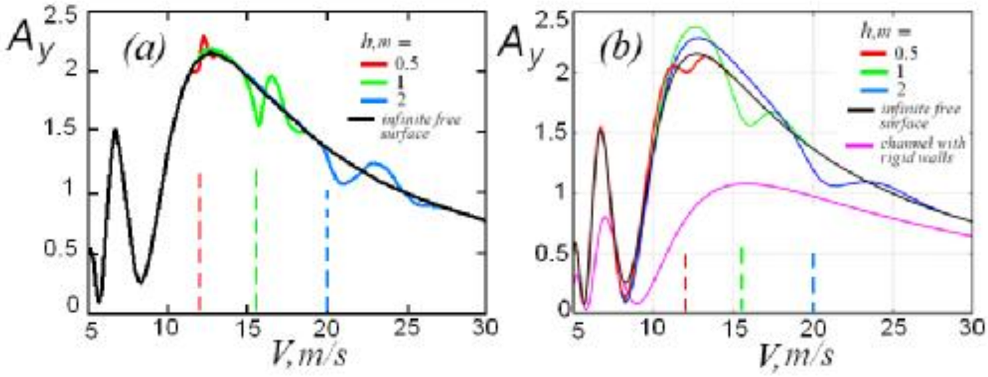

Figure 8. The wave resistance for the vehicle moving along the edge of ice cover at different ice thickness (h=0.5, 1, 2 m) and H=100 m in semi-infinite free surface (a) and along the ice channel (b). Black lines show the wave resistance for an infinitely extended free surface (Doctors and Sharma, 1972). Pink line shows the wave resistance acting on the vehicle as it moves through a channel with solid vertical walls (Newman and Poole, 1962).

4. Conclusion

The presented results show the significant difference wave forces, ice deflections and strains due to moving load in the case of inhomogeneous ice cover from their values for infinitely extended ice cover, especially large distinctions are reached in the case of ice cover near the wall. Edge waves exist in the cases of two identical plates or the ice sheet with free edge near the wall and in the ice channel. The movement of the load on the free surface along the edge of the ice sheet can lead to its destruction so this fact should be accounted for during rescue operations. For the effective destruction of an ice cover by moving ACV, it should move on water surface along the edge. The fluid is more pliant than an ice cover, and amplitudes and the energy of waves generated by the moving load on water are larger than those for the case of motion on an ice sheet.

References

Brocklehurst, P., Korobkin, A.A. and Parau, E.I., 2010. Interaction of hydro-elastic waves with a vertical wall. J. Eng. Math. 68, 215-231.

Doctors, L.J. and Sharma, S.D., 1972. The wave resistance of an air-cushion vehicle in steady and accelerated motion. J. Ship Res. 16(4), 248–260.

Kozin, V.M. and Pogorelova, A.V., 2003. Wave resistance of amphibian aircushion vehicles during motion on ice fields. J. Appl. Mech. Tech. Phys. 44(2), 193-197.

Li, Z.F., Wu, G.X. and Shi, Y.Y., 2019. Interaction of uniform current with a circular cylinder submerged below an ice sheet. Appl. Ocean Res., 86, 310-319.

Newman, J.N. and Poole, F.A.P., 1962. The wave resistance of a moving pressure distribution in a canal. Schiffstechnik, 9, 21-26.

Squire, V., Hosking, R., Kerr, A. and Langhorne, P., 1996. Moving loads on ice plates. Kluwer.

Squire, V. and Martin, A., 1980. A field study of the physical properties, response to swell, and subsequent fracture of a single ice floe in the winter Bering sea. Technical report 18, Univ. Washington.

Sturova, I.V., 2017. Action of periodic surface pressure on an ice cover in the vicinity of a vertical wall. J. Appl. Mech. Tech. Phys. 58(1), 80-88.

Sturova, I.V., 2018. Motion of an external load over a semi-infinite ice sheet in the subcritical regime. Fluid Dyn . 53(1), 49-58.

Tkacheva, L.A., 2017a. Vibrations of an ice sheet with crack under a time-periodic load. Fluid Dyn. 52(2), 219-229.

Tkacheva, L.A., 2017b. Behavior of a semi-infinite ice cover under periodic dynamic impact. J. Appl. Mech. Tech. Phys. 58(4), 641-651.

Tkacheva, L.A., 2017c. Edge waves in a fluid under ice cover with a crack. Doklady Physics. 62(4), 202-207.

Tkacheva, L.A., 2017d. Action of a local time-periodic load on an ice sheet with a crack. J. Appl. Mech. Tech. Phys. 58(6), 1069-1082.

Tkacheva, L.A., 2018. Behavior of a semi-infinite ice cover under a uniformly moving load. J. Appl. Mech. Tech. Phys. 59(2), 258-272.

Tkacheva, L.A., 2019a. Wave motion in an ice sheet with crack under uniformly moving load. Fluid Dyn. 54(1), 14-32.

Tkacheva, L.A., 2019b. Wave pattern due to a load moving on the free surface of a fluid along the edge of an ice sheet. J. Appl. Math. Tech. Phys. 60(3), 462-472.

Tkacheva, L.A., 2019c. Edge waves produced by the motion of a vessel in an ice channel. J. Appl. Math. Tech. Phys. 60(5), 850-864.

25th IAHR International Symposium on Ice
Trondheim, 23 - 25 November 2020

Uncertainty in ocean wave estimate in the Arctic Ocean

T. Waseda[1], T. Nose[1], T. Kodaira[1], K. Nakano[1], J. Inoue[2], and K. Sato[3]
[1]The University of Tokyo; [2]National Institute of Polar Research;
[3]Kitami Institute of Technology
[1]Kashiwa, Chiba, Japan; [2]Tachikawa, Tokyo, Japan; [3]Kitami, Hokkaido, Japan

The Arctic sea ice is retreating at an accelerating rate and ocean waves in the emerging open waters are increasing. While the possible positive feedback of wave-ice-breakup is an environmental concern, the widely open ice-free waters are providing economic opportunities to the Arctic Circle communities. The need for accurate prediction of ocean waves in the open waters, coastal region, and in the Marginal Ice Zone is imminent. The Japanese R/V Mirai has conducted three expeditions in the Arctic Ocean in 2016 September and October 2018 November, and 2019 October in the Beaufort Sea and the Chukchi Sea. Through the collected knowledge based on wave buoy observations and modeling, we have identified that the largest sources of uncertainties of wave estimates are not necessarily the wave-ice interaction physics, but the uncertainty in the wind and sea-ice forcing. By analyzing the reanalysis wave field, we have shown that the extreme waves in the open waters are increasing as the chances of Arctic Storms generating ocean waves increase with the enlarged open water area. For those extreme events, the location of the ice-edge is not necessarily important as the storm size is smaller than the open water area. In such a case, the source of uncertainty is the reanalysis wind field. On the other hand, waves near the MIZ is highly uncertain, not because of inaccurate wave-ice interaction physics but is because of the uncertainty in the sea ice concentration. The satellite-derived S.I.C. estimates are highly variable depending on the sensors and analysis algorithms, and the associated uncertainty of ocean wave model-estimates is larger than the uncertainty related to the wave-ice interaction physics.

1. Introduction

The sea-ice conditions in the Arctic region are changing as the atmospheric and oceanic temperature gradually rises. While the emerging open waters open up economic opportunities for Arctic Circle countries, increased ocean waves and drifting sea ice are imposing risks to ships navigating through the Northern Sea Route. Considerable lack of knowledge of the nature of the wave and ice interaction is overcome by new expeditions. An extensive coordinated observation was conducted in 2015 by the Sea State DRI program funded by the Office of Naval Research during the period from 30 September to 9 November 2015 in the Beaufort Sea (Thomson et al. 2019). The extensive study of the air-ice-ocean-wave system revealed that the Arctic ocean is becoming more "seasonal" and impacts of episodic wave events during autumn are imprinted in the winter sea-ice. Moreover, in the western Arctic Ocean, the evidence is acquired to show the remote influence of the Pacific waters in delaying the sea-ice advance triggered by a rare episodic weather event (Kodaira et al. 2020b). In essence, the nature of wave and ice interactions drastically varies from year to year. New observations inevitably provide new knowledge.

Japan, as being an observer of the Arctic Council, is determined to contribute to the scientific research of the Artic to clarify the mechanisms of its environmental changes (Kohno 2018[1]). Two research initiatives funded by the Ministry of Education, Culture, Sports, Science, and Technology (MEXT) were completed; GRENE (Green Network of Excellence) Program from 2011 to 2016 and the Arctic Challenge for Sustainability (ArCS) from 2015 to 2020. A new 5-year program ArCS-II will start in 2020. The program encompasses science, engineering, and social science research. During the ArCS program, several Arctic expeditions were conducted by the R/V Mirai of the Japan Agency for Marine-Earth Science and Technology (JAMSTEC). Among those cruises, three wave-observations were conducted in 2016, 2018, and 2019. We here summarize the collected knowledge from these expeditions and conclude that the largest missing piece is yet the knowledge of where the sea-ice is.

In section 2, a brief overview will be provided regarding wave modeling in the Arctic Ocean in an effort to identify possible sources of uncertainty. The aim of the 2016 expedition, unlike the Sea State DRI, was to validate wave model outputs in the open waters. Coincidentally, two storm events caused by passing depression was observed by the two buoys. The study of these events led to the depiction of the Arctic Ocean transitioning from inland-water-like open waters to basin-wide open waters encompassing the storm. The overview of these results will be presented in section 3. The second expedition conducted in 2018 included unique repeat transect observations across the marginal ice zone. 12-day repeated observations and the associated modeling study revealed that the biggest uncertainty of the modeled wavefield is not the wave-ice interaction physics but the lack of precise knowledge of the ice edge location, ice concentration, and the types of sea-ice. The conjecture will be augmented by preliminary analysis results from the 2019 observation in which another MIZ transect observations were conducted. These results will be detailed in section 4. And finally, a concluding remark will be presented in section 5.

2. Sources of uncertainty in wave-in-ice modeling

Waves evolve in the ocean by the action of wind forcing and its evolution is characterized by the concurrent increase of energy and wave period. The fetch law first presented by Sverdrup

[1] https://www.mofa.go.jp/files/000410409.pdf

and Munk (1946) and can be derived from a coupled equation of the peak energy density $\tilde{e}$ and the wave group velocity $\tilde{c}_g$ of the wind waves (Tulin et al. 1996):

$$\frac{\partial \tilde{e}}{\partial t} + \tilde{c}_g \frac{\partial \tilde{e}}{\partial x} = -\tilde{e}\frac{\partial \tilde{c}_g}{\partial x} + \dot{e}_w - D_b \quad \textbf{[1]}$$

$$\frac{\partial \tilde{c}_g}{\partial t} + \tilde{c}_g \frac{\partial \tilde{c}_g}{\partial x} = \gamma \tilde{c}_g \frac{D_b}{\tilde{e}} \quad \textbf{[2]}$$

Here, $\dot{e}_w$ is the time rate of energy transfer from the wind and D_b is the time rate of energy dissipation due to breaking. The somewhat mysterious $\gamma \tilde{c}_g\, D_b/\tilde{e}$ term derives from a scaling consideration and a heuristic choice of a functional form seeking a solution of power law (Fontaine 2013). It represents the excess of momentum to the energy loss of wave breaking, and the positive sign of the γ assures that the system downshifts (e.g. Tulin and Waseda 1999).

Let us now consider an appropriate modification of the dual equation for waves propagating under sea-ice. The wind pumping $\dot{e}_w$ is often ignored but there is observational evidence that waves grow under sea-ice; under fast ice (Crocker and Wadhams 1988), and in the MIZ (Gemmrich et al. 2018). More recently, waves under grease ice were found to grow under the action of wind (Kodaira et al. 2020a). In fact, there is no reason not to believe that the growth mechanism of Miles type or a sheltering mechanism would work. Both mechanisms can be associated with a variation of surface normal pressure. Indeed, the growth of waves under grease ice or ice sheet by wind may resemble the growth of mechanically generated waves in which the short wind-wave ripples are suppressed by surfactants (Mitsuyasu and Honda 1982). However, the majority of the study focuses on the identification of the dissipation term D_b regardless of the presence of wind. Thus, *the neglect of the wind pumping* is a source of uncertainty that indirectly affects the accuracy of the wave modeling through the inappropriate dissipation rate.

Next, the expression for the dissipation needs to be changed. When the sea surface is not fully packed by ice-floe the breaking energy loss may be present, but otherwise, the loss of wave energy is primarily due to non-breaking causes such as the transfer of energy to the ice motion or ice deflection, and turbulent dissipation due to differential velocity between ice and water (Voermans et al. 2019). The D_b term thus depends on the type of sea-ice and ice concentration. The dissipation rate or the attenuation rate for different types of sea ice are formulated and implemented in the third generation wave models. However, in most cases, *attenuation rates are estimated without distinguishing the type of sea ice*. This is a large source of uncertainty and the numerous parameters of the attenuation rate merely serve as tuning nobs (Nose et al. 2020).

The spectral down or upshifting expressed in terms of equation [2] derives from the conservation of wave momentum:

$$\frac{\partial}{\partial t}\left(\frac{\tilde{e}}{\tilde{c}}\right) + \frac{\partial}{\partial x}\left(\frac{\tilde{e}}{2}\right) = \Delta M \quad \textbf{[3]}$$

where ΔM is the rate of change of momentum. When the energy is lost as a propagating wave, the lost momentum can be expressed as $\Delta M = -D_b/\tilde{c}$ and equation [2] becomes identical to [1] without wind pumping; no down or upshifting occurs. Therefore, to express downshifting due to wave breaking, the parameter γ was introduced to represent energy loss, not in the form of propagating waves. From various observations, the averaged wavelength is considered to lengthen as the waves propagate into the sea covered by packed ice (e.g. Collins et al. 2017). In which case, the expression $\gamma\tilde{c}_g D_b/\tilde{e}$ may be appropriate but a different choice of γ is warranted. Now, in case of wave scattering by ice floes, ΔM represents reflected wave momentum. Indeed, the ΔM is equivalent to the force acting on the sea ice. So, the excess momentum can be expressed as $\Delta M = -\alpha(\tilde{e}/\tilde{c})$ where α is the reflection coefficient which depends on the combination of ice concentration and relative size of the ice floe to the wavelength. Since $\tilde{c}$ of the reflected wave does not change, this term will not appear in equation [2]. In other words, the wave scattering does not contribute to the spectral downshifting. However, the α is the attenuation rate of the wave energy due to scattering and therefore $-\alpha\tilde{e}$ appears on the right-hand side of [1].

Finally, by imposing boundary conditions, modified equations [1] and [2] can be integrated to obtain a fetch law. This seems like an easy task but it turns out that the largest source of uncertainty in wave modeling in the Arctic Ocean is the boundary condition. In the following sections, we first present a case when the lateral boundary condition is unimportant. The large wave event is caused by an Arctic Cyclone whose scale is smaller than or equivalent to the open water area. In this case, the uncertainty of the wave estimate depended largely on the surface boundary condition, i.e. the wind. The next case is regarding the waves in the marginal ice zone. In this case, the lateral boundary condition is the dominant source of uncertainty. To our surprise, the satellite-derived sea ice concentration was erroneous and the possible reason for that will be discussed based on observed in-situ sea ice concentrations.

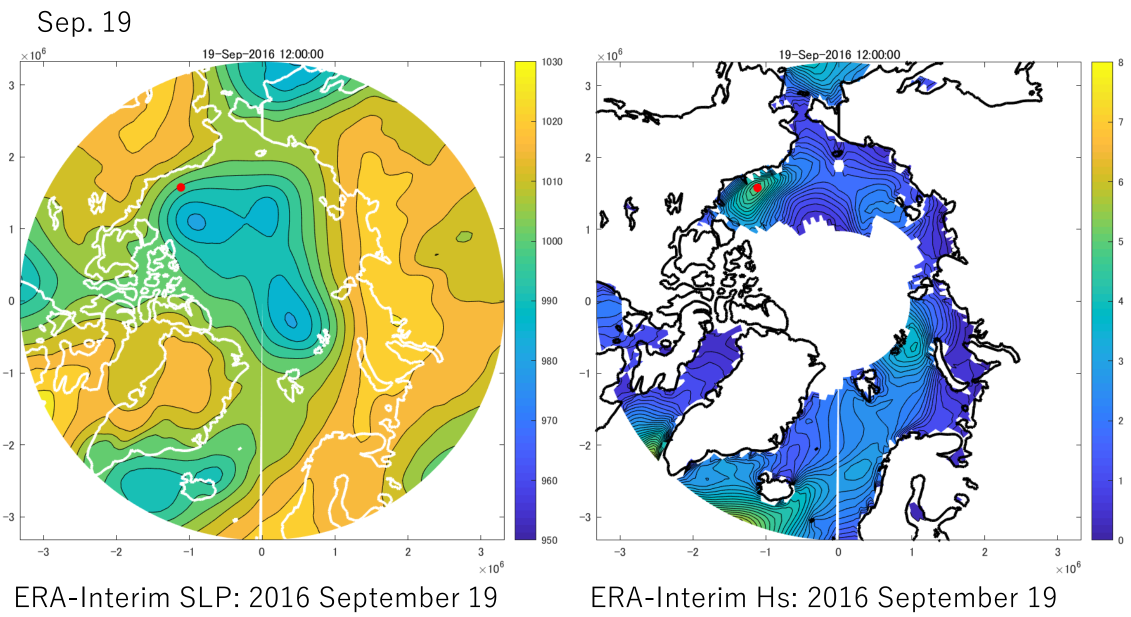

Figure 1. Sea level pressure (left) and the significant wave field (right) from ERA-Interim when the highest wave (denoted by the red dot) in 2016 September occur in the Beaufort Sea.

Our study showed that there is no discernible evidence that the strength of the AC is enhancing over the last 40 years. Moreover, for the particular case shown in Figure 1, the upwind open water was wide open and the effective fetch was not affected by the ice-edge location. Therefore, the removal of the sea-ice from the wave model had practically no effect on the estimated wave heights (Nose et al. 2018). This remarkable finding that the lateral sea-ice boundary condition does not affect the wave modeling is a consequence of the Arctic Ocean losing its Mediterranean nature for the ocean wave development and that it started to bear the character of an ocean basin encompassing the storms.

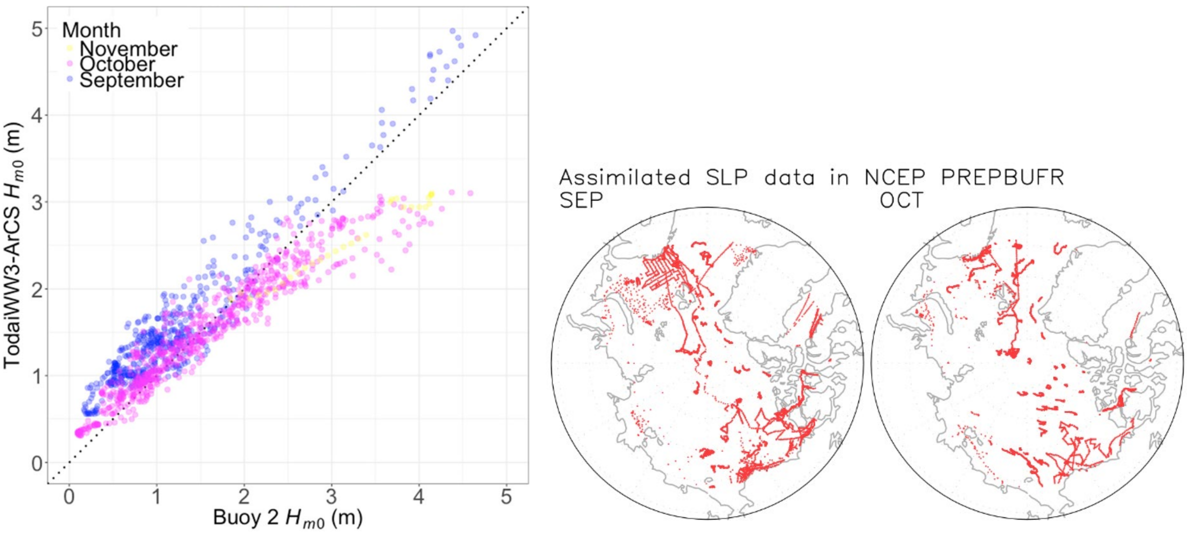

Figure 2. (left) Scatter plots of the significant wave heights from the model (TodaiWW3-ArCS) and the buoy in September (blue), October (magenta) and November (yellow) of 2016. (right) The available in-situ sea level pressure data in September and November of 2016. The plates are adapted from Nose et al. (2018).

3. Open waters; transition from waves in inland water to waves in a basin

During the 2016 cruise, two wave buoys were deployed in the middle of the open waters off point Barrows. The buoys successfully measured waves from Sep. 10 to Nov. 2, 2016. Two extreme events were observed and the registered significant wave height reached around 5 m. Unlike the extreme events during the 2015 Sea State DRI expedition, the events were related to the passage of the Arctic Cyclones (AC) and not related to the enhanced easterly due to a strengthened high-pressure system. These observations led us to look into historical events and learned that as the open water area enlarges, the extreme wave height and wind speed concurrently increase (Waseda et al. 2018). During the 2016 buoy observation, the two ACs developed near the north pole, migrated south, and gradually veered eastward. The area with enhanced waves is thus located at the south of the cyclone which coincided with the open water area (Figure 1).

Under conditions when fetch is not limited, the uncertainty of wave estimates originate from the surface boundary condition. The wave model simulations based on NOAA WAVEWATCH III® were executed and compared against buoy observations (Figure 2). Notably, the accuracy of the September estimates superseded the October estimates. While the September estimates well-correlated with the buoy observation up to the highest waves observed around 5 m, in October, the model largely underestimated the significant wave height. The conjecture was unaffected by the presence of sea-ice in the model. After some sensitivity tests, we have finally come to the conclusion that the reason for the deteriorated wave estimates in October is the lack of observational data to correct the reanalysis winds. Both CFSRv2 and ERA-I winds were used to force the wave model and both showed similar tendencies. This was further confirmed with ERA-I and ERA-5 wave reanalysis as well. All the wind products are assimilating the same in-situ data. For example, in October, the number of sea-level pressure data reduced by more than 20% from September. Considering the shortages of atmospheric observational data in the Arctic Ocean, it is known that the accuracy of the reanalysis wind field improves when additional observational data is made available (Inoue et al. 2009, 2013, 2015). We, therefore, conjectured that the model underestimation of the October 2016 wave field in the Beaufort Sea is because of the quality of the wind.

4. Marginal Ice Zone

In 2018, a unique repeated MIZ transect observation was conducted for 12 days by R/V Mirai from Nov 9 to Nov 20 in the Chukchi Sea (Inoue 2018). Two buoys were deployed on Nov 6 and the one closest to the marginal ice zone survived whereas the one in the open water failed after deployment for an unknown reason. The ship-born microwave wave gauge provided in-situ wave data throughout the MIZ transect observation. The anomalously warm Chukchi Sea SST delayed the autumn refreezing even under favorable off-ice wind conditions (Kodaira et al. 2020b) allowing this unique MIZ observation in November. While the daylight was limited, the sequence of sea-ice images showed a gradual increase of ice floe size during the 12 days yet revealing the presence of patches of the packed ice field and open water. This motivated us to compare the visual impression against satellite radiometer derived sea ice concentration (s.i.c.) (Nose et al. 2020). To our surprise the s.i.c. derived from two different satellites and four different algorithms showed variability much larger than we have anticipated. An example of the boundary of the MIZ denoted by s.i.c. 0.85 (dotted lines) are shown in Figure 3 (left) for three different products. Particularly a notable difference is found between BST-AMSR2 and the others (ASI-3km and OSSISAF-SSMIS). A few hundred-kilometer difference in the MIZ boundary can result in a large difference in the estimated wave field. The uncertainty associated with the lateral boundary condition was compared against the uncertainty associated with the choice of wave-ice interaction physics (IC2, IC3, and IC5 of WWIII). The Quantile-Quantile plot of the uncertainty estimates defined as a supremum of the differences is shown in Figure 3 (right) comparing uncertainties due to lateral boundary condition (vertical axis) and the wave-ice interaction physics (horizontal axis). Clearly, the uncertainty associated with the satellite-derived s.i.c., as a lateral boundary condition, is the dominant factor. It is worthwhile to point out that the majority of the studies in existing literature fine-tunes the wave-ice interaction physics for the particular choice of satellite-derived s.i.c. Therefore, the tuned parameters may be suitable for that particular product but may not be suitable for the other product.

In 2019, a similar MIZ transect observation was conducted during the R/V Mirai cruise on October 17 to 25. In this cruise, two CMOS video cameras were installed on the upper deck of the ship to obtain stereo-image sequences. Here we present preliminary analysis results of the images. Stereo-reconstruction is not made and only the images from one camera are analyzed to estimate the s.i.c. Binary images were obtained from the gray scale images following a standardized technique similar to Zhang and Skjetne (2014). The s.i.c. was estimated as a fraction of the sea-ice area in the analysis domain. Image rectification to a Cartesian coordinate is not necessary but areas with low resolution was excluded from the analysis.

One example is shown to highlight the significance of the sub-grid scale modeling of the wave-ice interaction. The 20-minute video sequence was obtained as the ship navigated at around 5 knots, thereby covering the distance of about 3 km. The ship track (in black) is overlaid on top of the BOOTSTRAP satellite-derived s.i.c. map (Figure 4 upper left). The s.i.c. was estimated every minute and a time series is obtained showing how the s.i.c. change along the cruise track (Figure 4 upper right). The s.i.c. of around 0.95 and 0.2 correspond to fields covered with pancake ice (Figure 4 lower left) and ice band open water area (Figure 4 lower right), respectively. Apparently, the imaging view is limited to only one side of the ship. Following a protocol such as ASPeCT, the s.i.c. should be an average of the ice fraction within the visible area covering a few kilometers distance from the ship. It is then appropriate to average the s.i.c. time-series to compare against visual observation, which will be roughly 0.6 or so. This value, equivalent to the visual observation, is larger than the two satellite products which range around 0.2-0.3 in this case (Figure 4 upper right). This difference is not an indication of a systematic bias of the satellite product and the difference in other cases varied. On average, there seemed to be a difference of about 10 km in the ice edge location between satellite data and the in-situ image-based analysis.

What is more important is the large deviation of the s.i.c. within the cruise track. It is of course well known that the sea ice field is patchy but as in the ASPeCT protocol, s.i.c. was reported only as an average and the scale and extent of the patchiness are not documented. The scale, however, is close to the surface waves, and therefore, cannot be neglected. The patchiness of the ice field is equivalent to the gustiness of the wind. Such sub-grid scale forcing is not necessarily taken into consideration in the third-generation wave model, but for wave propagation under the sea-ice field, the consideration of the patchiness seems critical. More work is warranted.

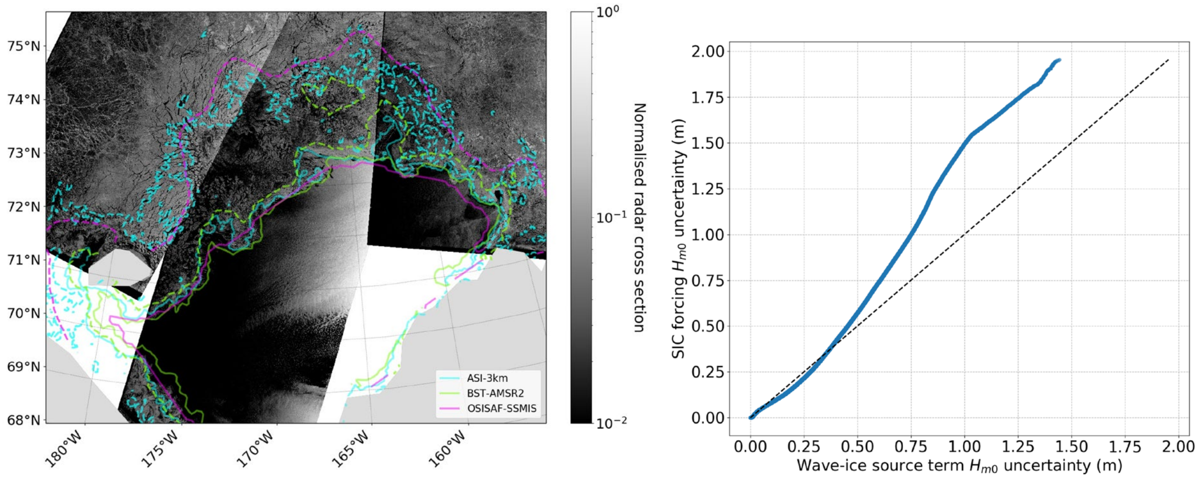

Figure 3. (left) Sea ice concentration contours (0.85 dashed and 0.15 solid lines) from three different satellite products (AIS-3km, BST-AMSR2, OSSOSAF-SSMIS) are overlaid on top of the Sentinel-1 Normalized Radar Cross Section image; (right) Q-Q plot of uncertainty estimates from the sensitivity wave model runs changing the s.i.c. products (vertical axis) and the wave-ice physics (horizontal axis). The plates are adapted from Nose et al. (2020)

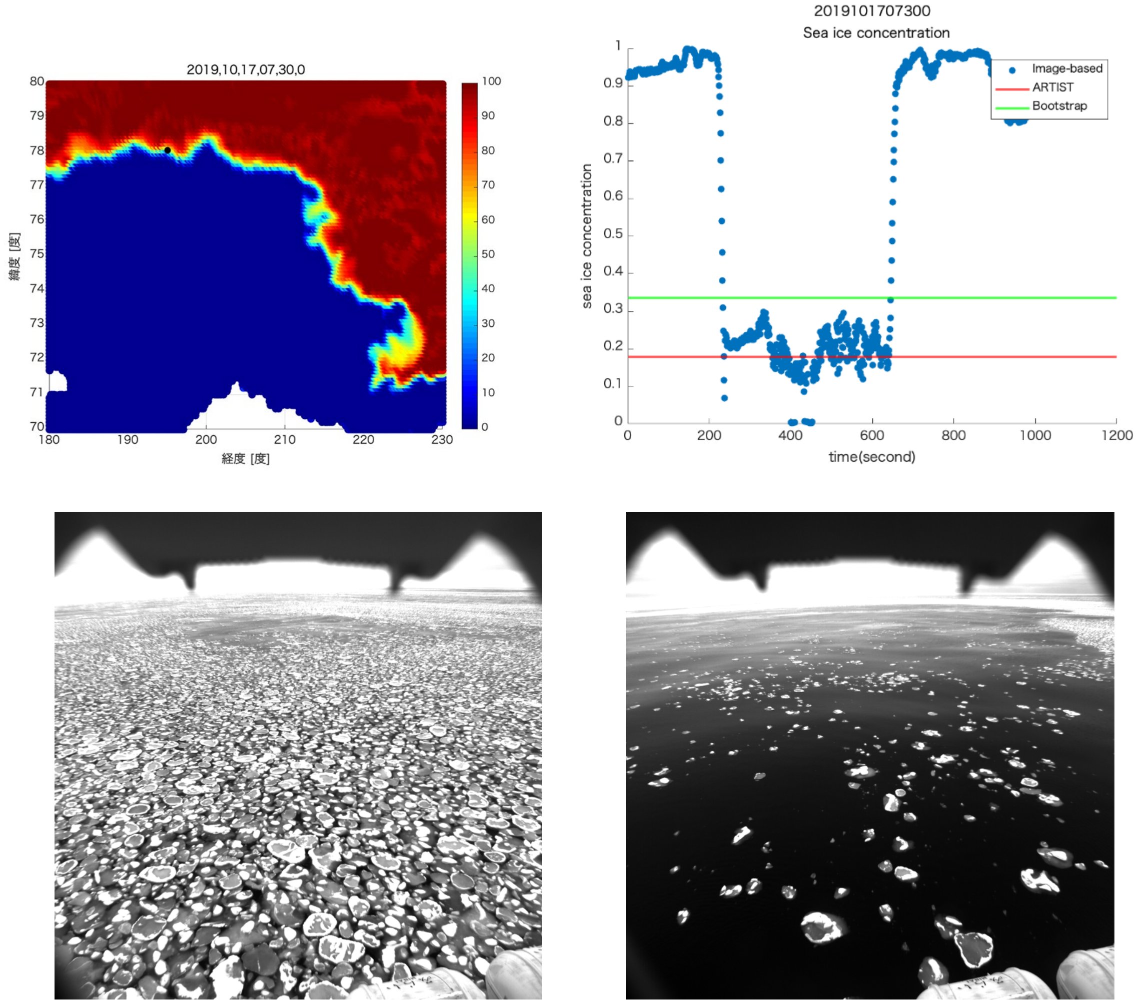

Figure 4. (upper left) Satellite-derived (BOOTSTRAP) s.i.c.; (upper right) Time series of image-based s.i.c., 20 minutes long at a minute interval; (lower left) An image of the pancake ice field; (lower right) An image of open water.

5. Concluding remark

Causes of uncertainty in wave modeling in the Arctic Ocean were discussed in this paper. We have identified the following:

i) The neglect of wind pumping under sea-ice coverage
ii) The neglect of sea ice type distinction and subgrid-scale patchiness
iii) Accuracy of surface boundary condition
iv) Accuracy of lateral boundary condition

The comparison of in-situ image-based s.i.c. against satellite-derived products revealed that the type of ice and the sea ice concentration changes a lot within 3 km or so. Such patchiness of the ice field is not taken care of in the wave modeling yet and should be considered in the future. However, it turns out that the largest source of error, at this point, was the lateral boundary condition provided by the satellite-derived s.i.c. Improvement of the s.i.c. estimates from satellite data is crucial as the sea ice field in the Arctic Ocean is changing year to year and a new set of calibration and validation campaign might be needed.

Acknowledgments
The first author acknowledges T. Toyota for his insightful discussion about wave and ice interaction. The work was conducted under sponsorship of the Japanese Ministry of Education, Culture, Sports, Science, and Technology through the ArCS and ArCSII project and JSPS KAKENHI Grant Number JP 16H02429 and 19H00801.

References

Collins, C. O., Rogers, W. E., & Lund, B. (2017). An investigation into the dispersion of ocean surface waves in sea ice. Ocean Dynamics, 67(2), 263-280.

Crocker, G. B., & Wadhams, P. (1988). Observations of wind-generated waves in Antarctic fast ice. Journal of physical oceanography, 18(9), 1292-1299.

Fontaine, E. (2013). A theoretical explanation of the fetch-and duration-limited laws. Journal of physical oceanography, 43(2), 233-247.

Gemmrich, J., Rogers, W. E., Thomson, J., & Lehner, S. (2018). Wave evolution in off‐ice wind conditions. Journal of Geophysical Research: Oceans, 123(8), 5543-5556.

Inoue J, Enomoto T, Miyoshi T, Yamane S (2009) Impact of observations from Arctic drifting buoys on the reanalysis of surface fields. Geophys Res Lett 36(8)

Inoue J, Enomoto T, Hori ME (2013) The impact of radiosonde data over the ice-free Arctic Ocean on the atmospheric circulation in the Northern Hemisphere. Geophys Res Lett 40(5):864–869.

Inoue J, Yamazaki A, Ono J, Dethloff K, Maturilli M, Neuber R, Edwards P, Yamaguchi H (2015) Additional Arctic observations improve weather and sea-ice forecasts for the Northern Sea Route. Scientific Reports 5:16,868.

Inoue, J. R/V Mirai Cruise Report MR18-05C. (2018)

Kodaira, T., Waseda, T., Nose, T., Sato, K., Inoue, J., Voermans, J., & Babanin, A. (2020a). Observation of on-ice wind waves under grease ice in the western Arctic Ocean. Polar Science, 100567. https://doi.org/10.1016/j.polar.2020.100567

Kodaira, T., T. Nose, T. Waseda and J. Inoue (2020b) Record high Pacific Arctic seawater temperatures and delayed sea-ice advance in response to episodic atmospheric blocking, Scientific Reports, submitted

Mitsuyasu, H., & Honda, T. (1982). Wind-induced growth of water waves. Journal of Fluid Mechanics, 123, 425-442.

Nose, T., Webb, A., Waseda, T., Inoue, J., and Sato, K. (2018) Predictability of storm wave heights in the ice-free Beaufort Sea, Ocean Dynamics, 625 68, 1383–1402

Nose, T., T. Waseda, T. Kodaira, and J. Inoue (2020) Satellite retrieved sea ice concentration uncertainty and its effect on modelling wave evolution in marginal ice zones, The Cryosphere, 14(6), 2029-2052. https://doi.org/10.5194/tc-14-2029-2020

Sverdrup, H. U., & Munk, W. H. (1946). Empirical and theoretical relations between wind, sea, and swell. Eos, Transactions American Geophysical Union, 27(6), 823-827.

Thomson, J., Ackley, S., Girard‐Ardhuin, F., Ardhuin, F., Babanin, A., Boutin, G., ... & Fairall, C. (2018). Overview of the arctic sea state and boundary layer physics program. Journal of Geophysical Research: Oceans, 123(12), 8674-8687.

Tulin, M.P., Y. Yao, A.K. Magnusson (1996). The Evolution and Structure of Energetic Wind Waves, The Sixth International Offshore and Polar Engineering Conference, 26-31 May, Los Angeles, California

Tulin, M. P., & Waseda, T. (1999). Laboratory observations of wave group evolution, including breaking effects. Journal of Fluid Mechanics, 378, 197-232.

Voermans, J. J., Babanin, A. V., Thomson, J., Smith, M. M., & Shen, H. H. (2019). Wave attenuation by sea ice turbulence. Geophysical Research Letters, 46(12), 6796-6803.

Waseda, T., Webb, A., Sato, K., Inoue, J., Kohout, A., Penrose, B., & Penrose, S. (2018). Correlated increase of high ocean waves and winds in the ice-free waters of the Arctic Ocean. Scientific reports, 8(1), 1-9.

Zhang, Q., & Skjetne, R. (2014). Image processing for identification of sea-ice floes and the floe size distributions. IEEE Transactions on geoscience and remote sensing, 53(5), 2913-2924.

25th IAHR International Symposium on Ice
Trondheim, June 14 to 18, 2020

Theoretical model for predicting the breakup of ice covers due to wave ice interaction

Changpeng Zhang and Xin Zhao*
Department of Mechanics, Beijing Institute of Technology, Beijing, 100071, China
**Corresponding author, Email: 6120160101@bit.edu.cn*

Abstract:
An approximate solution for wave transmission and reflection between open water and a finite viscoelastic ice cover is developed in present study, in which both the water and the ice cover were treated as a continuum, each governed by its own equation of motion. The interface conditions included matching velocity and stresses between the two continua. The analysis is useful for modeling the wave-in-ice climate on a geophysical scale. In this study, only two modes of the dispersion relation are considered and the horizontal boundary conditions are approximated by matching the mean values. The reflection and transmission coefficients are determined for simplified cases to compare with earlier theories. Behaviors of the resonance are then obtained for a range of pure elastic ice covers. The effect of viscosity is also be investigated for viscoelastic ice covers. According to the above wave-ice interaction model, the stress and strain are calculated in the ice cover. By using the stress failure criterion, the breakup condition of ice covers with different thicknesses and lengths under the interaction of waves and sea ice is determined. Finally, a dynamic evolution model of ice floe size distribution function in the marginal ice zone is established.

Keywords: Wave Propagation; Viscoelastic; Transmission and Reflection Coefficients, Finite Ice Cover, Ice breakup

1. Introduction

Present existing operational wave models, such as WAVEWATCH III (WW3), can provide the viscous attenuation model by ice covers (Tolman, 2014). However, the viscoelastic sea ice model (Wang and Shen, 2010) adopted in current WW3 needs parametrization for the viscoelastic parameters. The shear modulus in the viscoelastic model is critical to the size of the ice floe and ice concentration. The accuracy for estimating the size distribution of ice floes will strongly influence the computational accuracy of WW3. Therefore, a theoretical model for wave induced ice breakup is needed to simulate the size distribution in the marginal ice zone.

In the previous studies, Meylan and Squire (1993, 1994) calculated this problem using the semi-infinite thin elastic plate model method and Green function method. They found a resonance behavior for wave amplitude. In present study, we also investigate this phenomenon with the viscoelastic model and two-mode approximate method. The results are consistent with the previous studies by Meylan and Squire (1993, 1994). Using such viscoelastic model, Wang and Shen (2011) calculated the reflection and transmission of wave energy from open water into a semi-infinite ice cover with the two-mode approximate method. Further, Zhao and Shen (2013) applied the same method to calculate the wave reflection and transmission by two adjacent inhomogeneous ice covers. The two-mode approximate method was shown to be efficient with certain accuracy recently (Zhao and Shen, 2015).

The organization of this paper is as follows. Section 2 briefly outlines the theoretical formulation of the viscoelastic model. In section 3, the approximation method is presented. Section 4 gives the result of special cases to compare with previous studies for pure elastic ice covers and viscoelastic covers. The discussion and conclusions are given in section 5. A linear wave regime is assumed in this study.

2. The theoretical formulation

2.1 Definition of the domain

The problem to be analyzed is two dimensional. The ice cover with finite length and thickness are assumed to be fully submerged. The coordinate system used in this study is shown in Fig. 1. The x direction is aligned with the incoming wave direction, and the z direction is opposite to gravity. The origin is set at the bottom of the leading edge of the ice cover. As shown in Fig. 1, there are four regions: ice region 1; water region 2, 3 and 4. A monochromatic wave propagates from left to right. The ice thickness for region 1 is h. The total depth of the domain is H.

2.2 Governing equation

For the ice cover, we use a Voigt viscoelastic continuum model shown below (Wang and Shen, 2011):

$$\tau_{mn} = -p\delta_{mn} + 2GS_{mn} + 2\rho_{ice}\nu\dot{S}_{mn}, \qquad \textbf{[1]}$$

Where ρ_{ice} is the density of the ice layer; τ_{mn}, S_{mn} and $\dot{S}_{mn}$ represent the stress tensor, the strain tensor and the strain rate tensor, respectively; m and n represent x or z; G and ν are the effective shear modulus and the effective kinematic viscosity of the ice layer, respectively; p is the pressure and δ_{mn} the Kronecker delta. The equation of motion is

$$\frac{\partial \boldsymbol{U}_i}{\partial t} = -\frac{1}{\rho_{ice}}\nabla p_i + \nu_e \nabla^2 \boldsymbol{U}_i + \boldsymbol{g} \quad i = 1, \qquad \textbf{[2]}$$

Where $\boldsymbol{U}_i$ is the velocity vector, $\boldsymbol{g}$ the gravitational acceleration, and ν_e the viscoelastic parameter:

$$\nu_e = \nu + iG/\rho_{ice}\omega \quad i = 1, \qquad \textbf{[3]}$$

In which, ν and G are the effective parameters in ice region, and ω is the angular frequency of the incoming wave. Using the decomposition with potential function ϕ_i and stream function ψ_i for the velocity (Lamb, 1932),

$$\boldsymbol{U}_i = -\nabla\phi_i + \nabla \times (0, \psi_i, 0) \quad i = 1, \qquad \textbf{[4]}$$

we obtain

$$\nabla^2\phi_i = 0 \qquad \textbf{[5]}$$

$$\frac{\partial\psi_i}{\partial t} - \nu_e\nabla^2\psi_i = 0 \qquad \textbf{[6]}$$

$$\frac{\partial\phi_i}{\partial t} - \frac{p_i}{\rho_{ice}} - \Phi = 0 \quad i = 1 \qquad \textbf{[7]}$$

Here, $\Phi = gz$ is the gravitational potential.

For water regions 2, 3 and 4, we assume an inviscid fluid. The governing equations are

$$\frac{\partial\boldsymbol{U}_i}{\partial t} = -\frac{1}{\rho_{water}}\nabla p_i + \boldsymbol{g}, \qquad \textbf{[8]}$$

$$\nabla^2\phi_i = 0, \qquad \textbf{[9]}$$

$$\frac{\partial\phi_i}{\partial t} - \frac{p_i}{\rho_{water}} - \Phi = 0 \quad i = 2, 3, 4. \qquad \textbf{[10]}$$

The water velocity is related to the velocity potential only:

$$\boldsymbol{U}_i = -\nabla\phi_i \quad i = 2, 3, 4. \qquad \textbf{[11]}$$

In terms of the Fourier modes, the solution for a sinusoidal wave with two modes can be written as (Wang and Shen, 2011)

$$\phi_i(x, z, t) = \sum_{n=1}^{2}(A_i(n)\cosh k_i(n)z + B_i(n)\sinh k_i(n)z)e^{ik_i(n)x}e^{-i\omega t}, \qquad \textbf{[12]}$$

$$\psi_i(x, z, t) = \sum_{n=1}^{2}(C_i(n)\cosh \alpha_i(n)z + D_i(n)\sinh \alpha_i(n)z)e^{ik_i(n)x}e^{-i\omega t}, \qquad \textbf{[13]}$$

for the ice region $i = 1$ and $0 \le z \le h$, and

$$\phi_i(x, z, t) = \sum_{n=1}^{2} E_i(n)\cosh k_i(n)\,(z + H)e^{ik_i(n)x}e^{-i\omega t}, \qquad \textbf{[14]}$$

for the water region $i = 2$ and $-H \le z \le 0$.

$$\phi_i(x, z, t) = E_i \cosh k_0\,(z + H)e^{ik_0(n)x}e^{-i\omega t}, \qquad \textbf{[15]}$$

for the water region $i = 3, 4$ and $-H \le z \le 0$. The coefficients $A_i(n)$, $B_i(n)$, $C_i(n)$, $D_i(n)$, and $E_i(n)$ are complex constants. As shown in Zhao and Shen (2013) Appendix B, the solution of these constants can be obtained by matching the vertical boundary conditions. In the above, ${\alpha_i}^2(n) = {k_i}^2(n) - i\omega/\nu_e$ for $i = 1$ and $n = 1{,}2$ from Eq. (6). Here $k_i(n)$ is the wave number for ice-covered region.

2.3 Boundary conditions in the horizontal direction

We now proceed to determine the horizontal boundary conditions between open water region and ice cover region. In the horizontal direction between the two regions, we need to match the velocities, and stresses.

a) Water-Water interface

The boundary conditions between water region 2 and 3 include continuity of the potential and the horizontal velocity

$$\phi_2(0, z) = \phi_3(0, z), \ -H \le z \le 0, \qquad \textbf{[16]}$$

$$\frac{\partial \phi_2(0,z)}{\partial x} = \frac{\partial \phi_3(0,z)}{\partial x}, \ -H \le z \le 0, \qquad \textbf{[17]}$$

For water region 2 and 4,

$$\phi_2(L, z) = \phi_4(L, z), \ -H \le z \le 0, \qquad \textbf{[18]}$$

$$\frac{\partial \phi_2(L,z)}{\partial x} = \frac{\partial \phi_4(L,z)}{\partial x}, \ -H \le z \le 0, \qquad \textbf{[19]}$$

b) Water-Ice interface

Between water region 3 and ice region 1, the kinematic condition is

$$u_1(0, z) = u_3(0, z), \ 0 \le z \le h. \qquad \textbf{[20]}$$

Likewise, the dynamical boundary condition is

$$\tau_{xx1}(0, z) = \tau_{xx3}(0, z), \ 0 \le z \le h. \qquad \textbf{[21]}$$

For water region 4 and ice region 1,

$$u_1(L, z) = u_4(L, z), \ 0 \le z \le h, \qquad \textbf{[22]}$$

$$\tau_{xx1}(L, z) = \tau_{xx4}(L, z), \ 0 \le z \le h. \qquad \textbf{[23]}$$

To summarize, the following equations are the approximated eight horizontal boundary conditions in terms of the potential and stream functions. As shown in Zhao and Shen (2013), Eqs. (16-23) may be approximated by the following equations, where the pointwise matching at interfaces are replaced by matching only the mean values over the interface.

$$\int_{-H}^{0} \phi_2(0, z) dz = \int_{-H}^{0} \phi_3(0, z) dz, \qquad \textbf{[24]}$$

$$\int_{-H}^{0} \frac{\partial \phi_2(0,z)}{\partial x} dz = \int_{-H}^{0} \frac{\partial \phi_3(0,z)}{\partial x} dz, \quad \textbf{[25]}$$

$$\int_{-H}^{0} \phi_2(L,z) dz = \int_{-H}^{0} \phi_4(L,z) dz, \quad \textbf{[26]}$$

$$\int_{-H}^{0} \frac{\partial \phi_2(L,z)}{\partial x} dz = \int_{-H}^{0} \frac{\partial \phi_4(L,z)}{\partial x} dz, \quad \textbf{[27]}$$

$$\int_{0}^{h} \left(-\frac{\partial \phi_3(0,z)}{\partial x}\right) dz = \int_{0}^{h} \left(-\frac{\partial \phi_1(0,z)}{\partial x} - \frac{\partial \psi_1(0,z)}{\partial z}\right) dz, \quad \textbf{[28]}$$

$$\int_{0}^{h} i\omega\rho_{water}\phi_3(0,z) dz = \int_{0}^{h} \left[i\omega\rho_{ice}\phi_1(0,z) + 2\rho_{ice}\nu_e \left(-\frac{\partial^2 \phi_1(0,z)}{\partial x^2} - \frac{\partial^2 \psi_1(0,z)}{\partial x \partial z}\right)\right] dz\ , \quad \textbf{[29]}$$

$$\int_{0}^{h} \left(-\frac{\partial \phi_4(L,z)}{\partial x}\right) dz = \int_{0}^{h} \left(-\frac{\partial \phi_1(L,z)}{\partial x} - \frac{\partial \psi_1(L,z)}{\partial x}\right) dz, \quad \textbf{[30]}$$

$$\int_{0}^{h} i\omega\rho_{water}\phi_4(L,z) dz = \int_{0}^{h} \left[i\omega\rho_{ice}\phi_1(L,z) + 2\rho_{ice}\nu_e \left(-\frac{\partial^2 \phi_1(L,z)}{\partial x^2} - \frac{\partial^2 \psi_1(L,z)}{\partial x \partial z}\right)\right] dz\ , \quad \textbf{[31]}$$

An improved matching method using a variational method was provided in Zhao and Shen (2015). It was found that results from the approximation method was very close to the more accurate results from the variational method. We thus adopt the approximate method in the present study.

3. Solutions

In general, the full solution of the wave propagation through a viscoelastic cover consists of an infinite series of modes, each with a different wave number, all of them roots of the dispersion relation. Truncation of this infinite series provides approximate solutions. Following Wang and Shen (2011), the two wave numbers closest to the open water case are chosen to form the approximate solution. Shown in Fig. 1 and Fig. 2, the incoming wave from water region 3 is represented by an incoming magnitude I. When entering the ice cover, multiple reflections between the leading and trailing edges occur. Each time partial reflection and transmission would take place until reaching a steady state. At which, the reflection back into the upstream open water is represented by R and the transmission forward into the downstream open water is represented by T. Within the ice cover, there is a superposition of forward and backward going wave components. These components are approximated by two modes only in this study. Thus the total potential function and the stream function in the ice covered region may be written in terms of these two modes as follows, where the individual modes denoted by $n = 1,2$.

$$\phi_1(x,z,t) = \sum_{n=1}^{2} T_n(A_1(n)\cosh k_1(n)z + B_1(n)\sinh k_1(n)z)e^{ik_1(n)x}e^{-i\omega t}$$
$$+ \sum_{n=1}^{2} R_n(A_1(n)\cosh k_1(n)z + B_1(n)\sinh k_1(n)z)e^{ik_1(n)x}e^{-i\omega t}; \quad \textbf{[32]}$$

$$\psi_1(x,z,t) = \sum_{n=1}^{2} T_n(C_1(n)\cosh \alpha_1(n)z + D_1(n)\sinh \alpha_1(n)z)e^{ik_1(n)x}e^{-i\omega t}$$
$$+ \sum_{n=1}^{2} R_n(C_1(n)\cosh \alpha_1(n)z + D_1(n)\sinh \alpha_1(n)z)e^{ik_1(n)x}e^{-i\omega t}; \quad \textbf{[33]}$$

$$\phi_2(x,z,t) = \sum_{n=1}^{2} T_n E_1(n) \cosh k_1(n)\,(z+H) e^{ik_1(n)x} e^{-i\omega t}$$
$$+ \textstyle\sum_{n=1}^{2} R_n E_1(n) \cosh k_1(n)\,(z+H) e^{ik_1(n)x} e^{-i\omega t}, \qquad \textbf{[34]}$$

And in the open water regions,

$$\phi_3(x,z,t) = \frac{ig \cosh k_0(z+H)}{\omega \cosh k_0(z+H)} \left(I e^{ik_0 x} + R e^{ik_0 x}\right) e^{-i\omega t}; \qquad \textbf{[35]}$$

$$\phi_4(x,z,t) = \frac{ig \cosh k_0(z+H)}{\omega \cosh k_0(z+H)} T e^{ik_0 x} e^{-i\omega t}. \qquad \textbf{[36]}$$

In the above,

$$\alpha_i^{\,2}(n) = k_i^{\,2}(n) - i\omega/\nu_{ei},\ i = 1 \text{ and } n = 1{,}2. \qquad \textbf{[37]}$$

The solution matrix for $A_i(n)$, $B_i(n)$, $C_i(n)$, $D_i(n)$ and the equation for solving $E_i(n)$ can be found in Zhao and Shen (2013) Appendix B. After which we can substitute the solutions of $A_i(n)$, $B_i(n)$, $C_i(n)$, $D_i(n)$, $E_i(n)$ into the horizontal boundary conditions to form eight linear equations for I, R, T, R_1, R_2, T_1, and T_2. Following the above steps, substituting equations (32-36) into equations (24-31) gives an over-determined system of eight equations involving only seven unknowns I, R, T, R_1, R_2, T_1, and T_2. We solve this using singular value decomposition method based on the least-square error method to find the pseudo-inverse. When matching the boundary conditions at the leading edge, we need to consider the phase change, $2k_1(n)L$, between R_1, R_2, T_1, and T_2. This is implemented by multiplying $e^{2k_1(n)L}$ to R_n in Eqs. (24), (25), (28), and (29).

4. Results

In this section we study the behavior of wave propagation involving pure elastic ice covers and viscoelastic ice covers. For all cases shown in this study, $\rho_{ice} = 917\,kg/m^3$, $\rho_{water} = 1000\,kg/m^3$, and $H = 1000\text{m}$.

We consider introducing different numbers of evanescent modes to obtain a more accurate solution, but Zhao and Shen's (2015) paper has proved that introducing evanescent waves or the third complex mode will not improve the result significantly. In addition, from the energy point of view, the third mode contains very little energy, so it can be removed. For the present model, two modes are sufficient for the calculation of transmission and reflection coefficients. They also compared the approximation method with the variational method. From the perspective of error analysis, compared with the exact solution of the variational method, the most significant error of the approximation method is from the first term. For this term with two modes, the error is slightly above 0.2%. By including 30 modes, the error drops to 0.1% (Zhao and Shen, 2015). Therefore, within the allowable error range, we can ignore the evanescent mode to save calculation time.

To compare with previous studies, we calculate the reflection and transmission coefficients with respect to the length of ice cover. Fig. 2 shows the effect of the ice thickness on reflection coefficients. The results are qualitatively agree with Meylan and Squire's results (1993, 1994). The shear modulus used in Fig. 2 is calculated from the Young's modulus $6GPa$ and Poisson ration 1/3, which are the same as Meylan and Squire (1994). The incoming wavelength is 100m, and the wave period is about $8s$ based on the deep water dispersion relation. The resonant behaviors are found in the reflection coefficients. For the thin ice cover with 1m ice thickness, the resonance occurs at nearly every half wavelength, and this is consistent with previous studies. Because the wavelength will become longer in the ice covered region, the resonant length of the ice cover will be longer than the half of the incoming wavelength. Fig. 3 also shows the transmission coefficient for $h = 2\text{m}$. We can find the reflection and transmission coefficients satisfy the relation $R^2 + T^2 = 1$ in Fig. 3a for zero viscosity. So when the resonance occurs the reflection coefficient approach to zero, and the transmission coefficient will be close to 1. Adding a large viscosity, such as the case in Fig. 3b, the reflection coefficient will be not change, but the transmission coefficient will decrease its amplitude by the viscous damping. The longer length of the ice cover will cause more viscous damping during the wave propagating in the ice cover.

In Fig. 4, we also plot the reflection and transmission coefficients with respect to the wave period for pure elastic cases. For the length of the ice cover varying from 10m to 1000m, the resonance behavior will be different. Compared with the reflection and transmission by the semi-infinite ice cover (Fox and Squire, 1990; Wang and Shen, 2011), we do not obtain the convergence trend by increasing the length of the ice cover. We find the longer length of the ice cover will produce more resonance behaviors in Fig. 4, which is consistent with Meylan and Squire (1994).

After comparing with previous results, we will calculate the elastic energy of the ice cover and determine the effective shear modulus for an ice field with many identical elastic ice floes. Firstly, we introduce the definitions of the stress τ, strain rate $\dot{\varepsilon}$, strain ε, and elastic energy U_e:

$$\tau_{xz} = \tau_{zx} = \rho_{ice} v_e \dot{\varepsilon}_{xz} = \rho_{ice} v_e \left(\frac{\partial u_1}{\partial z} + \frac{\partial w_1}{\partial x}\right); \quad \textbf{[38]}$$

$$\tau_{xx} = -p + \rho_{ice} v_e \dot{\varepsilon}_{xx} = -p + 2\rho_{ice} v_e \frac{\partial u_1}{\partial x}; \quad \textbf{[39]}$$

$$\tau_{zz} = -p + \rho_{ice} v_e \dot{\varepsilon}_{zz} = -p + 2\rho_{ice} v_e \frac{\partial w_1}{\partial z}; \quad \textbf{[40]}$$

$$\varepsilon_{xz} = -\frac{1}{i\omega} \dot{\varepsilon}_{xz}; \quad \textbf{[41]}$$

$$\varepsilon_{xx} = -\frac{1}{i\omega} \dot{\varepsilon}_{xx}; \quad \textbf{[42]}$$

$$\varepsilon_{zz} = -\frac{1}{i\omega} \dot{\varepsilon}_{zz}; \quad \textbf{[43]}$$

$$U_e = G \int_0^h \int_0^L (\varepsilon_{xx}\varepsilon_{xx}^* + 2\varepsilon_{xz}\varepsilon_{xz}^* + \varepsilon_{zz}\varepsilon_{zz}^*)\, dxdz. \quad \textbf{[44]}$$

We assume that the incident wave energy is given by the JONSWAP spectrum (Hasselmann e t al., 1973). given by:

$$E_{JONSWAP}(f) = \alpha g^2 2\pi^{-4} f^{-5} exp\left[-\frac{5}{4}\left(\frac{f}{f_{peak}}\right)^{-4}\right] \gamma^{exp\left[-\frac{1}{2}\left(\frac{f/f_{peak}-1}{\sigma}\right)^2\right]}, \quad \textbf{[45]}$$

where α is the energy parameter, γ is a peak-enhancement factor, and σ is a peak-width parameter ($\sigma = 0.07$ for $f \leq f_{peak}$ and $\sigma = 0.09$ for $f > f_{peak}$ to account for the slightly different widths on the two sides of the spectral peak), peak frequency f_{peak} is taken as 0.125. We input the JONSWAP spectrum to calculate the stress of a sea ice with a length of $500m$ and a thickness of $0.5m$, and we obtain the stress distribution of the sea ice. Fig 5 and Fig 6 show the stress distribution of the sea ice for pure elastic case and viscoelastic case respectively. It can be seen from the results in the figure that the maximum values (abs value) of stress τ_{xx} and stress τ_{zz} and stress τ_{xz} are located in the left half of the sea ice, that is, the side of wave incidence. With the depth of the incident wave, the stress value gradually decreases, and the maximum values of stress τ_{xx} and stress τ_{zz} are far greater than the maximum value of stress τ_{xz}. For stresses τ_{xx} and τ_{zz} in the case of pure elasticity and viscoelasticity, their maximum positions locate at same points along x direction, but their signs are changed. For shear stress τ_{xz}, we find their maximum positions locate at the points that stresses τ_{xx} and τ_{zz} nearly equal to zero, in the middle layer of the sea ice.

Based on the above analysis, a sea ice fracture model for the marginal ice zone (MIZ) caused by the stress-based can be established. According to the mechanical properties of sea ice, if waves cause enough stress in the sea ice, the sea ice will break. By using the proper instrumentation and experimental design, it is possible to measure the stress value at failure, and this stress value is the sea ice fracture threshold ($\tau_{threshold}$). We calculate the stress applied to the sea ice by the passing wave, and use the fact that we know the stress threshold at failure, to arrive at the MIZ sea ice fracture criterion, which can be written as: $\max(\tau_{xx}, \tau_{xz}, \tau_{zz}) \geq \tau_{threshold}$. We input the size distribution function of ice floes in the MIZ and calculate the break point of each sea ice according to the above fracture criterion. The size and number of multiple small ice floes can be obtained based on the ice breakup model. A new MIZ ice floes size distribution function can be calculated.

5. Discussion and Conclusions

Present study employs the viscoelastic model with the finite ice thickness and two-mode approximate method to investigate the reflection and transmission by a finite length ice cover. The resonance behavior is obtained for different ice length and wave period. The present results agree with previous studies of the thin elastic plate model (Meylan and Squire, 1993, 1994). We also show that the including of the large viscosity in the ice cover will damp the wave energy.

We also find that the maximum stress caused by waves on the ice cover lies on the upper and lower surface of the sea ice. Based on this, we present a two-dimensional model based on stress fracture criterion for predicting the ice floe breakup under ocean wave forcing in the MIZ. This model is designed to facilitate the prediction of the ice floe size. In this model, the original ice floe size distribution function and the wave spectrum are taken as the input, and the new ice floe size distribution function is taken as the output. Our findings provide a theoretical understanding of the wave-induced ice break-up process in the MIZ.

Acknowledgment

This work is supported in part by the National Natural Science Foundation of China, #41776194.

References

Fox, C. and Squire, V.A., 1990. Reflection and transmission characteristics at the edge of shore fast sea ice. J. Geophy. Res., 95:11629-11639.

Hasselmann, K., T. P. Barnett, E. Bouws, H. Carlson, D. E. Cartwright, K. Enke, J. A. Ewing, H. Gienapp, D. E. Hasselmann, P. Kruseman, A. Meerburg, P. Müller, D. J. Olbers, K. Richter, W. Sell and H. Walden, 1973. Measurements of wind-wave growth and swell decay during the Joint North Sea Wave Project (JONSWAP), Deutsch. Hydrogr. Z., Suppl., A8, 12, 95 pp.

Lamb, S. H., 1932. Hydrodynamics. Dover, New York.

Meylan, M., & Squire, V. A. 1993. Finite-floe wave reflection and transmission coefficients from a semi-infinite model. J. of Geophy. Res., 98: 12537-12542.

Meylan, M. and Squire, V. A., 1994. The response of ice floes to ocean waves. J. Geophy. Res., 99: 891-891.

Wang, R. and Shen, H.H., 2010. Gravity waves propagating into an ice-covered ocean: a viscoelastic model. J. Geophys. Res. 115, C06024.

Wang, R. and Shen, H.H., 2011. A continuum model for the linear wave propagation in ice-covered oceans: An approximate solution. Ocean Modeling, 38: 244-250.

Zhao, X. and Shen, H. H., 2013. Ocean wave transmission and reflection between two connecting viscoelastic ice covers: An approximate solution. Ocean Modelling, 71: 102-113.

Zhao, X. and Shen, H. H., 2015. Ocean wave transmission and reflection by viscoelastic ice covers. Ocean Modelling, 92: 1-10.

Figures

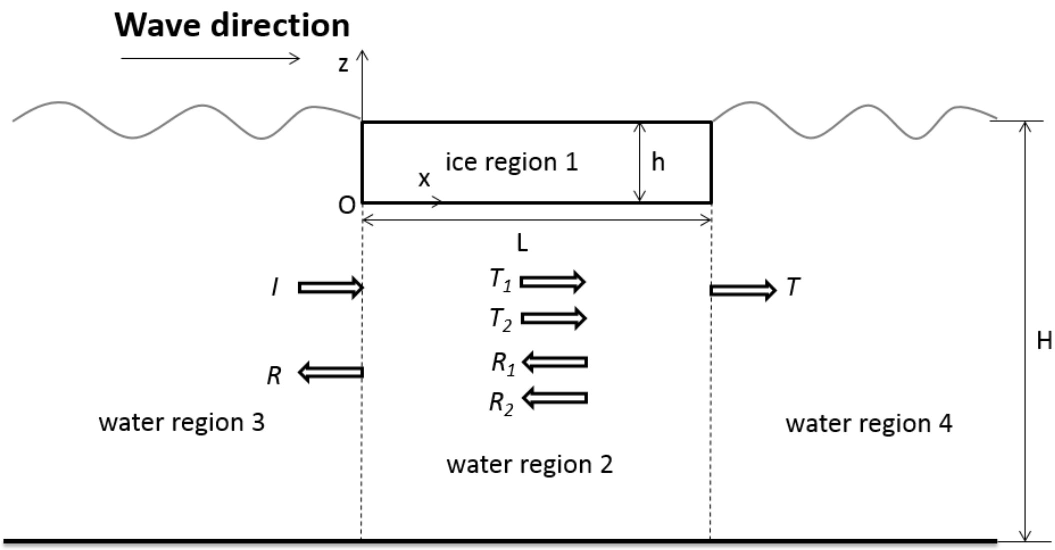

Figure 1. Schematic of the coordinate frame of the problem.

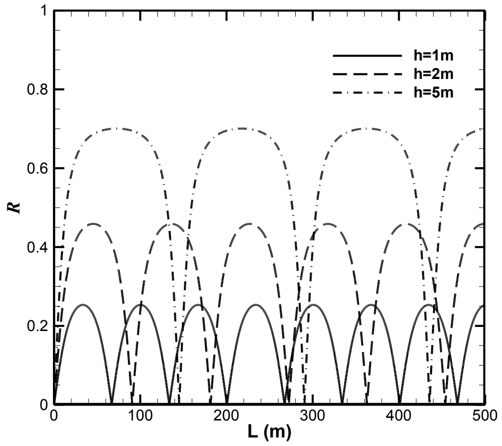

Figure 2. Reflection coefficients: $G = 2.3GPa$, $\upsilon = 0\, m^2/s$, $H = 1000$m, $T = 8s$.

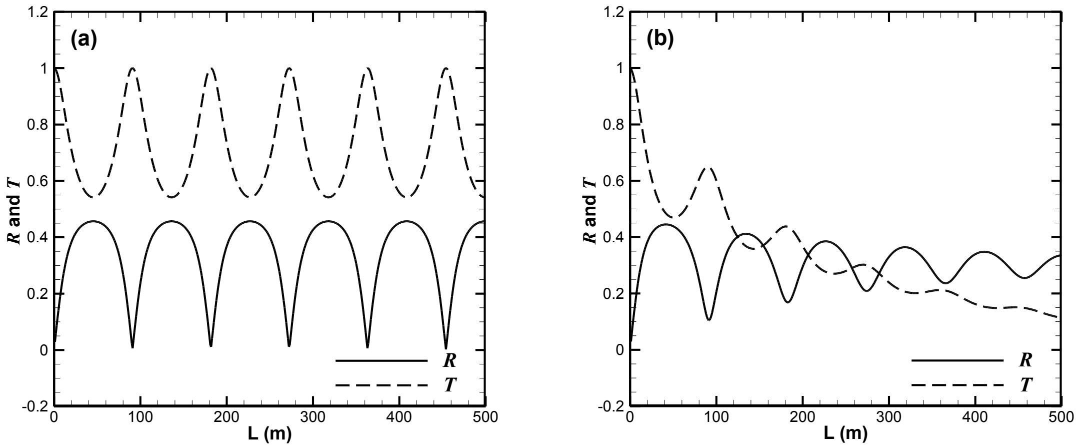

Figure 3. Reflection and transmission coefficients: $G = 2.3GPa$, $h = 1m$, $H = 1000$m, $T = 8s$. (a) $\upsilon = 0\, m^2/s$; (b) $\upsilon = 10^6\, m^2/s$.

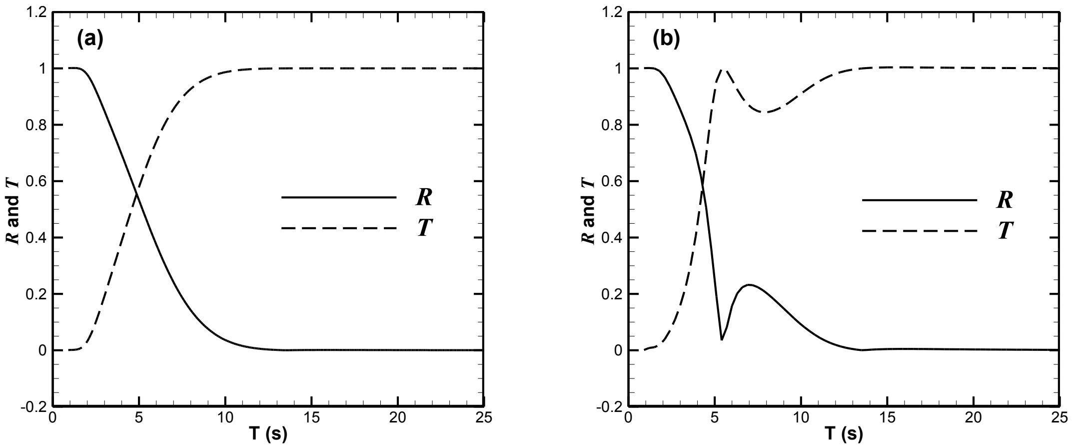

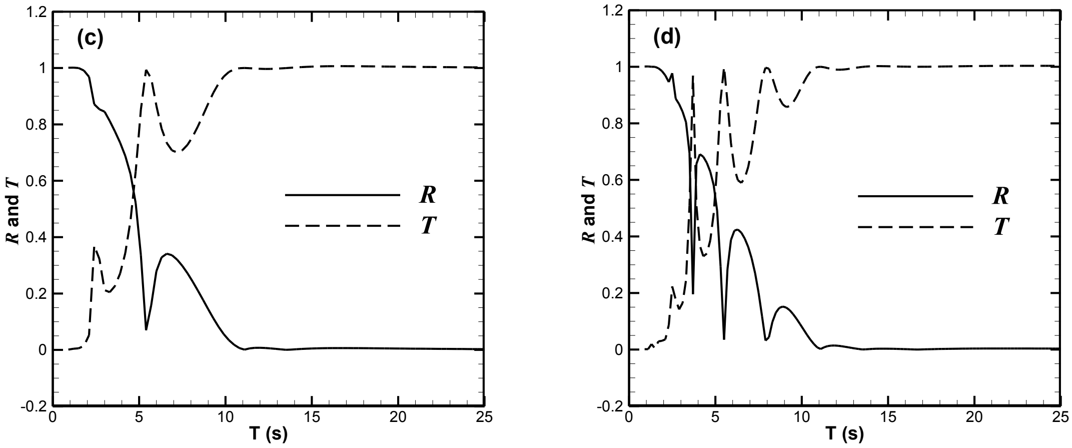

Figure 4. Reflection and transmission coefficients: $G = 2.3GPa$, $\upsilon = 0\,m^2/s$, $h = 1m$, $H = 1000$m. (a) $L = 10m$; (b) $L = 50m$; (c) $L = 100m$; (d) $L = 200m$.

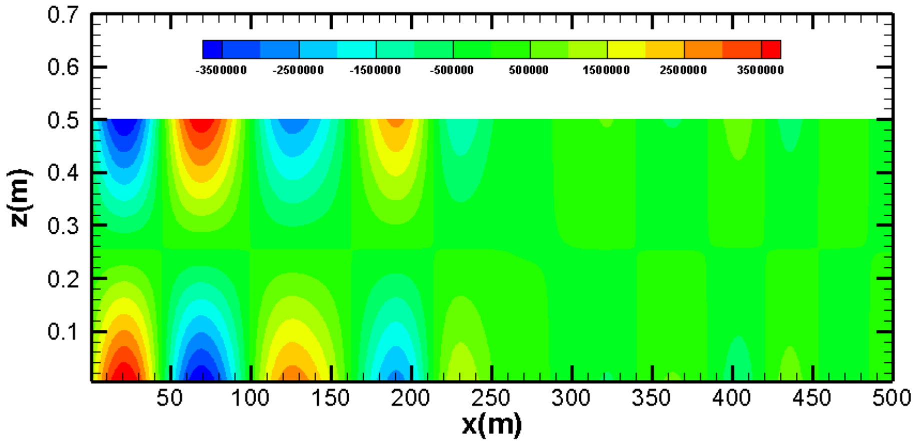

Figure 5a. Stress distribution of τ_{xx}: $G = 2.3GPa$, $\upsilon = 0\,m^2/s$, $h = 0.5m$, $H = 1000$m, $L = 500m$.

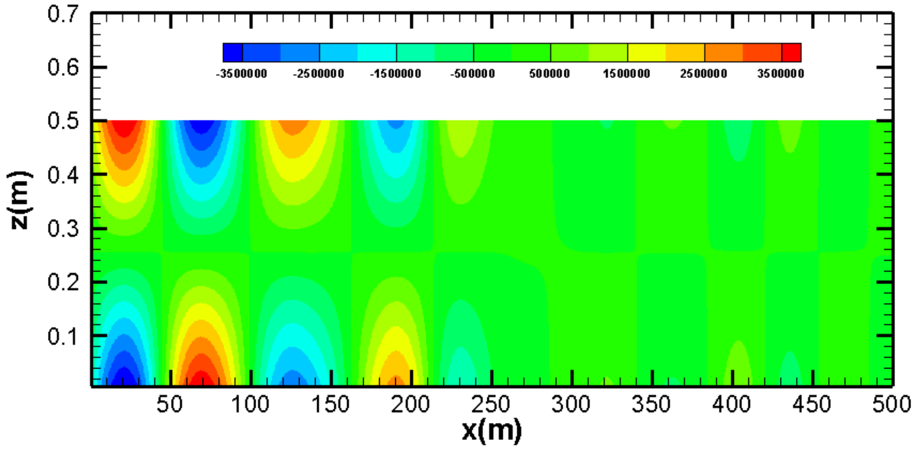

Figure 5b. Stress distribution of τ_{zz}:, $G = 2.3GPa$, $\upsilon = 0\,m^2/s$, $h = 0.5m$, $H = 1000$m, $L = 500m$.

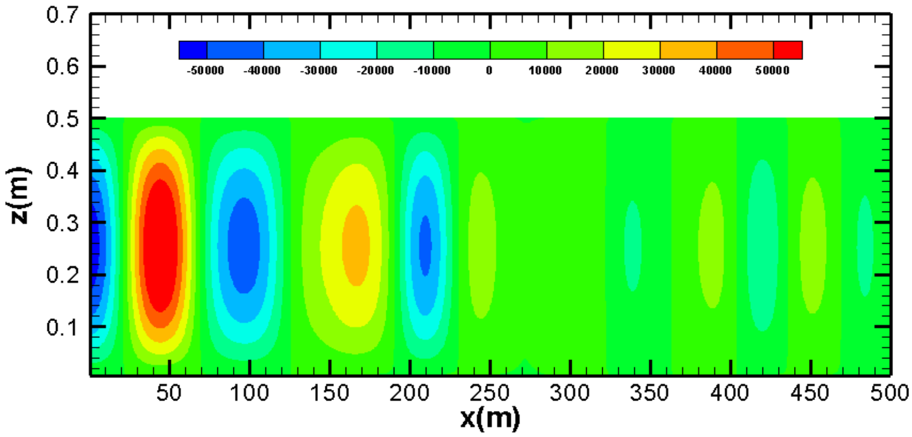

Figure 5c. Stress distribution of τ_{xz}: $G = 2.3GPa$, $\upsilon = 0\, m^2/s$, $h = 0.5m$, $H = 1000$m, $L = 500m$.

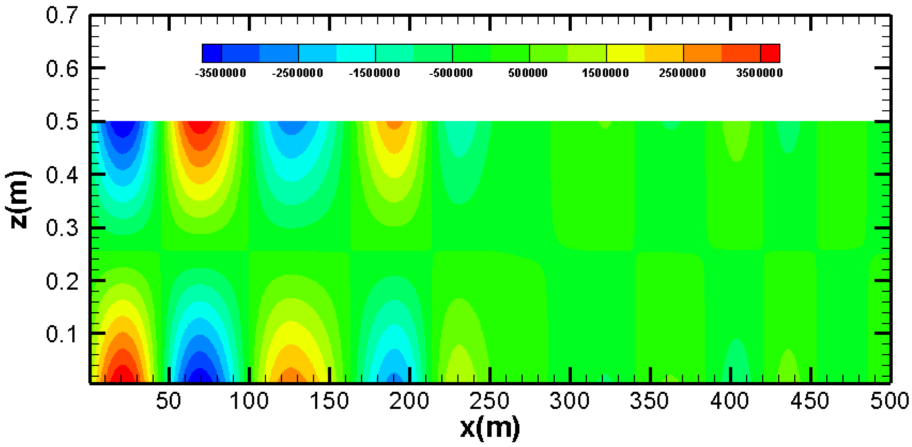

Figure 6a. Stress distribution of τ_{xx}: $G = 2.3GPa$, $\upsilon = 0.1\, m^2/s$, $h = 0.5m$, $H = 1000$m, $L = 500m$.

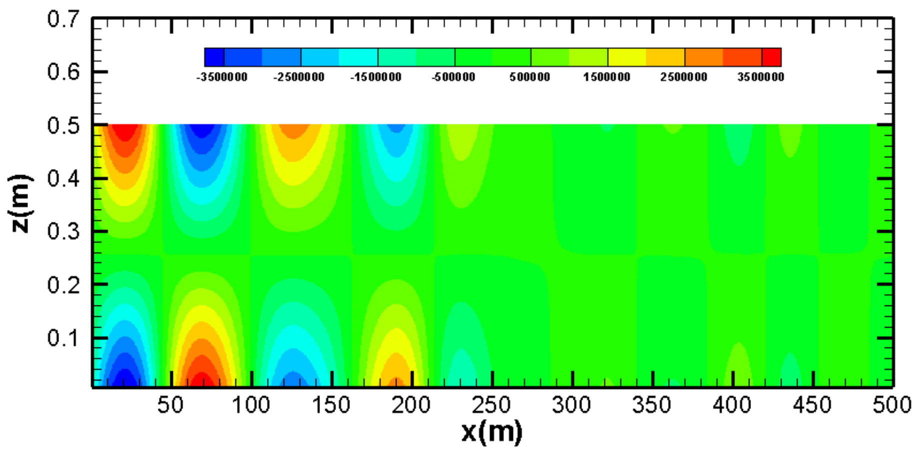

Figure 6b. Stress distribution of τ_{zz}: $G = 2.3GPa$, $\upsilon = 0.1\, m^2/s$, $h = 0.5m$, $H = 1000$m, $L = 500m$.

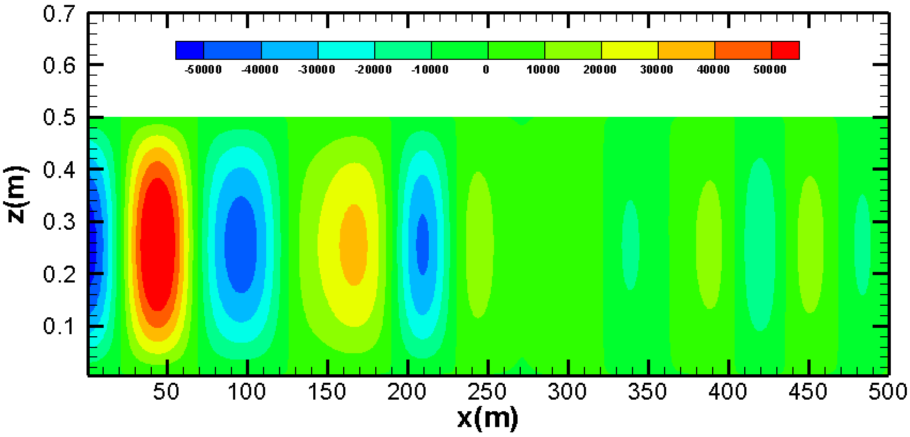

Figure 6c. Stress distribution of τ_{xz}: $G = 2.3GPa$, $\upsilon = 0.1\, m^2/s$, $h = 0.5m$, $H = 1000$m, $L = 500m$.

07
Oil and pollution in ice

25th IAHR International Symposium on Ice
Trondheim, 23 - 25 November 2020

Possibly approaches for under ice oil pollution detection

V.K. Goncharov, I.V. Aleshin, R.D. Smolin, A.V. Sudakov
Saint-Petersburg State Marine Technical University
Lotsmanskaya str., 3, 190008, Saint-Petersburg, Russian Federation
vkgonch@mail.ru, Smolin.rostislav@mail.ru, sudakov.ant@gmail.com

This paper contains analysis the problems of oil pollution detection that formed under the ice cover surface due to accidental oil spills from platforms and terminals or as result of the emergencies while the ice navigation of the cargo vessels and tankers in the Arctic seas, where application of the oil spills monitoring tools developed for non-freezing seas is impossible. The outcomes of the under ice oil spill spreading and the oil film formation investigations are presented. The spatial scales of the oil spreading and pollution at the ice-water interface were evaluated for the most probable volumes of accidental spills. Effect of the oil film under the ice cover on the heat flow from the water space to the atmosphere was studied on basis of the thermal physics methods. In the issue the possible contrasts of the snow layer or the ice surface temperature above oil film in comparison with surrounding space was evaluated. Known methods and equipment for detection of the oil pollution are considered with regard to the under ice spillage, and their effectiveness is assessed in terms of the sensitivity and possibility of being used for observation “from above”, that is through ice cover, and “from below” - from water space. It is justified the infrared tools application for the under ice oil film detection on the ice cover (or snow layer) by means of the incipient temperature contrast. The paper contains also recommendations for equipping autonomous and remotely controlled underwater vehicles (ROV) with the most effective means for detecting under ice spill sites: sonars and fluorescent lidars. Outcomes of the studies can be used for development and application the special equipment and tools for the oil pollution monitoring in the shelf water areas with drill and mining platforms and on the navigation routs in the Arctic seas.

1. Introduction

Intensive development of oil deposits on the Arctic shelf is accompanied by the risk of accidental oil spills due to crashes on platforms, wellhead structures and oil pipelines, as well as damage of tankers hulls while the ice cover compression. Accidental oil spill under an ice cover is the most dangerous one in the case of the environment oil pollution. Ice cover with a concentration of 9 – 10 points exists in the Arctic seas for 6 – 7 months: from December to June (Arikainen, 1990). This period is the most dangerous from the platforms operation and navigation from the point of view, which is caused by the lack of natural light in the polar night, extremely low temperatures (below minus 50 degrees Celsius), icing of the upper structures of platforms and ship deck-erections, and often occurring movements and compression of ice (Zubakin, 2006). The same circumstances require application of special instruments, which are capable to detect oil pollution located under the ice cover.

In the event of accident with oil spill, the primary task is to assess the extent of oil pollution and monitor its dynamics until the time, when climatic and weather conditions will be acceptable for usage one or another method for oil spill recovery. Detection of the oil contamination of an ice cover lower surface from under water seems to be a natural method, and therefore it has been studied experimentally in sufficient details in laboratory conditions and field tests (Wilkinson, 2013). Performed researches have given reasons to recommend autonomous and remotely controlled underwater vehicles (ROV) to detect oil pollution of ice. On the base of experiments under model conditions, the sonar (ultrasonic locator) on ROV was accepted as the most effective sensor.

An adequate assessment of the applicability of various methods for oil film detection requires representations of the possible spatial and temporal scales of under ice oil pollution. Paper presents research outcomes of the process of oil spreading along the ice-water interface, and an estimation of the sizes of sub-ice oil films for the characteristic volumes of accidental oil spillage. Outcomes of this problem studies was presented in partly (Aleshin et al, 2019). This paper contains much detail statement of the developed for the under ice oil film dimensions evaluation method and the effect of oil film on the heat flow from water space to atmosphere.

The under-ice oil film dimensions and its effect on the heat flow through an ice cover was the basis for analyze the possibilities of the optic sensors (fluorescence lidar and infrared camera) for the sounding water space under ice cover and justify the prospects of their application for detecting oil films on the underwater surface of ice.

2. Features of oil film formation on the ice-water interface under ice cover

Studies of various aspects of the oil-and-ice-surface interactions have been in process for a long time with the aim to prevent freezing seas oil pollution (Hollebone and Fingas, 2001; Goncharov, 2007). The main feature of the oil-and-ice-surface interaction (in contrast with oil to water surface interaction) is the fact that an ice is unwettable one for the crude oil both in air and water spaces. This effect is being characterized by a contact angle, which differs tremendously from 0° for oil on the water surface. In first case (on ice surface in air space) it consists in the range $0 << \theta_u < 90°$, whereas in the water space contact angle of oil on an ice surface lies within range $90° << \theta_d < 180°$ (Liukkonen et al, 1997).

Oil film thickness on an ice surface is determined by the balance of surface tension force which prevents oil from spreading, and force of gravity or buoyancy, which in turn helps to increase its transverse size via compressing it. A diagram of surface tension forces acting on the oil film is shown in Figure 1 for films located on the upper and lower surfaces of the ice.

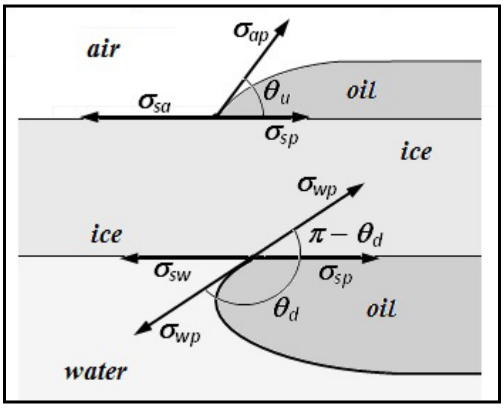

Figure 1. Forces acting on the oil film while spreading above and beneath ice surface.

The equilibrium shape of the film at the point of contact with the ice surface is characterized by a contact angle θ_u (on ice) or θ_d (under ice), and are determined by the balance of surface tension forces. This condition corresponds to the Young equation (Adamson, 1979), and for the upper and lower surface of the ice it has the following form

$$\cos\theta_u = \frac{\sigma_{sa} - \sigma_{sp}}{\sigma_{pa}}, \qquad \cos\theta_d = \frac{\sigma_{sw} - \sigma_{sp}}{\sigma_{pw}}. \quad \textbf{[1]}$$

Here: σ_{sa}, σ_{sp}, σ_{pa}, σ_{sw}, σ_{pw}, - surface tension coefficients at the ice-air, ice-oil, oil-air, ice-water and oil-water interfaces, respectively. The σ_{pa} value is a known tabular value that depends on the brand of oil and its temperature. To solve the problem, it is necessary to estimate the values σ_{sa} and σ_{sw}, which determine the equilibrium of the oil film, compensating for the force of gravity on ice or buoyancy under ice. The surface tension along solid and gas boundaries and solid and liquid boundaries cannot be determined in any way (Schukin et al, 2004). It can be assumed that each liquid has its own combination of σ_{sp}, σ_{pa} and θ_u, which is the same for all liquids, since the surface tension at the solid(ice)–air interface does not depend on liquid.

Evaluation of the value of σ_{sa} can be constructed in approximation based on Antonov rule (Adamson, 1979; Schukin et al, 2004) that being applied to the ice-oil boundary, determines

$$\sigma_{sp} = \sigma_{pa} - \sigma_{sa}. \quad \textbf{[2]}$$

The surface tension at the oil-water interface is estimated approximately also according to Antonov rule, which means

$$\sigma_{pw} = \sigma_{wa} - \sigma_{pa}. \quad \textbf{[3]}$$

As a result following equation determines the surface tension coefficient at the ice - water interface

$$\sigma_{sw} = \sigma_{pa}\left[1 - \omega\left(1 + \cos\theta_u\right) - \cos\theta_d\right] + \sigma_{wa}\cos\theta_d. \quad \textbf{[4]}$$

The coefficient ω takes into account the possible difference between oil and ice surface tension on the upper and lower ice surface, due to the difference in its temperature. An oil film is kept from spreading by a force, which is determined by a surface tension coefficient on the ice-water-oil contact line. The hydrostatic pressure per length unit of the oil film contact with ice is determined by the buoyancy of the oil film

$$P_u = \frac{1}{2}(\gamma_w - \gamma_p)h_u^2. \qquad \textbf{[5]}$$

In this equation, h_u is the thickness of the oil film on the lower surface of the ice, γ_w is the density of water; γ_p is the density of oil. Equating [4] and [5], it is possible to find the thickness of the oil film at the ice-water interface

$$h_d = \sqrt{\frac{2\sigma_{pa}}{\gamma_w - \gamma_p}\left[\frac{1}{2}(1-\cos\theta_u) + \cos\theta_d + \frac{\sigma_{wa}}{\sigma_{pa}}\cos(\pi - \theta_d)\right]}. \qquad \textbf{[6]}$$

The obtained result shows that the thickness of the oil film under the ice surface depends on the contact angles θ_u and θ_d, which is only experimentally possible to determine. Figure 2 shows the dependence of an oil film thickness under the ice surface on the contact angle θ_d for three values of the contact angle of the film of the same oil on the ice surface: $\theta_{u1} = 60°$, $\theta_{u2} = 40°$, $\theta_{u3} = 20°$. (For each brand of oil, there should be a pair of contact angles θ_d and θ_u, depending on the properties of ice surface). Figure 2 shows that the thickness of the oil film on the lower surface of the ice can exceed a centimeter, while on the free surface of the water the oil spreads under the influence of surface tension to a monomolecular layer.

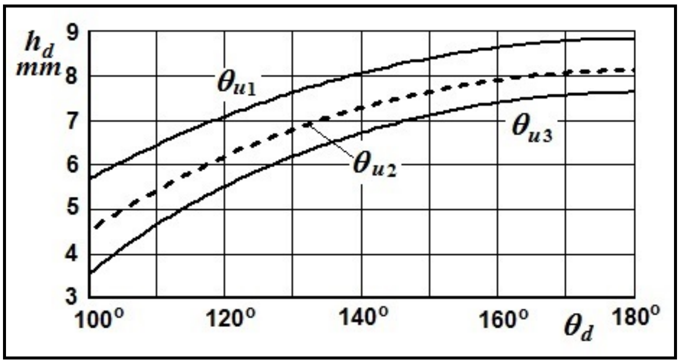

Figure 2. Dependence of an oil film thickness under ice cover on the contact angle θ_d.

3. Oil spreading beneath the ice surface

The laws of physical chemistry of surfaces, limiting the spreading of oil under ice to its thickness reaching a certain finite value, respectively, also determine the spatial dimensions of the oil film at a given spill volume. For a spill of Q volume, the final spreading diameter of the circular oil film under ice at the interface with the water mass is determined by the following equation:

$$D_{df} = 2\sqrt{\frac{Q}{\pi}\sqrt{\frac{\gamma_w - \gamma_p}{2\sigma_{pa}}\left[\frac{1}{2}(1-\cos\theta_u) + \cos\theta_d + \frac{\sigma_{wa}}{\sigma_{pa}}\cos(\pi - \theta_d)\right]^{-1}}}. \qquad \textbf{[7]}$$

The balance of gravity, inertia and viscosity forces, that the resistance to oil flow depends on, determine the rate of oil spreading along the ice surface. There are various models of this process (Hollebone & Fingas, 2001). Their common drawback is that they did not pass verification under the conditions of a real spill, as happened with oil spills in ice-free waters. Under these conditions, solutions were chosen for modeling that were experimentally verified in the largest range of spatiotemporal scales

$$D_d\left(t\right)=1.282\left(\frac{\gamma_w-\gamma_p}{\mu_p}Q^3\right)^{0.125}t^{0.125}. \quad \textbf{[8]}$$

Here μ_p is the viscosity of the oil. This solution allows us to estimate the spreading time of the oil spill before the end of this process T_{df}, that is, before the formation of a stable film with a thickness of h_d and diameter D_{df}.

$$T_{df}=0.36\frac{\mu_p Q}{\left(\gamma_w-\gamma_p\right)h_{un}^4}. \quad \textbf{[9]}$$

Using equations [6] – [9] it is possible to trace the process of oil spreading after a spill under a close ice cover and to estimate the scale of ice pollution. Figure 3 shows the final size D_{df} of oil films and their spreading time T_{df}, depending on the volume of the spill. These spatial and temporal scales should be targeted by means of detecting under ice oil spills.

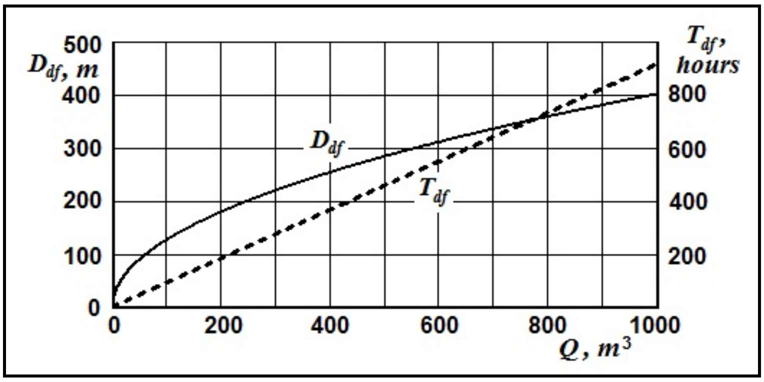

Figure 3. Dependence of the oil films final size D_{df} and spreading time T_{df} on spill volume.

4. Contrast of the ice cover temperature above the thick oil film under ice

In the winter conditions, the heat flow from water to atmosphere takes place through snow-ice cover of the underlying water space. This flow includes two components: the flow due to difference between the water temperature and the atmospheric air temperature and the flow of the ice crystallization heat on the interface ice-water. The difference of temperature of water and air determines the first component. The Stephen condition determines this heat flow for the immovable water space (Krass and Merzlikin, 1990: Goncharov et al, 2016).

The thick oil film on lower surface of an ice cover changes the heat flow to the atmosphere because its smaller heat conductivity than ice and owing to the ice crystallization termination. Therefore the ice cover temperature over the under ice thick oil film should be above temperature of ambient ice or snow surface (Goncharov et al, 2017).

It is possible to suppose that the temperature in horizontal plane in all mediums (atmosphere, snow, ice and water) is identical one and do not vary with the course of time. (It is considered the quasistationary problem). The origin of the vertical axis OZ is situated on the boundary snow - atmosphere. The heat transfer within the snow layer and the ice cover is realized by the heat conductivity. The thermal boundary layer is located on the surface of the snow layer in which the convective heat transfer into the atmosphere occurs (Krass and Merzlikin, 1990).

The oil film takes up the part of lower surface of the ice cover. It is supposed that dimensions of the oil film are sufficiently large to provide the temperature within ice and snow uniformity in the horizontal plane. The lifetime of the oil film is sufficiently small for the oil encapsulation into ice. Figure 4 presents the heat flow from water to atmosphere diagram.

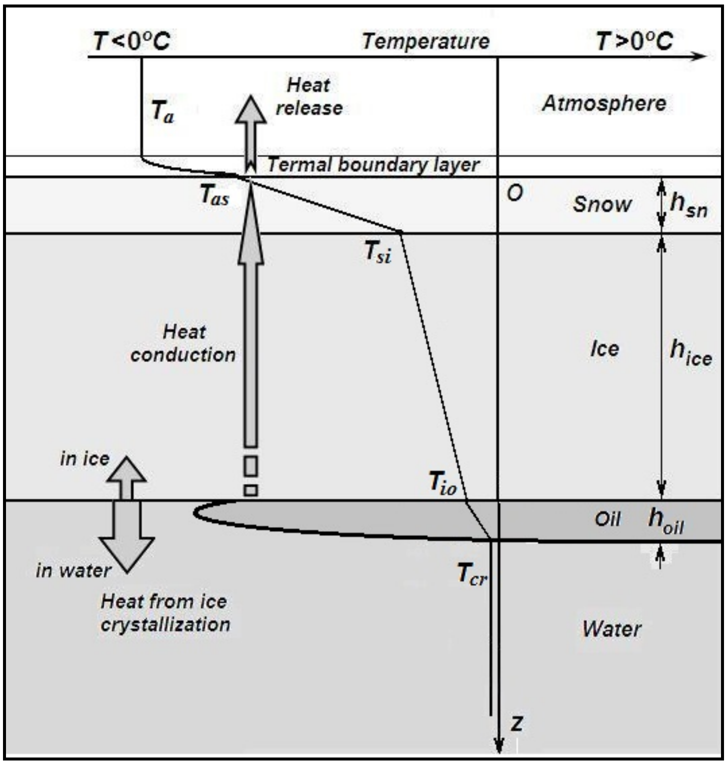

Figure 4. Diagram of the heat flow from water space to the atmosphere through oil film, ice and snow layers.

It is accepted the following notations: the thickness of ice cover h_{ice}, its heat conductivity coefficient λ_{ice}, the thickness of snow layer h_{sn}, its heat conductivity coefficient λ_{sn}, the thickness of oil film h_{oil}, heat conductivity coefficient of crude oil λ_{oil}. Temperature on the boundary snow - atmosphere T_{as}, on the boundary snow - ice T_{si}, on the boundary ice - oil T_{io}, the water temperature corresponds the ice crystallization for given salinity T_{cr}, the temperature of an atmospheric air T_a.

The problem of the heat field within the multilayer plate: water - ice - snow is the subject of the first step investigation (the oil film is absent). The specific heat flux (per unit area) from water space to the atmosphere through the system that includes two solid and one gaseous medium was presented as sum of two components:

– the heat flow from the high temperature medium to medium with smaller temperature in accordance with the Fourier's law (Kreiht and Black, 1980) (temperature of air $T_a < 0$ºC) and
– the heat flow F_{h0} from the ice crystallization on the interface ice - water:

$$q_{wa} = \frac{T_{cr} - T_a}{R_{hc}} - \mu F_{h0} T_a. \qquad \textbf{[14]}$$

In this equation μ - coefficient that defines the portion of the ice crystallization heat which diffuses into the ice cover (the rest part of heat defuses into the water space under an ice). R_{hc} is the coefficient of thermal resistance (heat transfer) that is determined by the heat conductivities of ice and snow and the heat irradiation from the snow layer surface to the atmosphere (α_{sa} - coefficient of the heat irradiation - convective heat transfer)

$$R_{hc} = \frac{1}{\alpha_{sa}} + \frac{h_{ice}}{\lambda_{ice}} + \frac{h_{sn}}{\lambda_{sn}}. \qquad \textbf{[15]}$$

The ice crystallization heat flow F_{h0} was evaluated on base of representation for the rate of the ice cover growth as result of freezing, which was the increment of an ice thickness h_0 per time unit and 1ºC of an atmospheric air (Goncharov et al, 2016). Base for applied approach was the equation for an ice cover thickness forecast on base of the sum of negative average day temperatures of air for Siberian rivers (Donchenko, 1987) that was similar to known N. Zubov's equation (Zhukov, 1976). This approach and derived equation were verified by measurements of air temperature and ice cover thickness on the Heilongjiang (Amur) River.

$$W_{fr}\left(h_0\right) = 2.06 \cdot 10^{-5}\left(1.176\, h_0^{-0.125} - 1\right). \qquad \textbf{[16]}$$

After introduce in this equation L_{ice} – specific heat of the ice crystallization and γ_{ice} – density of ice and substitution into [14] the following equation for the heat flow was derived

$$F_{h0} = 2.06 \cdot 10^{-5}\, L_{ice}\, \gamma_{ice}\left(1.176\, h_{ice}^{-0.125} - 1\right). \qquad \textbf{[17]}$$

The special parameter "modified" temperature of the atmospheric air T_{ah} depending on the ice crystallization rate was applied for following analyze that connected with the real temperature of air T_a by equation

$$T_{ah} = \left(1 + R_{hc}\, \mu\, F_{ho}\right) T_a. \qquad \textbf{[18]}$$

In this statement it is possible to reduce the problem in point to the known problem of the heat transfer through the multilayer plate, where the equation for heat flow has the following canonical form

$$q_{wa} = \frac{T_{cr} - T_{ah}}{R_{hc}}. \qquad \textbf{[19]}$$

The solution of this problem is known one (Kreiht and Black, 1980) and defines the temperature of the snow layer surface by following way

$$T_{as} = T_{ah} + \frac{q_{wa}}{\alpha_{sa}}. \qquad \textbf{[20]}$$

For simplification of the subsequent equations it is reasonable to introduce the coefficient of "heat supply", which is determined for each medium by following way

$$\varepsilon_a = \frac{1}{\alpha_{sa}}, \quad \varepsilon_{sn} = \frac{h_{sn}}{\lambda_{sn}}, \quad \varepsilon_{ice} = \frac{h_{ice}}{\lambda_{ice}}, \qquad R_{hc} = \varepsilon_a + \varepsilon_{sn} + \varepsilon_{ice}. \qquad \textbf{[21]}$$

Temperature of the snow layer surface is possible to present on this base as following

$$T_{as} = \frac{\varepsilon_a}{R_{hc}} T_c + \left(1 - \frac{\varepsilon_a}{R_{hc}}\right)\left(1 + R_{hc}\,\mu F_{ho}\right) T_a. \qquad \textbf{[22]}$$

When the oil film exists between the lower surface of ice and water space the ice crystallization does not run, and only the heat transfer from the water space to the atmosphere through the three-layer plate values the snow surface temperature: crude oil film - ice cover - snow layer. Coefficients of the "heat supply" and coefficient of the thermal resistance are determined as following

$$\varepsilon_a = \frac{1}{\alpha_{sa}}, \ \varepsilon_{sn} = \frac{h_{sn}}{\lambda_{sn}}, \ \varepsilon_{ice} = \frac{h_{ice}}{\alpha_{ice}}, \ \varepsilon_{oil} = \frac{h_{oil}}{\lambda_{oil}}, \quad R_{hf} = \varepsilon_a + \varepsilon_{sn} + \varepsilon_{ice} + \varepsilon_{oil}. \qquad \textbf{[23]}$$

Equation for the heat flow from water space to the atmosphere has following form

$$q_{waf} = \frac{T_{cr} - T_a}{R_{hf}}. \qquad \textbf{[24]}$$

After substitution form [23] for the thermal resistance and heat flow [24] into known solution for the heat transfer through the multilayer plate (similar to [20]), the following solution for the snow surface temperature while the crude oil film under the ice cover was derived

$$T_{asf} = \frac{\varepsilon_a}{R_{hf}} T_{cr} + \left(1 - \frac{\varepsilon_a}{R_{hf}}\right) T_a. \qquad \textbf{[25]}$$

The difference between the snow surface temperature without crude oil film under ice [22] and the one, when the oil film exists [25], defines the contrast of temperature due to the oil film under ice cover that decrease the heat flow from water space to the atmosphere. (It is supposed that outside the oil film the heat flow is unchanged). Therefore temperature of the of the snow layer surface above the oil film is higher one than on surrounding area.

$$\vartriangle T_{as} = \frac{\varepsilon_a\,\varepsilon_{oil}}{R_{hc}\,R_{hf}} T_{cr} + \left[\left(\varepsilon_{sn} + \varepsilon_{ice}\right)\mu F_{ho} - \frac{\varepsilon_a\,\varepsilon_{oil}}{R_{hc}\,R_{hf}}\right] T_a. \qquad \textbf{[26]}$$

Solution [26] can be transformed in other form, in which the first component is the contribution in the temperature contrast of the insulation effect of the oil film and the second component is the effect of the ice freezing interruption.

$$\vartriangle T_{as} = \frac{\varepsilon_a\,\varepsilon_{oil}}{R_{hc}\,R_{hf}} \left(T_c - T_a\right) + \left(\varepsilon_{sn} + \varepsilon_{ice}\right)\mu F_{h0}\, T_a. \qquad \textbf{[27]}$$

Figure 5 presents the dependence of the temperature contrast of the snow surface on the atmospheric air temperature for various thickness of the sea ice cover while the snow layer thickness is h_{sn} = 0.05 m. These data shows the temperature contrast of the snow surface above the oil film under ice cover increases while temperature of atmospheric air and the ice cover thickness increases.

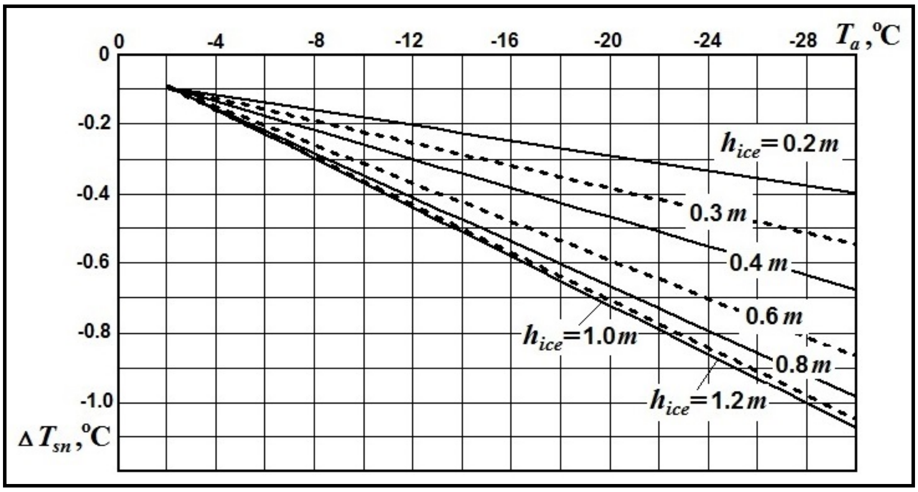

Figure 5. Dependence of the temperature contrast of the snow layer surface on the atmospheric air temperature for various thicknesses of the ice cover.

5. Analysis of existing methods for detecting oil pollution at the ice - water border when observed from under water

The results of studies of various methods for detecting oil in a various ice conditions are contained in reports (Wilkinson et al, 2013; Pegau et al, 2016). The following methods (sensors) were considered and experimentally tested as possible for application in the underwater media: video camera, sonar, multispectral radiometer, and fluorescent laser.

The acoustic location (sonar) detects oil pollution by the difference in the dispersion of acoustic energy from the ice-water and oil-water boundaries and this method is rated as the most effective, when using a sonar and receiver with a variable frequency of radiation. A fluorescent laser is only evaluated as an additional means to sonar, capable of detecting oil in conditions, where the sonar is not effective. For instance, to detect small amounts of oil in "grated" or broken ice, in narrow canals in ice cover, etc.

It should be noted that lidar methods for sensing natural environments, in particular the marine environment, are being intensively improved nowadays. The effect of lidar sensing of oil pollution of ice is based on the difference in reflectance with respect to laser emitting of oil, snow, ice or sea water.

When the rough target sounding with a specular reflection coefficient R by lidar with an output power of emitting P_0, the divergence of the sounding radiation θ_D, the area of the receiving device pupil A_{int}, the transmittance T of the medium between the lidar and the target, the power of the specular component P_R of the scattered target sounding for a statistically rough surface of the target will have the following form (Gulkov et al, 1984):

$$\frac{P_R}{P_o} \approx \frac{R\,T\,A_{int}}{\pi\,L^2(4\,a_{sf}^2 + \theta_D^2)}. \qquad \textbf{[28]}$$

Under deriving this form, it was assumed that there is a distance L between lidar and the target, the optical axes of the lidar emitting and receiving devices are aligned, the sounding is carried out in “nadir”, i.e. perpendicular to the target surface, and $4a^2_{sf}$ is a statistical parameter that takes into account the macro roughness of the target.

It is possible to apply this approach for detection the oil film on the ice floe bottom that is sounding "from below" - from the water space. Seawater has much less transparency than the atmosphere (especially in the coastal water areas). Therefore it is necessary to take into account attenuation of sounding radiation during double passage along the sounding path from the lidar to the target and backward. To simplify the solution, it is reasonable to assume that the lower surface of the ice cover and the oil film are absolutely smooth. In this case, equation [28] takes the following forms for oil and ice

$$\frac{P_R^{oil}}{P_o} \approx \frac{R_{oil}\, T_w\, A_{int}}{\pi L^2 \theta_D^2}. \qquad \textbf{[29]}$$

$$\frac{P_R^{ice}}{P_o} \approx \frac{R_{ice}\, T_w\, A_{int}}{\pi L^2 \theta_D^2}. \qquad \textbf{[30]}$$

The transmittance of seawater T_W can be represented in the following form (k_W is the attenuation coefficient of the sounding radiation within seawater)

$$T_w = \exp\left(-2 k_w L\right). \qquad \textbf{[31]}$$

Using equations [29] and [30], the “lidar contrast” s of the oil film on the ice floe bottom when observed “from below” can be determine as following

$$s = \frac{P_R^{oil} - P_R^{ice}}{P_R^{ice}}. \qquad \textbf{[32]}$$

The lidar contrast value in this case is defined, first of all, by the ratio of the reflectivity of oil and ice. The exponential dependence of the attenuation of the power of sounding radiation in the water space with the sensing distance increasing [31] is the main obstacle for the wide application of this method. It was evaluated (Aleshin et al, 2006) that, with an integral transparency of sea water corresponding to a white disk visibility of 25 m (the most favorable option for coastal waters), oil pollution on the lower ice surface can be detected by the lidar method at a distance of about ten meters.

6. Conclusion

The dynamics of oil spreading over the ice surface in air and in the aquatic environment differs significantly from oil spreading over the sea surface. This is because oil does not wet the ice surface, and cannot spread to the monomolecular layer. Under non-wettability conditions, surface tension limits the spreading of oil along the ice surface and forms a film of relatively large thickness. On the lower ice surface - at the interface with the water mass, the thickness of the oil film can reach 1 cm. Such oil pollution is an object for detection by various methods applied for monitoring the ecological state of the marine environment.

Thick oil film on the ice-water interface decreases the heat flow from the water space to the atmosphere because of its insulation effect and ice crystallization termination. Originated contrast of the temperature of the snow layer on ice cover can be detected with infrared gears.

In the specific conditions of the Arctic ice cover, the most effective carrier of equipment for monitoring oil pollution of the lower ice surface from below are an autonomous or remotely controlled underwater vehicles (ROV). Laboratory studies performed in Canada gave reason to consider the most promising use of a sonar with a tunable frequency in comparison with optical means that can only be used as auxiliary ones.

The results of the analysis of the applicability of the lidar for detecting oil films under ice from below showed this method as a perspective one also. This allows to recommend the use of lidar in conjunction with a sonar on submarine carriers to detect and localize emergency oil spills that can occur due to damage of bottom oil pipelines and wellhead devices of oil wells.

Implementations of the method under consideration for monitoring oil pollution of the ice cover should be preceded by systematic laboratory and field studies using sonar and lidar to assess their real ability to detect oil films under ice and to develop appropriate detection methods and algorithms that are required for their use in autonomous underwater vehicles (ROV).

Acknowledgement
Study was implemented within projects SIMREC – "Simulators for improving Cross-border Oil Spill Response in Extreme Conditions". Projects are co-funded by the European Union, the Russian Federation and the Republic of Finland.

Reference

Adamson, A.,1979. Physical chemistry of surfaces. M.: Mir, 568 p.

Aleshin, I.V., Yakovlev, V.A., 2003. Modern informationally-optical technologies for operational monitoring the state of the sea surface. Morskoy Vestnick. No 3(7), pp. 83–87.

Aleshin I.V., Goncharov V.K., Osadchy V.Y., Levin I.M., Radomyslskaya T.M., Klementieva N.Y., Kolobkov V.S., Zelensky V.V., Li Z., 2006. Modern methods and technical means for detecting deep sea accidental oil leakages. Morskoy Vestnik. No 2(18). pp. 78 - 83.

Aleshin, I.V., Goncharov V.K., Smolin R.D., Sudakov A.V., 2019. Application of marine robots for monitoring of oil spills under the ice. MarineRobotics 2017/2019 International Conferences on Marine Robotics in Ocean Exploration. Saint-Petersburg, Russia. Collection of Papers. pp. 51 – 60.

Arikainen, A.I., 1990. Shipping in the ice of the Arctic. M.: Transport, 247 p.

Donchenko, R. V. 1987. The Ice Regime of the USSR Rivers. L.: Gidrometeoizdat, 242 p.

Goncharov, V.K., 2007. Technogenic pollution of the marine environment and methods for its forecast. Textbook. Publishing Center of Saint-Petersburg State Marine Technical University. 188 p.

Goncharov, V.K., Edush N.Yu., Klementeva N.Yu., Zueva E.S., Jianmin Qin, Liqin Cui, Li Zhang, Xiao Deng, Peng Chen, 2016. Investigation of Correlation between the Temperature on Air-Snow and Snow-Ice Interfaces and the Atmospheric Air Temperature. Journal of Earth Science and Engineering. vol. 6. pp 245 – 253.

Goncharov, V.K., Aleshin I.V., Zueva E.S., Klementieva N.Yu., 2017. Evaluation of the Heat Contrast on Ice Cover Surface while the under Ice Oil Spill. Proceedings of the 40th AMOP Technical Seminar on Environment Contamination and Response, Calgary, Canada, CD-ROM, 8 p.

Gulkov, V.N., Zaitsev, V.A., Kropotkin, M.A., Pashchenko, E.G., Tikhonov, V.V., 1984. Optical and physical means of ocean research. L.: Sudostroenie, 264 p.

Hollebone B.P., Fingas M., 2001. The fate and Behavior of Oil in Freezing Environments. Permann D.N.S. and Mullin J. Draft. Environment Canada, Ottawa, Ontario, Canada, 488 p.

Krass, M.S. and V.G. Merzlikin, 1990. Radiation thermophysics of the snow and ice, L.: Gidrometeoizdat, 262 p.

Kreiht, F. and Black W.Z., 1980. Basic heat transfer, Harper & Row Publishers, NY, 512 p.

Liukkonen, S., Rytkonen J., Alhimenko F., Kniazeva E., 1997. On the Adhesion of Oil to Ice. Proceedings of the 7th International Offshore and Polar Engineering Conference, Honolulu, USA, vol.1, pp. 579-586.

Pegau, W. S., Garron, J., Zabilansky, L., 2016. Detection of oil on-in-and-under ice. Final Report 5.3. Report from Join Industry Program on oil spill detection and mapping in low visibility and ice: experimental results, 40 p.

Schukin, E.D., Pertsov, A.V., Amelina E.A., 2004. Colloid chemistry. Manual for Universities. M.: Vysshaia Shkola, 446 p.

Wilkinson, J., Maksim, T., Singh, H., 2013. Capabilities for detection of oil spills under sea ice from autonomous underwater vehicles. Final Report 5.2. Report from Join Industry Program on oil spill detection and mapping in low visibility and ice: focus on undersea remote sensing, 104 p.

Zhukov, L.A., 1976. General Oceanology, L.: Gidrometeoizdat, 376 p.

Zubakin G.K. (Ed.), 2006. Ice formations of the seas of the western Arctic. Collection. Publishing Center of Arctic and Antarctic Research Institute. 272 p.

08
Harbours and coastal challenges

25th IAHR International Symposium on Ice
Trondheim, 23 - 25 November 2020

Thermal Deformations of Frozen Clay Caused by Cyclic Changes of Temperature and Thermal Impacts

Artem Nesterov
Peter the Great Saint-Petersburg Polytechnic University
artyom_nesterov-@mail.ru
Aleksey Marchenko
The University Centre in Svalbard (UNIS)
aleksey.marchenko@unis.no
Nicolai Vasiliev
JSC "Vedeneev VNIIG"
nicolaivasiliev@hotmail.com

Construction and operation of port, transport, residential and other large coastal facilities in Arctic region are complicated by spreading of frozen soils. With a natural change in temperature, compression (expansion) deformations of frozen soils arise. As a result of the action of frost heaving forces, destruction of engineering structures (retaining walls, pile-shells with soil aggregate, dams, pipelines, embankments etc.) can occur. The laboratory experiments were performed in the cold laboratory of the University Centre in Svalbard at November 2019 to investigate thermal response of clay samples due to cyclic changes of the room temperature from -5 to -20ºC and due to the freezing of water in the soil cracks. Both fresh and sea water were used. Clay samples were made by hand with pre-prepared cracks, and the chain saw was used to repeat experiments with freezing water. The horizontal dimension of clay samples was of about 50x35 cm, and the thickness was of about 14 cm. Fiber optics sensors AOS GmbH were used to measure clay strains and temperature in the laboratory. Micro-SHM System MISTRAS was used to register acoustic emission in the tests. For comparison results experiments with fresh and sea ice samples were conducted. Test on ice were carried out in 2018-2019 independently of the clay tests. The results of measuring deformations of frozen soils according to the proposed methodology can reveal the mechanism of stress-strain state formation for such soils in a wide range of thermal and mechanical loads and the time of their impact. The results can be used for estimating stability of harbor and coastal engineering structures.

1. Introduction

The growing attention to the development of coastal zone resources is notable not only for moderate and southern latitudes but also in the Arctic regions. The construction and operation of ports, transport, residential and other large facilities in this region are complicated by the spread of frozen soils. Much attention initially focused on the problems of frost heave, but the problems associated with the behavior of frozen soils under cyclic changes of negative temperatures are also important due to the presence of unfrozen water in frozen soils (Grechishchev, et al., 1983). The phase transformations influence thermal deformations of frozen soils (Ershov, 1990). Compressive or tensile deformations arising in the soils under the action of the air temperature changes influence the formations of frost cracks passing through the active soil layer into permafrost (Chzhan, Velikin, 2014). It may create settlement and destruction of engineering structures.

Cementation of mineral particles by ice in frozen soils is of primary importance for assessing of their mechanical properties estimated by the ice content and the quantitative content of unfrozen pore water at a given negative temperature (Cheverev, 2004). At the same time, the construction of hydraulic structures on the shelf is affected by both sea water and fresh water, when erecting structures in the deltas of northern rivers. Therefore, in this work, a new technique for experimental studies of temperature deformations of frozen soils saturated with water of various salinity is proposed and implemented. Knowledge of the processes of thermal expansion of such soils is necessary for the design of berthing and soil structures the Arctic regions (Marchenko, Nesterov, Vasiliev, et. al., 2020). This paper describes the method and results of direct measurement of temperature deformations of frozen clay samples with different salinity under cyclic changes of negative temperatures.

2. Instrumentation

Fiber Bragg Grating sensor (FBG) is a periodic grid with 40,000 cells burned by two laser beams inside the fiber with diameter of 9 μm. The grid length is 1 cm. Each FBG sensor reflect the light signal of a certain wavelength, depending on the grid characteristics, tension and temperature of the fiber. The incoming light signal is generated in the optical fiber by the source LED in the spectral range 1,500~1,600 nm. The wavelengths reflected by the FBG sensors are registered and analyzed by a spectrometer. To register changes inside a calibration device, a constant temperature is maintained in one of the sensors. The spectrometer, calibrator, and analyzer of the incoming optical signals are combined in one unit with four channels designed and manufactured in the company Advance Optic Solutions GmbH (Dresden). Every channel of the unit can transfer information from 16 FBG sensors embedded in the same fiber (Marchenko, Lishman, Wrangborg, et al., 2016).

FBG thermistor string and strain sensor are shown in Figure 1. Fiber cable with FBG temperature sensor is protected from mechanical deformations by thin metal tube of 1 mm diameter. The FBG thermistor string includes 12 FBG sensors embedded in the same fiber with 1 cm distance between neighbor sensors. The FBG thermistor string is protected from mechanical deformations by thin metal tube of 1 mm diameter and 25 cm length. The thermistor string is welded with optical fiber protected by blue plastic. The accuracy of temperature measuring, and nominal resolution is correspondingly equal to 0.4 °C and 0.08 °C. Strain sensor is embedded in the middle part of the fiber protected by transparent plastic with working length about 20 cm. The fiber inside transparent plastic is going through the screw and welded to fiber cable protected by yellow plastic. The strain sensor is mounted on a sample and pretended using two screws and bolts. The resolution of the strain sensors is 10^{-6}, and the accuracy is 5×10^{-6}.

The change of the wavelength ($\Delta\lambda$) of the light reflected by the Bragg grating is proportional to the fiber extension ($\Delta L/L$) and the change of the fiber temperature (ΔT):

$$\Delta\lambda/\lambda = GF*\Delta L/L + TK*\Delta T \qquad \textbf{[1]}$$

where GF = 0.719, "calibration factor"; TK = 5.5×10^{-6}, "thermal elongation factor"; L is the reference length of the fiber; λ is the reference length of the light reflected by the Bragg grating. The value of $\Delta\lambda$ is measured by the spectrometer. From Equation 1 it follows that temperature changes of the fiber ΔT should be known for the calculation of the fiber strain $\Delta L/L$. In the experiment, the temperature of the strain sensor was measured by the FBG temperature sensor. The FBG thermistor string was installed to measure temperature inside the soil sample.

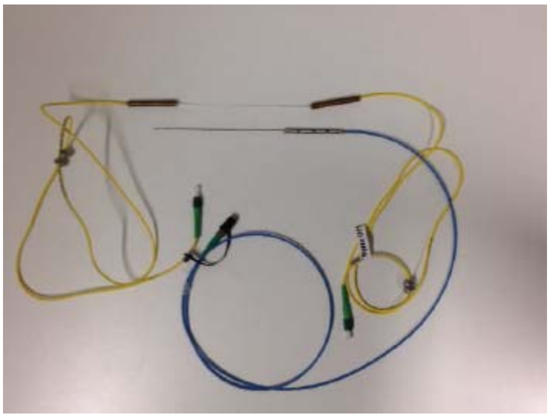

Figure 1. FBG thermistor string with blue plastic housing of the fiber and strain sensor with yellow plastic housing of the fiber.

3. Organizing of experiments

We prepared and pre-frozen two clay samples 50×35×13 cm saturated with fresh and saltwater (34 ppt), respectively. The basic physical properties of the clay (gray-green color) are given in Table 1.

Table 1. The basic physical properties of the clay.

<table>
<tr><td colspan="3">Moisture content, %</td><td rowspan="3">Plasticity index P_l, %</td><td rowspan="3">Consistency index C_l, %</td><td colspan="3">Density, g/cm^3</td><td rowspan="3">Porosity, e</td><td rowspan="3">Water holding capacity, W_{ct}</td></tr>
<tr><td rowspan="2">Moisture, W</td><td colspan="2">Limits (GOST)</td><td rowspan="2">Particles, ρ_s</td><td rowspan="2">Soil, ρ</td><td rowspan="2">Dry soil, ρ_d</td></tr>
<tr><td>Liquid, W_l</td><td>Plastic, Wp</td></tr>
<tr><td>35.0</td><td>37.4</td><td>19.1</td><td>18.3</td><td>0.87</td><td>2.67</td><td>1.82</td><td>1.35</td><td>0.978</td><td>0.366</td></tr>
<tr><td rowspan="3">Degree of saturation, S_r</td><td colspan="9">Size of particles, mm</td></tr>
<tr><td colspan="9">Composition of grains, %</td></tr>
<tr><td colspan="2">1-0.5</td><td>0.5-0.25</td><td>0.25-0.1</td><td>0.1-0.05</td><td>0.05-0.01</td><td>0.01-0.005</td><td>0.005-0.002</td><td><0.002</td></tr>
<tr><td>0.96</td><td colspan="2">–</td><td>0.3</td><td>6.1</td><td>8.5</td><td>21.2</td><td>14.5</td><td>11.1</td><td><0.003</td></tr>
</table>

One not through cut (0.8×10×7 cm) was made in the center of each sample for subsequent investigation of the water penetration and water freezing effects on the clay deformations. FBG temperature string and FBG strain sensors were used to measure soil temperature and deformations. Strain sensors were mounted on the surface of soil samples with brackets and screws, temperature strings were placed in drilling holes with diameter of 2 mm. Temperature probes Testo-176 were placed in the cuts to measure water-ice temperature. SHM transducers were glued to the soil surface by silicon lubrication. Soil samples with installed measurement systems is shown in Fig. 2. Similar FBG sensors were installed on the samples of fresh and sea ice in the same room. The sea ice salinity was 4 ppt.

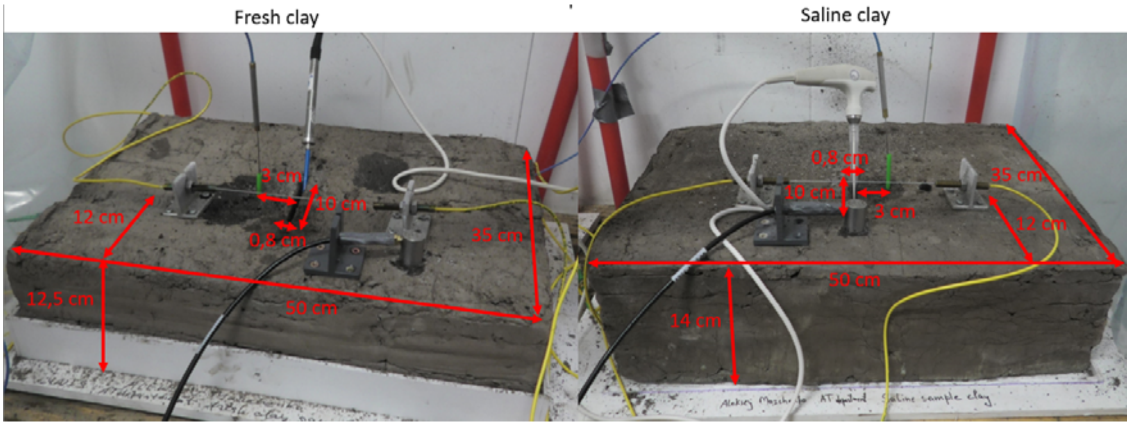

Figure 2. Clay samples and measurement installation.

4. Temperature and strain measurements

Figure 3 shows the dependencies of the mean temperature in the soil and sea ice sample versus the time. The dependence of the air temperature near the soil surface is shown in the sane figure. The air temperature amplitude was about 10ºC in the air. The ice temperature amplitude was smaller on 1ºC. The amplitude of the fresh soil temperature was about 6ºC, and the amplitude of the saline soil temperature was only 4ºC. It means that the specific temperature conductivity of the soils is smaller the sea ice conductivity. It is probably related with larger amount of unfrozen water in the soil samples in comparison with amount of liquid brine in sea ice.

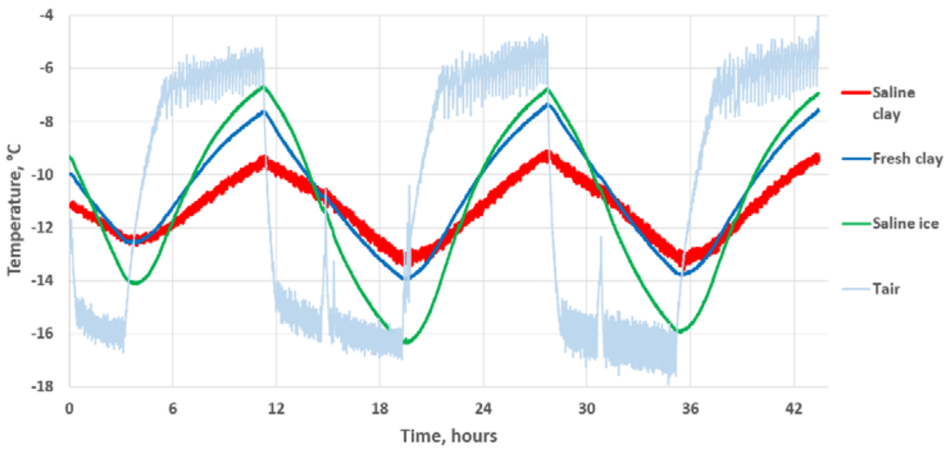

Figure 3. The mean temperatures of the ice and soil samples and the air temperature versus the time

Measured strains of the ice and clay samples are shown in Fig. 4 versus the time. At the beginning of the deformation curve and at each subsequent temperature switching rapid jumps of strains were observed in the soil samples. It is explained by softening of soil skeleton due to uneven crystallization of pore moisture leading to the appearance of local micro-stresses and microcracks (Votyakov, 1975). With a further increase in temperature, the acquired decompaction of the soil structure is preserved. This effect was not observed in the ice samples. Maximal strain amplitudes were observed in the fresh ice sample. The strain amplitude in sea ice sample were smaller, and the strain amplitudes in fresh and saline soils samples were similar and smaller than in sea ice sample.

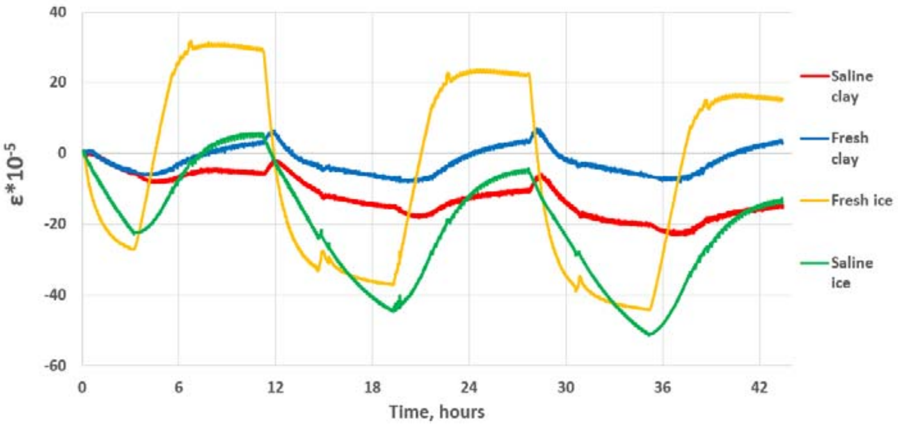

Figure 4. Strains measured in the ice and soil samples versus the time.

Figure 5 shows the dependence of strains in the soil samples and sea ice from their mean temperature. The mean temperature was calculated as the mean value of 10 temperature values measured by FBG temperature string at different depths in the soil. The hysteresis loops are well visible in the samples of saline soil and sea ice, and it is very thin in the fresh soil sample. The mean slope of the strain-temperature curves shown in Fig. 5 equals to the mean value of the linear coefficient of thermal expansion (CTE). Based on Fig. 5 the following values of CTE for saline soil, fresh soil and sea ice were calculated: $CTE_{ss}=0.8\cdot10^{-5}K^{-1}$, $CTE_{fs}=1.6\cdot10^{-5}K^{-1}$, $CTE_{si}=5.6\cdot10^{-5}K^{-1}$. Herewith, studies of the CTE of frozen soils show that the deformability of the tested frozen soils does not directly depend on their mineral composition (salinity), but through values of the moisture content, porosity and structural features (Brushkov, 1998). Frozen soils are characterized by abnormally high CTE up to $2\cdot10^{-3}K^{-1}$ and more (for clays), while for the mineral skeleton of the soil CTE=$(0.4\text{-}8)\cdot10^{-6}$ K^{-1} (Volokhov, Nikitin, Lavrov, 2017).

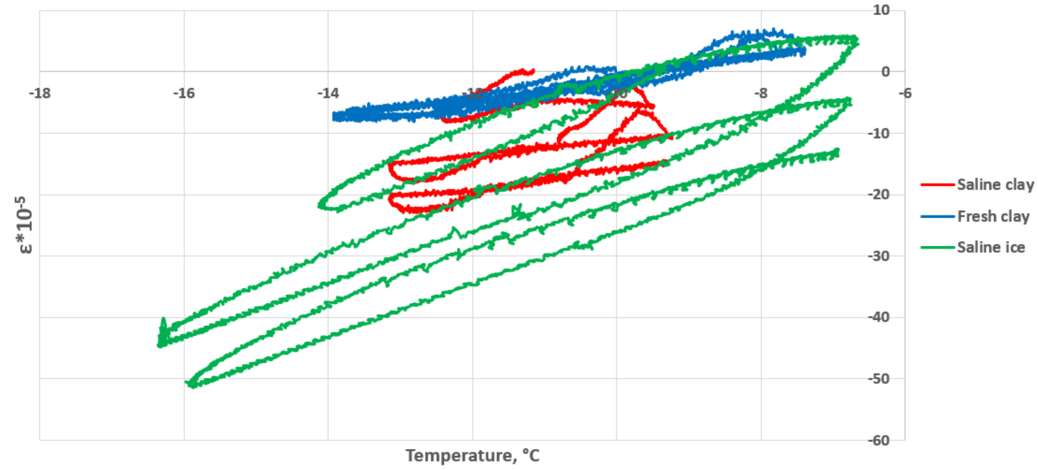

Figure 5. Dependences between average temperature inside sample and deformation.

Figure 6 shows temporal evolutions of the strain (red line) and temperature inside saline soil sample after sea water (salinity is 34 ppt) was added in the cut. The added water was at the freezing point (~ -1.9ºC). The air temperature near the soil surface (gray line Tair) and water/ice temperature inside the cut (green line Temp inside hole) are also shown in Fig. 6. The air temperature near the soil surface was around -9ºC during the experiment. Significant part of the sea water was frozen inside the cut probably during several minutes, and after that only liquid brine with high salinity left inside the soil. The moment when sea water was added in the cut coincides with sharp increase of the temperature inside the cut. The temperature stabilization inside the hole occurred in 1.5 h. The soil temperature returned to the initial temperature after 2.5 h. The strain response in tension extended over 6 h. Maximal tensile strain accounted from the moment when the water was added in the cut reached $6 \cdot 10^{-5}$.

Figure 7 shows temporal evolutions of the strain (red line) and temperature inside fresh soil sample after fresh water at the freezing point was added in the cut. The air temperature near the soil surface (light blue line Tair) and water/ice temperature inside the cut (green line Temp inside hole) are also shown in Fig. 7. The air temperature near the soil surface was around -9ºC during the experiment. The fresh water was frozen inside the cut probably during several minutes or faster. This moment coincides with sharp increase of the temperature inside the cut. The temperature stabilization inside the hole occurred in 1.5 h. The soil temperature returned to the initial temperature after 2.5 h. The strain response in tension extended over 2 h. Maximal tensile strain accounted from the moment when the water was added in the cut reached $4 \cdot 10^{-5}$.

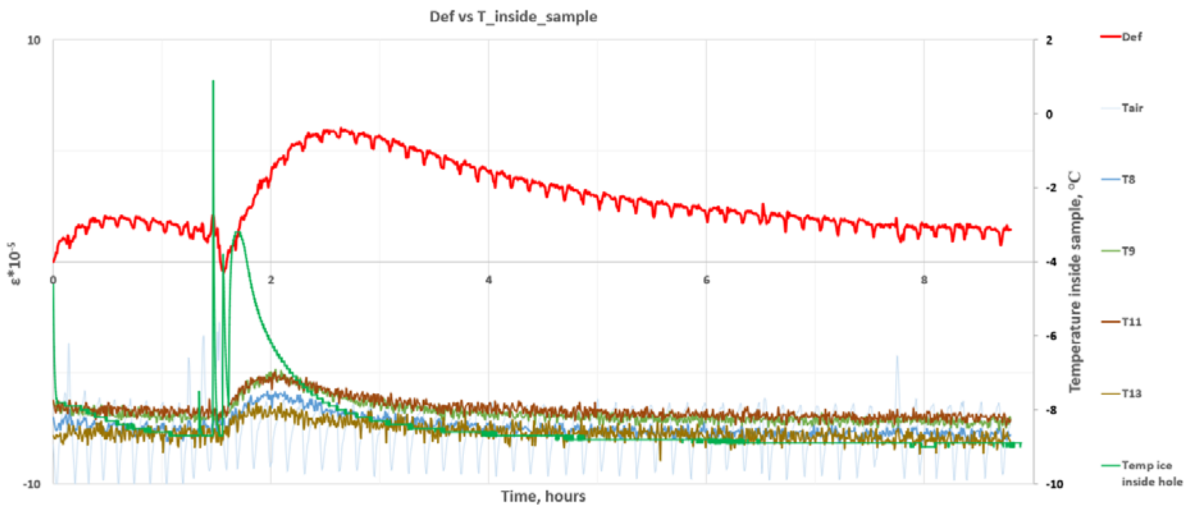

Figure 6. Water penetration effect on saline clay sample.

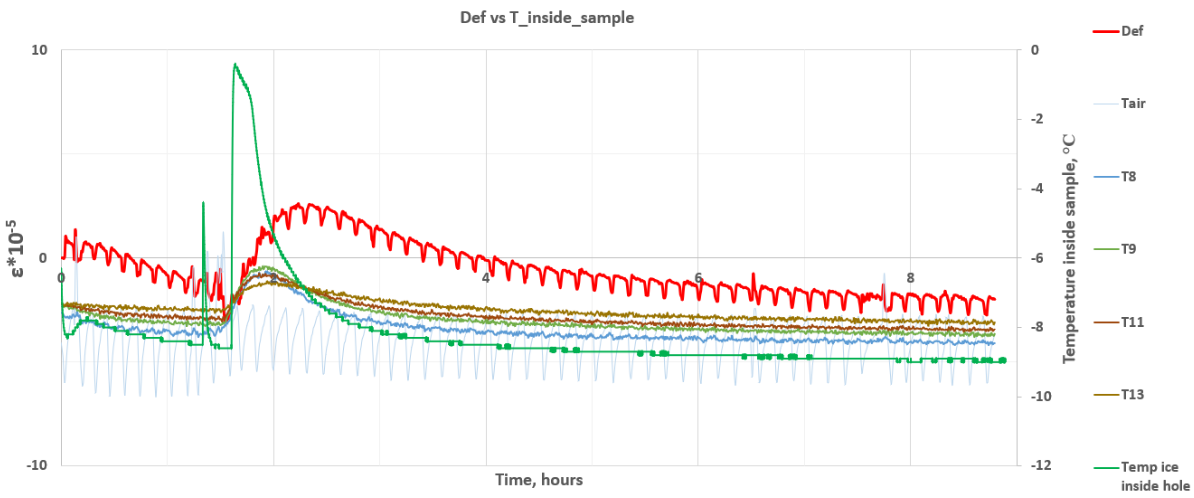

Figure 7. Water penetration effect on fresh clay sample.

5. Acoustic emission

Acoustic emission was recorded during tests with cyclic changes of the air temperature on stages of active deformations of the samples. Figure 8 shows records of acoustic emission at around 16 h later after the beginning of the experiment. Local peak of the air temperature was recorded in this time (Fig. 3) because the door in the laboratory was open and closed. Temperature and strain rates were around their maxima at that time. Figure 8 show that energy and number of emitted acoustic heats was greater in the fresh soil sample than in the sample of saline soil. Figure 9 shows that the hit numbers registered in the fresh and saline soil samples during 20 s were respectively around 280 and 35. Figure 5 demonstrates that the strain amplitude was higher in the fresh soil sample than in the saline soil sample. Thus, the energy and the number of hits correlate with the strain amplitude.

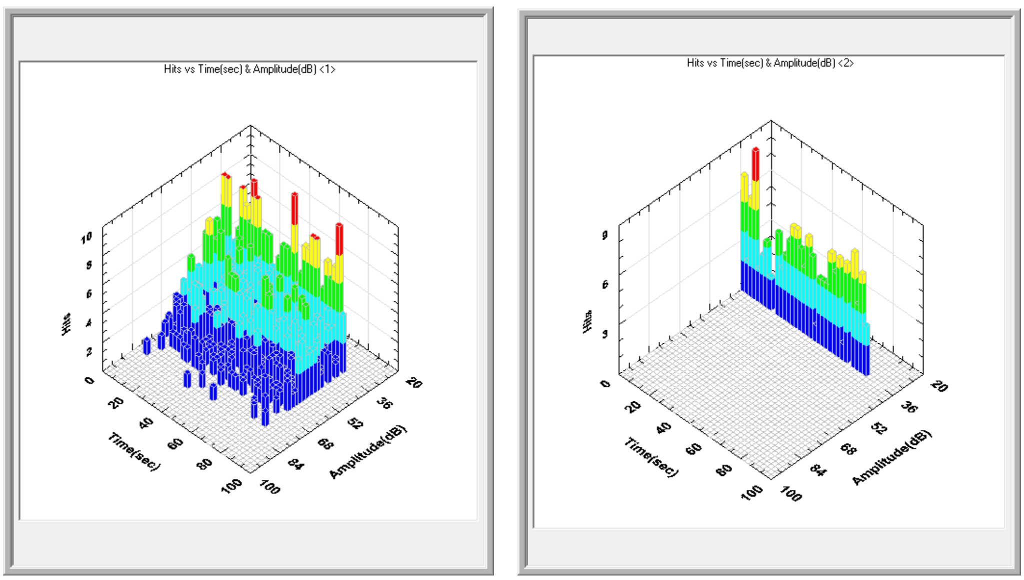

Figure 8. Acoustic emission in the experiment when soil deformations were caused by cyclic changes of the air temperature: hits as a function of amplitude and time in fresh soil (left panel) and saline soil (right panel).

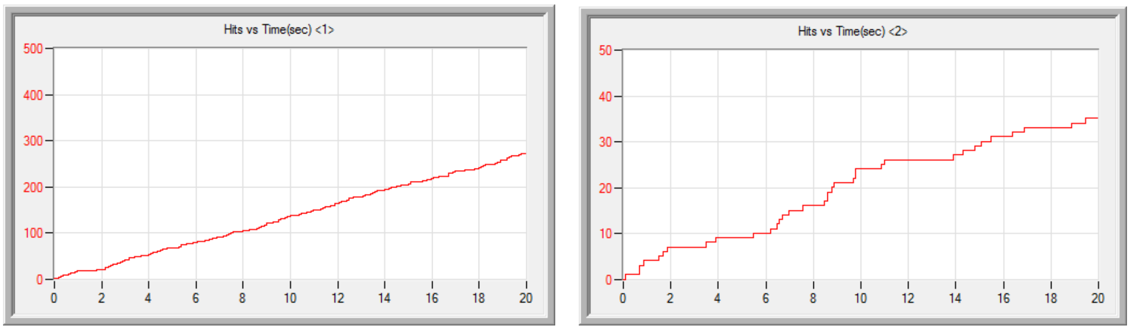

Figure 9. Acoustic emission in the experiment when soil deformations were caused by cyclic changes of the air temperature: number of hits versus time in fresh soil (left panel) and saline soil (right panel).

Acoustic emission was recorded during tests when cyclic changes of the air temperature on stages of active deformations of the samples when soil deformations were caused by the adding of water in the cuts of soil samples. Figure 10 shows records of acoustic emission at the time when the cuts were filled by water. The amount and energy of registered acoustic hits were higher in the saline soil sample. Figure 11 shows that the hit numbers registered in the fresh and saline soil samples during 20 s were respectively around 35 and 600. Figures 6 and 7 demonstrate that the strain amplitude was higher in the saline soil sample than in the fresh soil sample. Thus, the energy and the number of hits correlate with the strain amplitude.

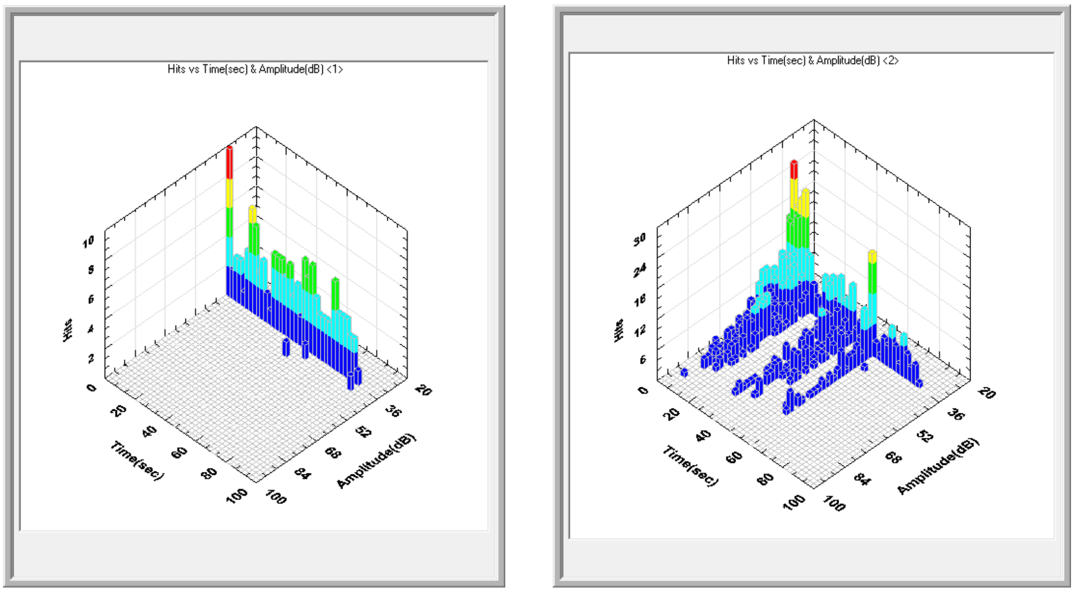

Figure 10. Acoustic emission in the experiment when soil deformations were caused by the adding of water in the cuts of soil samples: hits as a function of amplitude and time in fresh soil (left panel) and saline soil (right panel).

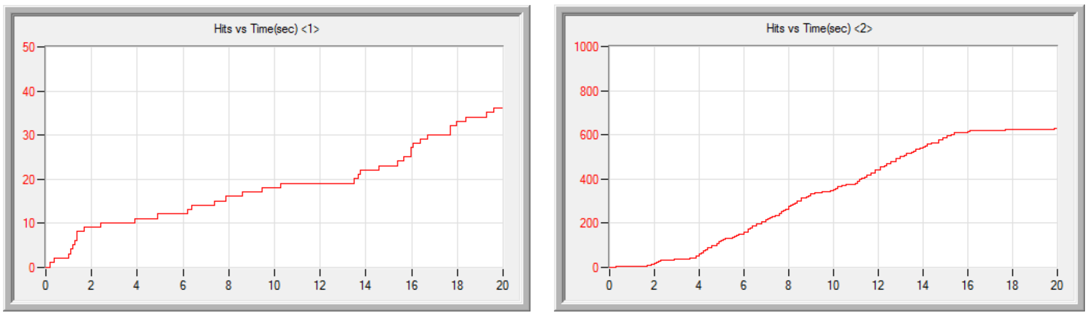

Figure 11. Acoustic emission in the experiment when soil deformations were caused by the adding of water in the cuts of soil samples: number of hits versus time in fresh soil (left panel) and saline soil (right panel).

5. Conclusion

Cyclic change of the air temperature in the range from -5ºC to -20ºC with 12 h period influenced cyclic deformations of the saline soil and fresh soil samples, and sea ice sample placed in the same room. Deformations were caused by thermal expansion. Maximal strain amplitudes were registered in sea ice. The strain amplitudes in the fresh soil sample were approximately in two times greater the strain amplitudes in the saline soil sample. The mean values of the linear coefficients of thermal expansion of saline soil, fresh soil and sea ice, fresh were $CTE_{ss}=0.8\cdot10^{-5}K^{-1}$, $CTE_{fs}=1.6\cdot10^{-5}K^{-1}$, $CTE_{si}=5.6\cdot10^{-5}K^{-1}$. The hysteresis loops were greater in the saline soil and sea ice samples. Strain rates of tensile and compressive deformations accompanying respectively the temperature increase and decrease were not similar in the considered temperature range. Differense of the temperature and the thermally induced strains in the samples is explained by the difference in their thermodynamic characteristics including the specific heat capsity and the thermal conductivity. Probably the specific heat capacity of the saline soil sample was highest because of the liquid brine content. Temperature changes were associated with phase transformations in the soil and as a result temperature variations were smallest in the saline soil sample. Respectively, the thermal expansion was also smallest in this sample.

Freezing of water inside the cuts made in the saline soil and fresh soil samples influences tensile deformations. Temporal response on the fast filling of the cuts by sea water at the freezing point in the saline soil sample and fresh water at the freezing point in the fresh soil sample consists of the temperature increase and extension. Representative time of the response was greater in the saline soil sample. Tensile strains were also greater in saline soil sample. Since the air temperature was constant (-9ºC) during the experiments the soil heating is exlained by the latent heat release by the water freezing in the cuts. The latent heat released in the cuts volume and the heat flux propagated mainly in the soil, because the contact area of the cuts with the air was much smaller the contact area with the soil. Thermodynamic properties of the soils influenced temperature changes near the cuts, and it influenced in its turn the thermal expansion of the soil samples.

Measurements of acoustic emission accompanying processes of thermal expansion showed that the energy and the number of acoustic heats were proportional to the strain amplitude. The acoustic emission was higher in the samples subjected to larger deformations. In the experiments on the water freezing in the cuts maximal acoustic emission was registered in the beginning of the experiment just after the water was added in the cuts and started to freeze. It shows that the water crystallization may be potential sourse of the registered emission.

Acknowledgments
The team of authors expresses great appreciation to the project – Safety of Industrial Development and Transportation Routes in the Arctic, 2015–2019 (SITRA), with the financial support of which it became possible to conduct these studies.

References

Cheverev V.G., 2004. Nature of cryogenic soils. Moscow: Nauchnui Mir., pp. 234 (in Russian).

Chzhan R.V., Velikin S.A., 2014. Safety of small and medium dams in permafrost regions. Sciences in Cold and Arid Regions, 6(4), 331–339.

Ershov E.D., 1990. Geocryology. Moscow: Nedra, pp. 559 (in Russian).

Grechishchev S.E., et al., 1983. New methods of studying the composition, structure and properties of frozen soils. "Nedra", Moscow (in Russian).

Marchenko AV, Lishman B, Wrangborg D, et al., 2016. Thermal Expansion Measurements in Fresh and Saline Ice Using Fiber Optic Strain Gauges and Multipoint Temperature Sensors Based on Bragg Gratings, Hindawi Publishing Corporation. Journal of Sensors, pp. 13.

Votyakov I.N., 1975. Physical and mechanical properties of frozen and thawed soils of Yakutia. Novosibirsk: Nauka. pp. 176 (in Russian).

Marchenko A.V., Nesterov A.A., Vasiliev N.K., et. al., 2020. Temperature Deformations of Soil Influencing Transportation Continuity in the Arctic Region. Transportation Soil Engineering in Cold Regions, Volume 1, Lecture Notes in Civil Engineering 49, 25-34.

Brushkov A.V., 1998. Saline frozen soils of the Arctic coast, their origin and properties [Book]. - M.: Moscow State University. - p. 330.

Volokhov S.S., Nikitin I.N., Lavrov D.S., 2017. Temperature deformations of frozen soils caused by rapid changes in temperature // Moscow University Geology Bulletin – Vol. 72, no. 3 – p. 224–229.

25th IAHR International Symposium on Ice

Trondheim, June 14 to 18, 2020

Ice Formation in Norwegian Fjords – Findings from the 2018 - 2019 Field Season

M. O'Sadnick[1,2], C. Petrich[1], Ø. Kleven[1], J. Skarðhamar[3] & C. Brekke[2]

[1] *SINTEF Narvik, Narvik, Norway*

[2] *UiT The Arctic University of Norway, Tromsø, Norway*

[3] *Institute of Marine Research, Tromsø, Norway*

megan.osadnick@sintef.no, christian.petrich@sintef.no, oystein.kleven@sintef.no, jofrid.skardhamar@imr.no, camilla.brekke@uit.no

Understanding ice conditions in fjords is imperative to ensure safe operations and to protect the surrounding environment. Seven fjords in northern Norway were visited in March 2019, six with significant ice cover. In each location, measurements of ocean temperature and salinity, and $\delta^{18}O$ for ocean water and river water leading into the fjords were gathered. In addition, where ice was present, measurements of ice bulk salinity and $\delta^{18}O$ were obtained along with an extra core to examine ice stratigraphy and pore structure. Results show ice of low bulk salinity, < 1.5 psu, and $\delta^{18}O$, < -7.67 ‰, in five fjords holding ice with maximum ice thickness being upwards of 0.46 m. This result combined with examination of stratigraphy cores reveals ice closely resembling freshwater ice in structure despite lying atop an ocean of average salinity 32 – 33.5 (psu). Ice salinity profiles elude to varying environmental conditions impacting ice formation throughout the winter season. Due to the impact of significant freshwater flux, ice properties differed significantly from sea ice forming in the open ocean, an important characteristic when considered in application to coastal operations.

1. Introduction

The coast of mainland Norway is dominated by the presence of fjords cutting into the adjacent mountains, with the glaciers that carved these fjords receded into higher terrain if not gone entirely (Holtedahl, 1967; Porter, 1989). Often subjected to temperatures below freezing, ice has the possibility to form in Norwegian fjords. While the Norwegian pilot guide offers brief descriptions of ice conditions in selected areas to assist boat and ship captains (Hughes, 2006), no studies exist that make direct observations of sea ice thickness, extent and properties in fjords found throughout mainland Norway. Ice conditions in the pilot guide are themselves based primarily off aging data published in older editions mixed with examination of visible and infrared satellite images gathered in February and March 2005.

The fjords in mainland Norway are influenced by the North Atlantic current bringing warm waters into the fjords, which therefore are mainly ice free all year. However, smaller side fjords and the inner parts of larger fjords often freeze up during winter, a subject of little focus in scientific research until now (O'Sadnick et al 2018; 2020). There is a wide breadth of published work from mainland Norwegian fjords during ice free conditions (for example Asplin et al., 1999; Eilertsen & Skardhamar, 2006; Lalande et al., 2020; Mankettikkara, 2013; Myksvoll, 2008; Myksvoll et al., 2013; Skardhamar et al., 2018). These studies examine the fjord system from physical and biological perspectives, both of which are potentially impacted by the presence of ice. When ice forms on the surface of a fjord, it creates a barrier between the ocean and air, altering the exchange of mass and energy (Petrich & Eicken, 2010) . In addition, ice creates a biologically rich environment of brine-filled pores that offers a sheltered place for algae and other microbiota to grow (Arrigo et al, 2010; Brandon et al., 2010). These processes are well understood in studies of sea ice in the open ocean. In addition, studies of sea ice in the Baltic Sea offer descriptions of ice grown from sea water of lower salinity, brackish in character, as well as the impact of fresh water plumes on local ecology (Granskog et al. 2005a; Granskog et al., 2005b; Kaartokallio et al., 2007). While such knowledge can be applied to fjord ice, adaptations must be made to account for a stratified water column with saline sea water overlain by a layer of very low or even fresh water, different from the brackish water of the Baltic. Given increasing interest in Norway from both shipping and resource exploration industries, the safety hazard and potential obstacle ice presents to operations are of concern. Therefore, understanding ice conditions and how they vary from fjord to fjord, throughout the year, and between years as the climate changes is important from both a scientific and operational perspective.

2. Methods

2.1. Ice sampling

Seven fjords were chosen based on previous observations of ice formation in recent years. For the 2018 – 2019 season, all but one fjord, Storfjord, held ice. Ice sampling location was chosen based on accessibility and total extent of the ice. The locations of sampling sites are shown in Fig. 1. Typically, samples were gathered in approximately the center of the fjord, 1 – 2 km from the head of the fjord where a river input was present. Snow depth was first measured and samples collected for $\delta^{18}O$ measurements before a section was cleared of snow. A Kovacs ice core barrel, 10 cm in diameter, was used with a hand drill to collect at least two ice cores at each location – one for bulk salinity and the other for stratigraphy analysis. For the former, ice was sliced into 5 cm sections and bagged for melting on return to the lab. Sample salinity was measured using a YSI Pro-30 salinometer with an accuracy of 0.1 on the practical salinity scale (psu) and resolution of ±0.1 (psu) or ±1% of the reading, whichever is greater. Once melted samples were measured, they were poured into glass viles and closed with a cone lined cap before being stored at 5 °C until $\delta^{18}O$ could be measured. Samples were analyzed at the Stable Isotope Laboratory at the Centre for Arctic Gas Hydrate, Environment and Climate (CAGE) located at UiT – The Arctic University of Norway, Tromsø, Norway. A 0.3 mL sample from each melted core slice was pipetted into a 12 mL Labco glass vial which was next flushed with a 0.3% CO2 in He gas mixture, equilibrated at 25°C for <24h. Calibration was done through measuring three inhouse standards of $\delta^{18}O$ between -1 ‰ and -36 ‰ that had previously been calibrated against international standards VSMOW2, GISP, and SLAP2. When a line was fit to true vs. measured vales of $\delta^{18}O$, the R^2 value of the line was 1.0, with error between separate readings most often being less than 0.01 ‰ but with a standard deviation <0.05 ‰. A Thermo-Fisher MAT253 IRMS with a Gasbench II was used to measure the quantity of $\delta^{18}O$ defined as

$$\delta^{18}O = \left(\frac{\left(\frac{^{18}O}{^{16}O}\right)_{sample}}{\left(\frac{^{18}O}{^{16}O}\right)_{standard}} - 1 \right) * 1000 \tag{1}$$

where the standard is Vienna Standard Mean Ocean Water (VSMOS).

Brine volume fraction was calculated using measured values of bulk salinity and a modelled linear temperature profile that assumed an air/ice temperature of -2 °C and an ice/ocean temperature of 0 °C (Leppäranta & Manninen, 1988).

Stratigraphy samples were kept in a cooler during transport to their storage location. They were stored at -30 °C and processed in a cold room at -15 °C. They were sliced to a thickness of 12 – 16 mm and examined on a light table for pore structure and layering. Additionally, cross polarized filters were used to clarify crystal structure and further highlight transitions in the ice.

2.2. Water sampling

In addition to melted ice samples, seawater and river water was also gathered for measurement of $\delta^{18}O$. For seawater measurements, a tube, 1 cm in diameter, was lowered to the pre-determined depth with the end above water plugged. The plug was then released, allowing water from that depth to fill the tube, before being plugged again and raised to the surface to fill the same cone lined bottles described above. Each bottle was first rinsed with water from the same depth before being filled. In addition to seawater, water samples from rivers leading into each fjord were gathered.

2.3. Satellite and photo image processing

UOVision UM 565 and UM785 trail cameras were used to collect timelapse images of several fjords. Examples of the photos obtained are presented in Fig. 2. Additionally, images from the SENTINEL-1 C-band Synthetic aperture radar (SAR), vertical transmit/vertical received (VV) were examined to determine when ice formed, termed a freeze-up date here, to within 2 – 3 days for fjords having no camera (Copernicus, 2019). Due to the difficulty of identification, visual inspection of individual images was needed to confirm the presence of ice.

Imagery from the Terra satellite MODIS sensor, specifically MOD09A1.006 Terra Surface Reflectance 8-Day Global 500m was also used to track ice from February, when sunlight has returned to northern Norway, through May to determine a date when fjords were ice free to within 8 days (Vermote, 2015). MODIS Images were first processed to exclude any pixels of low quality or marked as having clouds. Next, the following formula was applied:

$$Ice\ band = Band\ 3\ [459 - 479\ nm] - (Band\ 6\ [1628 - 1652\ nm] + Band\ 7\ [2105 - 2155\ nm]) \quad (2)$$

Pixels having above a certain value were then classified as ice. This method is similar to that used in Petrich et al. (2017) but automated to allow for a larger number of images to be processed. Processing steps are described in more depth in O'Sadnick et al. (2020).

3. Results & Discussion

3.1. Linking source water to ice

A summary of the dates of ice formation and breakup are presented in Table 1. Ice was observed in Sørbotn/Ramfjord for the longest period of time, 20 December 2018 to 7 May 2019. Kattfjord was second with ice being present from 14 January to 26/27 April 2019. In the remaining fjords, the ice season was shorter: 27 – 29 January to 16 - 24 April 2019 in Gratangen, 3 March to 21 April 2019 in Beisfjord, 20 – 23 January to 16 - 24 April 2019 in Lavangen, and 29 – 30 January to 16 - 24 April 2019 in Nordkjosbotn. Additionally, Storfjord was shown to hold small amounts of ice through the season but only near the outlet river and over short stretches of time. This is supported by timelapse and MODIS images (not shown). The conditions that enable ice formation in fjords are difficult to define due to the changing balance between ocean salinity and temperature (conditions influenced by weather, tides, and currents), freshwater flux into the fjord, the resultant stratification, and air temperature. To fully understand the evolution of fjord ice from beginning to end, further observation and study is needed to determine the dominant factors and how these may change between fjords and with time.

Measurements of water temperature and salinity gathered in each fjord are shown in Fig.3. Gratangsbotn was warmest with water temperatures above 6 °C at depth while Nordkjosbotn was coldest, dipping below 1 °C The other four fjords had temperatures generally between 3 – 4 °C. All had a fairly constant salinity between 32 and 33.5 psu with the most variation seen in the upper 2 m. Note, the upper 1 m of each profile is not shown as it may have been disturbed by the coring. At five fjords, a single location was selected to collect measurements and acquire ice cores for further processing. At one fjord, Beisfjord, several locations were visited (Fig. 1). Thick sections, measurements of salinity and $\delta^{18}O$, and calculated brine volume fraction for Sørbotn/Ramfjord, Kattfjord, and four location in Beisfjord, are presented in Figs. 4 – 9 respectively. Additionally, bulk salinity and brine volume fraction are provided in Fig.10 for Gratangsbotn, Lavangen, and Nordkjosbotn.

In six out of the seven cores gathered, salinity did not increase above 1.2 psu with Sørbotn/Ramfjord, Kattfjord, and Gratangsbotn having bulk salinity consistently below 0.5 psu. In all other cores where $\delta^{18}O$ was measured, values ranged from -7.73 ‰ (Kattfjord) down to -12.17 ‰ (Beisfjord 1). In cores from Ramfjord, Beisfjord 3, and Beisfjord 4, bulk salinity and $\delta^{18}O$ largely parallel each other having similar increases and decreases through their entire depth. In cores from Kattfjord, Beisfjord 1, and Beisfjord 2, these two measurements sometimes mimic each other but also show instances of being opposite- in the core gathered from Kattfjord for example, an increase in bulk salinity at a depth of 20-25 cm from 0.2 to 0.3 psu, coincides with a decrease in $\delta^{18}O$ from -7.67 to -8.76 ‰. The relationship between bulk salinity and $\delta^{18}O$ is non-trivial being dependent on the source of water as well as the ice growth rate. Seawater has a $\delta^{18}O$ value between – 1 to 0 ‰ while fresh water, from river runoff specifically, ranged here from -10.24 to -12.49. Values of $\delta^{18}O$ in the upper 1 m of ocean water from each sampling site as well as river water entering the fjord are summarized in Table 2. While a decrease in salinity is often linked to a decrease in $\delta^{18}O$, in fjord ice this is not always the case. As growth rate of ice slows, the ratio of ^{18}O to ^{16}O increases due to ^{18}O being incorporated preferentially, the reason related to differences in molecular vibration energy (Eicken, 1998). Resultantly, $\delta^{18}O$ will be greater (less negative, or at times positive) in ice formed at a slower versus a faster rate. Bulk salinity is also affected by growth rate with slower growth leading to lower salinity, faster growth to higher salinity (Petrich et al., 2011). Therefore, ice formed from water of comparatively higher salinity but grown quickly may have a comparable $\delta^{18}O$ value for ice formed from water of lower salinity but at a slow growth rate. In such a case however, values for bulk salinity would further diverge.

In only one core were values of salinity higher than 2 psu and $\delta^{18}O$ higher than -7 ‰ measured, that being Beisfjord 4 (Fig. 9). Bulk salinity decreased from 5.6 psu in the upper 3 cm to 0.6 psu at the ice/ocean interface, a depth of 18 cm. Similarly, this core also had the highest value of $\delta^{18}O$, -2.58 ‰ in the upper 3 cm, decreasing to -9.41 ‰ at its bottom. The highest values for bulk salinity and $\delta^{18}O$ occur in granular ice formed likely through the flooding of the snow-covered surface. The core was collected at the edge of a transition -- nearer to the head of the fjord and entrance of the river, ice was consistently > 20 cm, on the other side of the transition, ice was < 10 cm (Beisfjord 3 core, Fig.8). Beisfjord 3 presumably formed at a later time given its thickness of only 8 cm. Comparing the two cores, a change in microstructure and crystal structure approximately 10 cm in the Beisfjord 4 core, aligns with the top of the Beisfjord 3 core in salinity and $\delta^{18}O$. Additionally, a layer of transparent, glass-like ice was found at the bottoms of both cores. This indicates consistency in the water that formed the lower section of Beisfjord 4 sample and the entirety of the Beisfjord 3 sample. The weather leading up to the field visit was consistently cold, with a daily average air temperature consistently below -4 °C. While this would indicate likely no large increase in fresh water, snowfall was recorded twice in the short period of time from ice formation to the field visit (not shown). This snowfall may have led to an increase in flux from the river or alternatively, a layer of freshwater to form on the surface of the fjord that enabled the formation of the Beisfjord 3 core and which later flowed under the ice as the tide rose.

Each core has a mixture of granular (frazil) and congelation ice with all also displaying several changes in microstructure. For example, in the upper 10 cm of the Beisfjord 1 core, texturally classified as granular, pores are spherical and large in comparison to the next 5 cm of granular ice where pores decrease significantly is size and increase in density. At a depth of 15 cm, where a transition to congelation ice occurs, the number of pores decreases with their shape also changing to be generally thin and elongated. Layers exist within this microstructure however where there are several pores clearly larger in size, lengthening in steps downwards, from approximately 0.5 cm, to 1.0 cm, 1.5 cm, and finally 2.5 cm in the lower 10 cm of the core. Salinity relatedly decreased slightly from 0.3 to 0.2 psu while $\delta^{18}O$ increased from -10.50 to -10.06 ‰. This provides one example where salinity and $\delta^{18}O$ not aligning may be due to growth rate. We hypothesize that the water at the interface remained constant in its $\delta^{18}O$ and salinity values as ice grew while ice growth slowed due to the thickening of ice, the accumulation of snow on the surface, changes in air and ocean temperature, or a mix of these factors.

In cores gathered in Ramfjord and Kattfjord, several transitions in microstructure and relatedly bulk salinity and $\delta^{18}O$ are evident. It is difficult to define with certainty the cause of each change. However, examining weather data from these two fjords both experienced snowfall and rainfall/snowmelt that may have altered properties of the water at the ice/ocean interface. Additionally, abrupt changes in pore size like that found at 25 cm in the Kattfjord core bring to light other factors that may disrupt conditions at the ice/ocean interface. While the ice protects much of the underlying ocean from turbulence, wind and tides/currents still have potential to disrupt conditions at the ice/water interface that may lead to variations in ice microstructure. To better understand how these layers of differing microstructure, salinity, and $\delta^{18}O$ develop, continuous observation of environmental conditions is needed.

3.2. Implications

As marine traffic increases, the risk of an oil spill, either from ships or oil production, is becoming more of a concern. Oil emplaced under and frozen into sea ice having a well-understood microstructure of connected brine pores and channels would have a pathway to rise to the surface during spring warming as pores connect (Dickens, 2011; Petrich et al., 2013). If layers of lower porosity or possibly impermeable, freshwater, ice are present, this process will be disrupted resulting in a different oil clean up scenario. In Figs 4 - 9, brine volume fraction was investigated to examine how ice may evolve in warm temperatures when one would expect the pore space to become more connected. In a previous studies by Karlsson et al. (2011), it was estimated that oil migration occurred around 10% brine volume fraction but often not until ice reached even greater values of upwards 15 % brine volume fraction. In five out of the six cores collected, brine volume fraction does not exceed 6 %. It is only the Beisfjord 4 sample, where portions of the ice are above the 10 % threshold with no ice above 15 %. Parts of the core do remain below 10 % however meaning that while oil would possibly be able to migrate upwards it would likely hit a barrier slowing or preventing oil movement to the surface.

Transitions in sea ice microstructure from congelation, columnar ice to granular, frazil ice have also been shown to disrupt and alter how oil rises to the surface even when values for brine volume fraction are high (Oggier et al., 2019). The cores presented here all had transitions as well as several layers of clearly differing pore size and density which could potentially impact the behavior of oil in the ice. Hence, for the cores included in this study, timing of oil surfacing for potential clean up would be likely be difficult to predict.

4. Conclusions

Seven fjords were visited in the northern Norway in March of 2019 with six having ice of thickness ranging from 8 – 46 cm, that was subsequently cored and sampled. Seawater ranged in salinity from 32 to 33.5 psu underneath the ice while bulk ice salinity stayed below 1.5 psu for five out of six fjords, increasing up to 5.8 psu in the remaining core. Measurements of $\delta^{18}O$ largely stayed below -7.67 ‰. The sixth core with high salinity, remained an outlier however having $\delta^{18}O$ values reaching as high as -2.58 ‰.

When examining thick sections, pores of varying shape and size were apparent with many cores holding a mixture of spherical pores of differing diameter and density, thin elongated pores interspersed in relatively transparent ice, occasional brine channels several centimeters in length, and also sections of ice devoid of any pores. The date of ice formation was determined through timelapse images and estimations from ice thickness and air temperature. It is hypothesized here that changing weather conditions resulting in fluctuations in air temperature, snowfall, and runoff from rainfall/snowmelt contributed to layers of differing pore structure. Continuous observations are needed to observe ice formation as well as changes in river input to further support this point. In addition, a greater number of $\delta^{18}O$ measurements taken consistently at the same locations and throughout the year, will further clarify how river water influences ice formation throughout the winter season.

Acknowledgements

This work was funded by the Centre for Integrated Remote Sensing and Forecasting for Arctic Operations (CIRFA), a Centre for Research- based Innovation (Research Council of Norway project number 237906).

References

Anderson, D. L. (1961). Growth rate of sea ice. *Journal of Glaciology*, *3*(30), 1170–1172.

Arrigo, K. ., Mock, T., & Lizotte, M. . (2010). Primary Producers and Sea Ice. In D. . Thomas & G. . Dieckmann (Eds.), *Sea Ice* (1st ed., pp. 283–326). Oxford: Wiley-Blackwell.

Asplin, L., Salvanes, A. G. V., & Kristoffersen, J. B. (1999). Nonlocal wind-driven fjord-coast advection and its potential effect on plankton and fish recruitment. *Fisheries Oceanography*, *8*(4), 255–263. https://doi.org/10.1046/j.1365-2419.1999.00109.x

Brandon, M. ., Cottier, F. ., & Nilsen, F. (2010). Sea Ice and Oceanography. In D. N. Thomas & G. Dieckmann (Eds.), *Sea Ice* (1st ed., pp. 79–112). Oxford: Wiley-Blackwell.

Copernicus Sentinel data (2019) for Sentinel data, processed by ESA.

Dickens, D. (2011). Behavior of oil spills in ice and implications for Arctic spill response. In *OTC Arctic Technology Conference*. Offshore Technology Conference.

Eicken, H. (1998). Deriving Modes and Rates of Ice Growth in the Weddell Sea from Microstructural, Salinity and Stable-Isotope Data. *Antarctic Sea Ice: Physical Processes, Interactions and Variability, Antarct. Res. Ser*, *74*, 89–122. https://doi.org/10.1029/ar074p0089

Eilertsen, H. C., & Skardhamar, J. (2006). Temperatures of north Norwegian fjords and coastal waters: Variability, significance of local processes and air-sea heat exchange. *Estuarine, Coastal and Shelf Science*, *67*(3), 530–538. https://doi.org/10.1016/j.ecss.2005.12.006

Granskog, M. A., Ehn, J., & Niemelä, M. (2005). Characteristics and potential impacts of under-ice river plumes in the seasonally ice-covered Bothnian Bay (Baltic Sea). *Journal of Marine Systems*, *53*(1–4), 187–196. https://doi.org/10.1016/j.jmarsys.2004.06.005

Granskog, M. A., Kaartokallio, H., Thomas, D. N., & Kuosa, H. (2005). Influence of freshwater inflow on the inorganic nutrient and dissolved organic matter within coastal sea ice and underlying waters in the Gulf of Finland (Baltic Sea), *65*, 109–122. https://doi.org/10.1016/j.ecss.2005.05.011

Holtedahl, H. (1967). Notes on the Formation of Fjords and Fjord-Valleys. *Geografiska Annaler.*

Series A, Physical Geography, *49*(2), 188–203.

Hughes, N. (2006). *NP57A, NP57B, NP58A, NP58B Norway Pilot. Sea Ice Conditions: West coast of Norway from: Lindesnes to Statlandet, Statllandet to Risværfjorden. Offshore and coastal waters of Norway from: Risværfjorden to the north part of Vesterrålen, Andfjorden to Varang*. Argyll, UK: Scottish Association for Marine Science.

Kaartokallio, H., Kuosa, H., Thomas, D. N., Granskog, M. A., & Kivi, K. (2007). Biomass , composition and activity of organism assemblages along a salinity gradient in sea ice subjected to river discharge in the Baltic Sea. *Polar Biology*, *30*, 183–197. https://doi.org/10.1007/s00300-006-0172-z

Karlsson, J., Petrich, C., & Eicken, H. (2011). Poac'11, (Amsa 2009).

Lalande, C., Dunlop, K., Renaud, P. E., Nadaï, G., & Sweetman, A. K. (2020). Seasonal variations in downward particle fluxes in Norwegian fjords. *Estuarine, Coastal and Shelf Science*, *241*. https://doi.org/10.1016/j.ecss.2020.106811

Leppäranta, M., & Manninen, T. (1988). *The brine and gas content of sea ice with attention to low salinities and high temperatures*. Helsinki.

Mankettikkara, R. (University of T. (2013). Hydrophysical characteristics of the northern Norwegian coast and fjords. *Dissertation for the Degree of Philosophiae Doctor*, (August).

Myksvoll, M. S. (2008). *Mechanisms affecting the transport of early stages of Norwegian coastal cod - a fjord study*. The University of Bergen.

Myksvoll, M. S., Erikstad, K. E., Barrett, R. T., Sandvik, H., & Vikebø, F. (2013). Climate-driven ichthyoplankton drift model predicts growth of top predator young. *PLoS ONE*, *8*(11). https://doi.org/10.1371/journal.pone.0079225

O'Sadnick, M., Petrich, C., Brekke, C., & Skarðhamar, J. (2020). Ice extent in sub-arctic fjords and coastal areas from 2001 to 2019 analyzed from MODIS imagery. *Annals of Glaciology*. https://doi.org/10.1017/aog.2020.34

Oggier, M., Eicken, H., Petrich, C., Wilkinson, J., & O'Sadnick, M. (2019). Crude oil migration in sea-ice: Laboratory studies of constraints on oil mobilization and seasonal evolution. *Cold Regions Science and Technology*, 102924.

Petrich, C., & Eicken, H. (2010). Growth, Structure, and Properties of Sea Ice. In D. Thomas & G. Dieckmann (Eds.), *Sea Ice* (2nd ed., pp. 23–78). Oxford: Wiley Blackwell.

Petrich, C., Karlsson, J., & Eicken, H. (2013). Porosity of growing sea ice and potential for oil entrainment. *Cold Regions Science and Technology*, *87*, 27–32.

Petrich, C., Langhorne, P., & Eicken, H. (2011). Modelled Bulk Salinity of Growing First-Year. *Proceedings of the 21st International Conference on Port and Ocean Engineering under Arctic Conditions*.

Petrich, C., O'Sadnick, M. E., & Dale, L. (2017). Recent ice conditions in North-Norwegian porsangerfjorden. *Proceedings of the International Conference on Port and Ocean*

Engineering under Arctic Conditions, POAC.

Porter, S. C. (1989). Some geological implications of average Quaternary glacial conditions. *Quaternary Research*, *32*, 245–261. https://doi.org/10.1016/0033-5894(89)90092-6

Skardhamar, J., Albretsen, J., Sandvik, A. D., Lien, V. S., Myksvoll, M. S., Johnsen, I. A., … Bjørn, P. A. (2018). Modelled salmon lice dispersion and infestation patterns in a sub-arctic fjord. *ICES Journal of Marine Science*, *75*(5), 1733–1747. https://doi.org/10.1093/icesjms/fsy035

Vermote, E. (2015). MOD09A1 MODIS/terra surface reflectance 8-day L3 global 500m SIN grid V006. *NASA EOSDIS Land Processes DAAC*, *10*.

Figures and Tables

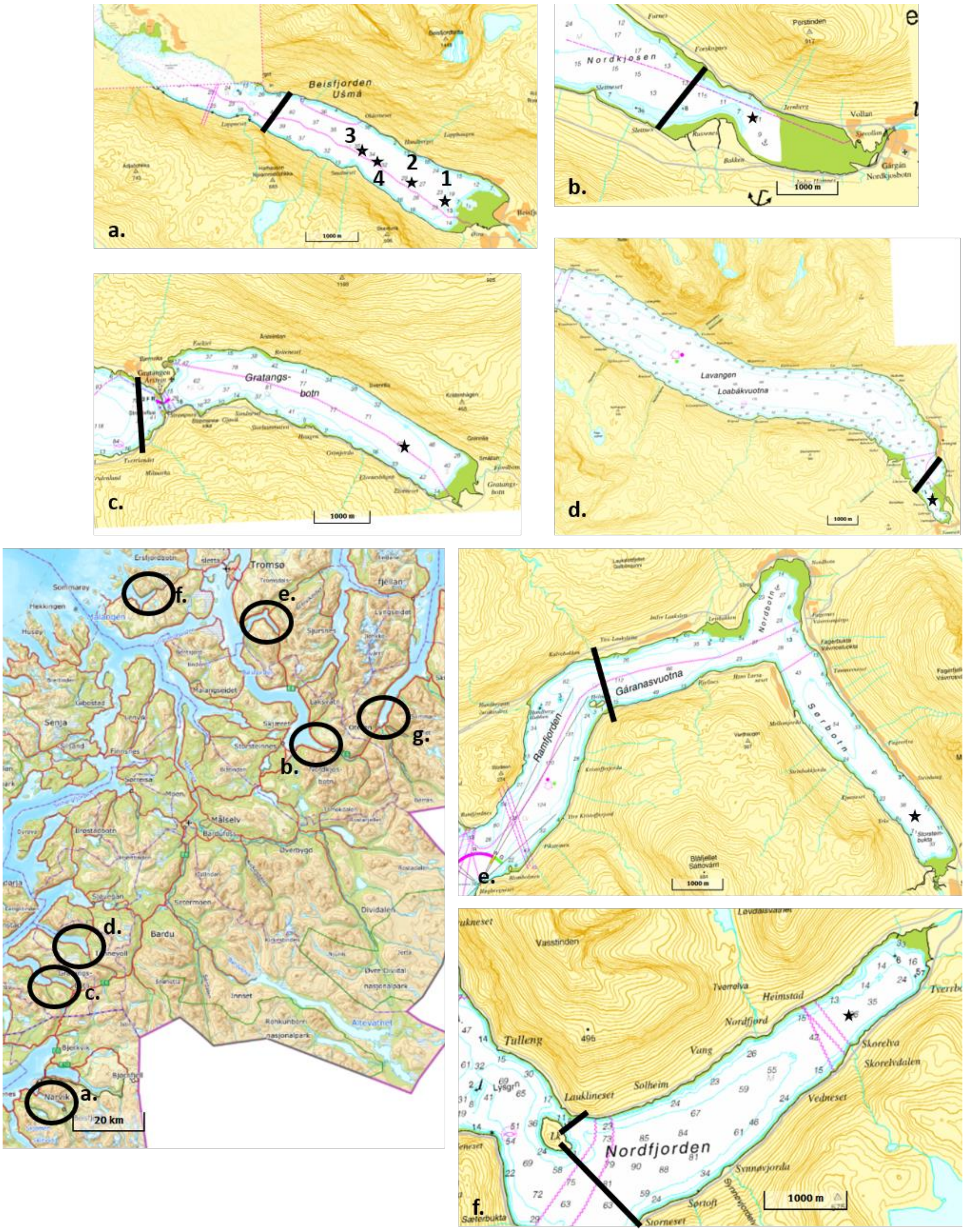

Figure 1. Location of fjords where ice samples were collected, marked with star, with a seventh fjord marked where no ice was present on the day of visit. a) Beisfjord, four locations, marked according to how they are referred in following; b) Nordkjosbotn; c) Gratangsbotn; d) Lavangen; e) Sørbotn/Ramfjord; f) Kattfjord; g) Storfjord (ice- free, no close-up presented).

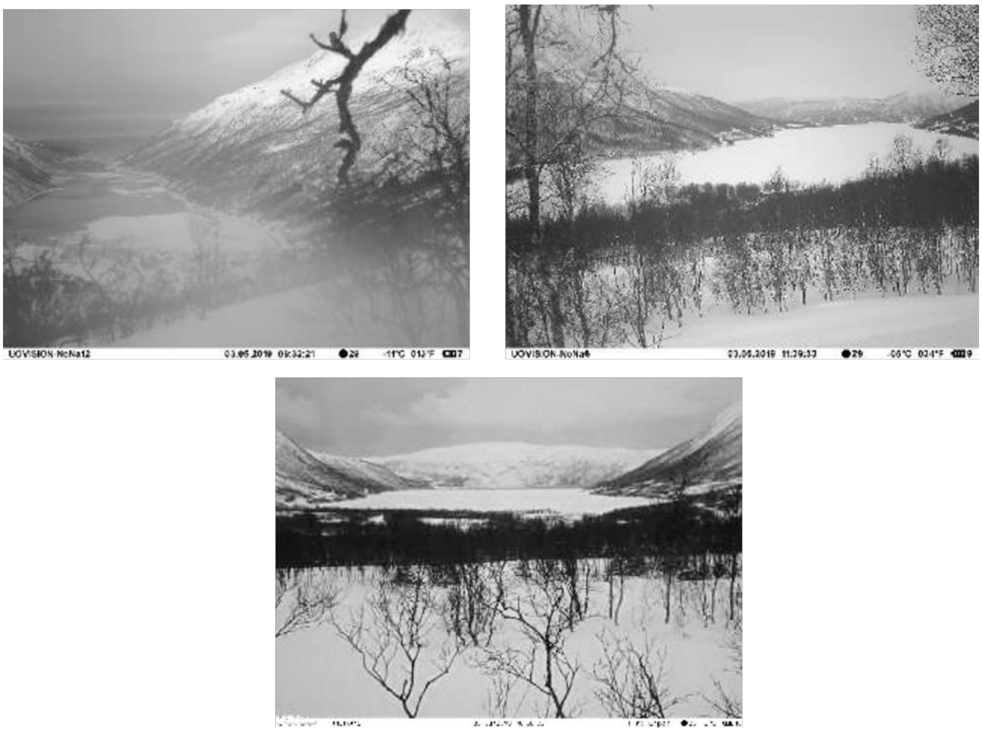

Figure 2. Example of timelapse images gathered on 6 March 2019 at Beisfjord (top, left), Sørbotn/Ramfjord (top, right), Kattfjord (bottom).

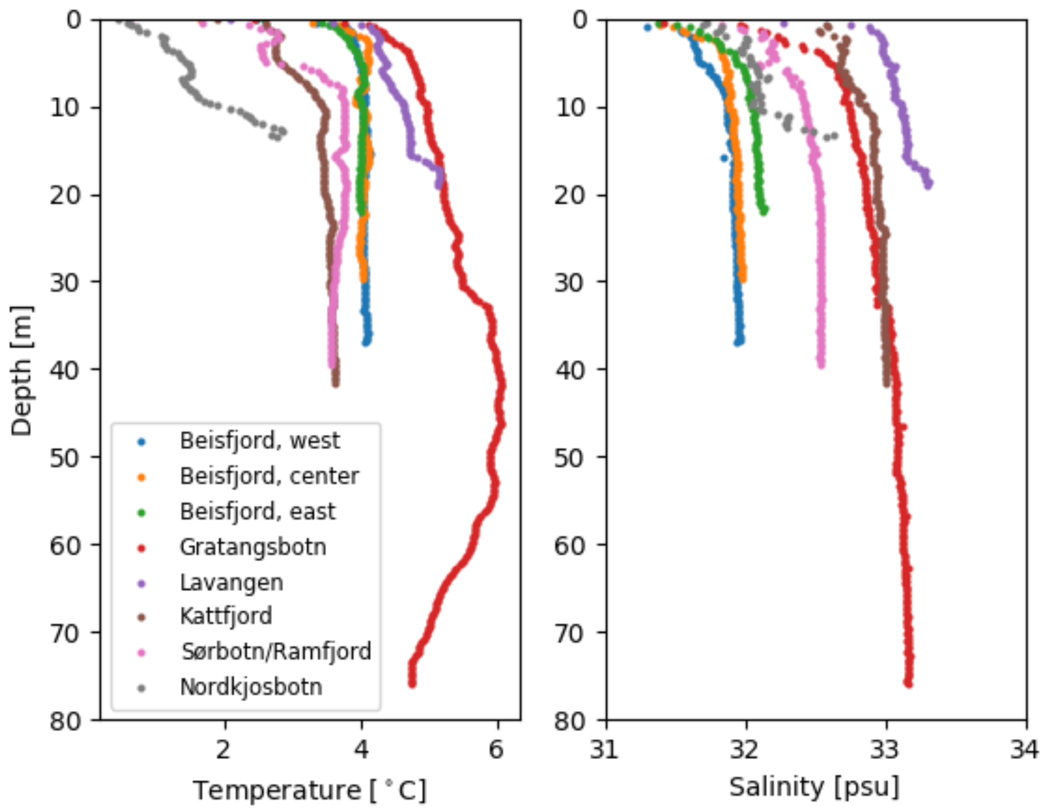

Figure 3. Seawater temperature and salinity under the ice of each core

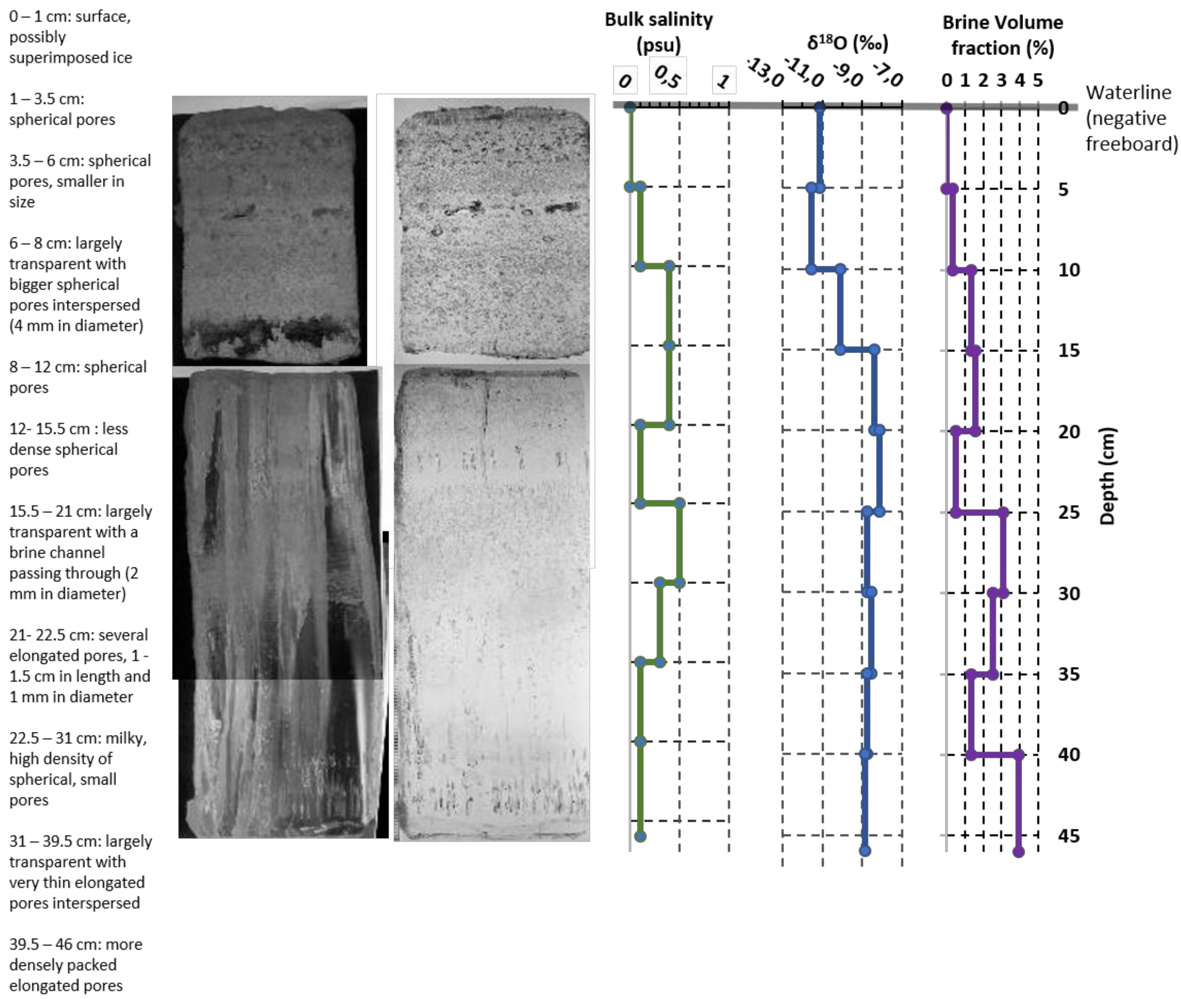

Figure 4. Core sample from Sørbotn/Ramfjord: From left to right- description of layers, cross-polarized imaged, light transmission image, bulk salinity, $\delta^{18}O$, and brine volume fraction.

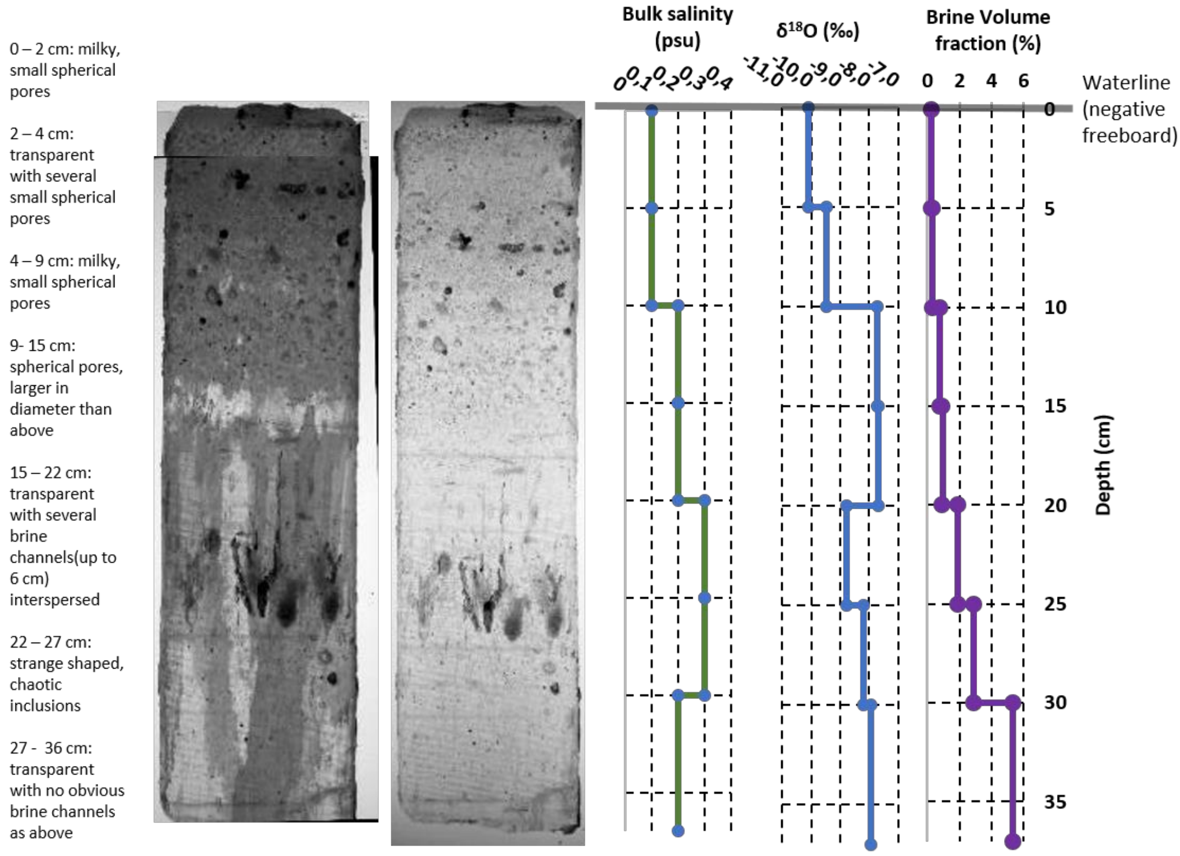

Figure 5. Core sample from Kattfjord: From left to right- description of layers, cross-polarized imaged, light transmission image, bulk salinity, δ^{18}O, and brine volume fraction.

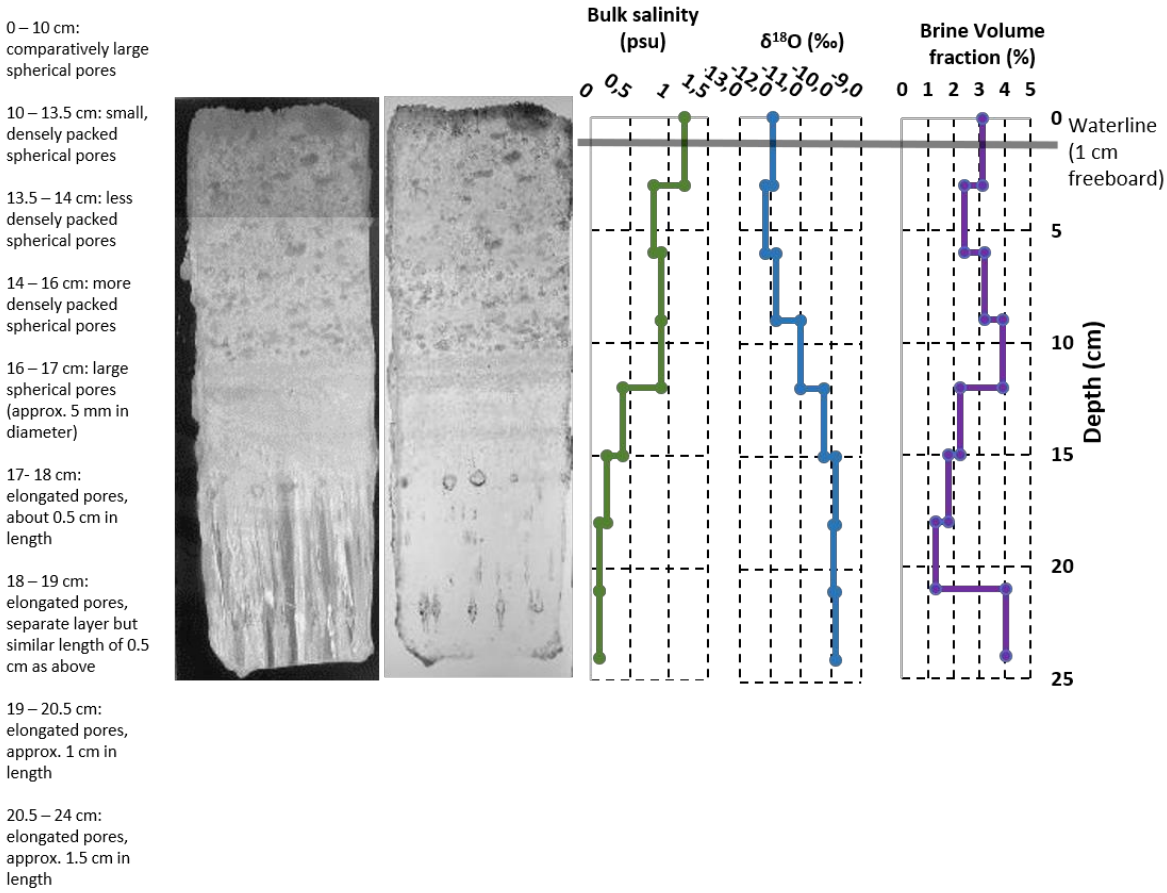

Figure 6. Core sample from Beisfjord 1: From left to right- description of layers, cross-polarized imaged, light transmission image, bulk salinity, $\delta^{18}O$, and brine volume fraction.

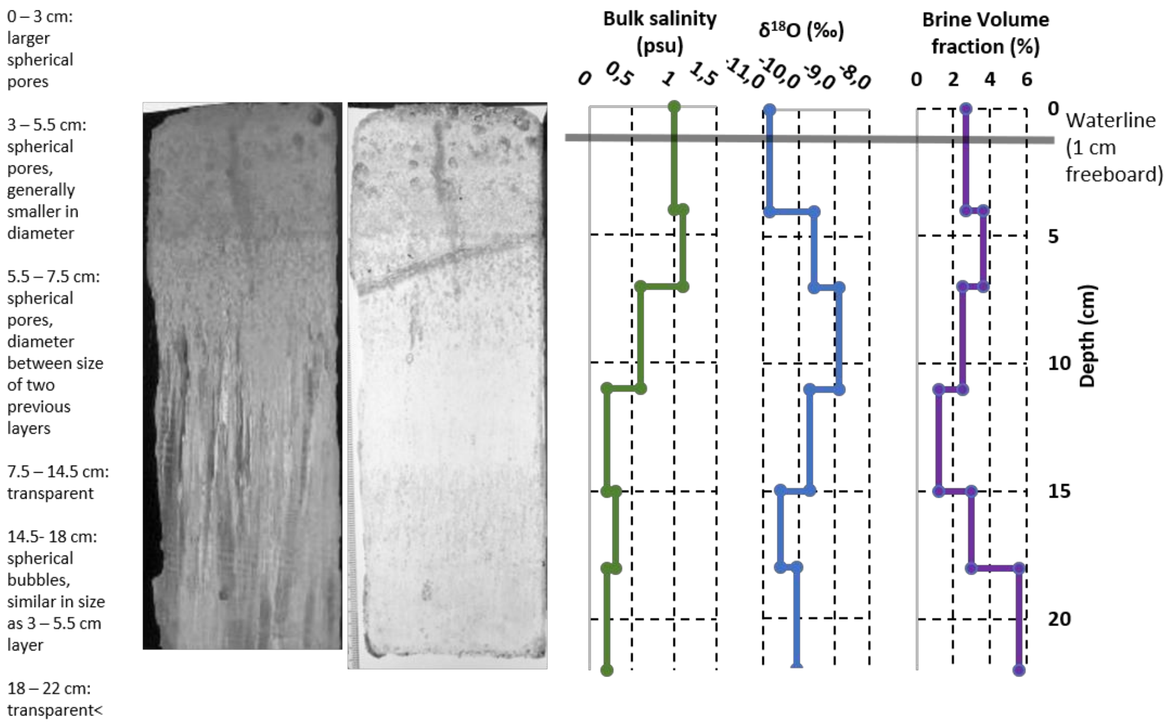

Figure 7. Core sample from Beisfjord 2: From left to right- description of layers, cross-polarized imaged, light transmission image, bulk salinity, δ^{18}O, and brine volume fraction.

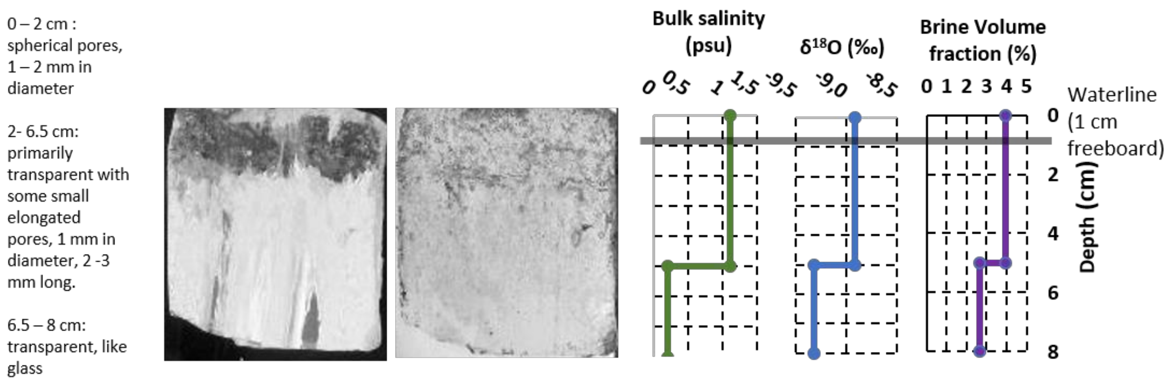

Figure 8. Core sample from Beisfjord 3: From left to right- description of layers, cross-polarized imaged, light transmission image, bulk salinity, δ^{18}O, and brine volume fraction.

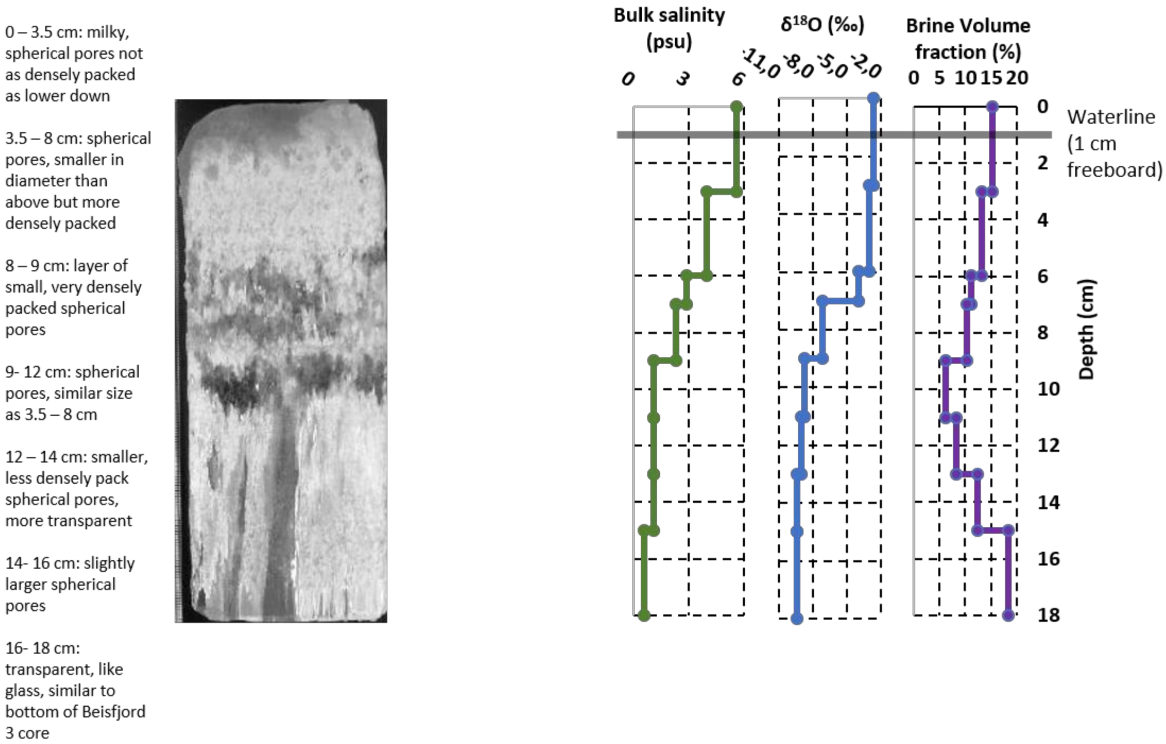

Figure 9. Core sample from Beisfjord 4: From left to right- description of layers, cross-polarized imaged, light transmission image, bulk salinity, $\delta^{18}O$, and brine volume fraction.

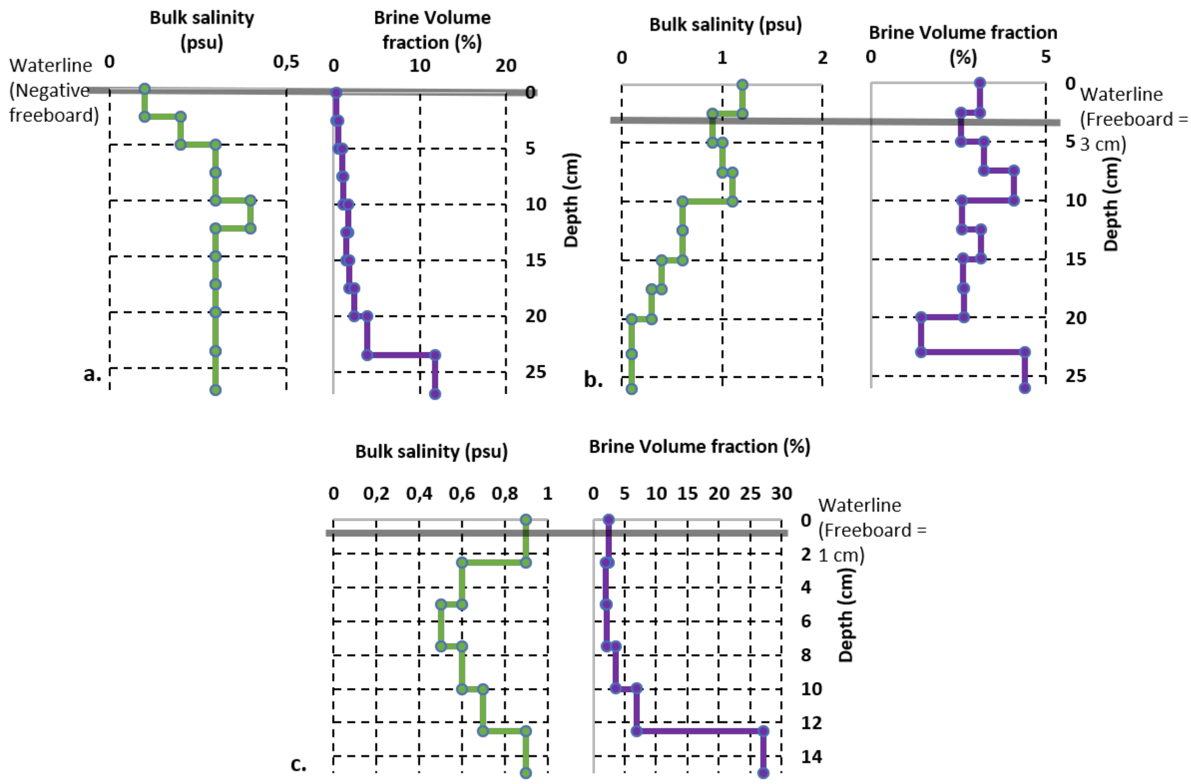

Figure 10. Bulk salinity and brine volume fraction for core samples from a) Gratangsbotn; b) Lavangen; c) Nordkjosbotn

Table 1. Measured ice thickness, freeze-up date, and first day without ice.

Fjord	Ice thickness (cm)	Freeze-Up	Ice Free
Beisfjord	24 (1), 22 (2), 8 (3), 18 (4)	3 March 2019* (from camera)	21 April 2019 (from camera)
Sørbotn/Ramfjord	46	20 December 2018 (from camera)	7 May 2019 (from camera)
Kattfjord	35	14 January 2019 (from camera)	26-27 April 2019 (from camera)
Nordkjosbotn	15	29 – 30 January 2019 (from SAR)	16 – 24 April 2019 (from MODIS)
Lavangen	26	20 – 23 January 2019 (from SAR)	16 – 24 April 2019 (from MODIS)
Gratangen	27	27 – 29 January 2019 (from SAR)	16 - 24 April 2019 (from MODIS)

*Dispersed in bands across fjord, was evidence of ice formation prior near to mouth of fjord but disappeared quickly.

Table 2. $\delta^{18}O$ measurements in ‰ for rivers leading into each fjord and ocean water where ice sampled. Measurement obtained for one ice free fjord, Storfjord, also.

Fjord	River	Ocean
Beisfjord	-12.49	-0.99 (1.0 m)
Sørbotn/Ramfjord	-11.14	-1.06 (0.8 m)
Kattfjord	-10.24	-0.72 (0.8 m)
Gratangen	-10.86	-0.92 (1.0 m)
Nordkjosbotn	-12.15	-0.56 (1.4 m)
Lavangen	-11.34	-0.53 (1.0 m)
Storfjord	-11.55	-0.08 (1.5 m)

25th IAHR International Symposium on Ice

Trondheim, 23 - 25 November 2020

Sufficient independence between barriers

Stian Ruud, (cand. real.)

Department of Civil and Environmental Engineering
Norwegian University of Science and Technology (NTNU)
Høgskoleringen 7a, 7491, Trondheim

Stian.Ruud@ntnu.no

The Norwegian Petroleum Safety Authority (PSA) has requirements for risk reduction described in the Management regulation §5 Barriers. The second paragraph in §5 is stating that *Where more than one barrier is necessary, there shall be sufficient independence between barriers*. In this paper ice management (IM) barriers are described by means of event trees with Boolean barrier events. The number of barriers may be based on the risk related to the end events of the barrier system, but the basic requirement is the single failure requirement. In order to analyze and verify sufficient independence there is a need for precise descriptions of the barrier elements and the logic relations between the elements. Four type of barrier dependency properties are described and related by studying dependencies in a two-barrier system based on 16 truth tables and 16 related Boolean operators. The relations between the four barrier dependency properties are compared by inserting the truth tables in a diagram where the barrier properties are related to different subsets of the diagram. The two-barrier system is then enhanced by an additional common cause. A Boolean model of the enhanced system is motivated by an established FMEA analysis of the single failure requirement of redundant systems. The model will be extended with a formal Boolean method for describing the systems and the associated barrier elements events, thus establishing barrier models where dependencies and common causes may be included, analyzed and verified to be acceptable.

1. Introduction

Design decisions for safe and efficient ice management (IM) systems can be based on performance models and decision criteria for the overall, or parts of the IM system. It is assumed that the PSA requirements (Ref PSA, Regulatory principles 2019) for risk reduction and barriers is the main and superior source of the requirements hierarchy for operations on the Norwegian Continental Shelf and in the Norwegian Arctic Waters.

1.1 Requirements, objectives and assumptions

The PSA 2019 Management regulation §5 Barriers states that: *…Where more than one barrier is necessary, there shall be sufficient independence between barriers…* In the guideline to §5 Barriers the following clarification of sufficient independence is that it: *...should not be possible for multiple important barriers to be impaired or malfunction simultaneously, e.g. as a result of a single fault or a single incident.'…* Further, the PSA 2019 Framework HSE regulation §11 Risk reduction principles states that *'The requirement in this provision for reducing the risks entails that the established minimum level for health, safety and environment, including acceptance criteria for major risk'.* Similar requirements on single failure criterion may also be found in offshore standards e.g. (Ref DNV GL 2018 OS E101).

The objectives of this paper are to

- Interpret *sufficient independency* in Boolean barrier systems with two barriers in the situation of the qualitative approach due to unavailability of frequency data of initial events, barrier probability performance data and quantified dependency data.
- Clarify possible dependency types for Boolean two-barrier systems
- Categorize and compare the 16 possible dependency types by the properties originating from the requirements: 1) sufficient independency, 2) single failure criterion, 3) barrier system risk reduction, and 4) minimum requirements to independency
- Extend the comparison with an additional common cause factor for a two-barrier system

The main assumptions in the paper are a top-down approach with qualitative barrier event trees with (Boolean) performance descriptions (Ref Ruud, S and Skjetne, R. (IMDC 2018). Ruud, S., POAC 2019). This approach is motivated by the lack of quantitative frequency of initial event, and barrier performance probability data. Quantitative common cause/dependency factors may in general be available as beta-factors (Ref Stein Hauge et al. (SINTEF 2015)), but in this paper, it is assumed that quantitative data are not available. The need for more than one barrier may originate from minimum requirements, best industry practice, or ALARP estimates for risk reduction.

1.2 The Boolean barrier event tree modelling approach

Assume that there are two barriers (A, B) which shall be demanded in order to avoid that an end event $€_4$ should occur. In the Boolean equation below, A and B are Boolean variables which may take the value *True* if the barrier *function* and *False* if the barrier *fails*. The initial event $€_0$ will be *True* when the initial event occurs (Figure 1). The conditions for the undesired Boolean variable end event $€_4$ are:

$$€_4 = €_0 \cap \neg A \cap \neg B$$

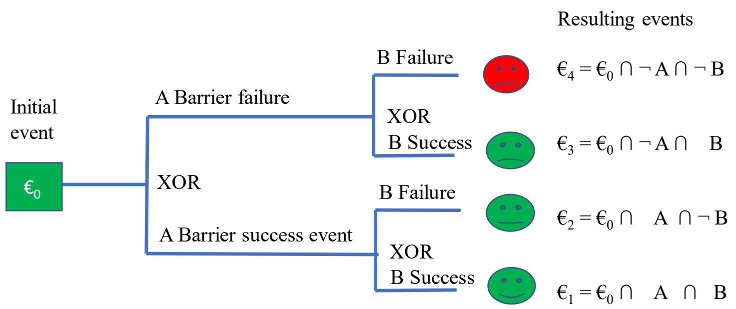

Figure 1. Barrier system consisting of two barriers, A and B. The undesired end event $€_4$ will occur if both barriers A and B have failed after demand of the initial event $€_0$.

A truth table for the four end events with given Boolean performance is given in Figure 2.

B False	$€_2$	$€_4$
B True	$€_1$	$€_3$
	A True	**A False**

Figure 2. Truth table (A∩B) ($€_1€_2€_3€_4$) functions for barrier A and B where the Boolean end events for the barrier system in Figure 1 are inserted.

The end event $€_4$ is acceptable if the failures of A and B are *sufficiently independent*. One of the objectives of the paper is to describe the types of dependencies between A and B which are in compliance with the *sufficiently independent* requirement by means of truth tables Figure 2.

1.3 Categories for barrier system properties

The requirements in §5 Barriers are related to 'sufficient independence' and the 'single failure criterion' in the guideline. However, the overall objective with a barrier system is to provide 'sufficient risk reduction' in order to comply with the performance requirements of the barrier system. In our Boolean approach we must limit the analysis to Boolean performance requirements and the Framework regulation §11 first sets requirements to *'minimum requirements'* and in this context, we assume that minimum requirements also apply for the independency between barriers.

A truth table with two variables may have [0-4] True values. For a two-barrier system, there are $2^4 = 16$ possible truth tables and 16 associated binary operators for defining dependencies. The 16 truth tables will all be categorized with regard to the proposed four types of barrier system properties with given categories (a,..,e) as presented in the list below:

1. Independency/dependency category according to number of True (T) values in the truth table
   a. Boolean independency (4T)
   b. Sufficient and necessary cause dependencies (3T)
   c. Causal dependencies or A or B dependencies (2T)
   d. Dependency (1T)
   e. Barrier system not available (0T)
2. Single failure criterion
   a. All truth tables with (***F), and/or (TTTT) will comply with the failure criterion
   b. All truth tables with (***T) except (TTTT) will not comply to this criterion
3. Barrier system risk reduction
   a. High risk reduction (T**F)
   b. Medium risk reduction (T**T)
   c. Low risk reduction (F**T)
4. Minimum level of barrier independency
   a. Minimum level of independency complied with (TTTT)
   b. Minimum level of independency complied with by monitoring of dependencies in the barrier system (***T)
   c. Minimum level of independency not complied with (F**T)

where * means that either T or F may appear in this position of the truth table.

2. Truth tables with proposed dependency properties

The 16 truth tables are presented according to the number of true values (#T) in the truth tables in the following sections.

2.1 Modelling independency for truth table (4T+0F)

Probabilistic independency between A and B is defined by

$$P(B|A) = P(B)$$

This motivate the definition of independent Boolean variables:

$$B|A=B, \text{ and } A|B=A,$$

with truth table (A B) (TTTT). The table indicates that all 4 combinations of A and B are possible and there are no dependencies between the variables which is also shown in Figure 3.

B False	T	T
B True	T	T
(A indep B)	A True	A False

T	T
T	T

Truth table (TTTT)
A and B independent
Single failure criterion
compliance (green)

Figure 3. Truth table with four true (4T) values representing independent A and B Boolean variable barriers. The green color in the middle truth table represents that the single failure criterion is complied with.

2.2. Modelling sufficient and necessary causes for truth tables with (3T+1F)

In general, we have that if x is a sufficient cause of y, then the presence of x necessarily implies the subsequent occurrence of y. However, another cause z may alternatively cause y. Thus the presence of y does not imply the prior occurrence of x.

Above definition of 'sufficient cause' means that x and y must be assumed to be dependent in some way and such dependencies may be modelled in terms of Boolean algebra and truth tables for A and B barriers. In formal logic the sufficient cause dependency type may also be denoted as A→B or described as *Material implication* or *Modus ponens* and the table is given in **Figure 4.**

B False	F	T
B True	T	T
(A →B)	A True	A False

F	T
T	T

A function is sufficient
function cause of B.
(A→B) (TFTT)

Figure 4. If A function is sufficient cause function of B, then the truth table is (A → B) (TFTT)

The above dependency case where *function of A is sufficient cause of function of B* means only that one can be sure that if A is functioning, then B will be functioning. There is also an implication that B cannot be failing if A is functioning. But if A is failing (F), B may function (T) or be failing (F).

In a similar manner the 4 truth tables for 4 possible different combinations (3T+1F) of *sufficient cause* of A and B are shown in Figure 5 below.

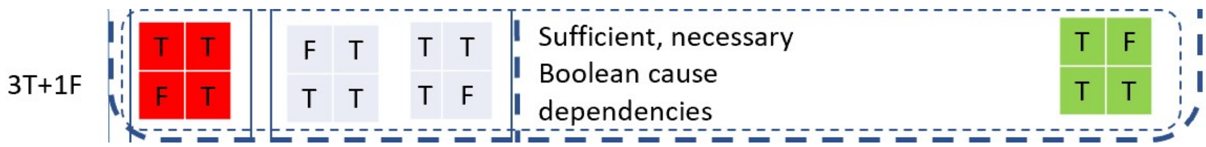

Figure 5. Truth tables for 4 sufficient causes and combinations of A and B values. The single failure criterion will always be complied with for (¬A→ B) (TTTF) (green) since this dependency type will always lead to either end event €$_1$, €$_2$ or €$_3$ and not the end event €$_4$.

In general, we have that 'If x is a necessary cause of y, then the presence of y necessarily implies the prior occurrence of x. The presence of x, however, does not imply that y will occur.'

The truth table for 'A function is necessary cause for B function' is $(A \leftarrow B)$ (TTFT) where the operator 'Converse implication' is denoted $\leftarrow$. In a similar manner as shown for sufficient causes the truth tables for 4 combinations of necessary causes will be the same as shown in Figure 5, but with changed sequence and property associations.

2.3. Positive and negative dependencies for truth tables (2T+2F)

Boolean positive dependency for barrier A and B is proposed to be defined as

If $A|B = B$ or if $B|A = A$, and the truth table for both relations is $(A=B)$ (TFFT), (Figure 6.)

The relations for our barrier system may also be stated as shown below:

$$€_4 = €_0 \cap \neg A \cap \neg B = €_0 \cap \neg A \cap \neg A = \underline{€_0 \cap (\neg A)}$$

This means that if barrier A fails, then barrier B will always fail, thus meaning that the end event $€_4$ will occur and meaning that the single failure criterion is not complied with for positive dependency between barriers A and B. It also means that the *sufficient independency* requirements are not complied with for positive dependency between barrier A and B.

B False	F	T
B True	T	F
(B=A)	A True	A False

B dependent positively of A (TFFT)

Figure 6. Truth table for B positively dependent of A (TFFT). The single failure criterion and sufficient independency requirements are not complied with.

Positive dependency may also be described as causal dependency, IF AND ONLY IF, sufficient and necessary causes. An example of an ideal operational forecast and start decision of an operation is assuming positive dependency between the forecast barrier A and the decision barrier B of the operation (Figure 7).

Negative result	Too positive F	Negative justified, T
Positive result	Positive justified, T	Too negative F
(B=A)	Positive forecast	Negative forecast

Figure 7. The perfect operational forecast for decision of running a future operation should be positive dependent. Barrier A is the forecast and Barrier B is the start decision of the operation.

Positive dependency types may be desired and acceptable in an operation if the state of barriers and independency may be monitored and used for operational decisions.

If A|B = ¬ B, or if B|A = ¬A, can be denoted as *negative dependency* between A and B or Exclusively OR, (XOR) and the truth table is (A⨁B) (FTTF) as shown in Figure 8. The single failure criterion will always be complied with and is denoted by green truth table.

B False	T	F
B True	F	T
(A⨁B)	**A True**	**A False**

T	F
F	T

B is negatively dependent of A, Exclusive or, XOR, (A⨁B) (FTTF)

Figure 8. Truth table for negative dependency or exclusive disjunction.

An example of negative dependency is for lifeboats on port and starboard side (Figure 9) of a sinking ship (initial event $€_0$). For the negative dependency (B= ¬ A), either the port side or starboard lifeboats may be applied, and the undesired event may be expressed as

$$€_4 = €_0 \cap \neg A \cap \neg B = €_0 \cap \neg A \cap \neg(\neg A) = €_0 \cap (\neg A \cap A) = €_0 \cap Ø = Ø$$

which means that the undesired end event $€_4$ will never occur since either A or B may be used.

This means that the negatively dependent barrier system will provide complete risk reduction for $€_0$ and that the single failure criterion is always complied with.

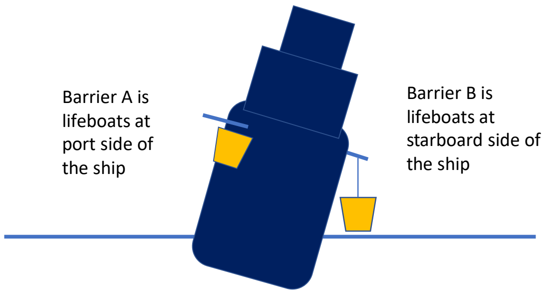

Figure 9. Lifeboats at port side (Barrier A) of the ship cannot be lowered to the sea due to heeling of the ship to starboard. The lifeboats at the starboard side (Barrier B) may be lowered as the lifeboats on port side are stuck due to the heeling.

Another example of two negatively dependent barriers is positioning of a supply ship which will normally be on the leeward side of the platform, so if the power of the supply ship is lost, the barrier function is to drift with the wind and away from the platform (Figure 10).

There are six truth tables with (2T+2F). Above the positive (TFFT) and negative (FTTF) dependency are described. The four others are (TTFF), (TFTF), (FFTT), (FTFT) will be included and categorized in the overall truth table diagram later in the paper.

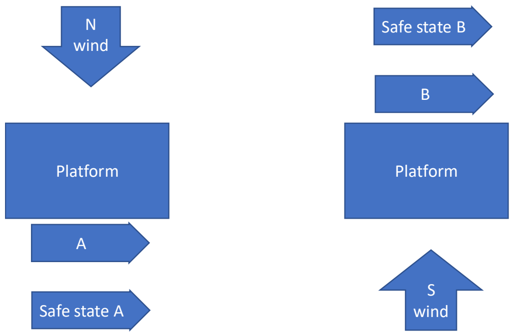

Figure 10. Positioning of a supply ship on the leeward side (A, B) of a platform represent barriers which are negatively dependent.

2.4 Boolean dependency for truth tables (1T+3F)

There are four truth tables with 1T which are (TFFF), (FTFF), (FFTF), (FFFT).

The truth table (TFFF) will give the maximum risk reduction because $€_1$ will always occur and the single failure criterion will always be complied with. The dependency between A and B will always be fixed and there will be full dependency.

The truth table (FFFT) will give minimum risk reduction because $€_4$ will always occur and the single failure criterion will never be complied with. The dependency between A and B will always be fixed and there will be full dependency.

The truth tables (FTFF) and (FFTF) will always comply with the single failure criterion and in both cases, there will be full dependency between A and B.

2.5. Summary of properties for 16 Boolean dependency types for two-barrier systems

Figure 11 illustrates how the four barrier dependency property types may define a diagram where the 16 truth tables may be located in specific table truth subsets according to the property subcategories. This enables us to relate the different verbal barrier dependency properties in a strictly logic manner.

§5 Barriers assumes that sufficient independence should be related to the single failure criterion. The diagram in Figure 11 shows that for Boolean barrier variables the sufficient independence is assumed in the upper part (3T-4T) of the diagram with two green, two grey, and one red truth tables. The single failure criterion is however complied with in the right part (8 green truth tables) of the diagram. This indicates that the sufficient independence criterion is weakly connected to the single failure criterion.

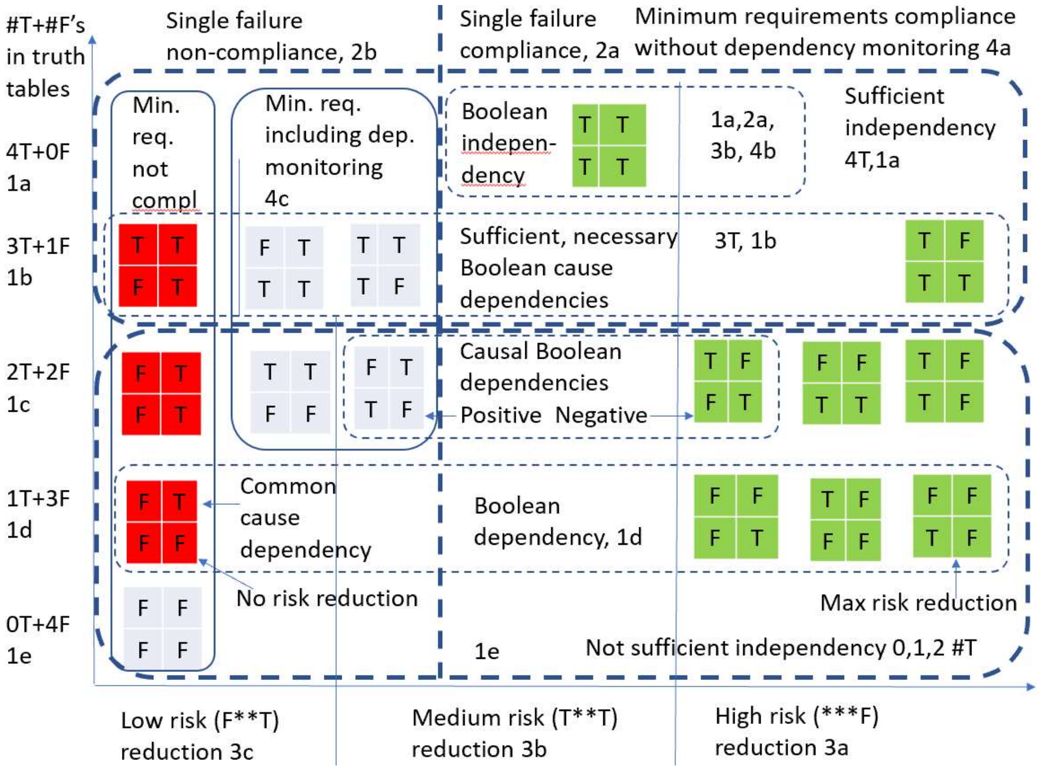

Figure 11. The four dependency property types for 16 truth tables for two-barrier systems

Minimum requirements to independency without monitoring of dependency elements are complied with for green truth tables in the right part of the diagram. The green truth tables are also complying with the single failure criterion and the high barrier risk reduction. This indicates that the three properties: 1) minimum requirements to independency, 2) the single failure criterion and 3) high barrier risk reduction are strongly connected.

3. Common cause dependencies for two-barrier systems

Common causes influencing the barriers may provide external dependency of the barriers. The definition of common causes is chosen to be

Common cause failures*, IEV 192-03-18, failures of multiple items, which would otherwise be considered independent of one another, resulting from a single cause (Ref Electropedia).*

The following example of a common cause X for the independent barrier system A and B provide an example of how one may analyse the single failure criterion and sufficient independency for an external common cause X.

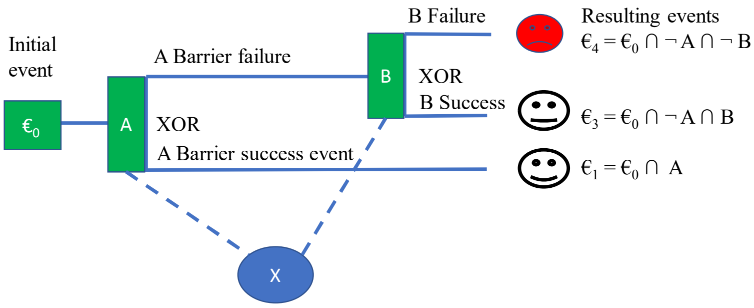

Figur 12. The common cause X failure will cause barrier A and B to fail so that the barrier system is not complying to the single failure criterion and the system is not sufficiently independent.

Barrier A and B have a common cause failure X. Assume that A and B are independent, and that X failure may be a common failure cause to A and B, so that if A or X fails, then the A' barrier will fail. The failure propagation from X to A and B is similar and assumed to be described by

$$A' = A \cap X$$
$$B' = B \cap X$$

and the undesired end event $€_4$ will occur with the following conditions:

$$€_4 = €_0 \cap \neg (A \cap X) \cap \neg (B \cap X)$$
$$€_4 = €_0 \cap \neg ((A \cup B) \cap X)$$
$$\underline{€_4 = €_0 \cap (\neg A \cap \neg B \cup \neg X)}$$

Variables A, B and X are independent, but A and B are both dependent (conjunction, ∩) of X in the barrier structure. If X is not causing failure, the single failure criterion is complied with, but if X is failed X will propagate to both A and B such that the barrier system will fail with one single failure. This means that the single failure criterion is not complied with for this barrier system. The barrier system will not comply with the sufficient independence criterion either since both A and B will fail simultaneously if the common cause X fails. A similar approach is described in a recommended practice for FMEA of redundant systems (Ref DNV-RP-D102 (2012)).

4. Summary and conclusion

This paper is based on PSA requirements and possible interpretations of verbal descriptions of dependencies into a Boolean model context with some practical examples. In a situation with lack of quantitative data for barrier performance and dependencies, it is proposed to describe the barrier systems with Boolean variables and binary operators to represent the barrier functions and possible dependencies in the barrier systems. Sixteen dependency types are presented, and four barrier properties are assigned to the 16 truth tables. The main conclusions so far are:

- A Boolean model for representation of qualitative barrier system may provide a viable method for representation of the performance of the barriers and dependencies between the barriers
- The regulative requirement of *sufficient independence* and the guideline for using the *single failure criterion* is weakly connected
- The properties of the dependencies may be used for analyzing and designing improved barrier structure e.g. negative causal dependency
- Truth tables like (A→ B) (TFTT) is communicating dependency relations better than verbal dependency descriptions like *sufficient cause, modus ponens, material implication, converse implication, disjunction, exclusive and inclusive conjunction.*
- Truth tables and binary operators may be quite straightforward to be prepared for computer representation and calculations. Visual presentation of the logical structures for computer display is viable to develop both for design decisions and operative decisions.

5. Further work

The work presented must be considered as ongoing research. In order to make the proposed theoretic results applicable for future industrial use the following projects are proposed:

- The ice management (IM) barrier system designer should take benefit of increased risk reduction by searching for possible negatively or positively dependent barrier systems which may give higher risk reduction than an independent barrier system
- In the operational phase, dependencies may be subject to variable operational conditions. The designer must consider if positive conditions should allow for safe operational windows. Such cases must be based on monitoring of the operational conditions
- In the design phase, possible barrier independencies must be identified and claimed independencies must be justified by the designer
- Justification of claimed independencies may be based on analyses, testing and data collection. Data collection should be planned to be carried out during IM operations
- Practical case for demonstration of operational barrier display of barriers and operational interpretation of sufficient independency, and dependencies displaying what is the actual barrier system state. Apply the knowledge of dependencies to design barrier systems.
- Practical case for demonstration of operational status presentation of barriers and dependencies for operational decisions
- Develop methods for examination of barrier performance and provision of objective proof for confirmation of the requirements to the barriers system

- The first stage of barrier independency performance is based on minimum requirements performance assuming a Boolean model. The next step is to carry out an ALARP performance of independency based on quantitative analyses

6. Acknowledgements

This work was supported by the Research Council of Norway through the SFI SAMCoT, RCN project. no. 203471. The paper has been commented by Åke Rohlen Arctic Marine Solutions (AMS) and Roger Skjetne NTNU. The work must be considered as ongoing research and is not applicable for practical industrial use in its current form.

7. References

DNVGL-OS-E101: 2018, Drilling facilities, Offshore Standards, 2018

DNV-RP-D102 (2012) Failure Mode and Effect Analysis (FMEA) of Redundant Systems

Electropedia: The World's Online Electrotechnical Vocabulary, http://www.electropedia.org/

ISO 14224:2006 -- Collection and exchange of reliability and maintenance data for equipment Petroleum, petrochemical and natural gas industries

ISO 35104:2018, Arctic operations — Ice management

PSA 2019 Framework HSE §11 Risk reduction principles, https://www.ptil.no/en/regulations/all-acts/?forskrift=158

PSA 2019 Management regulation §5 Barriers https://www.ptil.no/en/regulations/all-acts/?forskrift=611

PSA 2019 Regulatory principles http://www.psa.no/regulatory-principles/category932.html

Ruud, S and Skjetne, R. IMDC 2018. Ice management and design philosophy, International Marine Design Conference 2018

Ruud, S., POAC 2019, Minimum requirements to ice management barrier systems,

Stein Hauge et al. (SINTEF 2015), A2692 Common cause failures in Safety Instrumented Systems,

11
Icebergs

25th IAHR International Symposium on Ice

Trondheim, 23 - 25 November 2020

Monitoring of 3D motion of drifting iceberg with an ice tracker equipped with accelerometers

Aleksey Marchenko[1], Alex Zenkin[2], Nataly Marchenko[1], Chris Paynter[3], Yiyi Whitchelo[4], Thea J. Ellevold[4], Atle Jensen[4]

[1]*The University Centre in Svalbard*
PO Box 156, N-9171 Longyearbyen, Norway
Aleksey.Marchenko@unis.no
Sinaptics, San Jose, USA
Oceanetic Measurement (2011) Limited, B.C., Canada
University of Oslo, Oslo, Norway

The ice tracker (Oceanetic Measurements LtD) was deployed on a bergy bit on April 27, 2019, during the cruise of Polarsyssel in the Barents Sea. The tracker was recording GPS coordinates and yaw angle with sampling interval of 30 min, and 3D accelerations with sampling frequency of 2 Hz during 2048 s each hour. Iridium modem transmitted GPS coordinates, yaw angles, and complex spectrum of the accelerations. The FFT was programmed in C to reduce amount of transmitted data and keep useful information about wave induced motions with periods of wind waves and swell (5-30 sec). The bergy bit was scanned from the ship by the Laser scanner Riegl Vz-1000 and observed from below by ROV. Obtained data are analyzed and discussed in the paper. It is discovered that the bergy bit motion includes component corresponding to the action of swell with the period of 11 s. The action of swell influences maximal accelerations of the bergy bit over the period of observations.

1. Introduction

Investigation of iceberg drift is important for offshore development and navigation in the Barents Sea. Approaching of icebergs to offshore installations on small distances should be prevented by iceberg management according to ISO-19906. Small icebergs and bergy bits not always can be recognized remotely. Their collisions with constructions and ships are still dangerous and influence greater damage than collisions with drift sea ice. Typical example is the collision of oil tanker Overseas Ohio with an iceberg in Prince William Sound caused strong damage of the bulb with formation of a through hole with diameter of several meters. The iceberg mass was estimated only between 4000 and 7500 tons (Tangborn et al, 1994).

A review of iceberg and bergy bit hydrodynamic interaction with offshore structures was performed by Sayeed et al (2017). The review includes information about experiments and mathematical models of iceberg drift in the vicinity of structures, iceberg collisions, and multi-body hydrodynamic interaction. Effect of wave action on ice drift and effect of the excitation of steady waves between small iceberg and fixed structure are pointed out as important effects for the acceleration of icebergs in wave conditions. Modelling of ship collision with bergy bit was performed by Gagnon and Wang (2012).

Observations of icebergs drift was performed in different regions by radars (Sodhi and Mona El-Tahan, 1980) and ice trackers mounted on the icebergs and transmitting the coordinates of their geographical locations by satellites (Løset and Carstens, 1996; Turnbull et al., 2015; Buzin et al., 2019). Yulmetov et al (2016) investigated rotation of icebergs relative to the vertical axis using the records of two ice trackers deployed on the same icebergs. Rotation of drifting iceberg relative to the vertical axis was observed visually in the Barents Sea (Marchenko et al., 2019). Usually the iceberg motion recorded with sampling interval of 10 minutes or greater. This sampling interval is very large to investigate iceberg motions caused by swell or natural oscillations.

In the present paper we investigate motions of drifting bergy bit recorded by the ice tracker equipped with an accelerometer designed for the monitoring of surface waves in drift ice. Ice trackers equipped with accelerometers were used earlier for the monitoring of waves in ice environment (Doble et al., 2017; Rabault et al., 2020), but not for the monitoring of iceberg drift. The paper is organized as follows. In the second section geometrical properties of drifting bergy bit are described and the frequency of natural oscillations is estimated. The construction of ice tracker deployed on the bergy bit, in-situ data processing and data transmission are described in the third section of the paper. Characteristics of the bergy bit drift reconstructed with recorded data are described in the fourth section. Main finding are formulated in the conclusions.

2. Field investigations of drift ice in the West Barents Sea

Field works on drift ice to the South of Spitsbergen and Hopen Island were performed in April-May 2017-2019 during the cruises of Polarsyssel organized within the study program of the Arctic Technology Department at UNIS. It was discovered that drifting ice includes sea ice floes with diameter of 20-30 m and drafts up 5-9 m, small icebergs and bergy bits (Marchenko, 2019a). Floes consisted of sea ice are recognized as consolidated ice ridges (Marchenko, 2019b). Icebergs and bergy bits look different from these floes because of bigger drafts, different shape and colors. The iceberg surface is usually smooth and has free board greater than 1 m. At the same time big blocks of glacier ice can be at the surface of icebergs and bergy bits. An example of typical bergy bit is shown in Fig. 1 (left panel).

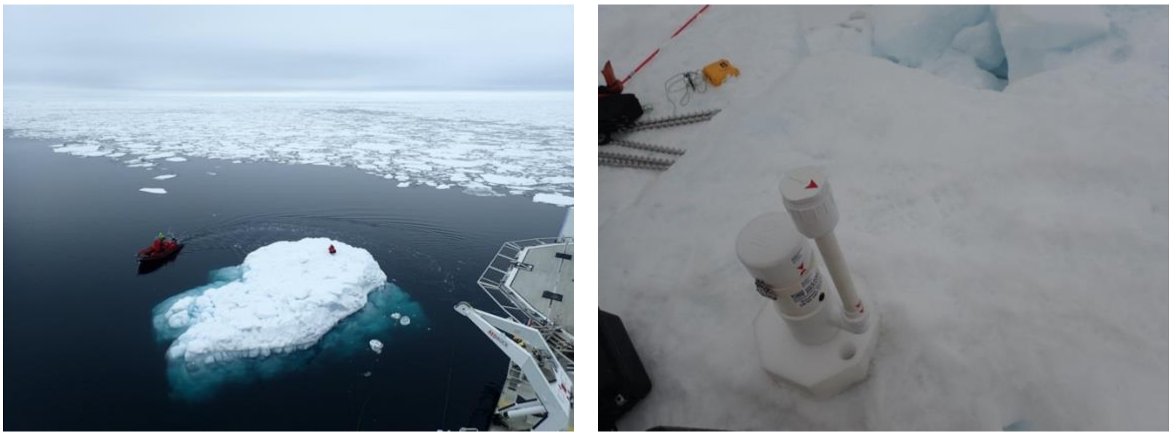

Figure 1. Deployment of ice tracker on the bergy bit on April 27, 2019 (left panel). Ice tracker deployed on a floe (right panel).

Laser scanning was performed from several location onboard of Polarsyssel with laser scanner Riegl-Vz 1000 (Fig. 2). The horizontal dimensions of the bergy bit varied within 15-25 m. The volume of above water part of the bergy bit was estimated as V_{fb} = 600-650 m^3, and the mean free board was h_{fb} = 1.75 m. The bergy bit keel was investigated visually with ROV. It had a conical shape with maximal draft of around 16 m. The volume of bergy bit is estimated with the formula

$$V_i = \frac{\rho_w}{\rho_w - \rho_i} V_{fb}, \qquad [1]$$

where ρ_w ≈1020 kg/m^3 is sea water density, and ρ_i ≈916 kg/m^3 is density of ice. From (1) it follows that V_i = 5884 – 6375 m^3, and the bergy bit mass is M_i =5.39 – 5.84 ·10^3 t. Maximal length of the sail is estimated from Fig. 2 about L =23 m, and the ratio M_i/L^3 is 0.44-0.48. The ratio is higher the average ratio 0.3 discovered for icebergs on Canadian shelf (Bruneau, 2004) because the widest part of the bergy bit was below water level and not visible on the laser scan image.

Natural frequency of bergy bit oscillations in a calm water is estimated from the balance of the inertia, gravity and buoyancy forces

$$M_i \ddot{z} = -M_i g + \rho_w \left(V_{d,0} - S_w z\right) g, \qquad [2]$$

where z is the vertical displacement of bergy bit relative to the water surface at $z = 0$, $\ddot{z}$ is the vertical acceleration of the bergy bit, $V_{d,0} = V_i - V_{fb}$ is the volume of submerged part of the bergy bit in hydrostatic equilibrium, and S_w is the bergy bit area at the water line estimated by the formula $S_w \approx V_{fb}/h_{fb}$. In hydrostatic equilibrium $M_i = \rho_w V_{d,0}$, and the natural frequency is determined by the formula

$$\omega_i^2 = \rho_w g S_w / M_i. \qquad [3]$$

Numerical estimates give $\omega \approx 0.127$ Hz. Corresponding period of the natural oscillations is 7.87 s.

If water level changes due the propagation of long waves (swell), then equation (2) modifies to

$$M_i \ddot{z} = \rho_w S_w (z_w - z) g, \quad [4]$$

where $z = z_w(t)$ is the vertical position of water surface near the bergy bit disturbed by waves relative to the calm water surface, and t is the time.

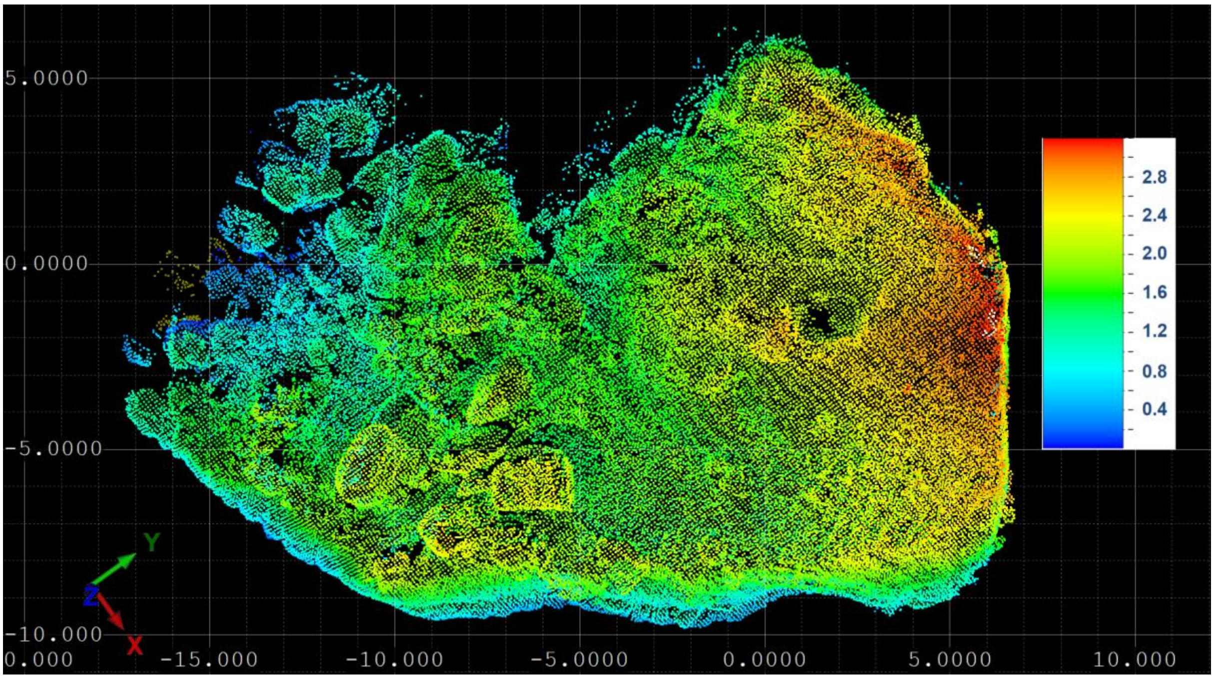

Figure 2. Bergy bit surface after the laser scanning from Polarsyssel.

Assuming that $z_w = a_w \sin(\omega t)$, where ω and a_w are the swell frequency and amplitude, we find

$$a_i = \gamma a_w, \gamma = \frac{\omega_i^2}{\omega_i^2 - \omega^2}, \quad [5]$$

where a_i is the amplitude of forced oscillations of bergy bit. The forced vertical oscillations of bergy bit are described by the formula $z = \gamma a_w \sin(\omega t)$. The amplitude of displacement of bergy relative to the water level equals $(1 - \gamma) a_w$.

3. Characteristics of ice tracker

The buoy Oceanetic Model 703-1901 uses a VectorNav VN-100 Inertial Measurement Unit (IMU) to measure acceleration of ice floes due to water waves. Acceleration is measured in the three axes True North, East, and Down at a selectable rate and duration. A Fast Fourier Transform (FFT) of each axis is programmed in C, and the real and imaginary FFT results are broadcast over the Iridium satellite network. Along with the FFT results, the buoy measures its yaw or heading angle relative to the True North at the beginning of each sampling session, so that rotation of the buoy and ice floe may be monitored. The buoy also measures GPS position every 30 min. All raw acceleration data and FFT results are recorded on an SD card.

The buoy may be remotely programmed with the following parameters:

- Transmit up to 160 FFT bins, selectable in groups of 5 from bins 0-239 (default bins 30-99)
- FFT length 512 or 1024 (default 1024)

- IMU sample rate of 200, 250, 400, or 500 ms (default 500 ms)
- Number of IMU samples of 512, 1024, 1536, or 2048 (default 2048)
- Period of sample collection from 1-24 hours (default 4 hours)
- IMU data are generated at 800 Hz sampling frequency and can be averaged over 4, 100, 200, or 400 samples (default 200).

The VN-100 uses its internal magnetometer, gyroscope and accelerometers to determine its orientation relative to True North, and uses GPS location in conjunction with the Magnetic World Model. As such, the VN-100 is sensitive to magnetic fields, and is therefore mounted on a boom away from the body of the buoy. The VN-100 is calibrated at the factory for soft and hard iron effects, and does not require a calibration step for the magnetometer. Figure 1 (right panel) shows ice tracker deployed on a floe during Polarsyssel cruise 2019. The default settings were used with the period of sample collection of 1h. It means that raw data were recorded during the interval of 512s two times per hour. Then, 70 complex FFT amplitudes of the North, East and Down accelerations were transmitted via Iridium for each interval of 512s.

4. Analysis of obtained data

Location of the field works and the trajectory of the ice tracker (IT) deployed on the bergy bit are shown in Fig. 3. General direction of IT drift was to the South-West. The trajectory had several lopes and "corner" points with high curvature because of combined action of semidiurnal tide and wind drag. Black points in the right panel of Fig. 3 show IT locations over the semidiurnal period M2 of 12.42 h. Figure 4 shows drift speed and acceleration versus the time reconstructed from the GPS positions of IT recorded with 30 min sampling interval.

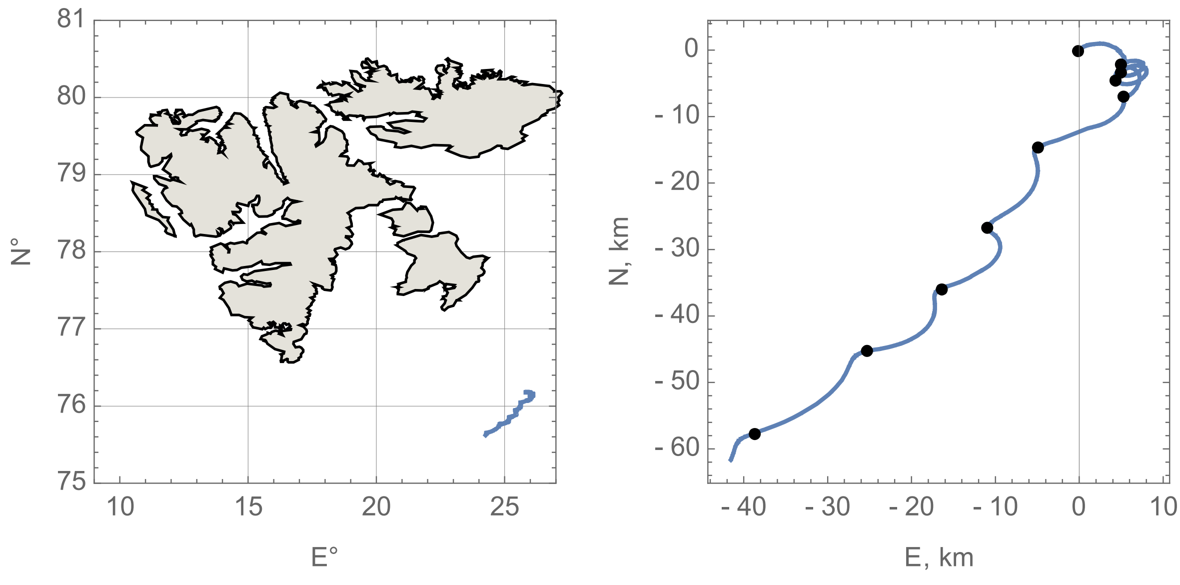

Figure 3. Map of Svalbard with the trajectory of the bergy bit (left panel). Bergy bit trajectory (right panel). Black points show locations of IT after each semidiurnal period of 12.42 h starting from the initial position.

The dependencies of IT velocities from the time were obtained with using the following procedure realized in Wolfram Mathematica software. On the first step the function GeoDistance was applied to get distances between consequent IT positions in the Metric System. Then Interpolation with Interpolation Order 1 was used to build continuous function describing the dependence of IT positions from the time. On the next step the function D (partial derivative) was used to calculate IT velocities in the North and South directions in discrete times with step of 6 min. The absolute IT velocity calculated after this procedure is shown in the left panel of Fig. 4 versus the time. For the calculation of IT accelerations, the function Interpolation was applied to the lists of IT velocities, partial derivatives were used to calculate IT accelerations in the North and South directions, and then the function Moving average over 2 h was applied. The last operations was applied to the lists of IT accelerations with different intervals of the averaging to get stable result with small noise. The absolute IT acceleration is shown in the right panel of Fig. 4 versus the time. The left panel in Fig. 4 tells that representative variation of IT velocity was of about 0.2 m/s per 5 hours. It gives the acceleration of 0.01 mm/s2. The right panel in Fig. 4 shows accelerations of the same order.

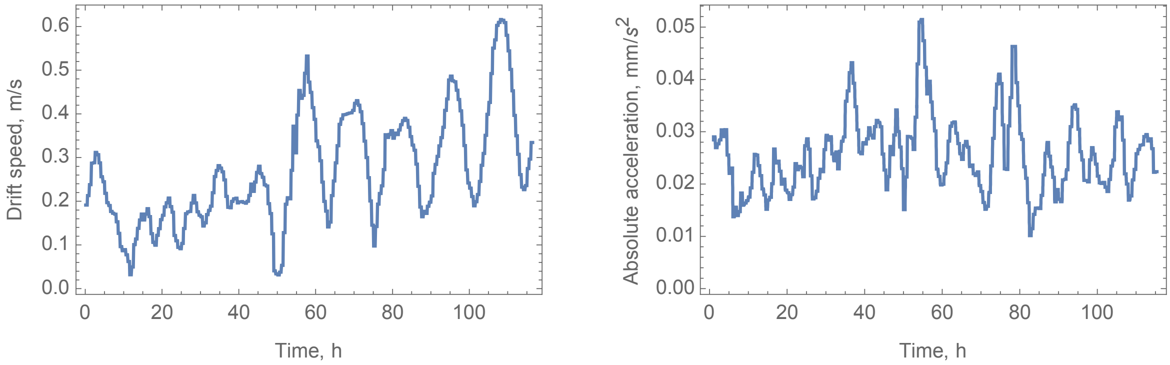

Figure 4. Drift speed (left panel) and accelerations (right panel) of IT computed using GPS locations recorded with sampling interval 30 min.

Figure 5 (right panel) shows the heading angle of IT versus the time over the entire deployment time. One can see that in the first 60 h of the motion the heading angle of IT several times changed on 200º – 300º (Fig. 5, right panel). It can be explained by the interaction of the bergy bit with surrounding floes. Then changes of the heading angle became smoother. Smooth temporal oscillations of the heading angle can be explained by hydrodynamic interaction of the bergy bit with water (Marchenko et al, 2019).

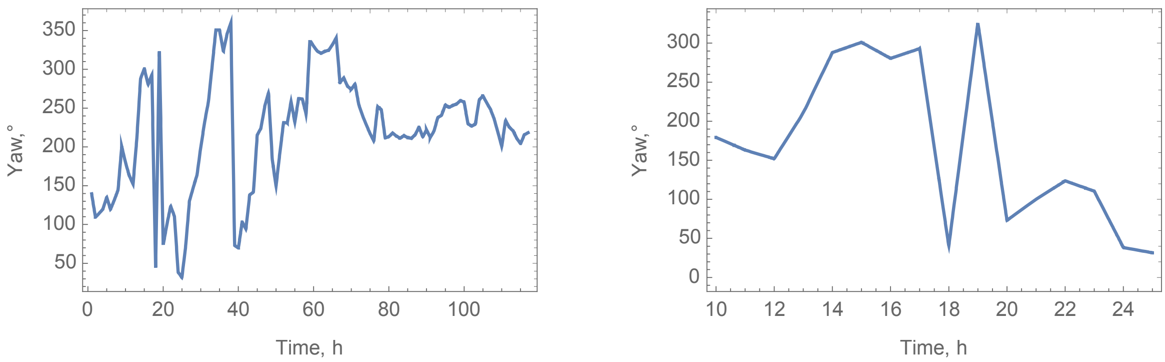

Figure 5. Yaw angle of IT versus the time over the deployment time (left) and zoomed for selected time (right).

Figures 6-8 show spectral densities of the East (SEA), North (SNA) and Vertical (SVA) accelerations of IT transmitted via Iridium. One can see that the frequency of most energetic oscillations is varied within 0.08-0.01 Hz. It corresponds well to the swell periods 10s - 12.5s in the Barents Sea (Marchenko et al, 2015), but smaller than estimated period (7.87 s) of natural oscillations of the bergy bit. Black points on the figure frames on the right panels of Fig. 6-8 correspond to the local minima of the drift speed shown on the left panel in Fig.4.

Inverse FFT was applied to the transmitted spectrums of the accelerations. Left panel in Fig. 9 shows spatial distribution of IT accelerations on the horizontal plane. One can see that there is dominant direction of the oscillating motion during each interval of 512 s. The dominant directions change with the time, but they are mostly oriented from South-West to North-East, that corresponds to dominant direction of swell propagating from North Atlantic into the Barents Sea. Right panel in Fig. 9 shows that an increase of the acceleration amplitudes in the vertical direction is accompanied by an increase of their horizontal amplitudes. It also can be explained by the increasing of horizontal orbital water velocities in swell with increasing of the swell amplitude.

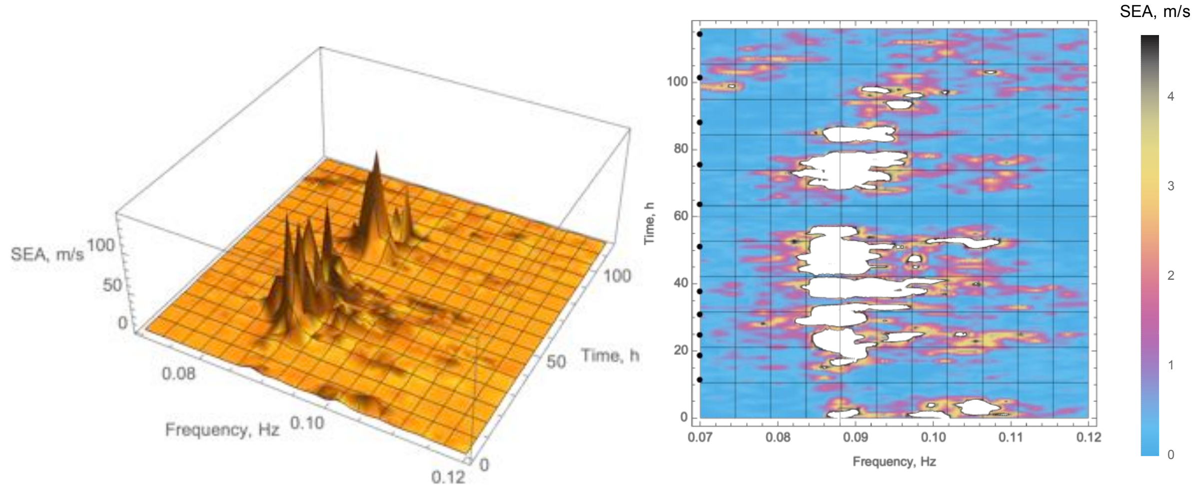

Figure 6. Spectral density of the East acceleration of IT measured with 2 Hz sampling frequency versus the time: 3D plot (left panel) and Density Plot (right panel) of spectral density of the East acceleration of IT versus the time.

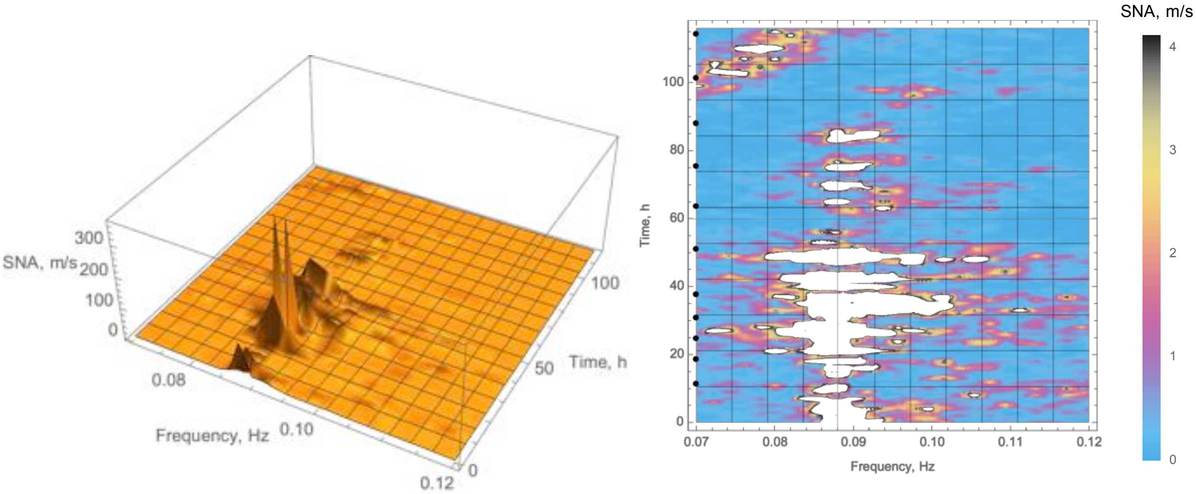

Figure 7. Spectral density of the North acceleration of IT measured with 2 Hz sampling frequency versus the time: 3D plot (left panel and Density Plot (right panel) of spectral density of the East acceleration of IT versus the time.

Figure 10 shows maximal absolute horizontal and vertical accelerations versus the time calculated for each interval of 512 s. Blue and yellow lines correspond to two consequent intervals of 512 s within the same hour. Figure 11 shows the mean absolute horizontal and vertical accelerations versus the time calculated for each interval of 512 s. One can see that the maximal and the mean horizontal accelerations are much higher than accelerations shown in Fig. 4 (right panel).

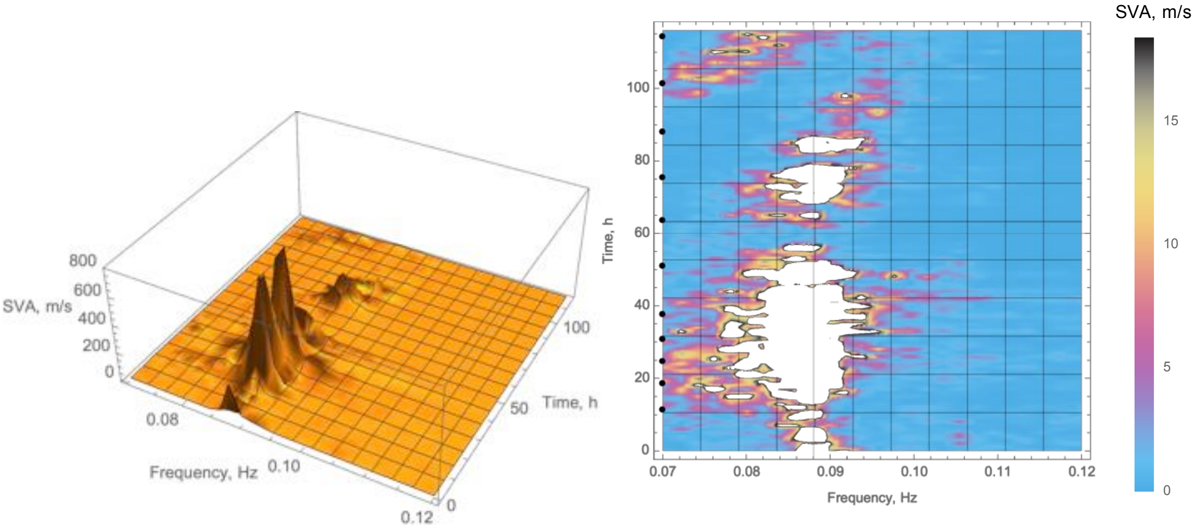

Figure 8. Spectral density of the vertical acceleration of IT measured with 2 Hz sampling frequency versus the time: 3D plot (left panel and Density Plot (right panel) of spectral density of the East acceleration of IT versus the time.

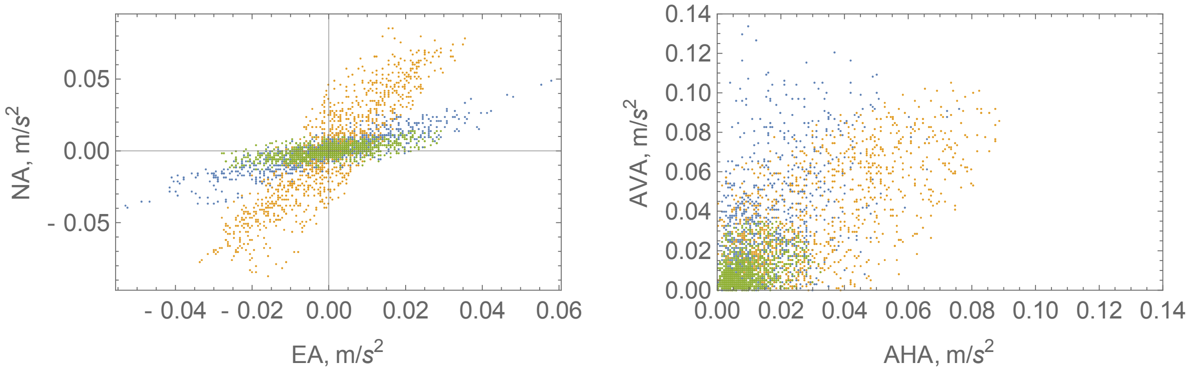

Figure 9. IT accelerations in the horizontal plane (left panel). Absolute vertical accelerations versus absolute horizontal accelerations (right panel). Blue, yellow and green dots correspond to the times 25h, 50h and 75h.

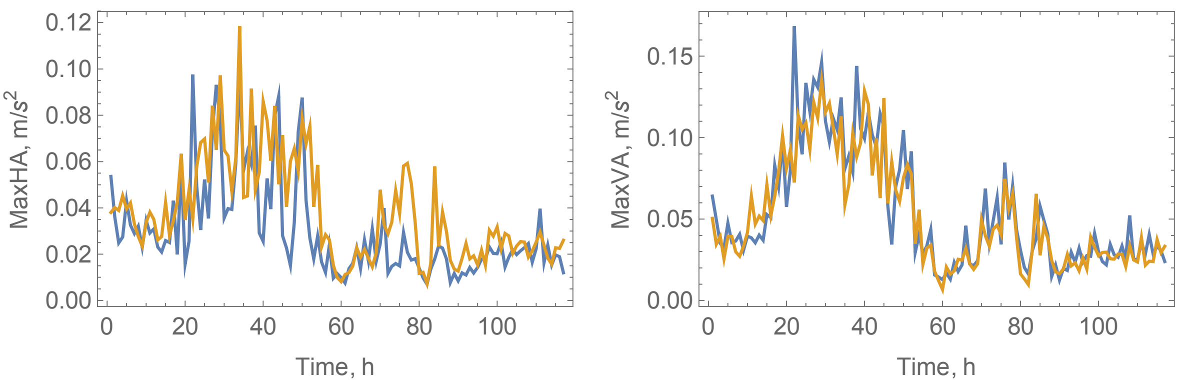

Figure 10. Maximal horizontal (left panel) and vertical (right panel) accelerations of IT measured with 2 Hz frequency versus the time.

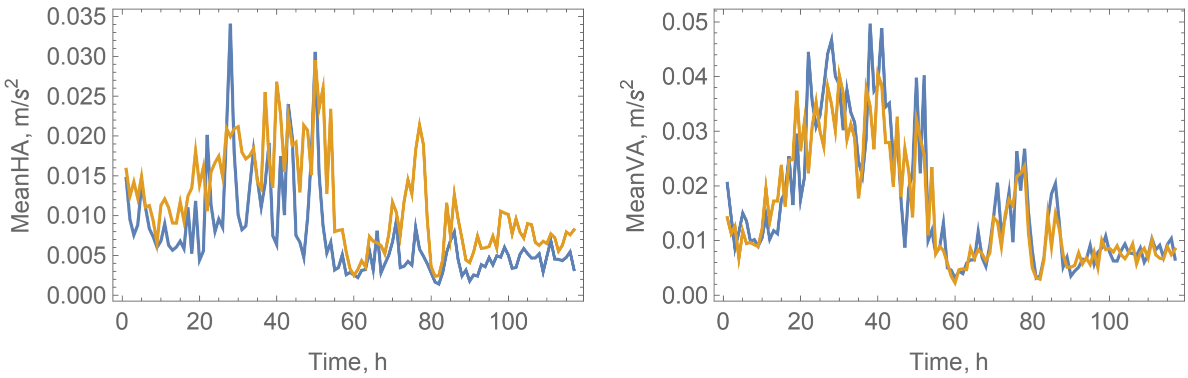

Figure 11. Mean horizontal (left panel) and vertical (right panel) accelerations of IT measured with 2 Hz frequency versus the time.

4. Discussion and conclusions

Ice tracker designed and constructed by Oceanetic Measurements LtD for wave monitoring was deployed on a drifting bergy bit in the Barents Sea to monitor its drift, yaw and accelerations. Raw data were collected with sampling frequency of 800 Hz, and then smoothed to the series with temporal resolution of 2 Hz using Moving Average procedure provided by IMU. Then FFT was programmed in C to get complex spectrum of the North, South and Down accelerations. 70 complex coefficients of the complex spectrum of each component of the accelerations were transmitted via Iridium two times per each hour. Spectral range of transmitted data corresponds to typical frequencies of swell and wind waves in marginal ice zones. The shortening of transmitted data in comparison to the raw data reduced the cost for the Iridium time significantly. The ice tracker communicated well around 120 h, and then the connection was broken.

Main direction of the bergy bit drift was to South-West, and total displacement of the bergy bit over the period of observations was of around 72 km with mean speed of 17 cm/s. Maximal drif speed according to GPS data collected with 30 min sampling interval reached 60 cm/s. The dependence of the yaw angle from the time shows rotations of the bergy bit relative to the vertical axis. The resulting rotation over the time of observations was in clockwise direction. Similar directions of icebergs rotation were observed and modeled by Yulmetov et al (2016) and Marchenko et al (2019).

The spectrum of accelerations had maximum at the frequency of about 0.09 Hz, which is lower than estimated natural frequency of the bergy bit of 0.127 Hz. The estimation of the natural frequency was made using the data on the bergy bit shape obtained by laser scanning from the board of Polarsyssel. The period of recorded bergy bit oscillations is similar the swell periods in the region (10-12 s). The length of swell of 0.09 Hz frequency propagating in the sea with depth of 120 m is 193 m. It is much greater than the diameter of the bergy bit. The forced amplitude of the bergy bit oscillations estimated with formula [5] is greater than the swell amplitude in 2 times ($\gamma = 2$).

It is possible to assume that horizontal accelerations of the bergy bit are similar the horizontal accelerations of water particles caused by the swell. Inverse FFT applied to the transmitted data showed that maximal horizontal acceleration of the bergy bit was of about 0.1 m/s^2. The amplitude of horizontal acceleration of water particles near sea surface is estimated with the formula $A_w = a_w\omega^2$, where ω is the angular frequency of swell measured in rad/s. Assuming that A_w =0.1 m/s^2 and ω =0.56 rad/s we find a_w =0.3 m. Then the amplitude of the vertical oscillations of the bergy bit can reach 0.6 m, and the amplitude of the bergy bit displacement relative to the water level can reach 0.3 m. Natural frequencies of floes are much higher than the frequency of swell. For example, according to formula (3), where $M_i = \rho_i S_w h_i$, the natural frequency of 1 m thick floe (h_i=1 m) is ω_i =3.3 Hz. Therefore, in this case $\gamma \approx 1$, and the amplitude of flow oscillations relative to the water surface is very small. This conclusion corresponds well to the field observations. Spatial variations of the horizontal direction of the bergy bit oscillations shown in the left panel of Fig. 9 are explained by different directions of swell propagation in the region.

The bergy bit accelerations reconstructed from the transmitted GPS data (right panel in Fig. 4) are much lower than the horizontal acceleration obtained from the transmitted spectral data of high frequency measurements by IMU (left panels in Figs. 10,11). It shows the importance of wave induced motion of drifting icebergs on their accelerations.

Acknowledgments
The work was supported by the Research Council of Norway through the Petromks-2 project Dynamics of Floating Ice and IntPart project Arctic Offshore and Coastal Engineering in Changing Climate.

References

Bruneau, S.E., 2004. Icebergs of Newfoundland and Labrador, Flanker Press, 1894463684, 64 pp.

Buzin, I.V., Nesterov, A.V., Gudoshnikov, Yu.P., Pashali, A.A., Kornishin, K.A., Efimov, Ya.O., Styragnikov, D.S., 2019. The main results of iceberg drift studies in the Russian Arctic Through 2012-2017. Proc. of 29th Int. Ocean and Polar. Eng. Conf., Honolulu, Hawaii, USA, 691-698.

Doble, M.J., Wilkinson, J.P., Valcic, L., Robst, J., Tait, A., Preston, M., Bidlot, J-R., Hwang, B., Maksym, T., Wadhams, P., 2017. Robust wavebuoys for the marginal ice zone: Experiences from a large persistent array in the Beaufort Sea. Elem. Sci Anth, 5: 47, DOI: https://doi.org/10.1525/elementa.233

Gagnon, R.E., Wang, J., 2012. Numerical simulations of a tanker collision with a bergy bit incorporating hydrodynamics, a validated ice model and damage to the vessel. CRST. 81, 26–35.

Løset, S. , Carstens, T., 1996. Sea ice and iceberg observations in the western Barents Sea in1987. CRST, 24, 323-340.

Marchenko, A.V., Gorbatsky, V.V., Turnbull, I.D., 2015. Characteristics of under-ice ocean currents measured during wave propagation events in the Barents Sea. POAC15-00171, Trondheim, Norway.

Marchenko, N., 2019a. Ice at its southern limit in the Barents Sea: field investigation near Bear Island in April 2017-2018. POAC19-58.

Marchenko, A.V., 2019b. Thermo-hydrodynamics of sea ice ridges. Proceedings of the IUTAM Symposium on Physics and Mechanics of Sea Ice. June 3-7. Aalto University, Finland.

Marchenko, A., Diansky, N., Fomin, V., 2019. Modeling of iceberg drift in the marginal ice zone of the Barents Sea. Applied Ocean Research. 88, 210-222.

Rabault, J., Sutherland, G., Gundersen, O., Jensen, A., Marchenko, A., Breivik, O., 2020. An open source, versatile, affordable waves in ice instrument for scientific measurements in the Polar Regions. Cold Regions Science and Technology, 170, 102955.

Sayeed, T., Colbourne, B., Quinton, B., Molyneux, D., Peng, H., Spencer, D., 2017. A review of iceberg and bergy bit hydrodynamic interaction with offshore structures, CRST,135,34-50.

Sodhi, D.S., Mona El-Tahan, 1980. Prediction of an iceberg trajectory during a storm. Journal of Glaciology, 1, 77-82.

Tangborn, A., Kan, S., Tangborn, W., 1994. Calculation of the Size of the Iceberg Struck by the Oil tanker Overseas Ohio. Proc. of 14th IAHR Ice Symp., Potsdam, NY, Balkema, Rotterdam, 237-242.

Turnbull, I.D., Fournier, N., Stolwijk, M., Fosnaes, T., McGonigal, D., 2015. Operational iceberg drift forecasting in Northwest Greenland. Cold Reg. Sci. Techn., 110, 1-18.

Yulmetov, R., Marchenko, A., Loset, S., 2016. Iceberg and sea ice drift tracking and analysis off north-east Greenland. Ocean Engineering, 123, 223-237.

12
River and lake ice processes

25th IAHR International Symposium on Ice
Trondheim, 23 - 25 November 2020

A tabulated review of 83 laboratory studies on frazil ice

Paul D. Barrette
Ocean, Coastal and River Engineering (OCRE)
National Research Council (NRC)
1200 Montreal Rd, Ottawa, ON Canada K1A 0R6
paul.barrette@nrc-cnrc.gc.ca

Frazil ice is a term used to designate ice particles of various shape occurring in a turbulent and supercooled water column, in both freshwater and saline water bodies. That ice is known to promote flooding, and also tends to clog water intakes and other structures below the water line. This paper present a succinct summary of different laboratory studies – the earliest reported in 1936 – that were found to focus on various aspects of frazil dynamics (growth, formation, velocity, particle/floc size and concentration, effects of water turbulence, sediment and algal entrainment), grease ice and pancake ice (their evolution and the effects of wave propagation on that ice), facilities and instrumentation (flume concepts, frazil/water monitoring tools) and interaction between structures and frazil (booms, screens, turbine, trash rack).

1. Introduction

Frazil ice consists of individual sub-mm to mm-sized particles in the form of disks, hexagonal stars, needles and other shapes. It is observed in both freshwater and saline water bodies where turbulence and supercooled water coexist (Osterkamp, 1978, Martin, 1981, Hicks, 2009, Daly, 2013). As seed crystals are introduced into that water, depending on hydraulic conditions, their concentration may rise abruptly. They may then coalesce into flocs, slush, ice pans, pancake ice and, eventually, form an ice cover. Frazil ice in river is notorious for the challenges it poses to engineered structures. For instance, it may clog water intakes and turbines, and interfere with shipping and hydroelectric generating stations. It can induce ice jamming and flooding when it develops into hanging dams especially if it links with anchor ice. These challenges have been recognized for quite some time (Barnes, 1906, 1928), and a significant amount of attention was dedicated to better understand frazil ice so as to mitigate the issues it engenders. Studies addressing frazil ice in saline water have also been conducted, to answer questions related with physical and biological processes related with sea ice dynamics.

2. Purpose

The National Research Council of Canada is ramping up its efforts to study frazil ice, including work that would be conducted in a controlled environments (laboratory). To that end, and in order to identify knowledge gaps, a thorough literature search was conducted, which identified a substantial number of different laboratory investigations, spanning the last several decades. The purpose of this paper is to provide a succinct summary of that previous laboratory work.

3. Overview of the literature survey

All studies are summarized in , which contains three columns: authorship (time sequence), water type and a brief summary of each study. A large variety of containments and sizes were used: vessels, cylinders, tanks, flumes (straight, track race). The length of the flume used by J. Wang, D.J. Kerr and collaborators is noteworthy (more than 35 m), as is the counter-rotating flume of J.C. Doering and collaborators. Modeling laws were used: Froude, Reynolds, Richardson. The effects of wave action on grease ice has been investigated by several people. A recent study (Belore and colleagues) also addressed oil evolution in frazil ice, namely evaporative losses and dispersant effectiveness. Overall, the studies can roughly be divided into four categories:

- Frazil dynamics (45 studies): Growth, formation, velocity, particle size, effects of water turbulence, sediment and algal entrainment.
- Grease, pancake and anchor ice (11 studies): Evolution, wave propagation.
- Facilities and instrumentation (18 studies): Flume concepts, frazil monitoring tools.
- Interaction between structures and frazil (9 studies): booms, screens, turbine, trash rack.

4. Conclusion

The purpose of this paper is to inform the readership on the number of frazil ice studies that have already been conducted in a laboratory. It is also to provide researchers that are new to this field of investigation with a basis onto which to build their own research plan. Why 83? Because that is the number of studies that had been found when the survey was stopped. A follow-up paper is being prepared, which will dissect the material contained in these studies and hopefully identify knowledge gaps and way forward with frazil ice investigations.

Acknowledgments

Sincere thanks go to R. Frederking and H. Babaei, and to an anonymous referee, for their review of earlier drafts.

Table 1. Summary of experimental studies (F: freshwater, S: saline).

Citation	Water	Summary/Outcome/Comments
Altberg (1936)	F	Frazil ice and anchor ice are considered identical ("underwater ice"). A basis for heat balance explaining their formation is offered, including role of dust and silt particles and existing ice-water interfaces.
Kumai and Itagaki (1953)	F	Seeding of supercooled water with ice allowed observation of crystal growth and resulting shapes. Silver iodide, kaolin, carbon, clay particles were not effective nucleus. Changes in the temperature with time showed the temperature-time pattern typical of frazil-producing water.
Arakawa (1954)	F	Growth rates of ice crystals were observed from supercooled water, with and without seeding, with size and shapes of crystals.
Bukina (1961)	F	The growth rate and diameter/thickness ratio of crystals in stirred supercooled water was investigated.
Williams (1962)	F	The formation of frazil in supercooled water caused it to warm up to the freezing temperature (it was no longer supercooled).
Michel (1963)	F	Included are conditions required for frazil formation, the short lifespan of a transitory nature (i.e. active state) on the supercooling time history, the relationship between cooling rate and quantity, as well as materials onto which active frazil would not attach (plastics).
Carstens (1966)	F	A higher cooling rate led to a higher supercooling. The rate of heat loss (from water surface) increases supercooling more so with weaker turbulence (lower heat transfer). A reduction of supercooling was achieved by bubble-generated turbulence.
Williams (1967)	F	At supercooling of 0.1^{o}C, frazil adhered to steel but not to plastic. With supercooling of 0.2-0.3oC, it will adhere to plastic. Silicon grease prevented frazil adhesion.
Bukina (1967)	F	Systematic supercooling temperature vs time traces, and corresponding crystal size distribution, for seven groups of experiments - in each, the temperature history was about the same.
Martin and Kauffman (1974)	F&S	A theoretical basis validated against experimentation showed that heat transfer from saltwater to freshwater is 5-10 more effective than classic heat diffusion.
Schmidt and Glover (1975)	F	Using a laser doppler velocimeter, the concentration/mass of frazil was determined as a function of time, and correlated with water temperature.
Tsang (1975)	F	Description of a '?'-shaped flume, with a wave generator, an observation window and a wave absorption section.
Hanley and Michel (1977)	F	Frazil and border formation as a function of water displacement rate, air temperature and time was investigated. Air temperature and higher velocities were the most important parameters to generate border ice and frazil, respectively.
McClimans et al. (1978)	F&S	The heat transfer from the freshwater to saltwater was maximum when salinity is 18ppt, because thermal convection in the lower saline layer was largest.
Muller (1978)	F	Frazil could only be generated by seeding with ice nuclei, arguing in favor of secondary nucleation as an important mechanism in nature. The number of ice particles increased, so did the growth rate at higher supercooling and heat transfer.
Martin and Kauffman (1981)	S	Generation of frazil with a wave maker led to a grease ice layer. Information on ice concentration/thickness and wave amplitude in this layer were related to viscosity.
Perham (1981)	F	Parallel cables, mostly nylon, a few mm in diameter, collected active and passive frazil. Ice volume and drag forces were measured, and field applications (collecting boom and reinforced ice cover) are discussed.
Andres (1982)	F	Low air temperature favored frazil multiplication and ice cover formation if turbulence was low. High turbulence precluded ice cover formation and raised the nucleating temperature.
Tsang (1983)	F&S	A relationship was obtained on the concentration of frazil in time as a function of amount of supercooling. Seawater and freshwater frazil differed in shape, cohesiveness and adhesiveness.
Ettema et al. (1984)	F	The growth rate and volume increased with increasing turbulence and decreasing water temperature. Particle size decreased with increased turbulence.
Hanley and Tsang (1984)	F&S	Formation and physical properties of frazil was affected by salinity, supercooling, number of seeding nuclei, flow turbulence and ambient pressure. For nucleation with either one or multiple seeds, seeding point, minimum temperature, temperature recovery were documented as a function of supercooling temperatures. Several trends in these relationships are discussed.
Tsang (1984)	F&S	An instrument was designed to measure frazil concentration in flowing water. Frazil in freshwater formed cohesive flocs, not observed with saline frazil, which formed a continuous flow of interlocked crystals.

Wuebben (1984)	F	Rising frazil crystals indicated Reynolds number above Stokes range. Rising velocity as a function of diameter was obtained, along with aspect ratio. Artificial frazil showed unstable rising patterns.
Tsang and Hanley (1985)	F&S	A relationship between normalized frazil concentration vs normalized time allowed to predict frazil content in the water as a function of time. Initial supercooling and salinity affected that relationship.
Tsang (1985)	F	An instrument was designed to measure frazil concentration in flowing water. It was able to quantify concentration, but with a calibration factor.
Daly and Colbeck (1986)	F	Data were obtained on crystal dimensions and diameter/thickness ratio, as a function of slope, bottom roughness and water velocity.
Ford and Madsen (1986)	F	The quantity of frazil ice was monitored using a device based on calorimetry.
Mussalli et al. (1987)	F	A cross-polarized lighting technique was used to detect frazil.
Garrison et al. (1989)	S	Frazil is able to capture and concentrate algal cells.
Tsang and Trapp (1990)	F	Commissioning of a newly designed flume to monitor frazil dynamics, and preliminary semi-quantitative results on the formation of frazil and anchor ice.
Axelson (1990)	F	Four flow stages were identified: orifice flow, transitional, permeable, weir flow. Rapid blockage of the fence screen will minimize scour, thereby maximizing the effectiveness in raising the water level upstream.
Foltyn (1990)	F	Time progression of channel depths upstream and downstream and of velocity was generated. Extending the structure above the water line and an upstream ice boom are suggested improvements.
Daly and Rand (1990)	F	The system tested in this study successfully allowed the detection of an intake blockage in the flume, followed by shut-down of the intake pump, deicing, air purge.
White (1991)	F	Successful application of the borehole dilution test to determine the intrinsic permeability of frazil ice.
Krylov and Zatsepin (1992)	F&S	Supercooling of freshwater was determined from the difference between heat diffusion and salt diffusion, in the presence of turbulence, yielding a rate of freezing.
Lever et al. (1992)	F	Using a calorimeter, the concentration/mass of frazil was determined, and correlated with water temperature.
Andersson and Daly (1992)	F	The progress of frazil build-up on a thrash racks is described, including flow velocity and water temperature.
Kempema et al. (1993)	F&S	Frazil in saltwater was more effective for sediment transport and their shape differed from that in freshwater. Anchor ice was more common in freshwater ice - information on its dynamics is provided.
Ushio and Wakatsuchi (1993)	F&S	Rate of frazil production salt flux increased with wind speed and salinity is presented and a process to explain these observations is described.
Reimnitz et al. (1993)	S	Observations on the rising dynamics of frazil and 'various types of suspended particulate' are presented: flocs formation, interaction with settling particles, resulting in ice enrichment.
Tsang and Cui (1994)	F	A functional relationship was determined empirically, describing the vertical distribution of frazil and containing three parameters: maximum concentration gradient, position of this gradient and the depth gap over which there are significant changes in frazil concentration.
Ackermann et al. (1994)	F	Sediment entrainment by frazil was observed, with sand-sized particles sinking and smaller-sized particles accumulated in the ice cover.
Voropayev et al. (1995)	F&S	Frazil production due to heat diffusion from saltwater to freshwater, and the influence of external turbulence, were documented. The rate was higher in a turbulent environment and was a function of the interfacial Richardson number.
Pegau et al. (1996)	F	Two optical instruments, a beam transmissometer and a three-wavelength absorption meter, were used to measure frazil concentration.
Gooch (1996)	F	Physical modeling at 1:25 scale, with 3-mm plastic beads meant to simulate frazil, was used to test the performance of various types of booms.
Newyear and Martin (1997)	S	Wave damping in grease ice was exponential with the traveled distance and also depended on ice thickness. The observations were more consistent with a Newtonian-fluid model than a mass-loading model of wave propagation.
Lindemann and Smedsrud (1998)	S	Sediment concentration was up to four times higher in the ice than in the water, likely due to scavenging by frazil.
Eicken et al. (1998)	S	The presence of wind was a deciding factor in the frazil to pancake ice process. Wave damping was also investigated. An increase in sediment content within the ice is attributed to scavenging by frazil.

Smedsrud (1998)	S	An 'aggregation' model between sediments and frazil ice, validated against the experiments, is presented. This process was related with sediment concentration, turbulence levels and the size of sediment particles and frazil ice.
Tyshko and Cherepanov (1998)	F&S	The amount of supercooling was higher in sodium chloride solutions than in distilled water and freshwater. A mechanism is proposed to explain phenomena related with frazil's active state and anchor ice formation.
Haas et al. (1999)	S	Wave damping by frazil and pancake ice was investigated. Langmuir circulation contributed to sediment entrainment by frazil ice.
Yankielun and Gagnon (1999)	F	A time-domain reflectometer and a specially-designed transmission line sensor documented an increase in volumetric ice fractions.
Doering et al. (2001)	F	The maximum anchor ice growth occurred when the Froude number was 0.27, with some indications that density increases with increasing Froude number. Anchor ice release from the flume's floor was observed with Reynolds numbers < 42,000.
Smedsrud (2001)	S	As a result of 'suspension freezing', the ice contained an average of two to ten times more sediment than the water column, which was a function of initial sediment concentration, air temperature and turbulence.
Clark and Doering (2002)	F	Information on the number of particle size and number of particles with time, as well as particle shapes and sintering is provided.
Kerr et al. (2002)	F	A growth-transition-final stage development from frazil ice was identified and three types of anchor ice are documented, which depended on Froude. Anchor ice hydraulic resistance to flow and the various parameters involved were also investigated.
Doering and Morris (2003)	F	An image processing system using cross-polarized light allowed to observe the evolution frazil ice size, concentration and vertical distribution.
Ettema et al. (2003), Chen et al. (2004)	F	The amount of frazil ingestion, collected with a wire mesh above a conical intake, varied with time, as a function of the ratio of height of the mesh above the intake and the intake diameter.
Dikarev et al. (2004)	S	A study of convection below an ice cover identified a 'congelation' regime and a 'frazil' regime. Frazil production was high at high supercooling rates. Crystal size decreased with salinity increase.
Ye et al. (2004)	F	Effects of air temperature, water velocity/depth on supercooling, and frazil development (size, number, volume) are documented. A relationship with Reynolds number was established.
Clark and Doering (2006)	F	The number of particles increased at maximum supercooling. The higher water velocity, the larger the crystals. Diameter/thickness ratios are reported. Some evidence showed that a higher bottom roughness increased the supercooling of the water column.
Dethleff and Kempema (2007)	S	Langmuir circulation with the production of frazil ice was simulated, providing information on frazil dynamics and sediment entrainment by frazil.
Unduche and Doering (2007a)	F	Four shapes of skim ice particles are shown, which depend on level of turbulence.
Qu and Doering (2007)	F	Development by anchor ice via frazil production is presented. Froude number influenced ice shape. A higher Reynolds number led to denser anchor ice.
Unduche and Doering (2007b)	F	The Froude number and shear stress velocity were factors that determined how much skim ice versus frazil ice existed in the ice cover.
Clark and Doering (2009)	F	High turbulence tended to reduce the number of large frazil flocs.
Wang and Shen (2010)	F	A wave regime was sent across a grease ice layer to study wave attenuation. The influence of pancake ice development is also discussed.
De la Rosa et al. (2011)	S	The temporal evolution of ice temperature, salinity and volume fraction of frazil ice is presented during the transition from frazil to grease ice to pancake ice.
Ghobrial et al. (2012)	F	An empirical relationship was established between the output of two sonars of different frequencies and the frazil concentration in the water column.
De la Rosa and Maus (2012)	S	Evolution of frazil accumulation on the surface, identified in terms of ice solid fraction and ice thickness.
Wang et al. (2012)	F	Using model ice, the Froude number was correlated with stability of ice accumulation/distribution at different locations.
Cook et al. (2012)	F	The preferential entrainment of coarse silt to medium sand from sediment-laden water was observed.
Ogasawara et al. (2013)	S	Information is provided on the temperature evolution of pancake ice (center vs rim) as a function of water temperature, taking into account ice coverage and thickness.
McFarlane et al. (2014)	F	The rise velocity of frazil as a function of crystal size, for various Reynolds numbers, is documented.

McFarlane et al. (2015)	F	The evolution of particle number and sizes during supercooling phases is documented, so is the influence of turbulent kinetic energy rate on crystal size.
Marko and Topham (2015)	F	Using model ice, acoustic back scattering theory was verified against observation of size, shape and concentration.
Belore et al. (2016)	S	The evaporative losses, viscosity and water contents of two crude oils in frazil ice, and their dispersant effectiveness, are compared.
Schneck et al. (2017)	F&S	The difference between particle number, shape and size formed in water of 0, 15 and 35ppt is discussed.
Hashiba et al. (2018)	F	The performance of three acoustic devices (Shallow Water Ice Profiler, Acoustic Doppler Current Profiler, Echo-Sounder) is compared.
Richard (2018)	F	Despite the extensive production of frazil, no accumulation was observed on a small vertical-axis cross-flow turbine.
Schneck et al. (2019)	F&S	The particle size and floc growth rate decreased with increasing salinity (0, 15, 25 and 35ppt). Freshwater growth rate was 4 times that in saline water.
Richard and Cornett (2019)	F	The outcome of two direct (visual observation, sampling) and two indirect (water temperature, acoustic backscatter) frazil observation methods are discussed.
Wang et al. (2019)	F	Model ice was used to study frazil accumulation and wave-forming behavior below and ice cover.

References

Ackermann, N.L., Shen, H.T. and Sande, B., 1994. *Experimental studies of sediment enrichment of arctic ice covers due to wave action and frazil entrainment*. Journal of Geophysical Research, 99(C4), p. 7761-7770.

Altberg, W.J., 1936. *Twenty years of work in the domain of underwater ice formation*. International Association of Scientific Hydrology, 23, p. 373-407.

Andersson, A. and Daly, S.F., 1992. *Laboratory investigation of trash rack freezeup by frazil ice*. CRREL Report 92-16. U.S. Army Cold Regions Research and Engineering Laboratory (CRREL). Hanover, N.H.

Andres, D.D., 1982. *Nucleation and frazil production during the supercooling period* Proceedings of the Workshop on Hydraulics of Ice-Covered Rivers, pp. 148-175.

Arakawa, K., 1954. *Studies on the freezing of water - (II) Formation of disc crystals*. Journal of the Faculty of Science, Hokkaidô University, Ser. II, IV(5), p. 311-339.

Axelson, K.D., 1990. *Freezeup dynamics of a frazil ice screen*. CRREL Special Report 90-4. U.S. Army Cold Regions Research and Engineering Laboratory (CRREL). Hanover, N.H.

Barnes, H.T., 1906. *Ice formation with special reference to anchor-ice and frazil*. John Wiley and Sons, New York.

Barnes, H.T., 1928. *Ice engineering*. Renouf Publishing Co., Montreal.

Belore, R.C., Faksness, L.-G., Dunnebier, D., Brandvik, P.J. and Daling, P., 2016. *Meso-scale flume testing of dispersant effectiveness in frazil Ice*, Proceedings of the 39th AMOP Technical Seminar, Environment and Climate Change, Ottawa, pp. 714-727.

Bukina, L.A., 1961. *A laboratory method of investigation of the rate of growth of frazil ice crystals*. Izv. Geophys. Ser., p. 947-950.

Bukina, L.A., 1967. *Size distribution of frazil ice crystals in turbulent flows*. Izvestiya, Atmospheric and Oceanic Physics, 3(1), p. 58-68.

Carstens, T., 1966. *Experiments with supercooling and ice formation in flowing water*. Geofysiske Publikasjoner: Geophysica Norvegica, 26(9-18).

Chen, Z., Ettema, R. and Lai, Y., 2004. *Ice-tank and numerical study of frazil ingestion by submerged intakes*. Journal of Hydraulic Engineering, 130(2), p. 101-111.

Clark, S. and Doering, J.C., 2002. *Laboratory observations of frazil ice*, Proceedings of the 16th International Symposium on Ice. Association of Hydraulic Engineering and Research (IAHR), Dunedin, New Zealand, pp. 127-133.

Clark, S.P. and Doering, J.C., 2006. *Laboratory experiments on frazil-size characteristics in a counterrotating flume*. Journal of Hydraulic Engineering, 132(1), p. 94-101.

Clark, S.P. and Doering, J.C., 2009. *Frazil flocculation and secondary nucleation in a counter-rotating flume*. Cold Regions Science and Technology, 55, p. 221-229.

Cook, S.J., Knight, P.G., Knight, D.A. and Waller, R.I., 2012. *Laboratory observations of sediment entrainment by freezing supercooled water*. Geografiska Annaler: Series A, Physical Geography, 94, p. 351-362.

Daly, S.F., 2013. *Frazil ice*. In: S. Beltaos (Editor), River Ice Formation. Committee on River Ice Processes and the Environment, CGU-HS, Edmonton, Alberta, p. 107-134.

Daly, S.F. and Colbeck, S.C., 1986. *Frazil ice measurements in CRREL' s flume facility*, Proceedings of the 8th International Symposium on Ice. Association of Hydraulic Engineering and Research (IAHR), Iowa City, USA.

Daly, S.F. and Rand, J.H., 1990. *Development of an underwater frazil-ice detector*. Cold Regions Science and Technology, 18, p. 77-82.

De la Rosa, S. and Maus, S., 2012. *Laboratory study of frazil ice accumulation under wave conditions*. The Cryosphere, 6, p. 173-191.

De la Rosa, S., Maus, S. and Kern, S., 2011. *Thermodynamic investigation of an evolving grease to pancake ice field*. Annals of Glaciology, 52(57), p. 206-214.

Dethleff, D. and Kempema, E.W., 2007. *Langmuir circulation driving sediment entrainment into newly formed ice: Tank experiment results with application to nature (Lake Hattie, United States; Kara Sea, Siberia)*. Journal of Geophysical Research, 112(C02004).

Dikarev, S.N., Poyarkov, S.G. and Chuvil'chikov, S.I., 2004. *Laboratory modeling of small-scale convection under a growing ice cover in winter Arctic leads*. Oceanology, 44(1), p. 62-70.

Doering, J.C., Bekeris, L.E., Morris, M.P., Dow, K.E. and Girling, W.C., 2001. *Laboratory study of anchor ice growth*. Journal of Cold Regions Engineering, 15(1), p. 60-66.

Doering, J.C. and Morris, M.P., 2003. *A digital image processing system to characterize frazil ice*. Canadian Journal of Civil Engineering, 30.

Eicken, H., Weissenberger, J., Bussmann, I., Freitag, J., Schuster, W., Delgado, F.V., Evers, K.-U., Cottier, F., Hall, R., Wadhams, P., Reisemann, M., Kousa, H., Ikävalko, J., Leonard, G.H., Shen, H., Ackley, S.F. and Smedsrud, L.H., 1998. *Ice-tank studies of physical and biological sea-ice processes*. In: H. Shen (Editor), Ice in Surface Waters. Balkema, Rotterdam, p. 363-370.

Ettema, R., Chen, Z. and Doering, J., 2003. *Making frazil ice in a large ice tank* Proceedings of the 12th Workshop on the Hydraulics of Ice Covered Rivers. CGU HS Committee on River Ice Processes and the Environment (CRIPE), Edmonton.

Ettema, R., Karim, M.F. and Kennedy, J.F., 1984. *Frazil ice formation*. CRREL Report 84-18. U.S. Army Cold Regions Research and Engineering laboratory (CRREL). Hanover, N.H.

Foltyn, E.P., 1990. *Laboratory and field tests of a wire mesh frazil collector*. CRREL Special Report 90-35. U.S. Army Cold Regions Research and Engineering Laboratory (CRREL). Hanover, N.H.

Ford, J.S. and Madsen, N.M., 1986. *Frazil ice recorder test*, Proceedings of the 4th Workshop on Hydraulics of River Ice. Committee on River Ice Processes and the Environment (CRIPE), Montreal.

Garrison, D.L., Close, A.R. and Reimnitz, E., 1989. *Algae concentrated by frazil ice: evidence from laboratory experiments and field measurements*. Antarctic Science, 1(4), p. 313-316.

Ghobrial, T.R., Loewen, M.R. and Hicks, F., 2012. *Laboratory calibration of upward looking sonars for measuring suspended frazil ice concentration*. Cold Regions Science and Technology, 70, p. 19-31.

Gooch, G., 1996. *Effects of ice boom geometry on ice capture efficiency*. CRREL Special Report 96-17. U.S. Army Cold Regions Research and Engineering Laboratory (CRREL). Hanover, N.H.

Haas, C., Cottier, F., Smedsrud, L.H., Thomas, D., Buschmann, U., Dethleff, D., Gerland, S., Giannelli, V., Hoelemann, J., Tison, J.-L. and Wadhams, P., 1999. *Multidisciplinary ice tank study shedding new light on sea ice growth processes*. Eos Transactions, 30(43), p. 507, 509, 511.

Hanley, T.O.D. and Michel, B., 1977. *Laboratory formation of border ice and frazil slush*. Canadian Journal of Civil Engineering, 4, p. 153-160.

Hanley, T.O.D. and Tsang, G., 1984. *Formation and properties of frazil in saline water*. Cold Regions Science and Technology, 8, p. 209-221.

Hashiba, M., Yoshikawa, Y. and Yokoyama, H., 2018. *Verification of ice measurement data by SWIP and ADCP and observation of river ice time series behavior in Teshio River* Proceedings of the 24th International Symposium on Ice. Association of Hydraulic Engineering and Research (IAHR), Vladivostok, Russia.

Hicks, F., 2009. *An overview of river ice problems: CRIPE07 guest editorial*. Cold Regions Science and Technology, 55, p. 175-185.

Kempema, E.W., Reimnitz, E., Clayton, J.R. and Payne, J.R., 1993. *Interactions of frazil and anchor ice with sedimentary particles in a flume*. Cold Regions Science and Technology, 21, p. 137-149.

Kerr, D.J., Shen, H.T. and Daly, S.F., 2002. *Evolution and hydraulic resistance of anchor ice on gravel bed*. Cold Regions Science and Technology, 35, p. 101-114.

Krylov, A.D. and Zatsepin, A.G., 1992. *Frazil ice formation due to difference in heat and salt exchange across a density interface*. Journal of Marine Systems, 3, p. 497-506.

Kumai, M. and Itagaki, K., 1953. *Cinematographic study of ice crystal formation in water*. Journal of the Faculty of Science, Hokkaidô University, Ser. II, 4(4), p. 235-246.

Lever, J.H., Daly, S.F., Rand, J.H. and Furey, D., 1992. *A frazil ice concentration meter*, Proceedings of the 11th International Symposium on Ice. Association of Hydraulic Engineering and Research (IAHR), Banff, Alberta, pp. 1362-1376.

Lindemann, F. and Smedsrud, L.H., 1998. *Sediment entrainment into sea ice in Arctic leads: An experimental approach*. In: H. Shen (Editor), Ice in surface waters. Balkema, Rotterdam, p. 387-390.

Marko, J.R. and Topham, D.R., 2015. *Laboratory measurements of acoustic backscattering from polystyrene pseudo-ice particles as a basis for quantitative characterization of frazil ice*. Cold Regions Science and Technology, 112, p. 66-86.

Martin, S., 1981. *Frazil ice in rivers and oceans*. Annual Review of Fluid Mechanics, 13, p. 379-397.

Martin, S. and Kauffman, P., 1974. *The evolution of under-ice melt ponds, or double diffusion at the freezing point*. Journal of Fluid Mechanics, 64(3), p. 507-527.

Martin, S. and Kauffman, P., 1981. *A field and laboratory study of wave damping by grease ice*. Journal of Glaciology, 27(96), p. 283-313.

McClimans, T.A., Steen, J.E. and Kjeldgaard, J.H., 1978. *Ice formation in fresh water cooled by a more saline underflow*, Proceedings of the 5th International Symposium on Ice. Association of Hydraulic Engineering and Research (IAHR), Luleå, pp. 13-26.

McFarlane, V., Loewen, M. and Hicks, F., 2014. *Laboratory measurements of the rise velocity of frazil ice particles*. Cold Regions Science and Technology, 2014, p. 120-130.

McFarlane, V., Loewen, M. and Hicks, F., 2015. *Measurements of the evolution of frazil ice particle size distributions*. Cold Regions Science and Technology, 120, p. 45-55.

Michel, B., 1963. *Theory of formation and deposit of frazil ice*, Proceedings of the 20th Annual Eastern Snow Conference, Quebec City, pp. 129-149.

Muller, A., 1978. *Frazil ice formation in turbulent flow*. Iowa Institute of Hydraulic Research (IIHR). Iowa City.

Mussalli, Y.G., Gordon, L.S. and Daly, S.F., 1987. *Frazil ice control using electromechanical vibrators and ice-resistant coatings*, Proceedings of ASCE Water Power '87. American Society of Civil Engineers (ASCE), Portland.

Newyear, K. and Martin, S., 1997. *A comparison of theory and laboratory measurements of wave propagation and attenuation in grease ice*. Journal of Geophysical Research, 102(C11), p. 25,091-25,09.

Ogasawara, T., Ogasawara, A. and Sakai, S., 2013. *Thermodynamics on grease-pancake ice growth in a sea ice-wave tank*, Proceedings of the 23rd International Offshore and Polar Engineering (ISOPE). International Society of Offshore and Polar Engineers, Anchorage, Alaska.

Osterkamp, T.E., 1978. *Frazil ice formation: A review*. Journal of the Hydraulics Division, 104(9), p. 1239-1255.

Pegau, W.S., Paulson, C.A. and Zaneveld, J.R.V., 1996. *Optical measurements of frazil concentration* Cold Regions Science and Technology, 24, p. 341-353.

Perham, R.E., 1981. *Tests of frazil collector lines to assist ice cover formation*. Canadian Journal of Civil Engineering, 8, p. 442-448.

Qu, Y.X. and Doering, J., 2007. *Laboratory study of anchor ice evolution around rocks and on gravel beds*. Canadian Journal of Civil Engineering, 34(1), p. 46-55.

Reimnitz, E., Clayton, J.R., Kempema, E.W., Payne, J.R. and Weber, W.S., 1993. *Interaction of rising frazil with suspended particles: tank experiments with applications to nature*. Cold Regions Science and Technology, 21, p. 117-135.

Richard, M., 2018. *Frazil ice generation in NRC's Ottawa ice tank for the testing of a cross-flow turbine*. OCRE-TR-2018-021. National Research Council.

Richard, M. and Cornett, A., 2019. *NRC frazil ice research facility*, Proceedings of the Annual Conference. Canadian Society for Civil Engineering (CSCE), Laval, Canada.

Schmidt, C.C. and Glover, J.R., 1975. *A frazil ice concentration measuring system using a laser doppler velocimeter*. Journal of Hydraulic Research, 13(3), p. 299-314.

Schneck, C., McFarlane, V. and Loewen, M., 2017. *Laboratory measurements of frazil ice properties in saline water*, Proceedings of the 19th Workshop on the Hydraulics of Ice Covered Rivers. CGU HS Committee on River Ice Processes and the Environment (CRIPE), Whitehorse.

Schneck, C.C., Ghobrial, T.R. and Loewen, M.R., 2019. *Laboratory study of the properties of frazil ice particles and flocs in water of different salinities*. The Cryosphere, 13, p. 2751–2769.

Smedsrud, L.H., 1998. *Estimating aggregation between suspended sediments and frazil ice*. Geophysical Research Letters, 25(20), p. 3875-3878.

Smedsrud, L.H., 2001. *Frazil-ice entrainment of sediment: large-tank laboratory experiments*. Journal of Glaciology, 47(158), p. 461-471.

Tsang, G., 1975. *A preliminary investigation and experimental set-up for the study of frazil formation in water with surface waves*. Technical Memo No. 114 (NRCC 14407). National Research Council of Canada. Ottawa.

Tsang, G., 1983. *Formation and properties of frazil formed in seawater at different supercoolings*, Proceedings of the 7th International Conference on Port and Ocean Engineering under Arctic Conditions (POAC), Helsinki, pp. 222-241.

Tsang, G., 1984. *Concentration of frazil in flowing water as measured in laboratory and in the field*, Proceedings of the 7th International Symposium on Ice. Association of Hydraulic Engineering and Research (IAHR), Hamburg.

Tsang, G., 1985. *An instrument for measuring frazil concentration*. Cold Regions Science and Technology, 10, p. 235-249.

Tsang, G. and Cui, W., 1994. *Laboratory study of frazil distribution in a flow*. Canadian Journal of Civil Engineering, 21, p. 696-709.

Tsang, G. and Hanley, T.O.D., 1985. *Frazil formation in water of different salinities and supercoolings*. Journal of Glaciology, 31(108), p. 74-85.

Tsang, G. and Trapp, B., 1990. *Preliminary findings from experiments on frazil and anchor ice in a circular flume*. In: T.D. Prowse and C.S.L. Ommanney (Editors), Northern Hydrology: Selected Perspectives : Proceedings of the Northern Hydrology Symposium, Saskatoon, pp. 405-418.

Tyshko, K.P. and Cherepanov, N.V., 1998. *Supercooling of large water volumes: Laboratory experiments and hypotheses*. In: H. Shen (Editor), Ice in surface waters. Balkema, Rotterdam, p. 371-378.

Unduche, F.S. and Doering, J.C., 2007a. *A laboratory observation of skim ice particles*, Proceedings of the 14th Workshop on the Hydraulics of Ice Covered Rivers CGU HS Committee on River Ice Processes and the Environment (CRIPE), Quebec City.

Unduche, F.S. and Doering, J.C., 2007b. *Experimental study of the formation of different types of surface ice runs*, Proceedings of the 14th Workshop on the Hydraulics of Ice Covered Rivers CGU HS Committee on River Ice Processes and the Environment (CRIPE), Quebec City.

Ushio, S. and Wakatsuchi, M., 1993. *A laboratory study on supercooling and frazil ice production processes in winter coastal polynyas*. Journal of Geophysical Research, 98(C11), p. 20321-20318.

Voropayev, S.I., Fernando, H.J.S. and Mitchell, L.A., 1995. *On the rate of frazil ice formation in polar regions in the presence of turbulence*. Journal of Physical Oceanography, 25, p. 1441-1450.

Wang, J., Sui, J.-y., Zhang, H.-y., Chen, P.-p. and Hirshield, F., 2012. *Mechanisms of ice accumulation in a river bend – an experimental study*. International Journal of Sediment Research, 27 p. 521-537.

Wang, J., Wu, Y., Sui, J. and Karney, B., 2019. *Formation and movement of ice accumulation waves under ice cover – an experimental study*. Journal of Hydrology and Hydromechanics, 67(2), p. 171-178.

Wang, R. and Shen, H.H., 2010. *Experimental study on surface wave propagating through a grease–pancake ice mixture*. Cold Regions Science and Technology, 61, p. 90-96.

White, K.D., 1991. *Determining the intrinsic permeability of frazil ice. Part 1. Laboratory investigations*. CRREL Report 91-23. U.S. Army Cold Regions Research and Engineering Laboratory (CRREL). Hanover, N.H.

Williams, G.P., 1962. *Two notes relating to frazil ice formation*. Research Paper No. 162. National Research Council. Ottawa.

Williams, G.P., 1967. *Adhesion of frazil ice to underwater structures*, Proceedings of the 24th Annual Eastern Snow Conference, Niagara Falls, pp. 82-92.

Wuebben, J.L., 1984. *The rise pattern and velocity of frazil ice*, Proceedings of the 3rd Workshop on Hydraulics of River Ice. Committee on River Ice Processes and the Environment (CRIPE), Fredericton.

Yankielun, N.E. and Gagnon, J.J., 1999. *Laboratory tests of a time-domain reflectometry system for frazil ice detection*. Canadian Journal of Civil Engineering, 26, p. 168-176.

Ye, S.Q., Doering, J. and Shen, H.T., 2004. *A laboratory study of frazil evolution in a counter-rotating flume*. Canadian Journal of Civil Engineering, 31, p. 899-914.

25th IAHR International Symposium on Ice
Trondheim, 23 – 25 November 2020

Observations of Supercooling in Rivers

Sean Boyd[1], Tadros R. Ghobrial[2], and Mark R. Loewen[1]

[1] *Dept. of Civil and Environmental Engineering*
University of Alberta, Edmonton, AB, Canada

[2] *Department of Civil and Water Engineering*
Laval University, Québec, Qc, Canada

srboyd@ualberta.ca, tadros.ghobrial@gci.ulaval.ca mrloewen@ualberta.ca

Supercooling events occur in northern rivers when the turbulent water is cooled below the freezing point. This leads to the formation of frazil ice crystals in the water column and/or anchor ice formation on the bed. The heat flux at the air-water interface and the latent heat released by ice formation are the dominant factors controlling the water temperature. If the air-water heat flux is approximately constant the water temperature decreases until it reaches a peak supercooling value, then it increases and eventually reaches a stable value slightly below zero called the residual temperature. At this time the heat being lost through the air-water interface is balanced by the heat being added by frazil or anchor ice formation. However, because the air-water heat flux is typically not constant due to changing environmental conditions the relationship between the water temperature and ice generation is likely more complicated. There are very limited measurements of supercooling in rivers reported in the literature. In this study field measurements were made in three rivers in Alberta, Canada (Kananaskis, North Saskatchewan, and Peace Rivers) over several winters using precision water temperature loggers (accuracy ±0.002 ^{0}C). The loggers were mounted in metal casings and anchored to the riverbed. The temperature time series were used to compute the characteristics of supercooling events including the timing, duration, and peak supercooling temperature. The characteristics of these events are analysed to determine significant patterns and trends within the data across all three rivers, and within each river. These patterns are compared to the recorded climate conditions from nearby weather stations such as solar radiation, air temperature and relative humidity.

1. Introduction and Background

Starting in late fall, northern rivers are exposed to freezing temperatures which can cool the turbulent water to sub-zero temperatures. This process, called supercooling, induces rapid production of frazil ice crystals when seed crystals are present to provide nucleation sites (Daly 1994). Highly adhesive frazil ice crystals quickly flocculate and either adhere to the bed as anchor ice, or grow large enough that buoyancy raises them to the surface (Daly 1994). At the surface, these flocs agglomerate as slush, then freeze into frazil pans (Daly 1994). Moving downstream, large concentrations of these pans may bridge the river at a constriction, starting the progression of an intact ice cover upstream. The ice cover insulates the water surface, preventing further supercooling. In steep fast flowing streams or seasons with milder winters, a complete ice cover may never form. In spring, supercooling may occur as the break-up of the ice cover exposes the water to cold air temperatures once more.

Figure 1 presents an idealized supercooling curve as observed in the laboratory under constant heat loss, and visualizes a few parameters of a supercooling event: the event start, the drop in temperature to a minimum temperature (called the peak supercooling temperature), and the rise in temperature from exothermic ice production to a residual temperature. For this paper, the period between the start of an event and the first occurrence of the peak supercooling temperature is defined as the principal supercooling period. The variations of the water temperature during a supercooling event is dependent on the net heat flux at the water boundaries (Hicks 2016). The temperature fluctuations in rivers are driven by the sensible and latent fluxes at the air water interface, along with the precipitation, the riverbed and banks, groundwater, and absorbed solar radiation. The different heat flux in nature change dynamically which means that while supercooling behavior similar to the constant heat flux curve shown in Figure 1 is possible, more erratic behavior is expected. Difficulties in measuring these heat flux components means approximations are often made when modeling river ice processes. Upstream storage dams that release water into the river may significantly alter the river ice regime downstream of the dam by maintaining open water conditions (Maheu et al. 2014). This enables supercooling and frazil ice production to continue throughout the winter.

This paper presents the analysis of water temperature time series measured on three Canadian rivers during the winter seasons from 2015 to 2018: the Kananaskis, North Saskatchewan and Peace Rivers (referred to as KR, NSR, and PR respectively). Supercooling events were identified in the time series, and their properties analyzed. Preliminary results from the analysis of the NSR data was presented in Kalke et al. (2019). This paper considers the event start and end time, duration, peak supercooling temperature, and the time from the event start to the first occurrence of the peak supercooling temperature referred to as the principal supercooling duration. The objective of this analysis is to improve our understanding of the supercooling in rivers, as it is crucial to the frazil ice production process.

2. Literature Review

A small number of studies report field measurements of supercooling in rivers. Two of these studies were focused on the St. Lawrence River near Quebec City, Canada: (Richard and Morse 2008; Morse and Richard 2009). These studies observed water temperatures fluctuating between -0.06°C to above 0.06°C at air temperatures below -5.4°C. Full season measurements in Newfoundland and New Brunswick by Nafziger et al. (2013) found that freeze–up supercooling events stabilized at a residual temperature specific to each site, while break up events had no residual period. Nafziger et al. (2013) measured peak supercooling up to -0.07 °C, and durations up to 42.7 hours.

Kalke et al. (2019), reported on supercooling events on the NSR from 2015 – 2018, and analysed both freeze-up and break–up events in detail. They found freeze-up peak supercooling values ranged from -0.005ºC to -0.106ºC, with 80% of these events occurring between 6:00 PM and 9:00 AM. Break-up events were found to have a smaller range of peak supercooling from -0.006ºC to -0.025ºC, and all events occurred between 9 PM and 9 AM.

3. Field Sites and Methods

All three rivers are regulated by dams at varying distances upstream of the study reaches. The approximate location of the upstream end of each reach, and all upstream dams, are shown in Figure 2 and the reach characteristics are summarized in Table 1. On the KR, the study reach lies within the 47 km between the Pocaterra Dam and Barrier Lake. Extreme hydropeaking causes flow fluctuations between 2 – 20 m^3/s daily, preventing the formation of a stable ice cover (McFarlane et al. 2017). Three observation sites were located on the river ~10, 15, and 26 km downstream of the dam. The Brazeau and Bighorn Dams on the NSR are approximately 230 km and 430 km upstream of Edmonton, respectively (McFarlane et al 2017). The regimes of these dams have little impact on the frazil ice production within the study reach. This ~100 km reach contains four sites, one ~80 km upstream of Edmonton, and the remaining three sites over a ~19 km reach in Edmonton. The W.A.C. Bennett Dam and Peace Canyon Dam, respectively 300 and 277 km upstream of the PR study reach, release warm water into the river during winter. This extends the freeze-up season and delays the ice front advancement upstream (McFarlane et al. 2017). Eleven sites are placed over a 15.8 km reach, eight of which are paired and placed near the left and right banks of a river station.

Measurements were collected for one, two and three winters on the KR, PR and NSR, respectively from 2015 to 2018. Water temperature was measured at a 1-minute sampling rate using RBR Solo T temperature loggers (±0.002ºC) placed inside protective casings and anchored to the riverbed. The KR and NSR loggers were housed and fastened to the bed using the casings and pins as shown in Figure 3 at a depth of ~0.75 m. On the PR, the RBR casings were attached to large pieces of flat iron, deployed in deeper water by boat, and anchored to the shore using steel cables. In total, 3, 11, and 9 time series were collected from the KR, NSR, and PR respectively. The time series run from late October – early November until after spring break-up. While these measurements are taken at the river bottom, turbulence is expected to keep the water column relatively well mixed, maintaining similar water temperatures throughout the water column.

A MATLAB program was developed to analyze the site time series, and catalogue identified supercooling events. The time series was only analysed during open water conditions. A supercooling event was assumed to start just before the temperature dropped below -0.002ºC and ended at the last data point before it rose above -0.002ºC. This definition was chosen so that all temperatures within the event were confirmed supercooling temperatures, regardless of the sensor accuracy at the time of measurement. After defining the start and end time of an event, the program also determined the peak supercooling temperature, as well the time when the peak supercooling temperature was measured during the event. Once the time of peak supercooling temperature have been determined, the principal supercooling duration could be calculated. Events less than 10 minutes in duration, were excluded due to being too short in duration. Events with a peak supercooling temperature below -0.2ºC, along with events that occurred within an hour of the start and end of the event, were excluded as likely influenced by exposure to air or ice.

4. Results

A total of 513 supercooling events were observed in the three rivers, 94, 175, and 245 in the KR, NSR, and PR, respectively. 452 events occurred during freeze-up, with the remaining 61 events during break–up. Figure 4 presents the time series of air and water temperatures during freeze-up in 2016 at a site on the North Saskatchewan River. It shows how supercooling events are defined within a time-series along with the water temperature's response to the measured air temperature, which reached a minimum of -8.2°C. In this 18-day period, 28 supercooling events were identified, including an event with a peak supercooling temperature of -0.105°C, the 2nd highest value observed. The duration of these events ranged from 15 minutes to 21.8 hours.

Figure 5 shows an example of a supercooling event that lasted ~10 days measured near the left and right banks of a PR station during the 2016 – 2017 season. The water was exposed to air temperatures well below freezing for most of its duration, reaching a low of -33.7°C. A peak supercooling temperature of approximately -0.043°C was reached within the first few hours on February 1st, with a residual temperature of approximately -0.008°C for ~8 days. Despite a 23°C drop in air temperature from February 2nd to 6th, the water temperature remained near the residual temperature, with minor fluctuations observed near the right bank.

Figure 6 presents the break-up water temperatures at a site on the NSR in 2017-2018 with weather parameters obtained from the Alberta Climate Information Service (ACIS) database St. Francis station (Climate ID 3012799) 9.54 km from the study site. Figure 6a shows the water and air temperatures over a two-week period, and the air temperatures ranged from 2°C to 25°C. In Figure 6b, the solar radiation, relative humidity, and wind speed measured by ACIS (2020) during this period are plotted. During the five significant supercooling events that occurred in this time period, peak supercooling varied from -0.006 °C to -0.024°C, air temperatures ranged from 1 to 7 °C, relative humidity from 35 to 75% and wind speeds from 2.5 to 25 km/hr. The first event was the only one to have wind speeds exceeding 20 km/hr. Solar radiation during the events was negligible since all the events occurred between midnight and early morning. The following day after each event, solar radiation was 760-820 W/m^2 which suggests clear skies and potentially high net long wave radiation the previous night. Under clear skies and open water conditions, Ashton (2013) estimates a net longwave radiation range of -60 to -80 W/m^2 when the air temperature is between 0°C and 5°C.

Histograms were used to analyze the start and end times of all events, along with the peak supercooling temperatures, as shown in Figure 7. Start times, shown in Figure 7a, occur evenly throughout the day with a slight peak between 4 PM and 6 PM. Figure 7b shows events ending predominately between 10 AM and 1 PM. The peak supercooling temperature histogram in Figure 7c follows an exponential probability distribution, with 95% smaller in magnitude than -0.05°C.

The statistics of each parameter is summarized in Table 2. The peak supercooling values in all rivers ranged from – 0.002°C to -0.106°C with a median and mean value of -0.010°C and -0.016°C, respectively. The results in individual rivers are comparable with mean values of -0.012, -0.015, and -0.018°C for the KR, NSR, and PR, respectively. Event durations in all rivers ranged from 10 minutes to ~13.5 days with a mean value of 21.1 hours with 88% less than 24 hours in duration. The event durations in the KR and NSR are comparable, with mean values of 10.4 and 7.82 hours, respectively. In contrast, events in the PR were considerably longer with a median and mean of 5.25 and 34.8 hours, respectively. Principal supercooling durations ranged from 1 minute to ~53 hours in all rivers with a mean of 1.74, 1.81, and 2.31 hours for the KR, NSR and PR, respectively.

5. Discussion and Conclusions

During the event shown in Figure 5 the water temperature remained at approximately the residual temperature despite the drop of 23ºC in air temperature. For the water temperature to remain at the residual for ~8 days, the heat budget in the water in the reach upstream of the measurement site must have remained balanced for this entire time. That is, no net heat flux into or out of the water column. However, many of the air-water heat fluxes would have varied substantially due to fluctuating air temperatures and therefore, the latent heat flux associated with frazil and anchor ice production must have varied to keep the net heat flux close to zero.

The occurrence of multiple supercooling events during spring break-up when air temperatures were above 0°C was surprising (see Figure 6). The events all started at around midnight and ended in early or mid-morning. Since the solar radiation data indicated that there were clear skies overnight, the net longwave radiation was likely the dominant factor. Heat fluxes will be analysed in greater depth in a future paper.

Figure 7a and 7b show that the start and end of an event tended to correlate with the average setting and zenith of the sun respectively. However, since the peak of these distributions is only ~10%, direct solar radiation is likely not the dominant influence on the timing of an event. In Figure 7c, the peak supercooling data appears to be well described by an exponential probability distribution function with 95% of the events having peak supercooling magnitudes less than 0.05˚C. The largest peak supercooling that was observed was -0.106ºC.

Supercooling event duration was the parameter that varied the most between the three rivers, likely due to upstream dam flow regulation. The extreme daily hydropeaking on the KR likely shortens the duration of many supercooling events and reduces the peak supercooling. The flow regulation on the PR is related to continuous or base load power generation at the upstream dams. Continuous release of relatively warm water maintains open water conditions for 100-400 km downstream depending on the season's severity. The extended time period of open water enables the long duration supercooling events. Flow regulation on the NSR causes daily water level fluctuations of 30-50 cm in amplitude but did not appear to have a significant impact on the properties of the observed supercooling events.

Observations indicate that a typical supercooling event on these three Canadian rivers had an average peak supercooling of -0.016oC and a duration of 21 hours. However, because both the duration and the peak supercooling data are significantly skewed, the median values of -0.010oC and 3.6 hours, respectively, might be more meaningful. A few outlier events had peak supercooling exceeding -0.1oC and durations exceeding 300 hours. However, 95% of the events had peak supercooling temperature magnitudes ≥ -0.05oC and 88% of them had durations of ≤ 24 hours. Therefore, we can conclude that the supercooling events observed in this study were typically less than 24 hours in duration with water temperatures ranging from -0.002 to -0.05ºC.

References

Alberta Climate Information Services (ACIS), 2020, *Current and Historical Alberta Weather Station Data Viewer,* Retrieved February 20, 2020 from https://acis.alberta.ca/acis/weather-data-viewer.jsp

Ashton, G. Thermal Processes. River Ice Formation. Edited by Beltaos, S. Committee on River Ice Processes and the Environment and Hydrology. Canadian Geophysical Union Hydrology Section, Edmonton, Alberta, Canada. ISBN 978-0-9920022-0-6 Pg. 19 - 76

Buehler, H. 2013. Impact of a hydropeaking dam on the Kananaskis River: changes in geomorphology, riparian ecology, and physical habitat (T). Electronic Theses and Dissertations (ETDs) 2008+. University of British Columbia. Retrieved February 20, 2020, from https://open.library.ubc.ca/collections/ubctheses/24/items/1.007354

Daly, S., 1994. Report on frazil ice. US Army Corp of Engineers, Cold Regions Research & Engineering Laboratory, Hanover, New Hampshire, Report 94-23, 50 pages.

Hicks, F., 2016. An introduction to river ice engineering for civil engineers and geoscientists. CreateSpace Independent Publishing Platform, Charleston, SC, USA.

Kalke, H. et al., 2019. Field Measurments of Supercooling in the north saskatchewan river, CGU HS Committee on River Ice Processes and the Environment Ottowa, Ontario

Kellerhals, R. C., C. R. Neil, and D. I. Bray. 1972. Hydraulic and geomorphic characteristics of rivers in Alberta. Cooperative Research Program in Highway and River Engineering Technical Report. Alberta Environment, Edmonton

McFarlane, V. Loewen, M., Hicks, F. 2017. Measurements of the size distribution of frazil ice particles in three Alberta rivers. Cold Regions Science and Technology 142, 107-117. https://doi.org/10.1016/j.coldregions.2017.08.001

Maheu, A., St-Hilaire, A., Caissie, D. 2014. The impact of dams on the winter thermal regime of streams: progress report. Rapport de recherche R1506, INRS-ETE, III+32 pages.

Morse, B., Richard, M., 2009. A field study of suspended frazil ice particles. Cold Regions Science and Technology 55, 86–102. https://doi.org/10.1016/j.coldregions.2008.03.004

Nafziger, J., Hicks, F., Thoms, P., Mcfarlane, V., Banack, J., Cunjak, R.A., 2013. Measuring supercooling prevalence on small regulated and unregulated streams in New Brunswick and Newfoundland, Canada, CGU HS Comittee on River Ice Processes and the Environment. Edmonton, AB.

Richard, M., Morse, B., 2008. Multiple frazil ice blockages at a water intake in the St. Lawrence River. Cold Region Science and Technology 53, 131–149. https://doi.org/10.1016/j.coldregions.2007.10.003

Figures

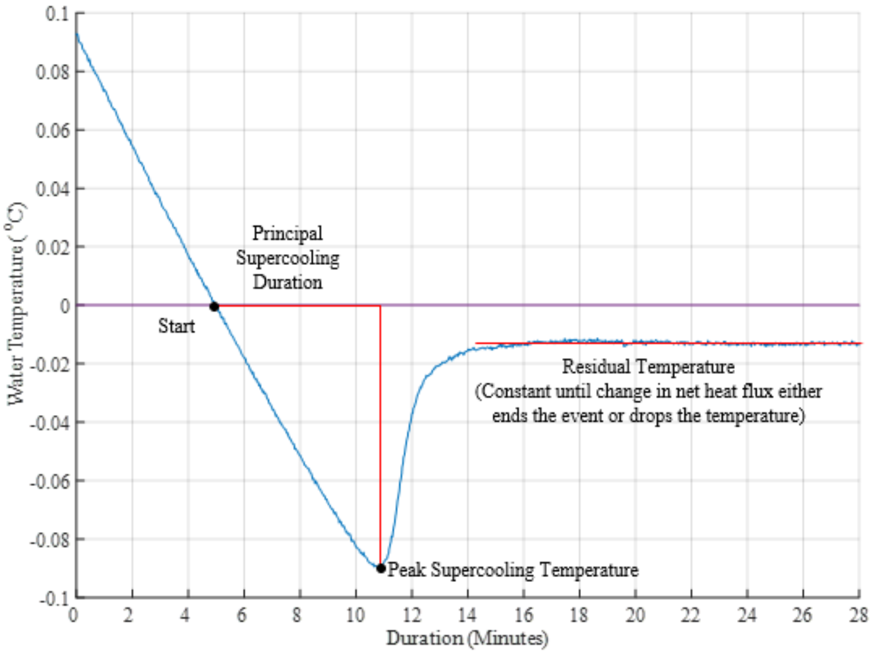

Figure 1. Laboratory generated supercooling temperature time series with key characteristics labeled.

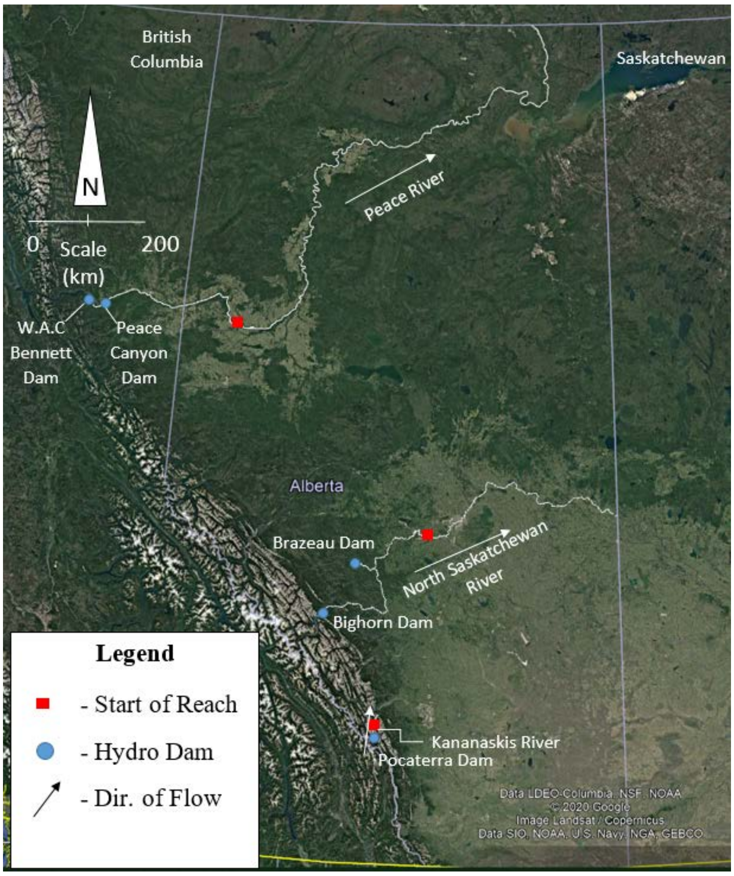

Figure 2. Approximate study site and hydropower dam locations in Alberta, Canada. [Image taken from Google Earth (2020)]

Figure 3. Metal casing and anchoring pins used to fasten the RBR Solo T temperature loggers on the bed in the North Saskatchewan and Kananaskis deployments.

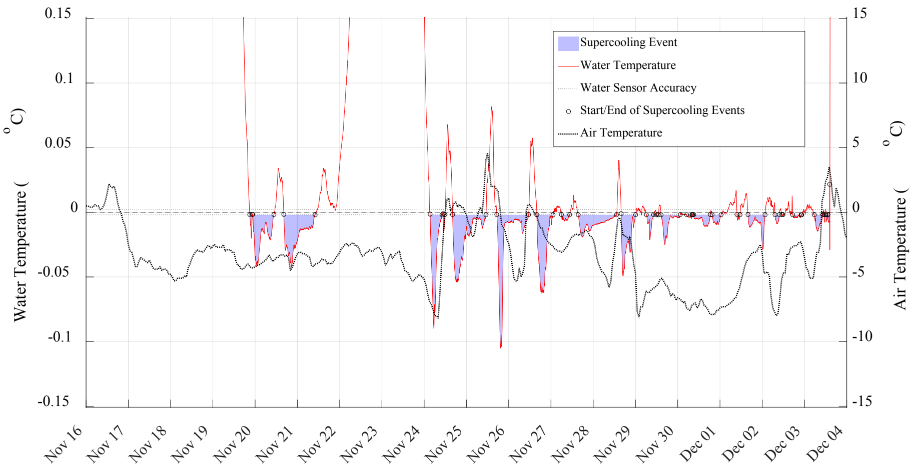

Figure 4. Freeze-up season time series of water and air temperature at a site on the North Saskatchewan during Nov-Dec 2016.

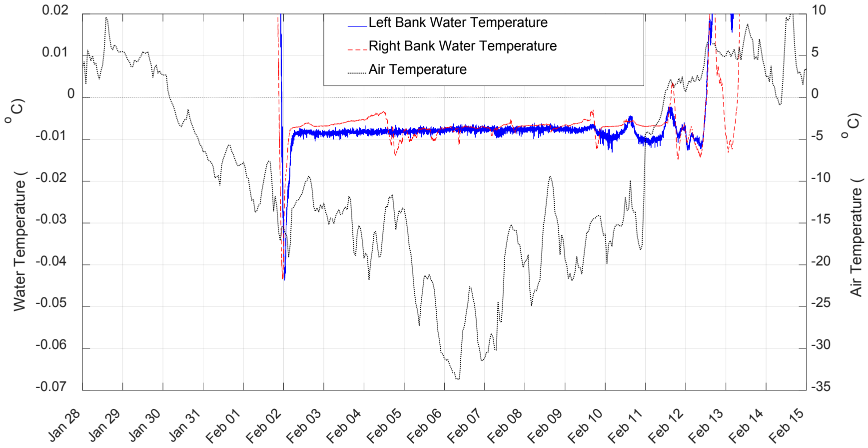

Figure 5. Water and air temperature time series at a station on the Peace River during the 2016 – 2017 season.

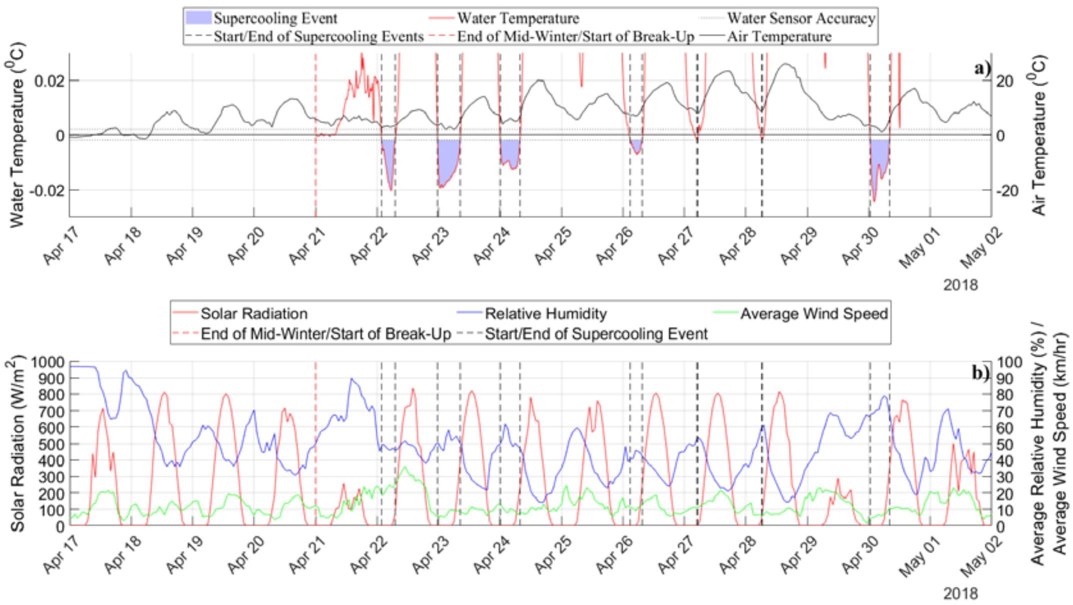

Figure 6. Time series plots of; a) water and air temperatures at a site on the North Saskatchewan during –break-up in 2018; b) solar radiation, relative humidity, and average wind speed during the same time period from the St. Francis station

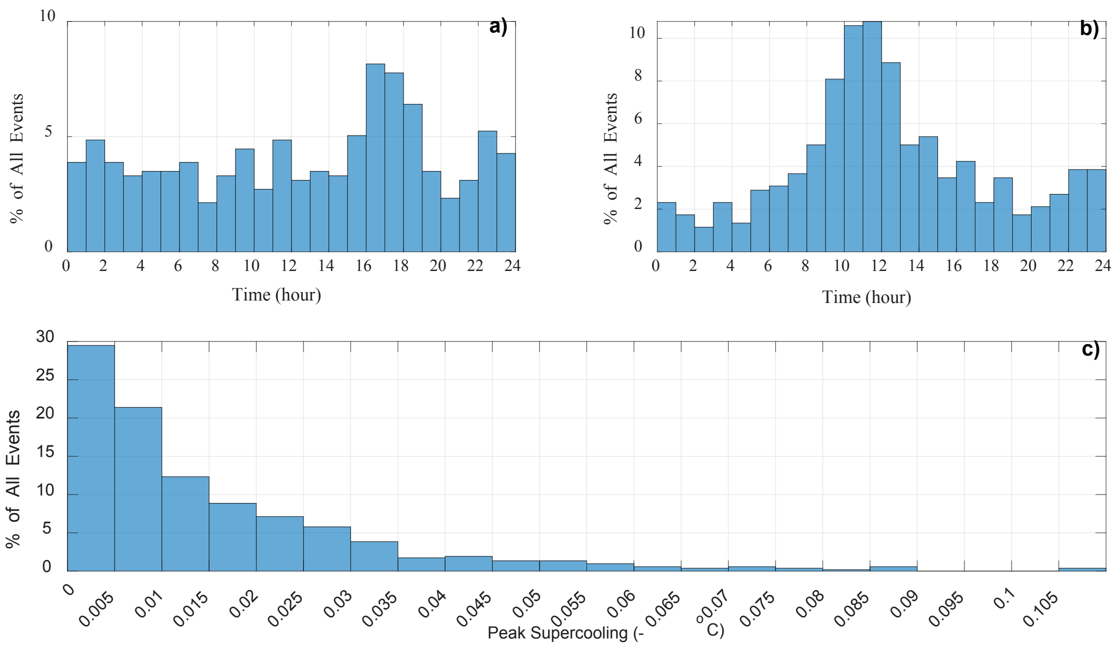

Figure 7. Histograms of various properties for all supercooling events; a) Start time of event b) End time of event c) Peak supercooling temperature.

Tables

Table 1. Summary of the characteristics of the three study reaches.

River	Drainage Basin Area at study site [km^2]	Average Annual Flow Rate [m^3/s][a]	Average Slope	Width [m][a]	Depth [m][a]
Kananaskis	[c]748	11 – 15	[c]0.0034	32	0.61
North Saskatchewan	[b]5.67×10^3	220	[a]0.00035	136	1.40
Peace	[b]1.30×10^5	1.59×10^3	[a]0.00025	227	2.56

Sources: [a] McFarlane et al (2017); [b]Kellerhals et al. (1972); [c]Buehler, H. (2013)

Table 2. Statistics of supercooling event properties.

	Statistical Parameters	Peak Supercooling [°C]	Event Duration [Hours]	Principal Supercooling Duration [Hours]
All Rivers	**Minimum**	-0.002	0.167	0.017
	Median	-0.010	3.58	0.850
	Mean	-0.016	21.1	2.04
	Maximum	-0.106	325	53.4
Kananaskis	**Minimum**	-0.002	0.183	0.067
	Median	-0.009	3.77	0.750
	Mean	-0.012	10.4	1.74
	Maximum	-0.059	162	15.4
North Saskatchewan	**Minimum**	-0.002	0.167	0.017
	Median	-0.007	1.87	0.75
	Mean	-0.015	7.82	1.81
	Maximum	-0.106	165	41.4
Peace	**Minimum**	-0.002	0.167	0.017
	Median	-0.015	5.25	1.09
	Mean	-0.018	34.8	2.31
	Maximum	-0.087	325	53.4

Analysis of factors affecting ice use in winter landscape——With the case of Harbin

Chang-lei Dai[a,b],Yi-ru Wei[a,b],Yu Wang[a,b],Nan Mi[a,b],Jin-wu Pang[d],Li-quan Wang[b],Xiao-hong Zhang[a,c]

[a] *Institute of Groundwater in Cold Region,Heilongjiang University,Harbin 150080,China*

[b] *School of Hydraulic and Electric power,Heilongjiang University,Harbin 150080,China*

[c]*Institute of East, North-Eastern Federal University,Yakutsk 677000,Russia*

[d]*Green Development Institute,Beijing Normal University 100875,China*

Abstract: In recent years Harbin has vigorously developed the ice and snow tourism industry and the demand for ice landscape has increased significantly. Analysis of influencing factors of ice landscape --with a case of Harbin has not only contributed to the prediction of ice conditions but also has important significance for river protection.Taking Harbin 2017 as an example，Analysis of the conditions of ice demand,ice picking and ice transporting .It is concluded that:(1) The demand for ice landscape is very large in Harbin,but the ice utilization rate is very low， and the ice loss is also very high;(2) Ice landscape mainly includes concentrated landscape ice and scattered ice in Harbin;(3) The Songhua River in Harbin can provide abundant ice storage in winter;(4) On considering ice safoty and ice thilneces the ice-picking time generally starts from December of each year,the ice size is 1.6m*0.8m*0.3m;(5) Because of its unique geographical conditions,the Songhua River in Harbin can provide convenient conditions for the transportation of ice.

Key words: Ice landscape; ice volume; ice picking; Songhua River;Harbin

Ice landscape is an indispensable factor for ice and snow tourism. However, there are many researches on the art of ice and snow landscapes, and there are few studies on ice and snow attractions. As a famous winter tourist city, Harbin attracts thousands of tourists every year to enjoy the charm of ice and snow. With the Ice and Snow World becoming one of the world's important ice and snow landscape theme parks, Harbin's ice and snow is not only naturally endowed by nature. Wealth, together with the important task of spreading Harbin urban culture. Therefore, the analysis of the factors affecting the use of ice in Harbin landscape is very necessary.

1 Overview of Harbin

1.1 Geographic location

Harbin is the capital of Heilongjiang Province in China and is the transportation, political, economic, cultural and financial center of northeastern China. Due to the special historical process and geographical location, it has become an attractive city with exotic customs. It not only brings together the history and culture of the northern minorities, but also integrates with other national cultures, making it a historical and cultural tourist city.

Harbin is located at E125°42′—E130°10′, N44°04′—N46°40′. The terrain of the whole area is flat and open, slightly inclined from the southeast to the northwest. The landform types are mainly floodplain, terrace and high plain.

1.2 Meteorological hydrology

As the capital city of China's highest latitude, Harbin has four distinct seasons. The winter is long and cold, and the summer is short and cool. The spring and autumn seasons are excessive seasons. The climate of Harbin is a humid continental monsoon climate. The annual precipitation is unevenly distributed during the year. The heavy rains are mostly concentrated in July and August, and the average annual precipitation is 540 mm. Snowfall is mainly concentrated from November of each year to January of the following year. The average daytime temperature in

Foundation project: The National Science and Technology Support Program of the 12th Five Year, for research on groundwater safety and security patterns based on highly efficient irrigation (2014BAD12B01-03).

Author: Chang-lei Dai, male, born in 1969 , Prof, Ph.D, magor in groundwater in cold regions and international rivers, E-mail：daichanglei@126. com.

winter is about -19 °C, and the average daytime temperature in summer is around 25 °C. Harbin is rich in water resources, with large and small rivers interlaced, mainly including Songhua River, Hulan River and Ash River, all of which belong to the Songhua River system. The surface water systems passing through Harbin City are mainly Yijiang, Erhe and Sangou. These water resources also provide protection for the ice in the winter ice landscape.

2 Analysis of ice demand factors in landscape

As one of the important ice and snow tourist cities, Harbin is in great demand for ice and snow every year. There are two types of ice for landscape use in Harbin: concentrated landscape ice and scattered ice.

2.1 Concentrated landscape ice

The concentrated landscape ice mainly refers to the large amount of ice used in large ice and snow parks, ice and snow festivals and other places in a certain place at a certain time. Harbin Ice and Snow World has become the most important ice project in Harbin.

The Ice and Snow World is to meet the Millennium Festival of the Millennium Festival. The Harbin Municipal Government, based on the advantages of the Harbin Ice and Snow Festival, launched the large-scale ice and snow art project in 1999, demonstrating the ice and snow culture and tourism charm of Harbin as a famous city in the north. Harbin Ice and Snow World has become the most popular ice and snow theme park in the country.

In 2017, the 19th Ice and Snow World covers an area of 800,000 m^2, with an ice capacity of 180,000 m^3, a snow consumption of 150,000 m^3, and a total of more than 2,000 ice and snow landscapes.

In addition to the Ice and Snow World in Harbin, the Ice Lantern Art Garden and the Wanda Ice Lantern World are all concentrated ice projects that attract many tourists to watch and watch. The Harbin Ice Lantern Art Garden was founded in 1963. It is located in Zhaolin Park and covers an area of 65,000 m^2. In 2017, the amount of ice used was about 2,000 m^3, and the number of ice landscape works reached more than 1,500 pieces. Wanda Ice Light World is located in Harbin Wanda Theme Park, covering an area of 500,000m^2 and using about 50,000 m^3 of ice. It is a new landmark for Harbin ice and snow tourism, adding rich interactivity and amusement.

2.2 Scattered ice

Disperse ice mainly refers to small amounts of ice used for municipal ice, street ice and other decorations. At present, there are 48 streets and 78 ice and snow spots in Harbin.

The shaping of the ice scene of Harbin Municipal Square not only considers the expression of culture, but also represents a city of ice and snow. The street ice and snow landscape plays a finishing touch to the landscape of the winter city streets, making the night landscape of the city streets more beautiful. The street ice landscape is a landscape aimed at Harbin culture, with ice elements as the main means of construction and ultimate purpose.

2.3 Total amount of ice

The amount of ice used in urban areas is 230,000 m^3 according to the number of [2011] No. 29 issued by the Harbin City Administration. The ice volume of the Ice and Snow World is 150,000 m^3 according to the survey in 2010 and 180,000 m^3 in 2017, and it was added in 2017. The Wanda Ice Light World uses ice of 50,000 m^3, and the increase rate of concentrated landscape ice is (3+5)/15*100%=53%.

The ice volume of the city's ice landscape is calculated according to the increase rate of ice used in the concentrated landscape. The total ice demand of the city is 352,700 m^3. According to the amount of ice in the concentrated ice landscape, the amount of ice used for dispersal of municipalities and streets is estimated: the total amount of ice minus the amount of ice used for concentrated landscape is 352,700-232,000=120,700 m^3.

In addition to the above-mentioned ice and snow parks, the Ice and Snow Festival and other projects that are held and carried out every year, there are other competitions or projects on ice and snow. It is assumed that the amount of ice used in the ice landscape accounts for about 90% of the ice used in the city's ice landscape. The annual ice consumption in Harbin is at least 391,900 m^3.

3 Ice source factor analysis

In order to meet the ice use of various ice and snow tourist attractions and ice and snow culture and art festivals, it is necessary to have a stable ice source and sufficient ice. The ice materials used in Harbin's current ice landscape are from the river ice of the Songhua River. During the ice picking period, the professional cuts the river ice by size, and then the ice picker removes the cut ice from the surface and finally loads it with the truck. Go to the ice site for sculpture.

3.1 Songhua River ice mining area

In order to meet the requirements of ice landscape construction, mining safety and transportation convenience, the selection of ice source has the following requirements:

(1) shorter transportation distance and convenient transportation;

(2) thicker ice layer to keep the ice intact, Ensure the safety of ice pickers;

(3) away from existing buildings, attractions and residents' living places.

The Songhua River is rich in water resources and passes through the urban area of Harbin. It can provide enough ice for the shaping of the ice landscape and has the characteristics of close proximity. Therefore, it is a very good choice for the ice source of Harbin ice and snow tourism.

3.2 The amount of ice produced

In 2017, the ice volume of the city's ice landscape was 391,900 m^3. Based on the cold temperature in Harbin winter, the maturity of ice landscape engraver technology and the experience of ice material transportation, the assumed breakage rate is 1%, which is obtained every year in Harbin. The amount of ice should be at least 391,900/(1+0.01)=395,800 m^3.

In order to meet the demand for ice use, ice picking needs to be planned, taking traffic and transportation distance into consideration. There are 6 mining areas on the north bank of Songhua River on the west side of Songhua River Highway Bridge, the north bank of the Songhua River on the east side of the Songhua River Highway Bridge, the north bank on the east side of the spillway bridge, the south bank on the west side of the spillway bridge, both sides of the Songpu Bridge, and near the spillway shipyard. Set up a spare mining area between Wangwan Railway and Fourth Ring Bridge. A total of 425,000 m^3 can be mined, as shown in Table 1.

Tab.1 River ice-picking area

Location		Volume / Million m^3
Minable area	the east side of the Songhua River Highway Bridge	4.0
	the west side of Songhua River Highway Bridge	6.0
	the east side of the spillway bridge	5.0
	on the west side of the spillway bridge	2.0
	and near the spillway shipyard	3.5
	the east side of the Songpu Bridge	1.0
	the west side of the Songpu Bridge	1.0
Spare mining area	the east side of the Wangwan Railway Bridge	20.0
total		42.5

4 Ice picking and transportation factor analysis

4.1Analysis of ice picking factors

Taking into account the safety of ice picking, ice cube size and other factors, the choice of mining area has the following requirements:

(1) to ensure stability of the river, flood control and protection of the water environment, can not bring river, flood control, water environmental protection, etc. Adverse effects;

(2) to ensure the normal use of coastal industries and agricultural facilities;

(3) does not conflict with existing developed ice areas, avoid crowded areas;

(4) transportation distance is short, transportation is convenient;

(5) back river channel flow rate is small The ice layer is thicker;

(6) away from the infrastructure areas such as bridges, wetlands, and famous tourist areas. The annual ice collection is mainly concentrated on both sides of the Songhua River Highway Bridge, Jinshui River and the flood discharge canal.

Statistics on the ice conditions of the Harbin hydrological station show that the average annual sealing date is November 24th of each year, and the opening date is April 9 of the following year. The average freezing time is 135d and the maximum ice thickness is 1.25m (March 1957). The thickness of each month's ice layer in Harbin in the past 50 years is shown in Figure2.

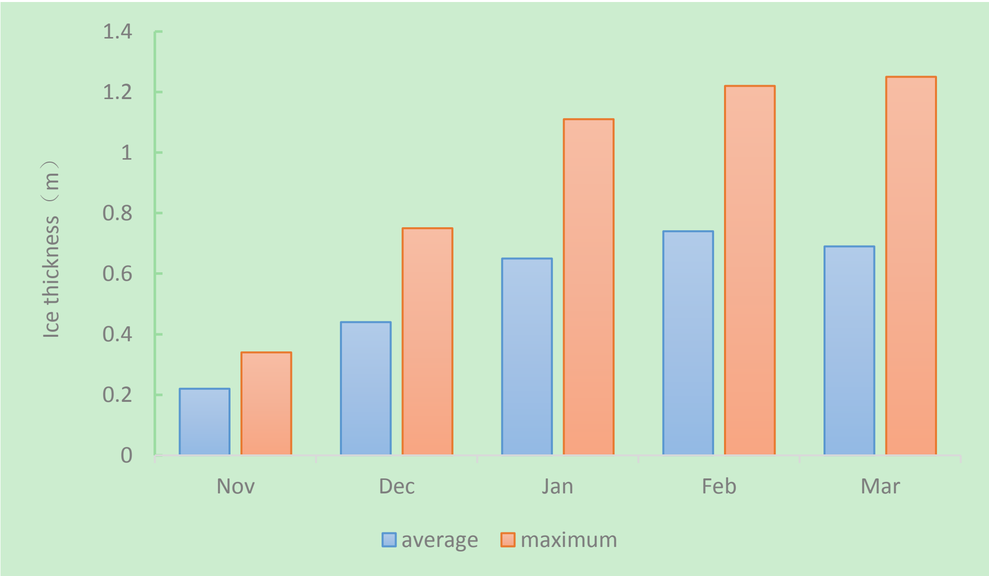

Fig.2 Results of ice thickness in each month of Harbin Station in winter

The annual Ice and Snow Festival begins on January 5, and the Ice and Snow World is also open in January. There is plenty of time for ice landscapes and attractions to be built. Every year, ice picking begins in December.

According to the construction of the ice landscape, the safety of the ice pickers and the convenience of transportation, the ice cubes are fixed in size. The ice is generally 1.60 m long and 0.80 m wide , and the thickness of the ice is based on the river water knot. The ice thickness in the ice-harvesting area from 2006 to 2010 in December is shown in Figure 3..

In recent years, the temperature rises and the thickness of ice increases, and the thickness of the ice layer is about 0.30 m. In order to ensure the quality of the ice landscape and the safety of the ice-picking work, it is necessary to observe the designated ice-picking site during the icing period:

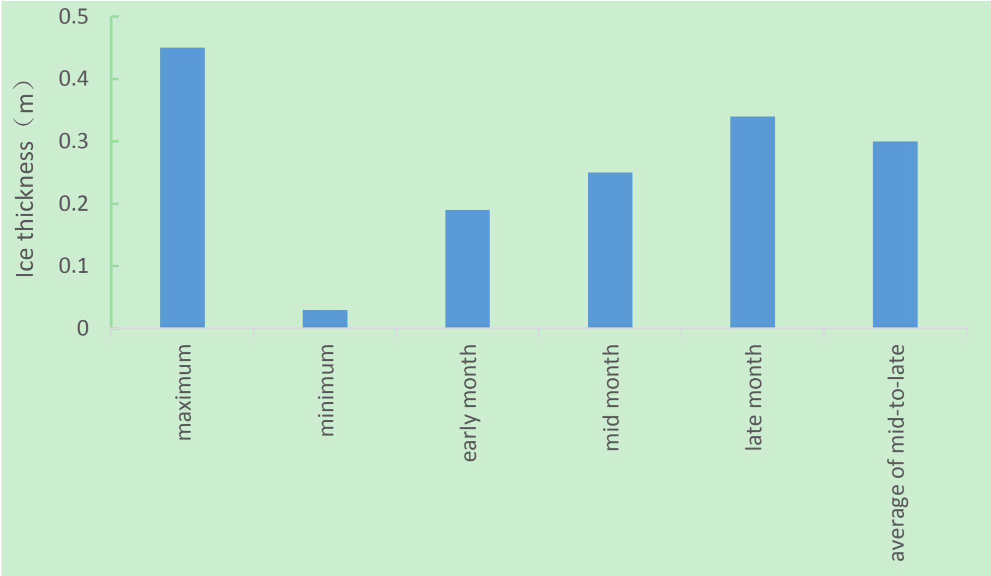

Fig.3 Ice thickness in the ice mining area in December

(1) Whether the water quality is clear and judge the ice quality;

(2) Ensure that roads are safely transported to avoid the risk of rollovers and ice slips.

4.2 Transportation factor analysis

Because of the existence of the Songhua River, the ice picking location is easy to determine and can provide a rich amount of ice. The distance between the freezing point and the ice site in Harbin is very short, and the transportation of ice is convenient and the cost is low. Harbin transports ice in the winter is relatively simple, usually carried by trucks loaded with ice. Ice transport is also one of the factors affecting the ice landscape.

5 Conclusions and suggestions

In 2017, the ice consumption in the world of ice and snow and Zhaolin Park reached 180,000 m^3 and 2,000 m^3 respectively. The added ice in the world of Wanda Icelight reached 50,000 m^3, and street ice and municipal ice were about 120,700 m^3; Harbin's ice source has sufficient ice volume, although the annual ice requirement is 395,800 m^3, but the planned ice picking capacity can reach 425,000 m^3, which can support the long-term and sustainable development of Harbin ice and snow tourism; Ice time generally begins in December each year, and the ice size is 1.6 m*0.8 m*0.3 m.

Harbin has been engaged in ice and snow tourism for a long time, and its form and culture have matured. However, there are still some problems due to some factors:

(1) It is necessary to improve the utilization rate of ice and plan for ice mining. At the same time, the treatment of ice landscape is completed;

(2) The choice of ice-picking area should not only ensure sufficient ice volume, ensure the safety of safety workers, but also ensure that no damage to the natural environment is caused;

(3) For transportation problems, the loss of ice during transportation should be considered to reduce unnecessary natural resources. waste.

References

[1]Yang K L, Wang J, Guo X L, et al.. Numerical simulation of water delivery during glacial period of water transfer project and key technology of ice forecasting[M]. China Water & Power Press, 2015:2-9.

[2]Guo Z H, Yu C G, Dai C L. Change of snow depth and snow melt equivalent over both time and space in Daxinganling[J].

Journal of Engineering of Heilongjiang University, 2013, 4(3):23-28.
[3]Dai C L, Yu C G, Liao H C, et al.. Survey and forecast of river ice[M]. China Water & Power Press, 2010: 3-7.
[4]Dai C L, Li Z J, Yu C G, et al.. Introdution of water science in cold region[M]. Heilongjiang Education Press, 2014: 145-155.
[5]Wang X N. On Public Human Resources Management of Urban Community[D]. Northeast Agricultural University, Harbin, 2017.
[6]Qin D H. Introduction to Cryosphere Science[M]. Science Press, 2017:142.
[7]Sun Q Q, Song G, Qi M L. Analysis of Land Ecological Safety Evaluation of Harbin City Based on Principal Component Analysis[J]. Research of Soil and Water Conservation, 2012, 19(1):234-238.
[8]Xie Y Y, Meng J, Guo L F. REE geochemistry of modern eolian dust deposits in Harbin City, Heilongjiang Province, China:implications for provenance[J]. Catena, 2014, 123: 70-78.
[9]Zhong H, Su A S, Li Z Y, et al.. Application of water conservancy project technological achievement in cold region[J]. Hydro Science and Cold Zone Engineering, 2018, 1(6): 63-67.
[10]Wen J W. A preliminary discussion on the implementation plan of urban hydrological monitoring, analysis and evaluation in Harbin[J]. Water Conservancy Science and Technology and Economy, 2017, 23(4): 55-57.
[11]Gong W F, Yuan L, Fan W Y. Analysis on land use pattern changes in Harbin based on terrain gradient[J]. Transactions of the Chinese Society of Agricultural Engineering, 2013, 29(2): 250-259, 303.
[12]Wang W J, Wang Q, Zhou W. Glomalin changes in urban-rural gradients and their possible associations with forest characteris-tics and soil properties in Harbin City, Northeastern China[J]. Journal of Environmental Management, 2018, 224(7): 47.
[13]Wu J C, Xue Y Q. Groundwater Hydraulics[M]. China Water & Power Press, 2009: 162-169.
[14]Huo L. Ice and Snow World "Leading Dance" Four Seasons Ice and Snow Tour[N]. Harbin Daily, 2016-07-15(1).
[15]Dong Y Z. The 19th China • Harbin Ice and Snow World Highlights. [EB/OL]. (2017-11-25)[2018-04-21], http://www. hlj. xin-huanet. com/bcrd/2017-11/25/c_ 136776926. htm.
[16]United States Army Corps of Engineers. River Ice Control Engineering Design Manual[M]. China Water & Power Press, 2013: 245-262.
[17]Wang T. Ice and Snow Landscape Construction Research on City Streets in Harbin[D]. Northeast Agricultural University, Harbin, 2016.
[18]Yao L. The Research of The Landscape Design for China’s Northern Ice and Snow Characteristics[D]. Beijing Institute of Fashion Technology, Beijing, 2008.
[19]Wang E L, Zhang D, Liu C L, et al.. Research progress of the application of ice surface sunken fascine mattress in revetment engineering in cold area[J]. Journal of Engineering of Heilongjiang University, 2018, 9(1):17-26.
[20]Xu G S. Ice picking: the "wealth effect" created by ice scenes[N]. Harbin Daily, 2011-01-05(1).

25th IAHR International Symposium on Ice
Trondheim, 23-25 November 2020

Observations of anchor-ice in a Canadian river using photographic and acoustic devices

Tadros R. Ghobrial[1], Sean Boyd[2], and Mark R. Loewen[2]

[1] *Department of Civil and Water Engineering*
Laval University, Québec, Qc, Canada

[2] *Dept. of Civil and Environmental Engineering*
University of Alberta, Edmonton, AB, Canada

tadros.ghobrial@gci.ulaval.ca , *srboyd@ualberta.ca*, *mrloewen@ualberta.ca*

Anchor ice can alter river hydraulics, affect fish habitat, reduce hydropower generation, and change the sediment budget of northern rivers. Although detailed laboratory experiments have been conducted to study anchor ice, much fewer field observations of anchor ice processes that have been reported. In this study, a field measurement program was undertaken to monitor anchor ice formation and release on the North Saskatchewan River in Edmonton, Alberta during freeze-up in 2019. The monitoring program included the deployment of a custom-built imaging system (camera and lighting), precision water temperature loggers, depth sensors, an upward looking sonar, Acoustic Doppler Velocimeter (ADV), and an acceleration and tilt sensor. Preliminary results showed that anchor ice formation and release can be reliably detected by the upward looking sonar, the ADV and the accelerometer. In addition to the formation and release of anchor ice, the underwater camera system was able to detect the growth rate of anchor ice.

1. Introduction

The formation of anchor ice occurs every winter on many northern rivers, and can alter river hydraulics, affect fish habitat, reduce hydropower generation, and change the sediment budget (Tsang, 1982; Beltaos, 2013). In order to mitigate the effects of anchor ice, we need to better understand the physical processes controlling its formation, growth and release in rivers. Although detailed laboratory experiments have been conducted to study anchor ice (e.g. Kerr et al., 2002; Doering et al., 2001), there are very few field observations of anchor ice processes that have been reported (e.g. Hirayama et al., 1997; Kempema et al., 2008). Previous field studies have relied on either direct sampling of anchor ice accumulations from the river bed, or qualitative observations of its formation and release. The main reason for a lack of quantitative field measurements is likely the harsh and challenging field conditions under which anchor ice forms.

This study explores the capabilities of different underwater acoustic instruments and sensors to detect the formation, growth and release of anchor ice. These sensors include: An Acoustic Doppler Velocimeter (ADV), an upward looking Shallow Water Ice Profiler Sonar (SWIPS), an accelerometer, temperature sensor, and a pressure sensor. In addition to these instruments, a custom-built imaging system (camera and lighting) was also deployed. Results from an earlier study (Ghobrial and Loewen, 2020) showed that the underwater camera system was able to detect anchor ice formation, growth and release. Therefore, images from the underwater camera were used (when available) to visually validate anchor ice effects on the data collected from the acoustics instruments and sensors. Also, an onshore trail camera was mounted on a nearby tree to take time lapse photographs of the surface ice conditions. This paper describes the field setup and presents preliminary results from this field study.

2. Instrumentations and Methods

Measurements of anchor ice were conducted on the North Saskatchewan River in the City of Edmonton at the Quesnell Bridge (53° 30′ 20″ N 113° 33′ 60″ W) during freeze-up October to December of 2019. The river in this reach has a slope of ~ 0.0002 and a width of ~ 200 m. The water depth ranges between ~ 0.6 m near the banks to ~ 3.0 m at the thalweg. Three instrumentation platforms were deployed on the river bed between the right (south) bank and the first bridge pier (at a depth of ~ 0.6 m) as shown in Figure 1a. The first platform (Platform 1) was fixed to the river bed early in the season before ice appeared in the river and housed an RBR SoloT (accuracy ±0.002°C) temperature logger and a Van Essen Micro-Diver (accuracy ±1 cmH2O) water level logger (Figure 1b) sampling every 1 and 5 min, respectively. The temperature data were used to identify supercooling events and correlate it with anchor ice appearance. The water depth data were used to investigate the effect of hydropeaking on anchor ice formation as well as documenting the stage up of the river leading to stable ice cover formation. On October 15th, Platform 1 was anchored on the river bed approximately 15 m from the shore at a water depth of 0.60 m. The platform was removed from the river immediately before the ice front reached the study reach on Dec 5th.

A 6 MHz field ADV (Vector, Nortek USA) and a 545 kHz SWIPS (ASL Environmental Inc.) were mounted on the second platform (Platform 2) as shown in Figure 1c. The ADV is a high-accuracy single-point current meter that is capable of acquiring 3D velocity and small-scale turbulence measurements. The ADV was programmed to sample velocity data at a frequency of 1 Hz at a point approximately 15 cm from the bed. The SWIPS is an upward looking sonar developed for ice thickness measurements (ice draft) in shallow water. It has been shown to be capable of detecting anchor ice and suspended frazil ice (e.g. Jasek and

Marko, 2007; Ghobrial et al., 2013) in rivers. The sonar returns from the SWIPS are recorded on a 16-bit board i.e., based on the strength of the return from insonified targets, the recorded counts range from 0 (no target) to 65,535 (full return) counts. More information on the SWIPS can be found in Ghobrial et al. (2013). The SWIPS was programmed to sample at 1 Hz and the data were processed and plotted in a 2D time series plot of profiles with color coded strength of the return signal. Sonar signals were used to identify the presence of anchor ice, suspended frazil ice as well surface pans. The ADV was powered internally but the SWIPS was powered by a 100 m long cable laid out along the river bed and connected to a Subaru R1700i gas generator secured on the river bank.

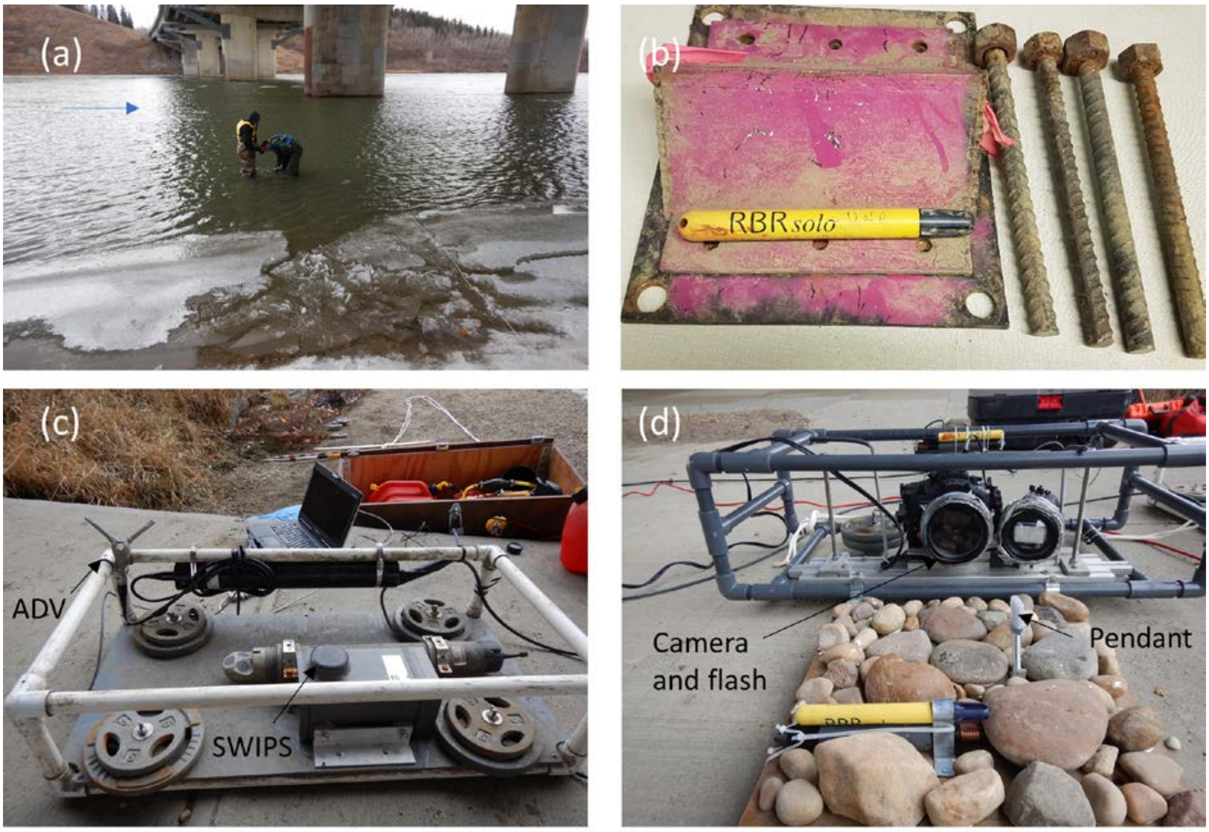

Figure 1. Images of the study site and instrumentation during freeze-up in 2019: (a) deployment location flow from left to right, (b) Platform 1, (c) Platform 2, and (d) Platform 3.

Platform 3 consisted of a custom-built underwater camera and lighting system. An artificial substrate was built using gravel/cobbles gathered from the river bed at this same location. It was bolted to the imaging system frame as shown in Figure 1d. In order to prevent frazil and anchor ice from forming on the camera and flash lenses, a heat trace cable was wrapped around the lenses casings and connected to the generator on the river bank. The underwater camera was programmed to take a photograph each 5 min of anchor ice accumulation on the artificial substrate. This sampling frequency resulted in a camera battery life of ~24 hours. Therefore, the research team visited the site once a day during each deployment to replace the camera batteries and fill-up the generator gas tank. It is important to note that during this freeze-up season, water levels were significantly higher than normal which resulted in increased turbidity in the water. As a result, the clarity of the underwater photographs was reduced and we were only able to determine the extent of the anchor ice formation above the substrate but could not discern any detailed features. Figure 2 presents examples of two underwater photographs taken by the camera with and without anchor ice accumulation. The images were processed in two stages. First, the images were enhanced to improve clarity using image processing software (BatchPhoto Pro ®). Second, the enhanced images were imported into MATLAB and the top of anchor ice accumulation thickness was manually tracked and scaled as a function of time using the image processing toolbox. Details of the image processing used in the analysis can be found in Ghobrial and Loewen (2020).

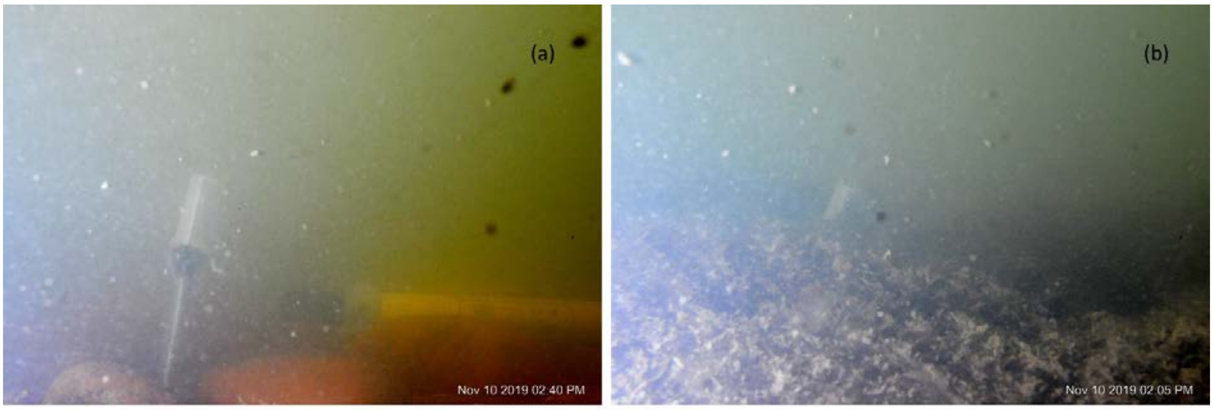

Figure 2. Example images taken with the underwater camera system. (a) No anchor ice is visible but the substrate, Pendant and RBR temperature logger are visible. (b) Anchor ice accumulation is visible.

In addition to the camera and lighting, Platform 3 had a HOBO Pendant G acceleration and tilt data Logger (Onset ®) that was bolted to a 2-inch spring that was fastened vertically on the substrate, so that it protruded into the flow and was visible in the camera field of view (Figure 1d and 2a). The pendant accelerometer was programmed to sample the acceleration (and therefore movement of the sensor) in 3 directions at 1 min intervals. The premise was to use the acceleration data as an indicator of anchor ice presence. If the sensor is covered with anchor ice, then we would expect a fixed tilt and acceleration value during the time the sensor is covered with ice. If the sensor was free to vibrate due to flow, then the acceleration signal would continually fluctuate. Platforms 2 and 3 were removed from the river bed after each deployment.

On the shore, a trail camera (Reconyx HyperFire PC800) was mounted on a nearby tree and programmed to take images of surface ice conditions every 15 min. Images from the trail camera were used to understand freeze-up processes and identify different surface ice conditions during anchor ice events. Meteorological data was downloaded from the Alberta Climate Information Service (ACIS) website. The closest weather station (approximately 2.0 km southeast of the study site) was the “Edmonton South Campus UA” station (Climate ID 3012220) which provides hourly weather data for the air temperature, solar radiation, wind speed and direction, rainfall/snowfall depth and relative humidity.

During the freeze-up season, the weather forecast was monitored and the dates of the instrumentation deployments were determined based on when supercooling events were expected to occur and the availability of the research team. Platforms 2 and 3 were deployed concurrently two times during the 2019 freeze-up season at the study site. The first deployment was from Nov 4th to Nov 13th and the second deployment was from Nov 22nd to Dec 1st. During the second deployment, the instrumentation experienced several malfunctions due to power failures as well as the formation of a local ice jam atop the platforms which damaged some of the instrumentation and therefore no meaningful data were collected during this period. Only data collected during the first deployment with Platform 2 and 3 (between November 4th and 13th) are presented in this paper.

3. Results and Discussion

Figure 3 presents time series of the air and water temperatures and the water depth measured at the study site from 14-Oct-2019 to 9-Dec-2019. Between October 14th and 25th, the air temperature fluctuated between ~ 14°C and 0°C, dropped below 0°C starting on the 25th and reached -12°C on Oct 29th. During this time period, the water temperature gradually decreased until the first supercooling event occurred on Oct 29th. After this, the air temperature fluctuated between 10°C and -20°C for the rest of the season and the first ice pans were observed on Nov 6th. The water depth at the deployment locations fluctuated between 0.6 and 1.0 m following a diurnal hydro-peaking cycle for most of freeze-up season. The surface concentration of ice pans varied during the season and eventually increased until a temporary bridging of the river occurred at the study site on Dec 1st, when the water level staged up to a depth of 2 m. On Dec 4th at 15:00, the water levels peaked to 3 m in about 30 min. and then suddenly released producing a brief ice jam release wave that was recorded by the Water Survey of Canada hydrometric station (North Saskatchewan River at Edmonton gauge #05DF001) located approximately 10.7 km downstream of the study site. The majority of the river channel was clear of ice after the jam release, but the section of the river between the right bank and the first bridge pier (where the instruments were deployed) remained ice covered for the rest of the season. A complete ice cover was observed forming over the rest of the cross-section on Dec 14th, 2019.

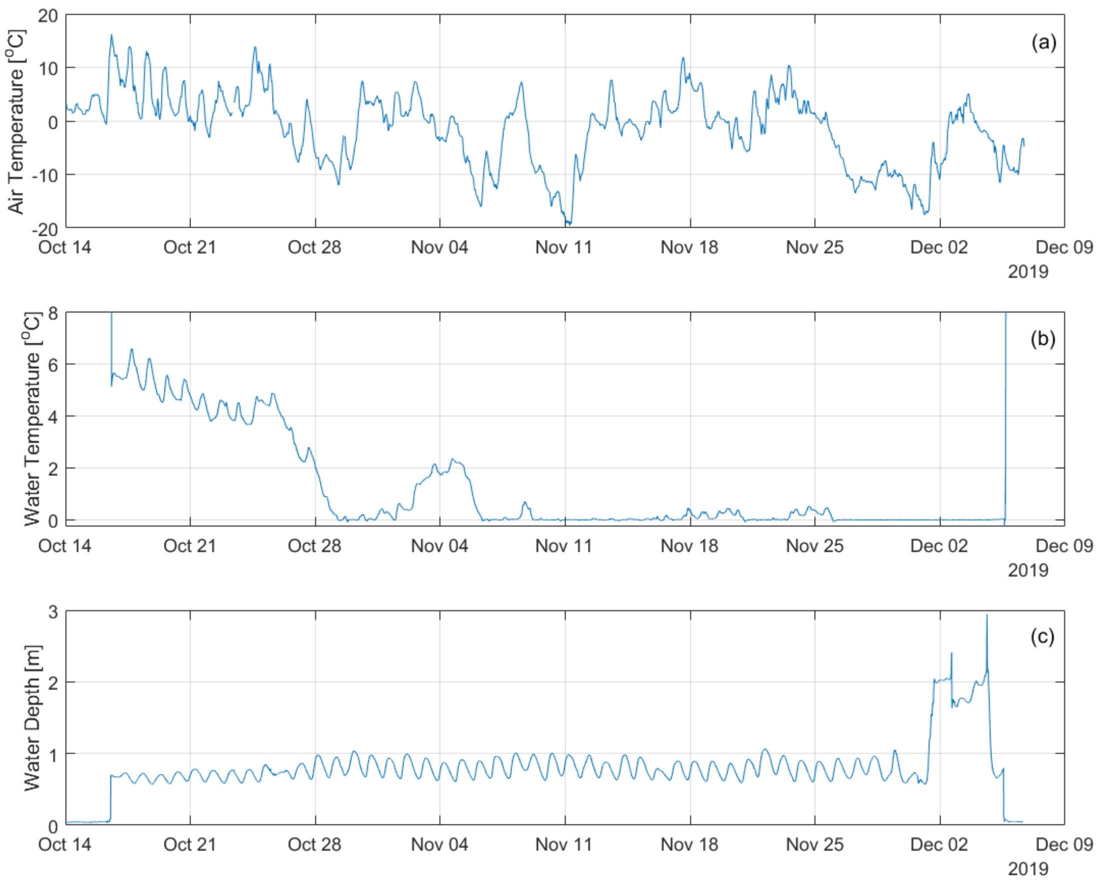

Figure 3. Time series of the (a) air temperature, (b) water temperature and (c) water depth during the 2019 freeze-up season on the North Saskatchewan River in Edmonton.

Two anchor ice events were observed during the first deployment: Event#1 on 6-7 Nov, and Event#2 between 10-12 Nov. Figures 4 and 5 present time series of air temperature, solar radiation, water temperature, sonar signal, water velocity, and local acceleration for Event#1 and Event#2, respectively. Note that the discontinuity of the data in the sonar signal (Figure 4d and 5d) was due to power failures. Platform 3 which had the pendant and camera was removed from the river on Nov 11th (See Figure 5f). Figure 6 presents the growth of anchor ice thickness as measured from the underwater photographs during both events.

As shown in Figure 4b, during Event#1, the water temperature was above 0°C on Nov 4th and 5th, and then it became supercooled at ~8:00 on Nov 6th and stayed supercooled for 28 hours until 12:00 on Nov 7th reaching a minimum of ~ -0.05°C. Evidence of anchor ice accumulation on the sonar transducer can clearly be observed in Figure 4d (as saturation of the signal near the bed) starting from 20:00 on Nov 6th and the signal indicates it released at ~12:30 on Nov 7th after a duration of 16.5 hours. The water velocity above the platform consistently varied between 0.50 to 0.75 m/s as the water depth varied from ~0.60 to 1.0 m due to the hydro-peaking cycle (Figure 4e). At the same time as anchor ice was accumulating on the sonar, the ADV signal was corrupted indicating that anchor ice was simultaneously accumulating on its transducers. Examining the acceleration signal from the Pendant (Figure 4f), it is also clear that the sensor signal was fixed at a constant value during approximately the same time period of anchor ice formation on the acoustic instruments, which is an indicator that the sensor was not free to move. It is interesting to note that anchor ice started to form immediately after the solar radiation reached zero although the water started to supercool earlier in the day. But anchor ice release did not coincide with the increase in solar radiation, but rather with the warming of the water above zero at about 12:30 on Nov 7th. The anchor ice thickness measured by the camera (Platform 3) in Figure 6a show that anchor ice started to form at 18:00 on Nov 6th and released at 12:30 on Nov 7th, a duration of 18 hours. The total anchor ice thickness was 12 cm with an approximate linear rate of growth of about 0.7 cm/hr. One interesting finding can be noted when comparing the thickness of anchor ice from the camera of 12 cm at the end of the event with the sonar signal saturation depth of 0.6 m seen in Figure 4d. Assuming the same thickness, density and composition of anchor ice accumulation did form above both the sonar transducer and the substrate, the sound speed to be used by the sonar to estimate the thickness of the anchor ice accumulation has to be ~ 5 times smaller than the sound speed in water at ~0°C. Lab slush experiments conducted by Ghobrial (2012) estimated sound speed in porous slush (formed of flocculating frazil particles) of about 1200 m/s, which is only 0.85 of the sound speed in water at zero degree. Therefore, more research is needed to investigate the effect of air bubbles, sediment, and internal composition of anchor ice on the sonar sound speed.

During Event#2, there were several cycles of daily supercooling that began at ~ 18:00 and ended the next day at ~ 12:00 (Figure 5b). Although there were multiple power failures of the SWIPS resulting in some discontinuity in the sonar data, it is clear that the sonar transducer was covered with anchor ice (indicated by the saturation of the signal near the bed) starting sometime on Nov 11th until 13:00 on Nov 12th (Figure 5d). The ADV velocity data in Figure 5e shows that the signal was continually corrupted (similar to Event#1) from ~20:30 on Nov 9th until 13:00 on Nov 12th. Note that before and after anchor ice formation on the probe, the flow velocity and depth are very similar to the values observed during Event#1. It was not possible to detect a clear signature of anchor ice formation or release in the Pendant acceleration time series in Figure 5f. Anchor ice formation and release on the substrate was observed in the underwater photographs from 3:00 until 14:00 on Nov 10th (Figure 6b). Before the release of anchor ice, the total thickness was 12.5 cm with a growth rate of 1.0

cm/hr. It is important to note that after this period the camera experienced some programming issues and was not collecting images. In both cases of anchor ice formation detected by the sonar, ADV, and camera, the release of anchor ice coincided with the warming of the water to above 0°C.

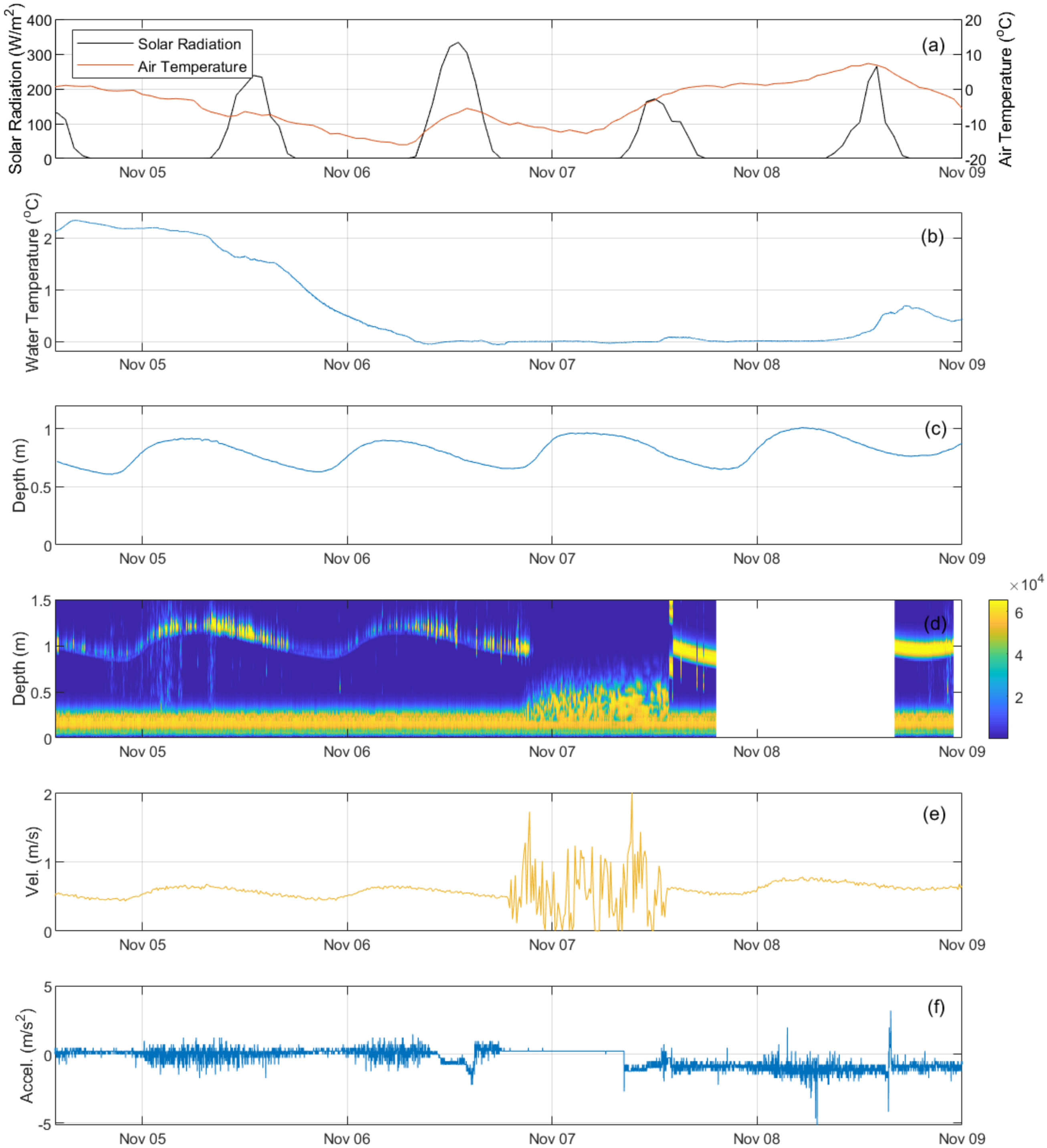

Figure 4. Time series of measurements during anchor ice Event#1; (a) air temperature and solar radiation, (b) water temperature, (c) water depth, (d) 2D SWIPS counts, (e) ADV absolute velocity, and (f) Pendant acceleration.

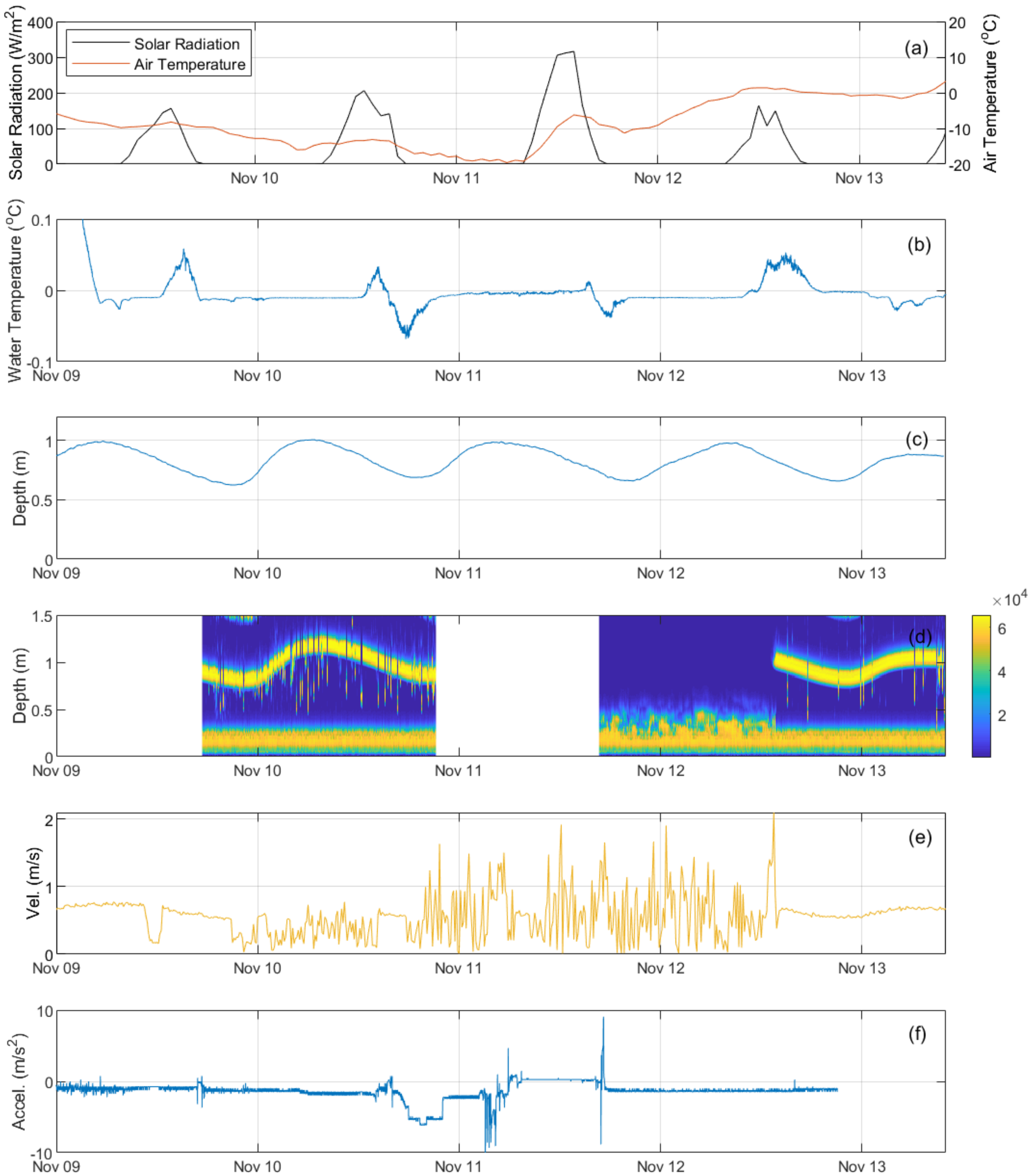

Figure 5. Time series of measurements for anchor ice Event#2; (a) air temperature and solar radiation, (b) water temperature, (c) water depth, (d) 2D SWIPS counts, (e) ADV absolute velocity, and (f) Pendant acceleration.

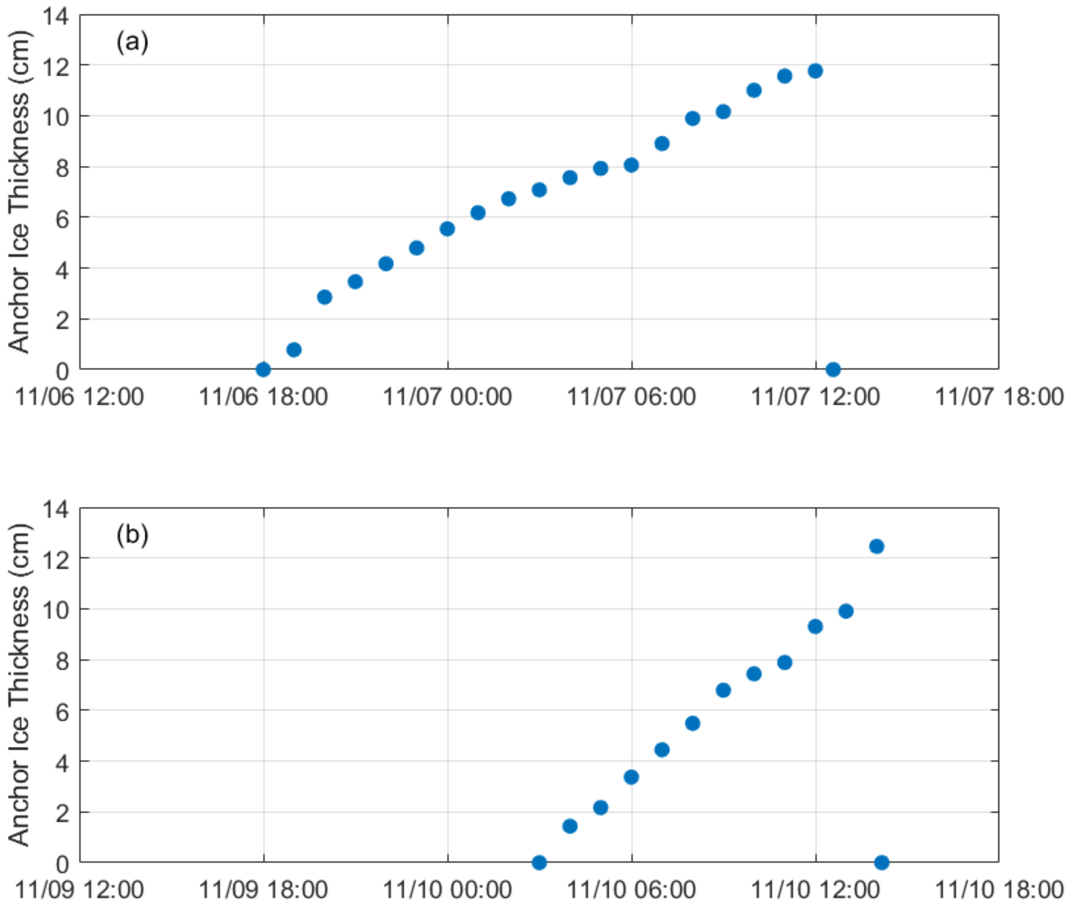

Figure 6. Time series of anchor ice thickness above the substrate as estimated from the underwater photographs during the 2019 freeze-up season for (a) Event#1 and (b) Event#2.

4. Conclusions

The duration and timing of anchor ice formation and release can be effectively detected using upward looking sonars and field velocity Doppler profilers. The Pendant, which is much cheaper and relatively easier to deploy than the acoustic instruments, was successful in detecting anchor ice formation and release during Event#1, but during Event#2 it was not clear how anchor ice formation affected the signal. More research is needed to investigate its performance. Results from the underwater camera confirmed the ability of the camera and lighting system to track the thickness and the rate of growth of anchor ice formations. The growth rates of anchor ice ranged between 0.7 and 1.0 cm/hr which is in agreement with previous measurements reported by Ghobrial and Loewen (2020). Due to the high turbidity in the water, the clarity of the photographs did not allow for distinguishing between the different mechanisms of anchor ice formation (i.e. crystal growth versus frazil deposition). Formation of anchor ice events appeared to start when solar radiation is 0 W/m^2 and the release of anchor ice coincided with the end of supercooling of the water.

Acknowledgments

This research was supported by the Natural Sciences and Engineering Research Council of Canada (NSERC) (RGPIN-2015-04670 and RGPAS 477890-2015). We would like to thank Perry Fedun for technical assistance with the project.

References

Beltaos, S., 2013. River Ice Formation. 1st edition, Committee on River Ice Processes and the Environment, Edmonton, AB, 2013.

Doering, J., Bekeris, L., Morris, M., Dow, K., Girling, W., 2001. Laboratory study of anchor ice growth. J. Cold Reg. Eng. 15, 60–66.

Ghobrial, T.R., 2012. Characterization of Suspended Frazil and Surface Ice in Rivers Using Sonars. PhD thesis, University of Alberta.

Ghobrial, T.R., Loewen, M.R., Hicks, F.E., 2013. Characterizing suspended frazil ice in rivers using upward looking sonars. Cold Regions Science and Technology 86 (2013) 113–126

Ghobrial, T.R. and Loewen, M. R., 2020. Continuous in situ measurements of anchor ice formation, growth and release. The Cryosphere Discuss., https://doi.org/10.5194/tc-2020-161, Accepted, 2020.

Hirayama, K., Terada, K., Sato, M., Hirayama, K., Sasamoto, M., Yamazaki, M., 1997. Field measurements of anchor and frazil ice. Proceedings of the 9th Workshop on the Hydraulics of Ice-Covered Rivers, Fredericton, NB.

Jasek, M., Marko, J., 2007. Instrument for Detecting Suspended and Surface Ice Runs in Rivers. Proceedings of the 14th Workshop on the Hydraulics of Ice-Covered Rivers, Quebec City, June 19 - 22, 2007.

Kempema, E., Ettema, R., McGee, B., 2008. Insights from anchor ice formation in the Laramie River, Wyoming. Proceedings of the 19th International Symposium on Ice, (Vancouver, BC).

Kerr, D.J., Shen, H.T., Daly, S.F., 2002. Evolution and hydraulic resistance of anchor ice on gravel bed. Cold Reg. Sci. Technol. 35, 101–114.

Tsang, G., 1982. Frazil and Anchor Ice - A Monograph. National Research Council of Canada, Associate Committee on Hydrology Subcommittee on Hydraulics of Ice-Covered Rivers, Ottawa.

25th IAHR International Symposium on Ice
Trondheim, June 14 to 18, 2020

Study on the occurrence factors of anchor ice in observation of actual rivers

Hashiba M [1] , Yoshikawa Y [2] , Yokoyama H [3] , Haga S [1]
1 Fukuda Hydrologic Centre
Sapporo/Kita-ku/N24W15 Hokkaido, Japan
hashiba@f-suimon.co.jp
s-haga@f-suimon.co.jp
2 Kitami institute of technology
Kitami/Koen-cho/165 Hokkaido, Japan
yoshi@mail.kitami-it.ac.jp
3 Civil Engineering Research Institute for Cold Region
Sapporo/Toyohira-ku/1-jyo,3-cho-me Hokkaido, Japan
yokoyama-h22ab@ceri.go.jp

In order to study the occurrence and release of anchor ice, we conducted continuous observations for about a week in three different actual rivers (the Yubetsu River, Nayoro River, and Bebetsu River). These rivers were the depth of about 0.3-0.4 m, and the Froude number was at Fr> 0.2; shear stress in anchor ice was 0.08 on average. The observation system has the following equipment installed into the water. 1) Time-lapse camera with LED light on the riverbed. 2) Precision water thermometer (resolution ±0.001degree). 3) The precision thermometer was embedded in the stone on the riverbed. 4) Underwater illuminance. Anchor ice occurred from the gaps between the stones and spread for the whole of the river bed. It was shown that the water temperature and riverbed stone temperature of the river bed decreased simultaneously with the disappearance of solar radiation. 1) Occurrence; In Yubetsu River, the anchor ice occurred from 6:00 P.M. to 11:00 A.M. before noon, where the temperature dropped to around -20 degrees. The anchor ice occurred when the water temperature was supercooling, but the stone temperature on the riverbed was almost over 0 degrees. In the Nayoro river, it occurred from 6:00 P.M. to 9:00 A.M. in the morning, where the temperature dropped to around -10 degrees. The anchor ice occurred at the timing of both supercooling of the water temperature, and the riverbed stone temperature dropped below freezing. 2)Releasing; The peaks of solar radiation, water temperature, and stone temperature increased, the anchor ice released to delay by 3-4 hours after the riverbed stone temperature rose. Although the illuminance and riverbed stone temperature are directly and indirectly related to the occurrence and release of anchor ice, it can be assumed the water temperature is the largest factor.

1. Introduction

Anchor ice is initiated by frazil ice formation and spread on riverbed widely. It is known as a derivative of frazil ice growth. Previous studies reported the risk of ice jam floods and water intake disturbances caused by the occurrence of anchor ice or frazil ice. Steven F. Daly(2006) reported municipal water supply and thermal power plants drawing water from the Great Lakes face the problem of their water intakes becoming blocked by frazil ice formed in the lakes. Tremblay et al. (2013) observed that both surface and former anchor ice layers merged to form thick blocks of ice during multi-day cycles. It was suggested that this process might promote the size and frequency of ice jam formation. Anchor ice occurrence and growth depend on the effect of several factors associated with the thermal condition between air and water and river flow conditions. A study of the anchor ice occurrence factor is essential to prevent the ice jam disasters and to keep the intake waters. According to the previous studies, Shen et al. (1995) clarified the growth of anchor ice was caused by heat exchange between the frazil ice at the supercooling and the riverbed by the equation of anchor ice formation. Malenchak et al. (2006) constructed a numerical calculation model (CRISS 2 D) using Shen's equation. They clarified that the growth rate of anchor ice affected frazil ice concentration, flow velocity, and water depth. Bisaillon et al. (2007) were defined as the anchor ice occurrence factor was that the average flow velocity was fast, and the depth of water was shallow. Also, for the occurrence of anchor ice, the Froude number was needed above 0.22 on average and did not occur below 0.10. Suzuki et al. (2018) indicated the occurrence of anchor ice was related to the balance between riverbed temperature and water temperature. Ghobrial et al. (2019) succeeded in observing an average rate of crystal growth of anchor ice on an artificial substrate using a high-resolution underwater camera system. In this study, to elucidate the occurrence condition of anchor ice, we conducted a time series observation from the occurrence to release at three different rivers.

2. Field observation method

a) Field observation point and observation period

The site observation point and observation period are shown in Table 1. All sites are located in Hokkaido, Japan.

Table 1. Observed fields

No.	River	Observation period	Anchor ice occurrence	River width(m)	Average depth(m)
1	Yubetsu river	10 Jan.-14 Feb.2017.	○	50.0	0.4
		26 Feb.-28 Feb.2019.	×	50.0	0.4
2	Nayoro river	20 Feb.-26 Feb.2018.	○	30.0	0.4
3	Bebetsu river	7 Feb.-10 Feb.2020.	○	10.0	0.3

b) Observation method

The observation system has the following equipment installed into the water as shown in Figure 1.

1) Time-lapse camera with LED light with 12V battery all in the waterproof housing case on the riverbed. Time-lapse camera (Brinno TLC-200f1.2) capable of continuously acquiring image data of 640 × 480 pixels was installed, and photographing was performed at one-minute intervals.

2) Precision water thermometer (JFE Advantec. MDS-Mk V / T, resolution: 0.015 ° C, accuracy: ± 0.05 ° C)

3) The precision thermometer was embedded in the stone on the riverbed. (JFE Advantec.

MDS-Mk V / T, resolution: 0.015 ° C, accuracy: ± 0.05 ° C)
4) Underwater illuminance gauge. To acquire continuous weather data, a thermometer (MC accuracy: ± 0.15 ° C or less), a water temperature gauge, and a hydraulic pressure gauge Electrical Industry Co., Ltd. MC-1100, accuracy ≤ ± 0.1% FS) was installed on river bank and riverbed.
5) Image velocimetry camera (only for Bebetsu river). Hike inc manufactured Hyke-cam SP2, full HD video 1920×1080P, daytime for RGB and nighttime for NIR(Near Infrared), the power generation section used two solar panels of 195 W and made eight storage batteries of 12 V - 105 A / hr.
The image velocimetry method was used STIV(Space-Time Image Velocimetry). STIV utilizes a space-time image (STI) generated from time-change of brightness variation in a searching line set parallel to the main flow direction. In the case of STI, the horizontal axis shows the distance of the searching line, and the vertical axis shows elapsed time as shown in Figure 2. The gradient of the oblique line is the flow velocity as shown in Eq(1).

$$U = \frac{S_x}{S_t} \tan \emptyset \quad (1)$$

Where U [m/sec] is velocity, S_x [m/pixel] is the unit length scale of the line segment, S_t [sec/pixel] is unit scale of time axis, $\emptyset$ is angle of STI.

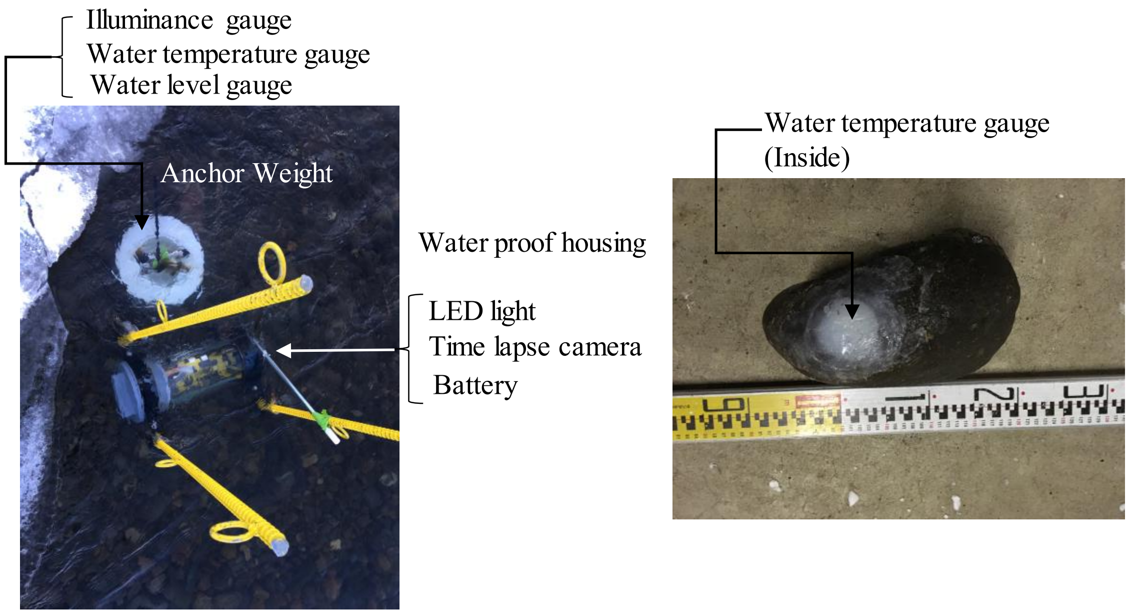

Figure 1. Observation device settings

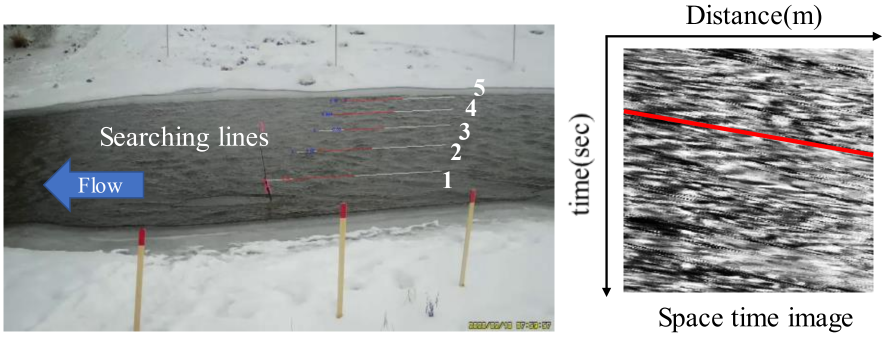

Figure 2. Method of STIV

3. Field observation result

a) Yubetsu River

Figure 3 shows the time series of observations. The anchor ice occurred from 6:00 p.m. to 11:00 before noon. When the water temperature dropped below zero degrees, at this time, the riverbed stone temperature also drops to the same extent. Although the water temperature recovered quickly to around zero degrees, the riverbed stone temperature was delayed to recover. During this super cooling condition, anchor ice continuously occurred. Also, since sunshine rose and the underwater illuminance increased, the temperature of the stone rose and becomes higher than the water temperature. At the same time, the anchor ice released. Figure 4 shows the results of time series observation for three days when the anchor ice did not occur. Air temperature at night was around -5 to -10 degrees, and water temperature and riverbed stone temperature were below zero degrees. Mainly, water temperature and riverbed stone temperature tended to fluctuate continuously. Figure 5 shows the situation of the anchor ice occurred. The air temperature tended to be down around -20 degrees. Although the riverbed stone temperature tended to fluctuate, the water temperature became constant around zero degrees, and it was kept the supercooling conditions about 12 hours. The anchor ice occurred during this supercooling period. As a result, it was found that the most necessary factor for the occurrence of anchor ice is a super cooling condition.

On the other hand, Shen et al. (1995) showed that as anchor ice is not filled the space between the bed particles, a channel of substrate flow will form in the pore space beneath the anchor ice. And he showed the bed heat flux might heat the water in the substrate and melt the anchor ice deposit from its underside. Near future, we considered it was possible to express a heat exchange of substrate flow using the time-series change between the water temperature and the riverbed stone temperature that could be observed.

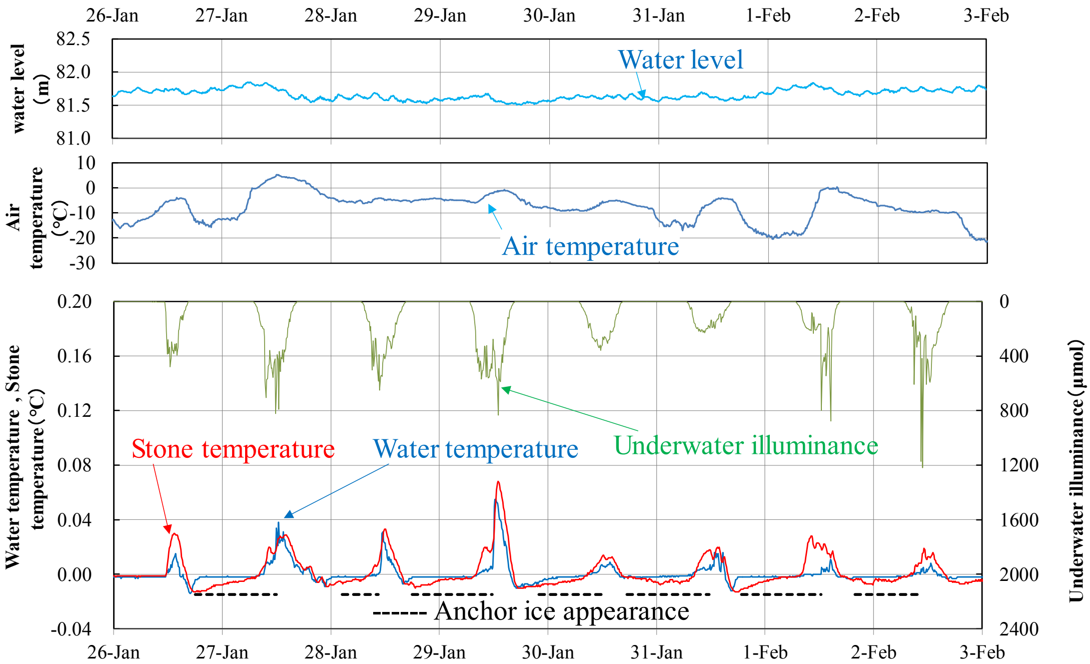

Figure 3. Time series observation in Yubetsu river,2017.

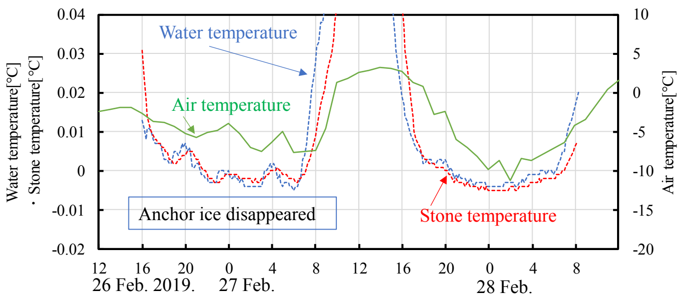

Figure 4. Time series observation at anchor ice released (in Yubetsu river,2019.)

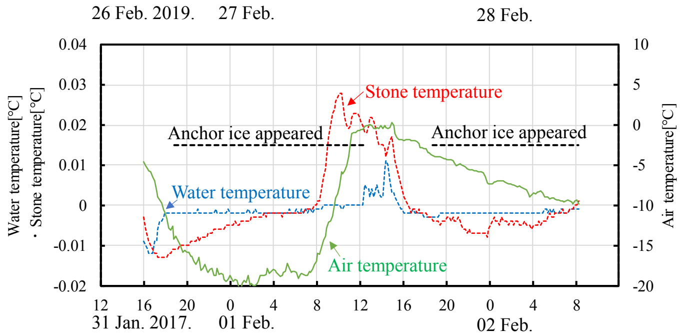

Figure 5. Time series observation in Nayoro river,2018.

b) Nayoro River

The anchor ice occurred from 6:00 p.m. to 9:00 in the morning, where the temperature dropped to around -10 degrees. The anchor ice occurred at the timing of both supercooling of the water temperature, and the riverbed stone temperature dropped below freezing. When this condition, which was in a super cooling occurred, anchor ice occurred and existed until the water and riverbed stone temperature rose with increasing solar radiation.

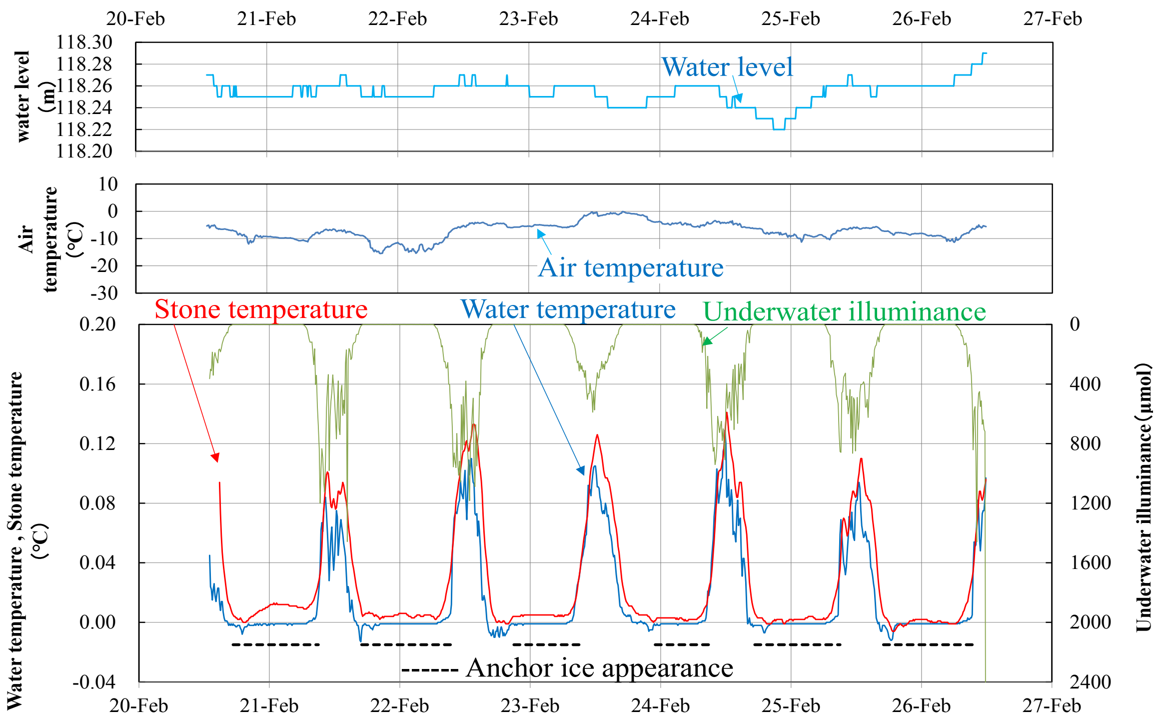

Figure 6. Time series observation at anchor ice appeared (in Nayoro river,2018.)

① When the illuminance reached underwater, and the ground temperature and water temperature were above plus degree, the anchor ice did not appear. It was shown that the water temperature and riverbed stone temperature decreased simultaneously with the disappearance of solar radiation. ②As the air temperature decreased, the water temperature became around zero degrees. Moreover, it was showed fluctuated slightly under zero degrees. However, at this time, the anchor ice had not appeared. ③When the water temperature kept on near-zero degree, and after that, the ground temperature stabilized around zero degrees, the anchor ice had appeared. Anchor ice occurred from the gaps between the stones and spread for the entire of the river bed. ④The water temperature and the ground temperature-stabilized around zero degrees during the anchor ice kept on appearance. At this time, the anchor ice grew up in thickness on the surface of the riverbed without separated by the flow. ⑤As the sun rose, the underwater illuminance increased. First, the ground temperature with low specific heat was increased. Then about 2 hours after, the water temperature with high specific heat began to increase. At this point, the anchor ice began to release. ⑥Anchor ice released when the water and ground temperature began to increase significantly. The anchor ice separated from the surface of riverbed stones and flowed away. At this time, anchor ice was seen running throughout the river. The peaks of solar radiation, water temperature, and stone temperature increased, the anchor ice released to delay by 3-4 hours after the riverbed stone temperature rose.

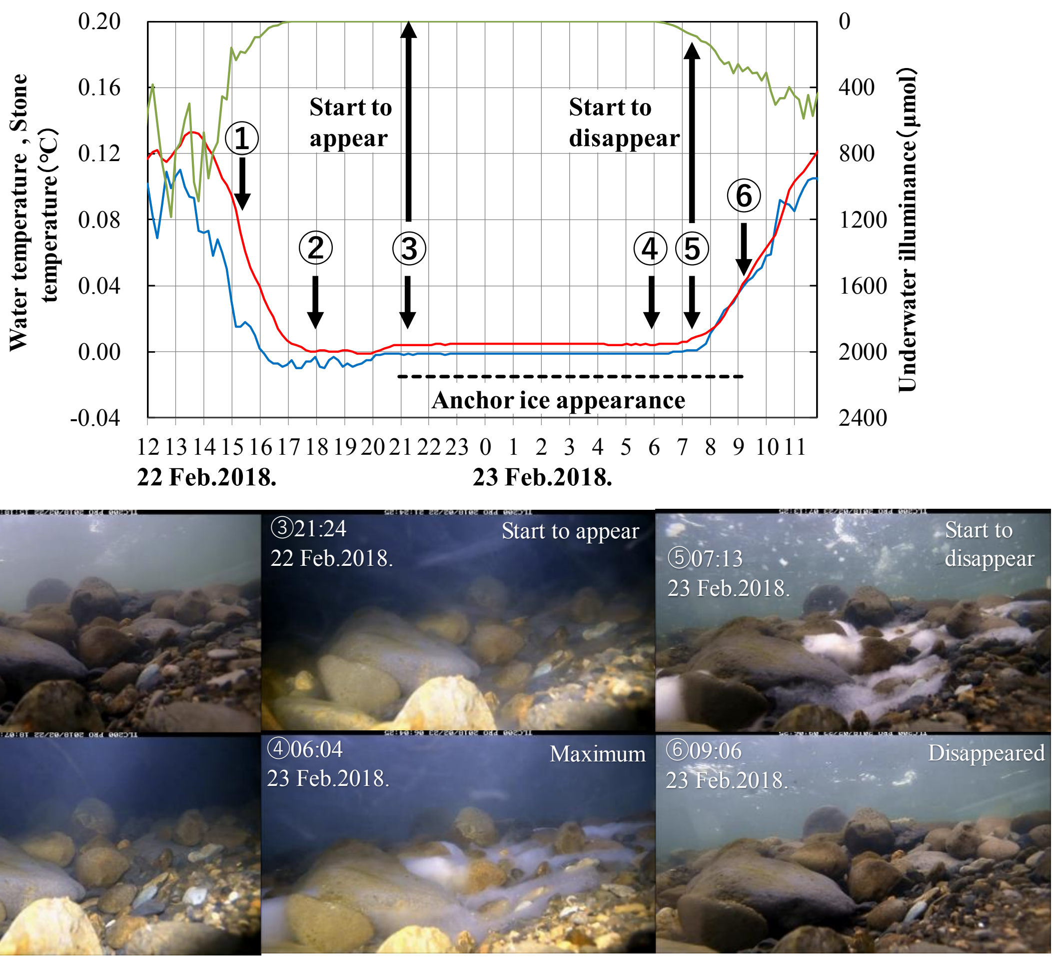

Figure 7. Feature of anchor ice occurrence and release (in Nayoro river,2018.)

c) Bebetsu River

The air temperature dropped nearly -30 degrees. Water temperature and riverbed stone temperature tended to be similar to the Yubetsu river, as shown in Figure 8. When the water temperature and the riverbed stone temperature also dropped to below zero degrees. Although the water temperature recovered quickly to around zero degrees, the riverbed stone temperature delayed recovering. During this super cooling condition, anchor ice continuously appeared. Also, when sunshine rose, and the underwater illuminance increased, the temperature of the stone rose and became higher than the water temperature. The reason why riverbed stone responded more strongly than water temperature was because the specific heat of stones was lower than waters, and the depth about 0.2m was shallow, which makes it more susceptible to air temperature and solar radiation. At 9 A.M., the anchor ice began to release from the riverbed. From 9 to 11 A.M., the debris of anchor ice flowed the whole surface of the river, as shown in Figure 10. Water level and discharge and stream velocity were not showed directly effect for anchor ice occurrence and release.

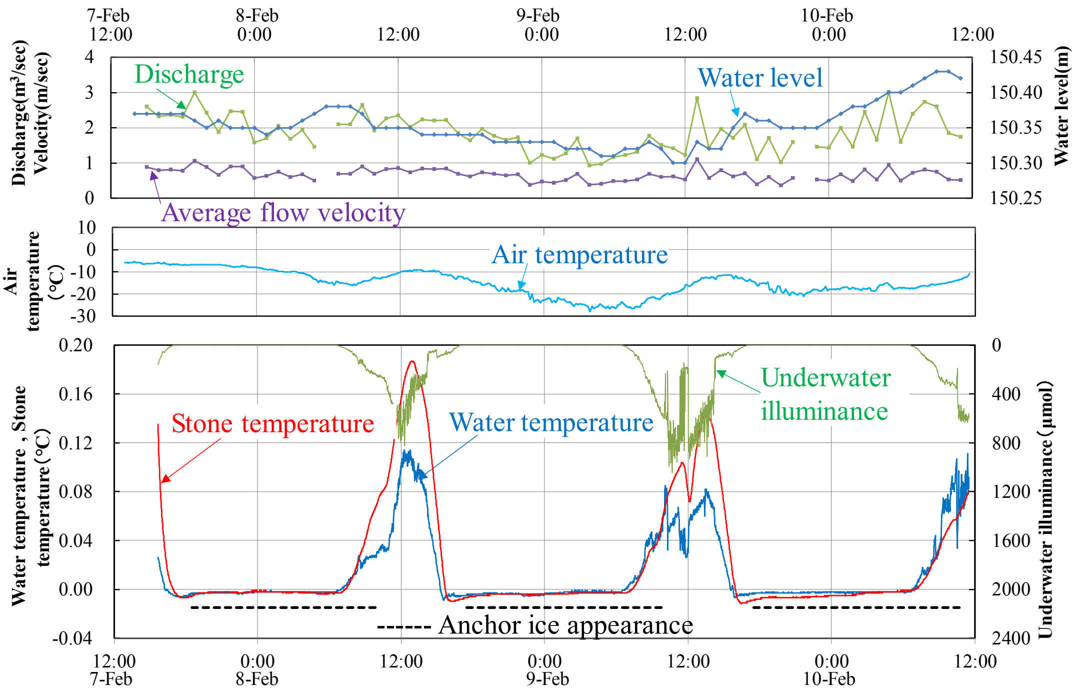

Figure 8. Time series observation in Bebetsu river,2020.

Figure 9. Debris of anchor ice releasing

4. Froude number and shear stress between anchor ice and stream flow

Figure 10 shows the anchor ice released in Bebetsu River. The searching lines from 1 to 5 were calculated the flow velocity by the STIV method. The anchor ice on the whole riverbed released from 9 A.M. to 11 A.M., and it removed in the transverse section from No.1 to No.5.

a) Froude number

Figure 11 shows the Froude number for each searching line calculated in time series. The observed Froude number was between 0.1 to 0.7, and the average is 0.32. Bisaillon et al. (2007) defined as the occurrence condition was that the average flow velocity was fast, and the depth of water was shallow. Also, the Froude number needed above 0.22 on average. If it was below 0.10, anchor ice did not occur. The results were consistent with these conditions, and it was showed that this river was conditions under which anchor ice appeared.

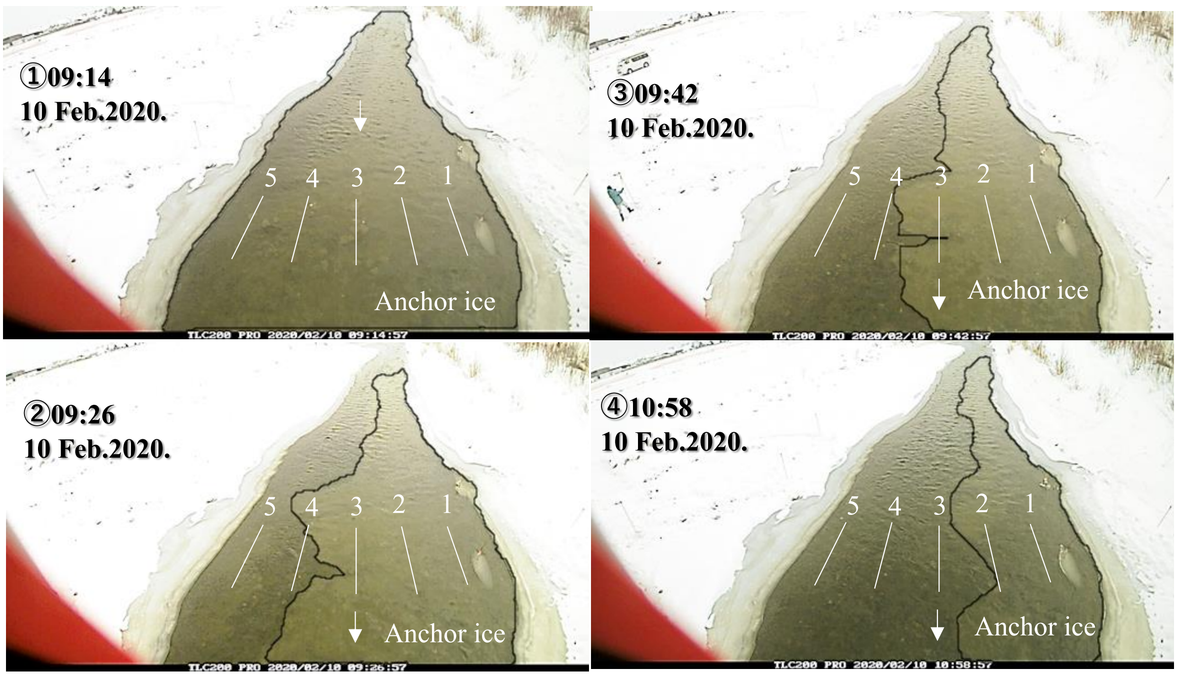

Figure 10. Anchor ice releasing

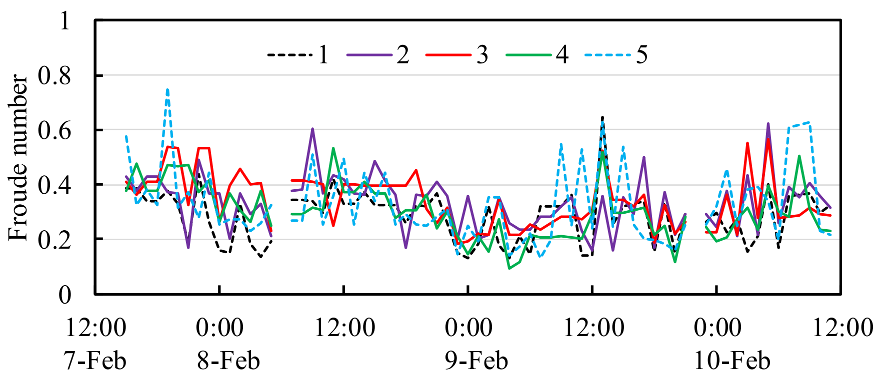

Figure 11. Froude number in Bebetsu river,2020.

b) Shear stress

Shen et al. (1995) proposed as follows; the critical shear velocity criterion introduced with the understanding that when the shear velocity is too small, the vertical mixing will not be strong enough to transport frazil ice to the bottom of the river. On the other hand, when the shear velocity is large, frazil particles will not be able to attach to the channel bottom. Therefore, we calculated the dimensionless shear stress from the shear velocity as Eq.(2) in time series for each searching line, as shown in Figure 12. The Manning equation obtained the energy gradient as Eq.(3). Dimensionless shear stress calculated as the same equation of sediment. In this case, we used the field observed average thickness of anchor ice instead of anchor ice particle (d) because it was hard to measure in the field the particle size(d) of the anchor ice.

$$u *= \sqrt{gRI_e} \tag{2}$$

Where $u*$[m/sec]=shear velocity; g=acceleration gravity;R[m]=hydraulic radius; I_e=energy gradient(calculated by Manning Eq.(3))

$$\bar{u} = \frac{1}{n} R^{\frac{2}{3}} I^{\frac{1}{2}} \tag{3}$$

Where u[m/sec]=velocity(observed by STIV method), R[m]= hydraulic radius(≒observed depth), n=roughness(≒0.035)

$$\tau *_{ice} = \frac{{u_*}^2}{(\sigma/\rho - 1)gd} \tag{4}$$

$\tau *_{ice}$=dimensionless shear stress of anchor ice ; $u*$[m/sec]=shear velocity; σ[g/m^3]=mass density of anchor ice particles(=0.8);ρ[g/m^3];mass density of water(=1.0) ;g=acceleration gravity;d[m]=size of anchor ice particle(anchor ice thickness=0.05)

The dimensionless shear stress in anchor ice was 0.07 on average in Figure 12. The dimensionless shear stress, of No. 1 where anchor ice was always present showed 0.29 at the maximum, 0.06 on average, and 0.04 with standard deviation. On the other hand, No.5 where the anchor ice was almost releasing showed 0.36 at the maximum, 0.08 on average, and 0.07 with standard deviation. The dimensionless shear stress of No. 1 where anchor ice was always present tended to be low and fluctuation range tended to be small and No.5 where anchor ice was easy to release tended to be higher and fluctuation range tended to be large.. As a result, it was suggested that the dimensionless shear stress was related to the release of the anchor ice. However, in this field study, it was not possible to clearly indicate the shear stress required for the release of anchor ice. Therefore, in the future work, it will be necessary to improve the accuracy of uncertain parameters such as the particle size of anchor ice.

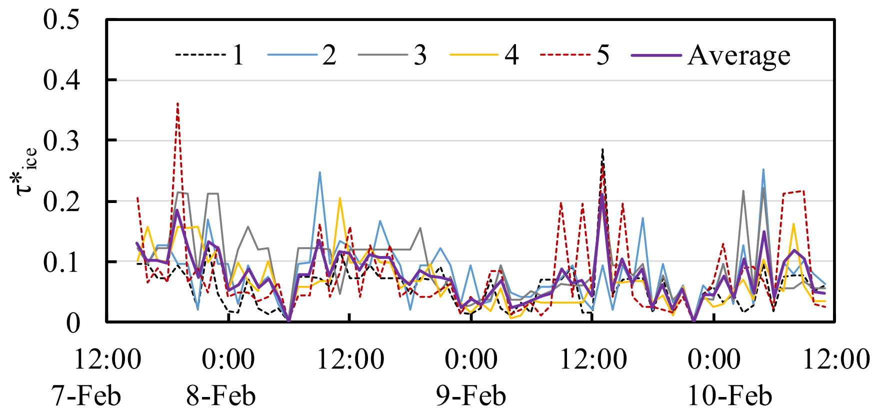

Figure 12. Time series change of shear stress in transverse section

5. Conclusions

- Although the illuminance and riverbed stone temperature are directly and indirectly related to the occurrence and release of anchor ice, it can be assumed that the water temperature is the largest factor. The anchor ice occurrence is keeping the stable condition of supercooling.
- It seems to be useful for the heat exchange between water temperature and riverbed stone temperature instead of substrate flow, which will form in the pore space beneath the anchor ice.
- The average Froude number in the Bebetsu river was 0.32 in the occurrence field of anchor ice. It was consistent with a previous study which needed over 0.22.
- Dimensionless shear stress in anchor ice was 0.07 on average; it was related to the release of the anchor ice. However, it could not be clearly indicate the shear stress required value for the release of anchor ice. So, it will be necessary to improve the accuracy of uncertain parameters near future.

Acknowledgments

We would like to express our gratitude to Asahikawa Development and Construction Department, Hokkaido Reginal Development Bureau for greatly help of field study.

References

Ashton.G.D.(1986):River and Lake Ice Engineering Colorado, USA,Water Resource Pubulication.

BisaillonJ.F.,Bergeron N.E.(2007) :Modelling anchor ice presence-absence in gravel bed streams，Proceedings of the 14th CRIPE Workshop on Hydraulics of Ice Coverd Rivers.

Fujita, I., Watanabe, H., Tsubaki, R. :Development of a non-intrusive and efficient flow monitoring technique : The space-time image Velocimetry (STIV), International Journal of River Basin Management 5(2):105-114,2007.

Malenchak J. ,Morris M.,Shen H.T. ,Doering J.(2006) :Modeling Anchor Ice Growth at Sundance Rapids, Proceedings of the 18thIAHR International Symposium on Ice.

Shen H.T. ,Wang D.S. ,WasanthaLal A.M.(1995) :Numerical Simulation of River Ice Processes，Journal of Cold Regions Engineering , ASCE9(3),107-118.

Suzuki.H.,Hashiba.M.,Yoshikawa.Y.,Yokoyama.H.(2018):Field study of anchor ice occurrence and disappearance and material circulation in cold regions river, 24th IAHR International Symposium on Ice.

Tadros R. Ghobrial, Vincent McFarlane and Mark R. Loewen(2019): In-situ measurements of anchor-ice formation andrelease, 20th Workshop on the Hydraulics of Ice Covered Rivers.

Tremnlay P., Leconte R., Lacey R.W.J., Bergeron N.(2013) :Anchor ice cycles :observations from field study on the Stoke River，CGU HS Committee on River Ice Processes and the Environment 17th Workshop on River Ice，pp.47-54．

25th IAHR International Symposium on Ice

Trondheim, 23 - 25 November 2020

A Modeling Study of Complex River Ice Processes in an Urban River

Rhodri Howley[1], Yuntong She[1], and Tadros Ghobrial[2]

[1]*Department of Civil and Environmental Engineering, University of Alberta*
7-203 Donadeo Innovation Centre for Engineering, Edmonton, Alberta, T6G 1H9

[2] *Department of Civil and Water Engineering, Laval University,*
Pavillon Adrien-Pouliot, 1065 av. de la Médecine, Québec, Qc, G1V 0A6

howley@ualberta.ca, yshe@ualberta.ca, tadros.ghobrial@gci.ulaval.ca

The winter regime of a northern river in an urban environment is often affected by many urban features such as municipal outfalls and bridges. The North Saskatchewan River (NSR) flowing through Edmonton, Alberta is one such example. Several previous studies on the NSR resulted in a relatively comprehensive database containing over a decade of ice related measurements. Analyses of these data have revealed several interesting and complex phenomena. The conditions at freeze-up are highly variable. Between the years 2009–2016, the degree days of freezing for the formation of a stable ice cover ranged between 50–130 °C·Days. The rate of ice front progression ranged between 3.7–8.6 km/day. The water level stage-up caused by the ice front passing a gauge station varied between 0.8–1.5 m, suggesting that both frontal progression through a juxtaposed mode and consolidation or shoving events can occur. There are multiple bridging locations within the study reach, which adds complexity to the freeze-up process. Urban outfalls including the Gold Bar Wastewater Treatment Plant (GBWTP) affects ice cover formation and can cause large open leads to form shortly after freeze-up. This study utilizes the University of Alberta's River1D Ice Process model to explore these complex river ice processes during the 2010-11 winter season. The 29 km reach that is simulated includes discharges from the GBWTP. Simulation results are compared to the water surface elevation, ice front progression, surface pan concentration, border ice fraction, ice thickness, suspended frazil concentration, and water temperature data measured at several locations along the reach.

1. Introduction

The ice regime of the North Saskatchewan River (NSR) through Edmonton is very complex (Howley et al. 2019). The NSR is a large, irregularly meandering river and is partially entrenched. Since the construction of the Brazeau and Bighorn dams in 1963 and 1972, respectively, the discharge of the NSR has been regulated and a mean winter discharge of approximately 120 m^3/s is observed (Total E&P Canada Ltd 2007). The river ice processes are significantly affected by the urban environment, several water intakes, urban outfalls and the Gold Bar Wastewater Treatment Plant (GBWTP) all situated within the study reach. The effluent from GBWTP causes an open lead to develop each year. Blockage of water intakes by frazil ice is known to be a recurring problem. The study site, shown in Figure 1, extends from Riverbend, Station 0 km, in the south-west of the city to Clover Bar, Station 28.84 km, in the east.

This study investigates the ice processes of the NSR using the University of Alberta's public domain River1D ice process model. To the best of the authors' knowledge, no previous river ice modeling study has focused on such an urban setting. Results from simulations of the 2010-11 freeze-up period are compared to the hydrodynamic and river ice data captured by Shallow Water Ice Profiling Sonar (SWIPS), Mini-Divers, cameras and a Water Survey of Canada (WSC) gauge.

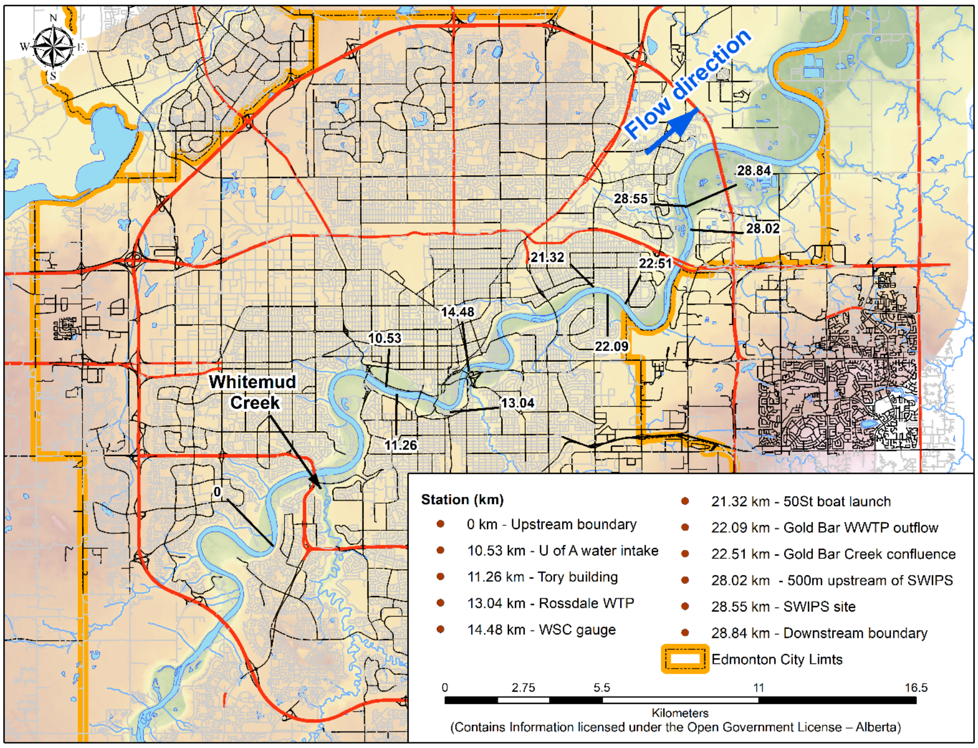

Figure 1. Map of the study reach; the North Saskatchewan River through Edmonton. [Image Source: Government of Alberta].

2. Model configuration

A detailed description of the River1D software used in this study, including the hydrodynamic and ice equations, is provided by Blackburn and She (2019). Since then the software has been enhanced with the capability to simulate multiple bridging locations which was used in this study. River geometry for the study site was originally collected in-house by Alberta

Environmental Protection in 1991 (IDG 1995). It was later converted to HEC-RAS format by NHC (2007). Additional cross-sections have been interpolated to provide a maximum cross-section spacing of 50 m. The simulation was conducted with a time-step of 18 seconds.

2.1 Boundary conditions

Discharge data were not available at the upstream boundary of the model domain but were available at the WSC gauge (Station 14.48 km). During the 2010-11 winter season, the WSC collected direct winter discharge measurements at Hawrelak Park footbridge, Station 6.87 km, on three occasions: (i) January 3rd 2011; (ii) February 1st 2011; and (iii) March 8th 2011. Winter discharge between these points and open water conditions was estimated using linear interpolation. Subsequently, a hydropeaking pattern was artificially created, maintaining a similar magnitude to what had been observed prior to the freeze-up period. The timing of peak and low flows was determined using water surface elevation data from the WSC gauge. This estimated winter discharge was shifted by wave travel time to the upstream boundary and its magnitude was adjusted to account for attenuation within the study reach.

Water temperature was recorded by resistance temperature detectors (RTDs) on a one-minute interval at the University of Alberta's chilled water systems intake, Station 10.53 km. Spikes in the dataset, caused by warm and pressurized backwater flushes, were removed. There is additional uncertainty in this data as the RTDs are inaccessible and are rarely calibrated. It is assumed that there is no diffusion or temperature change between the upstream boundary of the model and Station 10.53 km. As such, this water temperature was also shifted by wave travel time to the upstream boundary for use as a boundary condition. Hourly images captured by a game camera positioned at the upstream boundary were visually analyzed to generate an estimate of the surface ice flux. MATLAB image processing was used to binarize a sample of images and to validate the estimated surface ice flux. Incoming pan thickness data were not available at the upstream boundary. Estimates of the ice pan thickness were made using a weak relationship between the surface ice concentration and pan drafts, as measured by the SWIPS instrumentation at Station 28.55 km. The incoming suspended frazil flux was not measured and was assumed to be zero.

The lateral inflow from all tributaries, stormwater systems and combined sewage outfalls within the study reach was assumed to be negligible. As such, the only lateral inflow included in the model was from GBWTP at Station 22.09 km. Hourly data, which included the effluent discharge and the temperature, were provided by EPCOR Utilities Inc. who operate GBWTP.

The River1D model of the NSR was extended 10 km downstream of the study reach to allow a fixed water surface elevation to be used as a downstream boundary. A sensitivity analysis showed that the backwater effects caused by the downstream boundary is minimal within the study reach.

2.2 Meteorological and ice data

Air temperature was collected within the River Valley, on a 5-minute time-step, by a Campbell monitoring station at Station 28.55 km. Solar radiation data were collected on an hourly time step from the University of Alberta's climate station atop the EAS building, adjacent to Station 11.26 km. The depth of the river valley and the presence of coniferous trees along the south bank contribute to significant shading effects, especially in stretches of the river which flow from the west to the east. The model was divided into two atmospheric zones based upon channel orientation. A shading factor of 0.18 was applied to the solar radiation data in the shaded atmospheric zone. This shading factor was based on the first author's extensive experience of working in the river valley and on the NSR.

The timing and exact location of bridging events were not recorded in 2010. However, approximate bridging locations were identified from aerial photographs taken during a flight over the study reach on December 3rd, 2009 (Maxwell et al. 2011; Ghobrial et al. 2013). It is known that bridging typically occurs at the same locations each year (Beltaos 1995). The timing and location of bridging events was estimated based on the ice front progression as observed by game cameras installed at the upstream boundary and at Stations 11.26, 13.04, 21.56, 28.02, 28.55 and 28.84 km. The bridging events used in this study are given in Table 1.

Table 1. Location and timing of estimated bridging events.

Bridging location (km)	Time of bridging
39.35	18-Nov-2010 18:30
18.37	20-Nov-2010 16:00
14.01	20-Nov-2010 23:00

The data available for model calibration for the 2010-11 season is shown in Table 2. The ice front progression through the study reach was also observed by the cameras. It should be noted that both the SWIPS and the Mini-Divers measured depths. Depth measurements were combined with bathymetry data (Maxwell et al. 2011) and channel geometry to estimate water surface elevations. Estimates of surface ice concentrations and border ice fractions were generated by visual inspection of the available imagery. With exception of the WSC winter discharge measurements, all data were either averaged or interpolated to a 30-minute time-step.

Table 2. Summary of hydrodynamic and river ice data available for the NSR during the 2010-11 winter season.

Variable	Station (km)	Instrument	Time interval
Water surface elevation	14.48	WSC gauge	15 minutes
	21.32	Mini-Diver	15 minutes
	22.51	Mini-Diver	15 minutes
	28.02 - Left	Mini-Diver	15 minutes
	28.02 - Right	Mini-Diver	15 minutes
	28.55	SWIPS	1 second
	28.84	Mini-Diver	15 minutes
Water temperature	21.32	Mini-Diver	15 minutes
	22.51	Mini-Diver	15 minutes
	28.02	Mini-Diver	15 minutes
	28.55	SWIPS	1 second
	28.84	Mini-Diver	15 minutes
Surface ice concentration & border ice fractions	11.26	EAS Camera	Hourly
	13.04	Game Camera	Hourly
	21.56	Game Camera	Hourly
	28.02	Game Camera	Hourly
	28.55	SLR Camera	5 – 30 minutes
	28.55	SWIPS	1 minute
	28.84	Game Camera	Hourly
Pan draft/ Ice thickness	28.55	SWIPS	1 second
	6.87	WSC measurement	3 times throughout winter
Suspended frazil concentration	28.55	SWIPS	1 second

2.3 Model calibration

The model was first calibrated for open-water conditions by adjusting the Manning's roughness values of the channel bed for four regions within the model reach. The calibrated roughness values range from 0.030 - 0.034. This is a slight increase on the values used by NHC (2007) and IDG (1995) in their respective Flood Risk Mapping Studies. Open water simulation performance was assessed using data from Stations 14.48 km, 21.32 km, 22.51 km and 28.84 km. During the open water simulation period of October 13th to November 4th, 2010, the simulated water level remained within 0.06 m of the observed. This calibration tolerance was deemed acceptable given uncertainty relating to the datum of the depth recording equipment, two-dimensional flow effects and potential errors in measuring water levels.

Ice related parameters were adopted from Blackburn and She (2019), with several exceptions which are listed in Table 3. Parameter values were calibrated for the NSR so that simulated results best matched observed data. The value used in this study for new frazil pan thickness is lower than values previously used in the literature but is justified by the average pan draft of 0.14 m measured by the SWIPS instrumentation.

Table 3 Adopted values for ice modeling parameters (adapted from Blackburn & She 2019).

Parameter name	Adopted value	Values in literature
Albedo, α	0.15	0.05 – 0.15 (Hicks 2016)
Linear heat transfer coefficient, h_{wa} (W/m^2/°C)	14	8 – 20 (Andres 1988)
Linear heat transfer coefficient, h_{ia} (W/m^2/°C)	12	10 – 20 (Ashton 2011)
Rate of frazil rise (m/s)	0.001	0.0001 – 0.001 (Timalsina et at 2013)
Porosity of frazil slush	0.6	0.43 – 0.85 (Hicks 2016)
New frazil pan thickness (m)	0.14	0.3 (She et al. 2012)
Maximum fraction of channel covered by border ice	0.75	0.7 (Blackburn & She 2019)
Maximum velocity for dynamic border ice growth	0.8	0.4 – 1.2 (Lal and Shen 1991)
Max Froude number for ice front progression	0.13	0.08 - 0.13 (Ashton 1986)
Porosity between Ice floes at the ice front	0.6	0.6 (Jasek et al. 2011)

3. Results and discussion

Figure 2 shows a comparison of the simulated water temperatures with the observed. For Stations 10.53, 28.02, 28.55 and 28.84 km (two examples shown), the model performed exceptionally well, with r^2 values greater than 0.978 and RMSEs of between 0.15 – 0.45°C. Additionally, the model accurately captured the point of zero degree isotherm, at which water temperatures dropped to 0°C at these locations. The model also closely captured the trend of the observed water temperature at Station 21.32 km except when approaching 0°C. The observed water temperature was not recorded as having dropped as low as 0°C. The authors are not aware of any outfalls or other urban features which contribute warm water near this location. At Station 22.51 km, the observed water temperatures were collected towards the right bank of the river and within the effluent plume of GBWTP. The model should not be expected to perform well in this location where the water temperature is clearly two dimensional.

The simulated ice front progression is shown in Figure 3, along with the points at which the front was observed by the river-side cameras. The simulated ice front passed within 11.5 hours of the observed ice front at each of the observed data points. The average simulated progression through the study reach is 12.20 km/day. Progression of the ice front was most sensitive to the maximum Froude number for ice front progression and the frazil slush porosity. It was also determined that the surface ice flux and the incoming pan thicknesses included in the upstream boundary condition had a strong influence on the front progression through the study reach. It would be reasonable to expect some improvement in the timing of the simulated front propagation through the reach if the precise bridging locations and times had been recorded and more robust data were available for the upstream boundary condition. In the model, bridging at Station 14.01 km was delayed until 2.5 hours after the user defined bridging time. This is because the Froude number at this location exceeded the parameter value for the maximum Froude number for ice front progression until the downstream ice front approached.

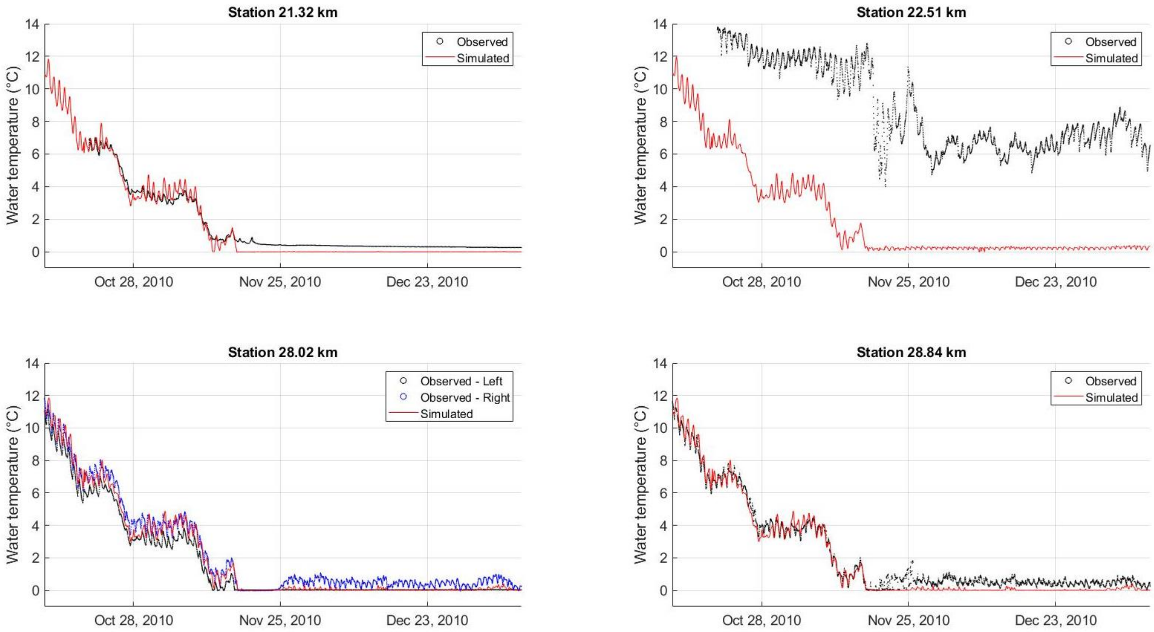

Figure 2. Comparison of simulated and observed water temperatures at Stations 21.32, 22.51, 28.02 and 28.84 km.

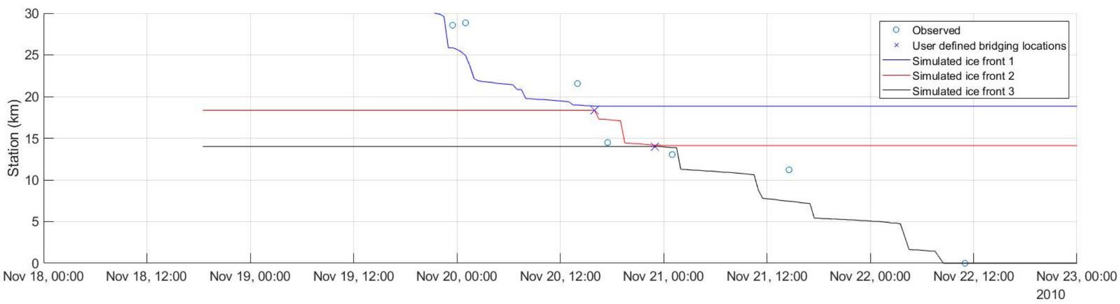

Figure 3. Observed and simulated ice front progression through the study reach.

Once the ice front progression had been simulated with a reasonable degree of accuracy, little calibration of the other parameters was required to achieve good agreement between simulated and observed values for the remaining variables. The rate of frazil rise was set as 0.001 m/s, leading to more reasonable simulated values for suspended frazil concentrations and minor improvements in the simulation of ice thicknesses and border ice fractions. Although the maximum fraction of border ice was set to 0.75, the simulated border ice did not grow to this extent anywhere within the study reach.

Simulated concentrations of suspended frazil ice were compared with the observed results collected by the SWIPS instrumentation at Station 28.55 km (Figure 4). During the freeze-up period, the simulated suspended frazil concentrations are of the correct order of magnitude when compared to the observed. The timing of the increases in suspended ice concentration is also very good; the first simulated peak on November 17th, 2010, begins to rise within an hour of the observed rise in suspended frazil concentration. Following freeze-up, the model returned a suspended frazil concentration of 0% for most of the simulation. However, small, isolated spikes of less than 0.01% suspended frazil concentration were simulated, for example on December 1st, 2010 and January 7th, 2011. These spikes coincided with open water conditions around Station 23.74 km and when air temperatures of -12°C or less were observed. The mid-winter spikes in simulated suspended frazil concentration did not always coincide with spikes in the observed suspended frazil concentration, likely because the model did not fully capture the formation of the GBWTP open lead.

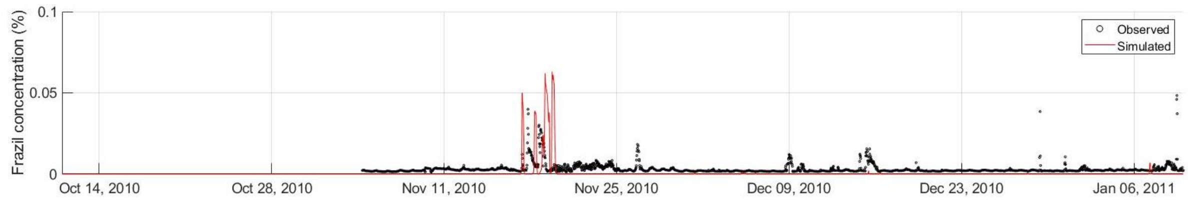

Figure 4. Simulated and observed suspended frazil concentrations at Station 28.55 km.

Figure 5 shows the observed ice thicknesses and the simulated frazil slush and solid ice thicknesses at Stations 6.87 and 28.55 km. The model performed well in simulating ice thicknesses at Station 6.87 km. A large and sudden increase in ice thickness was simulated on November 21st, 2010 and this coincided with the passing of the ice front. The simulated solid ice thickness trends in the right direction and is within 7 cm of the ice measured on January 3rd, 2011. Providing the rate of simulated solid ice growth were to continue at a similar rate, the simulated results should be within a reasonable tolerance of the observed WSC thicknesses. At Station 28.55 km, the simulated results can be compared with the draft measurements obtained by the SWIPS. There is good agreement in the timing of increased and decreased ice thicknesses, with both observed and simulated ice thicknesses climbing sharply on November 16th and decreasing between November 24th – 26th, 2010. Following this period, the model did simulate the growth and reduction of solid ice, but it was always significantly lower than the draft measurements obtained by the SWIPS. A sensitivity test was conducted to assess the influence of the GBWTP outflow on the ice thickness. When the GBWTP outflow was removed from the model, an ice thickness of 1 m was simulated at Station 28.55 km in January 2011. This confirms that although the model is not completely capturing the openings that appeared after the passing of the ice front, the outflow is influencing the simulated slush and solid ice thicknesses.

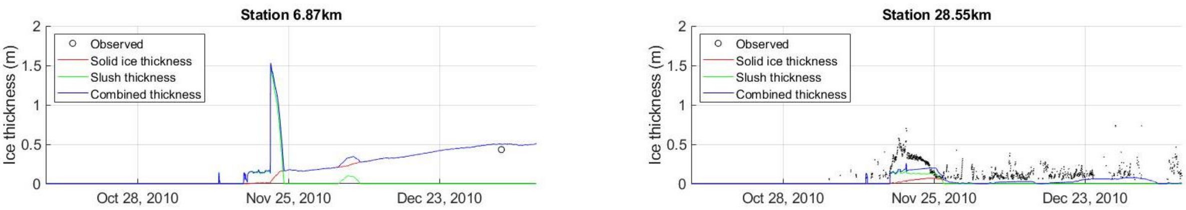

Figure 5. Observed and simulated ice thicknesses at Stations 6.87 km and 28.55 km.

Figure 6 presents the simulated and observed border ice fractions at Stations 13.4 and 21.56 km. There was a tendency for the model to underestimate the border ice fractions, especially at Stations 13.04, 21.56, 28.55 and 28.84 km. Border ice growth in the model did start at the correct time at all stations.

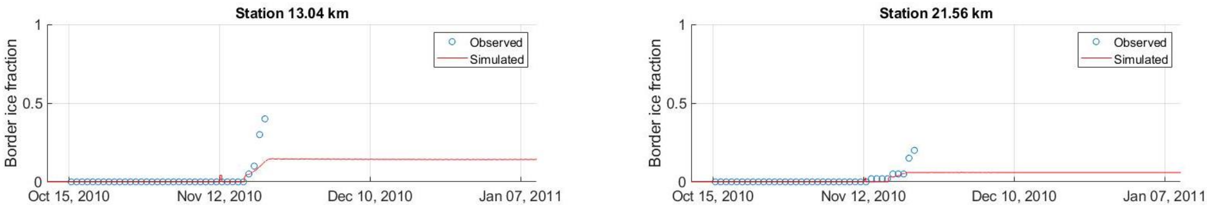

Figure 6. Observed and simulated border ice fractions at Stations 13.04 and 21.56 km.

Figure 7 shows the observed and simulated surface pan concentrations. The simulated results correspond well with the observed and follow the general trend of increasing surface ice concentration. In particular, the model performed well in capturing the timing of rapid increase in surface pan concentration. The simulated surface ice concentrations remained at 100% following freeze-up at all stations upstream of GBWTP. With the exception of a small open lead which forms downstream of an outfall at the University of Alberta (not included in the model due to a lack of data), this matches the observed data.

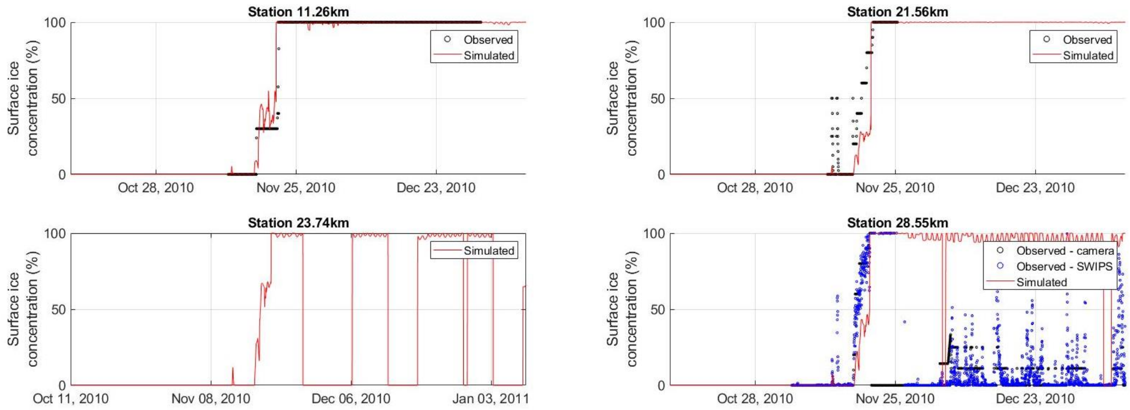

Figure 7. Observed and simulated surface pan concentrations at Stations 11.26, 21.56, 23.74 and 28.55 km.

Formation of the GBWTP open lead caused the observed surface ice concentrations downstream of the plant's outfall, Station 22.09 km, to reduce following the freeze-up period. The size of the open lead is known to fluctuate but at times it extends at least 13.5 km downstream of GBWTP and occupies more than 60% of the channel width. Modeling efforts to simulate the open lead were partially successful. Downstream of GBWTP, the surface ice concentration continuously fluctuated between 90-100% and longer periods of complete open water conditions were simulated, most frequently between Stations 23.37 km and 27.34 km. When the GBWTP inflow was removed from the model, neither the fluctuations in surface ice concentration nor the formation of an open lead were simulated.

As can be seen in Figure 8, which presents the simulated and observed water surface elevations, the timing of stage-up is well captured at all locations. The model performed well in simulating the magnitude of stage-up at stations upstream of GBWTP. Downstream of GBWTP the model underestimated the magnitude of stage-up by 0.20 – 0.25 m. Following freeze-up, the model overestimated water surface elevations upstream of GBWTP and underestimated water surface elevations downstream of GBWTP. The model calculates ice roughness values based on the ice thickness, according to Nezhikhovskiy (1964), and does not account for smoothing. Several smaller outfalls which may contribute to the thinning of the ice cover in the central part of the city have not been included in the model. The decrease in water surface elevations downstream of the plant is caused by a reduction in the simulated solid ice thicknesses and increased hydraulic efficiency. On November 29th, 2010, the average simulated solid ice thickness throughout the study reach was 0.16 m while the simulated solid ice thickness downstream of GBWTP was only 0.01 m, with several cross sections showing no solid ice.

Stage-up is inextricably linked to the ice front progression and bridging locations. It is noticeable that the drop of approximately 0.5 m in observed water surface elevations at Stations 14.48 and 21.32 km, immediately prior to stage-up, was not replicated in the model. An additional upstream bridging event(s), unaccounted in the model or boundary condition, could be responsible for this drop in water levels.

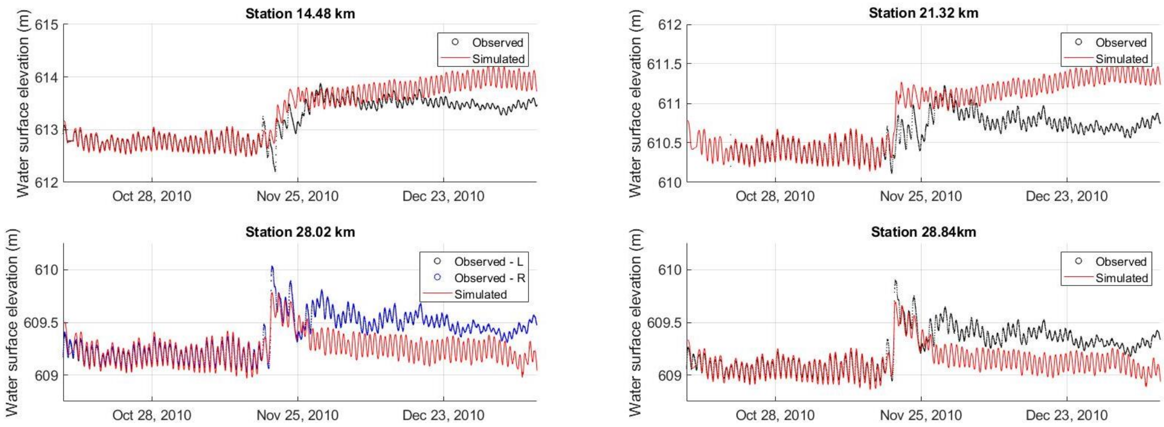

Figure 8. Observed and simulated water surface elevations at Stations 14.48, 21.32, 28.02 and 28.84 km.

4. Conclusion

The River1D ice process model was used to simulate the 2010-2011 freeze-up of the highly urban reach of the NSR. Strong agreement between the observed and simulated data was achieved for an unprecedented number of river ice variables. The particularly strong simulation results for suspended frazil concentration are encouraging and there is potential for the model to be used to identify periods where there is a heightened risk of water intake blockages. However, acquisition of data relating to the timing and magnitude of such blockages would be required for such an exercise. Further modeling efforts are underway to increase the simulation period to include break-up. The underestimation of the magnitude of "stage-up" highlights the need for accurate bridging data and more robust discharge data to be included in the upstream boundary condition. Although the model did not perfectly replicate the open lead, the effect of the warm water discharge was apparent in the simulated surface ice concentrations, and the solid and frazil slush thicknesses. Future work includes validating the model with another season of field data.

Acknowledgments

This study was funded through the Natural Science and Engineering Research Council of Canada (NSERC) Discovery Grant. This support is gratefully acknowledged. The authors would also like to acknowledge the contributions of Joshua Maxwell and EPCOR Utilities Inc. for data collection and provision, respectively.

References

Andres, D.D., 1988. Observation and prediction of the 1986 breakup on the Athabasca River upstream of Fort McMurray, Alberta. Alberta Research Council Report No. SWE-88/03.

Ashton, G.D. (Ed.), 1986. River and Lake Ice Engineering. Water Resources Publications, Littleton, Colorado.

Ashton, G.D. 2011 River and lake ice thickening, thinning, and anow ice formation. Cold Regions Science and Technology. **68**, 3-19.

Beltaos, S. (Ed), 1995. River Ice Jams. Water Resources Publications, Littleton, Colorado.

Blackburn, J., She, Y., 2019. A comprehensive public-domain river ice process model and its application to a complex natural river. Cold Regions Science and Technology. **163**, 44-58.

Ghobrial, T., Loewen, M., Hicks, F., 2013. Continuous monitoring of river ice during freeze-up using upward looking sonar. Cold Regions Science and Technology. **86**, 69-85.

Hicks, F. (Ed), 2016. An Introduction to River Ice Engineering for Civil Engineers and Geoscientists. CreateSpace Independent Publishing Platform.

I.D.G., 1995. North Saskatchewan River at Edmonton Flood Risk Mapping Study (Phase II – Upper Reach). Submitted to Alberta Environmental Protection.

Jasek, M., Ghobrial, T., Loewen, M., Hicks, F., 2011. Comparison of CRISSP modeled and SWIPS measured ice concentrations on the Peace River. Committee on River Ice Processes and the Environment. Proc. 16th Workshop on River Ice, Winnipeg, Manitoba, September 18-22.

Lal, A.M., Shen, H.T., 1991. A mathematical model for river ice processes. Journal of Hydraulic Engineering. **117** (7), 851-867.

Maxwell, J., Hicks, F., Loewen, M., 2011. Study of Freeze-up ice characteristics on the North Saskatchewan River. Committee on River Ice Processes and the Environment. Proc. 16th Workshop on River Ice, Winnipeg, Manitoba, September 18-22.

Nezhikhosky, R.A., 1964. Coefficent of roughness of bottom surface of slush ice cover. Soviet Hydrology, Selected Papers. **2**, 127-150.

NHC., 2007. North Saskatchewan River Flood Risk Mapping Study; Devon to Fort Saskatchewan (Excluding Edmonton). Submitted to Alberta Environment.

She, Y., Hicks, F., Andrishak, R., 2012. The role of hydro-peaking in freeze-up consolidation events on regulated rivers. Cold Regions Science and Technology, **73**, 41-49.

Timalsina, N., Charmasson, J., Alfredsen, K., 2013. Simulation of the ice regime in a Norwegian regulated river. Cold Regions Science and Technology, **94**, 61-73.

Total E&P Canada., 2007. Environmental Baseline Study: Hydrology. Calgary, Alberta, Canada. 36 pages.

IAHR AIRH

25th IAHR International Symposium on Ice

Trondheim, 23 – 25 November 2020

Examination of the Applicability of a Model for Predicting Ice Sheet Thickness

Yu INAMI [1], Hiroshi YOKOYAMA [1], Yasuhiro YOSHIKAWA [2], Hiroki YABE [1]

[1] Civil Engineering Research Institute for Cold Region
Sapporo, Japan
inami-y@ceri.go.jp
yokoyama-h22ab@ceri.go.jp
yabe-h@ceri.go.jp
[2] Kitami Institute of Technology
Kitami, Japan
yoshi@mail.kitami-it.ac.jp

By considering the Hokkaido Ice Jam Disaster of March 2018, the Civil Engineering Research Institute for Cold Region developed a program for calculating the thickness of river ice in collaboration with Associate Professor Yasuhiro Yoshikawa of the Kitami Institute of Technology.

In this study, we first calculated the changes in ice thickness using the ice jam prediction program for the Kenufuchi River in Hokkaido, Japan, and discussed the results. The program was confirmed to reproduce the time-series of phenomena from river ice formation at sub-freezing temperatures to melting at above-freezing temperatures. The program also demonstrated that the time at which the calculated river ice thickness suddenly decreases can be regarded as the start of an ice jam. Next, the possibility of using the ice jam prediction program in the field was discussed by comparing the calculation results with the results of field observation conducted on the Kenufuchi River on March 12, 2018. This comparison revealed that predicted time of ice jam occurrence roughly agreed with the actual time of ice jam occurrence estimated from field observations. Therefore, it is suggested that the ice jam prediction program can be roughly predict the time of ice jam occurrence. Finally, the accuracy of the ice jam prediction program was examined by comparing its calculation results with those of the one-dimensional unsteady flow calculation model CERI1D, developed by Associate Professor Yasuhiro Yoshikawa of Kitami Institute of Technology. The ice jam prediction program was found to be accurate enough for practical use, although the accuracy is slightly lower than that of CERI1D, which is a commonly used program for calculating river ice thickness fluctuations. From the viewpoint of usability at field offices, the ice jam prediction program may be regarded as an effective tool for detecting ice jams.

1. Introduction

During the coldest season, freezing occurs in many rivers in cold regions, and river ice flows down them. In some cases, this ice accumulates at narrow sections or bends in the river, or near river structures such as bridge piers and sluices. The accumulated ice causes the river water level to rise. There have also been reports of river ice damaging embankments by striking them or of river ice causing water intake failures by accumulating near water intake facilities. These phenomena are generally called ice jams, and they often occur in rivers in Hokkaido. However, there have been few observations on ice jams worldwide, and the phenomenon is not fully understood. Therefore, knowledge about ice jams has been scarce.

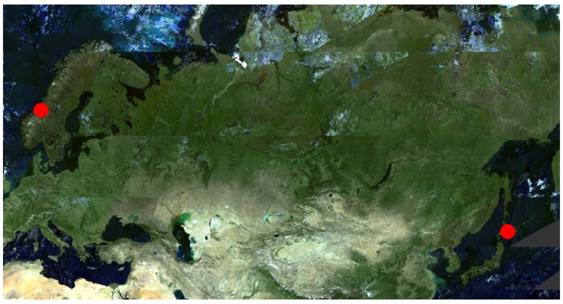

Figure 1 (a). Locations of Trondheim and Sapporo

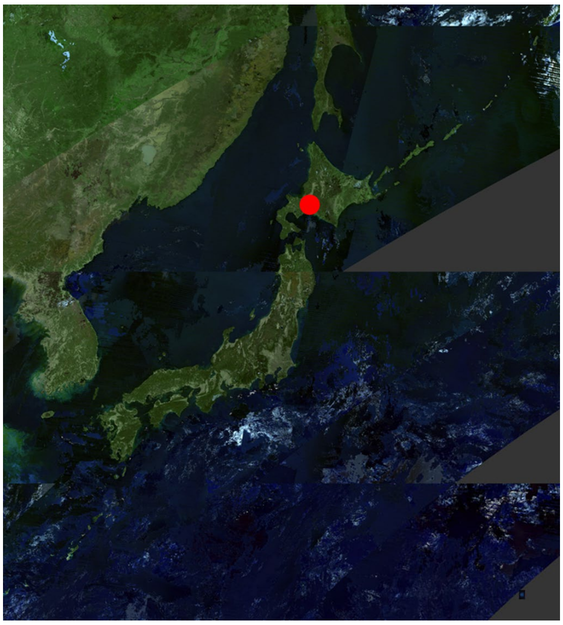

Figure 1 (b). Location of Sapporo in Japan

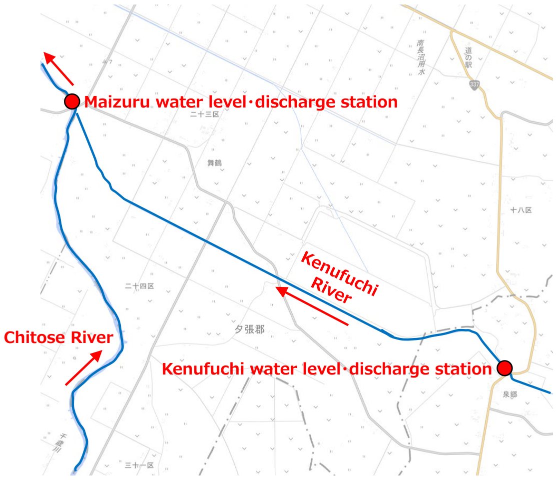

Figure 1 (c). Kenufuchi River

The Kenufuchi River is a tributary of the Chitose River in the Ishikari River System. It joins the Chitose River at KP 28.6 (Figure 1). The Kenufuchi is a small river with a water surface width of about 10 m during the normal water stage. In the river section from KP 0.2 to KP 7.2, which is administered by the Minister of Land, Infrastructure, Transport and Tourism (MLIT), there are many river structures, including 9 sluice gates, 8 bridges, 1 aqueduct bridge and 1 dike sluice. Ice jams had not occurred on the Kenufuchi River until March 9, 2018, when they occurred on many rivers in Hokkaido due to rainfall and high temperatures. Considering the effects of long-term climate change, it can be predicted that water disasters will become more intense and frequent. The number of rivers that will have ice jams may increase in Hokkaido.

By considering the Hokkaido Ice Jam Disaster of March 2018, the Civil Engineering Research Institute for Cold Region (CERI), in collaboration with Associate Professor Yasuhiro Yoshikawa of the Kitami Institute of Technology, developed a program for calculating the thickness of river ice. On a trial basis, we have been distributing the program to administrative agencies that manage rivers. This program uses the Excel VBA function; therefore, the user is able to use the program in Excel format, from input to calculation of the input data to output of the calculation results. The program was created so as to be usable without much effort by river administrators, who are often not very knowledgeable about

numerical calculation programs. Another feature of the program is that input data (temperature, wind speed, sunshine duration, snow depth, water level) can be acquired free of charge. However, many unclear points remain regarding the adaptability of this program to each local area due to the limited number of ice jam observations at each river. Furthermore, toward the social implementation of this program, its calculation accuracy needs to be verified by comparison to those of generally used river ice thickness fluctuation calculation methods.
In this study, the changes in ice thickness are first discussed using the ice jam prediction program. Next, the possibility of using that program in the field is discussed by comparing the calculation results with the results of field observations conducted on the Kenufuchi River on March 12, 2018. Finally, we compare the calculation results of the program with those of the one-dimensional unsteady flow calculation model CERI1D developed by Associate Professor Yoshikawa while he was on the cold river team of CERI and published in 2013.

2. Model for Predicting Ice Sheet Thickness

To predict the future state with high accuracy using numerical calculations, it is necessary to assume actual phenomena as accurately as possible. However, the greater is the accuracy of the assumptions, the greater is the complexity of the calculation scheme. As a result, input conditions necessary for numerical calculation increase, and the program becomes difficult to handle for those who are not skilled at numerical calculation. Also, when judging the success or failure of a calculation result, it is not easy to determine which part of the formula contributes to the result. Therefore, a program for calculating river ice thickness on Excel has been developed and distributed to relevant organizations on a trial basis.
In this study, the Kenufuchi River, a tributary of the Chitose River in the Ishikari River System, was the subject area; the river ice thickness was calculated by giving the representative river width, and changes in ice thickness were examined.

2.1 Equation

In the ice jam prediction program, river ice thickness is calculated by using the following equation.

$$h_i = h_i' - \left(\frac{65.2}{10^5}\right)\alpha\frac{T_a}{h_i'} - \left(\frac{45.8}{10^2}\right)\beta^{4/5}T_w h_w^{1/3} \tag{1}$$

Where, h_i (m) is the ice sheet thickness, h'_i (m) is the ice sheet thickness Δt before the target time, T_a (°C) is the air temperature, T_w (°C) is the water temperature, and h_w (m) is the water depth. α and β are calculated by using the following equation.

$$\alpha = 0.906 - 2.770\frac{I_b B}{h_w} \tag{2}$$

$$\beta = \frac{u_w}{h_w^{2/3}} \tag{3}$$

Where, I_b (-) is the river bed slope, B (m) is the river width and u_w (m/s) is the water velocity. α represents the degree of ice sheet formation corresponding to the air temperature at the target time. The greater is this value, the greater is the increase in ice sheet thickness. β represents the degree of ice sheet melting corresponding to the water temperature and the effective water depth. This is a coefficient whose increase means increases in the degree of melting of the ice sheet. When snow or frazil ice accretes to an ice sheet and becomes part of the ice sheet, the

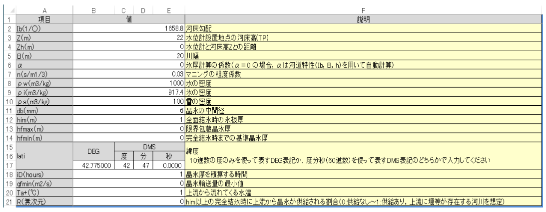

	A	B	C	D	E	F
1	項目	値				説明
2	Ib(1/〇)				1658.8	河床勾配
3	Z(m)				22	水位計設置地点の河床高(TP)
4	Zh(m)				0	水位計と河床高Zとの距離
5	B(m)				20	川幅
6	α				0	氷厚計算の係数(α=0の場合，αは河道特性(Ib, B, h)を用いて自動計算)
7	n(s/m1/3)				0.03	マニングの粗度係数
8	ρw(m3/kg)				1000	水の密度
9	ρi(m3/kg)				917.4	氷の密度
10	ρs(m3/kg)				100	雪の密度
11	db(mm)				6	晶氷の中間径
12	him(m)				1	全面結氷時の氷板厚
13	hfmax(m)				0	限界包蔵晶氷厚
14	hfmin(m)				0	完全結氷時までの基準晶氷厚
15	lati	DEG	DMS			緯度
16			度	分	秒	10進数の度のみを使って表すDEG表記か、度分秒(60進数)を使って表すDMS表記のどちらかで入力してください
17		42.775000	42	47	0.0000	
18	iD(hours)				1	晶氷厚を積算する時間
19	qfmin(m2/s)				0	晶氷輸送量の最小値
20	Ta+(℃)				1	上流から流れてくる水温
21	R(無次元)				0	him以上の完全結氷時に上流から晶氷が供給される割合(0:供給なし~1:供給あり，上流に堰等が存在する河川を想定)

Figure 2. Input data for predicting ice sheet thickness

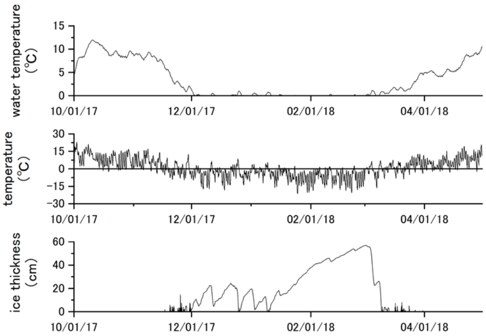

Figure 3. Results of model for predicting ice sheet thickness

value of α increases, and when the snow or frazil ice acts as a heat insulation for the ice sheet, this value decreases. β increases when the hydraulic gradient is great and the roughness is small, and decreases when the hydraulic gradient is small and the roughness is great.

Usually, in order to assume and calculate the river ice thickness as realistically as possible, it is necessary to calculate the balance of the amount of river ice at each point in addition to equation (1). However, to do so, it is necessary to divide the river channel into small areas and create a computation grid, but this requires specialized knowledge and increases the difficulty of using the computation model. The main feature of this ice jam prediction program is that it is not necessary to calculate the balance of river ice amount at each location but to calculate the river ice thickness at one representative location without using a calculation grid for determining ice jam occurrence.

2.2 Setting of the Input Condition

Figure 2 shows the data given as fixed values among the input data. The water temperature flowing from upstream is an input condition, and a constant value is given for simplicity. In this calculation, the water temperature is assumed as 1°C, because the measured water temperature is unknown. For the air temperature, we use the website of the Japan Meteorological Agency, and select the air temperature at Eniwa-shimamatsu, which is close to the target location.

2.3 Results and Discussion

Figure 3 shows the changes in the water temperature, air temperature and river ice thickness from 1:00 on October 1, 2017 to 24:00 on April 30, 2018.

From November 19 to 30, 2017, the river ice repeatedly forms and melted. This is because the air temperature drops below freezing from nightfall and river ice forms, but the air temperature rises above 0°C with sunrise and the river ice melts completely during the day. This freezing and melting cycle is repeated during these days. At this time, the water temperature is 0.89°C at the lowest, and it is found that river ice easily forms and melts from heat flux exchange between the water and the air.

After December 1, hours with sub-zero temperatures increase during the day and the water temperature stays around 0°C throughout the day; therefore, river ice continuously forms without melting, even during the daytime. Nevertheless, on days with high daytime air temperatures, such as December 3, December 10, December 24, 2017, and January 1 and January 8, 2018, river ice of about 20cm in thickness melts. The marked decrease in river ice thickness suggests that the originally formed river ice melts and flows down as broken ice sheets. Therefore, it can be determined that the possibility of occurrence of ice jam is high.

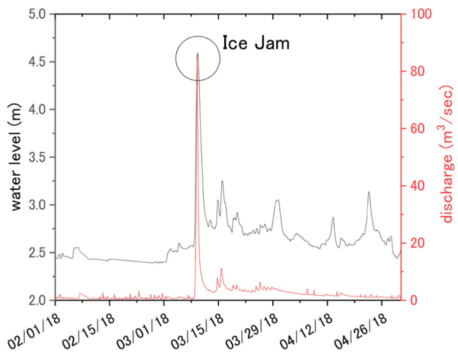

Figure 4. Water level and discharge

Figure 5. River ice sheets in Kenufuchi River

Figure 6. River ice sheet (Flat)

Figure 7. River ice sheet (Cross section)

No significant melting is observed on January 9 on and the river ice thickness reaches a maximum of about 57cm on March 3. From March 3 to March 9 the river ice melts extensively, and the ice thickness decreases from 57cm to 0cm. At this time, both the water temperature and the air temperature have risen remarkably. Therefore, the likelihood of an ice jam is considered to be high.

From the melting of ice on March 9, both the water and the air temperatures are high, and no significant river ice forms. However, river ice forms only on days when the air temperature falls below the freezing point after sunset.

3. Overview of the On-Site Investigation

The onsite survey conducted on March 12, 2018 will be outlined, and the causal factors behind the ice jam that occurred in the Kenufuchi River will be described. Issues to be examined further will also be presented in this chapter.

3.1 Overview of the Ice Jam

From March 8 to 9, 2018, an extratropical cyclone developed and approached Hokkaido, resulting in unseasonal rainfall and rising air temperatures. Rainfall and rising air temperature, which promote the melting of rive ice and increase the river discharge, can be direct causes of ice jams. The peak river discharge was approximately 85m^3/s at 13:00 on March 9, indicating extremely severe flooding given the normal discharge of 1m^3/s (Figure 4). According to the

Chitose River Office, which manages the Kenufuchi River, river ice clogged the bend from KP 5.0 to KP 6.2 at 13:00 on March 9. It is presumed that the ice jam occurred during the flooding.

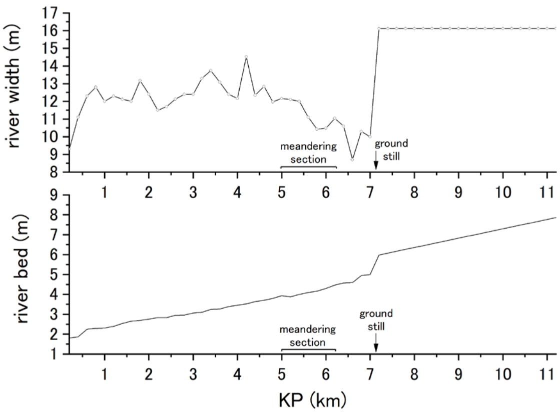

Figure 8. Width and elevation of Kenufuchi River

3.2 Onsite Survey Results

The onsite survey was conducted on March 12, three days after the ice jam. The surveyed range was KP 6.8 to KP 7.2, where the existence of river ice in the high-water channel was confirmed. At the time of the onsite survey on March 12, pieces of river ice with a maximum length of 3.0m and a thickness of 0.1 to 0.5m were piled up in the high flood channel of the Kenufuchi River. During the ice jam, pieces of river ice larger than those found in the high flood channel on March 12 were observed to flow down the river channel (Figure 5, 6, and 7).

River ice had entered the areas near the intakes of Tosaka Sluice (KP 7.0, left bank) and Matsubara Sluice (KP 7.0, right bank); however, no water intake failures or damage from ice striking the sluice gate was observed. The Kenufuchi River is narrow; therefore, once an ice jam has occurred, the river ice that flows down covers the entire width of the river, so the risk of a potential ice jam is considered to be high. The sluices downstream of these two sluices were not investigated.

3.3 Comparison between the Onsite Survey Results and the Results from the Ice Sheet Thickness Predicting Model

First, the appropriateness of the timing of the ice jam predicted by the program will be examined. According to the ice jam prediction program, the river ice continues to melt gradually from March 3 to March 9, and an ice jam occurs. However, in reality, it is speculated that the river ice melted in a short period of time from March 8 to 9, and the ice jam occurred. This is probably because the ice jam prediction program does not take the discharge into account. In the ice jam prediction program, rising air temperatures are a major factor in the melting of river ice, and this melting is considered to possibly result in an ice jam. However, in the actual phenomena, the river ice melts and flows down the river when the air temperatures rise, and ice jams do not necessarily occur under such conditions. When the increase in the discharge coincides with the melting of river ice, it is conceivable from the onsite survey that the river ice does not flow down, but instead clogs the bend or narrow part, resulting in an ice jam. Therefore, it is suggested that the ice jam prediction program can roughly predict the time of ice jam occurrence.

4. Numerical Simulations of an Ice Jam Using CERI1D

To simplify the calculation, the ice jam prediction program makes calculations for only one location. Therefore, the influence of the conditions immediately upstream and downstream of that location is not considered in the program. However, the target location is actually under the influence of the inflow of river ice from upstream and the freezing conditions downstream. To compare the result of this program with the general calculation of river ice thickness, which takes into account these effects from upstream and downstream, we performed simulations of

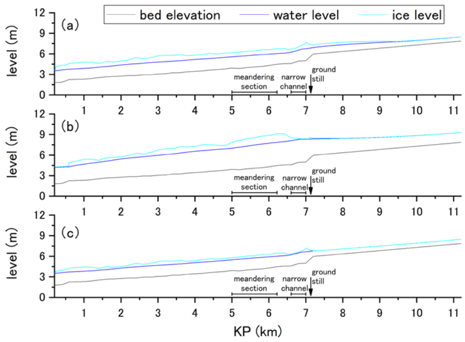

Figure 9. The longitudinal profiles of river bed elevation, water level and ice surface elevation
(a) before ice jam, (b) ice jam,
(c) after ice jam

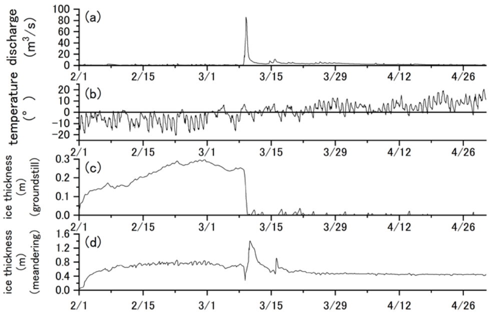

Figure 10. Results of CERI1D
(a) discharge, (b) temperature,
(c) ice thickness at ground still,
(d) ice thickness at meandering point

flow regimes and river ice formation and melting using CERI1D, a one-dimensional unsteady flow solver that is included in iRIC.
This model consists of equations that address the conditions for the occurrence of an ice jam, including the river flow, the river ice flow, the formation and melting of ice sheets, and the breakup of river ice. River ice is roughly categorized into two types: a hard ice sheet and frazil ice underlying the ice sheet. In this calculation model, however, river ice is categorized into a fixed hard ice sheet and flowing ice (including broken ice sheets). The generation of frazil ice due to temperature drop and snowfall, ice formation from frazil ice, the melting of frazil ice, and bridge piers in the river channel are not considered.

4.1 Boundary Condition
In this study, the boundary condition at the downstream end is the water level at the Maizuru Water Level and Discharge Observation Station (Chitose River, KP 28.5, Figure 1). The boundary condition at the upstream end is obtained by converting the water level at the Kenufuchi Water Level and Discharge Observation Station (Kenufuchi River KP 7.2, Figure 1) into a discharge by using the HQ equation (Figure 4). The calculation area is set as the section from KP 0.2 to KP 11.2 (Figure 8). For the transverse data for KP 0.2 to KP 7.2, which is a section under the jurisdiction of MLIT, the data measured by the Chitose River Office in November 2015 are used. The transverse cross-section at KP 7.2 is given uniformly to the entire target section, and the riverbed gradient is set as the average gradient for the section from KP 0.2 to KP 7.2. The reasons for these treatments are as follows: 1) For the area upstream of KP 7.2, there are no transverse data, and it is determined, based on reports from the office in charge of that area, that no ice jam has occurred upstream of KP 7.2 at the time of the onsite survey; and 2) it is considered that an ice jam is unlikely to occur based on the river channel shape of the section. The upstream end of the calculation area is assumed as the head of a river, and the supply of river ice at the upstream end is set as $0m^3/s$. The river ice area at the downstream end is set to hi = $0m^2$ after confirming that the confluence with the Chitose River is not frozen, based on videos taken by CCTV cameras installed by the Hokkaido Regional Development Bureau. The calculation period is set as the three months from February 1, 2018, when it is thought that ice formed, to April 30, 2018, when the period of ice jams finishes and melting starts.

4.2 Results of Numerical Simulations (CERI1D) and Discussion

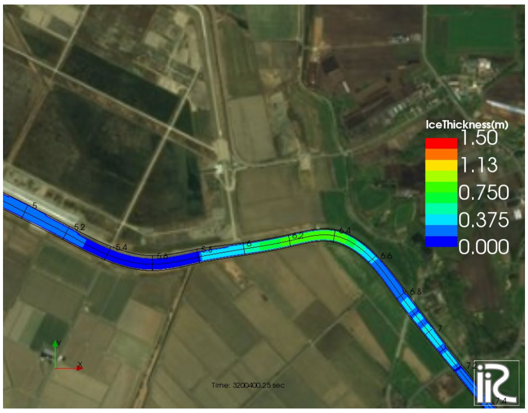

Figure 11. Contour diagram of ice thickness 8 March 2018 13:00

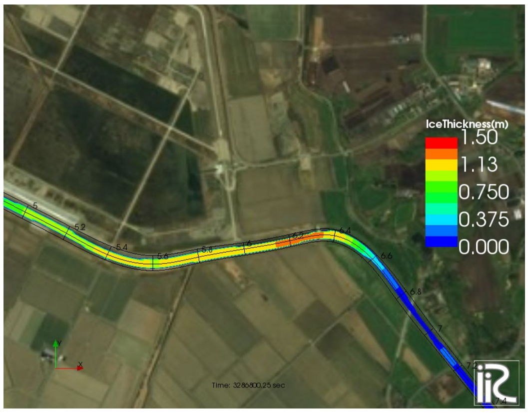

Figure 12. Contour diagram of ice thickness 9 March 2018 13:00

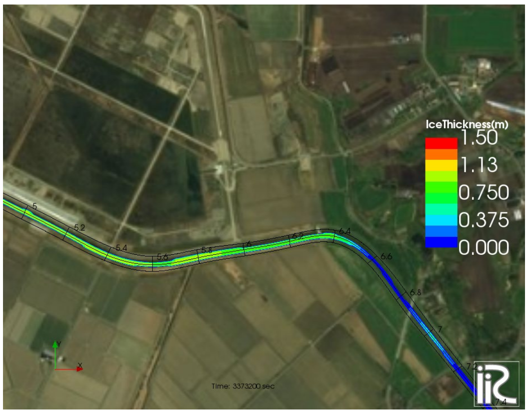

Figure 13. Contour diagram of ice thickness 10 March 2018 13:00

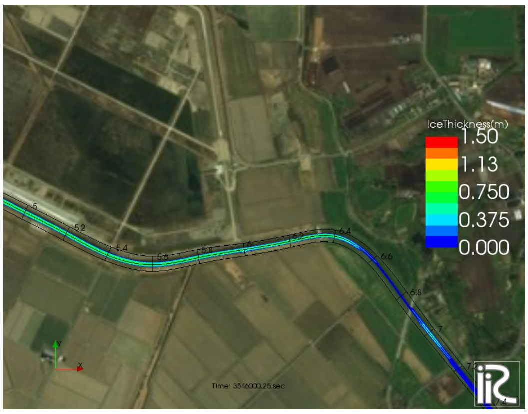

Figure 14. Contour diagram of ice thickness 12 March 2018 13:00

A longitudinal profile of the target river section is shown in Figure 9 (a), in which the riverbed height, water level, and river ice height before the ice jam are plotted. The river ice height is the elevation of the top surface of ice floating on the river water. To understand the state of river ice formation before the ice jam, the values calculated for March 7 are used. From Figure 9 (a), it is understood that river ice markedly forms in the section immediately downstream of KP 7.1 where the Kenufuchi River No. 2 Groundsill is installed. The discharge is as small as $1m^3/s$ (Figure 10 (a)), and the air temperatures are roughly below 0°C (Figure 10 (b)). From Figure 10 (c) and (d), it is understood that river ice continuously forms during this period.

A longitudinal profile of the target river section is shown in Figure 9 (b), in which the riverbed height, water level, and river ice height at the occurrence of an ice jam are plotted. The calculation results are considered to be satisfactory based on the fact that the thickness of the ice sheet at KP 7.0 at 12:30 on March 12 is calculated to be 0.32m, and the measured values are from 0.1m to 0.5m. By comparing Figure 9 (b) with (a), it is understood that the thickness of the ice sheet has decreased on the upstream side of the groundsill, while the thickness of the ice sheet has increased on the downstream side of the groundsill, particularly at the bend. From Figure 10 (a), the peak discharge can be estimated, from the HQ equation, to be about $85m^3/s$. On some days, the air temperature exceeds 0°C (Figure 10 (b)), indicating that river ice is melting. From Figure 10 (c), it is understood that the thickness of the ice sheet has decreased on the upstream of the groundsill. It is considered that the upstream ice sheets decrease because the increased discharge from melting ice under the rising temperature promotes the flowing down of the ice. At the same time, the ice sheet is thicker at the bend (Figure 10 (d)). Therefore, it is suggested that the bend is clogged with the flushed river ice and that an ice jam has occurred.

The longitudinal profile of the target river section, which shows the riverbed height, water level, and river ice height after the ice jam occurrence, is shown in Figure 9 (c). Figure 9 (c) shows that thin ice covers the area immediately downstream of the groundsill. The discharge is as small as $1m^3/s$ (Figure 10 (a)), and the air temperature is above 0°C (Figure 10 (b)). The river ice is not fully melted. From Figure 9 (c), it is understood that no river ice has formed upstream of the Kenufuchi River No. 2 Groundsill. This is probably because there is no supply of river ice at the upstream end and the temperature is rising. As described above, thin ice is seen in the section immediately downstream of the groundsill (Figure 10 (d)). It is considered that river ice which formed during the ice jam remains in this section.

4.3 Comparison between Numerical Simulations (CERI1D) and the Results from the Ice Sheet Thickness Predicting Model

First, the appropriateness of the timing of the ice jam predicted by the program will be examined. Figures 11, 12, 13, and 14 show the spatial distribution of river ice thickness at the bend before and after the occurrence of the ice jam. From Figure 11, it is understood that the ice sheet is thicker at a part of the bend while the discharge increases on March 8. From Figure 12, which shows the river ice conditions on March 9, it can be inferred that the ice sheet is thicker and an ice jam occurs in the sections at and near the bend. Finally, from Figures 13, and 14, it is understood that the discharge decreases and the river ice thickness decreases on March 10. From the above, it is possible to determine, from the calculation results of CERI1D, that an ice jam occurs from March 8 to 9. The calculation results of CERI1D are closer to the results of the onsite survey than are the results obtained using the ice jam prediction program. This is probably because the discharge is considered in CERI1D, as described earlier.

Here, the time required to perform the calculation and the degree of difficulty of these two programs will be discussed. For CERI1D, it is necessary to create a computational grid before performing the calculation. The calculation grid can be automatically generated on iRIC; however, depending on the construction of the calculation grid, the calculation may not be performed properly and may diverge, or the calculation results may deviate from the actual phenomena. Furthermore, in the case of calculation for a complicated flow path, the user needs to manually recreate the calculation grid, which is not always easy. The calculation for an ice jam occurrence by the ice jam prediction program is for only one location; therefore, there is no need for a calculation grid, and the calculation can be performed only by inputting the air temperature, water level, representative river width, and a few other items. In light of the above, the ice jam prediction program may be considered as an effective tool for detecting ice jams at the field offices.

5. Conclusion

The changes in river ice thickness in the Kenufuchi River were examined using an ice jam prediction program. Next, the possibility of using that program in the field is discussed by comparing the calculation results with the results of field observations conducted on the Kenufuchi River on March 12, 2018. Finally, we compared the calculation results of the CERI1D, a one-dimensional unsteady flow calculation model developed by Associate Professor Yoshikawa with the results of the ice jam prediction program. The major findings are as follows.

- It was suggested that the ice jam prediction program can roughly predict the time of ice jam occurrence. However, it is necessary to be aware that this program does not consider the discharge of the river.
- The ice jam prediction program is considered to be sufficiently good for practical use, although its accuracy is slightly lower than that of the generally used river ice thickness calculation program. From the viewpoint of usability, the ice jam prediction program is considered an effective tool for ice jam detection at field offices.

References

Johnson, G.C., 1999. Format for preparation of camera-ready papers. Proc. 10th Workshop on River Ice, Winnipeg, Manitoba, 1-8.

Li, M., Wu, H., and Chen, W.F., 2008. Format for preparation of camera-ready papers. Proc 19th IAHR Symposium on Ice, Dalian, China. 1-8.

CERI1D solver manual [http://i-ric.org/ja/download/get/mTmjY5]

Bray, D. : Estimating Average Velocity In Gravel-Bed Rivers, Journal of the Hydraulics Division,Vol.105, No.HY9, pp.1103-1122, 1979.

Yoshikawa, Y., Watanabe, Y., Hayakawa, H., and Hirai, Y., 2010. The influence factor given to an observation discharge and development of the discharge formula for ice covered river

Shen, H.T., Shen, H., Tsai, S.M. : Dynamic transport of river ice, Journal of Hydraulic Research 28,pp.659-671, 1990.

Yoshikawa, Y., and Watanabe, Y., 2009. Investigation of an ice thickness simulation considering the transition of frazil into ice sheet in the Shokotsu and Yubetsu rivers

25th IAHR International Symposium on Ice
Trondheim, November 23 - 25 2020

Investigation of flow velocity in ice-covered channels

Delaram Kazemian* and Mahmoud F. Maghrebi
Civil Engineering Department, Faculty of Engineering, Ferdowsi University of Mashhad, P.O. Box 91775-1111 Mashhad, Iran
Dkaz1371@gmail.com

Abstract: Determination of velocity distribution profiles at hydraulic sections has always been important in river and hydraulic engineering. There are several factors which influence the velocity distribution in the channels cross-section. One of them is ice as it forms in open channels basically alters velocity distribution by increasing the magnitude of wetted perimeter and hydraulic resistance. River ice processes include complex interactions among the hydrodynamic, mechanical, and thermal processes. There are various methods to estimate distribution of isovel contours. The single point velocity measurement method (SPM) is a relatively new method of estimating distribution of isovel contours in the channels. In this paper, the verification of this method is investigated in terms of the presence of full ice cover in the rectangular channels and compared with the experimental results. An experimental program was developed at the Hydraulics laboratory of Ferdowsi University, Mashhad, Iran. A 8-m-long, 0.4-m-wide rectangular channel was used, and a simulated ice cover was installed on the bed and top of the channel. Experiments were designed in order to quantify the effects of channel-bed and ice roughness on the flow characteristics within a completely ice-covered rectangular channel. Measurements are performed from ice cover by means of a current meter attached to a vertical rigid rod supported on the channel bed. It was found that roughness had a significant impact on isovel counters below the ice cover. The results of the experiments showed that the presence of the full ice cover caused an almost symmetrical development of the velocity distribution profiles in the flow cross-section. A rough surface was shown to decrease water velocity near to the rough boundary. The minimum error occurs in the central position of the flow and as moving to the upper and lower rough boundaries the error in estimating the velocity is increased.

1. Introduction

Determining the flow velocity distribution profile in turbulent open channels has always been the focus of researchers. The issue matters since the velocity distribution profile allows us to determine the shear stress distribution as well as the flow rate in the channels. Several factors influence the velocity distribution profile, including the formation of ice layers on the flow surface. Most of the rivers in the highlands are covered by ice during the winter. Ice layer formation depends on the temperature conditions of water and the surrounding environment. Decreasing the water temperature to zero and its cooling are not sufficient conditions for ice layer formation. Rather, the ice nucleus around, which the ice crystals are formed, is the main factor.

Ice formation in flowing water (rivers, channels, reservoirs) and stagnant water (lakes, ponds) is a very complex chain of physical processes that appears as a result of heat exchange between water and the environment (Majewski, 2007). The process of forming ice cover in flowing water is much more complicated than in the stagnant water. These processes occur regularly in the annual hydrological cycles due to the significant interaction between the thermal conditions and the flow regime. The freezing of rivers produces different morphological and hydraulic properties compared to the open channels flow as a result of the additional boundary layer creation on top of the river. This boundary layer also affects the rate and distribution of flow velocity, flow regime, discharge (flow rate), and the sediment transport (Morse and Hicks, 2005). The location of maximum velocity at the cross-section of the ice-covered river is somewhere between the river bed and the ice layer, which is affected by the roughness of the lower surface of the ice cover and the riverbed roughness.

Sui et al. (2010) studied the velocity distribution profile and the movement of frazil particles under the ice cover. They concluded that under the same flow conditions, the mean average velocity across the channel in the open flow state is significantly higher compared to both cases of the presence of rough and smooth ice. Peters et al. (2018) investigated the effects of bed and ice on flow characteristics by considering partial ice cover (67% ice coverage) and using two acoustic Doppler accelerometers in the laboratory. Zare et al. (2016) introduced a new method to estimate composite roughness based on measured velocity profiles. The validity and applicability of this new method's main assumptions are tested using four-month continuous field data collected under the ice by acoustic instruments.

Kimiaghalam et al. (2018) studied the velocity profile and shear stress in a partially-covered trapezoidal channel for the first time. They examined seven different cases of roughness and ice layer, four states of which were related to the different percentages of ice coverage (without ice, 25%, 50% and 67% of ice layer cover) and the other three were related to the roughness (rough partial ice layer, rough walls and bed, and all rough boundary). Lau (1981) calculated the velocity distribution in a large number of flow channels with different bed and top roughness rates. The calculated velocity distribution shows that velocity profiles follow a logarithmic velocity distribution only for about 60% of the flow depth and the velocity value is lower than that obtained by the logarithmic distribution for 40% of the flow depth approximately near the maximum velocity location. Majewski (2007) conducted a field study on the effects of ice layer on the flow in the Vistula River and showed that the changes range of Manning roughness coefficient of the lower surface of the ice layer varies from 0.02 to 0.15. Chen et al. (2019) performed an experimental study on the stage-discharge curve of the ice-covered flow in rectangular channels. Comparing the predicted results of the proposed model and the data collected from previous papers suggests that the proposed method provides an appropriate estimation of the stage-discharge relationship in the rectangular channels covered by an ice layer. Teal et al. (1994) evaluated the point measurement methods to estimate the average velocity along the vertical direction of flow, including the single-

point, two-point, and three-point methods. They finally concluded that the two-point method shows less error than the other methods.
A new approach was introduced by Maghrebi (2006) to predict dimensionless velocity contours, in which was assumed that the velocity at any desired point is influenced by the hydraulic properties of the channel boundaries. According to this approach and by calculating the average velocity, Maghrebi (2006) obtained the discharge in different levels of the rectangular channels and plotted the stage-discharge curve for the rectangular channels.
In this study, in order to investigate the effect of ice layer on the flow, an experimental model was used for simulation. Then, the observational data was used to validate the single point measurement method under the conditions of the presence of an ice layer. Also, the MAPE statistical error parameter was used to analyze the method error under these conditions.

2. Materials & Methods

2.1. Experimental set-up

The experiments were carried out by using a flume located at the Hydraulic Laboratory of Ferdowsi University of Mashhad. The flume is made of a metal chassis channel with glass walls to observe the water flow path. This flume with the dimensions of 8 m long, 40 cm width, and 50 cm height is set in the laboratory with metal bases. There are two lever arms below the device. By rotating the lever and changing its height, one can create the desired longitudinal slope in the channel.
In this experiment, the slope of the channel was adjusted as 1: 5000. The water temperature varied from 10 °C to 15 °C on different days during the experiments. Depending on the water temperature, the physical properties of the water had some variations, including the fluid density 999.1 to 999.7 kg/m^3 and the kinematic viscosity about 1.31×10^{-6} to 1.14×10^{-6} m^2/s. A metal slide gate is embedded at the end of the channel to regulate the depth of flow, which is guided up and down by a lever. The laboratory water supply and transfer system consisting of a ground tank is equipped with a radial flow pump system and an elevated tank at the beginning of the channel, which directs water from the ground tank to the laboratory flume through metal pipes. A digital gauge is embedded along these pipes to determine the inlet flow rate to the channel. The amount of discharge can be changed by rotating the control valve embedded on the path of this pipe. In fact, the desired flow intensity is entered into the channel by opening and closing this valve and reading the discharge on the digital gauge.
In order to keep the submergence state of the sand grains used in the upper area of the flume, the flow rate always varied about 26.66-27 liters/s. The experiments were performed for two different cases. In the first mode, the channel walls were smooth with the height of 20 cm and the roughness height was 8 mm. The reason for choosing this height is to modeling an ice cover with some accumulation of frazil. In the second case, the channel walls were smooth with the height of 15 cm and the roughness was similar to the former state. The points for velocity measurement in each case were selected in both vertical and transverse directions.
The local velocity of the current was measured by a micro-propeller. The device consists of a 5-blade propeller with a diameter of 9mm mounted on a 42 cm thin steel rod. The velocity measurement device is connected to a digital indicator by a cable and the appropriate pulse is shown in the indicator in terms of Hz proportionate to the number of blade rotations. The velocity was measured by a micro-propeller and a digital indicator device at a distance of two meters of the channel downstream. A slot with the size of 1.5 × 40 cm was embedded across the channel to allow the probe to move along the cross-section, in order to measure velocity at different points across the channel. The micro-propeller was placed for 120 seconds at each point to measure the velocity and the time average of the velocities was considered as the local average velocity.

2.2. Single point velocity measurement method

Maghrebi proposed a simple model in 2003 derived from Biot–Savart law in Electromagnetism presented in 1820. This method is able to plot the velocity dimensionless contours at the cross-section of ducts, open channels, and irregular natural rivers at the roughness and geometry without the longitudinal curvature. The method is based on the similarity between the magnetic field of a current wire and the isovel contours in a channel cross-section. It is assumed that a current passing through a wire creates a current intensity of "I", which will create a magnetic field around it. An element of wire with a length of dL is now considered to produce the field around the wire. Then, according to the Biot–Savart law, for an arbitrary point such as M, the magnitude of the magnetic field intensity created by any differential element would be proportional to the current passing intensity, the length of the wire element, and the angle between the wire and the line connecting the wire to the desired point. In terms of the orientation of the magnetic field intensity, according to Fig. 1(a), and with respect to the right-hand rule, the field is perpendicular to the plane consisting of the vector element of the wire and the vector drawn from the wire to the examined point.

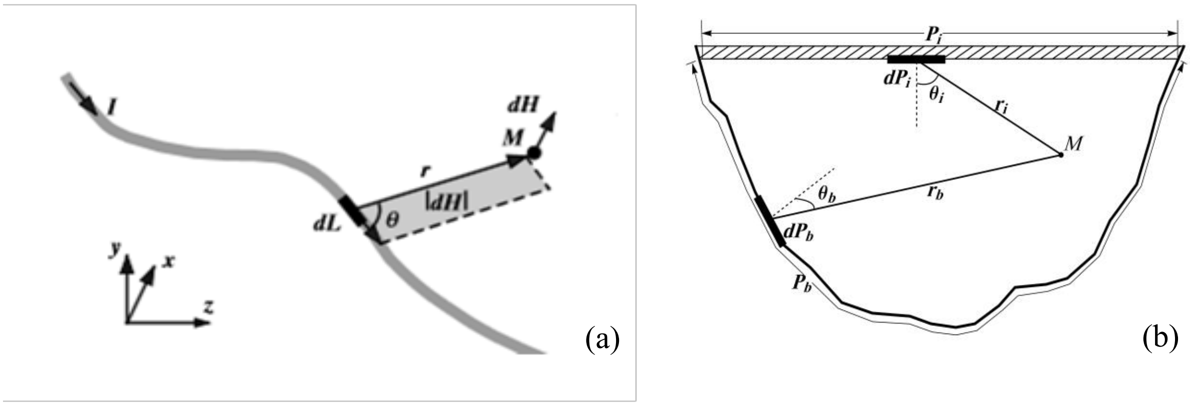

Figure 1. (a) The effect of the magnetic field on the charged particle, and (b) The effect of the boundary element on the desired point in the current section

The Biot–Savart law can be presented as relation (1) based on the vector structure:

$$\mathrm{d}\mathbf{H} = \frac{I d\boldsymbol{L} \times \mathbf{r}}{4\pi r^3} \quad [1]$$

where **H** is the intensity of the magnetic field, **r** is the position vector that connects the element to the desired point, I is the current intensity and $d\boldsymbol{L}$ is an element of wire.
Now, according to the Biot–Savart law, a model for flow section from an open channel is presented. To this end, as seen in Fig. 1(b), a limited length of the flow boundary (dP) on an arbitrary point on the cross section will have an effect equivalent to du_{SPM}:

$$\mathrm{d}\mathbf{u}_{SPM} = f\left(\mathbf{r}\right) \times c_1 d\boldsymbol{P} \quad [2]$$

where du_{SPM} is the deviation of velocity changes due to the boundary element such as $d\boldsymbol{P}$, $\boldsymbol{r}$ is the vector between the boundary element and the desired point, c_1 is the constant related to the boundary roughness and $f(\boldsymbol{r})$ is the velocity function.

In this method, to determine the effects of the whole flow boundary on a point, the length of the wet environment from left bank to the right bank is divided into boundary elements of $d\boldsymbol{P}$. Then, we calculated the value of u_{SPM} by integrating the effects of all the boundary elements on each point of the flow:

$$u_{SPM}\,\mathbf{i} = \int_{boundary} f\,(\mathbf{r}) \times c_1 d\boldsymbol{P} \tag{3}$$

where "**i**" is the unit vector, which is co-directional with the flow, or in other words, parallel to the X axis. On the other hand, we know that the cross product of two $\boldsymbol{r}\times d\boldsymbol{P}$ vectors generates a field with the magnitude of $r.dP.\sin\theta$ perpendicular to the plane; thus, we will have:

$$u_{SPM} = \int_{\text{boundary}} c_1 \cdot \sin\theta \cdot f\,(r) \cdot \mathrm{d}P \tag{4}$$

where θ is the angle between the position vector and the boundary element vector. Normally, the pattern of velocity distribution in open channels follows the velocity power law in closed and open channels due to the flow turbulence. Therefore, the velocity function is expressed as follows:

$$f\,(r) = u_*\left(c_2 r^{\frac{1}{m}}\right) \tag{5}$$

where c_2 is the coefficient related to the turbulence and shear stress of the walls. By substituting Eq. (5) in Eq. (4), the value of $u_{SPM}\,(y,z)$ can be obtained at any point with the coordinates of (y,z):

$$u_{SPM}\,(y,z) = \int_{\text{boundary}} c_1 \cdot c_2 \cdot \sin\theta \cdot u_* \left(r^{\frac{1}{m}}\right) \cdot \mathrm{ds} \tag{6}$$

Considering $c_3 = u_* c_1 c_2$ and $m = 7$, the recent equation would be as follows:

$$u_{SPM}\,(y,z) = \int_{boundry} c_3 \left(r^{\frac{1}{7}}\right) \sin\theta\,\mathrm{ds} \tag{7}$$

Using the Eq. (8), the average value u_{SPM} at the flow section, i.e., U_{SPM} is obtained. If we divide the U_{SPM} value by the u_{SPM} value at a point in the coordinates (y, z), the parameter for the dimensionless velocity contour C is obtained from Eq. (9):

$$U_{SPM} = \frac{\int_A u_{\mathrm{SPM}}\,(y,z)\,dA}{A} \tag{8}$$

$$C\,(y,z) = \frac{u_{SPM}\,(y,z)}{U_{SPM}\,(y,z)} \tag{9}$$

Applying the above relation, we can plot the dimensionless velocity contours at any desired point.

3. Results

In order to investigate the effects of the formation of ice layer in the channel, we simulated the flow in a laboratory flume, which its bed and top had been roughened by aggregates with a diameter of d_{50}=8 mm. The meshing was made at 1 cm intervals in both dimensions of the depth and width of the channel as shown in Fig. 2.

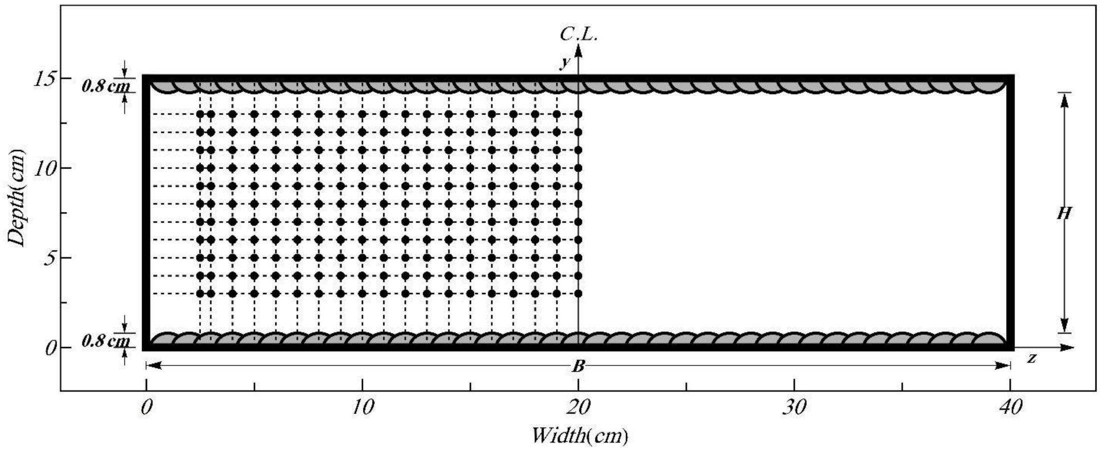

Figure 2. The display of the points measured in the laboratory

Using the observational data in both cases, the dimensionless velocity contours were first plotted in the laboratory flume. Fig. 3 shows the comparison between dimensionless velocity contours based on the observational results and the model. As can be seen in Figs. 3(a) and 3(c), as the *z/B* ratio increases, the ratio of velocity to average velocity has increased and reached its maximum value in the central part of the channel. Also, the Figs. 3(b) and 3(d) suggest that the model provides acceptable results in the condition of ice layers compared to the experimental results.

Then, the velocity distribution profiles were plotted at different points. In Figs. (4) and (5), *U* is the flow average velocity, u is velocity at each point, *H* is channel height, *y* is water depth and *z* are the distance from the left wall of the channel to the channel central line. The plotted velocity distribution profiles show that the velocity distribution profile is also approximately symmetric when the ice layer exists. As can be seen in Fig. 4(a), the velocity distribution profile obtained from the experimental model has many fluctuations due to the proximity to the side wall of the channel. However, with the gradual departure from the wall, the drawn profile based on the observed data has become more regular. Also, it was found by comparing the profiles drawn using the single point method with the laboratory model that the single-point method in the areas near the central line of the channel is in good agreement with the experimental model. As can be seen in this figure, by gradually increasing the distance from the bottom of the channel to about *y/H*=0.5, the plotted velocity distribution profile based on the single point method is in good agreement with experimental observations.

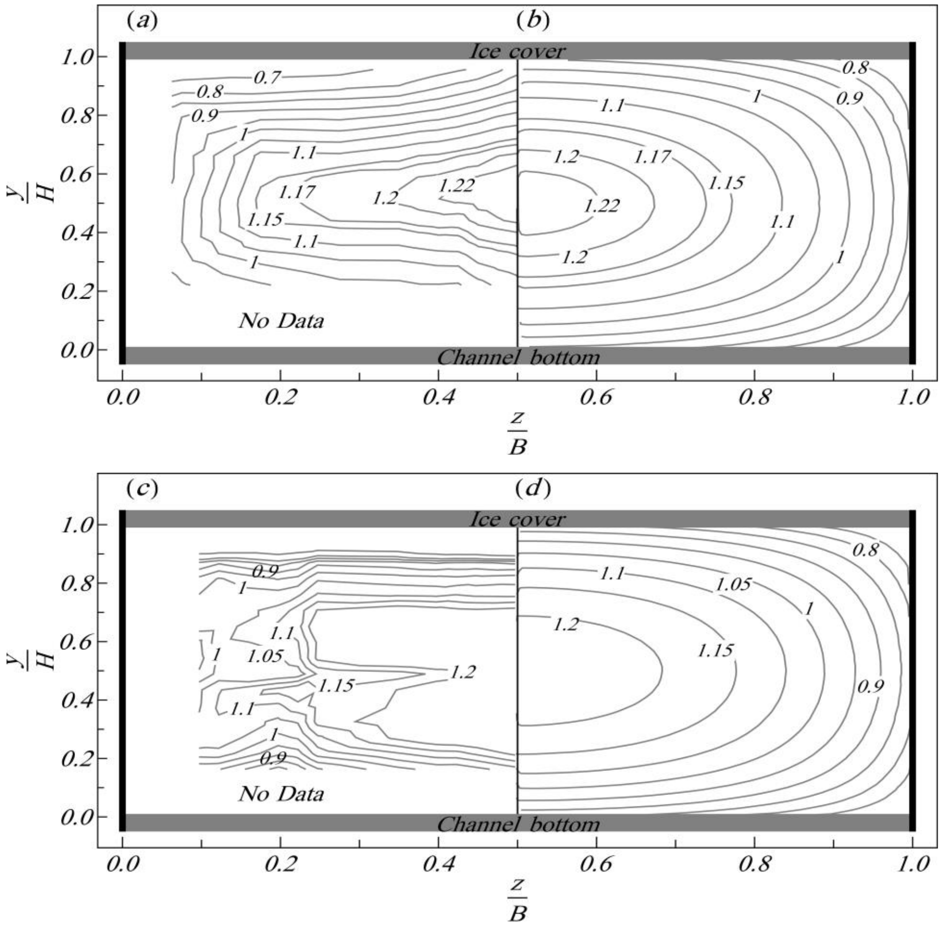

Figure 3. Comparison between the observed (a and c) and calculated contour lines (b and d) for *H=15* and *20 cm*, respectively.

The statistical parameter of *MAPE* was used to quantify the error in Figs. (4) and (5):

$$MAPE = \frac{100}{N}\sum_{i=1}^{N}\left|\frac{u_m - u_c}{u_m}\right| \quad \textbf{[10]}$$

where u_c is the velocity calculated by the single point method, u_m is the same velocity measured in the laboratory and *MAPE* is the statistical parameter which indicates the percentage of mean absolute error

After analyzing the results of the error, it was found that the maximum value of the error in Fig. (5) is about 15%, which occurs at *z/B=0.2* and the percentage of error has reduced in the areas, near the central line of the channel to 7.5%.

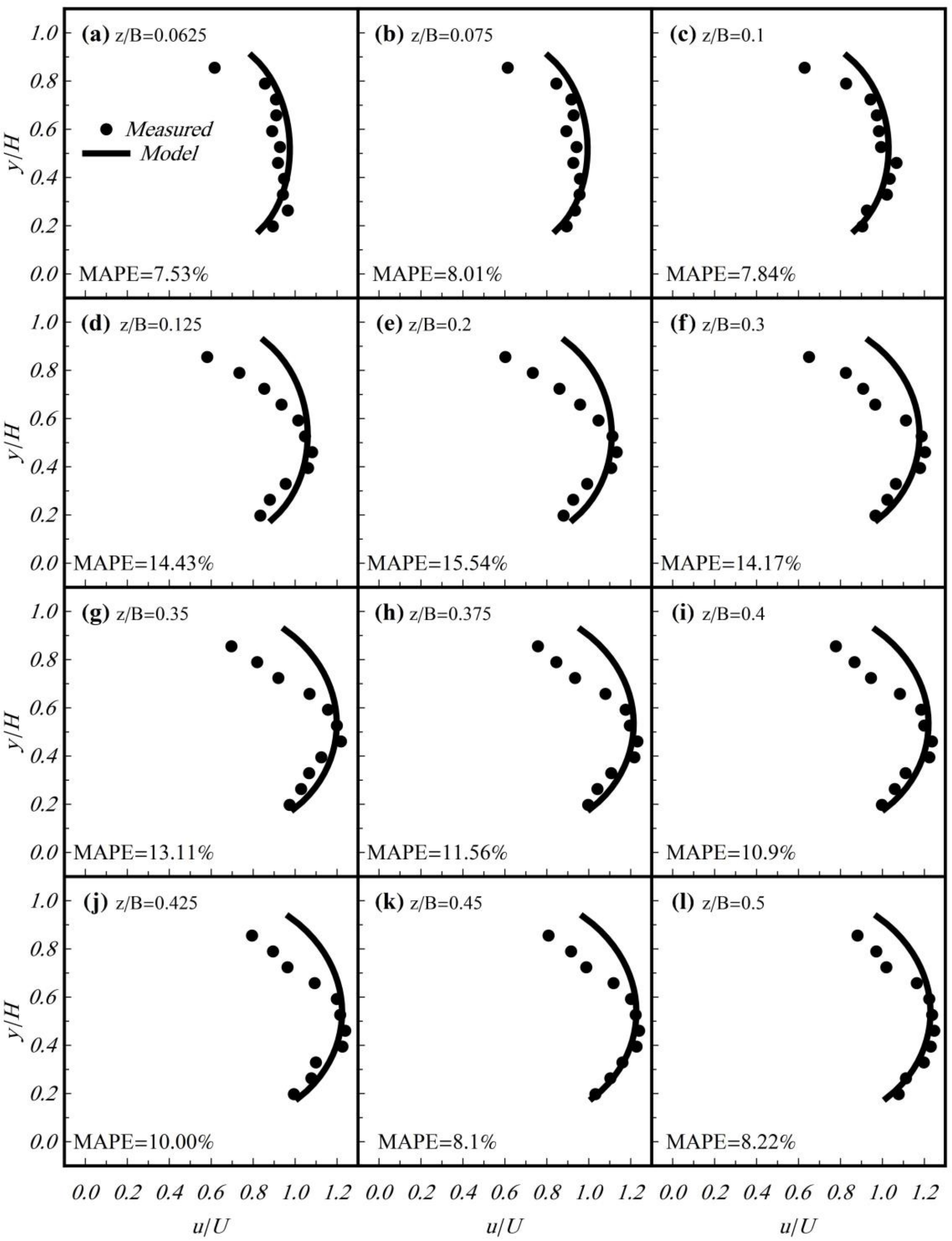

Figure 4. Plotting the velocity distribution profiles in the case of *H=15* (cm), using the single point method and comparing with the experimental model at different distances from the wall by *MAPE*.

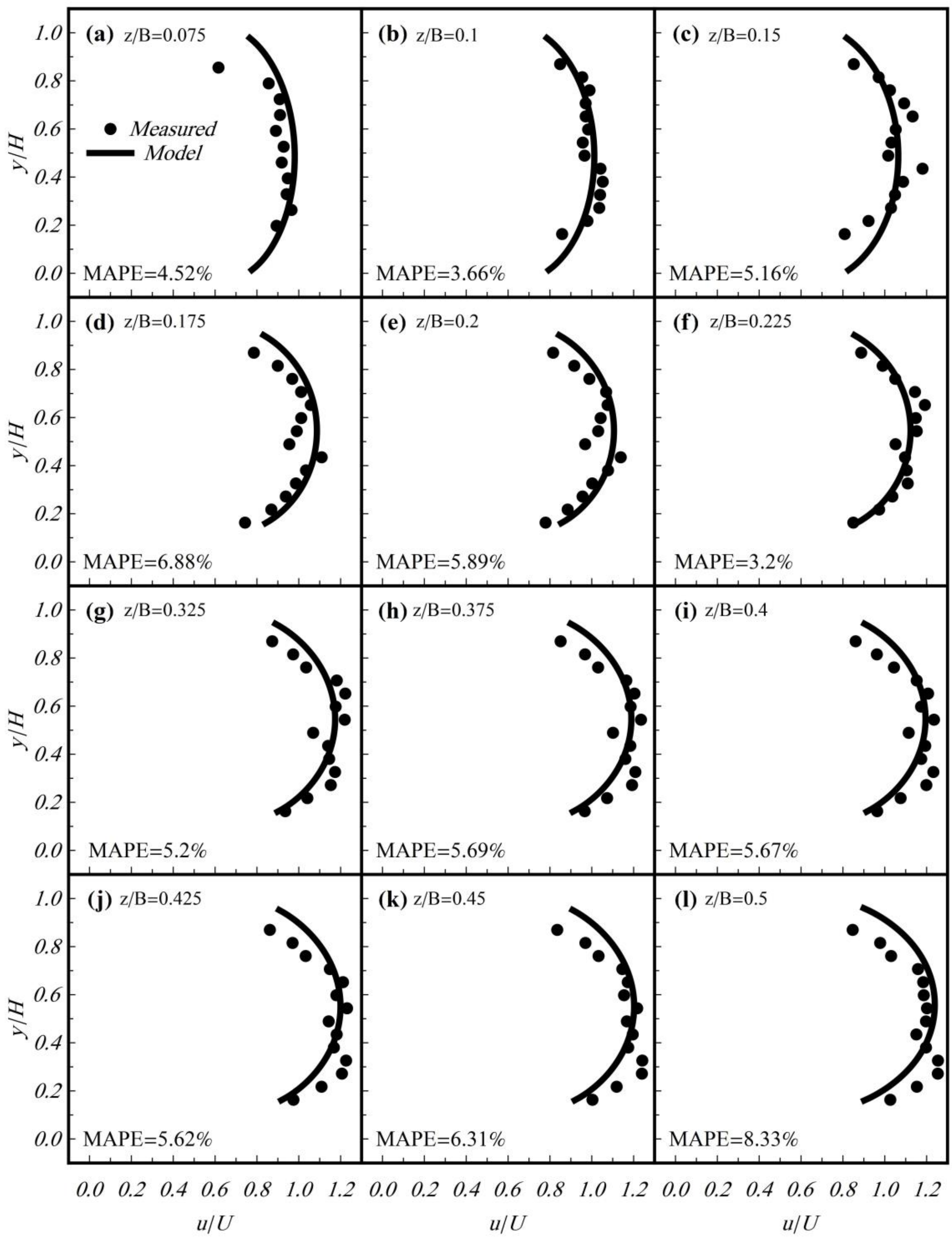

Figure 5. Plotting the velocity distribution profiles in the case of *H=20* (cm), using the single point method and comparing with the experimental model at different distances from the wall by *MAPE*.

4. Conclusion

Ice formation on rivers is common in cold areas and can change the velocity distribution of the rivers. Understanding the effect of ice layer on the velocity distribution is essential to design hydraulic structures, operate hydroelectric generating stations and flood control in cold regions. In this study, the method proposed by Maghrebi (2006), used to estimate isovel contours, in the presence of ice layer was validated for the first time. After drawing velocity distribution profiles, it was observed that the maximum velocity occurs at the maximum distance from the lower and upper walls of the duct, in the mid-depth position. The comparison of profiles drawn by single point method with the experimental model as well as the results of the error analysis show that the SPM method is in good agreement with the observed data and the statistical analysis have shown a low value of error.

References

Chen, G., Li, B., Gu, S. and Zhong, Y., 2019. Discharge Assessment in Straight Open Channels with Partial Ice Cover. Journal of Cold Regions Engineering, 33(2), p.04019002.

Ghareh Aghaji Zare, S., Moore, S.A., Rennie, C.D., Seidou, O., Ahmari, H. and Malenchak, J., 2016. Estimation of composite hydraulic resistance in ice-covered alluvial streams. Water Resources Research, 52(2), pp.1306-1327.

Kimiaghalam, N., Clark, S.P. and Dow, K., 2018. Flow characteristics of a partially-covered trapezoidal channel. Cold Regions Science and Technology, 155, pp.280-288.

Lau, Y.L., 1982. Velocity distributions under floating covers. Canadian Journal of Civil Engineering, 9(1), pp.76-83.

Maghrebi, M.F., 2006. Application of the single point measurement in discharge estimation. Advances in water resources, 29(10), pp.1504-1514.

Majewski, W., 2007. Flow in open channels under the influence of ice cover. Acta Geophysica, 55(1), pp.11-22.

Morse, B. and Hicks, F., 2005. Advances in river ice hydrology 1999–2003. Hydrological Processes: An International Journal, 19(1), pp.247-263.

Peters, M., Clark, S.P., Dow, K., Malenchak, J. and Danielson, D., 2018. Flow characteristics beneath a simulated partial ice cover: Effects of ice and bed roughness. Journal of Cold Regions Engineering, 32(1), pp.04017017.

Jueyi, S.U.I., Jun, W.A.N.G., Yun, H.E. and Faye, K.R.O.L., 2010. Velocity profiles and incipient motion of frazil particles under ice cover. International Journal of Sediment Research, 25(1), pp.39-51.

Teal, M.J., Ettema, R. and Walker, J.F., 1994. Estimation of mean flow velocity in ice-covered channels. Journal of Hydraulic Engineering, 120(12), pp.1385-1400.

25th IAHR International Symposium on Ice
Trondheim, 23-25 November 2020

Two-Dimensional Modeling of Pier Type Ice Control Structures

Ian M. Knack[1], Jason Shaw[2], S. Thomas Lavender[3], Kelvin Jamieson[4], Leo Friday[5]

[1]Department of Civil and Environmental Engineering, Clarkson University
Potsdam, NY 13699-5710, USA
iknack@clarkson.edu

[2]Discipline Director – Hydrotechnical Engineering, Hatch, Ltd.
Niagara Falls, ON, Canada

[3]River Ice Engineering Specialist, Chemainus, BC, Canada

[4]President, FHR, Inc.
Christian Island, ON, Canada

[5]Chief, Kashechewan First Nation
Kashechewan, ON, Canada

Ice jamming in northern rivers is becoming increasingly prevalent and severe. In order to protect communities along these rivers, ice control structures are often considered. Ice control is used to arrest large volumes of ice to jam predictably in a safe location until sufficient melting facilitates benign passage through critical areas. Ice control can include ice booms, pier type ice control structures, weirs, or combinations of different ice control. Ice control is often combined with physical channel conditions that allow for bypassing high flows while retaining the ice to reduce the forces on the structures and maximum flood levels. This paper presents a study on the Albany River in Ontario, Canada to develop ice control as a potential means for mitigating ice jam flooding at the Kashechwan First Nation community. Numerical modeling was conducted using the two-dimensional ice dynamics model DynaRICE. A method was developed to simulate pier type ice control structures within the model. The model allowed detailed simulation of ice retention, resulting inundation, and the forces on the individual piers. Simulations with varying ice, flow, and pier conditions were simulated to optimize the design of the piers, including pier spacing, height, and size. In turn, numerical modeling facilitated a comparative examination of flood risk reduction to the Kashechewan community borne from the implementation of various ice control options.

1. Introduction

The Kashechewan First Nation (KFN) community is located on a floodplain of the north branch of the Albany River, on the west coast of James Bay, in Ontario, Canada (Figure 1). Each spring the community faces the uncertain prospect of evacuation to limit damages caused by ice-jam flooding. The community has been evacuated on a precautionary basis on at least 10 occasions of ice-jam related flooding since 1976. To reduce the impacts of flooding to the community, a Ring Dyke was constructed in the early 1990s to surround the site (Figure 2). While this dyke reduced the frequency of flooding, its poor design and construction and lack of maintenance spawned dam safety hazards; specifically, potential failure due to slope instability and piping. In the spring of 2006, the Ring Dyke was nearly overtopped (Figure 2).

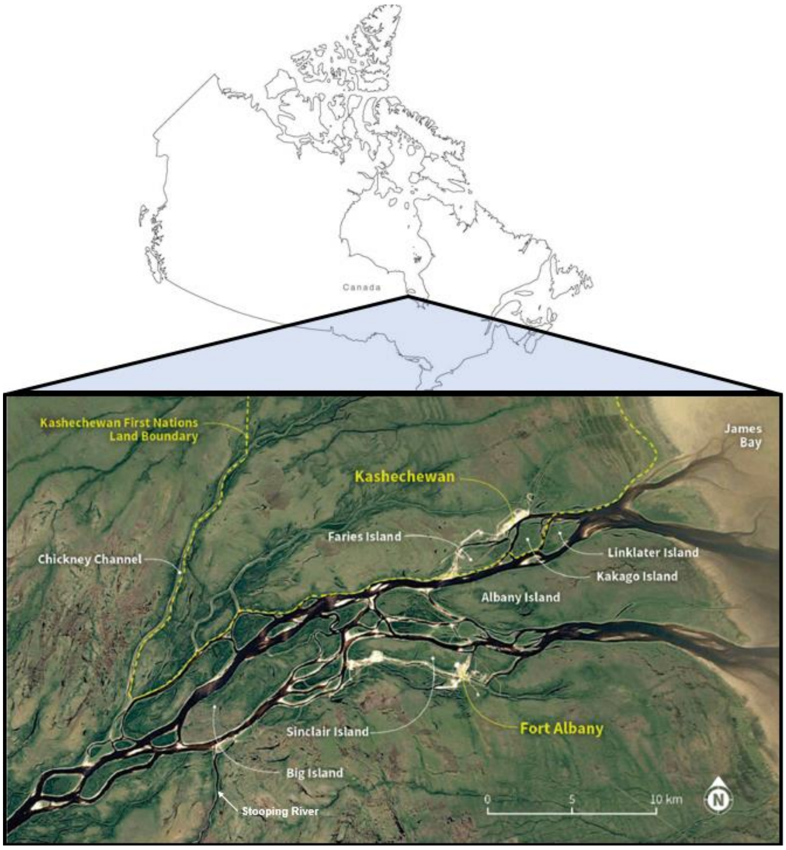

Figure 1. Lower Albany River and Study Area

Following the near miss in 2006, a remedial action plan was developed for reducing the flood risk due to ice-jamming at the community. The work was divided into two phases; 1. High Priority Emergency Measures; 2. Option Development for Permanent Remedial Works. Phase 2 commenced in 2015 with the initiation of a Flood Reduction Study. The objective of this study was to develop long-term options for reducing the flood risk to the KFN community. Phase 2 was divided into four stages. Stage 1 consisted of a detailed land survey that used airborne LiDAR remote sensing techniques to collect above water topography data and SONAR based techniques to collect under water bathymetry data. Stage 2 included a screening exercise to develop long-term "far-field" solutions (hereinafter referred to as ice control options) which refer to new structural measures not physically integral with the dyke. Ultimately, three "far-field" solutions, consisting of concrete weirs with piers and associated embankment dams were identified for further assessment in Stage 3. Stage 4 consisted of an environmental screening and high-level capital cost estimates. This paper serves to summarize Stage 3 of the study; the technical assessment of structural ice jam flood risk mitigation options for the KFN community.

Figure 2. Kashechewan Ring Dyke during 2006 Ice Jam Flood

1.1. Approach

The hydraulic characteristics of the Albany River delta are extremely complicated and necessitated the development of a two-step modeling approach using two computer simulation models. In the first step, a one-dimensional numerical hydraulic model was set up to represent the river delta and determine the open channel flow hydraulic characteristics of the study reach. These characteristics can be achieved more efficiently with a one-dimensional tool because of its relative simplicity to determine key river hydraulic parameters. The second step (and the focus of this paper) utilized the two-dimensional river ice dynamic model, DynaRICE (Shen et al. 2000), to conduct a detailed examination of ice jam formation and associated river hydraulics. This examination facilitated the assessment of ice jam flooding in the delta and the effectiveness of breakup ice control structures. DynaRICE was used to:

- Evaluate potential ice jam locations and combinations to predict the critical ice jam scenario;
- Estimate inflow discharge during the critical ice jam event;
- Estimate maximum flood levels to determine the adequacy of Kashechewan Ring Dyke crest elevation;
- Determine the quantity of ice downstream of the potential ICS locations and evaluate the potential for secondary ice jamming and ice jam related flooding at the KFN community;
- Estimate the complimentary diversion and/or storage capacity needed for ice control solution;
- Specify and layout out potential solution options; and
- Determine design criteria for, and characteristics of, potential structures such as location, elevations of key features (e.g. crest, channel bottom), and physical dimensions.

1.2. Numerical Model

Many ice processes and ice problems in river engineering projects (especially ice jam related flooding problems) cannot be adequately analyzed by a conventional model if it does not correctly account for ice dynamics. A two-dimensional ice dynamic model is required to properly assess sites with complex flow patterns and river geometries that include braided and multiple channel networks. The simulation tool selected for this study was the coupled two-dimensional river ice dynamic model DynaRICE (Shen et al. 2000). The model is capable of simulating the breakup of ice covers and the dynamic transport and jamming of surface ice in rivers. The model couples hydrodynamics and ice dynamics, including the flow through and under ice rubble. Hydrodynamics is simulated by solving the depth-integrated two-dimensional hydrodynamic equations for shallow water flows, including the effects of surface ice. The hydrodynamic component of the model uses a finite element method based on streamline upwind Petrov-Galerkin (SUPG) concept and with improved treatment of shallow water depths developed by Knack and Shen (2017). This improvement allows the model to be used for simulations that involve changes between wet and dry bed conditions, including floodplain flows. The model has been used to simulate a number of river ice jams (Shen, 2010) and river ice breakup scenarios (Knack and Shen, 2018) and provides ice cover breakup options which allow user specified breakup conditions, including breakup time, critical water surface elevation, critical water level change, or water level change relative to the ice thickness. Details of the ice breakup model are provided in Knack and Shen (2018).

1.3. Ice Management Overview

Ice jam flooding is the consequence of a combination of a high-water inflow rate to a flood vulnerable site and the accumulation of a large volume of ice in a jam downstream of that site. It follows logically that ice jam flood risk may be mitigated by: reducing the peak water inflow rate to the site by regulation or diversion, or reducing the volume of ice available to form a jam downstream of the site, or a combination of the first two, or channel modification at the downstream jam site to encourage ice to move further downstream to a ‘harmless’ location. In the case of the Albany River, the last possibility is unrealistic as harmful ice jams occur at the river’s tidal interface with James Bay and channel modifications could not improve the transport of ice into and through the estuary reaches of the river. Therefore, reducing the inflow and/or volume of ice were the only feasible objectives and could be achieved with some form of control structure(s). Fundamental, and essential, to the siting and selection of ice control structures is an adequate description of the hydraulics of the candidate river reaches. The initial location and low-level screening of candidate sites can be done most cost effectively with open water backwater calculations through the subject river reaches. Final screening and detailed design require the sophistication of two-dimensional ice mechanics modeling.

2. Model Calibration

Water level and flow data was essentially non-existent for the study area. The tidal levels at the downstream boundary (James Bay) provided the only known water levels for open water conditions. The nearest flow gauge on the Albany River with historical records was located 180 km upstream of the upstream boundary of the domain at Hat Island. Due to the lack of local open water data, selection of the channel bed and floodplain roughness parameters were based on interpretations of land cover data. This interpretation yielded a bed Manning’s n of 0.036 and a floodplain roughness of 0.15.

Limited data were available for calibration of ice parameters as well. An ice jam flood that occurred in April 2006 was the worst flood on record at the community. Anecdotal observations were used to calibrate key ice parameters. Peak water levels and flood extents were extrapolated from observations by KFN community members. The peak water level at the community was estimated to be 10.1 m. Ice thickness at breakup was estimated by scaling images of the ice chunks stranded on the riverbanks during the event. This thickness was estimated to be 1.0 m and compares well with historically observed mid-winter thickness between 1995 and 2008. The location of the ice jam during peak flooding was estimated from aerial photos which showed the toe to be just downstream of the KFN community. The flow rate during the ice jam event was estimated at the upstream boundary of the model and based on a drainage area proration relative to the Hat Island gauge. Additional secondary variables that were not possible to extract from observations were calibrated using a number of different flow and ice conditions to match the water level at the KFN community and the general ice jam observations. These secondary variables are discussed below.

- A thicker ice cover existed in both the north and south channels near James Bay, which is an extension of the cover that forms in James Bay. This thicker ice cover provided resistance to the ice jam progressing downstream during the breakup. This thicker cover and restricted progression resulted in simultaneous jams in the south branch and across the north branch.
- Breakup was initiated by a higher than the average breakup flow. This flow ensured that broken ice was flushed to the downstream end of the community. Using lower flows caused the ice to jam upstream of the community on the north branch which, in turn, shifted flows to the south branch. This shift caused flooding at the Fort Albany First Nations Community (FAFN) on the south branch of the river. However, flooding at FAFN was not observed in 2006.
- There was no ice flow into the domain from upstream during the beginning of the breakup scenario. It was assumed that this was due to an ice jam upstream of the model domain.
- When the ice jam upstream of the model domain released, ice flow resumed, as well as a sharp increase in flow. The inflow of ice traveled down to the existing ice jams and increased the volume of ice in the jams. The flow pulse consolidated the ice jam downstream of the community, significantly increasing the thickness of the jam and water levels at the community.
- There was a second period of no ice influx to the domain due to another assumed ice jam upstream of the domain. This absence of ice inflow allowed maximum flood inundations levels to be achieved at the community by eliminating the upstream progression of the ice.

Based on the calibrated ice and flow conditions noted above, the simulation of the 2006 ice breakup and jamming event proceeded as follows. Starting at hour 0 of the simulation, flow rates in the Albany River and Stooping Creek (a tributary to the south branch of the Albany River within the study domain) begin to rise (Figure 3). At hour 0.5, the ice cover broke up everywhere except for the thicker ice near James Bay. No ice comes into the model domain between hours 0 and 64, due to the assumed ice jam upstream of the model domain. At hour 50 there is a noticeable spike in flow rate due to the release of the ice jam, followed by the ice reaching the domain at hour 64. There is then a steady inflow of ice until hour 96 when the ice inflow stops again due to a second assumed ice jam upstream of the domain. A constant tidal level equal to the mean tide level, 0.75 m was used, and provided the maximum flood levels at the community. The strength of the ice cover was calibrated to be 5,000 N/m. The simulated ice jam flooding at the dyke was found to be 0.25 m below the anecdotal peak water level reported in 2006. Figure 4 shows the simulated flood inundation and peak water levels. Figure 5 shows the simulated ice jam conditions. Simulated ice and flow conditions compared well with the observations during the 2006 ice jam event.

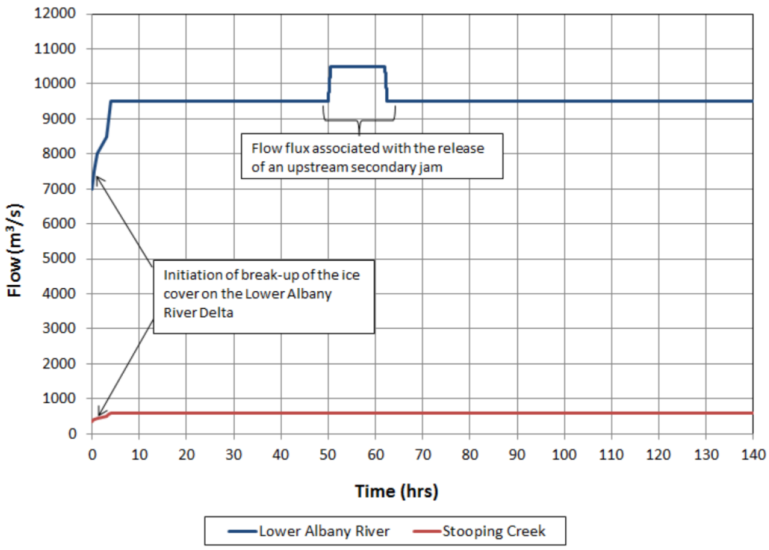

Figure 3. Upstream flow rate boundary conditions during 2006 ice jam event.

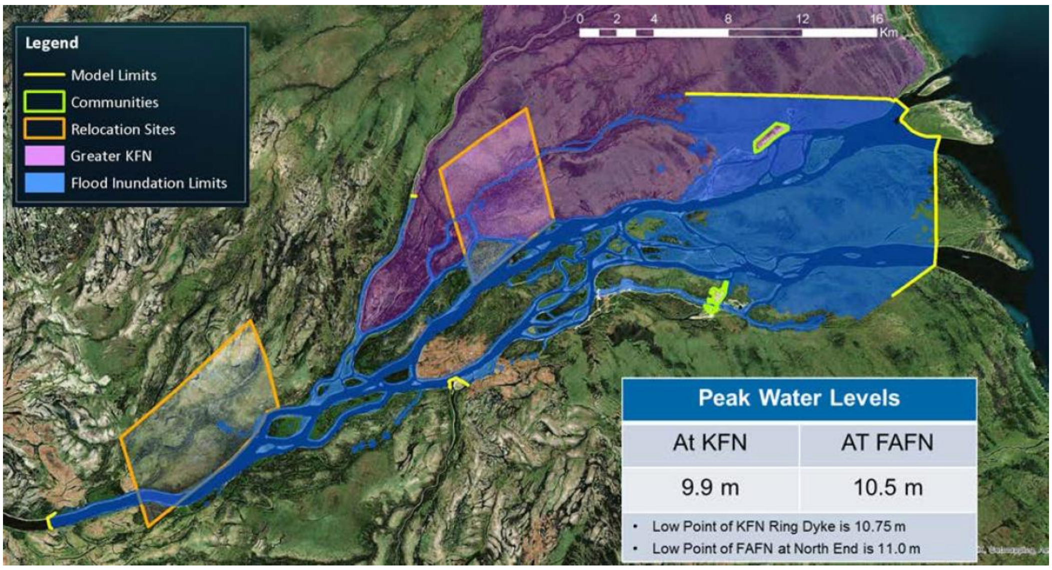

Figure 4. Peak flood inundation during 2006 ice jam event.

3. Ice Control Structure Options

The design of an Ice Control Structure (ICS) must take into account the conditions specific to a design ice event which includes discharge, ice thickness, and volume. However, equally important is the foundation conditions and river channel characteristics (e.g. bank to bank distance and length and profile of the river section in the desired ICS location). Consequently, a selection of different ICS options has historically been developed and applied to control ice breakup and limit the impact of jamming on communities. These options include: 1) Dams and Overflow Weirs – Large dam and weir structures used to retain ice; 2) Intermittent Piers Alone – Consists of boulder or concrete piers spaced across the river; 3) Weir with Intermittent Piers – Same as 2 but with a weir for improved hydraulics; 4) Ice Booms for Breakup Retention – Floating steel pipe booms positioned across the river; and 5) Wire Rope Structures – Single wire rope across the river channel.

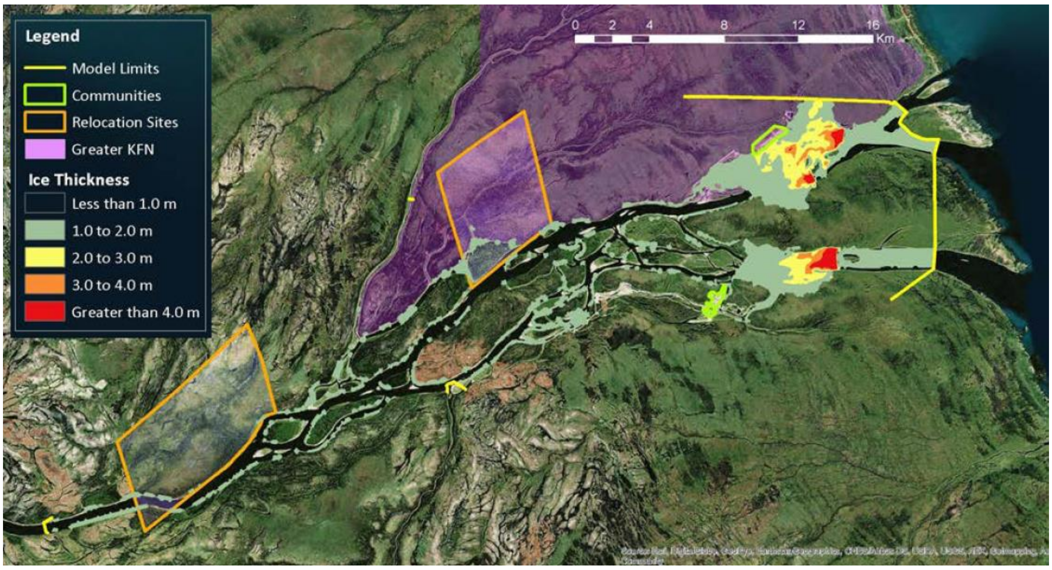

Figure 5. Ice jam conditions during 2006 ice jam event.

Each of these options can be combined with one of three flow bypass alternatives intended to pass high flows and mitigate rises in upstream water level. The bypass alternatives include: designed or naturally existing channel that diverts flow away from the ICS channel during high flow events; floodplain relief channel that passes the flow around the ice jam to the same channel using a designed or naturally existing feature; and in-channel bypass feature which directs flow around one end of the piers, used when there is insufficient floodplain area to achieve this.

Ice booms and wire ropes can be effective means to arrest ice, depending on the magnitude of the Froude number at the section of interest. The prescreening study using the open channel model determined that the Froude number was not below the critical level of 0.08 at any point of the river. Therefore, booms and ropes were dismissed as options. Large dams can also be effective in retaining ice. However, their implementation on the Lower Albany could result in significant inundation and be characterized by relatively large environmental impacts. Therefore, a large dam(s) was dismissed. The remaining two pier-based options differ only in the incorporation of a weir at the base of the piers. Both options have been proven to arrest ice and were deemed to be the most technically feasible and cost-effective means of ice retention on the Lower Albany.

The concept design of the piers was based on the equilibrium ice jam equation of Pariset et al. (1966). Assuming negligible ice cohesion during breakup, a stable ice jam will form when:

$$\frac{B'V^2}{C^2H^2} = \frac{B'Q^2}{B'^2C^2H^4} = \frac{\sqrt{B_1}Q}{B'CH^2} \leq 0.058 \qquad \textbf{[1]}$$

where, B' = open water surface width; V = flow velocity; H = the hydraulic mean depth of the section; C = Chezy flow resistance coefficient; Q = flow discharge; $B_1 = B'/(1+N)$ = width between piers; and N = number of piers. Therefore, by increasing the number of piers, thereby decreasing the value of B_1, the greater the likelihood that the value of the equation on the left will fall below the limiting value of 0.058 and a stable ice cover will form at the piers.

3.1. Ice Control Options

The site selection and ICS design procedure were based on the internal stability criterion (Eq. 1), with the Froude criterion serving as the second point of evaluation. It is acknowledged, however, that the multi-channel, braided nature of the Lower Albany River, adds to the layout and design complexity, and these criteria alone are not the sole factor in the selection and design process.

The channel geometries of the North and South branches support the majority of the flow and ice passage in the Lower Albany River delta. Therefore, to protect the community of Kashechewan and cause no additional harm to the community of Fort Albany from ice related flooding, the proposed ICS Options will need to include a method of arresting ice on the North Branch and possibly the South Branch upstream of the communities. This approach will certainly limit the volume of ice available and, depending upon design, could reduce the amount of flow contributing to the delivery of ice to a secondary jam location in close proximity to the community. In addition, locations where proposed ice control structures would offer more control of overflow distribution and intended diversion, i.e. upstream of the highly braided region, were appealing.

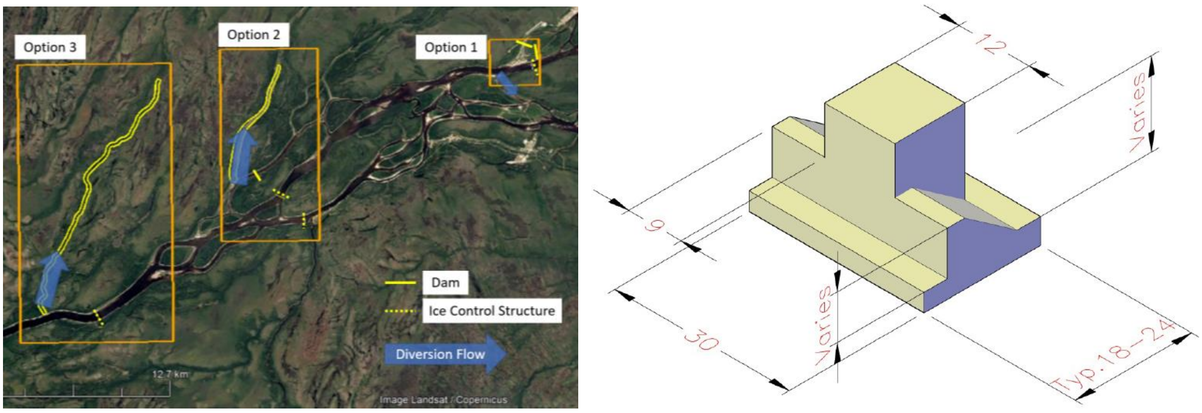

Figure 6. a) Ice Control Options for Albany River Ice Jam Protection and b) Dimensions of a Representative Concrete ICS Structure

An overall image of the relative locations of the three proposed ICS Options is presented in Figure 6a. Of the two pier-based ice retention methods, the Weir with Piers option was selected for the following reasons. The weir aids in creating favorable hydraulic conditions upstream of the structure for ice jam potential. A sizeable foundation extending from the channel invert to below the overburden layer is necessary for either option, and the additional mass of the weir structure provides added structural stability to the piers under the significant anticipated ice loads. An image of a representative ICS cell is shown in Figure 6b. The weir height above the channel invert varies and depends upon the river section geometry and associated hydraulic characteristics at each proposed location. The pier and base slab dimensions are also approximate. The design accounted for design ice forces, the riverbed soil profile and depths at the ICS location and the corresponding frictional resistance parameter values against sliding. The final design procedure for these components are described in Section 3.2.

During the screening and design process it was identified that a potential ancillary benefit of the

ICS would be the conversion of the structure to an intercommunity transport or access route by adding bridge decks for car and/or pedestrian traffic. The construction roads required to build the ICS(s) would later serve as public access roads to the bridge and possibly other locations. The maximum spacing of the ICS piers was, therefore, set at 30 m to allow for the possibility of installing a road bridge across the piers. It is acknowledged that the practicality of this additional feature is largely dependent upon the proximity of the ICS placement to the two communities.

3.2. Numerical Modeling of Ice Control Structures

It was deemed critical to evaluate the ICS design using the two-dimensional numerical model with the 2006 ice jam event as the test condition. Two-dimensional modeling allowed for the complex hydraulics and ice dynamics of the river delta to be evaluated. Several options for including the ICS in the model were considered. The structures could be removed from the finite element mesh which would automatically calculate the driving and resisting forces on the ice accumulation due to each pier. It would also include more accurate hydrodynamics at the piers by excluding the piers from the flow area. It was decided, however, that if the initial pier design was not adequate to stop the ice, that additional iterations would require remeshing the domain for each trial and would not be efficient for design. Alternatively, the ice boom option in DynaRICE could be used to determine the force distribution required to arrest the ice at the ICS location. The model calculates and outputs the force distribution and ice thickness at output times set by the user. The force distribution across the ICS location could then be used to determine the required pier spacing and dimensions at each ICS location. This method for designing the ICS piers was selected for efficiency in the design process. The force on the ice boom in the model is output as a force per unit length on each boom section, which can be defined as a model input. The highest boom load would be taken as the design load on the ICS pier used for design. The thickness of the ice jam at the boom is also recorded. Therefore, the resolution of the output can be adjusted to increase the resolution of the design parameter. The length of boom section used for output of boom force was selected as the initial pier spacing design from Eq. 1, which is 30m. This spacing was determined to have a high enough resolution for initial analysis and design. The model also considers leading edge Froude number stability as well as the critical erosion velocity for ice pieces on the underside of the jam.

The boom subroutine in the DynaRICE model was altered such that it did not start to stop ice unless the ice concentration exceeded 0.5. In this way, individual ice pieces could move through the ICS until the ice transport was high enough to cause the ice to jam at the ICS. The resisting force on the ice jam, was determined to be:

$$F_R = F_{frict} + F_N = 2\rho'\left(1-\frac{\rho'}{\rho}\right)\frac{gt}{2}(1-e)tan^2\left(\frac{\pi}{4}+\frac{\phi}{2}\right)(tL)\mu_s + F_{boom}w \qquad \textbf{[2]}$$

where, F_R = resisting force from the ICS; F_{frict} = frictional force on the pier sides; F_N = normal force on the upstream edge of the pier; ρ' is the density of ice; ρ is the density of water; t is the ice thickness at the ICS piers; e is the porosity of the ice accumulation; ϕ is the internal friction angle of ice rubble (46°); tL is contact area between the ice and the pier where L is the length of the piers in the flow direction; μ_s is the coefficient of static friction between the piers and the ice; F_{boom} is the force per unit width from the ice boom output; and w is the width of the ICS pier. For the normal force, only one pier width was used in the equation because half of each bounding pier is considered for each pier opening. Eq. 2 was then used to calculate the required pier spacing to balance the driving force with the resisting force generated from the piers.

4. Results and Discussion

The design procedure discussed in Section 3.2 was used to calculate the optimal pier spacing. Based on the initial analysis it was determined that the minimum pier length had to be 49m or the minimum pier width had to be 12m or the minimum pier spacing had to be 12m. A detailed design process was then conducted to optimize the dimensions and spacing of the piers. This method was used to evaluate the pier spacing and dimensions for all three ICS Options being considered. The analysis showed that all three options required modification to initial pier design for optimal performance for the 2006 ice jam event. The results of the simulation for ice stoppage at each ICS option also allowed for detailed analysis of the weirs and other flood protection that was associated with each option. Model results showed the need for modifications to the weirs and channel bypass design for Options 1 and 3 (see Figure 6a). Overall, two-dimensional numerical modeling proved to be critical for the design of ice control options to reduce ice jam flooding in the Albany River.

5. Conclusions

A numerical model study to evaluate ice mitigation options and to protect communities near the outlet of the Albany River in northern Ontario, Canada was conducted using the two-dimensional river ice dynamics model DynaRICE. The model was calibrated to available, and mostly anecdotal, hydraulic and ice jam observations from the 2006 ice jam event. The 2006 ice jam event was produced the most severe flood of record at the Kashechewan First Nation community. Three ice control options were developed that combined pier type ice control structures with flow diversions and weirs. Each of the three options were derived to provide the best storage of ice volume during an event while reducing flood risk for the two communities in the lower Albany River delta. Initial pier design was conducted using the equilibrium ice jam stability equation from Pariset et al. (1966). A method was developed to simulate pier type ice control structures within the model. The model allowed detailed simulation of ice retention, resulting inundation, and the forces on the individual piers. Simulations with varying ice, flow, and pier conditions were simulated to optimize the design of the piers, including pier spacing, height, and size. These simulations facilitated an examination of reducing flood inundation at the Kashechewan First Nation and Fort Albany communities by controlling river ice.

References

Knack, I.M. and Shen, H.T., 2017. Numerical modeling of ice transport in channels with river restoration structures. Canadian Journal of Civil Engineering, 44(10): 8130819. doi:10.1139/cjce-2017-0081.

Knack, I.M. and Shen, H.T., 2018. A numerical model study on Saint John River ice breakup. Canadian Journal of Civil Engineering, 45(10): 817-826. doi:10.1139/cjce-2018-0012.

Pariset, E., Hausser, R., and Gagnon, A. 1966. Formation of Ice Covers and Ice Jams in Rivers. Journal of the Hydraulics Division, ASCE, HY6: 1-24.

Shen, H.T. 2010. Mathematical modeling of river ice processes. Cold Regions Science and Technology, 62(1): 3-13. doi:10.1016/j.coldregions.2010.02.007.

Shen, H.T., Su, J., and Liu, L. 2000. SPH Simulation of river ice dynamics. Journal of Computational Physics, 165(2): 752-770. doi:10.1006/jcph.2000.6639.

25th IAHR International Symposium on Ice

Trondheim, 23 - 25 November 2020

Ice jam flood experiment using real ice around bridge piers

Taro KOIKE[1], Yasuhiro YOSHIKAWA[2], Hiroshi YOKOYAMA[3]

[1]Kitami Institute of Technology
165 Koen-cho, Kitami, Hokkaido, 0908507, Japan
m1952200121@std.kitami-it.ac.jpice
[2]Kitami Institute of Technology
165 Koen-cho, Kitami, Hokkaido, 0908507, Japan
yoshi@mail.kitami-it.ac.jp
[3]Civil Engineering Research Institute for Cold Region, PWRI
1-3-1-34 Hiragishi, Sapporo, Hokkaido, 0628602, Japan
yokoyama-h22ab@ceri.go.jp

In this study, we aimed to clarify the phenomenon of ice-jam flooding generated around bridge piers. Depositing real ice in a river channel is an integral part of investigating ice-jam flooding around river structures. However, the effects of flooding and the destructive mechanism of deposited ice have not been considered in most previous experimental studies. We chose here to conduct an ice-jam flooding experiment in a compound river channel. In the experiment, polypropylene plates and real-ice plates were used to model the river ice. In a series of experiments, we examined the speed and number of jammed plates around bridge piers according to the modeled-ice at the time of the ice-jam occurrence, the flooding situation in the high-water channel, and water level changes.

The study results are the following. (1) Because of the experimental ice jams, speed was decreased and number of plates was increased in the modeled-ice; (2) the ice in the model detoured around bridge piers and flowed in the high-water channel, but eventually flowed into the low-water channel downstream; (3) after the ice jam developed, flooding began on the upstream side of the ice-jam site. Over time, floodwaters flowed downstream from the ice-dam site; (4) flooding speed was fast when discharge was large. Over time, the flooded area stabilized; (5) in the vicinity of ice-jam sites, upstream water level increased and downstream water level decreased until sudden reversals after ice jams broke; (6) ice-jam occurrence was greatly influenced by discharge; (7) the rise in water depth apparently had a big influence on the discharge of ice.

1. Introduction

In cold regions, decreases in air temperature and flow velocity in winter cause ice formation in rivers. As temperature and flow velocity increase, river ice begins to melt, break, and flow downstream, potentially causing ice jams such as the one that occurred in Hokkaido, Japan, in March 2018 (Yokoyama et al., 2018).

An ice jam occurs with changes in river structures or characteristics. This may be where there is a gradient change, or near a river junction, at a sandbar, in a meander or curved section of a river, or around bridge piers or pylons. To model these alternatives, we designed an underground-waterway experiment by which we were able to clarify the phenomenon of ice-jam.

Researchers have in the past run ice-jam experiments using artificial ice made of polypropylene (Hara et al., 1995) or polyethylene (Wang et al., 2016). However, those materials could not reproduce the effect of ice fusion in an ice jam. Also, because the waterway shape used in those earlier experiments was a single section, they could not reproduce the multichannel flooding phenomenon characteristic of ice jams.

In our experiment, we used a compound channel that included low- and high-water channels with structural components intended to model the ice-jam phenomenon around bridge piers.

In our modeled-ice experiment, we used both polypropylene (as in past studies) and true ice (for a few study samples).

By analyzing the results of these modeled-ice experiments, we examined the speed of the modeled phenomena at the time of ice-jam occurrence around bridge piers, the area of flooding, and water level changes.

2. Ice-jam flood experimental conditions

Experimental variables include water-channel shape, discharge, discharge of ice, and model ice size relative to the ice jam that occurred in the Shokotsu River in Hokkaido in February 2010 (Yoshikawa et al., 2011a) (Yoshikawa et al., 2011b). We set up two parallel experiments: Case 1 using the modeled-ice made of polypropylene, which has a specific gravity of 0.92 (comparable to river ice); and Case 2 using the modeled-ice made of real ice, which has a specific gravity of 0.89. We tried to reproduce ice-jam breakup in Case 2.

The method for setting waterway shape was as follows: At the surface, the waterway was modeled as averaging 40.8 m in width, ranging 21.3–82.0 m; riverbed incline ranged from 1/769 to 1/126 (based on the public-section inequality-style calculation (Yoshikawa et al., 2014) result) for sections 11–20 km from the river mouth, which became the ice-jam-occurrence section.

An experimental setup and cross-section plan of the experimental water channel as well as a cross-section plan 6 m from the downstream edge are diagrammed in Figure 1. There is a bridge-pier model as a factor of ice-jam occurrence at this point. The reduced scale of the model is 1/100. The discharge of Case 1 is set to 1.4 L/s, and Case 2, to 0.7 L/s. The discharge for the emplaced- modeled-ice is the same as for Case 1 and Case 2. The size of the modeled ice was 4 cm x 4 cm and 0.6 cm thick.

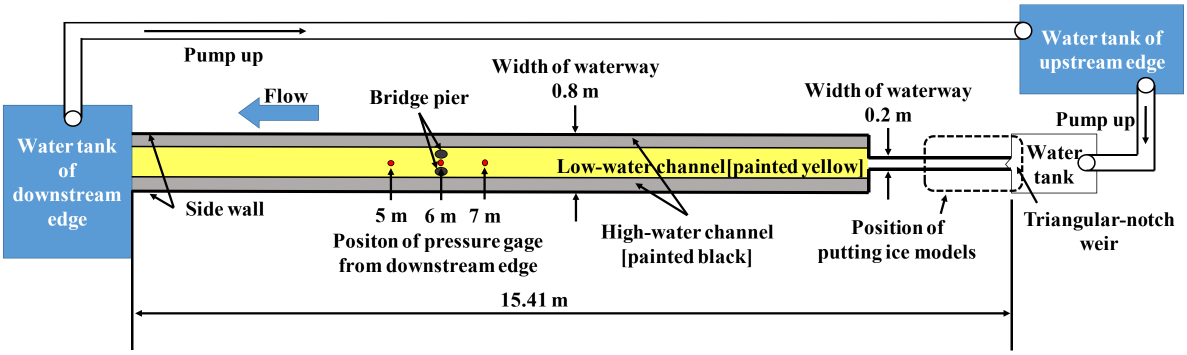

1) Experimental setup (plan)

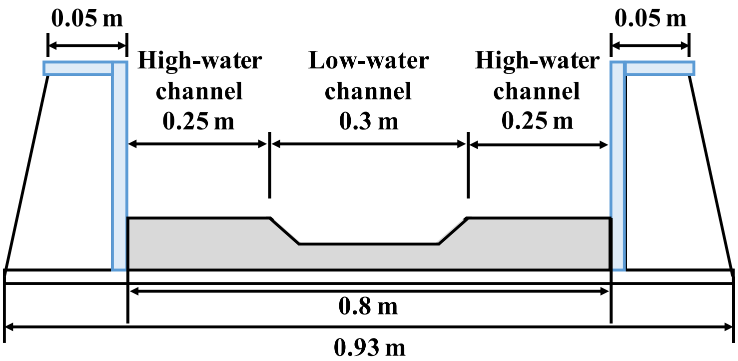

2) Cross-section

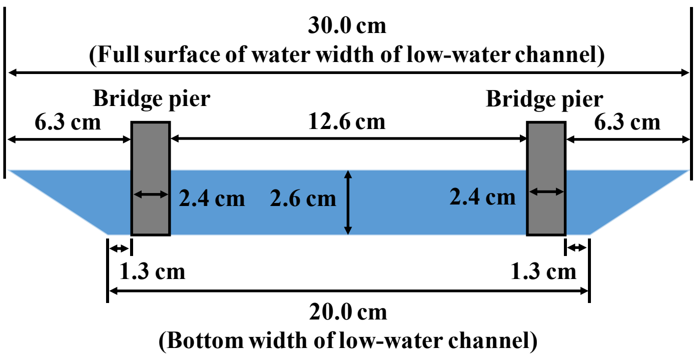

3) Cross-section 6 m from downstream edge

Figure 1. Experimental water channel.

3. Ice-jam flood experimental results

3.1 Experimental results

The experimental channels in Case 1 and Case 2 are shown in Figure 2. In Case 1, an ice jam occurred at 17 seconds from experiment start. Modeled-ice formed arching at the upstream faces of rounded bridge piers. Emplaced-modeled-ice totaled 500 pieces. There were 300 modeled-ice pieces in a low-water channel and 49 in a high-water channel. In Case 2, an ice jam occurred at 29 seconds from experiment start. At 70 seconds, modeled-ice pieces flowed downstream, as the ice jam had broken. Emplaced-modeled-ice totaled 500 pieces. In case 1, the water is colored white. In case 2, a white powder sprayed on the high-water channel. Therefore, there are differences in the appearance of the high-water channel.

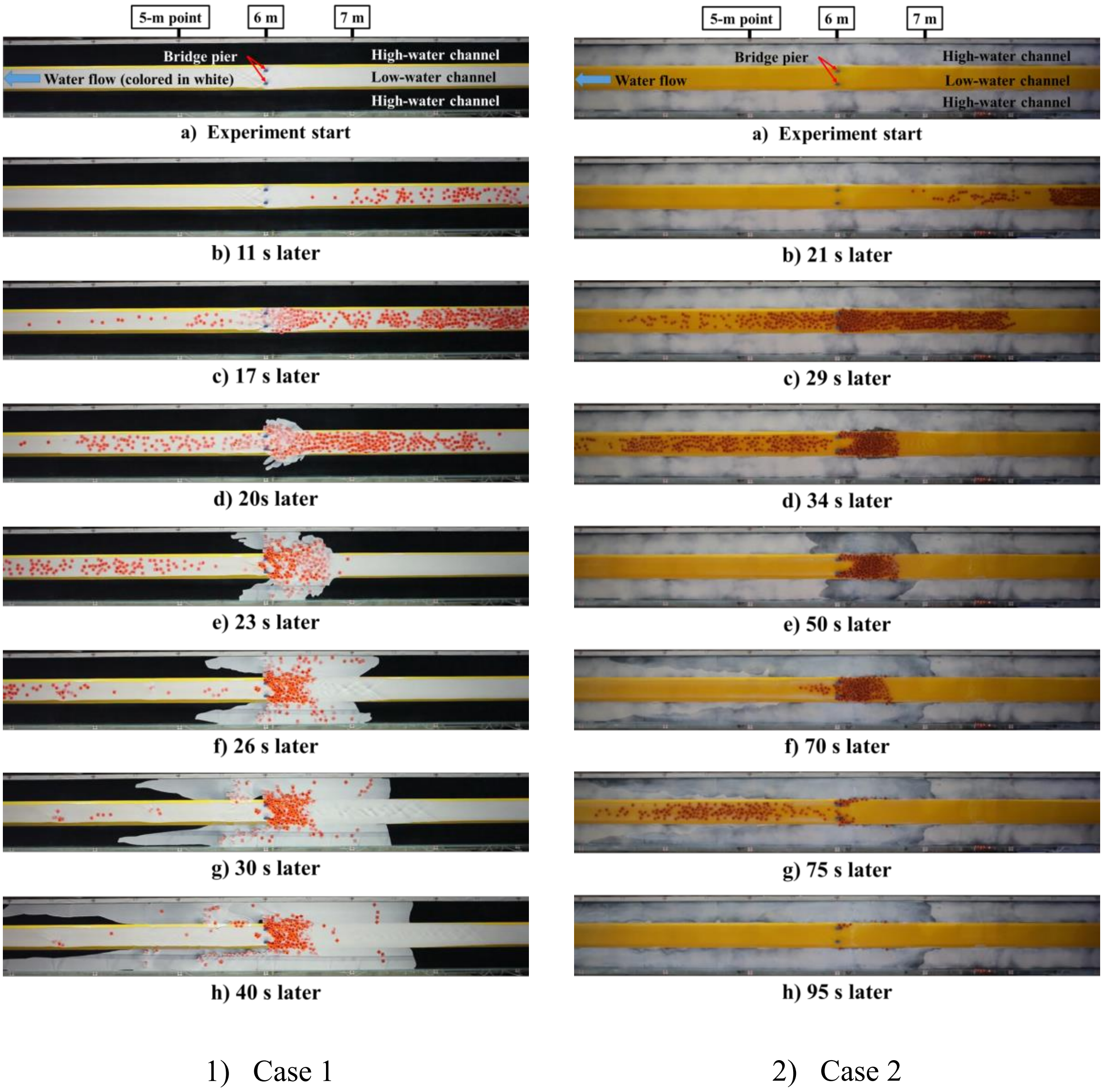

Figure 2. Experimental channels.

3.2 Modeled-ice speed and number of modeled-ice deposited on modeled ice jam

For Case 1, the change in modeled-ice speed is shown in Fig. 3, and the change over time in the number of modeled-ice deposited on the modeled ice jam is shown in Fig. 4. For Case 2, the change in modeled-ice speed is shown in Fig. 5, and change over time in the number of modeled-ice deposited on the modeled ice jam is shown in Fig. 6.

The modeled-ice speed was analyzed by particle-image-velocimetry analytical software, using a 0.0033-s analysis interval. The number of modeled-ice deposited on the modeled ice jam is the number of modeled-ice of the water surface of the range of ice-jam-occurrence (1-s analysis interval). The ice-jam-occurrence section of Case 1 is 0.5 m upstream from the bridge pier. The ice-jam occurrence section of Case 2 is at 0.7 m from the bridge pier. In Fig. 3, 5, this speed of modeled-ice is average value at ice-jam-occurrence section.

In Case 1, 300 modeled-ice pieces were deposited in the low-water channel, and water-surface modeled-ice numbered 70 pieces. About four levels (300/70 = 4.29) of 70 modeled-ice pieces exist as layers in the low-water channel of the ice-jam occurrence section. Also, modeled-ice exist across the whole area in the low-water channel, because when there are four 0.006-m-thick modeled-ice, the four-layer total is 0.024-m thick, and the height of the low-water channel is 0.026 m. The modeled-ice ran for the number of seconds needed for deposits in the low-water channel. Therefore, we estimated that the number of modeled-ice becomes small within 25 s of the experiment start. We also found no change in speed and number of modeled-ice 40 s later. In Case 2, the peak speed was reached 22 s later. At the time of ice-jam occurrence, there were 100 modeled-ice pieces. At 70 s from experiment start, ice-model pieces flowed downstream as the ice jam was breaking down.

Because of the ice jams, the speed of the modeled-ice decreased and the numbers of modeled-ice pieces increased. In Case 1, at the time of ice-jam occurrence, the modeled-ice pieces (polypropylene) detoured around the bridge piers and flowed in the high-water channel and then into the low-water channel downstream. In Case 2, the speed of the real-modeled-ice at the time of the ice-jam breakup was slower than at the time of ice-jam occurrence.

3.3 Flooding area

Areas of the high-water channel (upstream and downstream) at ice-jam occurrences in Case 1 and Case 2 are shown in Figs. 7 and 8.After an ice-jam occurrence, flooding began from the upstream side of the ice-jam site. Over time, floodwaters flowed to the downstream site. The flooding speed was fast when discharge was large. Eventually, the flooding area stabilized.

4. Water level change with ice-jam occurrence

Water level change is the value that should receive attention in the field in ice-jam occurrences. For the experiment, we measured water depth with a pressure gage.

Water level changes in Case 1 and Case 2 are shown in Figs. 9 and 10. We also calculated the water-depth ratio calculated, as h/h', where h' is the initial water depth and h is the water depth at every second.

In Case 1, by 17 s after the ice-jam occurrence, the water level of the position of 7 m from the downstream edge had risen, and the water levels of 6 m and 5 m from the downstream edge had been reduced. The 7-m water level had risen notably three times since the experiment start.In Case 2, by 34 s after the ice-jam occurrence, form of ice-jam had become similar to Case 1. By 70 s later, by which time the ice jam had broken out, the 6-m and 5-m water levels had risen rapidly about once or twice since the experiment start.

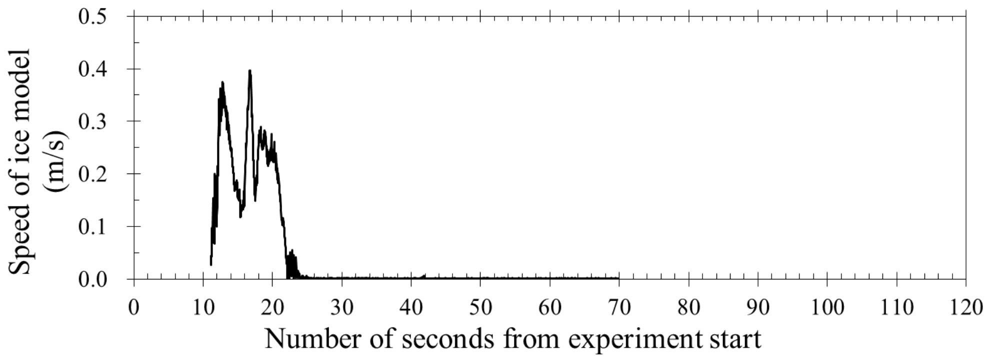

Figure 3. Change of modeled-ice speed in Case 1.

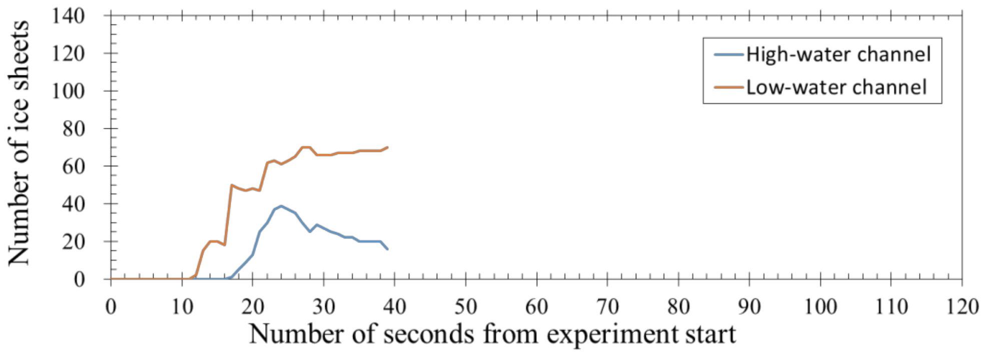

Figure 4. Number of modeled-ice in Case 1.

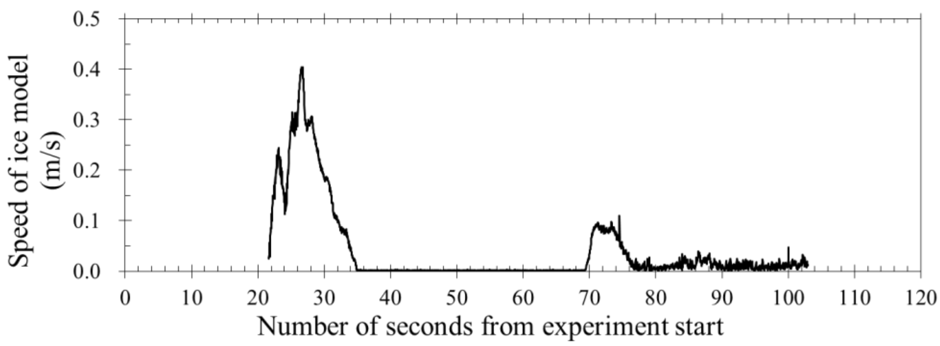

Figure 5. Change of modeled-ice speed in Case 2.

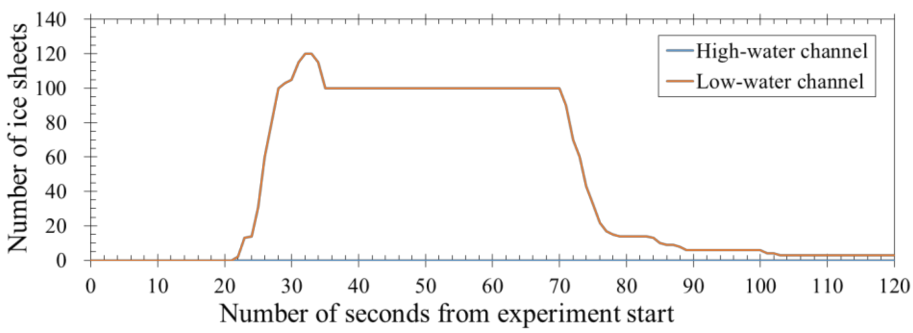

Figure 6. Number of modeled-ice in Case 2.

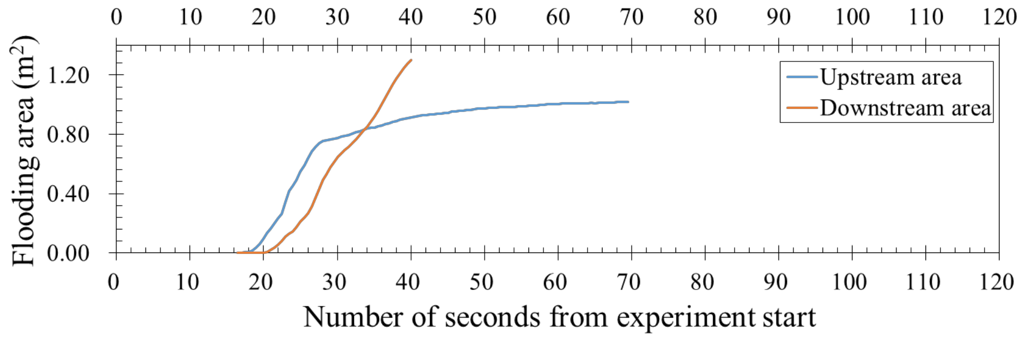

Figure 7. Areas of high-water channel at ice-jam occurrence in Case 1.

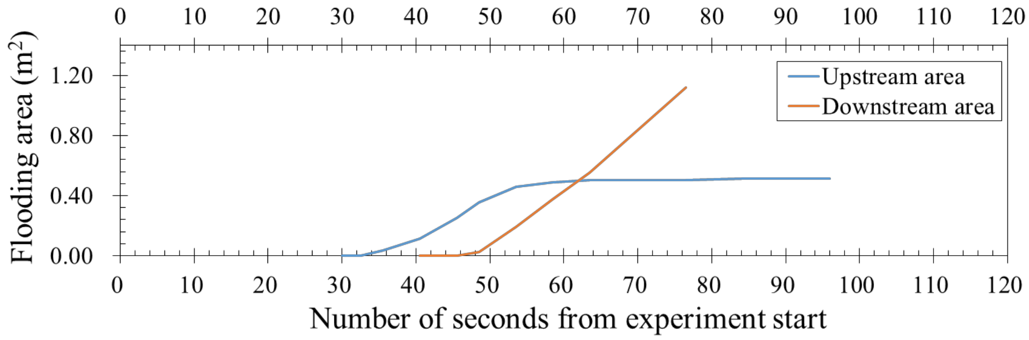

Figure 8. Areas of high-water channel at ice-jam occurrence in Case 2.

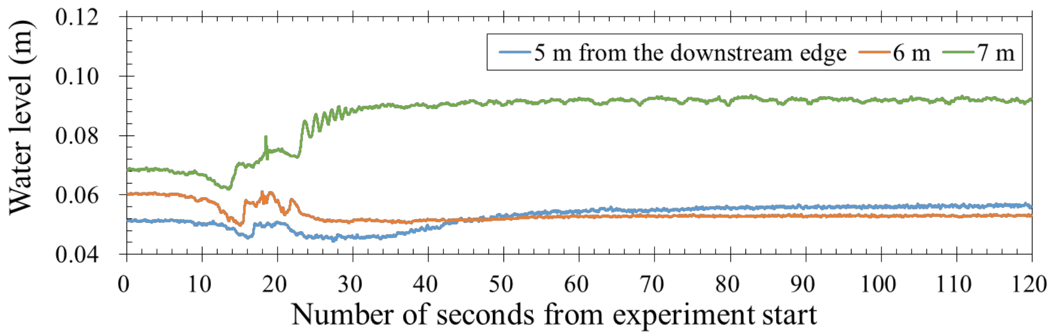

Figure 9. Water level in Case 1.

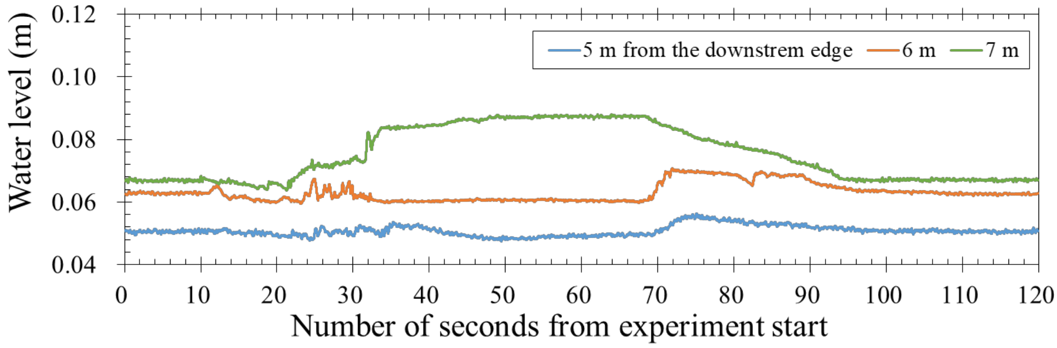

Figure 10. Water level in Case 2.

5. Conclusions

In this study, we aimed to clarify the phenomenon of ice jams generated around bridge piers. Our investigation clarified the following: We confirmed multiple changes with time as being characteristic of ice-jam occurrences, including changes in the speed and the number of ice pieces at the ice-jam site; changes in water levels in general; and, in particular, changes in high-water level as flooding progressed, and from the ice-jam breakup, changes in water level where the ice jam occurred; and in water level, changes in flooding speed; and changes in discharge.

Because of ice jams, the speed of the modeled-ice decreases and the number of modeled-ice pieces increases. The modeled-ice pieces detoured at bridge piers and flowed in the high-water channel and then into the low-water channel downstream. After ice-jam occurrence, flooding began from the upstream site and later floodwaters flowed to the downstream site. The flooding speed was fast when discharge was large. As time passed, the flooding area stabilized. At the ice-jam site, the upstream water level rose, while the downstream water level fell. Downstream, the water level increased suddenly after the ice-jam breakup.

Acknowledgments
This work supported in part by River Center of Hokkaido, Japan Society for the Promotion of Science Grants-in-Aid for Scientific Research JP18K04361 and JP17H01870.

References

Yokoyama, H., Yoshikawa, Y., Inami, Y., Maeda, S., and Yabe, H. 2018. Process understanding on the phenomena of flood damage caused by ice jam in march 2018 and future problems. Annual Journal of Hydraulic Engineering, Vol.74, No.5, pp.I_1039-I_1044.

Hara, F., Enoki, K., and Saeki, H., 1995. Study on the condition on arch formation due to ice floes at bridge piers. Annual Journal of Hydraulic Engineering, Vol.39, pp.607-612.

Wang, J., Hua, J., Sui, J., Wu, P., Liu, T., Chen, P., 2016. The impact of bridge pier on ice jam evolution – an experimental study. Journal of Hydrology and Hydromechanics, Vol. 64, pp.75–82.

Yoshikawa, Y., Watanabe, Y., Hayakawa, H., Hirai, Y., 2011a. Study of a river ice jam in the shokotsu river in february 2010. Advances in River Engineering, Vol.17, pp.353-358.

Yoshikawa, Y., Watanabe, Y., Hayakawa, H., Hirai, Y., 2011b. A study of ice break and ice flow during river ice breakup. Annual Journal of Hydraulic Engineering, Vol.67, No.4, ppI_1075-I_1080.

Yoshikawa, Y., Kuroda, Y., Itoh, A., Watanabe, Y., 2014. The relationship between ice jam occurrence and the cross-sectional profile of ice-covered rivers. Advances in River Engineering, Vol.20, pp.241-246.

25th IAHR International Symposium on Ice
Trondheim, 23 – 25 November 2020

Ice transport in rivers with training structures - the Odra River case study

Tomasz Kolerski
Gdańsk University of Technology, Department of Civil and Environmental Engineering
Narutowicza 11/12, 80-233, Gdańsk Poland
tomasz.kolerski@pg.edu.pl

Training structures are used to prevent erosion and maintain stable channels; however, their impact is also largely evident in ice transport and habitat conditions. Many European rivers were modified in the mid XVIII century to establish stable conditions for navigation and reduce side erosion. River engineering works on the Odra River were initiated in 1745 and were mainly carried out by the construction of closure structures built across secondary channels to reduce floodplain conveyance and increase the main channel depth. This river modification was proceeded until the mid XX century. This mitigation resulted in shortening the Odra length by approximately 20%; however, it does not eliminate winter floods. Flood risk reduction mainly constituted an attenuation of ice jam flooding risk in the area of Lower Odra. Currently, within the Odra-Vistula Flood Management Project (OVFMP) a number of initiatives are planned to prevent ice jam flooding. In the scope of this task, the restoration of spur dikes and construction of new structures such as stepped-up dikes or vanes is being considered. The impact of the proposed structures on ice transport along the boundary section of the Odra River is being investigated by means of applying a previously calibrated mathematical model. The DynaRICE model has been implemented at a location along the Odra River, previously selected as an ice-prone area.

1 Introduction

Major river-engineering works on large rivers in central Europe started in the middle of the XVIII century and continued over next decades. All works were aiming at prevention of side erosion and winter flooding, and insurance of rivers' navigability which was achieved by straightening and shortening the river course, island removal and dredging the riverbed and channels. In rivers like Elbe, Odra or Vistula, river course was stabilized by extensive river engineering works including closing structures built across secondary channels to reduce floodplain conveyance and increase the main channel depth. In the Odra River the process was carried out until middle of the XX centaury and caused significant reduction of large winter flood (Mudelsee et al., 2004), however it did not affect the ice jam potential of the river. Currently, according to the Regional Water Management Authority in Szczecin (RWMA Szczecin), low section of the Odra river (about 200 km), which is a border between Poland and Germany, has 28 jam prone locations stretching over more than one fourth of the river. The situation is mainly caused by negligence but also discontinuance in good engineering practices or abandonment in surveillance of river engineering structures.

Being aware of the possible flooding, Polish National Water Management Authority, recognized the urge to increase flood control in living areas at the vicinity of the Odra River valley. Therefore, Odra-Vistula Flood Management Project (OVFMP) is currently being processed. Amongst others, one of the project components aims at boosting protection against winter floods to the cities of Szczecin and Słubice, and smaller towns along the Odra River. Technically the goal should be achieved by various activities including the (re)construction of dikes and other protective works on banks, dredging the Odra riverbed and its channels and river training works. The purpose of this paper is to assess the impact of the proposed river regulation on the ice run on the Odra River in the vicinity of the city of Słubice. Two dimensional mathematical model DynaRICE is used to estimate the efficiency of selected river engineering solutions. The DynaRICE model is based upon known physical laws of ice processes , and it proves its robustness and strengths due to its computational effectiveness (Shen, 2010).

2 Hydrological data for the Odra River case study

In the duration of OVFMP, number of river training structures are planned to be renovated along the entire reach of the Lower Odra Rive. One of the locations which is planned for extensive renovation and reconstruction, is 5 km river reach near Słubice. The Polish city of Słubice is located on the right bank of the Odra River, which forms the border with Germany. According to the RWMA Szczecin, the river in the vicinity of the city is particularly susceptible to the ice jamming. As shown in (Kolerski, 2018), it is caused by river narrowing and an additional cross section reduction trigged by single bridge pier (Słubice-Frankfurt bridge). In recent years, the city was at risk of flooding caused by jamming in February 2010. All existing structures on the 5 km river reach are planned to be renovated. Structures mainly damaged to high extend are submerged spur dikes which are to be rebuilt into L-shaped and non-submerged structures.

Since winter flow characteristics were required to conduct numerical simulation of ice jam potential, the data obtained from a ten year period of water discharge recorded at Słubice gauging station were analyzed. Data are provided by hydrologic surveillance service of the Institute of Meteorology and Water Management – National Research Institute (IMWM–NRI) and for current study were retrieved at < https://dane.imgw.pl/ >. In Poland the water year is used for hydrological statistics, thus time series used for the study starts on November 1st, 2006 ending on October 31st, 2017. More recent data were not available at the time the study was conducted. The raw flow data are presented in Figure 1, and the discharge-time duration plot for average year in Figure 2. The winter season (December 1st – March 31st) is indicated in Figure 1. Since winter season is social construct, the water temperature data were also presented. However, the time series is shorter because, it ends on December 31st 2014 (Figure 1).

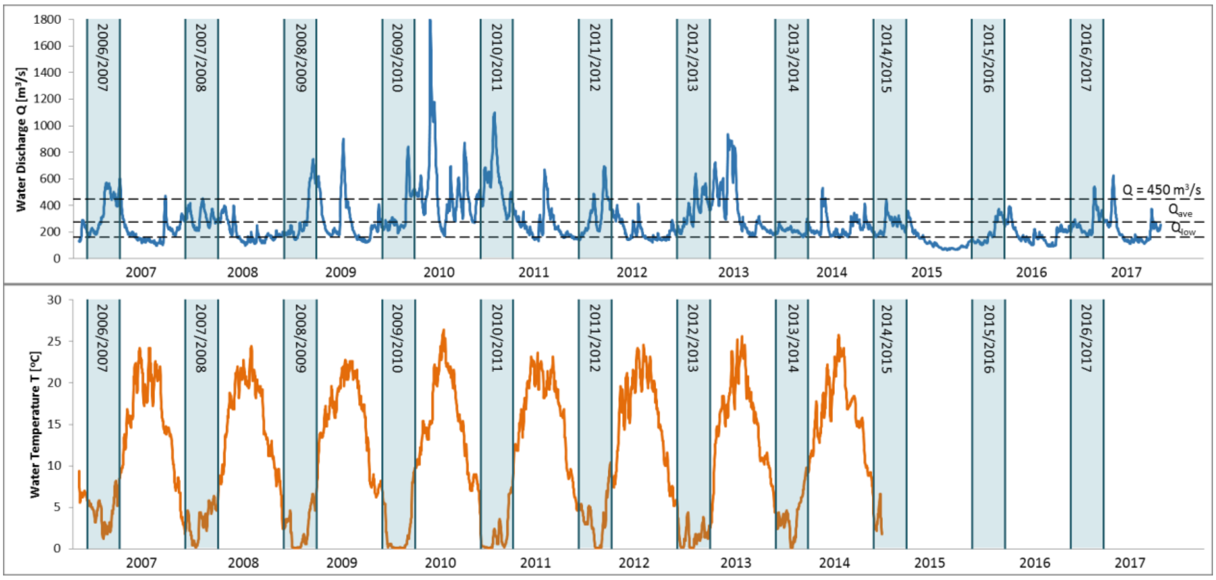

Figure 1. Water discharge and water temperature measured at Słubice gauging station; winter seasons were marked with blue, and characteristic flows by dash lines (data from https://dane.imgw.pl/).

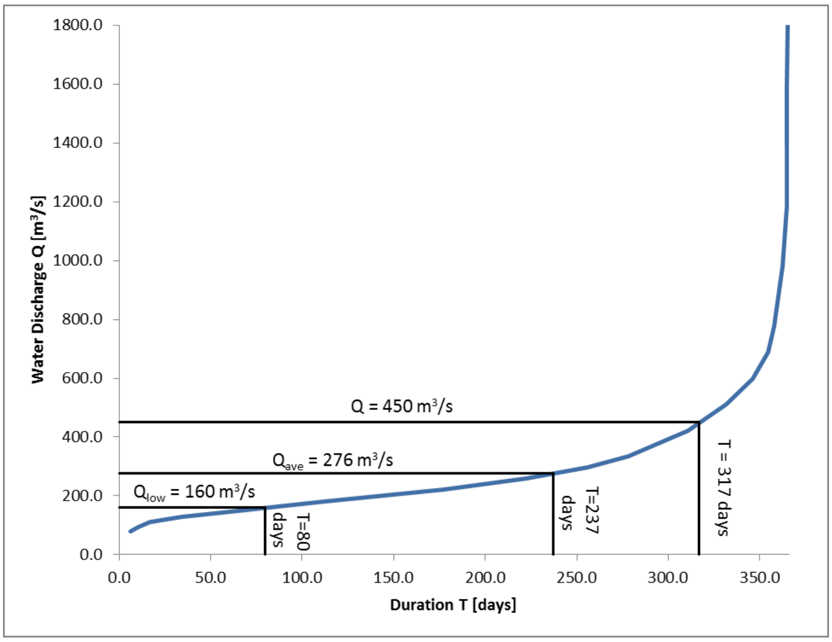

Figure 2. Water discharge duration for average year at Słubice gauging station; flows used in a study and its duration were marked with black lines (data athttps://dane.imgw.pl/).

The study considered three water discharge conditions (base on the 10 years daily average data): yearly-average flow Q_{ave}=276 m^3/s, low flow Q_{low} = 160 m^3/s and flow referring to breakup condition Q = 450 m^3/s. Regarding the beginning of the winter season, the flow in the Odra River is reduced below the average flow, barely dropping to the low flow range. In recent years the only exception was 2015/16 time period, which was affected by extreme drought in summer season. As a consequence of this drought, during the entire winter season low water level and discharge were observed. At the beginning of 2016, the water level started to rise; however, it were still in the range of low stages, which caused serious problems in releasing ice jams from the Odra River above Bielinek (km 677.2). Due to low depths (reported as 120 -160 cm), icebreakers which require up to 2 m draught, were not able to proceed upstream of mentioned location. As a result, only a part of the ice jam accumulations were released using icebreakers. Fortunately, meteorological conditions were favorable to embrace the risk of threat naturally. Air temperature in February and March stay above zero although it did not change abruptly, causing majority of the ice to melt in the place and no occurrence of rapid breakup. Based on this respect, not removing ice cover and ice accumulation could bring many problems referred to breakup ice jams.

The so called ‘breakup conditions’ ($Q = 450\ m^3/s$) are referred to the average flow starting from March. It is also the flow recorded on February 27th 2010 during the mid-winter breakup, when ice jam case in Słubice was developed due to ice sluicing. In many seasons and second half of the winter, the water discharge was rising due to increased air temperature and snow melting, as well as ice breakup. The increased discharge is more common for the mid-winter in recent years while it previously used to happen in core winter months, which is caused by changes in long-term state of the atmosphere at the region. Resultantly, mid-winter breakup may occur leading to potential jamming.

3 Jam potential

The ice cover on the Odra River is dominantly formed from dynamic ice accumulation. Typically, the process of cover development is initiated at Dąbie Lake (see Figure 3), where static cover is first formed. Next, the incoming ice floes may stop at the leading age of the ice cover on lake or flow underneath the cover. The rate of cover progression in upstream direction is affected by water flow and ice condition as well as the high water levels on the Sothern Baltic Sea through the backwater effect. Cover formed from dynamic floes accumulation has big potential for jam formation as evidenced by yearly ice reports provided by Regional Water Management Authority in Szczecin.

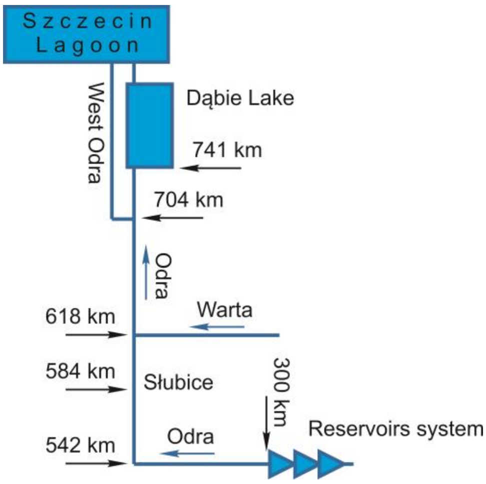

Figure 3. Schematic view of the Middle and Lower Odra River (Note: figure out of scale)

Figure 4. Polish and German icebreakers escaping to the Warta River on February 28th 2010 (railroad bridge at 615.1 river km) (RWMA, 2010)

For lower Odra, ice jams can also be unintentionally created due to ice sluicing from the system of low-head reservoirs in the middle section of the Odra River (see Figure 3). It is noteworthy that lack of coordination of the icebreaking operation on the Odra and mentioned reservoirs could significantly increase the thread of jamming in the downstream section of the river. It could be referred to the case from February 2010, when the ice sluicing started without prior consultation with management of the Polish-German icebreaking operation. Breaking the ice on reservoirs and sluicing through the spillways requires increased discharge to form a flow surge in the downstream section of river, which might causes a threat and risky situation. This is due to the fact that, if the downstream section still contains intact ice, the surge will break the cover and cause uncontrollable break up. If such actions are taken long before the icebreakers reach the leading edge of ice cover, the ice flow should be redistributed over time. In winter season of 2009/10 the 250 km of the Odra covered by ice, and the leading edge of the cover reached 491,4 km of the river. In the second part of February due to air temperatures above zero, the ice cover reduced its strength, however still remained intact in the river (km 645 - 491). Regardless of the situation on the lower section of the river, ice sluicing operation form the reservoirs was started. Realizing the threat, icebreaker crews worked with great effort nearly without stop on the Odra. On February 27th icebreakers reached the bridge in Słubice and a channel free from ice was formed. At the night of February 28th the weakened cover started to collapse due to the additional ice mass released from reservoirs and large amount of ice was shoved forming dangerous uncontrolled breakup. Under the life-threatening condition, icebreakers must flee downstream hiding in the Warta outlet (see photo taken on February 28th 2010 shown on Figure4).

To estimate the ice jam formation potential, the criteria developed by (Knack and Shen, 2017; Shen et al., 2005) were used; however some modifications were also implemented. In the current study 4 types of jam conditions were distinguished: none (0); jam weakly possible (1); jam strongly possible (2) and jam (3). No ice jam condition shows that ice proceeds without stoppage and increase in thickness, and reduction of the ice velocity. Jam conditions (1) and (2) refer to some ice velocity reduction; they also refer to increase in surface ice concentration. The weak jam condition (1) indicates increased concentration due to velocity reduction leads to some thickening. However, for this case the surface ice thickness is less than double the initial ice thickness. Strong ice jam conditions representing case with increased ice thickness to more than 2 times the initial ice thickness. Moreover, for this case the averaged-area ice velocity in initially specified location drops below 50% of averaged-area water velocity. Ice jam conditions are defined by further velocity reduction to 15% of water velocity and ice thickness increasing to 3 times the initial and single ice floe thickness. All conditions are summarized in Table 1.

Table. 1. Conditions used in the numerical modeling to determine jam potential

Jam potential	$\frac{\text{Ice velocity } (V_i)}{\text{Water velociy } (V_w)}$	$\frac{\text{Ice thinckness } (\eta_i)}{\text{Single floe thickness } (\eta_0)}$
(0) No jam	>0.9	<1.1
(1) Jam weakly possible	0.9 – 0.5	1.1 – 2.0
(2) Jam strongly possible	0.5 – 0.15	2.0 – 3.0
(3) Ice jam	< 0.15	> 3.0

4 Model application and simulation results

To check the ice condition in the vicinity of the Słubice-Frankfurt bridge, a mathematical model was applied to a 5 km stretch of the Odra River. The model was set up to simulate the ice run in the typical flow conditions expected at the beginning of the winter season and for ice breakup. The DynaRICE model was used as the most reliable model, allowing the simulation of a dynamic balance between ice dynamics and river hydrodynamics. The model was widely tested and successfully applied to a number of domains including the Vistula River (Kolerski, 2014) , Vistula Lagoon (Kolerski et al., 2019), etc.

Boundary conditions for river hydrodynamics were set to represent the flow conditions observed during core winter months. The data from Słubice gauging station were analyzed, where daily water surface elevation is recorded. Water discharge is also provided for the Słubice station. The station also has some ice thickness observations; however, this is mostly qualitative information on the ice type (Marszelewski and Pawłowski, 2019). Since detailed ice conditions for the Lower Odra River are not known, the input data for the model was set at the upstream boundary at initial ice floe thickness of 0.3 m. Calculations includes neither border ice nor cover existing in the river; it was assumed that river is free of ice and is subjected to possible jamming from breakup ice transported from upstream. This case with ice free channel was close to the situation from February 2010, when the most severe jamming condition was recorded in the vicinity of Słubice – Frankfurt bridge.

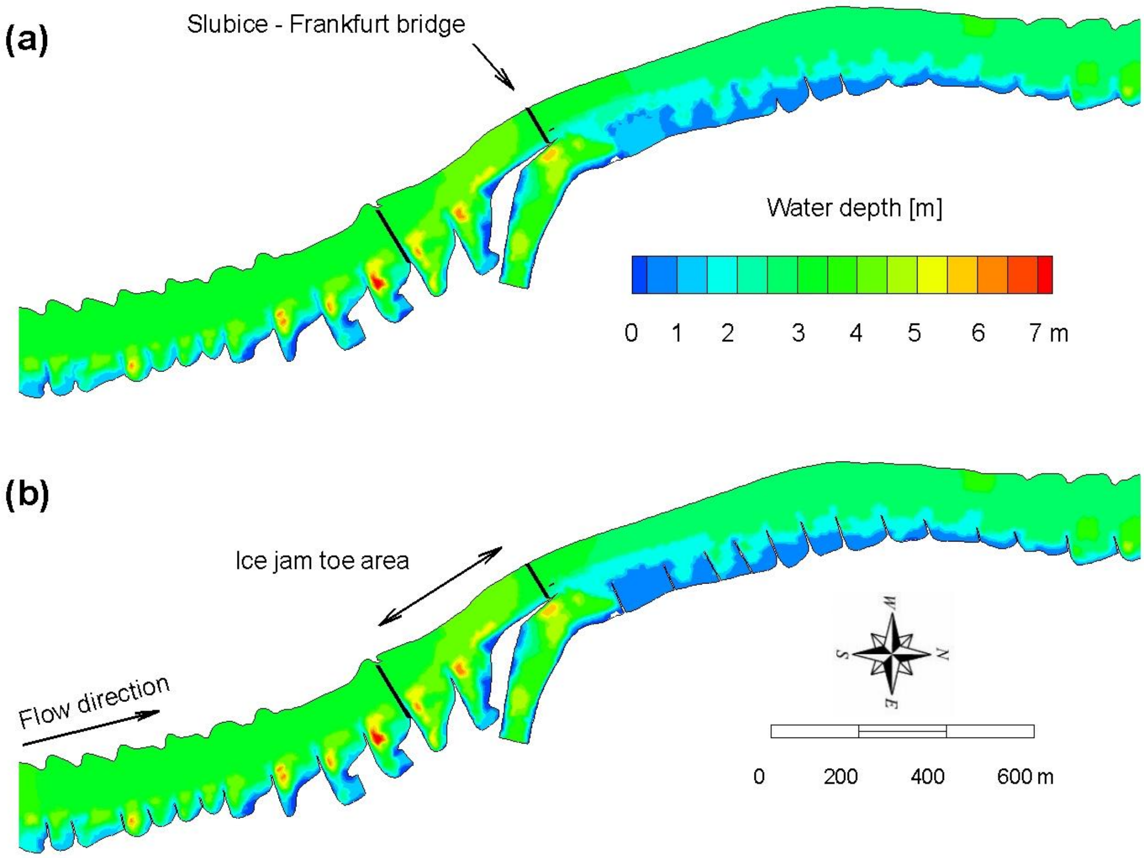

Figure 5. Water depth at average flow (Q = 276 m^3/s) for current (a) and proposed (b) conditions; sub-domain for numerical jam analysis are designated by black lines

Detailed river bathymetry and shoreline data, measured in 2017 for OVFMP, were used for the study. The data were considered to represent current state of the river which is considered to be substantially rebuilt by reconstruction or construction of spur dikes within the OVFMP. In the model domain the conditions after project implementation was taken into account by changing the shore line and including all proposed structures. Quantitative comparisons for both current and proposed river conditions are presented in Figure 5 showing water depth at average flow and outline of the existing and proposed river training structures.

Within the model domain, the sub-domain was selected where quantitative jam analysis were preceded (see Figure 5). The area includes river section of about 450 m long upstream of the Słubice – Frankfurt bridge. The location was selected based on the general trend in ice transport and high potential of that area for ice jamming and accumulation.

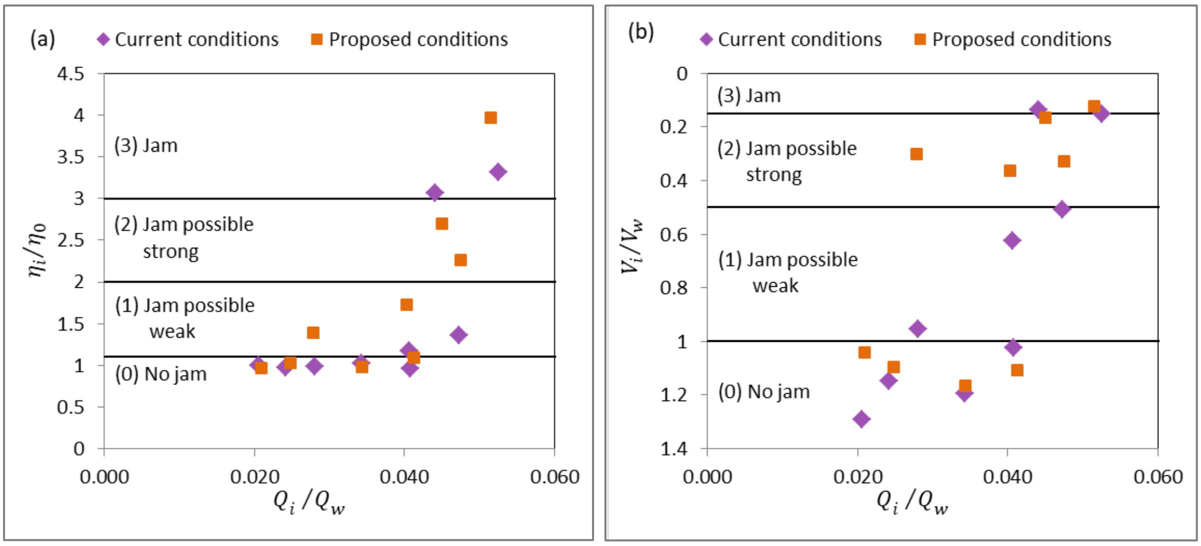

Figure 6. Numerical simulation results for Słubice showing jamming potential according to ice thickness increase (a) and ice velocity reduction (b) criteria; purple and orange clusters refer to current and proposed conditions

5 Conclusions

Simulation results are summarized on Figure 6, showing the ice jam potential for the beforehand selected location. The sensitivity analysis include wide variation of water and ice discharge, covering the conditions typical for winter months during freeze-up (most commonly low flow and low ice concentration) and breakup (flow above average with increased ice discharge). Numerical model results demonstrate that for most cases ice run was hampered by new structures. The proposed system of spur dikes are designed in extensive forms of existing structures damaged to a varying degree (Kreft and Parzonka, 2007). The spur dike extensions will perform towards flow conversion and velocity increase in the main channel; however, in the vicinity of the bridge the cross section will be reduced by newly designed structures. As a consequence, the congestion of ice due to convergence of the flow is observed. In addition, at the upstream of the river, the conveyance of the channel is increased, which results in increased ice inflow to the location prone for jamming. On the other hand, the river training structures will cause more compact and uniform main channel with increased depth, which is highly anticipated outcome from the ongoing project. That river feature will significantly facilitate ice breaking operation which is incorporated into winter flood protection program. Current river conditions preclude safe ice breaking and may lead to increased thread of flooding.

Acknowledgments
The bathymetry data used in the study were provided by Sweco Consulting and was part of the Odra-Vistula Flood Management Project – 8524 Pl, Sub-component 1A: Flood protection of areas in Zachodniopomorskie Voivodeship

References

Knack, I.M., Shen, H.T., 2017. Numerical modeling of ice transport in channels with river restoration structures. Can. J. Civ. Eng. 44, 813–819. https://doi.org/10.1139/cjce-2017-0081

Kolerski, T., 2018. Mathematical modeling of ice dynamics as a decision support tool in river engineering. Water 10, 1241.

Kolerski, T., 2014. Modeling of ice phenomena in the mouth of the Vistula River. Acta Geophys. 62, 893–914. https://doi.org/10.2478/s11600-014-0213-x

Kolerski, T., Zima, P., Szydłowski, M., 2019. Mathematical Modeling of Ice Thrusting on the Shore of the Vistula Lagoon (Baltic Sea) and the Proposed Artificial Island. Water 11, 2297. https://doi.org/10.3390/w11112297

Kreft, A., Parzonka, W., 2007. Issues related to the modernization of river regulation structures on the border section of the Lower Odra river. Infrastruct. Ecol. Rural Areas 123–134.

Marszelewski, W., Pawłowski, B., 2019. Long-Term Changes in the Course of Ice Phenomena on the Oder River along the Polish–German Border. Water Resour. Manag. 33, 5107–5120. https://doi.org/10.1007/s11269-019-02417-2

Mudelsee, M., Börngen, M., Tetzlaff, G., Grünewald, U., 2004. Extreme floods in central Europe over the past 500 years: Role of cyclone pathway "Zugstrasse Vb." J. Geophys. Res. Atmospheres 109.

RWMA, 2010. Icebreaking operation 2009/2010 report. Regional Water Management Authority in Szczecin, Szczecin.

Shen, H.T., 2010. Mathematical modeling of river ice processes. Cold Reg. Sci. Technol. 62, 3–13. https://doi.org/10.1016/j.coldregions.2010.02.007

Shen, H.T., Jayasundara, N.C., Tuthill, A.M., Mihm, J.E., 2005. Frequency and Severity of Past Ice Jams on the Grass River. Presented at the 13 th Workshop on the Hydraulics of Ice Covered Rivers, Hanover, NH, USA, p. 8.

25th IAHR International Symposium on Ice
Trondheim, 23 - 25 November 2020

Will there be an ice bridge this winter? Predicting spatio-temporal freeze-up patterns along the Yukon River, Canada

Benoit Turcotte
Formerly: Senior Hydrologist, Environment, Government of Yukon
Now: Senior Research Professional – Hydrology, Yukon Research Center, Yukon University
500 University Drive, Whitehorse, Yukon, Canada, Y1A 5K4
bturcotte@yukonu.ca

The City of Dawson, located is central Yukon, northwestern Canada, was founded at the end of the 1890s during the Klondike Gold Rush. For decades, residents of Dawson and West Dawson were able to cross the thick Yukon River ice cover every winter, from December to April. However, in the fall of 2013, a persistent open water lead in front of town prevented the preparation and certification of an ice bridge by the department of Highways and Public Works, despite a normal winter coldness (more than 3000 cumulated degree-days of freezing). Similar freeze-up scenarios occurred again during winters 2016-17 to 2018-19, when hundreds of thousands of (Canadian) dollars were spent to promote the formation of an ice cover at the usual ice bridge location.

Satellite images combined with weather and hydrometric data were used to create a model that would predict freeze-up timing and patterns on the Yukon River during the fall of 2019. Results were partially successful, confirming that more information needs to be analyzed and suggesting that some residual uncertainty would probably prevent the model from becoming perfectly accurate, especially in a context of evolving climate and morphology.

This work presents river ice formation observations on 300 km of the Yukon River, proposes a hypothesis on the potential cause of the change in freeze-up dynamics at Dawson in 2013-14, describes the empirical freeze-up model, and discusses potential research avenues and adaptation measures to improve the safe crossing of people and vehicles on the Yukon River during winter.

1. Introduction

Located in central Yukon, northwestern Canada, in the heart of the Tr'ondek Hwech'in Traditional Territory, Dawson is the historic heart of the 1898 Klondike Gold Rush. During its early days, it was one of the largest settlement in Western Canada, with a population of approximately 40,000 people, mostly gold miners. For decades, life in Dawson was dictated by ice conditions on the Yukon River (referred to as the "River" in this paper). The last sternwheeler of the season had to leave before freeze-up while people were busy preparing to survive the long, cold and dark sub-arctic winter. During the cold period, the ice cover was used for transportation and dog teams would travel 1000 km on the River to reach Dawson. In the spring, the first sternwheeler full of supplies from the south was expected with great enthusiasm after breakup. The exact date and time of breakup eventually became a lottery that continues to this day.

The relationship between the population and the river ice cover was not limited to supply transportation. Dawson was also flooded during its early days by major ice jams, as the town had been established on a low floodplain confined by Midnight Dome Mountain. Snowmelt runoff in the south reached Dawson in May and Dawsonites would watch for potential ice jams. This remained one of the only threats from the River after Dawson was connected to Whitehorse and to the rest of Canada by the Klondike highway in the 1950s. A dike was built in the mid-1980s to reduce the impact of ice jams at Dawson and it finally seemed that the population could live in peace with the River.

However, new concerns about the ice cover of the River at Dawson recently emerged. During winter 2013-14, a persistent open water lead at the normal ice bridge location prevented the certification of an official crossing from Dawson to West-Dawson. This scenario repeated in 2016-17 and 2017-18. The ice cover has once again become an important discussion topic.

In 2018, the Department of Highways and Public Works (HPW), responsible for the preparation and sanctioning of a safe winter crossing for people and vehicles, hired Canada's National Research Council (NRC) to investigate potential causes of this unusual freeze-up pattern in Dawson. The NRC concluded that (1) evolving bars (especially at the Tr'ondek [Klondike River] confluence located just upstream of town) and evolving bed conditions could have an impact on hydraulic conditions, affecting water velocities and the formation of an ice cover. Climate change (2) was also pointed out as a potential cause of altered ice formation processes. Finally, other factors such as (3) low flow conditions, (4) groundwater heat and (5) human activity were identify as potentially influencing freeze-up. The NRC also proposed potential mitigation measures to promote ice formation and thickening.

During winter 2018-19, a persistent open water lead remained in front of Dawson and HPW hired a contractor to force the formation of an ice cover and to certify an ice bridge. However, after losing a snow cat through the ice in January 2019, the effort was abandoned. Meanwhile, discussion continued between HPW and the Water Resources Branch (WRB) of the Department of Environment in Yukon to identify the most probable cause of the presence of the open water lead in front of Dawson, as well as to identify mitigation avenues. This paper presents what has been found to date.

2. Freeze-up processes along large low-gradient northern rivers

The objective of this paper is to learn more about freeze-up patterns on the Yukon River. The most relevant questions for this research are:

1. How can freeze-up processes be efficiently documented on the Yukon River?
2. Can freeze-up patterns on the Yukon River be predicted?

Beyond observing and monitoring local ice conditions, it is of interest to document ice processes happening far upstream and downstream of a location of interest, especially if the gradient and morphology are fairly constant. The best approach to answer the first question, given the remote study location, is to rely on satellite imagery. The use of optical or radar satellite imagery, often referred to as remote sensing, has been described in numerous publications (e.g., Jasek et al., 2013; van der Sander et al., 2009). Since 2013, satellites have been taking pictures of the Dawson reach of the River until mid-November; this work is described in Section 3.

To the second question, readers will be reassured that the river ice literature presents a diversity of theories and case studies about river ice formation, most of which has been summarized in *River Ice Formation* (Beltaos, 2013). Upstream progression and consolidation of an ice cover has been described (Michel, 1984) and intensively monitored (e.g., Wazney et al., 2018), and previous publications have presented ice cover formation equations that can be used to forecast freeze-up progression in large rivers since the 1960s (e.g., Pariset et al., 1966). Freeze-up jamming, an apparently chaotic process, has even been simulated (Huang et al., 2016)

Most large, low-gradient rivers present a very predictable initial freeze-up pattern. Therefore, the literature about freeze-up processes has mostly focused on resulting ice cover types, upstream progression rates and associated water levels. However, very few publications have focused on the initial part of the story: Predicting the initial ice congestion location that significantly affects subsequent freeze-up patterns and progression rates. Beltaos (2013) simply expresses that "natural constrictions or constrictions created by border ice growth are potential ice bridging sites". Referring back at the second research question, this work investigates what happens when there are several potential congestion sites and when drifting ice mostly consists of small particles (compared with the river width). Moreover, an important concept that has received little attention in the literature is that immediately downstream of a dominant ice congestion site, the formation of an ice cover only relies on the thermal migration of border ice, which can be so gradual that an open water lead may persist throughout the entire winter, even a Dawson winter.

3. Yukon River ice formation observations

A historical photo of the Yukon River taken from the Midnight Dome, 550 m above Dawson, hangs on the wall by the photocopy machine in the WRB office (Fig. 1). It clearly shows an open water lead downstream of Dawson during what appears to be late winter. This photo reveals that (on that unknown year) a congestion point was located immediately downstream of town and that this would translate into the presence of a complete ice cover in front of Dawson. This photo, generally overlooked by busy office scientists, suggests that changes in freeze-up patterns represent the most probable cause of the occasional absence of a complete ice cover in front of Dawson (especially since 2013).

After an initial interpretation of satellite imagery, it was decided that almost 300 km of river would need to be included in the chronological investigation of freeze-up patterns. Km zero of the reach of interest is located at the outlet of the White River, which mixes its turbid, opaque water with the Yukon River (Fig. 2). The reach of interest extends past the Yukon-Alaska Border to Eagle, Alaska (km 290). Optical satellite images (Sentinel 2, Landsat 8) were initially used to identify freeze-up processes such as drifting ice (mostly unconsolidated frazil slush and small floes), ice flow choking points (100% ice concentration at the water surface), congestion (stagnation of the ice cover at choking locations) and upstream progression of the ice cover by drifting ice interception.

Figure 1. Looking north (downstream) at the Yukon River (km 125 to km 135, see Fig. 2) from Midnight Dome, Dawson. River width is 500m. Date and photographer unknown.

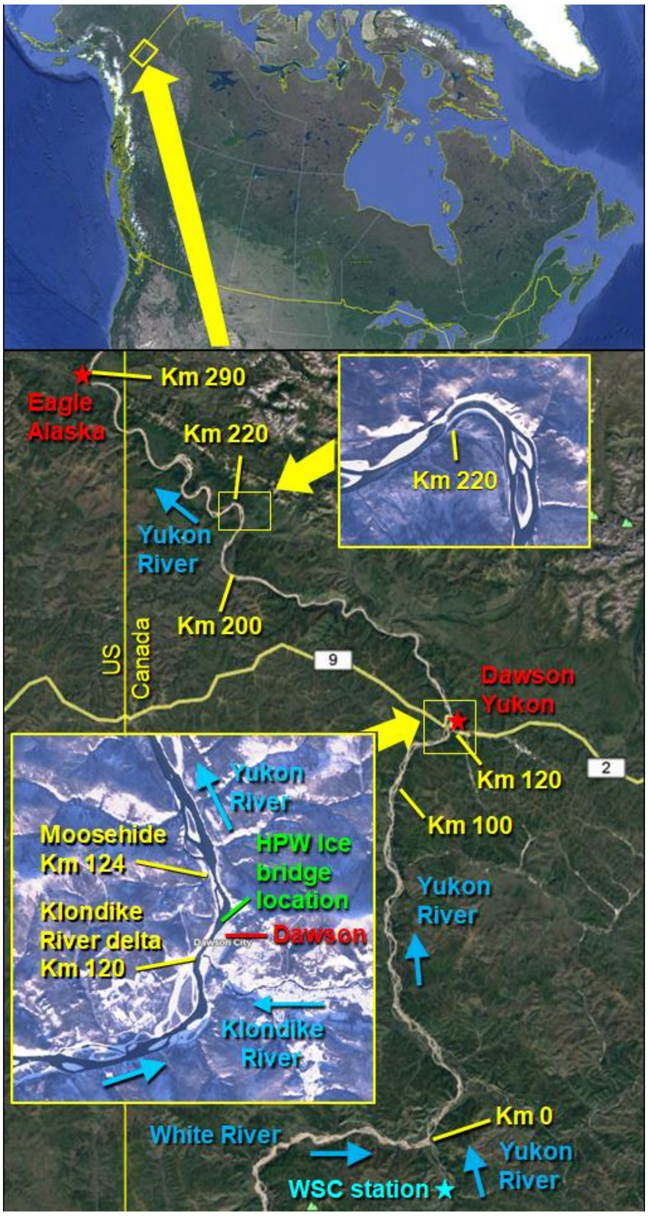

Figure 2. Location of the studied reach of the Yukon River, focusing on the Dawson segment (km 120 to 124) and on the tight meander bend located 100 km downstream (km 220).

Each relevant image was linked to a corresponding discharge (Q) estimate from the Water Survey of Canada (WSC) upstream of the White River junction (Km -20, Fig. 2), as well as to corresponding cumulated degree-days of freezing (CDDF) and daily-averaged air temperature at the Dawson City airport. The freeze-up period in Dawson is often cloudy (this was especially true in November 2016), so radar-derived ice maps from Sentinel 1 and Radarsat-2 were used, when available, to reveal freeze-up information. Key observations were:

- Primary congestion sites were located at km 220, 124 (a site called "Moosehide" just downstream of Dawson), 120 (Klondike River delta), and 0 (White River delta)
- Secondary congestion sites were located at km 240, 111, 80, 66, 27, 22 and 11
- There was no obvious congestion location between km 220 and 124
- The fastest confirmed ice front progression was about 30 km/day with an upstream ice contributing reach of 110 km (Nov 5, 2018) down to only 54 km (Nov 7, 2018)

Figure 3 shows optical satellite images of ice congestion at km 220 (a channel narrow, only 250m-wide, downstream of a tight bend). The Nov. 2 image displays loose slush being laterally compacted and released in the form of large frazil rafts (that disintegrate downstream). The Nov. 4 (estimated Q of about 720 m^3/s at km -20, 157 CDDF in Dawson) image shows the tail of the ice run, indicating very recent congestion, as well as incoming ice in the form of ice rafts. This was followed by upstream progression of the ice front, but later that process did not last (see next paragraph).

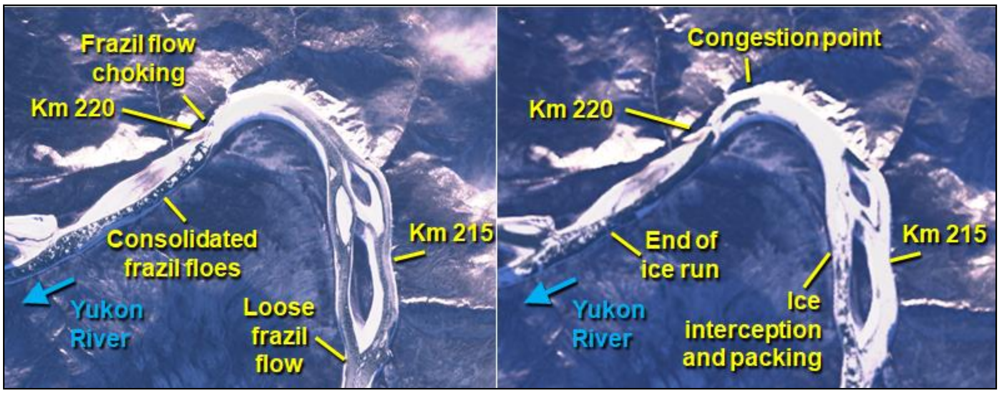

Figure 3. Ice flow choking (left, Nov. 2) and congestion (right, Nov. 4) at km 220 in 2018.

Figure 4 presents a congestion process taking place at km 120 (100 km upstream of what is presented in Figure 3), the upstream tip of Dawson, between Nov. 4 and Nov. 5, 2018. On Nov. 4 (720 m^3/s, 157 CDDF), two choking sites were competing for initial congestion: km 120 and 124. Ultimately, on Nov. 5 (710 m^3/s, 184 CDDF), Km 120 congested first, leaving the downstream segment open, with no further drifting ice to form an ice bridge at the usual km 122.5 location (and reducing ice front progression rate at km 210).

Figure 5 presents an example of a radar-derived ice map of the same Dawson reach in 2017. The dark blue color is either a very smooth ice cover (border ice) or open water with no drifting ice, the green color corresponds to moderate drifting ice concentration and the red color is a consolidated ice cover. From Nov. 7 (750 m^3/s, 195 CDDF) to Nov. 10 (610 m^3/s, 264 CDDF), 2017, moderate to intense drifting ice evolved into congestion at km 120 and upstream progression of an ice cover by packing and shoving of incoming ice, leaving the downstream reach open, including the usual ice bridge location. On Nov. 10, the ice front was located at km 105, suggesting a recent (< 24 hours) congestion at km 120.

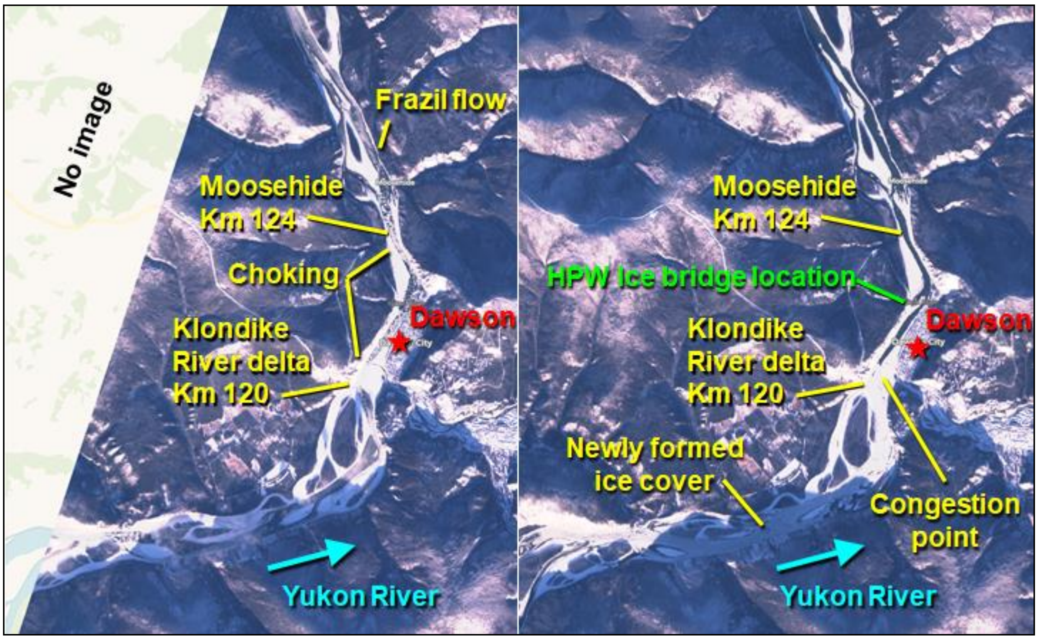

Figure 4. Ice flow choking (left, Nov. 4) and congestion (right, Nov. 5) at km 120 in 2018.

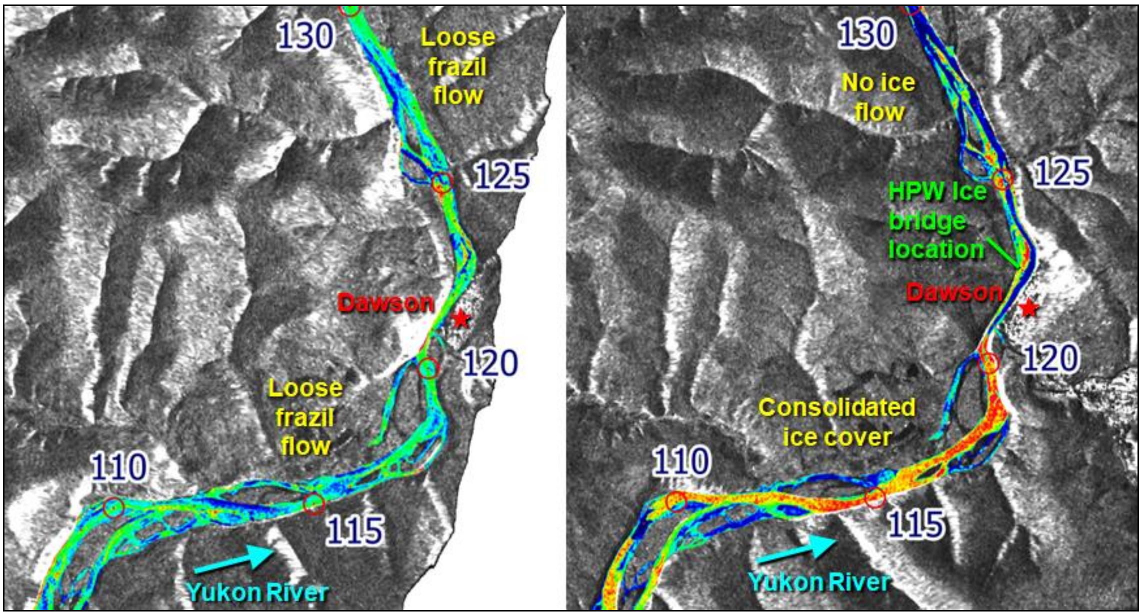

Figure 5. Radar-derived ice map showing drifting ice (left, Nov. 7) and congestion (right, Nov. 10) at km 120 in 2017.

Based on the 2013 to 2018 observations as well as local knowledge, congestion at km 120 before Km 124 (even several days after congestion at Km 220) is problematic for the preparation and sanctioning of an ice bridge at the usual location. Here is what observations revealed:

- 2018: Congestion at km 120 on Nov. 4, a day or so after congestion at km 220
- 2017: Congestion at km 120 on Nov 9 (probably), followed by km 0 and km 220
- 2016: Congestion at km 120 on Nov. 16 (probably), several days after km 220 and following a long mild period with limited ice production and transport
- 2015 and 2014: Ice cover formed at the normal ice bridge location, but no satellite data could confirm the exact location of initial congestion (probably km 220 or km 124)
- 2013: Congestion at km 120 (probably) on Nov. 14, at the same time as km 220

The reason why the ice cover was forming "normally" at Dawson before 2013 is likely due to a consistent initial congestion at Moosehide (km 124), but the reason why this initial congestion started to occur at km 120 is still a mystery. However, it is hypothesized that the combination of a major ice jam in the Klondike River in the spring of 2013 immediately followed by the highest maximum freshet flow on record contributed to mobilize a significant amount of sediment that settled on the Klondike River delta, partially obstructing the Yukon River channel. This combination of events could have created a primary ice congestion location at Km 120. Unfortunately, no satellite image was available to document freeze-up patterns or the shape of the delta before the 2013 event and this will be the topic of a future investigation, including Traditional Knowledge.

4. 2019 freeze-up predictive model results

The author believes that the timing of freeze-up and freeze-up patterns are relatively predictable, at least compared with breakup processes. This is because limited fall and early winter hydro-meteorological factors influence freeze-up sequences compared with the sum of a tremendous number of fall, winter and spring ice and hydro-meteorological factors that affect breakup. However, this does not mean that predicting freeze-up is always simple.

After winter 2018-19, an attempt was made to develop a model that would predict the timing of freeze-up in Dawson as well as to forecast the presence or absence of an open water lead in front of Dawson once dynamic freeze-up processes have ended:

- Freeze-up timing mostly depends on the heat budget. The air temperature, a readily available data, is a dominant heat budget parameter. The timing of freeze-up was therefore associated with two thresholds (Fig. 6A): Minimum CDDF (to let the water cool down to 0°C) and Maximum daily-averaged air temperatures (for enough heat loss to support massive ice production and consequent congestion).
- Freeze-up sequences often depend on water velocity and on the presence of obstacles such as emerging bars. For a given river channel (morphology), the discharge (Q) represents an indicator of both hydrodynamic conditions and emerging obstacles. It was hypothesized that a high freeze-up Q would prevent initial congestion at km 120, a relatively new congestion location. The occurrence of initial congestion at km 120 was therefore associated with a Q threshold relative to freeze-up timing (CDDF; Fig. 6B).

The resulting empirical model is summarized in Figure 7.

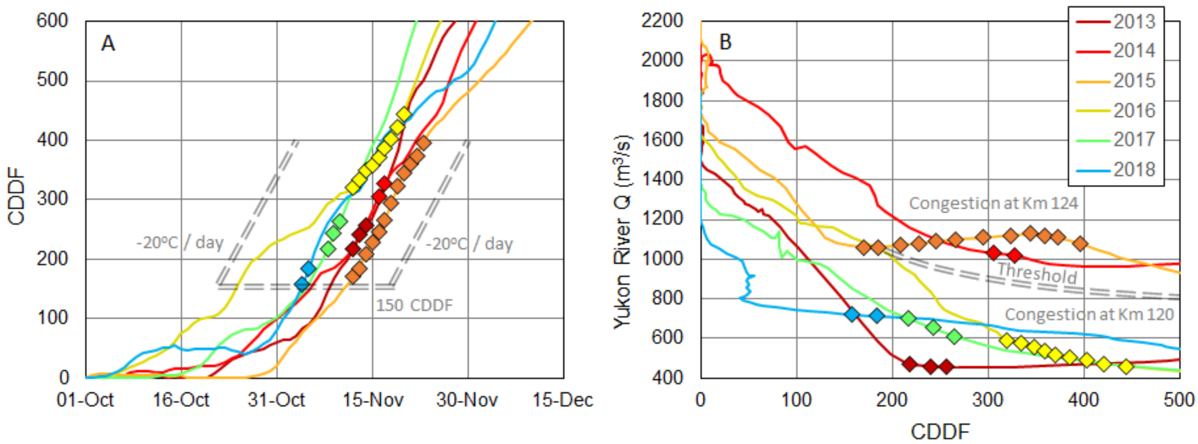

Figure 6. (A) Freeze-up timing (diamonds indicate days of initial congestion) occurring at more than 150 CDDF with daily-average air temperature below -20°C. (B) Initial congestion (same diamonds) occurring first at km 120 if Q is below the specified (approximate) threshold.

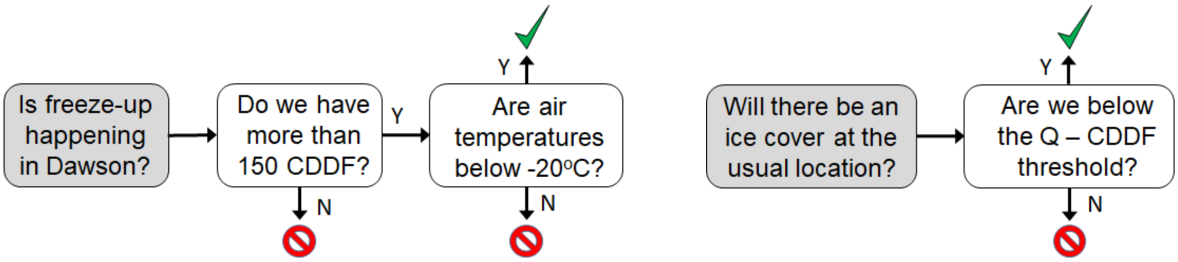

Figure 7. Summary of the empirical model derived from Figure 6.

The model was tested during the 2019 freeze-up period. Based on weather forecasts and hydrological trends, the author confidently stated on Nov. 5 that freeze-up in Dawson would occur between Nov. 7-11 and that initial congestion would occur first at km 120. This meant that another challenging winter was ahead to prepare and certify an ice bridge at the usual location. Figure 8 shows the data associated with the freeze-up of 2019 (in purple). Figure 8A confirms that the timing was reasonably predicted, with an observed congestion between Nov. 10 and 12. However, the initial congestion occurred at Moosehide (Km 124; Fig. 9) despite data points located below the approximate threshold. Hence, the author should have not been so confident about the pattern component of his model (Fig. 8B).

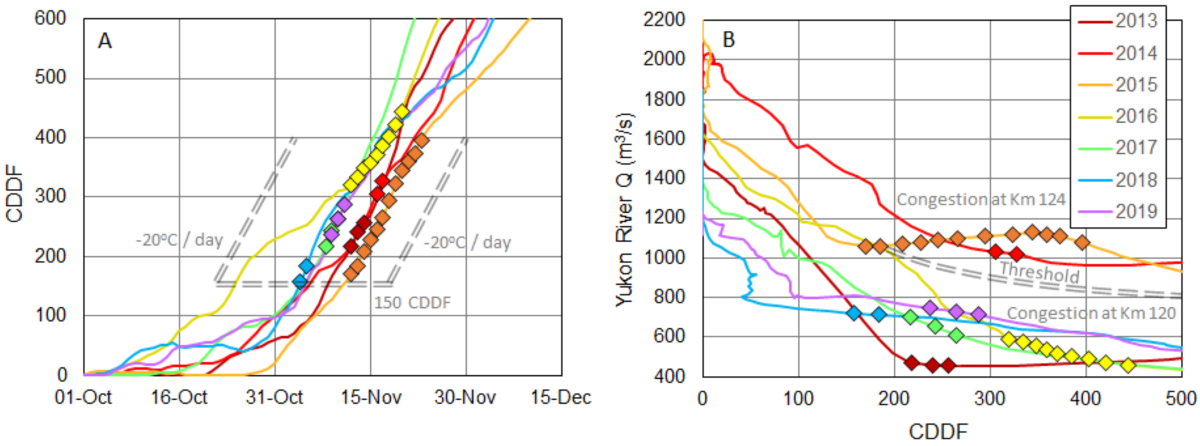

Figure 8. Copy of Figure 6 including the data of 2019. The data set in B suggests that initial congestion should have taken place at km 120, which was not the case.

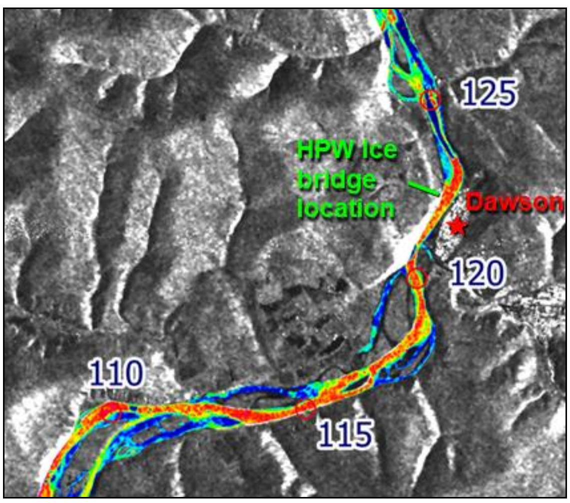

Figure 9. Radar-derived ice map of Nov. 12, 2019, confirming initial congestion at km 124, downstream of Dawson. A complete ice cover is present at the ice bridge location.

5. Future Work

The newspaper reminded the author several times during winter 2020 that the good old Dawson ice bridge was open for the first time in 4 years. Freeze-up patterns along the Yukon River from the White River to Eagle are now better understood and the timing of the initial drifting ice congestion can be predicted with reasonable accuracy. However, the location of the first congestion point (km 220, km 124 or km 120) cannot be forecasted yet with great confidence. It is a possibility that the impact of the 2013 Klondike River hydrological events on Yukon River freeze-up processes are beginning to fade through sediment remobilization. Freeze-up patterns may also simply be somewhat chaotic and the segregation presented in Fig. 6B could have been a coincidence. Freeze-up patterns in river reaches with several choking locations represent a topic to investigate further. Choking locations definitely influence one another:

- A lateral constriction of the drifting ice flow may generate enough backwater to reduce water velocities and generate initial congestion at a nearby upstream choking site (this could partially explain initial congestion at km 120 despite severe choking at km 124).
- Large rafts of compacted frazil can jam at the next downstream choking location if there are no rapids to loosen the newly compacted ice (which would be the traditional freeze-up sequence at km 124).

The later process would explain the formation of a rather smooth ice cover despite relatively high water velocities, as described by Michel (1984). In 2018, NRC determined that flow velocities in the open water lead at Dawson were above 1 m/s.

To better understand freeze-up processes in the Yukon River, the author recommends:

- Documenting the longitudinal elevation profile of the Yukon River from km 0 to 290.
- Further investigating the role of other parameters (e.g., wind or snowfall) on freeze-up patterns in order to improve the spatial component of the freeze-up prediction model.
- Creating a complementary energy budget model that would calculate, for specific congestion points and weather conditions, the amount of ice and the time needed for the ice front to reach Dawson. For example, Fig. 10 reveals that even if no congestion would have happened at Km 124 in 2019, chances are that the ice front caused by the km 220 congestion would have transited through Dawson before Nov. 16.

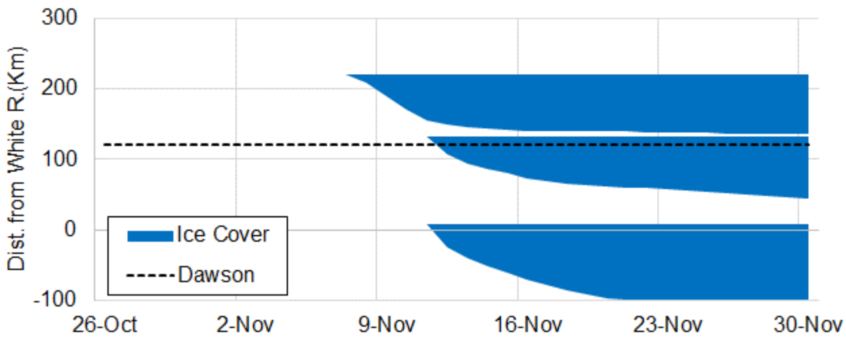

Figure 10. Spatial-temporal ice cover progression on the Yukon River between km -100 (upstream of White River) and km 300 (past Eagle, Alaska), based on 2019 satellite imagery.

Creating an ice cover at the usual ice bridge location in Dawson with an ice boom has been proposed and tested. However, beyond high surface velocities and the slushy nature of drifting ice at Dawson, it seems that the main limitation of this approach would be that drifting ice may be intercepted immediately upstream of town. In this context, a better approach, from an energy and resource consumption point of view, would be to maximize the ice conveyance capacity of the Yukon River at the Klondike River Delta (Km 120) by:

- Breaking border ice, thereby limiting any lateral choking of the drifting ice flow and releasing large border ice floes that may generate congestion at Moosehide (Km 124).
- Breaking any recently formed ice congestion, which would re-establish the flow of drifting ice and also potentially release large freeze-up ice jam floes that may generate congestion at Moosehide.

A potentially more sustainable and safer approach to promote ice formation at Dawson could also consist in removing part of the side bar formed by the Klondike River Delta, thereby improving the ice conveyance capacity of that cross-section. Nature may actually already be working in that sense, therefore explaining the poor result of Figure 8B. A similar measure would consist in modifying the gravel bar on the left side of the Yukon River at Moosehide to promote early ice congestion. However, this could be problematic, as it would increase the probability of spring ice jam flooding in Dawson, a flood-prone community.

Readers may wonder, considering the time and money invested to certify an ice bridge and to operate a ferry, why HPW has not considered a permanent bridge option at Dawson. This has been discussed in the past and the conversation continues. However, this bridge would need to be built without any pier in the channel to avoid ice jamming, which represents a span of approximately 400m. Besides technical solutions to avoid having to deal with Nature, life at Dawson has always depended on the Yukon River and the *status quo* might be appropriate.

Acknowledgments
The author would like to acknowledge that Brian Crist, Bill Stanley and Paul Murchison from the Department of Highways and Public Works have considerably facilitated this project. The National Research Council and the team led by Paul Barrette also contributed to this project through their 2018 report and subsequent discussion. The author would also like to thank Dromadaire Géo-Innovations for producing ice maps as well as Ellen Ward for providing comments to improve this work.

References

Beltaos, S., 2013. River Ice Formation. Committee on River Ice Processes and the Environment CGU-HS, Edmonton, AB, Canada.

Jasek, M., Gauthier, Y., Poulin, J., Bernier, M., 2013. Monitoring of Freeze-up on the Peace River at the Vermilion Rapids using RADARSAT-2 SAR data. Proc 17th CGU-HS-CRIPE Workshop on River Ice. Edmonton, Alberta, Canada. 1-29.

Huang, F., Shen, H.T., Li, C., 2016. Ice Transport and Jamming in Channel Bends. Proc 23rd IAHR International Symposium on Ice, Ann Arbor, MI, USA. 1-6.

Michel, B., 1984. Comparison of field data with theories on ice cover progression in large rivers. Canadian Journal of Civil Engineering 11, 798-814.

Pariset, E., Hausser, R., Gagnon, A., 1966. Formation of ice covers and ice jams in rivers. ASCE Journal of Hydraulic Division 92 (HY6), 1-24.

Van der Sanden, J.J., Drouin, H., Hicks, F.E., Beltaos, S., 2009. Potential of RADARSAT-2 for the Monitoring of River Freeze-up Processes. Proc 15th CGU-HS-CRIPE Workshop on River Ice. St-John’s, Newfoundland and Labrador, Canada. 1-14.

Wazney, L., Clark, S.P., Wall., A.J., 2018. Field monitoring of secondary consolidation events and ice cover progression during freeze-up on the Lower Dauphin River, Manitoba. Cold Regions Science and Technology 148, 159-171.

25th IAHR International Symposium on Ice
Trondheim, 23 - 25 November 2020

Creation of Artificial Mountain Glaciers as a Way of Water Supplying in Arid Regions of Central Asia

Nicolai Vasiliev
JSC «Vedeneev VNIIG»
21,Ghzatskaya, , St Petersburg, 195220, Russia
Vasiliv NK@vniig.ru
Vladimir Moiseev
Emperor Alexander I State Transport University
9, Moskovki Ave, 190031 St. Petersburg, Russia
moiseev_V_I@list.ru
Tatyana Komarova
Scientific Center «DISIST»
40, Novocherkaski Ave., 195112 St. Petersburg, Russia
komarova_tanusha@mail.ru
Olga Komarova
Scientific Center «DISIST»
40, Novocherkaski Ave., 195112 St. Petersburg, Russia
komarova_olga@list.ru

A new method of combating desertification of vast territories in south-eastern regions of Russia and in the countries of Central Asia has been proposed. The proposed method is described in detail in this paper. The essence of the method is to create artificial glaciers. It has been established that the growing threat of the transformation of vast territories into a waterless desert can be eliminated only by preserving and recreating mountain glaciers. It is assumed that the process of creating artificial glaciers will take at least 10 years. After this period, the thickness of the formed glacier can be 20 - 30 meters, and the length of two - three kilometers.This method implies the artificial creation of mountain glaciers feeding new rivers that do not yet exist at present.

1 Introduction

South-eastern regions of Russia, northern regions of India and China, as well as all the states of Central Asia are experiencing an acute shortage of water.

Without water, vast territories in these countries, where millions of people now live and work, will become a dead desert. A significant part of the water in central Asia is provided by the rivers, which are formed by the melting of mountain glaciers and masses of snow falling in the mountains in winter. The share of precipitation in the form of spring and summer rains is not large and rainwater utilization systems are not developed.

In the past three decades, there has been a global warming of the Earth's climate. Monitoring showed that the average annual air temperature on the planet during the specified time increased by 0.9 °C, while in the mountains of Central Asia it rose by almost 2.5 °C [1].

While the amount of precipitation (rain and snow) renewing snow reserves in the mountains over the past decades has remained unchanged, the rise in air temperature has caused rapid melting and "retreat" of glaciers and an irreparable loss of water contained in them. Thirty years ago in the Pamir and Tian Shan Mountains there were more than 18,000 glaciers with a total area of more than 17 thousand km^2, containing about 650 billion tons of water, but during the period 1960–2015 their total area has decreased by more than one-sixth of the original, and the increasing rise in air temperature continues and intensifies the process of their melting [2]. For example, here is a quote from press release of United Nations [3]: UN Secretary-General António Guterres stressed that Tajikistan faces unique threats from the impacts of climate change, with almost 30 per cent of its glaciers having melted in the last 10 years alone. The growing threat of turning vast territories into a waterless desert can only be eliminated by preserving and recreating mountain glaciers. It is shown [4] the key conditions necessary for glacier formation are possible at nearly all latitudes. The needs for their conservation as permanent water sources are not only for the countries of Central Asia, but also India, China, Russia, France and the countries of South America.

2 Goals and objectives

The paper addresses the challenge of providing water to arid plains of foothill areas in Central Asia and offers a solution to this challenge.

Glaciers are effective "water towers" [5], accumulating seasonal snow and ice above the snowline. Snowline is a moving border. Spring thawing of snow begins at the bottom of the mountain, and is caused by both an increase in air temperature and exposure to solar radiation. The thermal radiation power per 1 m^2 of the Earth's surface depends on the latitude of the terrain, the height above sea level, and the orientation of the section of the mountain slope relative to the Sun. On average, it can be assumed that at the latitude and altitude of the mountain slopes of the Pamir and Tien Shan, the thermal power of solar radiation is close to 1 kW / m^2 [6].

Snow and ice have a high (about 90%) reflection coefficient of solar radiation and a large (330 kJ / kg) specific heat of fusion [7].

Granite, pebbles and soil have a low (about 10%) reflection coefficient of solar radiation and a relatively small (about 1 kJ/kg ^{o}C) specific heat capacity. The specificity of the sharply continental and dry alpine climate of the countries of Central Asia is such that winter air temperatures there are very low, often there are snowfalls, summer days are hot and dry, and the nights are cold and without precipitation [8,9].

Spring melting of snow lying on the slopes of the mountains, an area of tens of square kilometers occurs in a matter of days, and hours, and is accompanied by the formation of turbulent water flows and mudflows, rushing through the mountain gorges. The high speed of snow melting is due to the fact that the sun's rays warm the open ground to a fairly high temperature, including directly at the snow line itself. The snow on the heated ground quickly melts, and the resulting water flows down the mountainside. The soil dries and heats, while the snow line moves up. After a quick snowfall, the soil and stones on the mountain slopes remain dry for weeks and months. In dry regions mountain rivers or streams dry up completely for several weeks or months in summer time. Water, precious in summer, is irretrievably lost on the foothill plains, and the steepness of the mountain slopes plays a significant role in all this.

3 Solution

The solution to the problem of stable water supply to the arid lowland foothill territories is to create artificial mountain glaciers that feed existing rivers with water.

Imagine now that in the mountains at a height close to the summer position of the snow line there is a long horizontal platform with a cold base, which does not have a slope. The snow that fell on it in winter can not melt during the whole spring - summer period and remain in this state until the next winter. This is due to the fact that the bulk of the incident solar radiation is reflected by snow. Due to its high specific heat of melting and the absence of runoff of water formed, due to the low night-time temperatures of the air, the absorbed heat of solar radiation is already insufficient to heat the soil under the snow cap. Low air temperatures and snowfall in winter will lead to the result that the snow cap on the cold ground will grow from year to year, turning into a glacier.

Extended horizontal ice platforms can be created on the basis of ice basins erected on small mountain rivers with their subsequent transformation into artificial mountain glaciers.

The idea of preserving water for spring irrigation of arid fields in ice pools was implemented by Indian engineer Chevang Norphel in Ladakh (India, west of the Tibetan Plateau) [10,11]. He created a cascade of ice pools, shown in Figures 1 - 2. The water had accumulated in the pools by the fall, in the winter it froze to the very bottom of the pool, and in the spring the ice accumulated in the pool slowly melted, forming water. Water flows through pipes to irrigation fields. These ice pools exist and they are up to 300 meters long, up to 45 meters wide and about 1 meter deep. Each pool provides periodic spring irrigation of an area of 5-10 hectares.

The mountain river is fed on an existing glacier located upstream. Typical mountain rivers have a depth of about one meter, high rocky shores, a narrow channel (several tens of meters). In summer they have a very high water consumption and high (up to 20 m/s) flow rate. The bed of mountain rivers usually consists of granite and pebbles which impede earth work and especially pile works. Also the location of the construction site at height of two-three thousand meters above the sea level hampers the delivery of heavy construction equipment. In winter, with the cessation of the melting of the feeding glacier, the flow of water in a small mountain river drops sharply until its cessation, and the river bed is exposed.

All these circumstances lead to the requirement that at the construction site assembly of structures is made of easily transportable elements only. The main work is carried out in localities in enterprises. Construction materials and structures are wood beam, screw piles and auxiliary products that provide fasteners for buildings. The main building material is also ice.

The layout of the structures necessary for the creation of an artificial mountain glacier on the mountain glacier fed river is shown in Figure 3. Five to six small reservoirs in future ice pools (two of them are shown in Fig. 3) are erected on a selected slope with ratio of inclination about 0.05 section of the glacier fed river, at a distance $l_1, l_2 \approx 100\text{-}150$m from each other.

In the proposed solution to the problem, the creation of primary ice pools having extremely low evaporation compared to evaporation from water basins is considered as the basis for the created artificial glacier.

The first stage of construction is produced in the fall at low water.

In open areas of the mountain river canyon 20 ... 30 the shallow funnels 0.5-1.0 m deep are organized using explosives. Metal heels 3 with a wide lower base are inserted into these cavities, into which short metal piles 4 with a length of 2... 2.5m are screwed. The funnels 2 are reinforced with stones and cement. Wooden beams are attached to piles 4, blocking the riverbed with barriers 5 and 6 with a height of $h_1 \sim 0.3 \ldots 0.5$ m. The very shallow reservoir 7/2 with a depth of $h_1 \sim 0.3 \ldots 0.5$ m is formed between the barriers 5 and 6.

The reservoirs are fed by streams flowing from under the glacier 1 and the practically calm water inside it is first cooled, then at air temperatures t = -10 ... -15°C it is guaranteed to freeze in 4 ... 5 days. The excess water flowing into the reservoir 7/2 is poured over the edge of the downstream barrier, forming another small reservoir behind it.

The barriers 5 and 6 provide only the quenching of the vortices characteristic of developed turbulent flows and transfer the water flow to a slightly turbulent mode of its flow.

Consequently, if a cascade of five or six small reservoirs (ice pools) 7/1, 7/2 and 7/N is located along the river, then the water flowing into the upper one from under the feeding glacier 1 completely freezes. So the artificial glacier is formed with a length of about 1000 ... 1500m. If necessary, wooden beams are attached to metal piles 4 in the following row, which increases the height of the barriers 5 and 6 to 1m. Then, the length of piles 4 can be increased by screwing another row of piles into their upper end. Pile field is completely frozen in the ice of the glacier. Piles and wooden beams can be considered as a relatively cheap consumable item and irretrievably lost, but they can also be reused by reinstalling to new places.

During the first four winter months, a mass of ice of approximately 0.5 million tons can be accumulated in the artificial glacier. With a length of 1500m and a width of the river valley 80m, the artificial glacier will have a base area 120,000m^2 and a thickness close to 4m. Thus, within 5 ... 6 years the feeding glacier can be completely restored.

Note that in summer the water flowed from the supply glacier increases rapidly and very cold glacial water will flow along the surface of the created ice pools (the artificial glacier), creating a layer that protects the ice from high warm air temperature and exposure to sunlight.

It is planned that the process of creating an artificial glacier will take from five to ten years with the gradual movement of prefabricated wooden barriers both up and downstream.

.

Fig.1. Artificial ice pool in summer, in June.

Fig.2. Artificial ice pool in winter

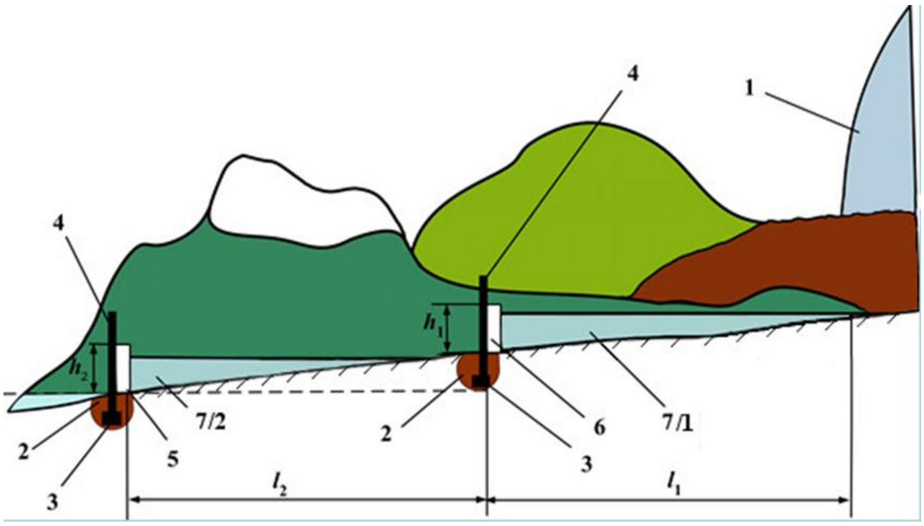

Fig.3 The layout of the structures for the creation of artificial mountain glacier.

1) – feeding glacier; 2) – funnels; 3) – metal heels; 4) – metal piles;
5) and 6) – barriers; 7/1) and 7/2) – reservoirs (ice pools).

4 Conclusions

A new method has been developed for water supply in arid foothills and combating desertification of vast territories in the south-eastern regions of Russia and in the countries of Central Asia. This method involves the artificial creation of mountain glaciers, in which the accumulation of solid precipitation during the year exceeds the amount of its melting, followed by runoff, feeding existing, now drying up rivers, and evaporation (ablation).

References

1. NOAA National Centers for Environmental Information, State of the Climate: Global Climate Report for Annual 2017. https://www.ncdc.noaa.gov/sotc/global/201713.
2. Bach, E., Radic, V., Schoof, C., 2018. How sensitive are mountain glaciers to climate change? Insights from a block model. Journal of Glaciology. **64** (244):247-258. doi:10.1017/jog.2018.15
3. Press release of United Nations SG/T/3175. https://www.un.org/press/en/2017/sgt3175. doc.htm
4. Mark, B.G. et al., 2015. Glaciers as water resources. In book: The High-Mountain Cryosphere Environmental Changes and Human Risks. Edition: FirstChapter: Glaciers as Water Resources Publisher: Cambridge University Press Editors: Huggel C., Carey M., Clague M., Kääb A.DOI: 10.1017/CBO9781107588653.011
5. Viviroli, D. et al., 2007. Mountain of the world. Water towers for humanity: typology, mapping, and global significance. Water Resources Research, 43:7, WO7447.10.10219/2006WR005653.
6. Dolgushin, L.D., Osipova, G.B., 1989. Glaciers. Mysl, Moscow, 447 p. (in Russian)
7. Paterson, W.S.B.,1981. The physics of glaciers. Oxford, Pergamon Press.
8. Shumskiy, P.A.,1978. Dynamic glaciology. New Delhi, Amerind Publishing Company.
9. Chizhov, O.P.,1969. On the Hypothesis of Ice Ages Suggested by Captain E. S. Gernet. Journal of Glaciology, **8** (63): 225-228.
10. Nelson, D.,2009. Indian engineer 'builds' new glaciers to stop global warming. The Telegraph. 28 October 2009. https://www.telegraph.co.uk/news/earth/environment/globalwarming/6449982
11. Shrager, H., 2008. 'Ice Man' vs. Global Warming. Time. 25 February 2008. http://content.time.com/time/world/article/0,8599,1717149,00.html

25^{th} IAHR International Symposium on Ice

Trondheim, 23 - 25 November 2020

Creation of Artificial Mountain Glaciers as a Way of Water Supplying in Arid Regions of Central Asia

Nicolai Vasiliev
JSC «Vedeneev VNIIG»
21,Ghzatskaya, , St Petersburg, 195220, Russia
Vasiliv NK@vniig.ru
Vladimir Moiseev
Emperor Alexander I State Transport University
9, Moskovki Ave, 190031 St. Petersburg, Russia
moiseev_V_I@list.ru
Tatyana Komarova
Scientific Center «DISIST»
40, Novocherkaski Ave., 195112 St. Petersburg, Russia
komarova_tanusha@mail.ru
Olga Komarova
Scientific Center «DISIST»
40, Novocherkaski Ave., 195112 St. Petersburg, Russia
komarova_olga@list.ru

A new method of combating desertification of vast territories in south-eastern regions of Russia and in the countries of Central Asia has been proposed. The proposed method is described in detail in this paper. The essence of the method is to create artificial glaciers. It has been established that the growing threat of the transformation of vast territories into a waterless desert can be eliminated only by preserving and recreating mountain glaciers. It is assumed that the process of creating artificial glaciers will take at least 10 years. After this period, the thickness of the formed glacier can be 20 - 30 meters, and the length of two - three kilometers.This method implies the artificial creation of mountain glaciers feeding new rivers that do not yet exist at present.

1 Introduction

South-eastern regions of Russia, northern regions of India and China, as well as all the states of Central Asia are experiencing an acute shortage of water.

Without water, vast territories in these countries, where millions of people now live and work, will become a dead desert. A significant part of the water in central Asia is provided by the rivers, which are formed by the melting of mountain glaciers and masses of snow falling in the mountains in winter. The share of precipitation in the form of spring and summer rains is not large and rainwater utilization systems are not developed.

In the past three decades, there has been a global warming of the Earth's climate. Monitoring showed that the average annual air temperature on the planet during the specified time increased by 0.9 °C, while in the mountains of Central Asia it rose by almost 2.5 °C [1].

While the amount of precipitation (rain and snow) renewing snow reserves in the mountains over the past decades has remained unchanged, the rise in air temperature has caused rapid melting and "retreat" of glaciers and an irreparable loss of water contained in them. Thirty years ago in the Pamir and Tian Shan Mountains there were more than 18,000 glaciers with a total area of more than 17 thousand km^2, containing about 650 billion tons of water, but during the period 1960–2015 their total area has decreased by more than one-sixth of the original, and the increasing rise in air temperature continues and intensifies the process of their melting [2]. For example, here is a quote from press release of United Nations [3]: UN Secretary-General António Guterres stressed that Tajikistan faces unique threats from the impacts of climate change, with almost 30 per cent of its glaciers having melted in the last 10 years alone. The growing threat of turning vast territories into a waterless desert can only be eliminated by preserving and recreating mountain glaciers. It is shown [4] the key conditions necessary for glacier formation are possible at nearly all latitudes. The needs for their conservation as permanent water sources are not only for the countries of Central Asia, but also India, China, Russia, France and the countries of South America.

2 Goals and objectives

The paper addresses the challenge of providing water to arid plains of foothill areas in Central Asia and offers a solution to this challenge.

Glaciers are effective "water towers" [5], accumulating seasonal snow and ice above the snowline. Snowline is a moving border. Spring thawing of snow begins at the bottom of the mountain, and is caused by both an increase in air temperature and exposure to solar radiation. The thermal radiation power per 1 m^2 of the Earth's surface depends on the latitude of the terrain, the height above sea level, and the orientation of the section of the mountain slope relative to the Sun. On average, it can be assumed that at the latitude and altitude of the mountain slopes of the Pamir and Tien Shan, the thermal power of solar radiation is close to 1 kW / m^2 [6].

Snow and ice have a high (about 90%) reflection coefficient of solar radiation and a large (330 kJ / kg) specific heat of fusion [7].

Granite, pebbles and soil have a low (about 10%) reflection coefficient of solar radiation and a relatively small (about 1 kJ/kg ^{o}C) specific heat capacity. The specificity of the sharply continental and dry alpine climate of the countries of Central Asia is such that winter air temperatures there are very low, often there are snowfalls, summer days are hot and dry, and the nights are cold and without precipitation [8,9].

Spring melting of snow lying on the slopes of the mountains, an area of tens of square kilometers occurs in a matter of days, and hours, and is accompanied by the formation of turbulent water flows and mudflows, rushing through the mountain gorges. The high speed of snow melting is due to the fact that the sun's rays warm the open ground to a fairly high temperature, including directly at the snow line itself. The snow on the heated ground quickly melts, and the resulting water flows down the mountainside. The soil dries and heats, while the snow line moves up. After a quick snowfall, the soil and stones on the mountain slopes remain dry for weeks and months. In dry regions mountain rivers or streams dry up completely for several weeks or months in summer time. Water, precious in summer, is irretrievably lost on the foothill plains, and the steepness of the mountain slopes plays a significant role in all this.

3 Solution

The solution to the problem of stable water supply to the arid lowland foothill territories is to create artificial mountain glaciers that feed existing rivers with water.

Imagine now that in the mountains at a height close to the summer position of the snow line there is a long horizontal platform with a cold base, which does not have a slope. The snow that fell on it in winter can not melt during the whole spring - summer period and remain in this state until the next winter. This is due to the fact that the bulk of the incident solar radiation is reflected by snow. Due to its high specific heat of melting and the absence of runoff of water formed, due to the low night-time temperatures of the air, the absorbed heat of solar radiation is already insufficient to heat the soil under the snow cap. Low air temperatures and snowfall in winter will lead to the result that the snow cap on the cold ground will grow from year to year, turning into a glacier.

Extended horizontal ice platforms can be created on the basis of ice basins erected on small mountain rivers with their subsequent transformation into artificial mountain glaciers.

The idea of preserving water for spring irrigation of arid fields in ice pools was implemented by Indian engineer Chevang Norphel in Ladakh (India, west of the Tibetan Plateau) [10,11]. He created a cascade of ice pools, shown in Figures 1 - 2. The water had accumulated in the pools by the fall, in the winter it froze to the very bottom of the pool, and in the spring the ice accumulated in the pool slowly melted, forming water. Water flows through pipes to irrigation fields. These ice pools exist and they are up to 300 meters long, up to 45 meters wide and about 1 meter deep. Each pool provides periodic spring irrigation of an area of 5-10 hectares.

The mountain river is fed on an existing glacier located upstream. Typical mountain rivers have a depth of about one meter, high rocky shores, a narrow channel (several tens of meters). In summer they have a very high water consumption and high (up to 20 m/s) flow rate. The bed of mountain rivers usually consists of granite and pebbles which impede earth work and especially pile works. Also the location of the construction site at height of two-three thousand meters above the sea level hampers the delivery of heavy construction equipment. In winter, with the cessation of the melting of the feeding glacier, the flow of water in a small mountain river drops sharply until its cessation, and the river bed is exposed.

All these circumstances lead to the requirement that at the construction site assembly of structures is made of easily transportable elements only. The main work is carried out in localities in enterprises. Construction materials and structures are wood beam, screw piles and auxiliary products that provide fasteners for buildings. The main building material is also ice.

The layout of the structures necessary for the creation of an artificial mountain glacier on the mountain glacier fed river is shown in Figure 3. Five to six small reservoirs in future ice pools (two of them are shown in Fig. 3) are erected on a selected slope with ratio of inclination about 0.05 section of the glacier fed river, at a distance $l_1, l_2 \approx 100$-150m from each other.

In the proposed solution to the problem, the creation of primary ice pools having extremely low evaporation compared to evaporation from water basins is considered as the basis for the created artificial glacier.

The first stage of construction is produced in the fall at low water.

In open areas of the mountain river canyon 20 ... 30 the shallow funnels 0.5-1.0 m deep are organized using explosives. Metal heels 3 with a wide lower base are inserted into these cavities, into which short metal piles 4 with a length of 2... 2.5m are screwed. The funnels 2 are reinforced with stones and cement. Wooden beams are attached to piles 4, blocking the riverbed with barriers 5 and 6 with a height of $h_1 \sim 0.3…0.5$ m. The very shallow reservoir 7/2 with a depth of $h_1 \sim 0.3…0.5$ m is formed between the barriers 5 and 6.

The reservoirs are fed by streams flowing from under the glacier 1 and the practically calm water inside it is first cooled, then at air temperatures t = -10 ... -15°C it is guaranteed to freeze in 4 ... 5 days. The excess water flowing into the reservoir 7/2 is poured over the edge of the downstream barrier, forming another small reservoir behind it.

The barriers 5 and 6 provide only the quenching of the vortices characteristic of developed turbulent flows and transfer the water flow to a slightly turbulent mode of its flow.

Consequently, if a cascade of five or six small reservoirs (ice pools) 7/1, 7/2 and 7/N is located along the river, then the water flowing into the upper one from under the feeding glacier 1 completely freezes. So the artificial glacier is formed with a length of about 1000 ... 1500m. If necessary, wooden beams are attached to metal piles 4 in the following row, which increases the height of the barriers 5 and 6 to 1m. Then, the length of piles 4 can be increased by screwing another row of piles into their upper end. Pile field is completely frozen in the ice of the glacier. Piles and wooden beams can be considered as a relatively cheap consumable item and irretrievably lost, but they can also be reused by reinstalling to new places.

During the first four winter months, a mass of ice of approximately 0.5 million tons can be accumulated in the artificial glacier. With a length of 1500m and a width of the river valley 80m, the artificial glacier will have a base area 120,000m^2 and a thickness close to 4m. Thus, within 5 ... 6 years the feeding glacier can be completely restored.

Note that in summer the water flowed from the supply glacier increases rapidly and very cold glacial water will flow along the surface of the created ice pools (the artificial glacier), creating a layer that protects the ice from high warm air temperature and exposure to sunlight.

It is planned that the process of creating an artificial glacier will take from five to ten years with the gradual movement of prefabricated wooden barriers both up and downstream.

.

Fig.1. Artificial ice pool in summer, in June.

Fig.2. Artificial ice pool in winter

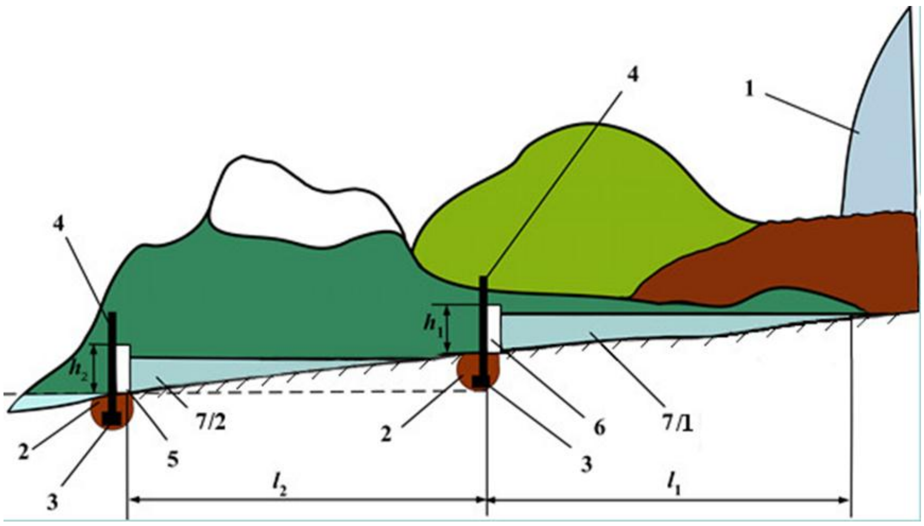

Fig.3 The layout of the structures for the creation of artificial mountain glacier.

1) – feeding glacier; 2) – funnels; 3) – metal heels; 4) – metal piles;
5) and 6) – barriers; 7/1) and 7/2) – reservoirs (ice pools).

4 Conclusions

A new method has been developed for water supply in arid foothills and combating desertification of vast territories in the south-eastern regions of Russia and in the countries of Central Asia. This method involves the artificial creation of mountain glaciers, in which the accumulation of solid precipitation during the year exceeds the amount of its melting, followed by runoff, feeding existing, now drying up rivers, and evaporation (ablation).

References

1. NOAA National Centers for Environmental Information, State of the Climate: Global Climate Report for Annual 2017. https://www.ncdc.noaa.gov/sotc/global/201713.
2. Bach, E., Radic, V., Schoof, C., 2018. How sensitive are mountain glaciers to climate change? Insights from a block model. Journal of Glaciology. **64** (244):247-258. doi:10.1017/jog.2018.15
3. Press release of United Nations SG/T/3175. https://www.un.org/press/en/2017/ sgt3175. doc.htm
4. Mark, B.G. et al., 2015. Glaciers as water resources. In book: The High-Mountain Cryosphere Environmental Changes and Human Risks. Edition: FirstChapter: Glaciers as Water Resources Publisher: Cambridge University Press Editors: Huggel C., Carey M., Clague M., Kääb A.DOI: 10.1017/CBO9781107588653.011
5. Viviroli, D. et al., 2007. Mountain of the world. Water towers for humanity: typology, mapping, and global significance. Water Resources Research, 43:7, WO7447.10.10219/2006WR005653.
6. Dolgushin, L.D., Osipova, G.B., 1989. Glaciers. Mysl, Moscow, 447 p. (in Russian)
7. Paterson, W.S.B.,1981. The physics of glaciers. Oxford, Pergamon Press.
8. Shumskiy, P.A.,1978. Dynamic glaciology. New Delhi, Amerind Publishing Company.
9. Chizhov, O.P.,1969. On the Hypothesis of Ice Ages Suggested by Captain E. S. Gernet. Journal of Glaciology, **8** (63): 225-228.
10. Nelson, D.,2009. Indian engineer 'builds' new glaciers to stop global warming. The Telegraph. 28 October 2009. https://www.telegraph.co.uk/news/earth/environment/ globalwarming/6449982
11. Shrager, H., 2008. 'Ice Man' vs. Global Warming. Time. 25 February 2008. http://content.time.com/time/world/article/0,8599,1717149,00.html

IAHR AIRH

25th IAHR International Symposium on Ice
Trondheim, June 14 to 18, 2020

Flow Discharge Estimation Method considering River and Crystal Ice Thickness, HQ Equation, and Measured Values during the Freezing Period

Hiroki YABE[1), Osamu OHNO[1), Hiroshi YOKOYAMA[1)
[1) *Civil Engineering Research Institute for Cold Region*
Public Works Research Institute
Sapporo and Kushiro, Japan
yabe-h@ceri.go.jp
oono-o22aa@ceri.go.jp
yokoyama-h22ab@ceri.go.jp

Continuous flow discharge at the period of a frozen river is the important data for estimating water intake problems, water level rise and flooding caused by ice jams.

The observation of water level and discharge is measured three times a month, and we estimate the continuous flow discharge using water level-discharge curve (H-Q equation) during periods other than the observational day. However the automatic water level observed during the freezing period is not accurate because it includes the thicknesses of river and crystal ice. These ice obstruct river flow, and change with time. Therefore, we have to substitute the water level considering these thicknesses into the H-Q equation in order to improve the accuracy of continuous flow estimation. Furthermore, since the river roughness coefficient during freezing period is different from it during the non-freezing period, it is necessary to apply the H-Q equation using the flow observation data during freezing. In this study we propose a continuous flow discharge estimation method that combines the estimated values of river and crystal ice thickness using the heat balance method, the H-Q equation considering these thickness during the freezing period, and the measured values.

We obtained the hourly temperature, sunshine, wind speed, snowfall depth, and river water level data to apply the heat balance method at the target point. As a result of applying this model to the data for 12 years, it was divided into cases where the river ice thickness could be estimated approximately, the estimated values were oversized, underestimated, etc. When there is a difference between the estimated value and the measured value, the modified model with the measured value added as additional information was constructed and applied. As a result, the accuracy of river ice thickness estimation after the actual measurement date was improved.

1. Introduction

Understanding the continuous discharge of rivers that freeze in winter is vital in estimating water intake failures for water supply system, rising water levels, and inundation due to ice jams. Discharge observations are generally performed about three times a month, and the continuous discharge (Q) during the period in which measurements are not done is estimated from the continuously measured water level (H) using the H-Q equation. However, the accuracy of the continuous water level observed by the automatic water level gauge during the freezing period is often low because the measurements often include the thicknesses of river ice and frazil ice. The thicknesses of river ice and frazil ice are not included in the sectional flow area, and they change with time.

Therefore, to improve the accuracy of the continuous discharge data, the discharge (Q) must be obtained by substituting the water level (H') into the H'-Q equation after taking these thicknesses into consideration (i.e., subtracting these thicknesses from the measured water level). In addition, when the river is frozen over, it becomes a pipe channel instead of an open channel. Since the river roughness coefficient differs from that during the open-water season, it is necessary to apply an H'-Q equation that is constructed using flow observation data from the freezing season.

From the above, we proposed a method for estimating river ice thickness using a heat balance method, an H'-Q equation that considers river ice thickness during the freezing period, and a continuous flow rate estimation method that combines the measured values.

We collected data on hourly air temperature, sunshine, wind speed, snow depth, and river water level during the freezing period from December 2007 to March 2019 to estimate the temporal changes in river ice thickness at the target point. We applied the data to a model that uses the heat balance method. The values estimated by this model were modified using the measured values according to the degree of difference between the estimated value and the measured value of river ice thickness. And the H'-Q equation for the freezing period was constructed using the water level and discharge observation data from January 2008 to March 2018.As a result of this model modification, we were able to improve the estimation accuracy of river ice thickness and discharge for the period during which ice thickness measurements were not performed between the measurements.

2. Estimation of river ice thickness

2. 1 River freezing, and the discharge estimation

Ice formation patterns in rivers are categorized roughly into two. One freezing pattern takes place in a calm section without considerable currents. Border ice gradually forms along the bank and grows toward the center of the river section until the river freezes over. The other pattern takes place in most natural channels with turbulent flows, where fine crystals called frazil ice first form, before bonding together while flowing down the river. Frazil ice gradually aggregates, increases in size and floats to the water surface, which stops the flow at a section with mild currents and causes that section to freeze over. It has been confirmed that the freeze-over of a calm river section is greatly affected by the air and water temperatures. The conditions for the freeze-over of a river section where frazil ice and its stagnation are the main factors in the freeze-over also include river hydraulic factors (flow velocity, water depth, etc.)[1).

An example of the cross-section at the time of river freezing is shown in **Fig. 1**. For estimating the discharge at such a cross-section for which continuous river water level data are available, there are two methods. One is an estimation performed directly from the water

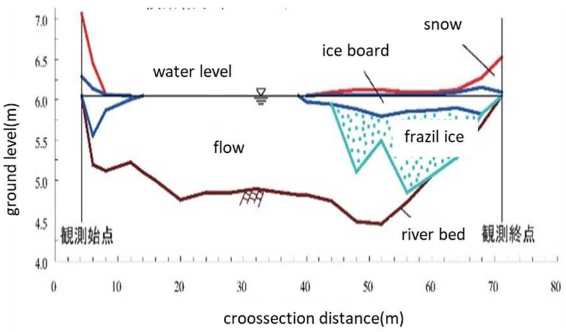

Fig. 1 An example of a transverse survey of a frozen-over river

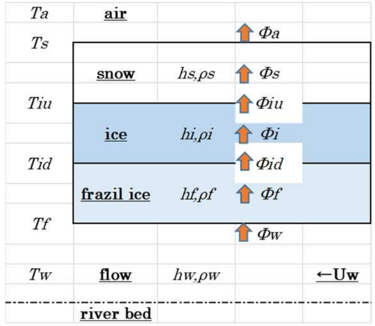

Fig. 2 A conceptual diagram of the heat balance in a frozen-over river

level using the H'-Q equation for the time of freezing. In the other, the water level is obtained from a relational expression between the cross-sectional area of the river flow and the discharge at the time of freezing. Then, the discharge is obtained by using the cross-sectional area. Both estimation methods need river water level data, and in this study, we examined a simpler H'-Q equation estimation method for the time of freeze-over.

When calculating the river water level at a cross-section with flowing water, we need to subtract the river ice thickness from the river water level that is automatically and continuously observed. Therefore, the following estimation formula was applied to estimate the continuous river ice thickness.

2. 2 Estimation of river ice thickness using the heat balance method[2),3)]

(1) Derivation of the formula for estimating the river ice thickness

The process of deriving an equation for estimating river ice thickness (ice sheet thickness) is outlined below. The heat balance method is applied to construct the basic formula. The heat balance is the balance between heat that comes in and heat that goes out. It is expressed by the law of conservation of energy: [(thermal energy input) - (thermal energy output) = thermal energy storage].

A conceptual diagram of the components of heat balance in a frozen river is shown in **Fig. 2**. In this figure, T: temperature [°C], h_i: layer thickness [m], ρ: density [kg/m^3], U_w: flowing water velocity [m/s], and ϕ: heat flux (thermal energy per unit area per unit time) [W/m^2]. Each suffix indicates whether the value is for the atmosphere(***a***), the snow(***s***), the ice sheet(***i***), the frazil ice(***f***), or the flowing water(***w***).

The figure expresses the idea that the ice sheet layer exchanges heat with the layer of snow on the ice sheet and with the layer of frazil ice under the ice sheet. When heat moves from the ice sheet layer to the snow layer or from the ice sheet layer to the frazil ice layer, the ice sheet thickens. From the heat balance, it is understood that when "the thermal energy input" < "the thermal energy output", the thermal energy of the ice sheet layer decreases, and the ice sheet layer thickens. Therefore, Equation **[1]** can be expressed by assuming that the heat flux reduction is equal to the product of the density, the latent heat L_i [Ws/kg], and the increase in ice sheet layer thickness.

$$\rho_i L_i \frac{dh_i}{dt} = \phi_{iu} - \phi_{id} \qquad \textbf{[1]}$$

Similarly, this equation can express the idea that when thermal energy transfers from the snow layer to the atmosphere or from the snow layer to the ice sheet, the thickness of the snow layer h_s increases and that when thermal energy is transferred from the frazil ice layer to the ice sheet or from the frazil ice layer to running water, the thickness of the ice layer h_f increases. When this heat balance equation is constructed for each layer of the atmospheric layer, the ice sheet layer, and the frazil ice layer and the results are totaled, the following Equation **[2]** is derived. When this equation is simplified for the thickness of the ice sheet (h_i), Equation **[3]** is obtained.

$$\rho_s L_s \frac{dh_s}{dt} + \rho_i L_i \frac{dh_i}{dt} + \rho_f L_f \frac{dh_f}{dt} = \phi_a - \phi_w \quad \textbf{[2]}$$

$$h_i = h_i' + \frac{\Delta t}{\rho_i L_i}(\phi_a - \rho_s L_s \frac{dh_s}{dt} - \rho_f L_f \frac{dh_f}{dt} - \phi_w) \quad \textbf{[3]}$$

The heat flux of each layer of the atmosphere ϕ_a, snow ϕ_s, ice sheet ϕ_i and frazil ice ϕ_f is approximately expressed as the product of the heat exchange coefficient h_{sa} [W/m^2 ·°C] (or thermal conductivity k_i [W/m·°C]/the thickness of each layer h_s, h_i, h_f [m]) and the temperature difference at the boundary between the layers. Assuming that the fluctuations at the interface of every layer at a given time are in an equilibrium state, $\phi_a=\phi_s=\phi_i=\phi_f$ is obtained, and ϕ_a is expressed by Equation **[4]**.

The heat flux from the flowing water to the bottom surface of the river ice ϕ_w is affected by the flow velocity and water depth of the river (running water), and Equation **[5]** used in the previous study[2),3)] was applied. C_{wi} is 1622 [W·S$^{0.8}$·°C^{-1}·m$^{-2.6}$], U_w [m/s] is the average vertical flow velocity, and h_w [m] is the effective water depth from the riverbed to the undersurface of the river ice. The Manning formula for U_w and h_w, $U_w = \beta \cdot h_w^{2/3}$, is used. n_c is Manning's roughness coefficient, which is the combined roughness of the riverbed and that of the river ice, and i is the hydraulic gradient.

$$\phi_a = \frac{T_f - T_a}{\frac{1}{h_{sa}} + \frac{h_s}{k_s} + \frac{h_i}{k_i} + \frac{h_f}{k_f}} \quad \textbf{[4]}$$

$$\phi_w = C_{wi}\frac{U_w^{4/5}}{h_w^{1/5}}(T_w - T_f) = C_{wi}\beta^{4/5}T_w h_w^{1/3} \quad \textbf{[5]}$$

(2) The practical estimation formula for river ice thickness

When the temperature of the undersurface of the river ice T_f in Equations **[4]** and **[5]** is set as 0°C and substituted into Equations **[3]**, then Equation **[6]**, which is an equation for calculating the ice sheet thickness, is derived. The ice sheet thickness h_i' [m] is an arbitrary value given to the initial condition; after that, the ice sheet thickness before any Δt is given. Similarly, the coefficient α is obtained by giving the thickness of each layer at Δt before to h_s', h_f' [m]. Further, by substituting the values in **Table.1** into Equation **[6]**, a practical equation for ice sheet thickness calculation, Equation **[7]**, is derived.

$$h_i = h_i' - A\frac{T_a}{h_i'} - WT_w h_w^{1/3} \quad \textbf{[6]}$$

$$A = (\frac{k_i \Delta t}{\rho_i L_i})\alpha \quad W = (\frac{C_{wi}\Delta t}{\rho_i L_i})\beta^{4/5}$$

$$\alpha = \left\{1 - \left(\rho_s L_s \frac{dh_s}{dt} - \rho_f L_f \frac{dh_f}{dt}\right)/\phi_a\right)\right\} \times \left\{\frac{h_i'}{k_i}/(\frac{1}{h_{sa}} + \frac{h_s'}{k_s} + \frac{h_i'}{k_i} + \frac{h_f'}{k_f})\right\} \qquad \beta = U_w/h_w^{2/3} = \frac{1}{2^{2/3}}\frac{\sqrt{i}}{n_c}$$

$$h_i = h_i' - (\frac{65.2}{10^5})\alpha\frac{T_a}{h_i'} - (\frac{45.8}{10^2})\beta^{4/5}T_w h_w^{1/3} \quad \textbf{[7]}$$

The ice sheet thickness h_i [m] can be calculated by giving observed values to the air temperature T_a [°C], the water temperature T_w [°C], and the effective water depth h_w [m] in Equation **[7]** . The coefficients α and β in Equation **[7]** are given from the observation data of the previous study. Substituting β obtained from the observation data into Equation **[7]** and comparing the calculated ice sheet thickness to the observed thickness, the α that is more likely and predictable is obtained using the least squares method. When there is no observation data, the value of α is set by considering the conditions of the previous examination results. There is an example in a past study where the coefficient α is set as 0.6 and the coefficient β is set as 0.2381.

When snow or frazil ice accretes to an ice sheet and becomes part of the ice sheet, the value of coefficient α increases, and when the snow and frazil ice depths are great and they act as heat insulation for the ice sheet, this value decreases. α represents the degree of ice sheet formation with respect to air temperature. Coefficient β increases when the hydraulic gradient is great and the roughness is small, and decreases when the hydraulic gradient is small and the roughness is great. From Equation **[7]**, if the air temperature T_a of the second term that includes α is minus (negative), the river ice thickness tends to increase, and if it is plus (positive), the river ice thickness tends to decrease. The third term that includes β expresses that the river ice thickness tends to decrease with increase in water temperature and water depth, and that the river ice thickness tends to increase with decrease in water temperature and water depth. Therefore, the third term expresses the degree of melting of the ice sheet with respect to the water temperature, the effective water depth, the hydraulic gradient, and the roughness.

This estimation formula applies the heat balance method in determining the change in snow depth and frazil ice thickness. However, no consideration is given to the following factors: the changes in the snow depth caused by snowfall that increases the snow depth or winds that melt snow, the increase in the frazil ice thickness due to the supply of frazil ice in the flow from upstream, or the decrease in the frazil ice thickness due to downstreamward outflow.

Table. 1 List of physical properties of ice

	h_{sa}	ρ_i	L_i	k_i
	Heat exchange coefficient	density	latent heat	Thermal conductivity
unit	W/m^2・℃	kg/m^3	Ws/kg=J/kg	W/m・℃
value	25	917.4	3.336×10^5	2.31

3.Application of the river ice estimation model to an actual river

The subject river was the Uryu River, a tributary of the Ishikari River, a first-class river, which is in northern Hokkaido, a cold snowy region of Japan. The location for estimating the ice thickness and the discharge during the freezing period was the Tadoshi Site, where the water level observation had been done.

3 -1. Estimated and measured river ice thicknesses

The hourly air temperature, sunshine, wind speed, snowfall depth, and the river water level measured at and around the Tadoshi Site from November 1 to March 31, which is the winter period, from 2007 to 2019 were collected and applied to a model using the heat balance method. These values for river ice thickness estimation (riverbed gradient:1/480, river width:68m, the coefficient for ice thickness calculation (α):0.9, Manning's roughness coefficient:0.03, water density: 1000 kg/m^3, ice density: 917.4 kg/m^3, snow density : 100 kg/m^3, mean particle size of frazil ice :6 mm, the latitude 44.37 DEG) are inputted. As an example of estimation, the results for the winter of 2007-2008 are shown in **Fig. 3**.

At the Tadoshi Site, the measurements of the cross-sectional area and the width of river ice were done at the time of a discharge observation. The average measured river ice thickness was obtained by using the river ice data for the freezing period from January through March of the years 2008 to 2019. Next, the river ice thickness obtained by using the heat balance method was compared to that estimated by using the estimation model.

Three estimation models (regression formulas) were constructed for three cases : (x:estimated value, $\hat{y}$:mesured value) : (1) the difference between the estimated river ice thickness and the measured river ice thickness was within ±10% : $\hat{y} = 0.9785x + 1.7813$ $(R^2 = 0.8834)$, (2) the measured values were 110% of the estimated values : $\hat{y} = 0.9598x + 21.005$ $(R^2 = 0.694)$, and (3) the measured values were less than 90% of the estimated values : $\hat{y} = 1.0886x - 19.618$ $(R^2 = 0.9301)$, and the estimated values were overestimated. The results of the three estimation models are shown in **Figs. 4 to 6**.

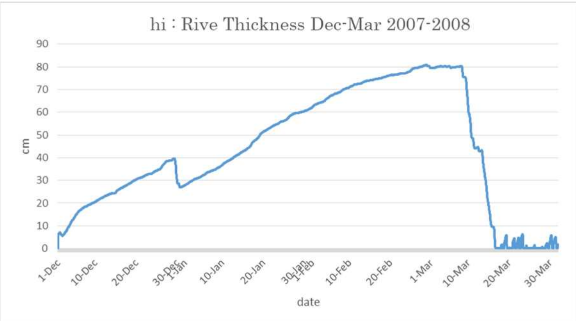

Fig. 3 Example of estimation for the river ice thickness

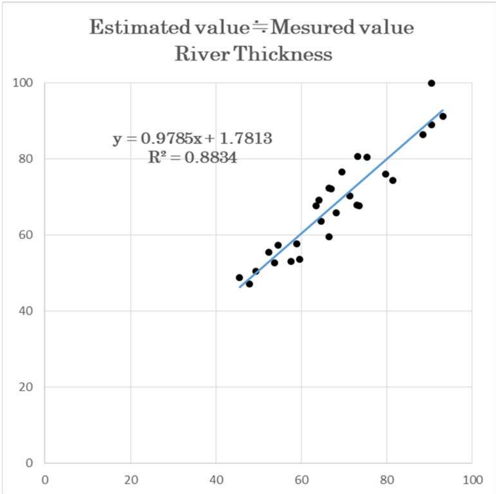

Fig. 4 Estimation model (1)

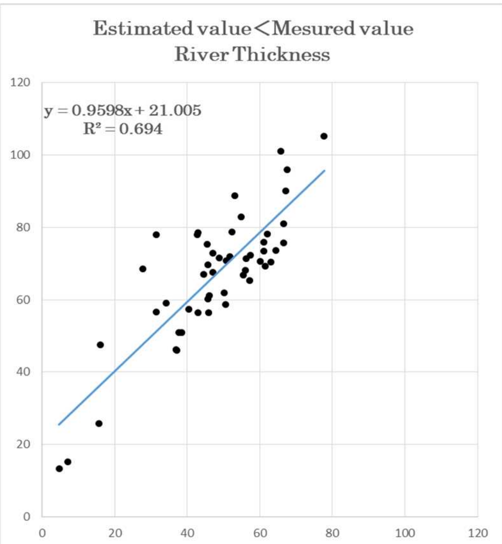

Fig. 5 Estimation model (2)

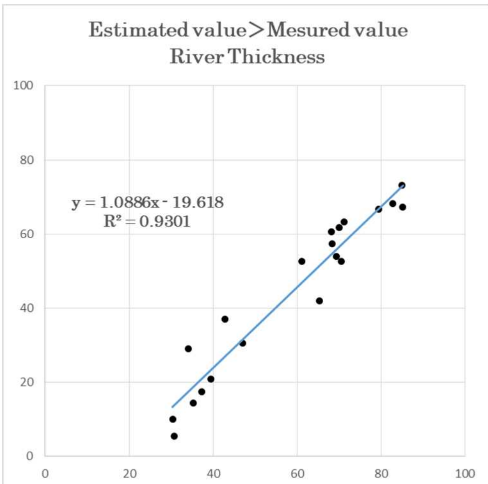

Fig. 6 Estimation model (3)

3 -2. Estimation for river ice thickness for the days between the measurement days

To predict the river discharge during the freezing period in real time in the future, these estimation models (1) to (3), were selected according to the degree of difference between the estimated value and the measured value of river ice thickness, and the models were modified using the measured value as additional information. The constant term (the intercept) was modified to reproduce the measured value, and the coefficient of the estimation equation was used as is for the regression coefficient and was applied to the equation for the days from January through March of the 2019. **Fig. 7** shows the results of the estimation that was performed by using the values modified based on the measured values.

In light of the above, we modified the river ice thicknesses estimated for the period without measurement values. The problem with the prediction of the initial period of freezing from January to February is that the predicted value differs from the actually measured value. The corrected predicted values after February are consistent with the measured values. Moreover, the phenomenon that the ice thickness in late March rapidly decreases can be expressed, and there is a possibility that information on the occurrence of ice jam can be provided with higher accuracy. In the future, we plan to extract the conditions in which it is difficult to predict and to examine the correction method.

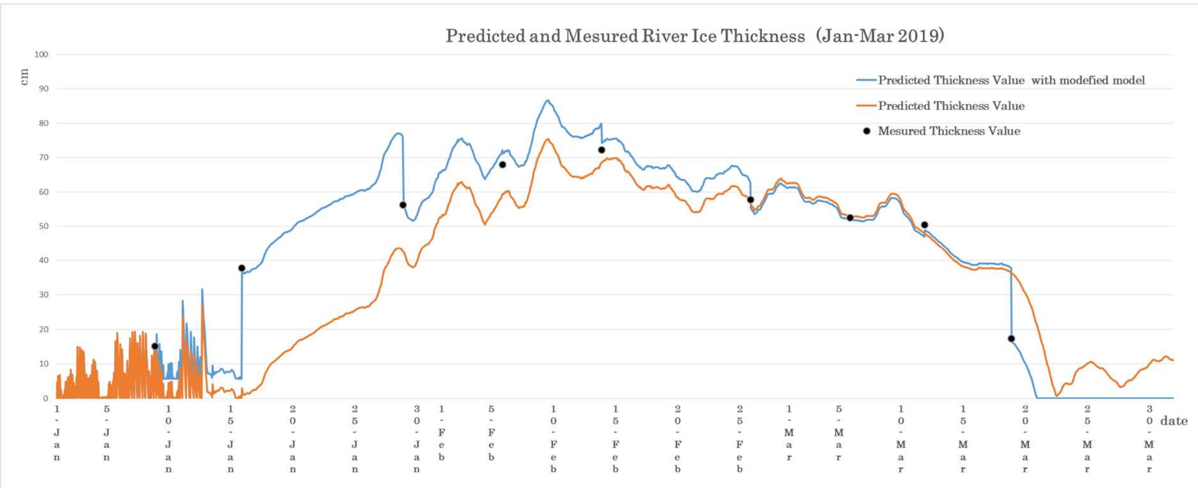

Fig. 7 River ice thickness predicted values from January through March of 2019 (with and without modified model using measured values)

4. Estimation of discharge considering the river ice thickness

4-1 Creation of an H'-Q equation for the frozen-over river

A H'-Q equation was created by using the discharge data measured during the freezing period from January through March of the years 2008 to 2018. For the river ice thickness and the frazil ice thickness, the average values were obtained by using the observed area and the width of the ice sheet below the water surface and those of the frazil ice. Next, the water depth that corresponded to the flowing water in the river channel was obtained by subtracting the river ice thickness and frazil ice thickness from the standard water level measured using the water level gauge. By using this corresponding water depth and the measured discharge, the H'-Q equation was created. Discharge observation was done three times during each of the freezing months. A total of 99 data were collected for 11 years. A regression equation was created by using the 94 data points that were left after eliminating the values that were considered to be abnormal in the H'-Q relationship distribution graph (Equation **[8]**, **Fig. 8**).

The water level distributed in the range between 53.88m and 54.77m, and the discharge distributed in the range between $1.04m^3/s$ and $33.87m^3/s$.

$$\hat{y} = 6.0215x - 323.38 \;\; (R^2 = 0.7951) \qquad \textbf{[8]}$$
$$\hat{y}: \sqrt{Q}\,, \quad x: H' = H - d$$

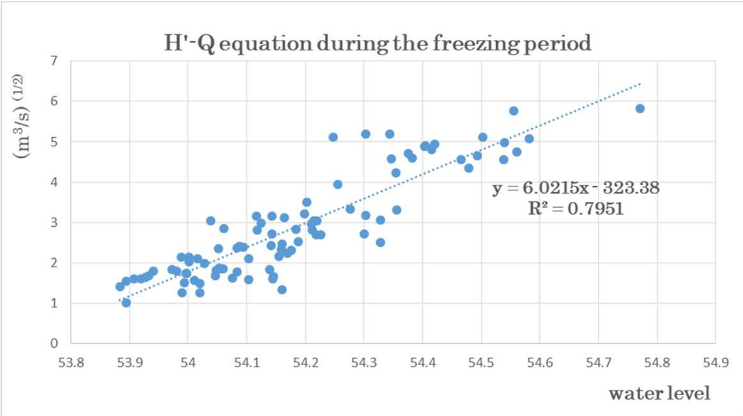

Fig. 8 H'-Q equation that considers river ice thickness during the freezing period

4-2. Estimation of discharge considering the river ice thickness

A continuous estimation of discharge was done for the period from January through March of 2019. The estimated river ice thickness was subtracted from the automatically measured water level. **Fig. 9** shows the discharge estimated by substituting this water level in the H'-Q equation for the frozen-over river (Equation **[8]**). **Fig. 9** also shows the discharge obtained without considering the river ice thickness and the discharge obtained by subtracting the estimated river ice thickness without a modification using the measured discharge.

The applied water level of the H'-Q formula during freezing ranges from 53.88 to 54.77m, and it is necessary to construct a new H-Q formula at high water levels during snow melting. In the future, conditions to be applied when melting snow, such as when river ice is not taken into consideration and when river ice flows down, and the new H-Q equation will be examined.

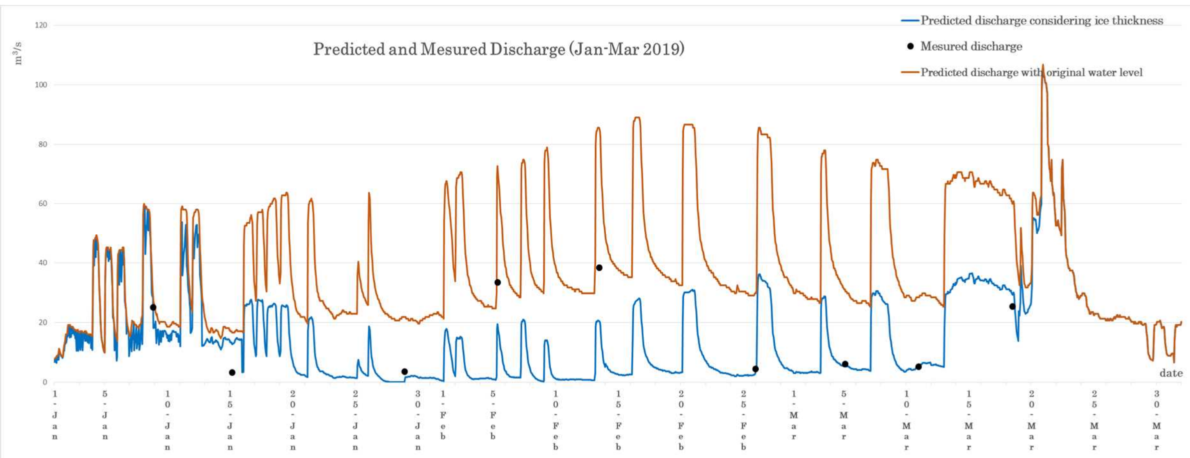

Fig. 9 Estimation of continuous discharge for the freezing period that considers the river ice thickness

5. Conclusion

In this study, examinations for the estimation of continuous river discharge during the freezing period were done, focusing on one location. We will conduct further examinations for many locations on various rivers and attempt to clarify the spatiotemporal characteristics of continuous discharge in frozen rivers.

Based on the current examination, we will further improve the accuracy of the river ice thickness estimation model by examining a greater amount of river ice thickness data and comparing them with the estimated values. We will also develop the estimation model for practical application by taking the estimation limit (e.g., setting of the confidence interval) into consideration.

The authors consider it useful to construct the H'-Q equation that is applicable according to the characteristics of the target location and the conditions of river ice with various roughness coefficients and sectional flow areas.

References

1) Japan Society of Hydrology and Water Resources: *Hydrology and Water Resources in Snowy and Cold Regions*, Shinzansha Scitech, pp.73-78, 1998.

2) River Engineering Research Team , Cold-Region Technology Promotion Division, Civil Engineering Research Institute for Cold Region: Clarification of the Phenomenon of Salt Water Intrusion in the Freezing Season and Development of Discharge Observation Technology for Ice-covered Rivers, FY2010 Key Project Research Report (Individual Research Issue), 2010.

3) River Engineering Research Team (Hiroki Yabe, Hiroshi Yokoyama, Yu Inami), River Ice Thickness Estimated Model during freezing period, Civil Engineering Research Institute for Cold Region Report No.792 - May number 2019, pp.34-37, 2019.

IAHR AIRH

25th IAHR International Symposium on Ice

Trondheim, 23 - 25 November 2020

Observation and simplified simulation of ice melting process in ice covered river

Hiroshi YOKOYAMA[1], Yasuhiro YOSHIKAWA[2], Yu INAMI[1], Hiroki YABE[1]

[1] Civil Engineering Research Institute for Cold Region, PWRI
1-3-1-34 Hiragishi, Sapporo, Hokkaido 0628602, Japan
yokoyama-h22ab@ceri.go.jp
[2] Kitami Institute of Technology
165 Koen-cho, Kitami, Hokkaido, 0908507, Japan
yoshi@mail.kitami-it.ac.jp

Ice jam flood is one of the problems for disaster prevention and maintenance of ice covered rivers in Hokkaido, cold snowy region in Japan. This study aimed to clarify the phenomena of ice melting process and to examine method to predict occurrence time of ice jam in ice covered river in spring thaw. First, we conducted continuous observation of ice melting process by measurement of inside the ice, river water, and longitudinal water level and capturing of river ice images with time-lapse camera. It was difficult to predict de-icing time only by visible information such as image of river ice. It was needed to consider more some invisible information such as continuous observation data of ice temperature, longitudinal water level to understand ice melting process and to predicted de-icing time. Next, we applied a simplified simulation model of time series change of river ice thickness. We assumed that possibility of ice jam occurrence increased when sudden decrease of river ice thickness appeared in the simulation. We compared actual ice jam occurrence time and sudden decrease of river ice thickness in simulations and discussed the applicability of the model for ice jam prediction.

.

1. Introduction

Many rivers in snowy cold regions freeze during winter. In early spring, the river ice starts to melt and breaks up due to rising air temperatures and rainfall. In a river whose discharge has been increasing, the amount of flowing river ice increases. Ice jams, which occur when river ice flows down and clogs the river channel, are a potential trigger for river disasters during the melting season. Such disasters include rapid water level rises, river water overflow, inundation, and damages caused by ice flows (Burrell et al., 2015).

Ice jam flood is one of the problems for disaster prevention and maintenance of ice covered rivers in Hokkaido, cold snowy region in Japan. As recent cases, worker accidents at river construction sites, and inundation caused by river ice that blocked a river channel at a bridge were reported (Yokoyama et al., 2018).

The prediction of the location and time of ice jam occurrence can be considered as a mitigation measure for ice jam disasters. Studies for developing practical prediction methods have been promoted. The authors have done an onsite survey (Yoshikawa et al., 2012), a hydraulic model experiment to clarify the behavior of river ice on a frozen river (Yoshikawa et al., 2016), an examination of a practical method for predicting the changes in river ice thickness (Yoshikawa et.al, 2014), and an examination of a method to extract river ice blockages from channels by using an ice-jam-scale (Toyabe et al., 2016). However, it is often unsafe to conduct onsite observations of river ice in the channel during the ice melting season. The accumulated data for verification studies are insufficient even since the development of various observation devices and methods.

We selected a river in which an ice jam occurred in March 2018 as the subject of this study, and observed the behavior of river ice in the channel from the freezing period to the melting period. We estimated the changes in the thickness of the river ice in the channel where the above observation had been done by using a simple model for predicting changes in river ice thickness that had been proposed by the authors and for which practical use had been considered. The examinations in this study were meant to contribute to the accumulation of information on ways to secure the safety of river construction works during winter in Hokkaido, to identify the times and locations of ice jams, to clarify the water level increase, and to acquire knowledge that might be used in decisions on the opening and closing of sluice gates.

2. Overview of the onsite observation

(1) Observation location

The subject section for the observation is shown in **Figure 1**. It was a roughly 4.5km-long channel section at the upper reaches of the Bebetsu River in the Ishikari River System. The Bebetsu River is a tertiary tributary of the Ishikari River. The downstream end of the surveyed river section is roughly 21km upstream from the Bebetsu River's confluence with the Biei River, a secondary tributary of the Ishikari River. The river channel in the surveyed section is relatively a straight section, although the channel slightly meanders. The right bank of this section abuts a mountain, and the left bank is on flat land. There are continuously installed longitudinal groundsills in the channel. The channel has a series of sandbars.

The longitudinal profile of the riverbed in the subject section is shown in **Figure 2**. Since there were not detailed survey data for the channel of the Bebetsu River, we created channel data by using the following procedure. The riverbed elevations were obtained by reading the longitudinal plane coordinates of the thalweg of the river section from the Google Earth satellite data for October 5, 2018, and obtaining the elevation for each plane coordinate by using “Map Sheet” tools published by the Geospatial Information Authority of Japan. In this study, the elevation of the water surface was assumed as the riverbed elevation; therefore, the obtained elevation values include certain degrees of error. Even so, it is considered that the

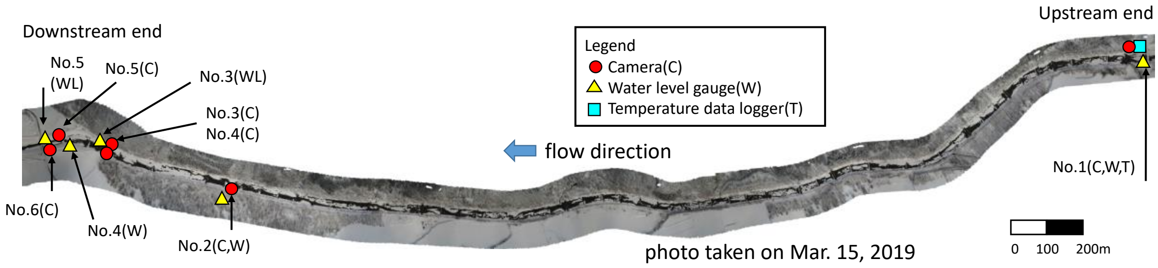

Figure 1. Surveyed section in the Bebetsu River

longitudinal changes in the riverbed elevations were sufficiently reproduced. The river width was about 30m throughout the target section. Although the water surface width varies from section to section, it varies between about 10m and 20m. The average longitudinal gradient was about 1/60.

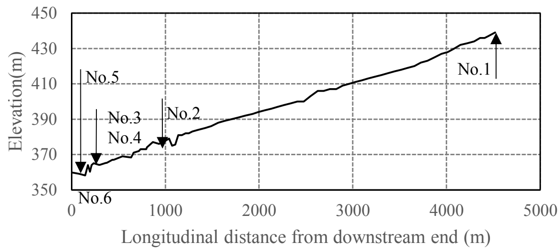

Figure 2. Longitudinal profile of the riverbed

(2) Observation method

To observe as many phenomena in the river channel as possible from the coldest time of the winter to the end of ice melting, the observation period was set from February 1 to April 12, 2019. The observation items include (1) the river ice behavior in the river channel as photographed by fixed-point still image interval photography using a trail camera (Hykecam SP2, Hyke, Inc.), (2) the water level continuously measured in the river channel using automatic recording water level gauges (S&DL mini, OYO Corporation), (3) ice and air temperatures measured continuously using ice thermometers (Kadec21-UHTV-C, North One Co., Ltd.), and (4) river water temperature measured continuously using water temperature data loggers (TidbiT v2, Onset). Shooting interval of trail cameras were 1 hour till March 4, 2019 and 30 second after March 5, 2019. Measurement interval of water level and temperatures were 1 minutes during the observation.

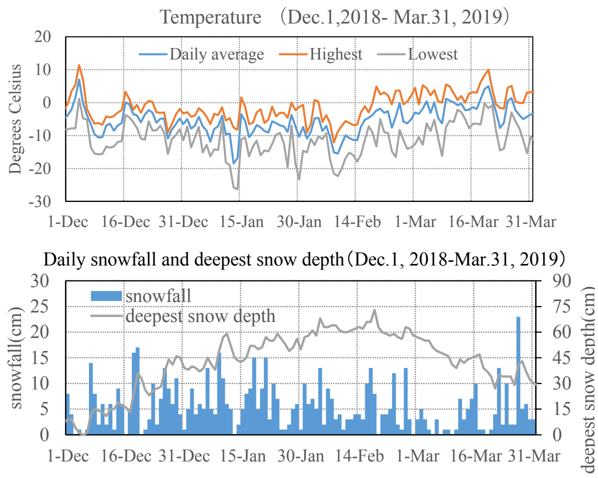

Figure 3. Weather data at Biei AMeDas station

(3) Overview of the weather conditions

Figure 3 shows the daily average, maximum, and minimum temperatures and the daily snowfall and deepest snow cover measured from December 1, 2018 to March 31, 2019 at the AMeDAS (Automated Meteorological Data Acquisition System, operated by Japan Meteorological Agency) observation station at Biei. The Biei AMeDAS station is about 14.5km west of site No. 1 in **Figure 1**. The Biei observation station is at the elevation of 250m, and No. 1 is at the elevation of 435m. The difference between these two elevations is 185m.
The deepest snow cover was recorded on February 18, 2019. The daily highest temperatures were below 0°C until February 18, and continued to be above 0°C from February 19 onward. It is estimated that the melting of river ice increased in late February. **Figure 4** shows the

changes in the daily deepest snow cover during the winter season from December 1 to March 31 for the past five years. In 2018 when an ice jam was observed, the daily deepest snow cover from January into February, which are the coldest months of the year, was higher than those in the other years. In 2014, the daily deepest snow cover during the coldest months was lower than those in the other years. In 2019, the depths of snow cover until mid-February were about the same as those for the other years; however, the snow cover depth did not increase after mid-February. The curve for 2019, which is about 20 to 30 cm lower than those for 2016, 2017, and 2018, continued to decrease, keeping the difference. It is estimated that the snow and river ice started to melt in late February, which was earlier than that of the ordinary year.

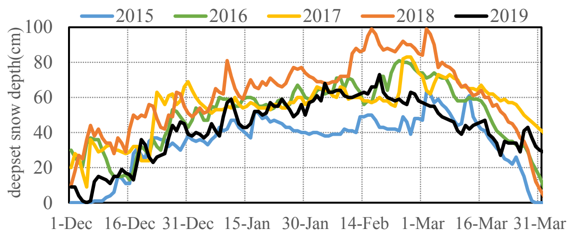

Figure 4. Deepest snow depth in the last 5 years at Biei AMeDAS station

3. Observation results

(1) Measurements of ice, water, and air temperatures

Next, the results of onsite observation are discussed. The purposes of measuring the ice temperature, water temperature, and air temperature are (1) to know the temperature inside of the river ice; and (2) to examine the applicability of the method for determining the river ice melting period. This method uses the characteristics of temperature changes inside the river ice. When the melting of river ice proceeds, parts of the equipment for measuring the inside temperature of river ice (hereinafter, the sensors) are exposed to the river water or the atmosphere, and the measurements of the sensor for the temperature inside the river ice follow the changes in the water and air temperatures.

The measured temperatures for the river ice and the river water are shown in **Figure 5**. This sensor was installed No. 1 (**Figure 1**). The depth of the sensor in the river ice was 12cm from the upper surface of the ice on February 5, which was the day that measurement began. At the inspection of equipment done on March 4, the river ice at the sensor was found to have disappeared and the sensor was exposed to the water; therefore, the sensor was re-installed at a location 5cm below the ice surface. At the inspection of equipment done on March 25, the river ice at the sensor was found to have disappeared and the sensor was exposed to the water again; therefore, the sensor was re-installed at a location 3cm below the ice surface. The ice temperature steeply decreased on March 4 and 25. This was from the re-installation of the sensor that had been in the river ice and had been exposed to the river water.

The river water temperature curve was flat, around 0°C, up to around February 20, but it showed great daily changes after February 20. The ice temperature was a constant -0.3°C from

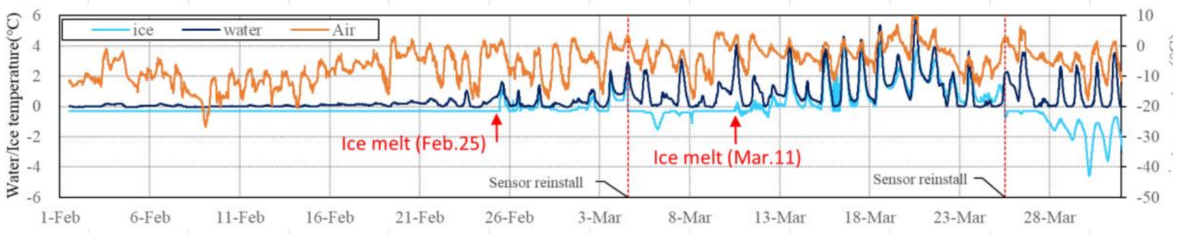

Figure 5. River water, ice and air temperature at Site No.1

the start of the observation until February 25. The ice temperatures changed to positive values sometime between 10:00 to 11:00 on February 25. After that change, the ice temperature roughly followed the changes in the river water temperature. Based on the above, it is considered that the melting of river ice at the location of the sensor continues and the exposure of the sensor to the river water started during this period.
Since the ice temperature turned positive again between 12:00 and 13:00 on March 11, after the sensor was re-installed in the river ice, and the ice temperature roughly followed the change in the river water temperature, it is estimated that the sensor was exposed to water due to ice melting. These results show that the timing of river ice melting can be determined to some extent by measuring the ice temperature, water temperature, and air temperature.

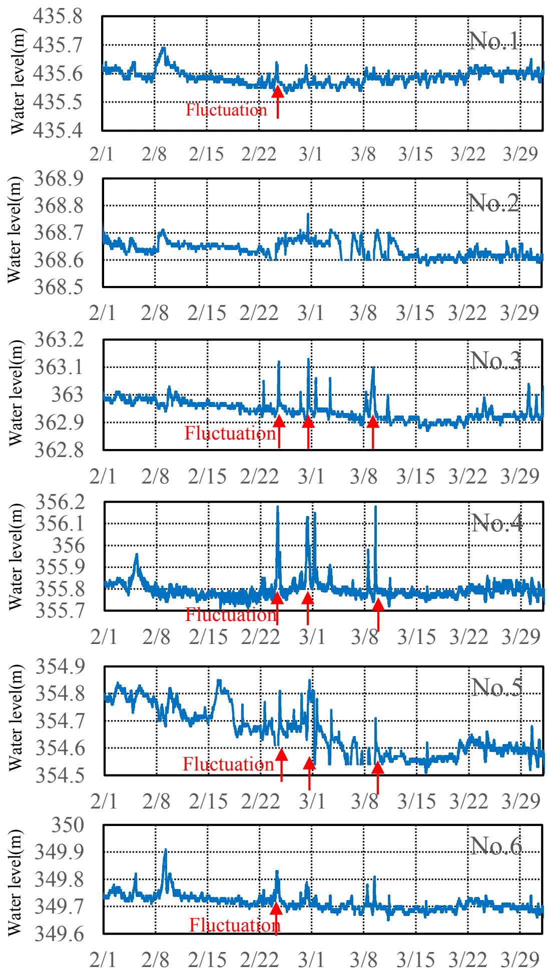

Figure 6. Longitudinal water level fluctuations (Feb. 1, 2019-Mar. 31, 2019)

(2) Measurement of water levels
Yoshikawa et al. showed, from field observations of rivers during ice jams, that river ice is lifted vertically due to the rapid rise in river water level when the melting of snow increases and that ice melting and the flow of river ice, which are further promoted by the vertical movement of the river ice, lead to ice jams (Yoshikawa et al., 2012). In light of the above, we performed a continuous observation of the longitudinal water level changes in the Bebetsu River during the melting period, and examined the relationship between the longitudinal water level changes and the melting process of river ice.
The changes in the water level at the measurement locations are shown in **Figure 6**. The part of the curve that indicates a marked change in water level is indicated with a red arrow. At No. 1, water level changes exceeding 10cm were observed on the morning of February 24. At No. 3 to No. 6 in the downstream sections, the water level rose during the day on February 24, indicating that the river discharge increased at this time. Similarly, on February 28 and March 9, the water level rose by 0.1 to 0.3m at No. 3, No. 4, and No. 5.
From the values observed at the Biei AMeDAS station from late February to early March, it is understood that there were no weather changes that could have caused sudden changes in river ice behavior, such as sudden increases in temperature or precipitation. However, on February 20 and after, the maximum temperature was positive on most days, and the increase in sunshine hours was thought to have caused the gradual melting of snow and river ice, which is a potential causal factor for local increases in water level in a channel.

(3) Images of river ice
This section examines the process of river ice melting with reference to the changes in images of the river ice. **Figure 7** shows the changes in the river ice from February 23 to March 1, and

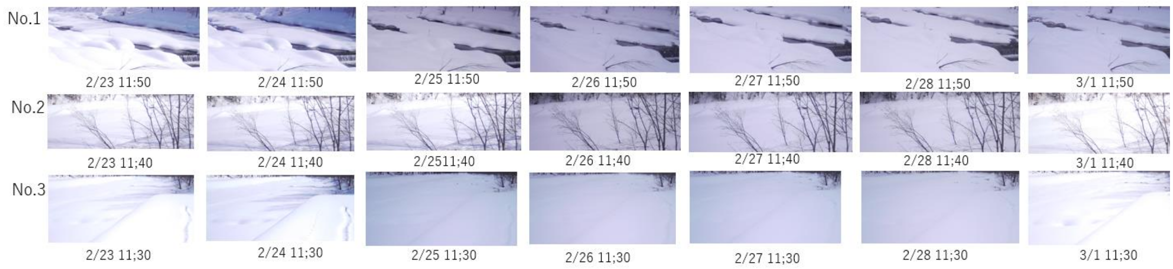

(a) Feb. 23, 2019- Mar. 1, 2019

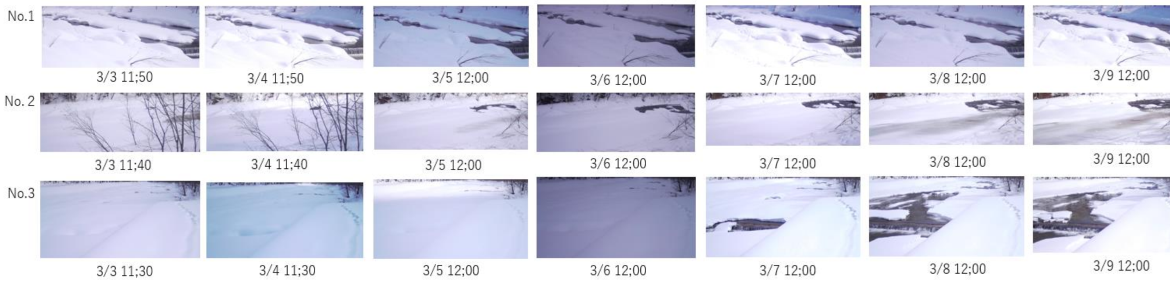

(b) Mar. 3, 2019- Mar. 9, 2019

Figure 7. Temporal change of river ice taken by trail cameras

those from March 3 to 9 at No. 1, which was at the upper reach within the survey section, at No. 2, which was at the middle part of the section, and at No. 3, which was at the lower reach within the survey section.

No changes in river ice are found in the images taken around February 24 and 25, when the ice temperature and water level fluctuations were observed. Similarly, no changes in river ice are found in the images taken around February 28, when the water level fluctuations were observed. The river ice images that were taken in early March clearly show that the river ice melting continued. At No. 2, small open water surfaces start to be seen on March 4, and they expand as the days go by. After March 8, changes in the color of the ice are observed, which seems to indicate the continued ice melting in the river channel. At No. 3, open water surfaces are found on March 7, and they expand as the days pass. No accumulation of river ice can be found in the image for March 9, but it is estimated that ice melting had progressed considerably.

(4) Examination of the ice-melting phenomena and the observation technique

The river ice melting will be examined as time series phenomena by discussing mainly the melting process observed at No. 1.

- Until mid-February, the daily maximum air temperature fluctuated between -2 and 0°C, the river water temperatures were around 0°C, and the ice temperatures were a constant -0.3°C. Neither water level changes, which are a sign of ice melting, nor the expansion of the open water surface were observed.
- In late February, the days with daily maximum air temperature exceeding 0°C started to increase. During this period, no expansion of the open water surface is observed in the river ice images. The melting of ice is not observed. On February 24, marked changes in water level were observed. On February 25, signs of full-fledged ice melting were detected, including the disappearance of river ice, which was shown in the measurements of ice, water, and air temperatures.
- In early March, when the air temperatures rose further, the expansion of open water surfaces is observed in the river ice images. The ice melting process was recorded, including the water level changes that occurred over the entire length of the river section on March 9 and that were

interpreted, based on the ice, water, and air temperatures on March 11, as indicating the disappearance of the river ice.
The process of ice melting is difficult to clearly observe from the ice images alone. The simultaneous measurement of the ice, river water, and air temperatures was effective in determining the timing of ice melting at the measurement locations. The simultaneous and longitudinal measurement of the river water level was effective in understanding the flow regime in the river channel, which closely related to the ice melting in the entire area of the channel. By combining multiple observation devices and methods, it is possible to examine a time-series of the ice-melting process on an actual river.

4. Application of the river ice thickness prediction model

(1) Overview of the prediction model
As an index for assessing the ice jam risk associated with river ice melting, which can trigger an ice jam, the prediction of river ice thickness is considered. We examine the applicability of the ice thickness prediction model by simulating predictions for the ice thickness at the observation locations in this study.
The basic equations for the time series changes in river ice thickness are given as the following equations (1) and (2) based on the heat balance among the atmosphere, river ice, and river water.

$$h_i = h'_i - \left(\frac{65.2}{10^5}\right)\alpha\frac{T_a}{h'_i} - \left(\frac{45.8}{10^2}\right)\beta^{4/5}T_w {h_w}^{1/3} \quad (1)$$

$$h_w = H - Z - \left(\frac{\rho_s}{\rho_w}h_s + \frac{\rho_i}{\rho_w}h_i + \frac{\rho_f}{\rho_w}h_f\right) \quad (2)$$

Where, h_i: ice sheet thickness (m), h'_i: ice sheet thickness at Δt before (m), T_a: air temperature (°C), T_w: water temperature (°C), H: water level (m), Z: riverbed elevation (m), ρ_s: snow density (kg/m^3), ρ_w: water density (kg/m^3), h_s: snow depth (m), ρ_i: ice sheet density (kg/m^3), ρ_f: frazil ice density (kg/m^3), h_f: frazil ice thickness (m), and h_w: effective water depth (m).
α in equation (1) is obtained based on the heat balance among the atmosphere, river ice, and river water when observation data are available, and when these are not available, it is determined by trial and error and observation records. In the current study, observation data were unavailable; therefore, we set α =0.2, which reproduces the measured river ice thickness satisfactorily. β (m$^{1/3}$/s) is expressed in the following equation (3).

$$\beta = U_w/{h_w}^{2/3} \quad (3)$$

For accuracy verification of the model, we compared observed ice sheet thickness and calculated ice sheet thickness. Afterward, we show ice sheet thickness for short with ice thickness unless we show it in particular.
In this study, under the assumption that this model would be used at river management offices, we simplified and limited the input hydrological conditions for the model by using constant values for the water level and the temperature of water flowing into the target river section and the input weather information by using the public data on air temperature, wind velocity, and sunshine hours (AmeDAS information). The wind velocity and the sunshine hours may influence α in equation (1); however, α in this study was a fixed value, so it did not influence the river ice thickness computation.
The location for computation by the model was No. 1. The longitudinal riverbed gradient was 1/60, and the river water surface width was 10m, based on the photos of the location.

For the water level at the location, a constant value obtained by adding 0.3m to the elevation of the location was used. For the weather data, the hourly observed values for Biei AMeDAS were input. The reason for not using the observed water level and air temperature for the prediction computation for 2019 was that, in conducting ice thickness predictions that include those for past years, we prioritized the unification of the input conditions for the computation. The start of prediction was set as 0:00 on December 1 of the previous year, and the end of the prediction was 24:00 on March 31 of the year when the prediction was done. The computation output was done with an interval of 1 hour, and the minimum ice thickness was 0.001m. The river ice thickness at the start of computation was set as 0.001m. The temperature of the river water flowing into the examined section fluctuated with the air temperature; however, for simplicity, it was set at a constant value of 2°C for the entire period of the computation.

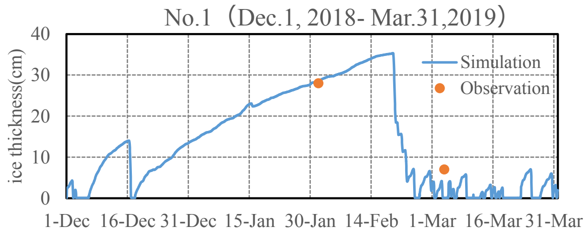

Figure 8. Estimated river ice thickness at Site No.1

The reproducibility of river ice thickness for the method presented in this study had been verified to be satisfactory in the examination using the river ice thickness measured at the winter discharge observation of a different river than that under examination in this study11).

(2) The results of the river ice thickness prediction

Figure 8 shows the ice thickness prediction result at No.1 from December 1, 2018 to March 31, 2019. The ice thickness was measured at No. 1 when the ice temperature sensor was installed and inspected. The measured ice thickness was 0.28m on February 1, 2019, and 0.07m on March 4. The prediction computation was done by adjusting the model parameters to match the observed values.

The prediction values for the river ice thickness show an increasing trend during the coldest period of the winter from mid-December to mid-February. The predicted values sharply decrease by nearly 20cm within 24 hours from noon on February 19 to noon on February 20. The predicted values further decrease to 0cm on February 25, and after that, the values fluctuate between 0cm and a few centimeters.

Next, we compare the changes in the predicted river ice thickness with the ice melting process observed onsite. On February 19, when the predicted value sharply decreases, the daily maximum temperature turns from negative to 0°C or higher. The timing of the predicted ice decrease roughly corresponds to the observed temperature changes. The predicted ice thickness became 0cm on February 25, and the disappearance of river ice, which was detected by the ice temperature sensor, was also on February 25. It can be said that the time when the predicted value of river ice thickness suddenly decreased overlapped with the occurrence time of phenomena that signal ice melting onsite.

A full-scale river ice breakup occurred in early March, and the model predicted that the river ice breakup occurred about 10 days earlier than observed. The reasons for this are considered to be that the Biei observatory, whose observation values were used as the input values for the model, had an elevation of 180m lower than that of No. 1 and that there was a temperature difference between the model input value and that at the actual site. The ice melting occurred earlier in the model than that onsite.

(3) Assessment of the possibility of an ice jam occurrence

Figure 9 shows the prediction results for river ice thickness for the past five years. In the previous report, the fluctuation characteristics of river ice thickness were qualitatively examined using the same model2). However, in this study, a recalculation was performed by applying the setting conditions used for the reproduction of the 2019 event to the other years.

In all these years, the river ice thickness continued to increase during the period from late December to January. In the years other than 2015, the river ice thickness shows a clear peak from late February to early March. The predicted annual maximum river ice thickness was roughly the same for all five years. A sudden decrease of about 10cm to 20cm in the river ice thickness during a 1- to 2-day period occurred in most of these years. In some years, the river ice thickness sharply decreased to 0cm in a short period of time. These sudden decreases in river ice thickness are able to be linked to continued ice melting and are phenomena that may lead to increased risk of ice jams.

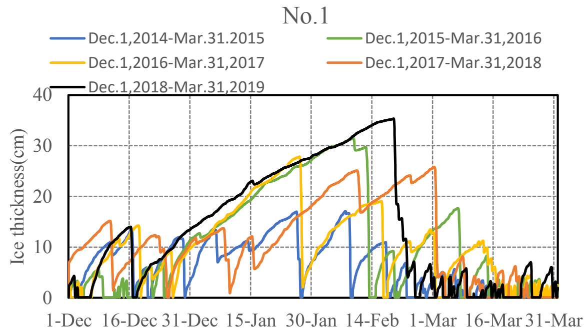

Figure 9. Estimated river ice thickness in the last 5 years at site No.1

As an effective use of this model, when the predicted value of river ice thickness decreases rapidly from the peak within 1 to 2 days, it is regarded as a sign of continued ice melting, and it is necessary to watch out for ice jams. However, to determine the decrease in river ice thickness that would warrant caution, it is necessary to set a standard by considering the results of multi-year ice thickness predictions and the past ice melting conditions for each site.

Currently, the estimated date and time of the sudden decrease in river ice thickness, which may indicate the occurrence of an ice jam, differ depending on the method. It is considered to be appropriate to assess the state of ice melting by combining observations of river ice images, water levels, ice temperatures, etc. with the predictions for river ice thickness fluctuations.

5. Summary

The findings in this study are summarized below.

- To understand the deicing process of a frozen river, we took river ice images and simultaneously measured the water levels longitudinally and simultaneously measured the ice temperatures, river water temperatures, and air temperatures. The simultaneous measurements of the ice, river water, and air temperatures were effective in determining the timing of ice melting at the measurement locations. An examination of the time series of the deicing process has become possible by combining several observation methods.
- The simplified ice thickness prediction model reproduced the measured river ice thickness satisfactorily. Furthermore, the time when the predicted value of river ice thickness suddenly decreased seemed to correlate with the degree of ice melting. Therefore, we were able to demonstrate the possibility of using the rapid decrease in river ice thickness as predicted by the model in order to predict an increase in the risk of an ice jam.

References

Burrell, B.C., Huokuna, M., Beltaos, S., Kovachis, N., Turcotte, B., Jasek, M. (2015): Flood Hazard and Risk Delineation of Ice-Related Floods: Present Status and Outlook, Proceedings of 18th Workshop on the Hydraulics of Ice Covered Rivers.

Geospatial Information Authority of Japan: Map Sheet ver 2.0.0.2, (https://renkei2.gsi.go.jp/renkei/130326mapsh_gijutu/index.html) (in Japanese)

Japan Meteorological Agency: AMeDAS observation data (http://www.data.jma.go.jp/obd/stats/etrn/index.php) (in Japanese)

Toyabe,T., Yoshikawa, Y., Abe, T., Kuroda, Y., Funaki, J., Tsumura, T., Inagaki, N.(2016) : Study on the identification of potential ice jam locations on Osobetsu River that takes into account snowstorms and the densimetric froude number of river ice, 23rd IAHR International Symposium on Ice.

Yokoyama, H., Yoshikawa, Y., Inami, Y., Maeda, S., Yabe, H.(2018): Process understanding on the phenomena of flood damage caused by ice jam in March 2018 and future problems, Journal of Japan Society of Civil Engineers, Ser. B1 (Hydraulic Engineering), Vol.74, No.5, I_1039-I_1044.

Yoshikawa, Y., Watanabe, Y., Hayakawa, H. and Hirai, Y. (2012): Field observation of a river ice jam in the Shokotsu River in February 2010. Proceedings of the 21st IAHR International Symposium on Ice, Dalian, China, pp. 105–117.

Yoshikawa, Y., Watanabe, Y., Itho, A. (2014): A simple equation for ice sheet thickness and ice formation/breakup prediction, Journal of JSCE, Vol.2, Issue1, pp.203-213.

Yoshikawa, Y., Kuroda, Y., Abe, T., Toyabe, T., Park, H., Oshima, K. (2016): Study on the ice-jam occurrence based on hydraulic experimentation, Proceedings of the 23rd International Symposium on Ice.

25th IAHR International Symposium on Ice
Trondheim, 23 - 25 November 2020

Simple ice jam simulation around bridge piers

Yasuhiro YOSHIKAWA[1], Hiroshi YOKOYAMA[2] and Yu INAMI[2]
[1] *Kitami Institute of Technology*
165 Koen-cho, Kitami, Hokkaido, 0908507, Japan
yoshi@mail.kitami-it.ac.jp
[2] *Civil Engineering Research Institute for Cold Region, PWRI*
1-3-1-34 Hiragishi, Sapporo, Hokkaido, 0628602, Japan
yokoyama-h22ab@ceri.go.jp

This study aimed to clarify the phenomenon of ice jams generated at the bridge piers place. The one-dimensional ice jams calculation model was built. The composition of this model is water flow, ice flow and ice jams. In order to check the accuracy of this model, we conducted an ice jam experiment. Experimental waterway has set up the channel of low-water and flood.

The study clarified the following. The time series phenomenon of ice jams generated at the bridge piers place was able to be expressed in the experiment. This calculation model can express water level variation by ice jams. Furthermore, in order to raise calculation accuracy, we understood that it was important to consider the influence of ice jams on water flow appropriately in this model.

1. Introduction

On March 9, 2018, during the winter season, river water levels in Hokkaido rose rapidly due to unseasonable heavy rain and warm air, causing damage in various places. A local agent was swept away and killed during revetment work on the Bebetsu River, and three vehicles were swept off of the intake weir and destroyed in the Sarukawa River. The damage from the inundation occurred in 28 and 26 instances above and below the floor level, respectively, and the disaster spread to all through the region of Hokkaido (Hokkaido 2nd report, 2019). Ice forms in Hokkaido rivers in winter and they freeze over; in the spring, the ice thaws and breaks up due to rising temperatures and enters the flow downstream. Ice jam are formed due to the accumulation of the flowing river ice in the river channel which leads to the rapid increase in the water level; as a result upstream flooding occurs followed by a sharp drop in downstream water level. Furthermore, when the ice jams are broken up, the ice flows downstream with a large amount of other river ice, causing widespread damage downstream. On-site observations have shown that many of the disasters that occurred on March 9 were caused by ice-jam phenomena and as places where ice-jams occurred, there were sandbars in river channels, slope change points, river structures (bridges), confluences with the main river, and increase in water levels (Yokoyama et al., 2018a). As a proactive measure, it is pertinent to properly understand ice jam phenomena as similar weather conditions may result in a similar disaster in the future.

The March 2018 Ice Jam Disaster was unprecedented; voices were heard in those places saying that "it was impossible to grasp what happened" and more information on the timing and location were earnestly sought. In regard to the “timing of occurrence,” because the ice jams occur after the river ice has thawed; the timing of thawing may be predicted. From the previous studies (Yoshikawa et al., 2014a), it has been shown that among ice sheet thicknesses that can be calculated using atmospheric temperature as an input value, there is a high possibility of thawing phenomena occurring during the period wherein the thickness of ice sheets decreases. Concerning the “place of occurrence,” studies have been conducted (Yoshikawa et al., 2014b) on places where the water surface width in the low channel narrows due to sandbars in the river channel or the flow speed decreases due to gradient change points. In another study on tributary confluences (Toyabe et al., 2017), it was reported that ice jams tend to occur when the water level of the main river rises and the flow decreases due to the influence of confluence with the main river. Moreover, there are also previous studies on ice jam phenomena in places where the downstream flow is completely frozen (Yokoyama et al., 2018b). However, adequate studies have not been carried out concerning ice jam phenomena at river structures (bridges). Numerical calculation models are effective as methods of understanding ice jam phenomena in time and space.

In this study, to elucidate ice jam phenomena at the pier part of the bridge, an ice jam calculation model was constructed; then, an ice jam experiment was conducted with a low channel and a high channel, and a lengthwise change in water level during the ice jam was measured. Furthermore, we attempted to reproduce the rise in water level due to ice jam phenomena utilizing this calculation model.

2. Ice Jam Calculation Model

This calculation model is composed of one-dimensional basic equations for water flow and ice flow. River ice is roughly classified into hard ice sheets (fixed ice includes ice sheets, floating ice flows downstream; if the size of the floating ice is 1m or larger it is an ice floe) and frazil ice, as well as accumulated snow on top of such ice sheets. In this calculation model, floating ice that flows downstream is the target. Fig. 1 shows a conceptual diagram of this calculation model. The cross-section was treated as a rectangular cross section.

2.1 Water flow calculations

The following equations of continuity and equations of motion were used as the basic equations for water flow. The first term on the right-hand side of equation [1], which is an equation of continuity, indicates the increase or decrease in the area of flowing water flowing through the gaps in the floating ice due to the increase or the decrease of the flowing ice.

$$\frac{\partial A_w}{\partial t} + \frac{\partial Q_w}{\partial x} = \lambda_i \frac{\rho_i}{\rho_w} \frac{\partial A_i}{\partial t} \qquad \textbf{[1]}$$

$$\frac{\partial Q_w}{\partial t} + \frac{\partial}{\partial x}\left(\frac{{Q_w}^2}{A_w}\right) + gA_w \frac{\partial H_z}{\partial x} + \frac{gn^2{U_w}^2S}{R^{1/3}} = 0 \qquad \textbf{[2]}$$

A_w (m^2) is the product of the flow, which is also the sum of the area in which only water flows and the area where water flows through the gaps in the floating ice. A_i (m^2) is the cross-sectional area of the ice floe, which is also the sum of the ice and the gaps in the ice. Q_w (m^3/s) is the discharge, while λ_i is the porosity of the floe ice, and 0.1 was provided by the reproduction calculation of this experiment. ρ_w (kg/m^3) = 1,000.0 in water density, ρ_i (kg/m^3) = 917.4 in ice density, t (sec) = time, x (m) = distance, U_w (m/s) = lengthwise direction of river, the running water speed, n ($s/m^{1/3}$): Manning's roughness coefficient was 0.008 in the reproduction calculation of this experiment. R (m): hydraulic radius and S (m): wetted perimeter; Calculations were made assuming complete freezing in the event regarding, when the thickness of the ice block H_i is twice the thickness of the ice model described later, 0.6 cm.

$\partial H_z / \partial x$ in the third term on the left side of equation [2], which is the equation of motion, is the water surface gradient. The water level and water surface gradient change due to the presence of floe, and this value is important in this calculation model because the speed of the floe changes as the flow velocity changes. The water level, H_z (m), was calculated as "the height of the riverbed + the water depth, taking the void space of the ice floe into consideration + the depth of the draft of the ice floe." The specific method used in the calculation is to divide A_w obtained by equation [1] by river width B to obtain water depth H_w taking into account the gaps of the ice floe; thus, the water level H_z was calculated as the bed height Z (m) by the following equation.

$$H_z = Z + H_w + \frac{\rho_i}{\rho_w}(1 - \lambda_i)H_i \qquad \textbf{[3]}$$

2.2 Calculation of Ice Flow

The ice flow calculation was carried out using the basic formula for the flow of the ice floes, which is the formula of continuity and river ice flow sedimentation, formula (Yoshikawa et al., 2018). The river ice deposition equation is derived from the assumption that river ice is an ice block of ice aggregates and assumes that the rotational moment of the force acting on the ice block is zero.

$$(1 - \lambda_i)\frac{\partial A_i}{\partial t} + \frac{\partial Q_i}{\partial x} = 0 \qquad \textbf{[4]}$$

$$Q_i = A_i U_i \qquad \textbf{[5]}$$

$$U_i = U_w - \sqrt{\frac{\frac{B_i}{B_d}\left(\frac{\rho_w - \rho_i}{\rho_w}\right)gH_i}{\frac{C_D}{2}\left(\frac{H_i}{L_i}\right)^2 + C_f\left(\frac{H_i}{L_i}\right) + \frac{C_L}{2}}} \qquad \textbf{[6]}$$

Where Q_i (m^3/s) is the ice block discharge, U_i (m/s) is the Speed of ice block in the lengthwise direction of the river, B_i (m) is the Width of ice mass in the transverse direction of the river, B_d (m) is the River width downstream from target section, ρ_w (kg/m^3) is the water density, ρ_i (kg/m^3) is the ice density, g(m/s^2) is the gravitational acceleration, H_i (m) is the vertical thickness of the ice block, L_i (m) is the Length of ice block along direction of the river, C_D is the Coefficient of drag, C_f is the Coefficient of friction, and C_L is the Coefficient of lift.

Regarding the calculation conditions, the Courant number was 0.005 and the cross-sectional area of the calculation section was 10 cm. In addition, by trial and error, the value of the river width of the cross-section was obtained from B_i and L_i and, in the case where the speed of the ice block becomes less than 0.5 times the speed of the running water, the calculation was performed with the speed of the ice blocks set to zero. These values need to be revalidated in subsequent studies.

3. Ice Jam Experiment and Reproduction Calculation at the Bridge Pier

3.1 Experimental Channel, Experimental Conditions, and Measurement Items

The shape of the experimental channel, the discharge, the amount of ice, and the ice size were investigated for the determination of ice jams (Yoshikawa et al., 2011) that occurred in the actual Shokotsu River in February 2010, for which detailed field observational data exists.

The method of setting the experimental channel shape is described as follows. The discharge before the ice jam occurred is 14 m^3/s and, from the results of the general cross-sectional unequal flow for the sections between 11 km and 20 km from the estuary where the ice jam occurs, the minimum water surface width was 21.3m, the average was 40.8m, the maximum was 82.0m, the minimum riverbed gradient was 1/769, and the maximum was 1/125. Considering the simplicity of hydraulic experiments, the model scale was set to 1/100, the width of the channel was set to 20 cm at the bottom of the low channel, the full water width of the low channel was 30 cm, the maximum width of the channel was 80 cm, and the slope was 1/120. The experimental channel is shown in Fig. 2, and the standard cross-section is shown in Fig. 3.

The length of the waterway is 15.41m, the height from the bottom of the low channel to the height of the high water channel bed is 2.6cm, the gradient of the low channel is 1:2, the width of the bed of the high water channel is 25cm (2 places on the left and right), and the downstream end of the channel has a step. The pier model installed two piers at the location shown in Fig. 4 at the point 6m from the downstream end in Fig. 2 with reference to the shortest distance between the piers for the Memorial Bridge of Shokotsu river. Part of side wall of the waterway was made of transparent acrylic material to better visualize the phenomenon, and other parts of the side wall, except for acrylic material and the bottom of the waterway, were made of wood. Waterproofing was performed through the application of a sealer, and the surface was painted twice. Concerning the color of the surface coating, the bed of the lower channel was painted yellow and that of the higher channel matted black so that it would be possible to distinguish between the ice model and the flood of the high water channel bed.

In order to decide the upstream discharge, we refer to the maximum discharge 286 m^3/s at the time of ice jam generating in actual river, and examined the conditions which ice jam generates. The result of examination, the value of the half of the maximum discharge was adopted and the discharge of the experiment was made into 1.4 L/s using the Froude similarity rule. The structure is such that the upstream end flow volume is pumped from the water tank installed at the downstream end to the upstream water tank (8.5m x 1.5m x 0.9m) with a submersible pump and then the water is pumped from the upstream water tank to the water tank directly connected to the water channel which overflows from the triangular weir, and the upstream discharge was controlled using the overflow depth from the triangular weir. Before this experiment, the discharge was verified with the capacity equation.

The running water was colored at a concentration of 2% using a white bath salt (Earth Pharmaceutical Co., Ltd., Basroman Premium Skin Care) for easy identification of flooding of the high water channel beds. The total amount of water used in this experiment is 8,288L. The specific gravity of the colored water was measured with a standard hydrometer and found to be 1.022.

The ice mass discharge of the experiment was made into 0.6 L/s using the Froude similarity rule. We refer to the ice mass discharge 60 m^3/s before ice jam generating in actual river. The ice size was 4 cm x 4 cm and the thickness was 0.6 cm based on the maximum ice size of 4 m and the thickness of 0.6 m of the ice that had accumulated in the river after the ice jam occurred. 500 ice models were made of polypropylene with a specific gravity of 0.92, which is equivalent to that of actual river ice. Assuming the ice model speed obtained by PTV analysis, to make the ice model easier to decipher, the entire surface of the ice model was colored with fluorescent orange on both sides, and a circle with a diameter of 2 cm was provided on both sides and was colored blue. The ice model input position was 13.5 m from the downstream end in Figure 2. At the loading position shown in Fig. 2, ice models were manually loaded for eight seconds at the rate of 62.5 ice model per second

As shown in Fig. 2, the water level was measured by installing six piezos (pressure sensors, STS ATM.1ST) on the bottom of the low channel, and the measured pressure was converted to water level and measured. The measurement interval was 0.01 seconds. A KEYENCE NR-600 stand-alone measurement unit was used as a data logger. The water temperature was measured before and after the experiment and was 14℃ both times.

A single-lens reflex digital camera (Canon EOS Mark II) was installed above the waterway to grasp the experimental situation, and images were taken over a range of 6 m along the waterway length.

The ice jam experiment was performed in two cases, one without the pier model and the other with the pier model installed.

3.2 Ice Jam Experiment Status

Figure 5 shows the experimental case where the pier was installed in the camera image taken from above the waterway. An ice jam occurred at around 17 seconds in Fig. 5 c). Specifically, the ice model was deposited first on the outside of the pier with the slow flow velocity, and the ice model was deposited in an arch shape with the pier as a fulcrum and drawing an arc upstream. From Fig. 5d) to h), the running water and the ice models are running on the high water channel bed on the left and right banks upstream from the pier after the occurrence of the ice jam. After that, the running water and the ice models returned to the lower channel below the pier, and some of the ice models were deposited on the low channel slope. Approximately 300 sheets were deposited in the low channel due to ice jam, and about 50 sheets were deposited on the high water channel bed, for a total of 500 pieces from among the ice models input.

3.3 Water Level Change in the Ice Jam Experiment

The study of water level change is a prerequisite for the proper understanding of the ice jam phenomenon and predicting the River water level rise. Figure 6 shows a case where no pier was installed, while Fig. 7 shows a case where a pier was installed. The experimental water level in the figure is a moving average value at 0.2-second intervals.

In the case without the pier in Fig. 6, the water level dropped at 15 seconds from the start of the experiment at the point of 8m. From the camera image, the ice models accumulated in the low water channel about 8.5 m upstream at 14 to 15 seconds from the start of the experiment;

then, the ice models accumulated 16 seconds from the start of the experiment and formed an accumulated mass that flowed downstream. The drop in the water level 15 seconds after the experiment began at the 8 m point may be caused by the blockage of the flowing water resulting from the accumulation of the ice model about 8.5 m upstream, so the water level downstream had dropped. The subsequent rise in the water level might be due to the rise in the downstream water level due to the flowing downstream of ice models accumulated at about 8.5 m upstream. One of the factors that caused the ice models to accumulate at the point of about 8.5 m was that the ice models were input manually, so it was not strictly possible to insert the ice model smoothly and evenly so as not to affect the water .The reason for the rise in the water level at about 45 seconds from the start of the experiment at the 2.0 m point and the drop in the water level at 50 seconds after the start of the experiment is that the ice models accumulated at the most downstream position at the end and the water level rose. After that, the ice models were removed manually and the water level dropped.

In the case with the pier shown in Fig.7, the water level drops at about 8 meters approximately 11 seconds from the start of the experiment. According to the camera images, ice models were accumulating in the low water channel at about 9.0 m upstream at about 11 seconds from the start of the experiment; then, at 12 seconds, the ice models became aggregated and moved downstream. The reason for the drop in water level 11 seconds after the start of the experiment at the 8 m point might be due to the dropping of water level on the downstream side which resulted from the accumulation of the ice models at about 9.0 m upstream, which blocked the flowing water. The subsequent rise in water level may be due to the rise in the downstream water level as a result of the ice model accumulation at about 9.0 m upstream that was eventually carried downstream. One of the factors that made the ice model to accumulate at about 9.0 m point is that the above-mentioned ice model was manually input.

In Fig. 7, the water level rises 16 to 17 seconds after the experiment at the 6 m point where the pier is installed and falls 23 seconds after the experiment started. From the camera image and Fig. 5, the ice models start to accumulate (ice jam) 16 to 17 seconds after the experiment started, and form an arc-shaped ice jam as the ice model draws an arc upstream at 23 seconds after the experiment started and the number of ice models flowing downstream was reduced. At the 6 m point where the pier is installed, the water level rose due to the ice jam of the ice models; however, it can be estimated that the water level at the pier dropped afterward due to the accumulation of the ice model at the arch. On the other hand, at 7 m upstream, which is affected by the ice jam, the water level rose from about 23 seconds after the start of the experiment to about 2.2 cm.

3.4 Reproduction Calculation of Ice Jam Phenomenon

In the change in water level between the experimental and calculated values, the cases with and without installed pier are shown in figures 7 and 6, respectively.

In the case without the pier, the calculated value reproduced the experimental value for the water level change at 10 m well. On the other hand, the calculated water levels do not reproduce the experimental water levels for the water level change at 8 m at around 15 seconds from the start of the experiment. Furthermore, the calculated water level peak and the experimental water level peak at 7, 6, 5 and 2 m after that are out of phase. These factors may be influenced by the ice model introduction method described above. Looking at the water levels at all points between 0 seconds and 60 seconds from the start of the experiment, it can be observed that the calculated values reproduced the experimental values to a large extent.

From this study, it has been shown that this calculation model can reproduce the water level change caused by the ice flow. In the case with the pier (Fig. 7), the calculated value well reproduced the experimental value for the water level change at 10 m. At the 8 m point, the calculated value was higher than the experimental value for the water level changes due to the downstream ice jam that occurred 29 seconds from the start of the experiment. In the experiment, the rise in water level was suppressed by the flooding of the high water channel bed; however, it is thought that the water level was higher than in the experiment because the high water channel bed was not considered in the calculation. The calculated value is lower than the experimental value for the water level change due to ice jams occurring 30 seconds from the start of the experiment at the 7 m point. On the other hand, the calculated values are higher than the experimental values at 6 m and 5 m; this observation may have resulted from the underestimation of the effect of ice jams on the running water during the calculation by the basic formulae of this calculation model. A possible way to remedy the situation may be to increase the value of Manning's roughness coefficient at the point the ice jam occurs. The calculated value was lower than the experimental value for the water level change at 40 seconds or more after the start of the experiment at 2 m.

This is thought to be a lower water level than in the experiment because, in the experiment, the running water that overflowed the high water channel bed due to the ice jam upstream circumvented the pier and flowed into the low water channel downstream, raising the water level. It is considered lower than the experiment.

This study showed that the calculation model can qualitatively reproduce the water level change of the ice jam phenomenon. On the other hand, it may be pointed out that in the basic formulae of the calculation model, the effect of ice jams on running water was properly evaluated and high water channel beds were considered to increase reproducibility.

4. Discussion

To elucidate ice jam phenomena at bridge piers, an ice jam calculation model was constructed, an ice jam experiment was performed with a low water channel and a high water channel bed, and the calculated and experimental values were compared for changes in water level caused by the ice jam. The following could be observed from the present study.

The result of the ice jam experiment showed that ice models began to accumulate from the location where the flow velocity was slow outside the pier, and the ice models accumulated in an arch shape facing upstream and forming an ice jam. It was observed that ice models were deposited on the high water beds and low water channel slopes due to the ice jam. For the water level change, it was found that the water level increased upstream of the ice jam occurrence point and decreased immediately downstream. The effects of the ice jam become smaller as the further one goes upstream. The water level rose further downstream from the ice jam occurrence point because the running water from the high water channel flowed into the low water channel again. An understanding of ice jam phenomena was achieved through this experiment.

Comparison of the calculated water level with the ice jam calculation model and the experimental water level showed that, in the case without a pier, the calculation model was able to reproduce the water level change due to the effects of ice flowing downstream. In the case with a pier, it was shown that this calculation model can qualitatively reproduce the water level changes of the ice jam phenomenon. However, to improve reproducibility, it was necessary to properly evaluate the effect of ice jams on the running water in the basic formula of the calculation model and to consider high water levels.

The results of this research will contribute to the study of ensuring the safety of river construction in winter, understanding the timing and location of ice jam occurrences, predicting the increase in the river water level, and quantitatively evaluating the effects of climate change.

Acknowledgments

This work was supported by the research grants of River Center of Hokkaido, JSPS KAKENHI Grant Number JP18K04361 and JP17H01870. We would like to express our gratitude for this.

References

Hokkaido Crisis Countermeasures Section, 2019. Damage from heavy rain and snow melting from March 8 to 9 (2nd report), http://www.pref.hokkaido.lg.jp/sm/ktk/higaiho2_2018 0308_ooame.pdf (Viewed: April 1, 2019)

Yokoyama,H., Yoshikawa,Y., Inami,Y., Maeda,S., Yabe,H., 2018a. Process understanding on the phenomena of flood damage caused by ice jam in March 2018 and future problems, Journal of JSCE, Ser. B1 (Hydraulic Engineering), Vol.74, No.5, I_1039-I_1044.

Yoshikawa,Y., Watanabe,Y., Itho,A., 2014a. A simple equation for ice sheet thickness and ice formation/breakup prediction, Journal of JSCE, Vol.2, Issue1, pp.203-213.

Yoshikawa,Y., Kuroda,Y., Itoh,A., Watanabe,Y., 2014b. The relationship between ice jam occurrence and the croos-sectional profile of ice-covered rivers, JSCE, Advances in River Engineering, Vol.20, pp.241-246.

Toyabe,T., Yoshikawa,Y., Okabe,H., Tanaka,T., 2017. Hydraulic model experiments on ice jam occurrence considering the effects of branch river junction, Journal of JSCE, Ser. B1 (Hydraulic Engineering), Vol.73, No.4, pp. I_1339-I_1344.

Yokoyama,H., Yoshikawa,Y., Yabe,H., 2018b. Ice Jam Occurrence Conditions at Completely Frozen Sites, Ministry of Land, Infrastructure, Transport and Tourism, Hokkaido Dev elopment Technology Research Conference, 61st, Disaster Prevention-9, Prevention 3 2.

Yoshikawa,Y., Park,H., Oshima,K., Yokoyama,H., 2018. Examination of simple ice jams calculation model, Journal of JSCE, Ser. B1 (Hydraulic Engineering), Vol.74, No.4, pp.I_351-I_356.

Yoshikawa,Y., Watanabe,Y., Hayakawa,H., Hirai,Y., 2011. A study of ice break and ice flow during river ice breakup, Journal of JSCE, Ser. B1 (Hydraulic Engineering), Vol.67, No.4, pp.I_1075-I_1080.

Figures

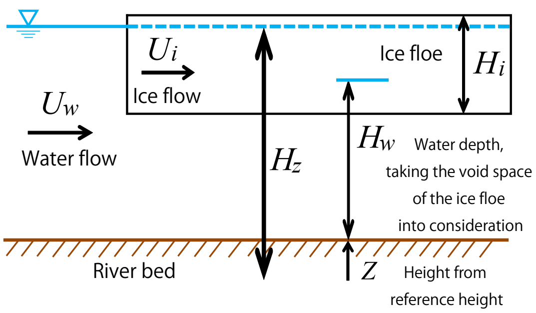

Figure 1. Conceptual diagram of ice jam calculation model.

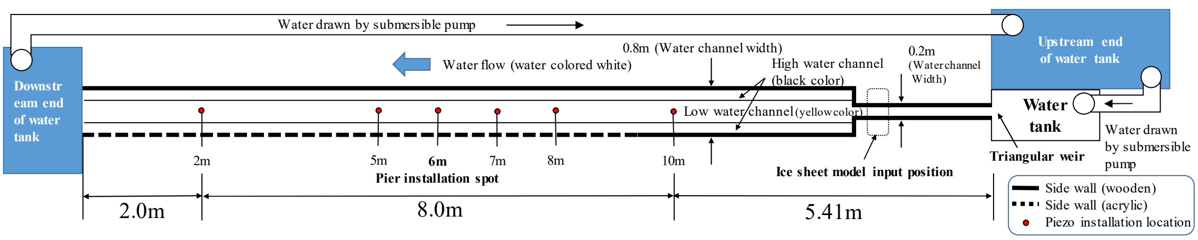

Figure 2. Plane view of the test channel.

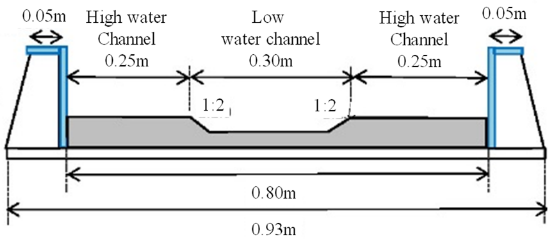

Figure 3.

Standard cross section of the test channel.

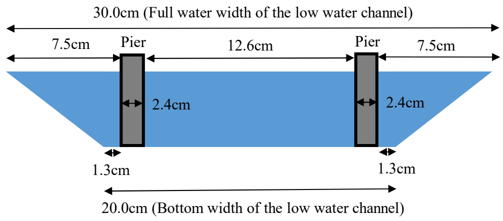

Figure 4.

Cross section of pier installation

(6m from downstream end).

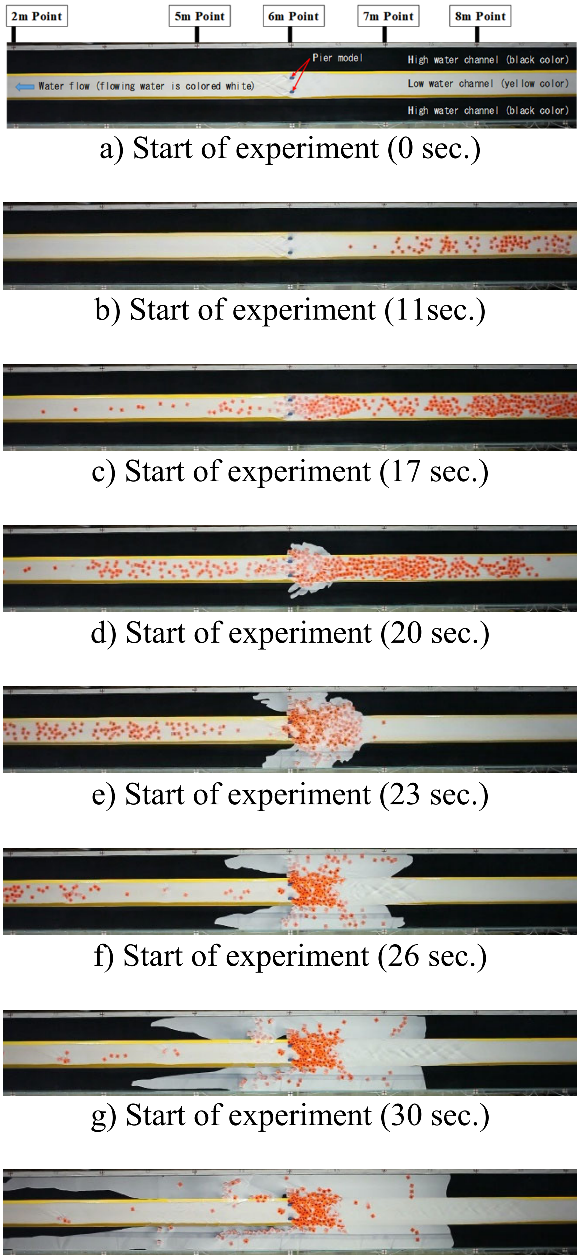

a) Start of experiment (0 sec.)

b) Start of experiment (11sec.)

c) Start of experiment (17 sec.)

d) Start of experiment (20 sec.)

e) Start of experiment (23 sec.)

f) Start of experiment (26 sec.)

g) Start of experiment (30 sec.)

h) Start of experiment (40 sec.)

Figure 5. Ice Jam Experimental State (planar image, including pier)

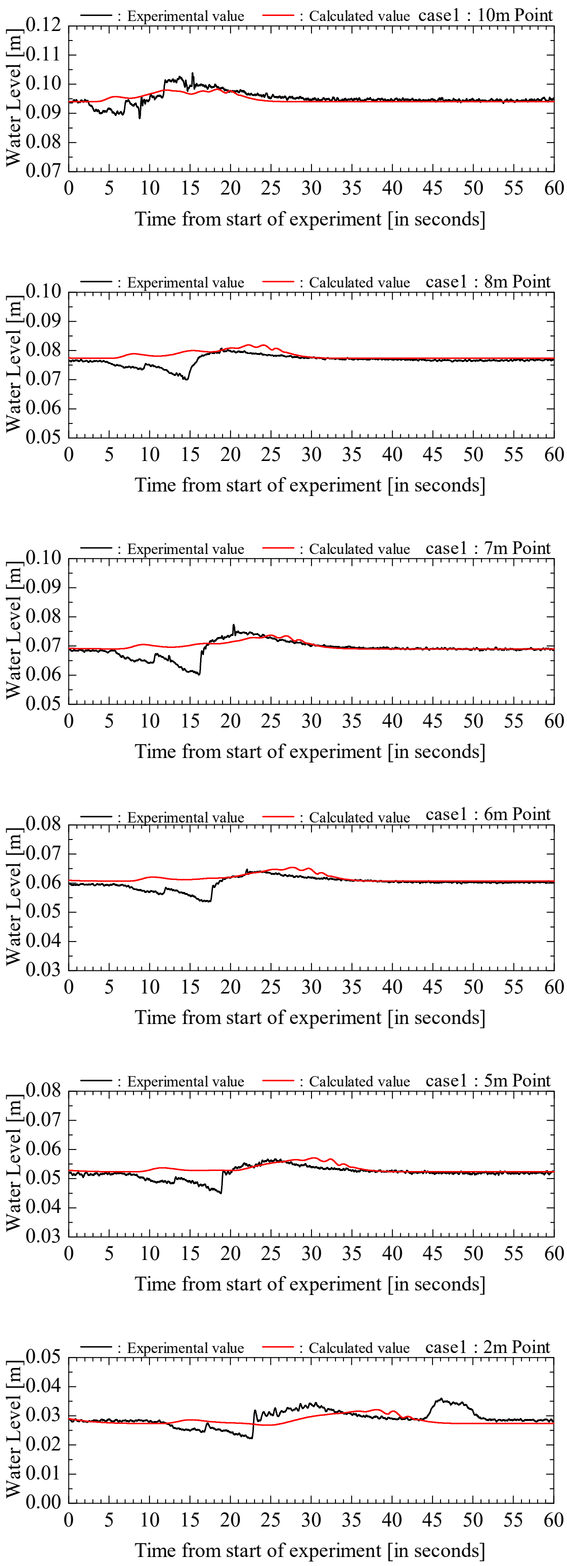

Figure 6. Comparison of Water Levels between Experimental and Calculated Values (Without Pier).

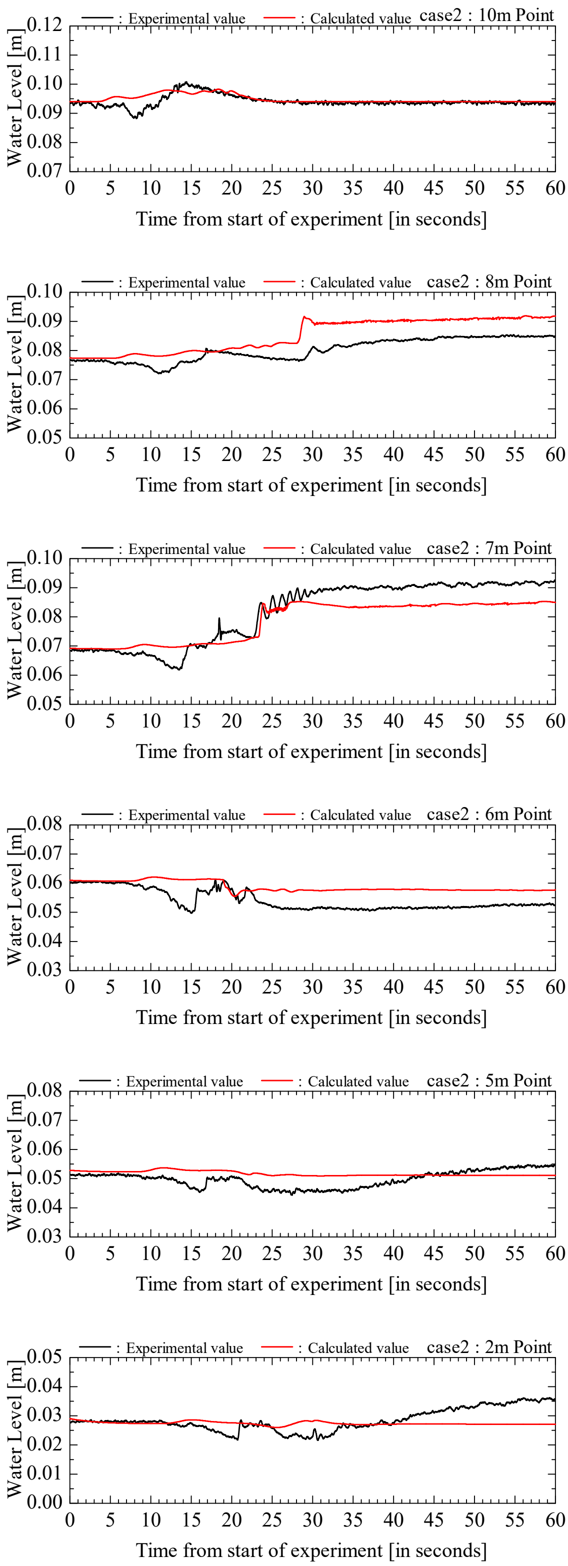

Figure 7. Comparison of Water Levels between Experimental and Calculated Values (With Pier).

13
Ice actions on dams and bridges

25th IAHR International Symposium on Ice

Trondheim, June 14 to 18, 2020

Measurement of static ice loads on dams, with varied water level

A.B. Foss
Sweco Norge AS,

Oslo, Norway aslakbohle.foss@sweco.no

ABSTRACT: A field program was undertaken in 2017 to (i) measure the forces in the ice sheet near a dam and (ii) observe the behavior of the ice sheet with controlled water level fluctuation of the reservoir. The field program was conducted at Dam Taraldsvikfossen outside Narvik town, located in northern Norway. Three different load scenarios were tested with 0.06, 0.22 and 0.35 m water level fluctuations. During the load scenario with 0.06 water level fluctuations it was considered that the ice pressure was reduced due to the variation in water level. The maximum ice load was registered at 85 kN/m during the load events with the highest variation in water level. It was concluded that the volume of the cracks, the number of cracks and the volume of refreezing of the cracks in an ice cover had a major impact on the ice load. These parameters, together with water level fluctuation, ice thickness and temperature variation, had the greatest impact on both the maximum value of the load and the ice sheet behavior. In an overall assessment of all the components presented in the paper, it was concluded that today‘s knowledge of ice loads is still limited. A general assessment of the measurement program and the measurement results has been conducted as a basis for continuing similar measurement programs.

1. INTRODUCTION

When a lake or a reservoir cools down, the water cools on the surface. This water will become heavier and therefore sink deeper at the same time as water flows up (Bergdahl, 1977). At stagnant water, the thin surface layer can reach the freezing point while the rest of the water volume has a temperature equal to 4°C. When the water in this layer reaches the freezing point, it begins to form ice (Ashton, 1986). An ice cover will be able to apply large loads to dam structures, either by thermal expansion or water level variations.

Design rules and practices have been established in several countries to ensure the safety of dams. One design parameter is static ice load, describes as a result of thermal expansion of the ice cover or water level fluctuations (Comfort, 2003). Ice loads are variable actions whose intensity and/or points of application vary frequently and significantly over time (CFBR, 2013). According to the guidelines of Norway (NVE, 2003), thermal ice loads are assumed to be a line load between 100 and 150 kN/m acting near the top of the dam. The ice load will have a major impact when calculating the stability of a dam. It will have a particularly large impact on low concrete and masonry dams. In many cases, ice loads would be the driving force for rehabilitation of a dam. It is therefore important to anticipate the correct maximum load and behavior of the load events.

Sensors used for ice stress measurements can be separeted into two categories (Cox and Johnson, 1983): cylindrical sensors having an effective modulus much greater than ice, and thin, wide sensors (flat-jacks), preferably having an effective modulus close to that of ice. Both cylindrical and flat-jacks stress gauges have been found to compare well during a series of field measurements in Canada (Morse et al., 2011, Taras et al., 2011).

New measuring equipment and new measuring methods, as described, have made measurements of ice load both easier and more accurate than before. Norut Narvik currently has an ongoing measurement program at the Taraldsvikfossen dam in Narvik. The reservoir in Taraldsvikfossen is small and can easily be regulated to manipulate water level fluctuations that will give particularly interesting load events. This study focuses on ice loads from water level fluctuations. Measurements were performed in a reservoir at a time of year when the ice level was kept steady.

2. ICE LOAD MEASSUREMENTS AT TARALDVIKFOSSEN DAM

The measurement program on dam Taraldsvikfossen started winter 2012/13 (Petrich,2015). The program was implemented as a basis for establishing measurement procedures, improving the design basis and increasing the understanding of ice load due to water level variation on dams. The load events presented in this paper was a result of measurements conducted in the winter of 2016/17. Recent research (Comfort et al., 2003, Blazevic, 2011) shows that load events on an ice-covered reservoir due to water level fluctuations combined with thermal expansion has greater measured maximum load and greater load variation, than load only generated from thermal expansion alone.

The motivation of the program was mainly to simulate a water level fluctuation, and to look at the behavior of the ice sheet and the loads occurring. Previous literature (Comfort et al., 2003) has only looked at uncontrolled fluctuations, and has therefore not had the opportunity to create such a load event. It is therefore completely unique to be able to simulate such load situations under nearly optimal conditions. To observe effects only due to ice jacking, the temperature should be almost constant throughout the measurement period. The temperature was therefore also measured during the load events.

Pressure Cells

In this measurement program, four oil filled GeoKon 4850 pressure cells were installed in the middle of the dam. The center of the second upper stress cell was 20cm below the ice surface at deployment. The cells consisted of two rectangular steel plates (10 * 20cm) which were welded together with air-free oil between the plates. A small tube connected the cell to a vibrating wire pressure transducer that also measures temperature with a temperature dependent resistor.

The pressure cells were calibrated with an accuracy of <0.5kPa. The cells were then mounted on a steel frame, with a vertical distance center distance of 18cm. In this article each individual pressure cell is named A1, A2, A3 and A4, where A1 is the top cell. The water level was between pressure cell A1 and A2 at the start of the load events. Pressure cell A1 was placed that way so we could measure the pressure if the ice grew above water level. The pressure cell could measure ice pressure, ice and water temperature and water level variation. A temperature sensor was also installed, two meters from the dam, which measured air temperature.

Figure 1. Three of the oil filled GeoKon 4860 pressure cells

Figure 2. Size and placement of the pressure cells

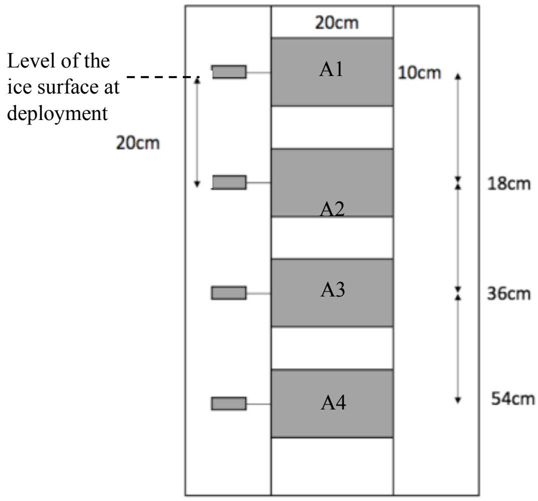

Measurement area

Dam Taraldsvikfossen is a gravity concrete dam with a vertical upstream surface. The reservoir functions as a backup source for drinking water to the city of Narvik. The reservoir is located in an area where there are stable low temperatures and with few external stresses in the form of wind. The reservoir alsohave the possibility of controlled fluctuations without major financial or environmental consequences. By agreement with Norut Narvik, it was chosen to carry out the measurement program at dam Taraldsvikfossen.

Logging

When the load panels were placed on the dam, they were also connected to recording equipment and a storage unit located in the dam. The events were monitored by remote sensing. The valve house had access to electricity which also made it possible to obtain measurement data directly when present at the dam. This had great utility value during the fluctuation of the reservoir.

All instruments were connected to a CR1000 data logger, and the ice load was recorded with a time interval of 5 minutes throughout the measurement period. Snow depth, freeboard and ice thickness were measured manually and logged before and during each test.

Fluctuations of the water level in the reservoir

Dam Taraldsvikfossen had two valves, one located in the valve housing and one located down in a drain downstream of the dam. Both valves were shut-off valves on the same drainpipe. It was important to control the fluctuations accurately. It was therefore chosen full opening on the valve in the drain, so that the fluctuation could be controlled more accurately from the valve in the valve housing. The water level variation was then registered by the pressure cells. The water level variation was also controlled manually by a ruler.

Since the knowledge on the field is still limited, there was great uncertainty about how the ice sheet would behave during the controlled fluctuations. According to previous measurement of ice loads it has been observed that Maximum ice loads occurs at water level fluctuations between 0.5h and h, where h is the average ice thickness (Comfort et al., 2003, Taras et al., 2011, Stander, 2006). Where *h* symbolizes ice thickness and *a* variation in water level. When the average ice thickness was measured at 600mm, it was expected that the ice load would reach the maximum value between $300\text{mm} < a < 600\text{mm}$ variation.

It was important to choose a measurement period that showed stable low temperatures with little temperature variation. Three different load events were selected. The duration of the load events is presented in Table 2. The water level variation is represented as the maximum decreasing of water level from the start of the fluctuation.

Table 2. Overview of the water level fluctuations and the duration of the load events

Load event no.	Water lever variation [m]	Duration [h]
1	0.06	11
2	0.22	11
3	0.35	24h

Load event 1 was conducted with a low water level variation as the motivation for this load event was to observe the behavior of the discharge mechanisms, the inflow and the ice cover.

Load event 2 was subjected to a larger water level variation, but with the same duration as load event 1. After about 0.1m water level variation, crack formations were observed in the ice cover. It was concluded to stop the fluctuation of 0.22m as there was a danger that the crack pattern would have an impact on load event 3.

In order to observe a longer load event, load event 3 was carried out with a longer duration. At a water level variation of 0.3 mm, it was considered that the cracks near the dam and in the surrounding terrain were of such large size that there was a danger that the ice cover would collapse. As such a break-up would significantly reduce the ice load, it was concluded to stop the fluctuation at 0.35m, so that the ice cover was intact during the entire load event.

Ice Conditions

Prior to the load events, measurements of ice conditions were conducted. The first measuring point was close to the dam body and the remaining measuring points were taken perpendicular on the dam (Table 1). The thickness of the ice sheet varied from 0.5m near the dam, and 0.7m at the center of the ice sheet. The same measurements were also performed during load event 3 to observe behavior of the ice sheet during water level fluctuations.

Table 1. Measurements of ice thickness, snow depth and freeboard before load event 1

Measurement point	Distance from dam [m]	Ice thickness [m]	Snow depth [m]	Freeboard [m]
M1	0.1	0.52	0.20	0.04
M2	0.5	0.49	0.15	0.03
M3	1	0.48	0.12	0.01
M4	2	0.51	0.30	0.02
M5	5	0.56	0.17	0.03
M6	10	0.66	0.60	0.04
M7	15	0.70	0.60	0.05
M8	20	0.72	0.80	0.06
M9	25	0.72	0.12	0.03

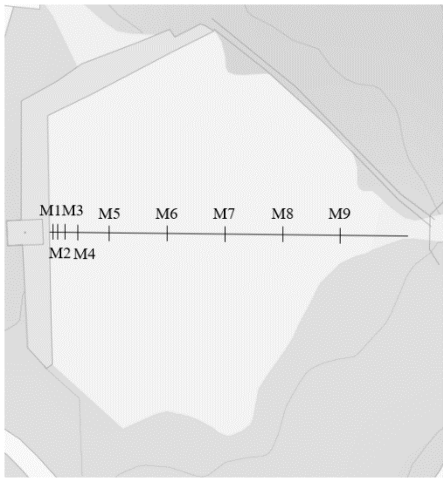

Two weeks before the start of the load events there were stable low temperatures without large rapid variations. This was the most stable period for air temperature in the winter of 16/17.

Temperature

The development of air temperature during the measurement period is based on measurements from the weather station installed on the dam body. The plot for ice temperature is based on measurements from the center of the three lowest pressure cells. In load event 1, the air temperature was stably low during the fluctuation, with little thermal variation. There was no marked rise in temperature that caused the build-up of a thermal ice pressure. The air temperature varied from -8ºC to -5ºC. The ice temperature had a low variance and dropped by 1ºC at all pressure cells. It is indicated that the ice was not largely affected by the temperature drop of 3ºC.

In load event 2, there were larger variations in the air temperature, and it was defined as a thermal load event. A thermal load event will occur in an ice cover if the average temperature, T, is lower than -2ºC and increases by more than 5ºC over two days. Individual load cases are separated at a temperature drop of 5ºC over one day or two days (Petrich et al., 2015).

The air temperature was -9ºC before the fluctuation, 1ºC at the lowest point of the water level decreasing and -5ºC when the water level was back to its normal level again. The ice temperature in the ice sheet was affected to a greater extent than in load event 1. In load event 2 the ice temperature increased at most by 2ºC in pressure cell A2. This indicated that the increase in air temperature influenced the ice. As the duration of the air temperature change only lasted for 5 hours and dropped to -5ºC after another 5 hours, it was expected that the thermal change did not have a large effect on the total ice load.

During load event 3, there were large temperature variations, and as load event 2, the change is defined as a load case (Petrich et al., 2015). The air temperature varied from -10ºC to 2ºC during the fluctuation. The temperature increase lasted for 40 hours before the temperature dropped again to -3ºC when the water level reached its normal level. The ice temperature was already 2ºC warmer at the start of the fluctuation compared to the other load events and had a much greater variation. The most noticeable case was that the ice temperature in pressure cell A2 varied from -4 ° C to -1 ° C. When the water level was decreased with 0.35m, water rose to the surface of the ice in some places. This may have affected the increase of the ice temperature.

The temperature of the ice can differ markedly from the air temperature (due to the insulating effect of snow and heat resistance in ice) and it is often 5 degrees warmer in cold periods. When weather changes from cold to hot, the temperature of the ice can also be calculated relatively easily hour by hour using non-stationary conditions using the heat conduction formula. This agrees well with measured temperatures as the heat conduction only takes place vertically.

Crack pattern

Cracks may form during water level fluctuations, or contraction due to temperature variations. These cracks will affect the stress distribution within the ice cover. Water filled cracks may refreeze at a later stage. Cracks, both dry and wet and refrozen, will always have an impact on the behavior and stress distribution (Ashton, 1986, Metge, 1976).

During all observed load events, there was crack formations visually to the naked eye, and the visible cracks increased in both depth, width and length with decreasing water level fluctuations.

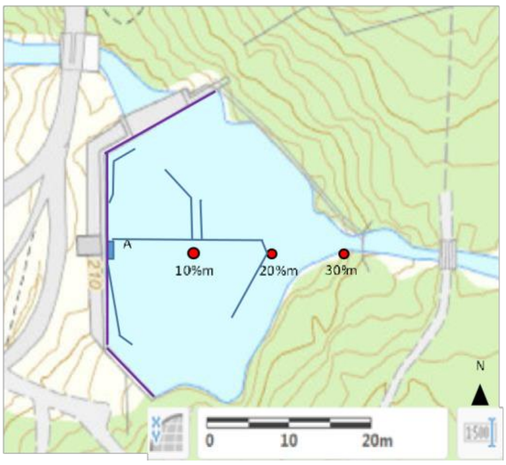

Figure 3 a). Observed crack pattern in the ice cover after load event 2

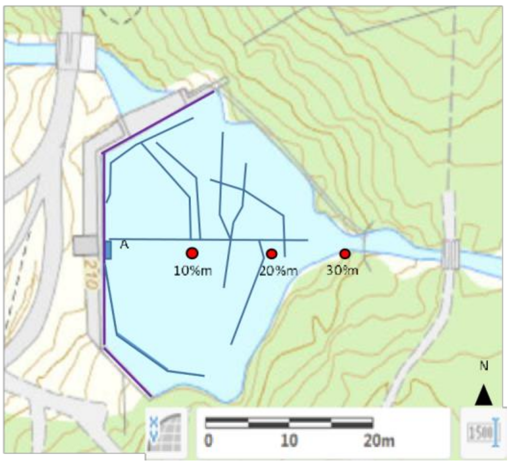

Figure 3 b). Observed crack pattern in the ice cover after load event 3

Observed crack pattern in the ice cover after load event 2 and 3 are illustrated in Figure 2 a) and b) respectively. The figure illustrates cracks that were open all the way to the surface. Both before and after load event 1, no visible cracks were observed.
During load event 2 a crack with width of 20mm quickly formed perpendicular on the dam.

The remaining cracks were formed towards the end of the fluctuations and had a width of 10mm. All observed cracks were dry. It was observed that the ice was firmly fixed in both the dam and in the surrounding terrain during the entire load event. 12 hours after the water level had returned to normal levels, the cracks had become significantly more narrow and shorter. The thickness of the crack perpendicular on the dam had been reduced by 10mm, and the crack length was reduced by 2m. The thickness of the remaining cracks was reduced by 5mm, and the crack lengths were reduced by 1-2m.

Figure 4. Water-filled crack during load event 3

Figure 5. Dry cracks 10m from the dam

Load event 3 was the only event where cracks were observed before the start of water level fluctuation. Shortly after the start of fluctuation, the crack pattern was almost identical to load event 2. New dry cracks were developed after 0.15m fluctuation. No further cracks were developed after this point, but the cracks increased in width and length with increased fluctuation. At 0.35mm fluctuation, the cracks in the ice sheet were in average 30mm wide, while the cracks parallel with the dam had a width of 50mm. It was observed that the ice cover was fixed in both the dam and the terrain during the entire load event 3.

After the water level had been decreased down to 0.25m, water-filled cracks were observed for the first time (Figure 4). These cracks were observed on the south and northeast sides of the reservoir. After 0.3m water level fluctuation, water-filled cracks were also observed 20m from the dam.
In contrast to load event 2, the cracks in load event 3 were not refrozen to the same extent. 12 hours after the water level fluctuation, the ice cover still had the original crack pattern (Figure 5) without any significant reduction in width or length.

Vertical motion of the ice sheet
In addition to observing the crack pattern, measurements of the vertical movement of the ice sheet perpendicular to the dam were also carried out during load event 3. These measurements are presented in figure 6 and show how the ice cover changes vertical position during the water level fluctuation. The measuring points were selected by observing at the crack pattern from load event 2. The measurements were conducted during load event 3 at 0.1m, 0.2m and 0.35m decreasing of the water level.

The largest vertical motion was expected near the cracks. Load event 3 had a water level fluctuation of 0.35m and a duration of 24 hours. The value of the water level variation is less than the thickness of the ice and will therefore be able to generate a high load component (Comfort et al., 2003).

The largest vertical displacement (35cm) was measured 26m from the front of the dam. The vertical displacement decreased near the opposite end of the dam, and the ice sheet had no displacement at the front of the dam. This indicates that the ice cover was fixed to the dam and fixed to a certain extent to the surrounding terrain.

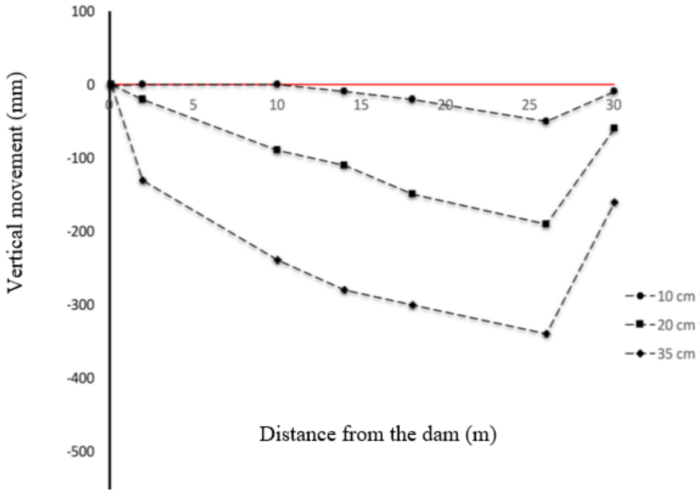

Figure 6. Vertical motion of the ice sheet during load event 3. Vertical movement (mm) on the x-axis and distance from the dam (m) on the y-axis

Cracks were observed parallel to the front of the dam at L = 0.5m, 13m, 18m and 24m (Figure 3 b). The measured cracks correspond well with the positioning of the ice sheet. Evidence of a wedging effect is substantiated by the gradient of the graphs changing in accordance with the position of the cracks. A wedging effect could generate a large load contribution against the dam structure.

As a result of the vertical motion, a rotation of the fixed ice sheet towards the front of the dam may occur. The crack formation led to the ice sheet being broken up into smaller ice blocks. The ice block that was attached to the front of the dam is therefore pulled out at the top when water level decreases and pressed up against the dam when the water level rises to its normal level. As the ice sheet was fixed to both the dam and the surrounding terrain, and the entire sheet was intact during the entire water level fluctuation, it was expected that this created a large pressure against the dam.

A load event can occur after a decreasing of water level, when the water level returns to its normal level. When the water level rises, water will seep into the cracks in the ice sheet. If the cracks are exposed to cold temperatures, the water will freeze. This repetitive cycle will be able to generate vertical layers of ice inside the cracks and the ice cover will expand. This effect will occur after the water level returns to its normal level. When water-filled cracks were observed during load event 3, it seems likely that such an effect occurred.

3. RESULTS

Maximal ice load

The results of the load events are shown in table 3 and show maximal measured ice pressure and ice load.

Table 3. Maximal measured ice pressure and ice load from load event 1, 2 and 3

Load event no.	Ice pressure [kPa]	Ice load [kN/m]
1	78	15
2	274	50
3	470	85

The pressure cells measured the ice pressure and was converted to ice load manually. The ratio between ice pressure and ice load is described as $\sigma = P * A$. Where σ is the ice load, P is the measured pressure and A is the crosssectional area of the ice towards the front of the dam. The pressure cells did not measure the pressure in the entire cross section of the ice, it was therefore divided into load zones that represented the registration area of each individual pressure cell. Such a conversion method has been developed by Carter et al (1998) and has been considered to work well in several measurement programs (Stander, 2006, Petrich et al., 2015). The ice load was then calculated by summing the ice load at all the pressure cells.

Load events

The measured ice pressure on the front of the dam varied from -100kPa to 470kPa. The properties of the pressure cells meant that they could not measure a value lower than -100kPa. Measurements with values below -100 kPa could cause the oil in the thick cells to boil, and such an event would lead to the measurements becoming very uncertain. The ice pressure will vary at different depths in the cross section of the ice sheet. In a typical load event for thermal ice load, the pressure will be greatest at the top of the cross-section and decrease with the depth of the ice cover (Bergdahl, 1977). In the case of a load event for ice load due to water level variation, the distribution seems to be different. In all the load events, the same distribution was observed; During the fluctuation, higher ice pressure was measured in pressure cell A4 than in A2. When the load event was completed, and the water returned to normal levels, the pressure in A2 increased, while the ice pressure in A4 decreased. Such a load sequence can be a result of the ice cover being firmly fixed to the dam.

When parts of the ice sheet move vertical downwards, the fixed part of the sheet will be pulled out at the top and at the same time press against the front of the dam at the bottom. When the water returns to normal levels, the effect will be reversed. Such a load distribution will be intensified by greater water level variation.

Load event 1 is presented in Figure 7. Before the fluctuation started (10h), the ice sheet had a residual load that corresponded to a line load of around 15 kN/m. After the fluctuation started, there was a clear reduction of the ice load, and this reduction was kept stable until the end of the fluctuation.

According to Comfort et al. (2003), a water level variation can both increase and decrease the total ice load. A reduction is due to the formation of cracks in the ice sheet, and the stresses in the ice is being "released". As no cracking was observed during the load event, this contrasts with this fact. However, cracks may have formed on the underside of the ice sheet. Such a phenomenon would not be observable from the upper side and would have the same reduction effect as crack formation on the upper side.

Another reason for a reduction may be contractions in the ice sheet due to low temperatures before and during the load event. As there were moderately low and stable air and ice temperatures both before, during and immediately after the load event, it was considered that a reduction of such magnitude seems unlikely to occur only by thermal contraction.

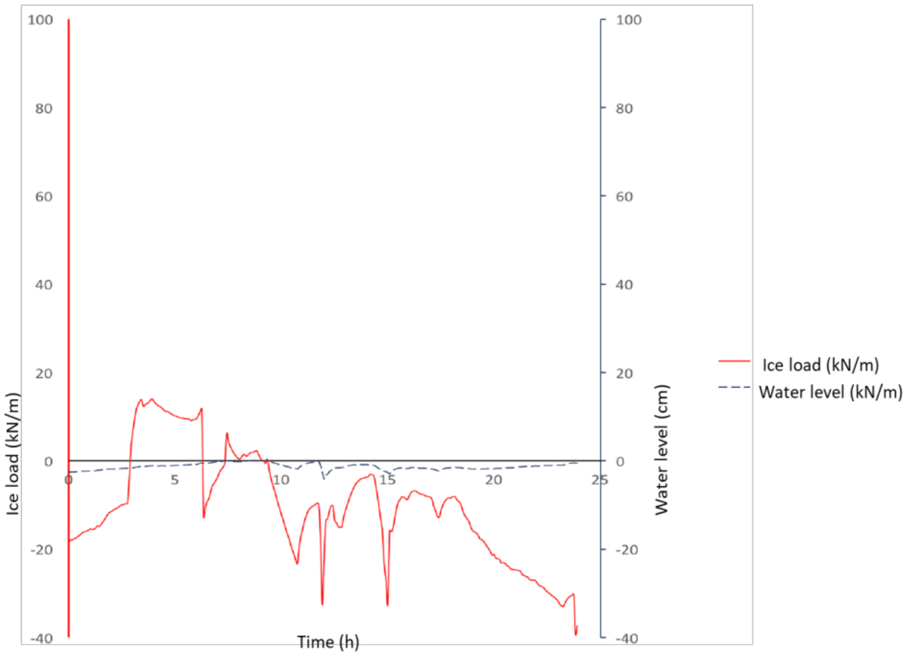

Figure 7. Load event 1. Time (h) on the x-axis and line load (kN/m) on the y-axis

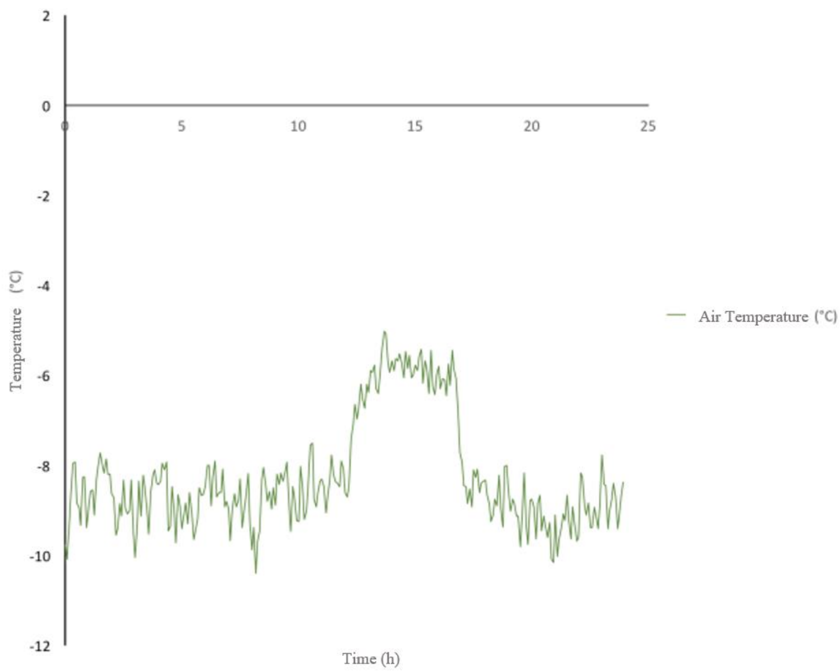

Figure 8. Air temperature of load event 1. Time (h) on the x-axis and temperature (ºC) on the y-axis

By studying the distribution of pressure at the different pressure cells, it was observed that the pressure reduced rapidly at pressure cell A2 at the start of the load event, while pressure cell A4 had no noticable results. It was considered that the reduction of the ice load was probably due to the ice cover being pulled out at the top, but that the water level variation was not of large enough amplitude for the sheet to press on the dam at the bottom. Load event 1 confirms Comfort et al (2003)'s claim that water level variation can reduce the occurring ice load.

Load event 2 is presented in Figure 9. Before the fluctuation started, the ice sheet had a residual load that corresponded to a line load equal to -40 kN/m. This indicates that the ice sheet compressed, and he ice sheet was exposed to a short cooling period before the load event that corresponds well with this load. The ice load increased considerably as soon as the fluctuation started (9h), and the total load increased by 70kN/m within 2 hours. If the residual load had not occurred, it seems likely that the ice load would have had a considerably higher value at this time.

When the fluctuation stopped, the ice load was reduced immediately. Such a phenomenon indicated that the ice sheet was fixed to the dam, and that a wedging effect occurred in that the sheet rotated towards the dam during the fluctuation. An occurrence of a wedging effect is confirmed by the fact that pressure cell A4 registered an increase in ice pressure during the period. When the water level went up to its normal level, an interesting case arose. Immediately after the water level stabilized, the ice load increased considerably. Such a phenomenon can be the result of two different load cases; (1) Thermal expansion will occur in an ice sheet where there are significant changes in air and ice temperature. During load event 2, there was a change in air temperature, and it increased by 8ºC. (2) Freezing of cracks leading to a volume expansion. Such a phenomenon occurs when cracks are frozen by being filled with water and exposed to cold temperatures.

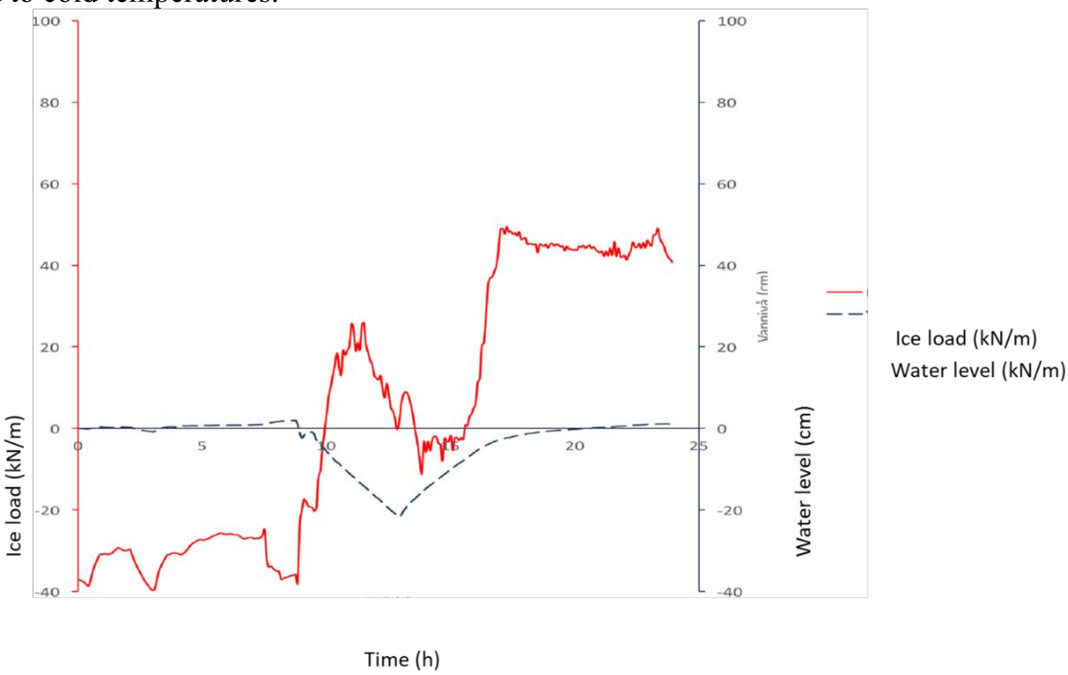

Figure 9. Load event 2. Time (h) on the x-axis and line load (kN/m) on the y-axis)

When the fluctuation stopped, the ice load was reduced immediately. Such a phenomenon indicated that the ice sheet was fixed to the dam, and that a wedging effect occurred in that the sheet rotated towards the dam during the fluctuation. An occurrence of a wedging effect is confirmed by the fact that pressure cell A4 registered an increase in ice pressure during the period.

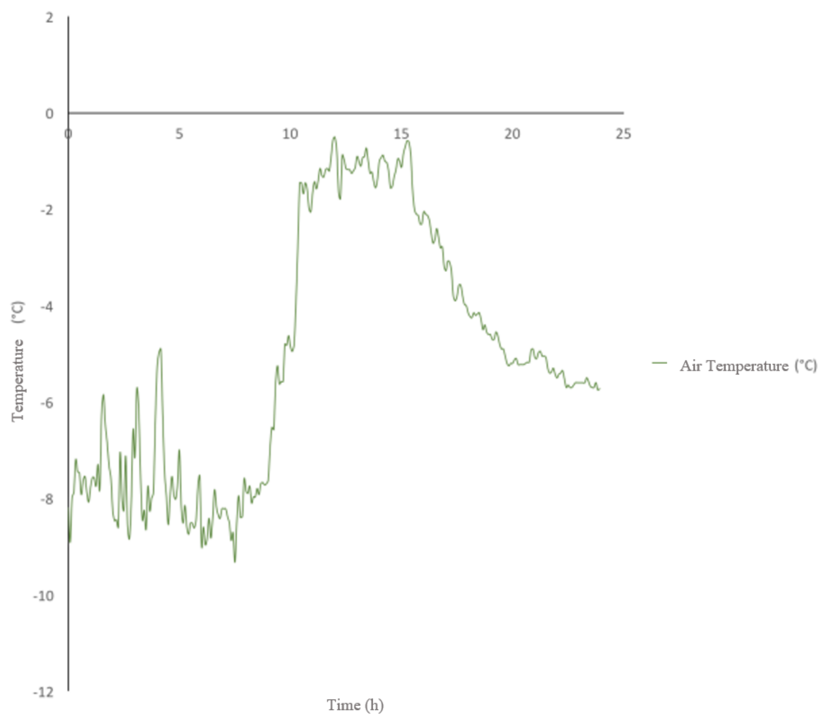

Figure 10. Air temperature of load event 2. Time (h) on the x-axis and temperature (ºC) on the y-axis

When the water level went up to its normal level, an interesting case arose. Immediately after the water level stabilized, the ice load increased considerably. Such a phenomenon can be the result of two different load cases; (1) Thermal expansion will occur in an ice sheet where there are significant changes in air and ice temperature. During load event 2, there was a change in air temperature, and it increased by 8ºC. (2) Freezing of cracks leading to a volume expansion. Such a phenomenon occurs when cracks are frozen by being filled with water and exposed to cold temperatures.

It seems likely that the ice sheet is expanding due to a change in temperature. On the other hand, the ice temperature did not change as much as the air temperature. This indicates that the change in air temperature did not have a large enough effect on the ice sheet to produce a load of such magnitude. It thus confirms that a load contribution arises in addition to the thermal expansion.

The formation of cracks, approximately 2mm wide, was observed during load event 2. As the air temperature dropped considerably just before the water returned to normal levels, it seems very likely that large parts of the cracks froze. Since the air temperature was stable and low at the end of load event 2, this corresponds with the fact that the largest load contribution comes from freezing the cracks.

Load event 3 is presented in Figure 11. The ice cover had almost zero residual load before the fluctuation. As the air temperature before the load event was very stable, it corresponds well with the measured load. When the fluctuation (17h) started, the ice load momentarily increased. The ice load increased almost linearly with the water level variation. As in load event 2, it seems likely that a wedging effect occurred. The measured pressure detected by pressure cell A4 increased markedly during fluctuation, and the measured pressure at pressure cell A2 was greatly reduced.

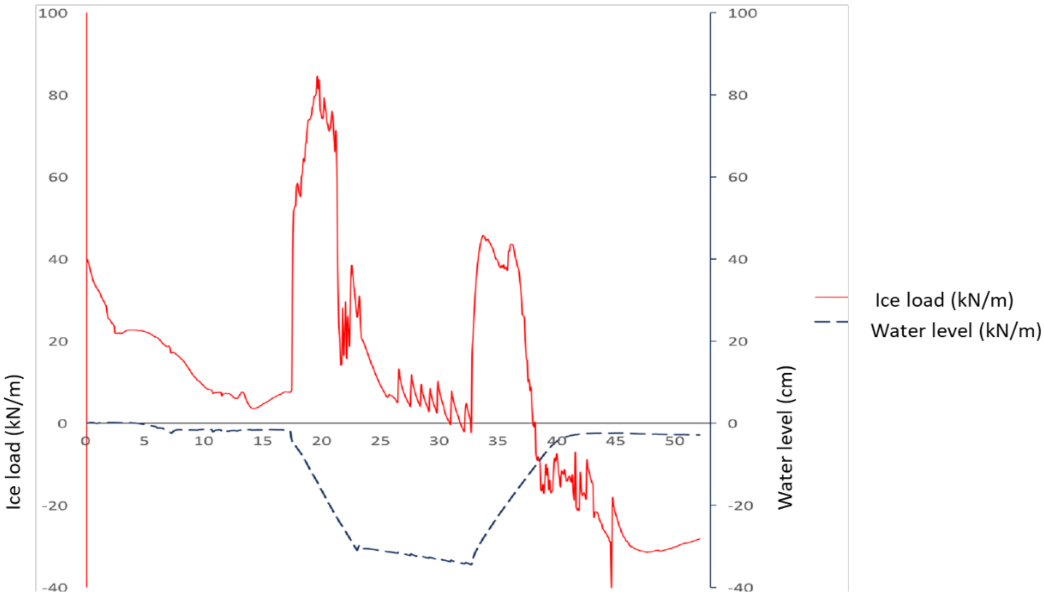

Figure 11. Load event 3. Time (h) on the x-axis and line load (kN/m) on the y-axis

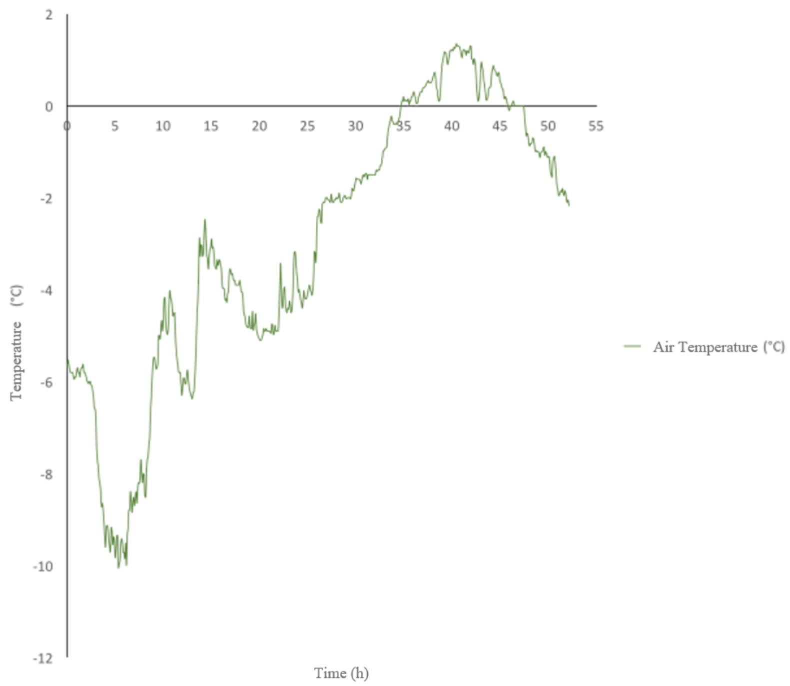

Figure 12. Air temperature of load event 3. Time (h) on the x-axis and temperature (ºC) on the y-axis

After 20 hours, the rate of fluctuation decreased, which led to a reduction in ice load. The water level was kept stable to look at the effects of such a phenomenon. An interesting observation here is that a new peak load occurs at the same time as when the water level started to return to normal level (33h). During the same period there was a large temperature change which probably led to a thermal expansion. Since the temperature change took place over such a short time, it seems unlikely that such a large ice load will only be produced by a thermal expansion. As the ice load decreases when the water was back to normal levels, it confirms the assumption. Since large cracks were observed, as well as water-filled cracks, it is likely that the load occurred due to freezing of the cracks.

4. CONCLUSION

In this paper, a measurement program on ice load with water level variation has been carried out. The measurement program took place in the winter of 2016/2017 at dam

Taraldsvikfossen in Narvik. Three different load events were conducted with 0.06m, 0.22m and 0.35m water level variation. As the winter of 2016/2017 was both warmer and had more precipitation than normal, it was not possible to carry out more experiments. Maximum ice load was measured to 85 kN/m during load event 3. During load event 1, a reduction of ice load was observed. There were no clear observations that explained the reduction.

The experiments confirm which load contributions occur during a load event with water level variation. There are mainly three major load contributions that affect the ice sheet: (1) Loads directly from a water level variation; (2) Load from thermal expansion. It is also likely that load from longitudinal extension of the ice sheet as a result of freezing of cracks had an impact on the measured ice pressure. The observations confirm theories from previous literature.

Acknowledgments

Helpful discussions with Leif Lia of the Norwgian University of Science and Technology (NTNU) and the excellent support of Tore Pettersen, Bård Arntsen and Christian Petrich of Norut in instrument preparation and deployment are gratefully acknowledged. Narvik Kommune kindly provided access to the Taraldsvikfossen Reservoir. The comments of anonymous reviewers helped to improve the manuscript.

References

ASHTON, G. D. 1986. *River and lake ice engineering*, Water Resources Publication.
BERGDAHL, L. 1977. *Physics of ice and snow as affects thermal pressure*.
BLAZEVIC, S. 2011. *Islast mot lukedammer; forventet fordeling av last*. NTNU.
CARTER, D., SODHI, D., STANDER, E., CARON, O. & QUACH, T. 1998. Ice thrust in reservoirs. *Journal of cold regions engineering*, 12, 169-183.
CFBR, 2013. Guidelines for The Justification Of The Stability Of Gravity Dams *French Dams and Reservoirs Committee* (CFBR), Le Bourget-du-Lac, France, 92
COMFORT, G., GONG, Y., SINGH, S. & ABDELNOUR, R. 2003. Static ice loads on dams. *Canadian Journal of Civil Engineering*, 30, 42-68. COMFORT, G., SINGH, S. & METGE, M. 1976. *Thermal cracks in lake ice*, publisher not identified.
Cox and Johnson. 1983 Stress measurements in ice. Report 83-82, *Cold Regions Research and Engineering Laboratories, Hanover, NH, USA*, 31
B. Morse, E. Stander, A. Côté, M. Richard, V. Desmet. Stress and Strain dynamics in a hydro-electric reservoir ice sheet. *Proceedings of the 16th Workshop on the Hydraulics of Ice Covered Rivers*, 303-316
NVE, 2003. Retningslinje for Laster og Dimensjonering til §§ 4–1 og 4–2 i *Forskrift om Sikkerhet og Tilsyn med Vassdragsanlegg Norges Vassdrags- og Energidirektorat*, 25
PETRICH, C., LANGHORNE, P. J. & HASKELL, T. G. 2007. Formation and structure of refrozen cracks in land\fast first\year sea ice. *Journal of Geophysical Research: Oceans*, 112.
PETRICH, C., SAETHER, I., FRANSSON, L., SAND, B. & ARNTSEN, B. 2015. Time dependent spatial distribution of thermal stresses in the ice cover of a small reservoir. *Cold Regions Science and Technology*, 120, 35-44.
STANDER, E. 2006. Ice stresses in reservoirs: effect of water level fluctuations. *Journal of Cold Regions Engineering*, 20, 52-67.
TARAS, A., CÔTÉ, A., COMFORT, G., THÉRIAULT, L. & MORSE, B. Measurements of ice thrust at Arnprior and Barrett Chute dams. Proceedings of the 16th Workshop on the Hydraulics of Ice-Covered Rivers, Winnipeg, MB, Canada, 2011. 18-22.

25th IAHR International Symposium on Ice
Trondheim, 23 - 25 November 2020

A parametric numerical study of factors influencing the thermal ice pressure along a dam.

Rikard Hellgren[1] and Richard Malm[1]
[1] KTH Royal Institute of Technology,
Department of Civil and Architectural Engineering, Stockholm, Sweden
rikard.hellgren@byv.kth.se

The uncertainty regarding size and variation of the ice pressure constitute one of the main significant sources of concern for condition assessment of concrete dams in cold regions. In most current dam safety guidelines, the design ice load is determined solely from the geographic location of the dam. However, factors such as variation in temperature and water level, the slope of the banks, wind etc. may also influence the size of the load. Previous measurements indicate that the pressure on a dam varies along the dam line during the same time and that the average ice pressure decreases as the area of the ice-structure interface is increased. This paper presents numerical studies on how the ice pressure varies along the dam wall. A finite element model that includes several dam monoliths, the ice and the beaches of the reservoirs are used to simulate thermal ice loads. The pure elastic load caused by the restrained expansion of an ice sheet subjected to a change in thermal gradient are greater than the design ice load in current dam safety guidelines and the loads measured. The simulations show that the ice load vary significantly along the dam, and the variation in cross-section stiffness along the dam greatly influence the magnitude of the total ice pressure. The parameter study shows that the elastic thermal ice load increases with an increased slope of the banks, reservoir length, and ice thickness and decreases as the angle of the connection between the dam and bank increases. However, the difference in ice load between the individual monoliths with the same geometry and temperature change are in several cases of the same magnitude as the variation in the external factors.

1. Introduction

For concrete dams in cold regions, the pressure caused by the formation, expansion or movement of the ice sheets may be significant. For the design of small dams, this ice load may constitute a significant fraction of the total horizontal load. Despite this, the maximum magnitude and its spatial distribution is uncertain, and the current understanding of ice loads is limited (Comfort et al., 2003; Gebre et al., 2013). The size and distribution of the ice loads are today, one of the greatest sources of uncertainty when assessing the stability of concrete dams in cold regions (Westberg Wilde & Johansson, 2016).

The following categories of the ice load acting on dams are often used;

- Thermal ice load, caused by the restrained thermal expansion of the ice sheet
- Ice load from water level changes and
- Ice load induced by shear forces from wind and flowing water.

From a mechanical perspective, these categories represent three different causes for loads on the ice-dam structure. However, the total ice pressure is caused by an interaction of the three loads described above.

In the current guidelines for ice load on dams, which are mainly based on the geographical location of the dam, the ice line-loads vary between 50 kN/m and 250 kN/m (RIDAS, 2017; NVE, 2003; USACE, 2016). Those guidelines were often created several decades ago without sufficient knowledge about the underlying mechanism, and have after a long time of use gained empirical validation. Many modern design standards use the partial coefficient method, which is a so-called semi-probabilistic method where statistical information about loads and the desired level of safety is included by converting basic variables into design values. The partial coefficients are calibrated so that the probability of failure does not exceed an acceptable probability of failure. In Eurocode (2015), characteristic values for climate loads should be chosen so that their time-dependent part is exceeded with a probability of 0.02 during a reference period of one year. This corresponds to an average value for a return period of 50 years. The load combination thus considers characteristic value, uncertainty and distribution for individual parameters (through the partial coefficients) and probability for loads to occur simultaneously. Thus, to define a suitable design value for the ice load requires knowledge of the variation and distribution in the maximum annual ice pressure.

Previous measurements show that the maximum annual ice load is within the range of 100 kN/m to 460 kN/m, with a log-normal distribution with the mean 81 kN/m and a standard deviation of 86 kN/m (Adolfi & Eriksson, 2013). That distribution is derived based on the assumption that all available ice load measurements belong to the same statistical distribution. Hence, any possible variations in the external conditions were not accounted for. One possible approach to determine the design ice load is to divide the load into sub-parameters, where each can be estimated separately. Such an approach is for example used for snow loads that, according to the Eurocodes (Eurocode 1, 2015), consist of a "natural snow load parameter" which depends on geographical location and altitude, combined with building-specific information such as roof slope and heat dissipation through the roof. A similar approach can be used for where the ice load is assumed to consist of a base ice load, I_{Base} and N other parameters. Then the design ice load I_{Design}, for one dam could be determined as the base ice load multiplied with factors that adjust for the other governing parameters

$$I_{\text{Design}} = I_{\text{Base}} \prod_{n=1}^{N} k_n \quad [1]$$

where k_n is a variable that considers the influence of an external factor *n*. In the literature, several external factors that may affect the magnitude of the ice load is mentioned.

- Ice thickness (Bergdahl, 1978; Bomeng, 1986; Carter, 1998)
- Air temperature (Fransson, 1988; Ko et al., 1994; Carter, 1998, Petrich et al. 2015)
- Snow thickness (Stander, 2006)
- Water level amplitude (Comfort et al., 2003, Foss 2017, Hellgren et al. 2020)
- Water speed (USACE, 2006)
- The dams structural properties (Comfort et al., 1997; Huang et al., 2017)
- The slope of beaches on the reservoir bank (Ko et al., 1994)
- Reservoir length-width ratio (Comfort et al.,2000b)
- Area of ice-structure interaction (Taras et al., 2011)

Many of these individual factors have only been studied in single studies, and there is today a lack of data to derive the influence of most of the mentioned factors. For quantification of the impact of the external factors, there is a need for additional theoretical predictions that can be validated with existing and new measurements.

This paper presents numerical studies investigating how the geometry of the reservoir and the ice thickness affects the elastic thermal ice load on several dam monolith. A parametric finite element model that includes several dam monoliths, the ice and the beaches of the reservoirs are used to simulate thermal ice loads. The influence of the restrain at the beaches, the reservoir geometry and ice thickness are studied by varying the slope of the banks, the width to length ratio of the reservoir and the ice thickness. The aim of this paper is to derive relationships for how these variations affect the structural behaviour of a concrete dam-ice system subjected to increasing air temperature. This includes the variation in ice pressure along the dam wall and the variation in total ice load between individual dam monoliths. This study is limited to thermal ice loads and do not consider material nonlinearities.

2. Method

2.1 FE-model

The mechanical effect of thermal ice loads on a dam was simulated using a model developed in the commercial finite element code Abaqus. The model consists of seven dam monoliths, the reservoir bank, the ice and a representation of the water. A dam monolith from the dam at Rätan hydropower plant was used. Rätan is a 28 m high traditional Swedish buttress dam constructed in 1968 and located in the northern region of Sweden. The dam, and ongoing measurements of the ice loads on the dam, are described more in detail in Hellgren (2019) and Hellgren et al. (2020). The model was created as a parametric model with the ability to alter the geometry of the reservoir, bank, and ice in accordance with the shape and dimensions shown in Figure 1.

All simulation was performed in two sequences, for temperature and static equilibrium. In the thermal analysis, a steady-state analysis were performed where the temperature on the top of the ice was increased via dirichlet boundary conditions, i.e. direct specification of nodal temperatures. Hence, the ice was heated from an even temperature distribution to a gradient.

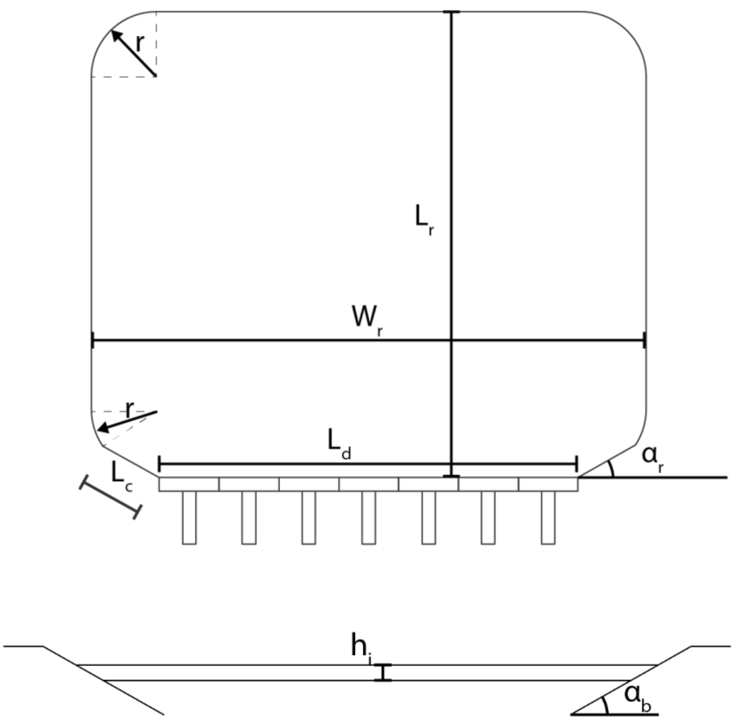

Figure 1. Geometry and dimensions of the ice and bank.

In the static simulations, two steps were used, dead load and temperature. In the first step, all dead loads were applied to the model. In the subsequent step, the calculated temperature was applied as a field in the static model with a one-way coupling. In the static simulations, transitional boundary condition was applied on the bottom of the dam and on the outer edges of the bank. The ice was held in place by contact interactions with the dam, bank and water. The dam-ice and bank-ice interaction are modelled using as hard contact in the normal direction and friction in the tangential direction. For both contacts, a friction coefficient of 0.3 was used, based on Shamsutdinova et al. (2018). For the ice-water interaction, a frictionless contact property is used in the tangential direction. The hard contact allows the ice to separate from, and prevents the ice from penetrating, the surrounding materials. A linear constitutive model with values according to Table 1 was used to describe the material behaviour of the concrete, bank and ice. All numerical analyses were performed with Abaqus (Dassault Systemes, 2017), version 2017 with the standard implicit solver.

The ice and buttress is modelled in 3D with 8-node linear brick elements with reduced integration and hourglass control (element DC3D8 and C3D8R in Abaqus), the bank with Theta (element DC3D4 and C3D4 in Abaqus). The average used element size is 0.5 m for the dam and one-fourth of the ice thickness for the ice.

Table 1. The material properties used in all simulations

Property	**Concrete**	**Ice**	**Rock**	**Unit**
Elastic modulus	33	4	2	GPa
Poisson's ratio	0.2	0.3	0	-
Density	2300	917	2700	kg/m^3
Thermal expansion	-	1.0e-5	-	K^{-1}
Thermal conductivity	-	3.0	-	W/(m*K)
Stress/strain free temperature	-	0.0	-	°C

2.2 Reference model

A reference model was used to more in detail study the behaviour of the ice-dam interaction and the variation of ice pressure along the dam line. For this simulation, the applied temperature change on the top of the ice was 100 ˚C, to ensure buckling of the sheet. The dimensions of the reference case are presented in Table 2.

Table 2. Dimensions for the base model with definitions according to Figure 1.

Property	Variable	Value	Unit
Dam length	L_d	63 (7 *9)	m
Reservoir length	L_r	100	m
Reservoir width	W_r	100	m
Reservoir radius	r	10	m
Connection length	L_c	10	m
Reservoir angle	α_r	0	°
Bank slope angle	α_b	30	°
Ice thickness	h_i	1.0	m

2.3 Parametric analyses

To study the influence of the reservoir on the thermal elastic ice load, a parametric analysis was performed with the reference case as a base. The slope angle, reservoir length and ice thickness were varied in accordance with Table 3. For these simulations, the applied temperature change on the top of the ice was 30 ˚C. From each simulation, the maximum line ice load, I_m, and the slope of the initial increase of line ice load per degree temperature change I'_i is extracted. The definition of the initial slope, I'_i, is illustrated in Figure 2a in section 3.1.

Table 3. Outline of parametric analysis.

Model	Reservoir length [m]	Reservoir angle [o]	Bank slope angle [o]	Ice thickness [cm]
Ref	100	0	30	100
1	100	0	15	100
2	100	0	30	100
3	100	0	60	100
4	100	0	30	25
5	100	0	30	50
6	200	0	15	100
7	200	0	30	100
8	200	0	45	100
9	100	45	30	100
10	100	90	30	100

3. Results

3.1 Analysis of reference case

Figure 2a shows the line load vs total temperature change for the reference case when the temperature on the top of the ice is increased with 100 ˚C. The results show three steps; at the first initial temperature rise (up to about 5 degrees), the load increase is linear, relatively steep and equivalently for the seven monoliths. After the initial increase, a plateau emerges where the load against the respective monolith stabilizes at an even, but between monoliths, variable level. After that, the ice buckles and an arch is formed along the dam. The continued thermal expansion of the ice occurs through arching with increased load on the four outermost monoliths, while the middlemost monoliths are initially unloaded. The final average line load of the two edge monoliths are more than twice as large as the load on the centre monolith. Figure 2c shows the displacement field, and hence the buckling mode of the ice after a temperature change of 100 ˚C, Figure 2b shows the area with the initial risk of cracking, where the principal stress in the ice first surpasses 1 MPa. This occurs at a temperature rise of 3.5 ˚C, on an area on the bottom of the ice, about four to ten meters from the edge of the ice along the banks but not the dam.

Figure 3 shows the relation between the displacement of the seven dam monoliths and the contact pressure on the dam-ice interface. Figure 3a and 3b show the integrated contact pressure as a line load and the displacement in the downstream direction, respectively. Together, these two plots show how the stiffness of the dam affects the ice load and how the deformations of the dam interplay with the load. The line load peaks over the buttress wall and has low points at the middle of the span. For the initial temperature increase, the difference between the peak load and the minimum is significant. This difference decreases as stresses are redistributed in the ice as the man load increases. The displacement of the dam crest shows the opposite relation with a local minimum at the canter of each monolith. Thus, at the end of each monolith, where the front-plate deforms the most, the expansion of the ice sheet is restrained to a lesser degree, which results in a lower ice load.

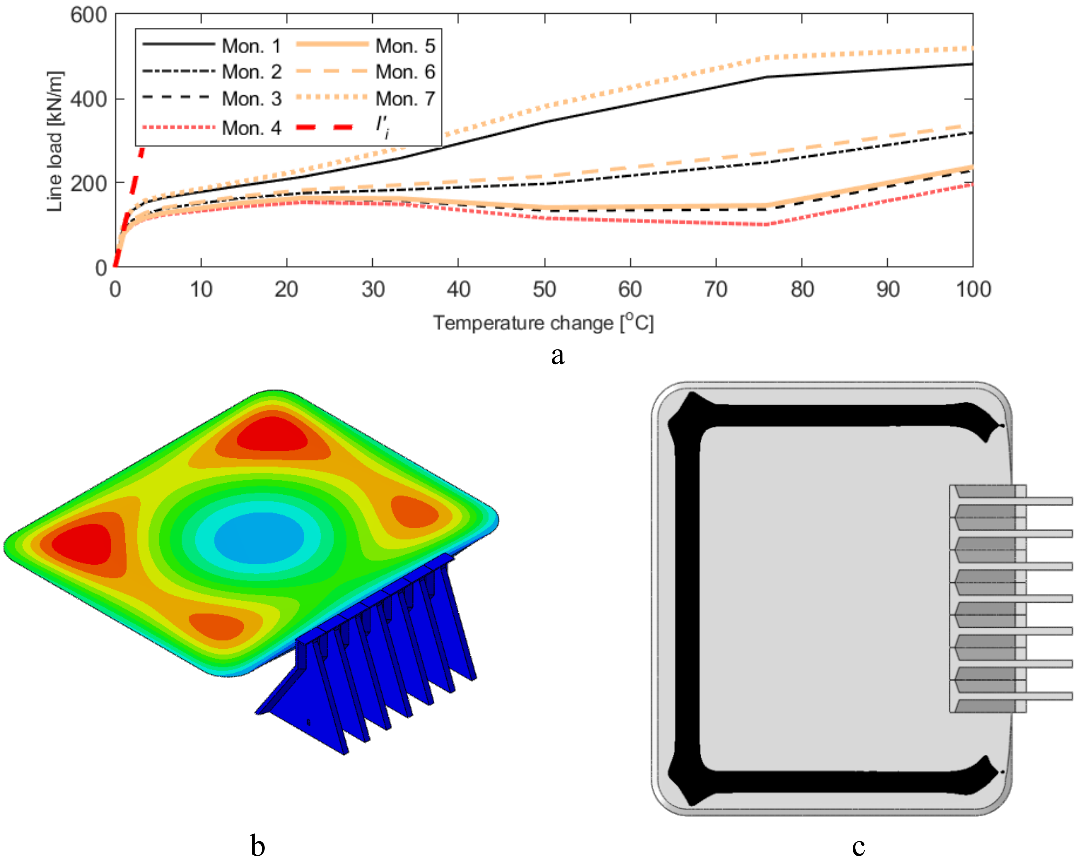

Figure 2. a) Ice load-temperature relationship for the seven monoliths, b) buckling displacement field for the reference model, c) area where the initial cracking is expected (view from below).

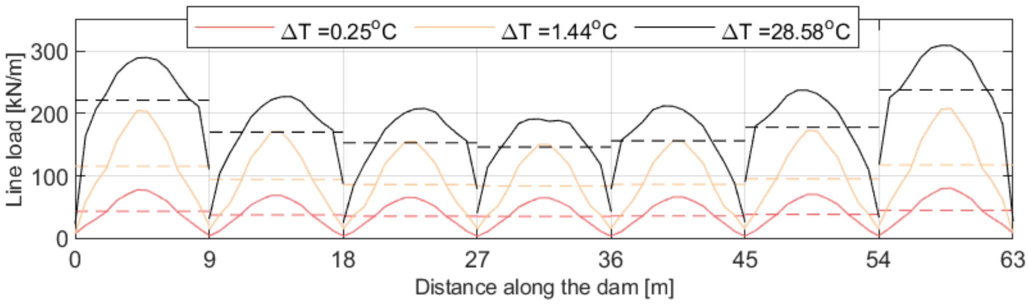

a

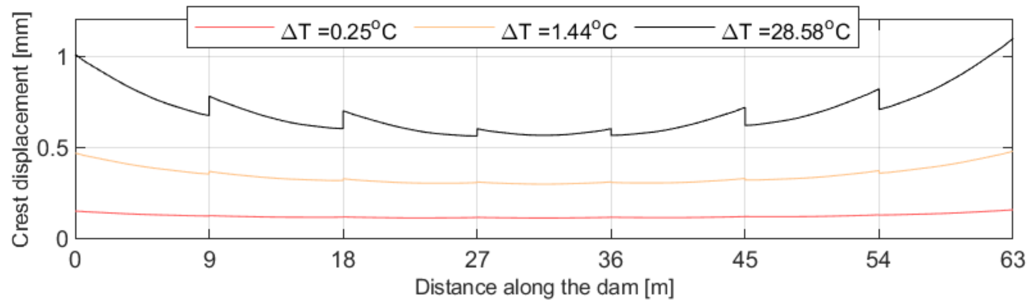

b

Figure 3. a) Solid lines are the line load along the dam and dashed lines are the average line load for the respective monolith b) displacement in the downstream direction along the dam line.

3.2 Parameter analysis

Figure 4 shows the variation in maximum ice load and the slope of the initial increase in ice load as a function of the bank slope, reservoir length, ice thickness and reservoir angle. The marks show the mean value of all monoliths and the error bar shows plus/minus one standard deviation. The elastic thermal ice load is positively correlated with increased bank slope ($\Delta I_m/\Delta\alpha_b$ = 16.1 [kN/m]/°, $\Delta I'_i/\Delta\alpha_b$=2.2 [kN/m˚C]/°), reservoir length ($\Delta I_m/\Delta L_r$=2.2 [kN/m]/m, $\Delta I'_i/\Delta L_r$ =1.1 [kN/m˚C]/m) and ice thickness ($\Delta I_m/\Delta h_i$ =1.1 [kN/m]/m, $\Delta I'_i/\Delta h_i$=0.4 [kN/m˚C]/m), and in general, negatively correlated with the angle of the connection between the bank and dam. However, for the 90° reservoir angle, the ice buckles and forms an arch between the two external monoliths and unloads the inertial monoliths. This shape completely unloads all internal monoliths while the load on the two outermost monoliths are increased greatly. The standard deviation in maximum ice load for the seven monoliths varies between 10 kN/m (α_b=30°, L_r=100 m, α_r=45 ° h_i=100 cm) to 140 kN/m (α_b=60 °, L_r=100 m, α_r=0 ° h_i=100 cm), if model 10 with α_r=90 ° is excluded.

4. Discussion

This paper simulates the elastic thermal ice load and does not consider nonlinearities such as creep or cracking. Further, the ice load caused by shear forces from wind and water currents as well as ice loads caused by water level changes not considered. As ice loads from water level changes are believed to cause the most severe ice loads (Comfort et al., 2003; Hellgren et al., 2020), this is a major limitation. It is probable that the variation in reservoir properties has other relations to the ice load caused by other mechanisms than the thermal ice load. The loads obtained in this study are greater than both the current guidelines and the loads measured. This indicates that there are other factors than the mechanical constrains that limits the maximum ice load and there might be little to gain by trying to quantify the ice load according to the external factors as proposed in Equation 1.

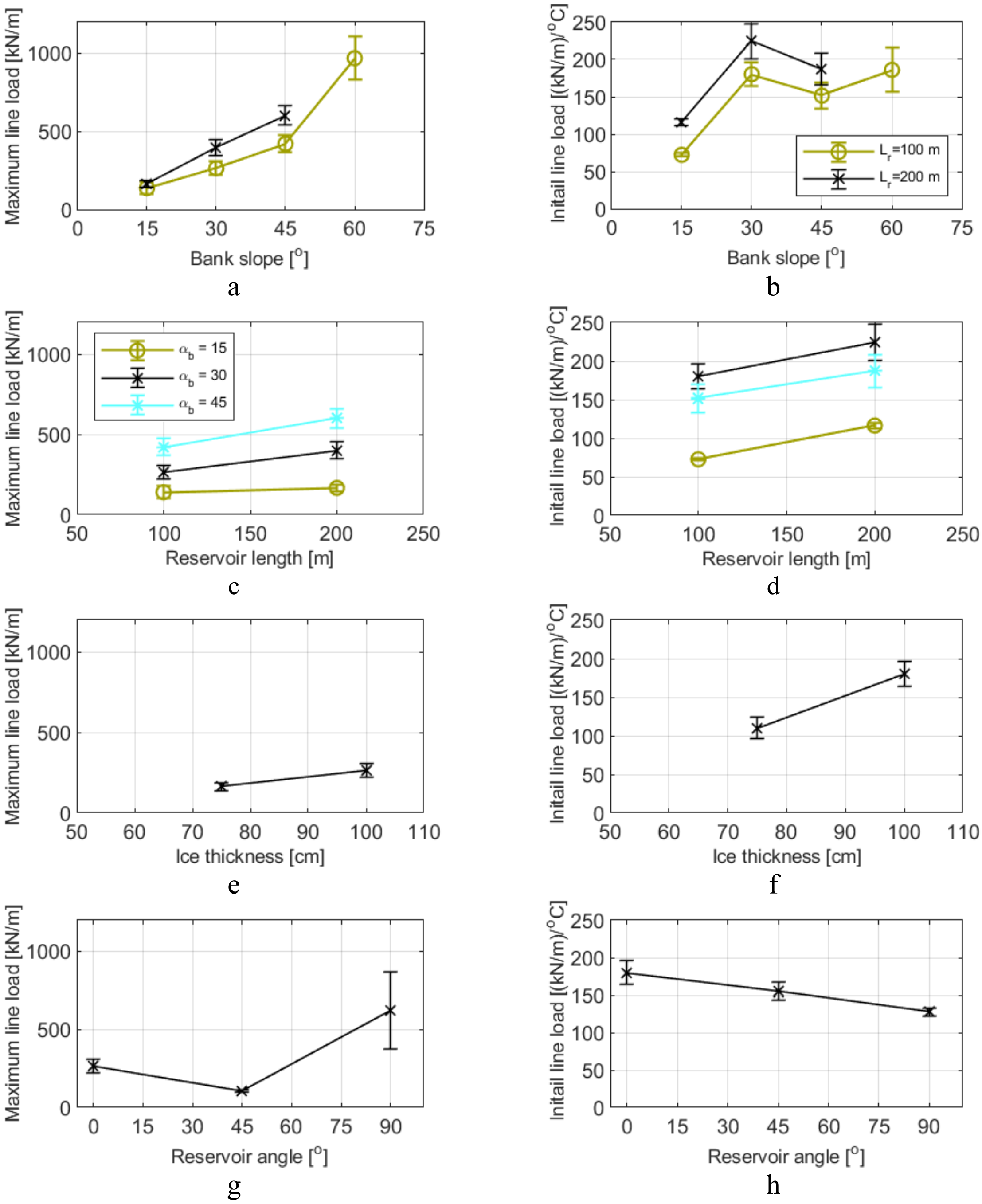

Figure 4. Impact of the external factors. a, c, e, g) maximum ice load and b, d, g, h) slope of the initial increase in ice load per degree temperature as a function of the bank slope, the reservoir length, the ice thickness and the reservoir angle, respectively.

Previous measurements have shown that the stress in the ice and the resulting load acting on the dam have a significant spatial variation and can vary significantly over a distance of a few meters along the dam at the same time (Taras et al., 2011). The simulations presented here shows that from a thermal elastic perspective, such variation is expected. The variation along the dam, within and between individual monoliths, are of the same magnitude as the variation in bank slope and reservoir length causes. Further, the results presented in Figure 3 show that the variation in ice pressure among an individual monolith can be significant. This means that measurement of ice load, which often occurs at only one point on the dam, provides limited information about the ice load acting on the dam. Furthermore, in the literature, the static ice load on dams are sometimes modelled as a function of the external conditions using a 2D model (Comfort et al. 2003; Kharik et al. 2018; Petrich & Arntsen 2018; Hellgren, 2019). Such an approach does not consider the spatial variation along the dam. Assume that a model is created which correctly predicts the ice load at one point along the dam during a winter. The same model could over- or underestimate the ice load only three meters from the first, with a factor of two. The external factors do not differ significantly over three meters which means that other factors such as the formation of cracks in the ice, and randomness in the wind, water, and snow may all affect the ice load. In the future, it is therefore essential to focus on the spatial variation of the ice load over an entire dam and try to establish how the average pressure decreases over an entire dam compared to local stresses.

5. Conclusion

This study presents numerical simulation of the elastic thermal ice load on dams. The pure elastic load caused by the restrained expansion of an ice sheet subjected to a change in thermal gradient are greater than the design ice load in current dam safety guidelines and the loads measured. As this study does not consider the nonlinear behaviour of ice, the main benefit of this study is the relative results rather than the absolute values. The simulations show that the ice load vary significantly along the dam, and the variation in cross-section stiffness along the dam greatly influence the magnitude of the total ice pressure. The parametric study shows that the elastic thermal ice load increases with the slope of the bank, reservoir length, and ice thickness and decreases as the angle of the connection between the dam and bank increases. However, the difference in ice load between the individual monoliths for the same geometry and temperature change are in several cases of the same magnitude as the variation in the external factors.

Acknowledgments

The research presented was carried out as a part of “Swedish Hydropower Centre -SVC”. SVC has been established by the Swedish Energy Agency, Energiforsk and Svenska Kraftnät together with Luleå University of Technology, KTH Royal Institute of Technology, Chalmers University of Technology and Uppsala University. www.svc.nu.

References

Adolfi, E., & Eriksson, J. (2013). Islastens inverkan på brottsannolikheten för glidning och stjälpning av betongdammar. KTH Royal Institute of Technology.

Bergdahl, L. (1978). Thermal ice pressure in lake ice covers. Chalmers University of Technology.

Bomeng, X. (1986). Design value of pressure due to expansion of ice sheet in reservoir. In lAHR Ice Symposium 1986 (pp. 231–238). Iowa City.

Carter, D., Sodhi, D., Stander, E., Caron, O., & Quach, T. (1998). Ice thrust in reservoirs. Journal of Cold Regions Engineering, 12(4), 169–183.

Comfort, G., Gong, Y., & Singh, S. (2000). The factors controlling static ice loads on dams. In Proceedings of the 15th International Symposium on Ice (pp. 189–198). Gdansk, Poland.

Comfort, G., Gong, Y., Singh, S., & Abdelnour, R. (2003). Static ice loads on dams. Canadian Journal of Civil Engineering, 30(1), 42–68. https://doi.org/10.1139/L02-080

Comfort, G., Gong, Y., Singh, S., & Abdelnour, R. (1997). Static ice loads on dams : Loads along a long dam face; and a comparison of the loads exerted on wooden and steel stoplogs. In Proceedings of the CDSA/CANCOLD Joint Dam Safety Conference Montreal: Canadian National Committee of International Commission on Large Dams.

Dassault Systemes. (2017). Abaqus Online documentation. Providence, USA.

Eurocode 1. (2015). EN 1991-1-3: Eurocode 1: Actions on structures - Part 1-3: General actions - Snow loads. Brussels.

Foss, A. B. (2017). Islast mot dammer med varierende vannstand [Ice loads on dams with water level variation]. NTNU: Norwegian University of Science and Technology.

Fransson, L. (1988). Thermal Ice pressure on Structures in ice covers. Luleå University of Technology. Retrieved from urn:nbn:se:ltu:diva-17625

Gebre, S., Alfredsen, K., Lia, L., Stickler, M., & Tesaker, E. (2013). Review of Ice Effects on Hydropower Systems. Journal of Cold Regions Engineering, 27(4), 196–222. https://doi.org/10.1061/(ASCE)CR.1943-5495.0000059

Hellgren, R. (2019). Condition assessment of concrete dams in cold climate (TRITA-ABE-DLT). KTH, Concrete Structures.

Hellgren, R., Malm, R., Fransson, L., Johansson, F., Nordström, E., & Wilde, M. W. (2020). Measurement of ice pressure on a concrete dam with a prototype ice load panel. Cold Regions Science and Engineering, 170.

Huang, W., Li, Z., Han, H., & Jia, Q. (2017). Limit resistive forces from ice frozen to concrete-revetment interface of an inclined dam wall. Cold Regions Science and Technology, 141(126), 181–187. https://doi.org/10.1016/j.coldregions.2017.06.012

Kharik, E., Morse, B., Roubtsova, V., Fafard, M., Côté, A., & Comfort, G. (2018). Numerical studies for a better understanding of static ice loads on dams. Canadian Journal of Civil Engineering, 45(1), 18–29. https://doi.org/10.1139/cjce-2017-0142

Ko, P. K., Ho, M. S., & Smith, G. F.. (1994). Thermal ice forces on concrete dams: recent developments. Dam Safety, 17–33.

NVE. (2003). Retningslinje for laster og dimensjonering til §§ 4-1 og 4-2 i forskrift om sikkerhet og tilsyn med vassdragsanlegg.

Petrich, C., Sæther, I., Fransson, L., Sand, B., & Arntsen, B. (2015). Time-dependent spatial distribution of thermal stresses in the ice cover of a small reservoir. Cold Regions Science and Technology, 120, 35–44. https://doi.org/10.1016/j.coldregions.2015.09.003

Petrich, C., & Arntsen, B. (2018). An overview of trends and regional distribution of thermal ice loads on dams in Norway. In Twenty-Sixth International Congress on Large Dams (pp. 1210–1224). Vienna, Austria: International Commission on Large Dams.

RIDAS. (2017). Swedish Hydropower companies guidelines for dam safety, application guideline 7.3 Concrete dams. Stockholm, Sweden.

Shamsutdinova, G., Hendriks, M. A. N., & Jacobsen, S. (2018). Concrete-ice abrasion: Wear, coefficient of friction and ice consumption. Wear, 416–417(September), 27–35.

Stander, E. (2006). Ice Stresses in Reservoirs: Effect of Water Level Fluctuations. Journal of Cold Regions Engineering, 20(2), 52–67.

Taras, A., Côté, A., Comfort, G., Thériault, L., & Morse, B. (2011). Measurements of Ice Thrust at Arnprior and Barrett Chute Dams. In 16th Workshop on the Hydraulics of Ice Covered Rivers (pp. 317–328). Winnipeg, Manitoba.

USACE. (2006). Engineering and design: ice engineering. EM 1110-2-1612 Change 3, 475.

Westberg Wilde, M., & Johansson, F. (2016). Probabilistic model code for concrete dams. Stockholm, Sweden.

25th IAHR International Symposium on Ice
Trondheim, 23 - 25 November 2020

Static ice loads on a dam in a small Norwegian reservoir

Chris Petrich[1], Irina Sæther[1], Megan O'Sadnick[1,2], Bård Arntsen[1]
[1] *SINTEF Narvik, Narvik, Norway*
[2] *UiT The Arctic University of Norway, Tromsø, Norway*
christian.petrich@sintef.no

Ice loads on a concrete dam have been calculated from stress measurements in Taraldsvikfossen Reservoir, a small reservoir in Narvik, Norway, during three winter seasons. Ice thickness was in the range of 0.5 to 1.0 m, and both thermal ice loads were observed and water level fluctuations up to 30 cm were observed when the ice cover froze to the spillway. The maximum global line load measured was 60 to 90 kN/m, in line with current design guidelines in Norway. Consistent with earlier reports, line loads were not evenly distributed along the dam face. A thermal line load model was able to reproduce the approximate shape and magnitude of many line load peaks even when the measured vertical stress profile could not be reproduced by the model. The results add to an extremely small body of data in Norway and motivate investigations in other parts of the country with expected higher or lower ice loads.

1. Introduction

Static ice loads form a significant contribution to the design load of dams of low height in cold climates. They have been attributed to thermal expansion of an ice cover during warm spells and refrozen fractures in the presence of water level fluctuations (e.g. Comfort et al., 2003; Stander, 2006; Petrich et al., 2015; O'Sadnick et al., 2016a). Design standards are based on empirical measurements as current understanding of the magnitude of ice loads is still limited (Comfort et al., 2003; Gebre et al., 2013; Timco et al., 1996). In Norway, static ice loads between 100 and 150 kN/m are generally assumed (NVE, 2003).

The only ice load measurements performed within Norway are those of Hoseth and Fransson (1999) at Silvatnet near Narvik, and the campaigns at Taraldsvikfossen Reservoir in Narvik, some of which form the basis of this study (Petrich et al. 2014, 2015; O'Sadnick et al., 2016a). All measurements targeted thermal ice loads and were performed in reservoirs with nominally constant water level. Hoseth and Fransson (1999) deployed three stress cells in front of a dam, rotated 120° with respect to each other 0.2 m below the ice surface. They derived line loads of up to 135 kN/m in 0.5 to 0.6 m thick ice by assuming a linear stress profile through the ice. They also found that the shapes of the peaks could be reproduced by an ice stress model after Bergdahl (1978). In the present study line loads were calculated for three winter seasons from vertical stress profiles. Since the vertical stress profiles observed were generally not linear, similar to observations in independent studies (e.g. Morse et al., 2009), an uncertainty arises from the extrapolation of stresses above and below the cell arrangement. Measured line loads are compared with thermal line loads calculated from ice temperature measurements in order to assess whether they are of thermal or mechanical origin.

Taraldsvikfossen Reservoir is a small (3400 m^2) drinking water backup reservoir fed by a creek (Taraldsvikelva) at 213 m elevation, 68.436782° N, 17.498563° E. The crown of the dam is 0.5 m above the nominal water level which is maintained by a spillway. The typical ice thickness is between 0.5 and 1.0 m, and the ice is attached to the dam. Aspects of the reservoir and ice stresses during the three winters covered in this study were presented in more detail elsewhere (Petrich et al. 2014, 2015; O'Sadnick et al., 2016). It became clear in those studies that Taraldsvikfossen Reservoir exhibits at least two different sources of ice stresses: thermal stresses in response to ice temperature changes, and mechanical in response to small (decimeter) water level fluctuations that typically coincide with partial flooding of the ice surface. The latter arose from a creek discharging into the reservoir while the ice cover was frozen to the spillway. Creek discharge while the ice cover was frozen to the spillway resulted in visible upward movement of the ice cover away from the dam. This resulted in the formation of several decimeters of superimposed ice at the dam.

2. Methods

2.1 Ice Stresses

Ice stresses were measured with custom designed oil-filled GeoKon 4850 stress cells that measured internal temperature at the same vertical level as pressure (Petrich et al., 2015). The cells consisted of two rectangular steel plates (100 mm×200 mm) welded together around the periphery with de-aired oil occupying the space between the plates. A short tube connected the cell to a vibrating wire pressure transducer that also measured temperature with a temperature-dependent resistor (cf. cells sketched in Figure 1). Between one and three cameras mounted around the reservoir took timelapse imagery every 30 minutes. A water pressure gauge had been installed at the dam at 1.3 m water depth in winter 2013/14. It froze in that winter but provided valuable data the following winter.

A limitation of the stress measurement method is that flatjacks cannot reliably measure tension because the ice may detach from the probes, or the oil inside the probes may start to boil in the presence of a vacuum. The latter problems may arise from approx. 100 kPa in tension. Hence, it is assumed in this study that measured line loads are systematically biased high in the presence of tensile stresses (cf. Section 3).
The configuration of stress cells differed between seasons. However, in each case there were both measurement stations that measured vertical profiles and measurement stations with only one cell. Only stations with multiple cells are used in this study, and those were located near the center of the dam. Cells that were frozen into the ice in 2012/13 and 2013/14 showed characteristic stresses during freeze-in (e.g., Fransson 1988), and data analysis stared after those freeze-in peaks had relaxed during warmer weather.

During winter 2012/13, stations were installed 1 m in front of the dam and in the middle of the reservoir, approx. 10 m from dam (cf. Petrich et al., 2015). At the time of measurement, ice thickness was approx. 0.85 m near the dam (Stations 3 and 5) and 1.0 m at Station W. During winter 2013/14, the first half of each station was installed at the dam early in the season and the second half in the ice 2 m in front of the dam in February. These were intended for inter-comparison but are interpreted as single stations here due to unexpected, excessive superimposed ice formation at the dam (Figure 2). During winter 2014/15, cells were installed at the dam with one cell placed above the water line to account for anticipated superimposed ice formation. As a result, only a comparatively small amount of superimposed ice formed above the upper-most cell (Figure 3).

Line loads were calculated as a lower and nominally upper bound. For lower bound calculations, each stress measurement was multiplied by the vertical separation of the stress cells, i.e. 0.15 m in all seasons (exception: 0.25 m at Station W in 2012/13), and the results were summed. However, due to the peculiar cell configuration in winter 2013/14, the lower-most cell 2 m in front of the dam was averaged with the upper-most cell at the dam (cf. Figure 2).

Simple stress extrapolations were performed to estimate nominally upper bound line loads, i.e., to account for ice above and below the stress cells. In season 2012/13 the depth weights of the upper and lower most cells at each station were changed to 0.25, and 0.35 m, respectively (0.275 and 0.45, respectively at Station W), in season 2013/14 they were 0.25 and 0.25 m, respectively, and in season 2014/15 they were 0.3 and 0.15 m, respectively. There was insufficient linearity in the stress profiles to justify a linear extrapolation.

Usually, loads to not act homogeneously along the dam which implies that the average load experienced by a section of the dam will be less than the peak load (e.g., Côté et al., 2016). Hence, a global line load was calculated as the average of the line loads of all stations at a given time (local line loads) to quantify the magnitude of the influence of dam design.

2.2 Thermal Modeling

Modeling of thermal ice loads assumes knowledge of ice thickness and temperature in addition to (implicit) assumptions about properties of ice and dam. While ice growth and temperatures are reasonably straight-forward to model (e.g., Bergdahl 1978; Petrich and Arntsen, 2018), measurements are used in this study since they are available. Temperature measurements at the stress cells have been used since the temperature sensors were at the same vertical position in the ice as the center of the respective stress cell.

Ice stresses are modeled as a linear spring in series with a non-linear dashpod (Bergdahl, 1978). Like Petrich and Arntsen (2018), we used the equation and coefficients derived for “Cell 4” in Petrich et al. (2015). This particular sensor is not used in the present study, i.e. the model is not fitted to data presented in this study, although it is based on measurements in the same reservoir (i.e. Taraldsvikfossen Reservoir, winter 2012/13).

Line loads were calculated by integrating the vertical thermal stress distribution normal to the dam through the thickness of the ice (Bergdahl, 1978; Petrich and Arntsen, 2018). Following earlier work (Bergdahl, 1978; Cox, 1984; Fransson 1988; Petrich et al., 2015), the thermal stress at a particular vertical position in the ice was calculated as

$$\frac{d\sigma}{dt} = A\frac{dT}{dt} - B\left(\frac{T_0}{\bar{T}}\right)^m \left(\frac{\sigma}{\sigma_0}\right)^n \quad [1]$$

where the stress σ is positive in compression (extension to negative stresses as in Petrich et al., 2015), dT/dt is the rate of temperature change and $\bar{T}$ is the temperature in °C at the same vertical level as the stress, T_0 = -1 °C and σ_0 = 100 kPa are scale constants, m=1.92 from Cox (1984), and A=200 kPa/K, B=342 kPa/day, and n=3.7 are parameters of Cell 4 from Petrich et al. (2015). The stress was fixed at 0 whenever $T \geq 0$ °C. Equation 1 was solved implicitly in time. Equation 1 does not account explicitly for elasticity of the dam or the movement of the dam in response to temperature changes.

Unlike earlier work, modeled stresses were capped at 30 kPa in tension to approximate measurement limitations of flat jacks (c.f. Section 2.1), i.e. if a modeled tensile stress exceeded this value at the end of a time step it was set to 30 kPa. For the purpose of this study, the impact of this cap on model results is largely cosmetic given the accuracy sought: it improves agreement with measurements of low ice loads dramatically while increasing some modeled peak thermal loads (by <40 kN/m). Note that this cap was not used to obtain the coefficients in Equation 1 (Petrich et al., 2015).

Thermal stresses were calculated from the temperature measurements within each stress cell and integrated using the approach for lower bound line loads described in Section 2.1. A limitation of this approach is that temperatures measured at the stress cells are not necessarily representative of the temperatures in most of the ice cover. For example, cells located at the dam may be affected by heat conduction through the dam, insulation form snow drifts caught by the dam, and may experience an unrepresentative thermal regime during partial flooding of the reservoir ice surface. Another limitation of the present approach is that no account was taken for any difference in ice physical properties with depth even though superimposed ice due to surface flooding, snow-ice, and congelation ice may have been present at the same time.

3. Results and Discussion

Measurements and thermal model results are compared for three seasons in Figures 4, 5, and 6, respectively. Measured ice thickness profiles perpendicular to the dam are shown in Figure 3. While no significant ice loads were registered anymore in winter 2014/15 after the profile in Figure 3 had been measured (phase 8), the profile serves to illustrate an actual thickening of ice close to the dam. The gap layer in the ice cover >5 m in front of the dam would have fixed the bulk of the ice at 0 °C, explaining the absence notable loads in spite of air and ice temperature variations at the dam.

3.1 Winter 2012/13

Figure 4 shows line load data of two stations mounted 2 m in front of the dam (Stations 3 and 5, Figure 4b and c, respectively), and one station mounted 10 m in front of the dam (Station W, Figure 4d). Ice thickness 1 m in front of the dam was 0.75 m on 9 February (0.3 m freeboard at the sites of deployment due to ice formation from surface flooding at the end of December).

Freeze-in artifacts lasted from probe deployment until a week-long warm spell at the end of February. The ice cover remained detached from the spill way following the warm spell and there were no further indications of water level fluctuations in the timelapse imagery or otherwise until break-up. After the warm spell, phase 1 started with a load event that, counter-intuitively, corresponded to a 10 °C drop in air temperature, followed by small load variations (Figure 4). The thermal model reacted on the initial decrease in air and ice temperature by predicting a negative load, i.e. ice pulling the dam, modulated by temperature fluctuations that correlate positively with the load variations at Stations 3 and 5, and negatively with loads calculated for Station W 10 m away from the dam. Phase 2 is characterized by five consecutive load events that are reasonably well reproduced by the thermal load model. Following an abrupt decrease in temperature, the thermal model and observations show fluctuations between tension and compression loads in phase 3. Like in phase 1, measured line load variations correlated positively with modeled loads at Stations 3 and 5, and negatively at Station W. The week-long load period of phase 4 and subsequent smaller variations in line load are reproduced reasonably well by the thermal load model. The ice decayed during phase 5 when no more load events were recorded or modeled.

There is a phase lag in the temperature data and stress signal from the top-most to the bottom-most stress cell as one would expect in the presence of vertical heat conduction through the ice (Figure 7).

With the exception of the initial peak in phase 1, the peak local line loads were between 60 and 90 kN/m, depending on how stresses are extrapolated. The nature of the initial peak in phase 1 is not clear. However, since they are entirely due to high stresses at the top-most cells they could potentially be a form of freeze-in artifacts. Peak global line loads (Figure 4e) were lower than local loads, i.e. 40 to 80 kN/m, depending on extrapolation.

3.2 Winter 2013/14

Figure 5 shows line load data of three stations that combine stress cells at the dam with stress cells in the ice. The period shown starts following the freeze-in period of the ice-borne sensors and ends prior to melt-out artifacts of the dam-borne sensors (i.e., dam-borne sensors were torn out of anchorage). No vertical movement was visible in the timelapse camera sequences since 4 February 2014. There was 50 cm superimposed ice at the dam since January, and ice thickness was 0.75 m during deployment on 11 February.

Three major load events (phases 1, 3, 7) appear to have been thermal loads based on their agreement with the thermal model. However, there is a small discrepancy in either time or magnitude between measurements and thermal model in phase 1. At this point we cannot assess whether this is a phenomenon that merits further investigation. Phases 2, 4, and 6 are marked by only small measured and modeled loads. In fact, the ice was flooded during phase

4 and all stress cells read 0.0 °C by the end of the phase. Line load peaks during phase 5 do not correlate with the thermal model and end suddenly, possibly due to some global rearrangement of the ice cover.

Ice temperature data show air temperature signals propagating downward compatible with vertical thermal conduction. However, unlike winter 2012/13, this pattern is not reflected in the stresses registered by the respective cells (Figure 8). Instead, stresses increased either more-or-less simultaneously (phase 7), or in non-intuitive order (e.g. phase 3, Station D: starting at both top and bottom-most and ending in the center). Hence, while the model performed reasonably well in predicting the over-all line load, it performed poorly at predicting stresses at individual cells.

Global thermal line loads reached close to 100 kN/m on three occasions this season with a measured maximum at 110 to 130 kN/m. However, loads derived this season are questionable in the light of the unconventional stress cell configuration.

3.3 Winter 2014/15

Ice stresses were recorded only at the dam and no freeze-in or break-up artifacts were observed. Only the most interesting part of the season is shown in Figure 6 as ice loads early and late in the season were low. Figure 6a shows water pressure data converted to water column equivalent in addition to air temperature. Ice thickness was 0.4 m on 5 January. On 5 February it was 0.8 to 0.9 m at the dam, reducing to 0.6 m 5 to 10 m in front of the dam. The sensors installed above nominal water level were exposed on 5 Jan but covered in ice by 22 January (Figure 9). Superimposed ice thickness at the dam was 0.25 m on 4 February.

Phases 1, 3, 5, and 6 had significant excursions of the water column equivalent (Figure 6a). Each excursion was readily visible in the site camera timelapses. Further confirmation was obtained as a result of a misunderstanding that led to holes being drilled in the ice cover close to the dam approximately 2 hours before the peak water level in phase 6. All holes had negative freeboard, i.e. they flooded the surface, with one hole creating a 0.1 m high water sprout.

Ice loads were small during phases 2 and 8 in spite of significant ice temperature changes that are reflected in the modeled thermal line loads. The absence of loads in phase 2 could be explained by assuming mechanical failure of the ice cover during phase 1. Measurements of the peaks during phases 4 and 7 are generally compatible with the thermal load model. The peak in phase 4 was lower than modeled, possibly because the water level was decreasing back to normal level at the same time. The shoulder in phase 7 appears to correlate well with the model.

In phase 6, the onset of the measured load peak appeared as the water level increased and before air or ice temperatures rose and had therefore been missed by the thermal model in Station C (Figure 6c). However, measured loads at Stations B and D only started to increase after air temperatures rose. The thermal model is catching up with the measurements toward the end of phase 6, presumably as a result of ice temperature increase from surface flooding. The initial peak appears to be related to water level increase. A peak of similar origin appears in phase 5: the thermal model eventually catches up once the surface flooded around the time of maximum deflection. The peaks in phases 1 and 3 correlate likewise with an upward movement of the ice cover. However, camera images show that the ice surface started to flood from the creek toward the dam around the same time. This should have created a thermal load. Since the flooding did not extend over the entire ice surface, no corresponding temperature signal was detected by the temperature sensors at any of the stations during phase 1, and at station D during phase 3 and hence those are not modeled as a thermal load (Figure 6b,c,d).

It is difficult to unambiguously distinguish loads due to waterlevel changes from thermal loads in phases 1, 3, 5, and 6 since water level changes were accompanied by partial flooding of the ice surface. The vertical stress profile that developed in the flooded areas could have averaged out in the regions that were not flooded closer to the dam where it got further modified by cracks and an upward-moving ice cover, removing the characteristic staggered stress development through depth that was observed in 2012/13. Similarly, the stress profiles during phases 4 and 7 do not show thermal characteristics (Figure 9) even though the aggregated local line loads do (Figure 6). Hence, the local line load may be a more robust measure of ice processes than the depth-resolved stress profile.

Peak line loads this season were related to inrush of water into the reservoir that caused upward-movement and partial flooding of the ice surface. Separating the contributions of the two mechanisms is not trivial.

The registered local peak line load was 170 to 240 kN/m at Station C, phase 6, just before readings at two stress cells exceeded 50 kPa in tension. The global line loads were 60 to 90 kN/m at this point.

4. Conclusion

Local line loads have been calculated for three years of ice stress measurements at Taraldsvikfossen Reservoir near Narvik. While the reservoir had nominally no waterlevel varions in winter it did show significant excursions while the ice cover was frozen to the spillway.

It was found that local line loads may follow development predicted by the thermal load model even when individual stress measurements within the corresponding profiles do not (2013/14 and 2014/15). It was hypothesized that this is related to inhomogeneous ice temperature profiles across the reservoir (in particular, local flooding) and cracks in the ice.

The maximum global line load registered was 60 to 90 kN/m with a local maximum of 170 to 240 kN/m. The ranges result from uncertainty because the measured vertical stress profiles did not extend through the entire depth of the ice and the stress profiles generally did not suggest linearity. The assessment excludes periods where at least one stress cell recorded tensile stresses >50 kPa due to systematic limitations of the method to measure tension. Season 2013/14 had been excluded from this assessment due to additional uncertainties that stem from the stress cell configuration. However, global line loads were probably in the same range. Since the maximum line load experienced by a section of the dam decreases with increasing width of the construction sections (e.g., Côté et al., 2016), the dam-dependent relevant peak line load should lie between local and global loads.

Rarely discussed aspects of the measurements include the observation of negative line loads, i.e. ice pulling the dam, and the implicit assumption that the dam is a rigid body that does not move in response to thermal or mechanical forces. The latter could potentially introduce dam-dependence of line load measurements.

Acknowledgments
This work was supported by the Research Council of Norway NORDSATSING program, grant number 195153 (ColdTech) and industry partners, by Statkraft and by the Norwegian Water Resources and Energy Directorate (NVE).

References

Côté, A., A. Taras, G. Comfort, and B. Morse, 2016. Static ice loads at dam face and at far field. In Proceedings of the 23rd IAHR International Symposium on Ice, Ann Arbor, MI, USA, 31 May–3 June 2016, 8 pp.

Cox, G. F. N., 1984. A preliminary investigation of thermal ice pressures. Cold Regions Science and Technology, 9, 221–229.

Fransson, L., 1988. Thermal ice pressure on structures in ice covers. Doctoral Thesis, Luleå University of Technology, Sweden, 161 pp.

Gebre, S., Alfredsen, K., Lia, L., Stickler, M., Tesaker, E., 2013. Review of ice effects on hydropower systems. Journal of Cold Regions Engineering 27 (4), 196–222.

Hoseth, K.A., Fransson, L., 1999. Istrykk på dammer, Måleprogram dam Silvann, vinter 98–99. Report 22/1999. Norwegian Water Resources and Energy Directorate (NVE), Oslo, 34 pp.

Morse, B., E. Stander, A. Coté, J. Morse, P. Beaulieu, A. Tarras, P. Noël, and Y. Pratt, 2009. Ice interactions at a dam face. In Proceedings of the 15th Workshop on River Ice, St. John's, Canada, June 2009, 11 pp.

NVE, 2003. Retningslinje for Laster og Dimensjonering til §§ 4–1 og 4–2 i Forskrift om Sikkerhet og Tilsyn med Vassdragsanlegg Norges Vassdrags- og Energidirektorat. Norwegian Water Resources and Energy Directorate (NVE), Oslo, Norway, 25 pp.

O'Sadnick, M., C. Petrich, B. Arntsen, and B. Sand, 2016. Observations of Ice Stress at Taraldsvikfossen Reservoir, Narvik, Norway. In Proceedings of the 23rd IAHR International Symposium on Ice, Ann Arbor, Michigan, USA, 31 May to 3 June 2016. 8 pp.

Petrich, C., I. Sæther, L. Fransson, B. Sand, and B. Arntsen, 2014. Preliminary results from two years of ice stress measurements in a small reservoir, In Proceedings of the 22nd IAHR International Symposium on Ice, Singapore, 11–15 August 2014, A. W.-K. Law (ed), NEWRI Nanyang Technological University, Singapore. 452-459.

Petrich, C., I. Sæther, L. Fransson, B. Sand, and B. Arntsen, 2015. Time-dependent spatial distribution of thermal stresses in the ice cover of a small reservoir. Cold Regions Science and Technology, 120, 35-44, https://dx.doi.org/10.1016/j.coldregions.2015.09.003.

Petrich, C., and B. Arntsen, 2018. An overview of trends and regional distribution of thermal ice loads on dams in Norway. In Proceedings of the 26th International Congress of the International Commission of Large Dams (ICOLD), Q.101, R.72, Vienna, Austria, 1-7 July 2018, 1210-1224.

Stander, E., 2006. Ice stresses in reservoirs: Effect of water level fluctuations. Journal of Cold Regions Engineering, 20(2), 52-67.

Timco, G.W., Watson, D.A., Comfort, G.A., Abdelnour, R., 1996. A comparison of methods for predicting thermally-induced ice loads. Proceedings of the 13th IAHR Symposium on Ice, Beijing, China. vol. 1, pp. 241–248.

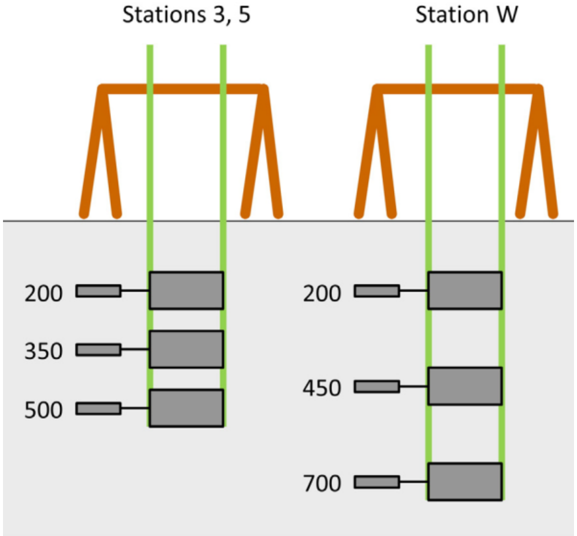

Figure 1. Sketch of the vertical positions of stress cells in winter 2012/13. Numbers indicate distance to the ice surface in mm at the time of depoyment. Stations 3 and 5, and Station W were placed 1 m and 10 m in front of the dam, respectively.

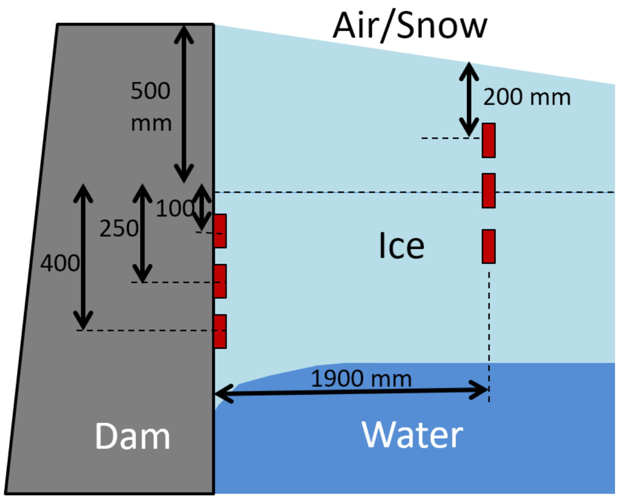

Figure 2. Sketch of the vertical positions of stress cells in winter 2013/14. The dashed horizontal line indicates the water level (i.e., approx. ice level) at the time of deployment of the dam-borne sensors. Sketch is not to scale.

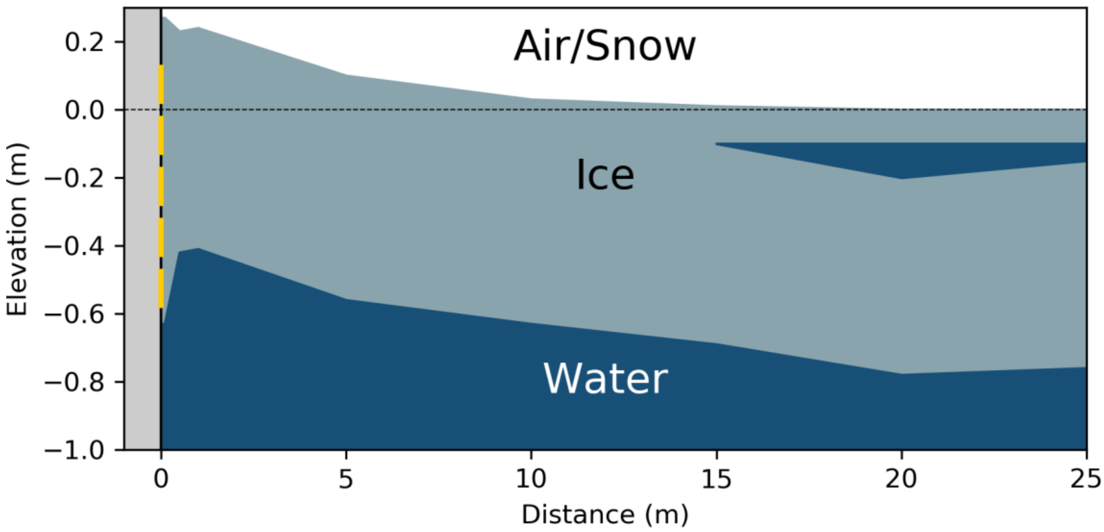

Figure 3. Measured vertical ice profile along a transect normal the dam (distance 0 m) on 6 March 2015 (phase 8), i.e. several weeks after significant load signals had been recorded. Positions of the stress cells at the dam during winter 2014/15 are marked (yellow lines at distance 0 m). 0 m elevation is the waterline at the time of measurement. Note the gap layer in the ice from 15 m onwards.

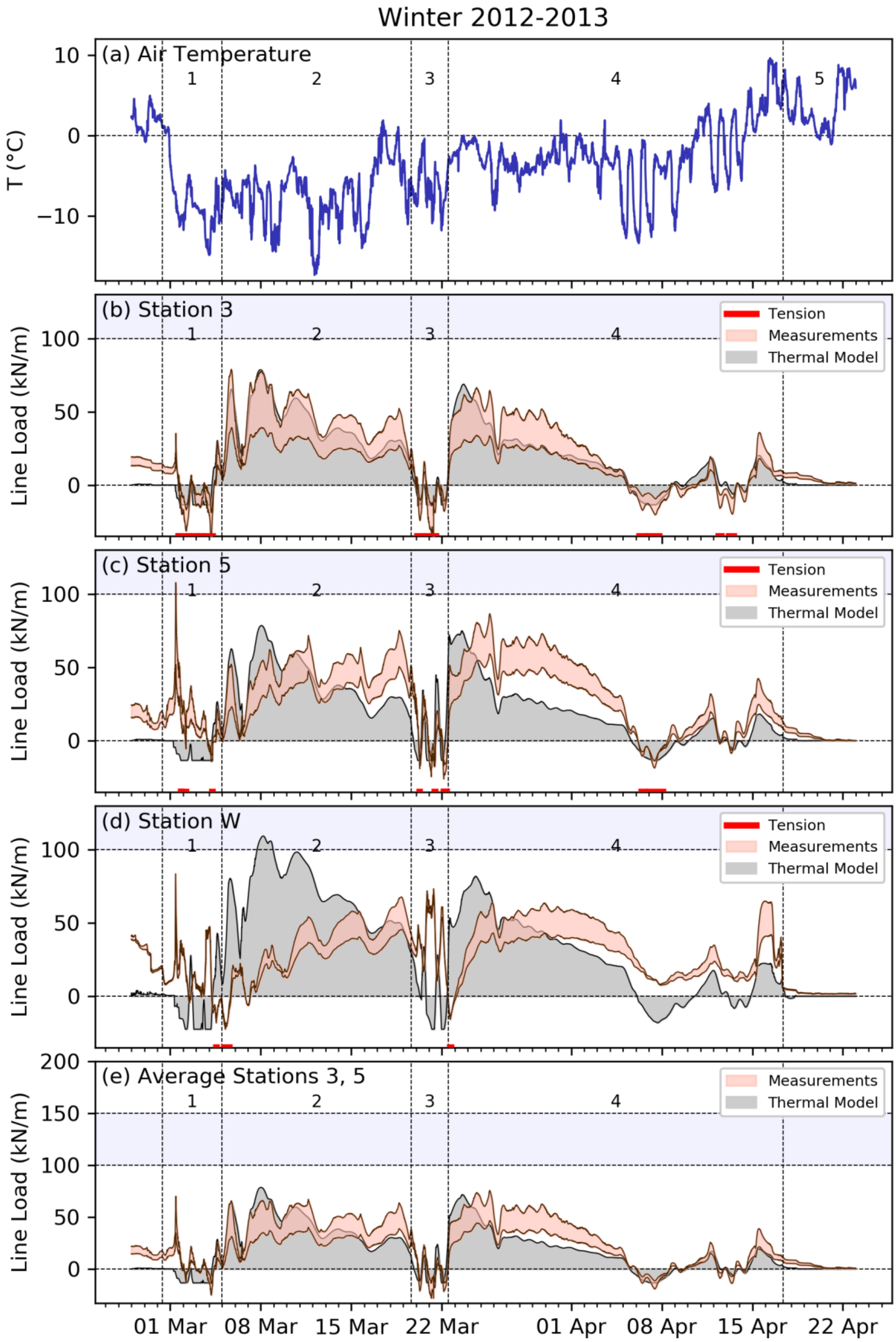

Figure 4. (a) Air temperature, (b,c) ice loads in winter 2012/13 measured and modeled at two stations, and (d) averaged loads. Red lines in (b) and (c) indicate that tensile stresses >50 kPa were measured.

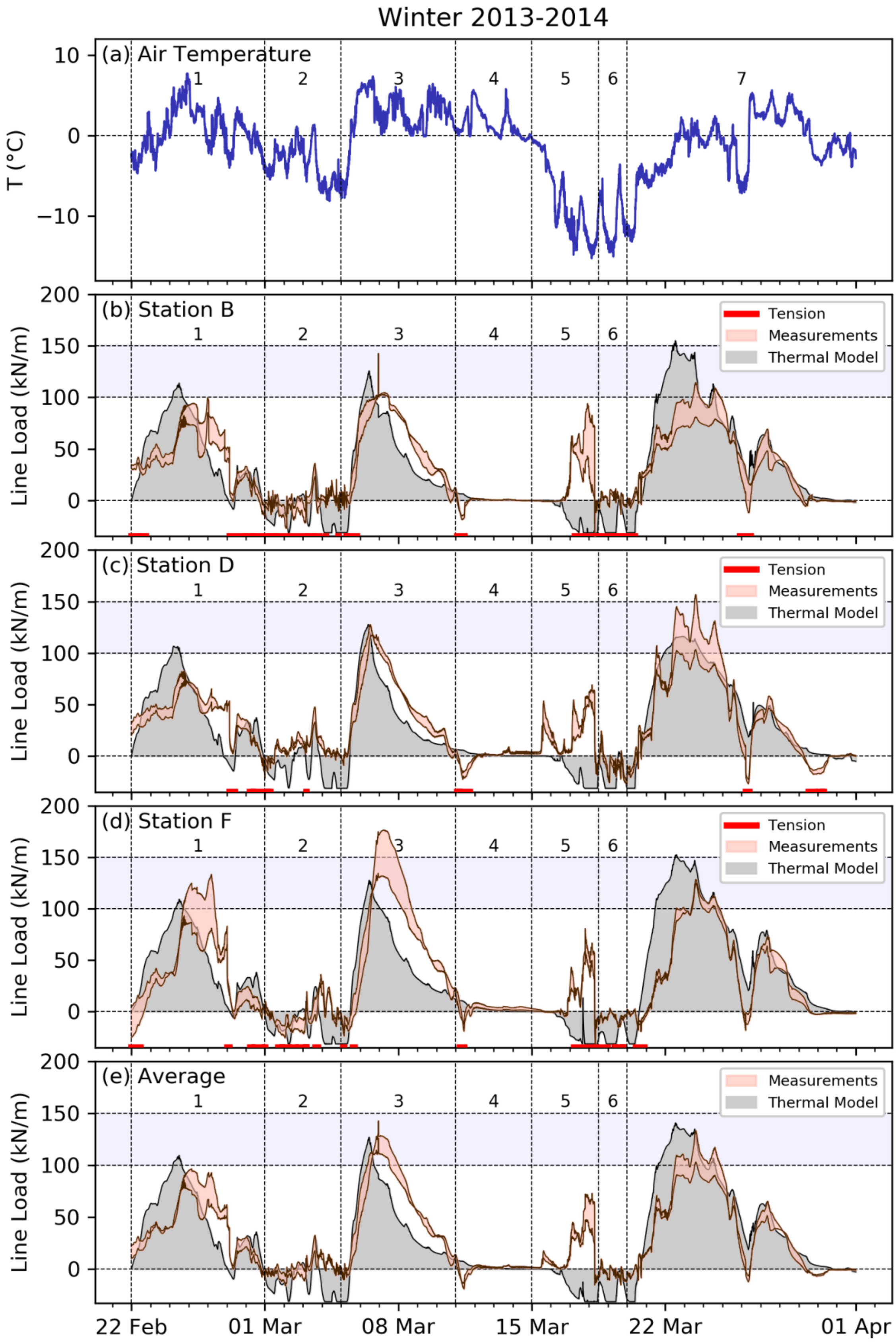

Figure 5. (a) Air temperature, (b,c,d) ice loads in winter 2013/14 measured and modeled at three stations, and (e) averaged loads. Red lines in (b), (c), and (d) indicate that tensile stresses >50 kPa were measured.

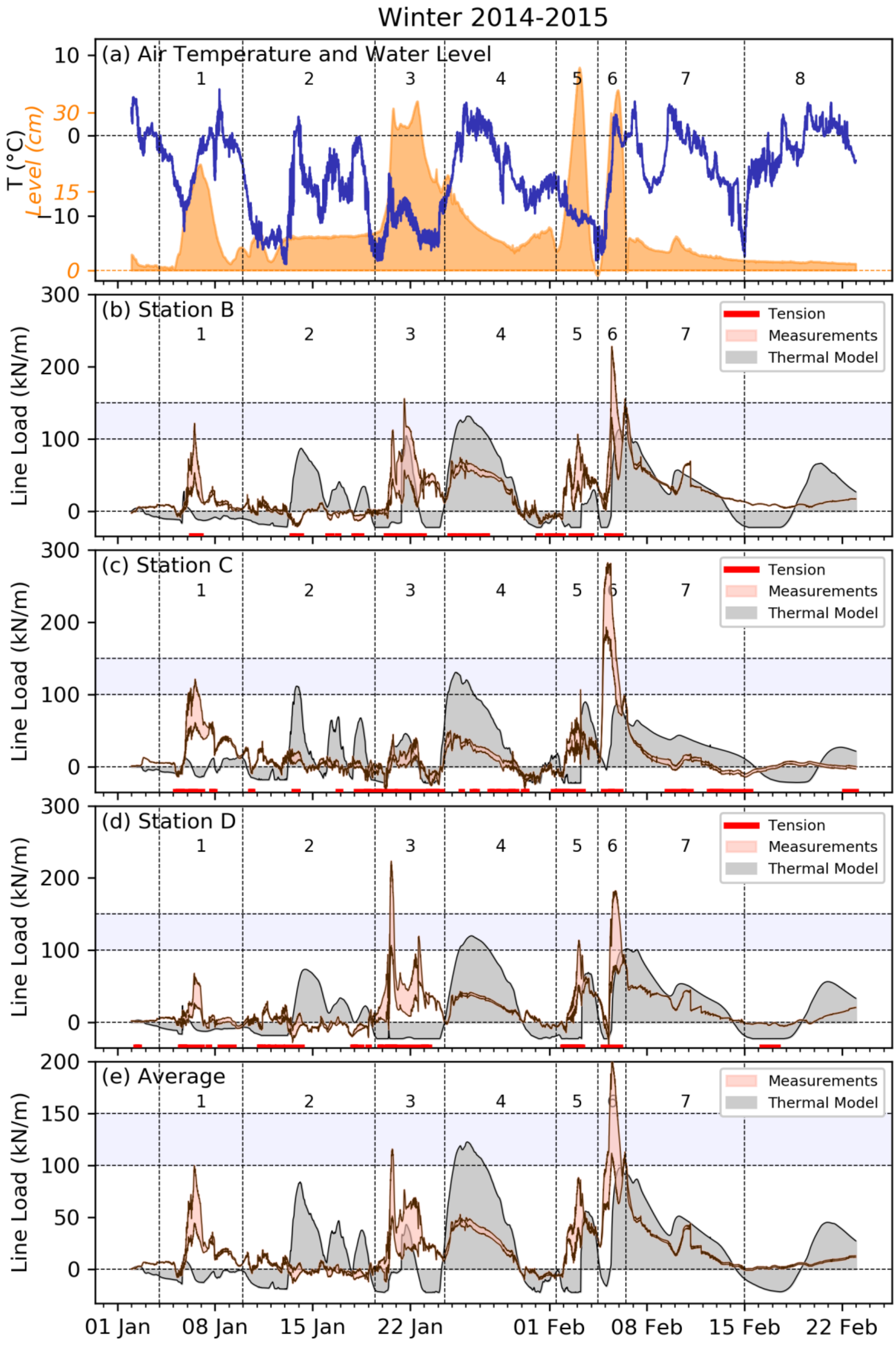

Figure 6. (a) Air temperature and water level, (b,c,d) ice loads in winter 2014/15 measured and modeled at three stations, and (e) averaged loads. Red lines in (b), (c), and (d) indicate that tensile stresses >50 kPa were measured.

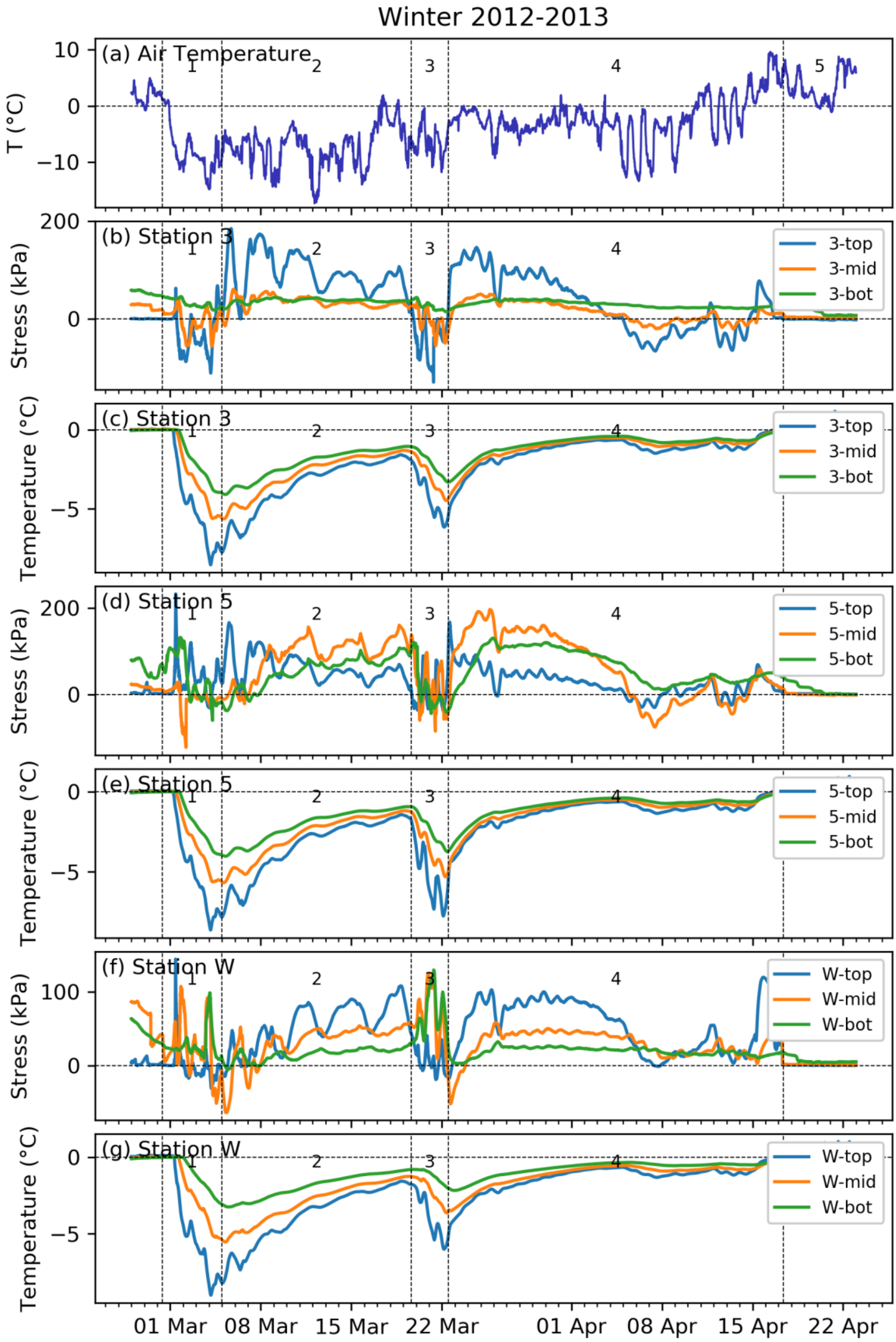

Figure 7. (a) Air temperature, (b,d,f) stresses positive in compression, and (c,e,g) ice temperatures measured in 2012/13. Cells are labeled top to bottom "top", "mid", "bot", respectively.

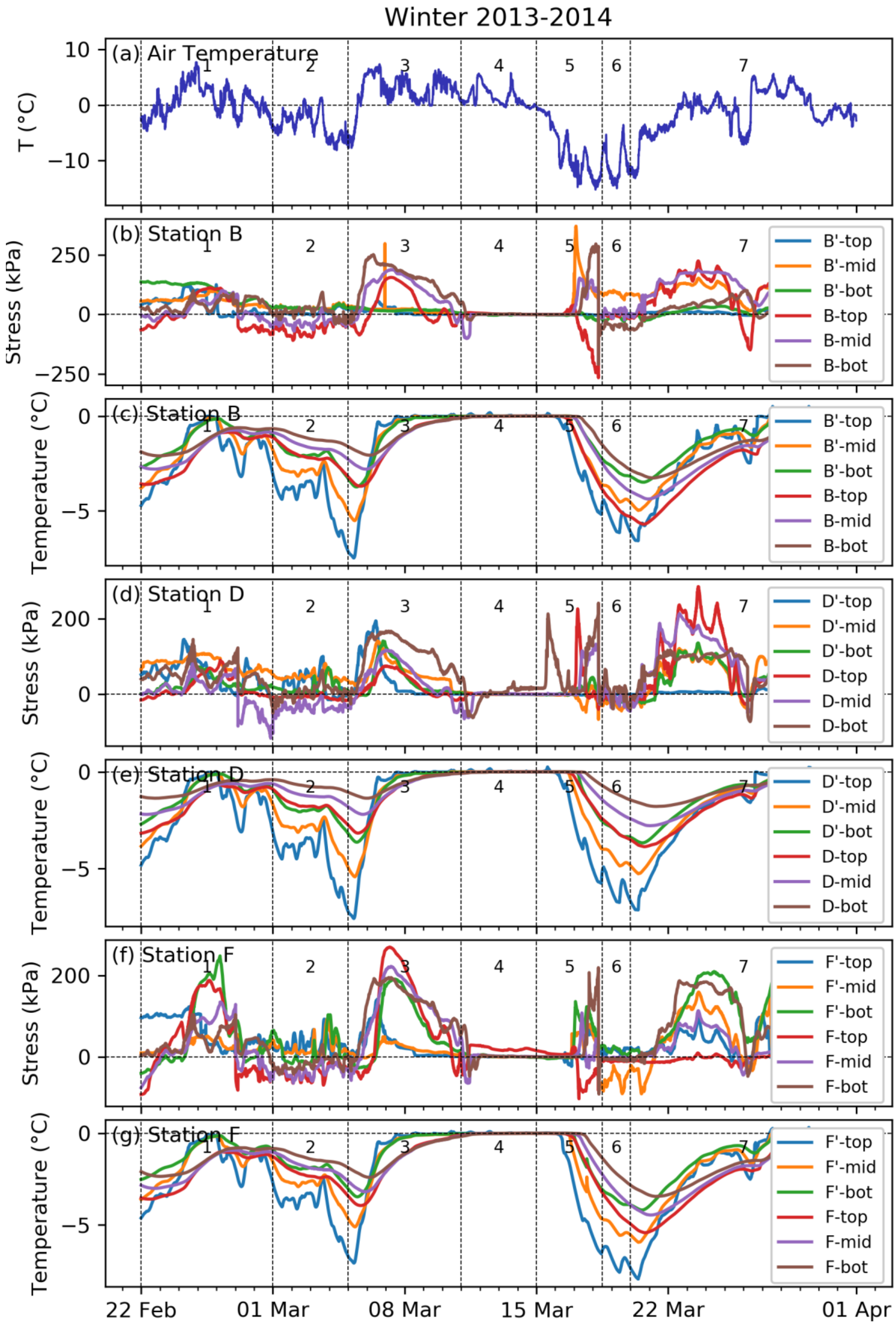

Figure 8. (a) Air temperature, (b,d,f) stresses positive in compression, and (c,e,g) ice temperatures measured in 2013/14. Cells are labeled top to bottom "top", "mid", "bot", respectively, with primed and unprimed cells in the ice and at the dam, respectively.

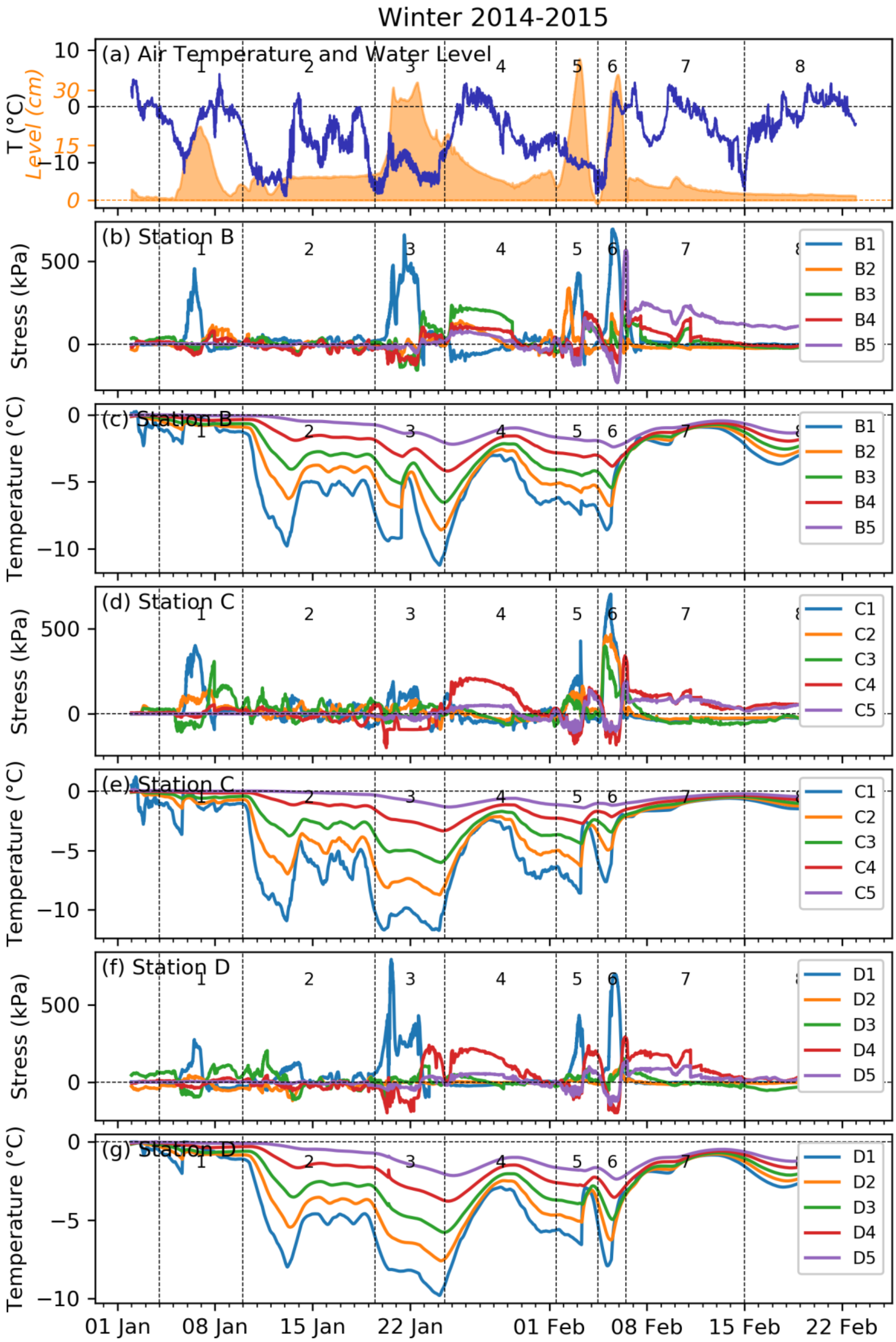

Figure 9. (a) Air temperature and water level, (b,d,f) stresses positive in compression, and (c,e,g) ice temperatures measured in 2014/15. Cells are labeled top to bottom from 1 to 5 where cell 1 had been installed above the nominal water line.

25th IAHR International Symposium on Ice

Trondheim, November 23 to 25, 2020

Investigating the sensitivity of small river bridge pier ice forces to parameter variation using SAMS

Einar Rødtang

Norwegian University of Science and Technology
S.P Andersens veg 5, 7491 Trondheim, Norway
einar.a.rodtang@ntnu.no

Predicting the forces caused by ice breakup on bridges is important because they are crucial for predicting erosion and sudden catastrophic failure. Simulator for Artic Marine Structures (SAMS) is a software package developed at the Centre for Research-based Innovation – Sustainable Arctic Marine and Coastal Technology (SAMCoT). SAMS was developed primarily to predict ice floe structure interactions in a marine environment. This paper aims to evaluate the parameter sensitivity of SAMS ice force prediction when predicting ice forces on bridge piers in small steep rivers. From a simulation point of view there are several key differences between small steep rivers and open marine environments, including river bed and bank shear forces and river slope. Furthermore, little is known about initial floe size distributions in such rivers. Few models currently provide satisfactory predictions of river ice forces on infrastructure, and those that do exist are developed and tested for moderate gradient large rivers and may be largely inapplicable to small and steep rivers. It was found that SAMS has a high sensitivity to the random seed used, low sensitivity to ice floe concentration and a linear sensitivity with increasing absolute variability to ice thickness.

1. Introduction

Accurate estimation of ice forces on river piers is important, because overestimation causes significant building costs, while underestimation entails a risk of collapse.

Accurate estimation of ice forces is a difficult problem due to the immense variability of ice properties and hydraulic conditions. This variability ensures a plethora of phenomena and failure mechanisms, making the development of a single analytical framework for ice force prediction difficult. Empirical methods are therefore often relied upon, however little river ice data and even less ice force data exists. Empirical methods therefore may have limited general applicability. A variety of software has been developed for modelling ice runs and ice jams(Carson et al., 2011). Evaluating the performance of various pieces of software is therefore of considerable interest.

This document seeks to use the SAMS software to investigate the sensitivity of small river bridge pier ice forces to parameter variation.

2. Background

SAMS (Simulator for Artic Marine Structures) is a numerical package for modelling ice floe interaction with marine structures. SAMS is being developed by ArcISo (Arctic Integrated Solutions AS). ArcISo is a spinoff company originating from SAMCoT (Centre for Research-based Innovation – Sustainable Artic Marine and Coastal Technology) hosted at NTNU (Norwegian University of Science and Technology). (Lubbad et al., 2018)

SAMS uses discrete element modelling (DEM) when simulating contact behaviour between ice floes. DEM methods are frequently either smooth or non-smooth (SDEM vs NDEM). SAMS utilizes NDEM. The primary difference between these groups of methods can be considered to be whether the methods use explicit or implicit time integration. In principle implicit integration should allow longer time steps while maintaining stability of the simulation.

When modelling contact behaviour SAMS distinguishes between 2 kinds of contacts; rigid and compliant contacts. Rigid contacts do not model the exact contact behaviour and doesn't have an upper bound on the contact force, they are however computationally cheaper and are able to estimate the average contact force. Hence rigid contact behaviour is acceptable for floe interactions that do not involve fracture. (Berg et al., 2018)

Furthermore, the NDEM method employed by SAMS is supplemented by closed-form analytical computations for simulating the fracture of ice. These analytical equations include closed form solutions for, bending failure, splitting and radial cracking of ice. SAMS also calculates hydrodynamic and aerodynamic drag applied to ice floes.

In short SAMS simulations have 3 modules. The NDEM multibody dynamics module, the closed form ice fracture module and the hydrodynamics module.

3. Investigation matrix

In this study a SAMS has been used to model an idealized version of Sokna bridge in Støren, Norway. The river Sokna is formed by the confluence of the two rivers Ila and Stavila and is a tributary of the Gaula river which discharges into Gaulosen. Gaulosen forms part of the Trondheim Fjord system in central Norway.

Sokna has an annual mean flood of 166 m^3⁄s. From the Ila/Stavila confluence to the Sokna/Gaula confluence the altitude drops from 238 m a.s.l to 64 m a.s.l. The distance between these confluences is 15km along the river and 12.5km as the crow flies. Giving an average river slope of 0.7° along the river. This however varies substantially along the river. Sokna for the purposes of river ice considerations can be considered a small steep river

This bridge was chosen in this study because it is prone to ice runs with thick, strong ice and a measurement campaign is underway that aims to provide accurate ice force data.

The simulation simplifies the real-world channel geometry to a rectangular channel since SAMS doesn't natively handle bathymetry.

To restrict the scope of this investigation a base case has been established. For each of the parameters considered the parameters and setting of the base case simulation will be used, except for the parameter under consideration which will be varied according to the investigation matrix.

Investigation matrix – Variation of parameters from base case			
	Ice field concentration	Ice field randomness (Seed number)	Ice thickness
Base Case	0.6	1579953051	0.8m
Case 1	0.1	1580045997	0.1m
Case 2	0.2	1580467661	0.2m
Case 3	0.3	1580467937	0.3m
Case 4	0.4	1580468094	0.4m
Case 5	0.5	1580468495	0.5m
Case 6	0.6	1580468712	0.6m
Case 7	0.7	1580469002	0.7m
Case 8		1580469168	0.8m
Case 9		1580469334	0.9m
Case 10		1580469820	1.0m
Case 11			1.1m
Case 12			1.2m
Case 13			1.3m
Case 14			1.4m
Case 15			1.5m

Simulation inputs		
Value	Unit	Parameter
0.1	s	Simulation time step
100	s	Simulation time

900	Kg/m^3	Ice density
1025	Kg/m^3	Water density
0.005	-	Skin friction coefficient
0.5	-	Form drag coefficient
1	m	Ice thickness
5	GPa	Young's modulus
0.3	-	Poisson ratio
150	kPa$\sqrt{m}$	Fracture toughness
2	MPa	Compressive strength of ice
500	kPa	Flexural strength of ice
0.15	-	Ice-ice and ice-structure friction coeff
3	m/s	Current velocity

3.1 Base case

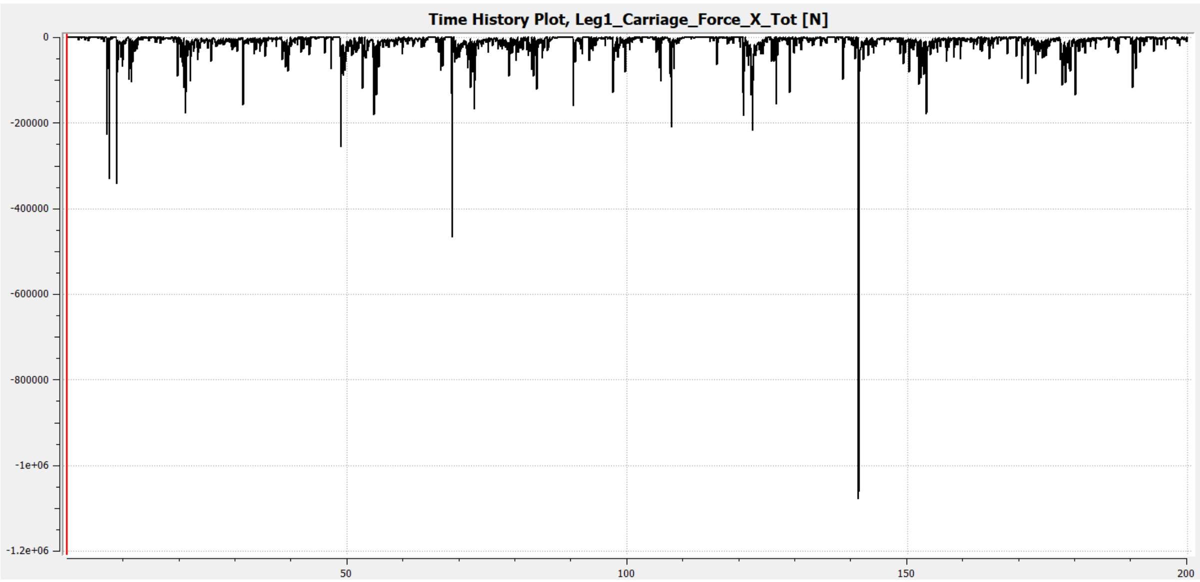

Figure 1. Pier 1 – Total X direction Carriage Force – Base case
Y-axis: Newton
X-axis: Seconds

The base case force plot displays some characteristics that are typical of the other force plots. Namely peak force being substantially higher than average forces and a substantial stochasticity.

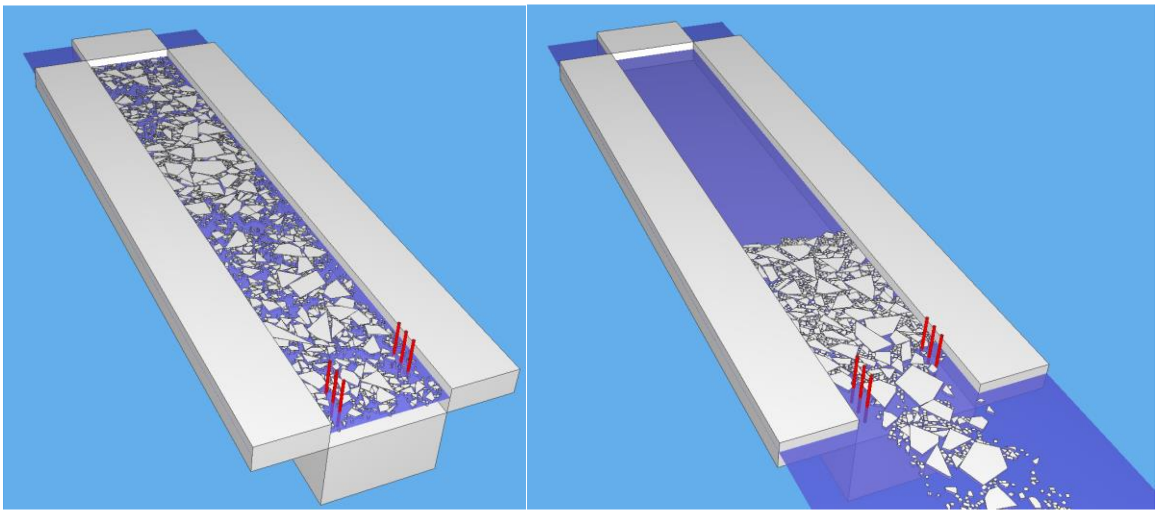

Figure 2. Base Case t=0s and t=200s

Figure 2 depicts the base case simulation at t=0s t=200 sec. Pier 1 is the pier that is furthest upstream amongst the piers. Pier 1 consistently saw higher forces than the shielded piers. The shielded piers saw much lower forces than the two upstream piers. The two upstream piers saw comparable forces.

3.2 Ice thickness

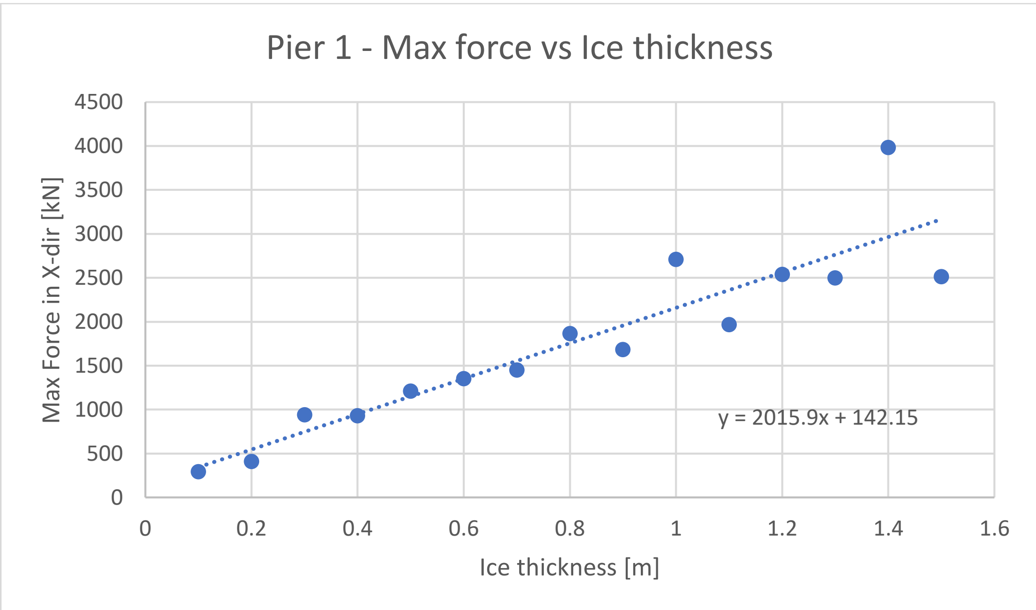

Figure 3. - Leg 1 - Total X direction Carriage Force - Variable ice thickness

15 trials were carried out with varying ice thickness. As can be seen from figure 3. Ice forces consistently rise with ice thickness, albeit with increasing absolute variability.

3.3 Ice field randomness

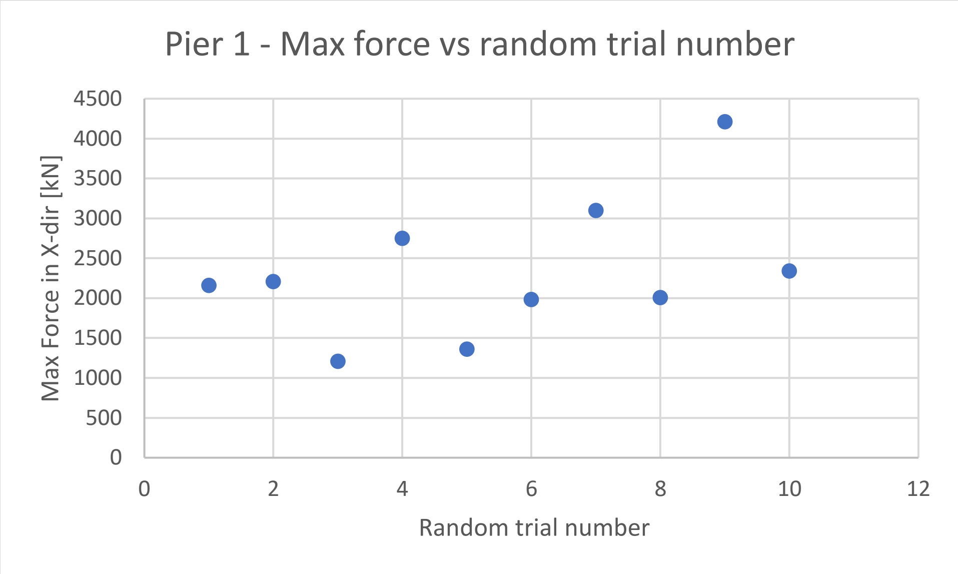

Figure 4. Leg 1 - Total X direction Carriage Force - Variable random seed

In order to determine expected variability in the obtained results a sequence of trials was carried out with the all the same parameters, except for varying the random seed used to generate the ice field. Key finding from this is that the range of variation (1.2MN vs 4.2MN) is very large compared to the variability due to other factors considered in other trials. Suggesting that far more trials should be conducted to obtain a statistically significant measure of the significance of the sensitivity of these other variables. Furthermore, trials to inspect any variable should include a variation of the random seed of the ice field.

3.4 Ice field concentration

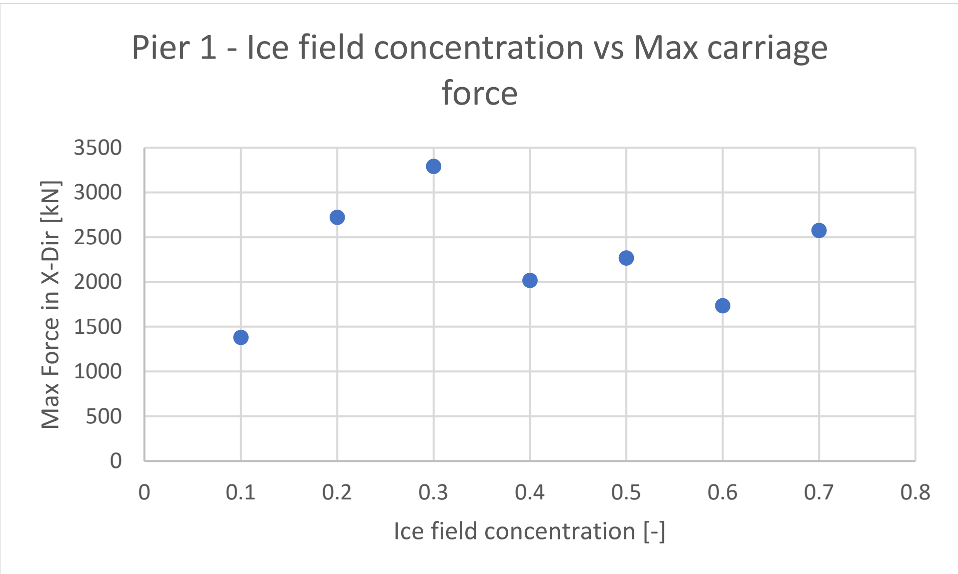

Figure 5. - Ice field concentration plot

The variation in carriage force due to variation in ice field concentration does not exhibit a clear trend and does not display variation in excess of what can be explained by the variation in random seed. Furthermore, inspecting the simulation footage it becomes clear that the significance of initial concentration quickly becomes insignificant as the ice field compacts due to interaction with the structures in the channel.

4. Comparison to theory

Various theoretical frameworks have been developed for predicting ice forces on river bridge piers(Ashton, 1986). It is instructive to compare the SAMS predictions to the predictions made by the Norwegian standard. The Norwegian standard is in turn based on the ISO standard(*Håndbok N400 - Bruprosjektering*, 2015, p. 71).

$$F_c = C \cdot h\left(\frac{D}{h}\right)^{-0,16}\left(\frac{h}{h_1}\right)^{(n)} \qquad \begin{array}{ll} n = -0,5 + h/5 & h \leq 1,0m \\ n = -0,3 & h > 1,0m \end{array}$$

hvor:

$$C = 1800\ \text{kPa}$$

$$h_1 = 1,0\ \text{m}$$

In our base case we consider 0.8m thick ice. Hence the predicted force evaluates to be approximately equal to 1.6MN. While the Norwegian standard calculates a characteristic force, it is intentionally conservative. Therefore, the peak force of 1.1MN achieved in the base case simulation is not unreasonable. 1.6MN is within the range of predictions realized in the random seed tests (1.2MN to 4.2MN). Although the peak force is considerably higher than that of the ISO prediction.

5. Conclusions

5.1 Sensitivity

In this simulation the realised peak ice force is clearly very sensitive to the random seed used in generating the ice field, peak ice force varying between 1.2 and 4.2MN. This suggests that at 3m/s current a 200m icefield at 100s of simulation is insufficient to get tightly bound results. One expects the peak force variability to go down the longer the ice field and simulation time is.

As expected, the ice force scales vaguely linearly with ice thickness. However, the absolute variability of ice forces increases with thickness.

Ice force displays little sensitivity to initial ice concentration. Provided the ice concentration is high enough to cause compaction.

5.2 Ice force prediction

Some comments can be made on the expected accuracy of the SAMS predictions based on the theoretical limitations of the model employed in SAMS.

SAMS assumes that all ice floes have similar uniform mechanical properties and thickness. This is far from the reality of river ice where ice properties vary substantially both within and between ice floes. By feeding SAMS the maximum thickness and ice strength an overestimate of forces is to be expected. Although in certain cases it can also cause an underestimate, namely when all floes having a high strength and thickness causes ice to jam up in front of the structure and thus shielding it from further direct impact. In these cases, one may see that reducing the strength and thickness of some floes causes the ice to clear the structure enabling future direct hits from thick strong ice.

5.3 Comparison of SAMS results to field data

An ice force measurement program is under way at Sokna bridge. During the winter 2020 the load panel measuring the forces had a battery failure on the day of the ice run, so ice force data was not obtained. Hindcast calculations based on the deformation of the load panel due to the ice run suggests that peak ice forces must have been between 1.1MN and 5.5MN. This is not inconsistent with the corresponding SAMS simulations. Peak ice thickness was measured to be 0.65m.

Observations suggest that ice floes flipping to vertical curing dynamic ice field compaction is common, the SAMS simulation did not exhibit this behaviour. This is likely due the rectangular channel assumption coupled with simplistic turbulence modelling.

5.4 Improving SAMS

Through the use of SAMS some lessons have been learned and suggestions can be made as to how to improve the software. It would be off great benefit to update the SAMS GUI and enable importation of multiple structures and bathymetry. Editing files manually to allow multiple structures is possible, and indeed this is what was done for this project. While this is straight forward enough once you know how, it is very time consuming to find out how to do this without help. Enabling batch simulations with variable properties would be a great quality of life improvement when using the software.

Manually editing files to include variable bathymetry should in principle be possible, but beyond the scope of this project to attempt. While bathymetry is not of great importance when modelling structures far out at sea, it is great importance when modelling ice transport in small rivers. Depending on the morphology and depth of the river ice jams may form and in its current state SAMS is incapable of predicting these. Furthermore, in order to enable SAMS to predict ice jam consolidation and breakup it would be necessary to include variable thermal and discharge conditions. Including more sophisticated fluid mechanical simulation is of course possible, however simply allowing the water level to vary according to a measured hydrograph and current velocity to vary according to according to table input would greatly improve predictions.

While SAMS may currently be applicable to large low gradient rivers, improvements need to be made before SAMS can confidently be applied to small steep gradient rivers.

Acknowledgments

I would like to thank Raed Lubbad for access to the SAMS software and Marnix Van Den Berg for helping me understand SAMS.

References

Ashton, G.D., 1986. River Lake Ice Engineering. Water Resources Publications.

Berg, M. Van Den, Lubbad, R., Løset, S., 2018. Cold Regions Science and Technology An implicit time-stepping scheme and an improved contact model for ice- structure interaction simulations. Cold Reg. Sci. Technol. 155, 193–213. https://doi.org/10.1016/j.coldregions.2018.07.001

Carson, R., Beltaos, S., Groeneveld, J., She, Y., Healy, D., Malenchak, J., Morris, M., Saucet,

J.-P., Kolerski, T., Shen, H.T., 2011. Comparative testing of numerical models of river ice jams. Can. J. Civ. Eng. https://doi.org/10.1139/l11-036
Håndbok N400 - Bruprosjektering, 2015th ed, 2015. . Vegdirektoratet.
Lubbad, R., Løset, S., Lu, W., Tsarau, A., van den Berg, M., 2018. Simulator for arctic marine structures(SAMS). OMAE2018.

25th IAHR International Symposium on Ice

Trondheim, 23 - 25 November 2020

Numerical analysis of ice loads on Taraldsvikfossen dam

Andreas Seger[1, 2], Bjørnar Sand[1], Bård Arntsen[1], Chris Petrich[1], Megan O'Sadnick[1,2]

[1] SINTEF Narvik, Narvik, Norway

[2] UiT-The Arctic University of Norway, Tromsø, Norway

andreas@tek.norut.no, bjoernar@tek.norut.no, baard@tek.norut.no, christian@tek.norut.no, megan@tek.norut.no,

Static ice loads (ice actions) are a key design parameter for dams in cold climates. Since 2012, ice stresses have been measured at Taraldsvikfossen reservoir located in Narvik, Norway. Similar to earlier observations in Canada, it became evident from the first three years of data that various effects resulted in stresses, including thermal expansion and water level fluctuations, and that the relative dominance of the processes varied between seasons. A numerical model, using the commercially available finite element software LS-DYNA, is presented for the prediction of the stress field in an ice sheet due to temperature changes and water fluctuations as a function of time, under a variety of conditions. The finite element model accounts for variable temperature and properties through the thickness, an elastic foundation representation of the underlying water, nonlinear constitutive behavior of the ice, temperature dependent mechanical properties, flexibility of resisting structures. For verification of the numerical model, results from simulation are compared with measured temperatures and stresses at Taraldsvikfossen reservoir.

1. Introduction

The age of the dams in Norway is increasing. The dams are a considerable value in terms of fixed capital assets and future profits. The consequences of a dam failure can often be very significant, causing both environmental and economic damage and loss of life. The safety of dams in Norway are regulated trough national regulations (Damsikkerhetsforskriften (2010)), in addition to this NVE has guidelines detailing how the stability calculation of dams should be done (e.g. NVE (2003) and NVE (2005)). One of the main changes that was introduced in 2010 was that ice load should be included in the stability calculation. It should be noted that the dams are reassessed every 10 – 20 years depending on the consequence a failure will have. The dam is reassessed according to the current regulations/guidelines. Ice loads where not considered as a load case, when many of the older dams were designed. Therefore, these dams do not fulfill the required theoretical safety factor with respect to stability as specified in the current guidelines. Approximately 90 % of the dams in Norway is what considered small dams, i.e. the maximum height is less than 15 meters. The ice load for these small dams is often the main issue when reassessing the stability of the dam according to the guidelines from 2003 by NVE (2003), this is due to the fact that the ice load in the guidelines (100 - 150 kN/m) is high in comparison with the self-weight of the dam body. This motivated a field measurement program that was implemented to measure the ice stresses at the Taraldsvikfossen reservoir, Narvik, Norway in 2012 and is still running. Some of these results can be found in Petrich et al., (2014), O'Sadnick et al. (2016). Thermal stresses in ice have been discussed in the context of elastic behavior over short periods of time, only (e.g. Comfort et al., (2003); Morse et al., (2011)). However, ice is clearly not an elastic material and alternative formulations of ice rheology have been proposed, e.g., Bergdahl (1978); Drouin and Michel (1974), Royen (1922). The model of Bergdahl (1978) enjoyed considerable success when compared with field measurements when the originally proposed coefficients were adjusted, Cox (1984); Fransson (1988), Petrich et al. (2015). Former work found encouraging agreement between numerical models and field and laboratory measurements Azarnejad and Hrudey (1998).

The overall problem of ice forces on dams is very complex. For instance, it will be important to study how the effects of rapid temperature change and the topology of the reservoir and infrastructure affects ice forces on dams. Initially, the problem is going to be simplified, and first look at how a temperature variations of the ice cover affects a dam, i.e. how the ice forces built up in the dam. Furthermore, take into account the stiffness and strength of the dam. Or if creep buckling occurs in the ice cover. These effects may reduce the estimated ice pressure acting on the dam face. The following knowledge gaps has been identified:

- The need for a physically meaningful constitutive model for freshwater ice. The model should include anisotropic behavior, and different compressive- and tensile strengths, (which are dependent on strain rate). The model should account creep and strain softening due to damage, and cracking caused by thermal contraction or mechanical loading.
- It is important to include the entire structural stiffness using the real shape and material properties of the structural components of the dam in the numerical model for ice-structure interaction process.
- Hydrodynamic forces acting on the floating ice sheet, as well as the dynamic coupling between ice and structure by means of contact and frictional forces at the ice-structure interface.

By implementing these effects, advanced numerical FE models can be developed to simulate ice loads on dams. The different mechanisms such as of thermal expansion and contraction, out of plane bending and buckling and ice jacking mechanisms on the ice action can then be differentiated in a realistic manner. It is necessary to carry out a stepwise development, and the complexity of the numerical models is extended during the project. The first step in the development of a numerical model will be in a simplified approach where the geometry, thickness of ice floes and boundary conditions are simplified, idealized and parameterized. To establish the temperature load in the ice cover, transient thermal analysis will also be simplified and idealized. The hypothesis that forms the basis for model development is based on the following: The temperature of the ice bottom is approximately equal to 0°C and constant, while the temperature on the top surface of the ice cover fluctuates with air temperature. The aim of this paper is to get a better understanding of how the measured ice load is influenced by environmental variables as temperature, water level fluctuations and interaction with dams and its structural stiffness. A numerical model, using the commercially available finite element software LS-DYNA, utilized for the prediction of the stress field in an ice sheet due to temperature changes and water fluctuations as a function of time, under a variety of conditions. The finite element model accounts for variable temperature and properties through the thickness. The most sophisticated method to account for hydrodynamic effects is by explicitly simulating the water medium by a coupled Arbitrary Lagrangian Eulerian (ALE) method. This approach is accurate, but not computationally efficient. Therefore, a mass-spring-dashpot model to account for hydrodynamic effects has been developed at SINTEF Narvik and implemented into the commercial FE code LS-DYNA and this approach will be employed in this project. In this manner, water level fluctuations, flooding, out of plane bending, buckling and ice jacking mechanisms of the ice sheet are accounted for. For verification of the numerical model, results from simulations are compared with measured temperatures, stresses and global load at Taraldsvikfossen reservoir. Better understanding of thermal and mechanical ice-structure interaction forces will contribute to reducing the rehabilitation costs of the existing Norwegian dams.

2. Field measurements

Taraldsviksfossen reservoir is a small reservoir of approximately 1650 m^2 located 212 m.a.s.l in the town of Narvik, Norway. Confined by a straight sided concrete dam 6 m in height, it is maintained to provide a backup water supply and not regulated (Fig. 1a). The reservoir is fed by a creek, called Taraldsvikelva. In winter, the creek freezes limiting the flow into the reservoir significantly. Given its relatively stable water level and accessibility, ice stress measurements were performed at Taraldsviksfossen reservoir. Five frames with stress sensors (A - E) was installed 6 m apart on 3 October 2014 as shown in Fig. 1. Stress was recorded using custom modified GeoKon 4850 pressure cells consisting of two rectangular steel plates (100 mm x 200 mm) separated by de-aired oil. In addition to stress, each cell measured temperature. Three frames (B, C, D) held five cells placed 0.15 m vertically apart (center-to-center) with the center of the uppermost cell placed 0.075 m above the nominal water line. Nominal waterline is 0.5 m below the top of the dam. The other two frames (A, E) held one cell each with the center placed 0.075 m below the surface. Cells are designed to measure normal compressive stresses up to 1 MPa. A detailed description of the setup is given by Petrich et al. (2015) and preliminary analysis of the ice stresses at Taraldsvikfossen for the season 2014-2015 is described by O'Sadnick et al. (2016).

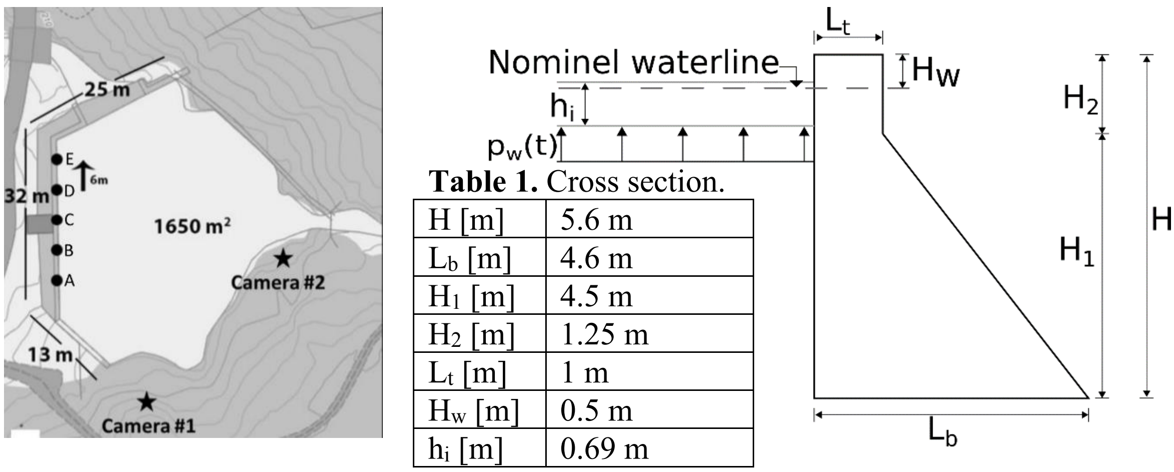

Table 1. Cross section.

H [m]	5.6 m
L_b [m]	4.6 m
H_1 [m]	4.5 m
H_2 [m]	1.25 m
L_t [m]	1 m
H_W [m]	0.5 m
h_i [m]	0.69 m

a) b)

Figure 1. a) Diagram of reservoir including position of frames (black dots) and cameras. From O'Sadnick et al. (2016). b) Dimension of the modelled cross-section.

The ice thickness, h_i, produced by static ice formation is most commonly predicted based on the accumulated Freezing Degree Days (FDDs), as given below:

$$h_i = \alpha_{ig}\sqrt{|FDD|} \text{ [m] with } \alpha_{ig} = 0.033 \text{ m/(day}^{\circ}\text{C)} \quad \textbf{[1]}$$

α_{ig} is an empirical coefficient that varies from site to site depending on local conditions such as the snow cover, winds, and solar radiation. The predicted ice thickness is compared with the average measured ice thickness in Fig. 2.

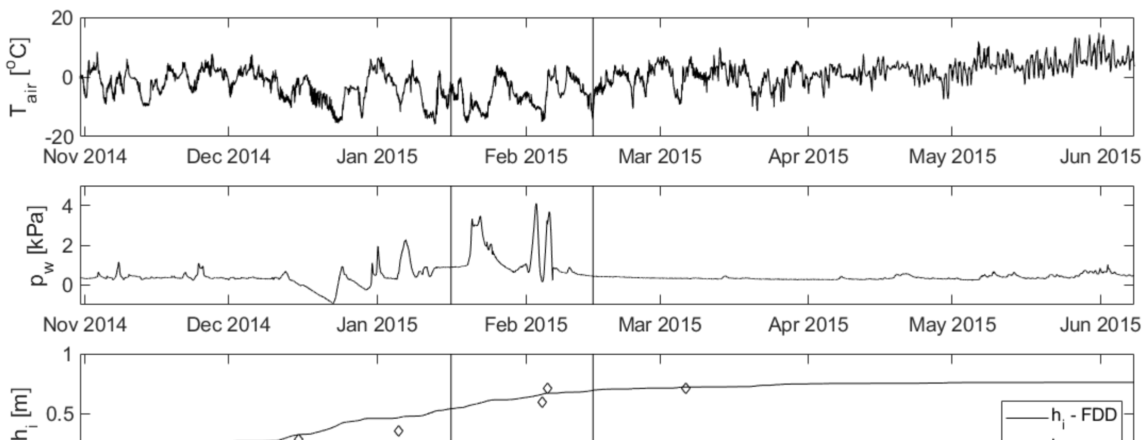

Figure 2. Measured air temperature, water pressure and ice thickness, Taraldsvikfossen dam for season 2014-2015. Vertical lines indicate the time span for numerical simulations, which starts at :16-Jan-2015 09:15:00 and ends at 15-Feb-2015 00:45:00.

Ice crack patterns are important as they are an indication of the motion of the ice cover near the wall of the dam as illustrated in Fig. 3. Similar crack patterns in the ice were observed for the ice at Taraldsvikfossen dam for season 2014-2015. The formation of ice cracks may be induced by either thermal contraction or mechanical loading most often associated with changes in water level. Crack formation due to thermal contraction is described by Ashton, 1986 and Bažant, 1992. Water level variations create hinge effects near the wall characterized by cracks in the ice. Two important cracks were found within meters from the wall, as shown on Fig. 3. They determine a segment of ice from the wall called the "crutch". As the water level changes, the ice cover moves up or down forcing the "crutch" to pivot about the "Ballycatter", a piece of ice that always stays frozen to the wall of the dam. This effect can contribute to generate an increase in load against the dam. As water level variations pivot the "crutch" up or down, it can snag at the hinges and develop a horizontal thrust against the dam, term called "ice jacking". Conditions that favor this effect are: (a) the presence of thermal ice expansion; and (b) the profile of the ice crack, for example: a jagged crack profile as opposed to a worn and rounded one. Another effect is when water rises and seeps through the cracks and refreezes, thereby increasing the aerial extent of the ice cover. Cracking and refreezing of water between cracks are described in detail by Ashton (1986). As water floods over the cold ice cover, it forces the surface temperature of the ice to increase, producing an expansion of the ice surface. A subsequent rise in water level then places the ice cover in compression as it is forced to fit into a now undersized basin. This phenomenon is called ice jacking. This repetitive cycle and a drop of the water level will produce tension in the upper part of the ice cover, and compression below, while a rise in water level will produce the inverse stress profile.

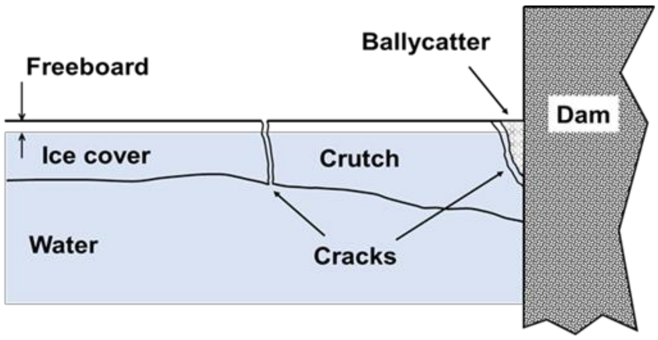

Figure 3. Observed cracks during field measurements.

2. Numerical model

Numerical analysis of ice loads on Taraldsvikfossen dam were with the LS-DYNA general purpose finite element code (Hallquist, 2006) as coupled thermal stress analysis using an implicit code. Simulations are driven by measured air temperature data.

The finite element model for simulation of ice forces acting on the dam is illustrated in Fig. 4 where both the concrete dam and the ice sheet are modeled with hexahedral elements. The ice thickness h_i and the total length of the ice sheet, L_i, is 36 m. As a first approach, only a unit width of 1 m is modeled. The cross-section dimensions of the dam are given in Fig. 2b). The concrete dam is modeled as a linear elastic material with elastic modulus E_c. The mechanical boundary conditions of the dam and ice sheet is modeled in such a way that plane strain is simulated. All the nodes at bottom of dam structure is fixed and all the nodes at the end of the ice furthest from the dam are also fixed. It is also assumed that the ice sheet is frozen to the face of the dam. This is achieved by specifying tied contact between the nodes on the ice and the surface of the structure at the ice-structure interface. The ice sheet is modelled with six hexahedral elements trough the thickness and two elements along the width as shown in Fig. 4. Buoyancy and gravity of the ice sheet is modeled with a nonlinear spring attached to all the nodes defining the bottom surface of the ice. In this manner, the effects of the elements on the ice sheet being lifted out of the water or being submerged is taken account for. Water level fluctuations is modelled by applying the water pressure p_w as a uniform surface pressure at the bottom of the ice sheet as function of time as shown in Fig. 2b).

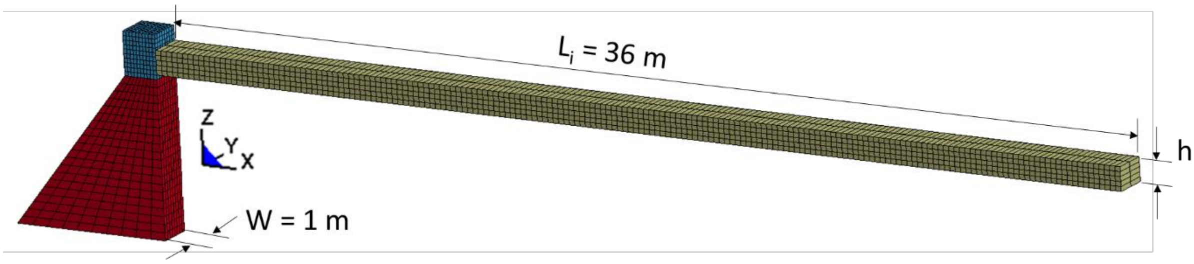

Figure 4. Finite element model for simulation of ice forces on Taraldsvikfossen dam with H = 5.6 m, h_i = 0.69 m and L_i = 36 m. Cross section dimensions are given in Fig. 1b).

For simplicity, the boundary condition at the top surface of the ice the surface is equal to the air temperature, which is function of time, i.e. $T_{air}(t)$ as shown in Fig. 2. It is assumed a linear distribution of temperature through the ice sheet with $T_{air}(t = 0)$ equal to -3 ^oC. as initial condition and the ice–water interface, the temperature is assumed to remain at the freezing point. One of the most difficult aspects of any stress analysis involving ice is the selection of values for the mechanical properties. Values adopted in this study are based on published data presented by others. However, finding appropriate data in the literature is complicated by the fact that the strain rates encountered in the thermal stress problem are of the order of 10^{-8} s^{-1} to 10^{-7} s^{-1}, whereas most published test results are for strain rates above 10^{-7} s^{-1}. Data from other studies concerned with thermal ice loads were also considered (Bergdahl 1978 and Cox 1984). In the uniaxial form, the total strain under both mechanical and thermal loading consists of three parts: an elastic strain, ε_e; a viscous strain, ε_v; and a thermal strain ε_T, eq.

$$\varepsilon = \varepsilon_e + \varepsilon_T + \varepsilon_v \qquad \textbf{[2]}$$

The elastic strain is related to the stress σ through the elastic constitutive relation:

$$\varepsilon_e = \frac{\sigma}{E_i} \qquad \textbf{[3]}$$

E_i is the elastic modulus of ice. Thermal strain due to a temperature change ΔT are given by

$$\varepsilon_T = \alpha_i \Delta T \qquad \textbf{[4]}$$

The viscous strain is provided by the Bailey-Norton law, sometimes called power law. This is given by Murat et al. (1989) as:

$$\varepsilon_v = A\sigma_e^n t^{m+1} \qquad \textbf{[5]}$$

Where A, m, n are temperature dependent material parameters and σ_e is the equivalent von Mises stress in multiaxial stress states and t is the time. Eq. 5 is often expressed in rate form as

$$\dot{\varepsilon}_v = K\sigma_e^n t^m \qquad \textbf{[6]}$$

where $K = A(m+1)$. In this study a material model already implemented in LS-DYNA (MAT_188) is employed. By neglecting effects of plasticity, i.e., viscous effects of plastic strain rate, isotropic and kinematic hardening in MAT_188 model, the thermo-elastic creep model, as outlined above is obtained. The thermal and mechanical properties are summarized in Tab. 2. In this approach, elastic modulus E_i and creep parameter A are assumed to be temperature dependent. Cracking of the ice, which is important for thermal and mechanical loads on structures is neglected.

Table 2. Thermal and mechanical properties

Latent heat, ice L_i	Jkg^{-1}	$3.34 \cdot 10^5$
Density ice ρ_i	kgm^{-3}	910
Density water ρ_w	kgm^{-3}	1000
Heat capacity, ice C_{pi}	$Jkg^{-1}K^{-1}$	2100
Thermal conductivity, ice k_i	$Wm^{-1}K^{-1}$	2.1
Coefficient thermal expansion, ice α_i	K^{-1}	$5.5 \cdot 10^{-5}$
Elastic modulus, ice E_i	MPa	$6.1(1-0.012T)$
Poisson's ratio, ice ν_i	-	0.3
Elastic modulus, concrete E_c	MPa	$2.8 \cdot 10^4$
Poisson's ratio, concrete ν_c	-	0.3
Creep parameter K	$MPas^{-1}$	$4.3 \cdot 10^{-6}$
Creep parameter A	$MPas^{-1}$	$K(1+m)\lvert T\rvert^{1.97}$
Creep parameter n	[-]	2.2
Creep parameter m	[-]	-0.22

3. Results

The ice load, P_{LL}, acting on the dam, calculated from the measured stresses at stations (St.) B, C, and D, is shown in Fig. 5, together with the line load obtained from the finite element analysis with ice thicknesses $h_i = 0.54$ m and $h_i = 0.69$ m. The maximum P_{LL} and time of occurrences are given in Tab. 3. Positive values of P_{LL} is defined as compressive line load. Fig. 5 shows that the ice load obtained with finite element analysis, is correlating with the one obtained from the measured data. It should be noted that the numerical results give higher negative values, this is most likely due to the material model used in these analyses. Furthermore, the variation of ice thickness during the period of measurements considered in these analyses here is not considered. The results for $h_i = 0.54$ m and $h_i = 0.69$ m show that the ice thickness will affect the magnitude of the ice load.

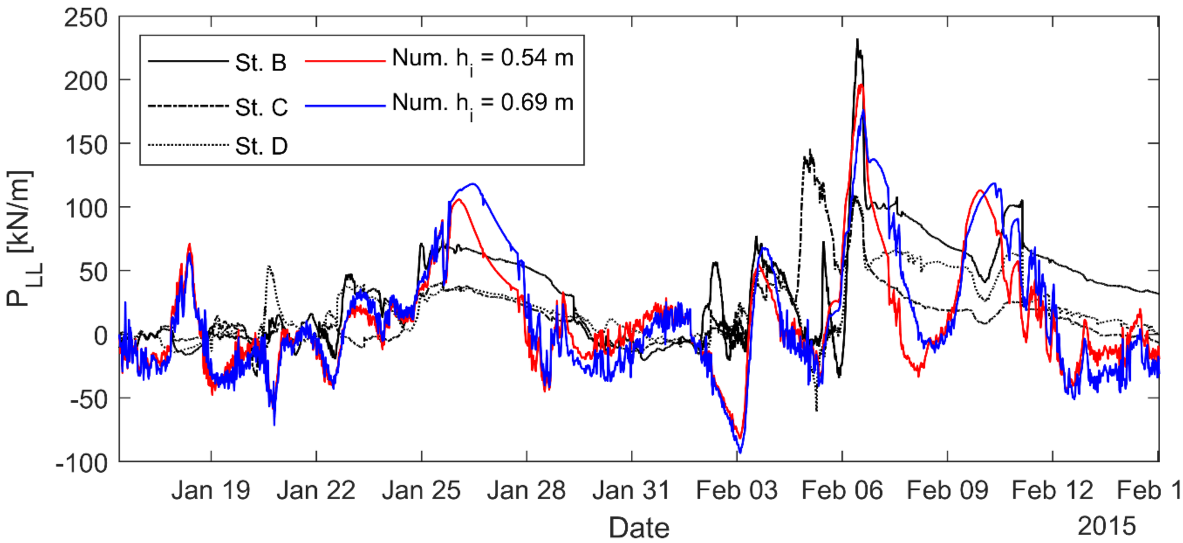

Figure 5. The line load acting on the dam obtained from the finite element analysis compared to the measured data.

The temperature profile obtained from the finite element analysis with $h_i = 0.54$ m at maximum ice load is shown in Fig 6a, and for $h_i = 0.69$ m is shown in Fig. 6b. For both analyses the temperatures are retrieved from the nodes in the intersection between the dam and ice sheet.

The measured temperature profile at maximum ice load at St. B, C and D is shown in Fig. 6c. In Fig. 6a and 6b the temperature profiles are plotted at the time of maximum ice load at the different stations (see Tab. 3). The z-coordinate of the temperatures measured was not recorded during the measurement and has here been estimated. This fact is likely to explain some of the differences in the profiles obtained from the finite element analysis and the measured data.

Table 3. The maximum ice load acting on the dam from the measured data and finite element analysis.

	Time [Date time]	*Maximum P_{LL} [kN/m]*
St. B	2015-02-06 10.25	230
St. C	2015-02-05 01.55	150
St. D	2015-02-06 07.05	110
h_i = 0.54 m	2015-02-06 13.18	200
h_i = 0.69 m	2015-02-06 14.25	180

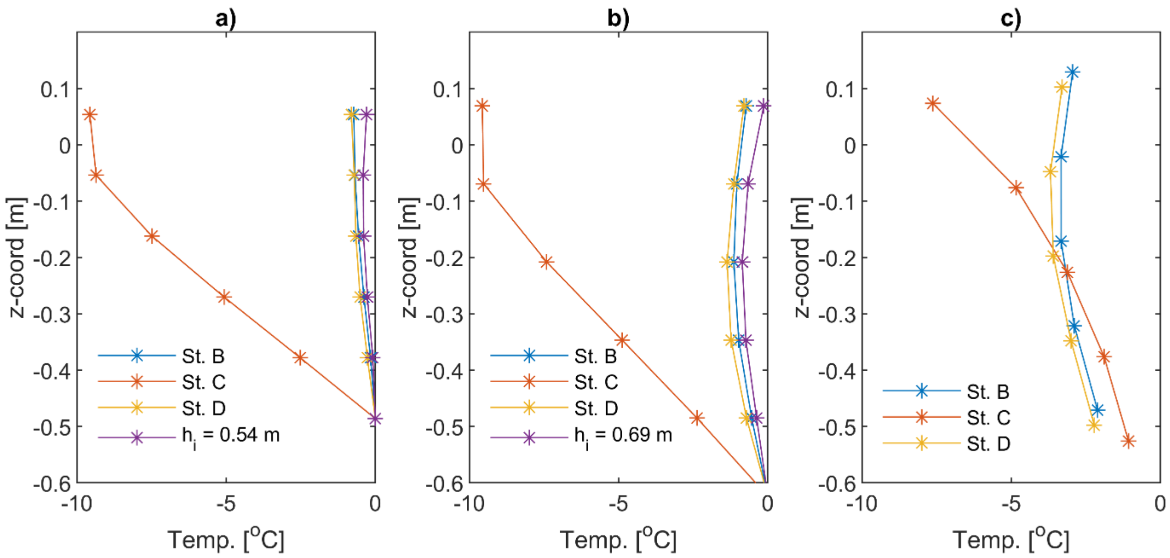

Figure 6. The temperature profiles at maximum ice load (P_{LL}) from the finite element analysis is shown with different ice thickness, h_i in a) h_i = 0.54 m and b) h_i = 0.69 m. c) The measured data.

The profile of the stress in x-direction (longitudinal direction of the ice sheet) in the ice are shown in Fig 7, with compressive stresses as negative. For the finite element analysis with h_i = 0.54 m and 0.69 m are shown in Fig 7a and Fig 7b, respectively, at the time of maximum ice load at the different stations (see Tab. 3). For both analyses the stresses are retrieved from the elements in the intersection between the dam and ice sheet. For h_i = 0.54 m the maximum compressive stress is -1.6 MPa and the minimum tensile stress is 1.12 MPa. For h_i = 0.69 m the minimum compressive stress is -1.4 MPa and the maximum tensile stress is 0.97 MPa. The measured stress is shown in Fig 7c, where the minimum compressive stress -0.56 MPa and the maximum tensile stress 0.02 MPa occurs at St. B. Fig. 7 shows that the numerical analysis highly overpredicts the tensile stresses in the ice, this is caused by the high tensile strength assumed in the material model used in the analyses. Furthermore, the numerical analysis overpredicts the compressive stresses. These differences is likely to errors in the water pressure ($p_w(t)$) applied to the ice and how the temperature loading was implemented (heat convection between the air temperature and ice was neglected).

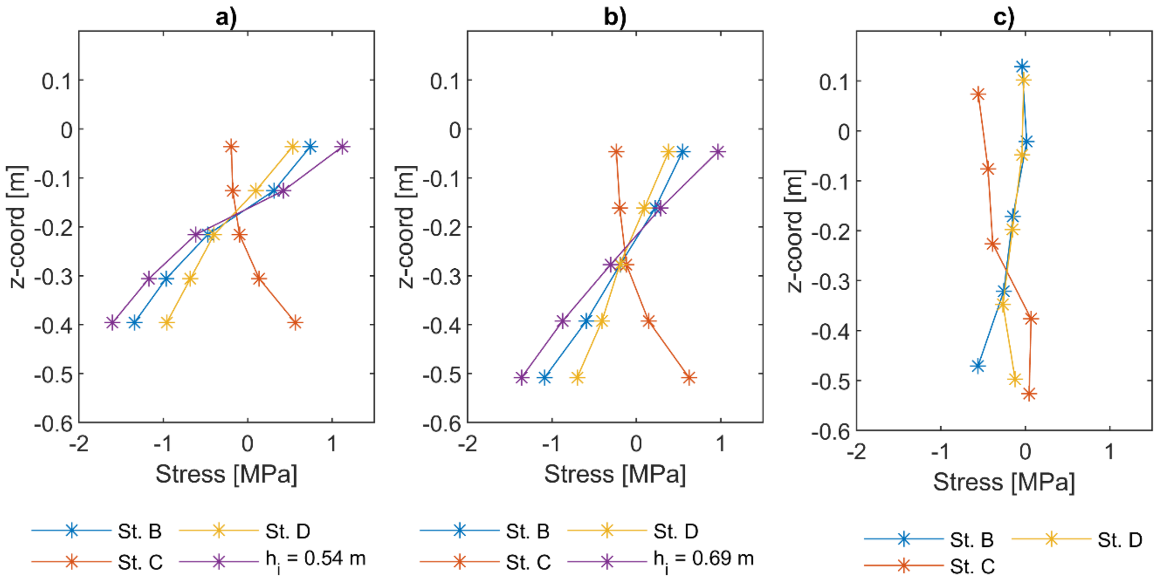

Figure 7. The stress profiles at maximum ice load (PLL) from the finite element analysis is shown for different ice thickness. a) h_i = 0.54 m and b) h_i = 0.69 m. c) Measured stress at stations B, C and D.

4. Conclusion

This paper presents a simplified numerical model for simulating ice-structure interactions forces on hydropower dam structures.

In these simulations the measured air temperature was used as the "driving" force for the thermal expansion of the ice sheet, and the heat convention at the air-ice, ice-water and ice-concrete interfaces was neglected. This is a likely source for the discrepancy between the measured temperature distribution and the resulting temperature distribution obtained by numerical simulations as shown in Fig. 6. Furthermore, the discrepancy in the temperature distribution also affects the predicted stress distribution within the ice cover and can be the source of the overprediction of the compressive stresses by the numerical model as shown in Fig. 7.

The numerical model for the mechanical properties of ice behavior presented herein does not take account for cracking of the ice cover. Therefore, this model overpredicts the tensile strength of the ice, as shown in Fig. 7, and thus gives to high tensile ice loads acting on the ice-structure interface as shown in Fig. 5. The simplified numerical model presented herein shows promising results in estimated ice pressure when compared to measured data. Further work will be to take account for tensile cracking which may lead to redistribution of stresses within the ice sheet and more realistic behavior of the ice cover.

Acknowledgments

This work was funded by the Research Council of Norway programme RFFNORD project number 295887 (ICEDAMS), and industry partners represented by Nordkraft Produksjon and Statkraft Energi. Narvik kommune kindly provided access to the Taraldsvikfossen reservoir.

References

Ashton G.D. (editor) 1986. River and Lake Ice Engineering, Water Resources Publications, Michigan.

Azarnejad, A., Hrudey, T.M., 1998. A numerical study of thermal ice loads on structures. Can. J. Civ. Eng. 25 (3), 557–568.

Bažant, Z. P. (1992), Large-scale thermal bending fracture of sea ice plates, J. Geophys. Res., 97(C11), 17739–17751.

Bergdahl, L., 1978. Thermal ice pressure in lake ice covers. Report Series A:2. Department of Hydraulics, Chalmers University of Technology, Göteborg, Sweden (164 pp.).

Comfort, G., Gong, Y., Singh, S., Abdelnour, R., 2003. Static ice loads on dams. Can. J. Civ. Eng. 30, 42–68.

Cox GFN. 1984. A preliminary investigation of thermal ice pressure. Cold Reg. Sci. Technol. 9, 221–229.

Damsikkerhetsforskriften, 2010. Forskrift om sikkerhet ved vassdragsanlegg (FOR-2009-12-18-1600). Retrieved from https://lovdata.no/dokument/SF/forskrift/2009-12-18-1600

Drouin, M., Michel, B., 1974. Pressures of Thermal Origin Exerted by Ice Sheets upon Hydraulic Structures. Draft Translation 427. Cold Regions Research and Engineering Lab, Hanover, NH, USA (429 pp.).

Fransson, L., 1988. Thermal Ice Pressure on Structures in Ice Covers (Ph.D. Thesis), Luleå University of Technology, Luleå, Sweden (161 pp.).

Hallquist, J.O., 2006. LS-DYNA Theory Manual. Livermore Software Technology Corporation, 680 pp.

Morse, B., Stander, E., Côté,A., Richard,M., Desmet, V., 2011. Stress and Strain dynamics in a hydro-electric reservoir ice sheet. Proc. of the 16th Workshop on the Hydraulics of Ice Covered Rivers,Winnipeg, MB, Canada, 18–22 September 2011, pp. 303–316.

Murat, J.R., Ladanyi, B., Huneault, P. 1989. In situ determination of creep properties of sea ice with the pressuremeter. Canadian Geotechnical Journal, 26: 575-594.

NVE, 2003. Retningslinje for laster og dimensjonering. Norges Vassdrags- og Energidirektorat, Retrieved from http://publikasjoner.nve.no/retningslinjer/2003/retningslinjer2003_01.pdf

NVE, 2005. Retningslinjer for betongdammer. Norges Vassdrags- og Energidirektorat, Retrieved from http://publikasjoner.nve.no/retningslinjer/2005/retningslinjer2005_01.pdf

O'Sadnick, M., Petrich, C., Arntsen B.,Sand, B., 2016, Observations of Ice Stress at Taraldsvikfossen Reservoir, Narvik, Norway, 2014/15, 23rd IAHR International Symposium on Ice, Ann Arbor, Michigan, USA, May 31 to June 3.

Petrich, C., Sæther I., Fransson L., Sand B., Arntsen B., 2014. Preliminary results from two years of ice stress measurements in a small reservoir, In Proceedings of the 22nd IAHR International Symposium on Ice, Singapore, 11–15 August 2014,

Petrich, C., Sæther I., Fransson L., Sand, B., Arntsen B., 2015. Time-dependent spatial distribution of thermal stresses in the ice cover of a small reservoir. Cold Regions Science and Technology, 120, 35-44.

Pounder, E. R. 1965. The physics of ice. Oxford, UK: Pergamon Press.

25th IAHR International Symposium on Ice
Trondheim, 23 - 25 November 2020

Riprap to resist wave and ice loads acting on the upstream slope of an embankment dam

Fjóla G. Sigtryggsdóttir
NTNU, Department of Civil and Environmental Engineering
S.P. Andersensveg 5, Trondheim
fjola.g.sigtryggsdottir@ntnu.no

In areas with cold climate formation of ice cover on a reservoir exerts loads on the upstream slope of an embankment dam which can cause degradation and erosion damages. Riprap is generally provided on the upstream slope of embankment dams to counteract both ice and wave action. The sizing of the riprap to resist wave action is well established with simple empirical formulas. First the wave height is estimated, usually through simple wave prediction formulas. Subsequently, wave height is inserted into empirical rock sizing formulas for determining the riprap stone size required to resist the wave action. Some dam design guidelines assume that riprap designed to resist the wave actions is also capable of resisting the ice action, while others, such as the Norwegian guidelines, consider ice action through a requirement on the minimum weight of individual riprap stones. The available riprap design measures for resisting wave and ice will be investigated. Furthermore, the conditions where the design against ice loading may be governing will be discussed.

Text (body) of paper then begins on the next page.

1. Introduction

The upstream slope of an embankment dam is typically protected with a layer of quarry stones, referred to as riprap. The riprap can be dumped or placed. Dumped riprap are randomly placed stones, while the term selectively placed riprap describes individually placed stones for enhanced interlocking and increased resistance. The purpose of the riprap on the upstream slope is to prevent erosion, scour or sloughing of the embankment. Thus, the riprap must counteract environmental loads, i.e. actions arising from wind generated waves and ice.

The ice action is the action of ice upon the surface of the upstream slope. The ice action includes: a) plucking of individual riprap stones embedded in the ice sheet due to water level fluctuations; b) ice shoving causing riprap stone displacement; c) and thrust from ice floes due to wind or current causing a slide or shear on the embankment slope. Ice action also includes freeze-thaw action that mainly may cause delamination and breakdown of individual riprap stones.

The resistance of the riprap to wave and ice actions relates to the individual stone size, weight and durability. Additionally, gradation and thickness of the riprap layer, as well as the interlocking between the stones, are important factors. Fig. 1 gives an example of an upstream slope of a rockfill dam with uniformly graded riprap selectively placed in an interlocking manner. Fig. 2 presents a riprap of less evenly sized stone that is partly dumped but arranged and ordered with an excavator.

In the European Rock Manual (CIRIA et al., 2007), individual stones in a protective layer are referred to as armour stone or armour unit, whereas the protective layer is referred to as the armour layer. The armour layer is to provide protection against waves and/or currents and/or ice loads. Furthermore, in the Rock Manual riprap is referred to as the term for wide-graded quarry stone, normally bulk-placed as a protective layer for mainly estuarial and riverbank applications. In dam engineering riprap refers to a protective layer of rock or rock fragments, that is either well graded within wide size limits (USBR, 2012), or uniformly graded (SEBJ, 1997). Thus, the word riprap in dam engineering also refers to individual stones, whereas the Rock Manual refers to this as the armour stone. Here, the dam engineering use of the word riprap (USBR, 2012; SEBJ, 1997), is generally applied. However, when the word armour stone is used the definition of the Rock Manual applies (CIRIA et al., 2007).

The sizing of the riprap to resist wave action is well established with simple empirical formulas (USBR, 2012; SEBJ,1997). Conversely, sizing of riprap in cold regions, such as the Artic to resist ice action is less understood (CIRIA et al., 2007; ICOLD, 1996) and guidance on the design limited. Available guidelines on the use of rock in hydraulic engineering, such as CIRIA et al. (2007) consider mainly marine structures in cold offshore regions, but is also of value for riprap protection on dams, although as stated in CIRIA et al. (2007), not comprehensive on this topic. Still, ice can cause degradation of riprap slopes, erosion damages and freeze-thaw breakdown (Fig. 2b). Furthermore, ice forces on the riprap protecting an embankment slope can be induced fluctuating water level, as well as, drifting ice (ice floe).

In practice, the emphasis is on designing riprap to resist the design wave action and assuming that riprap capable of absorbing wave energy is often also capable of absorbing ice forces (CIRIA et al., 2007; ICOLD, 1996). Nevertheless, the rock riprap guidelines from countries in cold region generally include some simple consideration of ice forces through minimum requirements. Furthermore, it is stressed that the impact of ice forces should be evaluated for each individual case. In the following the stone sizing formulas provided to resist wave action are reviewed as well as ice consideration in the sizing of riprap on dam slopes. Comparison of the stone sizing formulas is made, including also available minimum requirements regarding ice action. Finally, the results are discussed, and conclusions drawn from the simple study.

Figure 1. Placed riprap on the upstream slope of a rockfill dam in Norway. (Fig: FGS)

Figure 2. Riprap on the upstream slope of a rockfill dam in Iceland. (Fig: FGS) a) View on the upstream slope. b) Fractured stone from ice action (frost-thaw cycles).

2. Riprap sizing

The process of determining the size of riprap on embankment dams embraces sizing of riprap to resist wave action as well as ice action. The action that results in the largest stone size governs. Thus, here the riprap sizing for both wave action and ice action are shortly reviewed

Riprap sizing for wave action

Various researchers have developed empirical relationships to express the wave action and the resisting forces offered by the riprap. These relationships aim at predicting the size of riprap (and armourstones). Here only formulas that base on Hudson (Hudson, 1959, 1953) are reviewed as these are extensively used in dam engineering applications and presented in related manuals and guidelines, such as NVE (2012) (Norway), USBR (2012) (USA) and SEBJ (1997) (Canada). The Hudson formula is also presented in the European Rock Manual, CIRIA et al., (2007), as follows:

$$W_{50} = \frac{\rho_r g H^3}{K_D \Delta^3 \cot\alpha} \qquad [1]$$

where W_{50} is the median weight of the armour stone in N, H is the wave height in m at the toe of the structure, K_D is stability coefficient relating e.g. to the damage condition, ρ_r is the apparent rock density (kg/m^3), α is the embankment slope angle, and Δ is the relative buoyant density of the stone $\Delta=(\rho_r/\rho_w - 1)$ with ρ_w being the mass density of water. CIRIA et al., (2007) explain that K_D values suggested for design often correspond to the no damage condition.

In CIRIA et al., (2007) Eq (1) is rewritten as follows in Eq (2), to represent the so called stability number N_s, with the wave height H replaced by H = 1.27 H_s, where H_s is the significant wave height. Eq (2) also introduces a dimensionless damage level parameter S_d.

$$N_s = \frac{H_s}{\Delta D_{n50}} = 0.7\left(K_D \cot\alpha\right)^{1/3} S_d^{0.15} \qquad [2]$$

In dam engineering guidelines, such as NVE (2012), USBR (2012) and SEBJ (1997), the Hudson formula is however presented in a form similar to this of Eq. (1). Furthermore, definition of the wave height used varies, as well as the stability coefficients.

The Hudson formula in SI units is presented as follows in SEBJ (1997)

$$M_{\min} = \frac{\rho_r H_s^3}{K\left(S_r - 1\right)^3 \cot\alpha} \qquad [3]$$

where $M_{\min}$ is the minimum mass of the stone in kg , H_s is calculated according to SEBJ (1997), K is experimental stability coefficient that depends on damage level defined as no or limited damage associated respectively with a damage level S_d ≤2.5 and S_d = 5 and K values of respectively 1.75 and 3, ρ_r is the apparent rock density (kg/m^3), α is the slope angle, and S_r is the specific gravity of rock $S_r = \rho_r/\rho_w$.

In the Norwegian Guidelines (NVE, 2012) the Hudson formula in SI units is presented as follows:

$$W_{\min} = \frac{\gamma_r H_s^3}{K\left(\frac{\gamma_r}{\gamma_w} - 1\right)^3 n} \qquad [4]$$

where $W_{\min}$ is the minimum weight of the armour stone in kN, H_s is in m and predicted using method in NVE (2012) which bases on SEBJ (1997), K is defined as a constant that is dependent on the shape of the armour stone and how it is placed and given as ≤2.5 for Norwegian conditions, γ_r is the unit weight of the rock (kN/m^3), γ_w is the unit weight of the water (kN/m^3) set equal to 10 kN/m^3, n is the horizontal component of the inclination of the upstream dam slope, (cotα = n).

Finally, the Hudson formula in the US dam engineering guidelines USBR (2012) is presented as follows, the notation and coefficients are given in English Units and thus presented in the same manner here:

$$W_{50} = \frac{\gamma_r H^a}{K\left(G_s - 1\right)^3 (\cot\alpha)^b} \qquad \textbf{[5]}$$

where W_{50} is the median weight of riprap in kN, H is the design wave height in feets (determined according to USBR guidelines), γ_r is the unit weight of the rock (pounds per cubic foot), G_s is the specific gravity of rock, α is the slope angle measured from horizontal, K are experimentally determined coefficients and same for the exponents a and b.

Riprap sizing for ice action

As previously mentioned, sizing of riprap in cold regions to resist ice action is less understood compared to sizing to resist wave action (CIRIA et al., 2007; ICOLD, 1996). Still, investigation into the problem have been carried out e.g. by Daly et al. (2008), as well as Sodhi et al. (1997, 1996) and Sodhi and Donnelly (1999). In practice, the emphasis is generally on designing riprap to resist the design wave action and assume that riprap capable of absorbing wave energy is also capable of absorbing ice forces (CIRIA et al., 2007; ICOLD, 1996). However, some minimum weights of the riprap stone is for example specified in the Norwegian guidelines (NVE, 2012). Similarly, although not related to ice action, minimum weights are specified in USBR (2012), and minimum design wave heights are recommended in SEBJ (1997).

Laboratory tests of randomly and selectively placed riprap

Laboratory tests for the study of ice shoving on a riprap bank of randomly placed stones (dumped stones) conducted by Sodhi et al. (1996) and Sodhi and Donnelly (1999), suggested that the diameter of an average size stone must be two and three times the ice thickness, respectively for slopes of 3:1 (Horizontal (H):Vertical (V)) and 1.5:1 (H:V). These findings may however be difficult to incorporate for severe artic conditions resulting in ice thickness exceeding 1 m and consequently extremely large stone sizes. Sodhi et al. (1996) state for example that it may be more cost effective to carry out repairs than to design to these requirements. In the design of concrete dams in Norway, ice thickness of 0.5 m is to be considered. Transferring this design criteria to embankment dams with the consideration of the above-mentioned laboratory findings, would result in riprap diameter of 1 to 1.5 m. However, it must be considered that the riprap on dams in Norway is not randomly placed and thus it is not reasonable to apply the findings by Sodhi et al. (1996). Sodhi et al. (1996) found that smooth riprap surfaces resist the ice forces better in the case of the randomly placed riprap. McDonald (1988) also stated that smooth slopes of graded riprap resisted ice load better than rough uniformly graded riprap. Additionally, McDonald (1988) emphasized the importance of well keyed stones.

Daly et al. (2008) conducted laboratory tests considering ice shoves on riprap layers, using selective placement of armor stones (well keyed stones). The selective placement was described as carefully placing individual stone to maximize interlock and support between the stones. This was found to have a significant and positive impact on the stability. For example, a selectively placed 3600 kg (35 kN) armor stone (calculated to ca 1.3 m in diameter with γ_r = 27 kN/m^3, but Daly et al (2008) refer to larger diameter of 2 m (unit weight not given)) resisted ice shoves (of about 1.5 m thick ice sheet) very well on a 1.5:1 (H:V) slope. It is important that the riprap is selectively placed, and due care is taken in the design and placement of the toe stones. The results from Daly et al. (2008) can be simplified to indicate roughly that the diameter of the armour stone that is selectively placed into a riprap layer, should be 0.86 to 1.35 times the ice thickness. Considering an ice thickness of 0.5 m, this leads to a stone diameter of approximately 0.45 to 0.65 m.

Minimum weight requirements in dam engineering guidelines

In the Norwegian guidelines (NVE, 2012) the following minimum weight of the riprap stones are recommended to resist ice action: 2.5 kN for slopes of 1.5:1 (H:V), while for flatter slope such as 2:1and 3:1 (H:V), minimum weights of 1.6 kN should be used. For a stone γ_r = 27 kN/m^3, this gives a stone diameter of 0.55 for a slope of 1.5:1 (H:V). NVE (2012) does not provide a reference for this minimum weight requirement.

In the Canadian guidelines, SEBJ (1997), the use of a minimum design wave of 1.0 m is recommended for the riprap sizing, unless there are other special reasons. Furthermore, SEBJ (1997) considers "*that the influence of ice on the riprap is at the most marginal and that the minimum stone size resulting from the design wave calculations is adequate to resist ice forces*". However, it is interesting to calculate minimum weights from the minimum design wave recommended. Using the minimum design wave value, H_s = 1 m, into the Hudson formula as presented in SEBJ(1997) (same as the Norwegian guidelines (NVE, 2012)) with the SEBJ (1997) recommendation of K = 1.75, and additionally selecting the steepest slope recommended, 1.8:1 (H:V), and γ_r = 27 kN/m^3, results in W_{min}= 1.7 kN. Similarly, using this value, H_s = 1 m, into the Hudson formula as presented in the Norwegian guidelines (NVE, 2012), with K= 2.5, and the common upstream slope in Norway with n = 1.5 and γ_r = 27 kN/m^3, results in W_{min} = 1.5 kN.

In the US dam guidelines, USBR (2012), design situations including items such as ice or extreme freeze-thaw conditions are among other items mentioned as an examples of situation that may influence the design of riprap. However, no guidance is provided on how to design for these conditions other than these should guide the designer's judgment when selecting design parameters. USBR (2012), gives values for both minimum and maximum median weights of well graded riprap although these do not consider ice action. The minimum value, $W_{50,\ min}$, is set to 160 Pounds (or 0.7 kN) and the maximum value, $W_{50,\ max}$, is set to 2000 Pounds (or 8.9 kN). The maximum value is based on a research presented in an appendix to the guidelines indicating that 2000 pounds would have been adequate to avoid riprap failure by erosion for all the historical cases studied. The Rock Manual (CIRIA et al., 2007) discusses structural response related to ice, but does not specify additional sizing requirements due to ice action.

3. Simple comparison of methods

The methods above on riprap sizing due to wave and ice action are compared in this section with numerical examples (Fig. 3 and 4). A simplified comparison is to assume the same wind wave prediction (value of H_s) and use this in the stone sizing formulas. Thus, the method of calculating the significant wave height will further influence comparison between methods, but the different guidelines present different approaches and formulas for calculating this. For a given reservoir the different methods would result in different significant wave height. The minimum requirements considering ice action in the case of NVE (2012) and minimum wave height of 1 m in the case of SEBJ (1997) are also included in the figures.

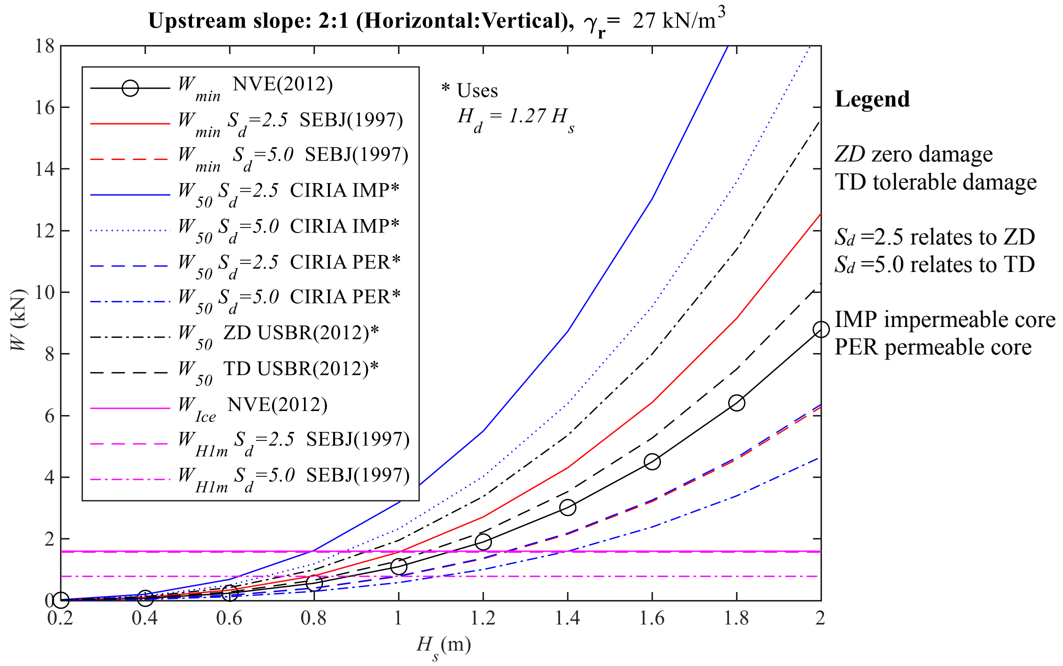

a)

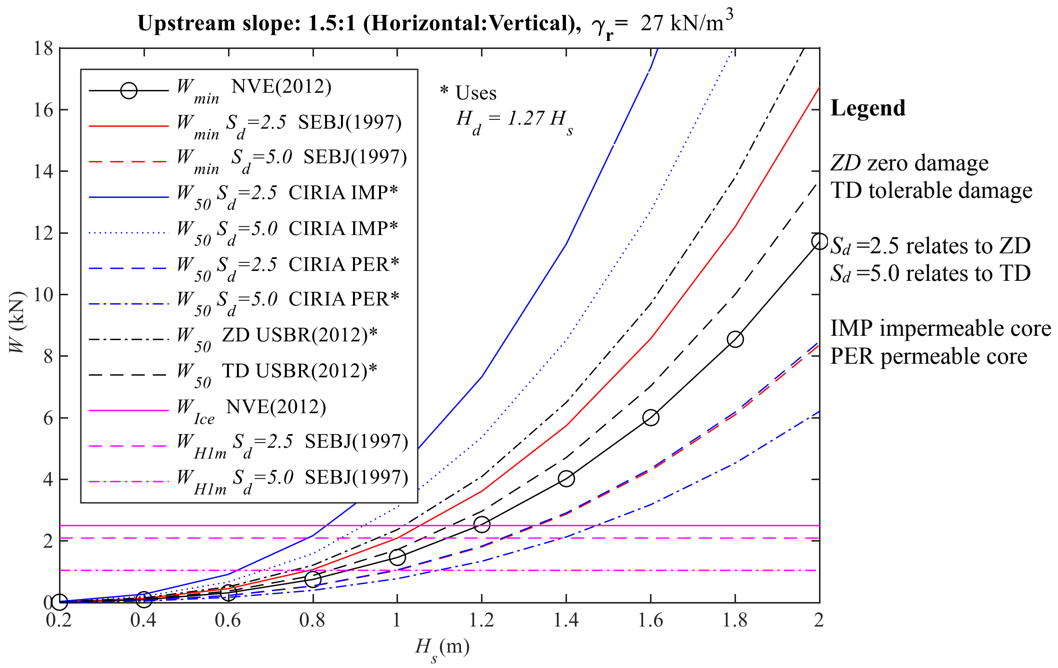

b)

Figure 3. Riprap sizing – comparison of formulas- H_s and H_d. Unit weight of riprap 27 kN/m^3. a) Slope of 2:1 (H:V). b) Slope of 1.5:1 (H:V).

The comparison in Fig. 3 and Fig. 4 assumes constant unit weight of the rock. The upstream slopes are 2:1 (H:V) and 1.5:1 (H:V) in Fig. 3 a) and b) respectively. The comparison for slope of 2:1 (H:V), is selected since all the guidelines, except NVE (2012), emphasise that the formulas and coefficients were not derived for steeper slopes than 2:1 (USBR, 2012) or 1.8:1 (H:V) (SEBJ, 1997). Slopes of 1.5:1 are common on rockfill dam slopes e.g. in Norway. Regarding the legend in the Fig. 3 and 4, it is important to note the notations IMP and PER for impermeable and permeable core respectively, refers to the core of a rubble mound breakwater.

Regarding Fig. 3, it is important to note that the significant wave height on the horizontal axis is multiplied with 1.27 into the USBR (2012) formulation, and that this effect is included in Eq. (2) from CIRIA et al. (2007). Furthermore, the USBR, (2012) method of predicting the significant wave height results in lower values than the methods associated with the other guidelines. To comprehend the difference, the same curves are plotted in Fig. 4 for a slope of 1.5:1 (H:V), however with the significant wave height into all the formulas (i.e. the value H on the horizonal axis). This entails for example, that the Eq. (1) from CIRIA et al. (2007), is divided by 1.27 to obtain the value for the significant wave height (the Eq. (1) as presented includes the design wave as 1.27 H_s). The CIRIA et al. (2007) curves in Fig. 4 are in the following referred to as modified CIRIA et al. (2007) curves.

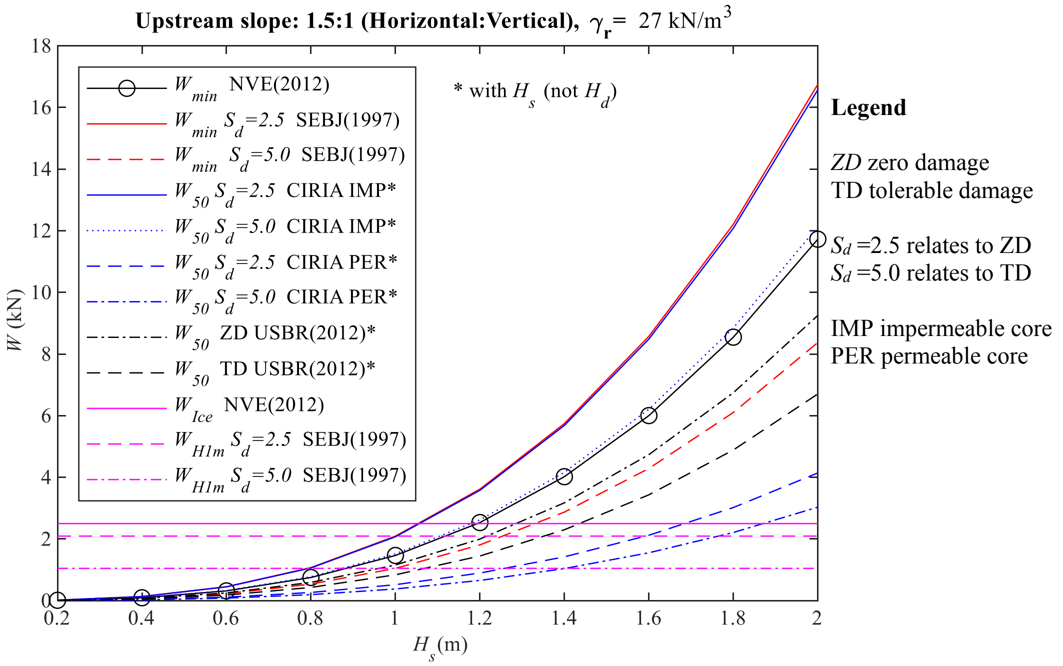

Figure 4. Riprap sizing – comparison of formulas- H_s and H_d. Unit weight of riprap 27 kN/m³. Slope of 1.5:1 (H:V).

4. Discussion

The comparison of the different riprap stone sizing methods as carried out here (Fig. 3 and 4) is a simplified comparison. The simplification relates to the different formulas employed for stone sizing to resist wave action, for this the following must be considered: The definition of the wave height used into the Hudson formula Eqs (1) to (5), is neither the same in all guidelines discussed here nor calculated with the same formula. The method of defining the fetch in the calculation is also different. In addition to the different calculation methods and definition of the wave heights, different criteria are given for the stability coefficients and damage levels. Thus, one cannot compare directly from the Fig. 3 and 4 the curves for the different damage levels since for a certain reservoir, different wave heights (return periods of the design event) will correspond to the different damage levels.

The riprap size required to resist the wave action increases with the wave height (Fig. 3 and 4). Furthermore, the significant wave height, and thus the wave action, increases with increased wind speed as well as with increased fetch. Similarly, increased wind speed and fetch should have effect on wind-driven ice actions. Such ice forces can develop as a strong wind blows during both freeze-up and breakup periods of the ice on a reservoir. The ice action on the riprap arise from the thrust of wind driven ice riding up the riprap slopes. Still, the dam engineering guidelines reviewed here, provide stone sizing strategies for the ice action; either with fixed values of minimum stone weights, regardless of both the wind conditions and the size of the reservoir influencing the fetch; or assume that a stone sizing for a certain minimum wave height is sufficient also for the ice action. For example, the consideration of ice with minimum requirements on the stone weight in the NVE (2012) guidelines for the rock density (27 kN/m^3) employed corresponds to a stone size to resist a wave height of 1.2 m for 1.5:1 slope, but roughly 1.1 m (1.13 m) in the case of 2:1 slope. This can be compared to the minimum wave height requirement in SEBJ (1997), i.e. 1 m high wave. The minimum weights requirement for the 1.5:1 slope and the density considered will result in a stone diameter of 0.55 m. This is within the range (0.45 to 0.65 m) obtained when considering beforementioned experimental results from Daly et al., (2008) and an ice thickness of 0.5 m. Thus, the minimum weight requirements seem to compare reasonably to conclusions drawn very roughly from experimental research on the impact of ice shoves. However, impact of ice thrust from movements of large ice floes due to wind and potential effects of the fetch is an additional consideration that would be interesting to investigate further for dams in artic regions. Furthermore, investigations relating to ice plucking of riprap from upstream slope of dams, might be relevant for dams on reservoirs with large or rapid water level variations during the winter period.

4. Concluding summary

Stone sizing formulas given in different dam safety guidelines and a rock manual have been compared. All the formulas base on the empirical Hudson formulae, which relates wave action and properties relevant for stability of the upstream riprap protection. The stability is important also for ice considerations and depends e.g. on the stone size (weight), upstream slope inclination, placement of the stones and more. The relation is established through experimentally determined stability coefficients. The guidelines considered here are issued in USA (USBR, 2012), Canada (SEBJ, 1997), Norway (NVE, 2012) and the manual is the European Rock Manual (CIRIA et al, 2007). Of those only the Norwegian guidelines define a specific minimum requirement considering ice load, while the Canadian guidelines specify design against minimum wave height, and the US guidelines specify minimum and maximum weight for general consideration (not particularly considering ice).

A comparison of the methods was conducted of the different riprap stone sizing method. However, the comparison is a simplification due to several reasons pointed out in the paper. The method of calculating the significant wave and the wind conditions are important in defining the conditions for which minimum requirements for ice may govern. In this the size and shape of the reservoir defining the fetch length is of importance. However, such site conditions may also influence the ice action and investigations into that are of interest.

Enhancing the current design procedure entails further research with combined evaluation from experiments and field surveys. This is required to compensate the uncertainties relating to the stone sizing, arising from both the action of ice and the reaction or resistance of the riprap protection. The assumption of minimum weights and/or that the stone sizes required to resist the wave action will also resist the ice action needs further investigations for embankment dams in artic regions.

Acknowledgments

The support from the Norwegian Water Resources and Energy Directorate (NVE) and cooperation with Morten Skoglund is acknowledged and appreciated.

References

CIRIA, CUR, CETMEF, 2007. The Rock Manual. The use of rock in hydraulic engineering. (2nd edition). C683, CIRIA, London.

Daly, S., Zufelt, J., Zabilansky, L., Sodhi, D., Bjella, K., Ginter, D., Eisses, K., Oliver, J., 2008. Estimation of Ice Impacts on Armor Stone Revetments at Barrow, Alaska, in: 19th IAHR Int. Symp. on Ice. Vancouver.

ICOLD, 1996. Dams and related structures in cold climate-Design guidelines and case studies. Bulletin 105., ICOLD. ICOLD, Paris.

McDonald, G.N., 1988. Riprap and armor stone. Arct. Coast. Process. Slope Prot. 190–207.

NVE, 2012. Veileder for fyllingsdammer. Oslo. (In Norwegian).

SEBJ, 1997. Practical Guide. Riprap Sizing. Société d'énergie de la Baie James (SEBJ).

Sodhi, D.S., Borland, S., Stanley, J., Tests, S., 1996. Ice Action on Riprap Small-Scale Tests.

Sodhi, D.S., Borland, S., Stanley, J.S., Donnelly, C., 1997. Ice effects on rip-rap: small scale tests, in: Energy and Water: Sustainable Developement. IAHR. ASCE, San Francisco.

Sodhi, D.S., Donnelly, C., 1999. Ice effects on rip-rap: Model tests, in: Putting Research into Practice, 10th ASCE Cold Regions Eng. Conf. ASCE, Lincoln.

Stewart, T.P., Newberry, S.D., Latham, J.-P., Simm, J.D., 2003. Packing and Voids for Rock Armour in Breakwaters, Report SR 621. Wallingford.

USBR, 2012. Design Standards No. 13: Embankment Dams. U.S. Department of the Interior. Bureau of Reclamation.

14
Environmental aspects of lake and river ice

25th IAHR International Symposium on Ice
Trondheim, November 23 to 25, 2020

Modelling stranded river ice using LiDAR and drone-based models

Knut Alfredsen and Ana Juárez
Department of civil and environmental engineering
Norwegian University of Science and Technology
7491 Trondheim, Norway
Knut.alfredsen@ntnu.no, ana.juarez@ntnu.no

Grounded and other remnants of ice in rivers influence flow and alter instream conditions in the period the ice is left in the river channel. Modelling the flow effects of ice have been difficult in the past due to difficulties in measuring the ice geometry both with regards to time needed to cover the ice formation and since moving on the ice for measurements can be difficult or even dangerous. The detailed river geometry could also be a challenge to find. Recent development in remote sensing from aerial vehicles have changed this and new technologies exist to capture such data. Here we show how the combination of a green LiDAR based river bathymetry can be merged with drone-based ice measurements to form a new river geometry suited for hydraulic modelling. The LiDAR bathymetry is collected from a plane and processed into a digital elevation model (DEM) covering the riverbed and the adjacent areas. The drone geometry is captured using a simple quadcopter with camera and processed into a DEM using structure from motion. Ground Control Points and randomly placed control points are measured with an RTK-GPS and used for georeferencing and to control the accuracy of the ice model. Using the drone for measurements provides a simple and efficient way to capture ice without the need for entering the ice to do traditional measurement campaigns using total stations or GPS software. The DEM representing the ice is merged with the LiDAR bathymetry in a GIS system, and the combined elevation model is used as input to the HECRAS 2D hydraulic model and the flow patterns for typical late winter discharges is simulated with and without ice to compare the impact of the grounded ice formations on the flow

1. Introduction

Development and release of river ice can have large impacts on several important processes in rivers related to physical and ecological factors (Prowse 2001b; Prowse 2001a). Of this, breakup of ice with the associated transport and potential jamming of ice can lead to flooding and changed hydraulic conditions in rivers with potential damage to infrastructure, altered morphology and severe effect on instream flora and fauna (Prowse and Culp 2003; Beltaos 2009). Establishing a relation between how ice behaves during the breakup period and the river hydraulics is therefore necessary to quantify important processes for understanding the dynamics and environment of river systems.

To understand and model the effect of grounded ice in rivers it is necessary to find the extent and the amount of ice. Field measurements of ice jams and grounded ice is difficult due to access and the complexity of the ice formations (Beltaos 1995). Working on grounded ice can also be dangerous due to unstable ice floes and crevasses in the ice. Therefore, remote sensing methods are an option to measure ice formations. There exists a number of examples where imagery and radar data from satellites have been used in mapping various forms of ice and ice dynamics, e.g. (Chu and Lindenschmidt 2016; Kääb et al. 2019; Lindenschmidt and Li 2019). For smaller streams and rivers, the resolution available in satellite data can be to coarse to be able to identify and quantify river ice at a scale relevant for the analysis of grounded ice, and it is also necessary to move from a qualitative assessment of ice types to a quantitative assessment of volumes which are not common in satellite analysis today.

An alternative approach to map geometry remotely that has seen increased use in aquatic systems is Structure from Motion (SfM) photogrammetry (Carrivick and Smith 2019). Through SfM, precise digital elevation models and orthophotomosaics can be built from aerial imagery. The imagery used in the SfM process can be collected from unmanned aerial vehicles (UAV) which simplify the process of collecting ice data in rivers. Related to applications in cryosphere science, both fixed wing and rotor wing devices are used with most applications so far in the areas of glacier and snow analysis (Gaffey and Bhardwaj 2019). In studies of river ice, Alfredsen et al. (2018) used a low cost drone to map an ice jam remnant and anchor ice formation in two Norwegian rivers. In a study on ice jams in the Mohawk river, Garver et al. (2018) used drones and SfM to map extent and topography of an ice jam.

Incorporating ice in hydraulic modelling can be done using different methods. Dedicated ice models have algorithms to predict and simulate the effect of ice formations on flow (Lindenschmidt 2017; Blackburn and She 2019). In such cases, SfM generated ice maps could probably be used to estimate extent and volume of ice jams for comparison. It is also possible to simulate the effects of ice jams of flow in the much used software package HEC-RAS (Beltaos and Tang 2013) and this requires data on the ice location and size as input (Beltaos and Tang 2013; Timalsina et al. 2016). A last option is to merge ice geometry into the bathymetry in rivers e.g. to see how flow patterns will change around a grounded ice mass. This would allow studies of water level rises, changed velocities and potential erosion around the ice. A drawback is the consideration of the ice as a fixed bed structure since melt, hydraulic forces and erosion processes will alter and eventually remove the ice over time. But for shorter duration analysis this method is interesting and ice erosion could be incorporated in the computation.

Here we show examples on how drone-based measurements of grounded ice formations can be combined with ice free river geometry and used as input to a hydraulic model to simulate the effect of the ice constrictions on river flow. Results will be relevant for assessing the impact of grounded ice on e.g. morphological changes, flooding potential and for assessment of instream ecological conditions by linking results to a habitat assessment strategy.

2. Materials and methods

Study site

The study site is located at Haga bridge (63.06º N, 10.29º E) on the river Gaula south of Trondheim (Figure 1). The site at Haga bridge often accumulates drifting ice during break-up, and stranded remnants of ice jams are common. For this study we collected data from two different situations, one ice run in December 2016 that lead to an ice jam and subsequent grounded ice covering parts of the river section, and a breakup event from January 2020 that left grounded ice that narrowed the river cross section. The drone flights were carried out in February 2017 and in January of 2020, under similar conditions with light winds and cloudy conditions.

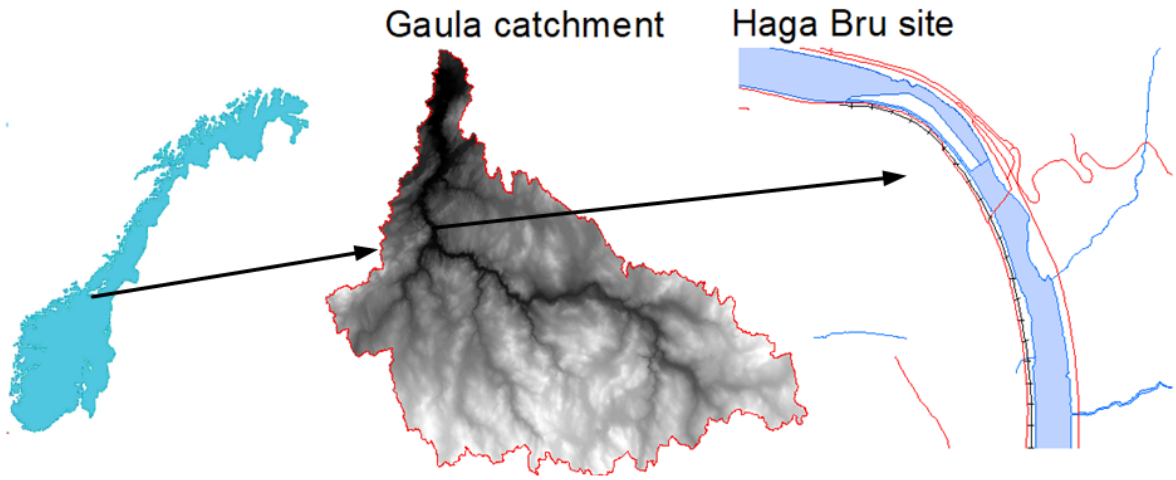

Figure 1The Haga bridge study site in river Gaula.

Ice mapping and river geometry

Aerial images for the 2017 case were collected using a DJI Phantom 3 Professional drone (www.dji.com) using 11 Ground Control Points (GCPs) measured with a Leica VIVA RTK GPS system (www.leica.com) for georeferencing. A total of 82 images were used in Agisoft Photoscan v 1.3.0 (www.agisoft.com) to create a digital elevation model (DEM) of the grounded ice and a orthophotomosaic of the reach using the SfM technique. For further details of measurement setup and processing see Alfredsen et al. (2018).

The second data set were collected in January 2020 using a DJI Phantom 4 RTK drone using the Norwegian C-pos system over a mobile phone connection for differential corrections for the GPS. A total of 435 images were collected and of these 408 were used in creating a DEM and an orthophotomosaic using Agisoft Metashape v.1.6.1. Using the RTK Drone precise location data can be transferred from the EXIF information for each picture and thereby potentially eliminate the need for GCPs. The SfM process from images to DEM followed the same steps as outlined in (Alfredsen et al. 2018) involving image matching, the generation of a dense point cloud and computing the DEM from the dense cloud. As a control of the quality of the DEM, we evaluated the precision by comparing the positioning of visible objects (railroad tracks and electricity poles) in the drone orthophotomosaic with digital maps of the same objects. We used this method mainly since measuring control points on the freshly grounded ice was not considered safe in this case.

River bathymetry for the reach was downloaded from the Norwegian mapping authority (www.hoydedata.no) as a DEM with a 1 by 1 meter resolution based on a flight using green LiDAR to collect below surface geometry data. Processing and merging of the digital elevation models were done in ArcMap v.10.6. Discharge data for the reach was collected from the Haga bridge gauge located 100 meters downstream of the study site.

Hydraulic modelling

The hydraulic modelling was carried out using the HEC-RAS 2D software version 5.0.7. The model was established for a 1500-meter long reach containing the areas with the grounded ice. We used a grid resolution of 1 x 1 meter and ran the model in the diffusive wave mode using a constant flow as the upper boundary condition and normal depth as the lower boundary condition. The lower boundary was placed well below the area with ice. We calibrated the model by adjusting a map of Manning n values along the reach. The basis for the calibration was an aerial image of the reach (www.norgeibilder.no) taken at a discharge of 45 m^3s^{-1} during ice free conditions. By simulating the same discharge in the model, we compared the observed wetted area with the simulated wetted area and adjusted the Manning n to obtain a matching water surface area.

3. Results

The model DEM and the calibration run overlaid the observed water surface area is shown in Figure 2. The observed area measured on the map was found to be 111800 m^2, while the simulated area after calibration is 108666 m^2 a difference of 2.8%. We therefore consider the calibration of the model to be good. The manning numbers ranged from 0.06 – 0.1 with the highest numbers for the lower end of the reach.

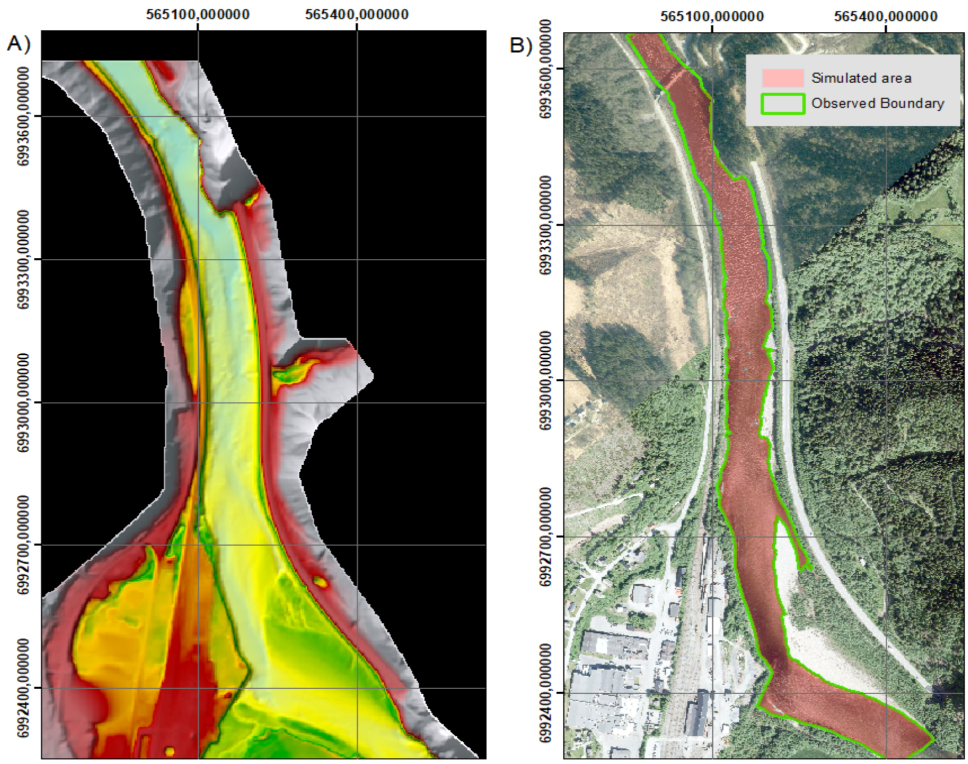

Figure 2 Bathymetry data for the model (A) and simulated water surface (red) compared to observed wetted area (green) for a discharge of 45 m^3s^{-1} (B). DEM and aerial image © Statens Kartverk, Geovekst og kommunene.

For the case in 2017 we used 82 images and generated a dense point cloud of 27 million points. For the 2020 case we used 283 images and made a dense point cloud of 82 million points. From this we generated the DEM and the orthophotomosaic (Figure 3). The error estimates for the cameras are shown for both cases in table 1.

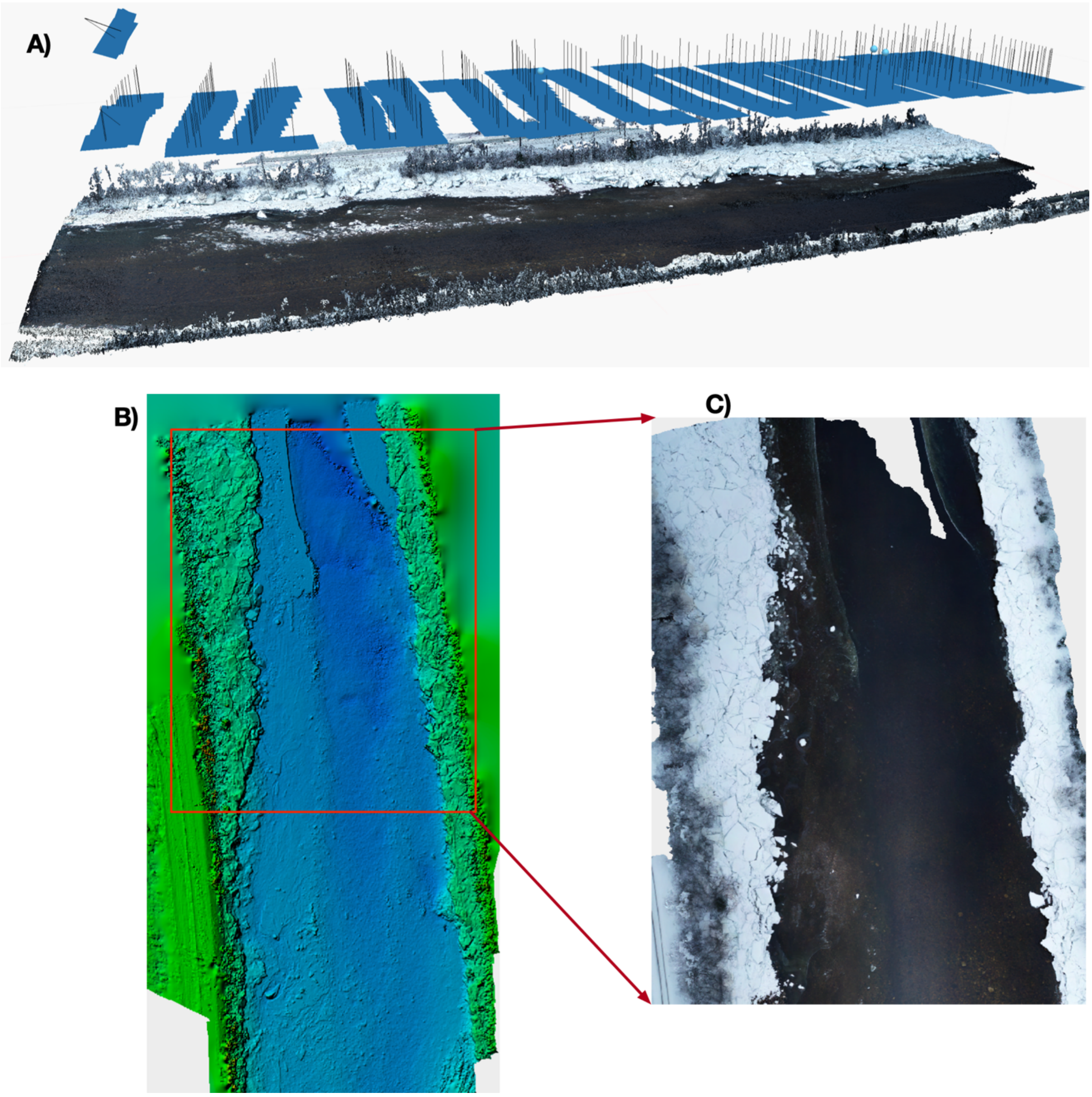

Figure 3 Dense point cloud with camera positions marked as blue squares (A), generated DEM from the dense point cloud (B) and orthophotomosaic showing the grounded ice (C).

Table 1 Errors reported from SfM processing

Field campaign	North (m)	East (m)	Altitude (m)
2017 GCP errors	0.048	0.051	0.013
2020 Camera position errors	0.006	0.009	0.012

The DEM representing the ice was then clipped and merged with the LiDAR bathymetry, and two different grids were made representing ice free conditions and conditions with the grounded ice in place (Figure 4).

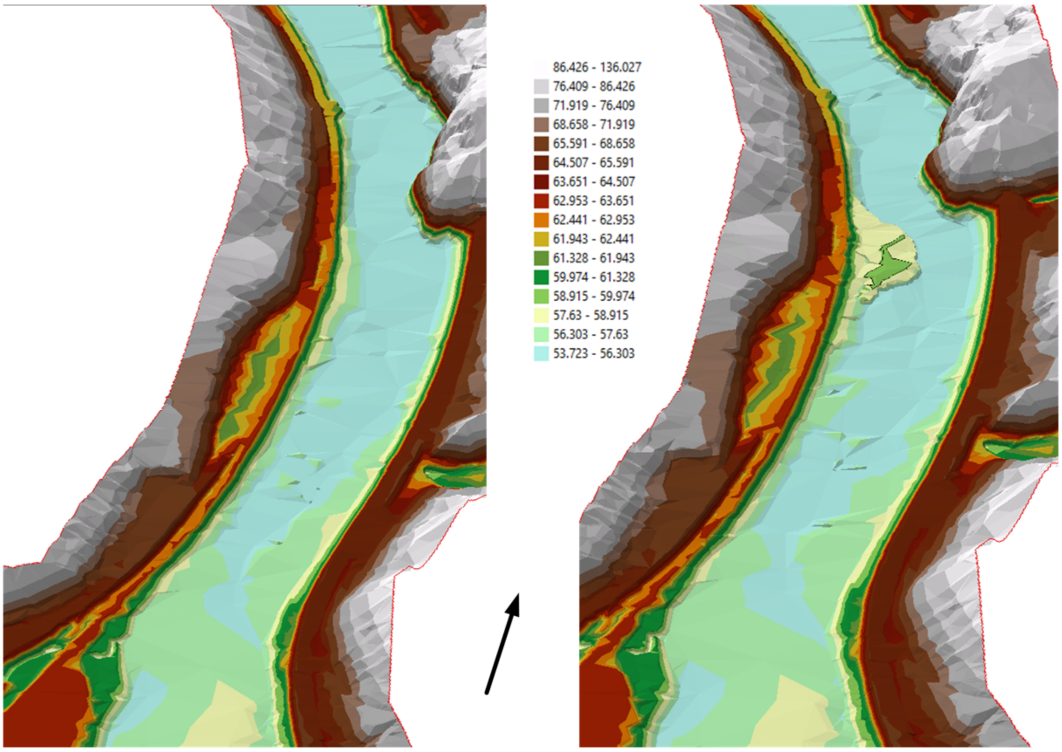

Figure 4 River bathymetry without ice (left) and with grounded ice (right)

We ran the model for different discharges. In Figure 5, the results from a simulation of a discharge of 90 m^3s^{-1} is shown. This represents the mean discharge of the river Gaula measured at the Gaulfoss gauge 1 km downstream of the study site. The figure shows the changed velocity profile where the ice blocks the river profile.

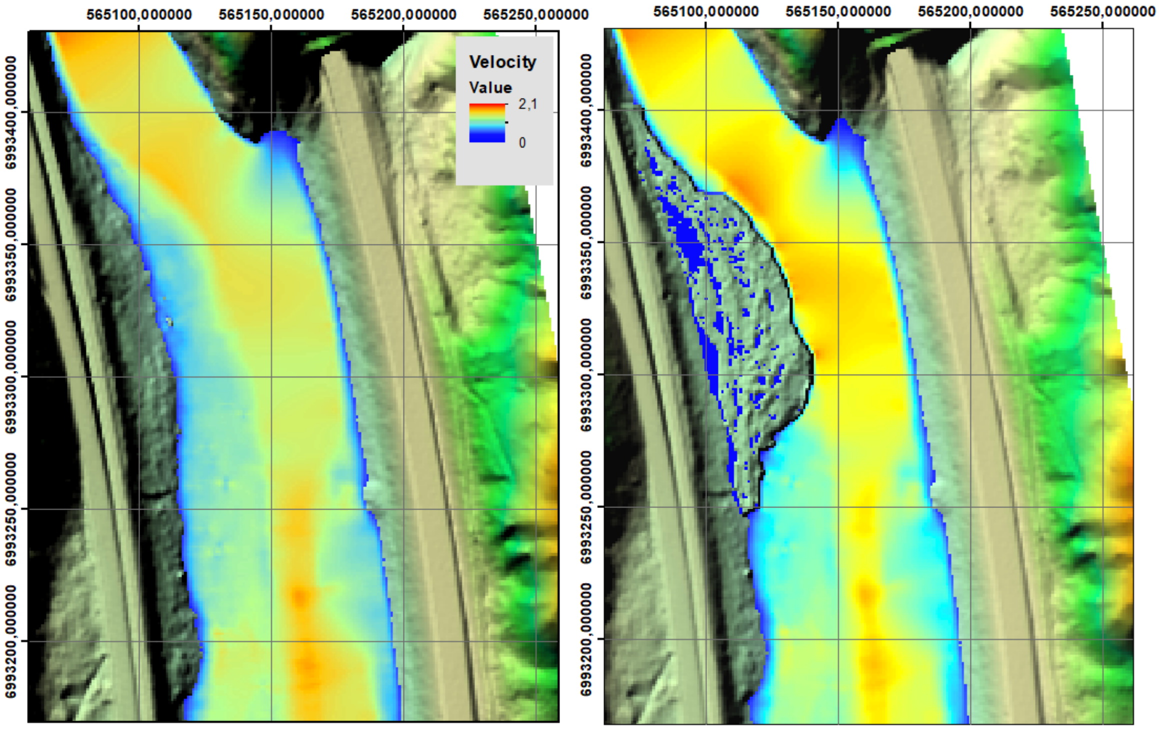

Figure 5 Simulated velocity for the 2017 case. River without ice in the left panel and river with grounded ice in the right panel. The discharge is 90 m^3s^{-1}.

A further evaluation of the depth and velocity distribution in the area influenced by the grounded ice for the discharge presented in Figure 5 shows changes in velocity (mean ± sd) without ice 0.85 ± 0.26 ms^{-1} and with ice 0.94 ± 0.27, and the max velocity increases from 1.29 to 1.49 ms^{-1}. Another observation related to velocity is a reduction in low velocity areas along the bank (see Figure 6) which could have effect on habitat availability for juvenile fish or on bed erosion. For depth the changes are from 1.7 ± 0.6 for the situation with ice and 1.58 ± 0.59 for the situation without ice. Here the max depth does not change since the depth in the downstream areas are not influenced by the ice.

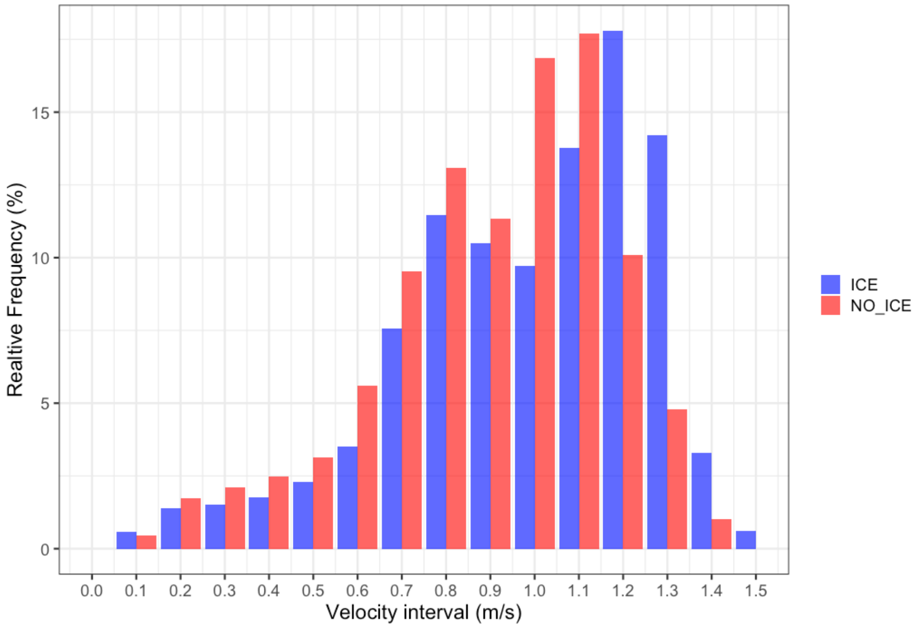

Figure 6 Relative frequency plot of velocities for the situation with and without ice. The velocity interval is 0.1 m/s.

The change in water level in front of the grounded ice is shown in Figure 7. We see that ice raise the water level compared to ice free conditions.

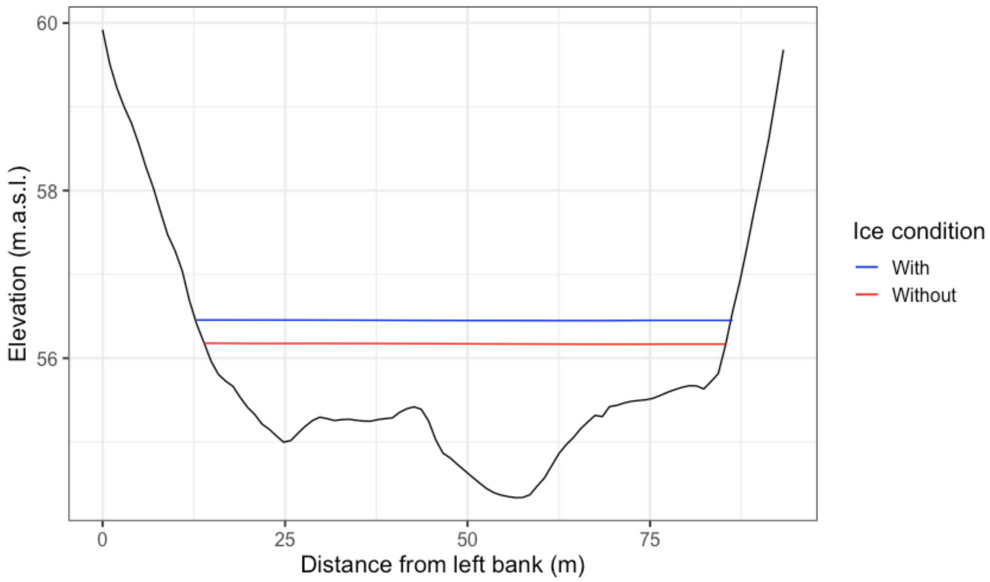

Figure 7 Water levels in front of the ice formation.

4. Discussion

In this study two different small unmanned drones have been used to map remnants of two ice runs in the river Gaula in Norway. The DEMs from the drone mapping have been merged into the river bathymetry and a two-dimensional hydraulic model have been used to simulate the impacts of the grounded ice on hydraulic conditions. The presented method is a potentially useful method of data collection from an environment that is notoriously difficult to access. The procedure can be used to investigate how changed hydraulics due to ice influences e.g. flooding, morphological changes and in-stream environmental conditions as outlined here, or to provide ice data for other forms of analysis and for ice model testing and verification.

In the example shown above we see changes in bankside velocity when ice is present and also an increase in depth along the ice edge. The loss of slow velocity habitat can be an issue in winter since this habitat is utilized by juvenile salmon and trout (Huusko et al. 2007) which is the species present in the Gaula river. The formation of ice ridges along the banks with deeper and faster water along the side can also block the access to suitable habitat for fish. Increased velocity due to a constricted channel also has a potential for erosion of the riverbed.
We found both drones to be efficient tools for data collection, and the study site could be mapped with relatively low effort. In the first case, two persons (one flying the drone the other measuring GCPs) used 35 minutes to cover the study site. The second flight in 2020 one person used 40 minutes to cover the study site with the RTK drone. In this case we did not collect any GCPs, but experiences from other applications of the same drone is that measuring a few points on the ground can be useful for the verification of the precision of the drone. Both the DEM of the ice structures and the orthophoto mosaics are useful data in analysis and modelling ice in rivers. Further, it is recommended to collect data on as low discharge as possible to capture as much of the dry riverbed as possible and to minimize the interaction between water and the ice. Weather conditions is another issue worth considering since the drone will be affected by wind and rain, and the quality of the images will be dependent on light conditions. This is particularly important for collecting ice data since this is often done in winter under low light conditions. Another factor to take into account is the GPS connection since the position hold and ease of flying requires good positioning.

The bathymetry data collected using the green LiDAR (LiDAR with the ability to penetrate the water surface) provides a very precise basis for modelling and for incorporating the ice DEMs into the hydraulic model. Previous experience working with LiDAR shows that the accuracy of the bathymetry provides a very good foundation for modelling river hydraulics (Mandlburger et al. 2015; Juarez et al. 2019).

Here we have assumed grounded ice based on the observations from the field for both cases. If the ice is bridged or floating on water this complicates the evaluation of ice volumes particularly under water, even if estimates of floating ice could be made by assuming the thickness of ice below the water surface. Garver et al. (2018) used the water level observed by the drone to estimate the topography of the ice above the water level. From our orthophotomosaic we clearly see the water surface elevation and also layers of fresh ice formed after the ice jam was established which could be used to find the level of water related to ice. Measuring during the jam formation, this could also be used to assess backwater effects and flooding related to the ice jam. The water levels established from analysis of the orthophotos could also be used in an evaluation of the hydraulic simulations with ice present.

The drone-based DEM also offers other possibilities to investigate the ice. Cross sectional profiles could be extracted from the drone-based DEM to compute the shear wall height along the banks. Further, from the orthophotos we can also identify and measure floe sizes and thickness and floe size distributions. The size and volume of floes is useful information for e.g. estimating loads on structures that should withstand the forces from the ice run during break up. Further, building on the Large Scale Particle Image Velocimetry (LS-PIV) methodology drones can be used to collect data to determine velocity fields in streams e.g. (Lewis and Rhoads 2018). This could also be utilized in rivers with ice, which allows for velocity and potentially discharge measurement from a safe location related to the ice formations. Another potential application relevant to ice assessments is mapping distributed water temperature. Dugdale et al. (2019) shows how drones with thermal imaging cameras can be used to collect temperature data distributed over the stream area in an efficient way, even if the current technology is better suited to assess relative differences than reporting the exact temperature.

Acknowledgements
The authors wish to thank Christian Haas, Jeffrey Thutan and Peggy Zinke who was instrumental in the planning, collecting and processing data for the 2017 event. We also wish to thank the Norwegian Mapping authority and Geovekst who has made digital data and aerial images available.

References

Alfredsen, K., C. Haas, J. Tuhtan and P. Zinke (2018). Brief Communication: Mapping river ice using drones and structure from motion. The Cryosphere **12**: 627-633

Beltaos, S. (1995). River ice jams. Highlands Ranch, Colorado, Water Resources Publishers LLC.

Beltaos, S., Ed. (2009). River Ice Breakup, Water Resources Publications LLC.

Beltaos, S. and P. Tang (2013). Applying HEC-RAS to simulate river ice jams: snags and practical hints. CGU HS Committee on River Ice Processes and the Environment. Edmonton, Alberta, CRIPE. **1:** 15.

Blackburn, J. and Y. She (2019). A comprehensive public-domain river ice process model and its application to a complex natural river. Cold Regions Science and Technology **163**: 44-58

Carrivick, J. and M. Smith (2019). Fluvial and aquatic applications of Structure from Motion photogrammetry and unmanned aerial vehicle/drone technology. Wiley Interdisciplinary Reviews: Water

Chu, T. and K.-E. Lindenschmidt (2016). Integration of space-borne and air-borne data in monitoring river ice processes in the Slave River, Canada. **Remote Sensing and Environment**(181): 65-81 doi:10.1016/j.rse.2016.03.041

Dugdale, S., C. Kelleher, I. Malcolm, S. Caldwell and D. Hannah (2019). Assessing the potential of drone‐based thermal infrared imagery for quantifying river temperature heterogeneity. Hydrological Processes **33**(7): 1152 - 1163 doi:doi.org/10.1002/hyp.13395

Gaffey, C. and A. Bhardwaj (2019). Applications of Unmanned Aerial Vehicles in Cryosphere: Latest Advances and Prospects. Remote Sensing **12**(6)

Garver, J., E. Capovani and D. Pokrzywka (2018). Photogrammetric models from UAS mapping and ice thickness estimated of the 2018 mid-winter Ice jam on the Mohawk River, NY. 2018 Mohawk Watershed Symposium. J. Cockburn and J. Garver. Union College, Schenectady NY. **1:** 19-24.

Huusko, A., L. Greenberg, M. Stickler, T. Linnansaari, M. Nykänen, T. Vehanen, S. Koljonen, P. Louhi and K. Alfredsen (2007). Life in the ice lane:The winter ecology of stream salmonids. River research and applications **23**: 469-491

Juarez, A., A. Adeva-Bustos, K. Alfredsen and B. Dønnum (2019). Performance of A Two-Dimensional Hydraulic Model for the Evaluation of Stranding Areas and Characterization of Rapid Fluctuations in Hydropeaking Rivers. Water **11** doi:doi:10.3390/w11020201

Kääb, A., B. Altena and J. Mascaro (2019). River-ice and water velocities using the Planet optical cubesat constellation. Hydrology and Earth System Science **23**: 4233-4247

Lewis, Q. and B. Rhoads (2018). LSPIV Measurements of Two‐Dimensional Flow Structure in Streams Using Small Unmanned Aerial Systems: 1. Accuracy Assessment Based on Comparison With Stationary Camera Platforms and In‐Stream Velocity Measurements. Water Resources Research **54**(10): 8000 - 8018 doi:/10.1029/2018WR022551.

Lindenschmidt, K.-E. (2017). RIVICE—A Non-Proprietary, Open-Source, One-Dimensional River-Ice Model. Water **9**(5): 314

Lindenschmidt, K.-E. and Z. Li (2019). Radar scatter decomposition to differentiate between running ice accumulations and intact ice covers along rivers. Remote Sensing **11**(307)

Mandlburger, G., C. Hauer, M. Wiesner and N. Pfeifer (2015). Topo-Bathymetric LiDAR for Monitoring River Morphodynamics and Instream Habitats—A Case Study at the Pielach River. Remote Sensing **2015**(7): 5 doi:10.3390/rs70506160

Prowse, T. (2001a). River-Ice Ecology. I: Hydrologic, Geomorphic, and Water-Quality Aspects. Journal of Cold Regions Engineering **15**(1): 1-16

Prowse, T. (2001b). River-Ice Ecology. II: Biological Aspects. Journal of Cold Regions Engineering **15**(1): 17-33

Prowse, T. and J. Culp (2003). Ice breakup: a neglected factor in river ecology. Canadian Journal of Civil Engineering **30**(1): 128-144

Timalsina, N. P., F. Beckers and K. Alfredsen (2016). Modelling winter operational strategies of a hydropower system. Cold Regions Science and Technology **122**: 1-9

25th IAHR International Symposium on Ice

Trondheim, 23 – 25 November 2020

Posteriori identification of a cold-region integrated catchment-river-lake water quality system

Karl-Erich Lindenschmidt[1], Eric Akomeah[1], Luis Morales-Marin[2], Elmira Hassanzadeh[3]

[1] *Global Institute for Water Security, University of Saskatchewan, 11 Innovation Boulevard, Saskatoon, Saskatchewan, Canada, S7N 3H5*
karl-erich.lindenschmidt@usask.ca; eric.akomeah@usask.ca

[2] *Environment and Climate Change Canada, 2121, route Transcanadienne, 4th Floor, Office 411, Dorval, Quebec, Canada, H9P 1J3 luis.morales-marin@canada.ca*

[3] *Department of Civil, Geological and Mining Engineering, Polytechnique Montreal, 2500 Chemin de Polytechnique, Montreal, Quebec, Canada, H3T 1J4*
elmira.hassanzadeh@polymtl.ca

Abstract

There is mounting evidence that ice phenology influences the biogeochemistry of aquatic ecosystems. For under-ice eutrophic aquatic ecosystems in saline environments, it is critical to delineate key parameters and processes for long-term management of such systems. Such systems are saddled with anoxic and bloom risks, with under-ice nutrient cycling being a precursor for spring and summer blooms. In this study, a novel top-down modelling and posteriori identifiability analysis in a Monte-Carlo framework is employed to highlight key parameters and processes contributing to rising eutrophication in the Prairie region of the North American Great Plains, Qu'Appelle River Basin. Landscape nutrient export processes and main stem in-stream processes were hypothesized and linked in VENSIM system-dynamics model and in-stream Water quality Analysis Simulation Program (WASP) models. Model integration was achieved using a python wrapper. Sensitivity metrics were estimated from an ensemble of 10,000 simulation runs. The interaction and cross-correlation of landscape and instream processes were inferred from these metrics. Results from the study showed that winter warming is critical to eutrophication in the studied system and the need to explicitly incorporate overwintering nutrient mechanisms in new generation integrated water quality models.

Key words: integrated catchment modelling, identifiability, uncertainty, cold region, ice processes,

1. Introduction

Incremental eutrophication is currently an issue in the Qu'Appelle River Basin (QRB). However, biogeochemical drivers required for effective nutrient management are unknown. The catchment is located in a Prairie ecozone and biogeochemistry is characterized by low N:P ratios, low iron, high sulphate, making it susceptible to algal blooms and anoxic risks. Furthermore, the river is heavily regulated with a chain of lakes under ice for almost half of the year (Orihel 2017, Akomeah et al., 2019a).

Data and knowledge gaps of catchment biogeochemistry, especially in Prairie cold regions are limiting the effective representation of eutrophication mechanisms in integrated models. The end results are unclosed mass balances with either simple structures or system un-identifiability (Beven, 2006; Fu et al., 2019; Frassl et al., 2019). The gaps have risen as a result of lack of appropriate measurement techniques, catchment heterogeneity, and the need to synchronize monitoring campaigns.

Single physical models and bottom-up modelling are current strategies employed in the development of integrated models (Eckhardt et al., 2003; Weiler and McDonnell, 2004). All feasible future states are still not delineated by these approaches and impacting model identifiability (Young and Parkinson, 2002). The gains of complex models are also only marginal (Perrin et al., 2001; Carpenter et al., 2001; Reed et al., 2004). It is therefore imperative to balance data needs and model complexity in the development and identification of catchment scale models. In this study, a stepwise model development and multi-stage practical identification framework is proposed for the development and improved identifiability of large-scale water quality models of data-poor catchments.

The framework combines systematic deduction of internal processes from catchments' overall responses to available measured data (Klemeš, 1983; Sivapalan et al., 2003) and phased screening of uncertain processes and parameters in the development of large-scale water quality models and their parameter identification. Model development progresses from the use of very simple structures to complex ones, optimizing system processes description based on available data. Bayesian inference and multi - Monte Carlo simulations are then applied to filter and highlight key processes and structural deficiencies for a more focused sampling campaign and model structure improvement.

The internal behavior of an aquatic ecosystem shapes the speciation and ultimate fate of fluxes. These mechanisms can be traced in water quality samples. The samples represent an aggregation of random processes over space and time. Consequently, the random behavior can be assigned to probability distribution parameters. Observation models are typically used to hypothesize and validate the functional relationship between water quality data and parameters. Bayes' axiom can also be used to estimate feasible parameters appropriate for the relationships and predict the behavior of the aquatic ecosystem (Kak, 2009). To this end, a new framework was developed to systematically deduce and identify integrated water quality models for complex catchments with scarce data. The approach was applied to delineate the internal mechanisms of the QR, especially for the under-ice conditions which is a knowledge gap. The framework was applied to identify critical controls on under-ice eutrophication in the QRB in Saskatchewan, Canada. The study is a synthesis of published and papers in submission: Akomeah et al. (2017), Hosseini et al. (2018), Akomeah et al. (2019a and 2019b), and Akomeah et al. (in submission). The reader is therefore encouraged to visit these publications for the details.

2. Study area

The Qu'Appelle River (QR) drains a 52,000 km^2 catchment area with mainly agricultural land use. Mixed farming, annual crop production, wetland drainage, and winter cattle feeding near river banks are some of the farming practices in the catchment (Fig. 1). The river is used to supply potable, irrigation, and industrial water to Saskatchewan. It is also used for fishing and recreation (Hassanzadeh et al., 2019). Mean annual flow is estimated as 6.5 m^3/s (Pomeroy et al., 2005). Incremental eutrophication, internal loading as a result of warming temperatures, high pH, and anoxia are persistent water quality issues in the Valley (Hall et al., 1999; Orihel et al., 2015). Typically, the coldest month is in January (a mean temperature of -20.1ºC) and the warmest month in July (28.5ºC).

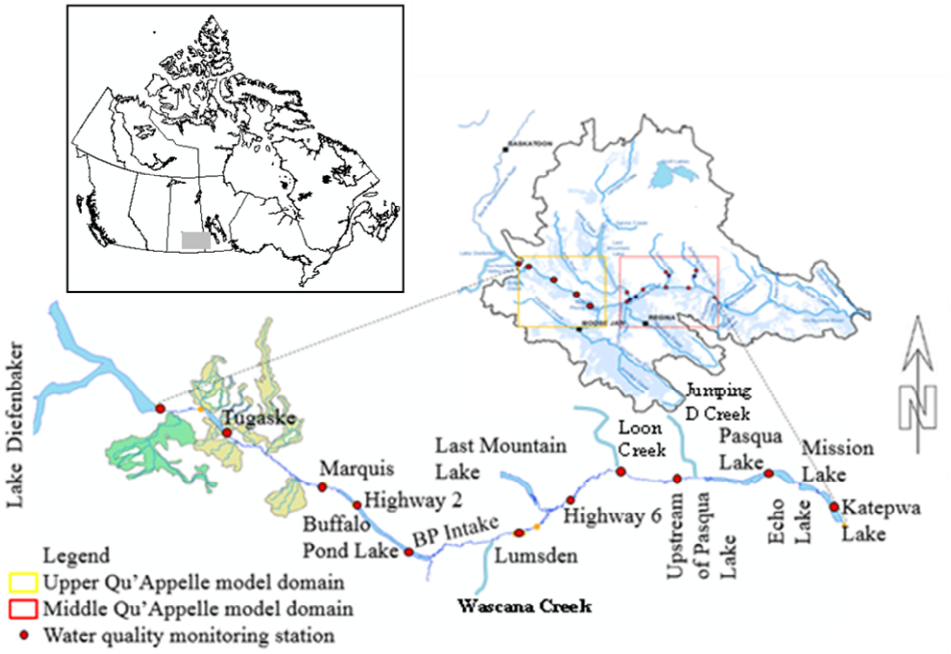

Figure 1. Qu'Appelle River basin showing the upper and middle Qu'Appelle River. The yellow box shows the upper Qu'Appelle River and the red box, middle Qu'Appelle River. Water quality monitoring stations are represented as red dots. Map is modified from Akomeah et al. (2018).

3. Methods

The proposed framework combines Bayesian inference techniques and global sensitivity analysis to identify the reliable expanse within which an unmeasured parameter falls, given a *prior* probability. Bayes theorem combines known information about ungauged parameters and typical system response for a target variable to improve the estimate of parameter distribution (Benjamin and Cornell, 1970). For a given model with a single unobserved parameter, the rule is given as:

$$P(\theta|x) = \frac{P(x|\theta)\,P(\theta)}{P(x)} = \frac{P(x|\theta)\,P(\theta)}{\int_{\theta} P(x|\theta).P(\theta)d\theta} \quad \textbf{[1]}$$

where

$P(\theta|x)$ = Posteriori distribution (probability that an estimated parameter is accurate for the given measurement)

$P(x|\theta)$ = Likelihood (probability of observed behaviour occurring given an accurate parameter)

$P(\theta)$	=	Preliminary estimate of the probability of each parameter value being accurate
$P(x)$	=	Probability of the data occurring

According to Eq. (1), the probability of an ungauged parameter estimate being accurate depends on the probability of that parameter causing the observed behaviour of a target variable and the probabilities of the parameter and observed data occurring. That is, the rule is interpreted as:

$$Posteriori = \frac{likelihood \times prior}{evidence} \quad \textbf{[2]}$$

where the likelihood distribution = observation model.

$P(x|\theta)$, thus, represents the mechanistic model, which in this study is an integrated catchment and instream water quality model. The Monte Carlo simulation solves the integrands with probabilities. Samples drawn from a probability distribution P(θ) are used to estimate the integrals.

For a given input I(x, t) and output M(x, t), a model (M) is globally identified if a unique solution exists (Ljung and Glad, 1994). That is:

$$f(I(x,t),\theta) = f(I(x,t),\theta^{*}) \leftrightarrow \quad \theta = \theta^{*} \quad \textbf{[3]}$$

This means that, for any given input and time, a model with a vector of parameters has the same output as a model with the true parameter set (θ^{*}).

In this study, a stepwise filtering strategy was applied to screen for error, noise, and bias associated with the identification of environmental models (Akomeah et al., in submission).

3.1 Application of the framework to the QRB

The top-down and identifiability framework was applied in the development and identification of an integrated model for the QR (Fig. 2). Catchment and instream nutrient cycling, stoichiometry, and eutrophication were hypothesized using two established models: the Water quality Analysis Simulation Program (WASP) and Vensim. Model development progressed from simple structure (Streeter-Phelps; catchment nutrient export) to complex structure, instream advanced eutrophication. Details of sub models and integrated model development, calibration, and identification can be found in (Akomeah et al., 2017, Hosseini et al., 2018, Akomeah et al., 2019a, Akomeah et al., 2019b, and Akomeah et al., in submission).

3.1.1 Under-ice variation in sediment oxygen demand

Aquatic ecosystems in the Prairies are prone to anoxia, bloom risks, and fish kills due to their unique biogeochemistry (Orihel et al., 2017). Biogeochemical processes at the sediment water interface and in the sediments play a key role in these issues. Sediment oxygen demand (SOD) was sparse in the study site. Meanwhile, SOD constitutes a number of microbial and biological processes within the sediments that draw dissolved oxygen (DO) from sediments and overlying water column. The drawdown rate is typically a precursor to anoxia, internal loading, and bloom risks in the aquatic system. SOD was therefore inferred from available water quality data.

Akomeah et al., (2017) discusses details of model development and calibration. The seasonal variation of SOD was modelled in the study. This study focuses on the variation of SOD in the winter and its implications.

To enhance the accuracy of SOD estimation, WASP model processes and parameters were constrained to a low complexity structure with few parameters to optimize. The modified Streeter and Phelps DO balance in WASP was utilized to improve SOD estimation. The model structure consists of the transport and transformation kinetics of biochemical oxygen demand and dissolved oxygen. Processes involved in these kinetics include atmospheric reaeration, total oxidation, SOD for DO balance, influent total biochemical oxygen demand, and settling of oxidizable organic material for biochemical oxygen demand (BOD) dynamics. In addition, the effect of ice on reaeration was incorporated in the model setup. Output of a verified Hydrologic Engineering Center River Analysis System (HEC-RAS) hydrodynamic model was used to drive the BOD-DO kinetics. Model forcings included temperature, flow, and dissolved oxygen (Wool et al., 2006).

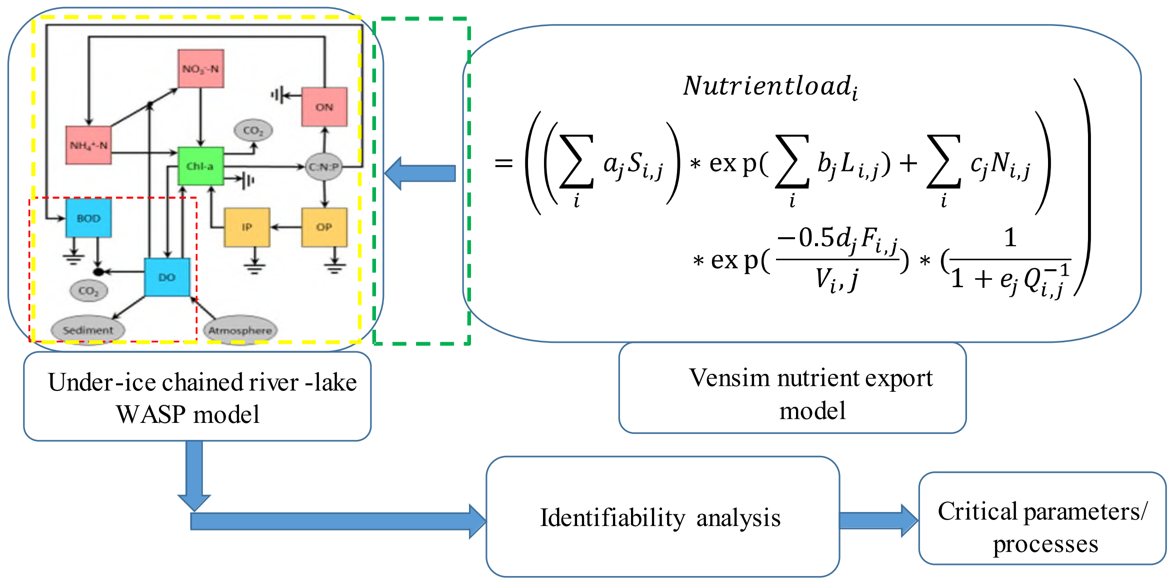

Figure 2. Conceptual model of the integrated catchment-surface water quality modelling framework including WASP and Vensim model structures and linkages. Map is modified from Akomeah et al. (in submission).

The estimation of SOD and its temperature coefficient included iteration within reasonable bounds of the parameter space derived from the literature using the dynamically dimensioned search algorithm of OSTRICH optimization software (Matott, 2017). The optimum parameter set and verification included those that closely predicted available DO data for typical summer and winter months for the period 2013 to 2015. Model bias and prediction error were assessed using mean error and mean absolute error (Akomeah et al., 2017).

3.1.2 Eutrophication model structure selection, setup, and seasonal controls for instream and in-lake

Phytoplankton, nitrogen, phosphorus cycles, and DO balance in the river and lake were linked in WASP (Akomeah et al., 2019a). The organic matter in the BOD-DO model structure was separated into carbonaceous biochemical oxygen demand, organic nitrogen, ammonium, nitrate, organic phosphorus, orthophosphate, and phytoplankton. Some of the transformations include photosynthesis, reaeration, respiration, grazing, death, dissolution, mineralization, nitrification, adsorption, desorption, settling, denitrification, and nitrogen fixation. Model calibration and validation were undertaken for the period 2012 to 2016, measuring predictive power with the mean absolute error metric. Global sensitivity analysis was then carried out to assess controls on eutrophication in the components of the QR: riverine, lake, and river-lake configuration (Hosseini et al., 2018).

3.2 Development of catchment nutrient export model and identification of integrated model

Seasonality was incorporated into the base structure of an existing model to allow its integration with the instream WASP model. The model includes hybrid statistical-process base mechanisms including nutrient mobilization, decaying, and delivery (Hassanzadeh et al., 2019). The two models were integrated using a python wrapper. The VENSIM model is first called and ran in Monte Carlo settings. Model outputs are then reformatted and parsed to WASP at specified segment locations. The wrapper then calls WASP's executables for a second Monte Carlo simulation. The framework was then used to constrain uncertainty propagation and to identify critical parameters and processes impacting nutrient enrichment in the integrated water quality model.

First, to limit the propagation of error with respect to model structure, parameters, and forcing, physically plausible parameter space for the Prairies was determined for the sub-models (Akomeah et al., in submission). Credible regions within which unobserved parameter values fall were identified given an *a prior* probability. A multi-stage Monte Carlo simulation was then undertaken to generate feasible ensemble loading. The ensemble loads were then parsed to WASP for a second Monte Carlo filtering simulation. Performance of the *posteriori* distribution generated from this global sensitivity analysis was then ranked from best to worst and grouped into 10 sets. A cumulative distribution pertaining to the probability of each parameter was then generated for all parameters in each set (Akomeah et al., in submission). Low error margin (α=0.001) was applied to further filter simulation results using the two-sample Kolmogorov–Smirnov (KS) statistic test to two cumulative distribution frequencies (CDFs).

The test is given as:

$$S_i = \max_{i,j}\left(\max_x\left(\left|F_i(x) - F_j(x)\right|\right)\right), \tag{4}$$

where $F_i()$ is the CDF of x in the *i-th* group and $F_j()$ is the CDF in the j-th group.

Thus, the double screening phases that the procedure affords provide a robust estimate of unique parameters for each target response observation in the integrated model (Akomeah et al., in submission).

4 Results and discussion

4.1 Under-ice sediment oxygen demand and eutrophication mechanisms in the Qu'Appelle catchment-river-lake system

Akomeah and Lindenschmidt (2017) provide details about model development, calibration and verification of the WASP's BOD-DO complexity module. Model calibration and validation covered typical winter months (November – April) for the period 2013 to 2015 using the OSTRICH software. Estimated mean error and mean absolute error ranged from 0.62 to 0.62 (mg DO/L) and 0.35 to 1.78 (mg DO/L), respectively.

Modelled SOD rates across the system (river and lakes) levelled off under ice conditions but marked up during ice breakup conditions (Fig. 3). Estimated SOD rates in the river ranged from 0.30 to 0.94 g/m^2/day compared to 0.83 to 0.95 g/m^2/day in the lakes (Akomeah and Lindenschmidt, 2017). Estimated SOD rates for 11 ice-covered lakes with similar trophic states in Alberta, Canada, also ranged from 0.243 to 0.848 g/m^2/day (Babin & Prepas, 1985). Accumulation of nutrients in the lake during the winter may have accounted for the higher SOD rates in the lakes. Ice breakup is often characterized by large deposition of organic matter in rivers with ensuing oxidation several days after the deposition (Elwood & Waters, 1969).

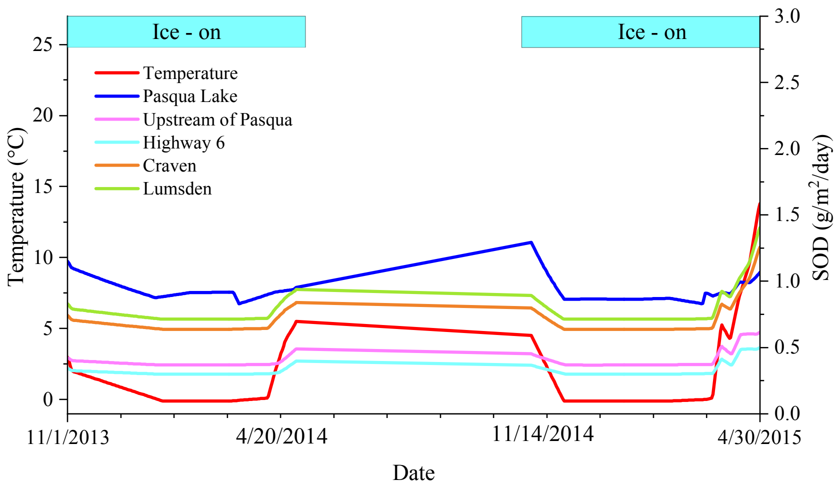

Figure 3. Winter sediment oxygen demand rates in the river and lake (middle Qu'Appelle).

The transport and biogeochemistry of the river and lake were linked in one framework using WASP. Model calibration and validation covered the period, 2012 to 2016 (Hosseini et al., 2018; Akomeah et al., 2019b). Estimated mean absolute error for DO, NH_4^+-N, and NO_3^--N ranged from 0.23 mg NO_3^--N/L to 1.45 mg DO/L. The model was able to capture the seasonal and spatial dynamics in nutrients and phytoplankton. Detailed results can be found in Hosseini et al. (2018) and Akomeah et al. (2019a).

Under-ice mineralization and nitrification were active as nutrients pooled while ON, DO, and Chl-a declined (Akomeah et al., 2019a). Organic substrate tends to accumulate in the sediment during the winter from summer bloom collapse and reduced microbial activities in the fall as the temperature declines. The substrate gets utilized during mineralization in the winter which is mediated by heat supply from sediment. During the process, ON and DO decline. Although nutrients abound in the winter, decreased illumination due to ice covers and low temperatures hindered phytoplankton growth (Akomeah et al., 2019a). Results from other studies are in harmony with these delineated winter mechanisms (Nürnberg et al., 1986, Hampton et al., 2017).

Posteriori identifiability analysis of the integrated model further showed that the water column nutrient pooling is also borne by episodic diffuse loading during the winter (Fig. 4). Warming winter accounted for the catchment nutrient export (Akomeah et al., in submission). Accumulated nutrients from fertilizer application, livestock farming areas, and plant residues are discharged into the river from meltwater during above zero temperatures in the winter. A grade is formed in snow crystals with ensuing fractionation and densification during this condition. As ions are separated from the snow crystals during the process, elution occurs with sporadic loadings to the nearby receptors (Pomeroy et al., 2006). A warm winter corresponds to NO_3^--N export in the winter (Casson et al., 2012). Elsewhere, external N flux has been attributed to the riverine accumulation of NO_3^--N in the winter (Knowles & Lean, 1987; Pettersson et al., 2003; George et al., 2010). In another study, NO_3^--N export in the winter contributed up to 40% of annual exports (Eimers et al., 2007). This was mainly due to events such as rain-on-snow and flow over frozen ground. In the winter, snow cover and frozen ground limit NO_3^--N contact with the soil and retard denitrification rates.

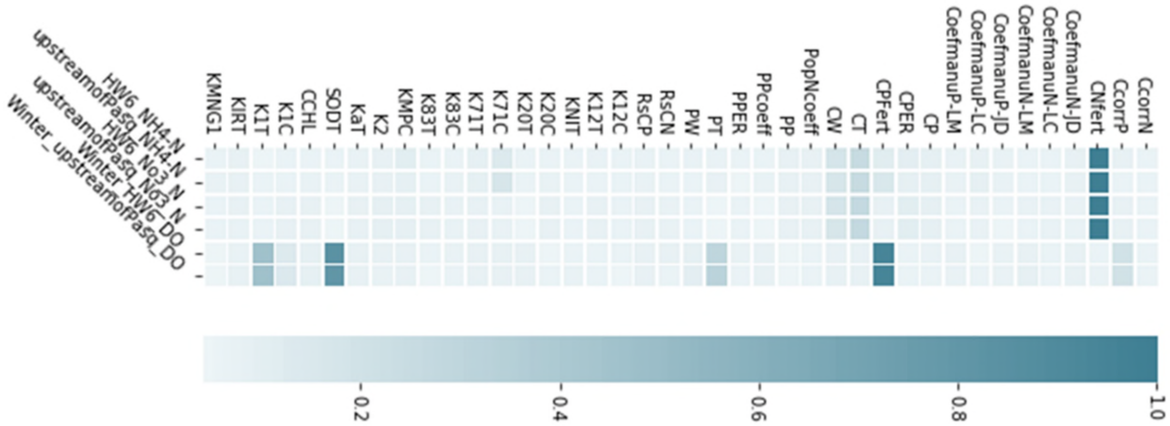

Figure 4. Sensitivity of NH_4^+-N, NO_3^--N, DO, and Chl a to variation in parameters in the winter (December) (Akomeah et al., in submission).

Microbial activities and temperature in the sediment play prominent roles in DO availability in winter (Fig. 4) (see also Hosseini et al., 2018). External mechanisms such as reaeration become limited due to the presence of ice cover. Thus, biogeochemical processes such as diffuse loading, organic matter mineralization, nitrification, and nutrient uptake are prevalent in the winter.

4.3 Controls on under-ice eutrophication in the Qu'Appelle catchment-river-lake system

Characterizing under-ice eutrophication in a river-lake system was a novel approach employed during the model development (Akomeah et al., 2017; Hosseini et al., 2018). The approach was therefore benchmarked against existing river only and lake only eutrophication modelling approaches. The comparison showed that, parameters in the river-lake system had the greatest control on eutrophication than those in either the river- or lake-only model. The ability to accurately characterize the transport (riverine, backwater, and ponding) in the river-lake model accounted for this (Hosseini et al., 2018).

Table 1 provides the results of a global sensitivity analysis carried out to delineate controls on under-ice eutrophication with the components of Qu'Appelle River system as objective functions. Some of the key winter sensitive eutrophication parameters included: dissolved organic nitrogen mineralization rate (K71C), phytoplankton nitrogen to carbon ratio (NCRB), phosphorus-to-carbon ratio (PCRB), maximum phytoplankton growth rate (K1C), and phytoplankton death rate (K1R) (Table 1). In a similar study by Hosseini et al. (2016) in a near-by catchment, sensitive parameters included K71C, K1C, and K1R.

Table 1. sensitivity of river (only), lake (only) and river and lake (together) models to eutrophication variables in the winter

Parameters	Description	river	lake	lake_river
SOD_r	Sediment oxygen demand for river			
SOD_l	Sediment oxygen demand for river	-		
SOD_temp	Sediment oxygen demand temperature coefficient			
K12C	Nitrification rate at 20°C			
K20C	Denitrification rate			
K71C	ON- mineralization rate at 20°C			
K83C	OP- mineralization rate at 20°C			
NCRB	Nitrogen-to-carbon ratio			
PCRB	Phosphorus-to-carbon-ratio			
CCHL	Carbon-to-chlorophyll-a-ratio			
K1C	Maximum phytoplankton growth rate			
K1R	Phytoplankton respiration rate			
K1D	Phytoplankton death rate			
KMNG	Half-saturation constant for phytolankton nitrogen uptake			
KMPG	Half-saturation constant for phytolankton phosphorus uptake			
fON	Fraction of dead and respired phytoplankton recycled to ON			
fOP	Fraction of dead and respired phytoplankton recycled to OP			

Critical under-ice winter parameters identified using the developed framework for the integrated model included nitrogen and phosphorus fertilizer export coefficients (CNfert and CPfert), catchment temperature coefficient (CT), wetland decay coefficient (CW), temperature coefficient (PT). Sediment temperature further regulates microbial activities (SOD and phytoplankton growth) in the winter (SODT and K1T).

From the foregoing and pending field validation, the above parameters are potential critical considerations in the development of eutrophication models in the region.

4 Conclusions

A new top-down and phased screening methodology is proposed for the development and improved identifiability of integrated water quality models. The approach combines systematic and judicious increments in the complexity of the model structure and filtering of uncertainties based on available measured data to develop and identify integrated models. Rather than engaging in detailed model development from the onset, low complexity model structure is adapted and gradually verified and increased to characterize system internal behaviour and Bayesian inference techniques and the Kolmogorov–Smirnov test are applied to highlight crucial parameters and processes of the system. The methodology was applied to the Qu'Appelle River Basin in Saskatchewan, Canada. Land-based activities and soils of the Qu'Appelle are increasing the trophic state of the river. Drivers of this eutrophication are, however, not known.

A modified Streeter and Phelps BOD-DO model structure was used to constrain and optimize SOD estimation for the system. The structure was gradually increased from intermediate eutrophication to advanced eutrophication. Global sensitivity analyses of upstream and middle reach model setups prompted model integration of the entire catchment. Two sub-models, one for the catchment and the other for the river, were then loosely coupled using a python wrapper. A multi-stage Monte Carlo simulation, global sensitivity analysis, and KS test were then used to screen and identify critical parameters and processes.

The proposed approach provides a platform for continuous improvement in model development for reliable and precise predictions through focused monitoring and the incorporation of new hypotheses. In the Anthropocene, where sub-components of aquatic systems are co-evolving due to altered and coupled biogeochemical cycling and rising mean temperatures, the approach provides a way to manage aquatic systems sustainably by tracking and incorporating new trajectories into model development.

References

Akomeah, E. and Lindenschmidt, K.-E., 2017. Seasonal Variation in Sediment Oxygen Demand in a Northern Chained River-Lake System, Water, 9(4), 254, doi:10.3390/w9040254.

Akomeah, E., Davies, J.-M. and Lindenschmidt, K.-E., 2019a: Water Quality Modeling of Phytoplankton and Nutrient Cycles of a Complex Cold-Region River-Lake System, Environ Model Assess, doi:10.1007/s10666-019-09681-x.

Akomeah, E., Lindenschmidt, K.-E. and Chapra, S. C. , 2019b: Comparison of aquatic ecosystem functioning between eutrophic and hypereutrophic cold-region river-lake systems, Ecological Modelling, 393, 25–36, doi:10.1016/j.ecolmodel.2018.12.004.

Akomeah, E., Lindenschmidt, K.-E., Morales-Marin L. and Hassanzadeh E., (in submission). A stepwise framework for posteriori identification of integrated catchment-river-lake water quality system.

Babin, J., & Prepas, E. E. (1985). Modelling Winter Oxygen Depletion Rates in Ice-Covered Temperate Zone Lakes in Canada. Canadian Journal of Fisheries and Aquatic Sciences, 42(2), 239–249. https://doi.org/10.1139/f85-031

Benjamin, J. R. and Cornell, C. A., 1970. Probability, statistics and decision for civil engineers, Infoscience [online] Available from: https://infoscience.epfl.ch/record/27691 (Accessed 1 February 2020).

Beven, K., 2006. Searching for the Holy Grail of scientific hydrology: Q_t=(*S, R, Δt*)*A* as closure, Hydrology and Earth System Sciences, 10(5), 609–618, doi:https://doi.org/10.5194/hess-10-609-2006.

Casson, N. J., Eimers, M. C. and Watmough, S. A., 2012. Impact of winter warming on the timing of nutrient export from forested catchments, Hydrological Processes, 26(17), 2546–2554, doi:10.1002/hyp.8461.

Eckhardt, K., Breuer, L. and Frede, H. G., 2003. Parameter uncertainty and the significance of simulated land use change effects, Journal of hydrology [online] Available from: http://agris.fao.org/agris-search/search.do?recordID=US201600119119 (Accessed 31 January 2020).

Eimers, M. C., Buttle, J. M. and Watmough, S. A., 2007. The contribution of rain-on-snow events to annual NO3-N export from a forested catchment in south-central Ontario, Canada, Applied Geochemistry, 22(6), 1105–1110, doi:10.1016/j.apgeochem.2007.03.046.

Frassl, M. A., Abell, J. M., Botelho, D. A., Cinque, K., Gibbes, B. R., Jöhnk, K. D., Muraoka, K., Robson, B. J., Wolski, M., Xiao, M. and Hamilton, D. P.,2019. A short review of contemporary developments in aquatic ecosystem modelling of lakes and reservoirs, Environmental Modelling & Software, 117, 181–187, doi:10.1016/j.envsoft.2019.03.024.

Fu, B., Merritt, W. S., Croke, B. F. W., Weber, T. R. and Jakeman, A. J., 2019. A review of catchment-scale water quality and erosion models and a synthesis of future prospects, Environmental Modelling & Software, 114, 75–97, doi:10.1016/j.envsoft.2018.12.008.

George, G., Järvinen, M., Nõges, T., Blenckner, T. and Moore, K., 2010. The Impact of the Changing Climate on the Supply and Recycling of Nitrate, in The Impact of Climate Change on European Lakes, edited by G. George, pp. 161–178, Springer Netherlands, Dordrecht.

Hall, R. I., Leavitt, P. R., Quinlan, R., Dixit, A. S. and Smol, J. P., 1999. Effects of agriculture, urbanization, and climate on water quality in the northern Great Plains, Limnol. Oceanogr., 44, 739–756.

Hampton, S. E., Galloway, A. W., Powers, S. M., Ozersky, T., Woo, K. H., Batt, R. D., & Stanley, E. H., 2017. Ecology under lake ice. Ecology Letters. 20(1), 98–111.

Hassanzadeh, E., Strickert, G., Morales-Marin, L., Noble, B., Baulch, H., Shupena-Soulodre, E. and Lindenschmidt, K.-E., 2019. A framework for engaging stakeholders in water quality modeling and management: Application to the Qu'Appelle River Basin, Canada, Journal of Environmental Management, 231, 1117–1126, doi:10.1016/j.jenvman.2018.11.016.

Hosseini, N., Akomeah, E., Davis, J.-M., Baulch, H. and Lindenschmidt, K.-E., 2018. Water quality modeling of a prairie river-lake system, Environ Sci Pollut Res, 25(31), 31190–31204, doi:10.1007/s11356-018-3055-2.

Kak, A. C., 2009. Monte Carlo in Bayesian Estimation Tutorial by Avi Kak Monte Carlo Integration in Bayesian Estimation.

Klemeš, V., 1983. Conceptualization and scale in hydrology, Journal of Hydrology, 65(1), 1–23, doi:10.1016/0022-1694(83)90208-1.

Knowles, R. and Lean, D. R. S., 1987. Nitrification: A Significant Cause of Oxygen Depletion Under Winter Ice, Can. J. Fish. Aquat. Sci., 44(4), 743–749, doi:10.1139/f87-090.

Ljung, L. and Glad, T., 1994: On global identifiability for arbitrary model parametrizations, Automatica, 30(2), 265–276, doi:10.1016/0005-1098(94)90029-9.

Matott, L., 2017: an Optimization Software Tool, Documentation and User's Guide, Version 17.12.19. 79 pages, University at Buffalo Center for Computational Research, www.eng.buffalo.edu/~lsmatott/Ostrich/OstrichMain.html.

Nürnberg, G. K., Shaw, M., Dillon, P. J., & McQueen, D. J., 1986. Internal phosphorus load in an oligotrophic Precambrian Shield lake with an anoxic hypolimnion. Canadian Journal of Fisheries and Aquatic Sciences, 43(3), 574–580.

Orihel, D. M., Schindler, D. W., Ballard, N. C., Graham, M. D., O'Connell, D. W., Wilson, L. R. and Vinebrooke, R. D, 2015. The "nutrient pump:" Iron-poor sediments fuel low nitrogen-to-phosphorus ratios and cyanobacterial blooms in polymictic lakes, Limnology and Oceanography, 60(3), 856–871, doi:10.1002/lno.10076.

Orihel, D. M., Baulch, H. M., Casson, N. J., North, R. L., Parsons, C. T., Seckar, D. C. M. and Venkiteswaran, J. J., 2017. Internal phosphorus loading in Canadian fresh waters: a critical review and data analysis, Can. J. Fish. Aquat. Sci., 74(12), 2005–2029, doi:10.1139/cjfas-2016-0500.

Perrin, C., Michel, C. and Andréassian, V., 2001. Does a large number of parameters enhance model performance? Comparative assessment of common catchment model structures on 429 catchments, Journal of Hydrology, 242(3), 275–301, doi:10.1016/S0022-1694(00)00393-0.

Pettersson, K., Grust, K., Weyhenmeyer, G. and Blenckner, T., 2003. Seasonality of chlorophyll and nutrients in Lake Erken – effects of weather conditions, Hydrobiologia, 506(1), 75–81, doi:10.1023/B:HYDR.0000008582.61851.76.

Pomeroy, J. W., de Boer, D. and Martz, L. W., 2005. Hydrology and water resources of Saskatchewan, Centre for Hydrology, University of Saskatchewan Saskatoon.

Pomeroy, J. W., Jones, H. G., Tranter, M. and Lilbæk, G., 2006. Hydrochemical Processes in Snow-Covered Basins, in Encyclopedia of Hydrological Sciences, American Cancer Society.

Reed, S., Koren, V., Smith, M., Zhang, Z., Moreda, F., Seo, D.-J. and DMIP, 2004. Participants and overall distributed model intercomparison project results, Journal of Hydrology, 298(1), 27–60, doi:10.1016/j.jhydrol.2004.03.031.

Sivapalan, M., Blöschl, G., Zhang, L. and Vertessy, R., 2003. Downward approach to hydrological prediction, Hydrological Processes, 17(11), 2101–2111, doi:10.1002/hyp.1425.

Weiler, M. and McDonnell, J., 2004: Virtual experiments: a new approach for improving process conceptualization in hillslope hydrology, Journal of Hydrology, 285(1), 3–18, doi:10.1016/S0022-1694(03)00271-3.

Wool, T. A., Ambrose, R. B., Martin, J. L., Comer, E. A. and Tech, T., 2006. Water quality analysis simulation program (WASP). User's Manual, Version, 6.

Young, P. C. and Parkinson, S., 2002: Chapter 13 Simplicity out of complexity, in Developments in Environmental Modelling, vol. 22, pp. 251–301, Elsevier.

25th IAHR International Symposium on Ice

Trondheim, November 23 to 25, 2020

A novel fully-operational fully-automated real-time ice-jam flood forecasting system

Lindenschmidt, K.-E.[1], Brown, D.[2], Khan, A.A.[3], Khan, H.[3], Khayer, M.[3], McArdle, S.[4], Mostofi, S.[3], Naumov, A.[4], Pham, T.[4] and Weiss, A.[2]

[1] *Global Institute for Water Security, University of Saskatchewan, 11 Innovation Blvd., Saskatoon, Saskatchewan, Canada, S7N 3H5 karl-erich.lindenschmidt@usask.ca*

[2] *KGS Group, 3rd Floor - 865 Waverley Street, Winnipeg, Manitoba, Canada, R3T 5P4*

[3] *Water Resources Management Division, Government of Newfoundland and Labrador, 4th Floor - Confederation Building (West Block), PO Box 8700, St. John's, Newfoundland and Labrador, Canada, A1B 4J6*

[4] *4DM Inc., Suite 803 - 920 Yonge Street, Toronto, Ontario, Canada, M4W 3C7*

This paper provides insight to one of the first fully operational ice-jam flood forecasting systems that has been implemented to forecast ice-jam floods in real-time. The system was developed for and is operated by the Government of Newfoundland and Labrador to forecast ice-jam floods along the lower Churchill River in Labrador, Canada. The system consists of a river ice model to simulate possible ice-jam backwater levels, for the next three days. The model is embedded in a Monte-Carlo framework to provide ensembles of backwater level profiles, from which exceedance probabilities are derived. A hydrological model of the basin upstream of the Churchill River's lower reach forecasts the runoff used as an upstream boundary condition for the river ice model. Space-borne remote sensing imagery provides an indication of the remaining extent of the ice cover along the reach upstream of the potential ice-jamming stretch. This provides an estimate of the volume of ice that is available to form jams. All data acquisitions and feeds and model runs are fully automated and synchronised to provide daily forecasts of the ice-jam flood hazard, always three days ahead of time. The model was tested successfully for the spring 2019 breakup event.

1. Introduction

Background and motivation

Major ice flooding occurred along the (Atlantic) Churchill River in Central Labrador on 17 May 2017 which caused extensive damages in and the evacuation of residents from riverside communities of Mud Lake and areas of Happy Valley-Goose Bay, particularly along Mud Lake Road (KGS, in prep.). The evacuation had to be performed using helicopters as water levels and ice conditions were not amenable to evacuation by boat. The flooding caused great stress to the residents of both Mud Lake and Happy Valley – Goose Bay and had a devastating effect on the community and surrounding area (KGS, in prep.).

The flooding prompted an independent review (Lindenschmidt, 2017) of the causes of the flood event. It was speculated that construction of the upstream Muskrat Falls dam and hydro-power generation plant may have contributed to the flooding, but the review found that "the high freshet discharge that occurred during May 2017 was caused by natural events, particularly the rain-on-snow event in the middle basin of the Churchill River and the high rainfall event just prior to and during the May 2017 flood in the Churchill River's lower basin" (Lindenschmidt, 2017, p. 29). The review recommended that "modelling capabilities [be developed] to make predictions regarding potential ice jamming and flooding along the lower Churchill River. Models should include those that can simulate the hydraulics and river ice behaviour along the lower Churchill River and estimate the runoff from the Churchill River watershed, particularly the middle and lower basins" (Lindenschmidt, 2017, p. 30).

In response to this recommendation, the Government of Newfoundland/Labrador issued a request for proposals for the development of a flood forecasting service for the Churchill River (NFLD, 2018). The award went to the proposal submitted by KGS Group in Winnipeg (KGS, 2018). A large portion of the work encompassed the development and testing of an automated and operational forecasting system to predict open-water and ice-jam floods in real time. This paper focuses on only the ice-jam flood forecasting component of the forecasting system. The flood forecasting system was based on the HydrologiX web platform developed by 4DM Inc. and advanced for ice-jam flood forecasting through the project. To date, it is the first fully-operational fully-automated real-time ice-jam flood forecasting systems in the world.

Ice-jam flood forecasting

Forecasting riverine floods caused by ice jams is more challenging than forecasting open-water floods due to the stochastic nature of ice jams and their backwater staging effects. For example, small changes in the volume of ice that forms the jams, the location of the ice-jam lodgements, the properties of the ice or the hydraulic conditions can lead to large shifts in the ice-jam morphology and backwater staging. **Figure 1** shows simulation results from a river ice model. The parameter and boundary condition settings are the same for each model run, except that the ice-jam lodgement (toe) is 200 m apart. Notice the difference in the ice-jam morphology, with maximum ice-jam thicknesses being respectively 3.94 and 4.41 m for the upstream and downstream lodgement locations, a difference of almost ½ m. Slight differences in the location of the ice jam compared to its fluvial geomorphological setting can be very sensitive to the outcome of water-level staging and ice-cover extent and thicknesses.

The use of computer models is a convenient way of representing and analysing ice jams and their flooding outcomes. Although river ice hydraulic models are generally set up in a deterministic modelling structure (one set of parameters and boundary conditions yields one output), the stochastic nature of ice jams and ice-jam floods can be represented in a probabilistic context by placing the deterministic model into a Monte-Carlo framework. Within the framework, the model is run many hundreds of times with each simulation having a different setting of the parameter and boundary condition values. The values are chosen randomly from frequency distributions that reflect the possible changes that may occur in the hydraulic and ice regimes of the jam during the ice-jam flooding event. Probability distributions of flood level threshold exceedances can then be derived from the resulting ensemble of backwater level profiles along the flood hazard area of interest.

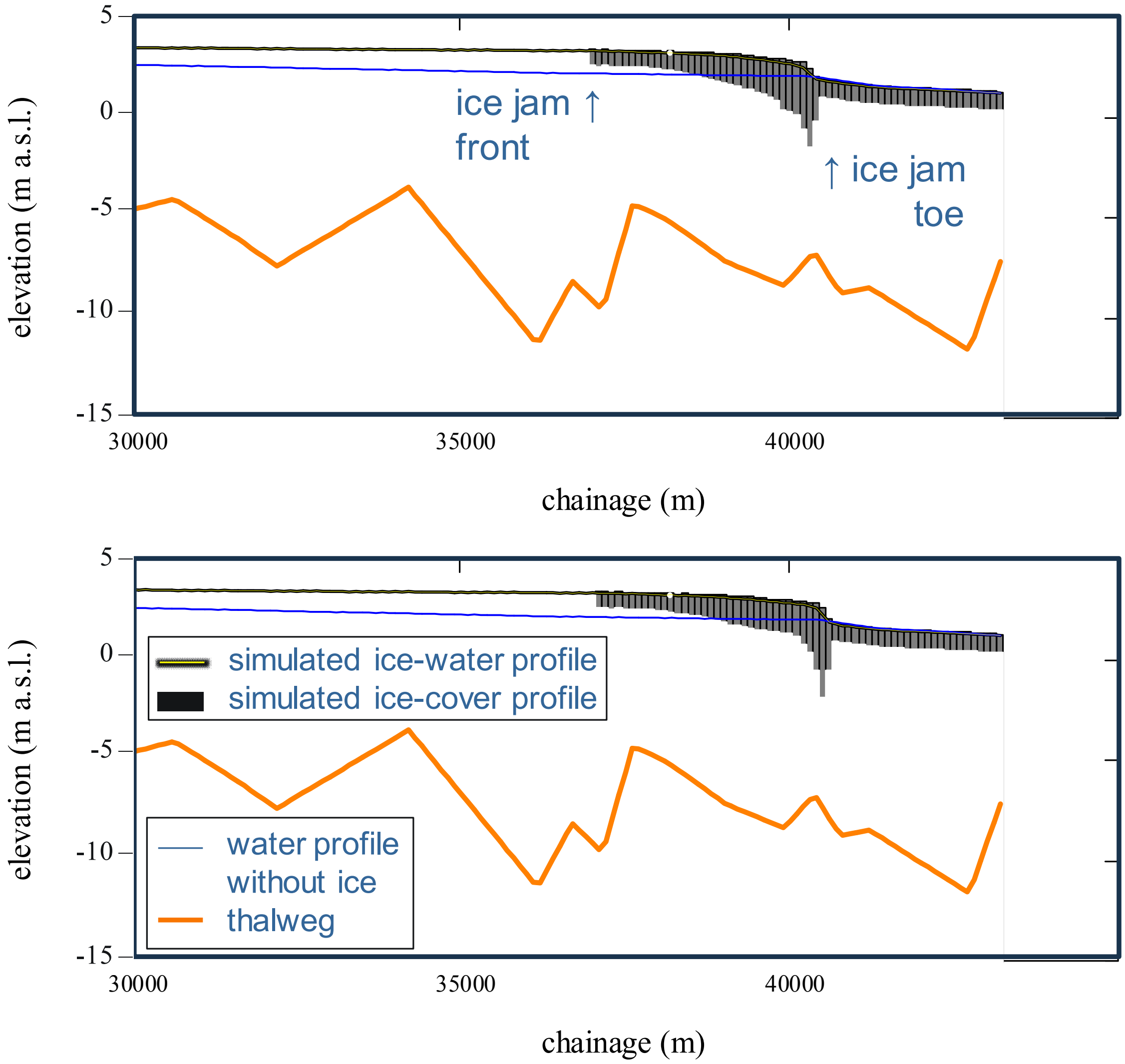

Figure 1. Ice and backwater level profiles of an ice jam along the lower Churchill River, with the same parameterisation and boundary conditions except for the ice-jam lodgement location being 200 m apart.

The stochastic characteristics of ice-jam formation and impacts may be an important reason why many river managers shy away from including ice-jam flooding in their flood forecasting tasks and portfolios. Forecasting "stochastic" ice-jam flooding is far more difficult than forecasting the more "deterministic" open-water flooding, increasing risks and liabilities for the forecaster. However, in northern cold-region rivers, the most extreme flood events and ensuing damages are often caused by ice jams (Rokaya et al., 2018a). For example in New Brunswick, approximately 40% of all floods and 70% of direct damages are caused by ice-jam events (Humes and Dubin, 1988). Past ice-jam flood events have led to hundreds of millions of dollars in direct damages, such as the ice-jam flooding along the Susquehanna River in 1988 (Jeffries et al., 2012) and the Yukon River at Galena, Alaska in 2013 (Kontar et al., 2015). Rokaya et al. (2018b) predict that flood magnitudes and severity could increase in the future for some areas due to climate change. Additionally flooding from ice jams can be much "flashier" than open-water flooding for the same river system with jam formation and subsequent rapid rises in backwater levels occurring in a very short period of time (Das and Lindenschmidt, 2019), sometimes within minutes (Lindenschmidt et al., 2019a), making it challenging to coordinate emergency response such as the implementation of flood mitigation measures or initiating evacuation procedures. Hence, forecasting ice-jam events and their flood hazard and risk is pertinent for many northern riverside communities.

To the authors' knowledge, very few attempts have been made to place ice-jam flood forecasting capabilities in an operational context. We stress "operational" since there are many studies in which ice-jam occurrences have been predicted through hindcasting exercises or in the context of climate change research. This paper introduces the implementation of a novel ice-jam flood forecasting methodology, based on the Monte Carlo analysis technique, into the operational real-time flood forecasting system for the Churchill River in Labrador.

2. Study site

The (Atlantic) Churchill River basin (see Figure 2) is approximately 95,000 km^2 in size and can be delineated into three subbasins: upper basin with the outlet at the Churchill Falls hydro-electric generating station, middle basin with the outlet at the Muskrat Falls hydro-electric generating station and the lower basin with the outlet at tidally-influenced Lake Melville. The areas of upper, middle and lower basin are respectively 72,100 km^2, 20,300 km^2 and ≈2,500 km^2. The length of the Churchill River from Churchill Falls to Lake Melville is approximately 335 km with an elevation difference of about 138 m (average slope = 0.0004).

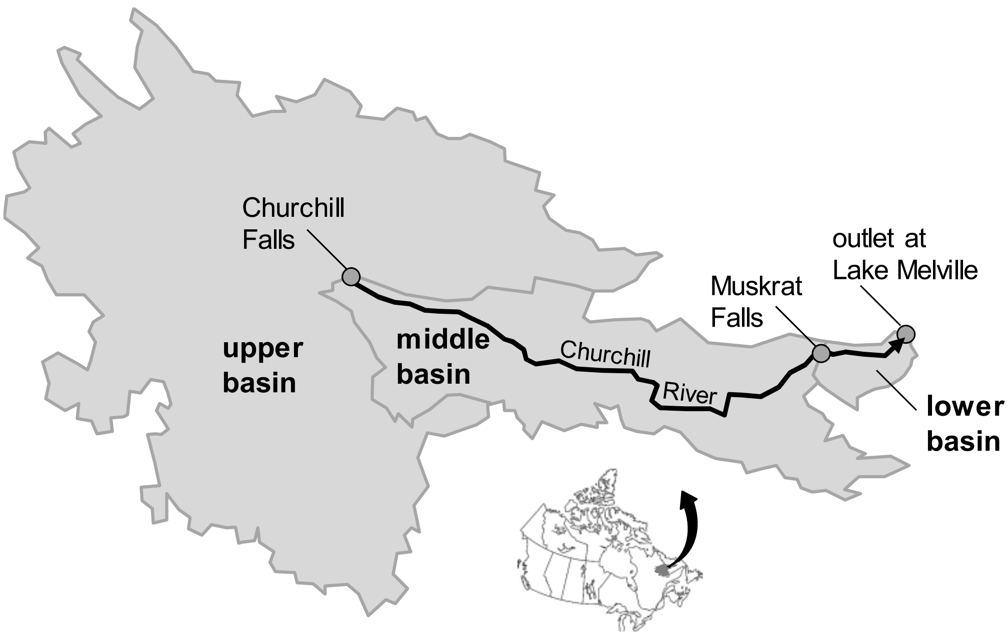

Figure 2. (Atlantic) Churchill River basin delineated into the upper, middle and lower subbasins.

The reach of interest for this study is the lower Churchill River which extends 47 km from Muskrat Falls to Lake Melville (see Figure 3). The average discharge recorded at Muskrat Falls is 1,747 m^3/s (data from 1948 to 2015 extracted from Water Survey of Canada). The river ice modelling domain extends immediately downstream of the falls to Lake Melville. Due to its low slope of the bed, widening of the channel and numerous islands and sandbars, this stretch is prone to ice-jam formation during ice-cover breakup in spring. The area at the mouth of the river is an inland delta making the settlements at Mud Lake and the Mud Lake (boat) access point particularly vulnerable to ice-jam flooding. The most extreme ice-jam flood event on record occurred in May 2017 which saw many properties at the settlements flooded requiring its residents to be evacuated.

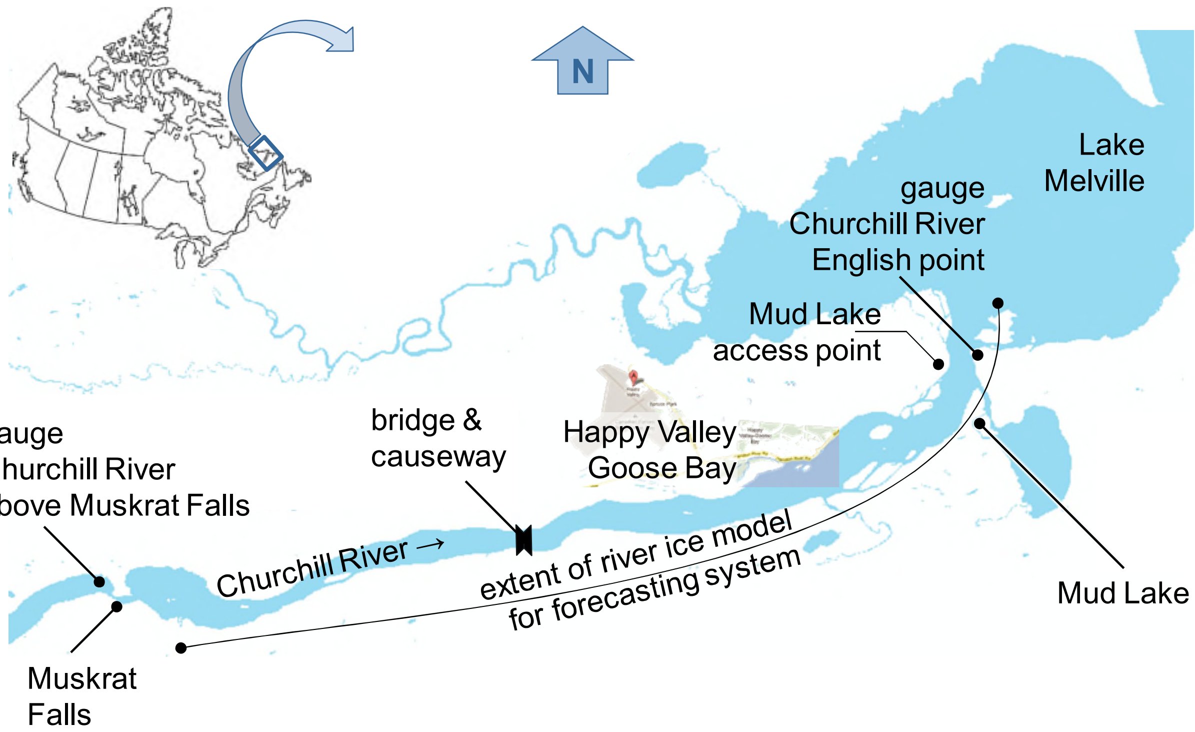

Figure 3. Lower Churchill River with modelling domain (adapted from Lindenschmidt, 2020)

3. River ice hydraulic model

The river ice hydraulic model RIVICE (Lindenschmidt, 2020) was used to simulate wide-channel ice jams along the lower Churchill River. RIVICE is a one-dimensional hydrodynamic model with river ice processes loosely coupled to the water flow simulations. For wide-channel jams, the forces exerted on the ice jam are tracked throughout the simulations. The forces include (refer to Figure 4):

- thrust F_T of the water flowing against the ice-jam cover front,
- drag F_D created as the water flows along the underside of the ice cover,
- component of the jam ice weight F_W in the sloping direction,
- friction F_F between the ice cover and the river banks and
- internal resistance F_I created by the thickening of the ice jam.

When $F_T + F_D + F_W > F_F + F_I$, the ice in the jam shoves in the downstream direction to thicken the ice (telescoping). The shoving and thickening increases F_I and persists until $F_T + F_D + F_W < F_F + F_I$. Shoving ceases and the rubble ice arriving at the ice jam abuts against the ice-cover front and accumulates to extend the ice cover in the upstream direction, a process known as juxtapositioning.

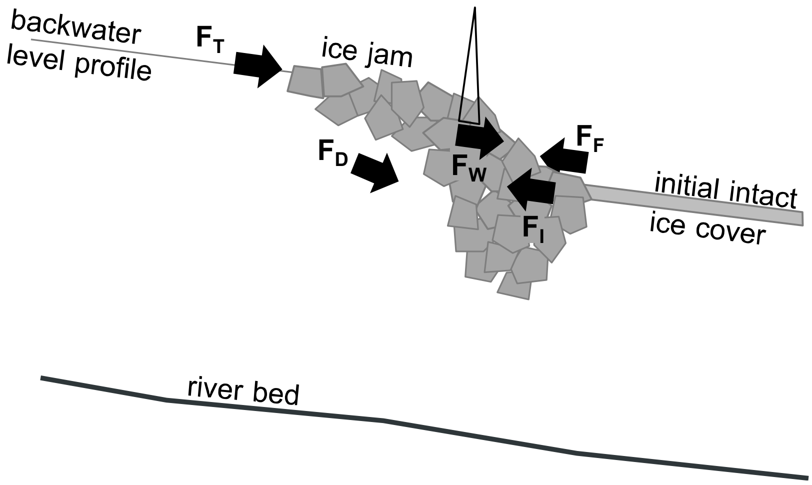

w

Figure 4. Forces applied to a wide-channel ice jam.

Several parameters (Figure 5) control the formation of the ice jam and cover including:

- porosity of the incoming ice floes and the ice-jam cover, respectively *PS* and *PC*,the thicknesses of the ice floes, ice-jam cover front and the intact ice cover downstream of the ice jam, respectively *PT*, *FT* and *h*,
- coefficients describing the roughness of the underside of the ice cover and the river bed, respectively n_{8m} and n_{bed},
- thresholds of the flow velocity above which ice erodes from the underside of the ice cover v_{er} or below which ice in-transit deposits onto the ice cover v_{dep} and
- coefficients controlling the transfer of longitudinal forces laterally to the banks *K1TAN* (determines the magnitude of the friction forces along the bank F_F) and vertically through the thickening ice of the jam cover *K2* (determines the magnitude of the internal resistive force F_I).

Boundary conditions (Figure 5) also influence the formation and morphology of the ice jams. These include:

- flow of water *Q* into the upstream boundary of the model domain,
- flow of ice V_{ice} into the upstream boundary of the model domain,
- water level elevation *W* at the model domain's downstream boundary and
- location of the ice-jam lodgement *x* along the model domain.

4. Stochastic modelling framework

Once calibrated, the model was inserted in a Monte-Carlo framework to allow stochastic simulations in which the model can automatically be run many 100s of times with each simulation having a parameter and boundary condition setting randomly selected from appropriate frequency distributions (Lindenschmidt et al., 2019b, Lindenschmidt, 2020). This yields an ensemble of backwater level profiles from which probabilities of backwater staging exceedances can be determined.

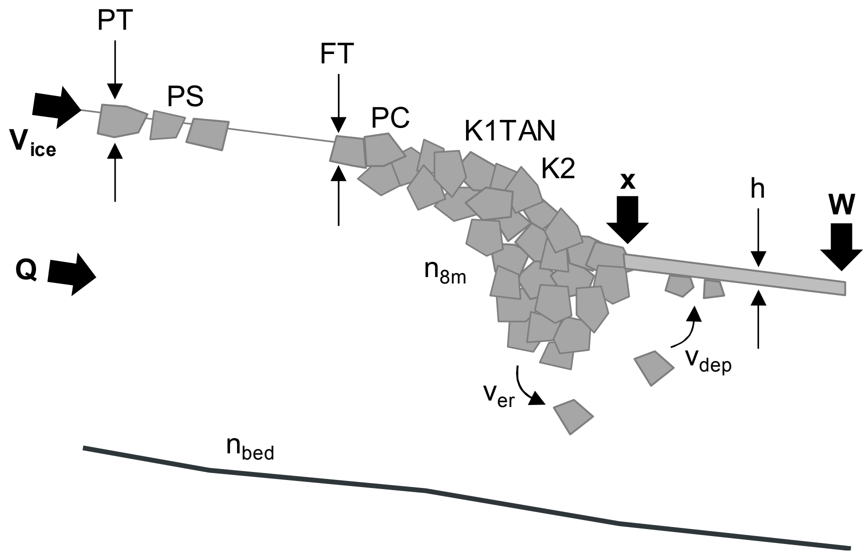

Figure 5. Parameters (normal font) and boundary conditions (bold font) controlling the formation and morphology of an ice jam.

Figure 6 depicts this Monte-Carlo methodology. At the top of the figure are histograms representing probability frequency distributions of the boundary conditions: upstream inflow Q, downstream water-level elevation W, location of the ice cover front x and the inflowing volume of rubble ice accumulating at the ice-jam lodgement V_{ice}. Either extreme value or uniform functions are used for the distributions, depending on the data richness. Parameter values (not shown) are typically extracted from uniform distributions. Many model runs are executed with parameter and boundary condition values extracted randomly from the frequency distributions. Many simulations produce an ensemble of backwater level profiles, shown in the bottom of Figure 6. The 10th, 50th (median) and 90th percentiles are then extracted to determine probabilities of overbank spill and hinterland flooding.

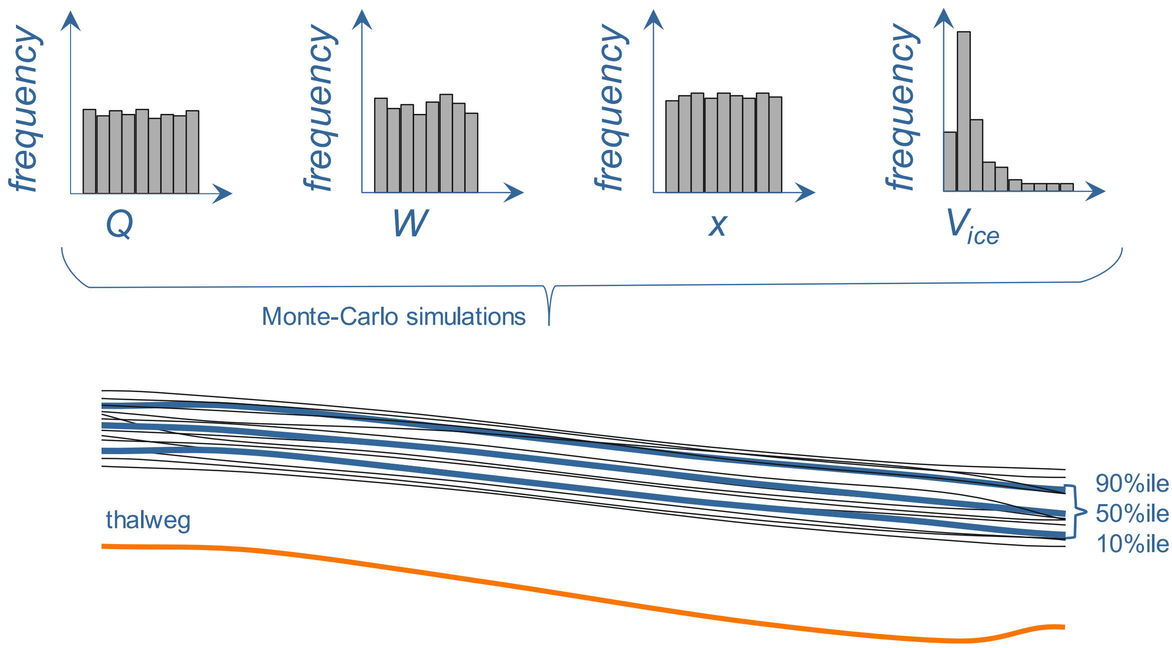

Figure 6. Conceptualisation for the ice-jam flood forecasting component.

5. Model Forecast Implementation

Ice-affected forecasts were carried out with RIVICE daily. Discharges for the next three day at Muskrat Falls, simulated from the HEC-HMS hydrological model, served as input for a range of discharges in the RIVICE model. Ice thicknesses were extracted from field surveys and instrumentation and, along with ice-cover extent extracted from satellite imagery, provided estimates of the volume of ice that could form an ice jam along the lower river stretch. RIVICE was then executed 50 times with different boundary conditions and parameters settings, selected randomly from frequency distributions. This provided an ensemble of 50 backwater level profiles, from which exceedance probabilities along the river banks could be placed within a probabilistic context.

6. Flood forecasting system

Screen shots of the Churchill River Flood Forecasting System (CRFFS) are shown in Figure 7 and Figure 8. The shots were acquired on 11 May 2019 during operational forecasting of ice-jams during the 2019 spring breakup event. Figure 7 shows the dashboard with real-time information in the top row "Process Status and Notification" providing current water levels (stage), flows and temperature and ice thicknesses at the time of the forecast. The middle row indicates the "Forecast Data" with predictions on water levels and flows over the course of the next three days (11, 12 and 13 May 2019). The bottom row provides a suite of "Watershed Environmental Maps" with total accumulated precipitation over the past 48 hours, air temperature forecasted 48 hours in the future and the ice coverage along the lower river reach.

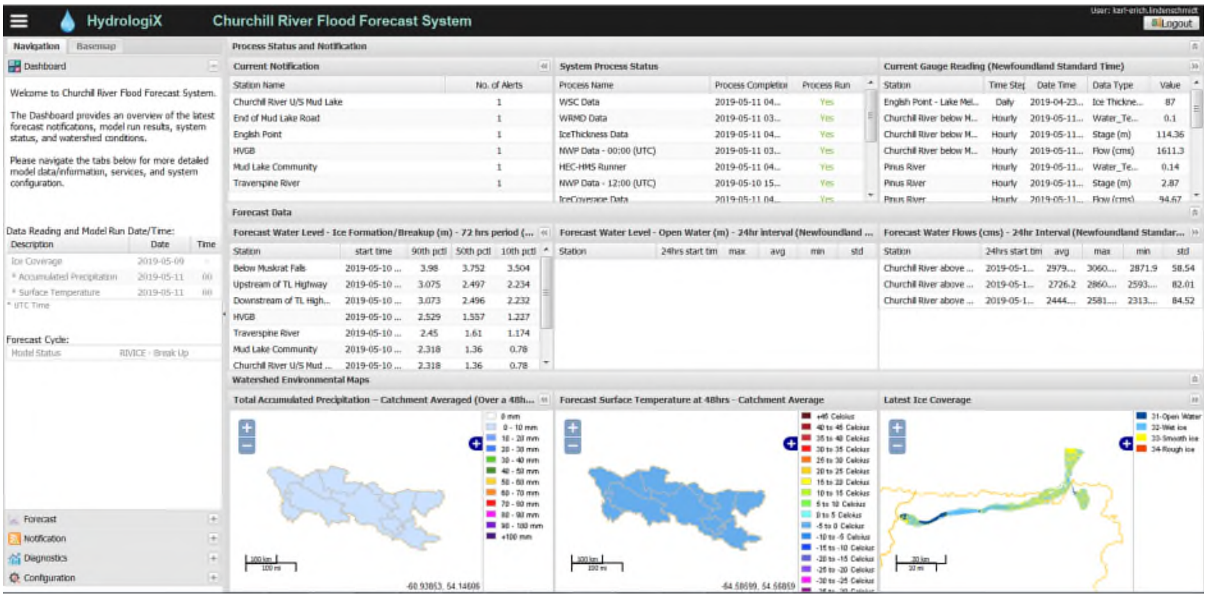

Figure 7. Dashboard of the Churchill River Flood Forecast System for operation forecasting on 11 May 2019.

Figure 8 shows forecasted model results for the following three days (11 – 13 May 2019). The top right window panel labelled "Flow Forecast" displays the forecasted flows for the lower Churchill River acquired from the HEC-HMS hydrological model. Different gauge locations can be selected from the dropdown "Select" button at the far left – the results are displayed for gauge 03OE017 at "Mud Lake Community". The window panel "Station Forecast Ice Affected Water Levels" indicates the 10th, 50th and 90th percentiles of the backwater level elevations summarized from the RIVICE ice-jam model ensembles. Juxtaposed for comparison are the observed water levels at the selected gauge, the elevations of the right and left bank at that river station, along the lowest levee crest elevation at the immediate vicinity of the river station. Longitudinal profiles of the percentile water levels are superimposed with the profiles of the left and right bank levee crest elevations on the bottom window panel, providing a quick overview of potential overbank flow and hinterland flood sites.

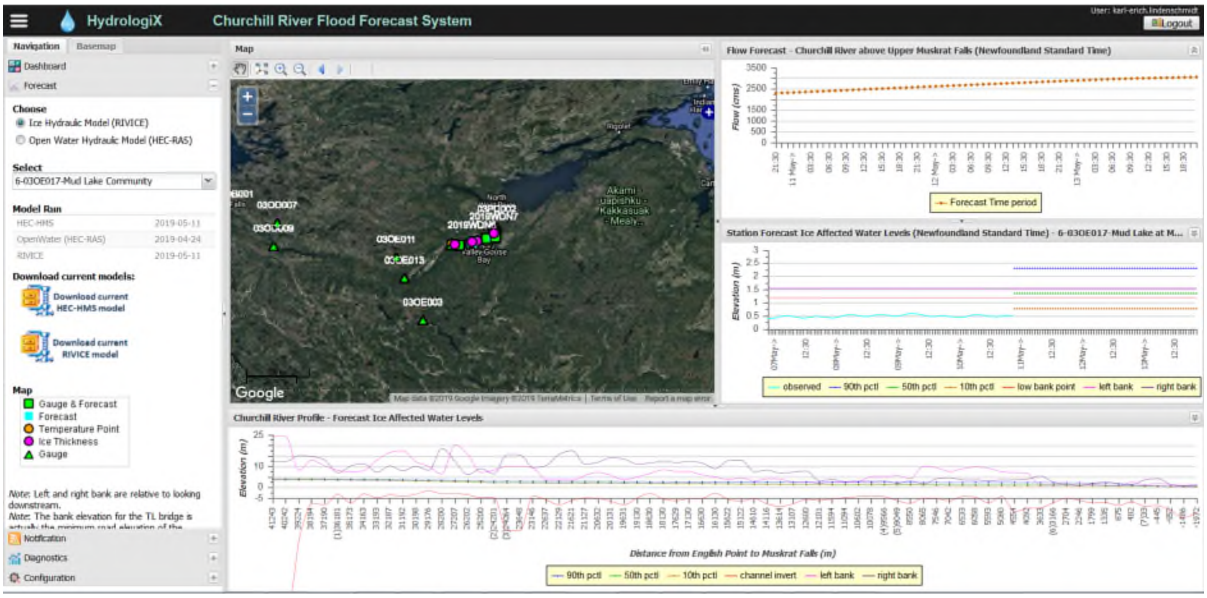

Figure 8. Forecast window of the Churchill River Flood Forecast System for operational forecasting on 11 May 2019.

7. Conclusions

The first worldwide fully-operational fully-automated real-time ice-jam flood forecasting system was successfully developed and implemented. The system has also been successfully utilised to form flood maps for annual exceedance probabilities of 1:20 and 1:100 years for ice-jam floods (not open-water floods, which are calculated separately).

In additional to flood forecasting, "expressing potential flood outcomes as exceedance probabilities provides many opportunities for flood management applications. Probabilities define flood hazard and are an important basis for flood risk assessment, in which expected annual damages can be quantified for communities prone to ice-jam flooding. A prediction in terms of a probability can also flow into cost-benefit analyses to better distinguish between cost-effective flood management and mitigation options. Expressing professional opinions in probabilistic terms ... allows better management decisions to be made ... for flood forecasting and mitigation. For example, a 20% exceedance of a flood level threshold may concentrate personnel and resources to focus on flood mitigation measures, whereas a 90% flood exceedance prediction may require these resources to be diverted to carry out evacuation protocols of the flood management plan." (Lindenschmidt, 2020, pp. 6-7).

References

Das, A. and Lindenschmidt, K.-E. (2019) Predicting rates of water-level rise for ice-jam flood hazard assessment. CGU HS Committee on River Ice Processes and the Environment 20th Workshop on the Hydraulics of Ice Covered Rivers, Ottawa, Ontario, Canada, 14-16 May 2019. http://www.cripe.ca/docs/proceedings/20/Das-Lindenschmidt-2019.pdf

Humes, T.M. and Dublin, J. (1988) A comparison of the 1976 and the 1987 Saint John River ice jam flooding with emphasis on antecedent conditions. Proceedings of the 5th workshop on Hydraulics of River Ice / Ice jams, Winnipeg, Manitoba, 22 – 24 June 1988. pp. 43 – 61. http://cripe.ca/docs/proceedings/05/Humes_Dublin_1988.pdf

Jeffries, M. O., Morris, K. and Duguay, C. R. (2012) Floating ice: lake ice and river ice. Satellite image atlas of glaciers of the world-state of the earth's cryosphere at the beginning of the 21st century: glaciers, global snow cover, floating ice and permafrost and periglacial environments. U.S. Geological Survey Professional Paper 1386-A, https://pubs.usgs.gov/pp/p1386a/

KGS (2018) Climate change flood risk mapping study and the development of a flood forecasting service: Happy Valley - Goose Bay. Proposal for engineering services KGS Group 18-000-0648. May 2018.

KGS (in prep.) Climate change flood risk mapping study and the development of a flood forecasting service: Happy Valley - Goose Bay and Mud Lake (final report). Prepared by KGS Group for the Water Resources Management Division of the Government of Newfoundland and Labrador.

Kontar, Y., Bhatt, U., Lindsey, S., Plumb, E. and Thoman, R. (2015) Interdisciplinary approach to hydrological hazard mitigation and disaster response and effects of climate change on the occurrence of flood severity in central Alaska. Proceedings of the International Association of Hydrological Sciences 369: 13–17. https://www.proc-iahs.net/369/13/2015/piahs-369-13-2015.html

Lindenschmidt, K.-E. (2020) River ice processes and ice flood forecasting – a guide for practitioners and students. Springer Nature Switzerland AG. 267 pp. https://doi.org/10.1007/978-3-030-28679-8

Lindenschmidt, K.-E., Carstensen, D., Fröhlich, W., Hentschel, B., Iwicki, S., Kögel, K., Kubicki, M., Kundzewicz, Z.W., Lauschke, C., Łazarów, A., Łoś, H., Marszelewski, W., Niedzielski, T., Nowak, M., Pawłowski, B., Roers, M., Schlaffer, S. and Weintrit, B. (2019a) Development of an ice-jam flood forecasting system for the lower Oder River – requirements for real-time predictions of water, ice and sediment transport. Water 11: 95. https://dx.doi.org/10.3390/w11010095

Lindenschmidt, K.-E., Rokaya, P., Das, A., Li, Z. and Richard, D. (2019b) A novel stochastic modelling approach for operational real-time ice-jam flood forecasting. *Journal of Hydrology* **575**: 381–394. https://dx.doi.org/10.1016/j.jhydrol.2019.05.048

Lindenschmidt, K.-E. (2017) Independent Review of the 17 May 2017 Churchill River (Labrador) Flood Event. Report submitted to the Government of Newfoundland & Labrador. http://www.mae.gov.nl.ca/waterres/flooding/Lindenschmidt_review_all.pdf

NFLD (2018) Climate change flood risk mapping study and the development of a flood forecasting service: Happy Valley - Goose Bay. Request for proposals. Issued for 2018-19 by the Water Resources Management Division, Government of Newfoundland and Labrador. https://www.mae.gov.nl.ca/waterres/flooding/RFP_HVGB-ML.pdf

Rokaya, P., Budhathoki, S. and Lindenschmidt, K.-E. (2018a) Ice-jam flood research: a scoping review. Natural Hazards 94(3): 1439–1457. https://dx.doi.org/10.1007/s11069-018-3455-0

Rokaya, P., Budhathoki, S. and Lindenschmidt, K.-E. (2018b) Trends in the Timing and Magnitude of Ice-Jam Floods in Canada. Scientific Reports 8: 5834. http://dx.doi.org/10.1038/s41598-018-24057-z

15
Ice and hydropower

25th IAHR International Symposium on Ice
Trondheim, 23 - 25 November 2020

The ice skimming spillway on the new intake for Laxá Power Plant III – North Iceland

Hörn Hrafnsdóttir
Verkís Consulting Engineers
Ofanleiti 2, 103 Reykjavík, Iceland
Faculty of Civil and Environmental Engineering
University of Iceland
hhr@verkis.is

The Laxá Power Plant III is a 14 MW run-of-the-river plant from 1973, that uses the dam constructed in 1939 for the Laxá Power Plant I. The power plant experienced severe operational and abrasional problems due to ice and sediment transport. In 2016/17, the dam and intake were rebuilt to reduce the operational problems.

During the problem analyzing phase, it became clear that the sediment transport is most likely highly linked to the ice slush transport, or more precisely, the resulting ice formations that increase sediment transport capacity considerably. This showed the importance of keeping the intake pond clear of ice formations.

The new design features a new outer intake with ice skimming spillway above it and two small sediment traps at the bottom. This paper covers the design considerations for the ice skimming spillway, the velocity within the intake pond, the location of the ice skimming spillway, the formation of the design and areas chosen for supercritical flow. The design time was limited, and no physical model tests were carried out. The design relied on observation of photos and videos of ice transport at the site, as well as knowledge on ice behavior and information from various papers and experience from other sites on ice skimming. Due to this the paper also covers a comparison of the ice skimming facilities at Búrfell Power Plant (built 1969) and the new ice skimming spillway at Laxá Power Plant III (2017).

The experience after the first two years in operation was good, even though the ice skimming did not always function due to ice accumulation upstream of the spillway. No operational problems due to ice and sediment around the intake area affected the power production during the first two winters. Some sand and stones still passed through the machinery but very little compared to before. The winter 2019-2020 was extreme in north Iceland, including conditions where the Laxá became porridge like due to ice slush. Such conditions were outside the design scope.

1. Background

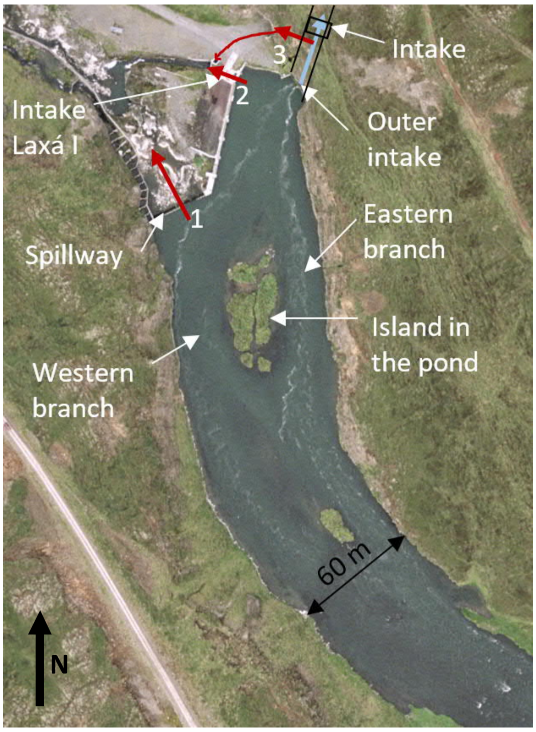

Figure 1. Aerial photo of the intake pond for Laxá III before 2016. Blue arrow: discharge to Laxá III. Red arrows: paths possible for ice flushing.

The Laxá Power Plant III, here after called Laxá III, is a run-of-the-river plant that uses a dam constructed in 1939 for a smaller power plant, Laxá I. Laxá III was commissioned in 1973 as the first phase of a bigger hydropower scheme. The second phase, including a big dam that should have raised the water level some 45 m creating a reservoir of 60,000,000 m^3, was never constructed due to the first major environmental protests in Iceland. This resulted in continuation of already well-known operational problems due to ice and sandtransport. The old dam only raised the water level about 3 m upstream of the dam. Under most operating conditions the top of the outer intake for the intake tunnel was above water. The dam was located within a relatively steep and narrow canyon, see Figure 1, creating a very small pond with volume of about 30,000 m^3. The sand transported to the Laxá by its tributary, the Kráká, is of the same order of magnitude (volume) per year and accumulated ice produced and carried by the river to the Laxá III site, can, during very cold spells, reach the same order of magnitude in only a few hours. The climate in Iceland is more temperate than would be expected this far north due to the North Atlantic Current and the landscape is very barren. The winters are relatively mild in temperature and there are continuous cycles of freeze-up and break-up periods throughout winter. The wind plays more active role than in most places as it both influences the temperature when ice starts to form in the rivers and adds huge amounts of snowdrift to the rivers. For this reason the operation of hydropower plants in Iceland can be challenging throughout the winter.

Following the environmental protests, the Laxá and Lake Mývatn, where the river originates, were protected by special laws in 1974. These laws allow no discharge or water level changes within the river. Attempts had been made a few times to get an exemption from the laws to heighten the old dam by a few meters (10 to 12 m) as it would improve ice and sediment conditions. In 2014 further attempts were considered futile and work started on finding ways to lessen the operational problems within the law's framework. The main aim was to lower the sand transport through the machinery and to implement the changes parallel to scheduled work on the turbine, starting in May 2016. The budget for research and new construction/ equipment was limited so all available sources of information had to be used. Many operational problems had been documented at the station and some research papers are available on the Laxá and Lake Mývatn. Before the construction of Laxá I in 1939, the mayor of Akureyri visited numerous farmers along the river in July 1936 to document their knowledge of the ice in the river (Steinsen, S., 1936). Useful information was also found in the documentation of modelling work made for two other Icelandic projects; the Búrfell ice skimming facilities (commissioned in 1970) (Carstens, T., & Tesaker, E., 1966) and the surface flow outlet at the planned Urriðafoss plant (Ágúst Guðmundsson, 2013). The only research made specifically for this study was recording of ice accumulation on the intake pond in the form of pictures taken every two minutes during the winters from 2014 to 2016.

2. The Laxá and the Þjórsá - Laxá III and Búrfell - Similarities and difference

The rivers in question are steep enough to prevent ice cover formation resulting in continuous ice production during cold spells. The frazil slush is not necessarily a problem per se, but it is a building material for other ice formations like wide river ice jams and hanging dams, and they cause head losses and influence sediment transport and can cause clogging of intakes. For this reason, the main aim with the ice skimming at both locations was to tackle the frazil slush during "normal" winter conditions. Other ice induced problems are present but not of the same magnitude.

On average, the ice skimming facilities, upstream of the Búrfell intake pond, worked well in the past. If, though, ice cover started to form upstream of the ice skimming facilities, it grew quickly as a combination of wide river ice jam and hanging dam. The formation narrowed the usable cross section for water discharge. This increased water velocity and soon the frazil slush was transported into the diversion canal and into the reservoir. There, it became a building material for a hanging dam within the reservoir, reducing the available stored water for diurnal fluctuations and increasing the possibility of blocking the path to the intake for the Búrfell power plant. Upstream of the diversion structure, ice jam formation sometimes grew a few kilometers upstream. If severe, the river bypassed the power station completely (Maríusson, Freysteinsson & Elíasson, 1975).

In Laxá III the problems are slightly different. The amount of sediment transported to the Laxá, mainly sand grains, is relatively stable throughout the year. The average velocity from Lake Mývatn to the intake pond is 1.3 m/s so the sand is steadily transported downstream. The bay, Birningsstaðaflói, is an exception. It is a shallow basin over 1 km in length located about 5 km upstream of the intake pond with estimated water volume of 100–200,000 m^3. It is a known location for ice jam formation according to both Sigurjón Rist (1979) and Hólmgeir Hermannsson (2014). The velocity is low enough for ice and sediment accumulation; thus, it must act as a big sediment trap when no ice is present and then change into a "flushing bay" when ice formations change the flow regime. This interaction between the two medium, sand and frazil slush, is caused by the difference in settling/erosion velocity, which is around 0.5 m/s for the sand and likely to lie in the range of 0.6–0.9 m/s for the frazil slush according to Ashton (1986). The same interaction between sand and ice should also take place within the intake pond and tunnel for Laxá III as the water velocity within the tunnel is low enough for accumulation of sand and frazil slush. The volume available for sand and ice accumulation within the intake tunnel and intake pond is relatively small, but the effects are very important. A fully formed ice accumulation forms quickly allowing the incoming frazil slush to flow under the upstream end of the ice formation. It, along with transported sand from upstream and the additional sand eroded from the bottom due to the increased water velocity, is then transported through the intake, into the tunnel and through the power plant, including the turbines. This shows the need for keeping the intake pond and tunnel free of ice formations.

Despite the difference between Laxá III intake pond and Búrfell diversion structure, the purpose is the same and the small pond in front of the diversion at Búrfell is actually not so small when compared to the narrow Laxá Canyon. The average discharge is about 44 m^3/s in the Laxá and tested discharges in the model with ice for Búrfell ranged from 100–300 m^3/s. The width of the rivers at the sites in question, is mostly in the range of 35–70 m in Laxá and in the range of 300–340 m in the Þjórsá, so the unit discharge covers a similar range.

3. Lessons learned from model tests for Búrfell

Búrfell was designed by Harza Engineering Company International, and the model tests were made at the River and Harbour Research Laboratory at the Technical University of Norway in Trondheim. A schematic drawing of the final layout of the diversion structure is given on Figure 2 along with a section through the diversion inlet. The original design from Harza was slightly different. Carstens and Tesaker (1966) report that polyethylene grains, 2–6 mm in diameter, with specific weight of 0.92 were used and “the material was found to reproduce the motion of “passive” ice to satisfaction.” According to Gunnar Sigurdsson (1970) the model tests showed a tendency of an ice bridge formation if the water level was too high upstream of the intake. The prototype was not as vulnerable to this behavior as the actual ice formed shear zones, allowing the movement of thicker ice flow than could be modelled. The bridging tendency in the model was mainly due to the interlocking between the polyethylene grains that prevented the formation of shear zones. Still, in the prototype the balance was very delicate so the tendency for ice bridging was always lurking.

a)

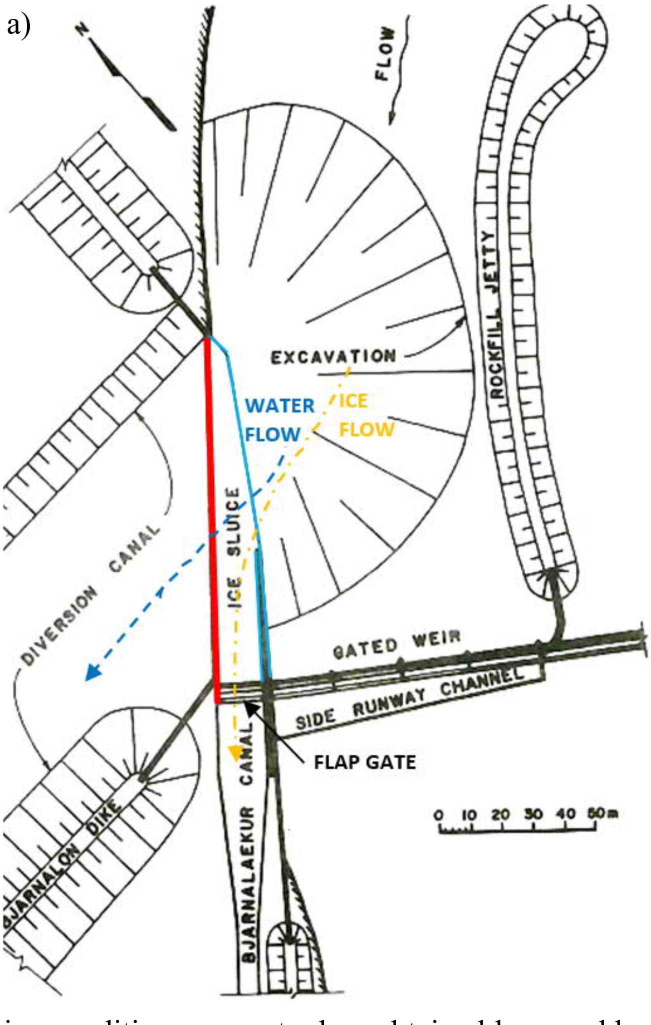

b)

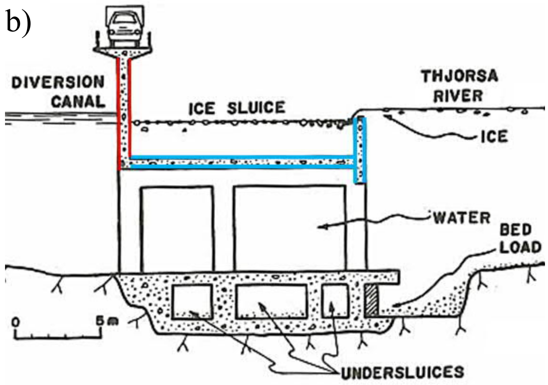

Figure 2. The diversion structure at Búrfell. a) Plan view; b) section through the diversion inlet. (Gunnar Sigurdsson, 1970).

Carstens and Tesaker (1966) gave some general design rules that emerged from the model tests. They include; not too low velocities to avoid irregular ice movement or ice bridging; not too high velocities where suspension of ice particles into the water is disadvantageous; sudden changes in flow direction tend to pile up ice and should be avoided at the inlet; sudden velocity reductions increase the risk of ice bridging; accelerations usually improve ice conditions, except when obtained by a sudden decrease in the depth; the necessary flush water to pass ice over the crest is dependent on the rate of ice to be transported, the necessary depth to prevent ice lumps from sticking to the crest, and the need of sufficient surface currents to carry the ice towards the gates.

The original design of the diversion structure from Harza aimed at keeping the upper part of the openings as deep as possible. This is commonly accepted as a good design for intakes leading water from a large reservoir, which is neither the case for Búrfell nor Laxá III.

According to Carstens and Tesaker (1966) the model tests showed that this was not an important design feature for the diversion structure for Búrfell. Different openings were tested without the ice sluice. The original openings were only 2 m heigh. Increasing the height by raising the upper crest by 4,6 m, did not make a difference. The main issue was to prevent ice accumulation upstream of the wall. If ice started to accumulate it did not matter how deep the openings were, the inevitable intrusion of frazil slush was only slightly delayed if the openings where deeper. This is very understandable when the accumulation is connected to the buildup of a hanging dam.

The original design did not include an ice sluice (colored blue on Figure 2), only a diversion wall above the intake openings (colored red on Figure 2). It was supposed to divert the ice towards a flap gate located at the end of the wall, leading into the Bjarnalækur canal. Two processes proved difficult; firstly, diverting the ice along the wall towards the ice flushing gate and secondly, getting the ice that moved to the gate to pass over it. Regarding the former, the flow path was the main issue. "A velocity component perpendicular to the wall causes the ice to accumulate and gradually build up an ice float in front of the wall, [...] Even a nearly parallel flow direction along the wall does not completely remove the ice accumulation as long as a plain wall like the original design is maintained." (Carstens og Tesaker 1966). Regarding the latter, the depth in front of the gate caused a problem. The sudden decrease in depth drew water from the depth to the surface and the vertical component excluded the surface flow from the flap gate. Adding the ice sluice made all the difference as long as enough water was used (Carstens og Tesaker 1966).

The streamlines within the intake pond were extremely important. Moving the openings away from the ice skimming flap gate (30–40 m) removed a vortex formation in the corner between the two main parts of the construction. The vortex had the ability to suck ice through the inlet (Carstens og Tesaker 1966). A rockfill jetty parallel to the intake wall improved the flow conditions considerably. Both the ice skimming flap gate leading to the Bjarnalækur canal and the gates on the dam were intended for ice flushing even though the ice skimming flap gate was considered the main canal for frazil ice flushing. The gates on the dam worked best if the streamlines were perpendicular to the gates and the depth upstream was kept small to prevent vertical upward water movement (Carstens og Tesaker 1966).

4. The design of the new intake for Laxá III

The old layout of Laxá III had three locations were ice skimming was possible. The first one was the spillway marked 1 in Figures 1 and 3. It was located some 60 m upstream from the outer intake. A good portion of the frazil slush passed over the spillway (26.8 m long) as it is ideally located in the outer bend of the western branch, see Figures 1 and 3. The second was located in the old intake for Laxá I, marked 2 in Figures 1 and 3, were a 4 m wide flap gate for ice skimming had been added. Ice skimming never worked there, most likely because it has a "dead zone" upstream of it as it is located in a corner some 20 m away from the main flow as can be seen on Figure 3. The third is located adjacent to the inner intake but at a 90° angle to the main flow direction, marked 3 in Figure 1. The opening is relatively small, 1.9 m × 2.1 m, with a

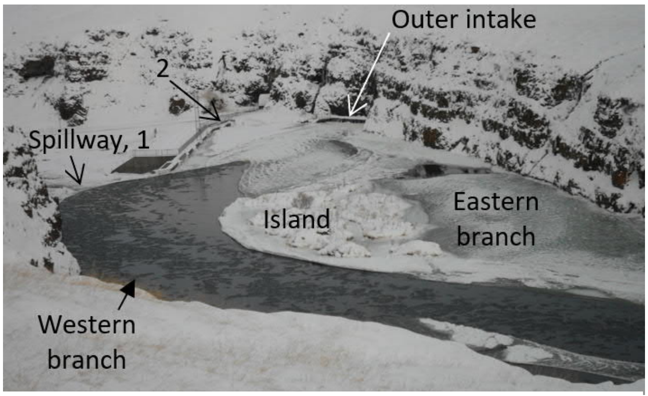

Figure 3. A winter view of the intake pond.

flap gate to control the flow. The reason why a sudden turn does not work for ice skimming comes down to the law of conservation of momentum. It explains why a part of the ice is always transported over the spillway at location 1 (an outer turn and secondary currents induced by momentum) and why the ice is more likely to hit the intake than to take a left turn at the intake at location 3.

During the brain storming time of the refurbishment of Laxá III different designs were considered. Some were too expensive, including flap gates, other focused on deepening the intake pond to create more space, but the amount of frazil slush produced by the river was too much for that idea to work. After consideration of various options, the only solution left was continuous ice skimming as in Búrfell.

4.1 Location

The location of the skimming facility is important. In Búrfell the ice skimming was taken to the upstream end of the intake pond which is not an option within the narrow Laxá canyon. Tuthill (1995) reports that experience from Norway, at Rygene and Fiskumfoss plants, indicated that the key is to locate the ice flushing as close to the intake as possible. The opposite was true for Búrfell, where the conditions were improved by moving the ice skimming some meters away. This indicates that the flow conditions in the pond upstream of the facility play a vital role. The videos of the ice formations on the intake pond of Laxá III were studied. The flow seemed well formed within the branches. Locations where sand settled were mapped as well as locations where frazil ice collected at the surface. The cost was also considered, and it was decided to use as much of the old structures as possible. Based on these studies it was decided to locate the ice skimming as close to the intake as possible. It was also decided to keep the old spillway as a secondary skimming location to lessen the load, keeping in mind that its performance might be enhanced later by adding ice booms or walls to help diverting ice towards it.

4.2 Ice skimming layout and hydraulic design

The first ideas focused on either a diversion wall or an ice sluice channel in front of the intake that would divert the ice towards a spillway north of the intake. The old structure had to be considered and access ensured both to the intake cave and the new construction. Based on the modelling work for Búrfell, a diversion wall was quickly dismissed. The idea of an ice sluice channel, similar to the one at Búrfell, was considered but still considered risky as the ice sometimes stopped within the ice sluice channel and at Laxá III there would be no additional gates on the spillway as backup to help get rid of ice. Two things were considered to be the main cause of ice accumulation in the ice sluice channel at Búrfell. Firstly, the flow took a 90° turn (between intake flow direction and the direction within the ice sluice channel) and secondly, the surface opening through the channel end was much shorter than the length of the surface inflow to the ice sluice channel (the narrow blue line in Figure 2a), increasing the risk of congestion within the ice sluice channel. Similar layout was though chosen for Laxá III but with a huge difference. Instead of using an ice sluice channel above the intake with an apron and similar water level across it, a spillway crown was used instead, that diverts the flow into a side channel, similar to the one used in Búrfell but with much lower water level. The channel then leads the water back to the river. During normal operating conditions, the spillway ensures a transition from subcritical (Froude number, $Fr < 1$) to supercritical ($Fr > 1$) flow at the spillway crown. This transition ensures that the water upstream of the spillway is not affected by the flow downstream of the spillway crown. The approaching frazil slush laden water flowing over the spillway will only be affected by the width of the spillway and the approaching flow, not the narrower channel downstream nor the turn the water is forced to take. To ensure that the ice would not pile up within the channel, the slope of the channel was kept steep enough for a supercritical flow to form in the direction of flow behind the hydraulic jump, see the arrow in Figure 5. The hydraulic jump and the collision with the back wall are intended to smash the ice to pieces and mix the frazil slush well with the water so it can be flushed on with ease. The side channel also has a slight side slope towards the back wall to increase the depth along the wall and facilitate the passage of ice. The river reach from the dam to the tailrace channel is very steep and narrow so all ice passing through the ice skimming facility should be carried on with ease.

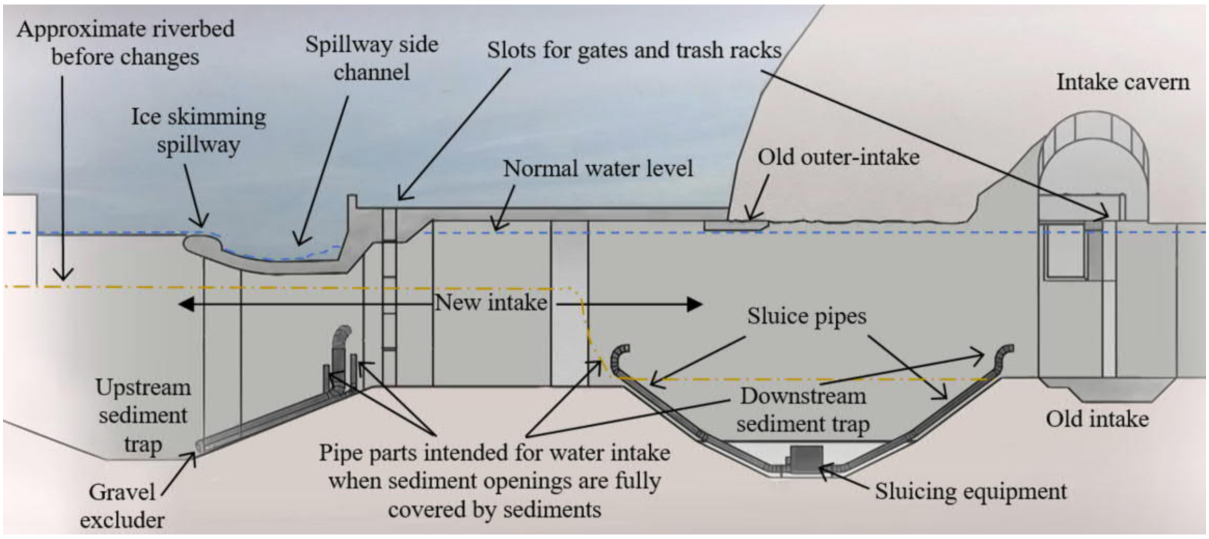

Figure 4. The new outer intake at Laxá III. Flow from left to right. Note: the crown of the spillway is not flat at the top. The longitudinal section of the intake cuts the spillway at 43° angle rather than 90°, skewing the section through the spillway crown.

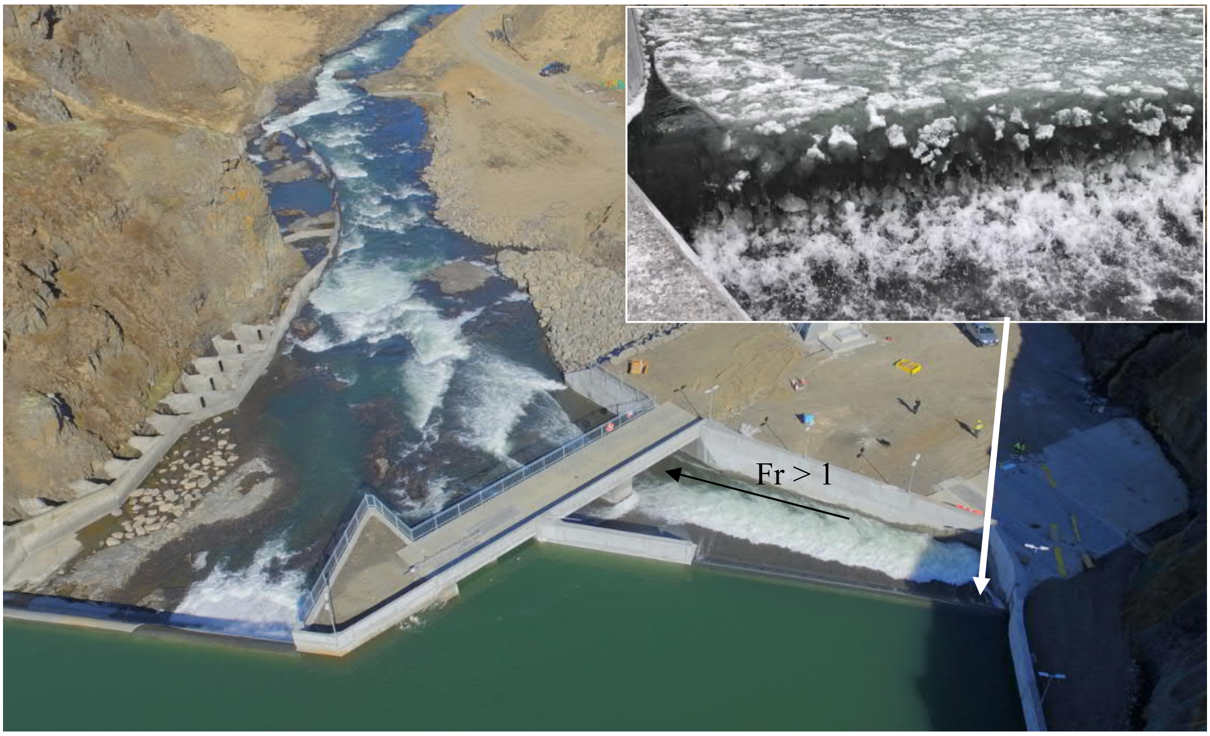

Figure 5. The new construction. Large picture: summer conditions. Corner picture: ice skimming during winter conditions.

Figure 4 shows a section through the new intake and Figure 5 shows a picture of it. The ice skimming spillway is located above the intake and the spillway side channel passes the ice back to the river through the openings in the old dam. The intake opening is 10 m wide, which was considered too short for the ice skimming spillway. Using the path (approximate streamlines) of the main flow in the old intake pond as a guidance and by drawing a line across it from the opening planned for passing the flow back to the river to the opposite side, the length was taken as 22.5 m.

4.3 The formation of the ice skimming spillway crown

Downstream of Búrfell three new hydropower plants are on the drawing table. There, salmon migration is an issue. A specially designed structure called surface flow outlet (SFO) is intended to facilitate the downstream migration of juvenile salmon at the most downstream plant, Urriðafoss. Model tests, (scaled physical model test, carried out at the hydraulic laboratories of the Icelandic Marine Administration, collaboration between Landsvirkjun, the University of Iceland, the Reykjavík University, the Icelandic Marine Administration and the designers; Mannvit and Verkís consulting engineers) and a computer model, have been carried out to optimize the design (Ágúst Guðmundsson 2013). Some design aspects important to the fish also apply to the frazil slush. The juvenile salmon is known to locate itself in the middle of the stream where boundary effects are at a minimum and flow velocities are high. This is not the case for the ice but still the bulk of the ice flow tends to be transported with the main current even though part of it ends up elsewhere due to boundary layers or momentum involvement. The juvenile fish is surface oriented and is known to locate itself in the uppermost part of the water column, just like frazil slush that has been allowed to surface. Dams in rivers can make the salmon disoriented and if their migration is delayed it can affect their mortality (Ágúst Guðmundsson 2013). Similarly, frazil ice can accumulate on the surface if the streamlines or the velocity is unfavorable.

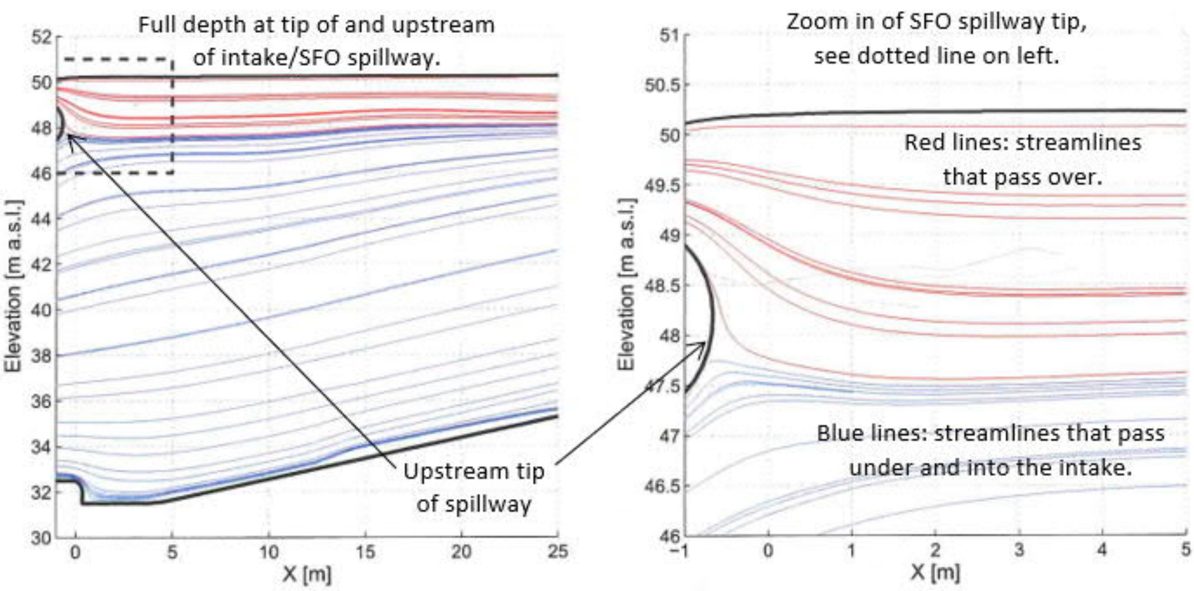

Figure 6. Streamlines. Flow from right to left (Ágúst Guðmundsson 2013).

After studying the report for the SFO it was decided to adopt a part of it for Laxá III, i.e. the design of the spillway crown and the upper most part of the wall/floor/roof separating the side channel and the intake. The spillway crown was scaled down and has a radius of 0.45 m upstream and 0.65 m downstream. The main reason for using this design is that the computer model tests showed very promising streamlines above and under the form, see Figure 6.

These smooth streamlines are likely to minimize risk of accumulation of frazil slush at the spillway, assuming the water level is high enough for the ice to pass over. The upward component of the flow should also help lift the frazil slush over the spillway.

4.4 Design aspects upstream of the ice skimming spillway

Two design aspects are left to discuss for Laxá III; water depth needed at the spillway and how to insure the passage of the frazil slush through the intake pond and to the spillway. Information on the former was not found. Based on videos of the frazil slush in the Laxá, both in the intake pond and downstream, it was estimated that 0.2 m depth on the ice skimming spillway was likely to be sufficient. It was also assumed that a learning period would be needed to find the optimum water level.

Regarding the latter, not much was available except; the idea of smooth streamlines, not too high and not too low velocity, no abrupt changes in direction, velocity or acceleration. The focus was first put on the velocity within the intake pond. The velocity must be high enough to prevent bridging of the incoming frazil slush. This velocity is dependent on the matureness of the ice, the weather or how quickly ice particles at the surface might freeze together, and other factors. In the intake pond for Laxá III the frazil slush is not "developed" as the river is steep just upstream of the intake pond and the ice has only about 200 m to float to the surface and develop before reaching the ice skimming spillway. According to Perham (1983) an ice cover will grow out across the river as if on a small lake if the mean velocity is low (0.15–0.3 m/s), mainly by the horizontal propagation of ice crystals. This of course would not be the case on the intake pond as the frazil slush would be the building material. Still, the same principles could apply, i.e. the ability to bond by freezing between frazil slush particles if the velocity is this low. Some might argue that the distance is short, only 200 m, but this velocity range over a distance of 200 m means a passing time of 11–22 minutes. If the air temperature is below freezing and the wind is blowing, that might be enough time for bonding. This velocity range is unlikely to create strong enough downstream force on the underside of the ice cover to carry the main ice cover downstream (sheer zones).

Perham continues, adding that if the mean velocity is 0.38 m/s or higher, ice cover is formed by accumulation upstream from an ice cover or other obstruction. Furthermore, if the ice floes, here the frazil slush, are numerous and the water velocity not too high the floes will jam mechanically in a neck or narrows of the river and form a stable ice arch. From there, the ice cover will proceed upstream until the velocity becomes about 0.69 m/s or greater, which happens before it would grow up to the upstream end of the intake pond. Based on this it was decided to keep the velocity within the intake pond over 0.38 m/s.

4.5 A deviation from the design criteria

Deepening of the riverbed at the intake entrance was necessary for sediment trapping and sluicing equipment. A smooth excavation was designed from the riverbed down to the trap in both branches. The excavation in the eastern branch was also used as access ramp for the contractor. The ramps became too large to keep the velocity within the design limits. Additionally, they were not as smooth as intended due to difficult tuff layers within the lava. This was not thought of as a major problem as sand would settle on the ramps, smoothen them and bringing the velocity back up to around 0.5 m/s within a reasonably short time. Similarly, for the sediment and ice collection locations identified within the old intake pond, sand is expected to settle at the bottom and frazil ice to cover the surface. Then sheer zones are estimated to form between the stationary ice and the main flow. The velocity needed for the sheer zones to form was though not known.

5. Experience since 2017

No operational problems due to ice and sediment around the intake area affected the power production during the first two winters. The winter 2019-2020 was extreme in north Iceland, including conditions where the Laxá became porridge like due to ice slush. Such conditions were outside the design scope. The ice skimming spillway and the spillway side channel have functioned as intended. The corner figure on Figure 5 shows how the ice skimming spillway works. This was taken during the last phase of construction when a cofferdam covered half of the intake pond allowing only the use of the eastern branch. After the work was finished and both branches were back in operation it happens that ice starts to accumulate on the intake pond. Two different processes causing the initiation of ice cover formation have been caught on video. Based on those the problems are most likely as follows:

- Sometimes the water level is left too low, much less than 0.2 m above the crest, so the incoming ice strands on the spillway. This can be fixed by changing the automation of the turbine.
- Sometimes the surface velocity within the intake pond becomes too low resulting in frazil ice not reaching the spillway. This scenario was caught on video during a northern storm with wind blowing strongly against the flow. At first the frazil slush is carried towards and over the ice skimming spillway. Later, the frazil slush came to a halt some 0.5 to 2 m upstream of the spillway, indicating that the surface velocity became too low.

6. Conclusion

The ice skimming spillway and the spillway side channel have functioned as intended, but more research and some adjustments must be made to the intake pond. Firstly, the water level on the ice skimming spillway must be kept heigh enough for ice skimming at all times. Secondly, the surface velocity within the intake pond has to be increased as it becomes too low during northern storms. It is possible that simple diversion structures, that would divert the flow into the eastern branch in the intake pond, would increase the surface velocity through the intake pond sufficiently. At present no additional work or research has been scheduled since commissioning of the new structure in 2017.

References

Ágúst Guðmundsson, 2013. Model Investigations of a Juvenile Fish Bypass System at Urriðafoss HEP. University of Iceland.

Ashton, G. D., 1986. River and Lake Ice Engineering. Water Resources Publications. Chelsea, Michigan.

Carstens, T., & Tesaker, E., 1966. Model Tests on Burfell Hydroelectric Power Project, Iceland. Vassdrags- og havnelaboratoriet, Oppdrag nr.: 600115. Trondheim.

Gunnar Sigurdsson, 1970. The Búrfell Project. A case study of system design for ice conditions. Proc 1st IAHR Symposium on Ice, Reykjavík, Iceland. 1-18 (4.0).

Hólmgeir Hermannsson, 2014. Interview with Hólmgeir. 23rd of July.

Maríusson, J. M., Freysteinsson, S., & E.B. Elíasson., 1975. Ice jam control. Experience from the Burfell power plant Iceland. Proc 3rd IAHR Symposium on Ice, Hanover, NH. 233–242.

Perham, R. E., 1983. Ice sheet retention structures. CRREL Report 83-30. Hanover, NH.

Sigurjón Rist, 1979. The hydrology of River Laxá. Oikos, 32(1), 271–280.

Steinsen, S., 1936. Steinn Steinsen's interview with farmers along the Laxá.

Tuthill, A. M., 1995. Structural Ice Control. Review of Existing Methods. CRREL Special Report 95-18. Hanover, NH.

25th IAHR International Symposium on Ice
Trondheim, November 23 to 25, 2020

Reducing ice accumulation on Coanda Screen intakes

Leif Lia[1], Hanne Nøvik[2] and Knut Alfredsen[1]
[1]Norwegian University of Science and Technology NTNU, [2]Multiconsult ASA
NO-7491 Trondheim, [2]Nedre Skøyenv. 2, NO-0276 Oslo
leif.lia@ntnu.no, hanne.novik@multiconsult.no, knut.alfredsen@ntnu.no

Abstract
Coanda screen intakes has proved to be a reliable and cost-effective low maintenance solution for numerous small hydro (SHP) intakes in the past two decades. In Norway 50 intakes are installed since 2012, the first intake was at Dyrkorn SHP in western Norway. The concept is based on a fine meshed screen with transverse bars with a spacing from 0,5 – 3 mm, most of installed intakes have a space of 1 mm. The narrow spacing prevent most kind of floating debris to approach the real intake which is placed downstream of the screen. Due to the steep inclination of the screen all floating debris like leaves, grass, branches, ice floes etc will slide on the screen and be deposited on the downstream side of the screen structure. Sediments will be trapped or flushed over the intake screens like debris.

International experience confirms that frazil ice accumulates on the screen itself in various different physical processes. Depending on the details of the screen ice accumulate in different ways and may cause blocking of the intake. This paper describes first the freezing process progress at the intake and how the ice by natural processes release from the intake after some time. Several winters with monitoring at the Dyrkorn intake give unique operational data from the ice accumulation and consequences for the hydropower production. Secondly, this paper describes how a general modification and two new innovations have reduced the ice accumulation on the screen. The innovations concentrate the flow on the intake in periods with low discharge, but the effect from siphoning water from the bottom of the pool may have even more positive effect to the reduced ice problems at the intake.

In the end limitations for Coanda screen intakes will be discussed based on extreme climate conditions.

1. Background

With more than 50 Coanda screen intakes installed for SHP in Norway in the last decade (Lia, 2019), a lot of experience with winter conditions is gained. Modifications like the 'Fossekallen' and the Grizzly intake has been developed, in parallel with smaller improvements developed locally. The Coanda screens cleans themselves with the spilling water and both debris, sediments, fishes etc will pass over the screens. The 'cleaned' water will be dropped down through the horizontal and transverse bars in the screen and enter the main intake basin beneath the screen, se typical layout in Figure 1. Coanda screens have in those years proved to be reliable in most conditions, but still there are challenges to overcome in steep rivers, unregulated discharge and shallow intakes. Field observations indicate that the most severe conditions that create water loss for the intake occur during winter, especially in situations with rapid changes in temperature and discharge. In long periods with low temperatures there is also a tendency that the entire intake may be covered by solid ice and stop functioning. The loss of income in such situation is not significant since the events are corresponding with extremely low discharge in the rivers. This situation is not unique for Coanda screen intakes, also other SHP intakes will experience blocking from solid ice.

With the Coanda intakes approach with self-cleaning and no-maintenance philosophy, extra focus must be made to ensure problem free winter operation. The performance and winter behavior is presented in Wahl (2001) and Nøvik et.al (2014) respectively and little other literature is available on this topic. Thus, monitoring, verification, innovations and proposals presented in this paper is a contribution to make the Coanda screen intakes more efficient during winter times in small and steep rivers.

2. Coanda screen effect in intakes

The Coanda screen effect is well documented and for SHP intakes most recently by Wahl (2001). The horizontal rotated steel bars force the water to be shaved from below, as shown in Figure 1. The Coanda effect will not occur without a required water velocity, and all Coanda screen are constructed with an acceleration section upstream of the screen, as seen in Figure 2.

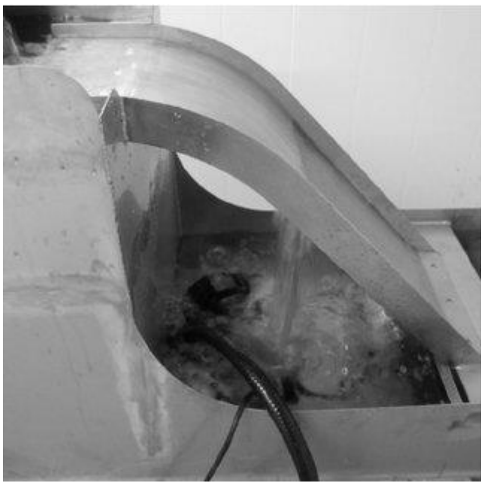

Figure 1 Water extracted by a Coanda full size screen in the laboratory, bar spacing is 1,0 mm.

Figure 2 Water flowing through the screen into the intake basin, full-scale intake at Dyrkorn SHP.

Coanda screens are commercially available from several global suppliers. The screens are made from stainless steel manufactured by robotic welding in narrow sections. For intakes, sections are attached side by side by flanges commonly constructed onto a frame of concrete, as seen in Figure 2.

The distance between the bars may vary from 0,5 – 3,0 mm by various steps. Most commonly used for Norwegian intakes is 1,0 mm. With increasing discharge more and more of the available screen is taken into use and the intake capacity is reached when the entire screen is covered by water, but due to operational issues the intake normally have larger capacity than the power plant, and the intake will start spilling before the screen capacity is fully utilized.
As seen in Figure 1 and Figure 4 most Coanda screens are protected by 'Boulder bars', vertical steel bars between the screens in the flow direction. Those bars will prevent debris like wood, ice floes, large stones etc hitting the screen.

3. Winter effects and freeze-up

Winter effects are described in detail in Nøvik et.al (2014), where the freezing is divided into two processes:

Type I clogging occurs when soft and wet ice slush clog by adhesion to the intake screen, as seen in Figure 3. The ice particles stick to the top surface of the screen and do not enter between the screen wedge wires; hence the screen is more or less open underneath the soft ice cover. Type II clogging is when the screen is so cold that solid ice forms between the wedge wires, Figure 4.

Figure 3 Frazil ice accumulation onto the Coanda screen.

Figure 4 Type II freezing from the boulder bars. The connection between two sections is visible as the double bar to the left.

The cooling of the screen itself is a contributor to the icing processes. With the screen exposed to low air temperatures T_a, wind and radiation from clear sky, cooling of 300 – 400 W/m^2 is to be expected, Ashton (1986). With temperatures in the water upstream of the intake of T_w = -0,02ºC, from Sæle (2019), the frazil ice will be supercooled and sticky along with the intake screen cooled down to temperatures below zero.

Clogging occurs when soft and wet ice slush clog by adhesion to the intake screen. The ice particles stick to the top surface of the screen and do not enter between the screen wedge wires; hence the screen is more or less open underneath the soft ice cover

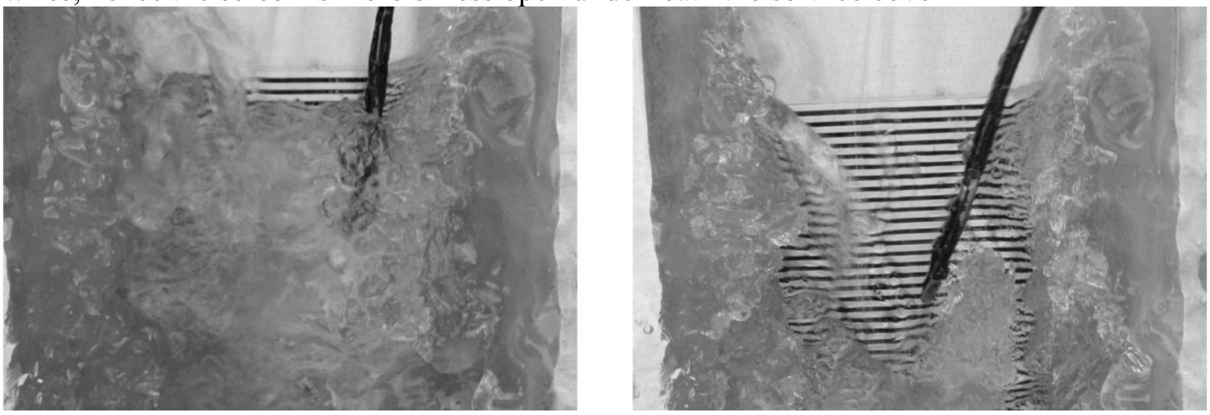

Figure 5 The photos prove that any frazil ice discs penetrated the screen with d = 1,0 mm.

4. Thawing processes on the screen

Approximately half of the Coanda-effect intake screens in Norway has experiences clogging of the intake at least once each winter, NVE (2020). Detailed studies presented in Nøvik et.al (2014), Aal (2018) and Sæle S.D. (2019) verify that the clogging of the intakes is temporary. Most clogging events with drop in energy production have according to Nøvik et.al (2014) a duration of 12 – 24 hours. All nine events recorded from Dyrkorn SHP intake in the winter 2012/2013 ended with a natural thawing process ('self-healing') where the accumulated frazil ice on the screen converted itself to passive slush and water started flowing under the ice cover and into the intake. The phenomenon with reopening is showed on the photos in Figure 6.

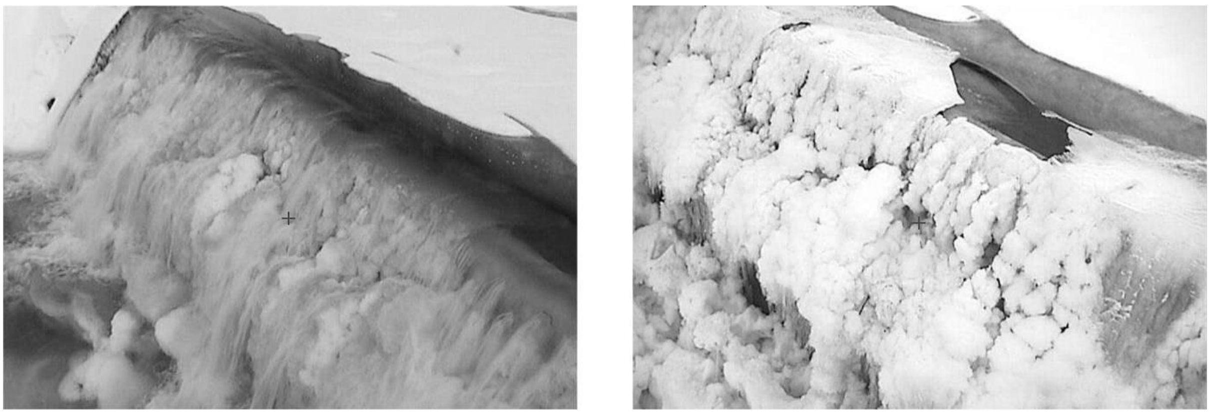

Figure 6 Coanda screen intake when active frazil clogs the intake (left) and the frazil converts to passive and water is flowing into the intake (right), photo: Tafjord kraft

Frazil ice eventually led to a reduced intake capacity or complete blockage of the Coanda screen, but the structure reopened without any intervention after all events of freezing. When the air temperature is low enough, accumulated soft ice on the wedge wires will freeze to a solid ice cover over the screen, and after a while, the water will start to flow under the ice. Since there are no ice particles between the wedge wires, the intake will reopen without any intervention. In Figure 6 the Coanda-effect screen is completely clogged with frazil ice and the water is flowing over the ice. In the picture taken two days later, a solid ice cover is protecting the screen, and the water is flowing beneath the ice blanket and a full flow capacity of the intake is re-established. The cause of the reopening of the screen is not fully understood but a combination of melting caused by the heat flux from the water to the ice particles, mechanical erosion of ice particles by the water flow momentum and the shear forces and uplifting forces from hydraulic pressure on the ice particles seems likely. Based on the data collected in field, the reopening of the Coanda screen, which is confirmed by the startup of the SHP, took place without any intervention for all the complete ice blockage events, and for most of the complete ice blockage cases, 1−10 h after the last measurement of supercooled water. For some of the ice blockage events, supercooled water was measured up to 10 hours after the screen was reopened. It can therefore be deduced that once the frazil ice production stops, after an event of ice clogging of Type I, the screen reopens without any intervention since the spacing between the wedge wires are free from ice. The intake may also start performing again if an ice cover protects the screen from more approaching suspended ice and the clogging ice particles are removed by erosion or melting underneath an ice cover. The ice may also be washed away by an increased water discharge in the river exceeding the screen capacity. Detailed studies at Dyrkorn SHP intake has led to detailed knowledge about the winter performance, Nøvik et.al. (2014). Time series with simultaneous development of different parameters were studied, an example is shown in Figure 7.

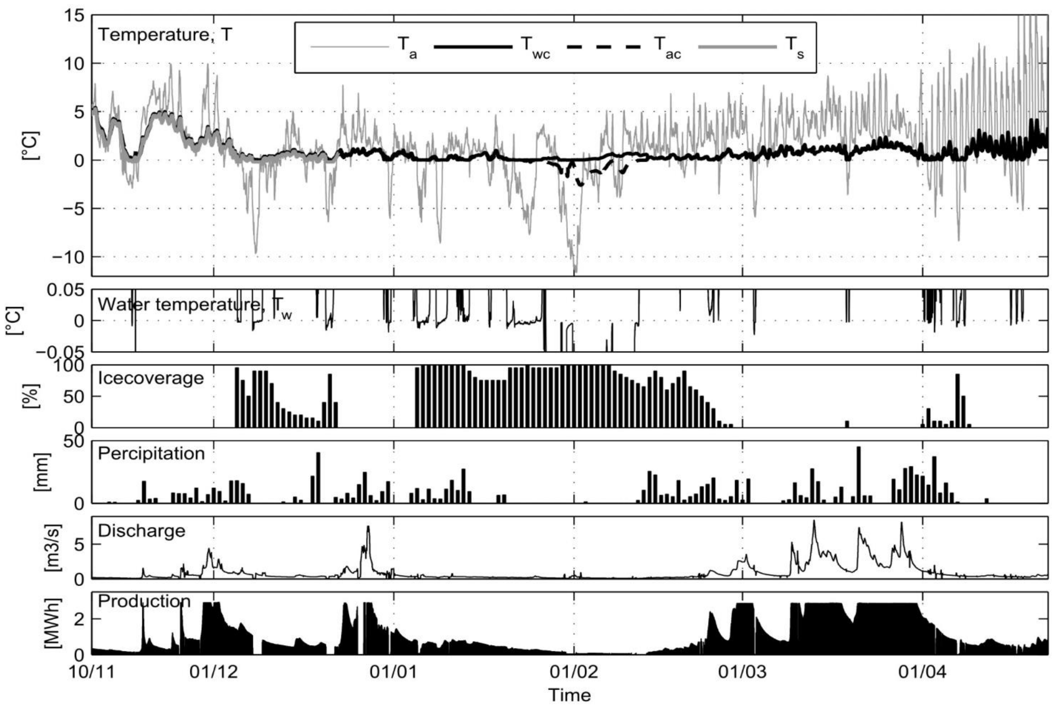

Figure 7 Overview of the hydrologic parameters at Dyrkorn SHP during the winter 2011/2012. Subplots shown in order from top outdoor air temperature and in the chamber, T_a and T_{ac} [°C], water temperature upstream and in downstream chamber, T_w and T_{wc} [°C], temperature on the Coanda screen, T_s [°C], ice coverage [%], precipitation [mm], discharge [m^3/s] and Energy production [MW], from Nøvik et.al. (2014).

These events costs energy production and should be avoided. On the other hand, none of the recorded events in the winter 2011/2012 required any kind of manual cleaning or maintenance. Any damages were registered to the intake structures or to the screen. In practical engineering this will lead to a compromise situation between manual work and loss of energy production. As long as water is spilled, the motivation is there to improve winter performance of the intake.

5. Correspondence between temperature and frazil ice production

To monitor frazil ice accumulation in accordance with temperatures T_a and T_w and energy production P [MW] a SWIPS (Shallow Water Ice Profiling Sonar) from ASL Environmental Sciences is used. The SWIPS profiler is placed on the bottom of the pond and 'shoots' sonar waves under the water surface. The SWIPS records the frazil ice passing in the water column over the unit. A photo of the equipment and a screenshot of one recorded period is shown in Figure 8 and Figure 9.

Figure 8 SWIPS equipment

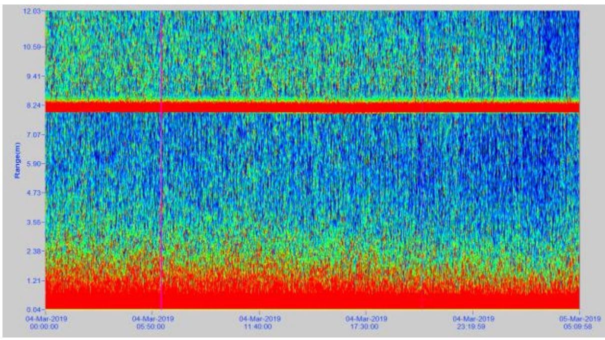

Figure 9 The SWIPS recording shows how particles are fully distributed in the water column from 4. March 2019 – 5. March 2019, from Sæle (2019). The range in the y-axis is in [Feet].

The recording from two winters 2017/2018 and 2018/2019 shows correspondence between temperatures, continuously camera recording, SWIPS data and operation of the power plant. Volumes of ice recorded from the SWIPS will be accumulated at the intake, recorded by the camera. Volumes over a specific amount leads to blocking of the intake and loss of energy production in specified time will be recorded in the power plant governing system. The methodology is presented in Sæle (2019). This methodology is the main content in a warning system for SHP operation with Coanda screen intakes in cold climate.

6. Coanda screen intakes with extreme low temperatures

In regions with low temperatures in long periods low discharge and stable ice covers will follow. In the beginning of the freeze-up period there will be a gap with free water surface between the ice cover and the weir on the Coanda screen. When the discharge is reduced and ice cover in the intake pond reach the weir, solid ice may forms onto the screen. If the discharge in the river/brook still decreases the ice will in few days cover the entire screen. Examples from two different intakes are shown in Figure 10 and Figure 11.

Figure 10 Solid ice cover the intake at Nybuelve river, 2017, the ice is around 300 mm thick

Figure 11 Solid ice cover the intake at Tverråne river, 2017, the top of the boulder bars can be seen in the ice

Formation of solid ice cover onto the intake pond is normally an advantage for a hydropower intakes, preventing further cooling of the water body. For Coanda screen intakes it represents a potential situation for permanent blocking of the intake. Rapid melting of the ice is not expected in melting periods, when the solid ice cover is 0,1 – 0,5 mm thick. Experience through several winters at Nybuelve and Tverråne in Hallingdal has highlighted the risk by using Coanda screen intakes. Severe challenges with ice through the first winters led to a reconstruction of the Tverråne intake, converted into a conventional intake for lower discharges. With higher discharge the Coanda screen will come into use. It is not verified how the reconstructions has increased its winter performance.

7. Innovations to prevent icing

One general principle and two different devices are developed to reduce ice problems: a narrowing of the intake, a snorkel device and a device for the release of environmental flow. All three innovations have been tested at the Dyrkorn SHP intake in the western part of Norway. The innovative solutions are developed by the engineers at Tafjord kraft power company but tested and verified in laboratory and field in cooperation with NTNU.

Narrowing the flow is a commonly used measure to prevent ground icing/aufeis on most structures, channels and natural rivers. On the Coanda screen intake narrowing the weir during wintertime may have two positive effects:

- Reducing the net heat loss from the screen and from the flow over the screen, by using just one specific length of the weir for the same discharge, e.g. increasing the unit discharge q [$m^3/s \cdot m$].
- Introducing stronger current in a narrow section for cleaning of the screen after an icing event.

The disadvantage of the narrowing is that when there are rapid changes between low and high discharges. Ideally the narrowing equipment should be removed before a time period with high discharge, e.g. regular spring floods.

The innovation of **the Snorkel** has been a great contribution and inspiration to improve the performance of the Coanda screen intake during winter time, and is previously described in Lia et.al. (2019). The idea of a Snorkel came up in Opaker (2012) and the Snorkel is a siphoning device to discharge water from the depth in the intake pool, where there should ideally be less super cooled water and frazil ice particles than in the upper part of the water column. The Snorkel should also protect the upper part of the intake screen from snow and ice, Opaker (2012). The power company Tafjord kraftproduksjon AS developed and installed a prototype of the Snorkel at Dyrkorn power plant in 2016. The prototype was manufactured from 10 mm thick sheets of PE (polyethylene). Further, monitoring of the prototype showed that the snorkel fetched water from 1.8 meters depth, and that it fully covered the crest in the crest length of 0.9 m. The Snorkel covered 0,5 m of the intake screen, of which 0,25 m was acceleration zone without spaces and 0,25 m was the bar section. To achieve the necessary difference in pressure, a 100 mm high wooden stop log raised the level that would allow water to flow through the snorkel over the weir. This was done along the entire weir, except for the part were the Snorkel is located, Sæten (2016). The Snorkel is shown in Figure 12 and Figure 13.

Figure 12 The Snorkel from the upstream side, reservoir drowned down, from Sæten (2016).

Figure 13 The Snorkel in operation at Dyrkorn intake, Norway, from Sæten (2016).

It was demonstrated in Opaker (2012) that the intake screen made in stainless steel could become supercooled itself. Adequate insulating properties are therefore a necessary requirement for the material used in the Snorkel.

Previously conducted laboratory tests showed that the Snorkel partly functioned as a siphon. The capacity could increase, and in some cases discharge more water than desirable. Later studies in both model and prototype scales, have shown that the Snorkel does not function as a siphon, but it is important to construct solutions that does provide this feature, Sæten (2016).

Measurements from November 2018 to May 2019 showed that the difference in temperature in the water column were minimal in a shallow intake basin, like the one at the Dyrkorn SHP. It is therefore possible to assume that the flow of water through the Snorkel would contain supercooled water. This could indicate that the Snorkel, as it functions and is constructed today would require certain size compared to the 100 mm opening in the prototype version, Sæle (2019). The measurements done by the SWIPS showed that there were frazil ice particles in the entire water column; however, it is not possible to determine if these particles were able to enter the Snorkel, Sæle (2019). Nevertheless, both this study and the work presented in Aal (2017) concludes that the Snorkel does not fully prevent the power plant stops in periods during the winter, were the discharge should indicate electricity production. Deformation of the prototype forced by the under-pressure in the siphoning part may also have reduced the discharge capacity significantly. Optimized design for the Snorkel will may improve the performance.

Release of environmental flow from Coanda screen intakes may impose various challenges. Most of the intakes in Norway are remotely located and advanced regulation or labor-intensive systems are not preferable due to costs and winter condition operational issues. Environmental flow must be documented for legal reasons, this is normally done by V-notches and pressure cells, causing even more challenges during wintertime. In many Coanda screen intakes, the environmental flow is released from the intake by a level-controlled pump from the lower intake chamber. The upstream intake pool is in a Coanda screen intake always full and the special **PK-Slipp** devise solves this by a rectangular tube section, which diverts exactly the specific discharge above the Coanda intake crest. The devise is shown in Figure 14 and Figure 15.

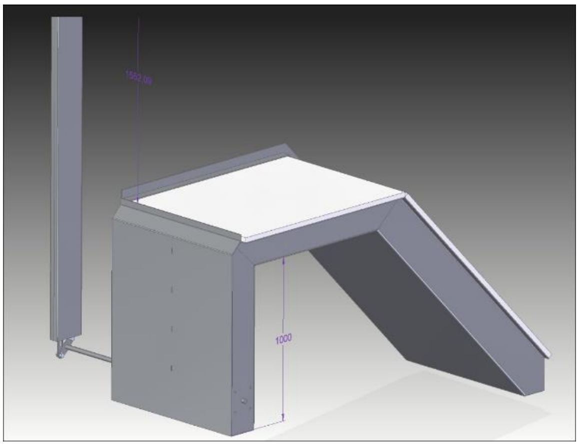

Figure 14 *A 3D illustration of the rectangular tube, from Lia et.al (2019)*

Figure 15 *The PK-Slipp installed at Dyrkorn SHP intake, photo: Tafjord kraftproduksjon*

The device appears similar to a siphon but behave as a regular pipe. If the device is placed at the same level as the screen, no build-up of under-pressure will be encountered. The device can be closed in periods during wintertime to ensure that all available discharge is diverted through the intake chamber before release in the river, to avoid freezing in the chamber. The device can be constructed employing different material. However, PE (polyethylene) is generally preferred due to production cost, heat exchange properties, reliability and abrasive strength.

8. Conclusions

Winter operation of Coanda screen intakes introduces two main challenges

- Frazil ice accumulation and temporary loss of water
- Development of long-term solid ice cover and loss of intake capacity.

The Coanda screen intakes has proven an impressive performance with reopening of the intake beneath the accumulated frazil/anchor ice. For removal of solid ice covering the intake screen no natural processes are observed.

Further research will be done in this project

- Modifications and improvements of the innovations presented in this paper
- Post-processing and development of SWIPS-data as a comparison with ice accumulation

Acknowledgments
The Authors like to thank Hallbjørn Brekke and Per-Kåre Skudal in Tafjord kraftproduksjon AS (power company) for their encouragement and innovative contribution to this research field. We also like to thank others in Tafjord kraftproduksjon AS for their willingness and support under our field studies. Funding from Energi Norge and NVE has made this research possible.

References

Ashton, G. (1986), "River and Lake Ice Engineering", Water Resources Publications, Colorado, USA

Lia, L., Sæle S.D., Skår, B., Skudal, P.K., Brekke, H. and Jensen, T. (2019), "Improvements on Coanda screen intakes for small hydro", Hydro2019, Porto, Portugal

NVE (2020), "Status of Coanda screen intakes", NVE-report 10/2020, Norwegian Directorate of Water Resources and Energy, Oslo, Norway

Nøvik, H., Opaker, H. and Lia, L. (2014), "Performance of a Coanda-Effect Intake Screen in a Cold Climate", Journal of Cold Regions Engineering, ASCE, https://doi.org/10.1061/(ASCE)CR.1943-5495.0000073

Marko, J.R, Fissel, D.B. and Jasek, M. (2006), "Recent developments in ice and water column profiling technology, IAHR 18th Ice Symposium, Sapporo, Japan

Opaker, H. (2012), "Performance of Coanda intake screen – Experiences from Dyrkorn Hydropower plant", Master thesis at NTNU, Department of hydraulic and environmental engineering, Trondheim, Norway

Sæle, S.D. (2019), "Development of snorkel device for reduction of winter problems at Coanda screen intakes", Master thesis NTNU, Trondheim, Norway

Sæten, N.K. (2016), "Testing of the Snorkel device for Coanda screen intakes", Master thesis at NTNU, Department of hydraulic and environmental engineering, Trondheim, Norway

Wahl, T.L. (2001), "Hydraulic performance of Coanda-effect screens", Journal of Hydraulic Engineering, ASCE, https://doi.org/10.1061/(ASCE)0733-9429(2001)127:6(480)

Aal, E. (2017), "Testing of winter conditions for modifies Coanda screen intakes", Master thesis at NTNU, Department of hydraulic and environmental engineering, Trondheim, Norway

16
Ice actions on river and lake morphology

25th IAHR International Symposium on Ice
Trondheim, 23 - 25 November 2020

Ice gouging conditions of the Northern Caspian depending on the severity of winters

Stepan Maznev
Lomonosov Moscow State University
119991, Leninskie Gory, 1, Moscow, Russia
maznev@geogr.msu.ru
Anastasiia Magaeva
Southern Scientific Centre of Russian Academy of Sciences
344006, Chehova, 41, Rostov-on-Don, Russia
a.magaeva@mail.ru
Stanislav Ogorodov
Lomonosov Moscow State University
119991, Leninskie Gory, 1, Moscow, Russia
ogorodov@aha.ru
Natalia Yaitskaya
Southern Scientific Centre of Russian Academy of Sciences
344006, Chehova, 41, Rostov-on-Don, Russia
yaitskayan@gmail.com

Ice gouging is mechanical plowing of bottom ground by ice features. Hydrometeorological conditions, changing from year to year, determine the intensity of ice features (ice hummocks, ice ridges and stamukhi) formation. In this paper, we consider the conditions of the ice gouging of the Northern Caspian seabed by ice features in winters of various severity. We used the cumulative freezing-degree days (CFDD) over a winter period as a criterion for dividing winters by severity. We used data from several nearshore meteorological stations to divide them into mild, moderate and severe. The analysis, based on aerial reconnaissance and modern satellite data, showed the variability of the number of stamukhi, their distribution and depths of grounding over recent years. We created charts of different ice gouging intensities for the different types of winters. The charts are consider not only analysis of stamukhi distribution, but also ice cover dynamics, typical position of fast ice rim and features of the bottom topography. The charts showed changes in the conditions of ice gouging at the Northern Caspian from year to year. The results allowed estimating the influence of the winters severity on the intensity of the ice features formation and ice gouging in different years. The results of this study must be considered when conducting economic activities in the Northern Caspian.

1. Introduction

The Caspian Sea is partially freezing every year. The ice conditions of the Caspian Sea are complex and variable. They vary from year to year depending on hydrometeorological conditions. The ice conditions determine the number and spatial distribution of ice features (ice ridges, hummocks, etc.). Ice features are a factor of the bottom microtopography dynamics. Grounded hummocks, named stamukhi, can move and plow the bottom. Ice gouging (ice scouring) is the process of mechanical plowing of the bottom ground by ice, associated with the ice cover dynamics, acting under the influence of hydrometeorological factors and the topography of the coastal zone (Ogorodov, 2011). Information on the stamukhi distribution and ice gouging processes is most important for pipeline design from offshore structures to shore, marine operations, including tracing and navigation of ships and air-cushion vehicles during the period of ice formation and melting. Along with changes in ice conditions in the Northern Caspian, the conditions for the ice gouging of the bottom by ice features change from year by year.

Earlier P.I. Bukharitsin (1984) suggested that the largest number of ice features form in moderate (normal) winters. The first chart of intensity of ice gouging by ice features in the Northern Caspian was created by Ogorodov (2017). Climate change should be considered when studying the conditions of bottom gouging by ice features. Under the conditions of climate warming, the character and intensity of ice impact on the coasts and seabed change significantly (Ogorodov et al., 2018). Due to the decrease of the ice thickness, ice ridging increases. The width and stability of fast ice also become lower. We analyzed the hydrometeorological conditions in the Northern Caspian and created charts showing how the ice gouging conditions vary depending on the severity of winters.

2. Materials and methods

Ice scours at the Northern Caspian were first discovered by B.I. Koshechkin (1958). The scientific research of the ice scours and gouging started along with exploration of oil deposits on the shelf (Ogorodov, Arkhipov, 2010). Now many researchers, prospectors and stakeholders pay attention to ice gouging processes (Ogorodov et al., 2019; Sigitov et al., 2019).

Ice conditions in the Northern Caspian strongly depend on the thermal type of winter (Kouraev et al., 2004). We classified winter seasons of the Northern Caspian by their severity to show, how ice-gouging conditions change depending on meteorological conditions. This classification reflects the interannual dynamics of winter temperatures, which define the formation of ice in the water area. Determining the types of winter seasons is a key parameter, both when analyzing the ice regime of the seas and assessing climate change.

The most common method of classification of winters by severity is calculating the cumulative freezing-degree days (CFDD). A similar approach for winters typing in the Northern Caspian was used by Tamura-Wicks et al. (2015). CFDD is usually calculated as a sum of average daily degrees below freezing for a winter season. Then we determine the type of winter season according to the preferred gradations. Dumanskaya (2013) classify moderate (normal) winters as winters with CFDD corresponding to the interval from “average minus 20% amplitude” to “average plus 20% amplitude”. Winters with CFDD in the interval above are classified as mild and in the interval below are indicated as severe. Moreover, two extreme abnormal winters (the coldest and the warmest) are excluded from statistics.

P.I. Bukharitsin (2008) and A.V. Fedorenko (2011) perform similar technique for winters typing of the Caspian Sea.

In this research, we summarized negative air temperatures of winter seasons (from December till March) from four hydrometeorological stations of the Northern Caspian – Astrakhan, Atyrau, Makhachkala and Fort-Shevchenko. The annual sums were used to classify 1950-2019 winter seasons according to their severity.

Two main sources were used to identify stamukhi distribution in years with different severity of winters:
1) aerial reconnaissance data from 1959 to 1974 (Bukharitsin, 1984);
2) stamukhi observation data from satellite imagery deciphering (mainly Sentinel-1, usable Sentinel-2 and Landsat) from 2014 to 2019 acquired by LLP ICEMAN.KZ (Sigitov et al., 2019).

The distribution of stamukhi and ridging zones are largely dependent on the bottom topography. Therefore, a high-resolution digital elevation model (DEM) of the bottom of the Northern Caspian is required. The DEM, developed in the laboratory of geoecology of the North, Faculty of Geography, MSU, is based on the bathymetric navigation map of 1998, reduced to an average level of the Caspian Sea minus 28 m below sea level. In 2017, Ogorodov was the first to publish a chart of the intensity of ice gouging in the Northern Caspian, based on this DEM. This chart considered only aerial reconnaissance data from 1959 to 1974 for moderate (normal) winters.

Using the analysis of ice ridges and stamukhi locations, the distribution of various types of ice conditions for different types of winters (Terziev et al., 1992) and the bottom topography (DEM), we created charts of the ice gouging intensity distribution for mild, moderate and severe winters.

3. Results

The winters of the Northern Caspian were divided into three categories according to their severity: mild, moderate and severe (Table 1). For the period from 1950 to 2019, moderate types of winters prevail with 59.4%. The number of severe and mild winters is the same and amounts to 14 of each type (20.3%). Fig. 1 shows their temporal pattern. From 1950 to 1985 severe winters in the Northern Caspian occurred every 2-5 years, but from 1985 to 2019 only 3 severe winters took place (2002/03, 2007/08, 2011/12).

Considering the aerial reconnaissance (Bukharitsin, 1984) and satellite data (Sigitov, 2019), we created charts of different ice gouging intensities for the different types of winters (Fig. 2). The charts are consider not only analysis of stamukhi distribution, but also ice cover dynamics, typical position of fast ice rim and features of the bottom topography.

According to Ogorodov, 2011 we divide all the ice gouging area of the Northern Caspian into four zones: 1) fast ice zone; 2) zone of fast and drifting ice interaction; 3) drifting ice zone within deep areas; 4) drifting ice area within banks and shoals.

Table 1. The Northern Caspian winter seasons classification

Winter type	Number	%	CFDD, °C	Seasons
Severe	14	20,3	≤ 1862,05	1950/51, 1953/54,1955/56, 1959/60, 1963/64, 1966/67, 1968/69, 1971/72, 1976/77, 1979/80, 1984/85, 2002/03, 2007/08, 2011/12
Moderate	41	59,4	from -1862,05 to -858,25	1951/52, 1952/53, 1954/55, 1956/57, 1958/59, 1960/61, 1962/63, 1964/65, 1967/68, 1969/70, 1970/71, 1972/73, 1973/74, 1974/75, 1975/76, 1977/78, 1978/79, 1981/82, 1983/84, 1985/86, 1986/87, 1987/88, 1989/90,1990/91, 1991/92, 1992/93, 1993/94, 1994/95, 1995/96, 1996/97, 1997/98, 2004/05, 2005/06, 2008/09, 2009/10, 2010/11, 2012/13, 2013/14, 2014/15, 2016/17, 2017/18
Mild	14	20,3	≥ 858,25	1957/58, 1961/62, 1965/66, 1980/81, 1982/83, 1988/89, 1998/99, 1999/00, 2000/01, 2001/02, 2003/04, 2006/07, 2015/16, 2018/19

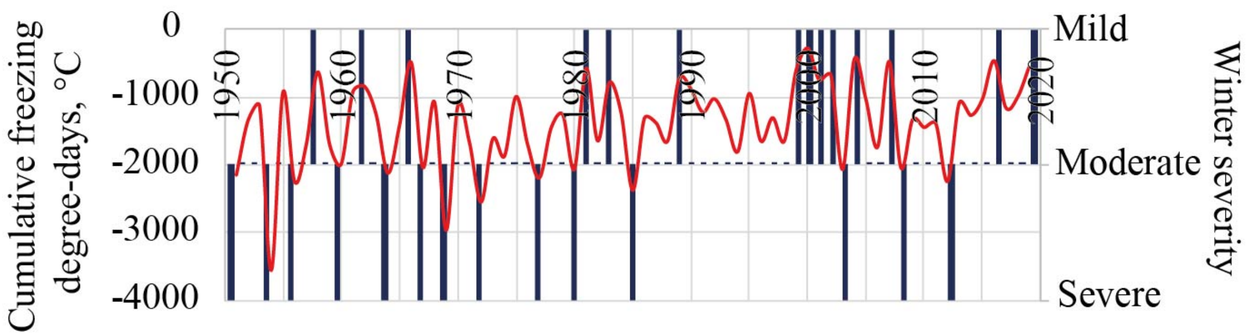

Figure 1. Winter severity timeline of the Northern Caspian

Fast ice zone is characterized by limited scour impact of ice features, mainly ice ridges and grounded hummocks. The intensity of ice gouging is determined by immobility of fast ice. Bottom scouring by ice floes with frozen ice ridges occurs only during the fast ice breack-up. The zone of fast and drifting ice interaction is characterized by intensive scour impact on seabed by keels of ice ridges on fast ice rim and ice hummocks frozen into drifting ice floes, rarely by stamukhi. Drifting ice zone within deep areas is characterized by intensive scour impact on seabed by keels of ice ridges frozen into drifting ice floes. Drifting ice zone within banks and shoals is characterized by the most intense scour impact on seabed by keels of ice ridges frozen into drifting ice floes and large stamukhi.

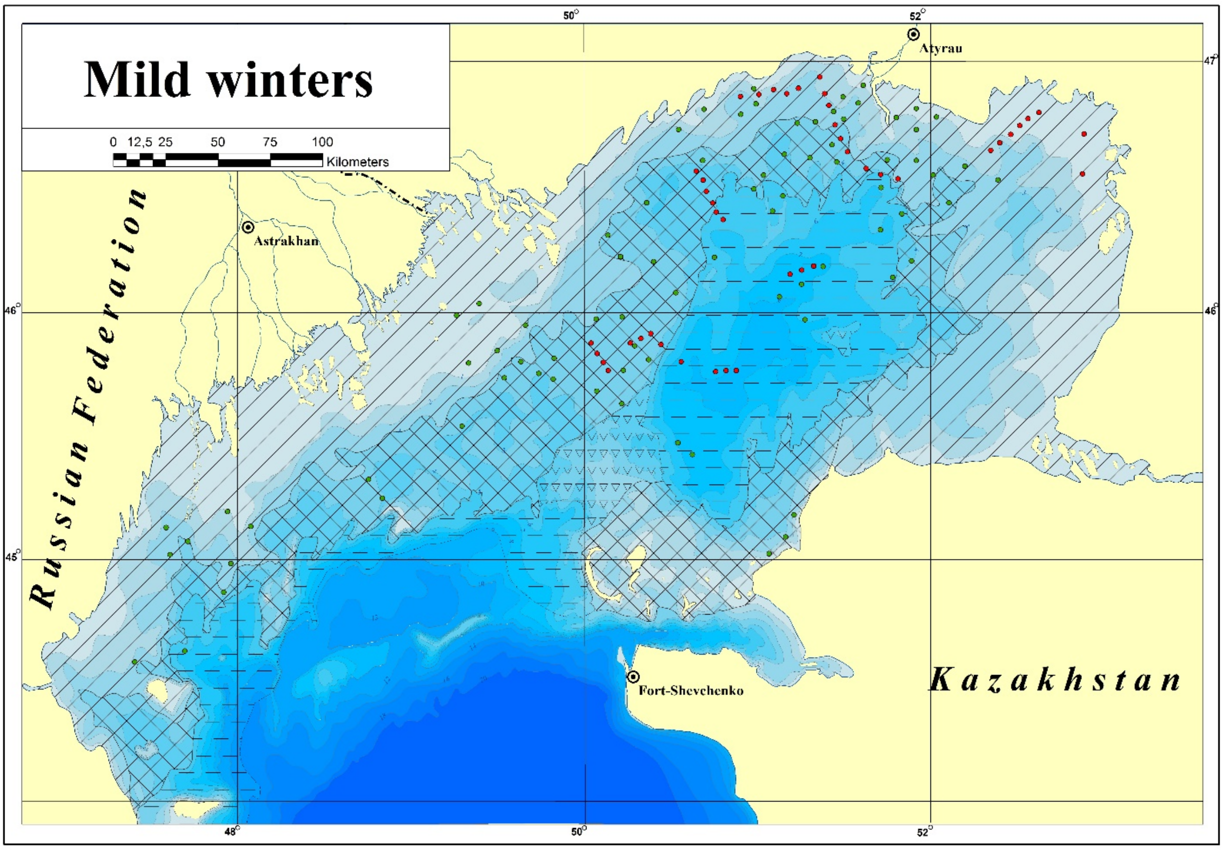

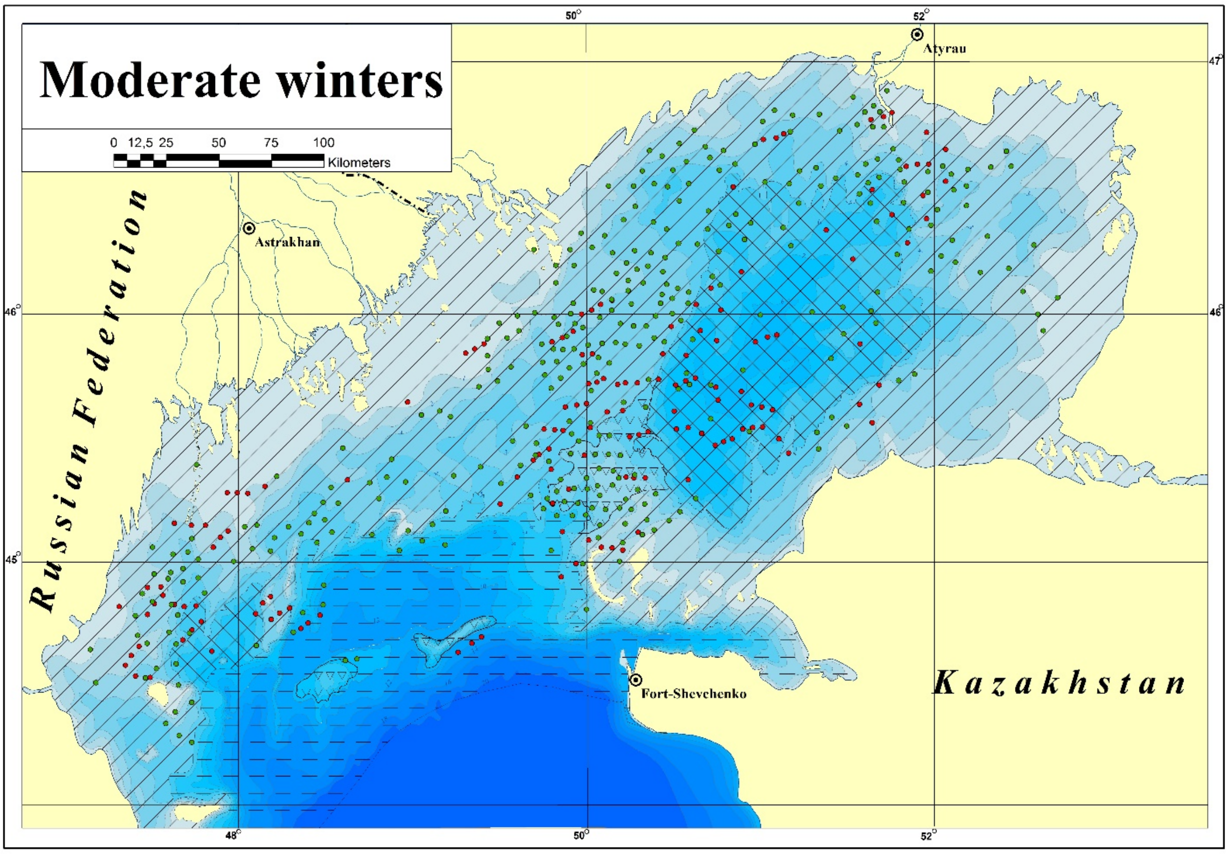

Figure 2. (Continued below)

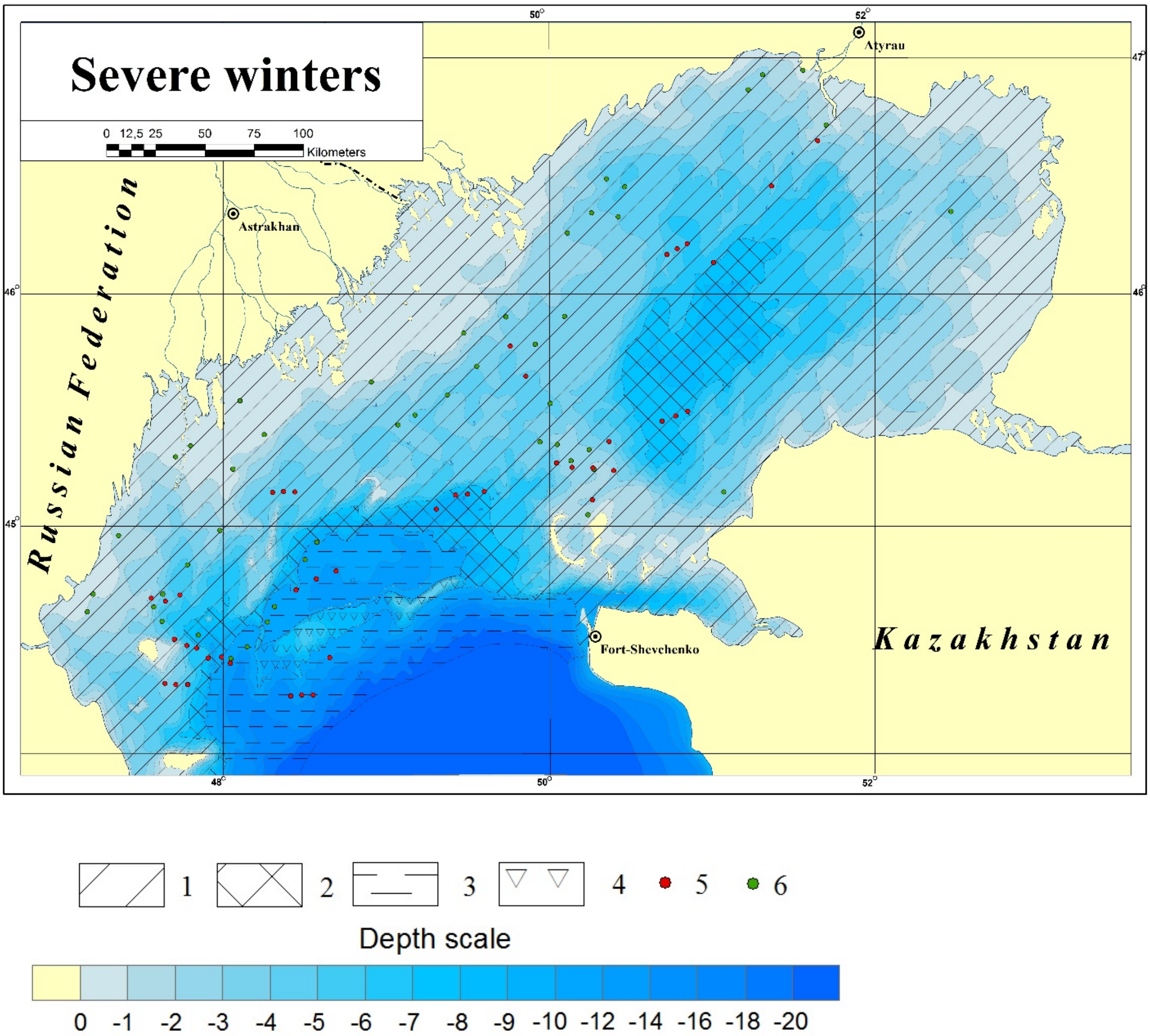

Figure 2. Charts of ice gouging intensity of the Northern Caspian: 1) fast ice zone; 2) zone of fast and drifting ice interaction; 3) drifting ice zone within deep areas; 4) drifting ice area within banks and shoals; 5) ice hummocks and ice ridges; 6) stamukhi.

4. Discussion

Severe winters in this region are caused by meridional activity, bringing cold air from the Arctic often. Surge of air far to the south leads to a cold snap and prolonged cooling. Mild winters occur when latitudinal activity takes place in Europe, the East European Plain, the Caucasus and the Caspian Sea (Solovjev, 1973). The winter season of 1953/54 was the most severe in the North Caspian region, the CFDD for Astrakhan station amounted -1166.5 °C. The mildest was the winter of 1999/00, the CFDD for Astrakhan station amounted minus 78.7 °C.

Depending on the temperatures, the beginning and the end of freeze-up can be shifted earlier or later. The ice coverage of the Caspian Sea also vary significantly - from 30% to 85% of the area of the Northern Caspian (winters 1999/2000 and 1953/1954, respectively) (Magaeva, 2017).

The classification of winter severity shows that in recent years (after 1985) severe winters occur less frequently, while moderate winters predominate. Earlier Bukharitsin (1984) supposed the largest number of ice features is formed in moderate (average in ice coverage) winters. In severe winters, landfast ice is more stable, and the width of the ridging zone is less. Ogorodov (2011) suggested that in mild winters, ridging is also low due to the limited fast ice extension.

The intensity of ice gouging depends primarily on the number of ice features scouring the seabed and the general ice coverage. Previously, the conditions of bottom scouring were considered depending on level fluctuations and ice coverage (Bukharitsin et al., 2015). The charts (Fig. 2) show that, the ice-gouging areas of various intensity change along with the number of ice features. The comparison of the ice-gouging intensity patterns showed the difference of them from year to year. The area of low intensity of ice-gouging (1) related to the extension of fast ice is reduced in mild winters both absolutely and relatively. We suppose that, during mild winters, fast ice is thinner and brasher, which favor to more active ridging in this zone. This fact is confirmed by modern data from 2014-2019, showing many ice features in fast ice. According to Sigitov (2019), the majority of stamukhi in mild years is formed in proximity to the coastline, and the most intense ridging and stamukhi formation is observed in the zone of fast ice. This provides a greater intensity of bottom scouring in this zone compared to moderate and severe winters.

At the same time, in mild winters, the area of the intensive ice-gouging (2) expands either relatively or absolutely. However, in mild winters, the intensity in this zone decreases significantly compared to the same zone for moderate or severe winters. Ice features in mild winters consist of weak ice, which reduces ice impact.

Moreover, the area of drifting ice in mild, moderate and severe winters remains almost unchanged both in relatively deep waters (3), and in banks and shoals (4). In severe winters, the fast ice area is maximum; it occupies about 75% of the Northern Caspian. Fast ice in severe winters is extremely strong, which prevents active ridging. The example cases show that, depending on the severity of winters, the ice-gouging conditions change. From year to year the ice-gouging intensity patterns vary significantly, but also the degree of intensity in different zones are diverse.

5. Conclusion

The study shows that in recent years the number of severe winters in the Northern Caspian decreased significantly, moderate winters predominate. The created charts of the ice-gouging intensity revealed changes in the conditions of bottom scouring depending on types of winters. Despite the climate warming, the intensity of bottom scouring in the Northern Caspian does not decrease. In moderate winters, the intensity of ice-gouging processes is highest, but in mild winters the intensity is also high. Studying the changes in ice-gouging intensity depending on the severity of winters allow us to predict the formation of ice scours in certain zones during ongoing climate changes. The results of this study must be considered when conducting economic activities in the Northern Caspian.

Acknowledgments

We are very grateful to Sergey Vernyayev, Anton Sigitov and Yevgeniy Kadranov (LLP ICEMAN.KZ) for the stamukhi observation data and brilliant ice consulting. We are also grateful to Peter Bukharitsin (Astrakhan State Technical University) for the aerial reconnaissance data. The reported study was funded by the RFBR, projects number 19-35-90100 and 19-35-50086.

References

Bukharitsin, P.I., 1984. Ice ridging characteristics in the northern part of the Caspian Sea. Water resources, 6, 115-123. (In Russian)

Bukharitsin, P.I., 2008 Comparative characteristics of the long-term ice cover variability the northern part of the Caspian and Azov Seas. Bulletin of Astrakhan state technical university, 3, 207-213 (In Russian).

Bukharitsin, P.I., Ogorodov, S.A. and Arkhipov, V.V., 2015. The impact of floes on the seabed of the northern Caspian under the conditions of sea level and ice cover changes. Bulletin of the Moscow State University, Series 5, Geography, 2, 101-108.

Dumanskaya, I.O. 2013. Typical conditions on the main shipping lanes of the seas of the European part of Russia for winters of varying severity // Transactions of the Hydrometeorological Research Center of the Russian Federation, 350, S.142-166. (In Russian)

Fedorenko, A.V., 2011. The study of seasonal and intra-annual variations of the main ice parameters on the southern seas (the Sea of Azov and the Caspian Sea). Proceedings of the SOI, 215, 15-25. (In Russian)

Koshechkin, B.I., 1958. Traces of the moving ice on the bottom of shallow water areas of the Northern Caspian. Proceedings of Airborne methods laboratory of AS USSR, 6, 227–234. (In Russian)

Kouraev, A.V., Papa, F., Mognard, N.M., Buharizin, P.I, Cazenave, A., Cretaux, J.-F., Dozortseva, J., Remy, F., 2004. Sea ice cover in the Caspian and Aral Seas from historical and satellite data. J. Mar. Syst., 47, 89– 100.

Magaeva, A.A., 2017. Preliminary analysis of the parameters of the ice regime of the Caspian Sea // XIII The annual youth scientific conference of students, PhD students and young scientists "Research and development of advanced scientific areas": abstracts, Rostov-on-Don, Publishing House of the SSC RAS, 46-47. (In Russian)

Ogorodov, S.A. and Arkhipov, V.V., 2010. Caspian Sea Bottom Scouring by Hummocky Ice Floes, Doklady Earth Sciences. 432 (1), 703-707.

Ogorodov, S.A., 2017. Ice gouging topography at the bottom of Caspian and Aral Seas. Proceedings of the Thirteenth International MEDCOAST Congress on Coastal and Marine Sciences, Engineering, Management and Conservation, MEDCOAST 17, Mellieha, Malta, 2, 711–721.

Ogorodov, S.A., 2011. The Role of Sea Ice in Coastal Dynamics. Moscow University Press, 173. (In Russian)

Ogorodov, S.A., Arkhipov, V.V., Baranskaya, A.V., Kokin, O.V, Romanov, A.O., 2018. The Influence of Climate Change on the Intensity of Ice Gouging of the Bottom by Hummocky Formations. Doklady Earth Sciences, 478, 2, 228–231.

Ogorodov, S.A., Maznev, S.V., Bukharitsin, P.I., 2019. Ice gouging topography on the Caspian and Aral Seas bottom. Proceedings of the Russian Geographical Society, 151, 2, 35-50.

Sigitov, A., Kadranov, Y., Vernyayev, S., 2019. Analysis of Stamukhi Distribution in the Caspian Sea. Proceedings of the International Conference on Port and Ocean Engineering under Arctic Conditions, POAC, 1-14.

Solovjev, D.V., 1973. Some features of ice formation in the Caspian Sea and synoptic processes causing them. The study of ice of USSR southern seas, Moscow, Nauka. 52-56. (In Russian)

Tamura-Wicks, H., Toumi, R., Budgell, W.P, 2015. Sensitivity of Caspian sea-ice to air temperature. Q. J. R. Meteorol. Soc. 141, 3088–3096.

Terziev, F. S., Kosarev, A.N., Kerimov, A.A., 1992. Hydrometeorology and Hydrochemistry of Seas, Vol. 4: Caspian Sea, No. 1, Saint Petersburg, Hydrometizdat, 280. (In Russian)